ELUCIDATING MICROBIAL PROCESSES IN SOILS AND SEDIMENTS: MICROSCALE MEASUREMENTS AND MODELING,
2nd Edition

EDITED BY: Philippe C. Baveye, Wilfred Otten and Alexandra Kravchenko

frontiers Research Topics

About Frontiers

Frontiers is more than just an open-access publisher of scholarly articles: it is a pioneering approach to the world of academia, radically improving the way scholarly research is managed. The grand vision of Frontiers is a world where all people have an equal opportunity to seek, share and generate knowledge. Frontiers provides immediate and permanent online open access to all its publications, but this alone is not enough to realize our grand goals.

Frontiers Journal Series

The Frontiers Journal Series is a multi-tier and interdisciplinary set of open-access, online journals, promising a paradigm shift from the current review, selection and dissemination processes in academic publishing. All Frontiers journals are driven by researchers for researchers; therefore, they constitute a service to the scholarly community. At the same time, the Frontiers Journal Series operates on a revolutionary invention, the tiered publishing system, initially addressing specific communities of scholars, and gradually climbing up to broader public understanding, thus serving the interests of the lay society, too.

Dedication to Quality

Each Frontiers article is a landmark of the highest quality, thanks to genuinely collaborative interactions between authors and review editors, who include some of the world's best academicians. Research must be certified by peers before entering a stream of knowledge that may eventually reach the public - and shape society; therefore, Frontiers only applies the most rigorous and unbiased reviews.
Frontiers revolutionizes research publishing by freely delivering the most outstanding research, evaluated with no bias from both the academic and social point of view. By applying the most advanced information technologies, Frontiers is catapulting scholarly publishing into a new generation.

What are Frontiers Research Topics?

Frontiers Research Topics are very popular trademarks of the Frontiers Journals Series: they are collections of at least ten articles, all centered on a particular subject. With their unique mix of varied contributions from Original Research to Review Articles, Frontiers Research Topics unify the most influential researchers, the latest key findings and historical advances in a hot research area! Find out more on how to host your own Frontiers Research Topic or contribute to one as an author by contacting the Frontiers Editorial Office: researchtopics@frontiersin.org

ELUCIDATING MICROBIAL PROCESSES IN SOILS AND SEDIMENTS: MICROSCALE MEASUREMENTS AND MODELING,
2nd Edition

Topic Editors:
Philippe C. Baveye, Université Paris-Saclay, France
Wilfred Otten, Cranfield University, United Kingdom
Alexandra Kravchenko, Michigan State University, United States

Table of Contents

Editorial: Elucidating Microbial Processes in Soils and Sediments: Microscale Measurements and Modeling

Philippe C. Baveye[1]*, Wilfred Otten[2] and Alexandra Kravchenko[3]

[1] UMR ECOSYS, AgroParisTech, Université Paris-Saclay, Paris, France, [2] School of Water, Energy and Environment, Cranfield University, Cranfield, United Kingdom, [3] Department of Plant, Soil and Microbial Science, Michigan State University, East Lansing, MI, United States

Editorial on the Research Topic

Elucidating Microbial Processes in Soils and Sediments: Microscale Measurements and Modeling

Over the last decade, soils have become increasingly central to a number of crucial debates on issues of great societal concern, related to climate change, environmental pollution, or feeding the estimated 10 billion people who will live on earth by 2050, a mere 30 years from now (Baveye, 2015). In order to successfully meet the extremely daunting challenges that confront us in these different contexts, we need to understand what controls the growth and activity of the soil microorganisms that mediate many if not most of the underlying processes. However, the information we have in this respect is still woefully inadequate, arguably at least in part because of a lack of appropriate technology.

Half a century ago, soil microbiologists reached the conclusion that a full understanding of the growth and activity of microorganisms in soils and sediments would require quantitative observations at spatial scales as near as possible to the size of the organisms themselves (Alexander, 1964). Back then, this type of observation was not feasible at all, unfortunately. The development of electron microscopes in the 60s and 70s provided qualitative insight into microscopic parameters that controlled the activity of bacteria, archaea, and fungi in pore spaces (Foster, 1988), but produced no quantitative information. It is only with the technological advances in X-ray computed micro-tomography (μCT), first at synchrotron facilities in the 90s, then with commercial table-top scanners in the early 2000s, that quantitative, micrometric data on the geometry of the pore space has finally become available. In the last decade, different methods have also been developed to measure the spatial distribution of microorganisms at fine resolution in thin sections (e.g., Nunan et al., 2001), as well as to map the composition of organic soil constituents (e.g., Solomon et al., 2005) or the nature of nitrogenous compounds at micrometric or even nanometric scales (e.g., Mueller et al., 2012, 2017).

After these novel techniques became available, an initial stage in the research has consisted of identifying and resolving the problems associated with their use to elucidate microbial processes in heterogeneous soils and sediments. Significant progress has been achieved in this respect, for example in the development of objective (operator-independent), local segmentation techniques

adapted for X-ray μCT images [e.g., (Schlüter et al., 2010; Hapca et al., 2013; Houston et al., 2013a,b)], in terms of improvements of hybridization (FISH) technologies to locate bacterial and archaeal cells in soil thin sections (Eickhorst and Tippkötter, 2008; Schmidt et al., 2012), or in the in elaboration of statistical tools to interpolate 2-D measurements to produce 3-D data (Hapca et al., 2011, 2015).

Shortly before the Research Topic on "Elucidating microbial processes in soils and sediments" was launched in August 2017, we felt that the time had come to switch to a higher gear, more focused on interdisciplinarity, in the research in this area, and we were convinced that encouraging our colleagues to submit jointly a number of manuscripts describing their work on this topic was the best approach to pave the way for this switch to occur. As part of the Research Topic, it was decided that a comprehensive review article would be put together, covering as much as possible of the relevant literature, and trying to identify major axes, or "paths," in it. In the resulting article (Baveye et al.), we identify three major disciplinary paths along which research efforts have taken place in the last 15 years, and which, when they will eventually converge in full interdisciplinary mode, should provide a far better grasp than what is currently available of what controls the activity of microorganisms in soils. The key take-home message of Baveye et al.'s review, visualized in **Figure 1**, is that significant progress has been achieved on a number of fronts, but that progress unfortunately is very uneven. At the extremes of the spectrum are the research on the physical characteristics of soils at the microscale and the (arguably more complicated) experimental observation of microbial processes. While the former has moved full speed ahead, the latter has been lagging far behind, casting doubt on the soundness of some of the modeling that has been carried out in this field, and hindering the needed integration of physical, (bio)chemical, and microbiological perspectives. Clearly, the picture that emerges from the extensive literature covered in Baveye et al.'s review suggests that, as of 2018, there was still a long way to go before reaching the Holy Grail, with many daunting challenges on the different paths leading to it.

In more ways than one, the various articles published as part of our Research Topic have managed, if not to reach the Holy Grail (that may have been a bit much to hope for), at least to address some of the challenges head on, and to make significant progress concerning quite a few of them.

A first group of articles focuses on the characterization of the geometry of the pore space, in which all the (bio)chemical and microbial processes take place in soils, and deepens our understanding of how this geometry as well as the architecture of the solid phase influence, or are symptomatic of, soil behavior. San José Martinez et al. explore the ability of Minkowski functionals of the connected soil pore space to discriminate between the pore geometries exhibited by soils with different managements and depths, and that are therefore expected a priori to be dissimilar. The crucial question of how well microscale measurements carried out via X-ray microtomography can help us unravel the relationship between microscopic soil architecture and macroscopic soil properties is addressed by Smet et al. These
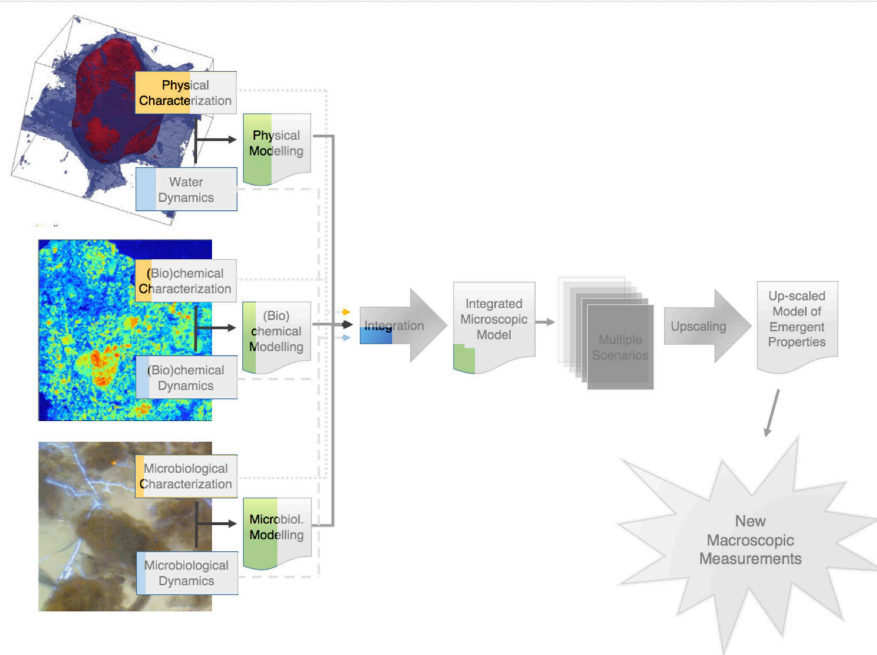
FIGURE 1 | Visual assessment of the level of progress along various paths in the research on the emergent properties of microbial activity in heterogeneous soil microenvironments. The colored parts correspond to Baveye et al.'s estimate of the progress achieved to date along each path. The shaded portions of the diagram still largely remain to be tackled.

authors deal in particular with practical questions associated with the implementation of X-ray computed microtomography, including how well the samples represent the uniqueness of the pore network or architecture, and the systemic compromise between sample size and resolution.

A second group of four articles deals with the "hot" topic of the distribution and fate of soil organic matter (SOM). Maenhout et al. are interested in the impact of soil structure on N availability to microbes, and thus on heterotrophic microbial activity and community structure. Their results with artificially reconstructed miniature soil cores with contrasting soil structures, viz. high or low degree of contact between soil particles ascertained via X-ray μCT, suggest that soil structure controls carbon mineralization through mediation of N diffusion and in turn N availability. Working with aggregates from a California forest and a Nevada shrubland soil subjected to different soil moisture and "heating" regimes, Jian et al. show that low-severity fires can accelerate the decomposition of soil organic carbon (SOC) protected in soil aggregates. Quigley et al. try to characterize the spatial heterogeneity of the soil matrix in macroaggregates obtained from soils associated with three contrasting long-term managements (conventionally-managed and biologically-based row-crop agricultural systems, along with a primary successional unmanaged system), and they explore the usefulness of grayscale gradients as proxies to determine the microscale spatial distribution of soil organic matter (SOM). Finally, Quigley et al. use the natural difference between carbon isotopes of C3 and C4 plants to determine how the presence of pores of different sizes affects spatial distribution patterns of newly added carbon immediately after plant termination and then after 1-month incubation. The results indicate that, in the studied soil, pores of 40–90 μm size range are associated with the fast influx of new C followed by its quick decomposition, whereas pores <40 μm tend to be associated with C protection.

The next group of articles deal with microscale aspects of soils related to the presence of plant roots. van Veelen et al. use correlative X-ray CT (resolution ∼20 μm) in combination with Magnetic Resonance Imaging (MRI, resolution ∼120 μm) to set up groundwork to enable *in situ* visualization of root-produced mucilage in soil. Benard et al. also focus their attention on this mucilage. They use a percolation approach to predict the flow behavior in the rhizosphere near the critical mucilage content. At that particular stage, a sufficient fraction of pores is blocked and the rhizosphere turns water repellent. Two other articles deal with the influence that plant roots, by themselves or through chemicals they exude, can have on microorganisms in their vicinity. Rodeghiero et al. combine planar optodes and spatial analysis to assess how tomato roots influence the metabolic activity and growth patterns of the fungus *Fusarium oxysporum f. sp. lycopersici* (Fol), one of the most destructive soil-borne diseases of tomatoes. Using fluorescence microscopy combined with automated image analysis and spatial statistics, Schmidt et al. carry out a gnotobiotic experiment using a potential nitrogen-fixing bacterial strain in combination with roots of wetland rice to explore the distribution of bacterial colonization patterns on rhizoplanes of the rice roots.

Another group of articles in this Research Topic deals with observations of the distribution and dynamics of microorganisms in soils. Chamizo et al. inoculated two cyanobacterial species, *Phormidium ambiguum* (non N-fixing) and *Scytonema javanicum* (N-fixing) on different textured soils (from silt loam to sandy), and used scanning electron microscopy to analyze the development of cyanobacteria biocrust and the evolution of selected physicochemical properties of the soils for 3 months under laboratory conditions. Couradeau et al. also worked on biocrusts. They developed methodologies to visualize and quantify the water dynamics within an undisturbed biocrust undergoing desiccation. In particular, using synchrotron-based X-ray microtomography, they were able to resolve the distribution of air, liquid water, mineral particles and cyanobacterial bundles at the microscale. Vermeire et al. assess the reciprocal interactions between soil minerals, SOM, and the broad composition of microbial populations in a 530-year chronosequence of podzolic soils. Choi et al. use a metagenomic sequencing method to assess the distribution of genes encoding for key cellulose-degrading enzymes among aggregate fractions in a fertilized prairie soil. Watteau and Villemin illustrate with studies involving a variety of soils in different contexts (i.e., five cropped soils, one forest soil, and one Technosol) that Transmission Electron Microscopy (TEM) can be used advantageously to localize microorganisms and deduce their influence within soil structures. In particular, organic matter turnover can be assessed within microhabitats through a combination of TEM, Electron Energy Loss Spectroscopy (EELS) or NanoSIMS. Finally, Juyal et al. address the extent to which it is possible to control the pore geometry at microscopic scales in microcosms made of repacked aggregates, through manipulation of common variables such as density and aggregate size. In addition, they analyze in these microcosms the effect of pore geometry on the growth and spread dynamics of *Pseudomonas* sp. and *Bacillus* sp. bacteria following their introduction into soil.

The next group of articles focuses on the use of artificial media to gain a better understanding of the factors that control the distribution and activity of microorganisms in pores. Schlüter et al. introduce an experimental framework relying on simplified porous media (consisting of aggregates of porous, sintered glass beads) that circumvents some of the complexities occurring in natural soils while fully accounting for physical constraints believed to control microbial activity in general, and denitrification in particular. They use this framework to explore the impact of aggregate size and external oxygen concentration on the kinetics of O_2 consumption, as well as CO_2 and N_2O production. Guo et al. are interested in how the pore geometry of a soil can affect the extent to which bacteria are able to influence local moisture conditions through the secretion of extracellular polymeric substances (EPS). They systematically measured the rate and extent of water evaporation from pore structures as a function of both EPS concentration and pore size. They used for that purpose three different types of two-dimensional chambers: glass capillary tubes with a uniform macropore geometry, emulated soil micromodels representing an aggregated sandy loam pore geometry, and microfluidic capillary arrays to represent a uniform micropore geometry. Using the

same type of micromodel of a sandy loam soil, Soufan et al. try to ascertain that the fungus *Rhizoctonia solani* can indeed grow in such an environment, and then to identify and analyze in detail the pattern by which it spreads in the tortuous pores of the micromodel.

Finally, a last group of articles uses theoretical calculations or computer modeling to describe processes that control the interaction of bacteria with pore surfaces, or the activity of bacteria in soils. Bradford et al. present a theoretical method to determine the mean interaction energy between a colloid and a solid-water-interface when both surfaces contain binary nanoscale roughness and chemical heterogeneity, and they illustrate the application of the method to bacterial retention on solid surfaces. Portell et al. explore *in silico* the hypothesis that the heterogeneous distribution of soil organic matter, in addition to the spatial connectivity of the soil moisture, might account for the observed microbial biodiversity in soils. The analysis rests on a multi-species, individual-based, pore-scale model that is parameterized with data from 3 *Arthrobacter* sp. strains, known to be, respectively, competitive, versatile, and poorly competitive.

One may wonder to what extent all these 22 manuscripts, published over the last year, have managed to put some color in the schematic diagram of **Figure 1**, i.e., dissipate a little bit the knowledge gap that existed on many questions at the time the graph was established. We lack the necessary perspective to determine if the articles contained in this Research Topic will contribute to make a serious dent in the gray zones of **Figure 1**, but it is comforting in this context to see that quite a few articles, either through experiments or modeling, deal head on

with the challenges associated with the distribution and activity of microorganisms in soils at the microscale. As mentioned earlier and as illustrated by Baveye et al. in Figure 1, microscale research on the microbial components of soil systems until recently has been seriously lagging behind the work on the physical and (bio)chemical characteristics. It is encouraging to see, among the various articles gathered in this Research Topic, several resolutely engage along this relatively unexplored path.

Arguably as a result of the Research Topic, or at least stimulated by it, the research on the microscale properties of soils is now entering into another phase, where different techniques and disciplinary outlooks will be systematically combined to apprehend more completely the characteristics of microhabitats in terrestrial systems. A number of research groups around the world are now trying to quantify the physical and (bio)chemical features of these microhabitats, as well as to describe as thoroughly as possible the composition and biodiversity of microbial populations they contain. The very recent article by Schlüter et al. (2019) is an excellent example of the type of work that is unfolding in this area. Using a combination of X-ray μCT, fluorescence microscopy, scanning electron microscopy and nanoSIMS, these authors are able to study the distribution of bacteria in a soil, and to show that they have a preference toward foraging near macropore surfaces and near fresh particulate organic matter. Juyal et al. (2019) combined X-ray CT with biological thin sections to elucidate the impact of pore architecture on bacterial distribution in soil. They highlighted that when different methods are being integrated, one needs to consider an "appropriate spatial scale" to understand the

FIGURE 2 | Group picture of the attendees of the *Microsoil 2018* workshop, held in the château of Saint Loup Lamairé (Deux Sèvres, France) in June 2018. The group comprised 50 researchers from 7 countries, who for 3 days, debated issues associated with the Research Topic in a very relaxed atmosphere.

factors that regulate the distribution of microbial communities in soils. It is hoped that these type of interdisciplinary efforts will not only help us understand better what controls the activity of microorganisms in soils, but will also enable us to (finally) make progress on the intimately linked topic of the dynamics of humic substances (e.g., Baveye and Wander, 2019).

We feel confident that within the next few years an increasing focus will be placed on integration of techniques. Progress in this respect will likely be fueled very significantly by the development of an array of new techniques, e.g., single-cell metabolomics or X-rays produced by plasma wave accelerators, which offer great promise for the research on soils and sediments. It may take a significant time, still, to develop the type of macroscopic descriptors of the emergent properties of microbial activity that are all the way in the gray zone in **Figure 1**, and that we desperately need to predict how soils are likely to react to the changes we impose on them, but at least we now seem to be on track to 1 day get there.

This brief description of the salient aspects of the Research Topic on "Elucidating microbial processes in soils and sediments" would not be complete without mentioning an event that took place in June 2018 and, although distinct from the Research Topic *per se*, was nonetheless intimately connected with it. A workshop, entitled *MicroSoil 2018*, was organized in the château of Saint Loup Lamairé (Deux Sèvres, France) in part to allow a sizeable number of authors of articles published in this Research Topic to get together and interact. A group of 50 researchers from 7 different countries gathered for 3 days (**Figure 2**), and actively debated about the status of the research, about impediments to its necessarily interdisciplinary character, and about plans for future research activities. A very positive outcome of the workshop is that several researchers from different institutions have decided to collaborate on joint projects (e.g., Vidal et al., 2019). A follow-up MicroSoil Summer school will take place in June 2019, again in Saint Loup Lamairé, and another workshop, MicroSoil 2020, similar to the 2018 one, will be held there in June 2020.

AUTHOR CONTRIBUTIONS

All authors listed have made a substantial, direct and intellectual contribution to the work, and approved it for publication.

REFERENCES

Alexander, M. (1964). Biochemical ecology of soil microorganisms. *Annu. Rev. Microbiol.* 18, 217–250. doi: 10.1146/annurev.mi.18.100164.001245

Baveye, P. C. (2015). Grand challenges in the research on soil processes. *Front. Environ. Sci.* 3:10. doi: 10.3389/fenvs.2015.00010

Baveye, P. C., and Wander, M. (2019). The (bio)chemistry of soil humus and humic substances: why is the "new view" still considered novel after more than 80 years? *Front. Environ. Sci.* 7:27. doi: 10.3389/fenvs.2019.00027

Eickhorst, T., and Tippkötter, R. (2008). Improved detection of soil microorganisms using fluorescence *in situ* hybridization (FISH) and catalyzed reporter deposition (CARD-FISH). *Soil Biol. Biochem.* 40, 1883–1891. doi: 10.1016/j.soilbio.2008.03.024

Foster, R. C. (1988). Microenvironments of soil microorganisms. *Biol. Fert. Soils* 6, 189–203. doi: 10.1007/BF00260816

Hapca, S., Baveye, P. C., Wilson, C., Lark, R. M., and Otten, W. (2015). Three-dimensional mapping of soil chemical characteristics at micrometric scale by combining 2D SEM-EDX Data and 3D X-Ray CT Images. *PLoS ONE* 10:e0137025. doi: 10.1371/journal.pone.0137205

Hapca, S. M., Houston, A. N., Otten, W., and Baveye, P. C. (2013). New local thresholding method for soil images by minimizing grayscale intra-class variance. *Vadose Zone J.* 12:vzj2012.0172. doi: 10.2136/vzj2012.0172

Hapca, S. M., Wang, Z. X., Otten, W., Wilson, C., and Baveye, P. C. (2011). Automated statistical method to align 2D chemical maps with 3D X-ray computed micro-tomographic images of soils. *Geoderma* 164, 146–154. doi: 10.1016/j.geoderma.2011.05.018

Houston, A. N., Otten, W., Baveye, P. C., and Hapca, S. (2013a). Adaptive-window indicator kriging: a thresholding method for computed tomography images of porous media. *Comput. Geosci.* 54, 239–248. doi: 10.1016/j.cageo.2012.11.016

Houston, A. N., Schmidt, S., Tarquis, A. M., Otten, W., Baveye, P. C., and Hapca, S. M. (2013b). Effect of scanning and image reconstruction settings in X-ray computed microtomography on quality and segmentation of 3D soil images. *Geoderma* 207, 154–165. doi: 10.1016/j.geoderma.2013.05.017

Juyal, A., Otten, W., Falconer, R., Hapca, S., Schmidt, H., Baveye, P. C., et al. (2019). Combination of techniques to quantify the distribution of bacteria in their soil microhabitats at different spatial scales. *Geoderma* 334, 165–174. doi: 10.1016/j.geoderma.2018.07.031

Mueller, C. W., Köbl, A., Hoeschen, C., Hillion, F., Hiester, K., Herrmann, A. M., et al. (2012). Submicron scale imaging of soil organic matter dynamics using NanoSIMS – From single particles to intact aggregates. *Organ. Geochem.* 42, 1476–1488. doi: 10.1016/j.orggeochem.2011.06.003

Mueller, C. W., Remusat, L., and Rumpel, C. (2017). "Characterization of biogeochemical processes at the microscale," in *Terrestrial Ecosystem Research Infrastructures*, eds A. Chabbi and H. Loescher (Boca Raton, FL: CRC Press), 193–212. doi: 10.1201/9781315368252-9

Nunan, N., Ritz, K., Crabb, D., Harris, K., Wu, K. J., Crawford, J. W., et al. (2001). Quantification of the *in situ* distribution of soil bacteria by large-scale imaging of thin sections of undisturbed soil. *FEMS Microbiol. Ecol.* 37, 67–77. doi: 10.1111/j.1574-6941.2001.tb00854.x

Schlüter, S., Eickhort, T., and Mueller, C. W. (2019). Correlative imaging reveals holistic view of soil microenvironments. *Environ. Sci. Technol.* 53, 829–837. doi: 10.1021/acs.est.8b05245

Schlüter, S., Weller, U., and Vogel, H.-J. (2010). Segmentation of X-ray microtomography images of soil using gradient masks. *Comput. Geosci.* 36, 1246–1251. doi: 10.1016/j.cageo.2010.02.007

Schmidt, H., Eickhorst, T., and Tippkoetter, R. (2012). Evaluation of tyramide solutions for an improved detection and enumeration of single microbial cells in soil by CARD-FISH. *J.Microbiol. Methods* 91, 399–405. doi: 10.1016/j.mimet.2012.09.021

Solomon, D., Lehmann, J., Kinyangi, J., Liang, B. Q., and Schafer, T. (2005). Carbon K-edge NEXAFS and FTIR-ATR spectroscopic investigation of organic carbon speciation in soils. *Soil Sci. Soc. Am. J.* 69, 107–119. doi: 10.2136/sssaj2005.0107dup

Vidal, A., Watteau, F., Remusat, L., Mueller, C. W., Nguyen Tu, T.-T., Buegger, F., et al. (2019). Earthworm cast formation and development: a shift from plant litter to mineral associated organic matter *Front. Environ. Sci.* 7:55. doi: 10.3389/fenvs.2019.00055

frontiers
in Environmental Science

Soil Microstructures Examined Through Transmission Electron Microscopy Reveal Soil-Microorganisms Interactions

Françoise Watteau* and Geneviève Villemin

INRA, LSE, Université de Lorraine, Nancy, France

Research over the last few decades has shown that the characterization of microaggregates at the micrometer scale using Transmission Electron Microscopy (TEM) provides useful information on the influence of microorganisms on soil functioning. By taking soil heterogeneity into account, TEM provides qualitative information about the state of bacteria and fungi (e.g., intact state of living organisms, spores, residues) at the sampling date within organo-mineral associations, from the soil-root interface to the bulk soil, and in biogenic structures such as casts. The degree of degradation of organic matter can be related to the visualized enzymatic potential of microorganisms that degrade them, thus indicating organic matter dynamics within soil aggregates. In addition, analytical TEM characterization of microaggregates by EELS (Electron Energy Loss Spectroscopy) or EDX (Energy Dispersive X-rays spectroscopy) provides *in situ* identification of microbial involvement in the biogeochemical cycles of elements. Furthermore, micrometer characterization associated with other methodologies such as Nanoscale Secondary Ion Mass Spectrometry (NanoSIMS) or soil fractionation, enables monitoring both incorporation of biodegraded litter within soil aggregates and impacts of microbial dynamics on soil aggregation, particularly due to production of extracellular polymeric substances. The present focused review suggests that such an approach using micrometer characterization of soil microhabitats provides relevant qualitative and quantitative information when monitoring and modeling microbial processes in dynamics of organo-mineral associations.

Keywords: bacteria, EPS, microhabitats, *in situ* localization, soil fractionation, micro-analyses, hotspots of biological activity

INTRODUCTION

How a soil functions is closely related to the dynamics of soil microbial communities. Microbial habitats and soil structure are so intimately related that knowledge of these interactions appears essential to understand soil processes and management. While microorganisms influence soil structure as aggregation agents (Tisdall and Oades, 1982), conversely, soil texture and structure form microhabitats (Stotzky, 1986) and thereby strongly influence the dynamics, ecology, and activity of microbial populations. Bacteria are distributed throughout pores of various sizes and within aggregates (Hattori and Hattori, 1976), while simultaneously organic matter provides

micro-niches adequate for microorganism growth (Guggenberger et al., 1999). Chenu and Cosentino (2011) described the role of microorganisms in the temporal and spatial dynamics of aggregation. They detailed the formation, stabilization and destruction of aggregates by microorganisms as well as impacts of soil structure evolution on microbial activity. Thus, the visualization of microorganisms within soils has long been, and is especially now, both a real need and a challenge in order to assess "life in inner space" (Ritz, 2011; Baveye et al., 2018).

The *in situ* observation of soil biota requires that the fabric of the soil be left as undisturbed as possible (Ritz, 2011). In their review of micrometer determinants of bacterial diversity in soils, Vos et al. (2013) presented several methods to describe micrometer-sized soil habitats, based on sieving, dissecting and visualizing individual soil aggregates. They cited advantages and disadvantages of associated techniques, such as Scanning Electron Microscopy (SEM) associated with Energy-Dispersive X-ray spectroscopy (EDX), Infrared Spectroscopy, Nanoscale Secondary Ion Mass Spectrometry (NanoSIMS) and Near Edge X-ray Absorption Fine Structure Spectroscopy. These techniques usually use polished, resin-embedded whole aggregates and thus, from a methodological point of view, require sample preparation similar to that used for Transmission Electron Microscopy (TEM) characterization. Nevertheless, results in the literature characterize and localize organic matter and elements more often than bacterial units. Micro-computed tomography and nuclear magnetic resonance or magnetic resonance imaging are also cited as non-destructive approaches in three-dimensional (3D) analysis of soil structure. Finally, fluorescence *in situ* hybridization (FISH) techniques combined with micro-pedological methods are promising, allowing specific classes of microorganisms to be localized in soils by using oligonucleotide probes (Eickhorst and Tippkötte, 2008). In addition, micro-cartography of digital-sequential images of soil thin sections combined with fluorescent microscopy improves understanding of the distribution and quantification of hotspots and biofilms in soils regardless of the micrometer scale (Nunan et al., 2001; Castorena et al., 2016). As a precursor, Foster emphasized the use of TEM to visualize *in situ* soil microstructures, particularly in the rhizosphere, which has been the main site of micrometer studies of soils and soil microorganisms (Foster et al., 1983; Foster, 1988). Within the rhizosphere, many physical, chemical and biological processes take place, stemming from root growth, water and nutrient uptake, respiration and rhizodeposition (Hinsinger et al., 2005). Microbial activity is therefore much greater there than in non-rhizopheric soil due to root activity (Lynch, 1990). TEM makes it possible to identify cellular components such as cellulose, lignin and condensed polyphenolic substances within plant tissues and soil aggregates and to localize bacteriaband fungi, while identifying their intact state at the sampling date, (e.g., alive, sporulated, dead) and their enzymatic activity within cellular components by visualizing areas of lysis around the microorganisms (Kilbertus, 1980; Foster et al., 1983). Roose et al. (2016) reviewed current developments in structural and chemical imaging of the rhizosphere. Although they focus on the influence

of pore structure in the rhizosphere on water and nutrients fluxes, the techniques and the main results they mention also concern soil-microorganism interactions. TEM combined with micro-analysis, immuno-labeling or specific staining procedures is extremely well-suited for localizing microorganisms within soil structures at the micrometer scale, whether inside or outside rhizospheres (Hattori and Hattori, 1976; Foster and Martin, 1981; Bartoli et al., 1986; Chotte et al., 1992; Ladd et al., 1993). In addition, image analysis of visualized soil parameters (e.g., pores, roots) can quantify impacts of soil-biota interactions and strengthens use of visualizing techniques. Nevertheless, using TEM requires the physical and chemical fixation of microstructures to avoid any shrinkage, staining procedures to enhance organic matter contrast, and preparation of ultra-thin sections despite the presence of potentially damaging minerals. This is why TEM, despite the large amount of information it can yield, may sometimes seem less approachable to all than other techniques.

In this article, we highlight the use of TEM to elucidate mutual interactions between soils and microorganisms, thereby identifying soil processes and microbial activity. The feasibility of using TEM to localize microorganisms and deduce their influence within soil structures is illustrated by studies involving a variety of soils in different contexts (i.e., five cropped soils, one forest soil and one Technosol). The results presented, most of them already published, are used as examples to highlight microbial contribution to (i) organic matter turnover within microhabitats, assessed through a combination of TEM, Electron Energy Loss Spectroscopy (EELS) or NanoSIMS; (ii) soil aggregation inside and outside rhizospheres and (iii) microaggregate dynamics as indicators of soil health. This focused review of using TEM to assess soil-microorganisms interactions at the micrometer scale is motivated by the need to visualize soil microhabitats efficiently for soil microbiology, providing both qualitative and quantitative data and considering soil heterogeneities. Samples must be representative and soil structure must be preserved to ensure the relevance of results. As hotspots of biological activity, rhizosphere, drilosphere (casts), and 0–20 μm size fractions of soil were sampled and morphologically or analytically characterized by TEM. We discuss relationships among microbial dynamics within these organo-mineral associations and how the soil functioned as a whole, with the aim of identifying data to improve modeling of microbial dynamics in soil processes, in particular soil organic matter evolution and soil aggregation.

MATERIALS AND METHODS

Soils

We review 5 soils from agrosystems (soils 1–5), one soil from a forest ecosystem (soil 6), and one constructed Technosol (soil 7). Soil names are given according the WRB classification (2014) (see **Table S1** of the main physico-chemical parameters):

- soil 1: a calcic Cambisol developed on silt deposits. It was cropped with maize (*Zea mays*) after moderate tillage and fertilization at an experimental station. Digested sewage sludge

was applied according to regulations. Sampling allowed us to monitor any impact of cropping practices on micro-aggregation (Watteau et al., 2012).

- soil 2: a Luvisol developed from aeolian silt on an alluvial terrace in western France and cropped with maize. The impact of cattle manure amendment on soil fertility was studied.
- soil 3: a Cambisol collected from a permanent grassland in northern France. It was used in a mesocosm experiment to study the incorporation of ^{13}C-labeled organic matter [roots or shoots of Italian ryegrass, (*Lolium multiflorum*)], in the presence or absence of earthworms (*Lumbricus terrestris*) (Vidal, 2016). It was sieved to 4 mm for homogenization, plant residues and macrofauna > 4 mm were removed, and then the soil was placed into PVC containers (80 cm long × 40 cm in diameter) for 6 months. Results of the treatment with incubation of ^{13}C-labeled ryegrass shoots with earthworms are presented.
- soil 4: a Luvisol developed on old gravelly alluvium sampled from a long-term field experiment in south-eastern France. It was cropped with maize and studied to highlight impacts of root on microaggregation (Watteau et al., 2006).
- soil 5: a Vertisol from south-eastern Martinique. Because of their high exchangeable sodium content, these soils have low structural stability and high susceptibility to erosion, in particular when intensively cropped, which leads to a loss of organic matter. Fallowing these soils, however, rebuilds organic matter content and thus makes them less erodible (Campbell et al., 1999). Results comparing a Vertisol under a former grassland to the same vertisol under former market gardens (Blanchart et al., 2000) are presented.
- soil 6: a Podzol under a beech (*Fagus sylvatica*) ecosystem in eastern France. This study was designed to identify root aging at the micrometer scale using TEM and EELS (Watteau et al., 2002).
- soil 7: a constructed Technosol. Constructing soil to reclaim derelict land is based on the recycling of secondary by-products. Using pedological engineering concepts, these by-products are combined to construct a new soil (Technosol) over *in situ* brownfield substrates (Séré et al., 2010). It consisted of three different parent materials deposited in layers (from top to bottom): (i) green-waste compost (10 cm) from urban trees and grass cuttings, (ii) a mixture (1:1 v/v) of paper-mill sludge and thermally treated industrial material extracted from a former coking plant (80 cm), and (iii) pure paper-mill sludge (25 cm). This Technosol was constructed during field tests in 2003 at the GISFI experimental station (http://gisfi.univ-lorraine.fr) in eastern France. The soil was seeded with Italian rye grass and lucerne (*Medicago sativa*).

Soil Fractionation

Three to five samples of 200 g of soils 1–7 were taken from the topsoil, pooled and kept wet until their conditioning for soil fractionation. The 0–20 μm size fractions were obtained after soil fractionation in water from the soil particles <2-mm obtained by dry sieving fresh soil. Thirty-gram samples were dispersed in 200 ml distilled water and stirred gently for 1 h. The 200 μm−2 mm fractions were obtained by wet sieving.

The 0–200 μm fractions were dispersed for 16 h in 500 ml distilled water. The 50–200 μm fractions were then obtained by wet-sieving. The 0–2, 2–20, and 20–50 μm fractions were collected by sedimentation using the Robinson pipette method. All fractions were oven-dried at 60°C and weighed. Weight distributions were adjusted to 100%, and percentages of the fractions were expressed as the means and standard errors of three replicates. From the resulting 0–50 μm residue, 0–2, 2–20, and 20–50 μm fractions were collected separately, according to Stokes' law. To obtain enough material for further analyses, 0–2 μm fractions were mainly collected by five serial elutions of 0–50 μm fractions without the addition of flocculating agents. Parts of these fractions were oven-dried at 110°C and finely ground for elementary analyses, while the remainders were left undried and stored at 8°C until they were processed for TEM.

Morphological and Analytical Characterization by TEM

Roots, casts and 0–20 μm size soil fractions were sampled and morphologically or analytically characterized by TEM. The roots more or less associated with rhizospheric soil were sampled because of the numerous soil-plant-microorganism interactions within the rhizosphere (Waisel et al., 2002). Earthworms are strongly involved in aggregate formation, microbial dynamics in the soil profile, and sequestration/mineralization of organic matter in tropical and temperate environments (Bossuyt et al., 2005; Jouquet et al., 2009). The fine soil fractions, with a particle diameter of 0–20 μm, are considered the most reactive, given their high cation exchange capacity, stable carbon (C) content, microbial (C) content (Anderson et al., 1981; Eliott, 1986; Chotte et al., 1992; Balabane and Plante, 2004), and their recalcitrance to biodegradation (Hassink, 1997). In addition, 2–20 μm micro-aggregates represent very favorable habitats for bacteria in most soils (Ranjart and Richaume, 2001).

Three replicates of a few cubic millimeters each were sampled from roots, casts, and 2–20 μm fractions for TEM examination. These sub-samples were fixed in 2% (w/v) osmium tetroxide in a cacodylate buffer (pH 7.2) for 1 h in order to chemically fix the organo-mineral structure. Osmium-fixed samples were dehydrated in graded acetone solutions, then embedded in epoxy resin (Epon 812) until complete polymerization (16 h at 60°C). Ultra-thin sections (80–100 nm) were cut with a diamond knife on a Leica Ultracut S ultramicrotome. Some sections were filed on nickel grids, stained with uranyl acetate and lead citrate to enhance organic matter contrast, and examined in a JEM 1200 EXII transmission electron microscope operating at 80 kV. A minimum of 15 observation fields at a magnification of 4000 were performed for each of the three replicates. Unstained ultra-thin sections were filed on nickel grids covered with a C film and used for *in situ* elementary analyses with EDX, EELS or NanoSIMS (Watteau and Villemin, 2001; Watteau et al., 2002; Vidal et al., 2016). EDX is a simple and fast technique but does not give access to light elements (from $Z = 3$) and is of lower resolution than EELS, whose results analysis is still more complicated (Egerton, 1986; Bauer, 1988).

RESULTS AND DISCUSSION

Microbial Activity Within Microstructures

TEM observations of the 2–20 μm fractions of soils 1–3 revealed different states of microorganisms in soil microstructures (**Figure 1**). Microorganisms can be observed in pores or in aggregates, individually or when gathered into colonies. Bacteria are present within microaggregates, associated either with the organic residues they degraded or with minerals, mainly due to production of extracellular polymeric substances (EPS) (**Figures 1.1**, **1.2**). Typical bacterial aggregate consisting of EPS-producing bacteria, on which minerals are adsorbed, are also frequently observed (**Figures 1.3**, **1.4**). At the time of sampling, bacteria within microaggregates of soil 2 were alive and intact (**Figure 1.4**), sometimes dividing (**Figure 1.5**), spores waiting for better conditions (**Figure 1.6**), or dead in the form of cell wall residues (**Figure 1.4**). Actinomycetes and fungi are also observed to be associated within soil 3 aggregates (**Figures 1.7, 1.8**). Certain typical intracellular features (cytoplasmic membranes) allow us to identify nitrogen-cycle bacteria in casts sampled from soil 7 (**Figure 1.9**). Because sampling and sample processing preserve the initial soil structure, TEM allow localization of the main microorganisms within aggregates.

These microhabitats visualized by TEM highlight their impact on two main parameters of soil-microorganism interactions: physical protection of microorganisms and nutrient availability. As an illustration of the ability of microorganisms to degrade organic matter, fungi and bacteria attack ligneous residues in soil 3 [**Figure S1**, (see Datasheet 2)]. Areas of lysis due to fungal activity are visualized in ligneous thickenings, suggesting fungal ligninolytic capacity. Cell intersections already persist, and many bacteria colonize these plant tissue residues until they get completely fragmented. Due to the spatio-temporal sampling, TEM allow us to monitor the successive microbial degradation of organic matter identified within microstructures. TEM microanalysis also identifies microbial enzyme production on beech roots sampled from soil 6 (Watteau et al., 2002). EELS analysis of the contrasting rings surrounding areas of lysis observed in polyphenolic substances contained in cortical cells detect a large amount of nitrogen [**Figure S1.2** (see Datasheet 2), EEL spectrum 2]. However, no nitrogen is detected in the polyphenolic substances themselves [**Figure S1.2** (see Datasheet 2), EEL spectrum 1]. This supplemental nitrogen came from enzymes produced by hyphae colonizing these cells. Another way to identify organic matter turnover is to combine TEM and NanoSIMS. Vidal et al. (2016) sample earthworm casts as newly formed aggregates in soil 3, to which ^{13}C-labeled shoot residues had been added. From ^{13}C labeling and NanoSIMS imaging of ultra-thin sections, these authors observe incorporation of ^{13}C-labeled carbon in casts and its microflora [**Figure S1.3** (see Datasheet 2) and NanoSIMS maps]. NanoSIMS imaging does not always allow them to recognize features of organic matter and microorganisms within aggregates because of the heterogeneity of the aggregates' organo-mineral components and arrangement. Previous TEM examination of the aggregates on the same ultra-thin sections used for NanoSIMS ensured the identification of the features analyzed. Thus, contribution of microorganisms

to degradation of freshly introduced litter can be monitored within aggregates at a micrometer scale. Supplementing such information about the C cycle, TEM-EDX and TEM-EELS can also be used to monitor microbial involvement in the biogeochemical cycles of other main elements (e.g., silicon; Watteau and Villemin, 2001).

Biologically promoted soil aggregates are of increasing interest in soil structure dynamics, as hotspots of biological activity influence soil biogeochemical cycles (Tecon and Or, 2017). The contribution of soil organic matter to different aggregate fractions and details of how organic C is organized within aggregates are of critical importance to the self-organization of microbial communities. Besides, only a small percentage of total microbial biomass found in soil is active; most is dormant or inactive (Blagodatskaya and Kuzyakov, 2013; Tecon and Or, 2017). As one way to obtain such data, TEM can identify activity of microflora observed within aggregates, revealing their state and their enzymatic potential. To confirm the nature of organic matter, it can be stained to enhance proteins, lipids or polysaccharides (Foster, 1981; Bisdom, 1983) and differentiate microbial from plant polysaccharides (Tiessen and Stewart, 1988). Furthermore, microaggregate turnover is high, as the rate of organic matter degradation by microorganisms is related to microhabitats. As shown, combining TEM and NanoSIMS is one promising way to identify this turnover (Vidal et al., 2016) and will add microbial information to the imaging of organic matter dynamics using NanoSIMS and SEM (Mueller et al., 2012). Likewise, combining soil organic matter fractionation and TEM typology of organo-mineral associations will likely become a promising method for confirming the biochemical composition of extracted organic matter regardless of the fractionation method used. It can determine the nature (polyphenolic, ligneous, EPS) of the organic matter observed according to its identified biochemical recalcitrance, in particular the presence of microbial components.

A combination of TEM and other techniques (e.g., EELS, EDX, NanoSIMS) can observe the contribution within soil of microorganisms to organic matter dynamics and biogeochemical cycles of several elements. TEM data on soil physico-chemical characterization or microbial diversity and abundance will improve knowledge about microbial contribution to soil processes. As part of this approach, combining FISH and immuno-labeling at the micrometer scale appears to be a promising way to carry out future research. Similarly, immunomarking techniques could be developed to detect of viruses within aggregates. Currently, *in situ* visualization of virus particles within undisturbed soil samples is far from obvious. Thus, direct counting methods using TEM or epifluorescence microscopy have relied on a two-step process of extraction and enumeration (Williamson et al., 2017). TEM allows for visualization of viral morphology and epifluorescence microscopy is more used for viral enumeration. Ashelford et al. (2003) reported that substantial populations of soil bacteriophage exist in soils. Considering the impact that viruses can have on the bacterial cycle and thus on the nutrient cycle, identifying viruses
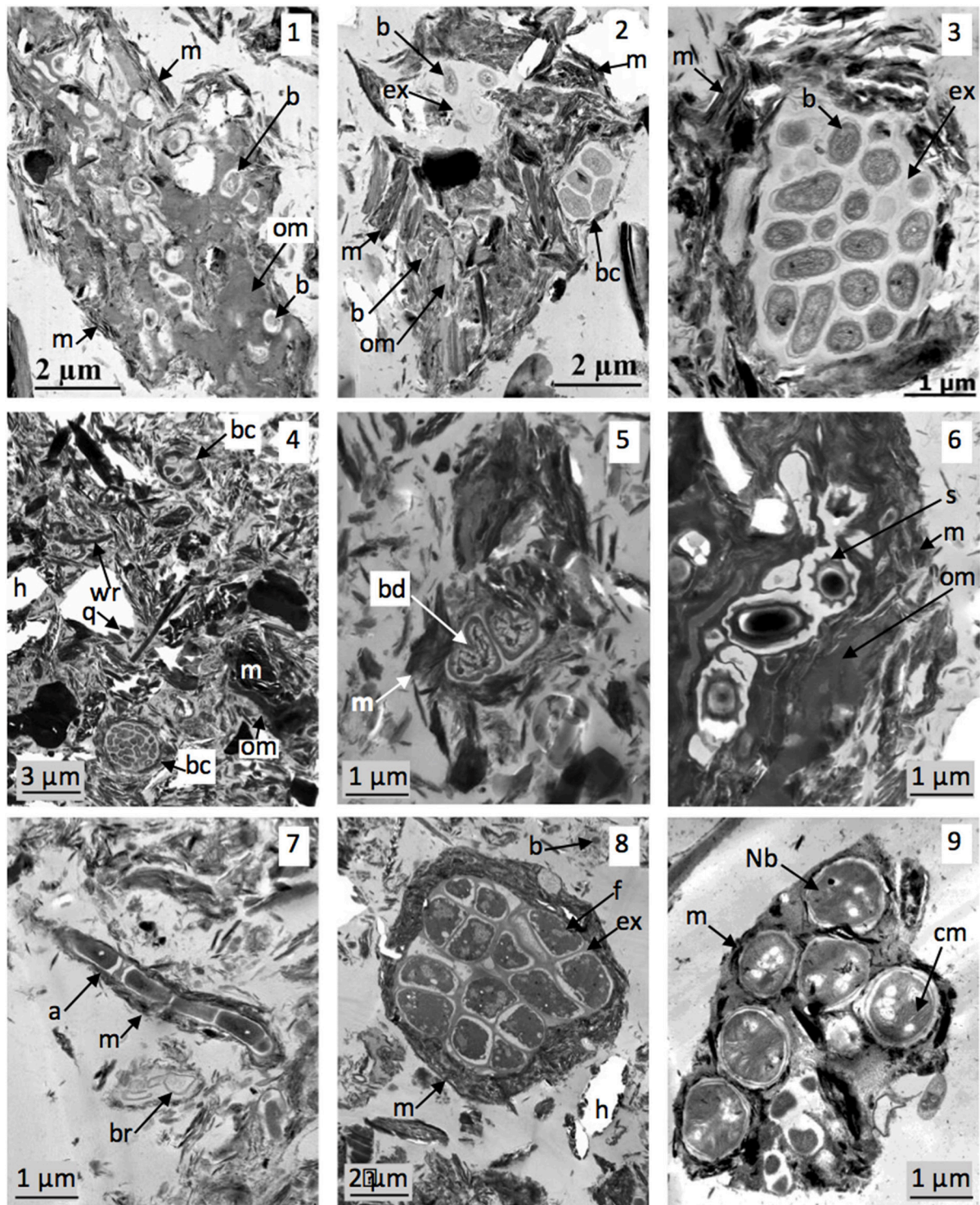
FIGURE 1 | Microorganism localization within soil microstructures. TEM views **(1–3)**: soil 1 microaggregates (already published in Watteau et al., 2012). **(1)** Organic residue colonized by bacteria and surrounded by with minerals; **(2)** mainly mineral aggregate containing few organic residues and EPS producing bacteria (individualized or in colony); **(3)** typical bacterial aggregate constituted by bacteria producing EPS on which are adsorbed minerals. TEM views **(4–6)**: soil 2 aggregates. **(4)** Global view of 2–20 μm fraction showing mineral or organic particles and bacterial aggregates as bacterial colony associated with minerals. **(5)** Bacteria in division within aggregate; **(6)** bacterial spores localized in organic residue associated with minerals. TEM views **(7,8)**: microorganisms in soil 3. **(7)** Actinomycete associated with minerals; **(8)** fungal aggregate. TEM view **(9)** Bacteria of N cycle in soil 4 (already published in Pey et al., 2014). a, actinomycete; b, bacteria; bc, bacterial colony; bd, bacteria in division; br, bacterial residue; cm, cytoplasmic membrane; ex, EPS; f, fungus hypha; h, hole in the resin as an artifact due to mineral presence; Nb, bacteria of nitrogen cycle; om, organic matter; m, mineral; q, microquartz; s, bacterial spore.

within soil microstructures may prove relevant in specifying carbon dynamics as a function of bacterial population dynamics.

Soil-Microorganism Interactions at Hotspots of Biological Activity

The rhizosphere is a soil hotspot, as microbial interactions impact soil functioning. We studied soil aggregation as a function of increasing distance from roots in soil 4 (Watteau et al., 2006). Coarse and fine roots at the soil interface generate stable 2–20 μm aggregates, whose organization depends on the nature of the plant or microbial organic matter. Distribution of aggregate types varies according to their proximity to roots (**Figure 2**). Microaggregates near roots contain mainly root cell walls and bacteria, whereas those further from roots contain mainly polyphenolic substances and bacterial aggregate residues. These results agree with the conceptual model of soil organic C dynamics under long-term maize cropping systems, in which C is distributed among four pools with different biodegradation kinetics (Balesdent et al., 2000; Ludwig et al., 2003).

Describing the rhizosphere with TEM enhanced the role of microbial EPS in forming organo-mineral associations in such coarse-textured soil. Bacteria adhered to roots because of EPS, on which minerals were aggregated and EPS are the main components of frequently observed bacterial aggregates (**Figures 1**, **2**). TEM visualization identified the involvement of EPS in microbial aggregation in the main soils, i.e., the cropped soils and the Technosol (**Figures 1.2–1.4**, **2.9**, **2.10**). EPS are thus a hotspot of soil-microorganism interactions, especially since they resist degradation. It is well-known that stable EPS influence soil structure dynamics, binding particles together and promoting the formation of a stable structure (Chenu and Guerif, 1993). EPS optimize functions at the microsite scale (Abiven et al., 2007), such as water availability in micropores (Rossi et al., 2012). Bacterial polysaccharide-mediated aggregation has been widely studied, particularly using SEM (Chaney and Swift, 1986; Dorioz et al., 1993). Thus, TEM could identify the contribution of EPS in most soils, even those as coarsely-textured as young Technosols, in which biofilms may predominate during pedogenesis, by analogy with biological crust development (Malam Issa et al., 2007; Weber et al., 2016).

Over short time scales, microbial interactions at hotspots (e.g., rhizosphere and aggregates) impact the soil physical environment greatly (Philippot et al., 2013). In this way, composts can also be considered as hotspots. Composts are added as a soil amendment or as parent materials at remediation sites (soil 7). Composted organic matter is expected to be biochemically and microbially stable because of its production process. However, TEM characterization of green-waste composts showed that they also have a microbial potential (Séré et al., 2010; Watteau and Villemin, 2011). Observation of spores or active microflora in identified organic residues indicates both enzymatic potential and dynamics of composted organic matter and associated microorganisms, as these composts will be added to the soil. TEM identification of the microbial potential of organic residues incorporated in the soil is particularly relevant for site remediation. Green-waste composts are currently used as

organic parent materials of Technosols (Bacholle et al., 2006), and paper-mill sludge is incorporated in large amounts throughout the entire soil depth (120 cm) (soil 7; Séré et al., 2010). As both residues can also contain bacteria and fungi, it is interesting to note that pedological engineering creates soil microhabitats, even deep in the soil and during soil construction (Watteau et al., 2018). TEM characterization of parent material-microorganism interactions at the micrometer scale can help monitor Technosol functioning. This is of great interest, as Technosols are increasingly used in new ecosystems. By definition, biofeatures (e.g., earthworm casts, burrows, fecal pellets) are also hotspots of microbial activity. TEM characterization of biofeatures indicates the ability of fauna to transform ingested organic matter before it is incorporated in soils and to form new aggregates [**Figure 1**, **Figure S1** (see Datasheet 2); Pey et al., 2014; Vidal et al., 2016]. TEM appears well suited to identify fauna-microorganism interactions in the context of soil functioning. Thus, TEM can identify microbial potential (i.e., presence, state, and enzymatic activity) and also biologically promoted aggregation, at hotspots of biological activity.

Microbial Aggregates as Soil Function Indicators

TEM can be used to characterize 2–20 μm stable soil fractions by comparing Vertisols under either former market gardens or former grassland (soil 5). TEM examination clearly shows that these size fractions consist mainly of microaggregates of three types [**Figure S2**, (see Datasheet 3)]:

- Type 1: organo-mineral, composed of plant cell residues associated with clays in various proportions. Microorganisms can colonize the organic residues.
- Type 2: bacterial, composed of bacteria producing EPS which were associated with clays.
- Type 3: mainly mineral, composed of clays aggregated by colloidal organic substances. EDX analyses confirmed the presence of organic matter by detecting osmium specifically bound to it [**Figure S2** (see Datasheet 3), EDX spectrum 1].

The relative proportions of these three types of microaggregates within the 2–20 μm fractions can be assessed for both Vertisols. Thirty naked-eye counts of 330 μm^2 were performed for each, corresponding to 135 and 253 aggregates from the Vertisol under former market gardens and former grassland, respectively. Whereas mineral aggregates predominate under former market gardens, bacterial and organo-mineral aggregates are more numerous under former grassland. These contrasting morphological descriptions may be related to other differing soil parameters, such as the soil stability index (AS500, the percentage of stable aggregates >500 μm after 18 h of stirring in water) and soil C content (Blanchart et al., 2000). AS500 is four times as high under former grassland (16%) compared to Vertisol under former market gardens (4%), and soil C content is almost three times as high under former grassland (39 g.kg^{-1}) than under former market gardens (14 g.kg^{-1}). Biological aggregates (bacterial and organo-mineral) predominate in stable situations (93%), whereas mineral aggregates predominate in erodible situations (67%). Moreover, this is also related to the measured

FIGURE 2 | Soil-microorganism interactions at hotspots of biological activity. TEM views **(1–8)** (soil 4): microaggregation from maize root soil interface **(1, 2)** to rhizospheric soil **(3–6)** and to bulk soil **(7, 8)** (issue from Watteau et al., 2006). **(1)** Fine root-soil interface; **(2)** coarse root-soil interface; **(3, 4)** degradation of root cell walls of fine root forming aggregates; **(5)** microaggregate with electron-dense root cell wall; **(6)** bacterial aggregate; **(7)** microaggegate with electron-dense cell residue; **(8)** old bacterial aggregate. TEM views **(9, 10)**: EPS as aggregation agents from bacterial and fungal origin in soil 3 (views **9**) and in soil 7 (view **10**). b, bacteria; bc, bacterial colony; br, bacterial residue; cwr, cell wall residue; ex, EPS; m, mineral; ps, polyphenolic substance; rt, root tissue.

biological activity, as the biomass of roots, the abundance of earthworms and microorganisms in these soils are lower than those in market gardens (Chotte et al., 1992; Blanchart et al., 2000). This clear relationship between microaggregate type and Vertisol stability under various crops was also verified for four other cropping situations [bare soil, sugar cane (*Saccharum* spp.), meadow, fallow land] of calcic Vertisols in Guadeloupe (Blanchart et al., 2000). Biological aggregates due to soil enrichment by plant debris and increased microbial activity in reclamation situations influence soil structural stability. The relative proportions of these three types of aggregates consequently appear to indicate a sensitivity of these soils

to erosion, and the typology of aggregates in the 2–20 μm fractions can be used as an indicator of impacts of cropping practices.

Micrometer characterization of these fractions is thus well suited to identify microhabitats in relation to soil use. Others studies highlighted using the same approach to examine impacts of biological activity (by roots and microorganisms) on the stability and composition of 0–20 μm aggregates in a maize-cropped soil (see section Soil-Microorganism Interactions at Hotspots of Biological Activity), the relationship between soil stability and the nature of aggregated organic matter from plants and microorganisms (Watteau et al., 2012) and the

impact of crop rotation on soil structure (Saad et al., 2017). The biochemistry and turnover of organic matter are closely related to the size of organic matter and its associations with mineral soil components, and thus influence aggregate stability (Oades, 1984; Tiessen and Stewart, 1988). We thus confirm that microaggregate type results from, and is an indicator of, soil biofunctioning.

Potential Contribution of TEM to Soil Process Quantification and Modeling

As shown, morphological and analytical characterization by TEM provides much qualitative information about microhabitats in relation to soil processes. It can identify soil-microorganism interactions by visualizing biota *in situ* while respecting their habitat in the state it has at the time of sampling. Data on the contribution of microorganisms to organic matter dynamics and biogeochemical cycles of main elements are available regardless of the soil compartment (e.g., root interface, undisturbed aggregates, size fractions, faunal dejections). The 0–20 μm soil fractions appear to indicate soil functioning according to soil use or assessment of spatiotemporal heterogeneity. This would provide an opportunity to scale up and use the experimental data obtained at the micrometer scale to take impacts of microorganisms on soil functioning into account at the soil profile or even plot scale. Thus, TEM can provide data for soil process modeling, especially as using or developing image analysis protocols can also yield quantitative results by obtaining representative samples and statistically analyzing the number of counts performed. Future research could focus on the feasibility of using image analysis to quantify certain microbial descriptors indicating the presence or activity of microorganisms in soil fractions (e.g., proportion of biological aggregates, number or size of bacterial aggregates, number of free microorganisms, area of organic matter lysed). Thus, meta-analysis may identify correlations between certain quantified descriptors and other soil characteristics depending on the process studied, then identify the best microhabitat parameters to serve as indicators of soil functioning. Moreover, the entire aggregate could be extrapolated by analyzing many TEM images and mathematically constructing a 3D soil structure from 2D data (e.g., Wu et al., 2006). These descriptors could then be used as input parameters of soil process models, as could the amount and C content of 0–20 μm organo-mineral fractions. Mechanistic representation of small-scale processes is one of the priorities for improving models of soil organic matter dynamics (Manzoni et al., 2009). Microbial degradation and competition are increasingly simulated in models of structured environments and microtomography provides information about soil-fungi interactions (Monga et al., 2014). However, TEM is most relevant for soil-bacteria interactions. Future research combining TEM with other visualization techniques and analyses, may provide information and quantitative parameters relevant for simulating bacterial contributions to soil processes in 2D and 3D models. Characterization of the pore network may become a relevant indicator of

soil functioning, while that of aggregation already seems to be one (Rabot et al., 2018). In addition to the micropore-microorganisms interactions already studied (Vos et al., 2013), we recommend using TEM to characterize microaggregates, and particularly microbial interactions within them, as potential soil health indicators. Soil health reflects ecological attributes of the soil for producing a particular crop, encompassing biodiversity, food web structure, soil biotic activity and the range of functions it performs (Pankhurst et al., 1997 in Bünemann et al., 2018). Micron-scale interactions must be considered in macroscale processes (Baveye, 2018). In this way, micrometer-scale soil studies aim to input microhabitat parameters in soil process models, thereby facilitating simulation of microbial dynamics in their organo-mineral environment.

AUTHOR CONTRIBUTIONS

All authors listed have made a substantial, direct and intellectual contribution to the work, and approved it for publication.

ACKNOWLEDGMENTS

SUPPLEMENTARY MATERIAL

The Supplementary Material for this article can be found online at: https://www.frontiersin.org/articles/10.3389/fenvs. 2018.00106/full#supplementary-material

Table S1 | Main physico-chemical characteristics of the 2 mm sieved topsoils.

Figure S1 | Microbial degradation of organic matter within soil microstructures. TEM view **1**: degradation of ligneous residue issue from cattle manure added to soil 2, showing lysis area due to microbial enzymatic activity.
TEM view **2** (soil 6): weathered features of polyphenolic substances contained in mycorrhizal beech root, showing area of lysis due to fungal activity, emphasized by N enrichment detected using EELS spectroscopy: EEL detection of C in the less-electron dense area of the polyphenolic substances (spectrum 1) and EEL detection of C and N in the contrasting ring around the less-electron dense area of the polyphenolic substances (spectrum 2) (already published in Watteau et al., 2002).
TEM view **3** (soil 3): cast microaggregates of *Lumbricus terrestris* and NanoSIMS maps of $^{12}C^{14}N$ and $\delta^{13}C$ highlighting the incorporation of labeled elements in fungi and bacteria (already published in Vidal et al., 2016). b, bacteria; bc, bacterial colony; ci, cell intersection; cw, cell wall; cwr, cell wall residue; f, fungi; fr, fungal residue; h, hypha; la, lysis area; lt, ligneous thickening; L, pure silica layer surrounding polyphenolic substances; m, mineral; ps, polyphenolic substance; q, microquartz; r, contrasted ring; s, spore; *1 and *2, localization of EEL analyses corresponding to EEL spectra 1 and 2.

Figure S2 | Microaggregates of Vertisol. TEM view **1**: 2–20 μm fraction presenting the 3 types of microaggregates; TEM view **2**: "organo-mineral" aggregate; TEM view **3**: bacterial aggregate; TEM view **4**: "mineral" aggregate and corresponding EDX spectrum 1 and 2 for respectively fine organic matter (presence of C and Os) and clay.
b, bacteria; ba, bacterial aggregate; cw, plant cell wall; ex, exopolymer; ma, mineral aggregate; m, mineral; om, organic matter; oma, organo-mineral aggregate; pr, plant residue; *1 and *2, localization of EDX analysis 1 and 2.

REFERENCES

Abiven, S., Menaserri, S., Angers, D. A., and Leterme, P. (2007). Dynamics of aggregate stability and biological binding agents during decomposition of organic materials. *Eur. J. Soil Sci.* 58, 239–247. doi: 10.1111/j.1365-2389.2006.00833.x

Anderson, D. W., Saggar, S., Bettany, J. R., and Stewart, J. W. B. (1981). Particle size fractionation and their use in studies soil organic matter: I. the nature and distribution of forms of carbon, nitrogen and sulfur. *Soil Sci. Soc. Am. J.* 45, 767–772. doi: 10.2136/sssaj1981.03615995004500040018x

Ashelford, K. E., Day, M. J., and Fry, C. (2003). Elevated abundance of bacteriophage infecting bacteria in soil. *Appl. Environ. Microbiol.* 69, 285–289. doi: 10.1128/AEM.69.1.285-289.2003

Bacholle, C., Leclerc, B., and Coppin, Y. (2006). Utilisation des produits organiques en reconstitution de sol – Inventaire des pratiques en France; Etat de l'art des connaissances liées aux impacts de ces pratiques. *Rapport ADEME.* 1–135.

Balabane, M., and Plante, A. F. (2004). Aggregation and carbon storage in silty soil using physical fractionation techniques. *Eur. J. Soil Sci.* 55, 415–427. doi: 10.1111/j.1351-0754.2004.0608.x

Balesdent, J., Chenu, C., and Balabane, M., (2000). Relationship of soil organic matter dynamics to physical protection and tillage. *Soil Tillage Res.* 53, 215–230. Available online at: http://citeseerx.ist.psu.edu/viewdoc/download?doi=10.1.1.458.7739&rep=rep1&type=pdf

Bartoli, F., Demai, J. J., Philippy, R., Gueniot, B., Hatira, A., Villemin, G., et al. (1986). Structure de matières organiques de sols en microscopie électronique à transmission. *Soil Biol. Bioch.* 18, 497–505. doi: 10.1016/0038-0717(86)90007-6

Bauer, R. (1988). Electron spectroscopic imaging: an advanced technique for imaging and analysis in transmission electron microscopy. *Methods Microbiol.* 20, 113–146. doi: 10.1016/S0580-9517(08)70050-3

Baveye, C. P. (2018). Book review: shifting paradigms on soil microbial biomass. *Front. Environ. Sci.* 6:10. doi: 10.3389/fenvs.2018.00010

Baveye, P. C., Otten, W., Kravchenko, A., Balseiro Romero, M., Beckers,É., Chalhoub, M., et al. (2018). Emergent properties of microbial activity in heterogeneous soil microenvironments: different research approaches are slowly converging, yet major challenges remain. *Front. Microbiol.* 8:1364. doi: 10.3389/fmicb.2018.01929

Bisdom, E. B. A. (1983). Submicroscopic examination of soils. *Adv. Agron* 36, 55–96. doi: 10.1016/S0065-2113(08)60352-1

Blagodatskaya, E., and Kuzyakov, Y. (2013). Active microorganisms in soil: critical review of estimation criteria and approaches. *Soil Biol. Biochem.* 67, 192–211. doi: 10.1016/j.soilbio.2013.08.024

Blanchart, E., Achouak, W., Albrecht, A., Barakat, M., Bellier, G., Cabidoche, Y. M., et al. (2000). Déterminants biologiques de l'agrégation dans les vertisols des Petites Antilles. Conséquences sur l'érodibilité des sols. *Etude et Gestion des Sols* 7, 309–328.

Bossuyt, H., Six, J., and Hendrix, P. F. (2005). Protection of soil carbon by microaggregates within earthworm casts. *Soil Biol. Bioch.* 37, 251–258. doi: 10.1016/j.soilbio.2004.07.035

Bünemann, E. K., Bongiorno, G., Bai, Z., Creamer, R. E., De Deyn, G., De Goede, R., et al. (2018). Soil quality - A critical review. *Soil Biol. Biochem.* 120, 105–125. doi: 10.1016/j.soilbio.2018.01.030

Campbell, C. A., Bierderbeck, V. O., McConkey, B. G., Curtin, D., and Zentner, R. P. (1999). Soil quality - Effect of tillage and fallow frequency. Soil organic matter quality as influenced by tillage and fallow frequency in a silt loam in southwestern Saskatchewan. *Soil Biol. Biochem.* 31, 1–7. doi: 10.1016/S0038-0717(97)00212-5

Castorena, E. V. G., Gutierrez-Castorena, M. C., Vargas, T. G., Bontemps, L. C., Delgadillo Martinez, J., Suastegui Mendez, E., et al. (2016). Micromapping of microbial hotspots and biofilms from different crops using digital image mosaics of soil thin sections. *Geoderma* 279, 11–21. doi: 10.1016/j.geoderma.2016.05.017

Chaney, K., and Swift, R. S. (1986). Studies on aggregate stability. I. Re-formation of soil aggregates. *J. Soil Sci.* 37, 329–335. doi: 10.1111/j.1365-2389.1986.tb00035.x

Chenu, C., and Cosentino, D. (2011). "Microbial regulation of soil structural dynamics," in *The Architecture and Biology of Soils: Life in Inner Space*, ed K. Ritz and I. Young (Croydon: CPI Group), 37–70.

Chenu, C., and Guerif, J. (1993). Mechanical strength of clay minerals as influenced by an adsorbed polysaccharide. *Soil Sci. Soc. Am. J.* 55, 1076–1080. doi: 10.2136/sssaj1991.03615995005500040030x

Chotte, J. L., Jocteur-Monrozier, L., Villemin, G., and Toutain, F. (1992). Effet du mode de dispersion du sol sur la localisation de sa biomasse microbienne; cas d'un vertisol. *Cahier de l'Orstom, Pédologie* 27, 81–95.

Dorioz, J. M., Robert, M., and Chenu, C. (1993). The role of roots, fungi and bacteria on clay particle organization. An experimental approach. *Geoderma* 56, 179–194. doi: 10.1016/0016-7061(93)90109-X

Egerton, R. F. (1986). *Electron Energy Loss Spectroscopy in the Electron Microscope.* New York, NY: Plenum Press.

Eickhorst, T., and Tippkötte, R. (2008). Detection of microorganisms in undisturbed soil by combining fluorescence *in situ* hybridization (FISH) and micropedological methods. *Soil Biol. Biochem.* 40, 1284–1293. doi: 10.1016/j.soilbio.2007.06.019

Eliott, E. T. (1986). Aggregate structure and carbon, nitrogen and phosphorus in native and cultivated soils. *Soil Sci. Soc. Am. J.* 50, 627–633. doi: 10.2136/sssaj1986.03615995005000030017x

Foster, R. (1981). Polysaccharides in soil fabrics. *Science* 214, 665–667. doi: 10.1126/science.214.4521.665

Foster, R. C. (1988). Microenvironments of soil microorganisms. *Biol. Fert. Soils* 6, 189–203. doi: 10.1007/BF00260816

Foster, R. C., and Martin, J. K. (1981). "*In situ* analysis of soil components of biological origin," in *Soil Biochemistry*, Vol. 5, eds E. A. Paul and J. N. Ladds (New York, NY: Marcel Dekker), 75–112.

Foster, R. C., Rovira, A. D., and Cock, T. W. (1983). *Ultrastructure of the Root-Soil Interface.* St Paul, MN: American Phytophathological Society.

Guggenberger, G., Elliott, E. T., Frey, S. D., Six, J., and Paustian, K. (1999). Microbial contributions to the aggregation of a cultivated grassland soil amended with starch. *Soil Biol. Biochem.* 31, 407–419. doi: 10.1016/S0038-0717(98)00143-6

Hassink, J. (1997). The capacity of soils to preserve organic C and N by their association with clay and silt particles. *Plant Soil* 191, 77–87. doi: 10.1023/A:1004213929699

Hattori, T., and Hattori, R. (1976). The physical environment in soil microbiology: an attempt to extend principles of microbiology to soil microorganisms. *Crit. Rev. Microbiol.* 4, 423–461. doi: 10.3109/10408417609102305

Hinsinger, P., Gobran, G. R., Gregory, P. J., and Wenzel, W. W. (2005). Rhizosphere geometry and heterogeneity arising from root-mediated physical and chemical processes. *New Phytol.* 168, 293–303. doi: 10.1111/j.1469-8137.2005.01512.x

Jouquet, P., Zangerle, A., Rumpel, C., Brunet, D., Bottinelli, N., and Tran Duc, T. (2009). Relevance and limitations of biogenic and physicogenic classification: a comparison of approaches for differentiating the origin of soil aggregates. *Eur. J. Soil Sci.* 60, 1117–1125. doi: 10.1111/j.1365-2389.2009.01168.x

Kilbertus, G. (1980). Etude des microhabitats contenus dans les agrégats du sol, leur relation avec la biomasse bactérienne et la taille des procaryotes présents. *Rev. Ecol. Biol. Sols* 17, 543–557.

Ladd, J. N., Foster, R. C., and Skjemstad, J. O. (1993). Soil structure: carbon and nitrogen metabolism. *Geoderma* 56, 401–434. doi: 10.1016/0016-7061(93)90124-4

Ludwig, B., John, B., Ellerbrock, R., Kaiser, M., and Flessa, H. (2003). Stabilization of carbon from maize in a sandy soil in a long-term experiment. *Eu. J. Soil Sci.* 54, 117–126. doi: 10.1046/j.1365-2389.2003.00496.x

Lynch, J. M. (1990). "Introduction: some consequences of microbial rhizosphere competence for plant and soil," in *The Rhizosphere*, ed J. M. Lynch (Chichester: John Whiley & Sons), 1–10.

Malam Issa, O., Défarge, C., Le Bissonnais, Y., Marin, B., Duval, O., Bruand, A., et al. (2007). Effects of the inoculation of cyanobacteria on the microstructure and the structural stability of a tropical soil. *Plant Soil* 290, 209–219. doi: 10.1007/s11104-006-9153-9

Manzoni, S., Schimel, J. P., and Porporato, A. (2009). Responses of soil microbial communities to water stress: results from a meta-analysis. *Ecology* 93, 930–938. doi: 10.1890/11-0026.1

Monga, O., Garnier, P., Pot, V., Coucheney, E., Nunan, N., Otten, W., et al. (2014). Simulating microbial degradation of organic matter in a simple porous system using the 3-D diffusion-based model MOSAIC. *Biogeosciences* 11, 2201–2209. doi: 10.5194/bg-11-2201-2014

Mueller, C. W., Kölbl, A., Hoeschen, C., Hillon, F., Heister, K., Herrmann, A. M., et al. (2012). Submicron scale imaging of soilorganic mater dynamics using NanoSIMS – From single particles to intact aggregates. *Org. Geochem.* 42, 1476–1488. doi: 10.1016/j.orggeochem.2011.06.003

Nunan, N., Ritz, K., Crabb, D., Harris, K., Wu, K., Crawford, J. W., et al. (2001). Quantification of the *in situ* distribution of soil bacteria by large scale imaging of thin sections of undisturbed soil. *FEMS Micro. Ecol.* 37, 67–77. doi: 10.1111/j.1574-6941.2001.tb00854.x

Oades, J. M. (1984). Soil organic matter and structural stability: mechanisms and implications for management. *Plant Soil* 76, 319–337. doi: 10.1007/BF022 05590

Pankhurst, C. E., Doube, B. M., and Gupta, V. V. S. R. (eds.). (1997). "Biological indicators of soil health: synthesis," *Biological Indicators of Soil Health* (Wallingford: CAB International), 419–435.

Pey, B., Cortet, J., Capowiez, Y., Nahmani, J., Watteau, F., and Schwartz, C. (2014). Technosol composition affects Lumbricus terrestris surface cast composition and production. *Ecol. Eng.* 67, 238–247. doi: 10.1016/j.ecoleng.2014.03.039

Philippot, L., Raaijmakers, J. M., Lemanceau, P., and van der Putten, W. H. (2013). Going back to the roots: the microbial ecology of the rhizosphere. *Nat. Rev. Microbiol.* 11, 789–799. doi: 10.1038/nrmicro3109

Rabot, E., Wiesmeier, M., Schlüter, S., and Vogel, H. J. (2018). Soil structure as an indicator of soil functions: a review. *Geoderma* 314, 123–137. doi: 10.1016/j.geoderma.2017.11.009

Ranjart, L., and Richaume, A. (2001). Mini-review: Quantitative and qualitative microscale distribution of bacteria in soil. *Res. Microbiol.* 152, 707–716. doi: 10.1016/S0923-2508(01)01251-7

Ritz, K. (2011). "*In situ* visualization of soil biota," in *The Architecture and Biology of Soils: Life in Inner Space*, eds K. Ritz and I. Young (Croydon: CPI Group), 1–12.

Roose, T., Keyes, S. D., Daly, K. R., Carminati, A., Otten, W., Vetterlein, D., et al. (2016). Challenges in imaging and predictive modeling of rhizosphere processes. *Plant Soil* 407, 9–38. doi: 10.1007/s11104-016-2872-7

Rossi, F., Potrafka, R. M., Pichel, F. G., and De Philippis, R. (2012). The role of exopolysaccharides in enhancing hydraulic conductivity of biological soil crusts. *Soil Biol. Biochem.* 46, 33–40. doi: 10.1016/j.soilbio.2011.10.016

Saad, R. F., Kobaissi, A., Machinet, G., Villemin, G., Echevarria, G., and Benizri, E. (2017). Crop rotation associating a legume and the nicckel hyperaccumulator Alyssum murale improves the structure and biofunctioning of an ultramafic soil. *Ecol. Res.* 645, 380–392. doi: 10.1007/s11284-017-1526-4

Séré, G., Schwartz, C., Ouvrard, S., Renat, J. C., Watteau, F., Villemin, G., et al. (2010). Early pedogenic evolution of constructed Technosols. *J. Soils Sediments* 10, 1246–1254. doi: 10.1007/s11368-010-0206-6

Stotzky, G. (1986). "Influence of soil mineral colloids on metabolic processes, growth, adhesion and ecology of microbes and viruses," in *Interactions of Soils Minerals With Natural Organics and Microbes*, ed P. M. Huang and M. Schnitzer (Madison, WI), 305–428.

Tecon, R., and Or, D. (2017). Biophysical processes supporting the diversity of microbial life in soil. *FEMS Microbiol. Rev.* 39, 599–623. doi: 10.1093/femsre/fux039

Tiessen, H., and Stewart, B. (1988). Light and electron microscopy of stained microaggregates: the role of organic matter and microbes in soil aggregation. *Biogeochemistry* 5, 312–322. doi: 10.1007/BF02180070

Tisdall, J. M., and Oades, J. M. (1982). Organic matter and water-stable aggregates in soils. *J. Soil Sci.* 33, 141–163. doi: 10.1111/j.1365-2389.1982.tb01755.x

Vidal, A. (2016). The fate of ^{13}C labelled root and shoot litter in soil and earthworm casts: a multidisciplinary approach based on mesocosm experiment.

Thesis, Pierre et Marie Curie University. Available online at: http://www.theses. fr/2016PA066264

Vidal, A., Remusat, L., Watteau, F., Derenne, S., and Quenea, K. (2016). Incorporation of ^{13}C labelled shoot residues in Lumbricus terrestris casts: a combination of transmission microscopy and nanoscale secondary ion mass spectrometry. *Soil Biol. Biochem.* 93, 8–16. doi: 10.1016/j.soilbio.2015.10.018

Vos, M., Wolf, A. B., Jennings, S. J., and Kowalchuk, G. A. (2013). Micro-scale determinants of bacterial diversity in soil. *FEMS Microbiol. Rev.* 37, 936–954. doi: 10.1111/1574-6976.12023

Waisel, Y., Eshel, A., and Kafkafi, U. (2002). *Plant Roots – The Hidden Half* New York, NY; Basel: Marcel Dekker Inc., 1136.

Watteau, F., Huot, H., Séré, G., Begin, J. C., Rees, F., Schwartz, C., et al. (2018). Micropedology to reveal pedogenetic processes in technosols. *SJSS.* 8, 148–163. doi: 10.3232/SJSS.2018.V8.N2.02

Watteau, F., and Villemin, G. (2001). Ultrastructural study of the biogeochemical cycle of silicon in the soil and litter of a temperate forest. *Eur. J. Soil Sci.* 52, 385–396. doi: 10.1046/j.1365-2389.2001.00391.x

Watteau, F., and Villemin, G. (2011). Characterization of organic matter microstructure dynamics during co-composting of sewage sludge, barks and green waste. *Bioresource Technol.* 102, 9313–9317. doi: 10.1016/j.biortech.2011.07.022

Watteau, F., Villemin, G., Bartoli, F., Schwartz, C., and Morel, J. L. (2012). 0–20 μm aggregate typology based on the nature of aggregative organic materials in a cultivated silty topsoil. *Soil Biol. Biochem.* 4, 103–114. doi: 10.1016/j.soilbio.2011.11.021

Watteau, F., Villemin, G., Burtin, G., and Jocteur-Monrozier, L. (2006). Root impact on the stability and constitution of the fine organo-mineral associations in a maize cultivated soil. *Eur. J. Soil Sci.* 57, 247–257. doi: 10.1111/j.1365-2389.2005.00734.x

Watteau, F., Villemin, G., Ghanbaja, J., Genet, P., and Pargney, J. C. (2002). *In situ* ageing of fine beech roots (*Fagus sylvatica*) assessed by transmission electron microscopy and electron energy loss spectroscopy: description of microsites and evolution of polyphenolic substances. *Biol. Cell* 94, 55–63. doi: 10.1016/S0248-4900(02)01182-6

Weber, B., Büdel, B., and Belnap, J., (eds.). (2016). "Biological soil crusts: an organizing principle in drylands," in *Ecological Studies* (Springer), 3–541.

Williamson, K. E., Furhrmann, J. J., Wommack, K. E., and Radosevich, M. (2017). Viruses in soil ecosystems: an unknown quantity within an unexplored territory. *Ann. Rev. Vir.* 4, 201–219. doi: 10.1146/annurev-virology-101416-041639

WRB, J. (2014). *World Reference Base for Soil Ressource*. World Soil Resources Reports No. 106. Rome: FAO.

Wu, K., Van Dijke, M. I. J., Couples, G. D., Jiang, Z., Ma, J., Sorbie, K. S., et al. (2006). 3D stochastic modelling of heterogeneous porous media – applications to reservoir rocks. *Transp. Porous Media* 65, 443–467. doi: 10.1007/s11242-006-0006-z

Spatial Structuring of Cellulase Gene Abundance and Activity in Soil

Jinlyung Choi[1], Elizabeth Bach[2,3], Jaejin Lee[1], Jared Flater[1], Shane Dooley[1], Adina Howe[1†] and Kirsten S. Hofmockel[2,4*†]*

[1] Department of Agricultural and Biosystems Engineering, Iowa State University, Ames, IA, United States, [2] Department of Ecology, Evolution, and Organismal Biology, Iowa State University, Ames, IA, United States, [3] Department of Biology and School of Global Environmental Sustainability, Colorado State University, Fort Collins, CO, United States, [4] Environmental Molecular Sciences Laboratory, Pacific Northwest National Laboratory, Richland, WA, United States

Microbial mechanisms controlling cellulose degradation in soil habitats remains a critical knowledge gap in understanding and modeling terrestrial carbon-cycling. We investigated land management and soil micro-habitat influences on soil bacterial communities and distribution of cellulose-degrading enzyme genes in three bioenergy cropping systems (corn, prairie, and fertilized prairie). Within the soil, aggregates have been examined as potential micro- habitats with specific characteristics influencing resource partitioning and regulation, thus we also investigated genes associated with cellulose degradation within soil aggregate fractions from the fertilized prairie system. Soil bacterial communities and carbon-cycling gene presence varied across land management and soil microhabitats. Examination of genes specifically involved in cellulose-degradation pathways showed high levels of redundancy across the bioenergy cropping systems, but medium macroaggregates (1,000–2,000 μm) supported greater cellulose-degrading enzyme gene abundance than other aggregate fractions and whole soil. In medium aggregates, the enriched cellulose-degrading genes were most similar to genes previously observed in Actinobacteria. These findings represent gentic potential only, and our previous work on the same samples found elevated cellulase exo-enzyme activity in microaggregates. These contrasting results emphasize the importance of measuring community, functional genes, and metabolic potentials in a coordinated manner. Together, these data indicate that location within the soil matrix matters. Overall, our results indicate that soil aggregate environments are hot-spots that select for organisms with functional attributes like cellulose degradation, and future work should further explore micro-environmental factors that affect realized C-cycling processes.

Keywords: microbiome, carbon cycling, metagenomes, aggregates, prairie, bioenergy

INTRODUCTION

Cellulose comprises 40–60% of plant residues (Lynd et al., 2002), contributing more than 70×10^9 Mg of carbon (C) annually to the global C budget (Paul, 2014). Cellulose is a simple polymer that forms insoluble crystalline microfibrils that are highly resistant to enzymatic hydrolysis (Béguin and Aubert, 1994). Therefore, a suite of enzymes is involved in depolymerizing cellulose into molecules that can be assimilated by soil microbes (Lynd et al., 2002; **Figure 1A**). Generally

cellulose degraders are not able to produce the full suite of enzymes involved in breaking down cellulose; therefore, it is considered a community process. Simultaneously, across and within phyla, multiple genes encode for similar enzymatic processes, contributing to functional redundancy within a microbial community. For example, many polysaccharide degraders harbor multiple glycoside hydrolases, promoting the coordinated activity among multiple enzymes (Wilson, 2011; Berlemont and Martiny, 2015). Further, many organisms have the ability to degrade oligosaccharides, but few lineages have been identified with enhanced potential for complex carbohydrate decomposition (Berlemont and Martiny, 2015; Berlemont, 2017). In fact, observations of complex carbohydrate deconstruction is limited to only a few lineages of potential polysaccharide degraders, while the majority of opportunistic microbes participate indirectly by maintaining low oligosaccharide concentrations to prevent enzyme inhibition (Xu et al., 2013; Berlemont and Martiny, 2016).

Recent studies considering large-scale patterns in microbial biogeography reveal that different locations harbor microorganisms that differ in genotypic composition (Langenheder and Prosser, 2008; Hanson et al., 2012). Yet few studies have considered the influence of the soil matrix itself, which contains micro-scale environments with stable soil structures that differ in size and breadth of resources (Tisdall and Oades, 1982; Six et al., 2001). This heterogeneity in resource availability can influence community assembly and the abundance and expression of genes contributing to a specific function (Salles et al., 2009). Within the soil matrix, soil aggregates have been examined as potential microbial habitats (or community niche; Leibold, 1995), where the level of complementarity in resource niche partitioning regulates the relative abundance of functional genes with in the soil matrix. Consequently, much of what we know of soil-associated carbohydrate decomposition has stemmed from the isolation of soil microbes that have been characterized with enhanced complex carbohydrate decomposition or potential enzyme measurements of cellobiohydrolase and β-glucosidases to understand how cellulose decomposition varies across ecosystems (Sinsabaugh et al., 2008) and land management regimes (Bowles et al., 2014).

Some studies have measured the potential activity of extracellular enzymes and taxonomic diversity among soil aggregate fractions (Marx et al., 2005; Allison and Jastrow, 2006; Bailey et al., 2012; Kim et al., 2015). In a comparison of individual soil aggregates, relative abundance of bacterial family Chitinophagaceae was greater in aggregates with high β-glucosidase activity (Bailey et al., 2013), suggesting that community membership of a functional group at the micro-scale may play a role in the potential for soil carbon cycling. Further evidence for variation among soil aggregates was observed in a mollisol under corn, prairie, and fertilized prairie bioenergy cropping systems in central Iowa, where increased plant inputs in the prairies correlated with increased potential cellobiohydrolase enzyme activity and microbial biomass carbon pools (Bach and Hofmockel, 2015, 2016). Within all three bioenergy systems, total carbon was greatest in soil macroaggregate fractions

in contrast to greater potential cellobiohydrolase activity in microaggregates ($<250 \mu m$) (Bach and Hofmockel, 2016). Further exploration of the soil microbial communities in these aggregates revealed that the bacterial (16S rRNA) and fungal (ITS) communities showed greater microbial diversity and distinct microbial communities in microaggregate fractions (Bach et al., 2018), evidence of the role of microbial membership within aggregate fractions to observed differences in enzyme activity potentials.

To identify genes encoding enzymes involved in cellulose degradation and the phylogenetic distribution of their bacterial hosts across cropping systems and aggregate scales, we performed full metagenomic sequencing on whole soil from three bioenergy systems (i.e., corn, prairie, and fertilized prairie) and five soil aggregate fractions from a fertilized prairie system. The fertilized prairie soils were strategically selected to examine aggregate-scale differences because our previous work showed it supports greater extracellular enzyme activity and microbial biomass than the corn and unfertilized prairie systems (Bach and Hofmockel, 2015). We hypothesize that cellulose degradation is enhanced in prairie systems due to enriched abundance of genes encoding for key cellulose-degrading enzymes, particularly more energetically expensive endocellulases, and support more phyla contributing those genes. Further, we hypothesize that cellulose degrading genes are not evenly distributed among micro-habitats, or aggregate fractions, due to differences in the distribution of carbon among aggregates. Specifically, we expected to see more genes encoding cellulose-degrading enzymes in microaggregates, where we previously observed increased cellobiohydrolase activity (Bach and Hofmockel, 2016).

MATERIALS AND METHODS

Soil Sampling and Sequencing

Soil samples were collected at the Comparison of Biofuel Systems (COBS) research site at Iowa State University (Ames, IA). Replicated plots growing continuous corn (C, corn planted every year without rotation), prairie (P, prairie without fertilizer), and fertilized prairie (FP, prairie with fertilizer, 84 Kg N ha^{-1}) were studied. The study site is a randomized complete block design with four replicate blocks containing each treatment ($n = 12$). Three replicate soil samples (5.5 cm diameter, 10 cm deep) were collected from each plot in July, 2012. Replicate cores from each plot were pooled and physically sieved into five different aggregate sizes after collection [whole soil, large ($>2,000 \mu m$), medium ($1,000–2,000 \mu m$), small ($250–1,000 \mu m$), and micro aggregate ($<250 \mu m$)] as previously described (Bach and Hofmockel, 2014). Among the resulting 60 samples (5 fractions × 4 replicates × 3 blocks), a total of 44 samples were selected for DNA extraction for this study, including whole soil from all plots and all fractions from fertilized prairie. DNA was extracted using PowerSoil®-htp DNA Isolation Kit (MoBio, Carlsbad, CA, United States) as previously described (Bach et al., 2018). Paired-end metagenome libraries (read length 100 bp) were prepared and sequenced using HiSeq at Argonne National Laboratory. All 44 metagenomes are publicly available at the

FIGURE 1 | (A) Cellulose decomposition enzymes from the KEGG database. Breaking down cellulose microfibrils requires endoglucanases that randomly attack the cellulose chain (EC 3.2.1.4) and exoglucanases including cellodextrinases (EC 3.2.1.74) that cleave from the end of the cellulose chains releasing cellobiose. Cellobiohydrolases (EC 3.2.1.91) are endoglucanases that can degrade cellulose or cellodextrin to cellobiose. Finally, β-glucosidases (EC 3.2.1.21) cellobiose phosphorylase (2.4.1.20) and 6-phospho-β-glucosidase (EC 3.2.1.86) release glucose from cellobiose and other soluble cellodextrins. **(B)** Abundance of reads encoding for KEGG enzymes in corn (C), unfertilized prairie (P), and fertilized prairie (FP) metagenomes. **(C)** Abundance of reads encoding for KEGG enzymes in aggregates from fertilized prairie (FP) metagenomes. WS, whole soil; LM, large; MM, medium; SM, small; Micro, micro aggregates. Normalized counts estimated with DeSeq2 package.

MG-RAST Metagenomics Analysis Server (https://www.mg-rast.org/mgmain.html?mgpage=project&project=mgp13620), **Supplementary Table 1**). In total, this study represents a total of 3.1 billion reads (average 71 million reads per sample).

Analysis of Metagenomes

Sequences were aligned to the KEGG prokaryote and eukaryote protein database (obtained January 17, 2017) using Diamond (v0.7.9.58), requiring a minimum E-value threshold of 0.001. The best-matching amino acid sequence with these criteria was selected as the KEGG protein annotation. Count data for the abundance of genes encoding for enzymes was analyzed with DESeq2 (version 1.16.1). Taxonomy associated with metagenomic reads was assigned by nucleotide homology to genes encoding enzymes in the KEGG database, requiring 97% similarity and a minimum E-value of 1e-5 (BLAST+, version 2.2.30). For estimation of taxonomy, abundances were calculated as total reads associated with an annotation normalized by the total number of reads in each metagenome. To characterize cellulose degradation, a subset of KEGG enzymes associated with cellulose decomposition were selected within the starch and sucrose metabolism pathway (Kanehisa et al., 2017), including endoglucanases (EC 3.2.1.4), β-glucosidases

(EC 3.2.1.21), 6-phospho-β-glucosidase (EC 3.2.1.86), cellobiose phosphorylase (EC 2.4.1.20), cellobiohydrolases (EC 3.2.1.91) (**Figure 1A**). Co-occurrence analysis was used to understand interactions of genes associated with cellulose decomposition. Spearman correlation coefficient values were calculated using co-occurrence software FastCoOccur (version 0.0.1) (https://github.com/germs-lab/FastCoOccur), which is based on methods previously described (Williams et al., 2014). Nodes representing genes associated with KEGG enzymes were considered significant if the Spearman's rank correlation coefficient, $\rho > 0.7$ or smaller than -0.7 and the $P < 0.01$. Visualization of networks was performed using the Force Atlas layout of Gephi software (version 0.9.2).

Statistical Analyses

All statistical analysis was performed in R v.3.4.1. Phyloseq (version 1.20.0) (McMurdie and Holmes, 2013) was used to for metagenome comparisons. All NMDS ordinations were plotted based on Bray-Curtis distances, and significance between treatments was determined based on permutational multivariate analysis of variance (PERMANOVA) using Adonis function in vegan package (version 2.4-4) (Oksanen et al., 2017). Cellulose decomposition genes that were significantly different between

treatments were determined using DESeq2 (version 1.16.1) (Love et al., 2014), requiring $p < 0.01$. All analysis associated with this study are available at https://github.com/germs-lab/cobs-study.

RESULTS

Genes Associated With Cellulose Decomposition Vary in Abundances Between Corn and Prairies

For each soil sample, a metagenome library was sequenced, and extracellular enzyme activity was measured. Specifically, carbon-degrading enzymes β- glucosidase and cellobiohydrolase were measured, and we observed greater potential activity of both in fertilized and unfertilized prairie crops compared with corn (Bach and Hofmockel, 2015, 2016). To better understand the genes associated with the observed differences in enzyme potentials, we sequenced metagenomes from the three crops (Howe et al., 2016). The microbial community membership between the corn, prairie, and fertilized prairie were compared based on the 16S rRNA gene distribution in soil metagenomes. We observed significant differences between 16S rRNA genes identified in corn and both prairie metagenomes (prairie vs corn: $p = 0.0021$, corn vs fertilized prairie: $p = 0.0001$) and between prairie and fertilized prairie ($p = 0.0173$; **Supplementary Figure 1**), suggesting distinct microbial membership among microbiomes. Comparing the distribution of all KEGG genes in the three cropping systems, we observed significant differences between corn and both prairie crop systems (prairie vs corn: $p = 0.0098$, corn vs fertilized prairie: $p = 0.0007$), but no significant differences between unfertilized and fertilized prairie metagenomes ($p = 0.4$; **Supplementary Figure 2**).

To investigate cellulose degradation in these cropping systems, we selected genes associated with the starch and sucrose metabolism pathway (KEGG map00500) and five cellulose degrading enzymes (**Figure 1A**). These enzymes were selected because of their consistent detection across soil metagenomes. Overall, genes associated with these cellulose degradation enzymes comprised only a small fraction of the soil metagenomes, ∼0.5% of total reads. Among these, genes associated with β-glucosidases (EC 3.2.1.21) were the most abundant, with an average abundance of 23,903 reads per total number of reads in fertilized prairie soil metagenomes (average, normalized), followed by endoglucanases (EC 3.2.1.4; 3,954 average reads), 6-phospho-β-glucosidase (EC 3.2.1.86; 1,481 average reads) and cellobiose phosphorylase (EC 2.4.1.20; 629 average reads) (**Figures 1B,C**). Cellulose degrading enzyme genes observed in low abundance were cellobiohydrolases (EC 3.2.1.91; 306 average reads) (**Figure 1B**). In comparison, the range of abundances of reads associated with any genes associated with a KEGG EC was 0 to 254,355, with an average of 933. Overall, the relative abundance of each cellulase gene was similar in all three cropping systems, suggesting that these genes are generally conserved within the same soil type across land management differences (**Supplementary Figure 3**). We identified the taxonomy associated with these cellulase

genes in the three cropping systems, observing that similar bacteria are associated with genetic potential for cellulose decomposition in these soils (**Supplementary Figure 4**). Overall, 25 phyla were associated with the 1,214 genes encoding the six enzymes associated with cellulose degradation (**Figure 2**). In all soils, we identified that Actinobacteria and Proteobacteria comprise the majority of phyla associated with endoglucanases (EC 3.2.1.4) and β-glucosidases (EC 3.2.1.21), while mainly Proteobacteria are associated with genes encoding for 6-phospho-β-glucosidase (EC 3.2.1.86). Cellobiohydrolases (EC 3.2.1.91) was associated with mainly Actinobacteria and Ascomycota (**Figure 2**).

Genes Associated With Cellulose Decomposition Vary in Abundances in Aggregates of Fertilized Prairie Metagenomes

To examine distribution of cellulase gene abundance within the soil matrix, four aggregate fractions and whole soil metagenomes were compared from the fertilized prairie treatment. Laboratory measures of extracellular enzyme activity across these same aggregate samples found increased cellobiohydrolase activity in microaggregates ($<250\,\mu m$) compared with other aggregate fractions (Bach and Hofmockel, 2016). To identify functional differences in aggregates, we compared KEGG genes in fertilized prairie metagenomes. In contrast to 16S rRNA gene distributions (**Supplementary Figure 5**, p-value between 0.28 and 0.79), we observed significant differences in gene abundances associated with KEGG enzymes (**Supplementary Figure 6**, medium vs other aggregates: $p < 0.05$; micro vs large: $p = 0.035$; among other aggregate: $p > 0.05$). For KEGG genes specific to cellulose degradation (**Figure 1A**), we observed consistent contributions of genes among aggregate fractions (**Supplementary Figure 7**). Further, the abundance of these genes in micro, small, and large aggregates were similar to whole soils (**Figure 1C**); however, in contrast to other aggregates, medium aggregates were observed to consistently be enriched for genes associated with enzymes in the cellulose degradation pathway ($p < 0.05$, **Figure 1C**). Specifically, we observed that genes encoding for enzymes cleaving cellobiose (EC 3.2.1.91) and subsequently D-glucose (EC 3.2.1.21, EC 2.4.1.20) were significantly enriched in medium aggregates compared to other soil fractions. Further, genes encoding for enzymes associated with extracellular cellulose degradation, specifically extracellular cellobiose (EC 3.2.1.86), were also observed in significantly greater abundances in medium aggregate soils (**Figure 1C**). This contrasts with our direct measures of extracellular cellobiose degradation, which were elevated in microaggregates (Bach and Hofmockel, 2016).

To further characterize the gene abundance differences we observed in medium aggregates, we identified the taxonomy of cellulose degradation genes observed to be significantly different in medium aggregates. In these aggregates, we observed a significantly greater abundance of genes associated with *Actinobacteria* in four cellulose decomposition enzymes [endoglucanases (EC 3.2.1.4) and β-glucosidases (EC 3.2.1.21),
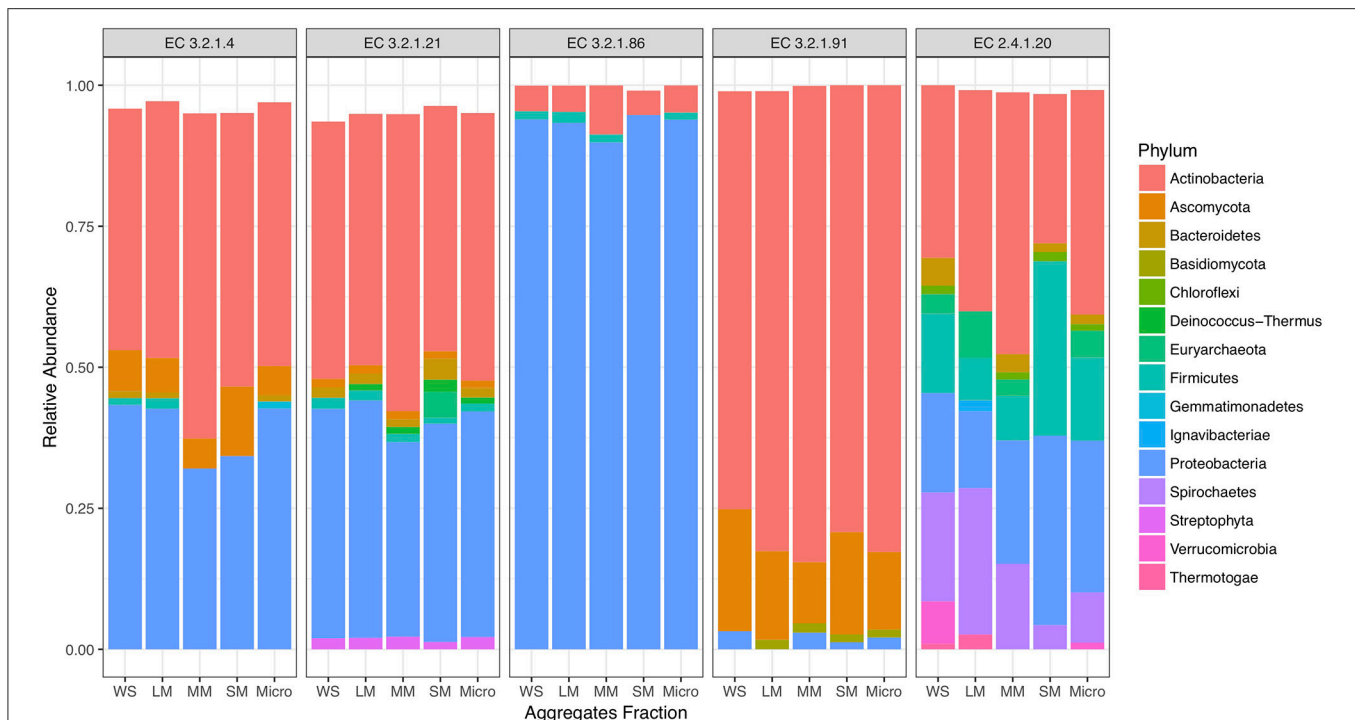
FIGURE 2 | Proportion of taxonomy associated with cellulose decomposition enzymes including endoglucanases (EC 3.2.1.4), β-glucosidases (EC 3.2.1.21), 6-phospho-β-glucosidase (EC 3.2.1.86), cellobiose phosphorylase (EC 2.4.1.20), and cellobiohydrolases (EC 3.2.1.91) in fertilized prairie aggregate metagenomes.

6-phospho-β-glucosidase (EC 3.2.1.86), cellobiohydrolases (EC 3.2.1.91), $p < 0.01$; **Figure 3**]. Overall, *Actinobacteria* comprised on average 7.5% of the taxonomy observed in soil (based on 16S rRNA gene abundances), suggesting despite its low presence in bulk soils, it may play an important role in medium aggregates. In endoglucanases (EC 3.2.1.4) and β-glucosidases (EC 3.2.1.21), genes associated with *Streptophyta* and *Basidiomycota* were observed at significantly greater abundance in medium aggregates ($p < 0.01$), suggesting that fungal organisms may play important roles in decomposing cellulose in the soil (**Figure 3**).

Genes Potentially Interacting With Cellulose Enzymes in Medium Aggregates in Fertilized Prairie Metagenomes

Broadening out beyond only cellulose decomposition enzymes, we examined the 3,546 genes within the KEGG database and found that 346 genes were observed to be significantly different between medium aggregates and whole soil. There were similar numbers of genes observed to be more or less prevalent in medium aggregates. A total of 162 genes (associated with 146 KEGG pathways) were observed enriched in medium aggregates relative to other aggregates and whole soils (**Supplementary Figure 8A**). In contrast, 184 genes (associated with 204 KEGG pathways), were less abundant in medium aggregates (**Supplementary Figure 8C**). Genes associated with similar KEGG pathways were observed as both

increased and decreased in medium aggregates. Similar results were observed in carbohydrate metabolism associated genes (**Supplementary Figures 8B,D**). In other words, we could not identify specific non-cellulose processing pathway genes that were enriched in medium aggregates. Consequently, to better understand the genes unique to medium aggregates, we next evaluated genes of enzymes that may interact with enzymes associated with cellulose degradation.

We performed a co-occurrence network analysis on all genes within metagenomes that were correlated to genes encoding enzymes in the cellulose degradation pathway (**Figure 1**). In total, we identified 192 and 121 KEGG genes that were either positively or negatively correlated with cellulase genes, respectively (**Figure 4**). We next evaluated whether these KEGG enzyme genes were significantly different (increased or decreased, $p < 0.01$) within medium aggregate metagenomes compared to other aggregates and bulk soil. A total of 54 positively-correlated KEGG genes were observed to be enriched in medium aggregate compared with whole soil (**Figure 4A**, green nodes, **Supplementary Table 2A**), and 42 negatively-correlated genes decreased abundances in medium aggregates (**Figure 4B**, red nodes, **Supplementary Table 2B**). EC class 4 (Lyases) were not observed in 54 positively-correlated genes that were enriched in medium aggregates. However all six EC classes were observed in negatively-correlated relationships with decreased abundance in medium aggregates. Among EC class 3 (Hydrolases), six of glycosidase class (EC 3.2.1.-) were observed in positive-correlations, but not observed among the negative-correlations.
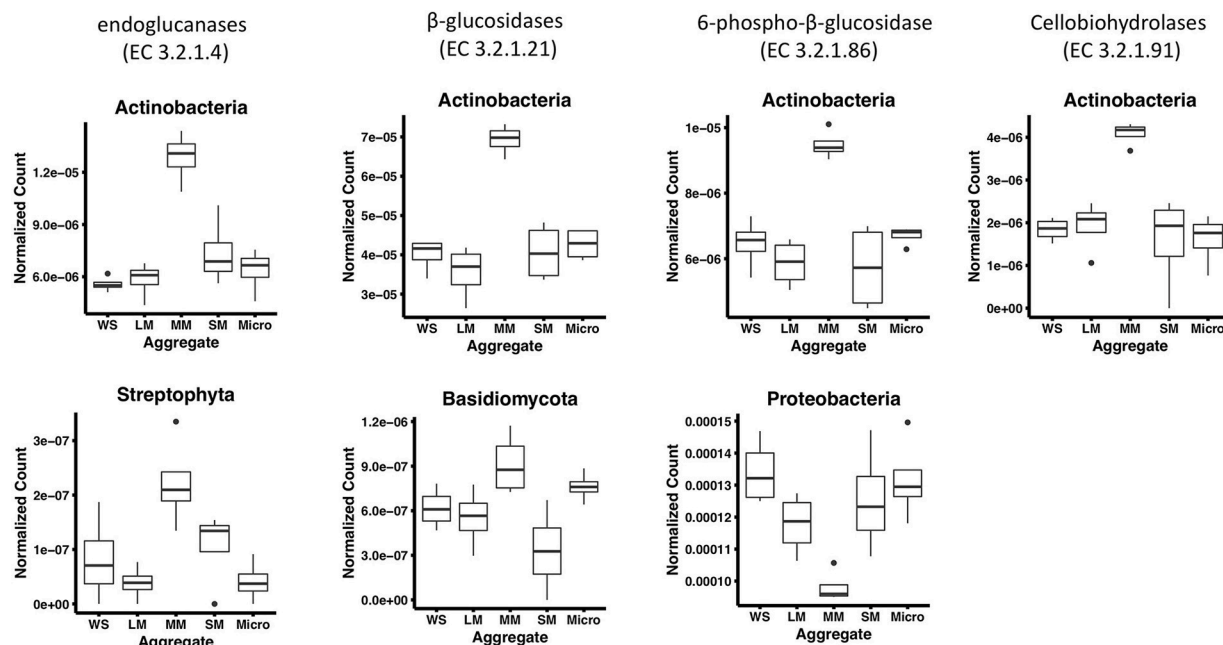
FIGURE 3 | Phyla that significantly differ among aggregates associated with cellulose decomposition enzymes in fertilized prairie aggregate metagenomes ($p < 0.01$, ANOVA). Cellobiose phosphorylase (EC 2.4.1.20) is exclude since no significantly different phyla were observed.

DISCUSSION

Microbial mechanisms controlling cellulose degradation in soil habitats remains a critical knowledge gap in understanding and modeling terrestrial C-cycling. Our metagenomic investigation of mollisols under three bioenergy cropping systems in central Iowa demonstrates that soil bacterial communities and KEGG associated genes vary across land management and soil microhabitats. Examination of genes specifically involved in cellulose-degradation pathways showed high levels of redundancy across the bioenergy cropping systems, but medium macroaggregates ($1,000–2,000\,\mu m$) supported greater cellulose-degrading enzyme gene abundance than other aggregate fractions and whole soil. In contrast, direct measures of potential cellobiohydrolase activity in these same soil samples were observed to be elevated in microaggregate fractions (Bach and Hofmockel, 2016). Hence, realized C-cycling functions like cellulose degradation do not necessarily reflect observed differences in microbial genetic potential (Frossard et al., 2012). Similar pattern is observed in higher level of taxonomic group (**Supplementary Figure 9**). Together, these data indicate that genetic potential and realized cellulase activity are redundant across bacterial taxa that respond to changes in land management but are sensitive to changes in soil microbial habitat.

Bacterial Communities and Cellulose Degradation Potential Differ Under Land Management

At an ecosystem scale, bacterial communities responded to stark differences in root input quantity and quality among the three bioenergy cropping systems. Corn systems had the least root biomass, fertilized prairie produced 8 times more root biomass than corn in 2011, and unfertilized prairie produced more than twice as much root biomass as unfertilized prairie (Dietzel et al., 2015). In addition, corn roots had a greater cellulose index than either prairie treatment, and unfertilized prairie roots had greater hemicellulose index, driven by greater concentrations of arabinose, galactose, glucose, and xylose (Rivas et al., 2014). These differences in root inputs likely contributed to our observed increased extracellular enzyme activity in both prairie systems compared with corn (Bach and Hofmockel, 2015) as well as the differences in the bacterial communities and KEGG C-cycling gene profiles among the three systems observed in this study (**Supplementary Figure 1**). However, we found genes associated with cellulose degradation pathways were relatively rare in the full metagenomes, only ~0.5% of total reads and were similarly distributed among the three cropping systems.

Across the cropping systems, there are several reasons the capacity for cellulose degradation may be highly conserved. First, these prairie plantings were only 4 years old at the time of sampling and had been managed as corn fields for many decades before the planting, so we may be observing a legacy effect on cellulose degradation capacity (Kulmatiski and Beard, 2011). Reciprocal transplant of organic matter among agricultural and natural systems detected management system effects on microbial consumption of organic matter, implying land use and organic matter inputs influence carbon decomposition (Hunting et al., 2017). Secondly, we did observe taxonomic shifts in bacterial communities among the systems, supporting several others studies showing functional redundancy
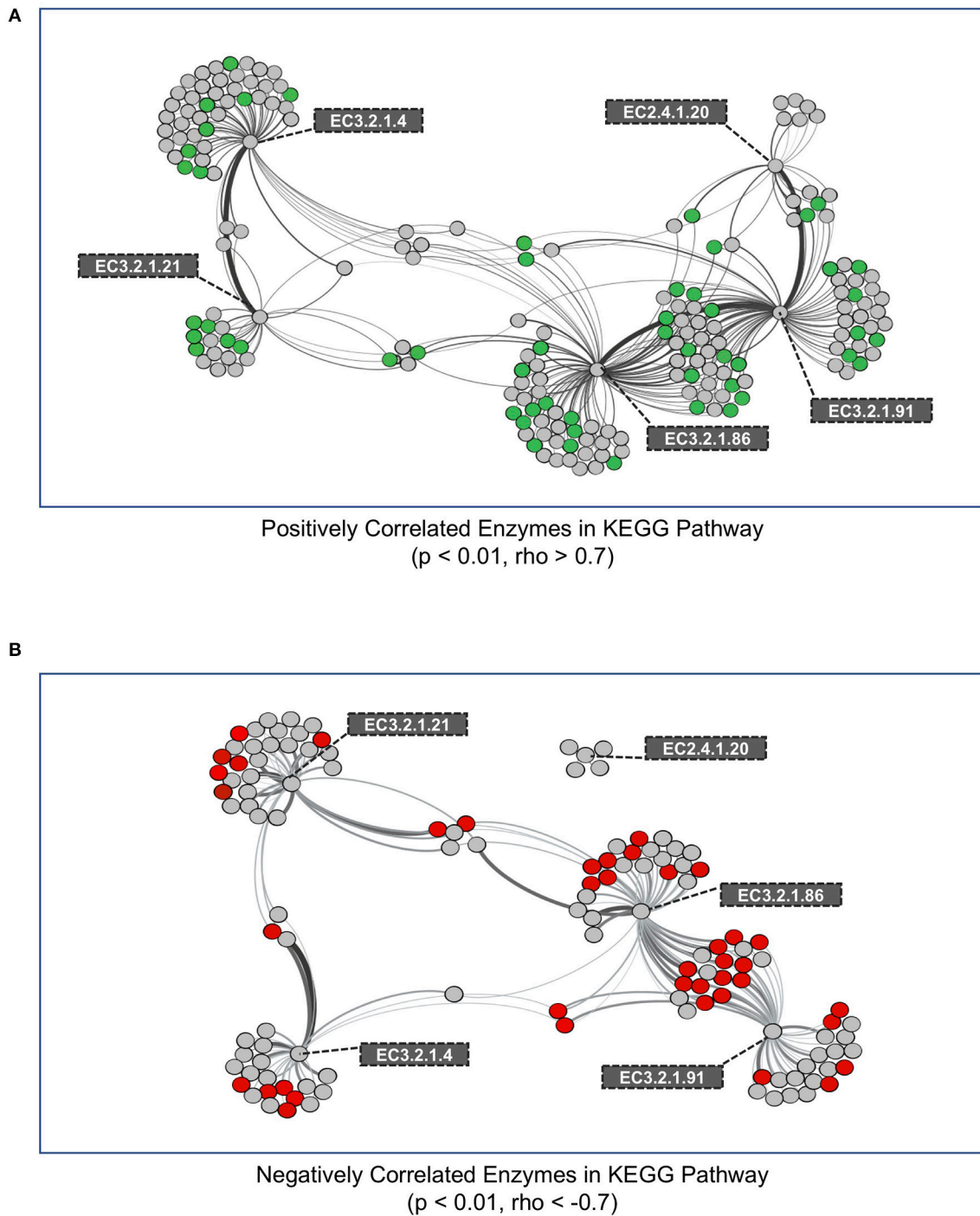
FIGURE 4 | Co-occurrence network of KEGG enzymes with significant interactions among cellulose decomposition enzymes. **(A)** Positively correlated KEGG enzymes with an enzyme in the cellulose decomposition pathway. Green nodes represent KEGG enzymes that are enriched in medium aggregates compared to whole soil. **(B)** Negatively correlated KEGG enzymes with an enzyme in the cellulose decomposition pathway. Red nodes represent KEGG enzymes that are observed in lower abundances in medium aggregate compared to whole soil. Thickness of edges represent the strength of correlation between nodes.

in bacterial and fungal communities (Fierer et al., 2013; Talbot et al., 2014). Given cellulose-degrading enzyme genes were such a small proportion of the total metagenome, it is likely these genes are hosted by a small portion of the total bacterial

community, and that portion may not be driving taxonomic shifts in the full community. Small changes in the phyla housing β-glucosidases (EC 3.2.1.21), endoglucanases (EC 3.2.1.4), 6-phospho-β-glucosidase (EC 3.2.1.86), cellobiose phosphorylase

(EC 2.4.1.20), and cellobiohydrolases (EC 3.2.1.91) indicate similar levels of functional genes were found overall in all the cropping systems, but were contributed by different bacterial community members (**Supplementary Figure 4**). Differences in cellulose input levels may also lead to differences in gene expression and/or enzyme efficiency. It is also possible that other soil organisms such as fungi, nematodes, collembolan, and/or earthworms may be the primary consumers of plant inputs, performing the initial stages of cellulose decomposition within their guts. To better understand micro-scale processes that may influence ecosystem-scale shifts in community and cellulose decomposition, we investigated microbial metagenomes from within soil aggregates.

Medium Macroaggregates Enriched in Genes Related to Cellulose Degradation

We identified medium macroaggregates as a "hot-spot" for genetic potential for cellulose degradation. Previous work on these same samples indicated microaggregates, not medium macroaggregates support elevated C-cycling enzyme activity and distinct bacterial or fungal communities(Bach and Hofmockel, 2016; Bach et al., 2018). Other studies have also found contrasting results. Allison and Jastrow (2006) also found elevated cellulase activity within microaggregates, but Kim et al. (2015) found no relationship between extracellular enzyme activity rates and microbial community composition within soil aggregates. Investigating enzyme activity within individual macroaggregates (<1,000 μm diameter), revealed higher cellulase activity in small volume macroaggregates, and microbial communities within aggregates with high β-glucosidase activity did not differ in overall microbial diversity and richness, but did differ in relative abundance of Chitinophagaceae family of bacteria (Bailey et al., 2013).

In this study, enrichment of genes encoding cellulose decomposing enzymes were predominantly associated with *Actinobacteria* and *Proteobacteria*. Previous field based experiments have noted the importance of *Actinobacteria* and *Proteobacteria* for predicting the activities of cellobiohydrolase activity (Trivedi et al., 2016). Phylogenetic investigations also support a predominance of cellulolytic capabilities among the order *Actinomycetales*, noting the trait-based advantage of filamentous morphology that preferentially enables penetration of cellulosic substrates within heterogeneous environments (Lynd et al., 2002). Enrichment of cellulose degrading *Actinobacteria* within the medium aggregates support the concept of niche differentiation, where sources of cellulose, such as plant residues, may accumulate in macroaggregates (Six et al., 2000, 2002) creating separate habitats that harbor functionally distinct communities. Here we build upon this understanding of macroaggregates along with previous evidence from the COBS field experiment by demonstrating microsite differences in cellulose degrading communities, genetic potential, and enzyme activity across soil aggregate fractions within whole soil.

Cellulose degradation is a community process involving multiple enzymes that cleave cellulose molecules from the end (exoglucanases) and within (endocellulases) of the polymer

(**Figure 1A**). Endocellulases are critical to decomposition, but energetically expensive, because cellodextrin cannot be assimilated intact, due to the large size. Yet breaking the interior bonds within a cellulose chain is essential for generating multiple fragments that can be cleaved into assimilable substrates. Our results indicate that despite the strong influence of endocellulases on cellulose decomposition, and in turn ecosystem functioning, these genes are rare, and may provide a keystone function (Chapin et al., 2000; Crowther et al., 2013). Endocellulases are much less prevalent relative to β-glucosidases, which are abundant and broadly distributed among taxa. In general, we observed that the proportion of phyla associated with cellulose degradation was consistent among soil aggregate fractions throughout the pathway of genes, including *Actinobacteria*, and *Proteobacteria* with contributions from *Basidiomycota* and *Ascomycota*.

While we observed that aggregate-specific dynamics resulted in the enrichment of genes associated with cellulose decomposition, we could not identify these trends for specific metabolic pathways. This result emphasizes the complexity of organic matter decomposition pathways in soil and the difficulty to unraveling microbial multifunctionality. Breaking down cellulose microfibrils requires endoglucanases that randomly attack the cellulose chain, but do not necessarily produce assimilable substrates (EC 3.2.1.4). Subsequently exoglucanases including cellodextrinases (EC 3.2.1.74) cleave from the end of the cellulose chains releasing cellobiose. Cellobiohydrolases (EC 3.2.1.91) are endoglucanases that can degrade cellulose or cellodextrin to cellobiose. Finally, β-glucosidases (EC 3.2.1.21) cellobiose phosphorylase (2.4.1.20) and 6-phospho-β-glucosidase (EC 3.2.1.86) release glucose from cellobiose and other soluble cellodextrins (Schimz et al., 1983; Singh and Hayashi, 1995; Lin et al., 2012; Montella et al., 2017). In addition to genes encoding for these enzymes, we found many genes that positively or negatively correlated with cellulose decomposition genes. However, the vast majority of these genes are not studied in association with cellulose decomposition. Our findings suggest hypotheses for future researcher aimed at understanding the genetic mechanisms underpinning microbial decomposition of cellulose in soil. Our results indicate that this metabolism is accomplished with diverse microbes with similar functions operating distinctively depending on their microenvironment.

CONCLUSIONS

Cellulose-degradation is an important, yet complex process involving multiple pathways and microbial species. Both natural and human-induced alterations can therefore constrain this process in numerous ways. Our deep exploration of soil metagenomes showed that bacterial communities were larger and more diverse in prairie plantings, across all aggregate sizes, and more diverse in microaggregates, regardless of land management. Presence of cellulose-degradation pathways were similar across land management regimes, but were modestly enriched in medium macroaggregate habitats. This finding contrasts our previous work on the same samples, which found elevated

cellulase exo-enzyme activity in microaggregates, emphasizing the importance of considering the potential nature of many standard soil measures. One consistent point in these data is that spatial structuring within the soil matrix differentiates the genetic and enzymatic potential as well as the distribution of organisms within the soil. Soil aggregate environments have substrate hot-spots that select for organisms with functional attributes. To identify the mechanisms driving *realized* functions *in-situ*, future work will continue to incorporate molecular information and substrate inputs that captures the pools and fluxes of metabolites and enzymes expressed by organisms under field conditions.

AUTHOR CONTRIBUTIONS

JC, EB, AH, and KH wrote the manuscript. EB performed the experiment. JC, JL, JF, and SD performed analysis. AH and KH designed the experiment and overall project.

FUNDING

ACKNOWLEDGMENTS

SUPPLEMENTARY MATERIAL

The Supplementary Material for this article can be found online at: https://www.frontiersin.org/articles/10.3389/fenvs.2018.00107/full#supplementary-material

Supplementary Figure 1 | NMDS of 16S rRNA genes from corn (C), unfertilized prairie (P), and fertilized prairie (FP) metagenomes.

Supplementary Figure 2 | NMDS of KEGG genes associated with corn (C), unfertilized prairie (P), and fertilized prairie (FP) metagenomes.

Supplementary Figure 3 | Proportion of KEGG enzyme associated with cellulose decomposition enzymes including endoglucanases (EC 3.2.1.4), β-glucosidases (EC 3.2.1.21), 6-phospho-β-glucosidase (EC 3.2.1.86), cellobiose phosphorylase (EC 2.4.1.20), and cellobiohydrolases (EC 3.2.1.91) in three bioenergy crops (CC, corn; P, prairie; FP, fertilized prairie).

Supplementary Figure 4 | Proportion of taxonomy associated with cellulose decomposition enzymes including endoglucanases (EC 3.2.1.4), β-glucosidases (EC 3.2.1.21), 6-phospho-β-glucosidase (EC 3.2.1.86), cellobiose phosphorylase (EC 2.4.1.20), and cellobiohydrolases (EC 3.2.1.91) in three bioenergy crops (CC, corn; P, prairie; FP, fertilized prairie). Phylum comprising <1% of the total community abundance were removed.

Supplementary Figure 5 | NMDS of 16S rRNA genes in metagenomes from aggregate fractions and whole soil of fertilized prairie metagenomes. (WS, whole soil; LM, large; MM, medium; SM, small; MM, micro aggregates).

Supplementary Figure 6 | NMDS of KEGG genes in aggregate fractions and whole soil of fertilized prairie metagenomes. (WS, whole soil; LM, large; MM, medium; SM, small; MM, micro aggregates).

Supplementary Figure 7 | Proportion of KEGG enzyme associated with cellulose decomposition enzymes including endoglucanases (EC 3.2.1.4), β-glucosidases (EC 3.2.1.21), 6-phospho-β-glucosidase (EC 3.2.1.86), cellobiose phosphorylase (EC 2.4.1.20), and cellobiohydrolases (EC 3.2.1.91) in aggregate fractions and whole soil. (WS, whole soil; LM, large; MM, medium; SM, small; MM, micro aggregates).

Supplementary Figure 8 | All enzymes significantly increased **(A)** or decreased **(B)** in abundance in medium aggregates relative to other soil metagenomes. Enzymes associated with carbohydrate metabolism increased **(C)** or decreased **(D)** in abundance in medium aggregates relative to other soil metagenomes. Z-score represents distribution of a numerical measurement of a value's relationship to the mean.

Supplementary Figure 9 | Proportion of taxonomy associated with cellulose decomposition enzymes including endoglucanases (EC 3.2.1.4), β-glucosidases (EC 3.2.1.21), 6-phospho-β-glucosidase (EC 3.2.1.86), cellobiose phosphorylase (EC 2.4.1.20), and cellobiohydrolases (EC 3.2.1.91) in aggregate fractions and whole soil. (WS, whole soil; LM, large; MM, medium; SM, small; MM, micro aggregates). Phylum comprising <1% of the total community abundance were removed.

Supplementary Table 1 | Summary of metagenomes used in this study. Aggregate fractions included whole soil (WS), large (>2,000 μm, LM), medium (1,000–2,000 μm, MM), small (250–1,000 μm, SM), and micro aggregate (<250 μm, micro) sieved fractions.

Supplementary Table 2 | All enzymes significantly positively and negatively correlated with cellulose decomposition enzymes in medium aggregates.

REFERENCES

Allison, S. D., and Jastrow, J. D. (2006). Activities of extracellular enzymes in physically isolated fractions of restored grassland soils. *Soil Biol. Biochem.* 38, 3245–3256. doi: 10.1016/j.soilbio.2006.04.011

Bach, E. M., and Hofmockel, K. S. (2014). Soil aggregate isolation method affects measures of intra-aggregate extracellular enzyme activity. *Soil Biol. Biochem.* 69, 54–62. doi: 10.1016/j.soilbio.2013.10.033

Bach, E. M., and Hofmockel, K. S. (2015). Coupled carbon and nitrogen inputs increase microbial biomass and activity in prairie bioenergy systems. *Ecosystems* 18, 417–427. doi: 10.1007/s10021-014-9835-8

Bach, E. M., and Hofmockel, K. S. (2016). A time for every season: soil aggregate turnover stimulates decomposition and reduces carbon loss in grasslands managed for bioenergy. *GCB Bioenergy* 8, 588–599. doi: 10.1111/gcbb.12267

Bach, E. M., Williams, R. J., Hargreaves, S. K., Yang, F., and Hofmockel, K. S. (2018). Greatest soil microbial diversity found in micro-habitats. *Soil Biol. Biochem.* 118, 217–226. doi: 10.1016/j.soilbio.2017.12.018

Bailey, V. L., Bilskis, C. L., Fansler, S. J., McCue, L. A., Smith, J. L., and Konopka, A. (2012). Measurements of microbial community activities in individual soil macroaggregates. *Soil Biol. Biochem.* 48, 192–195. doi: 10.1016/j.soilbio.2012.01.004

Bailey, V. L., Fansler, S. J., Stegen, J. C., and McCue, L. A. (2013). Linking microbial community structure to β-glucosidic function in soil aggregates. *ISME J.* 7, 2044–2053. doi: 10.1038/ismej.2013.87

Béguin, P., and Aubert, J. P. (1994). The biological degradation of cellulose. *FEMS Microbiol. Rev.* 13, 25–58. doi: 10.1111/j.1574-6976.1994.tb00033.x

Berlemont, R. (2017). Distribution and diversity of enzymes for polysaccharide degradation in fungi. *Sci. Rep.* 7:222. doi: 10.1038/s41598-017-00258-w

Berlemont, R., and Martiny, A. C. (2015). Genomic potential for polysaccharide deconstruction in bacteria. *Appl. Environ. Microbiol.* 81, 1513–1519. doi: 10.1128/AEM.03718-14

Berlemont, R., and Martiny, A. C. (2016). Glycoside hydrolases across environmental microbial communities. *PLoS Comput. Biol.* 12:e1005300. doi: 10.1371/journal.pcbi.1005300

Bowles, T. M., Acosta-Martínez, V., Calderón, F., and Jackson, L. E. (2014). Soil enzyme activities, microbial communities, and carbon and nitrogen availability in organic agroecosystems across an intensively-managed agricultural landscape. *Soil Biol. Biochem.* 68, 252–262. doi: 10.1016/j.soilbio.2013.10.004

Chapin, F. S., Zavaleta, E. S., Eviner, V. T., Naylor, R. L., Vitousek, P. M., Reynolds, H. L., et al. (2000). Consequences of changing biodiversity. *Nature* 405, 234–242. doi: 10.1038/35012241

Crowther, T. W., Stanton, D. W. G., Thomas, S. M., A'Bear, A. D., Hiscox, J., Jones, T. H., et al. (2013). Top-down control of soil fungal community composition by a globally distributed keystone consumer. *Ecology* 94, 2518–2528. doi: 10.1890/13-0197.1

Dietzel, R., Jarchow, M. E., and Liebman, M. (2015). Above- and belowground growth, biomass, and nitrogen use in maize and reconstructed prairie cropping systems. *Crop Sci.* 55, 910–923. doi: 10.2135/cropsci2014.08.0572

Fierer, N., Ladau, J., Clemente, J. C., Leff, J. W., Owens, S. M., Pollard, K. S., et al. (2013). Reconstructing the microbial diversity and function of pre-agricultural tallgrass prairie soils in the United States. *Science* 342, 621–624. doi: 10.1126/science.1243768

Frossard, A., Gerull, L., Mutz, M., and Gessner, M. O. (2012). Disconnect of microbial structure and function: enzyme activities and bacterial communities in nascent stream corridors. *ISME J.* 6, 680–691. doi: 10.1038/ismej.2011.134

Hanson, C. A., Fuhrman, J. A., Horner-Devine, M. C., and Martiny, J. B. H. (2012). Beyond biogeographic patterns: processes shaping the microbial landscape. *Nat. Publ. Group* 10, 497–506. doi: 10.1038/nrmicro2795

Howe, A., Yang, F., Williams, R. J., Meyer, F., and Hofmockel, K. S. (2016). Identification of the core set of carbon-associated genes in a bioenergy grassland soil. *PLoS ONE* 11:e0166578. doi: 10.1371/journal.pone.0166578

Hunting, E. R., Barmentlo, S. H., Schrama, M., van Bodegom, P. M., Zhai, Y., and Vijver, M. G. (2017). Agricultural constraints on microbial resource use and niche breadth in drainage ditches. *PeerJ* 5:e4175. doi: 10.7717/peerj.4175

Kanehisa, M., Furumichi, M., Tanabe, M., Sato, Y., and Morishima, K. (2017). KEGG: new perspectives on genomes, pathways, diseases and drugs. *Nucl. Acids Res.* 45, D353–D361. doi: 10.1093/nar/gkw1092

Kim, H., Nunan, N., Dechesne, A., Juarez, S., and Grundmann, G. (2015). The spatial distribution of exoenzyme activities across the soil micro-landscape, as measured in micro- and macro-aggregates, and ecosystem processes. *Soil Biol. Biochem.* 91, 258–267. doi: 10.1016/j.soilbio.2015.08.042

Kulmatiski, A., and Beard, K. H. (2011). Long-term plant growth legacies overwhelm short-term plant growth effects on soil microbial community structure. *Soil Biol. Biochem.* 43, 823–830. doi: 10.1016/j.soilbio.2010.12.018

Langenheder, S., and Prosser, J. I. (2008). Resource availability influences the diversity of a functional group of heterotrophic soil bacteria. *Environ. Microbiol.* 10, 2245–2256. doi: 10.1111/j.1462-2920.2008.01647.x

Leibold, M. A. (1995). The niche concept revisited: mechanistic models and community context. *Ecology* 76, 1371–1382. doi: 10.2307/1938141

Lin, L., Kan, X., Yan, H., and Wang, D. (2012). Characterization of extracellular cellulose-degrading enzymes from *Bacillus thuringiensis* strains. *Electron. J. Biotechnol.* 15. doi: 10.2225/vol15-issue3-fulltext-1

Love, M. I., Huber, W., and Anders, S. (2014). Moderated estimation of fold change and dispersion for RNA-seq data with DESeq2. *Genome Biol.* 15:550. doi: 10.1186/s13059-014-0550-8

Lynd, L. R., Weimer, P. J., van Zyl, W. H., and Pretorius, I. S. (2002). Microbial cellulose utilization: fundamentals and biotechnology. *Microbiol. Mol. Biol. Rev.* 66, 506–577. doi: 10.1128/MMBR.66.3.506-577.2002

Marx, M. C., Kandeler, E., Wood, M., Wermbter, N., and Jarvis, S. C. (2005). Exploring the enzymatic landscape: distribution and kinetics of hydrolytic enzymes in soil particle-size fractions. *Soil Biol. Biochem.* 37, 35–48. doi: 10.1016/j.soilbio.2004.05.024

McMurdie, P. J., and Holmes, S. (2013). phyloseq: an R package for reproducible interactive analysis and graphics of microbiome census data. *PLoS ONE* 8:e61217. doi: 10.1371/journal.pone.0061217

Montella, S., Ventorino, V., Lombard, V., Henrissat, B., Pepe, O., and Faraco, V. (2017). Discovery of genes coding for carbohydrate-active enzyme by metagenomic analysis of lignocellulosic biomasses. *Sci. Rep.* 7:42623. doi: 10.1038/srep42623

Oksanen, J., Blanchet, F. G., Friendly, M., Kindt, R., Legendre, P., McGlinn, D., et al. (2017). *Vegan: Community Ecology Package.* R package.

Paul, E. A. (2014). *Soil Microbiology, Ecology and Biochemistry.* London, UK; San Diego, CA; Waltham, MA; Oxford, UK: Academic Press.

Rivas, F. A., Tabatabai, M. A., Olk, D. C., and Thompson, M. L. (2014). Kinetics of short-term carbon mineralization in roots of biofuel crops in soils. *Biol. Fertil. Soils* 50, 527–535. doi: 10.1007/s00374-013-0870-y

Salles, J. F., Poly, F., Schmid, B., and Le Roux, X. (2009). Community niche predicts the functioning of denitrifying bacterial assemblages. *Ecology* 90, 3324–3332. doi: 10.1890/09-0188.1

Schimz, K. L., Broll, B., and John, B. (1983). Cellobiose phosphorylase (EC 2.4.1.20) of cellulomonas: occurrence, induction, and its role in cellobiose metabolism. *Arch. Microbiol.* 135, 241–249. doi: 10.1007/BF00413475

Singh, A., and Hayashi, K. (1995). Microbial cellulases: protein architecture, molecular properties, and biosynthesis. *Adv. Appl. Microbiol.* 40, 1–44. doi: 10.1016/S0065-2164(08)70362-9

Sinsabaugh, R. L., Lauber, C. L., Weintraub, M. N., Ahmed, B., Allison, S. D., Crenshaw, C., et al. (2008). Stoichiometry of soil enzyme activity at global scale. *Ecol. Lett.* 11, 1252–1264. doi: 10.1111/j.1461-0248.2008.01245.x

Six, J., Conant, R. T., Paul, E. A., and Paustian, K. (2002). Stabilization mechanisms of soil organic matter: implications for C-saturation of soils. *Plant Soil* 241, 155–176. doi: 10.1023/A:1016125726789

Six, J., Elliott, E. T., and Paustian, K. (2000). Soil macroaggregate turnover and microaggregate formation: a mechanism for C sequestration under no-tillage agriculture. *Soil Biol. Biochem.* 32, 2099–2103. doi: 10.1016/S0038-0717(00)00179-6

Six, J., Guggenberger, G., Paustian, K., Haumaier, L., Elliott, E. T., and Zech, W. (2001). Sources and composition of soil organic matter fractions between and within soil aggregates. *Eur. J. Soil Sci.* 52, 607–618. doi: 10.1046/j.1365-2389.2001.00406.x

Talbot, J. M., Bruns, T. D., Taylor, J. W., Smith, D. P., Branco, S., Glassman, S. I., et al. (2014). Endemism and functional convergence across the North American soil mycobiome. *Proc. Natl. Acad. Sci. U.S.A.* 111, 6341–6346. doi: 10.1073/pnas.1402584111

Tisdall, J. M., and Oades, J. M. (1982). Organic matter and water-stable aggregates in soils. *Eur. J. Soil Sci.* 33, 141–163. doi: 10.1111/j.1365-2389.1982.tb01755.x

Trivedi, P., Delgado-Baquerizo, M., Anderson, I. C., and Singh, B. K. (2016). Response of soil properties and microbial communities to agriculture: implications for primary productivity and soil health indicators. *Front. Plant Sci.* 7:990. doi: 10.3389/fpls.2016.00990

Williams, R. J., Howe, A., and Hofmockel, K. S. (2014). Demonstrating microbial co-occurrence pattern analyses within and between ecosystems. *Front. Microbiol.* 5:358. doi: 10.3389/fmicb.2014.00358

Wilson, D. B. (2011). Microbial diversity of cellulose hydrolysis. *Curr. Opin. Microbiol.* 14, 259–263. doi: 10.1016/j.mib.2011.04.004

Xu, Y., Tiago Guerra, L., Li, Z., Ludwig, M., Charles Dismukes, G., and Bryant, D. A. (2013). Altered carbohydrate metabolism in glycogen synthase mutants of *Synechococcus* sp. strain PCC 7002: cell factories for soluble sugars. *Metabol. Eng.* 16, 56–67. doi: 10.1016/j.ymben.2012.12.002

Bacterial Extracellular Polymeric Substances Amplify Water Content Variability at the Pore Scale

Yi-Syuan Guo[1], Jessica M. Furrer[2], Andrea L. Kadilak[1], Hector F. Hinestroza[2], Daniel J. Gage[3], Yong Ku Cho[1] and Leslie M. Shor[1,4,5]*

[1] Department of Chemical and Biomolecular Engineering, University of Connecticut, Storrs, CT, United States, [2] Department of Physics and Engineering, Benedict College, Columbia, SC, United States, [3] Department of Molecular and Cellular Biology, University of Connecticut, Storrs, CT, United States, [4] Center for Environmental Sciences & Engineering, University of Connecticut, Storrs, CT, United States, [5] School of Chemical Engineering, The University of Adelaide, Adelaide, SA, Australia

The function of microbial communities in soil is inextricably linked with the complex physical, chemical, and biological structure of the soil itself. Pore-scale water content controls the hydraulic connectivity of microbial communities and microbes' access to aqueous and gaseous substrates. In turn, soil bacteria directly influence local moisture conditions through the secretion of extracellular polymeric substances (EPS). However, the effect of a soil's physical geometry on EPS-mediated water retention is not well understood. In this study, we systematically measured the rate and extent of water evaporation from pore structures as a function of both EPS concentration and pore size. Three different chamber types were employed: (i) glass capillary tubes (1.2 mm pore diameter) to represent a uniform macropore geometry; (ii) emulated soil micromodels (pore widths ~10 to >300 μm) to represent an aggregated sandy loam pore geometry; and (iii) microfluidic capillary arrays (uniform channels 20 μm wide) to represent a uniform micropore geometry. All chambers were initially saturated with dilute EPS solutions collected from stationary-phase *Sinorhizobium meliloti* cultures and then the infiltration of air was tracked over time. In the largest chambers, EPS concentration had no effect on the extent of evaporation or on the magnitude or variability of the evaporation rate. However, in the chambers with micropore-sized physical features, EPS concentration strongly influenced rate, extent, and variability of pore water evaporation. In micropores, higher EPS concentrations enhanced water retention and led to greater variability in pore-scale water distributions. In real soil, these phenomena could act together to promote the intermediate water contents associated with productive soil systems, and more variable pore-scale water distributions could increase microbial community diversity and the resiliency of soil systems.

Keywords: extracellular polysaccharide, evaporation, micromodel, microfluidics, rhizosphere soil, soil aggregate, soil moisture

INTRODUCTION

Soil microbes strongly influence the productivity and composition of terrestrial ecosystems. Microbes enhance nutrient acquisition by plants, protect plants from disease, and promote fertile, well-aggregated soils. (Barrios, 2007; van der Heijden et al., 2008). Extracellular polymeric substances (EPS) produced by soil bacteria can have a strong influence on soil moisture (Roberson and Firestone, 1992; Bais et al., 2006; Bengough, 2012; Adessi et al., 2018; Zheng et al., 2018). Plants also produce mucilage, a hydrogel similar to bacterial EPS in function. The production of hydrogels by plants and microbes contribute to the higher local water content typically found in the rhizosphere as compared with bulk soil. (Carminati et al., 2010; Moyano et al., 2013; Sadeghi et al., 2017; Aufrecht et al., 2018).

EPS promotes retention of soil moisture by at least three separate mechanisms. First, the EPS material holds moisture directly within its polymeric matrix. EPS swells and shrinks to remain saturated despite large changes in overall moisture content. As a result, organisms associated with EPS remain hydrated and maintain access to dissolved constituents (Or et al., 2007). Second, EPS promotes the formation of soil aggregates (Amellal et al., 1998; Godinho and Bhosle, 2009; Büks and Kaupenjohann, 2016; Lehmann et al., 2017). Small pores typical of intra-aggregate spaces hold water tightly, while the increased abundance of large, inter-aggregate macropores facilitates drainage, and therefore gas exchange (Donot et al., 2012; Castellane et al., 2014). Third, EPS on surfaces can modify water repellency of a soil, leading to more hydrophobic micropores that inhibit water evaporation (Ahmed et al., 2016; Cruz et al., 2017). Each of these mechanisms are discussed in more detail below.

The composition of bacterial EPS is highly dependent on bacterial species (Wingender et al., 2001; Vaningelgem et al., 2004; Schaumann et al., 2007; Mora et al., 2008) and the environmental conditions under which it is formed (McSwain et al., 2005; Zhang et al., 2014). EPS may be composed of some or all of the following: polysaccharides, proteins (both structural proteins and enzymes), extracellular DNA, lipids, and surfactants. The various components enable attachment to soil surfaces, immobilization and degradation of macromolecules for use by cells, and cell-cell communication (Flemming and Wingender, 2010). Of primary interest from a soil physics standpoint are hydrophilic exopolysaccharides such as alginate which are responsible for retention of water within the EPS matrix.

The physical and chemical microstructure of soil influences the spatial distribution of soil water. In a real aggregated soil, water tends to reside in intra-aggregate spaces where capillary forces are strongest (Albers, 2014; Sakai et al., 2015), while the larger pore spaces between aggregates are less likely to be saturated at a given matric potential. The addition of EPS has been shown to shift the water retention curve of sand or soil toward higher water contents (Chenu and Roberson, 1996; Rosenzweig et al., 2012), thereby modulating the effects of drying conditions on bacterial cells embedded in the EPS matrix.

Soil surface properties are also extremely important to soil moisture retention. The presence of hydrogels and organic matter can lead to a heterogeneous distribution of hydrophobic and hydrophilic surface chemistries. EPS produced by different bacteria was observed to either increase or decrease water repellency in incubated soil (Schaumann et al., 2007). Studies on mixed wettability (i.e., variable contact angle) in soil have shown that surface properties modulate evaporation in soil (Shokri et al., 2008). In prior work, we have shown that pore water is retained longer in micromodels with more hydrophobic surfaces compared with micromodels with identical physical geometries but more hydrophilic surfaces (Cruz et al., 2017).

In real soils, soil composition, physical structure and surface hydrophobicity vary simultaneously and the contributions of each can be difficult to decouple. To better understand the physical, chemical, and biological mechanisms contributing to microbial processes in soil we have developed emulated soil micromodels featuring a realistic sandy loam pore geometry. Deng et al. (2015) employed these experimental systems to demonstrate that a small amount of EPS produced by the soil bacterium *Sinorhizobium meliloti* acts with soil microstructure to inhibit evaporation of pore water. Later, Cruz et al. (2017) found that both aggregation state and surface wetting properties are important in pore-sale water dynamics: while surface hydrophobicity dominated pore structure in influencing the overall water evaporation rate, pore structure was key to the spatial distribution (i.e., hydraulic connectivity) of pore water, especially at intermediate saturations.

Microbes are dramatically affected by the physical and chemical properties of their microenvironment (Sheng et al., 2010; Colica et al., 2014; Harimawan and Ting, 2016). Meanwhile, microbes also have the power to alter key physical and chemical features of their microenvironment through the production of EPS. The microscale variability of real soil and the dynamic feedback between microbial processes and microscale environment features makes for a dauntingly complex system. Prior work has suggested that soil bacteria and bacterial EPS can act synergistically microscale physical features to inhibit water loss (Deng et al., 2015). It is unknown if a bacteria-free solution of EPS retains this moisture retaining function, or how EPS-mediated moisture retention is influenced by pore size.

The purpose of this study was to systematically measure EPS-mediated moisture retention for bacteria-free EPS solutions as a function of both EPS solution concentration and pore size. Emulated soil micromodels were employed to reproduce the realistic physical geometry of an aggregated sandy loam soil. We also evaluated EPS-mediated moisture retention in glass capillary tubes, representing a fine macropore regime, as well as in microfluidic capillary arrays, representing a micropore regime. Bacterial EPS solutions were prepared from EPS collected from the common soil bacterium *Sinorhizobium meliloti*. The well-described EPS structures, biosynthetic pathways, EPS mutants and sophisticated genetic tools make *S. meliloti* a useful species for these and future studies. We report that EPS concentration had no effect on pore water retention in the larger chambers with a diameter of 1.2 mm. However, in the experimental systems with pores in the micropore regime, EPS concentration had a

dramatic effect on all aspects of moisture retention. These results have important implications on elucidating the mechanisms of EPS-mediated moisture retention at the microscale and for better understanding and predicting overall function of the rhizosphere system.

MATERIALS AND METHODS

Chemicals

Granulated agar and biotin (99%) were purchased from Fisher BioReagents. $CaCl_2$, $CoCl_2$, KH_2PO_4, $MgSO_4$, NaCl, NH_4Cl, $C_4H_4O_4Na_2 \cdot 6H_2O$ were all ACS grade and purchased from Fisher Chemical. Na_2HPO_4 was USP grade and purchased from MP Biomedicals. Artificial groundwater salts including $CaSO_4$, KNO_3, KH_2PO_4, $MgSO_4$, NaCl, $NaHCO_3$ were all ACS grade and purchased from Fisher Chemical.

Preparation of EPS Solutions

EPS was produced by a model organism commonly found in the soil rhizosphere that is known to both fix nitrogen and produce EPS. *Sinorhizobium meliloti* strain Rm1021 is a quorum-sensing mutant with a natural insertion in *expR* that results in relatively low-level production of the exopolysaccharide galactoglucan (EPSII) (Pellock et al., 2002).

S. meliloti wild type strain Rm1021 was streaked onto M9 (0.2 µg mL^{-1} biotin, 0.1 mM $CaCl_2$, 0.039 nM $CoCl_2$, 22 mM KH_2PO_4, 1 mM $MgSO_4$, 40 mM Na_2HPO_4, 8.6 mM NaCl, 19 mm NH_4Cl, 0.2% succinate) agar and grown for 5 d at 30°C. Individual colonies were inoculated into 35 mL M9 media and incubated 5 d at 30°C and 300 rpm shaking. Aliquots were collected and compared to optical density of growth curves measured at 595 nm in 48 well plates (Synergy HT plate reader, BioTek, Winooski, VT) to confirm that cultures had reached stationary phase.

To harvest EPS, supernatant from stationary-phase cultures was collected by centrifugation (20 min, 2500 × g and 4°C) and filtered by 0.22-µm polyvinylidene fluoride (PVDF) syringe filters (Fisherbrand^{TM} Syringe Filters) to produce so-called "1 × M9 EPS" solution (Alasonati and Slaveykova, 2012). This solution was diluted with 3 parts deionized (DI) water to produce "0.25 × M9 EPS" solution. Both of these solutions were used in the glass capillary and emulated soil micromodel experimental systems. The 1 × M9 EPS solution had a glucose-equivalent concentration of 58 µg mL^{-1} via the anthrone-sulfuric acid assay (Morris, 1948; Mendis et al., 2016). To prepare the "5 × EPS" solution also used in the glass capillary experimental system, M9 EPS supernatant was re-suspended in aqueous ethanol solution (v/v = 75%) and dialyzed (Fisher brand Regenerated Cellulose Dialysis Tubing, 3500 Da, Fisher Scientific) against DI water for 5 d, then lyophilized (Savant^{TM} SC210-115 SpeedVac system, Thermo Scientific) to remove excess water (González et al., 1996). This purified EPS solid was then dissolved in DI water. The glucose-equivalent concentration of this solution was 290 µg mL^{-1} via the anthrone-sulfuric acid assay.

Since salt concentrations in these EPS solutions varied, solutions with different concentrations of EPS but uniform salt compositions were also prepared. Here, purified EPS solid was dissolved in artificial groundwater (AGW) to produce the "1 × EPS in AGW" (58 mg L^{-1}) and "5 × EPS in AGW" (290 mg L^{-1}) solutions used in the microcapillary array experimental system.

Experimental Systems

Three different experimental systems were used to measure EPS-mediated moisture retention as a function of pore size (**Table 1**). Glass capillary tubes with an inner diameter of 1.2 mm were used in both the Macropore Evaporative Flux Experiments and Macropore Drying Experiments (**Figure 1A**). This is the simplest experimental system where it is easy to quantify evaporation rate by the linear retreat of the air-water interface in systems large enough to see without magnification. Second, emulated soil micromodels were used in Soil Micromodel Drying Experiments to systematically control and exactly replicate a physical microstructure similar to an aggregated sandy loam soil (**Figure 1B**). Finally, microfluidic capillary arrays were used in in the Micropore Drying Experiments to measure EPS-mediated moisture retention in the micropore regime (**Figure 1C**). The details of each of these experiments and experimental systems are describe in further detail below.

Macropore Evaporative Flux Experiments

Pseudo steady state evaporative flux was measured for three different EPS solutions (0.25 × M9 EPS, 1 × M9 EPS, and 5 × EPS, see **Table 1**) in separate chambers at three RH values (nominally 42, 50, and 80%). Each humidity regime was established inside a separate round petri dish (Corning^{TM} Falcon^{TM} Bacteriological Petri Dishes with Lid) containing different amounts (2, 1, or 0 g) of $CaCl_2$. For each humidity value, 3 replicate capillary tubes were filled with each solution via 100-µL Eppendorf Pipette, then affixed to the bottom of the dish at 5 mm spacing in parallel orientation (9 capillaries per dish). Dishes were closed and the junction between top and bottom dishes was tightly wrapped with a double-layer of Scotch tape. The length of liquid remaining inside each capillary tube was recorded every few hours over 25 h using a digital microscope (Dino-Lite Edge Digital Microscope AM7115MZT, AnMo Electronics Corporation, Taiwan). The temperature and humidity sensor recorded the actual temperature and RH inside the chamber during the experiment. Chambers with target RH of 42, 50, and 80% were actually maintained at 46 ± 5.1%, 49 ± 4.2% and 80 ± 16.9% RH with corresponding temperatures of 24 ± 0.8, 24 ± 0.5 and 26 ± 0.6°C over the 25-h duration of the experiment.

We also measured the pseudo steady state evaporative flux of DI water at different relative humidities as a control. Here, 80 µL of sterile DI water was loaded into 1 mm diameter micro haematocrit capillary tubes (non-heparinized, Eisco Labs, Rochester, NY) using a pipette. Three filled capillary tubes were placed inside a large petri dish (Fisher Scientific, Hampton, NY), alongside three lengths of measuring tape to aid in tracking the progress of the air-water interface. In some cases, two 100-µL wells of saturated hygroscopic salt solution (KCl or Na_2HPO_4) were also placed inside the petri dish to maintain constant RH. Then dishes were closed and sealed with Scotch tape. The experiment was conducted at 4 RH values, with humidity

TABLE 1 | Summary of the different solutions used in each experiment including number of replicates across all relative humidity (RH) treatments.

Experiment Name	Solutions tested (total replicates)			
	Control	**Low EPS**	**Medium EPS**	**High EPS**
Macropore Evaporative Flux	DI Water (12)	0.25 × M9 EPS (9)[a]	1 × M9 EPS (9)[b]	5 × EPS (9)[c]
Macropore Drying	DI Water (3)	0.25 × M9 EPS (3)[a]	1 × M9 EPS (3)[b]	-
Soil Micromodel Drying	DI Water (18)	0.25 × M9 EPS (6)[a]	1 × M9 EPS (9)[b]	-
Micropore Drying	1 × AGW (54)[d]	-	1 × EPS in AGW (54)[d]	5 × EPS in AGW (54)[d]
	5 × AGW (54)[e]			

[a] Salt composition: 0.25 × M9 media.
[b] Salt composition: 1 × M9 media.
[c] Salt composition: no salts; purified, solid EPS dissolved in deionized water.
[d] Salt composition: 1 × artificial groundwater.
[e] Salt composition: 5 × artificial groundwater.
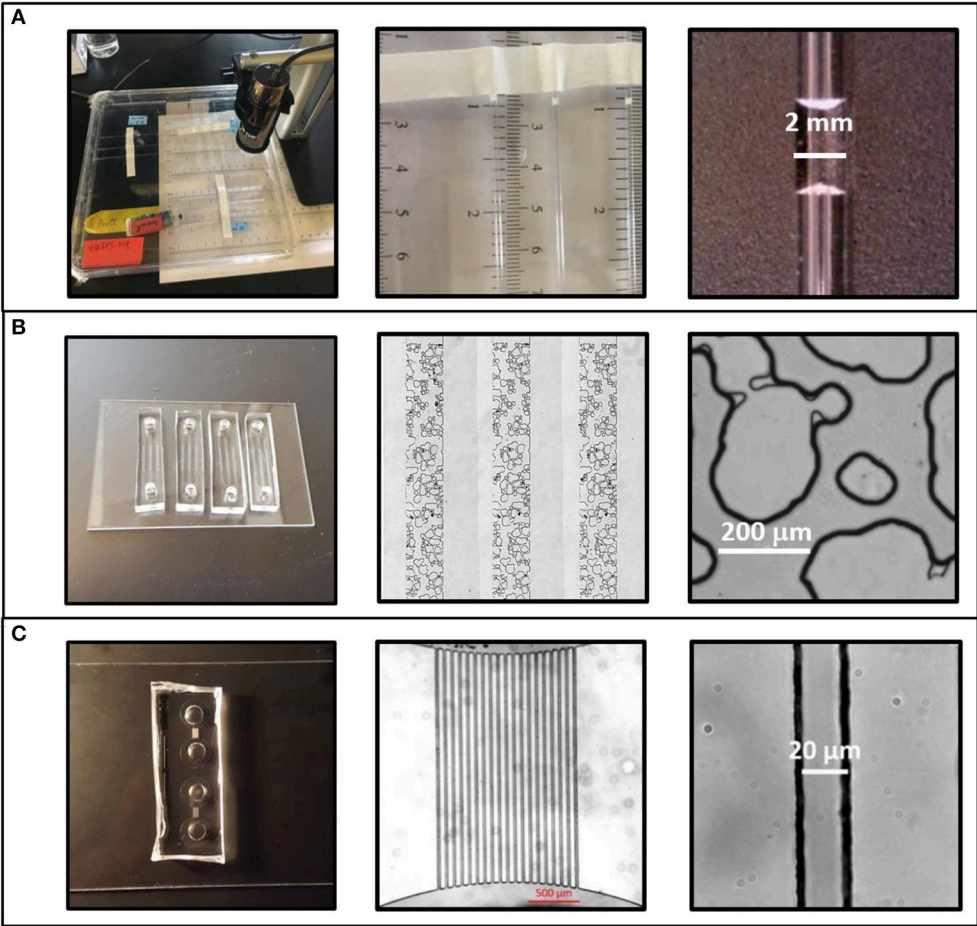
FIGURE 1 | Three experimental systems were used to test the effects of physical geometry on extracellular polymeric substance (EPS)-mediated drying behavior. **(A)** Intrinsic moisture retention behavior was measured in a macroscale regime using glass capillaries with an internal diameter of 1.2 ± 0.01 mm. **(B)** Drying behavior in soil-like geometries was measured using emulated soil micromodels. This systems features a 1 mm × 10 mm × 35 μm (w:l:h) microstructured region with a physical geometry similar to aggregated sandy loam soil. Pore widths range from 10 μm to >300 μm. **(C)** Microcapillary arrays were used for high-throughput determination of micropore regime effects. This system features bundles of 19 microchannels each measuring 20 μm × 34 μm × 2.2 mm (w:h:l).

control by different mechanisms: 42% (ambient lab RH), 95% (created with steam inside closed chamber), 85% (sealed petri dish with Na_2HPO_4), and 83% (sealed petri dish with KCl). For

the DI water controls, the position of the air-water interface was recorded either by a programmed smartphone suspended above the petri dish (every half hour), or manually approximately every

TABLE 2 | Average water flux for evaporative flux experiments performed at (a) pseudo steady state of water at four different relative humidity (RH) and at (b) three different RH for each of three different EPS solutions.

Average RH (%, mean and standard deviation)	Solution	Average flux (mg mm^{-2} h^{-1})
42 ± 0.4	DI Water	2.50 ± 0.89
83 ± 1.0		0.69 ± 0.42
85 ± 0.6		0.41 ± 0.15
95 ± 0.9		0.29 ± 0.10
46 ± 5.1	0.25 × M9 EPS[a]	0.71 ± 0.34
	1 × M9 EPS[b]	0.69 ± 0.29
	5 × EPS[c]	0.82 ± 0.27
49 ± 4.2	0.25 × M9 EPS[a]	0.69 ± 0.25
	1 × M9 EPS[b]	0.66 ± 0.18
	5 × EPS[c]	0.72 ± 0.36
80 ± 16.9	0.25 × M9 EPS[a]	0.26 ± 0.15
	1 × M9 EPS[b]	0.28 ± 0.12
	5 × EPS[c]	0.25 ± 0.13

[a]Salt composition: 0.25 × M9 media.
[b]Salt composition: 1 × M9 media.
[c]Salt composition: no salts; purified, solid EPS dissolved in deionized water.

2 h, except overnight. Smartphone images were culled down to one image every 2 h and analyzed after the conclusion of the experiment. RH was monitored and observed to be consistent (±7%) during the time domain used to compute evaporative flux.

For all evaporative flux experiments, water flux from capillary tubes in mg mm^{-2} hr^{-1} was calculated based on the moving position of the air-fluid interface and the known time interval. Here, specific gravity of the solutions was assumed to be unity since the combined concentration of all solutes is << 1% by mass. Flux calculations excluded the initial phase and included the next 20-60 h, as data were available. Values of instantaneous flux were averaged over a 4-h timespan to reduce variability in the dataset.

Macropore Drying Experiments

The rate of water loss was measured from 100 to 0% saturation for three different solutions (0.25 × M9 EPS, 1 × M9 EPS, and DI water, see **Table 1**) at one RH, nominally 65%. Here, Kimax® melting point glass capillary tubes (34500–99, length = 100 mm, I.D.:1.2 ± 0.01 mm, or similar) were filled using a MicroFil syringe needle (MF34G-5, I.D. 100 μm, O.D. 164 μm), then affixed to the bottom of a 25 × 25 cm square petri dish (Corning™ Untreated 245 mm Square BioAssay Dishes) at 5 mm spacing. The dish was closed with a double-layer of Scotch tape, and the remaining liquid inside each capillary tube was measured and recorded every few days using a digital microscope (Dino-Lite Edge Digital Microscope AM7115MZT, AnMo Electronics Corporation, Taiwan) until the tube completely dried. Temperature and humidity were 22 ± 2.5°C and 66 ± 15%, respectively, for the 2-month duration of the experiment.

Soil Micromodel Drying Experiments

Emulated soil micromodels consist of three parallel microchannels each featuring an identical 1 mm × 10 mm × 35 μm (width, length, height) microstructured region (**Figure 1B**). The microstructured region featured a pseudo-2D geometry that represents a "slice" from a real sandy loam soil. Microchannel geometry was uniform with height. Plan dimensions of "pillars" and "gaps" emulate a realistic particle size distribution and pore size distribution of an aggregated sandy loam soil. Key features of the micromodels are (1) the realistic pore scale soil geometry, and (2) precise replication of the geometry from channel to channel and experiment to experiment, and (3) the ease of directly observing the progress of the air-water interface over time. See our prior work (Deng et al., 2015; Cruz et al., 2017; Soufan et al., 2018) for additional details on the creation, validation, and use of the aggregated sandy loam pseudo-2D soil geometry.

Microfluidic devices were fabricated using standard photolithography and soft lithography methods as described previously (Deng et al., 2013). Briefly, polydimethylsiloxane (PDMS, Sylgard 184, Dow Corning, Midland, MI), a two-part silicone elastomer, was cast over a photolithography master, then cured at 60°C for 6 h, then cut out using a scalpel and punched on both side using a 4-mm biopsy punch (Integra® Miltex). PDMS castings and glass slides were cleaned with isopropyl alcohol (99%, Fisher Chemical) and methanol (Laboratory Grade, Fisher Scientific), respectively, dried at 60 °C at least 1 h, then cooled to room temperature.

After 30 s treatment with oxygen plasma, microdevices were bonded to a clean glass slide then loaded immediately with 5 μL EPS solution using a pipette. Solutions were loaded into devices immediately after plasma bonding to ensure a consistently low water repellency in all experiments, corresponding to a water-air-PDMS contact angle of ∼8° (Cruz et al., 2017). The hydrophilic surface chemistry causes the fluid added in one well to immediately wick through the emulated soil micromodels. After devices were filled with solutions, the excess fluid was removed from the well region by pipette (Eppendorf 10-μL Pipette) and the microchannel remained full. Then, devices were placed and sealed inside the control chamber, and the infiltration of the air phase was imaged over time. Rate and extent of water loss was measured in emulated soil micromodels for two different solutions (0.25 × M9 EPS and 1 × M9 EPS, see **Table 1**) at a target RH of 75%. Drying behavior for the 0.25 × M9 EPS and 1 × M9 EPS solutions is also compared with DI water using data reported previously (Cruz et al., 2017).

Air infiltration was imaged over time throughout each microstructured region using an AxioObserver Z1 AX10 inverted wide field microscope (CarlZeiss, Oberkochen, Germany) using transmitted light and a 2.5 × objective corresponding with a field of view of ∼4 × 4 mm. Overlapping frames encompassing the entire microstructured region of each device were collected every 20 min for 3 d or longer (depending on the time required to reach 0% saturation or apparent equilibrium).

Soil micromodel drying experiments were performed inside a custom-built control chamber designed to maintain consistent RH on a microscope stage. Full details on the design and

operation of the control chamber apparatus are available elsewhere (Deng et al., 2015). Briefly, the control chamber was comprised of custom-milled plastic base with that fit snugly into the stage of an AxioObserver Z1 AX10 inverted wide field microscope (CarlZeiss, Oberkochen, Germany). A gasket-lined opening in the base enabled one or more glass slides to be firmly mounted directly above the microscope objectives. A gasket-lined lid of clear polycarbonate was mounted via thumb screws to the side walls of the control chamber's base creating an open space large enough to permit air flow inside the control chamber but small enough to fit below the condenser of the inverted microscope. A second large mixing chamber was connected to the control chamber via plastic tubing. The mixing chamber contained a cigar humidifier (Cigar Oasis, Farmingdale, NY) producing a RH of ~75%. A MSR humidity sensor was placed inside the control chamber a few centimeters from the emulated soil micromodels to log both RH and temperature. The humidifier would be initiated at least 2 h prior to the start of each drying experiment to allow temperature and RH to equilibrate.

Image analysis followed a similar procedure as described previously (Cruz et al., 2017). Generally, mosaic images of the 1 mm × 1 cm microstructured region was converted into an 8-bit gray-scale image and thresholded by open source Fiji processing package ImageJ to resolve the continuous vapor interface along hydrated pore spaces or PDMS pillars (Schindelin et al., 2012). Then, the vapor area behind the vapor-liquid interface was manually filled with red pixels guided by the position of the vapor-liquid interface. Micromodel saturation (%) was calculated using the ratio of vapor area to total pore area:

$$Sat \ (\%) = (1 - \frac{A_V - A_C}{A_T - A_C}) \times 100\% \qquad (1)$$

where Sat is saturation, A_V is the vapor-phase area, A_C is the area of the channel in each image outside the 1 mm × 1 cm microstructure region, and A_T is the total pore area in the micromodel.

The start of the experiment was operationally defined as the time when the air interface had just reached the start of the microstructured region on both sides of the channel. The end of the experiment was operationally defined as three consecutive hours with no discernable change in saturation (see Cruz et al., 2017).

Micropore Drying Experiments

The microfluidic capillary array is a separate PDMS-on-glass microfluidic device comprised of bundles of 19 parallel microchannels (each channel is 20-μm wide and 35-μm high) and each microchannel bundle connects two inlet/outlet wells. The device is an "array" because the wells are arranged in the footprint of a 48-well plate to facilitate loading with a multichannel pipette and data analysis using a plate reader. The length of individual microchannels varies slightly due to curvature of the wells and averaged 2.2 mm (**Figure 1C**). The design enables rapid determination of changing saturation for 19 separate microchannels loaded simultaneously with an identical solution. Saturation changes are measured in one dimension and is visible via microscope along the entire length of all

microchannels in a bundle in a single field of view. Microcapillary array devices were produced using photolithography and soft lithography as described above.

The rate of pore water evaporation was measured in microcapillary arrays for five different solutions (5 × EPS in AGW, 1 × EPS in AGW, DI water, 1 × AGW, and 5 × AGW, see **Table 1**) at a target RH of 75%. Microcapillaries were loaded with each solution as described above. Excess fluid was removed from wells, then loaded devices were sealed inside the control chamber and the infiltration of air coupled with the evaporation of water from pores was imaged over time. Images were collected as above but at a magnification of 5 × and at a frequency of 1 min. Three replicates were performed for each solution. For each experiment, the time required to completely dry each of the 19 capillaries was recorded.

RESULTS AND DISCUSSION

Relation of Experimental Systems to Pore Regime

Three different experimental systems were employed to describe EPS-mediated moisture retention as a function of EPS concentration and pore size. The glass capillary tube experimental system is defined here as a bulk "macropore" regime by noting that pores >1,000 μm would be at least partially air-filled at a capillary pressure potential of −0.3 kPa. Field capacity (the degree of saturation after excess water has drained away) of soils ranges from about 8 to −10 kPa. Other prominent definitions for "macropore" include pores ≥ 1,000 μm (Luxmoore, 1981) or, alternatively, pores ≥ 75 μm (Brewer, 1965). These same authors define micropores as < 10 μm and <30 μm, respectively (**Table S1**). However, the most appropriate definition for macropore vs. micropore may be operational: Beven and Germann (1982) reviewed the topic and concluded that factors in addition to diameter such as pore connectivity determine preferential flow through soils.

In our simple system, bifurcated functionality from differences in structure can be understood by analyzing the differences in pore size distribution of our aggregated versus non-aggregated sandy loam emulated soil micromodel geometry (Cruz et al., 2017). The aggregated and non-aggregated micromodels have identical particle size distributions but different pore size distributions due to rearrangement of the "particles" in the photolithography mask used to create the microfluidic master. The non-aggregated geometry has a fairly uniform pore size distribution with no macropores (**Figure S1A**). By rearranging particles to create the aggregated structure, pores with diameter of 20–50 μm and pores with diameter of 200-240 μm were most increased, while pores with diameter of 60–140 μm were most decreased (**Figure S1A**). Based on the shape of the aggregated distribution we defined an operational micropore/macropore cutoff of 150 μm and fitted separate normal distributions to the pore size distributions. We find that the mean micropore is 44.8 ± 20.6 μm diameter, while the mean macropore is 212 ± 34.8 μm (**Figure S1B**). The sizes of our microfluidic capillary array (micropore regime) and glass capillary tube (macropore regime) experimental systems are consistent with these size domains.

Effect of EPS and RH on Evaporative Flux in the Macropore Regime

Evaporative flux was measured for DI water and EPS solutions in the glass capillary tube (macropore domain) experimental system. Sensitivity of evaporative flux to RH was also determined. RH was monitored throughout all evaporative flux experiments with mean and standard deviation for EPS solution evaporative flux experiment provided in **Table 2**. For the DI water experiments, RH was within ± 7% for all trials. For the EPS solution experiments, RH exhibited relatively high fluctuations. However, plotting flux against measured RH revealed there is little sensitivity of flux from EPS on RH (data not shown).

For DI water, evaporative flux ranged from 0.2 to 3.3 mg mm^{-2} hr^{-1}, depending on RH. For a given solution and RH value, evaporative flux was relatively constant over time (**Figure 2A**), indicating that a steady state was established within a few hours after drying began. Steady state fluxes for each replicate (with the initial transient values removed) were averaged together for further analysis. For DI water, the observed average evaporative flux was a strong function of RH (**Figure 2C**). The highest fluxes were observed for 42% RH, which was the driest experimental condition generated by the ambient cooling and air exchange system in the laboratory. Fluxes for 83, 85, and 95% RH were lower, with a sharp decrease in the differences between them as RH increased. Flux values were fitted with a natural log function of RH, with $R^2 = 0.99$.

For EPS solutions, evaporative flux varied from 0.1 to 1.5 mg mm^{-2} h^{-1} and exhibited a weaker dependence on RH than was observed for DI water (**Figures 2B,C**). EPS concentration had no obvious effect on magnitude of evaporative flux for a given RH. Averaged fluxes for the EPS solutions also exhibited a logarithmic dependence on RH, with $R^2 = 0.93$.

Evaporative flux from DI water or EPS solutions to the dryer air phase is dependent on the temperature of both phases (constant in our experiments), the saturation pressure of the liquid phase, and the vapor pressure in the gas phase (also dependent on the constant temperature) (Marek and Straub, 2001; Zhang et al., 2017). The pressures can be expressed as potentials, and the flux is proportional to the difference in water potential across the air-solution interface, with the magnitude determined by the transfer coefficient across the interface. The potential in the DI water phase is zero (fully saturated with no solute potential). The water potential in the air phase is given by Durner and Or (2005).

$$\psi_w = \frac{RT\rho_w}{M_w} \ln(RH) \qquad (2)$$

Our results showing a logarithmic dependence of averaged fluxes on RH can be explained by Equation (2) above, with the EPS transfer coefficient value 2-4 times lower than that for DI water.

No Evidence for EPS-Mediated Moisture Retention in the Macropore Regime

The effect of EPS concentration on moisture retention in the macropore regime was measured using glass capillary tubes loaded with either DI water, 0.25 × M9 EPS, or 1 × M9 EPS held

at 22 ± 2.5°C and at 66 ± 15% RH. Here, pore saturation (%) equals the length of the remaining water phase. In the initial stage of the drying process (0–15th day), all chambers exhibited rapid decline in saturation with little variance between replicates. From the 15 to 60th day, the drying rate declined slightly (**Figure 3A**) for all treatments, however at no point was there a statistically significant trend in the rate of moisture loss as a function of EPS concentration (Paired t-test, 2 tails: DIW vs. 0.25 × M9 EPS, $P = 0.98$; 0.25 × vs. 1 × M9 EPS, $P = 0.64$; DIW vs. 1 × M9 EPS, $P = 0.65$). All tubes reached 0% saturation on the 69th or 72nd day, with no statistically significant trend in the time required to reach 0% saturation among the treatments (unpaired t-test, 2 tails, equal variance: DIW vs. 0.25 × M9 EPS, $P = 1.0$; 0.25 × vs. 1 × M9 EPS, $P = 0.12$; DIW vs. 1 × M9 EPS, $P = 0.15$). Upon drying, the 0.25 × M9 EPS and the 1 × M9 EPS solutions left a clear white residue, corresponding to ∼0.19 and 0.22% of total capillary length, respectively. No residue was observed in the DI water capillaries, as expected.

These results show that EPS does not promote moisture retention in the macropore regime. All three solutions: 0.25 × M9 EPS and 1 × M9 EPS and DI water dried at the same rate and to the same extent.

Strong Evidence for EPS-Mediated Moisture Retention in Emulated Soil Micromodels

EPS-mediated moisture retention was also measured in emulated soil micromodels. For each experiment, two microfluidic devices each comprised of three microfluidic channels were filled with EPS solution, placed in the control chamber, and the infiltration of the air phase as pore water evaporated was imaged over time. Actual RH and temperature was 70 ± 2.5% (experiment with 0.25 × M9 EPS), 71 ± 1.3% (experiment with 1 × M9 EPS), and 76 ± 2.2% (additional experiment with 1 × M9 EPS).

In contrast with the results from the macropore drying experiments just discussed, in the emulated soil micromodels, EPS concentration clearly has a strong effect on the rate, on the extent, and on the variability of pore water retention (**Figure 3B**). Solutions identical to those used in the macropore drying experiments, above, now employed in a micropore regime slowed the drying rate by more than an order of magnitude compared with DI water. For example, in our previously-reported drying kinetics for DI water, the typical time for the saturation to drop below 50% was about 1 h (Cruz et al., 2017). The corresponding time for EPS solutions to drop below 50% saturation in similar emulated soil micromodels (same aggregated sandy loam geometry, same surface hydrophobicity) increased to about 8 h for the 0.25 × M9 EPS solution and to about 16 h for the 1 × M9 EPS solution (**Figure 3B**). Comparing the two EPS solutions, the drying rate slowed by a factor of 2. Chemically, the difference between the DI water and the 0.25 × M9 EPS solution are some simple salts and just 14.5 µg/ml glucose equivalent of EPS.

Perhaps even more important than the rate of water loss from a soil system is the quantity of water than can be held at a given
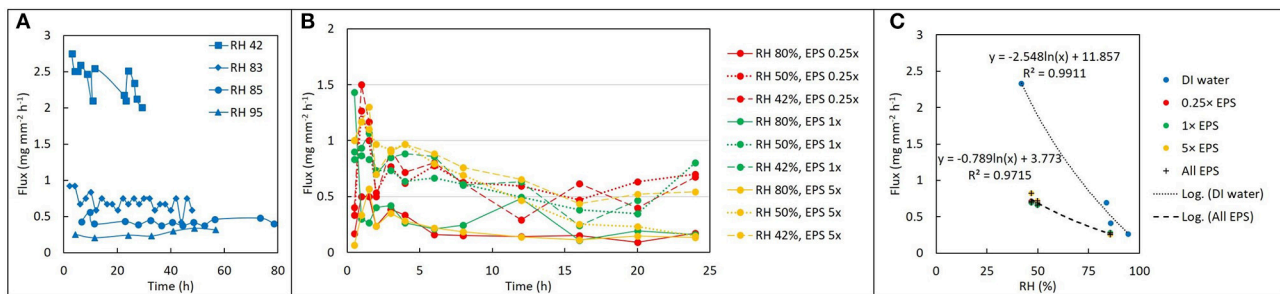
FIGURE 2 | Drying behavior as a function of EPS concentration and relative humidity (RH). **(A)** Change in water volume vs. time expressed as flux (mg mm^{-2} h^{-1}) for deionized water at four different values of RH. **(B)** Evaporative flux from different EPS solutions at different values of RH: after an initially higher rate, the flux becomes approximately constant over time. **(C)** Time-averaged flux decays exponentially with increase in RH for both water (blue) and EPS. Note that although concentration of EPS does not seem to influence the flux at a given RH, the difference between evaporative flux for EPS solutions versus deionized water varies by a factor of 2–4 times depending on RH.
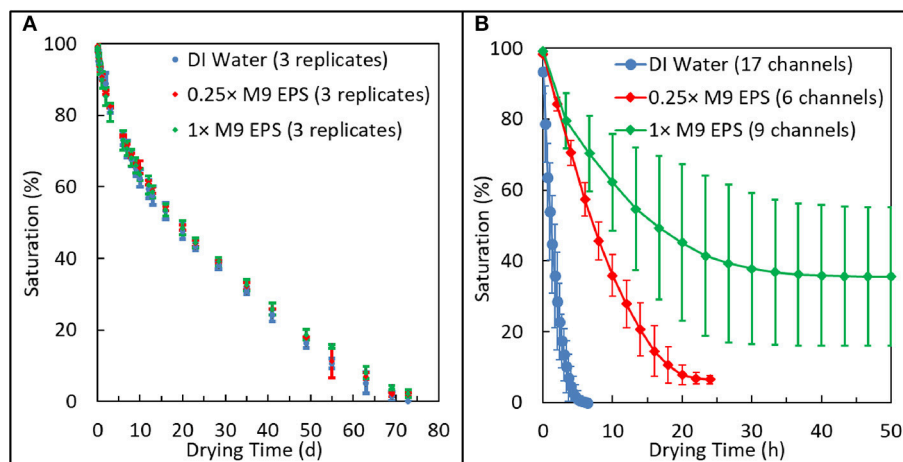
FIGURE 3 | Comparison of relative drying behavior of 1 × and 0.25 × extracellular polymeric substance (EPS) solutions suspened in M9 media at the macroscale and in an emulated soil geometry. **(A)** Glass capillary system shows all three solutions dried at similar rates and to similar extents in the macropore regime. **(B)** Emulated soil micromodel systems shows how EPS acts with microstructured physical geometry to dramatically reduce the rate and extent of drying and to enhance variability in pore-scale moisture retention.

matric potential. We define residual saturation as the saturation that persists in our experiments over time after the labile pore water has been evaporated. In similar emulated soil micromodels (same aggregated geometry, same surface hydrophobicity) at a similar RH, we previously reported a residual saturation for DI water of 0% for all 18 replicates (Cruz et al., 2017). However, with the addition of a small amount of EPS, residual saturation increased dramatically (**Figure 3B**). Average residual saturation was 6.4 ± 1.4% for the 0.25 × M9 EPS solution and 38 ± 19% for the 1 × M9 EPS solution (**Figure 3B**). Differences in residual saturation across treatments were highly significant (unpaired t-test, 2 tails, unequal variance: DIW vs. 0.25 × M9 EPS, $P <$ 0.0001; 0.25 × vs. 1 × M9 EPS, $P < 0.001$; DIW vs. 1 × M9 EPS, $P < 0.001$). These results are further evidence that small amounts of EPS act together with a microscale pore structure to limit water evaporation at narrow pore throats (Deng et al., 2015).

EPS-Mediated Variation in Microscale Water Content

Together with influencing the rate and extent of water evaporation in the micropore regime, we find strong evidence that EPS concentration also influences the variability of residual saturation (**Figure 3B**). Recall that residual saturation was 0 ± 0% for DI water ($n = 18$), while residual saturation ranged from 4.7 to 8.5% for the 0.25 × M9 EPS solution ($n = 6$) and from 15 to 74% for the 1 × M9 EPS solution (n=9). The difference in sample variance between the two EPS solution treatments was highly significant ($F = 183$, $P < 0.000001$).

Variability of residual saturation may be best understood by examining the time course of air infiltration within individual emulated soil micromodel channels. Time series of mosaic images of individual channels shows the air interface becomes "stuck" in certain positions and that this significantly impacts saturation (see **Videos V1-V6** provided in the Supplementary

Information). For example, representative mosaic images at 0, 20, and 40 h for three replicates channels loaded with the 1 × M9 EPS solution shows the air interface began at approximately the same position in all cases: flush with the "soil" structures to the left and right and just starting to infiltrate into the large central "macropore" (**Figure 4A**). However, 20 h later, Channel 1 and Channel 3 are at very nearly the same saturation of about 60% with nearly identical positions of the air-water interface, while progress of air infiltration of Channel 2 seems to be lagging well behind. These same trends can be seen graphically in the plot of saturation for these channels versus time (**Figure 4B**). At 40 h, not much additional progression on the right side of Channel 2 is observed, but infiltration has continued on the left side of Channel 2. In contrast, no infiltration on the left is observed in Channels 1 and 3, while progression from the right is observed in Channels 1 and 3. Channel 1 experiences the greatest degree of air infiltration, achieving a saturation of ~40% by 40 h compared with about 52 and 54%, respectively for Channels 3 and 2. The corresponding RH and temperature are provided in **Figure 4C**.

Although all channels exhibit similar invasion-percolation behavior as expected in emulated soil micromodels, and as observed previously (Deng et al., 2015; Cruz et al., 2017), there is substantial variation in the progression of water evaporation. Also, unlike in our prior work (Deng et al., 2015), variability cannot be attributed to potential biological growth or redistribution of bacteria in the device because here we are using a cell-free purified EPS suspension. We conclude that a combination of high interfacial velocity causing unsteady Haines jumps (Cruz et al., 2017) and solution properties of the EPS itself are contributing to this variability observed only in the micropore regime.

High-Throughput Investigation of EPS-Mediated Moisture Retention in the Micropore Regime

The soil micromodel drying experiments described above require several weeks to complete, including somewhat laborious image processing. To enhance uniformity and throughput, a microfluidic capillary array device was employed to quickly measure EPS-mediated drying resistance in the micropore regime in dozens of small capillaries simultaneously. Here, microcapillary devices were loaded with four different solutions and held at 75% RH. To avoid confounding factors from EPS and salts concentrations varying simultaneously, here, solutions with different concentrations of EPS were prepared from a salt-free lyophilized solid dissolved into a constant artificial groundwater (AGW) salt solution, as described earlier. Microcapillary drying of these 5 × and 1 × EPS in AGW solutions was also compared with 1 × and 5 × AGW alone (i.e., AGW and concentrated AGW with no EPS) to better understand the effects of salts versus EPS in mediating micropore regime drying resistance. Three replicate experiments were completed. In each replicate experiment, four separate microcapillary devices were each loaded with different solutions: 5 × EPS in AGW, 1 × EPS in AGW, 1 × AGW, or 5 × AGW. The actual RH and temperature in replicate experiments

was 75 ± 1.6%, 77 ± 0.9%, and 79 ± 1.3% and 23 ± 0.6°C, 23 ± 0.5°C, 23 ± 0.4°C, respectively.

Here, the time required to dry the entire channel was recorded from examination of microscope images collected of each microcapillary bundle every 1 min. Different EPS solutions (0×, 1 × and 5 × EPS all in 1 × AGW) dried in 22 ± 7 min, 37 ± 11 min, and 56 ± 20 min (**Figure 5**). Differences in drying time are statistically significant (Unpaired t-test, 2 tails, unequal variance: 1 × EPS vs. 0× EPS, $P < 0.000001$; 5 × EPS vs. 1 × EPS, $P < 0.000001$; 5 × EPS vs. 0× EPS, $P < 0.000001$). With higher EPS content but identical salt, the variance in drying time between these treatments increased as well. (1 × EPS vs. 0× EPS, $F = 171$, $P < 0.01$; 5 × EPS vs. 1 × EPS, $F = 171$, $P < 0.0001$; 5 × EPS vs. 0× EPS, $F = 171$, $P < 0.00001$.)

We also compared microcapillary drying time for different salt concentrations that contained no EPS. The drying time of 1 × and 5 × AGW solutions were similar and averaged 26 ± 9 min and 24 ± 10 min, respectively (**Figure S2**). There is no statistically significant difference in drying time as a function of salt concentration. There is a statistically significant difference in drying time as a function of EPS concentration.

In examining the drying time by channel, it seems apparent that the edge channels dried faster (**Figure 5**). Indeed, an analysis of relative drying rates across by channel shows that the 2 edge channels dry significantly faster than the others (data not shown). However, by pairing the data by channel and RH then comparing across solution treatments, the effect of solution type on drying time is easily determined despite variability among individual channels.

Interactions Among EPS, Salts, and Microstructure

Studies measuring evaporation of saline water from porous geometries are common in several fields, including environmental, agricultural, and engineering applications (El-Dessouky et al., 2002; Fujimaki et al., 2006). Pore structure is known to strongly influence the evaporation rate of water from soil (Norouzi Rad and Shokri, 2012; Shokri-Kuehni et al., 2017). We have shown that EPS dramatically inhibits the rate and extent of moisture loss and enhances variability of moisture content at the micropore scale. Our microfluidic capillary experiments definitively show that salts alone do not inhibit moisture loss at the micropore scale. However, salts are important for the proper function of EPS at the pore scale. As water evaporates, the local EPS and salt concentrations will be simultaneously increased, especially near the air-fluid interface. The resulting higher concentration of EPS and salt may affect the moisture distribution within the porous structure. Ionic polysaccharides are likely to interact with cations in groundwater especially divalent cations such as Ca^{2+} to form a cross-linked hydrogel structure that strongly retains moisture via hydrogen bonding and hydrophilic interactions (Fringant et al., 1996).

Both rate of water loss and the spatial distribution of water in a microenvironment are important to the function of soil systems. Rate of water loss will control the overall saturation of a soil as it dries after a rain event, while spatial distribution
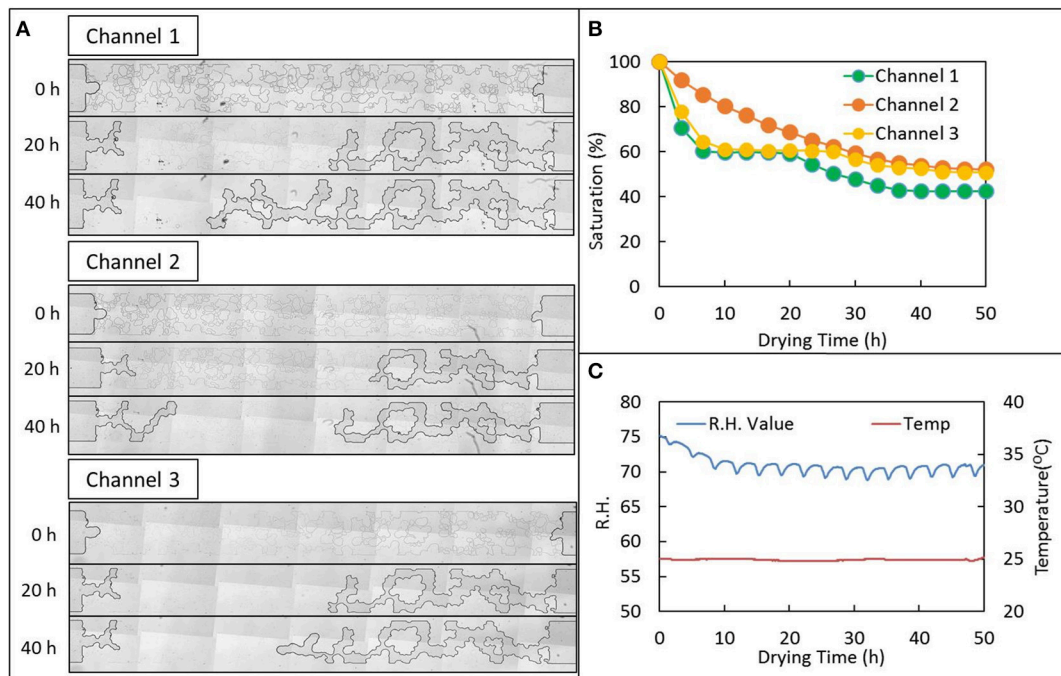
FIGURE 4 | Drying behavior of a 1 × extracellular polymeric substance (EPS) solution suspended M9 media loaded into an emulated soil micromodel geometry and held at 70-75% relative humidity (RH). **(A)** Tiled mages of individual replicate micromodel channels (see **Figure 1B**) at the operationally-defined start of the drying experiment and 20 and 40 h later. **(B)** Fraction of water remaining (saturation) for the same channels as in **(A)** vs. time. **(C)** RH and temperature recorded in the control chamber via USB recorder for the data shown in **(A,B)**. See **Supplemental Information** for movies of drying behavior.
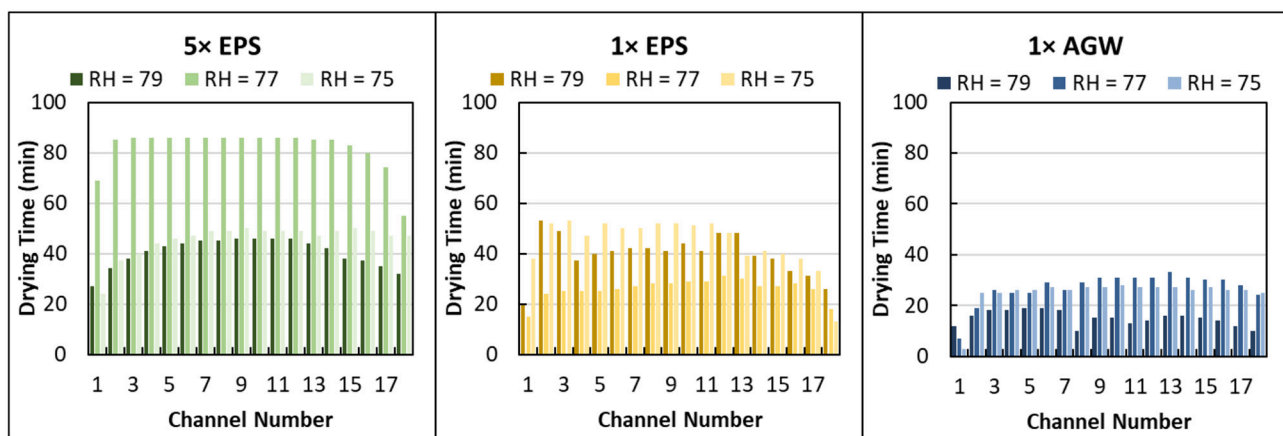
FIGURE 5 | Drying time distribution for different concentration extracellular polymeric substance (EPS) solutions suspended in artificial groundwater (AGW) in microcapillary arrays at different relative humidity (RH). Data are shown for 5 × EPS in 1 × AGW, 1 × EPS in 1 × AGW, and 1 × AGW (no EPS) at 79, 77, and 75% RH.

will determine proximity to soluble constituents in the aqueous (saturated) regions and proximity to gaseous constituents in the unsaturated regions. Position of water can therefore control whether aerobic or anaerobic conditions dominate, and if soils are net producers of greenhouse gasses. For example, Owens et al., estimated that pores $<26.8\,\mu m$ diameter remained full at a field potential of -11 kPa, which could lead to the creation of anaerobic microsites and influence overall N_2O

production (Owens et al., 2017). Microscale spatial and temporal variability of water distribution conditions is also a major factor driving diversity in soil microbial communities. Studies under a range of *in-situ* and experimental conditions have shown that hydraulic isolation caused by fragmentation of the water phase leads to higher bacterial diversity and richness (Zhou et al., 2002; Treves et al., 2003; Carson et al., 2009; Chau et al., 2011). Taxa that might otherwise compete for resources

are sequestered in disconnected water films in unsaturated soil, allowing them to coexist, but not compete, in very small volumes.

The mechanism for EPS enhancement of moisture content variability is not yet clear. One possibility is that a pore-clogging mechanism related to the precipitation of EPS or the formation of a local skin-like structure bridging narrow pore throats is responsible for reducing local water flux to near zero. Obtaining proof of this physical configuration in dilute, hydrated EPS systems is an analytical challenge. However, others have employed advanced technology, e.g., ToF-SIMS, NMR, and electron microscopy to probe the composition and microstructure of EPS within biofilms *in situ* (Marshall et al., 2006; Dohnalkova et al., 2011; Renslow et al., 2017) and found evidence for EPS structures such as fibers which could potentially reduce the water flux through the EPS matrix.

CONCLUSION

The inherent complexity of the rhizosphere makes for a fascinating system for study (Aleklett et al., 2017; Anbari et al., 2018; Borer et al., 2018). Emulated soil micromodels employed here offer complex yet reproducible and realistic physical pore geometries and the opportunity to directly observe microscale phenomena to enhance functional understanding of the soil system. In this study, relatively small quantities of EPS were found to dramatically affect drying behavior within emulated soil micromodels and at the micropore scale (but not at the macropore scale).

Soils at an intermediate saturation tend to be the most productive (Bouman and Tuong, 2001). Such soils have a mixture of water and gas-filled pore spaces, enabling organisms in soil to access both dissolved and gaseous substrates (Smith et al., 2003). The potential for EPS to *not* impede water evaporation from macropores at higher saturations yet strongly inhibit evaporation in a concentration-dependent fashion as the smaller pores empty at lower saturations is a remarkable microscale microbial process of the natural soil system. This functionality clearly promotes maintenance of the maximally-productive intermediate saturation condition over time.

Another key finding of this report is the enhancement in local variability of moisture content with EPS concentration. Taxa that might otherwise compete for resources are sequestered in disconnected water films in unsaturated soil, allowing them to coexist, but not directly compete, in very small volumes. This

could be a mechanism by which alpha diversity (in-site diversity) is maintained or enhanced in soil or the rhizosphere at larger scales, while enhancing beta diversity (between-site diversity) on the pore scale. Thus, enhanced variability of moisture, driven by bacterial synthesis of EPS, may lead to greater diversity of microbial communities and therefore greater resiliency of terrestrial ecosystems (Griffiths and Philippot, 2013). Testing the hypothesis that water film disconnections enhance these diversity indices will require careful, controlled studies and emulated soil micromodels may prove useful for such work.

AUTHOR CONTRIBUTIONS

Y-SG, JF, DG, YC, and LS created the overall concept and experiment design. Y-SG and AK designed and fabricated microfluidic devices. Y-SG, HH, and JF acquired primary data, and Y-SG, JF, and LS analyzed the data and drafted the manuscript. All authors discussed the results and contributed to the final manuscript.

ACKNOWLEDGMENTS

SUPPLEMENTARY MATERIAL

The Supplementary Material for this article can be found online at: https://www.frontiersin.org/articles/10.3389/fenvs.2018.00093/full#supplementary-material

Figure S1 | Pore size distribution of **(A)** aggregated and non-aggregated micromodel **(B)** aggregated micromodel pore geometries showing the bimodal normal distribution for miropores and macropores.

Figure S2 | Drying time distribution for 5 × AGW and 1 × AGW in microcapillary arrays at different relative humidity.

Table S1 | Summary of the experiments and experimental systems described in this report.

Videos V1–V6 | Air infiltration into individual emulated soil micromodel channels initially saturated with dilute extracellular polymeric substance (EPS) solutions suspended in M9 media.

REFERENCES

Adessi, A., de Carvalho, R. C., De Philippis, R., Branquinho, C., and da Silva, J. M. (2018). Microbial extracellular polymeric substances improve water retention in dryland biological soil crusts. *Soil Biol. Biochem.* 116, 67–69. doi: 10.1016/j.soilbio.2017.10.002

Ahmed, M. A., Kroener, E., Benard, P., Zarebanadkouki, M., Kaestner, A., and Carminati, A. (2016). Drying of mucilage causes water repellency in the rhizosphere of maize: measurements and modelling. *Plant Soil* 407, 161–171. doi: 10.1007/s11104-015-2749-1

Alasonati, E., and Slaveykova, V. I. (2012). Effects of extraction methods on the composition and molar mass distributions of exopolymeric substances of the bacterium *Sinorhizobium meliloti*. *Bioresour. Technol.* 114, 603–609. doi: 10.1016/j.biortech.2012.03.071

Albers, B. (2014). Modeling the hysteretic behavior of the capillary pressure in partially saturated porous media: a review. *Acta Mech.* 225, 2163–2189. doi: 10.1007/s00707-014-1122-4

Aleklett, K., Kiers, E. T., Ohlsson, P., Shimizu, T. S., Caldas, V. E., and Hammer, E. C. (2017). Build your own soil: exploring microfluidics to create microbial habitat structures. *ISME J.* 12, 312–319. doi: 10.1038/ismej.2017.184

Amellal, N., Burtin, G., Bartoli, F., and Heulin, T. (1998). Colonization of wheat roots by an exopolysaccharide-producingpantoea agglomerans strain and its effect on rhizosphere soil aggregation. *Appl. Environ. Microbial.* 64, 3740–3744.

Anbari, A., Chien, H.-T., Datta, S. S., Deng, W., Weitz, D. A., and Fan, J. (2018). Microfluidic model porous media: fabrication and applications. *Small* 14, 1703575–1703515. doi: 10.1002/smll.201703575

Aufrecht, J. A., Timm, C. M., Bible, A., Morrell-Falvey, J. L., Pelletier, D. A., Doktycz, M. J., et al. (2018). Microfluidics: quantifying the spatiotemporal dynamics of plant root colonization by beneficial bacteria in a microfluidic habitat (Adv. Biosys. 6/2018). *Adv. Biosys.* 2:1870051. doi: 10.1002/adbi.201800048

Bais, H. P., Weir, T. L., Perry, L. G., Gilroy, S., and Vivanco, J. M. (2006). The role of root exudates in rhizosphere interactions with plants and other organisms. *Annu. Rev. Plant Biol.* 57, 233–266. doi: 10.1146/annurev.arplant.57.032905.105159

Barrios, E. (2007). Soil biota, ecosystem services and land productivity. *Ecol. Econ.* 64, 269–285. doi: 10.1016/j.ecolecon.2007.03.004

Bengough, A. G. (2012). Water dynamics of the root zone: rhizosphere biophysics and its control on soil hydrology. *Vadose Zone J.* 11:vzj2011.0111. doi: 10.2136/vzj2011.0111

Beven, K., and Germann, P. (1982). Macropores and water flow in soils. *Water Resour. Res.* 18, 1311–1325. doi: 10.1029/WR018i005p01311

Borer, B., Tecon, R., and Or, D. (2018). Spatial organization of bacterial populations in response to oxygen and carbon counter-gradients in pore networks. *Nat. Commun.* 9:769. doi: 10.1038/s41467-018-03187-y

Bouman, B., and Tuong, T. P. (2001). Field water management to save water and increase its productivity in irrigated lowland rice. *Agric. Water Manag.* 49, 11–30. doi: 10.1016/S0378-3774(00)00128-1

Brewer, R. (1965). Fabric and mineral analysis of soils. *Soil Sci.* 100:73.

Büks, F., and Kaupenjohann, M. (2016). Enzymatic biofilm digestion in soil aggregates facilitates the release of particulate organic matter by sonication. *SOIL* 2, 499–509. doi: 10.5194/soil-2-499-2016

Carminati, A., Moradi, A. B., Vetterlein, D., Vontobel, P., Lehmann, E., Weller, U., et al. (2010). Dynamics of soil water content in the rhizosphere. *Plant Soil* 332, 163–176. doi: 10.1007/s11104-010-0283-8

Carson, J. K., Campbell, L., Rooney, D., Clipson, N., and Gleeson, D. B. (2009). Minerals in soil select distinct bacterial communities in their microhabitats. *FEMS Microbiol. Ecol.* 67, 381–388. doi: 10.1111/j.1574-6941.2008.00645.x

Castellane, T. C. L., Lemos, M. V. F., and de Macedo Lemos, E. G. (2014). Evaluation of the biotechnological potential of rhizobium tropici strains for exopolysaccharide production. *Carbohydr. Polym.* 111, 191–197. doi: 10.1016/j.carbpol.2014.04.066

Chau, J. F., Bagtzoglou, A. C., and Willig, M. R. (2011). The effect of soil texture on richness and diversity of bacterial communities. *Environ. Forensics* 12, 333–341. doi: 10.1080/15275922.2011.622348

Chenu, C., and Roberson, E. B. (1996). Diffusion of glucose in microbial extracellular polysaccharide as affected by water potential. *Soil Biol. Biochem.* 28,1–8. doi: 10.1016/0038-0717(96)00070-3

Colica, G., Li, H., Rossi, F., Li, D., Liu, Y., and De Philippis, R. (2014). Microbial secreted exopolysaccharides affect the hydrological behavior of induced biological soil crusts in desert sandy soils. *Soil Biol. Biochem.* 68, 62–70. doi: 10.1016/j.soilbio.2013.09.017

Cruz, B. C., Furrer, J. M., Guo, Y. S., Dougherty, D., Hinestroza, H. F., Hernandez, J. S., et al. (2017). Pore-scale water dynamics during drying and the impacts of structure and surface wettability. *Water Resour. Res.* 53, 5585–5600. doi: 10.1002/2016WR019862

Deng, J., Dhummakupt, A., Samson, P. C., Wikswo, J. P., and Shor, L. M. (2013). Dynamic dosing assay relating real-time respiration responses of *Staphylococcus Aureus* biofilms to changing microchemical conditions. *Anal. Chem.* 85, 5411–5419. doi: 10.1021/ac303711m

Deng, J., Orner, E. P., Chau, J. F., Anderson, E. M., Kadilak, A. L., Rubinstein, R. L., et al. (2015). Synergistic effects of soil microstructure and bacterial EPS on drying rate in emulated soil micromodels. *Soil Biol. Biochem.* 83, 116–124. doi: 10.1016/j.soilbio.2014.12.006

Dohnalkova, A. C., Marshall, M. J., Arey, B. W., Williams, K. H., Buck, E. C., and Fredrickson, J. K. (2011). Imaging hydrated microbial extracellular polymers:

comparative analysis by electron microscopy. *Appl. Environ. Microbiol.* 77, 1254–1262. doi: 10.1128/AEM.02001-10

Donot, F., Fontana, A., Baccou, J. C., and Schorr-Galindo, S. (2012). Microbial exopolysaccharides: main examples of synthesis, excretion, genetics and extraction. *Carbohydr. Polym.* 87, 951–962. doi: 10.1016/j.carbpol.2011.08.083

Durner, W., and Or, D. (2005). "Soil water potential measurement," in *Encyclopedia of Hydro- logical Sciences, Chapter 73*, eds M. G. Anderson and J. J. McDonnell (Chichester, UK: John Wiley and Sons, Ltd.), 1089–1102. doi: 10.1002/0470848944.hsa077a

El-Dessouky, H. T., Ettouney, H. M., Alatiqi, I. M., and Al-Shamari, M. A. (2002). Evaporation rates from fresh and saline water in moving air. *Indus. Eng. Chem. Res.* 41, 642–650. doi: 10.1021/ie010327o

Flemming, H.-C., and Wingender, J. (2010). The biofilm matrix. *Nat. Pub. Group* 8, 623–633. doi: 10.1038/nrmicro2415

Fringant, C., Desbrières, J., Milas, M., Rinaudo, M., Joly, C., and Escoubes, M. (1996). Characterisation of sorbed water molecules on neutral and ionic polysaccharides. *Int. J. Biol. Macromol.* 18, 281–286. doi: 10.1016/0141-8130(95)01087-4

Fujimaki, H., Shimano, T., Inoue, M., and Nakane, K. (2006). Effect of a salt crust on evaporation from a bare saline soil. *Vadose Zone J.* 5, 1246–1211. doi: 10.2136/vzj2005.0144

Godinho, A. L., and Bhosle, S. (2009). Sand aggregation by exopolysaccharide-producing microbacterium arborescens–AGSB. *Curr. Microbiol.* 58, 616–621. doi: 10.1007/s00284-009-9400-4

González, J. E., Reuhs, B. L., and Walker, G. C. (1996). Low molecular weight EPS II of Rhizobium meliloti allows nodule invasion in *Medicago sativa*. *Proc. Natl. Acad. Sci. U.S.A.* 93, 8636–8641. doi: 10.1073/pnas.93.16.8636

Griffiths, B. S., and Philippot, L. (2013). Insights into the resistance and resilience of the soil microbial community. *FEMS Microbiol. Rev.* 37, 112–129. doi: 10.1111/j.1574-6976.2012.00343.x

Harimawan, A., and Ting, Y.-P. (2016). Investigation of extracellular polymeric substances (EPS) properties of *P. aeruginosa* and *B. subtilis* and their role in bacterial adhesion. *Colloids Surf. B Biointerfaces* 146, 459–467. doi: 10.1016/j.colsurfb.2016.06.039

Lehmann, A., Zheng, W., and Rillig, M. C. (2017). Soil biota contributions to soil aggregation. *Nat. Ecol. Evol.* 1, 1828–1835. doi: 10.1038/s41559-017-0344-y

Luxmoore, R. J. (1981). Micro-, meso-, and macroporosity of soil. *Soil Sci. Soc. Am. J.* 45, 671–672. doi: 10.2136/sssaj1981.03615995004500030051x

Marek, R., and Straub, J. (2001). Analysis of the evaporation coefficient and the condensation coefficient of water. *Int. J. Heat Mass Trans.* 44, 1–15. doi: 10.1016/S0017-9310(00)00086-7

Marshall, M. J., Beliaev, A. S., Dohnalkova, A. C., Kennedy, D. W., Shi, L., Wang, Z., et al. (2006). c-Type cytochrome-dependent formation of U(IV) nanoparticles by *Shewanella oneidensis*. *PLoS Biol.* 4:e268–e210. doi: 10.1371/journal.pbio.0040268

McSwain, B. S., Irvine, R. L., Hausner, M., and Wilderer, P. A. (2005). Composition and distribution of extracellular polymeric substances in aerobic flocs and granular sludge. *Appl. Environ. Microbiol.* 71, 1051–1057. doi: 10.1128/AEM.71.2.1051-1057.2005

Mendis, H. C., Madzima, T. F., Queiroux, C., and Jones, K. M. (2016). Function of succinoglycan polysaccharide in sinorhizobium meliloti host plant invasion depends on succinylation, not molecular weight. *mBio* 7:e00606–16–11. doi: 10.1128/mBio.00606-16

Mora, P., Rosconi, F., Franco Fraguas, L., and Castro-Sowinski, S. (2008). *Azospirillum brasilense* Sp7 produces an outer-membrane lectin that specifically binds to surface-exposed extracellular polysaccharide produced by the bacterium. *Arch. Microbiol.* 189, 519–524. doi: 10.1007/s00203-007-0343-5

Morris, D. L. (1948). Quantitative determination of carbohydrates with dreywood's anthrone reagent. *Science* 107, 254–255. doi: 10.1126/science.107.2775.254

Moyano, F. E., Manzoni, S., and Chenu, C. (2013). Responses of soil heterotrophic respiration to moisture availability: an exploration of processes and models. *Soil Biol. Biochem.* 59, 72–85. doi: 10.1016/j.soilbio.2013.01.002

Norouzi Rad, M., and Shokri, N. (2012). Nonlinear effects of salt concentrations on evaporation from porous media. *Geophys. Res. Lett.* 39:L04403. doi: 10.1029/2011GL050763

Or, D., Phutane, S., and Dechesne, A. (2007). Extracellular polymeric substances affecting pore-scale hydrologic conditions for bacterial activity in unsaturated soils. *Vadose Zone J.* 6, 298–298. doi: 10.2136/vzj2006.0080

Owens, J., Clough, T. J., Laubach, J., Hunt, J. E., and Venterea, R. T. (2017). Nitrous oxide fluxes and soil oxygen dynamics of soil treated with cow urine. *Soil Sci. Soc. Am. J.* 81, 289–210. doi: 10.2136/sssaj2016.09.0277

Pellock, B. J., Teplitski, M., Boinay, R. P., Bauer, W. D., and Walker, G. C. (2002). A LuxR homolog controls production of symbiotically active extracellular polysaccharide ii by *Sinorhizobium meliloti. J. Bacteriol.* 184, 5067–5076. doi: 10.1128/JB.184.18.5067-5076.2002

Renslow, R. S., Marshall, M. J., Tucker, A. E., Chrisler, W. B., and Yu, X.-Y. (2017). *In situ* nuclear magnetic resonance microimaging of live biofilms in a microchannel. *Analyst* 142, 2363–2371. doi: 10.1039/C7AN00078B

Roberson, E. B., and Firestone, M. K. (1992). Relationship between desiccation and exopolysaccharide production in a soil *Pseudomonas sp. Appl. Environ. Microbiol.* 58, 1284–1291.

Rosenzweig, R., Shavit, U., and Furman, A. (2012). Water retention curves of biofilm-affected soils using xanthan as an analogue. S*oil Sci. Soc. Am. J.* 76, 61–69. doi: 10.2136/sssaj2011.0155

Sadeghi, S. H., Kheirfam, H., Homaee, M., Darki, B. Z., and Vafakhah, M. (2017). Improving runoff behavior resulting from direct inoculation of soil micro-organisms. *Soil Tillage Res.* 171, 35–41. doi: 10.1016/j.still.2017.04.007

Sakai, M., Van Genuchten, M. T., Alazba, A. A., Setiawan, B. I., and Minasny, B. (2015). A complete soil hydraulic model accounting for capillary and adsorptive water retention, capillary and film conductivity, and hysteresis. *Water Resour. Res.* 51, 8757–8772. doi: 10.1002/2015WR017703

Schaumann, G. E., Braun, B., Kirchner, D., Rotard, W., Szewzyk, U., and Grohmann, E. (2007). Influence of biofilms on the water repellency of urban soil samples. *Hydrol. Process.* 21, 2276–2284. doi: 10.1002/hyp.6746

Schindelin, J., Arganda-Carreras, I., Frise, E., Kaynig, V., Longair, M., Pietzsch, T., et al. (2012). Fiji: an open-source platform for biological-image analysis. *Nat. Methods* 9, 676–682. doi: 10.1038/nmeth.2019

Sheng, G.-P., Yu, H.-Q., and Li, X.-Y. (2010). Extracellular polymeric substances (EPS) of microbial aggregates in biological wastewater treatment systems: a review. *Biotechnol. Adv.* 28, 882–894. doi: 10.1016/j.biotechadv.2010.08.001

Shokri, N., Lehmann, P., and Or, D. (2008). Effects of hydrophobic layers on evaporation from porous media. *Geophys. Res. Lett.* 35, L19407-1–L19407-4. doi: 10.1029/2008GL035230

Shokri-Kuehni, S. M. S., Vetter, T., Webb, C., and Shokri, N. (2017). New insights into saline water evaporation from porous media: complex interaction between evaporation rates, precipitation, and surface temperature. *Geophys. Res. Lett.* 44, 5504–5510. doi: 10.1002/2017GL073337

Smith, K. A., Ball, T., Conen, F., Dobbie, K. E., Massheder, J., and Rey, A. (2003). Exchange of greenhouse gases between soil and atmosphere: interactions of soil physical factors and biological processes. *Eur. J. Soil Sci.* 54, 779–791. doi: 10.1046/j.1351-0754.2003.0567.x

Soil Science Society of America (2008). *Glossary Of Soil Science Terms.* Madison, WI: ASA-CSSA-SSSA.

Soufan, R., Delaunay, Y., Vieublé, L., Shor, L., Garnier, P., Otten, W., et al. (2018). Pore-scale monitoring of the effect of microarchitecture on fungal growth in a two-dimensional soil-like micromodel. *Front. Environ. Sci.* 6:68. doi: 10.3389/fenvs.2018.00068

Treves, D. S., Xia, B., Zhou, J., and Tiedje, J. M. (2003). A two-species test of the hypothesis that spatial isolation influences microbial diversity in soil. *Microb. Ecol.* 45, 20–28. doi: 10.1007/s00248-002-1044-x

van der Heijden, M. G. A., Bardgett, R. D., and van Straalen, N. M. (2008). The unseen majority: soil microbes as drivers of plant diversity and productivity in terrestrial ecosystems. *Ecol. Lett.* 11, 296–310. doi: 10.1111/j.1461-0248.2007.01139.x

Vaningelgem, F., Zamfir, M., Mozzi, F., Adriany, T., Vancanneyt, M., Swings, J., et al. (2004). Biodiversity of exopolysaccharides produced by streptococcus thermophilus strains is reflected in their production and their molecular and functional characteristics. *Appl. Environ. Microbiol.* 70, 900–912. doi: 10.1128/AEM.70.2.900-912.2004

Wingender, J., Strathmann, M., Rode, A., Leis, A., and Flemming, H.-C. (2001). "Isolation and biochemical characterization of extracellular polymeric substances from Pseudomonas aeruginosa," in *Methods in Enzymology*, ed R. J. Doyle (San Diego, CA: Elsevier; Academic Press), 302–314. doi: 10.1016/S0076-6879(01)36597-7

Zhang, L., Li, Y. R., Zhou, L. Q., and Wu, C. M. (2017). Comparison study on the calculation formula of evaporation mass flux through the plane vapour-liquid interface. *J. Phys. Conf. Ser.* 925, 012019–012017. doi: 10.1088/1742-6596/925/1/012019

Zhang, P., Fang, F., Chen, Y.-P., Shen, Y., Zhang, W., Yang, J.-X., et al. (2014). Composition of EPS fractions from suspended sludge and biofilm and their roles in microbial cell aggregation. *Chemosphere* 117, 59–65. doi: 10.1016/j.chemosphere.2014.05.070

Zheng, W., Zeng, S., Bais, H., LaManna, J. M., Hussey, D. S., Jacobson, D. L., et al. (2018). Plant Growth-Promoting Rhizobacteria (PGPR) reduce evaporation and increase soil water retention. *Water Resour. Res.* 178, 821–815. doi: 10.1029/2018WR022656

Zhou, J., Xia, B., Treves, D. S., Wu, L. Y., Marsh, T. L., O'Neill, R. V., et al. (2002). Spatial and resource factors influencing high microbial diversity in soil. *Appl. Environ. Microbiol.* 68, 326–334. doi: 10.1128/AEM.68.1.326-334.2002

Conflict of Interest Statement: The authors declare that the research was conducted in the absence of any commercial or financial relationships that could be construed as a potential conflict of interest.

frontiers
in Microbiology

Emergent Properties of Microbial Activity in Heterogeneous Soil Microenvironments: Different Research Approaches Are Slowly Converging, Yet Major Challenges Remain

Philippe C. Baveye[1]*, Wilfred Otten[2], Alexandra Kravchenko[3], María Balseiro-Romero[1,4], Éléonore Beckers[5], Maha Chalhoub[6], Christophe Darnault[7], Thilo Eickhorst[8], Patricia Garnier[6], Simona Hapca[9], Serkan Kiranyaz[10], Olivier Monga[11], Carsten W. Mueller[12], Naoise Nunan[13], Valérie Pot[6], Steffen Schlüter[14], Hannes Schmidt[15] and Hans-Jörg Vogel[14,16]

[1] UMR ECOSYS, AgroParisTech, Université Paris-Saclay, Thiverval-Grignon, France, [2] School of Water, Energy and Environment, Cranfield University, Cranfield, United Kingdom, [3] Department of Plant, Soil and Microbial Sciences, Michigan State University, East Lansing, MI, United States, [4] Department of Soil Science and Agricultural Chemistry, Centre for Research in Environmental Technologies, Universidade de Santiago de Compostela, Santiago de Compostela, Spain, [5] Soil–Water–Plant Exchanges, Terra Research Centre, BIOSE, Gembloux Agro-Bio Tech, University of Liège, Gembloux, Belgium, [6] UMR ECOSYS, INRA, Université Paris-Saclay, Thiverval-Grignon, France, [7] Laboratory of Hydrogeoscience and Biological Engineering, L.G. Rich Environmental Laboratory, Department of Environmental Engineering and Earth Sciences, Clemson University, Clemson, SC, United States, [8] Faculty 2 Biology/Chemistry, University of Bremen, Bremen, Germany, [9] Dundee Epidemiology and Biostatistics Unit, School of Medicine, University of Dundee, Dundee, United Kingdom, [10] Department of Electrical Engineering, Qatar University, Doha, Qatar, [11] Institut de Recherche pour le Développement, Bondy, France, [12] Lehrstuhl für Bodenkunde, Technical University of Munich, Freising, Germany, [13] Institute of Ecology and Environmental Sciences – Paris, Sorbonne Universités, CNRS, IRD, INRA, P7, UPEC, Paris, France, [14] Soil System Science, Helmholtz-Zentrum für Umweltforschung GmbH – UFZ, Leipzig, Germany, [15] Terrestrial Ecosystem Research, Department of Microbiology and Ecosystem Science, Research Network 'Chemistry meets Microbiology', University of Vienna, Vienna, Austria, [16] Institute of Soil Science and Plant Nutrition, Martin Luther University of Halle-Wittenberg, Halle, Germany

Over the last 60 years, soil microbiologists have accumulated a wealth of experimental data showing that the bulk, macroscopic parameters (e.g., granulometry, pH, soil organic matter, and biomass contents) commonly used to characterize soils provide insufficient information to describe quantitatively the activity of soil microorganisms and some of its outcomes, like the emission of greenhouse gasses. Clearly, new, more appropriate macroscopic parameters are needed, which reflect better the spatial heterogeneity of soils at the microscale (i.e., the pore scale) that is commensurate with the habitat of many microorganisms. For a long time, spectroscopic and microscopic tools were lacking to quantify processes at that scale, but major technological advances over the last 15 years have made suitable equipment available to researchers. In this context, the objective of the present article is to review progress achieved to date in the significant research program that has ensued. This program can be rationalized as a sequence of steps, namely the quantification and modeling of the physical-, (bio)chemical-, and microbiological properties of soils, the integration of these

different perspectives into a unified theory, its upscaling to the macroscopic scale, and, eventually, the development of new approaches to measure macroscopic soil characteristics. At this stage, significant progress has been achieved on the physical front, and to a lesser extent on the (bio)chemical one as well, both in terms of experiments and modeling. With regard to the microbial aspects, although a lot of work has been devoted to the modeling of bacterial and fungal activity in soils at the pore scale, the appropriateness of model assumptions cannot be readily assessed because of the scarcity of relevant experimental data. For significant progress to be made, it is crucial to make sure that research on the microbial components of soil systems does not keep lagging behind the work on the physical and (bio)chemical characteristics. Concerning the subsequent steps in the program, very little integration of the various disciplinary perspectives has occurred so far, and, as a result, researchers have not yet been able to tackle the scaling up to the macroscopic level. Many challenges, some of them daunting, remain on the path ahead. Fortunately, a number of these challenges may be resolved by brand new measuring equipment that will become commercially available in the very near future.

INTRODUCTION

Over the last decade, soils have become increasingly central to a number of crucial debates on issues of great societal concern. Because they contain a huge amount of carbon, soils could lead to a dramatic acceleration of global climate change, as mean temperatures increase and rainfall patterns are altered (Baveye, 2007; Baveye et al., 2011; Hamdi et al., 2013; Crowther et al., 2016). The idea, advocated by some (Paustian et al., 1997; Lal and Bruce, 1999), that on the contrary, with proper management, soils could store even more carbon than at present, and thereby help mitigate the production of greenhouse gasses resulting from the consumption of fossil fuels, has been adopted enthusiastically by politicians in a number of countries but has stirred intense discussions among scientists (Powlson et al., 2011; Cheng et al., 2012; Dungait et al., 2012; Kowalchuk, 2012; Verbruggen et al., 2012; Minasny et al., 2017, 2018; van Groenigen et al., 2017; Baveye et al., 2018; White et al., 2018). At the same time, humanity is faced with the prospect of having to significantly increase food production to feed the world population, which is expected to rise to 9 or 10 billion people by 2050 (Godfray et al., 2010). Since soil and water resources are already used at the maximum level of what some consider ecologically safe, a consensus seems to be emerging that as long as the focus is kept on land-based agricultural production, the best option to insure food security lies in exploiting plant-microbe partnerships to improve biomass production (Weyens et al., 2009; Glick, 2012, 2014; Blaser et al., 2016), or in stimulating so-called plant-soil feedback processes, whereby plants induce soil microbial communities to release nutrients and store water in the rhizosphere (Sposito, 2013; Baveye, 2015). In addition, even though the issue of soil contamination does not appear at the moment to be at the forefront of environmental concerns in many countries, the question remains of what to do with millions

of severely polluted sites around the globe, especially given the fact that this number is ever increasing, as a result of practices like shale gas production (Baveye, 2013c; Meckenstock et al., 2015). Given the prospect of a progressive warming of soils in decades to come, renewed threats caused by soil contamination will undoubtedly need to be addressed at some point in the near future.

The intimately connected microbial and physico-chemical processes at the core of all these soil-related issues have posed daunting challenges to researchers. Until a decade ago, in spite of sustained research efforts, progress was very slow or even non-existent, and in several cases serious hurdles arose, which no one had anticipated. Kirschbaum (2006) admitted that in the 10 years prior to the publication of his review of the field, no real advance had been made in understanding and predicting quantitatively the effect of temperature on the decomposition of soil organic matter (OM). Available models also routinely underestimated the pulses of CO_2 flux occurring when large rainfall events follow drafts (Blagodatsky and Smith, 2012; Evans et al., 2016). Recent work by Rabot et al. (2015) suggests that many of the previous measurements of the production by soil bacteria and fungi of nitrous oxide, a very potent greenhouse gas (Laughlin and Stevens, 2002; Crenshaw et al., 2008; Hu et al., 2015), probably missed very short emission bursts that occur at the onset of drying of soils, and therefore underestimated total N_2O production by soils. Concomitantly, research on carbon sequestration in soils provided evidence of the problematic "priming" effect, identified early on (Macura et al., 1965; Arsjad and Giddens, 1966), but routinely overlooked until a decade ago (Fontaine et al., 2007; Kuzyakov, 2010; Tian et al., 2015) and still poorly understood (Nunan et al., 2015; van der Wal and de Boer, 2017). Through this effect, the addition of fresh OM to soils can lead to the mineralization of very old humic substances, previously thought to be utterly stable and recalcitrant to further

degradation. In a similar fashion, in polluted soils, experiments showed that a slight change, for example brought about by the addition of a source of nutrients for microorganisms, could easily make supposedly "sequestered" contaminants once again bioavailable (Li et al., 2005). Some of these areas of ignorance remain "terra incognita" at this point, even with regard to the much ballyhooed biodiversity of soils (Baveye et al., 2016a,b). There is still no satisfactory explanation for the observation, made more than 60 years ago, that the mineralization of soil OM continues at the same rate even if 90% of soil microorganisms are wiped out by CHCl₃ fumigation (Jenkinson, 1966; Powlson et al., 2017; Baveye, 2018). A final example of a situation where our understanding of soil systems is still insufficient is related to the links between the diversity of soil microbial communities and various soil parameters. Some authors have found a close correlation between this diversity and specific parameters, like soil pH (Fierer and Jackson, 2006), but more detailed statistical analyses sometimes present a different picture. In a recent study, Terrat et al. (2017) use some of the most sophisticated molecular techniques currently available to analyze the biodiversity of soil samples across France, and try to relate it to various parameters of soils and of their environment. The results are systematically underwhelming. They find that less than half (48.2%) of the observed variance of the biodiversity could be accounted for by using soil parameters that are routinely measured. Clearly, at least in this particular study, something fundamental about soils is being missed.

In virtually all these instances, a common observation is that soil samples that appear alike in most of their overall measured characteristics can behave very differently, making replicated observations and good correlations difficult to achieve. Obviously, it is not sufficient to describe soils solely on the basis of traditional macroscopic measurements, such as the volumetric water content, microbial density, or contaminant concentration. Quantitative information on the spatial heterogeneity manifested at the micron scale, at which microorganisms operate, is also absolutely required.

In some respects, this is not as novel a perspective as it may appear. In another era, in literature that unfortunately seems to have become largely ignored since, soil microbiologists already reached the same conclusion. Sixty years ago, Rovira and Greacen (1957) subjected moist soil samples to compression and shearing to simulate tillage, and concluded, after ruling out other possible explanations, that the enhanced oxygen consumption observed in the soils after disruption was due to exposure of organisms to OM that was previously inaccessible to them. These and a number of other early observations pointing in the same direction prompted Alexander (1964, p. 219) to conclude that "microorganisms apparently in the same habitat are, in fact, often exposed to entirely different environmental influences and population pressures. To understand the forces actually affecting the organisms, a microenvironmental concept rather than the gross macroscopic view of interactions must be adopted." The review by Griffith (1965) of the extensive work carried out in the 40s and 50s on the opposite effect of microorganisms on their physical environment, and in particular on the development of soil architecture, also raises many

questions that could be addressed only from a microscopic perspective. Experimental evidence obtained since the mid-sixties has provided steadily strengthening support for this perspective (Hattori, 1973; Cheshire, 1977; Elliott et al., 1980; Tiedje et al., 1984; Stotzky, 1986; Crozat et al., 1987; Darrah et al., 1987; Parkin et al., 1987; Postma and Altemuller, 1990; Postma and van Veen, 1990; Killham et al., 1993; Renault and Stengel, 1993; Strong et al., 1997; Wachinger et al., 2000; Chenu and Stotzky, 2001; Attard et al., 2011; Chapman et al., 2012; Johnson et al., 2013; Vos et al., 2013; Uroz et al., 2015; Xun et al., 2015; Barcenas-Moreno et al., 2016; Keiluweit et al., 2017, 2018).

In the 50s and 60s, very little could be done to come up with better measurements, unfortunately. Alexander (1964, p. 219), again, observed that "because of inherent technical difficulties in biochemical experimentation at the microscopic level, progress in understanding of the microenvironment has been painfully slow." Even though more and more experiments over the years confirmed the significance of microenvironments, for a long time it was not feasible practically to characterize them in quantitative terms. The advent of transmission or scanning electron microscopes, and later of confocal laser microscopes as well, provided a wealth of qualitative information about microbial habitats in the form of micrographs of increasingly high quality (Foster, 1988; Vandevivere and Baveye, 1992a,b,c,d; DeLeo et al., 1997; Baveye et al., 1998), but the lack of related quantitative data prevented for several decades the development of satisfactory predictive models of soil microbial processes, accounting explicitly for the microheterogeneity of soils.

This situation has changed dramatically in the last decade and is continuing to evolve at a rapid pace. Significant technological advances have provided soil researchers, for example, with routine access to X-ray computed tomography (CT) systems, which provide increasingly reliable information about the geometry of pores and solids in soils at resolutions as small as 0.05 μm. Progress in near-edge X-ray spectromicroscopy (NEXAFS), scanning transmission X-ray microscopy (STXM), X-ray absorption spectroscopy, micro-fluorescence spectroscopy, and Nano-SIMS, applied to soil thin sections, has led to observations of sharp spatial heterogeneity in the chemical make-up of soils over minute distances, and in the accumulation of trace metals. Significant advances related to biological markers now allow specific bacteria to be identified in soils, and their spatial distribution at the micrometer scale to be determined in thin sections. This information can be translated into 3-dimensional distributions using recently developed statistical algorithms. In addition, very efficient modeling tools, like the Lattice-Boltzmann approach, allow the description of transport and physico-chemical processes occurring in soil pores at scales that are directly relevant to microorganisms, whereas individual-based or agent-based models, also developing rapidly, can describe the dynamics of microorganisms inhabiting the pore space (Gras et al., 2010, 2011; Muci et al., 2012; Hellweger et al., 2016; Kim and Or, 2016).

In the last few years, the application of each of these technologies and modeling methods to soils has been the object of a sizeable literature. Progress achieved in the use of each technology has already been expertly reviewed

(O'Donnell et al., 2007; Taina et al., 2008; Young et al., 2008; Behrens et al., 2012; Rennert et al., 2012; Helliwell et al., 2013; Tuller et al., 2013; Wildenschild and Sheppard, 2013; Schlüter et al., 2014; Calistru and Jitareanu, 2015; Kuzyakov and Blagodatskaya, 2015; Prosser, 2015; Roose et al., 2016; Xiong et al., 2016; Totsche et al., 2017). For some technologies, since advances are extremely rapid, it would be useful, conceivably, to provide an updated coverage of recent work, and no doubt new reviews will fill the gaps in the near future. Yet, a different type of critical overview might be even more fruitful at this stage, one that keeps sight firmly on what started out as the ultimate goal of the research: A thorough understanding of what one needs to measure at the macroscale in order to adequately describe emergent microbial processes. Instead of surveying the increasingly widespread application of specific technologies to soils, it is worth taking a step back and analyzing how the use of these technologies and their continual improvements help us, or are expected to help us, move steadily on paths leading to the goal we seek. For each path, we can try to assess how far along we are at present and, to the best of our knowledge, to estimate how much distance remains to be covered. Also, since at the scale of bacterial and archaeal cells, it is virtually impossible to dissociate physical, (bio)chemical, and biological aspects of soils, another key point of interest is the extent to which the combined uses of different technologies, meant to access information on these complementary aspects, make us now, or at least promise to make us soon, converge consistently toward meaningful insights. In this reflection on what remains to be done, it makes sense to try to gauge as well how much assistance we could derive from measurement technologies that are barely emerging at the moment but will in all likelihood become routinely available to us in the next few years. It is to scrutiny along these different directions that the present review article is devoted.

KEEPING ONE'S EYES ON THE ULTIMATE GOAL

First things first. As a famous microbiologist once wrote, "without the proper technological advances the road ahead is blocked. Without a proper vision, there is no road ahead" (Woese, 2004). So, it is vital to start from a clear perception of the goal that is being pursued, and then outline what paths lead to it. As pointed out above, it has been known for half a century at least that the type of macroscopic measurements that are carried out routinely on soils and sediments at the moment do not inform in a satisfactory way about the parameters that appear to be controlling the activity of microorganisms in these systems. Experience has shown clearly that knowledge of, e.g., the total microbial biomass and the total amount of OM present in a given volume of soil or sediment does not allow us to make reliable predictions about the activity of microorganisms or the fate of OM. Somehow, our usual measurements do not capture enough of the huge complexity that soils manifest at the microscopic scale to enable us to predict accurately various properties of soils, like the activity of microorganisms, at the macroscopic scale.

To describe the process by which microscale heterogeneity influences and generates macroscopic behaviors, researchers have used alternatively the terms of "emergence" (Holland, 1990; Addiscott, 2011) or "self-organization" (Smagin, 1989; Hallet, 1990; Phillips, 1995, 2000; Manson, 2001; Young and Crawford, 2004; Barot et al., 2007; Lavelle et al., 2007, 2016; Ebrahimi and Or, 2016; Tecon and Or, 2017a,b). For a number of reasons, explained in detail in **Appendix 1 (Supplementary Information)**, "emergence," implying a reality that is *less* than the sum of its parts and is therefore much simpler to describe, is far more appropriate than the term of "self-organization" to describe the type of soil-borne processes on which this review article focuses. In the following, we shall therefore refer consistently to "emergence."

This point of terminology being resolved, the crux of the matter is that information of an entirely different nature than that currently available is needed to describe soil microbial processes adequately. We clearly need new macroscopic measurements. There are probably different ways to envisage the paths that will lead us eventually to this "Holy Grail." **Figure 1** proposes one of these perspectives, which has served as a general strategy map to a number of us in our research efforts. It starts on the left with information about basic soil features. What we understand at this point of emergent processes in soils indicates that this topic has (at least) three clear, resolutely interdependent facets, associated, respectively, with physical-, (bio)chemical-, and microbiological aspects of soils. For each of them, it is crucial to gather experimental information, either on static properties (dealt with in the boxes "physical characterization," etc.), or on their dynamics. Alongside this evidence gathering, it is also important to develop theoretical and modeling frameworks that encapsulate experimental information and allow predictions to be made. In each case, experimental data should serve to refine theories and models, which in turn (e.g., through sensitivity analyses) can provide guidance in the procurement of additional data. The outcome of this type of iterative approach, hopefully, is a satisfactory description of each dynamic, which can then be integrated at first pairwise, and eventually all together, into a comprehensive model of soil processes at the microscale.

At that point, we are still somewhat far from the goal. Indeed, when this integrated model becomes available, running it on any given soil sample will require a tremendous amount of microscale information, which may take weeks or even months to gather, not to mention that the integrated model itself will likely take quite some time to run, which means that with this integrated microscale description of soils, only very few soil samples will ever be characterized and modeled. What we need instead is to come up with simple *macroscopic* measurements that can be carried out *routinely*.

One way to find out what these macroscopic measurements should be is suggested in **Figure 1**. It consists of expanding the available experimental database by simulating many different scenarios under different conditions of microscale heterogeneity of the soils, and of their properties. From these multiple scenarios, one can try to find out how one can simplify the description, in other words upscale the microscale model to the macroscale, while making sure that, in the process, the

FIGURE 1 | Schematic representation of the sequence of steps in the research on the emergent properties of soils, leading from a characterization of the various properties and dynamics at the microscale, onward to an upscaled macroscopic model, and finally to the ultimate goal of identifying macroscopic measurements that can be carried out routinely.
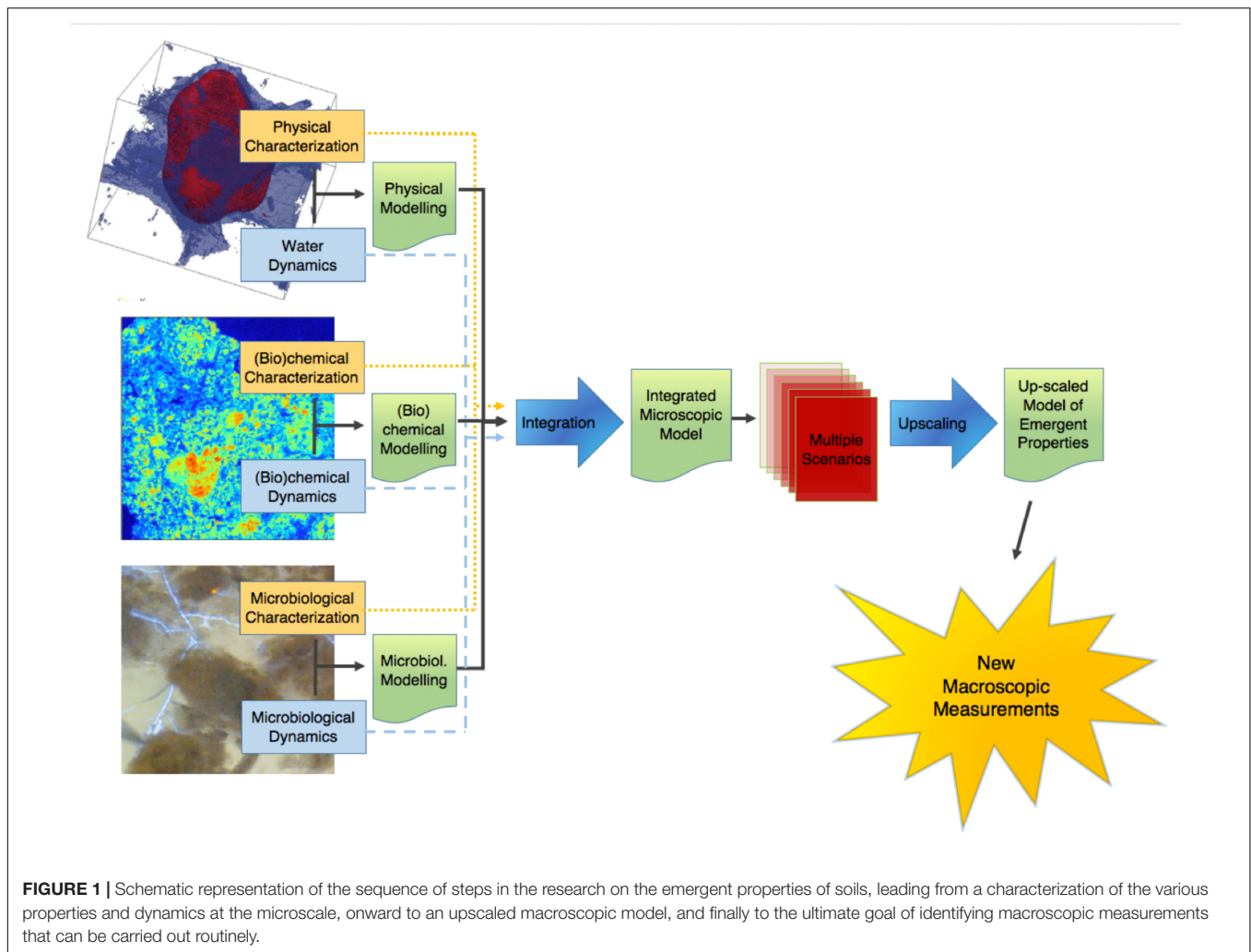
macroscopic parameters that appear in the resulting upscaled description are amenable to routine measurement in practice. This prospect of course rests on the assumption, at this stage very much open, that the simplification implied by the notion of "emergence" indeed occurs in soils. As discussed later, there is fortunately some circumstantial evidence that such simplification can be expected.

The research program, depicted in **Figure 1**, comprises a number of clear paths, which are discussed in the following. To the extent that some of the steps along these paths involve advanced technologies and elaborate methods of analysis or simulation, there is a definite risk of drift, i.e., to focus excessively on tools, perfect them, and progressively forget over time the reason for doing all this work in the first place, as one could argue has unfortunately happened occasionally in the past in other contexts in soil science (Baveye and Laba, 2015). One might argue that switching progressively from actual soils to very coarse sands or collections of clean 500 µm (or bigger) glass beads constitutes an example of such a drift. These systems admittedly pose far fewer technological challenges, which enable researchers to identify and isolate various microscale mechanisms, but, as

experience acquired in the past (e.g., in the sixties, when glass beads were used to research several soil processes, like water retention hysteresis) has shown, the relevance of the information acquired in these idealized systems for the functioning of real soils is unclear, at best. To avoid such drift, as much as possible, the descriptions of the various paths of **Figure 1** will focus exclusively on progress made to date with actual, living *soils*, in all their wonderful complexity and messiness.

One last comment that needs to be made before we embark in the description of the program of **Figure 1** is that there is no reason to be so wedded to it as not to be open to alternatives that may surface. If tomorrow, an experimentalist comes up with a robust empirical relationship among novel macroscopic measurements, similar to what is envisaged as the ultimate outcome of the program of **Figure 1**, every researcher interested in the field should probably rejoice, change gear, and adopt an entirely different perspective, for example to try to understand why the solution works. This is reminiscent of the debate about top-down vs. bottom-up approaches in hydrology (Basu et al., 2011; Baveye and Laba, 2015). Regardless of how strongly held one's philosophical beliefs are, what matters most is to find a

satisfactory answer to a number of questions, not necessarily the manner in which the answers are obtained. This being said, no experimentalist has stepped forward yet with a ready answer, and the stepwise plan of **Figure 1** appears to be our best bet at this point to ever obtain one in the limited time we have to do so.

PROGRESS ON THE PHYSICAL FRONT

Computed Tomography and Image Processing

Any overview of the quantitative research of the past 10 years on microscale processes in soils needs to start with their physical characterization. Indeed, soil physicists have undeniably led the charge. The pioneering work carried out in the early 1980s with medical and custom-made X-ray and gamma-ray computed tomography systems brought to the attention of the soil physics community the potential of this technology, then still in its infancy (Petrovic et al., 1982; Hainsworth and Aylmore, 1983; Crestana et al., 1985; Pires et al., 2010). The low (millimeter) resolution of scanners available at the time enabled researchers to characterize the geometry of macropores (e.g., earthworm burrows) in soils (Warner et al., 1989; Joschko et al., 1991; Heijs et al., 1995; Capowiez et al., 1998; Rogasik et al., 2003; Luo et al., 2010), but was much too coarse to provide information relevant to microorganisms. In the mid-1990s, various synchrotron facilities around the world began to devote beam time to soils, and researchers immediately took advantage of the significantly higher spatial resolution (down to a few μm) these facilities afforded, as well as the fact that the synchrotron X-ray beams are monochromatic (single-energy) (Anderson and Hopmans, 1994; Spanne et al., 1994; Garnier et al., 1998; Wildenschild et al., 2002; Feeney et al., 2006). However, access to synchrotron beam time was, and still is to a large extent, somewhat scarce and difficult to obtain, so that the extent of adoption of synchrotron-X-ray tomography has remained limited. The commercialization, around 2002, of the first tabletop, non-medical X-ray tomography systems, which were not excessively onerous and could therefore be entirely dedicated to soil science research, marked the beginning of a new era. The X-rays produced by these machines are polychromatic (i.e., are a mixture of X-rays of different energies), which in a number of ways is a disadvantage compared to the monochromatic X-ray produced by synchrotrons, but the resolution of these tabletop scanners has steadily improved since 2002 and several machines now allow resolutions that, in small soil samples of a few cm^3, can be as low as 0.3 μm, i.e., commensurate with the resolution afforded by synchrotrons (Voltolini et al., 2017) and with the size of some of the "ultra-small" bacteria and archaea found in soils. The very high resolution of X-ray CT has for a time at least made other types of measuring instruments, like dual-energy gamma-ray scanners, neutron radiography, or nuclear magnetic resonance micro-imaging systems, fall off the radar screen, at least in applications to soils. Nevertheless, as we shall see later, these instruments afford advantages over X-ray CT, and are therefore likely to play a more significant role in the future.

The "3-dimensional" soil images that CT scanners provide are in fact stacks of 2-dimensional, grayscale images associated with virtual slices within the soil sample. Very early on in the use of these images, researchers came to the conclusion that these grayscale images would not be very useful to quantify the geometry of the soil pore space and that it was necessary to derive binary (black and white) images from the original grayscale ones, a process alternatively referred to as "thresholding" or "segmentation." Significant progress has occurred over the years in how this thresholding is approached. Initially, it was carried out slice by slice, either manually by simple visual inspection ("eye-balling") or with the assistance of one of a number of available 2D algorithms (e.g., Nunan et al., 2006). The first improvement consisted of thresholding the whole 3-d image at once, using an algorithm to calculate a unique, global threshold value. Then, various researchers showed that in the presence of textural heterogeneities (e.g., stones) within the samples, it was preferable to instead use local thresholds, which can vary from location to location within a sample (Iassonov et al., 2009; Schlüter et al., 2014). Up to that point, all thresholding algorithms required operator input, to adjust one or more parameters. This introduced unavoidable subjectivity in the process, which in principle would make it improbable for different individuals to threshold a given soil sample the same way, or even for a single individual to threshold different soil samples (e.g., associated with different agricultural practices or with successive times) in a consistent manner (Baveye et al., 2010).

The question of objectivity in the generation of X-ray CT images of soils is in fact much broader than just this issue regarding thresholding/segmentation. Indeed, as a number of authors have pointed out (Vaz et al., 2011; Houston et al., 2013b), the process of obtaining CT images of soils requires many decisions to be made by operators, concerning in particular the value of scanning parameters (e.g., energy level, choice of filter, scanning resolution), the selection of one among a number of alternative image reconstruction and artifact correction algorithms, the format (8- or 16-bit) used to store the images, and the use of a method to increase image sharpness or reduce the noise that is unavoidably present in the images after reconstruction. As with thresholding 10 years ago, different groups, and sometimes even different individuals within a group, adopt alternative perspectives with respect to the various decisions that need to be made by operators, which can lead to sometimes significant differences in some of the metrics that are associated eventually with CT images (see, e.g., Houston et al., 2013b). Nevertheless, at this point, there appears to be no effort underway to develop a set of materials that could be used as "scanning standards," as suggested by Baveye et al. (2010), or simply to standardize analyzes. One way out of the difficulty would be to document exhaustively the parameter values used at each and every step of the image acquisition process, as well as, through detailed sensitivity analyses, the extent to which conclusions that are reached on the basis of CT images are affected by these parameter values.

Nevertheless, recognition a few years ago that the subjectivity in thresholding operations and in the manipulation of CT images

could be substantial, prompted the development of a number of automated thresholding algorithms requiring no operator input (Schlüter et al., 2010; Hapca et al., 2013; Houston et al., 2013a), regardless of the level of "supervision" (learning from training data) adopted. These objective algorithms have been used in a number of investigations (e.g., Beckers et al., 2014a,b; Houston et al., 2017), and new algorithms are appearing that do not require any parameter tuning (e.g., West et al., 2018), but so far they have not stopped the development of operator-dependent approaches (Kulkarni et al., 2012; Hashemi et al., 2014; Ojeda-Magana et al., 2014; Martin-Sotoca et al., 2017). Therefore, further progress is needed in this area, especially in order to segment images containing multiple distinct populations of voxels.

BIB- and FIB-SEM

Another approach that has recently been explored to obtain basically the same physical information as with X-ray CT consists of using broad- or focused ion beam scanning electron microscopy (BIB- or FIB-SEM). The ion beam can directly modify or "mill" a specimen surface, and this milling can be controlled with nanometer precision. By carefully controlling the energy and intensity of the ion beam, it is possible to perform very precise nano-machining to remove very thin layers of material, for example in a block of soil impregnated with resin. BIB milling produces cross-sections of a few mm^2 to cm^2, whereas FIB deals with surfaces that at most are a few hundred μm^2. Once a new surface has been exposed, it can be imaged via SEM, at resolutions typically between 10 and 500 nm (Cantoni and Holzer, 2014). The sequence of images obtained in successive layers can be assembled into a 3D image, similar to those resulting from X-ray CT tomography, and subsequently segmented (Salzer et al., 2015; Liu et al., 2017). In the last few years, this approach has been used extensively to investigate the morphological characteristics of dolomite rocks, shales, and clays using BIB alone (Houben et al., 2013), a combination of BIB- and FIB-SEM (Hemes et al., 2015), or the joint use of micro-CT and FIB-SEM (Devarapalli et al., 2017). In soils, FIB-SEM presents a tremendous potential, but its use appears to have been limited so far to observations of microbially induced calcite precipitation in sandy soils (Li et al., 2017) and to obtain high-resolution images of the colonization of soil–root interfaces (Vidal et al., 2018).

Soil Structure Versus Architecture

Early in the use of CT scanners to characterize the physical properties of soils, it became apparent that this technology afforded a convenient response to the age-old question of how to best quantify soil "structure," this term being understood either as "the arrangement or organization of the particles in the soil" (Hillel, 2004), or, following Dexter (1988), as "the spatial heterogeneity of the different components or properties of soils."

For many decades, the vast majority of the research on the topic has viewed soil structure as intimately linked with the fact that it is possible to fragment soils into distinct aggregates upon the application of mechanical stress (Rabot et al., 2018). Undoubtedly this perspective has its roots in the soil surveyors' traditional poking of exposed soil profiles with knives, leading to the detachment of chunks of soils, called "aggregates," whose size

and shape is used to diagnose the types of pedogenetic processes that might have taken place at that location, to classify soils, and to evaluate their agronomic potential. Since the 1940s, an extensive body of literature has been devoted to the assessment of the stability of soil aggregates under a variety of operational conditions, for example under dry or wet sieving. As Young et al. (2001) point out, "the ease and seeming reproducibility of the many standard stability tests are the main drivers behind the prevalence of this type of research."

A common criticism of the concept of aggregate in soils is that it is little more than an artifact. The hierarchical organization of aggregates, identified and described in detail by Tisdall and Oades (1982), suggests that the distribution of sizes of aggregates one obtains might depend on the amount of energy that is applied to take soils apart. This operational issue, discussed by Amézketa (1999), is particularly well illustrated by the experimental results of Díaz-Zorita et al. (2002), who show that the size of fragments obtained by sieving soils is inversely related to the mechanical stress applied. Hallett et al. (2013) also point out that breakdown of soils by dynamic or static mechanical loading yields different fragmentations of soil aggregates. This dependence of the aggregate size distribution on the operational conditions under which it is measured raises the question of whether aggregates exist in soils in their natural state (Young et al., 2001), calling into question the extensive literature that tries to analyze the influence of aggregate size on various processes, e.g., in terms of the sequestration of OM, the distribution of bacteria, a wide range of geochemical processes, or the release of greenhouse gasses (Ranjard and Richaume, 2001; Jasinska et al., 2006; Nunan et al., 2006; Razafimbelo et al., 2008; Goebel et al., 2009; Pallud et al., 2010; Chivenge et al., 2011; Masue-Slowey et al., 2011, 2013; Blaud et al., 2014; Rabbi et al., 2014, 2016; Ebrahimi and Or, 2015; Jiang et al., 2015; San José Martínez et al., 2015; Sheehy et al., 2015; Hausladen and Fendorf, 2017; Rillig et al., 2017; Zhao et al., 2017; Bocking and Blyth, 2018; Li et al., 2018), and explaining perhaps why some authors have failed to observe anticipated correlations between OM content and aggregation (Razafimbelo et al., 2013). Nevertheless, one might argue that this dependence problem can be alleviated somewhat by standardizing methods, and that, in any event, it does not particularly affect attempts to understand at a very local scale in soils the interactions between pore geometry, chemical composition, and microbial activity. As long as aggregates are viewed as chunks of soil that are convenient to manipulate because they do not fall apart too easily, e.g., when they are rotated on the stage of a CT scanner, and to the extent that no particular significance is associated with their external surfaces, which might just have been failure planes in some larger aggregate, no harm is done in using aggregates to gain insight into microscale processes, as various authors have done successfully (Remusat et al., 2012; Ananyeva et al., 2013; Kravchenko et al., 2013, 2015; Voltolini et al., 2017; Yu et al., 2017).

One could also consider that there is no problem either with repacking aggregates extracted from a soil, and trying to find out experimentally or through simulation how this now entirely artificial system behaves (e.g., Daly and Roose, 2014; Ebrahimi and Or, 2016). We are often forced by journals to use repacked soil columns in order to have actual replicates, and be able to

calculate statistics, which some reviewers view as sacred and indispensable. However, it is entirely unclear at this point to what extent the conclusions that one reaches from this kind of exercise relate to the behavior of real soils, including the very soil from which the aggregates that are used originated. The reason for this has to do fundamentally with the absence of any theoretical framework or set of procedures to, as it were, put the pieces of the puzzle back together, once a soil has been disaggregated and its aggregates have been characterized, e.g., relative to their size distribution and individual geometries. In the process of disaggregating a soil sample, as long as no information is obtained about the geometry and topology of the interstices that may have existed originally between what eventually becomes distinct aggregates, there is no way practically to "reconstruct" the original soil, even for computational purpose, and in particular to guarantee that the pores between aggregates in the repacked system be similar in shape to those that existed originally[1]. One could draw parallels here with architecture (Letey, 1991; Baveye, 2006) or even with card games: Indeed, one cannot say anything about the size and shape of a house of cards after it has been torn down, simply by looking at the pile of cards that is left.

Aware of these obstacles already many years ago, a number of authors argued for a different way to approach the structure of soils. Dexter (1988), in a thorough review of the then available methodology in this field, recommends that preference be given to methods involving direct observation of structural features by scanning electron microscopy and by optical scanning of resin-impregnated sections and fracture surfaces. A few years later, Letey (1991) vents his frustration in the face of many failed attempts to link soil structure, defined in terms of aggregates, to functionality within the soil system. He suggests that instead of focusing on the solid components of soil structure, as had been the tradition for decades, one should emphasize instead the arrangement of voids, and the properties that these voids confer to soils, just as to describe a building, it is not primarily the shape of the bricks or stones that matters, or the thickness of the walls, but the size of the rooms and openings (windows, door frames). Reiterating these same messages, Young et al. (2001) argue that "an investigation of discrete aggregates or distributions of aggregates does not offer any spatial information. Functional traits of soil structure, at all scales, rely on the connectivity, tortuosity, and heterogeneity of pore space in 3D." The same message is echoed in the recent thorough review of the literature by Rabot et al. (2018), who conclude that "although appealing, the aggregate perspective does not seem to be the most appropriate to link soil structure with soil functions and processes." Because of the historically close connection between "soil structure" and aggregates, Young et al. (2001) propose to drop the expression of "soil structure" in favor of that, less history-laden, of "soil architecture." This terminology has been routinely adopted since (e.g., Baveye, 2006; Lin et al., 2010; de Jonge et al., 2012; Lin, 2012; Bouckaert et al., 2013a,b; Cazelles et al., 2013; Helliwell

et al., 2013; Kravchenko and Guber, 2017; San José Martínez et al., 2017) and will be used consistently in the following.

In principle, it is feasible to analyze this architecture by taking 2D images of sequences of thin sections in resin-impregnated blocks of undisturbed soil, and then using dedicated software to reconstruct from these images a full 3D picture of the geometry of soil pores. This tedious, time-consuming approach has been adopted with success by Cousin et al. (1996, 1999), Vogel (1997), and Vogel and Roth (2001). However, access to X-ray beams at various synchrotron facilities, and especially the availability of table-top X-ray CT scanners, have allowed the work in this area to experience a quantum leap around the turn of the century. The new technology has made it possible to obtain 3D images of the pore space in intact soil cores much more rapidly, and at resolutions that have gradually improved over time (Mooney, 2002; Rozenbaum et al., 2012; Bouckaert et al., 2013a; Calistru and Jitareanu, 2015; Rabot et al., 2015).

The gradual conceptual shift from the aggregate-based "structure" to the "architecture" of soils has been accompanied by a refocus of the discourse on the voids within this architecture, following in that respect the suggestion of Letey (1991). Another conceptual shift as well is occurring in that respect. Conditioned to think in terms of a traditional analogy between the pore space of soils and a bundle or network of capillaries, soil physicists used to be concerned about the size of "pores" in soils. It is clear from CT images that there are no identifiable pores in soils, and that the delineation of individual pores is necessarily somewhat subjective. Some authors have tried to make the concept of pore size distribution less arbitrary by using automatic algorithms to determine locally the radii of maximum balls that are fully inside the pore space. Partly because of the historical weight of the capillary analogy and partly with the help of these "inscribed balls" algorithms, pore size distributions are still being computed (e.g., Kuka et al., 2007; Papadopoulos et al., 2009; Ostadi et al., 2010; Bouckaert et al., 2013a; Peng et al., 2014; Houston et al., 2017; Meira Cassaro et al., 2017). Yet, clearly, researchers have increasingly turned in recent years to other approaches to describe quantitatively the make-up of soils. Indeed, a whole panoply of mathematical tools is now available, and is steadily expanded, to characterize a number of aspects of the pore space. These tools include various algorithms to calculate the tortuosity and connectivity of the pore space on the basis of grayscale or binary 3D CT images (Gommes et al., 2009; Houston et al., 2017; Meira Cassaro et al., 2017). Another approach to describe the pore space quantitatively is provided by the fundamental set of Minkowski functional measures (Lehmann et al., 2006; Vogel et al., 2010; Falconer et al., 2012). These functional measures comprise the volume, surface area, integral mean curvature, and the Euler-Poincaré characteristic (or topological measure Chi). Karsanina et al. (2015) propose another set of descriptors, including two-point probability functions, linear functions, and two-point cluster functions, and they used the first two in simulated annealing optimization procedures to reconstruct soil architecture artificially, based on original images of soil thin sections. For a number of years, fractal geometry was thought to be an ideal tool to characterize the inner space of soils, since according to the way the theory was interpreted, a single

---

[1] There is one exception to this general statement, in the case of some oxisols in tropical areas, such as the La Selva soil investigated by Radulovich et al. (1992). This soil, containing 95% kaolinite clay, is made of "pseudo-sand" microaggregates that are very regular in shape and size, so that it is possible in practice to repack the soil in a state that is very close to what it was originally.

parameter, the fractal dimension, could inform about the make-up of soils over a range of scales. This vision of fractal geometry has since been confronted with the reality that a single dimension, whose value turns out to be itself scale- and resolution-dependent, does not suffice. As explained by Mandelbrot from the start, at least one other parameter, either the lacunarity (e.g., Pendleton et al., 2005; San José Martínez et al., 2017) or the succolarity (de Melo and Conci, 2013) is required to obtain an accurate description. Since the lacunarity (Pendleton et al., 2005) and likely also the succolarity are affected by the resolution of images, it is not clear at this point whether fractal geometry still offers much interest. Another approach that might (but has not yet) provide a solution to the resolution-dependence derives from the application of the theory of multifractal measures to CT images of soils (Lafond et al., 2012; Wang et al., 2016; Torre et al., 2018). From a different perspective, various authors have also tried to extract networks from 3D images of soils, to which graph theory principles can be applied to characterize the connectivity and topology of the pore space (Vogel and Roth, 2001; Perez-Reche et al., 2012).

Can We "See" Water and Organic Matter in Soils?

Since the ultimate objective of the research reviewed here is to eventually be able to predict the activity of microorganisms in soils, for whom the presence of water and readily biodegradable OM is crucial, it is important to be able to detect in what portion of the pore space they are located. In this respect, researchers have been confronted with the difficulty that, typically, if one places a wet soil sample in a table-top X-ray CT scanner, the outcome is a 3D grayscale image characterized by a histogram with a single, broad peak that is not suitable at all to tease apart the water from the solids without resorting to arbitrary assumptions (Tracy et al., 2015), nor to identify in the solid phase the portion that corresponds to OM. So far, to avoid this obstacle, researchers have either shifted their attention toward artificial media, or they have worked with actual soils but under special conditions that allow the identification of water and OM.

In terms of artificial porous media, researchers have used glass beads (Culligan et al., 2006; Schaap et al., 2007) and coarse sands (Brusseau et al., 2007) to quantify the 3-dimensional distribution of water in the pore space. If one scans these systems under partially saturated conditions, as these researchers did, evidence suggests that it is not very difficult to locate air-water interfaces. Another way to proceed, made possible by the low reactivity of glass beads or sands compared to soils, is to increase the contrast between the attenuation of X-rays in the solid phase and the liquid phase by using a contrast agent that increases X-ray attenuation in the liquid. Although the results obtained with glass beads and sands are definitely interesting and probably applicable to coarse aquifer materials, it is not clear at this stage how they help us identify water and OM in actual soils, which as a rule tend to be tremendously more heterogeneous, and have much smaller pores. There is no real answer at this point to the question of how one can transition from glass beads to actual soils. This is a perennial problem, also faced by researchers who for a time

carried out extensive work in the 1960s on the hysteresis of water retention in glass beads systems (Topp and Miller, 1966; Topp, 1971).

Another approach that can conceivably work in some soils, consists of scanning a soil sample when it is dry, and then re-scan it when it has been brought to the desired moisture content (e.g., Tracy et al., 2015). Comparison between the non-air phases in the "before" and "after" images yields the distribution of water in the system. In principle, this approach could work very well if the soil does not swell at all when its moisture content is increased. This apparently was the case in the experiments carried out by Tracy et al. (2015), who report that "no significant evidence of shrinkage was observed." Yet the problem is that most soils in the world do shrink/swell to some extent (Garnier et al., 1997), including soils like those described by Radulovich et al. (1992) whose kaolinitic mineralogy one does not traditionally associate with this phenomenon. The question remains at this point of what is significant enough evidence of shrinkage or swelling in a soil sample to prevent this "subtraction" method to be used to visualize the distribution of water.

Yet another strategy is to carry out CT measurements on real soils under conditions where water and OM are not intimately mixed with the solid constituents at very fine scales. This approach has been adopted by a number of researchers in the last few years who worked on plant residues within soils (De Gryze et al., 2006; Negassa et al., 2015; Kravchenko et al., 2017) or attempted to directly visualize soil moisture (Carminati et al., 2008; Tippkötter et al., 2009; Pot et al., 2015). Working with a real clay-loam soil material near water saturation, Carminati et al. (2008) focused on the water that occupies part of the volume in the larger pores. They were able under these conditions to clearly observe pendular rings of water in images at a resolution close to 6 μm. Tippkötter et al. (2009) adopted a similar focus, in undistributed soil samples, and were able with a table-top X-ray CT scanner to visualize the presence of water films coating the inner surfaces of meso- and macropores. Similarly, Pot et al. (2015), working with synchrotron X-rays, were able to generate CT images of repacked aggregates in whose histograms there was a good separation of voxels associated with the air, liquid, and solid phases (**Figure 2**).

A last approach that could work in principle to see the moisture in soils consists of adding various contrast agents to the water, to modify its X-ray attenuation (Van Loo et al., 2014). However, in practice, contrast agents need to diffuse sufficiently for the method to work, which again, in many cases, in undistributed soil samples, might be operationally workable only to image the largest pores near saturation.

It might thus be tempting to look elsewhere for a possible answer. Indeed, over the last decade, the resolution associated with 3D nuclear magnetic resonance (NMR) micro-imaging has become steadily better. Lee and Lee (2017), for example, managed to obtain images of 1.2 mm by 1.2 mm columns of glass beads and crushed silica gels particles, respectively, with a spatial resolution of 46.875 μm, which is still coarser than the resolution of CT scanners for this column width, but is not as far from it as it used to be. As encouraging as these results are, however, NMR micro-imaging as currently implemented still suffers from a major

FIGURE 2 | (A) two dimensional section of synchrotron X-ray computed tomography image of a soil cube equilibrated at −1 kPa and **(B)** histogram of the corresponding 3D SR-μCT image. In the tomographic sections, black is the air phase, dark gray is the water phase and light gray to white is the matrix phase. The scale bars represent 500 μm. (Reprinted with permission from Pot et al., 2015).

obstacle when it comes to real soils, and therefore is not a real solution in that context. Because of the very powerful magnets that are used to generate the signal, only soils that do not contain paramagnetic elements can be imaged. Since many if not most soils contain some iron, at least, this limits tremendously the conditions under which NMR is a viable alternative to X-ray CT to generate 3D images. An alternative to NMR would be to use neutron computed tomography (Tumlinson et al., 2008) to observe the distribution of water in soils, but at this stage the resolution of images that can be generated is still relatively low, comparable to that obtainable with medical or table-top X-ray CT equipment 15 or 20 years ago (Perfect et al., 2014).

The best option to "see" water at this point, even though it has not been implemented very much of late, appears to be

the use of dual energy X-rays in CT scanners. With gamma rays of two different energies, typically produced by [241]Am and ^{137}Cs sources, it has been possible for a while to simultaneous assess the moisture content and bulk density of soils (Soane, 1967; Hopmans and Dane, 1986; Biassusi et al., 1999), but the measurements are extremely slow, and their spatial resolution is low. Garnier et al. (1998) applied dual-energy synchrotron X-rays for the first time to soils, to assess rapid vertical soil density and water content changes in swelling soils during infiltration. Shortly thereafter, Rogasik et al. (1999) used a medical scanner that allowed them to scan silt loam subsoil samples at two energy levels (80 and 120 kV) to evaluate the distributions of water, air, and solids, as well as the voxel dry bulk density. The spatial resolution during scanning was 0.25 mm in the horizontal and 1 mm in the vertical direction, which was (and still is) standard for scanners routinely used in hospital settings. Since this work almost 20 years ago, there has been to our knowledge no application of dual-energy X-ray tomography to soils. Several table-top X-ray scanners currently commercialized offer the possibility to carry out dual-energy scanning sequentially on soil samples. The fact that nobody so far has reported on the use of this feature with table-top scanners suggests that polychromatic X-rays are not suitable for dual-energy scanning to work in the case of soil samples. Further research is needed to determine if with monochromatic X-ray beams, at synchrotron facilities, dual-energy scanning produces promising results.

Part of the reason for the limited use of dual-energy scanning — and it would be true as well for attempts to scan soils rich in OM with dual-energy gamma-rays — is that until not too long ago, it would have been difficult to tease apart water from soil OM in CT images (Taina et al., 2008). The problem is not OM *per se*. Kettridge and Binley (2011) demonstrate that X-ray CT can image beautifully the structure of peat samples of various compositions. The difficulty has to do with the fact that at the high X-ray energies required to penetrate through soil materials, there is very little difference in X-ray attenuation between water and water-filled OM, whose peaks in grayscale image histograms are often not clearly distinguishable from a broad peak associated with mineral constituents. This problem was resolved, at least in part, in 2014, when Van Loo et al. (2014) tested 52 different chemical compounds. They perfused aqueous solutions saturated with the compounds through undisturbed soil samples under partial vacuum and found that 4 of these chemicals [phosphomolybdic acid (PMA), silver nitrate, lead nitrate and lead acetate] successfully enhance the X-ray attenuation contrast of OM relative to soil minerals and allow particulate organic matter (POM) to be easily detected. Peth et al. (2014) tried to take advantage of the fact that osmium has a marked absorption K-edge[2] at a photon energy ∼74 keV. They exposed air-dry soil aggregates to a 25 w/w OsO_4 solution for 48 h at room temperature in a closed vial under a fume hood (because of the very high toxicity of OsO_4), and scanned

---

[2]K-edge is the binding energy of the K shell electron of an atom. There is a sudden increase in the attenuation coefficient of photons occurring at a photon energy just above the binding energy of the K shell electron of the atoms interacting with the photons.

FIGURE 3 | Illustrative two-dimensional spatial distributions of osmium-stained OM mapped onto the reconstructed image cross-sections of aggregates. In **(A)**, red colors are typically associated with particulate OM. Green colors reflect lower concentrations (Modified from Peth et al., 2014. Reprinted with permission). In **(B)**, the red patches correspond to OM (Modified from Rawlins et al., 2016. Reprinted with permission).

these aggregates at a synchrotron facility below and above the absorption K-edge, respectively. Preliminary results, obtained by Peth et al. (2014) and Rawlins et al. (2016), suggest that this technique makes it possible to visualize the distribution of OM in soils, and to distinguish between POM and OM that is distributed more diffusely throughout the soil architecture (**Figure 3**). One promising approach to identify POM in CT images consists of building on both the attenuation, thus gray scale, values of the organic materials and on the spatial distribution patterns of POM grayscale values, which uniquely separate it from the rest of the soil solids (Kravchenko et al., 2014a). Indeed, even from a "naked eye" examination, POM often stands out on CT images due to much greater uniformity of its grayscale values. Kravchenko et al. (2014a) successfully used geostatistical parameters of POM fragments as indicators of the presence of POM in intact soil samples. This approach has advantages over POM identification via Os staining, since, unlike Os staining, CT scanning has minimal effect on soil microorganisms (Bouckaert et al., 2013b; Kravchenko et al., 2014b; Schmidt et al., 2015). Thus, the samples can be used for exploring the decomposition of the identified POM fragments in a sequence of initial CT scanning, incubation, and post-incubation CT scanning activities, as done by Kravchenko et al. (2015). However, as of now the process of POM identification using this approach is time consuming and requires a substantial user input.

Sub-Resolution Pores

Another issue that, at the moment, is still awaiting a definite solution, is related to the soil pores having dimensions smaller than the resolution of CT images. From the mid-1980s to the

early 2000s, the resolution of X-ray CT scanners accessible to soil scientists improved by about 3 orders of magnitude, from a few hundred microns to a fraction of a micron in the best of cases. However, no matter how small this resolution is, a portion of the pore space unavoidably remains invisible to scanners. The practical significance of sub-resolution pores depends strongly on the resolution of CT images, of course, but also, critically, on the type of soil considered. For a coarse sandy soil, it is possible that at a 20 or 30 μm resolution, only a minute portion of the total porosity would not be visible in thresholded CT images. Contrastedly, in other types of soil, the portion of sub-resolution pores can be substantial. In microaggregated tropical soils like those investigated by Sollins and Radulovich (1988), pores with a diameter less than 5 μm make up approximately 70% of the pore space, and are key to understanding the unique physical and chemical properties of these systems (e.g., Radulovich et al., 1992). In the silty soils investigated by Piccoli et al. (2017), 82% of the pores a dimensions smaller than the resolution of 30 μm at which the CT scans were made. In clayey or clay-loam soils, like those whose pore size distribution was determined via mercury intrusion porosimetry by Churchman and Payne (1983), a resolution of 10 μm would be too large to identify any pore at all, and it would be of paramount importance to be able to somehow characterize the sub-resolution porosity in some fashion.

In some very special cases, grayscale CT images, before any thresholding or segmentation is carried out, may contain some information about sub-resolution features. In porous media like sandstone samples or columns filled with glass beads, which consist solely of a homogeneous mineral phase, grayscale values

intermediate between those of the pores and solids in CT images result from partial-volume effect if the solid particles are not porous. If, on the contrary, the solid particles are themselves porous, intermediate grayscale values are associated both with partial-volume effects and with sub-resolution pores, and blind application of a ternary segmentation approach, like that used by Scheibe et al. (2015), may yield meaningless results if interpreted solely as sub-resolution porosity. However, in these same simple systems, as long as partial-volume effects are negligible, grayscale values contain unambiguous information about sub-resolution pores, information that is lost entirely when the images are thresholded (Gommes et al., 2009; Baveye et al., 2010). To refine the analysis, insight obtained from images of these systems at different resolutions can be combined, as was done recently by various authors (Sok et al., 2010; Pini and Madonna, 2016; Shah et al., 2016) and applied to soils by others (Vogel et al., 2010; Dal Ferro et al., 2014), to try to get a better handle on predicting the properties of sub-resolution voids. Unfortunately, in real soils, in most cases of practical interest, both these single- and multiple-resolution approaches run into as yet insurmountable hurdles, related to the intimate, fine-scale mixing of minerals, OM, and water. The contribution of these different phases and constituents to the grayscale value of voxels in reconstructed CT images cannot at this stage be differentiated, and as a result, it is not possible in general to correlate this grayscale level with the porosity of the volume of soil to which it corresponds. It might be necessary to wait until tunable X-ray and gamma-ray scanners become routinely available, to resolve this issue.

Moving From 3D to 4D: Dynamical Measurements

In order to get a dynamical picture of physical processes in soils, one needs to transition from 3D to 4D, the fourth dimension of course being time. In many disciplines outside soil science, this transition has captured the attention of researchers over the last few years, and very interesting results have been obtained, in particular for very coarse-textured porous media (Berg et al., 2013; Dobson et al., 2016). Yet, as far as soils are concerned, forays along these lines have been timid. At the mesoscale, very interesting work, starting already 25 years ago, describing how earthworm burrow systems evolve over time (Joschko et al., 1991; Capowiez et al., 1998), how the geometry of macropores in paddy soils evolves during soil shrinkage (Bottinelli et al., 2016), or how loamy soils are compacted during centrifugation (Schlüter et al., 2016). Also, various researchers have used MRI systems to monitor the infiltration of water in clay and coarse sandy loam columns (Amin et al., 1994, 1996; Preston et al., 2001; Votrubová et al., 2003), γ-ray CT equipment to quantify the swelling of vertisols over time (Biassusi et al., 1999), or neutron CT systems to investigate the dynamics of water flows in soil, especially in the rhizosphere (Badorreck et al., 2010; Perfect et al., 2014; Tötzke et al., 2017). However, virtually all of this work has been carried out at relatively low resolutions, at best of 15 μm but more often than not of several tens or even hundreds of microns.

At the micron scale sensu stricto, very little 4D work has been carried out so far. None of this research includes water

movement, which is not very surprising, given the difficulties mentioned earlier concerning the detection of water at a sufficiently high resolution to be relevant to the microscale. Even under the various conditions where this detection is possible, water movement tends to be too fast to be monitored by X-ray CT, even at the fastest scanning times (of the order to 10–15 min, typically) available with table-top scanners. Ultrafast scanning techniques have been used recently with columns filled with gravel (Dobson et al., 2016), but similar research has yet to be conducted with soils. Because of these constraints, dynamic microscale measurements have been limited to situations that involve ice formation, or slow changes in the architecture of soils. Using a table-top X-ray CT scanner, Torrance et al. (2008) investigated the changes in structure and the redistribution of water to form ice lenses in saturated samples of an Aurora silt loam frost-susceptible soil that were thoroughly mixed to produce an initially homogeneous material, and of a Honeywood silt loam that was deliberately contaminated with motor oil. The soils were subjected to relatively rapid, downward freezing, with access to water at their base. The results indicate that CT can produce excellent images of the ice lens distribution within a frozen silt loam soil, the consolidation of soil between the ice lenses, and the effects of hydrocarbon contamination on ice formation. Also using X-ray CT in freezing soils, Starkloff et al. (2017) assessed the impact of a succession of freezing-thawing cycles on the pore network of a silty clay loam and a loamy sand topsoil. Also recently, Schlüter and Vogel (2016) quantified soil architecture turnover by labeling soil constituents in place with small garnet particles and tracking their fate in successive CT images. The particles adhere to pore boundaries at the beginning of the experiment but gradually change their position relative to the nearest pore as structure formation progresses and pores are destructed or newly formed.

Modeling the Physics

Over the last 2 decades, a significant body of literature has been devoted to the mathematical modeling of water retention and transport within the complex geometry of soil pores, revealed with increasing resolution by X-ray CT scanners. The bulk of this literature has dealt with the development and application of the Lattice-Boltzmann method (Martys and Chen, 1996; Genty and Pot, 2013, 2014; Liu et al., 2016; Cruz et al., 2017; Zhou et al., 2018), but in recent years, other methods have also been adopted, based on finite element or finite difference schemes, or on geometric primitives.

Most of the work in this area has involved a number of variants of the Lattice-Boltzmann method, in which a fluid is viewed as a collection of fictitious particles that, alternatively, propagate from node to node on a regularly spaced grid (lattice mesh), then collide with the particles that end up on the same nodes. In the modeling of soils, the nodes correspond to the centers of voxels in 3D CT images. The method originates from a molecular description of a fluid and can directly incorporate physical terms stemming from a knowledge of the interaction between molecules. Hence, in principle, it keeps the cycle between the elaboration of a theory and the formulation of a corresponding numerical model short, which undoubtedly

explains the enthusiasm it incited as soon as 3D CT images of soils became available. The key mathematical ingredient of the method is the probability $f_q(\vec{r}, t)$ of finding a particle at position $\vec{r}$ in one of the microscopic directions envisaged within the lattice, at time t, where the subscript q is an index associated with a set of microscopic directions that are selected arbitrarily. Several discretizations of space can be used and are traditionally classified via the DnQm scheme, where "Dn" stands for "n dimensions" and "Qm" denotes "m speeds." A common choice is $D3Q19$, in 3 dimensions and with 18 nearest neighbors considered around each node, described by the unit microscopic velocity vectors, $\vec{c}_q$. In this case, the subscript q takes on 19 different values (including rest particles).

Classical Lattice-Boltzmann models applied to soils require CT images to be thresholded and assume that voxels associated with pores in binary 3-D images are totally permeable to water molecules, whereas those associated with solids are completely impermeable. Recognition of the significance of the sub-resolution pore space has prompted a sizeable number of researchers in the last couple of years to investigate ways to take this pore space into account explicitly in Lattice-Boltzmann models of water movement in soils, following Gao and Sharma (1994) and Freed (1998). The resulting "Gray" or "Partial-Bounce-Back" (PBB) Lattice-Boltzmann models consider that each voxel in the original, grayscale CT images has a given probability of penetration by water or solutes, and therefore a complementary probability that water or solute particles that penetrate the voxel eventually bounce back to their previous positions (e.g., Sukop and Thorne, 2006; Chen and Zhu, 2008; Han et al., 2008; Walsh et al., 2009; Jones and Feng, 2011; El Ganaoui et al., 2012; Gottardi et al., 2013; Walsh and Saar, 2013; Zalzale et al., 2013; Chen et al., 2014; Li et al., 2014; Yoshida and Hayashi, 2014; Ginzburg et al., 2015; Xie et al., 2015; Yehya et al., 2015; Apourvari and Arns, 2016; Bultreys et al., 2016; McDonald and Turner, 2016; Pereira, 2016; Zhang et al., 2016). In all this work, considerable advances have been made recently and a number of technical issues have been clarified (Ginzburg, 2016), yet a major experimental hurdle related to the evaluation of the penetrability of sub-resolution pores, which at this point remains an arbitrary parameter in the models. As discussed in detail by Baveye et al. (2017), this penetrability cannot be deduced simply from grayscale values in CT images, and there is no practical alternative yet available.

The Lattice-Boltzmann method has indisputably become the de-facto standard in pore-scale studies of water retention and transport in soils. One of the drawbacks of the method, however, is the very long (sometimes weeks-long) computational time it typically requires on personal computers. Open Lattice-Boltzmann environments like Palabos[3] or OpenLB[4] offer options to run the code on massively parallel computers and arrays of graphics processing units (GPUs), or to decompose the flow domain into manageable subportions, and researchers are increasingly resorting to these speeding techniques

in applications of the Lattice-Boltzmann method to soils. Nevertheless, the relative slowness of the original method, unless one has access to large computer clusters, has encouraged various authors to explore other avenues to model soils at the microscale.

One of these avenues encompasses a technique called "smoothed particle hydrodynamics" (SPH) (e.g., Tartakovsky et al., 2007), which works by dividing a fluid into a set of discrete elements, referred to as particles. To these particles is associated a spatial distance (known as the "smoothing length"), over which their properties are "smoothed" by a kernel function. This means that the physical quantity of any particle can be obtained by summing the relevant properties of all the particles that lie within the range of the kernel.

Finite element or finite difference schemes are also among the alternative techniques that have been selected to solve Stokes' equation within the pore space of soils (e.g., Liu et al., 2016). In a recent article, for example, Gerke et al. (2018) introduce the free software Finite-Difference Method Stokes Solver (FDMSS) that solves Stokes' equation using a finite-difference method (FDM) directly on voxelized 3D pore geometries (i.e., without meshing). Based on explicit convergence studies, validation on sphere packings with analytically known permeabilities, and comparison against lattice-Boltzmann and other published FDM studies, these authors conclude that FDMSS provides a computationally efficient and accurate basis for single-phase pore-scale flow simulations. By implementing an efficient parallelization and code optimization scheme, permeability inferences can now be made from 3D images of up to 10^9 voxels using modern desktop computers. Tracy et al. (2015) use another numerical technique, based on the SIMPLE (Semi-Implicit Method for Pressure-Linked Equations) algorithm (Patankar, 1980) to solve Stokes' equation in the pore space of loamy sand and clayey loam soil samples. These authors did so with OpenFOAM, an open source Computational Fluid Dynamics toolbox.

A different path, beside the Lattice-Boltzmann method and the various numerical schemes just alluded to, consists of using a morphological model. Such a model involves the approximation of the soil pore space by a network of so-called volume primitives, i.e., simple geometric shapes that can be transformed at will and combined to represent more complex geometries (Monga et al., 2007; Ngom et al., 2012). One way to do so consists of using a geometrical algorithm based on Delaunay triangulation to determine the maximal balls of the pore space segmented from the 3D CT images. Maximal balls are defined as the balls included in the pore space but not included in any other ball included in the pore space. Then, a minimal set of maximal balls is extracted in order to obtain a compact representation of the pore space (Monga et al., 2009). The key advantage of the method is that it requires far fewer balls than voxels to cover the pore space, and one might hope in principle that this drastic simplification will carry over to the various processes (e.g., water retention, transport) that one wants to simulate. There is no guarantee in this respect, however, especially when models encompass not just physical processes but also (bio)chemical and microbiological ones. If the geometric primitives become too large, it may be necessary to divvy them up in smaller

---

[3]http://www.palabos.org
[4]http://www.openlb.net

subcomponents in order to account adequately for the spatial heterogeneity exhibited by chemical and microbial processes in soils. The added computational time that would result from this division might very well negate the speeding up that theoretically results from the scheme.

Since there are different ways to simulate the retention and transport of water in soil pores, one might ask which of these methods performs best. The intercomparison of models (e.g., Yang et al., 2016) provides some general idea of the agreement, or lack thereof, among the models, but clearly, benchmarking model predictions against actual experimental data is by far the most desirable approach. At this juncture, since dynamic data about the movement of water (or other liquid phases, e.g., NAPLs) are not (yet) readily available, direct comparison with experimental data is feasible only for water retention in the pore space. Pot et al. (2015) carried out the only such comparison to date, on the basis of quantitative data of the distribution of water and air in soil samples constituted of repacked aggregates, equilibrated at three matric potentials (-0.5, -1, and -2 kPa). The phase distribution data were derived from synchrotron X-ray CT images at a resolution of 4.6 μm. Water distribution was simulated by a two-phase Lattice-Boltzmann model (LBM) and a morphological model (MOSAIC). Results indicate that the lattice-Boltzmann model is able to predict remarkably well the location of air–water interfaces (**Figure 4**). When one lifts the assumption, motivated by capillary theory, that a pore can drain only if a connecting pore is already full of air, MOSAIC gives an acceptable approximation of the observed air–water interfaces (**Figure 4**). However, discretization of pores as geometrical primitives causes interfaces predicted by MOSAIC to have non-physical bulbous shapes. Nevertheless, given the huge difference in computing time required to run these two models (minutes for MOSAIC versus tens of hours for Lattice-Boltzmann), Pot et al. (2015) recommend that further research be carried out on the development of both modeling approach, in parallel. One might

argue that the same recommendation applies to other numerical schemes as well.

Visual Summary of the Status of the Physical Front

Now that we have covered in some detail the progress achieved to date in the description and modeling of the physics of soils, it is probably a good idea, and a nice way to summarize things, to go back to the schematic diagram of **Figure 1**, and, with it, attempt to represent visually where we are at the moment. In **Figure 5**, this is done by shading in the diagram of **Figure 1** the parts that correspond to work yet to be carried out. Admittedly, this is a subjective exercise, and different researchers, depending on how pessimistic or optimistic they are, may come up with contrasting evaluations. Yet, based on the detailed account provided above, the depiction in **Figure 5** of the status of the physical front seems reasonable.

In terms of the physics, **Figure 5** summarizes visually the conclusion that work is relatively well advanced. Certainly, some areas require further research. Among others, the sub-resolution porosity of soils needs to be better apprehended. Yet, overall, significant progress has already been achieved on the experimental side. This is true to a lesser extent insofar as the dynamics of water (and other liquid phases) is concerned, due to difficulties in measuring changes in water content over sufficiently short times. In terms of modeling of the physics, some success has been achieved in the past decade, but there is room for improvement, in particular relative to the speed of computations.

THE (BIO)CHEMICAL PICTURE

Limited 3D Microscale Measurements

Physical information is not sufficient to characterize microenvironments. Information about the chemistry, and

FIGURE 4 | Air-water interface surfaces of a region of interest (region p1bkk04a) in a silt-loam soil, measured via synchrotron X-ray computed tomography **(left)**, predicted using the Lattice-Boltzmann method **(center)**, and predicted by the geometric primitive-based model MOSAIC **(right)** (Modified from Pot et al., 2015. Reprinted with permission).

FIGURE 5 | Visual assessment of the level of progress on the various steps in the research on the emergent properties of soils. The un-shaded parts (relative to the schematic diagram of **Figure 1**) correspond to the authors' estimate of the progress achieved to date on each step. The shaded portion of the diagram still largely remain to be tackled.

in particular about the nature of reactive surfaces (e.g., Kotani-Tanoi et al., 2007) and of dissolved or adsorbed (bio)chemical species, is also important. Therefore, to complement the information available about the geometry and topology of the pore space in soils with similar information about the chemical properties, one should ideally be able, as a start, to measure in 3D the chemical composition of soils. A logical and relatively simple option in this respect, in principle (Egan et al., 2015), would be to take advantage systematically of the X-ray absorption K edge of all the elements we might be interested in, in a manner similar to the determination of the distribution of soil OM by adsorption of osmium (Peth et al., 2014). Unfortunately, the situation with osmium is somewhat unique. First, Os happens to have its K edge at 73.87 keV, in the middle of the range of energies that is typically required to deal with soil samples of a volume larger than a few cm^3. In the literature so far, that range has extended from 30 keV for synchrotron X-rays (Pot et al., 2015) up to nominally 225 keV for polychromatic X-rays (Houston et al., 2013b). Practically, the low end of this energy range means that, in soil samples of a reasonably large size, it is not possible to detect elements with an atomic number lower than 51 in the periodic table, i.e., before antimony (Sb), which

has an X-ray absorption K edge at 30.49 keV (Bearden and Burr, 1967). This constraint entails that only a few elements, like I, Cs, Ba, Hg, Tl, and Pb, can be mapped in 3D in soil samples, but even then, yet another condition has to be met, namely that these elements be present in soils in such high concentration that they affect appreciably the level of X-ray absorption in the voxels where they are located. In soils containing only trace-level concentrations of these elements, voxel grayscale values would be unlikely to differ much, if at all, immediately below and above the various K edges. This means in effect that, naturally or artificially, soils would have to be heavily laden, at least locally, with these elements for their spatial distribution to be detectable. For example, to be able to use the X-ray absorption K-edge of Cs to detect the distribution and movement of water in fine sand samples, Willson et al. (2012) had to use 10% (by mass) CsCl solutions. Similarly, to detect the transport of CaI_2 solutions within small sand columns using the K-edge of iodine, Shokri (2014) had to use concentrated (5% by mass) CaI_2 solutions. Altman et al. (2005) submerged soil aggregates in a 507 g L^{-1} CsCl solution in order to saturate the exchange complex with Cs, prior to scanning samples above and below the Cs K edge. Similarly, Keck et al. (2017) used a 0.3 mol L^{-1} $BaCl_2$ solution

to assess the distribution of cation adsorption sites in four undisturbed soils, three of which have a very high clay content (53.9–79.9% clay). In both Altman et al.'s (2005) and Keck et al.'s (2017) cases, the clay content of their soils makes one wonder whether the amount of CsCl and BaCl$_2$, respectively, needed for complete saturation of the exchange complex with Cs+ and Ba2+, which appears necessary to detect significant differences in X-ray attenuation, may have also caused, respectively, a dispersion of clay particles or a shrinking of clayey aggregates, and therefore, changes in the scanned images that could have been misinterpreted.

Another option for the 3D determination of soil composition is X-ray fluorescence. It is far less constraining in terms of the elements it can map (elements starting with Na, atomic number 11, are possible candidates), but unfortunately it suffers from a similar limitation on the size of soil samples that can be analyzed. The principle of the method is simple. When an atom is irradiated with X- rays of sufficient energy, it ejects an inner orbital electron. An electron from higher orbitals then falls to fill the vacancy in the lower energy state, resulting in the release of a fluorescent X-ray. The energy of the fluorescent X-ray given off is characteristic of the energy difference between the two orbital energy levels, which is specific to each element, while the intensity of the emitted X-rays is related to the elemental abundance in the sample being analyzed. In X-ray fluorescence tomography systems (Bleuet et al., 2010), also called confocal XRF scanners (Patterson et al., 2010; Lühl et al., 2013) or spectrometers (Smolek et al., 2012), the presence of focusing optic both on the path of the incoming X-ray beam and between the sample and the detector allows the 3D elemental profiling of the sample, provided the travel path of fluorescence X-rays within the sample, once they are produced, is not too long, so that their absorption is minimized. This re-absorption of X-rays limits the 3D measurements to minute samples, extending to at most a few mm in any direction. In that context, McIntosh et al. (2015) used 3D micro X-ray fluorescence spectroscopy to determine non-destructively the elemental composition of minute aggregates of a plutonium-contaminated soil, within which they could identify distinct 30 μm-size Pu particles with a limit of detection <15 ng.

Many 2D Measurements Are Feasible

Until direct 3D mapping of the chemical properties of soils becomes technically feasible and more accessible, an alternative approach to obtain 3-dimensional chemical information about soils at the microscale is to carry out the same procedure used a couple of decades ago by Cousin et al. (1996, 1999), Vogel (1997), and Vogel and Roth (2001), to obtain insight into the physical properties of soils. The idea is to perform multiple cuts through soil samples, analyze in turn the (bio)chemical make-up of each exposed surface within the soil, then, using an interpolation technique, generate a 3-D picture from the data associated with the various surfaces. This procedure is routinely used for biological samples, such as human tissues, in which the serial removal of layers can be carried out easily, either by using a traditional microtome or a cryo-ultramicrotome, or via ion-beam ablation.

To these exposed surfaces, it is now possible to apply a panoply of different spectroscopic techniques, a luxury that not too long ago, researchers would not even have dreamt of. Indeed, until the mid-1990s, beside the standard bulk analytical methods, requiring a sizeable sample of soils and therefore precluding microscale analysis, the only method that was available to researchers to determine local (bio)chemical properties of soils was based on energy dispersive X-ray spectroscopy, either in the so-called "electron microprobe" or SEM-EDX equipment, or on electron energy loss spectroscopy (EELS) (Villemin et al., 1995). The first two of these instruments, in scanner mode, can in principle produce elemental maps like that of **Figure 6A**. Starting in the mid- to late 1990s, synchrotron facilities around the world began offering soil scientists the opportunity to run various types of analyses, including X-ray absorption near-edge structure (XANES) and near-edge X-ray absorption fine structure (NEXAFS) spectroscopies, which rapidly became popular because of the very useful information it is able to provide on the molecular environment of atoms, and therefore on element speciation (Prietzel et al., 2003; Schumacher et al., 2005; Solomon et al., 2005, 2012; Kinyangi et al., 2006; Christl and Kretzschmar, 2007; Wan et al., 2007; Strawn and Baker, 2009; Hesterberg et al., 2011; Milne et al., 2011; Jassogne et al., 2012; Kopittke et al., 2017). In most cases, the target of interest in this type of analysis is extremely minute in extent, a most a few μm^2, but occasionally researchers have attempted to map properties over a slightly larger area, among other things to try to assess the heterogeneity of the composition of OM in soils (**Figure 6B**). Another synchrotron-based technique that has been used to some extent to obtain elemental maps involves X-ray micro-fluorescence (Hitchcock et al., 2004; Jacobson et al., 2007; Jassogne et al., 2012), which unfortunately does not provide information about speciation, but has the advantage that it can cover bigger surface areas (**Figure 6C**). Several other spectroscopic methods provide molecular- to micro-scale distributions of elements and isotopes and thus soil properties. Among them, the most commonly applied to soils in recent years is dynamic nanoscale secondary ion mass spectroscopy (NanoSIMS, **Figure 6D**). It uses a high-energy beam of ions (either Cs$^+$ or O$^-$) to eject secondary ions from a sample surface, which are then analyzed using a mass spectrometer, at a very high spatial resolution typically of the order of 100 nm for soil samples (Herrmann et al., 2007; Mueller et al., 2012, 2013, 2017). Slightly larger areas can be sampled with Static- or Time-of-flight Secondary Ion Mass Spectroscopy (Static SIMS or TofSIMS), which can target ions and small molecular fragments (Watrous and Dorrestein, 2011; Cerqueira et al., 2015; Worrich et al., 2017). Other spectroscopic methods, also working at spatial scales slightly larger than that of individual cells include Laser desorption/ionization (LDI), laser ablation inductively coupled plasma (LA-ICP), matrix-assisted laser desorption/ionization (MALDI) and desorption electrospray ionization (DESI) spectroscopies (Watrous and Dorrestein, 2011).

The fact that several of these techniques involve synchrotron X-ray beams, which are generally in extremely high demand, may explain why until now, their use has resulted in extremely few
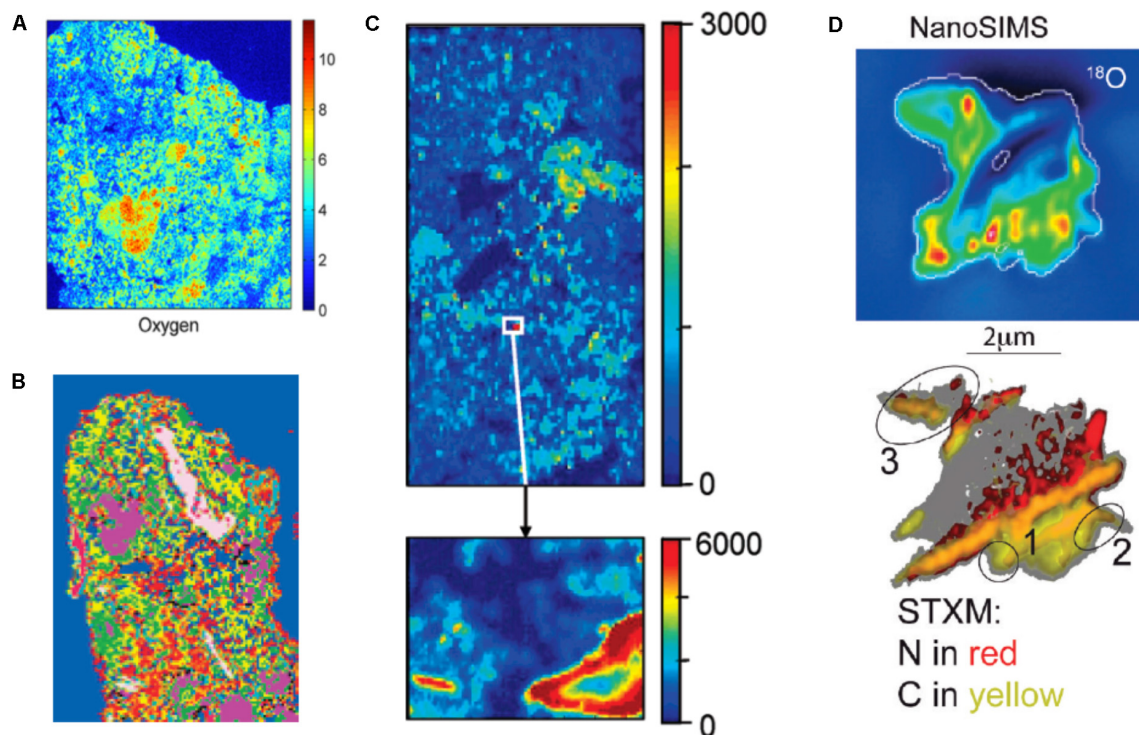
FIGURE 6 | Illustrative examples of various chemical measurements that are now routinely carried out on 2D cross-sections through soil samples: (A) SEM-EDX mapping of the distribution of oxygen in a section through a calcareous soil from Scotland. The intensity of the color indicates the concentration of oxygen (Adapted from Hapca et al., 2015). (B) Cluster map showing the large heterogeneity of carbon forms within a soil micro-assemblage from Nandi Forest (Kenya) determined by NEXAFS in combination with scanning transmission X-ray microscopy (STXM). The field of view is 5.4 μmm by 7.5 μm (adapted from Lehmann et al., 2008. Reprinted with permission). (C) Synchrotron-based μXRF maps of Cu in a calcareous soil vineyard soil from Burgundy (France). The large map on top (2 by 4 cm) was obtained with a 0.3-mm spot size, the small map at the bottom (1.5 by 1 mm) with a 20-μm spot size. The color, from blue to red, is correlated with the Cu concentration (Adapted from Jacobson et al., 2007. Reprinted with permission). (D) NanoSIMS map of ^{18}O in a soil aggregate (top) and C and N map of the same aggregate obtained by STXM (bottom). NEXAFS spectra were obtained in the three circled regions, whereas in the gray zones the sample was too thick to get NEXAFS spectra or was free of OM (Reprinted with permission from Remusat et al. (2012). Copyright {2012} American Chemical Society).

actual property maps of soil surfaces larger than microaggregates. Normally, experimentalists get "beam time" of 48–72 h at the most, during which it may be difficult to do a full scan of a thin section, for example. Due to the growing number of available instruments (soon to reach 50 worldwide), the situation for the use of NanoSIMS is improving, but access to all of them is highly coveted by researchers in many fields and only a hand full of laboratories routinely analyze soils. Fortunately, things might be getting better relatively soon in terms of NEXAFS since various groups of researchers (Peth et al., 2008; Müller et al., 2014; Kühl et al., 2016) have recently developed laser-based, benchtop-scale NEXAFS instruments, one of which is now commercially available. The results obtained to date, including on soil clays and OM, are very promising (Gleber et al., 2011; Sedlmair et al., 2012).

As exciting as the use of these various spectroscopic types of equipment might be, they afford measurements only of the concentration of various elements or their speciation, but not at all of the physico-chemical conditions in which specific (bio)chemical species are located. In particular, one would absolutely need information about the pH or redox potential locally in a porous medium, among other "thermodynamic" variables, to have a full picture of what is going on. Unfortunately,

once a block of soil has been impregnated with resin and has cured, none of these variables is accessible any more. If somehow, one could cut through a soil, and obtain a relatively flat surface in the process, without having to solidify the soil and denature it in any way, it would be possible to obtain information on pH and redox potential through the application of microelectrodes, microsensor probes or planar optodes (Pedersen et al., 2015; Rubol et al., 2016; Keiluweit et al., 2018; Wanzek et al., 2018). Other gel-based approaches such as diffusive gradients in thin films (DGT, Santner et al., 2015) could be used to obtain 2D maps of the distribution of labile chemical species. Zymography is a methodology similar to "optodes" in that a planar membrane is brought to contact with exposed soil to measure the activity of various enzymes (Spohn et al., 2013; Razavi et al., 2016). The development of new sensors is a very active field, offering perhaps interesting opportunities for microscale soil characterization in a few years.

Transitioning From 2D to 3D

Since many 2D measurements can be carried out on cuts through soil samples, it is feasible under certain circumstances to produce from them a 3D image of the soil (bio)chemical characteristics.

As with anything one does, it is useful to inquire whether this step is absolutely required. If methods were readily available to provide us with 3D images of the (bio)chemical composition of soils, we would not necessarily ask the question of why we need 3D images in the first place, but since the best we can get experimentally is 2D images of cuts through soils, it is worthwhile asking ourselves whether we really need to go through the added effort of the transition to 3D. Some researchers may be interested mostly in the relative distribution of chemical elements with respect to the pore system, to evaluate local gradients and accessibility of substrate for soil biota. They may consider that information in this respect can be obtained by single 2D slices of chemical maps that are projected on the 3D pore structure. From this standpoint, serial sectioning and interpolation are not necessary. A different perspective on the question, held for example by Hapca et al. (2011, 2015) is that, just like the degree of connectivity or tortuosity of the pore space in 2-dimensional cuts through a soil are generally different than in 3-dimensions, the spatial characteristics of the chemical make-up of soils, the distribution and local concentration gradients of targeted (bio)chemical compounds, also need to be estimated in 3D if one is to understand their influence on microbial processes. Experience will show in the future which one of these two perspectives is most conducive to progress.

Nevertheless, to obtain 3D information on (bio)chemical properties, the process of interpolation between 2D maps is complicated by the fact that cutting through soils is not as straightforward as it may seem. In mineral soils, the frequent presence of dense constituents reduces the range of techniques that can be used to cut or scrape away successive layers with minimal disturbance. Particularly when operating microtomes, the presence of constituents with markedly different densities often causes blades to deviate from their set course, so that eventually the exposed surfaces are not perfectly flat. Because of that, the correspondence of 2-D chemical or microbiological maps with the physical information obtained via computed tomography is likely to be poor, unless artifacts generated during soil cutting are accounted for.

Therefore, the first step in any attempt to simultaneously evaluate in 3D the physical, chemical, and biological

FIGURE 7 | Schematic diagram of the successive steps in the 2D–3D interpolation method proposed by Hapca et al. (2011, 2015). **(1)** Illustration of a typical method to isolate a layer from a soil cube, with a microtome blade. The cut may be at angles α and β, respectively, with the x–y plane in the x and y directions, respectively, resulting in layer surfaces that are not strictly parallel to each other, **(2)** rotation of the chemical analysis plane within the 3D CT image, **(3)** Reconstituted CT image of the soil surface. The dotted lines correspond to the limits of the different masks applied to the successive layers during the zonation process, **(4)** Spatial distribution, measured with SEM–EDX, of silicon in the top and bottom soil surfaces of an individual slice through the soil sample, **(5)** schematic representation of the interpolation layers and the corresponding sampling grids for the selection of the interpolation points, **(6)** 3D prediction of the silicon distribution in soil sample.

characteristics of soil samples is to find a way to correct for any distortion that may occur when cutting or grinding down soil samples to successively expose surfaces on which 2-D chemical mapping is carried out, and to geo-reference these 2-D maps within the geometry of the soil solid phase, determined via X-ray computed tomography. A practical, automated procedure to accomplish these tasks has been developed by Hapca et al. (2011). This procedure, depicted in **Figure 7**, involves three successive steps, namely the reconstitution of the physical structure of a given soil layer surface, the alignment of the chemical maps with the reconstituted soil surface image, and finally the 3D alignment of the 2D chemical maps with the internal structure of the soil cube. Once this alignment is carried out satisfactorily, one can proceed to a statistical interpolation between successive geo-referenced 2D planes. Hapca et al. (2015) suggested that, for this interpolation, the 3D information produced via X-ray CT could be used as a guide. They proposed a method based on a regression tree method and ordinary kriging applied to residuals, and used it to predict the 3D spatial distribution of carbon, silicon, iron, and oxygen at the microscale. The spatial correlation between the X-ray grayscale intensities and the chemical maps made it possible to use a regression-tree model as an initial step to predict the 3D chemical composition. For chemical elements, e.g., iron, that have high attenuation and are sparsely distributed in a soil sample, the regression-tree model provides a good prediction, explaining as much as 90% of the variability in some of the data. However, for chemical elements with lower attenuation coefficients that are more homogenously distributed, such as carbon, silicon, or oxygen, the additional kriging of the regression tree residuals improved significantly the prediction with an increase in the R^2 value from 0.221 to 0.324 for carbon, 0.312 to 0.423 for silicon, and 0.218 to 0.374 for oxygen, respectively. In principle, this method could be used for any (bio)chemical parameter that can be mapped on 2D cuts.

Dynamical Picture

Given the need to be able to work with 2D cuts through soils, e.g., by impregnating soils with resin and cutting through the resulting blocks in one way or another, to carry out measurements of (bio)chemical characteristics, it should come as no surprise that dynamical measurements *at the microscale* have been so far, and may remain for some time, impossible to achieve (Blaser et al., 2016). Of course, dynamical measurements of properties as they emerge at the macroscopic scale can be achieved relatively easily, for example breakthrough curves in column experiments serving as evidence of chemical transport. To some extent and for specific purposes, such macroscopic properties may suffice, but experience has shown time and again that in an of themselves, these macroscopic observations are not adequate to assess the soundness of microscale models of (bio)chemical dynamics.

Much of the energy, nutrient and information (signal molecules) flows in soil occur in aqueous phase. A broad range of organic and inorganic molecular forms are released into solution, taken up and metabolized, transformed by enzymes or immobilized on surfaces continuously. These constitute the most dynamic portion of the microbial environment. Although much research has been carried out on the soluble OM of soil (e.g., Rousk and Jones, 2010; Lerch et al., 2011), the scale at which the measurements have been made is inappropriate for understanding how the flows of energy, nutrients and information vary throughout the soil pore network; only an average value is obtained. Furthermore, extraction methods tend to introduce biases related to the choice of extractant and the disruption of the physical architecture of soil may release molecules not previously in solution (Inselsbacher et al., 2014). The use of miniaturized sampling devices (millimeter scale) such as microdialysis probes or micro-suction-cups offer the possibility of detecting gradients in the soil solution at scales that are getting closer to those relevant to microbial communities (Inselsbacher et al., 2014; Oburger and Schmidt, 2016), particularly in the rhizosphere where gradients are stronger. With microdialysis the soil solution is sampled by passive diffusion and is therefore likely to better reflect the soluble environment perceived by microbial communities. Recent research has shown that there are significant differences in the size and composition of soluble organic and inorganic N pools measured by microdialysis and those measured by the traditional extraction methods (Inselsbacher et al., 2014). The small size of the probes makes it possible to locate them precisely in soil samples using micro-CT imaging and to map diffusive fluxes in real time (Brackin et al., 2017).

Numerical Modeling

Over the last decade, a very significant amount of work has been devoted by geochemists and environmental engineers to the development of computer models able to describe the fate of a number of chemical species of interest in porous and fractured media (Tartakovsky et al., 2007; Valocchi, 2012; Steefel et al., 2013; Yoon et al., 2015). These models typically combine a transport component with a chemical speciation algorithm. Chemical transport is described using a variety of approaches, including the Lattice-Boltzmann method, smooth particle hydrodynamics (Tartakovsky et al., 2007), hybrid Lattice-Boltzmann-direct numerical simulation (DNS) (Yoon et al., 2012), and pore network models (Li et al., 2006). In terms of the chemical reactions that the speciation algorithms describe, as Iliev et al. (2017) accurately point out, many models focus on chemical reactions occurring in solution, with only a few models dealing with reactions controlled by the reactivity of the surfaces, like the dissolution of mineral phases. This bias makes sense for the type of systems researchers have been trying to describe, namely aquifer materials, calcareous formations, sandstones, or simply laboratory set-ups filled with glass beads. In that general context, one of the key predictions of these models has been that under a wide range of situations, macroscopic-scale descriptions with "effective" (i.e., volume-averaged) parameters do not account adequately for model predictions when non-linear reactive transport processes are associated with highly localized chemical reactions and incomplete mixing within the porous medium (Li et al., 2007a,b,c; Battiato et al., 2011; Steefel et al., 2013).

The different features of current microscale geochemical models of reactive transport probably explain to a large extent why none of them has been used so far to describe soil processes at the microscale. Given the extremely high specific surface area, and the significant surface reactivity of many soils, in addition to the fact that the reactions that take place in soils are complicated by the presence of very heterogeneous OM, the speciation portion of typical microscale geochemical models would have to be entirely overhauled before it could be applied to soils. Nobody, as far as we are aware, seems to have launched into this work yet. In addition, even if someone had done that work, model predictions could not at the moment be compared with actual microscale measurements at this stage, as discussed in detail in the previous two subsections.

Visual Summary of the Status of the (Bio)chemical Front

If we try to summarize graphically the state-of-the-art of the (bio)chemical characterization and modeling of soils at the microscale, it is clear that work in this area is far less advanced than on the physical front (**Figure 5**). Measurements of static features or of the dynamics of (bio)chemical species are still very limited. Some of this scarcity of data can, however, be addressed. There is indeed a great potential to generate many static, 2D data, using a wide array of experimental methods, and to extrapolate them to three dimensions. Modeling frameworks are available to describe the transport of reactive chemical species in porous or fractured media, but they would need to be modified substantially before they could be applied to soils, and that significant effort has not taken place yet.

THE MICROBIOLOGICAL SCENE

3D Microscale Distribution of Microorganisms: Absence of Direct Data

To complement the 3D data related to the geometry and topology of soil pores, as well as 3D data about the (bio)chemical properties of soils, generated by interpolation among 2D pictures, it would be ideal if detailed 3D information could be obtained about the distribution of microorganisms in soils. Such information can be readily obtained in the case of wood, at least for fungi (Van den Bulcke et al., 2009). But unfortunately, for exactly the same reasons that hinder the direct 3D determination of the distribution of OM in soils, it has proven impossible so far to quantify the spatial heterogeneity of the distribution of microorganisms *in actual soils*.

When direct 3D measurements of biomass distribution in porous media have been obtained, it has so far always been under conditions that bear little similarity to real soils. Lilje et al. (2013) describe the development of a culture system and staining protocol they have used to obtain 3D quantitative data of filamentous and zoosporic soil fungi in an artificial matrix that was "developed to simulate the particulate nature of soil." This artificial matrix consists of 500–900 μm diameter X-ray translucent polystyrene beads, which might be morphologically

similar, to some extent, to coarse sand particles, but would likely have very different surface and hydration properties than typically highly heterogeneous soils. In many ways, the same comment pertains to the use of nuclear resonance imaging to detect "biofilms" in systems composed of polystyrene beads (Vogt et al., 2013). Sanderlin et al. (2013) pioneered the use of a very promising low-field magnetic resonance system to visualize the 3D distribution of biofilms in glass beads and sand particles, whereas a number of other authors used X-ray tomography to assess the distribution of biofilms in systems of glass beads (Davit et al., 2011; Iltis et al., 2011; Peszynska et al., 2016) or 2.5 mm-diameter Nafion pellets (Carrel et al., 2017). In all these cases, the properties and geometry of the systems investigated are drastically different from those of actual soils, which are generally characterized by a spatially dispersed- rather than concentrated biomass, and it is not clear at all at this stage how the transition from artificial media to actual soils will be made.

Since *direct* methods are lacking to quantify the 3D microscale distribution of bacteria in whole soil samples in one go, a number of authors have developed sampling techniques to obtain 3D information in other ways. Dechesne et al. (2003) developed such a technique and tested it in repacked soil columns. Their approach consists of a number of steps. The soil is first micro-sampled within several small subunit volumes of roughly the same volume (minimum sample side: length of 50 μm) within the columns, and these microsamples are subsequently tested for the presence or absence of targeted microorganisms, which in the original study were two bacterial strains but could equally easily have been archaea or fungi. A subsequent statistical analysis involves a comparison of experimental sampling data with data expected from limited sampling of numerous theoretical spatial distributions. Since the exact spatial location of the microsamples was not determined by Dechesne et al. (2003), they could identify only which *statistical* distributions of patches occupied by bacteria were possible within their sample. However, now that with CT, it might be possible to geolocalize small subsamples within soil columns, a similar approach could now be used to determine spatial distributions of various microorganisms as well, albeit at a relatively low resolution. An implementation of this approach is reported by Kravchenko et al. (2014b). In that work, ≈5 mm-sized soil fragments (referred to as macro-aggregates) were subjected to CT scanning, which provided information on pore architecture. Scanning was followed by cutting the macro-aggregates into geolocalized subsections, that is, the position of each subsection on the CT images was determined. Then, microbial community analyses of each geolocalized subsection via 16S rRNA pyrosequencing was conducted, enabling exploration of associations between presence of certain groups of microorganisms and abundances of soil pores of different sizes.

Scarce Data on 2D Microscale Distribution of Microorganisms

Given the technical difficulties associated with 3D measurements, it is natural that researchers attempted to find out what information could be obtained from 2D cuts through soils.

Alexander and Jackson (1954, 1955) were apparently the first to suggest that thin sections of resin impregnated soil samples could be useful to observe algae, fungal hyphae, and bacteria, using either light or phase-contrast microscopy. They indicated that staining the soil before impregnation enhances the detection of hyaline mycelia and bacteria. Nevertheless, as soon as transmission and scanning electron microscope became available, microbiologists turned to the machines to obtain information about soil microorganisms. Consistently, they confirmed Clark's (1951) observations. Bacteria, often coated by clay platelets, were generally present, not as "biofilms," but as small colonies of a few cells, with many bacterial cells being dispersed in the rest of the soil as individual cells (Foster, 1988). As enlightening as these and other similar observations have been and still are[5], a drawback with TEM and SEM is the fact that at least until recently they could provide only *qualitative* information. To obtain *quantitative* data about the distribution of microorganisms, researchers found it necessary to return to staining cells in thin sections that could be georeferenced easily and viewed in their entirety (e.g., Jones and Griffiths, 1964; White et al., 1994; Nunan et al., 2001, 2002, 2003; Li et al., 2003, 2004). Aside from non-specific stains like calcofluor white M2R applied before impregnation (Postma and Altemuller, 1990), or basic fuchsin and methylene blue applied after impregnation (Tippkötter et al., 1986), researchers also have been interested in selective staining techniques of specific cells, e.g., using fluorescence-conjugated antibody techniques (Postma and Altemuller, 1990), to observe the distribution of bacteria and fungal hyphae in soils. In some cases, problem arose because of the crystallization of the stains when in contact with

---

[5] Anyone who is planning to simulate soils by using glass beads should have a long look at some of the images in Foster (1988) and in later work that has followed on his footsteps!

soils (Harris et al., 2002, 2003). Nevertheless, after these slight technical issues got resolved, images of soil thin sections obtained with these various staining techniques showed clearly that for fungal hyphae, given their size, it is relatively straightforward to identify them (**Figure 8A**). But for bacteria and archaea, as clearly indicated in **Figure 8B**, a tremendous amount of skill (or faith, or both) is required to be able to identify a cell conclusively. Experience shows that part of the problem is related to the difficulty, with traditional light microscopes to focus precisely on a specific depth. It is possible, but tricky, to focus on the top surface of a thin section, hoping that one would then have a sharp image of the first 1 or 2 μm at the surface (Nunan et al., 2001). An easier solution consists of using a confocal laser microscope (e.g., Caldwell et al., 1992; DeLeo et al., 1997; Li et al., 2004), which can produce sharp 2D images at selected shallow depths within a soil thin section. With special software, 3D images can be reconstructed from a set of z-dependent 2D images. In principle, an extension of Hapca et al.'s (2015) statistical interpolation technique, described earlier, should make it possible to assemble these very thin 3D images into a full 3D picture of microbial microscale distribution in soil columns.

A more difficult problem to resolve with traditional stains is related to their non-specific binding to OM or other soil constituents. As a result, many microbial cells may be undetectable against a very bright background of fluorescing soil constituents (**Figure 8B**). Luckily, that stumbling block too has found a solution in recent years, with the development of very reliable fluorescence *in situ* hybridization (FISH) techniques, which use fluorescent-labeled oligonucleotide probes (Pickup, 1995; Mcnaughton et al., 1996; Li et al., 2004; Eickhorst and Tippkötter, 2008a). Eickhorst and Tippkötter (2008b) have shown that when FISH is combined with tyramide
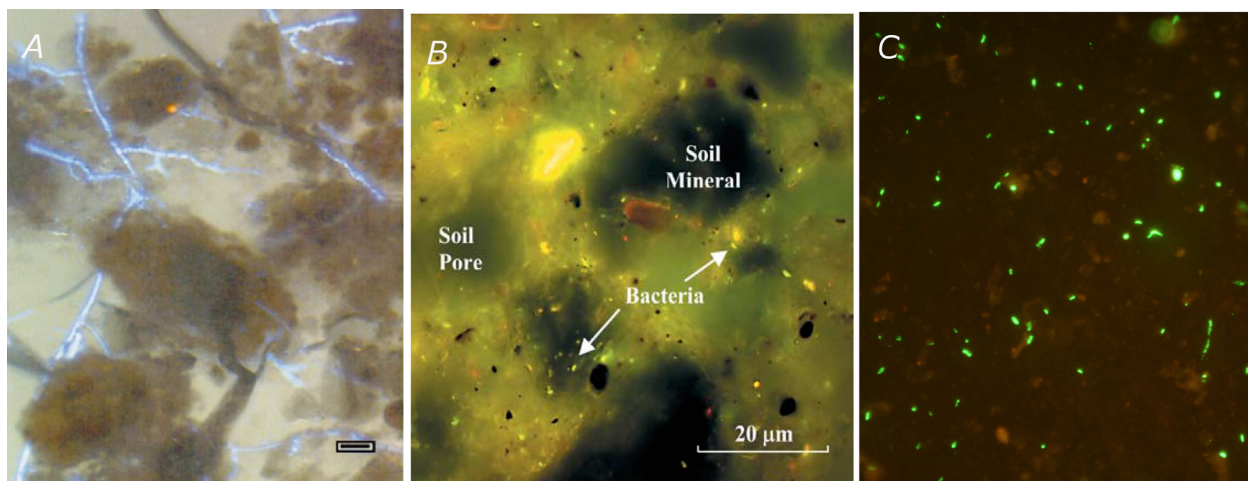
FIGURE 8 | Examples of experimentally determined microbial distribution in soils: **(A)** microscopic image of hyphae of the fungus *Rhizoctonia solani* growing in the pore space of a sandy loam. Scale bar 20 μm (Harris et al., 2002. Reproduced with permission of the British Mycological Society). **(B)** Micrograph of *ethidium* bromide-stained thin sections of a silt loam soil after inoculation by *Escherichia coli*. Image obtained using an epifluorescence microscope with blue excitation (Modified from Li et al., 2004. Reprinted with permission). **(C)** CARD-FISH stained *Bacillus subtilis* cells in soil filter sections under double excitation filter 643 (465–505 and 564–892 nm) (Modified from Juyal et al., 2018).

signal amplification, in what is referred to as Catalyzed reporter deposition (CARD)-FISH, one typically obtains higher signal intensity and reduced interference of the background fluorescence of the soil. This methodology, or variants of it, have been used by a few researchers in the past decade to assess the distribution of bacteria in soils (Schmidt et al., 2012a,b, 2015; Schmidt and Eickhorst, 2014). The combination of CARD-FISH, or one of its variants, with confocal laser microscopy, affords a very powerful tool to visualize and quantify the distribution of microorganisms in soils, with a satisfactory depth-resolution.

The (few) measurements that have been carried out in thin sections have shed some light on the spatial pattern of microbial distribution in soils, but many questions remain. Based on the analysis of 744 images of observed bacterial distributions in soil thin sections taken at different depths, Raynaud and Nunan (2014) found that the distance between neighboring bacterial cells was, on average 12.46 μm and that these inter-cell distances were shorter near the soil surface (10.38 μm) than at depth (>18 μm), due to changes in cell densities. These authors' analyses suggest that despite the very high number of cells and species in soil, bacteria only interact with a few other individuals. For example, at bacterial densities commonly found in bulk soil (10^8 cells per gram of soil), the number of neighbors a single bacterium has within an interaction distance of ca. 20 μm is relatively limited (120 cells on average). This analysis is based on calculations of Euclidean distances, which as Raynaud and Nunan (2014) acknowledge do not take into account the presence of solids, nor the tortuosity of the pore space.

A slightly different perspective on the distribution of bacteria is obtained when one proceeds to a simple back-of the-envelope calculation focused on the surfaces of soil pores, which may indicate somewhat better than Euclidean distances the degree of separation among bacterial cells. The specific surface area of soils varies between a low of 0.1 m^2 per gram, for coarse sand, to a high of 800 m^2 for a smectite clay, with most soils falling in between these extremes (Pennell, 2016). In a soil with a relatively low specific surface area of 10 m^2 per gram, a population of 10^8 bacteria, each having on average a 1 μm^2 cross section, would occupy a mere 0.0001 m^2 per gram of soil, i.e., about 1/100,000th of the specific surface area. Even if one assumes bacterial cells to be much bigger, with a longitudinal cross-sectional area of 4 μm^2, they would still cover only 1/25,000th of the specific surface. In other words, in either case, it is as if on the surface of soil solids, each cell would sit in the middle of an exclusion zone with an average radius of 178 μm. These numbers, in line with earlier estimates (Postma and van Veen, 1990; Grundmann, 2004; Young and Crawford, 2004; O'Donnell et al., 2007; Vos et al., 2013; Kuzyakov and Blagodatskaya, 2015) suggest a very lonely existence indeed, but of course, they are very crude estimates at best, ignoring any tendency cells may have to aggregate. Nevertheless, as more micrographs like that of **Figure 8C** become available in the coming years, and are combined with detailed information about the geometry of the pore space, it will become possible to refine our understanding of the patterns of spatial distribution

not only of bacterial cells, but also of archaea, fungi, and bacteriophages.

Background: Dominant Paradigm and Slow Shift to a New One

The relatively low number of articles dealing with the distribution of microorganisms in soils may surprise, especially given the tools that have been at our disposal for at least a decade (CARD-FISH) or even two (confocal laser microscopes). To understand why that has been the case, and especially to try to change this unfortunate state of affairs, it is useful to describe briefly in what context this work has been carried out. This background is of course familiar to soil microbiologists, but researchers in other disciplines may not necessarily be aware of it.

In the mid-1960s, contrary to the views that had prevailed earlier, a number of researchers, seeking to make their life easier, decided to start viewing the soil microbial biomass as a blackbox, which meant ignoring entirely both the diversity of microorganisms present in soils and their relation to their immediate physico-chemical environment (Baveye, 2018). This approach became dominant for a few years, but in the 1980s and 1990s, a slew of molecular methods were developed to characterize DNA or RNA extracted from soils (Maron et al., 2011; Mendes et al., 2015). Microbiologists in growing numbers jumped on these methods enthusiastically, with the hope that they would give them the opportunity to get information about the diversity of soil microorganisms, i.e., would allow them access inside the blackbox of soil biomass, but still with the convenience of not having to worry about where exactly microorganisms are located. Indeed, in what became known as "metagenomic" and, more recently, "high throughput sequencing" methods, all that was needed to carry out the analysis of a given soil was to extract its microbial DNA or RNA. Indeed, virtually all researchers adopting this approach have entirely ignored the geometry of the pore space in soils or the characteristics of microenvironments (e.g., Nannipieri et al., 2003). Even the so-called "high-resolution" metagenomics (Kalyuzhnaya et al., 2008) ignores the physico-chemical environment of microorganisms. The claim was also made initially, at least by some, that metagenomic methods would enable researchers to avoid having to culture microorganisms in the laboratory, a process that for an estimated 98% of soil microbes, had proven impossible until then (Vogel et al., 2009).

In terms of actual benefits of work carried out along those lines, one should mention the fact that knowledge of the diversity of nucleic acids present in soils paved the way for the design of oligonucleotide probes used in FISH. In itself, this is an important outcome, but in most other ways, experience over the years has demonstrated that many if not all of the initial claims made by proponents of metagenomics were unrealistically optimistic. Scores of researchers have shown that the extraction of DNA or RNA from soils in many cases manages to get at only a fraction of the total amount present (Terrat et al., 2012; Knauth et al., 2013; Dlott et al., 2015; Wagner et al., 2015), that some of this DNA or RNA material is associated with dead or dormant cells, or is extracellular (Carini et al.,

2016), and finally, that the information yielded by DNA or RNA analysis provides a picture of the genetic potential of microorganisms in a soil, not at all of what microorganisms actually do (Prosser et al., 2007; Blazewicz et al., 2013). Furthermore, it has become obvious that, far from alleviating the need to culture microorganisms, the metagenomic approach has increased the urgency of finding ways to identify and characterize vastly more organisms than is the case at the moment (Oremland et al., 2005; Baveye, 2009a,b; Pham and Kim, 2012; Puspita et al., 2012; Prakash et al., 2013). In spite of all these false hopes, limitations, and biases (Lombard et al., 2011; Prosser, 2015), it is fair to say that, at the moment, bulk "meta"-something-"omics" approaches (metagenomics, metatranscriptomics, metaproteomics, metabolomics) capture virtually all the funding dedicated to soil microbial diversity, and their use seems to be crucial to insure microbiologists' career advancement. Year after year, articles praising the merits of metagenomics to uncover the secrets of soils (e.g., van Elsas et al., 2008; Vogel et al., 2009; Delmont et al., 2011; Fierer, 2017; Popescu and Cao, 2018) still make headlines[6] and attract record numbers of citations.

But things may be changing. Roughly 12 years ago, partly in response to the inability of metagenomics to link functions to species and also because information needed to make sense of metagenomics data is lacking for a multitude of still uncultured microorganisms (Su et al., 2012; Shi et al., 2015), researchers started investigating ways to isolate and sequence the DNA and RNAs of individual cells. A number of articles (e.g., Wang and Bodovitz, 2010; Lasken, 2012, 2013; Pamp et al., 2012; Stepanauskas, 2012, 2015; Yilmaz and Singh, 2012; Blainey, 2013; Woyke et al., 2017) have recently retraced some of the key breakthroughs that have enabled what could probably be viewed as a fundamental revolution, in particular in the application of molecular biology techniques to environmental systems (Ishoey et al., 2008). The onset of that revolution is generally considered to be Raghunathan et al.'s (2005) proof-of-principle demonstration that it is possible to use the multiple displacement amplification (MDA) reaction to amplify genomic DNA from a single bacterium several billion fold, with a recovery of about 30% of the genome in the process. Marcy et al. (2007), Podar et al. (2007), and Kvist et al. (2007) applied MDA to environmental cells and established the feasibility of single-cell genome sequencing from uncultivated targets. Woyke et al. (2010) showed that it is possible to produce a completely closed genome from an individual cell. Progress has been very rapid since (**Supplementary Figure S1**), including in RNA sequencing (e.g., Pan et al., 2013; Svensson et al., 2017), single-cell transcriptomics (e.g., Kang et al., 2011), and single-cell metabolomics (e.g., Heinemann and Zenobi, 2011).

All these single-cell techniques offer tremendous potential for the study of soil microorganisms as various researchers have already pointed out (e.g., Ishii et al., 2010; Pedersen et al., 2015), provided two key challenges can be overcome. The first is related

---

[6] As an example of this type of repeated headlines, Charles (2018), on the National Public Radio website in the United States, describes the "Earth Microbiome Project," an initiative started a decade earlier, as a "new approach" to opening up the soil microbial blackbox.

to the fact that FISH, the technique that seems most promising at the moment to locate bacteria and archaea in 2D cuts through soils, has been documented to interfere with single-cell genome recovery (Woyke et al., 2017). This problem may be partly avoided by complementing FISH with other methods to detect and characterize microorganisms, like Raman spectroscopy (see below). The second challenge is related to isolating individual cells from their microenvironments in soils. In the past, various researchers have used micromanipulators of different types over the years, to extract hyphae fragments from soils (Söderström and Erland, 1986) or to sample bacteria on soil surfaces (Dennis et al., 2008). Ashida et al. (2010) and Nishizawa et al. (2012) adopted a micromanipulator originally developed by Fröhlich and König (1999, 2000) and Ishøy et al. (2006), and consisting of a microcapillary (with an outside tip diameter of $60–100\ \mu m$), to extract individual, artificially elongated bacteria from a rice paddy soil sample, and subsequently proceed to 16S rRNA gene analysis. More recently, Ringeisen et al. (2015) have used a laser printing technique, called BioLP, to isolate viable microorganisms from a thin layer of soil spread over a titanium-coated quartz plate. For both the micromanipulator and laser printing technologies, the technological challenge at this point is to design a sampling method that would have a far smaller footprint than is currently achievable, to make it possible to zero in on a single cell or a very small group of cells in a soil microhabitat. Since intracellular capillary microsensors with tip diameters less than $1\ \mu m$ have been used by microbiologists for at least 60 years (Draper and Weidmann, 1951) and the technology of "optical tweezers" has evolved tremendously in the last 2 decades (e.g., Fröhlich and König, 2006; Whitley et al., 2017), it may not be foolish to imagine that we could come up with a way to extract single bacterial cells from soils in a very efficient manner in the not too distant future.

An argument that could be put forth to downplay the interest of this type of single-cell analysis is that such a detailed description of microbial communities is an unnecessary luxury for understanding a large number of microbial functions in soil. It is widely accepted that microbial communities are characterized by a functional redundancy with respect to a range of functions, such as organic C mineralization (e.g., Wertz et al., 2006, 2007; Allison and Martiny, 2008), meaning that the loss of a large number of species does not have a significant effect on functions of interest. Where functional redundancy is apparent, it is possible that viewing microbial communities in soil as a distribution of active sites rather than a distribution of species might suffice. Further research is needed to determine under what conditions information about individual microbial cells is crucial and when it is superfluous.

Dynamical Picture: Are Micromodels a Way Forward?

Given the need to impregnate soils with resin and to cut through the resulting block in one way or another to obtain information about the distribution of microorganisms and the (bio)chemical features of the microenvironments where they reside, it is clear that it is not possible at this stage to monitor in real time, at the

microscale, the dynamics of microbial processes in actual soils. And, to be realistic in our expectations, for bacteria, archaea, and definitely viruses, it may be that we shall never be able to monitor their activity directly in soils.

We might be able, however, to observe the dynamics of these organisms or viruses in 2-dimensional, manufactured soil-like structures, generally referred to as micromodels or "microfluidic" devices. The development of these micromodels has been the object of significant research over the last 20 years (Karadimitriou and Hassanizadeh, 2012; Stanley et al., 2014, 2016; Stanley and van der Heijden, 2017; Aleklett et al., 2018). Early generations of micromodels, still in use to some extent (e.g., Dupin and McCarty, 1999; Stewart and Fogler, 2001; Lanning and Ford, 2002; Coyte et al., 2017; Borer et al., 2018) had idealized geometric properties, being basically two-dimensional networks of straight cylindrical segments, etched in glass or plexiglass. But as technology matured, second- and third-generation structures have become progressively closer to what one would find in a typical fine- to medium sandy soil. Of course, the material these micromodels are made of, often polydimethylsiloxane (PDMS), does not have the same surface properties as sand or silt particles. For some microbial processes this may be an issue, and it makes it impossible to reproduce surface chemical properties of soils, but at least the geometry of the pore space is realistic. With such a soil-like micromodel, Deng et al. (2015) have been able to observe the effect of extracellular polymeric substances (EPS), released by bacteria, on the drying kinetics of the pore space, whereas Rubinstein et al. (2015) have used it to demonstrate the effect a protist, the ciliate *Colpoda* sp., can have on the transport of nanoparticles through soils.

The use of micromodels opens up a number of very interesting avenues for further research, which may provide useful insight. For example, micromodels would seem to be ideal systems to instrument with optodes (Pedersen et al., 2015; Rubol et al., 2016), in order to access some of the physico-chemical parameters (pH, redox potential) that at the moment we cannot measure in soils at the microscale. The use of micromodels might also allow us to better understand how the moisture content of soils influences the activity of bacteria, archaea, and fungi. There is macroscopic evidence that these organisms react very differently to high or low moisture contents (e.g., Otten et al., 1999; Otten and Gilligan, 2006; Kaisermann et al., 2015; Baveye et al., 2016b), as do their predators, which we should not forget (Stefana et al., 2014), and it would be very useful to obtain direct evidence of this at the pore scale.

However, it is likely that for micromodels to give us valuable insight about actual soils, at least two significant challenges will have to be addressed and resolved. The first concerns the connectivity of the pore space. In nature, microorganisms evolve in a 3-dimensional space, which is significantly more connected than is achievable in 2D (e.g., discussion in Hapca et al., 2011). It will therefore be crucial to find a way to relate 2D observation made in micromodels with the more complex situation found in soils. The second challenge is related to what was referred to as "sub-resolution" pores in CT images. The issue, still very much an object of debate, is whether these pores are important to understand microbial activities

in soils, and therefore whether they should be present in micromodels. A body of literature, published over the last few decades, argues that pores in the 30 to 150 µm size range are particularly crucial to understand microbial activity (e.g., Kravchenko and Guber, 2017). Specifically, pores of this size group were found to harbor greater abundance of a number of bacteria groups, such as copiotrophic actinobacteria, firmicutes, and proteobacteria (Kravchenko et al., 2014b) and presence of such pores was associated with greater microbial activity and greater OM decomposition (Killham et al., 1993; Chenu et al., 2001; Strong et al., 2004; Ruamps et al., 2011, 2013), in spite of a higher predation pressure in larger pores, compared to small ones (e.g., Wright et al., 1995). Recently, it was also found that dissolved OM contained within such pores is more labile, having less lignin and tannin-like compounds, than that in small (<6 µm) pores (Bailey et al., 2017; Smith et al., 2017). One perspective on these data is that pores of this size range offer better micro-environmental conditions, e.g., O_2 and water supply, while providing enough space not only for individual organisms but for formation of microbial colonies, which then generate these sizeable experimentally detectable activities and changes in soil characteristics.

Based on this evidence, one would be temped to conclude that when constructing micromodels, one could safely ignore small pores, which would undoubtedly make everyone's life simpler. However, the much lower connectivity of the pore space that would result from that may prevent us from describing correctly some of the processes occurring in soils, both in terms of microbial movement and metabolism. To resist predation, it may be vital for bacteria and archaea to be able to find refuge in smaller pores in which amoebae and particularly ciliates are not able to penetrate. One expects motile bacterial and archaeal cells, sometimes as small as 0.3 µm in diameter or width in soils, to be able to move relatively easily in and out of 2–3 µm-wide pores filled with water. But, as the experiments of Männik et al. (2009) with micro-fabricated channels show, some bacterial cells (of *Escherichia coli*, but not of *Bacillus subtilis*), can penetrate pores smaller than themselves. Although organisms constricted in narrow channels had no mobility and were squeezed, they could still penetrate the channel by growth and division (Hallett et al., 2013). Perhaps more important still is the fact that, given their even smaller size, exoenzymes that bacteria and archaea, as well as fungal hyphae, release into the soil solution can move in and out of tiny pores. Likewise, solutes present in the soil solution can diffuse in and out of the smaller pores, including the very narrow 1.8 nm-wide spaces between clay particles (Dumestre et al., 2000, 2006). In particular, dissolved components of the OM that is located, and possibly to some extent is physically protected, in small pores can also diffuse out into wider pores, where they can be taken up by microorganisms or be transported with the percolating water. Results obtained by Michelson et al. (2017) using a microfluidic device also suggest that members of the *Geobacteraceae* family produce nanowires that are able to penetrate in pore spaces too small for cell passage and, there, up to 15 µm away from cell bodies, reduce Mn(IV) and Fe(III) oxides via long-range extracellular electron transport. Finally, the (so far virtually ignored) bacteriophages

swarming in the pore space of soils in huge numbers (Ashelford et al., 2003), with sizes sometimes as small as a few tens of nanometers, are likely to diffuse through tiny pores as well, and it may turn out that to understand the dynamics of phages in soils, a topic of increasing interest at the moment, it will be necessary to deal with sub-resolution pores in one way or another.

For all these reasons, inclusion of sub-micron pores in micromodels is a technological challenge that may need to be met if we want to use micromodels to gain knowledge about a range of soil processes, but in the meantime, a number of interesting processes, which are not or are only marginally influenced by sub-resolution pores, can still be studied with existing soil-like micromodels, such as the proliferation of fungal hyphae (as long as the release of exoenzymes is not the key mechanism by which fungi metabolize food sources), or the effect of bacterial activity on water or particle retention and movement in larger pores (e.g., Deng et al., 2015; Rubinstein et al., 2015).

Modeling of Microbial Spread and Activity in Soil Pores

Contrary to what has happened on the (bio)chemical scene, the least one can say is that the lack of experimental data about the spatial distribution and activity of microorganisms in soils has not discouraged at all a number of researchers from developing increasingly more sophisticated biokinetic models. On the contrary, work in this area, overwhelmingly carried out by soil physicists, mathematicians, and computer scientists, has been extensive over the last decade (e.g., Thullner and Baveye, 2008; Heße et al., 2009; Gras et al., 2010, 2011; Wang and Or, 2010; Gharasoo et al., 2012; Ebrahimi and Or, 2014, 2015, 2016, 2017; Vogel et al., 2015; Tecon and Or, 2017a,b; Wilmoth et al., 2018; Vogel H.J. et al., 2018; Vogel L.E. et al., 2018). Some of this research has consisted at first of a relatively straightforward extension to the microscale of macroscopic modeling approaches originally developed for saturated porous media, with the biomass consisting exclusively of bacteria, attached to surfaces and growing in response to the influx of a substrate, according to Monod's equation in its simplest formulation (e.g., Widdowson et al., 1988; Baveye and Valocchi, 1989; Loehle and Johnson, 1994; Vandevivere et al., 1995). Over the years, in addition to being extended to the microscale in variably saturated porous media, the original biokinetic model has also been greatly improved (e.g., Hron et al., 2015). Description of bacterial growth has included an explicit account of endogenous metabolism. Bacteria have been allowed to move via chemotaxis, in response to substrate concentration gradients (Olson et al., 2004; Ebrahimi and Or, 2014; Son et al., 2015), and to become dormant (Gras et al., 2011; Resat et al., 2012; Joergensen and Wichern, 2018), under a range of conditions. Instead of simply relying on population-level kinetic equations like Monod's, researchers have progressively turned to individual- or agent-based models, recognizing that locally in soils, the number of bacterial cells tends to be very small, and therefore the large-number assumption embodied in Monod's equation is no longer met (Hellweger et al., 2016). In all these respects, progress in the development of the models over the last decade has been very significant, although from a strictly bacteriological perspective, the models currently available still fail to include a number of processes that might be very significant in soils, like conjugation, quorum sensing, siderophore production, exopolymer and exoenzyme production, filamentous growth of some bacterial strains, or the release of antibiotics to compete with other bacteria or archea (Wolf et al., 2013; Abrudan et al., 2015; DeAngelis, 2016).

In parallel with this modeling effort related to bacteria, various researchers have endeavored to develop computer models to describe the 3-dimensional proliferation of fungi in various types of environments (Otten et al., 2001; Falconer et al., 2005, 2007, 2012, 2015; Boswell and Hopkins, 2008; Jeger et al., 2008; Pajor et al., 2010; Kravchenko A. et al., 2011; Kravchenko A.N. et al., 2011; Hopkins and Boswell, 2012; Cazelles et al., 2013; de Ulzurrun et al., 2017). These models include a number of processes, which for soils might be very relevant, like biomass recycling and the release of exo-enzymes. In applications of some of these models to soils, thresholded CT images can be used to establish the boundaries of the geometric domain in which fungal growth occurs.

Since most soils simultaneously harbor bacteria, archaea, and fungi (among many other organisms), one would expect that the two families of models developed so far to describe specifically the activity of these organisms would have been combined at some stage. This would seem to make a lot of sense, especially as far as bacteria are concerned. One might argue that, under a number of circumstances (e.g., discrete POM serving as exclusive carbon source to fungi), the presence or not of bacteria in the pore space is in general pretty much irrelevant for the proliferation of fungal hyphae. Exceptions occur when bacteria have fungicidal activity (Stanley et al., 2014), and influence the propagation of hyphae. But it is more common for fungi to exert an influence on the behavior and spread of bacteria. Over the last few years, evidence has accumulated that bacteria, "Hitchhikers on the fungal highway" as Warmink et al. (2011) put it, can hop on, or at least be passively carried by, fungal hyphae as they propagate through the pore space (Kohlmeier et al., 2005; Warmink et al., 2011; Ellegaard-Jensen et al., 2014; Stanley et al., 2014), with the consequence that mycelia may be having a very significant role in gene transfer in soils (Berthold et al., 2016; Nazir et al., 2017). Recent ToF- and NanoSIMS measurements carried out by Worrich et al. (2017) also demonstrate that fungal or fungal-like (oomycete) mycelia can reduce water and nutrient stresses experienced by bacteria in otherwise dry and nutrient-poor microhabitats. All these recent observations seem to run counter to previous research suggesting that the high biodiversity of bacterial populations in soils, as well as their community structure, could be accounted for by the low connectivity of the water-filled pore space (e.g., Tiedje et al., 2001; Fierer et al., 2003; Treves et al., 2003; Carson et al., 2010; Ebrahimi and Or, 2015).

Therefore, it would seem important for models describing the activity of microorganisms in soils to simultaneously involve bacteria, archaea, and fungi, and in particular describe the transport of bacterial or archaeal cells by fungal hyphae or the transfer of water and nutrients by mycelia in the pore

space. Unfortunately, this is far easier said than done, because of the difference in scale at which these various groups of organisms operate. In order to describe the activity of fungi realistically, one needs to model a volume of soil in which typically very large numbers of bacterial or archaeal cells would be located, making the prediction of microbial activity extremely CPU intensive, especially when using individual-based models. Within the context of this type of model, there is a possibility to deal with groups of cells, or "super-individuals," as if they were single individuals, to save computing time (e.g., Scheffer et al., 1995) but the approach does not appear to have been used yet to describe bacterial or archeal populations in soils, and it remains to be seen whether it really makes sense.

This hurdle we need to resolve, somehow, about including both bacteria and fungi in the same simulations, raises a broader question of how many other similar hurdles we need to face. How much biodiversity needs to be included in models, in order to have meaningful insights into what is occurring in soils, and in order for the label of "microbial" used abusively in the title of many articles dealing only with bacteria (e.g., Or, 2002; Ebrahimi and Or, 2015), is really justified? In principle, there is no problem in developing models that involve only one type of microorganism, as long as the conclusions reached are restricted to the organism(s) involved, under the conditions assumed in the modeling, and are not considered generally applicable to soils, which contain a multitude of other organisms beside the targeted one(s) (this point is discussed in detail in Baveye et al., 2016b). Clearly, however, such limited models, from which crucial components are missing, are not likely at all to be very useful in the long run in the context of the program defined in **Figure 1**. To make real progress, we need a model that includes as many as possible of the organisms that are relevant to the goal that is being pursued. In general, bacteria, archaea, fungi probably all need to be included, but so do their predators (e.g., DeLeo and Baveye, 1997; Ronn et al., 2012), as well as bacterial and archaeal phages that are present in the soil in large numbers and are more and more suspected to have a very significant, yet still largely misunderstood, influence on microbial dynamics (Williamson et al., 2017; Pratama and van Elsas, 2018). Likewise, the too often ignored aspects of mesofaunal and macrofaunal activity in soils (Briones, 2014), which directly relate to the growth and metabolism of microorganisms, probably also ought to be accounted for, somehow. Depending on the specific questions we try to address, it may be that, in addition to microorganisms, phages and the mesofauna all need to be taken into account in our description of soils, in which case individual-based techniques might not be workable, or only some organisms need to be involved explicitly. Further research is needed to enlighten us in this respect.

As we navigate among all these additional components that may, or may not, need to be added to current microbial models to make them encompass more of the known biodiversity of soils, it soon becomes apparent that progress vitally requires being able to compare model predictions with actual measurements,

which at this point, as was discussed in previous sections, are sadly lacking... Over the years, various soil scientists have reacted strongly, sometimes eloquently (Thomas, 1992), sometimes caustically (Philip, 1991), against modeling efforts that are not systematically backed by sound experimental support. A well-known philosopher and writer, David Henry Thoreau, offered a long time ago a more positive take on a similar situation (in a different context), when he wrote: "If you have built castles in the air, your work need not be lost; that is where they should be. Now put the foundations under them." (Thoreau, 1854). Clearly, in the case of models of microbial activity in the hugely complicated environment that soils constitute for microorganisms, it seems essential to heed this advice, and to obtain relatively quickly the type of experimental data that would enable us to establish our modeling efforts on a much stronger foundation.

Visual Summary of the Status of the Microbiological Front

In terms of measurements, the situation on the microbiological front is very similar to that found on the (bio)chemical one (**Figure 5**). Quantitative measurements of microbial distribution or dynamics are extremely limited and related only to a very small portion of the biodiversity found in soils. Unlike on the (bio)chemical front, however, efforts to model the activity of microorganisms in soils have been extensive, especially regarding bacteria, and have produced some interesting predictions. Nevertheless, this effort has so far been entirely focused on selected bacteria and just a few species of non-sporulating fungi, and in the absence of actual measurements, it is not clear at all how close to reality model predictions are.

INTEGRATION AND MODELING OF MULTIPLE SCENARIOS

The next step in the program of **Figure 1** consists of integrating disciplinary insights into a coherent integrated picture of microbial processes in soils. This integration should take place at both the static and dynamic experimental levels, and in terms of modeling, with the understanding that what is needed eventually, going into the next step, is a comprehensive, thoroughly tested microscale *model* of microbial activity. Right from the onset, one should expect this integration to pose significant challenges. Besides the usual institutional impediments to any kind of interdisciplinary research (see, e.g., Baveye, 2013b, 2014; Baveye et al., 2014), this integration is complicated by the fact that separate measurements that need to be made on the same soil samples often require heavy pieces of equipment that are not commonly found in a single location, causing logistic issues.

At the experimental level, one would expect that since data are still scanty on the (bio)chemical and microbiological scenes, very little integration would have taken place. And yet, encouragingly, some countries have set up a framework for efforts along these lines (e.g., Kögel-Knabner et al., 2008) and there have already been several attempts at integrating various types of experimental approaches. A case in point is the

very interesting article by Rawlins et al. (2016). These authors attempt to determine how soil heterotrophic respiration (SHR) is related to the accessibility of OM to microbes in aggregates of a soil from the United Kingdom. They use a combination of synchrotron X-ray CT, osmium staining, and total organic carbon (TOC) content measurements to quantify the 3D distribution of OM, pore space, and mineral phases, and eventually find a weak correlation ($r = 0,12$) between SHR and a measure of accessibility of OM, which they define as the probability that a given voxel, "filled" with OM be adjacent to a pore voxel. More recently, Yu et al. (2017) combine synchrotron-based 3D X-ray micro-computed tomography with scanning electron microscopy of 2D slices of two different soils, coupled with an energy –dispersive X-ray spectrometer (SEM-EDX) to establish the relation between pore architecture and cementing substances (iron oxide, carbon) in soil aggregates. In an even more recent article, Vidal et al. (2018) combine Nano-SIMS to FIB-SEM to gain information about the distribution of minerals and biomass in the vicinity of roots. They show in particular that bacteria near roots are surrounded by iron oxides, and that some microaggregates are intimately associated with the surface of fungal hyphae.

In terms of the integration of models, some limited work has been carried out as well. Falconer et al. (2012) focus on combining predictions of water retention in a soil, using a LB approach, with a model of the growth of fungal hyphae. Simulation results, based on X-ray CT images of three different soils, show that the water distribution in the soils is affected more by the pore size distribution than by the total porosity of the soils. The presence of water decreases the colonization efficiency of the fungi, as evinced by a decline in the magnitude of all fungal biomass functional measures, in all three samples. The architecture of the soils and water distribution have an effect on the general morphology of the hyphal network, with a "looped" configuration in one soil, due to growing around water droplets. These morphologic differences are satisfactorily discriminated by Minkowski functionals, applied to the fungal biomass.

Two other articles, also combining different models, demonstrate the large benefits that can be derived from the availability of models. Once an X-ray CT image of a soil have been obtained, one can artificially create all kinds of "what-if" scenarios, in which one can imagine that the OM or the microorganisms are distributed in the soil in a multitude of different manners, and one can determine the effect that these relative distributions have on some macroscopic outcome, like the amount of CO_2 evolved from a given soil sample. Of course, such "what-if" scenarios do not alleviate the need to secure actual measurements, of microbial and OM distribution, as well as of any macroscopic outcome one is interested in, but the scenarios can definitely complement and expand experimental data set in very advantageous ways, if only for the purposes of testing statistically various types of novel metrics of microscale heterogeneity (discussed later on). For example, Falconer et al. (2015) obtain strikingly different predictions of evolved CO_2 and fungal biomass production in soils, depending on how an identical amount of POM is distributed spatially in the pore space (**Figure 9**). When POM is present in relatively

FIGURE 9 | Boxplot diagram of simulated CO_2 production by fungi in soil samples with an identical Particulate Organic Matter (POM) content of 3%. The abscissa represents different scenarios with, respectively, (from left to right) 49.95, 51.06, 56.73, and 60.12% of POM accessible at pore-solid interfaces. Individual samples differ in the way POM is distributed in the pore space (Modified from Falconer et al., 2015).

large chunks (>200 μm in diameter, in scenarios 1 and 4), results in terms of both CO_2 evolution and biomass C produced show a large variability and in some cases a high level of production. On the contrary, when an identical amount of POM is more finely dispersed in the soil sample (scenarios 2 and 3), CO_2 evolution and biomass C production both vanish. This result may surprise, but as discussed by Falconer et al. (2015), it is entirely consistent with the foraging pattern of fungi. In another article also published just a few years ago, Vogel et al. (2015) analyze numerically the role of meso- and macropore topology on the biodegradation of a soluble carbon substrate in variably saturated and pure diffusion conditions. The simulations involve the coupling of a LB model to describe the retention of water in the pore space, and a simplified compartmental biodegradation model that does not allow bacterial motility. Not unexpectedly, Vogel et al. (2015) show that under these conditions, the biodegradation of the solute is strongly dependent on the separation distance between bacteria and solute, and is influenced by the moisture content of the soil.

Visual Summary of Integration
To summarize this inevitably quick overview of the work done so far on the integration of disciplinary perspectives on soils at the microscale (**Figure 5**), it seems fair to say that very little progress has been achieved, in large part because very few research projects have so far focused on integration. Such an integration is already largely feasible, for example by measuring in the same soil samples, both the characteristics of the pore space and the spatial heterogeneity of physico-chemical parameters, or either one of these parameters and the spatial distribution of microorganisms. And yet, at the time of the writing of this review article, very little integration at all has occurred at the experimental level. The tiny bit of work that has been carried out is encouraging, but a whole

lot of research remains to be done. This is even more so in the case of upscaling, which remains a virtual *terra incognita*.

UPSCALING, HOW?

Representativeness of Observations and the Imperative of Upscaling

To achieve a high resolution when scanning soil samples, it is necessary to restrict the size of the samples. Typically, with table-top scanners, samples cannot have a volume larger than 100 cm^3 to obtain micrometer resolution, and they have to be significantly less than that if one wants to reach the highest resolution (of about 0.3 μm) that is advertised by manufacturers. Meanwhile, the modeling of soil samples with lattice Boltzmann models is often limited at the moment to handling images of at most 500 $\times$ 500 $\times$ 500 voxels, which at a resolution of say, 20 μm, corresponds to a physical volume of only 1 cm^3.

This small size of soil samples has occasionally raised questions in terms of the "representativeness" of measurements or simulations carried out with these samples (e.g., Al-Raoush and Willson, 2005; Costanza-Robinson et al., 2011; Gao et al., 2014; Rab et al., 2014). These questions stem from the concept of Representative Elementary Volume (REV), which has served over the last few decades as a conceptual foundation for much of the description of transport processes in soils (Fowler, 1997; Vogel and Ippisch, 2008; Hemes et al., 2015; Tracy et al., 2015; Daly et al., 2016; Liu et al., 2016; Cooper et al., 2017; Gonzalez et al., 2018). From that standpoint, soil samples scanned via X-ray CT or simulated via LB, which are of a much smaller size than the REV, would not be sufficiently representative, and one should therefore try to work with larger samples, be it physically, or virtually by aggregating together, mosaic-style, images obtained on a number of small juxtaposed samples. The difficulty with this approach is that in general one has no idea how big an REV is in any particular situation or whether an REV indeed exists (Baveye and Sposito, 1984, 1985; Vogel et al., 2002; Koestel, 2017). One can try computationally to consider sequentially larger volumes of soil in CT images to ascertain that a given property, e.g., porosity or bulk density, tends to become constant as the volume grows, as was done by various authors (Baveye et al., 2002; Vogel et al., 2002). However, there is no guarantee that the REV associated with a particular soil property applies to any other parameter of interest, so that the volume-growing procedure has to be repeated in principle for every single parameter needed to fully describe soil dynamics. Therefore, what at first appears to be a sound physically based constraint on the size of soil samples turns out often not to be operationally meaningful, and the best one can do, as suggested by Baveye and Sposito (1984), is to carefully reference any observation that is made on a soil sample to the volume and shape of this sample.

Nevertheless, regardless of how one feels concerning the need to invoke the notion of REV, it is clear that observations made on cm^3-sized soil samples are not directly relevant to answering the questions raised by soil management, all of which relate to significantly larger spatial scales. Even the root zone of individual crop plants at maturation often encompasses several

m^3 (Baveye and Laba, 2015) and many societal concerns at the moment relate to the kilometric cells of typical climate and general circulation models used to predict global environmental change, or even to the much larger scales of watersheds and continents. Therefore, there is a definite need to upscale the observations made on small soil samples to the much larger scales at which answers are needed. In the words of Wachinger et al. (2000), "a path for translating small-scale understanding into large-scale phenomenology is required." At the moment, no solution is available for this upscaling, which turns out to be an extremely challenging step, but different options have been suggested, some of which can be eliminated right off the bat.

Are Increasing Sample Sizes or Volume Averaging Feasible Options?

One of the approaches that could be considered as an upscaling option consists of the process of mosaicking images obtained on small-sized soil samples, so as to obtain a virtual sample of much larger size. If this procedure results in soil samples of decimetric dimensions, one could be led to assume that the microscopic information and description relevant to the soil samples has been somehow "upscaled" to the macroscopic scale. However, even though the final sample considered may indeed be macroscopic in extent, the information one gets about it essentially remains microscopic in nature and does not necessarily provide the type of simplified description of reality that is sought in **Figure 1** and that corresponds to the notion of emergence.

Another option, which has been used by numerous authors over the last two decades, consists of averaging microscopic descriptions of porous media, over either a Representative Elementary Volume or an arbitrary volume (e.g., associated with a measuring instrument), in order to obtain macroscopic variables (Ayub and Bentsen, 1999; Lichtner and Kang, 2007a,b; Golfier et al., 2009; Valdes-Parada et al., 2009; Wood, 2009, 2010; Davit et al., 2010; Baveye, 2013a; Lugo-Mendez et al., 2015). Davit et al. (2013) have shown that in terms of outcome, this approach is equivalent to another popular upscaling method involving homogenization through multiscale asymptotics (e.g., Roose et al., 2016). In the classical literature on scales in hydrology, both methods are closely associated with what is often referred to as "coarse-graining," in analogy to a common practice in image analysis (Kitanidis, 2015). When applied to the type of soil processes we are interested in, the upshot of volume averaging, however, one looks at it, is a massive loss of information (Baveye, 2010), which takes us several steps backward in our understanding of emerging microbial processes. Indeed, if in a given soil, we perform a simple volume averaging of the concentration of a carbon source and, separately, of the biomass density, and if in so doing we ignore all the microscopic-scale information about the relative distributions of both, we are back to a situation we used to be in, with macroscopic parameters that have no causal relationship any more, and do not allow us to describe emerging processes accurately. Even if, as envisaged, e.g., by Wood (2010) and Porta et al. (2016), one goes beyond simple volume averaging, and somehow takes into account spatial

fluctuations or variance within the volume in which averages are computed, leading to non-local integrodifferential equations, the results still miss some of the key ingredients that we recognize intuitively that an upscaled description of emerging microbial processes should have, in particular a quantification of the disconnect between microorganisms and their carbon/energy sources.

Deep Learning?

Occasionally, in discussions, the suggestion is made that the very popular "machine" or "deep" learning techniques (LeCun et al., 2015; Willcock et al., 2018) could perhaps provide a way to upscale microscale modeling of soils to the macroscopic scale (Veres et al., 2015). *Machine learning* explores the study and construction of algorithms that can learn from data and make data-driven predictions. Machine learning algorithms have started to be employed in soil science, in particular for pattern analysis and image classification to predict material classes in single channel X-ray CT images (Chauhan et al., 2016) and multi-channel nanoSIMS images (Steffens et al., 2017; Schweizer et al., 2018). *Deep learning* is a class of machine learning algorithms that use a cascade of multiple layers of non-linear processing units for feature extraction and transformation; learn in supervised and/or unsupervised (e.g., pattern analysis) manners; learn multiple levels of representations that correspond to different levels of abstraction; and use some form of gradient descent for training via back-propagation.

The application of machine or deep learning techniques to soils might consist of feeding a computer with detailed information about a multitude of scenarios, like those depicted in **Figure 1**, as well as results of simulations carried out for each scenario with the integrated model. With this supply of "big data," deep learning algorithms would in principle search for patterns through all the simulations. Based on these patterns, it would then become feasible to predict the macroscopic behavior of a soil sample on the basis of microscopic data, without having to go through the likely time-consuming effort of re-running the integrated model. This type of outcome might conceivably be useful under specific circumstances, but it clearly does not correspond to what is expected of an upscaled model in **Figure 1**, namely the ability to predict the macroscopic behavior of soil samples *based on macroscopic data*. In other words, deep learning in itself does not automatically result in true upscaling. Nevertheless, deep learning algorithms might still be useful if somehow the patterns they identify in the data could (1) be revealed explicitly, (2) be related to specific macroscopic features of the soils, and (3) help in the development of appropriate macroscopic measurement techniques. At this point, further research is needed to determine whether any one of these different conditions can be met.

Disconnect Is the Key, but How Do We Measure It in Practice?

The research carried out to date, and in particular some of the scenario modeling alluded to earlier, point to a "disconnect" between microorganisms and their carbon/energy sources as being one of the keys to a proper understanding of emergent microbial processes in soils. In principle, this disconnect could be quantified in a number of ways. The Euclidean distance between microorganisms and OM might be a logical candidate, but it does not suffice, since closeness does not guarantee that OM be accessible either directly to a microorganism or indirectly to its extracellular enzymes (see illustration in **Supplementary Figure S2**). To convey the degree of direct or indirect accessibility of OM to microorganisms, a possibility is to consider the length of the most direct path through the pore space that connects a given bacterial cell or segment of fungal hyphae to a blob of OM, if pore connectivity allows such a path to exist at all. This shortest path, generally referred to as the "geodesic" distance, can be computed easily for individual pairs of points, using a number of algorithms developed in graph theory. In principle, a statistical mean of all relevant geodesic distances can then be generated within a specific soil sample. Within a range of CT image resolutions (which influence the apparent connectivity of soils, and therefore the calculation of shortest paths), the mean geodesic distance may prove to have merit, in particular if its use to characterize soil samples in investigations on the effect of temperature and precipitation on carbon mineralization manages to reduce the unexplained experimental variability observed so far.

Unfortunately, the geodesic distance in itself does not provide a complete answer. One issue with it is the fact that it does not take into account the geometry of the pore space along the shortest path, with which it is associated. In practice, this geometry matters tremendously. If a given geodesic path such as the one in **Supplementary Figure S2** goes through a tiny constriction (which used to be referred to as a "pore neck") between two adjacent voids in a soil, not only might bacterial cells or fungal hyphae have great difficulties passing through it, but chemical species (dissolved OM, exoenzymes, byproducts of enzymatic reactions) diffusing randomly through the pore space might also have a reduced likelihood of crossing over. From this perspective, instead of computing the geodesic distance, it might make more sense to quantify the average length of the path taken by molecules diffusing through the pore space. Even though conceptually, the geodesic and diffusion distances are very different, computationally they are not as distinct. Indeed, in order to compute the geodesic distance, algorithms typically track the diffusion paths of large number of random walkers, from which they eventually retain the shortest path. Therefore, the computation of an average diffusion distance between two points does not take a lot more time than the estimation of the geodesic distance.

Computer simulations, using the models under development at the moment and with a wide range of scenarios, could help determine under what conditions metrics like the mean geodesic distance, the mean diffusion distance, or some refinement of them, could be useful. The challenge at that point, then, will be to find a way to relate the metric that eventually turns out to be most suitable, to actual macroscopic measurements that make sense operationally. This is clearly a formidable challenge, whose practical importance cannot be downplayed. The end result of the program of **Figure 1** absolutely cannot require

extensive microbiological, chemical, and physical measurements at the microscopic scale. To be useful, the research needs to come up with simple measurement techniques, which can be used routinely, in a fully automated mode. It is far too early to have even a vague idea of what these routine measurements might be, but they need to remain front and center on our radar screen.

WHERE ARE WE, AND WHAT ARE THE NEXT STEPS?

One way to perceive the overall message conveyed by the visual assessment of **Figure 5** is that we are not very far along the way, and that a tremendous amount of work remains to be done. One could easily argue that this "half-empty glass" perspective is more than warranted. There is indeed a lot of work left, and a long way to go. From a more optimistic, "half-full glass" viewpoint, one could contend that, given the incredible complexity of soils and the fact that suitable technologies to deal with the various components of this complexity have been available for only a little over a decade, the progress achieved to date is remarkable.

Regardless of how one feels about the current state of affairs, it seems clear what the next steps in the research should be. The first step needs to address the clear imbalance that exists among the three core disciplines in the level of effort made to secure measurements in soils at the microscale. The current uneven level of knowledge, with some aspects of the research program that are far more advanced than others, if it is not alleviated in some way, is likely to dramatically hinder the credibility of any effort to make the basic disciplinary outlooks converge into a fully integrated microscopic model. At the moment, some integration of models has taken place, but one cannot actually assess how reliable the integrated descriptions are in practice, because in most situations, relevant microbiological observations are utterly lacking. Therefore, it seems fair to say that one of the key priorities of the research in this field will be to come up with the kind of microscale observations of the distribution and activity of microorganisms that are needed, whether that work be carried out by soil microbiologists or, as it has often happened in the last few decades, by non-microbiologists who have managed to gain the required expertise. When more precise information about the location and activity of microorganisms in soils becomes available, it will be useful to try to characterize as accurately as possible the physical and (bio)chemical nature of their microenvironments, and to determine how these microenvironments co-evolve with microorganisms over time.

A second step, which should be initiated now already, without waiting for the first step to be completed, consists of running multiple analyses on the same soil samples, in order to obtain an integrated view of the different parameters that control their functioning at the microscale. Some timid efforts have been made in this respect, but we have to shift to higher speed. In most cases, given the fact that the heavy equipment (e.g., scanners, NanoSIMS) used for some of these analyses are not located in the same institutions, this integration will require soil samples and possibly also researchers to travel from one institution to another. For some time, it has become well accepted that to

run synchrotron-based analysis of soils (e.g., μXRF, XANES, or NEXAFS), one had to take soil samples to one of the handful of synchrotrons around the world. But now, this same attitude will have to be generalized to a much wider range of investigations, including microbiological analyses.

The next activity we should delve into at this point, much more forcefully than has been the case so far, is to use the existing microscale models of soils to run multiple "what-if" scenarios, and thereby try to understand how, for example, a spatial disconnect between microorganisms and the POM in soils affects the mineralization of this POM. Little by little, as more and more scenarios are run, it is likely that we will progressively get a sharper idea of the features that control the emergent properties of microbial activity in heterogeneous soil microenvironments, and eventually guide us in terms of the still somewhat fuzzy (but crucial) upscaling to the macroscopic scale.

These steps should keep us busy over the next 5 years. Besides funding, several factors will determine how fast we can make progress. In particular, much could depend on how quickly we can take advantage of a number of tremendous technological advances that should become readily available to researchers in the next few years.

FORESEEABLE HELP FROM NOVEL TECHNOLOGIES?

As the preceding sections have documented in some detail, research on microscale aspects of emergent soil properties has been greatly stimulated by a number of major technological breakthroughs achieved at the turn of the century, especially in terms of X-ray CT but also with respect to other measurement techniques (e.g., CARD-FISH). The literature published in the last few years suggests that research is currently paving the way for another wave of phenomenal technological advances, which in several ways can be expected to be even more revolutionary than the previous one. Several of the new technologies are still at the development stage, such as zero-field nuclear magnetic resonance (Ledbetter and Budker, 2013) or quantum microscopes using molecular-scale MRI sensors built from diamonds (Reardon, 2017), but others have already become commercially available and could conceivably cause a huge leap in our ability to visualize and quantify processes in soils.

Years of efforts have been devoted to the development of near-synchrotron quality X-ray sources in facilities that are much smaller than the football stadium size of synchrotrons, and cost significantly less than the billions of euros a typical synchrotron does. Some of these efforts have resulted in 2015 in the installation in Munich (Germany) of the first commercially available mini particle accelerator, or "compact light source" (Eggl et al., 2016). With a very small 5 by 3 m footprint, it produces X-rays through Compton scattering, resulting from the interaction of low energy electrons and a high-powered laser pulse. The X-rays have high-brightness, intermediate between that of X-ray tube sources, used in table-top CT scanners, and large-scale synchrotrons. Another machine based on a similar principle, the ThomX compact light

source is currently under completion at Orsay (France). It has an 18 m long storage ring, and will produce photons with energies up to 90 keV with a maximum flux of 10^{13} photons per second, i.e., with a brightness similar to that of synchrotrons. Undoubtedly, this type of machine will become widely available in years to come, and will eventually afford soil scientists far more access to nearly monochromatic, tunable X-ray beams than is currently the case.

X-ray beams produced using a very different approach may prove to be of even greater interest to soil scientists, because of the very small footprint and, potentially, cost, of the technology. The principle of laser-wakefield accelerators (LWFAs) was proposed more than three decades ago, and technological advances are progressively bringing them closer and closer to practical applications. In a LWFA, not much larger than a shoebox, where an intense laser pulse focused onto a plasma forms an electromagnetic wave in its wake, electrons can be trapped and are now routinely accelerated to GeV energies. Betatron motion, Compton scattering, and undulators produce tunable x-rays or gamma-rays by oscillating relativistic electrons in the wakefield behind the laser pulse, a counter-propagating laser field, or a magnetic undulator (Malka et al., 2008; Ben-Ismail et al., 2011; Mourou et al., 2013; Albert et al., 2014; Cole et al., 2015a,b; Albert and Thomas, 2016). LWFAs still need to be improved, and in particular their brightness needs to increase significantly to the level of synchrotron sources. Nevertheless, progress has been very rapid in recent years, so much so that a number of researchers have been able to use the technology for microtomography of bones, insects, and small mammals (Cole et al., 2015a,b; Wenz et al., 2015; Döpp et al., 2018). It may not be very long before LWFAs are commercialized and become viable options to image soils.

Perhaps as a result of the appearance of novel sources of X-rays, there has also been an upsurge of interest in developing a variety of novel X-ray detectors (Gruner, 2012), such as the photon-counting silicon-strip detector allowing energy-resolved CT (Persson et al., 2014). Various research groups have also been keen to look beyond simply taking advantage of X-ray attenuation to produce 3D images of materials, including soils. Phase-contrast is a very good candidate in this respect (Bhreasail et al., 2012). Techniques that have received attention recently are edge-illumination phase-contrast tomography (Zamir et al., 2017), dark-field scatter tomography (Bech et al., 2010) and ptychographic X-ray computed tomography. In the latter, phase-contrast information can be used to generate high-contrast 3D electron density maps without having to invoke the usual assumptions of a weak phase object or negligible adsorption (Chapman, 2010; Dierolf et al., 2010). To our knowledge, even though they have been mentioned in the literature on natural porous media, these techniques have not yet been applied to soil samples, but this is bound to happen in the not too distant future, at which point it will be possible to determine exactly how much promise they hold.

A possible danger with these tremendous technological advances that are now on the not-very-distant horizon is that they will allow major progress to be made chiefly in the quantification of the physical aspects of soils, thereby widening the already large gap that exists relative to the (bio)chemical and microbiological aspects. But that does not need to be the case. High-brightness, monochromatic, tunable X-ray and gamma-ray beams, possible with LWFAs, could prove extremely useful to visualize water and OM in soils. Also, it may turn out that some of the alternative X-ray techniques, like phase-contrast or dark-field imaging, may offer great advantages to visualize OM or even fungal hyphae in soils. Techniques like 3D micro-XRF or micro-XANES (Silversmit et al., 2010), whose application to characterize the (bio)chemical make-up of soils is currently handicapped by the limited access to synchrotron facilities, may also benefit greatly from the widespread availability of much cheaper, versatile X-ray sources.

Progress is being achieved not only in terms of X-ray or gamma-ray. One area where progress has been tremendous, and that, clearly, holds a lot of promise to assess the distribution of microorganisms in soil thin sections is related to fluorescence microscopy. Light microscopy, including fluorescence microscopy, has experienced phenomenal advances in the last decade. Until about 40 years ago (Cremer and Cremer, 1978), the resolution achievable with light microscopy was strictly constrained by the diffraction of light. Over time, increasing numbers of "super-resolution" microscopes have been developed, relying either on deterministic super-resolution techniques, like the stimulated emission depletion (STED) and saturated structured illumination microscopy (SSIM), or on stochastic functional techniques, like the super-resolution optical fluctuation imaging (SOFI) and the omnipresent localization microscopy (OLM) (Min et al., 2011; Cremer and Masters, 2013; Duwé and Dedecker, 2017; Ji, 2017; Power and Huisken, 2017; Yang and Yuste, 2017). Again, most of these techniques have yet to be applied to soil samples. With more and more of this super-resolution equipment becoming commercially available, there is little doubt that this application to soils will occur in the near future. When super-resolution images become available, we might be surprised (or not) to find out that the individual spots of light in images like those of **Figure 8**, which at the moment are identified as single bacterial or archaeal cells, are in fact small groups of cells.

In terms of the identification of microorganisms, significant progress has also been achieved recently, which could be very helpful in soils. In parallel with single-cell omics methods, a number of other techniques have been developed in the last few years, which allow the less-detailed, but much more rapid, characterization of single microbial cells. For example, Single Cell Raman Spectroscopy (SCRS) allows the direct measurement of intrinsic information about single cells in a non-invasive, label-free, and *in vivo* manner (Li et al., 2012; Smith et al., 2016). SCRS measures vibrations of biomolecules resulting from the inelastic scattering of incident laser light, producing a Raman spectrum, which is associated with a small physical volume (<1 μm^3), of about the size of a bacterium. A typical single-cell Raman spectrum contains more than 1000 bands that can be assigned to different cellular compounds such as nucleic acids, protein,

carbohydrates and lipids. With this information, SCRS enables the characterization of different cell types and can show physiological and phenotypic changes in living single cells. At its inception, the SCRS technique was afflicted by weak Raman signal and significant difficulty in the interpretation of the spectral data, however, recent work on multi-laser beams techniques like the Coherent anti-Stokes Raman Spectroscopy (CARS) (Min et al., 2011) and stimulated Raman spectroscopy (SRS) (Freudiger et al., 2011) has allowed a three order of magnitude increase in the strength of the signal, and significant improvements in signal interpretation. Any of these techniques could be routinely used to complement single-cell omics analysis. Prior to carrying out such an analysis on a particular microorganism in a soil thin section, one could ascertain whether its Raman spectrum is similar to one obtained for another organism already analyzed. In the affirmative, there may not be a need to perform a full single-cell omics protocol, resulting in considerable time saving.

CONCLUSION

The key take-home message of this article is visualized in **Figure 5**. It presents our assessment of progress achieved to date toward what we view as the ultimate objective of the research about emerging soil microbial processes, namely the development of macroscopic measurement techniques that would provide us with the information needed to make reasonably accurate predictions. This **Figure 5** contains good news and bad news. The good news is that we have made significant progress. For forty years after prominent microbiologists argued in the mid 1960s that the *quantitative* microscale description of soil microbial processes was essential, the lack of suitable measurement techniques prevented the research from advancing at all. As a result, in spite of the publication of numerous articles on soil OM and on microbial processes in soils, very little progress has been achieved since the 1960s on several key questions in these areas. In the past 15 years, major technological breakthroughs have changed all that, with the result that our understanding of soils at the microscale has improved significantly on a number of fronts, experimentally as well as in terms of computer modeling. The bad news is that progress is very uneven. At the extremes of the spectrum, whereas research on the physical characteristics of soils at the microscale is moving full speed ahead, the (arguably more complicated) experimental observation of microbial processes is lagging far behind, casting doubt on the soundness on some of the extensive modeling that has been carried out in this field over the last decade, and hindering the needed integration of physical, (bio)chemical, and microbiological perspectives. Clearly, there is still a long way before reaching the holy grail, with many daunting challenges on the different paths leading to it.

There are reasons to be optimistic, however, and not to be intimidated by these challenges. For one thing, technological breakthroughs did not stop a decade ago. New measuring devices and new technologies in other respects as well (e.g., single-cell

"omics") are being developed and, for some of them, even getting commercialized, which should lead to many quantum leaps in our ability to carry out microscale measurements in soils. In addition, one can always hope that as we run more and more experiments to try to understand the emergent microbial properties of soils, someone will come up with an empirical equation that will provide a simple answer to all the questions we have at the moment, a little bit like what Henry Darcy did in his day for water movement in sand filters. Such an empirical description, if and when it becomes available, would completely change the game plan. But in the meantime, we need to keep in mind that we do not really have a choice but to move forward, no matter how challenging that might be. As was mentioned at the beginning of this article, the unresolved questions the research addresses are the object of extreme societal concern and it is not overblown to consider that they need to be answered urgently if we ultimately want humanity to survive. This message is not yet understood by decision makers in most countries, but as time goes by and it becomes more and more urgent to get answers, we should hope that even politicians will realize it will be in everyone's best interest to devote to this research more than the shoe-string budgets that have been allocated to it so far.

DATA AVAILABILITY

No new data were generated during the writing of this article.

AUTHOR CONTRIBUTIONS

PCB initiated the writing of this article, based on in-depth conversations he had over an extended period of time with all co-authors, and he revised several successive drafts of the text, after receiving substantial input from everyone (and very helpful suggestions from the associate editor and reviewers). All authors have approved publication of the final version.

FUNDING

ACKNOWLEDGMENTS

Finally, PCB, SS, TE, and CM acknowledge the financial support by the German Soil Science Society (DBG) for the workshop "Combined analysis of biochemistry and structural complexity of soil via imaging", held at the UFZ in July 2016 and during which many aspects of the topic reviewed in this article were discussed.

SUPPLEMENTARY MATERIAL

The Supplementary Material for this article can be found online at: https://www.frontiersin.org/articles/10.3389/fmicb.2018.01929/full#supplementary-material

REFERENCES

Abrudan, M. I., Smakman, F., Grimbergen, A. J., Westhoff, S., Miller, E. L., van Wezel, G. P., et al. (2015). Socially mediated induction and suppression of antibiosis during bacterial coexistence. *Proc. Natl. Acad. Sci. U.S.A.* 112, 11054–11059. doi: 10.1073/pnas.1504076112

Addiscott, T. M. (2011). Emergence or self-organization? Look to the soil population. *Commun. Integr. Biol.* 4, 469–470. doi: 10.4161/cib.15547

Albert, F., and Thomas, A. G. R. (2016). Applications of laser wakefield accelerator-based light sources. *Plasma Phys. Control. Fusion* 58. doi: 10.1088/0741-3335/58/10/103001

Albert, F., Thomas, A. G. R., Mangles, S. P. D., Banerjee, S., Corde, S., Flacco, A., et al. (2014). Laser wakefield accelerator based light sources: potential applications and requirements. *Plasma Phys. Control. Fusion* 56:084015. doi: 10.1088/0741-3335/56/8/084015

Aleklett, K., Kiers, E. T., Ohlsson, P., Shimizu, T. S., Caldas, V. E. A., and Hammer, E. C. (2018). Build your own soil: exploring microfluidics to create microbial habitat structures. *ISME J.* 12, 312–319. doi: 10.1038/ismej.2017.184

Alexander, F. E. S., and Jackson, R. M. (1954). Examination of soil micro-organisms in their natural environment. *Nature* 174, 750–751. doi: 10.1038/174750b0

Alexander, F. E. S., and Jackson, R. M. (1955). "Preparation of sections for study of soil microorganisms," in *Proceedings of the University of Nottingham Second Easter School in Agriculture Science: Soil Zoology*, ed. D. K. Kevan (London: Butterworths), 433–441.

Alexander, M. (1964). Biochemical ecology of soil microorganisms. *Annu. Rev. Microbiol.* 18, 217–250. doi: 10.1146/annurev.mi.18.100164.001245

Allison, S. D., and Martiny, J. B. H. (2008). Resistance, resilience, and redundancy in microbial communities. *Proc. Natl. Acad. Sci. U.S.A.* 105, 11512–11519. doi: 10.1073/pnas.0801925105

Al-Raoush, R. I., and Willson, C. S. (2005). A pore-scale investigation of a multiphase porous media system. *J. Contam. Hydrol.* 77, 67–89. doi: 10.1016/j.jconhyd.2004.12.001

Altman, S. J., Rivers, M. L., Reno, M. D., Cygan, R. T., and McLain, A. A. (2005). Characterization of adsorption sites on aggregate soil samples using synchrotron X-ray computerized microtomography. *Environ. Sci. Technol.* 39, 2679–2685. doi: 10.1021/es049103y

Amézketa, E. (1999). Soil aggregate stability: a review. *J. Sustain. Agri.* 14, 83–151. doi: 10.1300/J064v14n02_08

Amin, M. H., Hall, L. D., Chorley, R. J., Carpenter, T. A., Richards, K. S., and Bache, B. W. (1994). Magnetic resonance imaging of soil-water phenomena. *Magn. Reson. Imaging* 12, 319–321. doi: 10.1016/0730-725X(94)91546-6

Amin, M. H., Richards, K. S., Chorley, R. J., Gibbs, S. J., Carpenter, T. A., and Hall, L. D. (1996). Studies of soil-water transport by MRI. *Magn. Reson. Imaging* 14, 879–882. doi: 10.1016/S0730-725X(96)00171-3

Ananyeva, K., Wang, W., Smucker, A. J. M., Rivers, M. L., and Kravchenko, A. N. (2013). Can intra-aggregate pore structures affect the aggregate's effectiveness in protecting carbon? *Soil Biol. Biochem.* 57, 868–875. doi: 10.1016/j.soilbio.2012.10.019

Anderson, S. E., and Hopmans, J. W. eds (1994). *Tomography of Soil Water Root Processes*, Vol. 36. Madison, WI: Soil Science Society of America.

Apourvari, S. N., and Arns, C. H. (2016). Image-based relative permeability upscaling from the pore scale. *Adv. Water Resour.* 95, 161–175. doi: 10.1016/j.advwatres.2015.11.005

Arsjad, S., and Giddens, J. (1966). Effect of added plant tissue on decomposition of soil organic matter under different wetting and drying cycles. *Soil Sci. Soc. Am. Proc.* 30, 457. doi: 10.2136/sssaj1966.03615995003000040018x

Ashelford, K. E., Day, M. J., and Fry, J. C. (2003). Elevated abundance of bacteriophage infecting bacteria in soil. *Appl. Environ. Microbiol.* 69, 285–289. doi: 10.1128/AEM.69.1.285-289.2003

Ashida, N., Ishii, S., Hayano, S., Tago, K., Tsuji, T., Yoshimura, Y., et al. (2010). Isolation of functional single cells from environments using a micromanipulator: application to study denitrifying bacteria. *Appl. Microbiol. Biotechnol.* 85, 1211–1217. doi: 10.1007/s00253-009-2330-z

Attard, E., Recous, S., Chabbi, A., De Berranger, C., Guillaumaud, N., Labreuche, J., et al. (2011). Soil environmental conditions rather than denitrifier abundance and diversity drive potential denitrification after changes in land uses. *Global Change Biol.* 17, 1975–1989. doi: 10.1111/j.1365-2486.2010.02340.x

Ayub, M., and Bentsen, R. G. (1999). Interfacial viscous coupling: a myth or reality? *J. Petrol. Sci. Eng.* 23, 13–26. doi: 10.1016/S0920-4105(99)00003-0

Badorreck, A., Gerke, H. H., and Vontobel, P. (2010). Noninvasive observations of flow patterns in locally heterogeneous mine soils using neutron radiation. *Vadose Zone J.* 9, 362–372. doi: 10.2136/vzj2009.0100

Bailey, V. L., Smith, A. P., Tfaily, M., Fansler, S. J., and Bond-Lamberty, B. (2017). Differences in soluble organic carbon chemistry in pore waters sampled from different pore size domains. *Soil Biol. Biochem.* 107, 133–143. doi: 10.1016/j.soilbio.2016.11.025

Barcenas-Moreno, G., Baath, E., and Rousk, J. (2016). Functional implications of the pH-trait distribution of the microbial community in a re-inoculation experiment across a pH gradient. *Soil Biol. Biochem.* 93, 69–78. doi: 10.1016/j.soilbio.2015.10.024

Barot, S., Rossi, J. P., and Lavelle, P. (2007). Self-organization in a simple consumer-resource system, the example of earthworms. *Soil Biol. Biochem.* 39, 2230–2240. doi: 10.1016/j.soilbio.2007.03.021

Basu, N. B., Thompson Sally, E., and Rao, P. S. C. (2011). Hydrologic and biogeochemical functioning of intensively managed catchments: a synthesis of top-down analyses. *Water Resour. Res.* 47:W00J15. doi: 10.1029/2011WR010800

Battiato, I., Tartakovsky, D. M., Tartakovsky, A. M., and Scheibe, T. D. (2011). Hybrid models of reactive transport in porous and fractured media. *Adv. Water Resour.* 37, 1140–1150. doi: 10.1016/j.advwatres.2011.01.012

Baveye, P. (2006). Comment on "Soil structure and management: a review" by C.J. Bronick R. Lal. *Geoderma* 134, 231–232. doi: 10.1016/j.geoderma.2005.10.003

Baveye, P. (2010). Comment on "the role of scaling laws in upscaling" by BD Wood. *Adv. Water Resour.* 33, 123–124. doi: 10.1016/j.advwatres.2009.11.003

Baveye, P., Rogasik, H., Wendroth, O., Onasch, I., and Crawford, J. W. (2002). Effect of sampling volume on the measurement of soil physical properties: simulation with x-ray tomography data. *Measure. Sci. Technol.* 13, 775–784. doi: 10.1088/0957-0233/13/5/316

Baveye, P., and Sposito, G. (1984). The operational significance of the continuum-hypothesis in the theory of water-movement through soils and aquifers. *Water Resour. Res.* 20, 521–530. doi: 10.1029/WR020i005p00521

Baveye, P., and Sposito, G. (1985). Macroscopic balance-equations in soils and aquifers – The case of space-dependent and time-dependent instrumental response. *Water Resour. Res.* 21, 1116–1120. doi: 10.1029/WR021i008p01116

Baveye, P., and Valocchi, A. (1989). An evaluation of mathematical models of the transport of biologically reacting solutes in saturated soils and aquifers. *Water Resour. Res.* 25, 1413–1421. doi: 10.1029/WR025i006p01413

Baveye, P., Vandevivere, P., Hoyle, B. L., DeLeo, P. C., and de Lozada, D. S. (1998). Environmental impact and mechanisms of the biological clogging of saturated soils and aquifer materials. *Crit. Rev. Environ. Sci. Technol.* 28, 123–191. doi: 10.1080/10643389891254197

Baveye, P. C. (2007). Soils and runaway global warming: terra incognita. *J. Soil Water Conserv.* 62, 139A–143A.

Baveye, P. C. (2009a). Comment on "Conservation of protists: Is it needed at all?" by Cotterill et al. *Biodiv. Conserv.* 18, 503–505. doi: 10.1007/s10531-008-9525-y

Baveye, P. C. (2009b). To sequence or not to sequence the whole-soil metagenome? *Nat. Rev. Microbiol.* 7:756. doi: 10.1038/nrmicro2119-c2

Baveye, P. C. (2013a). Comment on "Averaging theory for description of environmental problems: what have we learned?" by William G. Gray, Cass T. Miller, and Bernhard A. Schrefler. *Adv. Water Resour.* 52, 328–330. doi: 10.1016/j.advwatres.2012.08.012

Baveye, P. C. (2013b). Addressing key challenges to interdisciplinary research on water-related issues: biologists' engagement and funding structure. *Biologia* 68, 1087–1088. doi: 10.2478/s11756-013-0280-5

Baveye, P. C. (2013c). Hydrology and the looming water crisis: It is time to think, and act, outside the box. *J. Hydrol. Hydromech.* 61, 89–96. doi: 10.2478/johh-2013-0012

Baveye, P. C. (2014). Learned publishing: who still has time to read? *Learn. Publish.* 27, 48–51. doi: 10.1087/20140107

Baveye, P. C. (2015). Grand challenges in the research on soil processes. *Front. Environ. Sci.* 3:10. doi: 10.3389/fenvs.2015.00010

Baveye, P. C. (2018). Book review: shifting paradigms on soil microbial biomass. *Front. Environ. Sci.* 6:10. doi: 10.3389/fenvs.2018.00010

Baveye, P. C., Baveye, J., and Gowdy, J. (2016a). Soil "ecosystem" services and natural capital: critical appraisal of research on uncertain ground. *Front. Environ. Sci.* 4:41. doi: 10.3389/fenvs.2016.00041

Baveye, P. C., Berthelin, J., and Munch, J.-C. (2016b). Too much or not enough: reflection on two contrasting perspectives on soil biodiversity. *Soil Biol. Biochem.* 103, 320–326. doi: 10.1016/j.soilbio.2016.09.008

Baveye, P. C., Berthelin, J., Tessier, D., and Lemaire, G. (2018). The "4 per 1000" initiative: A credibility issue for the soil science community? *Geoderma* 309, 118–123. doi: 10.1016/j.geoderma.2017.05.005

Baveye, P. C., and Laba, M. (2015). Moving away from the geostatistical lamppost: why, where, and how does the spatial heterogeneity of soils matter? *Ecol. Modell.* 298, 24–38. doi: 10.1016/j.ecolmodel.2014.03.018

Baveye, P. C., Laba, M., Otten, W., Bouckaert, L., Dello Sterpaio, P., Goswami, R. R., et al. (2010). Observer-dependent variability of the thresholding step in the quantitative analysis of soil images and X-ray microtomography data. *Geoderma* 157, 51–63. doi: 10.1016/j.geoderma.2010.03.015

Baveye, P. C., Palfreyman, J., and Otten, W. (2014). Research efforts involving several disciplines: adherence to a clear nomenclature Is needed. *Water Air Soil Pollut.* 225:1997. doi: 10.1007/s11270-014-1997-7

Baveye, P. C., Pot, V., and Garnier, P. (2017). Accounting for sub-resolution pores in models of water and solute transport in soils based on computed tomography images: are we there yet? *J. Hydrol.* 555, 253–256. doi: 10.1016/j.jhydrol.2017.10.021

Baveye, P. C., Rangel, D., Jacobson, A. R., Laba, M., Darnault, C., Otten, W., et al. (2011). From dust bowl to dust bowl: soils are still very much a frontier of science. *Soil Sci. Soc. Am. J.* 75, 2037–2048. doi: 10.2136/sssaj2011.0145

Bearden, J. A., and Burr, A. F. (1967). Reevaluation of X-ray atomic energy levels. *Rev. Mod. Phys.* 39, 125–142. doi: 10.1103/RevModPhys.39.125

Bech, M., Bunk, O., Donath, T., Feidenhans'l, R., David, C., and Pfeiffer, F. (2010). Quantitative x-ray dark-field computed tomography. *Phys. Med. Biol.* 55, 5529–5539. doi: 10.1088/0031-9155/55/18/017

Beckers, E., Plougonven, E., Gigot, N., Leonard, A., Roisin, C., Brostaux, Y., et al. (2014a). Coupling X-ray microtomography and macroscopic soil measurements: a method to enhance near-saturation functions? *Hydrol. Earth Syst. Sci.* 18, 1805–1817. doi: 10.5194/hess-18-1805-2014

Beckers, E., Plougonven, E., Roisin, C., Hapca, S., Leonard, A., and Degre, A. (2014b). X-ray microtomography: a porosity-based thresholding method to improve soil pore network characterization? *Geoderma* 219, 145–154. doi: 10.1016/j.geoderma.2014.01.004

Behrens, S., Kappler, A., and Obst, M. (2012). Linking environmental processes to the in situ functioning of microorganisms by high-resolution secondary ion mass spectrometry (NanoSIMS) and scanning transmission X-ray microscopy (STXM). *Environ. Microbiol.* 14, 2851–2869. doi: 10.1111/j.1462-2920.2012.02724.x

Ben-Ismail, A., Lundh, O., Rechatin, C., Lim, J. K., Faure, J., Corde, S., et al. (2011). Compact and high-quality gamma-ray source applied to 10 mu m-range resolution radiography. *Appl. Phys. Lett.* 98:264101. doi: 10.1063/1.3604013

Berg, S., Ott, H., Klapp, S. A., Schwing, A., Neiteler, R., Brussee, N., et al. (2013). Real-time 3D imaging of haines jumps in porous media flow. *Proc. Natl. Acad. Sci. U.S.A.* 110, 3755–3759. doi: 10.1073/pnas.1221373110

Berthold, T., Centler, F., Huebschmann, T., Remer, R., Thullner, M., Harms, H., et al. (2016). Mycelia as a focal point for horizontal gene transfer among soil bacteria. *Sci. Rep.* 6:36390. doi: 10.1038/srep36390

Bhreasail, A. N., Lee, P. D., O'Sullivan, C., Fenton, C. H., Hamilton, R., Rockett, P., et al. (2012). In-Situ observation of cracks in frozen soil using synchrotron tomography. *Permafrost Periglacial Process.* 23, 170–176. doi: 10.1002/ppp.1737

Biassusi, M., Pauletto, E. A., and Crestana, S. (1999). Estudo da deformação de um vertissolo por meio da tomografia computadorizada de dupla energia simultânea. *Rev. Brasi. Ciência Solo* 23, 1–7. doi: 10.1590/S0100-06831999000100001

Blagodatsky, S., and Smith, P. (2012). Soil physics meets soil biology: towards better mechanistic prediction of greenhouse gas emissions from soil. *Soil Biol. Biochem.* 47, 78–92. doi: 10.1016/j.soilbio.2011.12.015

Blainey, P. C. (2013). The future is now: single-cell genomics of bacteria and archaea. *FEMS Microbiol. Rev.* 37, 407–427. doi: 10.1111/1574-6976.12015

Blaser, M. J., Cardon, Z. G., Cho, M. K., Dangl, J. L., Donohue, T. J., Green, J. L., et al. (2016). Toward a predictive understanding of earth's microbiomes to address 21st century challenges. *MBio* 7:e00714-16. doi: 10.1128/mBio.00714-16

Blaud, A., Chevallier, T., Virto, I., Pablo, A.-L., Chenu, C., and Brauman, A. (2014). Bacterial community structure in soil microaggregates and on particulate organic matter fractions located outside or inside soil macroaggregates. *Pedobiologia* 57, 191–194. doi: 10.1016/j.pedobi.2014.03.005

Blazewicz, S. J., Barnard, R. L., Daly, R. A., and Firestone, M. K. (2013). Evaluating rRNA as an indicator of microbial activity in environmental communities: limitations and uses. *ISME J.* 7, 2061–2068. doi: 10.1038/ismej.2013.102

Bleuet, P., Gergaud, P., Lemelle, L., Tucoulou, R., Cloetens, P., Susini, J., et al. (2010). 3D chemical imaging based on a third-generation synchrotron source. *TrAC Trends Anal. Chem.* 29, 518–527. doi: 10.1016/j.trac.2010.02.011

Bocking, C. R., and Blyth, M. G. (2018). Oxygen uptake and denitrification in soil aggregates. *Acta Mech.* 229, 595–612. doi: 10.1007/s00707-017-2042-x

Borer, B., Tecon, R., and Or, D. (2018). Spatial organization of bacterial populations in response to oxygen and carbon counter-gradients in pore networks. *Nat. Commun.* 9:769. doi: 10.1038/s41467-018-03187-y

Boswell, G. P., and Hopkins, S. (2008). Linking hyphal growth to colony dynamics: spatially explicit models of mycelia. *Fung. Ecol.* 1, 143–154. doi: 10.1016/j.funeco.2008.10.003

Bottinelli, N., Zhou, H., Boivin, P., Zhang, Z. B., Jouquet, P., Hartmann, C., et al. (2016). Macropores generated during shrinkage in two paddy soils using X-ray micro-computed tomography. *Geoderma* 265, 78–86. doi: 10.1016/j.geoderma.2015.11.011

Bouckaert, L., Sleutel, S., Van Loo, D., Brabant, L., Cnudde, V., Van Hoorebeke, L., et al. (2013a). Carbon mineralisation and pore size classes in undisturbed soil cores. *Soil Res.* 51, 14–22. doi: 10.1071/sr12116

Bouckaert, L., Van Loo, D., Ameloot, N., Buchan, D., Van Hoorebeke, L., and Sleutel, S. (2013b). Compatibility of X-ray micro-Computed tomography with soil biological experiments. *Soil Biol. Biochem.* 56, 10–12. doi: 10.1016/j.soilbio.2012.02.002

Brackin, R., Atkinson, B. S., Sturrock, C. J., and Rasmussen, A. (2017). Roots-eye view: using microdialysis and microCT to non-destructively map root nutrient depletion and accumulation zones. *Plant Cell Environ.* 40, 3135–3142. doi: 10.1111/pce.13072

Briones, M. J. I. (2014). Soil fauna and soil functions: a jigsaw puzzle. *Front. Environ. Sci.* 2:7. doi: 10.3389/fenvs.2014.00007

Brusseau, M. L., Peng, S., Snaar, G., and Murao, A. (2007). Measuring air-water interfacial areas with X-ray microtomography and interfacial partitioning tracer tests. *Environ. Sci. Technol.* 41, 1956–1961. doi: 10.1021/es061474m

Bultreys, T., De Boever, W., and Cnudde, V. (2016). Imaging and image-based fluid transport modeling at the pore scale in geological materials: a practical introduction to the current state-of-the-art. *Earth-Sci. Rev.* 155, 93–128. doi: 10.1016/j.earscirev.2016.02.001

Caldwell, D. E., Korber, D. R., and Lawrence, J. R. (1992). Imaging of bacterial cells by fluorescence exclusion using scanning confocal laser microscopy. *J. Microb. Methods* 15, 249–261. doi: 10.1016/0167-7012(92)90045-6

Calistru, A.-E., and Jitareanu, G. (2015). Applications of X-ray computed tomography for examining soil structure: a review. *Bull. UASVM Agric.* 72, 31–36. doi: 10.15835/buasvmcn-agr:11145

Cantoni, M., and Holzer, L. (2014). Advances in 3D focused ion beam tomography. *MRS Bull.* 39, 354–360. doi: 10.1557/mrs.2014.54

Capowiez, Y., Pierret, A., Daniel, O., Monestiez, P., and Kretschmar, A. (1998). 3D skeleton reconstructions of natural earthworm burrow systems using CAT scan images of soil cores. *Biol. Fertil. Soils* 27, 51–59. doi: 10.1007/s003740050399

Carini, P., Marsden, P. J., Leff, J. W., Morgan, E. E., Strickland, M. S., and Fierer, N. (2016). Relic DNA is abundant in soil and obscures estimates of soil microbial diversity. *Nat. Microbiol.* 2:16242. doi: 10.1038/nmicrobiol.2016.242

Carminati, A., Kaestner, A., Lehmann, P., and Flühler, H. (2008). Unsaturated water flow across soil aggregate contacts. *Adv. Water Resour.* 31, 1221–1232. doi: 10.1016/j.advwatres.2008.01.008

Carrel, M., Beltran, M. A., Morales, V. L., Derlon, N., Morgenroth, E., and Kaufmann, R. (2017). Biofilm imaging in porous media by laboratory X-Ray tomography: combining a non-destructive contrast agent with propagation-based phase-contrast imaging tools. *PLoS One* 12:e0180374. doi: 10.1371/journal.pone.0180374

Carson, J. K., Gonzalez-Quinones, V., Murphy, D. V., Hinz, C., Shaw, J. A., and Gleeson, D. B. (2010). Low pore connectivity increases bacterial diversity in soil. *Appl. Environ. Microbiol.* 76, 3936–3942. doi: 10.1128/aem.03085-09

Cazelles, K., Otten, W., Baveye, P. C., and Falconer, R. E. (2013). Soil fungal dynamics: parameterisation and sensitivity analysis of modelled physiological processes, soil architecture and carbon distribution. *Ecol. Modell.* 248, 165–173. doi: 10.1016/j.ecolmodel.2012.08.008

Cerqueira, B., Arenas-Lago, D., Andrade, M. L., and Vega, F. A. (2015). Using time of flight secondary ion mass spectrometry and field emission scanning electron microscopy with energy dispersive X-ray spectroscopy to determine the role of soil components in competitive copper and cadmium migration and fixation in soils. *Geoderma* 25, 65–77. doi: 10.1016/j.geoderma.2015.03.026

Chapman, H. N. (2010). A new phase for X-ray imaging. *Nature* 467, 409–410. doi: 10.1038/467409a

Chapman, N., Miller, A. J., Lindsey, K., and Whalley, W. R. (2012). Roots, water, and nutrient acquisition: let's get physical. *Trends Plant Sci.* 17, 701–710. doi: 10.1016/j.tplants.2012.08.001

Charles, D. (2018). *Scientists Peek Inside the 'Black Box' of Soil Microbes to Learn Their Secrets*. Available at: https://www.npr.org/sections/thesalt/2018/01/18/578924748/scientists-peek-inside-the-black-box-of-soil-microbes-to-learn-their-secrets

Chauhan, S., Ruehaak, W., Anbergen, H., Kabdenov, A., Freise, M., Wille, T., et al. (2016). Phase segmentation of X-ray computer tomography rock images using machine learning techniques: an accuracy and performance study. *Solid Earth* 7, 1125–1139. doi: 10.5194/se-7-1125-2016

Chen, C., Geer, J., and Sammakia, B. (2014). Sub-continuum thermal transport modeling using diffusion in the lattice boltzmann transport equation. *Int. J. Heat Mass Trans.* 79, 666–675. doi: 10.1016/j.ijheatmasstransfer.2014.08.052

Chen, Y., and Zhu, K. (2008). A study of the upper limit of solid scatters density for gray lattice boltzmann method. *Acta Mech. Sin.* 24, 515–522. doi: 10.1007/s10409-008-0167-9

Cheng, L., Booker, F. L., Tu, C., Burkey, K. O., Zhou, L., Shew, H. D., et al. (2012). Arbuscular mycorrhizal fungiincrease organic carbon decomposition under elevated CO2. *Science* 337, 1084–1087. doi: 10.1126/science.1224304

Chenu, C., Hassink, J., and Bloem, J. (2001). Short-term changes in the spatial distribution of microorganisms in soil aggregates as affected by glucose addition. *Soil Biol. Biochem.* 34, 349–356.

Chenu, C., and Stotzky, G. (2001). "Interactions between microorganisms and soil particles: an overview," in *Interactions between Soil Particles and Microorganisms: Impact on the Terrestrial Ecosystem*, eds P. M. Huang, J. M. Bollag, and N. Senesi (London: Wiley), 3–40.

Cheshire, M. V. (1977). Origins and stability of soil polysaccharide. *J. Soil Sci.* 28, 1–10. doi: 10.1111/j.1365-2389.1977.tb02290.x

Chivenge, P., Vanlauwe, B., Gentile, R., and Six, J. (2011). Comparison of organic versus mineral resource effects on short-term aggregate carbon and nitrogen dynamics in a sandy soil versus a fine textured soil. *Agric. Ecosyst. Environ.* 140, 361–371. doi: 10.1016/j.agee.2010.12.004

Christl, I., and Kretzschmar, R. (2007). C-1s NEXAFS spectroscopy reveals chemical fractionation of humic acid by cation-induced coagulation. *Environ. Sci. Technol.* 41, 1915–1920. doi: 10.1021/es062141s

Churchman, G. J., and Payne, D. (1983). Mercury intrusion porosimetry of some New Zealand soils in relation to clay mineralogy and texture. *J. Soil Sci.* 34, 437–451. doi: 10.1111/j.1365-2389.1983.tb01047.x

Clark, F. E. (1951). Bacteria in the soil. *Experientia* 7, 78–80. doi: 10.1007/bf02153840

Cole, J. M., Wood, J. C., Lopes, N. C., Poder, K., Abel, R. L., Alatabi, S., et al. (2015a). Laser-wakefield accelerators as hard x-ray sources for 3D medical imaging of human bone. *Sci. Rep.* 5:13244. doi: 10.1038/srep13244

Cole, J. M., Wood, J. C., Lopes, N. C., Poder, K., Abel, R. L., Alatabi, S., et al. (2015b). Tomography of human trabecular bone with a laser-wakefield driven x-ray source. *Plasma Phys. Control. Fusion* 58:14008. doi: 10.1088/0741-3335/58/1/014008

Cooper, L. J., Daly, K. R., Hallett, P. D., Naveed, M., Koebernick, N., Bengough, A. G., et al. (2017). Fluid flow in porous media using image-based modelling to parametrize Richards' equation. *Proc. R. Soc. Lond. Ser. A Mathemat. Phys. Eng. Sci.* 473:20170178. doi: 10.1098/rspa.2017.0178

Costanza-Robinson, M. S., Estabrook, B. D., and Fouhey, D. F. (2011). Representative elementary volume estimation for porosity, moisture saturation, and air-water interfacial areas in unsaturated porous media: data quality implications. *Water Resour. Res.* 47, 1–12. doi: 10.1029/2010WR009655

Cousin, I., Levitz, P., and Bruand, A. (1996). Three-dimensional analysis of a loamy-clay soil using pore and solid chord distributions. *Eur. J. Soil Sci.* 47, 439–452. doi: 10.1111/j.1365-2389.1996.tb01844.x

Cousin, I., Porion, P., Renault, P., and Levitz, P. (1999). Gas diffusion in a silty-clay soil: experimental study on an undisturbed soil core and simulation in its three-dimensional reconstruction. *Eur. J. Soil Sci.* 50, 249–259. doi: 10.1046/j.1365-2389.1999.00215.x

Coyte, K. Z., Tabuteau, H., Gaffney, E. A., Foster, K. R., and Durham, W. M. (2017). Microbial competition in porous environments can select against rapid biofilm growth. *Proc. Natl. Acad. Sci. U.S.A.* 114, E161–E170. doi: 10.1073/pnas.1525228113

Cremer, C., and Cremer, T. (1978). Considerations on a laser-scanning-microscope with high resolution and depth of field. *Micros. Acta* 81, 31–44.

Cremer, C., and Masters, B. R. (2013). Resolution enhancement techniques in microscopy. *Eur. Phys. J. H* 38, 281–344. doi: 10.1140/epjh/e2012-20060-1

Crenshaw, C. L., Lauber, C., Sinsabaugh, R. L., and Stavely, L. K. (2008). Fungal control of nitrous oxide production in semiarid grassland. *Biogeochemistry* 87, 17–27. doi: 10.1007/s10533-007-9165-4

Crestana, S., Mascarenhas, S., and Pozzimucelli, R. S. (1985). Static and dynamic 3-dimensional studies of water in soil using computed tomography scanning. *Soil Sci.* 140, 326–332. doi: 10.1097/00010694-198511000-00002

Crowther, T. W., Todd-Brown, K. E. O., Rowe, C. W., Wieder, W. R., Carey, J. C., Machmuller, M. B., et al. (2016). Quantifying global soil carbon losses in response to warming. *Nature* 540, 104–108. doi: 10.1038/nature20150

Crozat, Y., Cleyet-Marel, J. C., and Corman, A. (1987). Use of the fluorescentantibody technique to characterize equilibrium survival concentrations of Bradyrhizobium japonicum strains in soil. *Biol. Fertil. Soils* 4, 85–90.

Cruz, B. C., Furrer, J. M., Guo, Y. S., Dougherty, D., Hinestroza, H. F., Hernandez, J. S., et al. (2017). Pore-scale water dynamics during drying and the impacts of structure and surface wettability. *Water Resour. Res.* 53, 5585–5600. doi: 10.1002/2016WR019862

Culligan, K. A., Wildenschild, D., Christensen, B. S. B., Gary, W. G., and Rivers, M. L. (2006). Pore- scale characteristics of multiphase flow in porous media: a comparison of air-water and oil-water experiments. *Adv. Water Resour.* 29, 227–38. doi: 10.1016/j.advwatres.2005.03.021

Dal Ferro, N., Sartori, L., Simonetti, G., Berti, A., and Morari, F. (2014). Soil macro- and microstructure as affected by different tillage systems and their effects on maize root growth. *Soil Tillage Res.* 140, 55–65. doi: 10.1016/j.still.2014.02.003

Daly, K. R., Keyes, S. D., Masum, S., and Roose, T. (2016). Image-based modelling of nutrient movement in and around the rhizosphere. *J. Exp. Bot.* 67, 1059–1070. doi: 10.1093/jxb/erv544

Daly, K. R., and Roose, T. (2014). Multiscale modelling of hydraulic conductivity in vuggy porous media. *Proc. R. Soc. Lond. Ser. A Mathemat. Phys. Eng. Sci.* 470:20130383. doi: 10.1098/rspa.2013.0383

Darrah, P. R., White, R. E., and Nye, P. H. A. (1987). Theoretical consideration of the implications of cell clustering for the prediction of nitrification in soil. *Plant Soil* 99, 387–400. doi: 10.1007/BF02370884

Davit, Y., Bell, C. G., Byrne, H. M., Chapman, L. A. C., Kimpton, L. S., Lang, G. E., et al. (2013). Homogenization via formal multiscale asymptotics and volume averaging: how do the two techniques compare? *Adv. Water Resour.* 62, 178–206. doi: 10.1016/j.advwatres.2013.09.006

Davit, Y., Debenest, G., Wood, B. D., and Quintard, M. (2010). Modeling non-equilibrium mass transport in biologically reactive porous media. *Adv. Water Resour.* 33, 1075–1093. doi: 10.1016/j.advwatres.2010.06.013

Davit, Y., Iltis, G., Debenest, G., Veran-Tissoires, S., Wildenschild, D., Gerino, M., et al. (2011). Imaging biofilm in porous media using X-ray computed microtomography. *J. Microsc.* 242, 15–25. doi: 10.1111/j.1365-2818.2010.03432.x

De Gryze, S., Jassogne, L., Six, J., Bossuyt, H., Wevers, M., and Merckx, R. (2006). Pore structure changes during decomposition of fresh residue: X-ray tomography analyses. *Geoderma* 134, 82–96. doi: 10.1016/j.geoderma.2005.09.002

de Jonge, L. W., Moldrup, P., Vendelboe, A. L., Tuller, M., and Wildenschild, D. (2012). Soil rchitecture and physicochemical functions: an introduction. *Vadose Zone J.* 11:vzj2011.0185. doi: 10.2136/vzj2011.0185

de Melo, R. H. C., and Conci, A. (2013). How succolarity could be used as another fractal measure in image analysis. *Telecommun. Syst.* 52, 1643–1655. doi: 10.1007/s11235-011-9657-3

de Ulzurrun, G. V.-D., Baetens, J. M., Van den Bulcke, J., and De Baets, B. (2017). Modelling three-dimensional fungal growth in response to environmental stimuli. *J. Theor. Biol.* 414, 35–49. doi: 10.1016/j.jtbi.2016.11.020

DeAngelis, K. M. (2016). Chemical communication connects soil food webs. *Soil Biol. Biochem.* 102, 48–51. doi: 10.1016/j.soilbio.2016.06.024

Dechesne, A., Pallud, C., Debouzie, D., Flandrois, J. P., Vogel, T. M., Gaudet, J. P., et al. (2003). A novel method for characterizing the microscale 3D spatial distribution of bacteria in soil. *Soil Biol. Biochem.* 35, 1537–1546. doi: 10.1016/s0038-0717(03)00243-8

DeLeo, P. C., and Baveye, P. (1997). Factors affecting protozoan predation of bacteria clogging laboratory aquifer microcosms. *Geomicrobiol. J.* 14, 127–149. doi: 10.1080/01490459709378039

DeLeo, P. C., Baveye, P., and Ghiorse, W. C. (1997). Use of confocal laser scanning microscopy on soil thin-sections for improved characterization of microbial growth in unconsolidated soils and aquifer materials. *J. Microbiol. Methods* 30, 193–203. doi: 10.1016/s0167-7012(97)00065-1

Delmont, T. O., Robe, P., Cecillon, S., Clark, I. M., Constancias, F., Simonet, P., et al. (2011). Accessing the soil metagenome for studies of microbial diversity. *Appl. Environ. Microbiol.* 77, 1315–1324. doi: 10.1128/aem.01526-10

Deng, J., Orner, E. P., Chau, F., Anderson, E. M., Kadilak, A. L., Rubinstein, R. L., et al. (2015). Synergistic effects of soil microstructure and bacterial EPS on drying rate in emulated soil micromodels. *Soil Biol. Biochem.* 83, 116–124. doi: 10.1016/j.soilbio.2014.12.006

Dennis, P. G., Miller, A. J., Clark, I. M., Taylor, R. G., Valsami-Jones, E., and Hirsch, P. R. (2008). A novel method for sampling bacteria on plant root and soil surfaces at the microhabitat scale. *J. Microbiol. Methods* 75, 12–18. doi: 10.1016/j.mimet.2008.04.013

Devarapalli, R. S., Islam, A., Faisal, T. F., Sassi, M., and Jouiad, M. (2017). Micro-CT and FIB-SEM imaging and pore structure characterization of dolomite rock at multiple scales. *Arabian J. Geosci.* 10:361. doi: 10.1007/s12517-017-3120-z

Dexter, A. R. (1988). Advances in characterization of soil structure. *Soil Tillage Res.* 11, 199–238. doi: 10.1016/0167-1987(88)90002-5

Díaz-Zorita, M., Perfect, E., and Grove, J. H. (2002). Disruptive methods for assessing soil structure. *Soil Tillage Res.* 64, 3–22. doi: 10.1016/S0167-1987(01)00254-9

Dierolf, M., Menzel, A., Thibault, P., Schneider, P., Kewish, C. M., Wepf, R., et al. (2010). Ptychographic X-ray computed tomography at the nanoscale. *Nature* 467, 436–482. doi: 10.1038/nature09419

Dlott, G., Maul, J. E., Buyer, J., and Yarwood, S. (2015). Microbial rRNA:rDNA gene ratios may be unexpectedly low due to extracellular DNA preservation in soils. *J. Microbiol. Methods* 115, 112–120. doi: 10.1016/j.mimet.2015.05.027

Dobson, K. J., Coban, S. B., McDonald, S. A., Walsh, J. N., Atwood, R. C., and Withers, P. J. (2016). 4-D imaging of sub-second dynamics in pore-scale processes using real-time synchrotron X-ray tomography. *Solid Earth* 7, 1059–1073. doi: 10.5194/se-7-1059-2016

Döpp, A., Hehn, L., Götzfried, J., Wenz, J., Gilljohann, M., Ding, H., et al. (2018). Quick x-ray microtomography using a laser-driven betatron source. *Optica* 5, 199–203. doi: 10.1364/OPTICA.5.000199

Draper, M. H., and Weidmann, S. (1951). Cardiac resting and action potentials recorded with an intracellular electrode. *J. Physiol. Lon.* 115, 74–94. doi: 10.1113/jphysiol.1951.sp004653

Dumestre, A., McBride, M., and Baveye, P. (2000). Use of EPR To monitor the distribution and availability of organic xenobiotics in model soil systems. *Environ. Sci. Technol.* 34, 1259–1264. doi: 10.1021/es990824k

Dumestre, A., Spagnuolo, M., Bladon, R., Berthelin, J., and Baveye, P. (2006). EPR monitoring of the bioavailability of an organic xenobiotic (4-hydroxy-TEMPO) in model clay suspensions and pastes. *Environ. Pollut.* 143, 73–80. doi: 10.1016/j.envpol.2005.11.015

Dungait, J. A. J., Hopkins, D. W., Gregory, A. S., and Whitmore, A. P. (2012). Soil organic matter turnover is governed by accessibility not recalcitrance. *Global Change Biol.* 18, 1781–1796. doi: 10.1111/j.1365-2486.2012.02665.x

Dupin, H. J., and McCarty, P. L. (1999). Mesoscale and microscale observations of biological growth in a silicon pore imaging element. *Environ. Sci. Technol.* 33, 1230–1236. doi: 10.1021/es981146p

Duwé, S., and Dedecker, P. (2017). Super-resolution imaging goes fast and deep. *Nat. Methods* 14, 1041–1044. doi: 10.1038/nmeth.4484

Ebrahimi, A., and Or, D. (2015). Hydration and diffusion processes shape microbial community organization and function in model soil aggregates. *Water Resour. Res.* 51, 9804–9827. doi: 10.1002/2015wr017565

Ebrahimi, A., and Or, D. (2016). Microbial community dynamics in soil aggregates shape biogeochemical gas fluxes from soil profiles – Upscaling an aggregate biophysical model. *Global Change Biol.* 22, 3141–3156. doi: 10.1111/gcb.13345

Ebrahimi, A., and Or, D. (2017). Mechanistic modeling of microbial interactions at pore to profile scale resolve methane emission dynamics from permafrost soil. *J. Geophys. Res. Biogeosci.* 122, 1216–1238. doi: 10.1002/2016jg003674

Ebrahimi, A. N., and Or, D. (2014). Microbial dispersal in unsaturated porous media: characteristics of motile bacterial cell motions in unsaturated angular pore networks. *Water Resour. Res.* 50, 7406–7429. doi: 10.1002/2014wr015897

Egan, C. K., Jacques, S. D. M., Wilson, M. D., Veale, M. C., Seller, P., Beale, A. M., et al. (2015). 3D chemical imaging in the laboratory by hyperspectral X-ray computed tomography. *Sci. Rep.* 5:15979. doi: 10.1038/srep15979

Eggl, E., Dierolf, M., Achterhold, K., Jud, C., Günther, B., Braig, E., et al. (2016). The munich compact light source: initial performance measures. *J. Synchrotron. Radiat.* 23, 1137–1142. doi: 10.1107/S160057751600967X

Eickhorst, T., and Tippkötter, R. (2008a). Improved detection of soil microorganisms using fluorescence in situ hybridization (FISH) and catalyzed reporter deposition (CARD-FISH). *Soil Biol. Biochem.* 40, 1883–1891. doi: 10.1016/j.soilbio.2008.03.024

Eickhorst, T., and Tippkötter, R. (2008b). Detection of microorganisms in undisturbed soil by combining fluorescence in situ hybridization (FISH) and micropedological methods. *Soil Biol. Biochem.* 40, 1284–1293. doi: 10.1016/j.soilbio.2007.06.019

El Ganaoui, M., Addakiri, S., and Semma, E. (2012). On the aptitude of the lattice Boltzmann approach for the treatment of the transient heat transfer with crack resistance. *Comptes Rendus Mecanique* 340, 518–525. doi: 10.1016/j.crme.2012.03.010

Ellegaard-Jensen, L., Knudsen, B. E., Johansen, A., Albers, C. N., Aamand, J., and Rosendahl, S. (2014). Fungal-bacterial consortia increase diuron degradation in water-unsaturated systems. *Sci. Total Environ.* 466, 699–705. doi: 10.1016/j.scitotenv.2013.07.095

Elliott, E. T., Anderson, R. V., Coleman, D. C., and Cole, C. V. (1980). Habitable pore space and microbial trophic interactions. *Oikos* 35, 327–335. doi: 10.2307/3544648

Evans, S., Dieckmann, U., Franklin, O., and Kaiser, C. (2016). Synergistic effects of diffusion and microbial physiology reproduce the Birch effect in a micro-scale model. *Soil Biol. Biochem.* 93, 28–37. doi: 10.1016/j.soilbio.2015.10.020

Falconer, R. E., Battaia, G., Schmidt, S., Baveye, P., Chenu, C., and Otten, W. (2015). Microscale heterogeneity explains experimental variability and non-linearity in

soil organic matter mineralisation. *PLoS One* 10:e0123774. doi: 10.1371/journal.pone.0123774

Falconer, R. E., Bown, J. L., White, N. A., and Crawford, J. W. (2005). Biomass recycling and the origin of phenotype in fungal mycelia. *Proc. R. Soc. B-Biol. Sci.* 272, 1727–1734. doi: 10.1098/rspb.2005.3150

Falconer, R. E., Bown, J. L., White, N. A., and Crawford, J. W. (2007). Biomass recycling: a key to efficient foraging by fungal colonies. *Oikos* 116, 1558–1568. doi: 10.1111/j.2007.0030-1299.15885.x

Falconer, R. E., Houston, A. N., Otten, W., and Baveye, P. C. (2012). Emergent behavior of soil fungal dynamics: influence of soil architecture and water distribution. *Soil Sci.* 177, 111–119. doi: 10.1097/SS.0b013e318241133a

Feeney, D. S., Crawford, J. W., Daniell, T., Hallett, P. D., Nunan, N., Ritz, K., et al. (2006). Three-dimensional microorganization of the soil–root–microbe system. *Microb. Ecol.* 52, 151–158. doi: 10.1007/s00248-006-9062-8

Fierer, N. (2017). Embracing the unknown: disentangling the complexities of the soil microbiome. *Nat. Rev. Microbiol.* 15, 579–590. doi: 10.1038/nrmicro.2017.87

Fierer, N., and Jackson, R. B. (2006). The diversity and biogeography of soil bacterial communities. *Proc. Natl. Acad. Sci. U.S.A.* 103, 626–631. doi: 10.1073/pnas.0507535103

Fierer, N., Schimel, J. P., and Holden, P. A. (2003). Influence of drying–rewetting frequency on soil bacterial community structure. *Microb. Ecol.* 45, 63–71. doi: 10.1007/s00248-002-1007-2

Fontaine, S., Barot, S., Barre, P., Bdioui, N., Mary, B., and Rumpel, C. (2007). Stability of organic carbon in deep soil layers controlled by fresh carbon supply. *Nature* 450, 277–281. doi: 10.1038/nature06275

Foster, R. C. (1988). Microenvironments of soil microorganisms. *Biol. Fertil. Soils* 6, 189–203. doi: 10.1007/BF00260816

Fowler, A. C. (1997). *Mathematical Models in the Applied Sciences*. Cambridge: Cambridge University Press.

Freed, D. M. (1998). Lattice-boltzmann method for macroscopic porous media modeling. *Int. J. Modern Phys. C* 9, 1491–1503. doi: 10.1142/s0129183198001357

Freudiger, C. W., Min, W., Holtom, G. R., Xu, B., Dantus, M., and Xie, X. S. (2011). Highly specific label-free molecular imaging with spectrally tailored excitation-stimulated Raman scattering (STE-SRS) microscopy. *Nat. Photon.* 5, 103–109. doi: 10.1038/nphoton.2010.294

Fröhlich, J., and König, H. (1999). Rapid isolation of single microbial cell from mixed natural and laboratory populations with the aid of a micromanipulator. *Syst. Appl. Microbiol.* 22, 249–257. doi: 10.1016/S0723-2020(99)80072-1

Fröhlich, J., and König, H. (2000). New techniques for isolation of single prokaryotic cells. *FEMS Microbiol. Rev.* 24, 567–572. doi: 10.1111/j.1574-6976.2000.tb00558.x

Fröhlich, J., and König, H. (2006). "Micromanipulation techniques for the isolation of single microorganisms," in *Intestinal Microorganisms of Termites and Other Invertebrates*, Vol. 6, eds H. König and A. Varma (Berlin: Springer), 425–437. doi: 10.1007/3-540-28185-1_18

Gao, J. F., Xing, H. L., Tian, Z. W., and Muhlhaus, H. (2014). Lattice Boltzmann modeling and evaluation of fluid flow in heterogeneous porous media involving multiple matrix constituents. *Comput. Geosci.* 62, 198–207. doi: 10.1016/j.cageo.2013.07.019

Gao, Y., and Sharma, M. M. (1994). A lga model for fluid-flow in heterogeneous porous-media. *Transp. Porous Media* 17, 1–17. doi: 10.1007/BF00624047

Garnier, P., Angulo-Jaramillo, R., DiCarlo, D. A., Bauters, T. W. J., Darnault, C. J. G., Steenhuis, T. S., et al. (1998). Dual-energy synchrotron X ray measurements of rapid soil density and water content changes in swelling soils during infiltration. *Water Resour. Res.* 34, 2837–2842. doi: 10.1029/98wr02367

Garnier, P., Perrier, E., Jaramillo, R. A., and Baveye, P. (1997). Numerical model of 3-dimensional anisotropic deformation and 1-dimensional water flow in swelling soils. *Soil Sci.* 162, 410–420. doi: 10.1097/00010694-199706000-00003

Genty, A., and Pot, V. (2013). Numerical Simulation of 3D liquid-gas distribution in porous media by a two-phase TRT lattice boltzmann method. *Transp. Porous Media* 96, 271–294. doi: 10.1007/s11242-012-0087-9

Genty, A., and Pot, V. (2014). Numerical calculation of effective diffusion in unsaturated porous media by the TRT lattice boltzmann method. *Transp. Porous Media* 105, 391–410. doi: 10.1007/s11242-014-0374-8

Gerke, K. M., Vasilyev, R. V., Khirevich, S., Collins, D., Karsanina, M. V., Sizonenko, T. O., et al. (2018). Finite-difference method stokes solver (FDMSS)

for 3D pore geometries: Software development, validation and case studies. *Comput. Geosci.* 114, 41–58. doi: 10.1016/j.cageo.2018.01.005

Gharasoo, M., Centler, F., Regnier, P., Harms, H., and Thullner, M. (2012). A reactive transport modeling approach to simulate biogeochemical processes in pore structures with pore-scale heterogeneities. *Environ. Modell. Softw.* 30, 102–114. doi: 10.1016/j.envsoft.2011.10.010

Ginzburg, I. (2016). Comment on "An improved gray Lattice Boltzmann model for simulating fluid flow in multi-scale porous media": intrinsic links between LBE Brinkman schemes. *Adv. Water Resour.* 88, 241–249. doi: 10.1016/j.advwatres.2014.05.007

Ginzburg, I., Silva, G., and Talon, L. (2015). Analysis and improvement of Brinkman lattice Boltzmann schemes: bulk, boundary, interface. Similarity and distinctness with finite elements in heterogeneous porous media. *Phys. Rev. E* 91:0233072. doi: 10.1103/PhysRevE.91.023307

Gleber, S. C., Vogt, S., Niemeyer, J., Finney, L., McNulty, I., and Thieme, J. (2011). "Hard X-ray fluorescence microscopy to determine the element distribution of soil colloids in aqueous environment," in *Proceedings of the 10th International Conference on X-Ray Microscopy*, Vol. 1365, eds I. McNulty, C. Eyberger, and B. Lai (College Park, MD: American Institute of Physics), 365–368. doi: 10.1063/1.3625379

Glick, B. R. (2012). Plant growth-promoting bacteria: mechanisms and applications. *Scientifica* 2012, 1–15. doi: 10.6064/2012/963401

Glick, B. R. (2014). Bacteria with ACC deaminase can promote plant growth and help to feed the world. *Spec. Issue Plant Growth Promot.* 169, 30–39. doi: 10.1016/j.micres.2013.09.009

Godfray, H. C. J., Beddington, J. R., Crute, I. R., Haddad, L., Lawrence, D., Muir, J. F., et al. (2010). Food security: the challenge of feeding 9 billion people. *Science* 327, 812–818. doi: 10.1126/science.1185383

Goebel, M.-O., Woche, S. K., and Bachmann, J. (2009). Do soil aggregates really protect encapsulated organic matter against microbial decomposition? *Biologia* 64, 443–448. doi: 10.2478/s11756-009-0065-z

Golfier, F., Wood, B. D., Orgogozo, L., Quintard, M., and Bues, M. (2009). Biofilms in porous media: development of macroscopic transport equations via volume averaging with closure for local mass equilibrium conditions. *Adv. Water Resour.* 32, 463–485. doi: 10.1016/j.advwatres.2008.11.012

Gommes, C. J., Bons, A.-J., Blacher, S., Dunsmuir, J. H., and Tsou, A. H. (2009). Practical methods for measuring the tortuosity of porous materials from binary or gray-tone tomographic reconstructions. *AICHE J.* 55, 2000–2012. doi: 10.1002/aic.11812

Gonzalez, J. L., de Faria, E. L., Albuquerque, M. P., Albuquerque, M. P., Bom, C. R., Freitas, J. C. C., et al. (2018). Representative elementary volume for simulations based on X-ray microtomography of sedimentary rock. *J. Petrol. Sci. Eng.* 166, 906–912. doi: 10.1016/j.petrol.2018.03.104

Gottardi, R., Kao, P.-H., Saar, M. O., and Teyssier, C. (2013). Effects of permeability fields on fluid, heat, and oxygen isotope transport in extensional detachment systems. *Geochem. Geophys. Geosyst.* 14, 1493–1522. doi: 10.1002/ggge.20100

Gras, A., Ginovart, M., Portell, X., and Baveye, P. C. (2010). Individual-based modeling of carbon and nitrogen dynamics in soils: parameterization and sensitivity analysis of abiotic components. *Soil Sci.* 175, 363–374. doi: 10.1097/SS.0b013e3181eda507

Gras, A., Ginovart, M., Valls, J., and Baveye, P. C. (2011). Individual-based modelling of carbon and nitrogen dynamics in soils: parameterization and sensitivity analysis of microbial components. *Ecol. Modell.* 222, 1998–2010. doi: 10.1016/j.ecolmodel.2011.03.009

Griffith, E. (1965). Micro-organisms and soil structure. *Biol. Rev. Camb. Philos. Soc.* 40, 129–142. doi: 10.1111/j.1469-185X.1965.tb00799.x

Grundmann, G. L. (2004). Spatial scales of soil bacterial diversity – The size of a clone. *FEMS Microbiol. Ecol.* 48, 119–127. doi: 10.1016/j.femsec.2004.01.010

Gruner, S. M. (2012). X-RAY imaging detectors. *Phys. Today* 65, 29–34. doi: 10.1063/pt.3.1819

Hainsworth, J. M., and Aylmore, L. A. G. (1983). The use of computer-assisted tomography to determine spatial distribution of soil water content. *Austr. J. Soil Res.* 21, 435–443. doi: 10.1071/sr9830435

Hallet, B. (1990). Self-organization in freezing soils: from microscopic ice lenses to patterned ground. *Can. J. Phys.* 68, 842–852. doi: 10.1139/p90-122

Hallett, P. D., Karim, K. H., Bengough, A. G., and Otten, W. (2013). Biophysics of the vadose zone: from reality to model systems and back again. *Vadose Zone J.* 12. doi: 10.2136/vzj2013.05.0090

Hamdi, S., Moyano, F., Sall, S., Bernoux, M., and Chevallier, T. (2013). Synthesis analysis of the temperature sensitivity of soil respiration from laboratory studies in relation to incubation methods and soil conditions. *Soil Biol. Biochem.* 58, 115–126. doi: 10.1016/j.soilbio.2012.11.012

Han, K., Feng, Y. T., and Owen, D. R. J. (2008). Modelling of thermal contact resistance within the framework of the thermal lattice Boltzmann method. *Int. J. Ther. Sci.* 47, 1276–1283. doi: 10.1016/j.ijthermalsci.2007.11.007

Hapca, S., Baveye, P. C., Wilson, C., Lark, R. M., and Otten, W. (2015). Three-dimensional mapping of soil chemical characteristics at micrometric scale by combining 2D SEM-EDX Data and 3D X-Ray CT Images. *PLoS One* 10:e0137025. doi: 10.1371/journal.pone.0137025

Hapca, S. M., Houston, A. N., Otten, W., and Baveye, P. C. (2013). New local thresholding method for soil images by minimizing grayscale intra-class variance. *Vadose Zone J.* 12:vzj2012.0172. doi: 10.2136/vzj2012.0172

Hapca, S. M., Wang, Z. X., Otten, W., Wilson, C., and Baveye, P. C. (2011). Automated statistical method to align 2D chemical maps with 3D X-ray computed micro-tomographic images of soils. *Geoderma* 164, 146–154. doi: 10.1016/j.geoderma.2011.05.018

Harris, K., Crabb, D., Young, I. M., Weaver, H., Gilligan, C. A., Otten, W., et al. (2002). In situ visualisation of fungi in soil thin sections: problems with crystallisation of the fluorochrome FB 28 (CalcofluorM2R) and improved staining by SCRI Renaissance 2200. *Mycol. Res.* 106, 293–297. doi: 10.1017/S0953756202005749

Harris, K., Young, I. M., Gilligan, C. A., Otten, W., and Ritz, K. (2003). Effect of bulk density on the spatial organisation of the fungus Rhizoctonia solani in soil. *FEMS Microbiol. Ecol.* 44, 45–56. doi: 10.1111/j.1574-6941.2003.tb01089.x

Hashemi, M. A., Khaddour, G., Francois, B., Massart, T. J., and Salager, S. (2014). A tomographic imagery segmentation methodology for three-phase geomaterials based on simultaneous region growing. *Acta Geotech.* 9, 831–846. doi: 10.1007/s11440-013-0289-5

Hattori, T. (1973). *Microbial Life in the Soil: An Introduction.* New York, NY: Marcel Dekker.

Hausladen, D. M., and Fendorf, S. (2017). Hexavalent chromium generation within naturally structured soils and sediments. *Environ. Sci. Technol.* 51, 2058–2067. doi: 10.1021/acs.est.6b04039

Heijs, A. W. J., de Lange, J., Schoute, J. F. T., and Bouma, J. (1995). Computed tomography as a tool for non-destructive analysis of flow patterns in macroporous clay soils. *Geoderma* 64, 183–196. doi: 10.1016/0016-7061(94)00020-B

Heinemann, M., and Zenobi, R. (2011). Single cell metabolomics. *Curr. Opin. Biotechnol.* 22, 26–31. doi: 10.1016/j.copbio.2010.09.008

Helliwell, J. R., Sturrock, C. J., Grayling, K. M., Tracy, S. R., Flavel, R. J., Young, I. M., et al. (2013). Applications of X-ray computed tomography for examining biophysical interactions and structural development in soil systems: a review. *Eur. J. Soil Sci.* 64, 279–297. doi: 10.1111/ejss.12028

Hellweger, F. L., Clegg, R. J., Clark, J. R., Plugge, C. M., and Kreft, J.-U. (2016). Advancing microbial sciences by individual-based modelling. *Nat. Rev. Microbiol.* 14, 461–471. doi: 10.1038/nrmicro.2016.62

Hemes, S., Desbois, G., Urai, J. L., Schröppel, B., and Schwarz, J.-O. (2015). Multi-scale characterization of porosity in Boom clay (HADES-level, Mol, Belgium) using a combination of X-ray (-CT, 2D BIB-SEM and FIB-SEM tomography. *Microporous Mesoporous Mater.* 208, 1–20. doi: 10.1016/j.micromeso.2015.01.022

Herrmann, A. M., Ritz, K., Nunan, N., Clode, P. L., Pett-Ridge, J., Kilburn, M. R., et al. (2007). Nano-scale secondary ion mass spectrometry – A new analytical tool in biogeochemistry and soil ecology: a review article. *Soil Biol. Biochem.* 39, 1835–1850. doi: 10.1016/j.soilbio.2007.03.011

Hesterberg, D., Duff, M. C., Dixon, J. B., and Vepraskas, M. J. (2011). X-ray microspectroscopy and chemical reactions in soil microsites. *J. Environ. Qual.* 40, 667–678. doi: 10.2134/jeq2010.0140

Heße, F., Radu, F. A., Thullner, M., and Attinger, S. (2009). Upscaling of the advection-diffusion-reaction equation with Monod reaction. *Adv. Water Resour.* 32, 1336–1351. doi: 10.1016/j.advwatres.2009.05.009

Hillel, D. (2004). *Introduction to Environmental Soil Physics.* San Diego, CA: Academic Press.

Hitchcock, A., Morin, C., Li, L., Brash, J., Scholl, A., and Doran, A. (2004). Methods and examples of quantitative chemical mapping using synchrotron soft X-ray spectromicroscopy. *Microsc. Microanal.* 10 1050–1051. doi: 10.1017/S1431927604886926

Holland, J. H. (1990). "Emergent models," in *Frontiers of Science*, ed. A. Scott (Oxford: Blackwell), 107–125.

Hopkins, S., and Boswell, G. P. (2012). Mycelial response to spatiotemporal nutrient heterogeneity: a velocity-jump mathematical model. *Fungal Ecol.* 5, 124–136. doi: 10.1016/j.funeco.2011.06.006

Hopmans, J. W., and Dane, J. H. (1986). Calibration of a dual-energy gamma radiation system for multiple point measurements in a soil. *Water Resour. Res.* 22, 1109–1114. doi: 10.1029/WR022i007p01109

Houben, M. E., Desbois, G., and Urai, J. L. (2013). Pore morphology and distribution in the shaly facies of opalinus Clay (Mont Terri, Switzerland): Insights from representative 2D BIB–SEM investigations on mm to nm scale. *Appl. Clay Sci.* 71, 82–97. doi: 10.1016/j.clay.2012.11.006

Houston, A. N., Otten, W., Baveye, P. C., and Hapca, S. (2013a). Adaptive-window indicator kriging: a thresholding method for computed tomography images of porous media. *Comput. Geosci.* 54, 239–248. doi: 10.1016/j.cageo.2012.11.016

Houston, A. N., Schmidt, S., Tarquis, A. M., Otten, W., Baveye, P. C., and Hapca, S. M. (2013b). Effect of scanning and image reconstruction settings in X-ray computed microtomography on quality and segmentation of 3D soil images. *Geoderma* 207, 154–165. doi: 10.1016/j.geoderma.2013.05.017

Houston, A. N., Otten, W., Falconer, R., Monga, O., Baveye, P. C., and Hapca, S. M. (2017). Quantification of the pore size distribution of soils: assessment of existing software using tomographic and synthetic 3D images. *Geoderma* 299, 73–82. doi: 10.1016/j.geoderma.2017.03.025

Hron, P., Jost, D., Bastian, P., Gallert, C., Winter, J., and Ippisch, O. (2015). Application of reactive transport modeling to growth and transport of microorganisms in the capillary fringe. *Vadose Zone J.* 14:vzj2014.07.0092. doi: 10.2136/vzj2014.07.0092

Hu, H.-W., Chen, D., and He, J.-Z. (2015). Microbial regulation of terrestrial nitrous oxide formation: understanding the biological pathways for prediction of emission rates. *FEMS Microbiol. Rev.* 39, 729–749. doi: 10.1093/femsre/fuv021

Iassonov, P., Gebrenegus, T., and Tuller, M. (2009). Segmentation of X-ray computed tomography images of porous materials: a crucial step for characterization and quantitative analysis of pore structures. *Water Resour. Res.* 45:W09415. doi: 10.1029/2009wr008087

Iliev, O., Lakdawala, Z., Neßler, K. H. L., Prill, T., Vutov, Y., Yang, Y., et al. (2017). On the pore-scale modeling and simulation of reactive transport in 3D geometries. *Mathemat. Modell. Anal.* 22, 671–694. doi: 10.3846/13926292.2017.1356759

Iltis, G. C., Armstrong, R. T., Jansik, D. P., Wood, B. D., and Wildenschild, D. (2011). Imaging biofilm architecture within porous media using synchrotron-based X-ray computed microtomography. *Water Resour. Res.* 47:W02601. doi: 10.1029/2010wr009410

Inselsbacher, E., Oyewole, O. A., and Näsholm, T. (2014). Early season dynamics of soil nitrogen fluxes in fertilized and unfertilized boreal forests. *Soil Biol. Biochem.* 74, 167–176. doi: 10.1016/j.soilbio.2014.03.012

Ishii, S., Tago, K., and Senoo, K. (2010). Single-cell analysis and isolation for microbiology and biotechnology: methods and applications. *Appl. Microbiol. Biotechnol.* 86, 1281–1292. doi: 10.1007/s00253-010-2524-4

Ishoey, T., Woyke, T., Stepanauskas, R., Novotny, M., and Lasken, R. S. (2008). Genomic sequencing of single microbial cells from environmental samples. *Curr. Opin. Microbiol.* 11, 198–204. doi: 10.1016/j.mib.2008.05.006

Ishøy, T., Kvist, T., Westermann, P., and Ahring, B. K. (2006). An improved method for single cell isolation of prokaryotes from meso-, thermo- and hyperthermophilic environments using micromanipulation. *Appl. Microbiol. Biotechnol.* 69, 510–514. doi: 10.1007/s00253-005-0014-x

Jacobson, A. R., Dousset, S., Andreux, F., and Baveye, P. C. (2007). Electron microprobe and synchrotron X-ray fluorescence mapping of the heterogeneous distribution of copper in high-copper vineyard soils. *Environ. Sci. Technol.* 41, 6343–6349. doi: 10.1021/es070707m

Jasinska, E., Wetzel, H., Baumgartl, T., and Horn, R. (2006). Heterogeneity of physico-chemical properties in structured soils and its consequences. *Pedosphere* 16, 284–296. doi: 10.1016/S1002-0160(06)60054-4

Jassogne, L., Hettiarachchi, G., McNeill, A., and Chittleborough, D. (2012). Characterising the chemistry of micropores in a sodic soil with strong texture-contrast using synchrotron X-ray techniques and LA-ICP-MS. *Soil Res.* 50, 424–435. doi: 10.1071/sr11312

Jeger, M. J., Lamour, A., Gilligan, C. A., and Otten, W. (2008). A fungal growth model fitted to carbon-limited dynamics of *Rhizoctonia solani*. *New Phytol.* 178, 625–633. doi: 10.1111/j.1469-8137.2008.02394.x

Jenkinson, D. S. (1966). Studies on the decomposition of plant material in soil: II. Partial sterilization of soil and the soil biomass. *J. Soil Sci.* 17, 280–302. doi: 10.1111/j.1365-2389.1966.tb01474.x

Ji, N. (2017). Adaptive optical fluorescence microscopy. *Nat. Methods* 14, 374–380. doi: 10.1038/nmeth.4218

Jiang, Y. J., Sun, B., Li, H. X., Liu, M. Q., Chen, L. J., and Zhou, S. (2015). Aggregate-related changes in network patterns of nematodes and ammonia oxidizers in an acidic soil. *Soil Biol. Biochem.* 88, 101–109. doi: 10.1016/j.soilbio.2015.05.013

Joergensen, R. G., and Wichern, F. (2018). Alive and kicking: why dormant soil microorganisms matter. *Soil Biol. Biochem.* 116, 419–430. doi: 10.1016/j.soilbio.2017.10.022

Johnson, R. A., Ellsworth, T. E., Hudson, R. J. M., and Sims, G. K. (2013). Diffusion limitation for atrazine biodegradation in soil. *Adv. Microbiol.* 3, 412–420. doi: 10.4236/aim.2013.35056

Jones, B., and Feng, Y. T. (2011). "Permeability assessment of heterogeneous porous media using the Lattice Boltzmann method," in *Particle-Based Methods: Fundamentals and Applications*, eds E. Oñate and R. Owen (Berlin: Springer), 865–881.

Jones, D., and Griffiths, E. (1964). The use of thin soil sections for the study of soil microorganisms. *Plant Soil* 20, 232–240. doi: 10.1007/bf01376452

Joschko, M., Graff, O., Muller, P. C., Kotzke, K., Lindner, P., Pretschner, D. P., et al. (1991). A non-destructive method for the morphological assessment of earthworm burrow systems in three dimensions by x-ray computed tomography. *Biol. Fertil. Soils* 11, 88–92. doi: 10.1007/BF00336369

Juyal, A., Eickhorst, T., Falconer, R., Baveye, P. C., Spiers, A., and Otten, W. (2018). Control of pore geometry in soil microcosms and its effect on the growth of *Pseudomonas* and *Bacillus* sp. *Front. Environ. Sci.* 6:73. doi: 10.3389/fenvs.2018.00073

Kaisermann, A., Maron, P. A., Beaumelle, L., and Lata, J. C. (2015). Fungal communities are more sensitive indicators to non-extreme soil moisture variations than bacterial communities. *Appl. Soil Ecol.* 86, 158–164. doi: 10.1016/j.apsoil.2014.10.009

Kalyuzhnaya, M. G., Lapidus, A., Ivanova, N., Copeland, A. C., McHardy, A. C., Szeto, E., et al. (2008). High-resolution metagenomics targets specific functional types in complex microbial communities. *Nat. Biotechnol.* 26, 1029–1034. doi: 10.1038/nbt.1488

Kang, Y., Norris, M. H., Zarzycki-Siek, J., Nierman, W. C., Donachie, S. P., and Hoang, T. T. (2011). Transcript amplification from single bacterium for transcriptome analysis. *Genome Res.* 21, 925–935. doi: 10.1101/gr.116103.110

Karadimitriou, N. K., and Hassanizadeh, S. M. (2012). A review of micromodels and their use in two-phase flow studies. *Vadose Zone J.* 11. doi: 10.2136/vzj2011.0072

Karsanina, M. V., Gerke, K. M., Skvortsova, E. B., and Mallants, D. (2015). Universal spatial correlation functions for describing and reconstructing soil microstructure. *PLoS One* 10:e0126515. doi: 10.1371/journal.pone.0126515

Keck, H., Strobel, B. W., Gustafsson, J. P., and Koestel, J. (2017). Quantitative imaging of the 3-D distribution of cation adsorption sites in undisturbed soil. *Soil* 3, 177–180. doi: 10.5194/soil-3-177-2017

Keiluweit, M., Gee, K., Denney, A., and Fendorf, S. (2018). Anoxic microsites in upland soils dominantly controlled by clay content. *Soil Biol. Biochem.* 118, 42–50. doi: 10.1016/j.soilbio.2017.12.002

Keiluweit, M., Wanzek, T., Kleber, M., Nico, P., and Fendorf, S. (2017). Anaerobic microsites have an unaccounted role in soil carbon stabilization. *Nat. Commun.* 8:1771. doi: 10.1038/s41467-017-01406-6

Kettridge, N., and Binley, A. (2011). Characterization of peat structure using X-ray computed tomography and its control on the ebullition of biogenic gas bubbles. *J. Geophys. Res.* 116:G01024. doi: 10.1029/2010JG001478

Killham, K., Amato, M., and Ladd, J. N. (1993). Effect of substrate location in soil and soil porewater regime on carbon turnover. *Soil Biol. Biochem.* 25, 57–62. doi: 10.1016/0038-0717(93)90241-3

Kim, M., and Or, D. (2016). Individual-based model of microbial life on hydrated rough soil surfaces. *PLoS One* 11:e0147394. doi: 10.1371/journal.pone.0147394

Kinyangi, J., Solomon, D., Liang, B., Lerotic, M., Wirick, S., and Lehmann, J. (2006). Nanoscale biogeocomplexity of the organomineral assemblage in soil: application of STXM microscopy and C 1s-NEXAFS spectroscopy. *Soil Sci. Soc. Am. J.* 70, 1708–1718. doi: 10.2136/sssaj2005.0351

Kirschbaum, M. U. F. (2006). The temperature dependence of organic matter decomposition - still a topic of debate. *Soil Biol. Biochem.* 38, 2510–2518. doi: 10.1016/j.soilbio.2006.01.030

Kitanidis, P. K. (2015). Persistent questions of heterogeneity, uncertainty, and scale in subsurface flow and transport. *Water Resour. Res.* 51, 5888–5904. doi: 10.1002/2015wr017639

Knauth, S., Schmidt, H., and Tippkotter, R. (2013). Comparison of commercial kits for the extraction of DNA from paddy soils. *Lett. Appl. Microbiol.* 56, 222–228. doi: 10.1111/lam.12038

Koestel, J. (2017). SoilJ: an ImageJ plugin for the semiautomatic processing of three-dimensional X-ray images of soils. *Vadose Zone J.* 17. doi: 10.2136/vzj2017.03.0062

Kögel-Knabner, I., Ekschmitt, K., Flessa, H., Guggenberger, G., Matzner, E., Marschner, B., et al. (2008). An integrative approach of organic matter stabilization in temperate soils: linking chemistry, physics, and biology. *J. Plant Nutr. Soil Sci.* 171, 5–13. doi: 10.1002/jpln.200700215

Kohlmeier, S., Smits, T. H. M., Ford, R. M., Keel, C., Harms, H., and Wick, L. Y. (2005). Taking the fungal highway: mobilization of pollutant-degrading bacteria by fungi. *Environ. Sci. Technol.* 39, 4640–4646. doi: 10.1021/es047979z

Kopittke, P. M., Wang, P., Lombi, E., and Donner, E. (2017). Synchrotron-based X-Ray approaches for examining toxic trace metal(loid)s in soil-plant systems. *J. Environ. Qual.* 46, 1175–1189. doi: 10.2134/jeq2016.09.0361

Kotani-Tanoi, T., Nishiyama, M., Otsuka, S., and Senoo, K. (2007). Single particle analysis reveals that bacterial community structures are semi-specific to the type of soil particle. *Soil Sci. Plant Nutr.* 53, 740–743. doi: 10.1111/j.1747-0765.2007.00200.x

Kowalchuk, G. A. (2012). Bad news for soil carbon sequestration? *Science* 337, 1049–1050. doi: 10.1126/science.1227303

Kravchenko, A., Chun, H. C., Mazer, M., Wang, W., Rose, J. B., Smucker, A., et al. (2013). Relationships between intra-aggregate pore structures and distributions of *Escherichia coli* within soil macro-aggregates. *Appl. Ecol.* 63, 134–142. doi: 10.1016/j.apsoil.2012.10.001

Kravchenko, A., Falconer, R. E., Grinev, D., and Otten, W. (2011). Fungal colonization in soils with different management histories: modeling growth in three-dimensional pore volumes. *Ecol. Appl.* 21, 1202–1210. doi: 10.1890/10-0525.1

Kravchenko, A. N., Wang, A. N. W., Smucker, A. J. M., and Rivers, M. L. (2011). Long-term differences in tillage and land use affect intra-aggregate pore heterogeneity. *Soil Sci. Soc. Am. J.* 75, 1658–1666. doi: 10.2136/sssaj2011.0096

Kravchenko, A. N., and Guber, A. K. (2017). Soil pores and their contributions to soil carbon processes. *Geoderma* 287, 31–39. doi: 10.1016/j.geoderma.2016.06.027

Kravchenko, A. N., Negassa, W., Guber, A. K., and Schmidt, S. (2014a). New approach to measure soil particulate organic matter in intact samples using X-Ray computed microtomography. *Soil Sci. Soc. Am. J.* 78, 1177–1185. doi: 10.2136/sssaj2014.01.0039

Kravchenko, A. N., Negassa, W. C., Guber, A. K., Hildebrandt, B., Marsh, T. L., and Rivers, M. L. (2014b). Intra-aggregate pore structure influences phylogenetic composition of bacterial community in macroaggregates. *Soil Sci. Soc. Am. J.* 78, 1924–1939. doi: 10.2136/sssaj2014.07.0308

Kravchenko, A. N., Negassa, W. C., Guber, A. K., and Rivers, M. L. (2015). Protection of soil carbon within macro-aggregates depends on intra-aggregate pore characteristics. *Sci. Rep.* 5:16261. doi: 10.1038/srep16261

Kravchenko, A. N., Toosi, E. R., Guber, A. K., Ostrom, N. E., Yu, J., Azeem, K., et al. (2017). Hotspots of soil N_2O emission enhanced through water absorption by plant residue. *Nat. Geosci.* 10:496. doi: 10.1038/ngeo2963

Kühl, F.-C., Mueller, M., Schellhorn, M., Mann, K., Wieneke, S., and Eusterhues, K. (2016). Near-edge x-ray absorption fine structure spectroscopy at atmospheric pressure with a table-top laser-induced soft x-ray source. *J. Vacuum Sci. Technol. A* 34, 041302. doi: 10.1116/1.4950599

Kuka, K., Franko, U., and Ruhlmann, J. (2007). Modelling the impact of pore space distribution on carbon turnover. *Ecol. Modell.* 208, 295–306. doi: 10.1016/j.ecolmodel.2007.06.002

Kulkarni, R., Tuller, M., Fink, W., and Wildenschild, D. (2012). Three-dimensional multiphase segmentation of X-Ray CT data of porous materials using a bayesian markov random field framework. *Vadose Zone J.* 11. doi: 10.2136/vzj2011.0082

Kuzyakov, Y. (2010). Priming effects: interactions between living and dead organic matter. *Soil Biol. Biochem.* 42, 1363–1371. doi: 10.1016/j.soilbio.2010.04.003

Kuzyakov, Y., and Blagodatskaya, E. (2015). Microbial hotspots and hot moments in soil: concept and review. *Soil Biol. Biochem.* 83, 184–199. doi: 10.1016/j.soilbio.2015.01.025

Kvist, T., Ahring, B. K., Lasken, R. S., and Westermann, P. (2007). Specific single-cell isolation and genomic amplification of uncultured microorganisms. *Appl. Microbiol. Biotechnol.* 74, 926–935. doi: 10.1007/s00253-006-0725-7

Lafond, J. A., Han, L., Allaire, S. E., and Dutilleul, P. (2012). Multifractal properties of porosity as calculated from computed tomography (CT) images of a sandy soil, in relation to soil gas diffusion and linked soil physical properties. *Eur. J. Soil Sci.* 63, 861–873. doi: 10.1111/j.1365-2389.2012.01496.x

Lal, R., and Bruce, J. P. (1999). The potential of world cropland soils to sequester C and mitigate the greenhouse effect. *Environ. Sci. Policy* 2, 177–185. doi: 10.1016/S1462-9011(99)00012-X

Lanning, L. M., and Ford, R. M. (2002). Glass micromodel study of bacterial dispersion in spatially periodic porous networks. *Biotechnol. Bioeng.* 78, 556–566. doi: 10.1002/bit.10236

Lasken, R. S. (2012). Genomic sequencing of uncultured microorganisms from single cells. *Nat. Rev. Microbiol.* 10, 631–640. doi: 10.1038/nrmicro2857

Lasken, R. S. (2013). Single-cell sequencing in its prime. *Nat. Biotechnol.* 31, 211–212. doi: 10.1038/nbt.2523

Laughlin, R. J., and Stevens, R. J. (2002). Evidence for fungal dominance of denitrification and codenitrification in a grassland soil. *Soil Sci. Soc. Am. J.* 66, 1540–1548. doi: 10.2136/sssaj2002.1540

Lavelle, P., Barot, S., Blouin, M., Decaens, T., Jimenez, J. J., and Jouquet, P. (2007). "Earthworms as key actors in self-organized soil systems," in *Ecosystem Engineers: Plants to Protists*, eds K. Cuddington, J. E. Byers, W. G. Wilson, and A. Hastings (Cambrdge, MA: Academic press), 77–106. doi: 10.1016/S1875-306X(07)80007-4

Lavelle, P., Spain, A., Blouin, M., Brown, G., Decaens, T., Grimaldi, M., et al. (2016). Ecosystem engineers in a self-organized soil: a review of concepts and future research Questions. *Soil Sci.* 181, 91–109. doi: 10.1097/ss.0000000000000155

LeCun, Y., Bengio, Y., and Hinton, G. (2015). Deep learning. *Nature* 521, 436–444. doi: 10.1038/nature14539

Ledbetter, M., and Budker, D. (2013). Zero-field nuclear magnetic resonance. *Phys. Today* 66, 44–49. doi: 10.1063/PT.3.1948

Lee, B. H., and Lee, S. K. (2017). Probing the water distribution in porous model sans with two immiscible fluids: a nuclear magentic resonance micro-imaging study. *J. Hydrol.* 553, 637–650. doi: 10.1016/j.jhydrol.2017.08.035

Lehmann, J., Solomon, D., Kinyangi, J., Dathe, L., Wirick, S., and Jacobsen, C. (2008). Spatial complexity of soil organic matter forms at nanometre scales. *Nat. Geosci.* 1, 238–242. doi: 10.1038/ngeo155

Lehmann, J., Wyss, P., Flisch Lehmann, E., Vontobel, P., Krafczyk, M., Kaestner, A., et al. (2006). Tomographical imaging and mathematical description of porous media used for the prediction of fluid distribution. *Vadose Zone J.* 5, 80–97. doi: 10.2136/vzj2004.0177

Lerch, T. Z., Nunan, N., Dignac, M. F., Chenu, C., and Mariotti, A. (2011). Variations in microbial isotopic fractionation during soil organic matter decomposition. *Biogeochemistry* 106, 5–21. doi: 10.1007/s10533-010-9432-7

Letey, J. (1991). The study of soil structure: science or art? *Austr. J. Soil Res.* 29, 699–707. doi: 10.1071/sr9910699

Li, J., Pignatello, J. J., Smets, B. F., Grasso, D., and Monserrate, E. (2005). Bench-scale evaluation of in situ bioremediation strategies for soil at a former manufactured gas plant site. *Environ. Toxicol. Chem.* 24, 741–749. doi: 10.1897/04-247r.1

Li, L., Peters, C. A., and Celia, M. A. (2006). Upscaling geochemical reaction rates using pore-scale network modeling. *Adv. Water Resour.* 29, 1351–1370. doi: 10.1016/j.advwatres.2005.10.011

Li, L., Peters, C. A., and Celia, M. A. (2007a). Applicability of averaged concentrations in determining geochemical reaction rates in heterogeneous porous media. *Am. J. Sci.* 307, 1146–1166. doi: 10.2475/10.2007.02

Li, L., Peters, C. A., and Celia, M. A. (2007b). Effects of mineral spatial distribution on reaction rates in porous media. *Water Resour. Res.* 43:W01419. doi: 10.1029/2005WR004848

Li, L., Peters, C. A., and Celia, M. A. (2007c). Reply to "Comment on upscaling geochemical reaction rates using pore-scale network modeling" by Peter C. Lichtner and Qinjun Kang. *Adv. Water Resour.* 30, 691–695. doi: 10.1016/j.advwatres.2006.05.002

Li, L., Wen, K., Li, C., and Amini, F. (2017). FIB/SEM imaging of microbial induced calcite precipitation in sandy soil. *Microsc. Microanal.* 23, 310–311. doi: 10.1017/S1431927617002239

Li, M., Xu, J., Romero-Gonzalez, M., Banwart, S. A., and Huang, W. E. (2012). Single cell Raman spectroscopy for cell sorting and imaging. *Curr. Opin. Biotechnol.* 23, 56–63. doi: 10.1016/j.copbio.2011.11.019

Li, R., Yang, Y. S., Pan, J., Pereira, G. G., Taylor, J. A., Clennell, B., et al. (2014). Lattice Boltzmann modeling of permeability in porous materials with partially percolating voxels. *Phys. Rev. E* 90:33301. doi: 10.1103/PhysRevE.90.033301

Li, Y., Dick, W. A., and Tuovinen, O. H. (2003). Evaluation of fluorochromes for imaging bacteria in soil. *Soil Biol. Biochem.* 35, 737–744. doi: 10.1016/s0038-0717(02)00196-7

Li, Y., Dick, W. A., and Tuovinen, O. H. (2004). Fluorescence microscopy for visualization of soil microorganisms – A review. *Biol. Fertil. Soils* 39, 301–311. doi: 10.1007/s00374-004-0722-x

Li, Z., Zhang, X., Wang, D., and Liu, Y. (2018). Direct methods to calculate the mass exchange between solutes inside and outside aggregates in macroscopic model for solute transport in aggregated soil. *Geoderma* 320, 126–135. doi: 10.1016/j.geoderma.2018.01.021

Lichtner, P. C., and Kang, Q. (2007b). Upscaling pore-scale reactive transport equations using a multiscale continuum formulation. *Water Resour. Res.* 43:W12s15.

Lichtner, P. C., and Kang, Q. J. (2007a). Comment on: "Upscaling geochemical reaction rates using pore-scale network modeling" by Li, Peters and Celia. *Adv. Water Resour.* 30, 686–690. doi: 10.1016/j.advwatres.2006.05.005

Lilje, O., Lilje, E., Marano, A. V., and Gleason, F. H. (2013). Three dimensional quantification of biological samples using micro-computer aided tomography (microCT). *J. Microbiol. Methods* 92, 33–41. doi: 10.1016/j.mimet.2012.10.006

Lin, H. (2012). "Understanding soil architecture and its functional manifestation across scales," in *Hydropedology*, ed. H. Lin (Amsterdam: Elsevier), 41–74.

Lin, H., Flühler, H., Otten, W., and Vogel, H. J. (2010). Soil architecture and preferential flow across scales. *J. Hydrol.* 393, 1–2. doi: 10.1016/j.jhydrol.2010.07.026

Liu, J., Pereira, G. G., Liu, Q., and Regenauer-Lieb, K. (2016). Computational challenges in the analyses of petrophysics using microtomography and upscaling: a review. *Comput. Geosci.* 89, 107–117. doi: 10.1016/j.cageo.2016.01.014

Liu, Y., King, H. E., van Huis, M. A., Drury, M. R., and Plümper, O. (2017). FIB-SEM tomography of porous geological materials: a state-of-the-art 3D characterization technique. *GIT. Imag. Microsc.* 2, 41–43.

Loehle, C., and Johnson, P. (1994). A framework for modeling microbial transport and dynamics in the subsurface. *Ecol. Modell.* 73, 31–49. doi: 10.1016/0304-3800(94)90096-5

Lombard, N., Prestat, E., van Elsas, J. D., and Simonet, P. (2011). Soil-specific limitations for access and analysis of soil microbial communities by metagenomics. *FEMS Microbiol. Ecol.* 78, 31–49. doi: 10.1111/j.1574-6941.2011.01140.x

Lugo-Mendez, H. D., Valdes-Parada, F. J., Porter, M. L., Wood, B. D., and Ochoa-Tapia, J. A. (2015). Upscaling diffusion and nonlinear reactive mass transport in homogeneous porous media. *Transp. Porous Media* 107, 683–716. doi: 10.1007/s11242-015-0462-4

Luo, L., Lin, H., and Li, S. (2010). Quantification of 3-D soil macropore networks in different soil types and land uses using computed tomography. *J. Hydrol.* 393, 53–64. doi: 10.1016/j.jhydrol.2010.03.031

Lühl, L., Mantouvalou, I., Schaumann, I., Vogt, C., and Kanngießer, B. (2013). Three-dimensional chemical mapping with a confocal XRF setup. *Anal. Chem.* 85, 3682–3689. doi: 10.1021/ac303749b

Macura, J., Szolnoki, J., Kunc, F., Vancura, V., and Babicky, A. (1965). Decomposition of glucose continuously added to soil. *Folia Microbiol.* 10, 44–54. doi: 10.1007/bf02869840

Malka, V., Faure, J., Gauduel, Y. A., Lefebvre, E., Rousse, A., and Phuoc, K. T. (2008). Principles and applications of compact laser-plasma accelerators. *Nat. Phys.* 4, 447–453. doi: 10.1038/nphys966

Männik, J., Driessen, R., Galajda, P., Keymer, J. E., and Dekker, C. (2009). Bacterial growth and motility in sub-micron constrictions. *Proc. Natl. Acad. Sci. U.S.A.* 106, 14861–14866. doi: 10.1073/pnas.0907542106

Manson, S. M. (2001). Simplifying complexity: a review of complexity theory. *Geoforum* 32, 405–414. doi: 10.1016/s0016-7185(00)00035-x

Marcy, Y., Ouverney, C., Bik, E. M., Lösekann, T., Ivanova, N., Martin, H. G., et al. (2007). Dissecting biological "dark matter" with single-cell genetic analysis of rare and uncultivated TM7 microbes from the human mouth. *Proc. Natl. Acad. Sci. U.S.A.* 104, 11889–11894. doi: 10.1073/pnas.0704662104

Maron, P. A., Mougel, C., and Ranjard, L. (2011). Soil microbial diversity: methodological strategy, spatial overview and functional interest. *CR Biol.* 334, 403–411. doi: 10.1016/j.crvi.2010.12.003

Martin-Sotoca, J. J., Saa-Requejo, A., Grau, J. B., and Tarquis, A. M. (2017). New segmentation method based on fractal properties using singularity maps. *Geoderma* 287, 40–53. doi: 10.1016/j.geoderma.2016.09.005

Martys, N. S., and Chen, H. (1996). Simulation of multicomponent fluids in complex three-dimensional geometries by the lattice Boltzmann method. *Phys. Rev.* E53, 743–750. doi: 10.1103/PhysRevE.53.743

Masue-Slowey, Y., Kocar, B. D., Jofre, S. A. B., Mayer, K. U., and Fendorf, S. (2011). Transport implications resulting from internal redistribution of arsenic and iron within constructed soil aggregates. *Environ. Sci. Technol.* 45, 582–588. doi: 10.1021/es1027663

Masue-Slowey, Y., Ying, S. C., Kocar, B. D., Pallud, C. E., and Fendorf, S. (2013). Dependence of arsenic fate and transport on biogeochemical heterogeneity arising from the physical structure of soils and sediments. *J. Environ. Qual.* 42, 1119–1129. doi: 10.2134/jeq2012.0253

McDonald, P. J., and Turner, M. N. (2016). Combining effective media and multi-phase methods of Lattice Boltzmann modelling for the characterisation of liquid-vapour dynamics in multi-length scale heterogeneous structural materials. *Modell. Simul. Mater. Sci. Eng.* 2. doi: 10.1088/0965-0393/24/1/015010

McIntosh, K. G., Cordes, N. L., Patterson, B. M., and Havrilla, G. J. (2015). Laboratory-based characterization of plutonium in soil particles using micro-XRF and 3D confocal XRF. *J. Anal. Atomic Spectros.* 30, 1511–1517. doi: 10.1039/C5JA00068H

Mcnaughton, S. J., Booth, T., Embley, T. M., and O'Donnell, A. G. (1996). Physical stabilization and confocal microscopy of bacteria on roots using 16S rRNA targeted, fluorescent-lavebeled oligonucleotide probes. *J. Microb. Methods* 26, 279–285. doi: 10.1016/0167-7012(96)00923-2

Meckenstock, R. U., Elsner, M., Griebler, C., Lueders, T., Stumpp, C., Aamand, J., et al. (2015). Biodegradation: updating the concepts of control for microbial cleanup in contaminated aquifers. *Environ. Sci. Technol.* 49, 7073–7081. doi: 10.1021/acs.est.5b00715

Meira Cassaro, F. A., Posadas Durand, A. N., Gimenez, D., and Pedro Vaz, C. M. (2017). Pore-size distributions of soils derived using a geometrical approach and multiple resolution microCT images. *Soil Sci. Soc. Am. J.* 81, 468–476. doi: 10.2136/sssaj2016.09.0291

Mendes, L. W., Tsai, S. M., Navarrete, A. A., de Hollander, M., van Veen, J. A., and Kuramae, E. E. (2015). Soil-borne microbiome: linking diversity to function. *Microb. Ecol.* 70, 255–265. doi: 10.1007/s00248-014-0559-2

Michelson, K., Sanford, R. A., Valocchi, A. J., and Werth, C. J. (2017). Nanowires of geobacter sulfurreducens require redox cofactors to reduce metals in pore spaces too small for cell passage. *Environ. Sci. Technol.* 51, 11660–11668. doi: 10.1021/acs.est.7b02531

Milne, A. E., Lehmann, J., Solomon, D., and Lark, R. M. (2011). Wavelet analysis of soil variation at nanometre- to micrometre-scales: an example of organic carbon content in a micro-aggregate. *Eur. J. Soil Sci.* 62, 617–628. doi: 10.1111/j.1365-2389.2011.01352.x

Min, W., Freudiger, C. W., Lu, S., and Xie, X. S. (2011). "Coherent nonlinear optical imaging: beyond fluorescence microscopy," in *Annual Review of Physical*

Chemistry, Vol. 62, eds S. R. Leone, P. S. Cremer, J. T. Groves, and M. A. Johnson (Palo Alto, CA: Annual Reviews), 507–530.

Minasny, B., Arrouays, D., McBratney, A. B., Angers, D. A., Chambers, A., Chaplot, V., et al. (2018). Rejoinder to comments on minasny et al., 2017 soil carbon 4 per mille geoderma 292, 59-86. *Geoderma* 309, 124–129. doi: 10.1016/j.geoderma.2017.05.026

Minasny, B., Malone, B. P., McBratney, A. B., Angers, D. A., Arrouays, D., Chambers, A., et al. (2017). Soil carbon 4 per mille. *Geoderma* 292, 59–86. doi: 10.1016/j.geoderma2017.01.002

Monga, O., Bousso, M., Garnier, P., and Pot, V. (2009). Using pore space 3D geometrical modelling to simulate biological activity: impact of soil structure. *Comput. Geosci.* 35, 1789–1801. doi: 10.1016/j.cageo.2009.02.007

Monga, O., Ngom, N. F., and Delerue, J. F. (2007). Representing geometric structures in 3D tomography soil images: aplication to pore space modelling. *Comput. Geosci.* 33, 1140–1161. doi: 10.1016/j.cageo.2006.11.015

Mooney, S. J. (2002). Three-dimensional visualization and quantification of soil macroporosity and water flow patterns using computed tomography. *Soil Use Manage.* 18, 142–151. doi: 10.1111/j.1475-2743.2002.tb00232.x

Mourou, G., Brocklesby, B., Tajima, T., and Limpert, J. (2013). The future is fibre accelerators. *Nat. Photon.* 7, 258–261. doi: 10.1038/nphoton.2013.75

Muci, A. L., Jorquera, M. A., Avila, A. I., Rengel, Z., Crowley, D. E., and de la Luz Mora, M. (2012). A combination of cellular automata and agent-based models for simulating the root surface colonization by bacteria. *Ecol. Modell.*, 247, 1–10. doi: 10.1016/j.ecolmodel.2012.07.035

Mueller, C. W., Köbl, A., Hoeschen, C., Hillion, F., Hiester, K., Herrmann, A. M., et al. (2012). Submicron scale imaging of soil organic matter dynamics using NanoSIMS – From single particles to intact aggregates. *Organ. Geochem.* 42, 1476–1488. doi: 10.1016/j.orggeochem.2011.06.003

Mueller, C. W., Remusat, L., and Rumpel, C. (2017). "Characterization of biogeochemical processes at the microscale," in *Terrestrial Ecosystem Research Infrastructures*, eds A. Chabbi and H. Loescher (Boca Raton, FL: CRC Press), 193–212. doi: 10.1201/9781315368252-9

Mueller, C. W., Weber, P. K., Kilburn, M. R., Hoeschen, C., Kleber, M., and Pett-Ridge, J. (2013). Advances in the analysis of biogeochemical interfaces: nanoSIMS to investigate soil microenvironments. *Adv. Agron.* 121, 1–46. doi: 10.1016/b978-0-12-407685-3.00001-3

Müller, M., Mey, T., Niemeyer, J., and Mann, K. (2014). Table-top soft x-ray microscope using laser-induced plasma from a pulsed gas jet. *Optics Express* 22, 23489–23495. doi: 10.1364/oe.22.023489

Nannipieri, P., Ascher, J., Ceccherini, M. T., Landi, L., Pietramellara, G., and Renella, G. (2003). Microbial diversity and soil functions. *Eur. J. Soil Sci.* 54, 655–670. doi: 10.1046/j.1351-0754.2003.0556.x

Nazir, R., Shen, J.-P., Wang, J.-T., Hu, H.-W., and He, J.-Z. (2017). Fungal networks serve as novel ecological routes for enrichment and dissemination of antibiotic resistance genes as exhibited by microcosm experiments. *Sci. Rep.* 7:1547. doi: 10.1038/s41598-017-15660-7

Negassa, W. C., Guber, A. K., Kravchenko, A. N., Marsh, T. L., Hildebrandt, B., and Rivers, M. L. (2015). Properties of soil pore space regulate pathways of plant residue decomposition and community structure of associated bacteria. *PLoS One* 10:e0123999. doi: 10.1371/journal.pone.0123999

Ngom, N. F., Monga, O., Mohamed, M. M. O., and Garnier, P. (2012). 3D shape extraction segmentation and representation of soil microstructures using generalized cylinders. *Comput. Geosci.* 39, 50–63. doi: 10.1016/j.cageo.2011.06.010

Nishizawa, T., Tago, K., Uei, Y., Ishii, S., Isobe, K., Otsuka, S., et al. (2012). Advantages of functional single-cell isolation method over standard agar plate dilution method as a tool for studying denitrifying bacteria in rice paddy soil. *AMB Express* 2, 50–50. doi: 10.1186/2191-0855-2-50

Nunan, N., Lerch, T. Z., Pouteau, V., Mora, P., Changey, E., Katterer, T., et al. (2015). Metabolising old soil carbon: simply a matter of simple organic matter? *Soil Biol. Biochem.* 88, 128–136. doi: 10.1016/j.soilbio.2015.05.018

Nunan, N., Ritz, K., Crabb, D., Harris, K., Wu, K. J., Crawford, J. W., et al. (2001). Quantification of the in situ distribution of soil bacteria by large-scale imaging of thin sections of undisturbed soil. *FEMS Microbiol. Ecol.* 37, 67–77. doi: 10.1111/j.1574-6941.2001.tb00854.x

Nunan, N., Ritz, K., Rivers, M., Feeney, D. S., and Young, I. M. (2006). Investigating microbial micro-habitat structure using X-ray computed tomography. *Geoderma* 133, 398–407. doi: 10.1016/j.geoderma.2005.08.004

Nunan, N., Wu, K., Young, I. M., Crawford, J. W., and Ritz, K. (2002). In situ spatial patterns of soil bacterial populations, mapped at multiple scales, in an arable soil. *Microb. Ecol.* 44, 296–305. doi: 10.1007/s00248-002-2021-0

Nunan, N., Wu, K. J., Young, I. M., Crawford, J. W., and Ritz, K. (2003). Spatial distribution of bacterial communities and their relationships with the micro-architecture of soil. *FEMS Microbiol. Ecol.* 44, 203–215. doi: 10.1016/S0168-6496(03)00027-8

Oburger, E., and Schmidt, H. (2016). New methods to unravel rhizosphere processes. *Trends Plant Sci.* 21, 243–255. doi: 10.1016/j.tplants.2015.12.005

O'Donnell, A. G., Young, I. M., Rushton, S. P., Shirley, M. D., and Crawford, J. W. (2007). Visualization, modelling and prediction in soil microbiology. *Nat. Rev. Microbiol.* 5, 689–699. doi: 10.1038/nrmicro1714

Ojeda-Magana, B., Quintanilla-Dominguez, J., Ruelas, R., Tarquis, A. M., Gomez-Barba, L., and Andina, D. (2014). Identification of pore spaces in 3D CT soil images using PFCM partitional clustering. *Geoderma* 217, 90–101. doi: 10.1016/j.geoderma.2013.11.005

Olson, M. S., Ford, R. M., Smith, J. A., and Fernandez, E. J. (2004). Quantification of bacterial chemotaxis in porous media using magnetic resonance imaging. *Environ. Sci. Technol.* 38, 3864–3870. doi: 10.1021/es035236s

Or, D. (2002). Physical processes affecting microbial habitats and activity in unsaturated poous media. *Agric. Sci.* 7, 39–45.

Oremland, R. S., Capone, D. G., Stolz, J. F., and Fuhrman, J. A. (2005). Whither or wither geomicrobiology in the era of 'community metagenomics'. *Nat. Rev. Microbiol.* 3, 572–578. doi: 10.1038/nrmicro1182

Ostadi, H., Rama, P., Liu, Y., Chen, R., Zhang, X. X., and Jiang, K. (2010). Threshold fine-tuning and 3D characterisation of porous media using X-ray nanotomography. *Curr. Nanosci.* 6, 226–231. doi: 10.2174/157341310790945623

Otten, W., and Gilligan, C. A. (2006). Soil structure and soil-borne diseases: using epidemiological concepts to scale from fungal spread to plant epidemics. *Eur. J. Soil Sci.* 57, 26–37. doi: 10.1111/j.1365-2389.2006.00766.x

Otten, W., Gilligan, C. A., Watts, C. W., Dexter, A. R., and Hall, D. (1999). Continuity of air-filled pores and invasion thresholds for a soilborne fungal plant pathogen, *Rhizoctonia solani. Soil Biol. Biochem.* 31, 1803–1810. doi: 10.1016/s0038-0717(99)00099-1

Otten, W., Hall, D., Harris, K., Ritz, K., Young, I. M., and Gilligan, C. A. (2001). Soil physics, fungal epidemiology and the spread of Rhizoctonia solani. *New Phytol.* 151, 459–468. doi: 10.1046/j.0028-646x.2001.00190.x

Pajor, R., Falconer, R., Hapca, S., and Otten, W. (2010). Modelling and quantifying the effect of heterogeneity in soil physical conditions on fungal growth. *Biogeosciences* 7, 3731–3740. doi: 10.5194/bg-7-3731-2010

Pallud, C., Masue-Slowey, Y., and Fendorf, S. (2010). Aggregate-scale spatial heterogeneity in reductive transformation of ferrihydrite resulting from coupled biogeochemical and physical processes. *Geochim. Cosmochim. Acta* 74, 2811–2825. doi: 10.1016/j.gca.2010.01.032

Pamp, S. J., Harrington, E. D., Quake, S. R., Relman, D. A., and Blainey, P. C. (2012). Single-cell sequencing provides clues about the host interactions of segmented filamentous bacteria (SFB). *Genome Res.* 22, 1107–1119. doi: 10.1101/gr.131482.111

Pan, X., Durrett, R. E., Zhu, H., Tanaka, Y., Li, Y., Zi, X., et al. (2013). Two methods for full-length RNA sequencing for low quantities of cells and single cells. *Proc. Natl. Acad. Sci. U.S.A.* 110, 594–599. doi: 10.1073/pnas.1217322109

Papadopoulos, A., Whitmore, A. P., White, R. P., Mooney, S. J., and Bird, N. R. A. (2009). Combining spatial resolutions in the multiscale analysis of soil pore size distributions. *Vadose Zone J.* 8, 227–232. doi: 10.2136/vzj2008.0042

Parkin, T. B., Starr, J. L., and Meisinger, J. J. (1987). Influence of sample size on measurement of soil denitrification. *Soil Sci. Soc. Am. J.* 51, 1492–1501. doi: 10.2136/sssaj1987.03615995005100060017x

Patankar, S. V. (1980). *Numerical Heat Transfer and Fluid Flow.* London: Taylor and Francis. doi: 10.1201/9781482234213

Patterson, B. M., Campbell, J., and Havrilla, G. J. (2010). Integrating 3D images using laboratory-based micro X-ray computed tomography and confocal X-ray fluorescence techniques. *X-Ray Spectrom.* 39, 184–190. doi: 10.1002/xrs.1245

Paustian, K., Andren, O., Janzen, H. H., Lal, R., Smith, P., Tian, G., et al. (1997). Agricultural soils as a sink to mitigate CO_2 emissions. *Soil Use Manage.* 13, 230–244. doi: 10.1111/j.1475-2743.1997.tb00594.x

Pedersen, L. L., Smets, B. F., and Dechesne, A. (2015). Measuring biogeochemical heterogeneity at the micro scale in soils and sediments. *Soil Biol. Biochem.* 90, 122–138. doi: 10.1016/j.soilbio.2015.08.003

Pendleton, D. E., Dathe, A., and Baveye, P. (2005). Influence of image resolution and evaluation algorithm on estimates of the lacunarity of porous media. *Phys. Rev.* E72:041306, doi: 10.1103/PhysRevE.72.041306

Peng, S., Marone, F., and Dultz, S. (2014). Resolution effect in X-ray microcomputed tomography imaging and small pore's contribution to permeability for a Berea sandstone. *J. Hydrol.* 510, 403–411. doi: 10.1016/j.jhydrol.2013.12.028

Pennell, K. D. (2016). "Specific surface area," in *Reference Module in Earth Systems and Environmental Sciences,* ed. S. A. Elias (Oxford: Elsevier), 1–8.

Pereira, G. G. (2016). Grayscale lattice Boltzmann model for multiphase heterogeneous flow through porous media. *Phys. Rev.* E93:063301. doi: 10.1103/PhysRevE.93.063301

Perez-Reche, F. J., Taraskin, S. N., Otten, W., Viana, M. P., Costa, L. d. F., and Gilligan, C. A. (2012). Prominent effect of soil network heterogeneity on microbial invasion. *Phys. Rev. Lett.* 109:098102. doi: 10.1103/PhysRevLett.109.098102

Perfect, E., Cheng, C.-L., Kang, M., Bilheux, H. Z., Lamanna, J. M., Gragg, M. J., et al. (2014). Neutron imaging of hydrogen-rich fluids in geomaterials and engineered porous media: a review. *Earth-Sci. Rev.* 129, 120–135. doi: 10.1016/j.earscirev.2013.11.012

Persson, M., Huber, B., Karlsson, S., Liu, X., Chen, H., Xu, C., et al. (2014). Energy-resolved CT imaging with a photon-counting silicon-strip detector. *Phys. Med. Biol.* 59, 6709–6727. doi: 10.1088/1361-6560/59/22/6709

Peszynska, M., Trykozko, A., Iltis, G., Schlueter, S., and Wildenschild, D. (2016). Biofilm growth in porous media: experiments, computational modeling at the porescale, and upscaling. *Adv. Water Resour.* 95, 288–301. doi: 10.1016/j.advwatres.2015.07.008

Peth, C., Barkusky, F., and Mann, K. (2008). Near-edge x-ray absorption fine structure measurements using a laboratory-scale XUV source. *J. Phys. D-Appl. Phys.* 41:10. doi: 10.1088/0022-3727/41/10/105202

Peth, S., Chenu, C., Leblond, N., Mordhorst, A., Garnier, P., Nunan, N., et al. (2014). Localization of soil organic matter in soil aggregates using synchrotron-based X-ray microtomography. *Soil Biol. Biochem.* 78, 189–194. doi: 10.1016/j.soilbio.2014.07.024

Petrovic, A. M., Siebert, J. E., and Rieke, P. E. (1982). Soil bulk density analysis in 3 dimensions by computed tomographic scanning. *Soil Sci. Soc. Am. J.* 46, 445–450. doi: 10.2136/sssaj1982.03615995004600030001x

Pham, V. H. T., and Kim, J. (2012). Cultivation of unculturable soil bacteria. *Trends Biotechnol.* 30, 475–484. doi: 10.1016/j.tibtech.2012.05.007

Philip, J. R. (1991). Soils, natural science, and models. *Soil Sci.* 151, 91–98. doi: 10.1097/00010694-199101000-00011

Phillips, J. D. (1995). Self-organization and landscape evolution. *Prog. Phys. Geogr.* 19, 309–321. doi: 10.1177/030913339501900301

Phillips, J. D. (2000). Signatures of divergence and self-organization in soils and weathering profiles. *J. Geol.* 108, 91–102. doi: 10.1086/314386

Piccoli, I., Camarotto, C., Lazzaro, B., Furlan, L., and Morari, F. (2017). Conservation agriculture had a poor impact on the soil porosity of Veneto low-lying plain silty soils after a 5-year transition period. *Land Degrad. Dev.* 28, 2039–2050. doi: 10.1002/ldr.2726

Pickup, R. W. (1995). "Sampling and detecting bacterial populations in natural environments," in *Population Genetics of Bacteria*, eds S. Baumerg, J. P. W. Young, E. M. H. Wellington, and J. R. Saunders (Cambridge: Cambridge University Press), 295–315.

Pini, R., and Madonna, C. (2016). Moving across scales: a quantitative assessment of X-ray CT to measure the porosity of rocks. *J. Porous Mater.* 23, 325–338. doi: 10.1007/s10934-015-0085-8

Pires, L. F., Borges, J., Bacchi, O., and Reichardt, K. (2010). Twenty-five years of computed tomography in soil physics: a literature review of the Brazilian contribution. *Soil Tillage Res.* 110, 197–210. doi: 10.1016/j.still.2010.07.013

Podar, M., Abulencia, C. B., Walcher, M., Hutchison, D., Zengler, K., Garcia, J. A., et al. (2007). Targeted access to the genomes of low-abundance organisms

in complex microbial communities. *Appl. Environ. Microbiol.* 73, 3205–3214. doi: 10.1128/aem.02985-06

Popescu, L., and Cao, Z.-P. (2018). From microscopy to genomic approach in soil biodiversity assessment. *Curr. Issues Mol. Biol.* 27, 195–198. doi: 10.21775/cimb. 027.195

Porta, G. M., Ceriotti, G., and Thovert, J. F. (2016). Comparative assessment of continuum-scale models of bimolecular reactive transport in porous media under pre-asymptotic conditions. *J. Contam. Hydrol.* 185, 1–13. doi: 10.1016/ j.jconhyd.2015.12.003

Postma, J., and Altemuller, H. J. (1990). Bacteria in thin soil sections stained with the fluorescent brightener calcofluor white M2R. *Soil Biol. Biochem.* 22, 89–96. doi: 10.1016/0038-0717(90)90065-8

Postma, J., and van Veen, J. A. (1990). Habitable pore space and survival of *Rhizobium leguminosarum* biovartrifolii introduced into soil. *Microb. Ecol.* 19, 149–161. doi: 10.1007/BF02012096

Pot, V., Peth, S., Monga, O., Vogel, L. E., Genty, A., Garnier, P., et al. (2015). Three-dimensional distribution of water and air in soil pores: comparison of two-phase two-relaxation-times lattice-Boltzmann and morphological model outputs with synchrotron X-ray computed tomography data. *Adv. Water Resour.* 84, 87–102. doi: 10.1016/j.advwatres.2015. 08.006

Power, R. M., and Huisken, J. (2017). A guide to light-sheet fluorescence microscopy for multiscale imaging. *Nat. Methods* 14, 360–373. doi: 10.1038/ nmeth.4224

Powlson, D., Xu, J., and Brookes, P. (2017). "Through the eye of the needle: the story of the soil microbial biomass," in *Microbial Biomass: A Paradigm Shift in Terrestrial Biogeochemistry*, ed. K. R. Tate (London: World Scientific), 1–40.

Powlson, D. S., Whitmore, A. P., and Goulding, K. W. T. (2011). Soil carbon sequestration to mitigate climate change: a critical re-examination to identify the true and the false. *Eur. J. Soil Sci.* 62, 42–55. doi: 10.1111/j.1365-2389.2010. 01342.x

Prakash, O., Shouche, Y., Jangid, K., and Kostka, J. E. (2013). Microbial cultivation and the role of microbial resource centers in the omics era. *Appl. Microbiol. Biotechnol.* 97, 51–62. doi: 10.1007/s00253-012-4533-y

Pratama, A. A., and van Elsas, J. D. (2018). The "neglected" soil virome: potential role and impact. *Trends Microbiol.* 26, 649–662. doi: 10.1016/j.tim.2017. 12.004

Preston, A. R., Bird, N. R. A., Kinchesh, P., Randall, E. W., and Whalley, W. R. (2001). STRAFI-NMR studies of water transport in soil. *Magn. Reson. Imaging* 19, 561–563. doi: 10.1016/S0730-725X(01)00305-8

Prietzel, J., Thieme, J., Neuhausler, U., Susini, J., and Kögel-Knabner, I. (2003). Speciation of sulphur in soils and soil particles by X-ray spectromicroscopy. *Eur. J. Soil Sci.* 54, 423–433. doi: 10.1046/j.1365-2389.2003. 00543.x

Prosser, J. I. (2015). Dispersing misconceptions and identifying opportunities for the use of 'omics' in soil microbial ecology. *Nat. Rev. Microbiol.* 13, 439–446. doi: 10.1038/nrmicro3468

Prosser, J. I., Bohannan, B. J. M., Curtis, T. P., Ellis, R. J., Firestone, M. K., Freckleton, R. P., et al. (2007). The role of ecological theory in microbial ecology. *Nat. Rev. Microbiol.* 5, 384–392. doi: 10.1038/nrmicro1643

Puspita, I. D., Kamagata, Y., Tanaka, M., Asano, K., and Nakatsu, C. H. (2012). Are uncultivated bacteria really uncultivable? *Microbes Environ.* 27, 356–366. doi: 10.1264/jsme2.ME12092

Rab, M. A., Haling, R. E., Aarons, S. R., Hannah, M., Young, I. M., and Gibson, D. (2014). Evaluation of X-ray computed tomography for quantifying macroporosity of loamy pasture soils. *Geoderma* 213, 460–470. doi: 10.1016/j. geoderma.2013.08.037

Rabbi, S. M. F., Daniel, H., Lockwood, P. V., Macdonald, C., Pereg, L., Tighe, M., et al. (2016). Physical soil architectural traits are functionally linked to carbon decomposition and bacterial diversity. *Sci. Rep.* 6:33012. doi: 10.1038/srep 33012

Rabbi, S. M. F., Wilson, B. R., Lockwood, P. V., Daniel, H., and Young, I. M. (2014). Soil organic carbon mineralization rates in aggregates under contrasting land uses. *Geoderma* 216, 10–18. doi: 10.1016/j.geoderma.2013.10.023

Rabot, E., Lacoste, M., Henault, C., and Cousin, I. (2015). Using X-ray computed tomography to describe the dynamics of nitrous oxide emissions during soil drying. *Vadose Zone J.* 14, 1–34. doi: 10.2136/vzj2014.12.0177

Rabot, E., Wiesmeier, M., Schlüter, S., and Vogel, H. J. (2018). Soil structure as an indicator of soil functions: a review. *Geoderma* 314, 122–137. doi: 10.1016/j. geoderma.2017.11.009

Radulovich, R., Sollins, P., Baveye, P., and Solorzano, E. (1992). Bypass water flow through unsaturated microaggregated tropical soils. *Soil Sci. Soc. Am. J.* 56, 721–726. doi: 10.2136/sssaj1992.03615995005600030008x

Raghunathan, A., Ferguson, H. R., Bornath, C. J., Song, W., Driscoll, M., and Lasken, R. S. (2005). Genomic DNA amplification from a single bacterium. *Appl. Environ. Microbiol.* 71, 3342–3347. doi: 10.1128/AEM.71.6.3342-3347. 2005

Ranjard, L., and Richaume, A. S. (2001). Quantitative and qualitative microscale distribution of bacteria in soil. *Res. Microbiol.* 152, 707–716. doi: 10.1016/ S0923-2508(01)01251-7

Rawlins, B. G., Wragg, J., Reinhard, C., Atwood, R. C., Houston, A. N., Lark, R. M., et al. (2016). Three-dimensional soil organic matter distribution, accessibility and microbial respiration in macroaggregates using osmium staining and synchrotron X-ray computed tomography. *Soil* 2, 659–671. doi: 10.5194/soil-2-659-2016

Raynaud, X., and Nunan, N. (2014). Spatial ecology of bacteria at the microscale in soil. *PLoS One* 9:287217. doi: 10.1371/journal.pone.0087217

Razafimbelo, T., Chevallier, T., Albrecht, A., Chapuis-Lardy, L., Rakotondrasolo, F. N., Michellon, R., et al. (2013). Texture and organic carbon contents do not impact amount of carbon protected in Malagasy soils. *Sci. Agricola* 70, 204–208. doi: 10.1590/S0103-90162013000300009

Razafimbelo, T. M., Albrecht, A., Oliver, R., Chevallier, T., Chapuis-Lardy, L., and Feller, C. (2008). Aggregate associated-C and physical protection in a tropical clayey soil under Malagasy conventional and no-tillage systems. *Soil Tillage Res.* 98, 140–149. doi: 10.1016/j.still.2007.10.012

Razavi, B. S., Zarebanadkouki, M., Blagodatskaya, E., and Kuzyakov, Y. (2016). Rhizosphere shape of lentil and maize: spatial distribution of enzyme activities. *Soil Biol. Biochem.* 96, 229–237. doi: 10.1016/j.soilbio.2016.02.020

Reardon, S. (2017). Diamond offers MRI for molecules. *Nature* 543, 162–162. doi: 10.1038/nature.2017.21573

Remusat, L., Hatton, P. J., Nico, P. S., Zeller, B., Kleber, M., and Derrien, D. (2012). NanoSIMS study of organic matter associated with soil aggregates: advantages, limitations, and combination with STXM. *Environ. Sci. Technol.* 46, 3943–3949. doi: 10.1021/es203745k

Renault, P., and Stengel, P. (1993). Modeling oxygen diffusion in aggregated soils: I. Anaerobiosis inside the aggregates. *Soil Sci. Soc. Am. J.* 58, 1017–1023. doi: 10.2136/sssaj1994.03615995005800040004x

Rennert, T., Totsche, K. U., Heister, K., Kersten, M., and Thieme, J. (2012). Advanced spectroscopic, microscopic, and tomographic characterization techniques to study biogeochemical interfaces in soil. *J. Soils Sediments* 12, 3–23. doi: 10.1007/s11368-011-0417-5

Resat, H., Bailey, V., McCue, L. A., and Konopka, A. (2012). Modeling microbial dynamics in heterogeneous environments: growth on soil carbon sources. *Microb. Ecol.* 63, 883–897. doi: 10.1007/s00248-011-9965-x

Rillig, M. C., Muller, L. A. H., and Lehmann, A. (2017). Soil aggregates as massively concurrent evolutionary incubators. *ISME J.* 11, 1943–1948. doi: 10.1038/ismej. 2017.56

Ringeisen, B. R., Rincon, K., Fitzgerald, L. A., Fulmer, P. A., and Wu, P. K. (2015). Printing soil: a single-step, high-throughput method to isolate micro-organisms and near-neighbour microbial consortia from a complex environmental sample. *Methods Ecol. Evol.* 6, 209–217. doi: 10.1111/2041-210x. 12303

Rogasik, H., Crawford, J. W., Wendroth, O., Young, I. M., Joschko, M., and Ritz, K. (1999). Discrimination of soil phases by dual energy x-ray tomography. *Soil Sci. Soc. Am. J.* 63, 741–751. doi: 10.2136/sssaj1999.634741x

Rogasik, H., Onasch, I., Brunotte, J., Jegou, D., and Wendroth, O. (2003). "Assessment of soil structure using X-ray computed tomography," in *Applications of X-ray Computed Tomography in the geosciences*, eds F. Mees, R. Swennen, M. Van Geet, and P. Jacobs (London: Geological Society, Special Publications), 151–165.

Ronn, R., Vestergard, M., and Ekelund, F. (2012). Interactions between bacteria, protozoa and nematodes in soil. *Acta Protozool.* 51, 223–235. doi: 10.4467/ 16890027ap.12.018.0764

Roose, T., Keyes, S. D., Daly, K. R., Carminati, A., Otten, W., Vetterlein, D., et al. (2016). Challenges in imaging and predictive modeling of

rhizosphere processes. *Plant Soil* 407, 9–38. doi: 10.1007/s11104-016-2872-7

Rousk, J., and Jones, D. L. (2010). Loss of low molecular weight dissolved organic carbon (DOC) and nitrogen (DON) in H2O and 0.5M K2SO4 soil extracts. *Soil Biol. Biochem.* 42, 2331–2335. doi: 10.1016/j.soilbio.2010.08.017

Rovira, A. D., and Greacen, E. L. (1957). The effect of aggregate disruption on the activity of microorganisms in the soil. *Austr. J. Agric. Res.* 8, 659–673. doi: 10.1071/ar9570659

Rozenbaum, O., Bruand, A., and Le Trong, E. (2012). Soil porosity resulting from the assemblage of silt grains with a clay phase: new perspectives related to utilization of X-ray synchrotron computed microtomography. *Comptes Rendus Geosci.* 344, 516–525. doi: 10.1016/j.crte.2012.09.004

Ruamps, L. S., Nunan, N., and Chenu, C. (2011). Microbial biogeography at the soil pore scale. *Soil Biol. Biochem.* 43, 280–286. doi: 10.1016/j.soilbio.2010.10.010

Ruamps, L. S., Nunan, N., Pouteau, V., Leloup, J., Raynaud, X., Roy, V., et al. (2013). Regulation of soil organic C mineralisation at the pore scale. *FEMS Microbiol. Ecol.* 86, 26–35. doi: 10.1111/1574-6941.12078

Rubinstein, R. L., Kadilak, A. L., Cousens, V. C., Gage, D. J., and Shor, L. M. (2015). Protist-facilitated particle transport using emulated soil micromodels. *Environ. Sci. Technol.* 49, 1384–1391. doi: 10.1021/es503424z

Rubol, S., Dutta, T., and Rocchini, D. (2016). 2D visualization captures the local heterogeneity of oxidative metabolism across soils from diverse land-use. *Sci. Total Environ.* 572, 713–723. doi: 10.1016/j.scitotenv.2016.06.252

Salzer, M., Prill, T., Spettl, A., Jeulin, D., Schladitz, K., and Schmidt, V. (2015). Quantitative comparison of segmentation algorithms for FIB-SEM images of porous media. *J. Microsc.* 257, 23–30. doi: 10.1111/jmi.12182

San José Martínez, F., Caniego, F. J., and García-Gutiérrez, C. (2017). Lacunarity of soil macropore space arrangement of CT images: effect of soil management and depth. *Geoderma* 287, 80–89. doi: 10.1016/j.geoderma.2016.09.007

San José Martínez, F., Muñoz Ortega, F. J., Caniego Monreal, F. J., Kravchenko, A. N., and Wang, W. (2015). Soil aggregate geometry: measurements and morphology. *Geoderma* 23, 36–48. doi: 10.1016/j.geoderma.2014.08.003

Sanderlin, A. B., Vogt, S. J., Grunewald, E., Bergin, B. A., and Codd, S. L. (2013). Biofilm detection in natural unconsolidated porous media using a low-field magnetic resonance system. *Environ. Sci. Technol.* 47, 987–992. doi: 10.1021/es3040686

Santner, J., Larsen, M., Kreuzeder, A., and Glud, R. N. (2015). Two decades of chemical imaging of solutes in sediments and soils – a review. *Anal. Chim. Acta* 878, 9–42. doi: 10.1016/j.aca.2015.02.006

Schaap, M. G., Porter, M. L., Christensen, B. S. B., and Wildenschild, D. (2007). Comparison of pressure-saturation characteristics derived from computed tomography and lattice Boltzmann simulations. *Water Resour. Res.* 43:W12S06. doi: 10.1029/2006wr005730

Scheffer, M., Baveco, J., DeAngelis, D., Rose, K., and VanNes, E. (1995). Super-individuals, a simple solution for modeling large populations on an individual basis. *Ecol. Modell.* 80, 161–170. doi: 10.1016/0304-3800(94)00055-M

Scheibe, T. D., Perkins, W. A., Richmond, M. C., McKinley, M. I., Romero-Gomez, P. D. J., Oostrom, M., et al. (2015). Pore-scale and multiscale numerical simulation of flow and transport in a laboratory-scale column. *Water Resour. Res.* 51, 1023–1035. doi: 10.1002/2014wr015959

Schlüter, S., Leuther, F., Vogler, S., and Vogel, H. J. (2016). X-ray microtomography analysis of soil structure deformation caused by centrifugation. *Solid Earth* 7, 129–140. doi: 10.5194/se-7-129-2016

Schlüter, S., Sheppard, A., Brown, K., and Wildenschild, D. (2014). Image processing of multiphase images obtained via X-ray microtomography: a review. *Water Resour. Res.* 50, 3615–3639. doi: 10.1002/2014wr015256

Schlüter, S., and Vogel, H. J. (2016). Analysis of soil structure turnover with garnet particles and X-ray microtomography. *PLoS One* 11:e0159948. doi: 10.1371/journal.pone.0159948

Schlüter, S., Weller, U., and Vogel, H.-J. (2010). Segmentation of X-ray microtomography images of soil using gradient masks. *Comput. Geosci.* 36, 1246–1251. doi: 10.1016/j.cageo.2010.02.007

Schmidt, H., and Eickhorst, T. (2014). Detection and quantification of native microbial populations on soil-grown rice roots by catalyzed reporter

deposition-fluorescence in situ hybridization. *FEMS Microbiol. Ecol.* 87, 390–402. doi: 10.1111/1574-6941.12232

Schmidt, H., Eickhorst, T., and Mussmann, M. (2012a). Gold-FISH: a new approach for the in situ detection of single microbial cells combining fluorescence and scanning electron microscopy. *Syst. Appl. Microbiol.* 35, 518–525. doi: 10.1016/j.syapm.2012.04.006

Schmidt, H., Eickhorst, T., and Tippkoetter, R. (2012b). Evaluation of tyramide solutions for an improved detection and enumeration of single microbial cells in soil by CARD-FISH. *J. Microbiol. Methods* 91, 399–405. doi: 10.1016/j.mimet.2012.09.021

Schmidt, H., Vetterlein, D., Koehne, J. M., and Eickhorst, T. (2015). Negligible effect of X-ray mu-CT scanning on archaea and bacteria in an agricultural soil. *Soil Biol. Biochem.* 84, 21–27. doi: 10.1016/j.soilbio.2015.02.010

Schumacher, M., Christl, I., Scheinost, A. C., Jacobsen, C., and Kretzschmar, R. (2005). Chemical heterogeneity of organic soil colloids investigated by scanning transmission X-ray microscopy and C-1s NEXAFS microspectroscopy. *Environ. Sci. Technol.* 39, 9094–9100. doi: 10.1021/es050099f

Schweizer, S. A., Hoeschen, C., Schlüter, S., Kögel-Knabner, I., and Mueller, C. W. (2018). Rapid soil formation after glacial retreat shaped by spatial patterns of organic matter accrual in microaggregates. *Global Change Biol.* 24, 1637–1650. doi: 10.1111/gcb.14014

Sedlmair, J., Gleber, S.-C., Peth, C., Mann, K., Niemeyer, J., and Thieme, J. (2012). Characterization of refractory organic substances by NEXAFS using a compact X-ray source. *J. Soils Sediments* 12, 24–34. doi: 10.1007/s11368-011-0385-9

Shah, S. M., Gray, F., Crawshaw, J. P., and Boek, E. S. (2016). Micro-computed tomography pore-scale study of flow in porous media: effect of voxel resolution. *Adv. Water Resour.* 95, 276–287. doi: 10.1016/j.advwatres.2015.07.012

Sheehy, J., Regina, K., Alakukku, L., and Six, J. (2015). Impact of no-till and reduced tillage on aggregation and aggregate-associated carbon in Northern European agroecosystems. *Soil Tillage Res.* 150, 107–113. doi: 10.1016/j.still.2015.01.015

Shi, X., Gao, W., Wang, J., Chao, S.-H., Zhang, W., and Meldrum, D. R. (2015). Measuring gene expression in single bacterial cells: recent advances in methods and micro-devices. *Crit. Rev. Biotechnol.* 35, 448–460. doi: 10.3109/07388551.2014.899556

Shokri, N. (2014). Pore-scale dynamics of salt transport and distribution in drying porous media. *Phys. Fluids* 26:012106. doi: 10.1063/1.4861755

Silversmit, G., Vekemans, B., Nikitenko, S., Schmitz, S., Schoonians, T., Brenker, F. E., et al. (2010). Spatially resolved 3D micro-XANES by a confocal detection scheme. *Phys. Chem. Chem. Phys.* 12, 5653–5659. doi: 10.1039/C004103N

Smagin, A. V. (1989). Soil as a product of biogeocenosis self-organization. *Doklady Akademii Nauk Sssr* 308, 729–731.

Smith, A. P., Bond-Lamberty, B., Benscoter, B. W., Tfaily, M.-M., Hinkle, C. R., Liu, C., et al. (2017). Shifts in pore connectivity from precipitation versus groundwater rewetting increases soil carbon loss after drought. *Nat. Commun.* 8:1335. doi: 10.1038/s41467-017-01320-x

Smith, R., Wright, K. L., and Ashton, L. (2016). Raman spectroscopy: an evolving technique for live cell studies. *Analyst* 141, 3590–3600. doi: 10.1039/C6AN00152A

Smolek, S., Pemmer, B., Folser, M., Streli, C., and Wobrauschek, P. (2012). Confocal micro-X-ray fluorescence spectrometer for light element analysis. *Rev. Sci. Instrum.* 83:083703. doi: 10.1063/1.4744934

Soane, B. D. (1967). Dual energy gamma-ray transmission for coincident measurement of water content and dry bulk density of soil. *Nature* 214, 1273–1274. doi: 10.1038/2141273a0

Söderström, B., and Erland, S. (1986). Isolation of fluorescein diacetate stained hyphae from soil by micromanipulation. *Trans. Br. Mycol. Soc.* 86, 465–468. doi: 10.1016/S0007-1536(86)80190-5

Sok, R. M., Varslot, T., Ghous, A., Latham, S., Sheppard, A. P., and Knackstedt, M. A. (2010). Pore scale characterization of carbonates at multiple scales: integration of micro-CT, BSEM, and FIBSEM. *Petrophysics* 51, 379–387.

Sollins, P., and Radulovich, R. (1988). Effects of soil physical structure on solute transport in a weathered tropical soil. *Soil Sci. Soc. Am. J.* 52, 1168–1173. doi: 10.2136/sssaj1988.03615995005200040050x

Solomon, D., Lehmann, J., Harden, J., Wang, J., Kinyangi, J., Heymann, K., et al. (2012). Micro- and nano-environments of carbon sequestration: multi-element STXM-NEXAFS spectromicroscopy assessment of microbial carbon

and mineral associations. *Chem. Geol.* 329, 53–73. doi: 10.1016/j.chemgeo.2012. 02.002

Solomon, D., Lehmann, J., Kinyangi, J., Liang, B. Q., and Schafer, T. (2005). Carbon K-edge NEXAFS and FTIR-ATR spectroscopic investigation of organic carbon speciation in soils. *Soil Sci. Soc. Am. J.* 69, 107–119. doi: 10.2136/sssaj2005. 0107dup

Son, K., Brumley, D. R., and Stocker, R. (2015). Live from under the lens: exploring microbial motility with dynamic imaging and microfluidics. *Nat. Rev. Microbiol.* 13, 761–775. doi: 10.1038/nrmicro3567

Spanne, P., Thovert, J., Jacquin, J., Lindquist, W. B., Jones, K., and Coker, D. (1994). Synchotron computed microtomography of porous media: topology and transports. *Phys. Rev. Lett.* 73, 2001–2004. doi: 10.1103/PhysRevLett.73. 2001

Spohn, M., Carminati, A., and Kuzyakov, Y. (2013). Soil zymography – A novel in situ method for mapping distribution of enzyme activity in soil. *Soil Biol. Biochem.* 58, 275–280. doi: 10.1016/j.soilbio.2012.12.004

Sposito, G. (2013). Green water and global food security. *Vadose Zone J.* 12:vzj2013.02.0041. doi: 10.2136/vzj2013.02.0041

Stanley, C. E., Grossmann, G., iSolvas, X., and deMello, A. J. (2016). Soil-on-a-Chip: microfluidic platforms for environmental organismal studies. *Lab Chip* 16, 228–241. doi: 10.1039/C5LC01285F

Stanley, C. E., Stockli, M., van Swaay, D., Sabotic, J., Kallio, P. T., Kunzler, M., et al. (2014). Probing bacterial-fungal interactions at the single cell level. *Integr. Biol. (Camb.)* 6, 935–945. doi: 10.1039/c4ib00154k

Stanley, C. E., and van der Heijden, M. G. A. (2017). Microbiome-on-a-chip: new frontiers in plant–microbiota research. *Trends Microbiol.* 25, 610–613. doi: 10.1016/j.tim.2017.05.001

Starkloff, T., Larsbo, M., Stolte, J., Hessel, R., and Ritsema, C. (2017). Quantifying the impact of a succession of freezing-thawing cycles on the pore network of a silty clay loam and a loamy sand topsoil using X-ray tomography. *Catena* 156, 365–374. doi: 10.1016/j.catena.2017.04.026

Steefel, C. I., Molins, S., and Trebotich, D. (2013). Pore scale processes associated with subsurface CO_2 injection and sequestration. *Rev. Mineral. Geochem.* 77, 259–303. doi: 10.2138/rmg.2013.77.8

Stefana, G., Cornelia, B., Jorg, R., and Michael, B. (2014). Soil water availability strongly alters the community composition of soil protists. *Pedobiologia* 57, 205–213. doi: 10.1016/j.pedobi.2014.10.001

Steffens, M., Rogge, D. M., Mueller, C. W., Höschen, C., Lugmeier, J., Kölbl, A., et al. (2017). Identification of distinct functional microstructural domains controlling C storage in soil. *Environ. Sci. Technol.* 51, 12182–12189. doi: 10. 1021/acs.est.7b03715

Stepanauskas, R. (2012). Single cell genomics: an individual look at microbes. *Curr. Opin. Microbiol.* 15, 613–620. doi: 10.1016/j.mib.2012.09.001

Stepanauskas, R. (2015). Wiretapping into microbial interactions by single cell genomics. *Front. Microbiol.* 6:258. doi: 10.3389/fmicb.2015.00258

Stewart, T. L., and Fogler, H. S. (2001). Biomass plug development and propagation in porous media. *Biotechnol. Bioeng.* 72, 353–363. doi: 10.1002/ 1097-0290(20010205)72:3<353::AID-BIT13>3.0.CO;2-U

Stotzky, G. (1986). "Influence of soil mineral colloids on metabolic processes, growth, adhesion, and ecology of microbes and viruses," in *Interactions of Soil Minerals with Natural Organics and Microbes,* eds P. M. Huang and M. Schnitzer (Madison, WI: Soil Science Society of America), 305–428.

Strawn, D. G., and Baker, L. L. (2009). Molecular characterization of copper in soils using X-ray absorption spectroscopy. *Environ. Pollut.* 157, 2813–2821. doi: 10.1016/j.envpol.2009.04.018

Strong, D. T., DeWever, H., Merckx, R., and Recous, S. (2004). Spatial location of carbon decomposition in the soil pore system. *Eur. J. Soil Sci.* 55, 739–750. doi: 10.1111/j.1365-2389.2004.00639.x

Strong, D. T., Sale, P. W. G., and Helyar, K. R. (1997). Initial soil pH affects the pH at which nitrification ceases due to self-induced acidification of microbial microsites. *Aust. J. Soil Res.* 35, 565–570. doi: 10.1071/ S96055

Su, C., Lei, L., Duan, Y., Zhang, K.-Q., and Yang, J. (2012). Culture-independent methods for studying environmental microorganisms: methods, application, and perspective. *Appl. Microbiol. Biotechnol.* 93, 993–1003. doi: 10.1007/ s00253-011-3800-7

Sukop, M. C., and Thorne, D. T. (2006). *Lattice Boltzmann Modeling: An Introduction for Geoscientists and Engineers.* Berlin: Springer Verlag.

Svensson, V., Natarajan, K. N., Ly, L.-H., Miragaia, R. J., Labalette, C., Macaulay, I. C., et al. (2017). Power analysis of single-cell RNA-sequencing experiments. *Nat. Methods* 14, 381–387. doi: 10.1038/nmeth.4220

Taina, I. A., Heck, R. J., and Elliot, T. R. (2008). Application of X-ray computed tomography to soil science: a literature review. *Can. J. Soil Sci.* 88, 1–20. doi: 10.4141/CJSS06027

Tartakovsky, A. M., Meakin, P., Scheibe, R. D., and Wood, B. D. (2007). A smoothed particle hydrodynamics model for reactive transport and mineral precipitation in porous, and fractured porous media. *Water Resour. Res.* 43:W05437. doi: 10.1029/2005WR004770

Tecon, R., and Or, D. (2017a). Biophysical processes supporting the diversity of microbial life in soil. *FEMS Microbiol. Rev.* 41, 599–623. doi: 10.1093/femsre/ fux039

Tecon, R., and Or, D. (2017b). Cooperation in carbon source degradation shapes spatial self-organization of microbial consortia on hydrated surfaces. *Sci. Rep.* 7:43726. doi: 10.1038/srep43726

Terrat, S., Christen, R., Dequiedt, S., Lelievre, M., Nowak, V., Regnier, T., et al. (2012). Molecular biomass and MetaTaxogenomic assessment of soil microbial communities as influenced by soil DNA extraction procedure. *Microb. Biotechnol.* 5, 135–141. doi: 10.1111/j.1751-7915.2011.00307.x

Terrat, S., Horrigue, W., Dequietd, S., Saby, N. P. A., Lelievre, M., Nowak, V., et al. (2017). Mapping and predictive variations of soil bacterial richness across France. *PLoS One* 12:e0186766. doi: 10.1371/journal.pone.0186766

Thomas, G. W. (1992). In defense of observations and measurements. *Soil Sci. Soc. Am. J.* 56, 1979. doi: 10.2136/sssaj1992.03615995005600060054x

Thoreau, H. D. (1854). *Walden: Life in the Woods.* Boston, MA: Ticknor and Fields. doi: 10.5962/bhl.title.146169

Thullner, M., and Baveye, P. (2008). Computational pore network modeling of the influence of biofilm permeability on bioclogging in porous media. *Biotechnol. Bioeng.* 99, 1337–1351. doi: 10.1002/bit.21708

Tian, J., Pausch, J., Yu, G., Blagodatskaya, E., Gao, Y., and Kuzyakov, Y. (2015). Aggregate size and their disruption affect C-14-labeled glucose mineralization and priming effect. *Appl. Soil Ecol.* 90, 1–10. doi: 10.1016/j.apsoil.2015. 01.014

Tiedje, J. M., Cho, J. C., Murray, A., Treves, D., Xia, B., and Zhou, J. (2001). "Soil teeming with life: new frontiers for soil science," in *Sustainable Management of Soil Organic Matter*, eds R. M. Rees, B. C. Ball, and C. A. Watson (Wallingford: CAB International), 393–412. doi: 10.1079/9780851994659.0393

Tiedje, J. M., Sexstone, A. J., Parkin, T. B., Revsbech, N. P., and Shelton, D. R. (1984). Anaerobic processes in soils. *Plant Soil* 76, 197–212. doi: 10.1007/ BF02205580

Tippkötter, R., Ritz, K., and Darbyshire, J. F. (1986). The preparation of soil thin sections for biological studies. *J. Soil Sci.* 37, 681–690. doi: 10.1111/j.1365-2389. 1986.tb00396.x

Tippkötter, R., Eickhorst, T., Taubner, H., Gredner, B., and Rademaker, G. (2009). Detection of soil water in macropores of undisturbed soil using microfocus X- ray tube computerized tomography ((CT). *Soil Tillage Res.* 105, 12–20. doi: 10.1016/j.still.2009.05.001

Tisdall, J. M., and Oades, J. M. (1982). Organic matter and water-stable aggregates in soils. *J. Soil Sci.* 33, 141–163. doi: 10.1111/j.1365-2389.1982.tb01755.x

Topp, G. C. (1971). Soil-water hysteresis: domain theory extended to pore interaction conditions. *Soil Sci. Soc. Am. Proc.* 35, 219–225. doi: 10.2136/ sssaj1971.03615995003500020017x

Topp, G. C., and Miller, E. E. (1966). Hysteretic moisture characteristics and hydraulic conductivities for glass-bead media. *Soil Sci. Soc. Am. Proc.* 30, 156–162. doi: 10.2136/sssaj1966.03615995003000020008x

Torrance, J., Elliot, T. R., Martin, R., and Heck, R. (2008). X-ray computed tomography of frozen soil. *Cold Regions Sci. Technol.* 53, 75–82. doi: 10.1016/j. coldregions.2007.04.010

Torre, I. G., Losada, J. C., Heck, R. J., and Tarquis, A. M. (2018). Multifractal analysis of 3D images of tillage soil. *Geoderma* 311, 167–174. doi: 10.1016/j. geoderma.2017.02.013

Totsche, K. U., Amelung, W., Gerzabek Martin, H., Guggenberger, G., Klumpp, E., Knief, C., et al. (2017). Microaggregates in soils. *J. Plant Nutr. Soil Sci.* 181, 104–136. doi: 10.1002/jpln.201600451

Tötzke, C., Kardjilov, N., Manke, I., and Oswald, S. E. (2017). Capturing 3D water flow in rooted soil by ultra-fast neutron tomography. *Sci. Rep.* 7:6192. doi: 10.1038/s41598-017-06046-w

Tracy, S. R., Daly, K. R., Sturrock, C. J., Crout, N. M. J., Mooney, S. J., and Roose, T. (2015). Three-dimensional quantification of soil hydraulic properties using X-ray computed tomography and image-based modeling. *Water Resour. Res.* 51, 1006–1022. doi: 10.1002/2014WR016020

Treves, D. S., Xia, B., Zhou, J., and Tiedje, J. M. (2003). A two-species test of the hypothesis that spatial isolation influences microbial diversity in soil. *Microb. Ecol.* 45, 20–28. doi: 10.1007/s00248-002-1044-x

Tuller, M., Kulkarni, R., and Fink, W. (2013). "Segmentation of X-Ray CT data of porous materials: a review of global and locally adaptive algorithms," in *Soil-Water-Root Processes: Advances in Tomography and Imaging*, eds S. H. Anderson and J. W. Hopmans, Vol. 61 (Madison, WI: American Society of Agronomy), 157–182.

Tumlinson, L. G., Liu, H., Silk, W. K., and Hopmans, J. W. (2008). Thermal neutron computed tomography of soil water and plant roots. *Soil Sci. Soc. Am. J.* 72, 1234–1242. doi: 10.2136/sssaj2007.0302

Uroz, S., Kelly, L. C., Turpault, M. P., Lepleux, C., and Frey-Klett, P. (2015). The mineralosphere concept: mineralogical control of the distribution and function of mineral-associated bacterial communities. *Trends Microbiol.* 23, 751–762. doi: 10.1016/j.tim.2015.10.004

Valdes-Parada, F. J., Porter, M. L., Narayanaswamy, K., Ford, R. M., and Wood, B. D. (2009). Upscaling microbial chemotaxis in porous media. *Adv. Water Resour.* 32, 1413–1428. doi: 10.1016/j.advwatres.2009.06.010

Valocchi, A. J. (2012). "Hydrogeochemical models," in *Delivery and Mixing in the Subsurface: Processes and Design Principles for In Situ Remediation*, eds P. K. Kitanidis and P. L. McCarty (New York, NY: Springer), 77–116. doi: 10.1007/978-1-4614-2239-6_4

Van den Bulcke, J., Boone, M., Van Acker, J., and Van Hoorebeke, L. (2009). Three-dimensional x-ray imaging and analysis of fungi on and in wood. *Microsc. Microanal.* 15, 395–402. doi: 10.1017/s1431927609990419

van der Wal, A., and de Boer, W. (2017). Dinner in the dark: illuminating drivers of soil organic matter decomposition. *Soil Biol. Biochem.* 105, 45–48. doi: 10.1016/j.soilbio.2016.11.006

van Elsas, J. D., Costal, R., Jansson, J., Sjoling, S., Bailey, M., Nalin, R., et al. (2008). The metagenomics of disease-suppressive soils – Experiences from the METACONTROL project. *Trends Biotechnol.* 26, 591–601. doi: 10.1016/j.tibtech.2008.07.004

van Groenigen, J. W., van Kessel, C., Hungate, B. A., Oenema, O., Powlson, D. S., and van Groenigen, K. J. (2017). Sequestering soil organic carbon: a nitrogen dilemma. *Environ. Sci. Technol.* 51, 4738–4739. doi: 10.1021/acs.est.7b01427

Van Loo, D., Bouckaert, L., Leroux, O., Pauwels, E., Dierick, M., and Van Hoorebeke, L. (2014). Contrast agents for soil investigation with X-ray computed tomography. *Geoderma* 213, 485–491. doi: 10.1016/j.geoderma.2013.08.036

Vandevivere, P., and Baveye, P. (1992a). Effect of bacterial extracellular polymers on the saturated hydraulic conductivity of sand columns. *Appl. Environ. Microbiol.* 58, 1690–1698.

Vandevivere, P., and Baveye, P. (1992b). Improved preservation of bacterial exopolymers for scanning electron microscopy. *J. Microsc. Oxford* 167, 323–330. doi: 10.1111/j.1365-2818.1992.tb03242.x

Vandevivere, P., and Baveye, P. (1992c). Sampling method for the observation of microorganisms in unconsolidated porous media via scanning electron microscopy. *Soil Sci.* 153, 482–485. doi: 10.1097/00010694-199206000-00007

Vandevivere, P., and Baveye, P. (1992d). Saturated hydraulic conductivity reduction caused by aerobic bacteria in sand columns. *Soil Sci. Soc. Am. J.* 56, 1–13. doi: 10.2136/sssaj1992.03615995005600010001x

Vandevivere, P., Baveye, P., Delozada, D. S., and Deleo, P. (1995). Microbial clogging of saturated soils and aquifer materials: evaluation of mathematical models. *Water Resour. Res.* 31, 2173–2180. doi: 10.1029/95wr01568

Vaz, C. M. P., de Maria, I. C., Lasso, P. O., and Tuller, M. (2011). Evaluation of an advanced benchtop micro-computed tomography system for quantifying porosities and pore-size distributions of two brazilian oxisols. *Soil Sci. Soc. Am. J.* 75, 832–841. doi: 10.2136/sssaj2010.0245

Verbruggen, E., Veresoglou, S. D., Anderson, I. C., Caruso, T., Hammer, E. C., Kohler, J., et al. (2012). Arbuscular mycorrhizal fungi – Short-term liability but long-term benefits for soil carbon storage? *New Phytol.* 197, 366–368. doi: 10.1111/nph.12079

Veres, M., Lacey, G., and Taylor, G. W. (2015). Deep learning architectures for soil property prediction. *Paper Presented at the 12th Conference on Computer and Robot Vision*, Halifax, NS, Canada. doi: 10.1109/CRV.2015.15

Vidal, A., Hirte, J., Bender, S. F., Mayer, J., Gattinger, A., Höschen, C., et al. (2018). Linking 3D structure and plant-microbe-soil carbon transfer in the rhizosphere. *Front. Environ. Sci.* 6:9. doi: 10.3389/fenvs.2018.00009

Villemin, G., Mansot, J. L., Watteau, F., Ghanbaja, J., and Toutain, F. (1995). Study of the biodegradation and humification of soil organic matter of plant origin by Electron Energy Loss Spectroscopy (EELS): distribution of carbon, nitrogen and C/N evaluation at ultrastructural level in situ. *Comptes Ren. Acad. Sci. Série 2. Sci. Terre Planèt.* 321, 861–868.

Vogel, H. J. (1997). Morphological determination of pore connectivity as a function of pore size using serial sections. *Eur. J. Soil Sci.* 48, 365–377. doi: 10.1046/j.1365-2389.1997.00096.x

Vogel, H. J., Bartke, S., Daedlow, K., Helming, K., Kögel-Knabner, I., Lang, B., et al. (2018). A systemic approach for modeling soil functions. *Soil* 4, 83–92. doi: 10.5194/soil-4-83-2018

Vogel, H.-J., Cousin, I., and Roth, K. (2002). Quantification of pore structure and gas diffusion as a function of scale. *Eur. J. Soil Sci.* 53, 465–473. doi: 10.1046/j.1365-2389.2002.00457.x

Vogel, H. J., and Ippisch, O. (2008). Estimation of a critical spatial discretization limit for solving Richards' equation at large scales. *Vadose Zone J.* 7, 112–114. doi: 10.2136/vzj2006.0182

Vogel, H. J., and Roth, K. (2001). Quantitative morphology and network representation of soil pore structure. *Adv. Water Resour.* 24, 233–242. doi: 10.1016/S0309-1708(00)00055-5

Vogel, H. J., Weller, U., and Schlüter, S. (2010). Quantification of soil structure based on Minkowski functions. *Comput. Geosci.* 36, 1236–1245. doi: 10.1016/j.cageo.2010.03.007

Vogel, L. E., Makowski, D., Garnier, P., Vieuble-Gonod, L., Coquet, Y., Raynaud, X., et al. (2015). Modeling the effect of soil meso- and macropores topology on the biodegradation of a soluble carbon substrate. *Adv. Water Resour.* 83, 123–136. doi: 10.1016/j.advwatres.2015.05.020

Vogel, L. E., Pot, V., Makowski, D., Garnier, P., and Baveye, P. C. (2018). To what extent do uncertainty and sensitivity analyses help unravel the influence of microscale physical and biological drivers in soil carbon dynamics models? *Ecol. Modell.* 383, 10–22. doi: 10.1016/j.ecolmodel.2018.05.007

Vogel, T. M., Simonet, P., Jansson, J. K., Hirsch, P. R., Tiedje, J. M., van Elsas, J. D., et al. (2009). TerraGenome: a consortium for the sequencing of a soil metagenome. *Nat. Rev. Microbiol.* 7, 252–252. doi: 10.1038/nrmicro2119

Vogt, S. J., Sanderlin, A. B., Seymour, J. D., and Codd, S. L. (2013). Permeability of a growing biofilm in a porous media fluid flow analyzed by magnetic resonance displacement-relaxation correlations. *Biotechnol. Bioeng.* 110, 1366–1375. doi: 10.1002/bit.24803

Voltolini, M., Tas, N., Wang, S., Brodie, E. L., and Ajo-Franklin, J. B. (2017). Quantitative characterization of soil micro-aggregates: new opportunities from sub-micron resolution synchrotron X-ray microtomography. *Geoderma* 305, 382–393. doi: 10.1016/j.geoderma.2017.06.005

Vos, M., Wolf, A. B., Jennings, S. J., and Kowalchuk, G. A. (2013). Micro-scale determinants of bacterial diversity in soil. *FEMS Microbiol. Rev.* 37, 936–954. doi: 10.1111/1574-6976.12023

Votrubová, J., Císlerová, M., Amin, M. H. G., and Hall, L. D. (2003). Recurrent ponded infiltration into structured soil: a magnetic resonance imaging study. *Water Resour. Res.* 39:1371. doi: 10.1029/2003WR002222

Wachinger, G., Fiedler, S., Zepp, K., Gattinger, A., Sommer, M., and Roth, K. (2000). Variability of soil methane production on the micro-scale: spatial association with hot spots of organic material and archaeal populations. *Soil Biol. Biochem.* 32, 1121–1130. doi: 10.1016/s0038-0717(00)00024-9

Wagner, A. O., Praeg, N., Reitschuler, C., and Illmer, P. (2015). Effect of DNA extraction procedure, repeated extraction and ethidium monoazide (EMA)/propidium monoazide (PMA) treatment on overall DNA yield and impact on microbial fingerprints for bacteria, fungi and archaea in a reference soil. *Appl. Soil Ecol.* 93, 56–64. doi: 10.1016/j.apsoil.2015.04.005

Walsh, S. D. C., Burwinkle, H., and Saar, M. O. (2009). A new partial-bounceback lattice-Boltzmann method for fluid flow through heterogeneous media. *Comput. Geosci.* 35, 1186–1193. doi: 10.1016/j.cageo.2008.05.004

Walsh, S. D. C., and Saar, M. O. (2013). Developing extensible Lattice-Boltzmann simulators for general-purpose graphics-processing units. *Commun. Comput Phys.* 13, 867–879. doi: 10.4208/cicp.351011.260112s

Wan, J., Tyliszczak, T., and Tokunaga, T. K. (2007). Organic carbon distribution, speciation, and elemental correlations within soil micro aggregates: applications of STXM and NEXAFS spectroscopy. *Geochim. Cosmochim. Acta* 71, 5439–5449. doi: 10.1016/j.gca.2007.07.030

Wang, D., and Bodovitz, S. (2010). Single cell analysis: the new frontier in 'omics'. *Trends Biotechnol.* 28, 281–290. doi: 10.1016/j.tibtech.2010.03.002

Wang, G., and Or, D. (2010). Aqueous films limit bacterial cell motility and colony expansion on partially saturated rough surfaces. *Environ. Microbiol.* 12, 1363–1373. doi: 10.1111/j.1462-2920.2010.02180.x

Wang, G., Guo, L., Bai, Z., and Yang, L. (2016). Using computed tomography (CT) images and multi-fractal theory to quantify the pore distribution of reconstructed soils during ecological restoration in opencast coal-mine. *Ecol. Eng.* 92, 148–157. doi: 10.1016/j.ecoleng.2016.03.029

Wanzek, T., Keiluweit, M., Baham, J., Dragila, M. I., Fendorf, S., Fiedler, S., et al. (2018). Quantifying biogeochemical heterogeneity in soil systems. *Geoderma* 324, 89–97. doi: 10.1016/j.geoderma.2018.03.003

Warmink, J. A., Nazir, R., Corten, B., and van Elsas, J. D. (2011). Hitchhikers on the fungal highway: the helper effect for bacterial migration via fungal hyphae. *Soil Biol. Biochem.* 43, 760–765. doi: 10.1016/j.soilbio.2010.12.009

Warner, G. S., Nieber, J. L., Moore, I. D., and Geise, R. A. (1989). Characterizing macropores in soil by computed tomography. *Soil Sci. Soc. Am. J.* 53, 653–660. doi: 10.2136/sssaj1989.03615995005300030001x

Watrous, J. D., and Dorrestein, P. C. (2011). Imaging mass spectrometry in microbiology. *Nat. Rev. Microbiol.* 9, 683–694. doi: 10.1038/nrmicro 2634

Wenz, J., Schleede, S., Khrennikov, K., Bech, M., Thibault, P., Heigoldt, M., et al. (2015). Quantitative X-ray phase-contrast microtomography from a compact laser-driven betatron source. *Nat. Commun.* 6:7568. doi: 10.1038/ncomms8568

Wertz, S., Degrange, V., Prosser, J. I., Poly, F., Commeaux, C., Freitag, T., et al. (2006). Maintenance of soil functioning following erosion of microbial diversity. *Environ. Microbiol.* 8, 2162–2169. doi: 10.1111/j.1462-2920.2006.01098.x

Wertz, S., Degrange, V., Prosser, J. I., Poly, F., Commeaux, C., Guillaumaud, N., et al. (2007). Decline of soil microbial diversity does not influence the resistance and resilience of key soil microbial functional groups following a model disturbance. *Environ. Microbiol.* 9, 2211–2219. doi: 10.1111/j.1462-2920.2007.01335.x

West, B. A., Hodgdon, T. S., Parno, M. D., and Song, A. J. (2018). Improved workflow for unguided multiphase image segmentation. *Comput. Geosci.* 118, 91–99. doi: 10.1016/j.cageo.2018.05.013

Weyens, N., van der Lie, D., Taghavi, S., Newman, L., and Vangronsveld, J. (2009). Exploiting plant–microbe partnerships to improve biomass production and remediation. *Trends Biotechnol.* 27, 591–598. doi: 10.1016/j.tibtech.2009.07.006

White, D., FitzPatrick, E. A., and Kilham, K. (1994). Use of stained bacterial inocula to assess spatial distribution after introduction into soil. *Geoderma* 63, 245–254. doi: 10.1016/0016-7061(94)90066-3

White, R. E., Davidson, B., Lam, S. K., and Chen, D. L. (2018). A critique of the paper 'Soil carbon 4 per mille' by Minasny et al. (2017). *Geoderma* 309, 115–117. doi: 10.1016/j.geoderma.2017.05.025

Whitley, K. D., Comstock, M. J., and Chemla, Y. R. (2017). "High-resolution "fleezers": dual-trap optical tweezers combined with single-molecule fluorescence detection," in *Optical Tweezers: Methods and Protocols*, ed. A. Gennerich (New York, NY: Springer), 183–256.

Widdowson, M. A., Molz Fred, J., and Benefield Larry, D. (1988). A numerical transport model for oxygen-and nitrate-based respiration linked to substrate and nutrient availability in porous media. *Water Resour. Res.* 24, 1553–1565. doi: 10.1029/WR024i009p01553

Wildenschild, D., Hopmans, J. W., Vaz, C. M. P., Rivers, M. L., Rikard, D., and Christensen, B. S. B. (2002). Using X-ray computed tomography in hydrology: systems, resolutions, and limitations. *J. Hydrol.* 267, 285–297. doi: 10.1016/S0022-1694(02)00157-9

Wildenschild, D., and Sheppard, A. P. (2013). X-ray imaging and analysis techniques for quantifying pore-scale structure and processes in subsurface porous medium systems. *Adv. Water Resour.* 51, 217–246. doi: 10.1016/j.advwatres.2012.07.018

Willcock, S., Martínez-López, J., Hooftman, D. A. P., Bagstad, K. J., Balbi, S., Marzo, A., et al. (2018). Machine learning for ecosystem services. *Ecosyst. Ser.* (in press). doi: 10.1016/j.ecoser.2018.04.004

Williamson, K. E., Fuhrmann, J. J., Wommack, K. E., and Radosevich, M. (2017). Viruses in soil ecosystems: an unknown quantity within an unexplored territory. *Ann. Rev. Virol.* 4, 201–219. doi: 10.1146/annurev-virology-101416-041639

Willson, C. S., Lu, N., and Likos, W. J. (2012). Quantification of grain, pore, and fluid microstructure of unsaturatedsand from X-Ray computed tomography images. *Geotech. Test J.* 35, 1–13. doi: 10.1520/GTJ20120075

Wilmoth, J. L., Doak, P. W., Timm, A., Halsted, M., Anderson, J. D., Ginovart, M., et al. (2018). A microfluidics and agent -based modeling framework for investigating spatial organization in bacterial colonies: the case of *Pseudomonas aeruginosa* and H1-Type VI secretion interactions. *Front. Microbiol.* 9:33. doi: 10.3389/fmicb.2018.00033

Woese, C. R. (2004). A new biology for a new century. *Microbiol. Mol. Biol. Rev.* 68, 173–186. doi: 10.1128/mmbr.00002-09

Wolf, A. B., Vos, M., de Boer, W., and Kowalchuk, G. A. (2013). Impact of matric potential and pore size distribution on growth dynamics of filamentous and non-filamentous soil bacteria. *PLoS One* 8:e083661. doi: 10.1371/journal.pone.0083661

Wood, B. D. (2009). The role of scaling laws in upscaling. *Adv. Water Resour.* 32, 723–736. doi: 10.1016/j.advwatres.2008.08.015

Wood, B. D. (2010). Reply to comment by Philippe Baveye on "the role of scaling laws in upscaling." *Adv. Water Resour.* 33, 125–127. doi: 10.1016/j.advwatres.2009.11.002

Worrich, A., Stryhanyuk, H., Musat, N., König, S., Banitz, T., Centler, F., et al. (2017). Mycelium-mediated transfer of water and nutrients stimulates bacterial activity in dry and oligotrophic environments. *Nat. Commun.* 8:15472. doi: 10.1038/ncomms15472

Woyke, T., Doud, D. F. R., and Schulz, F. (2017). The trajectory of microbial single-cell sequencing. *Nat. Methods* 14, 1045–1054. doi: 10.1038/nmeth.4469

Woyke, T., Tighe, D., Mavromatis, K., Clum, A., Copeland, A., Schackwitz, W., et al. (2010). One bacterial bell, one complete genome. *PLoS One* 5:e10314. doi: 10.1371/journal.pone.0010314

Wright, D. A., Kilham, K., Glover, L. A., and Prosser, J. L. (1995). Role of pore size location in determining bacterial activity during predation by protozoa in soil. *Appl. Environ. Microbiol.* 61, 3537–3543.

Xie, C., Wang, J., Wang, D., Pan, N., and Wang, M. (2015). Lattice Boltzmann modeling of thermal conduction in composites with thermal contact resistance. *Commun. Comput. Phys.* 17, 1037–1055. doi: 10.4208/cicp.2014.m360

Xiong, Q., Baychev, T. G., and Jivkov, A. P. (2016). Review of pore network modelling of porous media: experimental characterisations, network constructions and applications to reactive transport. *J. Contam. Hydrol.* 192, 101–117. doi: 10.1016/j.jconhyd.2016.07.002

Xun, W. B., Huang, T., Zhao, J., Ran, W., Wang, B. R., Shen, Q. R., et al. (2015). Environmental conditions rather than microbial inoculum composition determine the bacterial composition, microbial biomass and enzymatic activity of reconstructed soil microbial communities. *Soil Biol. Biochem.* 90, 10–18. doi: 10.1016/j.soilbio.2015.07.018

Yang, W., and Yuste, R. (2017). In vivo imaging of neural activity. *Nature Methods* 14, 349–359. doi: 10.1038/nmeth.4230

Yang, X., Mehmani, Y., Perkins, W. A., Pasquali, A., Schoenherr, M., Kim, K., et al. (2016). Intercomparison of 3D pore-scale flow and solute transport simulation methods. *Adv. Water Resour.* 95, 176–189. doi: 10.1016/j.advwatres.2015.09.015

Yehya, A., Naji, H., and Sukop, M. C. (2015). Simulating flows in multi-layered and spatially-variable permeability media via a new Gray Lattice Boltzmann model. *Comput. Geotech.* 70, 150–158. doi: 10.1016/j.compgeo.2015.07.017

Yilmaz, S., and Singh, A. K. (2012). Single cell genome sequencing. *Curr. Opin. Biotechnol.* 23, 437–443. doi: 10.1016/j.copbio.2011.11.018

Yoon, H., Kang, Q., and Valocchi, A. J. (2015). Lattice-Boltzmann-based approaches for pore-scale reactive transport. *Rev. Mineral. Geochem.* 80, 393–431. doi: 10.2138/rmg.2015.80.12

Yoon, H., Valocchi Albert, J., Werth Charles, J., and Dewers, T. (2012). Pore-scale simulation of mixing-induced calcium carbonate precipitation and dissolution

in a microfluidic pore network. *Water Resour. Res.* 48:W02524. doi: 10.1029/2011WR011192

Yoshida, H., and Hayashi, H. (2014). Transmission-reflection coefficient in the lattice boltzmann method. *J. Statist. Phys.* 155, 277–299. doi: 10.1007/s10955-014-0953-7

Young, I. M., and Crawford, J. W. (2004). Interactions and self-organization in the soil-microbe complex. *Science* 304, 1634–1637. doi: 10.1126/science.1097394

Young, I. M., Crawford, J. W., Nunan, N., Otten, W., and Spiers, A. (2008). "Microbial distribution in soils: physics and scaling," in *Advances in Agronomy*, Vol. 100, ed. D. L. Sparks (Amsterdam: Elsevier), 81–121.

Young, I. M., Crawford, J. W., and Rappoldt, C. (2001). New methods and models for characterising structural heterogeneity of soil. *Soil Tillage Res.* 61, 33–45. doi: 10.1016/s0167-1987(01)00188-x

Yu, X., Fu, Y., and Lu, S. (2017). Characterization of the pore structure and cementing substances of soil aggregates by a combination of synchrotron radiation X-ray micro-computed tomography and scanning electron microscopy. *Eur. J. Soil Sci.* 68, 66–79. doi: 10.1111/ejss.12399

Zalzale, M., McDonald, P. J., and Scrivener, K. L. (2013). A 3D lattice Boltzmann effective media study: understanding the role of C-S-H and water saturation on the permeability of cement paste. *Modell. Simulat. Mater. Sci. Eng.* 21, doi: 10.1088/0965-0393/21/8/085016

Zamir, A., Hagen, C., Diemoz, P. C., Endrizzi, M., Vittoria, F., Chen, Y., et al. (2017). Recent advances in edge illumination x-ray phase-contrast tomography. *J. Med. imAging (Bellingham, Wash.)* 4:040901. doi: 10.1117/1.jmi.4.4.040901

Zhang, X., Crawford, J. W., and Young, I. M. (2016). A Lattice Boltzmann model for simulating water flow at pore scale in unsaturated soils. *J. Hydrol.* 538, 152–160. doi: 10.1016/j.jhydrol.2016.04.013

Zhao, D., Xu, M., Liu, G., Yao, X., Tuo, D., Zhang, R., et al. (2017). Quantification of soil aggregate microstructure on abandoned cropland during vegetative succession using synchrotron radiation-based micro-computed tomography. *Soil Tillage Res.* 165, 239–246. doi: 10.1016/j.still.2016.08.007

Zhou, H., Yu, X., Chen, C., Zeng, L., Lu, S., and Wu, L. (2018). Evaluating hydraulic properties of biochar-amended soil aggregates by high-performance pore-scale simulations. *Soil Sci. Soc. Am. J.* 82, 1–9. doi: 10.2136/sssaj2017.02.0053

Conflict of Interest Statement: The authors declare that the research was conducted in the absence of any commercial or financial relationships that could be construed as a potential conflict of interest.

The reviewer PN and handling Editor declared their shared affiliation.

Microscale Heterogeneity of the Spatial Distribution of Organic Matter Can Promote Bacterial Biodiversity in Soils: Insights From Computer Simulations

Xavier Portell[1,2]*, Valérie Pot[2], Patricia Garnier[2], Wilfred Otten[1] and Philippe C. Baveye[2]

[1] School of Water, Energy and Environment, Cranfield University, Cranfield, United Kingdom, [2] UMR ECOSYS, Institut National de la Recherche Agronomique, AgroParisTech, Université Paris-Saclay, Paris, France

There is still no satisfactory understanding of the factors that enable soil microbial populations to be as highly biodiverse as they are. The present article explores *in silico* the hypothesis that the heterogeneous distribution of soil organic matter, in addition to the spatial connectivity of the soil moisture, might account for the observed microbial biodiversity in soils. A multi-species, individual-based, pore-scale model is developed and parameterized with data from 3 *Arthrobacter* sp. strains, known to be, respectively, competitive, versatile, and poorly competitive. In the simulations, bacteria of each strain are distributed in a 3D computed tomography (CT) image of a real soil and three water saturation levels (100, 50, and 25%) and spatial heterogeneity levels (high, intermediate, and low) in the distribution of the soil organic matter are considered. High and intermediate heterogeneity levels assume, respectively, an amount of particulate organic matter (POM) distributed in a single (high heterogeneity) or in four (intermediate heterogeneity) randomly placed fragments. POM is hydrolyzed at a constant rate following a first-order kinetic, and continuously delivers dissolved organic carbon (DOC) into the liquid phase, where it is then taken up by bacteria. The low heterogeneity level assumes that the food source is available from the start as DOC. Unlike the relative abundances of the 3 strains, the total bacterial biomass and respiration are similar under the high and intermediate resource heterogeneity schemes. The key result of the simulations is that spatial heterogeneity in the distribution of organic matter influences the maintenance of bacterial biodiversity. The least competing strain, which does not reach noticeable growth for the low and intermediate spatial heterogeneities of resource distribution, can grow appreciably and even become more abundant than the other strains in the absence of direct competition, if the placement of the resource is favorable. For geodesic distances exceeding 5 mm, microbial colonies cannot grow. These conclusions are conditioned by assumptions made in the model, yet they suggest that microscale factors need to be considered to better understand the root causes of the high biodiversity of soils.

Keywords: soil, pore scale, organic matter, resource allocation, bacteria, biodiversity, agent-based modeling

INTRODUCTION

During the last decade, soils have become increasingly central to a number of crucial debates on issues of great societal concern (e.g., Baveye et al., 2018). Because soils contain a very large stock of carbon, there is a risk that, with rising ambient temperatures associated with global climate change, soils will release vast amounts of greenhouse gases and thereby accelerate change. Biodiversity losses have also emerged as a major concern in many parts of the world. In this context, it is not surprising that in recent years, there has been a significant surge of interest into the biodiversity of soils, and the effect it has on traditional soil functions (Nannipieri et al., 2003).

Many aspects of the biodiversity of soils have proven very difficult to understand. Soils are highly complex media in which a huge number of bacteria, archaea, and fungi live. In a single gram of soil, it is not exceptional to find as many as 10^{10} bacterial cells and 5×10^4 species (Roesch et al., 2007), with commensurate numbers found for other microorganisms. To the extent that many microorganisms (an estimated 98.5% in the case of bacteria) have never been isolated or characterized, the measurement of soil biodiversity itself raises a number of fundamental questions (e.g., Nannipieri et al., 2003; Baveye et al., 2016a,b, 2018). Functionally, it is not clear at all to what extent this very large diversity of soil microbial populations is crucial and whether it needs to be preserved at all cost. Experimental results are contradictory in this respect. Whereas, e.g., Philippot et al. (2013) show that the loss of biodiversity in soils decreases denitrification activity and nitrogen cycling, the experimental results of Werts et al. (2006) suggest on the contrary that biogeochemical functions of soil such as carbon mineralization and denitrification are not impacted by a reduction of microbial diversity. Powlson et al. (2017) have recently described as an unresolved 60-year old paradox the fact that CHCl$_3$ fumigation, wiping out 90% of the soil microbial population and modifying drastically its diversity, does not appear to have an effect on soil organic carbon (SOC) mineralization in soils that have a pH above 5.5. SOC mineralization continues *at the same rate*, after fumigant removal, once the initial decomposition flush is over (Powlson et al., 2017).

A similarly high uncertainty surrounds the features of soils that allow such a large microbial diversity to exist in the first place. Some researchers consider that diversity is mainly caused by biotic interactions between cells (Hanson et al., 2012), but experimental observations increasingly suggest that a high biodiversity is associated with soil spatial heterogeneity (Rainey and Travisano, 1998) and is caused by biotic and abiotic interactions taking place in the soil architecture. Yet the exact mechanisms involved remain elusive. The often advocated explanation that the heterogeneous, disconnected distribution of moisture in unsaturated soils causes distinct groups of microorganisms to be physically isolated from each other (Treves et al., 2003; Long and Or, 2009) is appealing, but it does not apply to fungi or filamentous bacteria (Baveye et al., 2016b) and cannot account by itself for the biodiversity of soils that are periodically saturated after rainfall events. At this point, there is no real, satisfactory explanation of how the spatial heterogeneity of soils might foster the biodiversity of their microbial populations.

In this general context, the key objective of the present article is to explore the hypothesis that the heterogeneous distribution of the basic nutrient resources used by bacteria in soils can account to some extent for their diversity. The spatial distribution of organic matter in soils is known to be highly heterogeneous. Incorporation of plant residues by tillage results in patchy distribution at the centimeter scale (e.g., Elyeznasni et al., 2012) while at smaller millimeter scales, heterogeneous distribution of soil organic matter has been visualized by Peth et al. (2014) and Kravchenko et al. (2014). On the basis of these microscale observations, the effect of the heterogeneity of the spatial distribution of soil organic matter and of the connectivity of the aqueous phase on bacterial biodiversity was examined in a series of scenarios using a 3D pore-scale carbon dynamics model. Bacterial cells of three strains of the *Arthrobacter sp.* including highly competitive-, generalist-, and poorly competitive-strains, were randomly placed within the 3D pore space of a small soil sample (of volume size of 314 mm^3) imaged at a resolution of 68 μm, suitable to visualize meso- and macro-pores.

MATERIALS AND METHODS

Soil Image

Undisturbed soil cores were sampled in the surface horizon of a cultivated soil, a silty loamy (19% clay, 75% silt, 6% sand) Albeluvisol (Vogel et al., 2015). 3D images of the samples were obtained using an X-ray CT scanner (HMX 225, NIKON metrology, Tring, United Kingdom). A global threshold according to Elyeznasni et al. (2012) was used to obtain binary images in which the voxels of the gray CT image were classified either as soil or void voxels. We selected one sub-image (called G6 in Vogel et al., 2015) of 100^3 voxels size out of the set of segmented CT images. The voxel-resolution of the image is 68 μm, so that the pore space explored in this study encompasses most of the structural porosity made of meso- and macro-pores. This image corresponds to a volume size of about 314 mm^3, and it has a porosity of 18.82%. This number is undoubtedly smaller than the actual porosity of the soil, because of the fact that sub-resolution pores are ignored (Baveye et al., 2017).

The localization of the fluid and gas voxels corresponding to a given water saturation index, S_w (the proportion of the pore space filled with water), is calculated using a two-phase two-relaxation-times (TRT) lattice-Boltzmann model (LBM) as described by Genty and Pot (2013) and Pot et al. (2015). Three levels of water saturation of the CT-visible porosity are assumed in the present work, $S_w = 1.00$, $S_w = 0.50$, and $S_w = 0.25$. After a visual inspection of the 3D distribution of the gas phase in the images, we selected a few of the smallest visible pores containing gas and recalculated from the Young-Laplace law a rough estimate of the matric potential for $S_w = 0.25$ and $S_w = 0.50$. The matric potentials estimated in this manner are about -0.6 and -0.3 kPa, respectively. Therefore, even though a water saturation level of 0.25 would suggest that the soil is relatively dry, the fact that this number refers only to the CT-visible pore space means that the

scenarios reported in the present contribution correspond to wet conditions.

The image offers a tradeoff between resolution and sample size (constrained by X-ray computed tomography). It is a compromise that presents the advantage of reproducing the millimeter-scale variability of the microbial activity, as reported by Vieublé-Gonod et al. (2006), and of enabling us to work with a soil volume that is large enough for carbon mineralization to be measured in practice.

Model Description

The description below of the Ib-LBioS-Comp model follows the overview, design concepts, and details (ODD) protocol (Grimm et al., 2006, 2010), which was especially developed to communicate the features of agent and individual-based models.

Purpose

Ib-LBioS-Comp, which stands for Individual-based LBM for biodegradation affected by soil structure and competition, is a pore scale modeling approach developed to study the impact of the soil structure or, more appropriately, architecture (see discussion in Baveye et al., 2018), molecular diffusion, spatial heterogeneity of resource distribution, and competition among bacterial species on the biodegradation dynamics of organic matter in the soil.

Entities, State Variables, and Scales

Ib-LBioS-Comp combines a lattice-Boltzmann solute diffusion model and an individual-based biological module describing bacterial activity. The model involves single bacterial cells (biotic agents) of up to three different species or strains, dissolved organic carbon or DOC (abiotic lattice-Boltzmann populations), and particulate organic matter (POM, abiotic agents). Bacterial cells and DOC are distributed in the 3D volume of the soil pore volume and POM is distributed in the 3D volume of the soil solid matrix. Enzymatic hydrolysis of POM is assumed to continuously supply DOC to the liquid phase. Then DOC diffuses through the liquid phase toward the microenvironments where it is taken up by bacteria and used as nutrient source. The diffusion and uptake of oxygen are not accounted for explicitly in the model at the moment and are assumed not to limit microbial activity.

The simulated space is divided into a regular 3D grid made of cubic voxels that can be either solid or filled with a fluid (air or water).

A bacterial cell or individual (I_i) is defined by the variables Π_i, identifying its position in the domain, its species j_i, its mass m_i (mg C), its specific uptake rate $\upsilon_{DOC,i}$ (tu^{-1}), and its mass at reproduction $m_{R,i}$ (mg C). All masses in Ib-LBioS-Comp are expressed in terms of mass of carbon. Letting $P = I(t)$ denote the number of bacteria at time t, one obtains for the state of the population at time t:

$$Pn = \{I_i[\Pi_i, j_i, m_i, \upsilon_{DOC,i}, m_{R,i}]\}_{i=1,2,...,n(t)} \qquad (1)$$

where i is the index of individual bacteria and $n(t)$ the total number of cells at time t.

A POM agent (A_l) is defined by a variable indicating its position in the domain, Π_l, and its carbon mass, $m_{POM,l}$

(mg C). Letting $A(t)$ denote the number of POM agents, the POM population state at time t is:

$$POM_m = \{A_l[\Pi_l, m_{POM,l}]\}_{l=1,2,...,m(t)} \qquad (2)$$

where l is the index of the POM agents and $m(t)$ the total number of POM agents at time t.

The DOC solute is simulated by microscopic lattice-Boltzmann populations, f_q, that are microscopic solute entities defined in the Q microscopic directions at each liquid node of the 3D grid. The Q directions are defined by the unit microscopic velocity vectors, $\vec{C_q} = \{C_{q\alpha}\}_{q=0,...,Q-1;\alpha=1,...,d}$ where d is the dimension of the grid or lattice. We used the model D3Q7.

The DOC concentration in the liquid phase, C_{DOC} (t) (mg C lu^{-3}) can be calculated at each liquid node of the grid as the sum of the f_q populations:

$$C_{DOC} = \frac{1}{\triangle V_{xyz}} \sum_{q=0}^{Q-1} f_q \qquad (3)$$

with $\triangle V_{xyz}$ the volume of one voxel expressed in lu^3 where lu is the spatial unit of the lattice, in our case determined by the scanning resolution so that $1\ lu = 68\ \mu m$.

The temporal evolution of the system is divided into equal intervals associated with time steps or units (tu) of a time step length dictated by the lattice-Boltzmann submodel. The temporal extent of the simulations was set to 10 days according to previous simulations made by Vogel et al. (2015) in which exponential growth and decline of biomass were observed within this duration. The time step length is 3.44 s (see Sections "Abiotic Processes" and "Model Parameterization").

Process Overview and Scheduling

Global simulation comprises three sections (**Figure 1**): (i) the initialization of the simulated system, (ii) the time step loop, which is repeated until the end of the defined time steps, and (iii) the model output section, where the system-level (aggregated) and individual-level (non-aggregated) data are saved in files. Initialization of the system includes: reading of model parameters, initialization of the bacterial agents, and initialization of the LBM parameters and DOC populations. The time step loop includes, chronologically: (ii.i) storage of the simulation state in temporary data structures, (ii.ii) the POM agents actions loop, (ii.iii) the bacterial actions loop (**Figure 2**), and (ii.iv) the lattice-Boltzmann actions. Output files of aggregated and state variables are created from the temporary data structures saved previously.

At each time step, bacterial cells perform the following set of actions: uptake, metabolism, reproduction, and mortality. The order in which bacteria act is changed randomly every time step to avoid privileging always the same first-acting bacteria. At each time step, the existing POM agents undergo hydrolysis to produce DOC. The DOC lattice-Boltzmann populations, f_q, are then updated through the following set of actions: collision, propagation, and bounce-back when they encounter a solid or a gas neighbor. This last action is motivated by the premise that DOC occurs only in the water phase.

FIGURE 1 | General workflow of the lb-LBioS-Comp model.
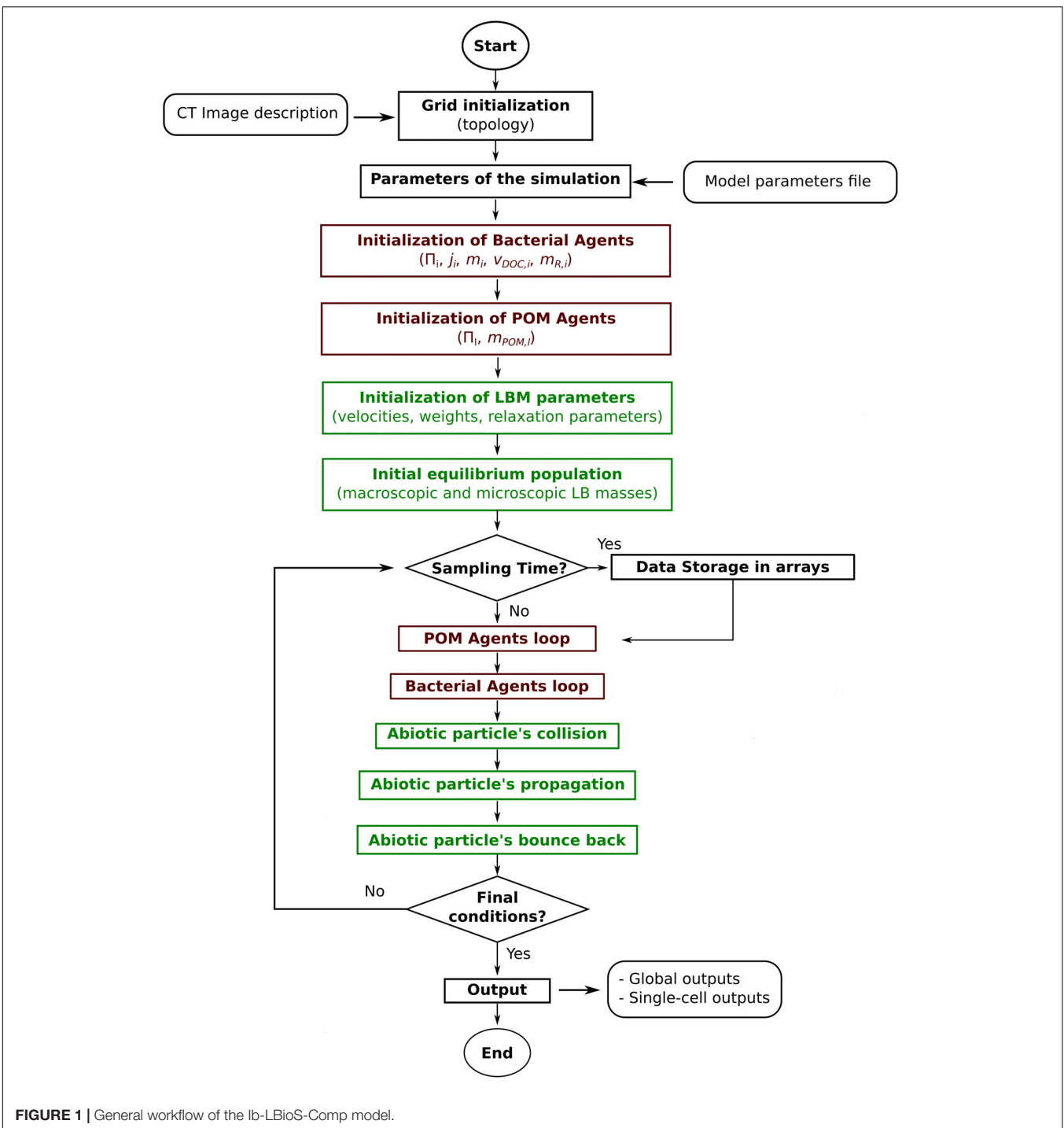
Design Concepts

Emergence

Bacterial processes (uptake, metabolism, reproduction, mortality) are defined at a single-cell level and the population or system level behavior emerges from the interactions among individuals and between the individuals and the media. The main population-level emerging characteristics are the population density (bacteria present in the media), the population biomass, the DOC taken up by the population, the CO_2 produced by the population and the bacterial size distribution. Solute diffusion processes (collision, propagation) are defined at the microscopic level of the Q directions of the lattice, and the solute behavior (diffusion) emerges from the interactions among the solute lattice-Boltzmann populations.

FIGURE 2 | General workflow of the bacterial agents loop of the lb-LBioS-Comp model.
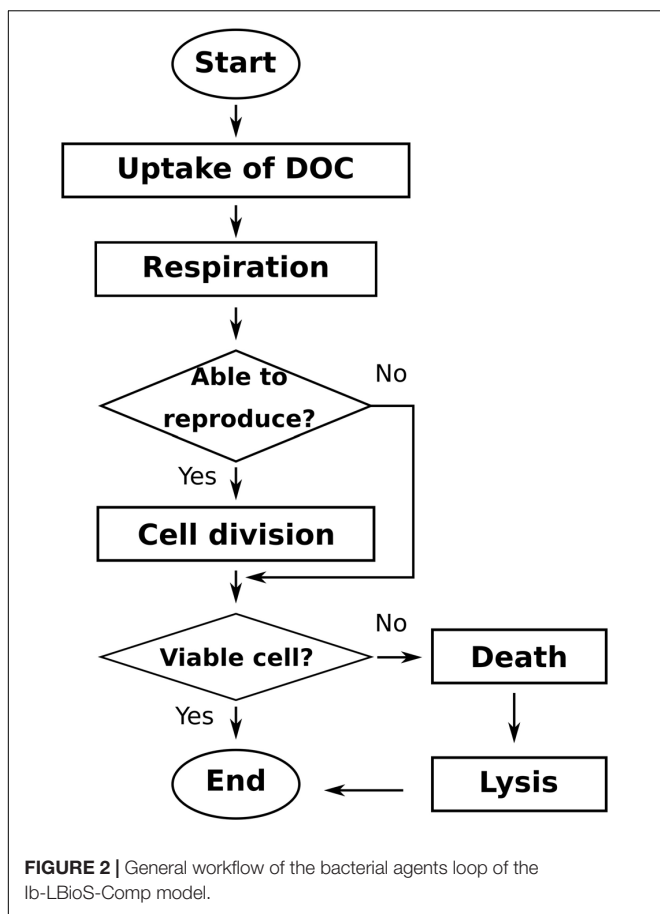
Interaction
Bacteria are considered to be immobile but they compete directly for space through the maximum carrying capacity of a voxel. Therefore, the presence of other bacterial cells in the local space can directly affect the fate of new-born bacteria. Indirect interactions among individual bacteria arises from competition for the DOC available in the local environment.

Stochasticity
Randomness is considered when the rules are applied to individuals by using probabilistic distributions to deal with or manage individual events. Random processes or events include the assignment of the position of new-born bacteria in the physical domain near the mother when the grid element of the mother reached maximum occupancy, and the occurrence for cell death. The sequence of actions of the simulated bacteria changes randomly at each time step to avoid privileging one over the others. The model can also introduce further stochasticity when setting the mass of the initial individuals, the individual specific uptake rate, and the mass at reproduction of the individual bacteria using folded normal distributions, but this is not considered in the current study.

Observation
Global and single-cell outputs are recorded at the beginning of the simulation, at regular intervals during the simulation, as well

as at the end of the simulation. Global variables calculated at the scale of the entire domain include: mass of DOC, POM, and CO_2 produced in the media, and, for each of the three bacterial species, the number of bacteria, and total bacterial biomass. The state of all the individual bacteria is saved at sampling times. These single-cell data include the position within the domain, species, mass, uptake rate, and mass at reproduction of the individuals. The carbon mass and position of all the POM spots (abiotic agents) are also saved at sampling times. The DOC concentration of the liquid voxels holding at least one bacterium is also recorded at sampling times. The final DOC concentration of all the liquid grid cells of the domain is recorded at the end of the simulation.

Initialization
The specific uptake rate ($v_{DOC,i}$), and the reproduction mass ($m_{R,i}$) of the initial individuals ($i = 4, ..., N_{B0}$) are assumed to be specific for each jth species. For the individuals of each species j, these properties are set using the model parameters v_{DOC}^{j} and m_{t0}^{j}, respectively, for the uptake rate and the reproduction mass. No intraspecific variability is considered in the present study. Similarly, the initial mass of the individuals starting the simulations (m_i) is initialized according to the model parameters m_{t0}^{j}.

Since it is generally assumed that bacteria in soil microenvironments tend to be sorbed to, or be at least very near, solid surfaces, the model assumes that bacteria can be located only in liquid voxels having at least one solid neighbor. What defines a neighbor here is the particular lattice-Boltzmann connectivity that is adopted in the calculations (D3Q7 in this case). The initial N_{B0} bacterial cells are randomly distributed among a number of bacterial spots (N_{SP0T}) that, in turn, are randomly chosen, with replacement, from the liquid voxels having one or more solid neighbors.

The POM agents are situated in the solid matrix of the soil. The initial POM agents are randomly distributed among solid voxels that have at least one liquid neighbor.

An initial amount of dissolved organic carbon, DOC_0, is distributed homogeneously among the liquid voxels of the image.

Input Data
The model uses soil structural data as described in see Section Soil Image.

Biological Processes
Several separate submodels describe quantitatively the uptake, metabolism, reproduction, and mortality, respectively, of individual bacteria.

In the *Uptake submodel,* the uptake (U_i) of carbon substrate by bacterium i, belonging to the species $j = j_i$, is given by the equation depending on the mass $m_i(t)$ of the bacterium

$$U_i(t) = \frac{v_{DOC,i}\, C_{DOC}^{(t)}}{C_{DOC}^{(t)} + k_{DOC}^{j}} m_i(t) \qquad (4)$$

where $v_{DOC,i}$ is the specific uptake rate of the ith bacterium (tu^{-1}), and the parameter k_{DOC}^j is the half saturation constant $(mg\ C\ lu^{-3})$ of the jth species.

In the *Metabolism submodel*, the mass of carbon taken up is used by the cell to create new biomass. Since catabolic reactions need energy, due to the respiration process, a fraction of the carbon that is taken up is released again to the media in the form of CO_2 emissions. Accordingly, the growth of the bacterial cell is modeled using the following equation:

$$m_i(t+1) = m_i(t) + U_i(t) - k_r^j m_i(t) \qquad (5)$$

where k_r^j is the respiration rate (tu^{-1}) of the species j. Equations (4) and (5) assume that growth respiration (traditionally calculated as a function of substrate during uptake) and maintenance respiration (proportional to the biomass) are not distinguished.

The Reproduction submodel adopts a simple bipartition condition (Banitz et al., 2015) according to which the bacterial cell has to attain a specific individual reproduction mass before dividing. Every time step, the mass of a bacterium is compared to $m_{R,i}$ (mg C), the reproduction mass of the ith individual. If $m_i(t+1) > m_{R,i}$, the mass of the bacterium is halved, and simultaneously a daughter cell of the same mass is created. If the number of bacteria occupying the voxel of the mother cell is less than N_{VOX}, the maximum carrying capacity of a voxel, the cell is created in the current voxel. Otherwise, the simulator chooses randomly a voxel that has not attained the maximum carrying capacity. The searching algorithm looks progressively to neighbors situated at increasing distances (in voxels) from the mother's voxel of origin, until all the tridimensional space is inspected. If all the voxels reach the maximum carrying capacity, the simulation stops. The daughter cell remains active but does not act until the next time step is reached. The specific uptake rate of the new-born individual $(v_{DOC,i})$ and its mass at reproduction $(m_{R,i})$ are inherited from the mother.

Finally, *the Mortality submodel* accounts for bacterial cell death derived from internal and external events (e.g., predation by other organisms). The cell cannot survive anymore due to internal events when the cell size decreases below the minimal cell size characteristic of its species j, m_{MIN}^j which can be attained due to a starvation process. Cell death due to external events is accounted by a probability, p_M^j (dimensionless), independent of the cell state. At every time step, the submodel compares r_p with p_M^j, where r_p is a random realization coming from a uniform distribution between 0 and 1. If $r_p > p_M^j$ the individual bacterium dies. The cell carbon lyses and creates new DOC in the current voxel.

Abiotic Processes

The main abiotic processes simulated by the model are the hydrolysis of POM and the diffusion of DOC in the 3D pore space. No convective movement of DOC was considered in the model. POM agents release DOC, decreasing as a result the mass of the POM agent. The model assumes only one homogeneous fraction of POM with a unique hydrolysis rate. The hydrolysis process is modeled assuming a first order kinetics of constant rate, k_{POM}. The underlying hypothesis is that exo-enzymes are ubiquitous in soil (Folse and Allison, 2012). Nannipieri et al. (2003) reported that newly produced exo-enzymes by bacterial cells are short-lived molecules because, for instance, proteases can degrade them. Thus, the ubiquitous enzymes are probably those physically protected though their adsorption to clay particles or humic molecules (Burns, 1982). Burns (1982) considers it a likely scenario that these enzymes become active when a POM fragment comes into contact with them. Then, the DOC released by the agent is distributed equally among the liquid voxels neighboring the solid voxels containing the POM agent.

We implemented the TRT lattice-Boltzmann approach of Ginzburg (2005). The evolution equation of the DOC microscopic entities at the liquid nodes (grid cell with k = lq), $\overrightarrow{V_{xyz}}$ from time t to $t+1$ is given by:

$$
\begin{aligned}
f_q(\overrightarrow{V_{xyz}} &+ \overrightarrow{c_q}, t+1) - f_q(\overrightarrow{V_{xyz}}, t) \\
&= \lambda_e[f_q^+(\overrightarrow{V_{xyz}}, t) - e_q^+(\overrightarrow{V_{xyz}}, t)] + \lambda_o[f_q^-(\overrightarrow{V_{xyz}}, t) \\
&\quad - e_q^-(\overrightarrow{V_{xyz}}, t)] + S_q
\end{aligned}
\qquad (6)
$$

in which the collision and propagation steps are described, respectively, by the two first terms of right hand side and left hand side of (7), respectively. The sink/source term of DOC, S_q, is calculated from the hydrolysis and bacterial processes. In the TRT scheme, the microscopic entities f_q are decomposed into symmetric,f_q^+ and antisymmetric components,f_q^- along their opposite velocities $\overrightarrow{c_q} = -\overrightarrow{c}_{\bar{q}}$ (Ginzburg, 2005). During the collision step, the relaxation of moments resulting from the entities' distribution at time t toward an equilibrium state $e_q = e_q^+ + e_q^-$ governs the reorganization of the entities. The relaxation parameter λ_e is a free parameter and the relaxation parameter λ_o is related to the molecular diffusion coefficient, D_m^{LBM} (lu^2tu^{-1}) along:

$$D_m^{LBM} = \frac{-1}{3}\left(\frac{1}{2} + \frac{1}{\lambda o}\right) \qquad (7)$$

Both parameters must be comprised between -2 and 0 for stability. The rescaling of lattice Boltzmann time units (tu) in real time units [T] is made through the relation:

$$T_R = \frac{D_m^{LBM}L_{R2}}{D_m^R L_{LBM}^2} T_{LBM} \qquad (8)$$

where T_{LBM} and L_{LBM} are the space and time in lattice units (respectively, tu and lu) and T_R and L_R are their corresponding time and space units in real units [respectively (T) and (L)].

Model Parameterization

Typical parameters for the three different strains 3R, 7R, and 9R of *Arthrobacter* sp. (see **Table 1**) were taken from the literature. The specific uptake rate, v_{DOC}^j, the half saturation constant of the uptake rate, k_{DOC}^j, and the respiration rate, k_r^j, of the three species were directly taken from Monga et al. (2014), while the population mortality rate, provided by the same authors, was reinterpreted as probability, P_m^j, dependent on the duration

TABLE 1 | Model parameters values used in the simulations. See text for an explanation of the computations and the bibliographic references used.

Symbol	Definition	Unit	Strain		
			j = 3R	j = 9R	j = 7R
BACTERIAL PARAMETERS					
v_{DOC}^{j}	Maximal uptake rate	d^{-1}	17	9.6	8.0
k_{DOC}^{j}	Half saturation constant	mg C cm^{-3} water	5.0×10^{-4}	1.0×10^{-3}	1.4×10^{-4}
k_{r}^{j}	Respiration rate	d^{-1}	0.2	0.2	0.3
m_{R}^{j}	Reproduction mass	mg C	1.32×10^{-10}	1.32×10^{-10}	1.32×10^{-10}
P_{m}^{j}	Mortality probability	–	1.5	0.5	1.0
m_{MIN}^{j}	Min bacterial mass	mg C	$0.1\, m_R$	$0.1\, m_R$	$0.1\, m_R$
m_{t0}^{j}	Initial mass of the bacterial cells	mg C	5.39×10^{-11}	5.39×10^{-11}	5.39×10^{-11}
N_{B0}^{j}	Initial bacterial number	Cells	230	230	230

		Unit	Value	
BIOTIC PARAMETERS				
N_{VOX}	Voxel Max. carrying capacity	Cells	751,423	
ABIOTIC PARAMETERS				
k_{POM}	POM decay rate	d^{-1}	0.25	
D_M	DOC mol. diff. coeff.	cm$^2 \cdot$s^{-1}	6.73×10^{-6}	

of the time step. These strains have different growth patterns, with 3R expected to be the fastest growing strain and strain 9R the least competitive one due to its highest value of the half saturation constant of the uptake rate. Strain 7R is supposed to be representative of a more generalist strain.

The maximum carrying capacity of a lattice-Boltzmann node, N_{VOX}, was calculated from the volume of a single image voxel (683 µm^3) and the mean cell volume of a bacterial cell. The mean volume of an *Arthrobacter* cell was calculated to be 0.418 µml according to data from Erlebach et al. (2000), assuming a spherical shape for the bacterial cell. We used this mean volume for the three strains of *Arthrobacter* sp. The mean reproduction diameter (i.e., the diameter attained by the cell before division) was also estimated from *Arthrobacter* cell size distributions (Erlebach et al., 2000) and assumed to be in the range 1.25 ± 0.15 µm, which includes the biggest diameters of the size distribution measured with a Coulter counter. The central value of 1.25 µm has been used in the present study.

Then, the mean carbon content of a single cell (m_{t0}^{j}, **Table 1**) and the value for the reproduction mass, m_{R}^{j}, were calculated from the mean cell volume and the mean reproduction volume calculated earlier, assuming a density of 1.1 g/cm^3, a ratio of dry to wet cell weight of 0.25, and a carbon content of 0.47 g C per gram of dry cells (Gras et al., 2011).

The value of the decay rate of the POM agents, k_{POM}, was set to 0.25 day^{-1} as reported by Iqbal et al. (2014) for the decomposition rate of maize (*Zea mays*) stem residues. These authors found "optimal decomposition conditions similar to those obtained with ground material" for fragments of POM of 0.02 cm length. Assuming a density of POM of 0.12 g cm^{-3} (Iqbal et al., 2013) and a volume of POM residue of about 0.02 cm × 0.02 cm × 0.01 cm, we calculated an initial POM mass of carbon, POM$_0$, of 1.92 10^{-4} mg C. We translated this fragment of POM into four fragments of parallelepiped shape

(1 × 1 × 3 voxels), located at the solid/liquid interface (**Figure 3**). When the POM hydrolyses, the DOC produced is included in the neighboring fluid site.

The molecular diffusion coefficient in lattice-Boltzmann units, D_m^{LBM}, is fixed to 0.5 lu^{2}tu^{-1} (Vogel et al., 2015, 2018). Since the DOC molecular diffusion coefficient, D_m^R, is 6.73 10^{-6} cm^{2}s^{-1} (Weast et al., 1986) and 1 lu = 68 µm, the rescaling equation (8) gives 1 tu = 3.44 s.

Simulation Scenarios

The scenarios were designed to investigate the effect of the local micro-environments of bacteria on the strains abundance. For all scenarios we randomly placed 230 bacteria of each strain in the medium which resulted in 690 bacterial spots. In one
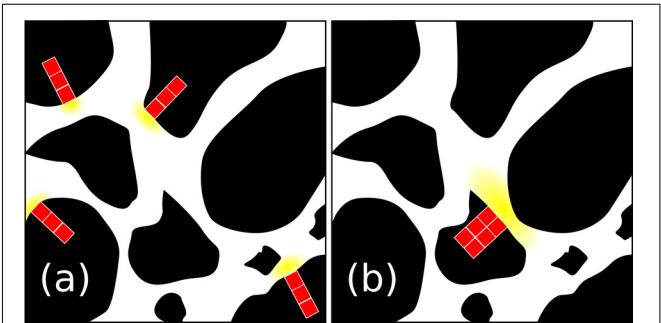
FIGURE 3 | 2D view of the POM initialization scheme used in the scenarios. In the figure, the POM (red), the DOC (yellow), the soil solid matrix (black), and the pore space (white) are depicted. In **(a)**, POM disaggregated, four parallelepiped POM fragments of 1 × 1 × 3 image voxels, were assumed to be present and connected to the pore space through a single voxel. In **(b)**, POM aggregated, a single 3D POM fragment of 4 × 4 × 3 was assumed to be present and connected to the pore pace through 4 of its voxels.

particular scenario (S4) the three strains systematically co-exist in the same bacterial spot, so that only 230 bacterial spots were generated. The local micro-environments of these bacterial spots were modified by introducing heterogeneity in the placement of the resource (POM and DOC) in the medium. The water content level was also modified. **Table 2** summarizes the characteristics of the different scenarios. Scenarios S1, S2, and S3 test the effect of the spatial distribution of organic matter on the global organic matter degradation and strain abundance. Scenario S4 tests the effect of the direct interspecific bacterial competition on strain abundance, whereas scenarios S5 and S6 are designed to test the effect of the water saturation level on organic matter degradation and strain abundance. Details of these scenarios are given below.

Scenario S1

The initial 690 bacteria were distributed among 690 randomly selected liquid voxels neighboring the soil solid matrix. Four POM fragments were randomly distributed in the medium (**Figure 3a**). Ten replicated simulations were performed with the position of POM fragments controlled by a random seed. The positions of the 690 bacterial spots were left unchanged for the ten replicated simulations. The water saturation level, S_w, was 0.50.

Scenario S2

The four fragments of POM were gathered in one fragment made of $2 \times 2 \times 3$ voxels with the base 2×2 voxels being contiguous solid sites neighboring 2×2 fluid sites (**Figure 3b**). Bacteria were located in the same 690 positions as for scenario S1 and the same water saturation level, $S_w = 0.50$, was adopted. Ten replicated simulations were again performed with the position of POM fragments controlled by a random seed Comparison of scenario 1 and 2 made it possible to assess the effect of the degree of spatial heterogeneity of POM.

Scenario S3

We assumed that all the carbon that can, potentially, be hydrolyzed and released to the liquid phase of the soil in the scenarios S1 and S2, was already homogeneously distributed in the liquid phase of the medium at the beginning of the simulations as a DOC. A water saturation index of $S_w = 0.50$ was also adopted. In ten replicated simulations, a random seed

controlled the position of 690 bacterial spots. This resulted in 9 extra configurations of the 690 bacterial positions tested in S1 and S2. Comparison of S3 with S2 and S1 allowed us to evaluate the impact of homogenously- vs. heterogeneously distributed C within the soil.

Scenario S4

This scenario was aimed at the effect of direct interspecific competition on strain abundance. Two simulations (identified as S4a and S4b) involved 3 bacteria, one of each strain, in selected 230 bacterial spots. In S4a, we took one particular repetition of scenario S2 in which the three strains had a noticeable growth (repetition S2r2) and we classified the 690 spots according to the amount of biomass growth of the colony in a descending order. The first 230 bacterial spots were selected and used to place the initial bacteria. In S4b, we took the repetition S2r2 but we just selected the 230 bacterial positions occupied by the less competitive strain (9R). In each of these spots, we placed initially 3 bacteria, one of each strain.

Scenarios S5 and S6

These scenarios are identical to scenario S2 except for the water saturation level that was fixed to 1.00 (S5) and 0.25 (S6). Because the positions of the 690 bacterial spots are left unchanged, in scenario S6 there were 165 bacterial spots that were found to be in the gas phase, and thus did not grow. In the 525 spots still placed in water filled grid cells, the three strains were found to be equally distributed as 178 cells of strain 3R, 172 cells of strain 9R and 175 cells of strain 7R.

RESULTS AND DISCUSSION

Effect of Spatial Distribution of Organic Matter on Global Organic Matter Degradation and Strain Abundance

Simulation scenarios S1 and S2 assume that the soil organic matter is found in a number of POM fragments that are distributed (S1) or aggregated (S2). In the proposed scenarios, the hydrolysis rate of POM is set to a constant value, so that

TABLE 2 | Simulation scenarios overview.

| Scenario | POM_0 | DOC_0 | N_{SPOT}^B | N_{SPOT}^{POM} | S_w | Randomness |
	mg C	mg C	Spots	Spots	[-]	
S1	1.92×10^{-4}	0.0	690	4	0.50	POM spots
S2	1.92×10^{-4}	0.0	690	1	0.50	POM spots
S3	0.0	1.92×10^{-4}	690	0	0.50	Bacterial spots
S4a	1.92×10^{-4}	0.0	230	1	0.50	–
S4b	1.92×10^{-4}	0.0	230	1	0.50	–
S5	1.92×10^{-4}	0.0	690	1	1.00	POM spots
S6	1.92×10^{-4}	0.0	690	1	0.25	POM spots

In the table: POM_0 is the initial carbon mass of POM, DOC_0 is the initial carbon mass of DOC, N_{SPOT}^B is the number of bacterial spots, N_{SPOT}^{POM} is the number of POM spots, and S_w is the saturation level of the media. Randomness indicates whether the POM fragments or the bacterial spots are randomly changed to generate 10 replicated simulations. The letter "a" denotes that the 230 bacterial spots are selected from the highest growing bacterial spots of repetition 2 of S2, while "b" denotes that the 230 bacterial spots occupied by the strain 9R in the repetition 2 of S2 are used.
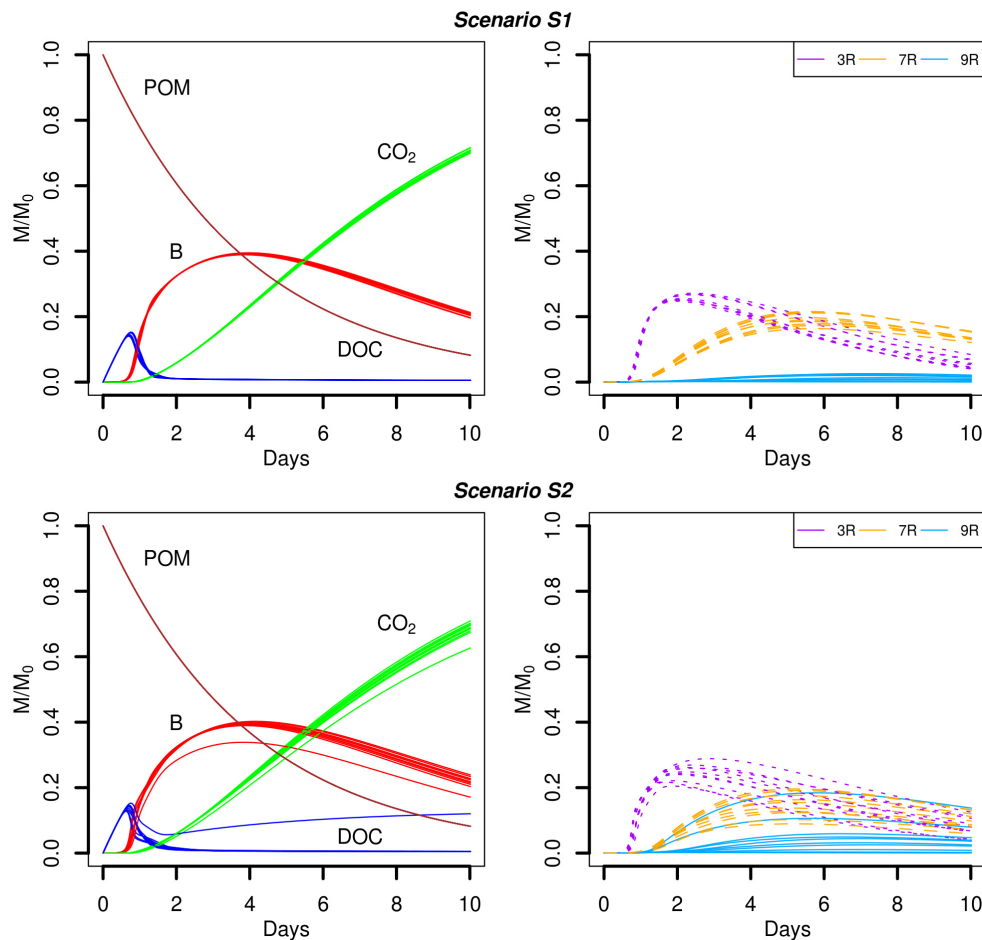
FIGURE 4 | Global biodegradation kinetics (left) and strains abundance (right) of scenarios with dispersed POM fragments (S1) and aggregated POM fragments (S2). M/M_0 is the ratio of the carbon mass (mg C) of each output over the total initial carbon mass M_0.

for k_{POM} = 0.25 d^{-1}, about 92% of the initial mass of carbon of the POM fragments is hydrolyzed at the end of the simulations. The predicted time evolutions of the POM, DOC, total biomass (B), and CO_2 are shown in **Figure 4**. At the beginning of the simulations, the carbon hydrolyzed from the POM particles cannot be totally consumed and accumulates in the liquid phase. After one day, when exponential growth of bacteria starts, the major part of the dissolved organic carbon is metabolized by the cells. At the end of the simulations, the CO_2 emitted has not yet reached a plateau although the slope of its cumulated increase begins to decrease. Except for one repetition of scenario S2, no differences are observed in the time evolutions of the POM, DOC, total biomass, and CO_2 between the two POM distributions.

Although the global model outputs are similar for both spatial distributions of POM, differences in the strains abundance are observed (**Figure 4**, right). When the POM is fragmented into 4 pieces, the less competitive strain 9R cannot grow significantly (**Figure 4**, scenario S1). The fastest growing strain 3R experiences an exponential growth up to two days before starting to decline. The more generalist strain 7R has a much smoother exponential increase compared to 3R, and even surpasses the biomass of 3R

after five days, before starting to decline after about the day seven. When the POM fragments are gathered into a single piece, 3R has the same overall dynamics, with comparable mean abundances but with higher dispersion between replicates. The coefficient of variation (CV) of the abundance peak is 0.03 for S1 and 0.10 for S2. The strain 7R has also the same dynamics as in scenario S1 but with a lower mean abundance peak that does not exceed 78% of the 7R mean abundance peak observed for the scenario S1. Again, the CV is highest in scenario S2 compared to S1 with the values of 0.24 and 0.10, respectively. On the contrary, the strain 9R shows a much higher growth variation among replicates when the POM is aggregated in a single piece of POM. In particular, two replicates (S2r2 and S2r5) show growth kinetics similar to those of strain 7R. In three other replicates, 9R grows without exceeding the abundance of the other species. In the last five replicates, 9R presents a similar growth as in the case of POM fragmented. The S2 replicate with lower global total biomass and emitted CO_2 (S2r9) corresponds to the lowest abundances of the strains 3R and 9R, and to the highest abundance of 7R. In that case, the highest abundance of 7R does not compensate the low abundances of strains 3R and 9R, while compensation

is observed for the other replicates at the scale of the whole soil sample.

A very different biodegradation kinetics is observed when the DOC is homogeneously distributed in the pore space (**Figure 5**, scenario S3). The global growth of the total biomass is much faster (**Figure 5**, left) with a maximum peak reached at day one. The value of the peak is 4.5 times higher than the peaks reached by the total biomass in scenarios with POM fragments. The higher amount of DOC available initially permits a higher bacterial uptake that translates into a faster growth of the bacteria. As a result, the amount of DOC quickly decreases within the same time interval (one day) and the cumulated CO_2 emitted is higher, with values of about 72% (**Figure 4**) and 91% (**Figure 5**), respectively. The different picture shown by the biodegradation kinetics has relevant implications for the species abundance (**Figure 5**, right). The most competitive 3R strain dominates from the very beginning. The high value of its maximal uptake rate (**Table 1**) makes 3R cells benefit more from the larger initial DOC concentration, and experience a quick and large exponential growth. This strain shows a more pronounced decline phase than in scenarios with POM fragments. Only when DOC becomes scarcer, the more generalist strain 7R with the lowest k_{DOC} values succeeds to grow at about the same extent as observed in previous scenarios with POM fragments. The strain 9R with intermediate growth rate but with a higher k_{DOC} value is not competitive enough to grow. A probable explanation is that, after two days, the DOC concentration at the local microbial habitat of strain 9R remains always lower than in the case of the POM fragments. In the latter case, some microbial habitats of strain 9R that are located close to the POM fragments can still benefit from a sufficient DOC concentration for them to grow. On the contrary, the more generalist strain 7R is not impacted by the lower DOC concentrations. **Figure 5** also shows that the position of the bacterial spots does not affect the predicted model outputs, and the ten replicated simulations almost overlap. Simulation scenario 3 is consistent with the nutritional state of the soil after a sudden flush of nutrients, which is typical of the anthropic addition of fertilizers to agricultural land, or as observed after rainfall following a period of drought.

Effect of Spatial Distribution of Organic Matter on Spatial Distribution of Strain Abundance

The spatial distribution of the abundances of the different strains in the scenarios S1 and S2 reveals a number of interesting patterns. In terms of the biomass in each of the 690 spots, we observe that the maximum peak abundance reached in the spots is 2.43 ± 1.01 higher in the case of scenario S2 compared to scenario S1 (**Figure 6**). In both scenarios, a few spots containing cells of the less competitive strain 9R can surpass spots of strain 3R and 7R and even be the most active spots (simulations S2r5 **Figure 6**, and simulation S2r2, not shown). When POM is fragmented, some spots containing 9R cells also end up with an amount of biomass that is similar to what is found with the strains 3R and 7R (simulations S1r2 and, to a lesser extent, simulation S1r9, **Figure 6**) showing that the global, per strain representation displayed in the graphic at right in **Figure 4** hides the very large dispersion of kinetics at the local scale (that of the microbial habitat).

A closer look at the microbial habitats suggests that $10 \pm 1\%$ of the spots do not experience any bacterial growth in scenarios S1. Among those spots, about 45% contain one initial bacterial cell of strain 3R, while 21% contain one initial 9R cell, and 34% contain one initial 7R cell. A higher proportion of non-active spots is found in scenario S2, $18.5 \pm 5\%$. A similar distribution of strains among those spots is observed for the scenario S1. When it comes to the active spots, when POM is fragmented in four pieces, only at $9.5 \pm 4.0\%$ of the spots does biomass exceed 10% of the maximum biomass registered among all the spots. Among these spots, about 60% contain 3R cells, 38% contain 7R cells and only 2% contain 9R cells. When POM is present in a single piece, the proportion of active spots exceeding 10% of the maximum simulated biomass, drops to $4.2 \pm 2.4\%$. Among those spots, about 58% contain 3R cells, 33% contain 7R cells, and 8% contain
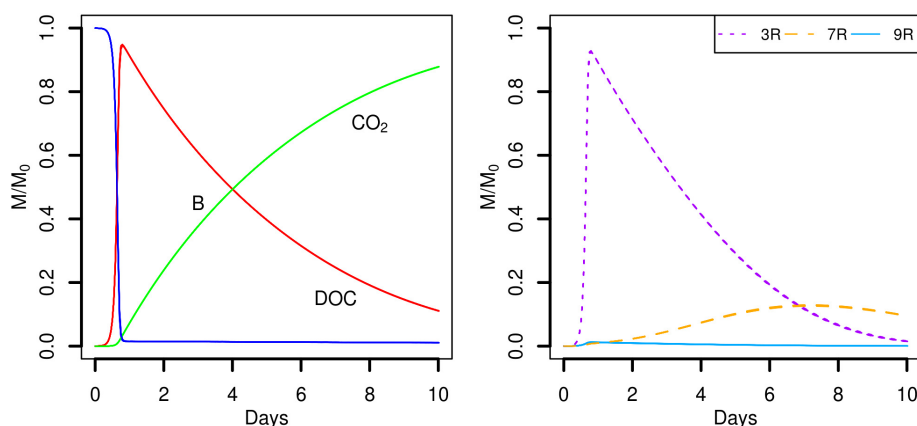

FIGURE 5 | Global biodegradation kinetics (left) and strains abundance (right) of the scenario with the C available as DOC and a water saturation level of 0.5 (S3). M/M_0 is the ratio of the carbon mass (mg C) of each output over the total initial carbon mass M_0.
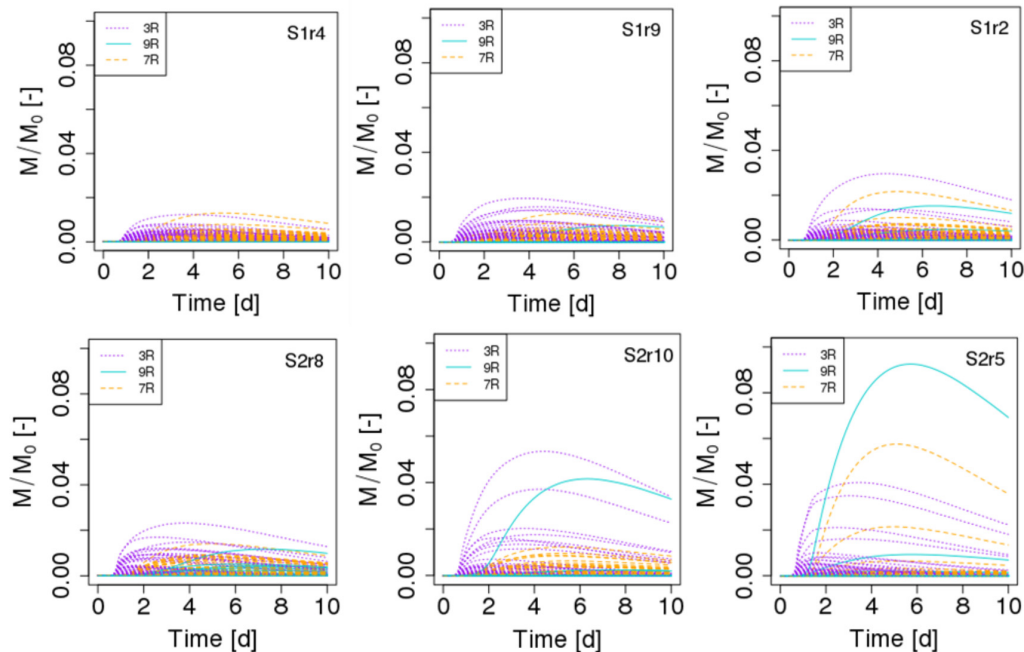
FIGURE 6 | Biomass growth kinetics of the three strains (3R, 9R, and 7R) of each of the 690 spots in scenarios of dispersed POM fragments (S1, Top figures) and aggregated POM fragments (S2, Bottom figures). M/M_0 is the ratio of the carbon mass (mg C) of the cells over the total initial carbon mass M_0. For each scenario, the replicate having the minimal, mean and maximum biomass growth is displayed from left to right.

9R cells. The higher proportion of 9R cells spots among the most active spots in scenario S2 compared to scenario S1 explains the observed higher abundance of this strain.

The general trend suggested by these results is that when POM is gathered into one piece, significantly fewer microbial habitats (almost half) are prone to grow, and a larger dispersion of the abundance is found compared to scenarios in which POM is fragmented. Therefore, under these conditions, it is not surprising that similar biomass growth is observed at the scale of a soil sample (**Figure 4**, left). In our scenarios, since the POM hydrolysis is constant and independent of the spatial position of bacteria, a lower amount of dissolved organic carbon is produced locally compared to the aggregated POM fragments when there are 4 fragments. Even if the probability of having more spots closer to these local sources of DOC is higher with dispersed POM, the available DOC concentration remains lower. Gaillard et al. (1999) show that an aggregated distribution of organic matter mineralized a lower amount of carbon than a dispersed distribution. They explain their results on the basis of a higher exchange surface with soil of the dispersed distribution. The simulation scenarios performed in this contribution were designated to create a similar contact surface area between the soil solid and liquid phases and, therefore, cannot account for the reported outputs. Nevertheless, in general, differences in the contact area still constitute a plausible explanation for differences in mineralization rate in soils.

Using an algorithm developed by Dijkstra (1971) and based on the 6-connexity of the lattice-Boltzmann grid, we further calculated the geodesic distance between each of the 690 spots and the POM fragments in order to relate biomass growth of the microbial habitats to their spatial remoteness of POM. The geodesic distance is the shortest pathway included in the liquid phase that connects two points in the pore space (Gommes et al., 2009). Divided by the Euclidian distance, the direct pathway between the two points, it gives the geometrical tortuosity as defined by Clenell (1997). Geometrical tortuosity and constriction are often considered to be good descriptors of the diffusive transport of solutes in complex pore spaces (Berg and Held, 2016). The mean geodesic distances of the bacterial spots to the POM fragments are about 1.6 times longer when POM fragments are gathered with $5,041 \pm 3,190\,\mu m$ and $8,144 \pm 3,983\,\mu m$ for scenarios S1 and S2, respectively. The mean smallest geodesic distances are $252 \pm 111\,\mu m$ and $490 \pm 262\,\mu m$ for S1 and S2, respectively. Within one replicate of either scenario, the most active spots are those having the shortest geodesic distance (**Figure 7**), however, when comparing the repetitions within a scenario it appears that spots where growth is maximum (S1r2) has a longer or similar minimal geodesic distance than spots having lower growth (S1r9 and S1r4). A large number of spots that do not have significant growth can have a very large range of geodesic distance values (**Figure 7**), which is an unexpected result. In some cases, the geodesic distance can even be close to the shortest values. However, when geodesic distances are longer than about $5000\,\mu m$ in the case of S1 and about $7500\,\mu m$ in the case of S2, the spots do not noticeably grow. When POM fragments are dispersed, the geodesic distances are shorter but also the DOC concentration that is emitted from the POM spots is lower.
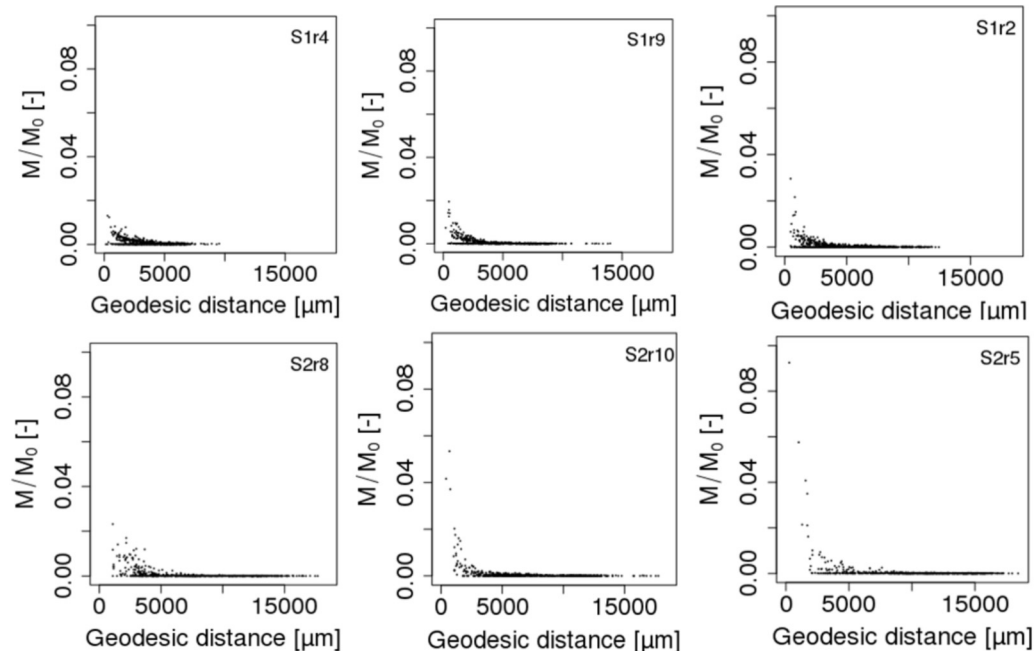
FIGURE 7 | Total biomass growth of each of the 690 spots against the geodesic distances between the spots and the POM fragments of scenarios S1 (Top figures) and S2 (Bottom figures). M/M_0 is the ratio of the carbon mass (mg C) of the cells over the total initial carbon mass M_0. For each scenario, the replicate having the minimal, mean and maximum biomass growth is displayed from left to right.

To our knowledge, it is the first time that geodesic distances between the nutrient resource and microbial habitats are calculated in 3D modeling scenarios of soil carbon dynamics. They reveal that beyond a distance of 5 mm to the POM fragments, the microbial colonies cannot grow. Interestingly, Euclidian distances of around 4 mm from straw labeled with ^{13}C have been reported to hold the sites of higher microbial assimilation and referred as "residusphere" (Gaillard et al., 1999). However, although the most active microbial spots are correlated with the lowest geodesic distances, a low geodesic distance is not a sufficient condition for the microbial colony to grow. We suggest that the size of the pores also matters (e.g., discussion in Baveye et al., 2018). Large cavities can dilute the concentration of DOC that reaches the bacteria, impacting ultimately the growth in the microbial habitat. Therefore, a bacterial spot can experience a microscale environment promoting more the bacterial growth than a spot placed at a shorter geodesic distance to the POM. Calculation of constriction in addition to diffusion length would be more appropriate. More effort is thus needed to calculate other metrics of importance for diffusive transport such as the constriction factor and the diffusion length in order to characterize and fully understand species abundance and functioning at pore scale.

Effect of Direct Interspecific Competition on Strain Abundance

Simulation scenarios S1, S2, and S3 suggest that when the strain 9R is closely competing with 3R or 7R, growth of 9R can occur only when it is located in an advantageous point with respect to

a sufficient source of DOC (for instance in the case of gathered POM fragments, **Figure 4**, scenario S2). To test this hypothesis, we chose one replicate of the scenario S2 (S2r2) in which a few 9R microbial habitats experienced growth, and we initially placed three cells in now 230 spots, one of each strains. The global outputs of the model are similar (**Figure 8**, left), but the strain abundances are very different (**Figure 8**, right). When the three strains co-exist in the same microbial habitat, the strain 9R cannot grow, even when it is located in the spots close to the POM fragments. The most competitive strain 3R grows to a much higher extent and the strain 7R has a delayed growth. There are no prominent differences observed between scenario S4a and S4b.

Effect of Water Saturation Level on Organic Matter Degradation and Strain Abundance

The role of the water saturation level of the pore space on the carbon dynamics was investigated in the scenarios S5 and S6. The global model outputs are similar when the pore space is fully saturated with water ($S_w = 1.00$, **Figure 9**, scenario S5). As mentioned in Section Entities, State Variables, and Scales, oxygen limitations are not yet considered in Ib-LBioS-Comp, so that the different water saturation levels do not impact the role of oxygen in the bacterial activity in these scenarios. Furthermore matric potentials considered in the scenarios S2 and S6 are very close (about -0.3 and -0.6 kPa, respectively) so that oxygen limitations are not expected to happen under the tested conditions. Since the local positions of the aggregated POM fragments and the 690 microbial habitats are not changed,
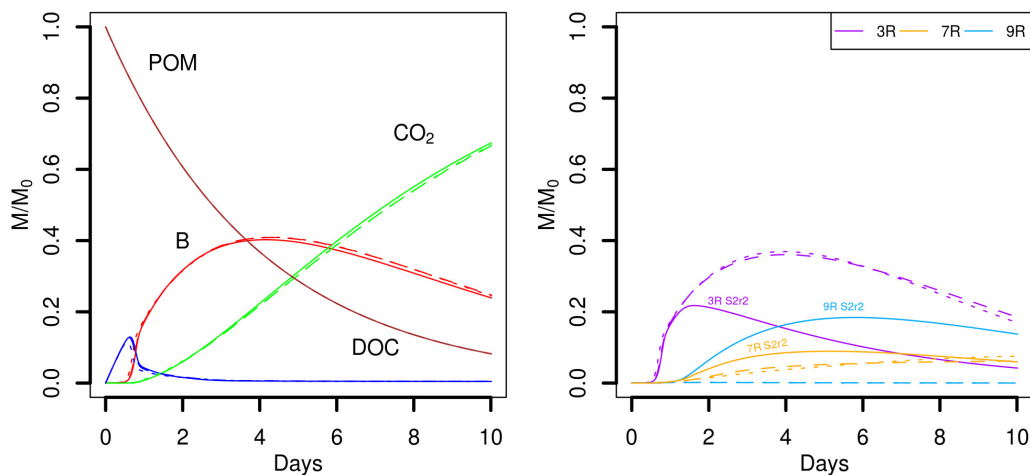
FIGURE 8 | Global biodegradation kinetics (left) and strains abundance (right) of replicate 2 of the scenario with aggregated POM fragments (S4) in which the three strains are initially alone in the spots (S2r2, solid lines) or gathered in the spots (S4a dotted lines and S4b dashed lines). M/M_0 is the ratio of the carbon mass (mg C) of each output over the total initial carbon mass M_0. Simulation outputs obtained in the second repetition of the scenario S2 (solid lines) are compared to the two simulations of the scenario S4 (dashed lines).
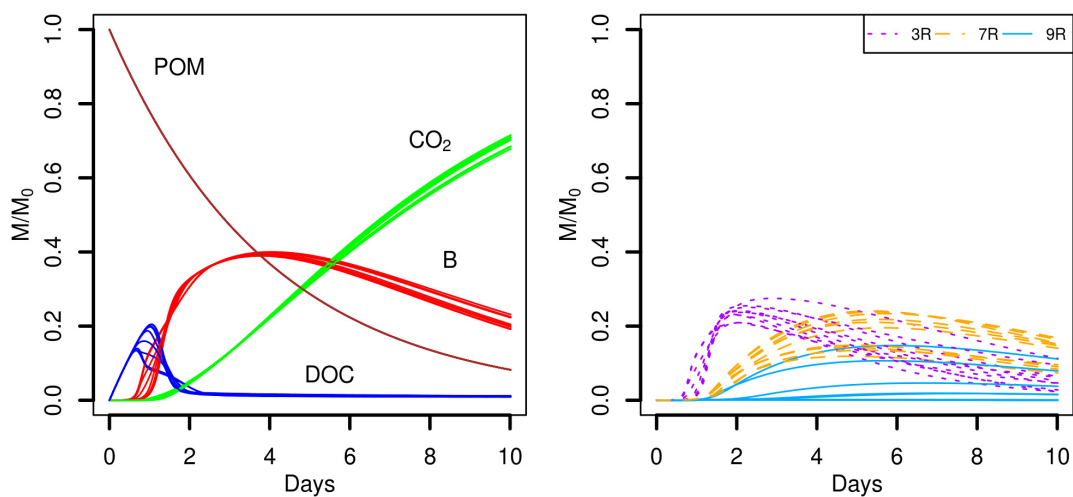

FIGURE 9 | Global biodegradation kinetics (left) and strains abundance (right) of the scenario with aggregated POM fragments and a water saturation level of 1.0 (S5). M/M_0 is the ratio of the carbon mass (mg C) of each output over the total initial carbon mass M_0.

the only effect of the higher water saturation is to decrease the DOC concentrations. However, the diffusive transport of DOC is also accelerated because all the pore space is now connected. The strain abundances are rather similar although this environment is comparatively more favorable for the generalist strain 7R, which becomes the most abundant strain after day 6. The establishment on the system for the simulations showing a noticeable growth of the less competing strain appear mostly driven by the spatial heterogeneity of POM distribution.

When the water saturation level decreases, the pore space filled with air increases and more disconnected aqueous regions appear. Consequently, some POM spots may not hydrolyze resource to the liquid phase, and, some bacterial microhabitats may not have access to the DOC hydrolyzed by the connected

POM agents. In particular, when the water saturation is divided by two (from $S_w = 0.50$ to $S_w = 0.25$), 525 of the original bacterial spots are still in the aqueous phase. In spite of that, five of the replicates (S6r2, S6r4, S6r5, S6r6, and S6r10) produced global model outputs similar to the ones observed for higher water saturation levels (**Figure 10**, upper panel). In one replicate (S6r1), the aggregated POM fragments are located in solid voxels whose neighbors are disconnected from the aqueous phase, preventing the release of DOC, and thus bacterial growth (**Figure 10**, lower panel). In three other replicates (S6r3, S6r7, and S6r9) one of the four gathered solid voxels containing the aggregated POM fragments also has a dry neighbor voxel. Furthermore, for two of them (S6r7 and S6r9), and for the replicate S6r8, no bacterial growth is recorded, resulting in the accumulation of DOC in
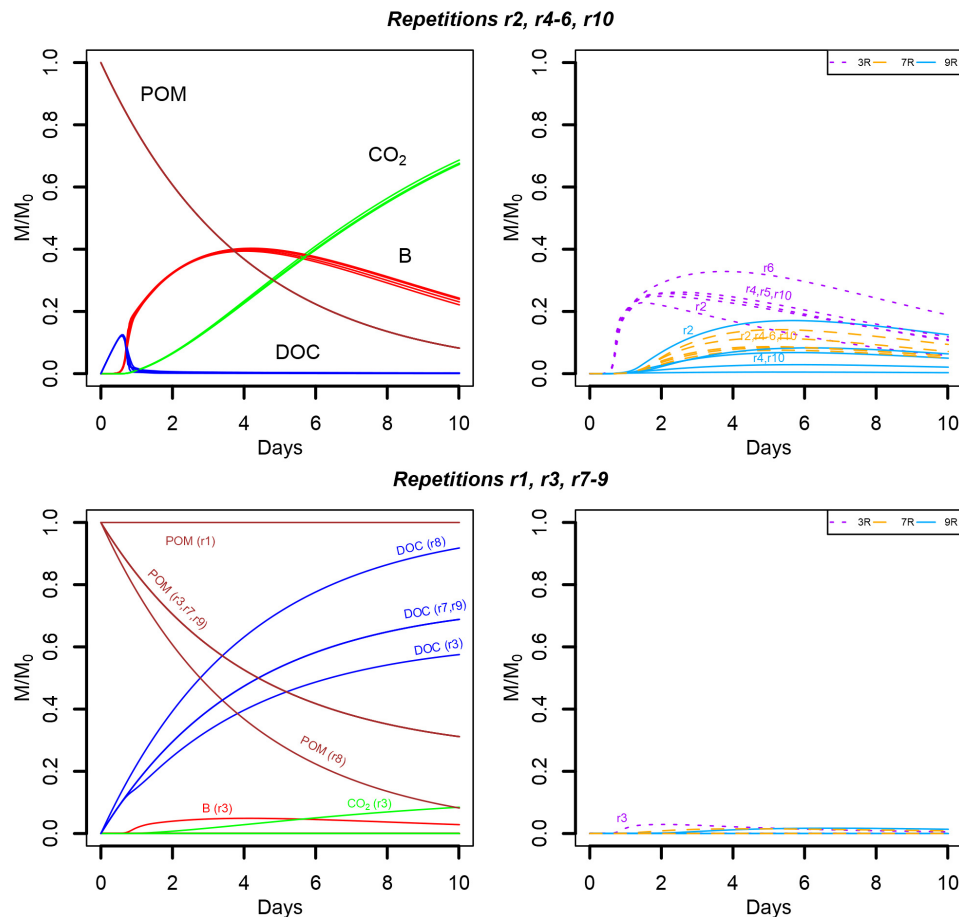
FIGURE 10 | Global biodegradation kinetics (left) and strains abundance (right) of the scenario with aggregated POM fragments and a water saturation level of 0.25 (S6). M/M_0 is the ratio of the carbon mass (mg C) of each output over the total initial carbon mass M_0. The repetition number generating the trends depicted are detailed in the figure.

the liquid phase (**Figure 10**, bottom left). In these three last situations, spatial disconnections between the microbial spots and the POM fragments are made possible by the aqueous phase fragmentation. Spatial disconnections are also observed in the repetition S6r3 where total biomass growth is very small (**Figure 10**, bottom). The strain abundances in the active spots are very similar to those observed when the water saturation is 0.50. In one repetition, the growth of strain 9R of all microbial spots surpasses the growth of strain 7R (**Figure 10**, upper right).

It is known that lack of competition resulting from spatial disconnection of soil microhabitats may promote biodiversity (Kim et al., 2008; Vos et al., 2013). Complete or partial spatial separation due to disconnection of liquid soil volumes in unsaturated soils is a common hypothesis used to explain biodiversity. For instance, one study using experimental setups with two bacterial strains competing for a dissolved resource in sand showed dominance of the more competitive strain under water-saturated conditions while drier conditions allowed the less competitive bacteria to establish (Treves et al., 2003). Regardless of the high variability on the model outputs found for the drier conditions ($S_w = 0.25$), our scenarios do not show

a clearly improved establishment of the less competing strain. Another study (Zhou et al., 2002), based on an rRNA-based cloning approach, reported differing biodiversity distributions in the microbial communities living in four geographically distinct sites at different soil depths. A uniform biodiversity distribution, which is thought to arise from a lack of microbial competition, was obtained for the saturated subsurface of both high and low carbon soils. Since the hypothesis of resource disconnection is difficult to hold under water-saturated conditions, the authors explain their observed pattern by a lack of competition due to specialization for different substrates. Although this hypothesis remains plausible, our simulations suggest that the spatial heterogeneity of the resource placement could also explain part of this biodiversity.

CONCLUSION

We have coupled a multi-species individual-based model describing bacterial growth to a 3D lattice-Boltzmann diffusion model to simulate organic matter dynamics in soil pore space.

The resulting model, Ib-LBioS-Comp, has been used to study the influence of the spatial heterogeneity of a nutrient source on the organic matter degradation and species abundance of a competitive-, a generalist-, and a poorly-competitive bacterial strain. The scenarios used three resource placements showing a gradient in the spatial heterogeneity of its distribution: organic matter dissolved in the aqueous phase (low heterogeneity), four fragments of organic matter (intermediate heterogeneity), and a single fragment of organic matter (high heterogeneity).

A number of results can be highlighted from the modeling scenarios performed: (i) In general terms, the greater the spatial heterogeneity of the location of the resource, the greater the variability in the output at the level of the soil volume imaged; (ii) When the resource is found as particulate organic matter, the fastest growing strain tends to dominate at first but then, when the resources becomes scarcer, it is overtaken by the generalist strain, showing that the spatial distribution of organic matter affects bacterial succession; (iii) the global bacterial growth is faster when the nutrient resource is available in the liquid phase at the beginning of the simulation. Under these circumstances, the fastest growing strain is able to reach much higher relative abundances, having a negative effect on biodiversity; (iv) When the resource is present as particulate organic matter, the total biomass created does not differ noticeably between the intermediate and high spatial heterogeneity schemes but in contrast the species abundance is impacted; (v) The least competing strain, which does not reach noticeable growth for the low and intermediate resource spatial heterogeneity schemes, is able to grow appreciably in the absence of direct competition, if the position of the nutrient resource is favorable. According to this observation, heterogeneity of the spatial distribution of the organic matter in soil would promote microbial diversity; (vi) the geodesic distance among the nutrient resources and the bacteria alone is not sufficient to explain this phenomenon; and, (vii) In the scenarios tested, the water saturation level does not seem to change much the observed biodiversity.

As a cautionary note, one needs to remember that the various predictions made in this article emanate from a relatively simple model, which ignores many different aspects of soils. In actual soils, microbial diversity and growth are potentially affected by a myriad of factors (e.g., resource quality, different nutritional requirements of individual bacteria, mutation, predation, transport by soil fauna, toxin production). In particular, bacterial motility and the diffusion of oxygen in the pore space are likely to have a significant influence on microbial activity. Subresolution pores, too small to be visible in X-ray CT images, are most probably playing a role in this context as well, especially in the dry range of the hydrological regime of soils. Future research will determine if the relationship between bacterial diversity and the spatial heterogeneity in resource distribution, highlighted in the present article, still holds when some of the assumptions of the model are lifted. It is possible that the same relationship will be observed, or that other, more complex behaviors will unfold.

DATA AVAILABILITY

Data underlying this paper can be accessed at https://doi.org/10.17862/cranfield.rd.6744158.

AUTHOR CONTRIBUTIONS

XP implemented the models. XP and VP ran simulations and analyzed the data. All authors conceived, designed the study, and contributed to the writing of the manuscript.

FUNDING

REFERENCES

Banitz, T., Gras, A., and Ginovart, M. (2015). Individual-based modeling of soil organic matter in NetLogo: transparent, user-friendly, and open. *Environ. Model. Softw.* 71, 39–45. doi: 10.1016/j.envsoft.2015.05.007

Baveye, P. C., Baveye, J., and Gowdy, J. (2016a). Soil "ecosystem" services and natural capital: critical appraisal of research on uncertain ground. *Front. Environ. Sci.* 4:41. doi: 10.3389/fenvs.2016.00041

Baveye, P. C., Berthelin, J., and Munch, J.-C. (2016b). Too much or not enough: reflection on two contrasting perspectives on soil biodiversity. *Soil Biol. Biochem.* 103, 320–326. doi: 10.1016/j.soilbio.2016.09.008

Baveye, P. C., Pot, V., and Garnier, P. (2017). Accounting for sub-resolution pores in models of water and solute transport in soils based on computed tomography images: are we there yet? *J. Hydrol.* 555, 253–256. doi: 10.1016/j.jhydrol.2017.10.021

Baveye, P. C., Otten, W., Kravchenko, A., Balseiro Romero, M., Beckers, É., Chalhoub, M.,et al. (2018). Emergent properties of microbial activity in heterogeneous soil microenvironments: different research approaches are

slowly converging, yet major challenges remain. *Front. Microbiol.* 8:1364. doi: 10.3389/fmicb.2017.01364

Berg, C. F., and Held, R. (2016). Fundamental transport property relations in porous media incorporating detailed pore structure description. *Transp. Porous Media* 112, 467–487. doi: 10.1007/s11242-016-0661-7

Burns, R. G. (1982). Enzyme activity in soil: location and a possible role in microbial ecology. *Soil Biol. Biochem.* 14, 423–427. doi: 10.1016/0038-0717(82)90099-2

Clenell, M. B. (1997). Tortuosity: a guide through the maze. *Geol. Soc. Lond. Spec. Publ.* 122, 299–344. doi: 10.1144/GSL.SP.1997.122.01.18

Dijkstra, E. W. (1971). *Ewd316: A Short Introduction to the Art of Programming.* Eindhoven: T.U. Eindhoven.

Elyeznasni, N., Sellami, F., Pot, V., Benoit, P., Vieublé-Gonod, L., Young, I., et al. (2012). Exploration of soil micromorphology to identify coarse-sized OM assemblages in X-ray CT images of undisturbed cultivated soil sores. *Geoderma* 179–180, 38–45. doi: 10.1016/j.geoderma.2012.02.023

Erlebach, C. E., Illmer, P., and Schinner, F. (2000). Changes of cell size distribution during the batch culture of *Arthrobacter* strain PI/1-95. *Antonie Van Leeuwenhoek* 77, 329–335. doi: 10.1023/A:1002632128921

Folse, H. J. III., and Allison, S. D. (2012). Cooperation, competition, and coalitions in enzyme-producing microbes: social evolution and nutrient depolymerization rates. *Front. Microbiol.* 3:338. doi: 10.3389/fmicb02012.00338

Gaillard, V., Chenu, C., Recous, S., and Richard, G. (1999). Carbon, nitrogen and microbial gradients induced by plant residues decomposing in soil. *Eur. J. Soil Sci.* 50, 567–578. doi: 10.1046/j.1365-2389.1999.00266.x

Genty, A., and Pot, V. (2013). Numerical simulation of 3D liquid-gas distribution in porous media by a two-phase TRT lattice boltzmann method. *Transp. Porous Media* 96, 271–294. doi: 10.1007/s11242-012-0087-89

Ginzburg, I. (2005). Equilibrium-type and link-type lattice Boltzmann models for generic advection and anisotropic-dispersion equation. *Adv. Water Resour.* 28, 1171–1195. doi: 10.1016/j.advwatres.2005.03.004

Gommes, C. J., Bons, H. J., Blacher, S., Dunsmuir, J. H., and Tsou, A. H. (2009). Practical methods for measuring the tortuosity of porous materials from binary or gray-tone tomographic reconstructions. *AIChE J.* 55, 2000–2012. doi: 10.1002/aic11812

Gras, A., Ginovart, M., Valls, J., and Baveye, P. C. (2011). Individual-based modelling of carbon and nitrogen dynamics in soils: parameterization and sensitivity analysis of microbial components. *Ecol. Modell.* 222, 1998–2010. doi: 10.1016/j.ecolmodel.2011.03.009

Grimm, V., Berger, U., Bastiansen, F., Eliassen, S., Ginot, V., Giske, J., et al. (2006). A standard protocol for describing individual-based and agent-based models. *Ecol. Modell.* 198, 115–126. doi: 10.1016/j.ecolmodel.2006.04.023

Grimm, V., Berger, U., DeAngelis, D. L., Polhill, J. G., Giske, J., and Railsback, S. F. (2010). The ODD protocol: a review and first update. *Ecol. Modell.* 221, 2760–2768. doi: 10.1016/j.ecolmodel.2010.08.019

Hanson, C. A., Furhman, J. A., Horner-Devine, M. C., and Martiny, J. B. (2012). Beyond biogeographic patterns: processes shaping the microbial landscape. *Nat. Rev. Microbiol.* 10, 497–506. doi: 10.1038/nrmicro2795

Iqbal, A., Beaugrand, J., Garnier, P., and Recous, S. (2013). Tissue density determines the water storage characteristics of crop residues. *Plant Soil* 367, 285–299. doi: 10.1007/s11104-012-1460-8

Iqbal, A., Garnier, P., Lashermes, G., and Recous, S. (2014). A new equation to simulate the contact between soil and maize residues of different sizes during their decomposition. *Biol. Fertil. Soils* 50, 645–655, doi: 10.1007/s00374-013-0876-875

Kim, H. J., Boedicker, J. Q., Choi, J. W., and Ismagilov, R. F. (2008). Defined spatial structure stabilizes a synthetic multispecies bacterial community. *Proc. Natl. Acad. Sci. U.S.A.* 105, 18188–18193. doi: 10.1073/pnas.0807935105

Kravchenko, A., Negassa, W., Guber, A. K., and Schmidt, S. (2014). New approach to measure soil particulate organic matter in intact samples using x-ray computed microtomography. *Soil Sci. Soc. Am. J.* 78, 1177–1185. doi: 10.2136/sssaj2014.01.0039

Long, T., and Or, D. (2009). Dynamics of microbial growth and coexistence on variably saturated rough surfaces. *Microb. Ecol.* 58, 262–275. doi: 10.1007/s00248-009-9510-3

Monga, O., Garnier, P., Pot, V., Coucheney, E., Nunan, N., Otten, W., et al. (2014). Simulating microbial degradation of organic matter in a simple porous system using the 3-D diffusion-based model MOSAIC. *Biogeosciences* 11, 2201–2209. doi: 10.5194/bg-11-2201-2014

Nannipieri, P., Ascher, J., Ceccherini, M. T., Landi, G., Pietramellara, G., and Renella, G. (2003). Microbial diversity and soil functions. *Eur. J. Soil Sci.* 54, 655–670. doi: 10.1046/j.1351-0754.2003.0556.x

Peth, S., Chenu, C., Leblond, N., Mordhost, A., Garnier, P., Nunan, N., et al. (2014). Localization of soil organic matter in soil aggregates using synchrotron-based X-ray microtomography. *Soil Biol. Biochem.* 78, 189–194. doi: 10.1016/j.soilbio.2014.07.024

Philippot, L., Spor, A., Hénault, C., Bru, D., Bizouard, F., Jones, C. M., et al. (2013). Loss in microbial diversity affects nitrogen cycling in soil. *ISME J.* 7, 1609–1619. doi: 10.1038/ismej.2013.34

Pot, V., Peth, S., Monga, O., Vogel, L. E., Genty, A., Garnier, P., et al. (2015). Three-dimensional distribution of water and air in soil pores: comparison of two-phase two-relaxation-times lattice-Boltzmann and morphological model outputs with synchrotron X-ray computed tomography data. *Adv. Water Res.* 84, 87–102. doi: 10.1016/j.advwatres.2015.08.006

Powlson, D., Xu, J., and Brookes, P. (2017). "Throught the eye of the needle: the story of the soil microbial biomass," in *Microbial Biomass: A Paradigm Shift in Terrestrial Biogeochemistry*, ed. K. R. Tate (London: World Scientific), 1–40.

Rainey, P. B., and Travisano, M. (1998). Adaptive radiation in a heterogeneous environment. *Nature* 394, 69–72. doi: 10.1038/27900

Roesch, L. F. W., Fulthorpe, R. R., Riva, A., Casella, G., Hadwin, A. K. M., Kent, A. D., et al. (2007). Pyrosequencing enumerates and contrasts soil microbial diversity. *ISME J.* 1, 283–290. doi: 10.1038/ismej.2007.53

Treves, D. S., Xia, B., Zhou, J., and Tiedje, J. M. (2003). A two-species test of the hypothesis that spatial isolation influences microbial diversity in soil. *Microb. Ecol.* 45, 20–28. doi: 10.1007/s00248-002-1044-x

Vieublé-Gonod, L., Chadoeuf, J., and Chenu, C. (2006). Spatial distribution of microbial 2, 4-dichlorophenoxyacetic acid (2,4-D) mineralization potential at a millimetre scale in soil. *Soil Biol. Biochem.* 35, 373–382. doi: 10.1016/S0038-0717(02)00287-0

Vogel, L., Makowski, D., Garnier, P., Vieublé, L., Coquet, Y., Raynaud, X., et al. (2015). Modeling the effect of soil meso- and macropores topology on the biodegradation of a soluble carbon substrate. *Adv. Water Res.* 83, 123–136. doi: 10.1016/j.advwatres.2015.05.020

Vogel, L. E., Pot, V., Makowski, D., Garnier, P., and Baveye, P. C. (2018). To what extent do uncertainty and sensitivity analyses help unravel the influence of microscale physical and biological drivers in soil carbon dynamics models? *Ecol. Modell.* 383, 10–22. doi: 10.1016/j.ecolmodel.2018.05.007

Vos, M., Wolf, A. B., Jennings, S. J., Kowalchuk, G. A. (2013). Micro-scale determinants of bacterial diversity in soil. *FEMS Microbiol. Rev.* 37, 936–954. doi: 10.1111/1574-6976.12023

Weast, R. C., Astle, M. J., Beyer, W. H. (eds). (1986). *CRC Handbook of Chemistry and Physics,* 66th Edn. Boca Raton, FL: CRC Press.

Werts, S., Degrange, V., Prosser, J. I., Poly, F., Commeaux, C., Freitag, T., et al. (2006). Maintenance of soil functioning following erosion of microbial diversity. *Environ. Microbiol.* 8, 2162–2169. doi: 10.1111/j.1462-2920.2006.01098.x

Zhou, J., Xia, B., Treves, D. S., Wu, L.-Y., Marsh, T. L., O'Neill, R. V., et al. (2002). Spatial and resource factors influencing high microbial diversity in soil. *Appl. Environ. Microbiol.* 68, 326–334. doi: 10.1128/AEM.68.1.326-334.2002

Check for
updates

Vulnerability of Physically Protected Soil Organic Carbon to Loss Under Low Severity Fires

Mathew Jian[1], Asmeret Asefaw Berhe[1], Markus Berli[2] and Teamrat A. Ghezzehei[1]*

[1] Life and Environmental Sciences Department, School of Natural Sciences, University of California, Merced, Merced, CA, United States, [2] Division of Hydrologic Sciences, Desert Research Institute, Las Vegas, NV, United States

Soil aggregate degradation during medium and high severity fires is often identified as the main mechanism that leads to loss of soil organic matter (SOM) due to fire. Low severity fires, however, are considered not to cause aggregate degradation assuming that temperatures <250°C, as occurring during low-severity burns, have only limited effects on the stability of the soil organic binding agents. Recent studies suggest that low severity burns may cause soil aggregate degradation due to rapid vaporization of soil pore water that can induce pressure on the soil aggregates beyond their yield stress. Such pressure-driven degradation of soil aggregates may expose physically protected organic carbon to decomposition. Our study investigated the effect of a low-severity fire on soil organic matter (SOM), water extractable organic C, and N as well as respiration for two initial soil moisture conditions undergoing three "heating regimes" using aggregates from a California forest and a Nevada shrubland soil. We found that initially moist soil aggregates that were rapidly heated up degraded the most, showing increased cumulative carbon mineralization when compared to aggregates that were not heated, aggregates that were dry before being heated, and initially moist soil aggregates that were slowly heated. Our results suggest that exposure of previously physically protected organic carbon within the soil aggregates to oxidative conditions was the most likely cause of increased rates of decomposition of organic matter after low-severity burns. Additionally, we show that for a shrubland soil, aggregates with relatively low organic carbon content, low severity burns increased cumulative carbon mineralization. We hypothesized that this was due to decomposition of cytoplasmic material from lysed microbes. Our results suggest that low severity burns can accelerate decomposition of soil organic carbon (SOC) protected in soil aggregates.

Keywords: aggregation, fire, soil carbon, decomposition, water extractable OM

INTRODUCTION

Fire is a major global controller of ecosystem processes exerting chief controls on soil processes through combustion of organic materials, production, and deposition of charred necromass (or pyrogenic carbon) and influencing several soil physico-chemical conditions (DeBano et al., 1998; Certini, 2005; Araya et al., 2016). The impact of medium-to-high-severity fires (with soil surface temperature of >250°C) on soil processes and properties is widely recognized and has been the

subject of many previous studies (DeBano et al., 1977; Certini, 2005; Carroll et al., 2007; Johnson et al., 2007; Knicker, 2007). Araya et al. (2016, 2017) performed systematic tests of temperature effect on physical properties of five different soils from the western Sierra elevation transect. They subjected the soils to six levels of maximum temperature (150–650°C) and observed statistically significant deterioration in water stable aggregation only for soils heated to 350°C or more. The decline in aggregate stability in the studies of Araya et al. (2016, 2017) was closely related to loss of carbon from macro- and micro-aggregate size classes. In contrast, samples that were subjected to 150–250°C heating did not exhibit loss of bulk soil organic carbon (SOC) nor water stable aggregation. Other field studies of low severity burns have also documented only a little or no effect on soil properties and processes immediately after the fires (DeBano et al., 1977, 1998; Mataix-Solera et al., 2002, 2011; O'Dea, 2007; Arcenegui et al., 2008; Jordan et al., 2011).

However, long-term observations of soil structure following low severity fires have revealed substantial loss of aggregate stability and porosity. These degradations in soil structure often are accompanied by reduced infiltrability and significantly increased susceptibility to wind and water erosion. For example, Úbeda and Bernia (2005) monitored aggregate stability of forest soils in northeastern Spain that experienced low, intermediate, and high severity burns. They noted that immediately after the burns, there was a consistent increase in aggregate stability across the entire burn severity spectrum, but aggregate stability in all the sites (including the low severity sites) was considerably below the control site after 8 months and remained so 2 years after the burn. Similar observations were made after a controlled, low-severity burn conducted in August 2009 at Upper Gleason Creek Watershed in the eastern Great Basin (Nevada). These observations showed a protracted process of soil structure degradation both under the shrub canopy and shrub interspaces (Chief et al., 2012; Kavouras et al., 2012). Under shrub canopies, soil structure degraded from moderate subangular blocky structure to coarse weak subangular blocky immediately after the fire and broke down further in the ensuing 9 months to a structureless soil. In interspaces, soil structure degraded from a moderate-to-strong coarse subangular blocky structure with hard dry consistency to a weak-to-medium subangular blocky structure with soft dry consistency immediately after the burn. The interspace soil became structureless 13 months after the burn. The above observations suggest that the mechanisms of soil structure degradation under low-intensity burns are characteristically different from medium-high severity fire conditions, and that effect of low-severity of fires on soil aggregation and dynamics of aggregate protected carbon in soil necessitates an in-depth investigation on effect of fires on these variables.

In previous study, we hypothesized that soil aggregates subjected to low severity burns can be degraded due to transient elevated gas-phase pressure caused by rapid vaporization of pore water (Albalasmeh et al., 2013). To simulate rapid

heating of surface soils, we placed soil aggregates in pre-heated muffle furnace for 30 min. These were contrasted with aggregates that were gradually heated to the same maximum temperature at 3°C/min. Aggregates subjected to rapid heating in 125–175°C range exhibited significantly lower water stability compared to aggregates heated to the same maximum temperature at a slow rate, although both sets of aggregates did not show measurable loss of SOM. Albalasmeh et al. (2013) was the first study to suggest the importance of rapid vaporization of pre water for soil aggregate degradation during low severity burns (Urbanek, 2013). In a follow up study (Jian et al., 2018), we showed that the gas-phase pressure directly measured inside moist aggregates rises to a level that is comparable to the tensile strength of the aggregates.

It follows then that deterioration of soil aggregates by the previously-described mechanism may also adversely impact physical protection of SOM from decomposition and leaching (Tisdall, 1996; Hassink and Whitmore, 1997; Piccolo and Mbagwu, 1999; Balesdent et al., 2000; Chenu and Plante, 2006; Schmidt et al., 2011). The mechanisms of physical protection of SOM within aggregates can include: adsorption of organic compounds on to solid mineral surfaces, with pockets of water-saturated pores where SOM decomposition is limited by oxygen availability, and complex pore geometry and tortuosity of diffusion pathways that limit diffusion of water, oxygen, and organic substrates to soil decomposers. SOM occluded within aggregates accounts for large fraction of the total SOM and tends to have significantly longer turnover time than bulk SOC (Flessa et al., 2008). Historically, the effects of low severity fires on soils on aggregation as well as carbon and nitrogen dynamics has received very little attention (Moghaddas and Stephens, 2007).

The present study was designed to test a follow up hypothesis that weakening of soil structure during low-severity burns leads to accelerated loss of SOM previously physically protected within aggregates. Specifically, we hypothesized that leaching loss of water extractable organic carbon (WEOC) and decomposition rate of SOC would be higher in soils subjected to rapid heating, albeit to <200°C. To test these hypotheses we conducted simulated burn experiments that can induce weakening of soil aggregates by rapid vaporization of pore water and compared with control samples in terms of (a) quantity and quality of water extractable C and N and (b) the rate of carbon mineralization in the burned samples with control treatments.

The often overlooked physical and biogeochemical impact of low severity fires is likely to cover a substantial proportion of the land exposed to natural and controlled fires. For example, half of the combined wildfire and prescribed burn area reported in the U.S. between 1984 and 2016 was characterized as low in intensity (time-averaged energy flux) and severity (degree of ecological effects) (Eidenshink et al., 2007; Keeley, 2009; MTBS, 2017) and appears to have been gradually increasing in aerial proportion over the last three decades (Jian et al., 2018). Similarly, about 80% of the burned area in Russia's boreal forest is characterized as low severity surface fire (Conard et al., 2002).

MATERIALS AND METHODS

Soil Sampling

Soil samples were collected from two distinct ecosystems that experience low severity fires in the western United States. The first soil was a sandy loam (Ultic Haploxeralfs, Holland series) collected from an undisturbed pine forest in Mariposa County, United States. The second soil was a loam (Calcic Petrocalcids, Purob series) collected from an unburned shrubland near Las Vegas, Nevada (adjacent to the burn boundary of the Carpenter 1 Fire) in Clark County, United States. In the subsequent sections of this paper, these soils will be referred to as forest and shrubland soils, respectively.

Soil samples were collected from 0 to 10 cm depth, which represents the soil layer that is most impacted by low severity surface fires. The samples, were air dried and separated into three aggregate size fractions (0.25–1, 1–2, and 2–4 mm) by dry sieving. The separated fractions were then homogenized by gentle manual mixing. Characteristics of the soils are provided in **Table 1**.

Simulated Burn Experiments

Low severity fire can affect dynamics of SOM via chemical, biological, or physical processes. Exposure of soil to elevated temperature can desiccate organic (e.g., sticky extracellular polymeric substances) and inorganic molecules (e.g., clay and carbonates) that bind soil particles together (Tisdall and Oades, 1982). This chemical transformation of binding agents can degrade aggregates thereby exposing physically protected SOM. Likewise, the population and community structure of soil microorganisms can be altered by high temperature in a way that can alter rate of mineralization. In this study, we were primarily concerned with additional mechanical disturbance of aggregates by rapid rise in the gas phase pressure, which arises when wet soil is exposed to direct source of heat (e.g., flame).

The effect of low severity burn on soil aggregates was simulated by placing aggregates equilibrated to a matric potential of −30 kPa ("field capacity") inside muffle furnace pre-heated to 175°C. The samples were exposed to this temperature for 30 min, which is equivalent to the time it takes for small dry logs to burn (Stoof et al., 2010). Direct placement in pre-heated furnace mimics the rapid temperature rise of surface soil that exposed to flame from burning biomass. These aggregates were expected to experience rapid rise in pneumatic pressure due to rapidly vaporizing pore water, which momentarily exerts destabilizing stress as it escapes (Albalasmeh et al., 2013; Jian et al., 2018). This form of heat treatment is referred to as "Rapid Burn" (RB) in the remainder of this paper. To distinguish the mechanical effect of the gas pressure from other biological or chemical effects due to elevated temperature (e.g., lysing of soil microbes or desiccation of organic molecules, respectively) we designed two additional heating experiments. In the first, which will be referred to as "Slow Burn" (SB), aggregates were prepared in identical manner as in the RB treatment but placed inside muffle furnace at room temperature (∼25°C) before being heated at 3°C/min until the furnace reached 175°C (which takes ∼1 h). The samples were then kept at 175° for 30 min

TABLE 1 | Characterization of studied soils (mean ± standard error, where $n =$ 3–5.

Soil	Aggregate size (mm)	Field capacity water content (g/g)	Organic carbon (%)	Clay (%)
Forest	0.25–1	0.328 ± 0.001	5.73 ± 0.07	11.55 ± 4.90*
	1–2	0.252 ± 0.003	4.67 ± 0.10	
	2–4	0.286 ± 0.012	3.58 ± 0.10	
Shrubland	0.25–1	0.165 ± 0.002	1.25 ± 0.02	21.05 ± 0.86
	1–2	0.145 ± 0.001	0.70 ± 0.01	
	2–4	0.120 ± 0.002	0.53 ± 0.01	

*Clay content is expressed in mean ± standard deviation, where $n = 4$ for forest soil and $n = 3$ for shrubland soil). *Value previously reported by Albalasmeh et al. (2013).*

so that exposure to the peak temperature is comparable to the RB treatment. However, the aggregates in the SB treatment receive higher total heat energy input and longer exposure (∼60 min) during the temperature rise phase. In a third heating experiment initially air-dried samples (matric potential of ∼30 MPa) were subjected to the same heating regime as for the RB treatment. This treatment, which will be referred to as "Slow Rapid Burn" (SRB) exposes the aggregates to the same total amount of heat energy and duration as the main RB treatment, but avoids the generation of potentially disruptive high water vapor pressure by keeping the initial moisture content of the aggregates at a minimum. As an overall control, untreated aggregates (denoted as UB) were kept at room temperature. Aggregates in the SB and DRB treatments were expected to exhibit chemical and biological effects on the quantity and quality of water extractable organic matter as well as the rate of mineralization. While aggregates in the RB treatment will exhibit additional physical effect of aggregate disruption by elevated pore pressure.

Moisture Equilibration of Soil Aggregates

The water content of the aggregates at field capacity ws determined using pressure plate apparatus (Soilmoisture Equipment Corp, Goleta CA). Briefly, triplicate sets of 5 g of soil aggregate samples from each soil type and aggregate size were placed on pre-wetted porous ceramic plates inside a pressure plate apparatus. Then, the aggregates were wetted by lightly spraying a fine mist of water and subsequently by capillary action from a thin film of water on top of the porous plates. Then, the aggregates were equilibrated to a matric potential of −30 kPa ("field capacity") for 24 h. Subsequently, the samples were transferred to aluminum weighing dishes and their gravimetric water content was determined by drying them in an oven at 105°C for 24 h. The gravimetric water contents of the soil aggregates are summarized in **Table 1.**

Leaching of Water Extractable Organic Matter

The goal of this experiment was to test whether low severity burn frees leachable organic matter previously protected inside stable aggregates. To achieve this, we measured the quantity and quality

of water extractable organic matter from aggregates subjected to the four treatments described above: RB, SB, DRB, and UB.

Prior to the heating treatments, 10 g of soil aggregates from the 2–4 mm size fraction were added to stainless steel cups with plastic lids. Water was slowly added onto the SB and RB treatment of soil aggregates by lightly spraying with a fine mist of water to get the water content of the soil aggregates to field capacity. The cups were then capped and the samples were allowed to equilibrate for 16 h. Then, the aggregates were subjected to the four burn treatments as described in Section Simulated Burn Experiments.

Soil aggregates were transferred onto pre-saturated porous plates in a Tempe Cell set-up (Soilmoisture Equipment Corp, Goleta CA). The aggregates were wetted by lightly spraying with a fine mist to avoid slaking. Then, additional 40 mL of deionized water was slowly added into the Tempe Cell and the aggregates were allowed to soak for 15 min. Afterwards, 10 kPa of pressure was applied for 10 min to extract the soil leachate from the Tempe Cell. The leachate was then further filtered through a 0.45 μm filter paper and stored in the dark at 4°C for a maximum of 14 days. The water extractable organic C and N concentrations (WEOC and TN, respectively) in the leachate were measured using a Shimadzu TOC-Vcsh analyzer.

Chemical composition of the soil leachate was analyzed using a Thermo Scientific Evolution 3000 Ultraviolet-Visible (UV-VIS) spectrophotometer Absorbance was measured between 200 and 560 nm, using ultrapure water as blank. Measurements were performed using a quartz cell with 1.25 cm path length. The specific UV absorbance at 254 nm ($SUVA_{254}$) was used to determine whether there were changes in aromaticity of the WEOC in the burned samples. $SUVA_{254}$ was calculated by normalizing the specific absorbance coefficient at 254 nm by the WEOC concentration. The ratio of absorption at 250–365 nm (A_{250}:A_{365}) was used to estimate the average molecular size of the WEOC in the soil leachate as high molecular weight. Molecules absorb light at longer wavelengths than at shorter wavelengths (Santos et al., 2016).

Mineralization of Organic Matter-Incubation Experiment

The goal of the heating experiments was to test whether degradation of aggregate stability by elevated steam pressure generated by rapid vaporization of pore water can lead to higher rates of SOC mineralization. Prior to the heating treatment, 5 g of soil aggregates in the 0.25–1 mm and the 1–2 mm size fraction per sample were placed into 50 mL glass vials with caps equipped with rubber septa. Then, the aggregates were subjected to the four burn treatments as described in Section Simulated Burn Experiments.

The samples were then wetted to field capacity with a micropipette, capped and allowed to equilibrate for 24 h. Afterwards, the caps were removed and the vials were covered with Parafilm® and incubated at 21°C in the dark for over 2 months. The vials were weighed every 3–7 days and water was added to maintain the initial moisture content. Gas samples were pulled from the forest sample vials on days 1, 2, 3, 5, 7, 10, 13,

17, 21, 26, 31, 37, 43, 50, 57, and 65 by capping the vial for 3 h and extracting 15 mL of gas through the septa on the vial caps. Gas samples were pulled from the shrubland samples in a similar fashion on days 1, 2, 3, 5, 7 10, and 13. Gas samples were also collected in subsequent days for the shrubland samples, but CO_2 flux rates were within measurement errors of the gas chromatographer used to analyze the samples. The samples were then analyzed on a gas chromatograph (Shimadzu GC-2014) fitted with a thermal conductivity detector to determine the concentration of carbon dioxide.

The change in SOC stock due to mineralization can be described using a first order kinetics model (Jenny, 1980).

$$\frac{dC}{dt} = -\kappa C \tag{1}$$

Where, C (C-mass/ soil-mass) is the quantity of mineralizable C and k (1/time) is the rate constant of mineralization. Assuming the soil remained under constant environmental conditions, the equation can be solved to provide an exponential decay of soil C content

$$C = C_0 e^{-\kappa t} \tag{2}$$

Where, C_0 is the initial stock of the biologically active C pool. The CO_2 efflux at time t can be given as

$$C_{CO_2} = C_0(1 - e^{-\kappa t}) \tag{3}$$

The linearity of the model permits expansion to multiple C pools that exhibit differing dynamics.

$$C_{CO_2} = \sum_{i=1}^{N} C_{0,i}(1 - e^{-\kappa_i t}) \tag{4}$$

A two-pool model appropriate for the rapid-burned soils will be introduced in subsequent section. The unknown parameters can be estimated by fitting the model to experimental data.

Statistical Analysis

Comparisons of burn treatments for WEOC concentration, $SUVA_{254}$, and A250:A365 in the soil leachate, and initial mineralizable C pool and rate constant of mineralization of for the CO_2 measurements were performed using one-way ANOVA, and pairwise comparison of burn treatments was performed using Tukey's test at $p < 0.05$ significance level when applicable. All analyses were conducted using R statistical software (r-project.org).

RESULTS

Water Extractable Organic C and N Concentrations

The mean WEOC concentration of the leachate from the UB forest aggregates was 3.38 ± 0.18 mg-C g-SOC^{-1} (**Figure 1**). All three heating treatments (RB, SB, and DRB) significantly increased the WEOC concentration when compared to the leachate from the UB aggregates ($P < 0.05$). Moreover, WEOC of the SB and DRB treatments were significantly higher than that

FIGURE 1 | Water extractableorganic carbon (mg L^{-1}) in the soil leachate from unburned (UB), dry rapidly burned (DRB), slowly burned (SB), and rapidly burned (RB) soil aggregates from **(A)** forest soil and **(B)** shrubland soil. Different letters represent significantly different means as determined from Tukey's HSD Test ($P < 0.05$).

FIGURE 2 | Carbon to Nitrogen ratio (C:N) of the water extractable organic matter **(A,B)** and the whole aggregates **(C,D)** for the forest **(A,C)** and shrubland **(B,D)** aggregates.

of the RB treatment ($P < 0.05$). Overall, heat treatment increased the WEOC concentration by a factor of $\times 2.1$– $\times 2.8$ relative to the UB treatment.

The mean WEOC concentration of the leachate in from UB shrubland aggregates was 2.23 ± 1.22 mg-C g-SOC^{-1}. The WEOC concentrations for the DRB, SB, and RB treatments were all significantly higher ($P < 0.05$) than for UB by factors of $\times 7.1$, $\times 9.88$, $\times 7.17$, respectively. The SB treatment yielded significantly higher WEOC than the DRB and RB treatments as well.

C:N Ratios of Leachate and Aggregates

The C:N ratios of the water extractable organic matter and the aggregates subjected to the four treatments are shown in **Figure 2**. The C:N ratios of the leachates were significantly ($P < 0.05$) higher in the burned samples (SB, DRB, and RB) compared to UB samples for both the forest and shrubland soils (**Figures 2A, B**, respectively). In addition, in the forest soils, the C:N ratio was significantly ($P < 0.05$) higher for the rapidly burned (RB) aggregates comparted to the dry-rapidly burned (DRB) and slow burned (SB) aggregates (**Figure 2A**). However, there were no significant differences between the burned samples of the shrubland soils (**Figure 2A**).

There were no significant differences in C:N ratio of the SOM remaining in the forest aggregates subjected to the four burn treatments (**Figure 2C**). For the shrubland aggregates, however, RB caused a decrease in C:N ratio of the aggregates compared to the UB aggregates. But there were no other significant differences among the burned samples (SB, DRB, and RB) or between the DRB and SB to the UB aggregates (**Figure 2D**).

Specific Ultraviolet Absorbance of Leachate

SUVA$_{254}$ of UB treatment of forest soil was 1.26 ± 0.03 L mgC^{-1} m^{-1} (**Figure 3A**). The DRB treatment of forest soil was not significantly different than the UB treatment ($P > 0.05$, SUVA$_{254} = 1.02 \pm 0.12$ L mgC^{-1} m^{-1}). The RB and SB treatment
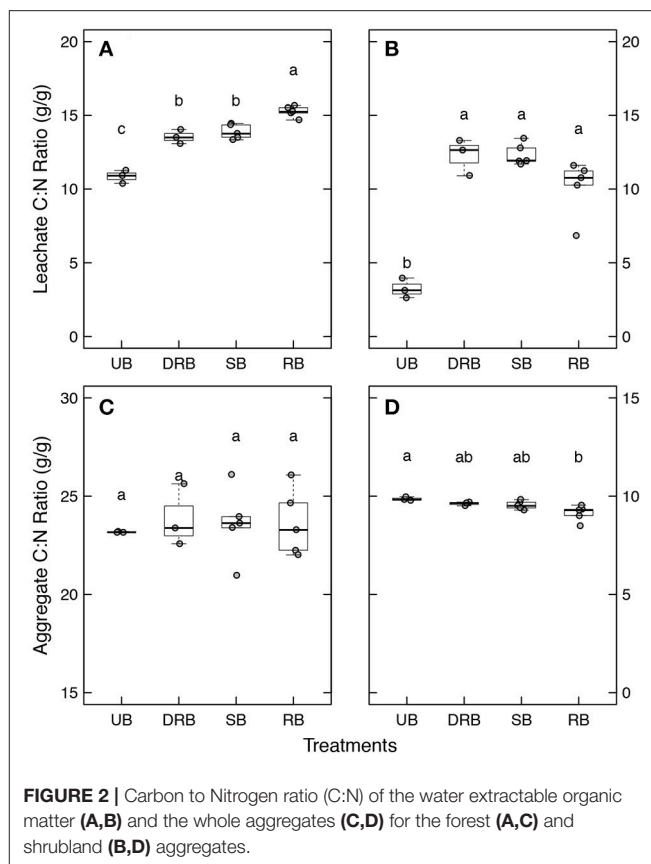
had SUVA$_{254}$ of 0.92 ± 0.03 and 0.88 ± 0.03 L mgC^{-1} m^{-1}, respectively. The SUVA$_{254}$ values for RB and SB treatment were significantly lower than the UB treatment ($P < 0.05$), but neither significantly differed from the DRB treatment ($P > 0.05$).
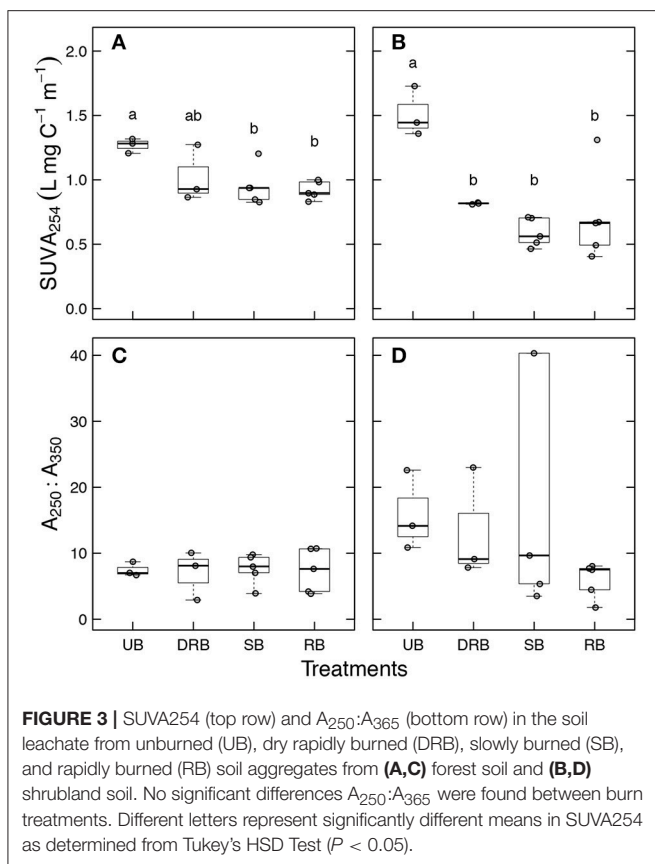
SUVA$_{254}$ of UB treatment of shrubland soil was 1.51 ± 0.11 L mgC^{-1} m^{-1} (**Figure 3B**). The DRB, RB, and SB treatments had DOC concentrations of 0.82 ± 0.00, 0.56 ± 0.07, and 0.59 ± 0.05 L mgC^{-1} m^{-1}, respectively. All three treatments had SUVA$_{254}$ significantly lower than the UB treatment ($P < 0.05$). None of the three treatments had SUVA$_{254}$ that significantly differed from each other ($P > 0.05$).

Average Molecular Size of WEOC

The heating treatments did not appear to have a significant effect on the average molecular size of SOC in the forest soil leachate (**Figure 3C**). A decrease in A$_{250}$:A$_{365}$ ratio indicates an increase in average molecular sizes. This appears to be the trend for RB and SB treatment in the shrubland soil (**Figure 3D**) with A$_{250}$:A$_{365}$ values of 5.9 ± 1.2, and 6.2 ± 1.8, respectively, and the UB treatment with an A$_{250}$:A$_{365}$ value of 15.9 ± 6.0. However, none of the burn treatments had an average molecular size of WEOC that significantly differed from each other ($P > 0.05$).

CO$_2$ Evolution

Figures 4, 5 show the cumulative CO$_2$-C loss over the course of the CO$_2$ measurements for the individual forest and shrubland soil samples, respectively. Each individual sample was shown in

FIGURE 3 | SUVA254 (top row) and A_{250}:A_{365} (bottom row) in the soil leachate from unburned (UB), dry rapidly burned (DRB), slowly burned (SB), and rapidly burned (RB) soil aggregates from **(A,C)** forest soil and **(B,D)** shrubland soil. No significant differences A_{250}:A_{365} were found between burn treatments. Different letters represent significantly different means in SUVA254 as determined from Tukey's HSD Test ($P < 0.05$).

order to highlight the variability in respiration between replicates. Analysis of the cumulative CO_2-C loss and rate constant of mineralization is shown in the succeeding paragraphs.

The RB of forest soil exhibits distinct two-pool pattern, indicated by the arrows in **Figure 4**. The second pool of carbon appears to have delayed onset of mineralization. To capture this bimodality

$$C_{CO_2} = \begin{cases} C_{0,1}(1-e^{-\kappa t}) & t < t_X \\ C_{0,1}(1-e^{-\kappa t}) + C_{0,2}(1-e^{-\kappa(t-t_X)}) & t \geq t_X \end{cases} \quad (5)$$

Where, t_X denotes the onset of mineralization in the secondary pool. The initial mineralizable C in both pools is C_0 is $C_0 = C_{0,1} + C_{0,2}$. To minimize the degrees of freedom of the fitted model, both pools were assumed to have identical decay rate. The fitted delayed onset of rapid mineralization (t_X) ranged between of 21.1 ± 2.4 and 19.9 ± 1.8 days for soil aggregates of size 0.25–1 and 1–2 mm, respectively. All the remaining CO_2 evolution datasets were individually fit with single-pool linear decomposition model, Equation (3).

C_0 of the UB treatment of forest soil with aggregate size from 0.25–1 mm was $1,988.1 \pm 158.5$ µgC g soil^{-1}. The DRB and SB treatment of forest soil with aggregate size 0.25–1 mm had C_0 of $2,229.2 \pm 192.7$ and $1,432.7 \pm 112.0$ µgC g soil^{-1}, respectively. Neither of these samples showed C_0 values that significantly differed from the UB treatment. The RB treatment has $C_0 = 3,884.6 \pm 716.7$ µgC g soil^{-1}, which significantly differed from

the other three treatments ($P < 0.05$). Similar results were found for the forest soil with aggregate sizes ranging from 1 to 2 mm in size ($P < 0.05$). The ratio of the biologically available pool of carbon to the total carbon pool (C_0:C_a) follows the same trend (**Table 2**) as C_0 to the treatments.

C_0 of the UB treatment of shrubland soil with aggregate size from 0.25 to 1 mm was 34.1 ± 9.1 µgC g soil^{-1}. The DRB sample had C_0 that did not significantly differ from the UB treatment (68.3 ± 13.6 µgC g soil^{-1}, $P > 0.05$). The SB and RB samples had C_0 values of 99.3 ± 18.2 and 93.8 ± 9.3 µgC g soil^{-1}, respectively. The SB and RB treatments had C_0 that were significantly higher than the UB treatment ($P < 0.05$). Neither of the samples significantly differed from the DRB treatment. For the shrubland soil with aggregate size from 1–2 mm, none of the treatments significantly differed each other ($P > 0.05$, 67.0 ± 14.3, 46.7 ± 5.0, 62.1 ± 7.2, 47.9 ± 2.9 µgC g soil^{-1} for the UB, DRB, SB, and RB treatment, respectively). The ratio of the biologically available pool of carbon to the total carbon pool (C_0:C_a) follows the same trend (**Table 2**) as C_0 to the treatments.

The decay rate of the active C pool (k) of the UB treatment of forest soil with aggregate size from 0.25–1 mm was 0.048 ± 0.003 day^{-1} (**Table 2**). The DRB, SB, and RB treatments had k values of 0.051 ± 0.002, 0.052 ± 0.004, and 0.035 ± 0.001 day^{-1}, respectively. None of the three treatments significantly differed from the UB treatment ($P > 0.05$), but the RB treatment significantly differed from the DRB and SB treatment ($P < 0.05$). The UB treatment of forest soil with aggregate size from 1 to 2 mm was 0.053 ± 0.006 day^{-1}. The DRB and SB treatment did not significantly differ from the UB treatment ($P > 0.05$, 0.049 ± 0.007 day^{-1}, and 0.040 ± 0.003 day^{-1}, respectively). The RB treatment significantly differed from the UB treatment ($P < 0.05$, 0.035 ± 0.004 day^{-1}), but did not significantly differ from the DRB and SB treatment ($P > 0.05$).

The decay constant k of the UB treatment of shrubland soil with aggregate size from 0.25 to 1 mm was 0.290 ± 0.032 day^{-1}. The DRB and SB treatments had k values of 0.328 ± 0.053, and 0.173 ± 0.016 day^{-1}, respectively. Both of these treatments did not significantly differ from the UB treatment. The RB treatment had $k = 0.450 \pm 0.037$ day^{-1}, which was significantly higher than the UB treatment ($P < 0.05$), but was not significantly higher than the DRB treatment ($P > 0.05$). A similar trend is observed for shrubland soil with aggregate size from 1 to 2 mm. However, DRB treatment differed significantly from the UB treatment ($P < 0.05$).

DISCUSSION

Water Extractable Organic Matter Quantity and Quality

The increase in the concentration of WEOC in leachate across all of the burn treatments when compared to the UB control is consistent with previous soil heating studies. For example, Santos et al. (2016) and Choromanska and DeLuca (2002) saw an increase in WEOC when burning
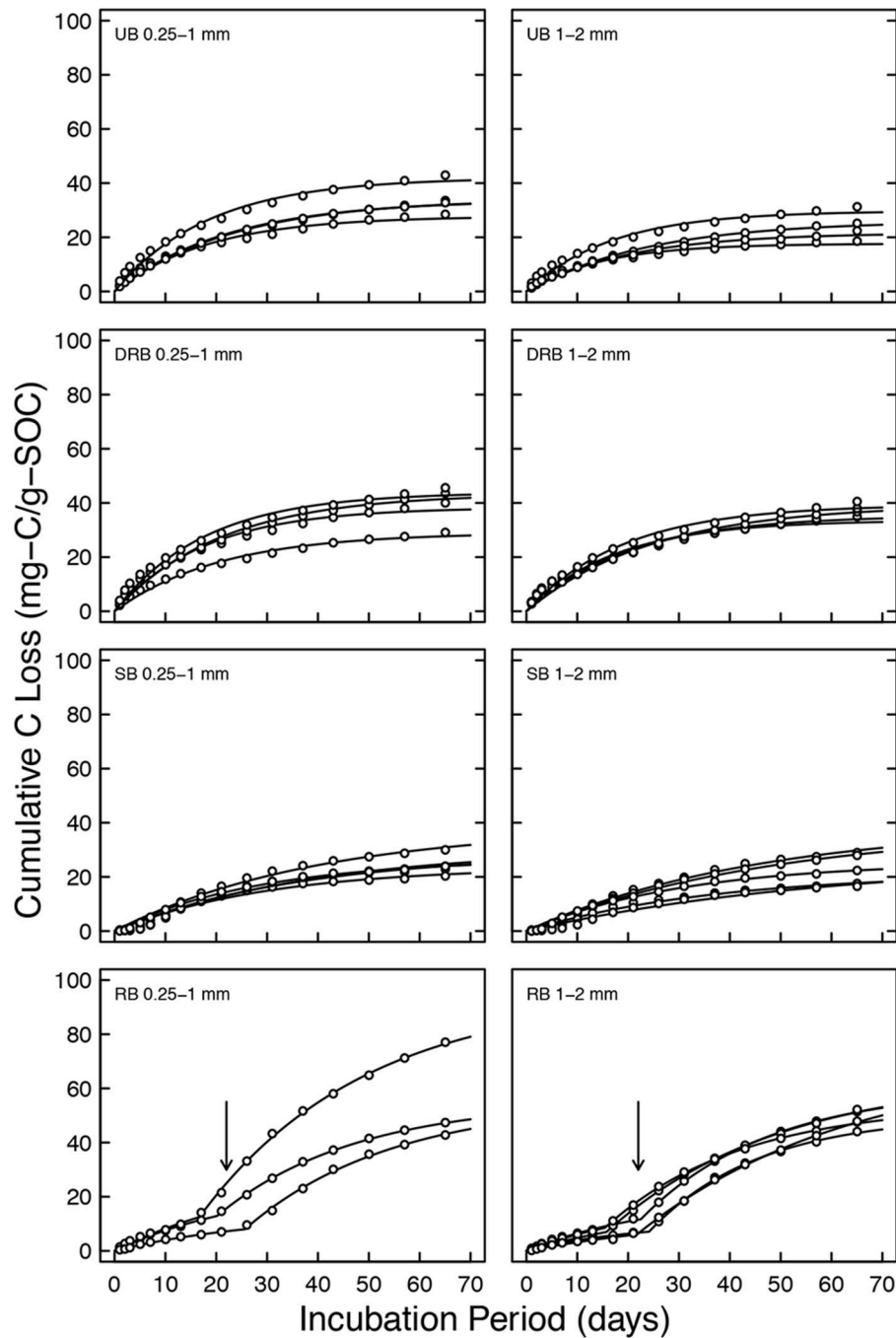
FIGURE 4 | Cumulative CO_2-C loss in μgC g soil^{-1} for forest soil with aggregate sizes of 0.25–1 and 1–2 mm. Solid lines are model fits. Arrows indicate delayed onset of rapid mineralization.

soils at around 150–250°C. Increase in WEOC concentration have been seen in burns as high as 400°C (Guerrero et al., 2005). Previous studies have suggested that the increase in WEOC in burned soil samples is attributed to soluble organic compounds derived from the lysis of microbial cells at such temperature (Serrasolsas and Khanna, 1995; Santos et al., 2016).

These C:N ratio of leachates results are consistent with the CO_2 evolution data we reported. Aggregates from the forest soil experienced substantial disruption during RB, which lead to release of previously occluded SOM by leaching (**Figure 3**) and delayed but higher rate of CO_2 release (**Figures 4**, **6**). Relatively faster loss of N vs. C could also lead to higher C:N ratio. But, considering the multiples line of evidence
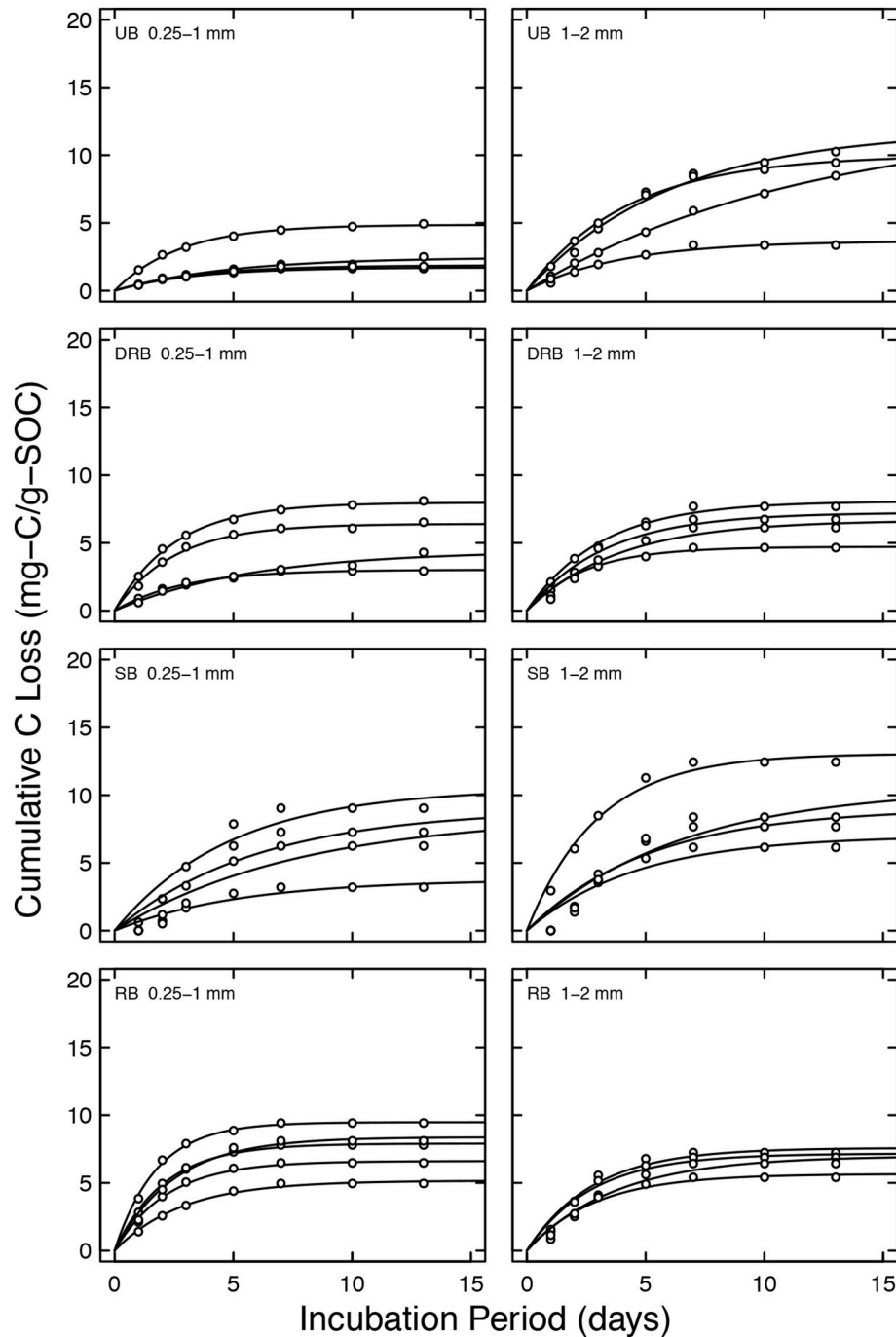
FIGURE 5 | Cumulative CO_2-C loss in μgC g soil^{-1} for shrubland soil aggregates of two size classes: 0.25–1 and 1–2 mm. Solid lines are model fits.
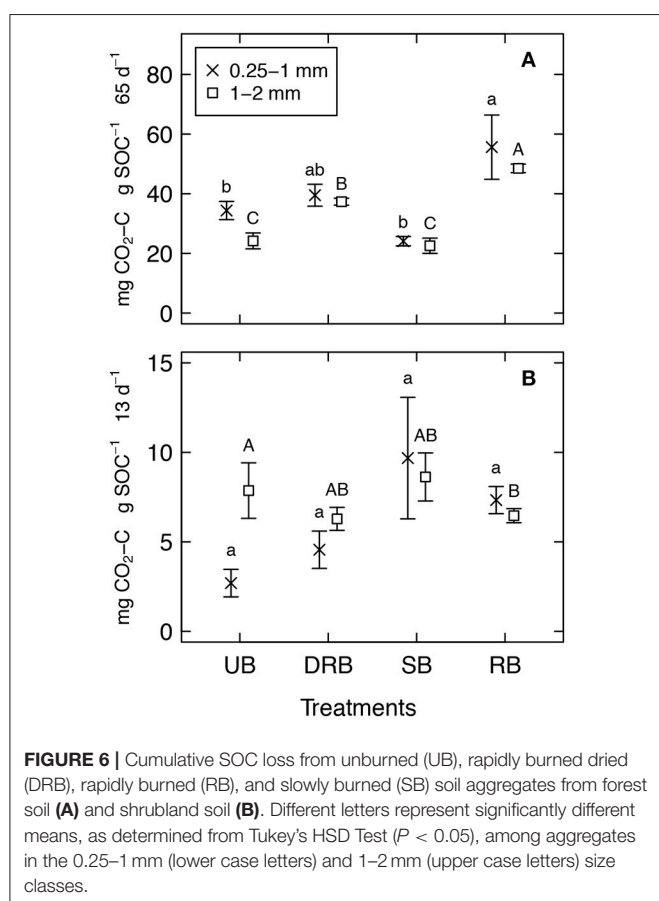
for aggregate breakdown, high rate of CO_2 flux post-burn, and the C:N of the leachate, it is more plausible that the observed increase in C:N ratio of leachate post-burn is due to release of microbially-processed organic matter due to aggregate disruption.

C:N ratio of the aggregates. This further supports the observation that rapid burn of moist soils liberates mobile and

easily decomposable SOM that does not remain in noticeable quantity after the incubation period, but does not have significant effect on the OM that remains associated with soil minerals physically (inside smaller aggregates) or chemically (through sorptive interactions). Many of these microbial derived organic compounds can include oxygenated (such as carbohydrates and proteins) and aliphatic groups. These microbial derived organic

TABLE 2 | C_0:C_a [the ratio of the biologically available carbon pool to the total carbon pool (C_a)] of unburned (UB), rapidly burned dried (DRB), rapidly burned (RB), and slowly burned (SB) soil aggregates from forest soil with aggregate sizes 0.25–1 and 1–2 mm, and shrubland soil with aggregate sizes 0.25–1 mm and 1–2 mm.

			Treatment			
	Soil	Aggregate size (mm)	UB	DRB	SB	RB
C_0:C_a	Forest	0.25–1	3.54 ± 0.29	3.75 ± 0.21	2.53 ± 0.24	7.01 ± 1.26
		1–2	2.19 ± 0.21	3.59 ± 0.12	2.37 ± 0.36	5.97 ± 0.46
	Shrubland	0.25–1	0.27 ± 0.07	0.55 ± 0.11	0.77 ± 0.13	0.71 ± 0.06
		1–2	0.90 ± 0.18	0.65 ± 0.07	1.00 ± 0.08	0.69 ± 0.04
k (day^{-1})	Forest	0.25–1	0.046 ± 0.003	0.051 ± 0.002	0.052 ± 0.004	0.035 ± 0.001
		1–2	0.053 ± 0.006	0.049 ± 0.003	0.040 ± 0.004	0.035 ± 0.004
	Shrubland	0.25–1	0.290 ± 0.032	0.328 ± 0.053	0.173 ± 0.016	0.450 ± 0.037
		1–2	0.183 ± 0.038	0.322 ± 0.031	0.189 ± 0.018	0.336 ± 0.023

FIGURE 6 | Cumulative SOC loss from unburned (UB), rapidly burned dried (DRB), rapidly burned (RB), and slowly burned (SB) soil aggregates from forest soil (A) and shrubland soil (B). Different letters represent significantly different means, as determined from Tukey's HSD Test ($P < 0.05$), among aggregates in the 0.25–1 mm (lower case letters) and 1–2 mm (upper case letters) size classes.

compounds may explain the decrease in SUVA$_{254}$ (aromaticity) in the burned treatments of the soil samples. Our results from the UV-Vis analyses are consistent with previous studies that showed that SUVA$_{254}$ decreased when soils were burned between 150 and 250°C (Santos et al., 2016). Generally, the existence of aromatic compounds in burned soil samples comes from enrichment of existing aromatic compounds or formation of new aromatic compounds from the thermal decomposition of existing organic matter. However, this generally occurs when soils are burned at above 300°C (González-Pérez et al., 2004). As there is probably

little to no addition of aromatic compounds into the dissolved state of the OC, while the addition of fresh, presumably labile, microbial derived organic compounds diluted the pre-existing aromatic component of WEOC, and thus causing a decrease in SUVA$_{254}$.

The average apparent molecular size of the WEOC in the leachate did not significantly differ from the UB control samples. This result differed from a previous study in which WEOC from soils heated to 150–250°C significantly increased average molecular size (i.e., higher A$_{250}$:A$_{365}$) (Santos et al., 2016). In their study, they suggested that heating samples at those temperatures resulted in small-size molecules undergoing polymerization reactions that resulted in larger molecules. It is also possible that smaller molecular size WEOC are preferentially lost when heated between those temperatures, resulting in a pool of carbon enriched with higher molecular size compounds. However, in the Santos et al. (2016) study the soil samples were heated at the maximum temperature for 1 h, whereas we heated our samples at the maximum temperature for 30 min. Such thermal degradation and/or polymerization of WEOC may be time duration dependent, or even moisture dependent as shown by the increase in average molecular weight of WEOC in the SB and RB treatment of the shrubland soil. However, the differences in average molecular weight of the SB and RB treatment were not significantly different than the UB control treatment. Since the average molecular weight does not differ amongst the treatments, it can be inferred that the WEOC diffuses within the soil pore water at relatively the same rate assuming that pore sizes and geometry remain the same. Diffusion and/or physical accessibility of organic substrate to microorganisms is an important factor in decomposition of the substrate as most soil microbial processes require water (Balesdent et al., 2000). It is also possible that there were changes in the average apparent molecular size of the WEOC in the leachate for the SB and RB sample when compared to the UB samples of the shrubland soil, but it was not apparent in the statistical analysis since there were large variability in the UB and DRB samples.

In conclusion, both the forest and shrubland soils had higher WEOC concentration for all three burn treatments when compared to the UB control treatment. The increase

in WEOC is likely from biodegradable cytoplasmic organic compounds from the lysis of microbial cells. Moreover, the average molecular weight of the WEOC in the burned treatments do not differ from each other nor when compared to the UB treatment, therefore the WEOC should diffuse at relatively the same rate to microbes for decomposition. These observations indicate that the burned treatments should have higher decomposition and respiration of CO_2 over a course of an incubation experiment since there is more WEOC to decompose.

CO₂ Measurements in Forest Soil

For both the forest soil with aggregate sizes 0.25–1 and 1–2 mm, the total respiration of C for the DRB and SB treatment did not significantly differ from the UB treatment for the respective sizes (**Figures 4**, **6A**), even though both of those treatments were shown to have significantly higher amounts of WEOC in the 2–4 mm sized aggregates. The only treatment to have significantly higher total respiration of C was the RB treatment. This is likely linked to the microscopic breakdown of the soil aggregates from the stress induced by the rapid vaporization of soil pore water as proposed by Albalasmeh et al. (2013) and Jian et al. (2018). Aggregated soils are known to have higher tortuosity (Horn and Smucker, 2005) and more complex soil pore geometries that limit diffusion pathways for microbes to have access to OC for respiration (Scow and Alexander, 1992; Balesdent et al., 2000). The degradation of soil aggregation by rapidly vaporized soil pore water from the low severity burn likely contributed to the decrease in tortuosity and complex soil pore geometries within the RB treatment of forest soil. This likely allowed the soil microbes to have easier access to the WEOC within the soil aggregates.

This is also evident as the RB treatments took a considerable amount of time (t_2 of 21.1 $\pm$ 2.4 and 19.9 $\pm$ 1.8 days for soil aggregates of size 0.25–1, and 1–2 mm, respectively) until increased CO_2 flux from the secondary pool commenced. Initially, the rapidly vaporized water slightly weakened the soil aggregate but did not fully break up the soil aggregate to expose physically protected OC. After some time, the soil aggregates break and weaken more to expose the previously physically protected OC. This is consistent with the long-term study made on the soil structure of a shrubland in the eastern Great Basin in Nevada after a controlled, low severity burn was conducted in August 2009 (Chief et al., 2012; Kavouras et al., 2012). Five days after the burn, the soil structure degraded slightly from a moderate subangular blocky structure to coarse weak subangular blocky structure. After around 9 months, the soil structure broke down further to a structureless soil. In another long-term study, the aggregate stability of forest soils from northeastern Spain that experienced a low severity burn was shown to increase immediately after the burn (Úbeda and Bernia, 2005). This was attributed to desiccation of inorganic cementing agents. However, after 8 months the aggregate stability decreased significantly when compared to unburned soil. Both of these study sites, and our findings, highlight the importance of how

the degradation of soil aggregates by rapidly vaporized soil pore water during low severity burns can take considerable amount of time.

The first order decay constant (k) across all treatments was relatively unchanged when compared to the UB control treatment. However, k was slightly lower in the RB treatments, which meant that the OC in the RB treatments decay at a slower rate. This is probably due to the pool of C being accessed to decomposition in the RB treatment being mostly particulate OC (POC). POC is generally the form of OC that is occluded within soil aggregates, and are known to be less labile and decomposable than free and loose organic matter (Christensen, 2001). This further highlight that the soil aggregates are degrading for the RB treatment, since the soil decomposers in the RB treatment are able to access the pool of C within the soil aggregates that the soil decomposers in the other treatments are not able to access.

CO₂ Measurements in Shrubland Soil

For the shrubland soil with aggregate size 1–2 mm, there were no differences in total respiration of C across all the treatments. One possible explanation for no difference in respiration could be that the total amount of organic carbon was very small. The TOC content in the shrubland aggregates of 1–2 mm in size is 0.70 $\pm$ 0.01%, whereas the TOC content for the forest aggregates of size 0.25–1 and 1–2 mm, and the shrubland aggregates of size 0.25–1 mm are 5.73 $\pm$ 0.07, 4.67 $\pm$ 0.09, and 1.25 $\pm$ 0.02%, respectively (**Table 1**). Since the shrubland aggregates of size 1–2 mm had such low amount of OC, the addition of DOC in the form of microbial lysis may not have contributed too much to additional respiration.

CONCLUSION

This study highlights the important effects that low severity burn may have on carbon mineralization rate of soil aggregates from two distinct ecosystems. For the forest soil, with high degree of aggregation, low severity burns can rapidly vaporize soil water thereby inducing mechanical stresses that cause soil disaggregation over time. This leads to liberation of previously, physically protected SOC, thus increasing the amount of carbon mineralized. We also showed that for a shrubland soil with low degree of aggregation and OC content, low severity burns can induce microbial lysis. The lysis of microbes can release biodegradable cytoplasmic organic compounds, which can also increase carbon mineralization in the shrubland soil. Results from both of these distinct ecosystems highlight that low severity burns may affect the geochemistry of soil aggregates, in particular SOM composition and content, leading to SOM loss and eventually aggregate degradation as reported in literature for weeks to months after a fire. Low severity fires were so far considered to have little effects on soil structure due to relatively low temperature and duration of the fire. Therefore, these results warrant further investigations of these types of fires onto soil properties, as low severity burns constitute

the majority of fires in the United States and there are limited numbers of studies on these types of fires on soil aggregation.

AUTHOR CONTRIBUTIONS

FUNDING

REFERENCES

Albalasmeh, A. A., Berli, M., Shafer, D. S., and Ghezzehei, T. A. (2013). Degradation of moist soil aggregates by rapid temperature rise under low severity fire. *Plant Soil* 362, 335–344. doi: 10.1007/s11104-012-1408-z

Araya, S. N., Fogel, M. L., and Berhe, A. A. (2017). Thermal alteration of soil organic matter properties: a systematic study to infer response of Sierra Nevada climosequence soils to forest fires. *Soil* 3, 31–44. doi: 10.5194/soil-3-31-2017

Araya, S. N., Meding, S. M., and Berhe, A. A. (2016). Thermal alteration of soil physico-chemical properties: a systematic study to infer response of Sierra Nevada climosequence soils to forest fires. *Soil* 2, 351–366. doi: 10.5194/soil-2-351-2016

Arcenegui, V., Mataix-Solera, J., Guerrero, C., Zomoza, R., Matalx-Beneyto, J., and Garcia-Orenes, F. (2008). Immediate effects of wildfires on water repellency and aggregate stability in Mediterranean calcareous soils. *Catena* 74, 219–226. doi: 10.1016/j.catena.2007.12.008

Balesdent, J., Chenu, C., and Balabane, M. (2000). Relationship of soil organic matter dynamics to physical protection and tillage. *Soil Tillage Res.* 53, 215–230. doi: 10.1016/S0167-1987(99)00107-5

Carroll, E. M., Miller, W. W., Johnson, D. W., Saito, L., Qualls, R. G., and Walker, R. F. (2007). Spatial analysis of a large magnitude erosion event following a Sierran wildfire. *J. Environ. Qual.* 36, 1105–1111. doi: 10.2134/jeq2006.0466

Certini, G. (2005). Effects of fire on properties of forest soils: a review. *Oecologia* 143, 1–10. doi: 10.1007/s00442-004-1788-8

Chenu, C., and Plante, A. T. (2006). Clay-sized organo-mineral complexes in a cultivation chronosequence: revisiting the concept of the "primary organo-mineral complex." *Eur. J. Soil Sci.* 57, 596–607. doi: 10.1111/j.1365-2389.2006.00834.x

Chief, K., Young, M. H., and Shafer, D. S. (2012). Changes in soil structure and hydraulic properties in a wooded-shrubland ecosystem following a prescribed fire. *Soil Sci. Soc. Am. J.* 76, 1965–1977. doi: 10.2136/sssaj2011.0072

Choromanska, U., and DeLuca, T. H. (2002). Microbial activity and nitrogen mineralization in forest mineral soils following heating: evaluation of post-fire effects. *Soil Biol. Biochem.* 34, 263–271. doi: 10.1016/S0038-0717(01)00180-8

Christensen, B. T. (2001). Physical fractionation of soil and structural and functional complexity in organic matter turnover. *Eur. J. Soil Sci.* 52, 345–353. doi: 10.1046/j.1365-2389.2001.00417.x

Conard, S. G., Sukhinin, A. I., Stocks, B. J., Cahoon, D. R., Davidenko, E. P., Ivanova, G. A., et al. (2002). Determining effects of area burned and fire severity on carbon cycling and emissions in Siberia. *Climatic Change* 55:197. doi: 10.1023/A:1020207710195

DeBano, L. F., Dunn, P. H., and Conrad, C. E. (1977). "Fire's effects on physical and chemical properties of chaparral soils," in *Environmental Consequences of Fire and Fuel Management in Mediterranean Ecosystems*, eds A. Harold and C. E. Conrad (Washington, DC: USDA), 65–74.

DeBano, L. F., Neary, D. G., and Ffolliott, P. F. (1998). *Fire Effects on Ecosystems*. New York, NY: John Wiley and Sons.

Eidenshink, J., Schwind, B., Brewer, K., Zhu, Z.-L., Quayle, B., and Howard, S. (2007). A project for monitoring trends in burn severity. *Fire Ecol.* 3, 3–21. doi: 10.4996/fireecology.0301003

Flessa, H., Amelung, W., Helfrich, M., Wiesenberg, G. L. B., Gleixner, G., Brodowski, S., et al. (2008). Storage and stability of organic matter and fossil carbon in a Luvisol and Phaeozem with continuous maize cropping: a synthesis. *J. Plant Nutr. Soil Sci.* 171, 36–51. doi: 10.1002/jpln.200700050

González-Pérez, J. A., González-Vila, F. J., Almendros, G., and Knicker, H. (2004). The effect of fire on soil organic matter - a review. *Environ. Int.* 30, 855–870. doi: 10.1016/j.envint.2004.02.003

Guerrero, C., Mataix-Solera, J., Gómez, I., García-Orenes, F., and Jordán, M. M. (2005). Microbial recolonization and chemical changes in a soil heated at different temperatures. *Int. J. Wildl. Fire* 14, 385–400. doi: 10.1071/WF05039

Hassink, J., and Whitmore, A. (1997). A model of the physical protection of organic matter in soils. *Soil Sci. Soc. Am. J.* 61, 131–139.

Horn, R., and Smucker, A. (2005). Structure formation and its consequences for gas and water transport in unsaturated arable and forest soils. *Soil Tillage Res.* 82, 5–14. doi: 10.1016/j.still.2005.01.002

Jenny, H. (1980). *The Soil Resources, Origin and Behavior*. New York, NY: Springer.

Jian, M., Berli, M., and Ghezzehei, T. A. (2018). Soil structural degradation during low-severity burns. *Geophys. Res. Lett.* 45, 5553–5561. doi: 10.1029/2018GL078053

Johnson, D., Murphy, J. D., Walker, R. F., Glass, D. W., and Miller, W. W. (2007). Wildfire effects on forest carbon and nutrient budgets. *Ecol. Eng.* 31, 183–192. doi: 10.1016/j.ecoleng.2007.03.003

Jordan, A., Zavala, L., Mataix-Solera, J., Nava, A., and Alanis, N. (2011). Effect of fire severity on water repellency and aggregate stability on Mexican volcanic soils. *Catena* 84, 136–147. doi: 10.1016/j.catena.2010.10.007

Kavouras, I. G., Nikolich, G., Etyemezian, V., DuBois, D. W., King, J., and Shafer, D. (2012). *In situ* observations of soil minerals and organic matter in the early phases of prescribed fires. *J. Geophys. Res. Atmos.* 117:D12313. doi: 10.1029/2011JD017420

Keeley, J. E. (2009). Fire intensity, fire severity, and burn severity: a brief review and suggested usage. *Int. J. Wildland Fire* 18, 116–126. doi: 10.1071/WF07049

Knicker, H. (2007). How does fire affect the nature and stability of soil organic nitrogen and carbon? A review. *Biogeochemistry* 85, 91–118. doi: 10.1007/s10533-007-9104-4

Mataix-Solera, J., Cerdà, A., Arcenegui, V., Jordán, A., and Zavala, L. M. (2011). Fire effects on soil aggregation: a review. *Earth Sci. Rev.* 109, 44–60. doi: 10.1016/j.earscirev.2011.08.002

Mataix-Solera, J., Gomez, I., Navarro-Pedreno, J., Guerrero, C., and Moral, R. (2002). Soil organic matter and aggregates affected by wildfire in a *Pinus halepensis* forest in a Mediterranean environment. *Int. J. Wildland Fire* 11, 107–114. doi: 10.1071/WF02020

Moghaddas, E. E. Y., and Stephens, S. L. (2007). Thinning, burning, and thin-burn fuel treatment effects on soil properties in a Sierra Nevada mixed-conifer forest. *For. Ecol. Manage.* 250, 156–166. doi: 10.1016/j.foreco.2007.05.011

MTBS (2017). *Monitoring Trends in Burn Severity*. Available online at: http://www.mtbs.gov/

O'Dea, M. (2007). Fungal mitigation of soil erosion following burning in a semi-arid arizona savanna. *Geoderma* 138, 79–85. doi: 10.1016/j.geoderma.2006.10.017

Piccolo, A., and Mbagwu, J. S. C. (1999). Role of hydrophobic components of soil organic matter in soil aggregate stability. *Water* 63:1801. doi: 10.2136/sssaj1999.6361801x

Santos, F., Russell, D., and Berhe, A. A. (2016). Thermal alteration of water extractable organic matter in climosequence soils from the Sierra Nevada, California. *J. Geophys. Res. Biogeosci.* 121, 1–9. doi: 10.1002/2016JG003597

Schmidt, M. W., Torn, M. S., Abiven, S., Dittmar, T., Guggenberger, G., Janssens, I. A., et al. (2011). Persistence of soil organic matter as an ecosystem property. *Nature* 478, 49–56. doi: 10.1038/nature10386

Scow, K. M., and Alexander, M. (1992). Effect of diffusion on the kinetics of biodegradation: experimental results with synthetic aggregates. *Soil Sci. Soc. Am. J.* 56, 128–134. doi: 10.2136/sssaj1992.03615995005600010020x

Serrasolsas, I., and Khanna, P. K. (1995). Changes in heated and autoclaved forest soils of S.E. Australia. I. Carbon and nitrogen. *Biogeochemistry* 29, 3–24. doi: 10.1007/BF00002591

Stoof, C. R., Wesseling, J. G., and Ritsema, C. J. (2010). Effects of fire and ash on soil water retention. *Geoderma* 159, 276–285. doi:10.1016/j.geoderma.2010.08.002.

Tisdall, J. (1996). "Formation of soil aggregates and accumulation of soil organic matter," in *Structure and Organic Matter Storage in Agricultural Soils*, eds M. Carter and B. Steward (Boca Raton, FL: CRC Press, LLC). 57–59.

Tisdall, J. M., and Oades, J. M. (1982). Organic matter and water-soluble aggregates in soils. *Eur. J. Soil Sci.* 33, 141–163. doi: 10.1111/j.1365-2389.1982.tb01755.x

Úbeda, X., and Bernia, S. (2005). "The effect of wildfire intensity on soil aggregate stability in the Cadiretes Massif, NE Spain," in *Geomorphological Processes and Human Impacts in River Basins*, eds R. J. Batalla and C. Garcia (International Association of Hydrological Sciences), 37–45.

Urbanek, E. (2013). Why are aggregates destroyed in low severity fire? *Plant Soil* 362, 33–36. doi: 10.1007/s11104-012-1470-6

Conflict of Interest Statement: The authors declare that the research was conducted in the absence of any commercial or financial relationships that could be construed as a potential conflict of interest.

Control of Pore Geometry in Soil Microcosms and Its Effect on the Growth and Spread of *Pseudomonas* and *Bacillus* sp.

Archana Juyal[1,2], Thilo Eickhorst[2*], Ruth Falconer[1†], Philippe C. Baveye[3], Andrew Spiers[1] and Wilfred Otten[1,4]

[1] School of Science Engineering and Technology, Abertay University, Dundee, United Kingdom, [2] Soil Microbial Ecology, FB 2 (Biology/Chemistry), University of Bremen, Bremen, Germany, [3] UMR ECOSYS, AgroParisTech, Université Paris-Saclay, Thiverval-Grignon, France, [4] School of Water, Energy and Environment, Cranfield University, Cranfield, United Kingdom

Simplified experimental systems, often referred to as microcosms, have played a central role in the development of modern ecological thinking on issues ranging from competitive exclusion to examination of spatial resources and competition mechanisms, with important model-driven insights to the field. It is widely recognized that soil architecture is the key driver of biological and physical processes underpinning ecosystem services, and the role of soil architecture and soil physical conditions is receiving growing interest. The difficulty to capture the architectural heterogeneity in microcosms means that we typically disrupt physical architecture when collecting soils. We then use surrogate measures of soil architecture such as aggregate size distribution and bulk-density, in an attempt to recreate conditions encountered in the field. These bulk-measures are too crude and do not describe the heterogeneity at microscopic scales where microorganisms operate. In the current paper we therefore ask the following questions: (i) To what extent can we control the pore geometry at microscopic scales in microcosm studies through manipulation of common variables such as density and aggregate size?; (ii) What is the effect of pore geometry on the growth and spread dynamics of bacteria following introduction into soil? To answer these questions, we focus on *Pseudomonas* sp. and *Bacillus* sp. We study the growth of populations introduced in replicated microcosms packed at densities ranging from 1.2 to 1.6 g cm^{-3}, as well as packed with different aggregate sizes at identical bulk-density. We use X-ray CT and show how pore geometrical properties at microbial scales such as connectivity and solid-pore interface area, are affected by the way we prepare microcosms. At a bulk-density of 1.6 g cm^{-3} the average number of *Pseudomonas* was 63% lower than at a bulk-density of 1.3 g cm^{-3}. For *Bacillus* this reduction was 66%. Depending on the physical conditions, bacteria in half the samples took between 1.62 and 9.22 days to spread 1.5 cm. *Bacillus* did spread faster than *Pseudomonas* and both did spread faster at a lower bulk-density. Our results highlight the importance that soil physical properties be considered in greater detail in soil microbiological studies than is currently the case.

Keywords: X-ray CT scanning, bacterial growth, bacterial spread, CARD-FISH, microcosm experiment, pseudomonas, Bacillus subtilis

INTRODUCTION

Simplified experimental systems, often referred to as microcosms, have played a central role in the development of modern ecological thinking on issues ranging from competitive exclusion to examination of spatial resources and competitive mechanisms, with important model-driven insights to the field (Drake et al., 1996; Jessup et al., 2004). In soil science, the complexity of soil ecosystems with interacting communities and their associated physico-chemical and biological processes has necessitated the development of simplified systems, with, for example, microcosms often used in transport studies and in studies quantifying dynamics of organic matter in soil. Microcosms help overcome problems associated with field studies that include difficulties in manipulative experiments and uncontrollability of temperature, wetness, and spatial heterogeneity. Other benefits include speed, repeatability, statistical power, and mechanistic insights (Carpenter, 1996). For the same reason, microcosms are often criticized based on the risks of investigating artifacts of the system and the absence of sound hypotheses that relate to real ecosystem functioning (Verhoef, 1996).

It is widely recognized that soil architecture is the key driver of biological and physical processes underpinning ecosystem services, and that the role of soil architecture and soil physical conditions is receiving growing interest (Nunan et al., 2001; Or et al., 2007; Tecon and Or, 2017). Nevertheless, the difficulty to capture the architectural heterogeneity in microcosms means that we typically disrupt physical architecture when collecting soils. Often this process is followed by drying and sieving, thereby exerting physical forces upon soil to disrupt its architecture. We then use surrogate measures of soil architecture such as aggregate size distribution and bulk-density, in an attempt to recreate conditions encountered in the field. These bulk measures are too crude and do not describe the heterogeneity at microscopic scales where microorganisms operate.

Recent years have seen a shift in soil science research toward non-destructive and explicit characterization of pore volumes. The complex pore geometry can offer refuge for microbes (Young et al., 2008), determine pathways of interaction, preferential pathways for fungal spread (Otten et al., 1999), and water flow, as well as provide surfaces for bacterial attachments, access to food sources, and nutrient adsorption (Young et al., 2008). Recent advances in the use of X-ray CT in research on soils enable these characteristics to be readily quantified, and various papers in the last few years have described the impact of management strategies and physical forces on soil architectural characteristics (e.g., Kravchenko et al., 2011). Soil characteristics that can be quantified using X-ray CT include the *porosity*, which quantifies the total volume available to microbial interactions and growth, the *connectivity*, which indicates how accessible the pore volume is for organisms to interact and find food sources, and the *pore-solid interface area*, which effectively defines the surface area accessible to microorganism in soils. Nevertheless, soil architecture and soil physical characteristics are poorly described in the majority of soil biological studies (Baveye et al., 2016), which often only give account of wetness without

consideration of packing of the solid phase. Therefore we can identify 3 shortcomings in our current use of soil microcosms: (1) we have little insight in the loss of naturally-occurring architectural characteristics when we prepare soil microcosms, hampering extrapolations to field research, (2) we are unaware to what extend we can control soil architecture in a pre-described manner, and (3) we still have little insight into the effect of soil architecture on the growth and activity of micro-organisms when studied in microcosms.

In the current paper we therefore ask the following questions:

- To what extent can we control the pore geometry in microcosm studies through manipulation of common variables such as density and aggregate size? Are replicated microcosms really replicated at the microscale?
- What is the effect of pore geometry on the growth and spread of bacteria following introduction into soil?

We focus on *Pseudomonas* sp. and *Bacillus* sp. Both species are abundantly present in the rhizosphere and bulk soils in many locations and are frequently studied for their growth-promoting ability, yet there is still very little knowledge available on how their growth and spread is affected by soil physical conditions such as pore geometry.

MATERIALS AND METHODS

Soil Sample Preparation

Samples were obtained from a sandy loam soil from an experimental site, Bullion Field, situated at the James Hutton Institute, Invergowrie, Scotland. Further description of the soil can be found in Sun et al. (2011). The soil was air-dried, sieved to size 1–2 and 2–4 mm, and stored in a cold room. Before usage, the soil was sterilized by autoclaving twice at 121°C at 100 kPa for 20 min within a 24 h interval time.

Bacteria and Preparation of Inoculum

Pseudomonas fluorescens SBW25-GFP (SBW25::mini-Tn7(Gm) P P_{rrnBP1} *gfp.ASV*-a, Gm^R (unpublished, A. Spiers), and *Bacillus subtilis* NRS1473 (NCIB3610 *sacA*::P$_{hy-spank}$-*GFPmut2*, Km^R; Hobley et al., 2013) cells were used as bacterial inoculum. *Pseudomonas* was grown on King's B medium (KB, 10 g Glycerol, 1.5 g K$_2$HPO$_4$, 1.5 g MgSO$_4$.7H$_2$O, 20 g Proteose peptone No.3 (Becton, Dickinson & Company, UK), 15 g Technical agar (1.5% w/v) per liter) (King et al., 1954). *Bacillus* was grown on Luria-Bertani medium (LB, 10 g NaCl, 10 g Tryptone, 10 g Yeast extract, 15 g Technical agar (1.5% w/v) per liter). Kanamycin (50 μg/ml) and Gentamycin (50 μg/ml) were added to the culture media.

For each experiment, an overnight culture was prepared by transferring a loop-full of colony in 10 ml of sterile broth and incubated at 28°C on a shaker at 200 rpm for 24 hr. The cells were harvested by centrifugation (4,000 × g) for 5 min and re-suspended in 10 ml PBS solution to a final concentration of OD$_{600}$ = 0.95. The cell density of the solution used to inoculate was 6.46E+08 cells/ml for *Pseudomonas* sp. and 7.85E+08 cells/ml for *Bacillus* sp. The method of inoculation of the microcosms is described below.

To study the spread from localized sources, a colonized agarose pellet was used to provide a reproducible source of inoculum. A small 1 ml aliquot of inoculum of washed cells with densities as described above was mixed with 30 ml of LMP agarose solution in a centrifuge tube. The mixture was poured onto a petri dish that was left in a laminar flow cabinet at room temperature to solidify. The solidified agarose was then cut into small circular pellets using the circular end of a 1 ml pipette tip. Each pellet was of a size of 2.5 mm in diameter and 5 mm in height. Control pellet without bacteria were prepared in a similar way.

Microcosms to Study Spread of Bacteria as Affected by Soil Physical Conditions

Following Otten et al.'s (2001) approach to monitor the spread of fungi through soil, placement experiments were used where the probability of colonizing a target placed at distances from a source of inoculum is quantified over time. In these experiments, replicated microcosms of various thicknesses are prepared and a source of inoculum is placed on one side. On the other side a target is placed, which can be replaced on a daily basis and assessed for colonization. A colonized agarose bead is placed at the bottom of the sample. One autoclaved aggregate (2–4 mm in size) is placed on top of each sample. Aggregates are removed from time to time and assessed for colonization as described below. Each sample is placed in upright position in a closed centrifuge tube to reduce evaporation, and is incubated at 23°C. Each microcosm (distance) is replicated 10 times and a control series is set up using an agarose bead without bacteria.

The effect of aggregate size on the rate of spread was quantified in microcosms with a height of 1.5 cm prepared by repacking aggregates sized 0.5–1, 1–2, or 2–4 mm. In a similar way the effect of bulk-density (BD) was quantified by comparing microcosms packed at a density of 1.3 or 1.5 g cm^{-3} with an aggregate size of 1–2 mm. A wetness equivalent of 60% of the pores filled with water was maintained for all samples. For all experiments the target aggregate was replaced daily with a fresh aggregate till the aggregate was tested positive for colonization after which the sample was removed from the series. The removed aggregates were placed on KB media plates for detection of *Pseudomonas* and on LB media for *Bacillus*. Plates were incubated at 28°C for 48 h after which colonies were clearly visible on the plates for aggregates that had been colonized. This was taken as positive colonization and evidence that bacteria had traveled through the soil from the source of inoculum. Absence of colonization for the control samples confirmed the validity of this assumption.

Microcosms to Study Growth of Bacteria as Affected by Soil Architecture

Growth dynamics were determined in microcosms packed at different bulk-densities and aggregate-sizes. Soil microcosms were prepared in PE rings of size 3.40 cm^3 (1.7 cm diameter and 1.5 cm height). The soil was wetted with sterile distilled water to achieve a moisture content so that 40% of the pores were water-filled. The gravimetric water content therefor differs per treatments, ranging from 0.13 to 0.06 g/g, and the amounts

added to each sample are listed in **Table 1**. Two experiments were conducted, one looking at the effect of bulk-density, and a second looking at the effect of aggregate-size. In the first experiment, sterilized, sieved 1–2 mm aggregates were packed at a range of bulk-densities. The amount of soil required to obtain each bulk-density was inoculated with 500 μl of the bacterial suspension, mixed well, and packed in PE rings using a push rod. Bulk-densities of 1.2, 1.3, 1.4, 1.5, and 1.6 g cm^{-3} were obtained. This way the density of bacteria per volume soil (or microcosm) was identical for all bulk-densities. Control samples were packed in a similar manner except that sterile distilled water was used instead of a cell suspension. Three replicates per treatment for each sampling day were prepared, and the microcosms were sampled destructively 4 times. In the second experiment, sieved 1–2 and 2–4 mm aggregates were used. They were wetted to the same moisture content as above and packed in a similar way in PE rings at a bulk-density of 1.3 g cm^{-3}. Soil in each ring was mixed with 500 μl of the bacterial suspension described above. The experiment was replicated 3 times and sampled 4 days after inoculation of the soil. All the microcosms were incubated at 23°C in the dark and sampled on 1, 5, 9, and 13 days after inoculation as described below.

Preparation of Samples for *in Situ* Hybridization

On sampling day, each microcosm was mixed with 10 ml of sterile 1 × PBS solution and shaken for 15 min at room temperature. CARD-FISH was applied on soil suspensions according to the protocol described by Eickhorst and Tippkötter (2008). Briefly, 500 μl of soil suspension prepared as described above was fixed in 4% formaldehyde solution (216 μl of 37% formaldehyde and 2 × 642 μl 1 × PBS) at 4°C for 2.5 hr. The fixed samples were then washed thrice with 1 × PBS solution, centrifuged at 10,000 g for 5 min at 4°C and stored in 1 × PBS/ethanol (1:1) solution at −20°C. These fixed samples were sonicated (Sonopuls HD2200, Bandelin, Berlin, Germany) twice at 10% power for 30 s and then filtered on white polycarbonate filter (0.2 μm pores, 25 mm diameter; Sartorious, Germany) by applying vaccum of 800 mbar. The filter membranes were then dipped in 0.2% low-melting-point agarose (Invitrogen Life Technologies) and dried at 46°C. To permeabilize cell walls, filters were incubated with 85 μl of lysozyme solution at 37°C for 60 min. The filters were

---

TABLE 1 | The gravimetric water content that results in a moisture content of 40% water filled pores, and the amount of soil per ring/microcosm to pack at a particular bulk-density.

Bulk-density (g cm^{-3})	Gravimetric water content (g/g)	Soil added/ring (g)
1.2	0.13	4.81
1.3	0.11	5.09
1.4	0.09	5.38
1.5	0.07	5.66
1.6	0.06	5.95

then washed in H_2O_{MQ} and dehydrated in ethanol. For *in-situ* hybridization the membrane filters were cut into small sections.

Catalyzed Reporter Deposition (CARD) on Filter Sections

For *in-situ* hybridization, filter sections were incubated in 400 μl of hybridization buffer [100 mg ml^{-1} dextran sulfate (Sigma-Aldrich), 5M NaCl, 1M Tris-HCl (v/v), 35% Formamide (Fluka), 10% (v/v) SDS, blocking reagent (Roche, Germany) and H_2O_{MQ}] and 1.5 μl of 50 ng μl^{-1} horseradish peroxidase-labeled oligonucleotide probe working solution for 2 h in a rotating incubator at 35°C.

After the hybridization step, filter sections were subsequently washed in a pre-warmed washing buffer (1M Tris-HCl, 0.5M EDTA, 10% SDS, 5M NaCl and H_2O_{MQ}, 5 min at 37°C), H_2O_{MQ} (2 min at RT) and with TXP [Triton-X 100 (Bio-Rad), 1 × PBS] for 10 min at RT. For amplification of tyramide signals, filter sections were incubated with the amplification buffer [100 mg ml^{-1} dextran sulfate (Sigma-Aldrich), blocking reagent, 5M NaCl, 1 × PBS] along with 0.15% H_2O_2 solution and 1 μl of fluorescein-labeled tyramide solution for 20 min in a rotating incubator at 35°C. Afterwards, filter sections were washed in Triton-X-PBS (0.05% v/v) and dH$_2$0 for 10 min each at RT and dehydrated with ethanol.

Enumeration of Bacterial Cells With Epifluorescence Microscopy

For evaluation of CARD-FISH signals, air-dried filter sections were placed on glass slides, mounted with VectaShield H-1200 containing DAPI (4′, 6-diamino-2-phenylindole) stain and covered with coverslips. A ZEISS Axioskop 2 microscope equipped with an HBO 100 W Hg vapor lamp and a 63x objective (Carl Zeiss) was used for evaluating the filter sections. The tyramide stained cells signal was examined under a double excitation filter (Filter set 24, Carl Zeiss) and total cells were enumerated under UV excitation and a DAPI filter (F46-000, AHF, Tübingen, Germany). Bacterial cells were counted using a counting grid (10 × 10, 1.25 mm^2; Carl Zeiss) integrated in the ocular of the microscope. The cells were counted at 15 random microscopic fields of views on each filter sections. Cell counts were extrapolated to obtain the number of cells per gram of soil.

Quantification of Soil Architecture With X-ray CT

An X-ray micro-tomography system, HMX225, was used to characterize and visualize the internal soil architecture (NIKON, Tring, UK). A series of samples packed at densities 1.2, 1.3, 1.4, 1.5, and 1.6 g cm^{-3} and with an aggregate size of 1–2 mm were prepared in triplicate as described above and scanned to quantify the effect of packing on pore geometry. In addition, samples with 1–2 or 2–4 mm aggregates (triplicate) were prepared to assess how aggregate-size affects pore geometry at a bulk-density of 1.3 g cm^{-3}. All soil samples were scanned at 105 kV, 96 μA, and 2,000 angular projections with 2 frames per second. A molybdenum target was used with a 0.5 mm aluminum filter to minimize beam hardening effects. Radiographs were reconstructed into

3-D volume using CT-Pro at a resolution of 24 μm for the series looking at bulk-density; the samples comparing the effect of aggregate size at a single bulk-density value were scanned and reconstructed at 13.4 μm. Data were imported into VGStudiomax (Volumegraphics, Heidelberg, Germany), and converted into stacks of voxel-thick, 8-bit gray scale bmp images. Image stacks were cropped around a fixed central point to a cuboid sized 512 × 512 × 512 voxels. Segmentation of solid and pore phases was performed with an Indicator Kriging method (Houston et al., 2013) and in-house developed software was used to calculate porosity, connectivity and interface-surface area of the visible pore space in the samples. The connectivity corresponds to the volume fraction of visible pore space that is connected with the external surface of the image volume (Houston et al., 2013; **Figure 1**). It is noted that these properties are dependent on the resolution of the obtained scans.

Data Analysis

Statistical analysis was performed with the statistical package SPSS version 2.1. An independent *t*-test with a 5% confidence interval was used to investigate architectural differences in mean porosity, connectivity and surface area across different bulk-densities and aggregate sizes. A generalized mixed effect Poisson model with the log link function was used to investigate significant differences in cell numbers between sampling days with day as a fixed factor. In different treatments, the significant difference between sampling days was investigated with treatments and days as fixed factor.

The rate and extent of spread was captured by 4-parameter sigmoidal curves following Otten et al. (2001). Curves were fitted to the data using Sigmaplot 11th Edition with the fraction of replicates with positive colonization, Y, given by: $Y = Y_o + a/(1 + \exp -((x-x_0)/b))$, where *a* is the maximum fraction of replicates with successful colonization in all replicates (1.0), x_0 is the point of inflection (when the fraction of replicates with positive colonization equals 0.5), and *b* is the steepness of the curve and reflects the variation in the rate of spread. The parameter Y_0 reflects the number of positive colonizations in the control samples and was equal to 0 in all our experiments. The fitted relationship means that the rate and extent of spread can be captured by a relatively small set of parameters and the effect of treatments on parameter values can be compared.

RESULTS

Effect of Bulk Soil Density and Aggregate Size on Pore Geometry

The effect of bulk-density on pore geometry is immediately apparent from the 2D slices selected from the 3D volumes with visibly less pore volume in the more compacted soil samples (**Figure 2**). In addition, the pore space looks more fragmented when the soil is packed at a higher density. This visual observation is confirmed by analysis of the thresholded 3D volumes, which showed a significant ($P < 0.05$) 57% decline in porosity with increasing bulk-density from 20.0% for
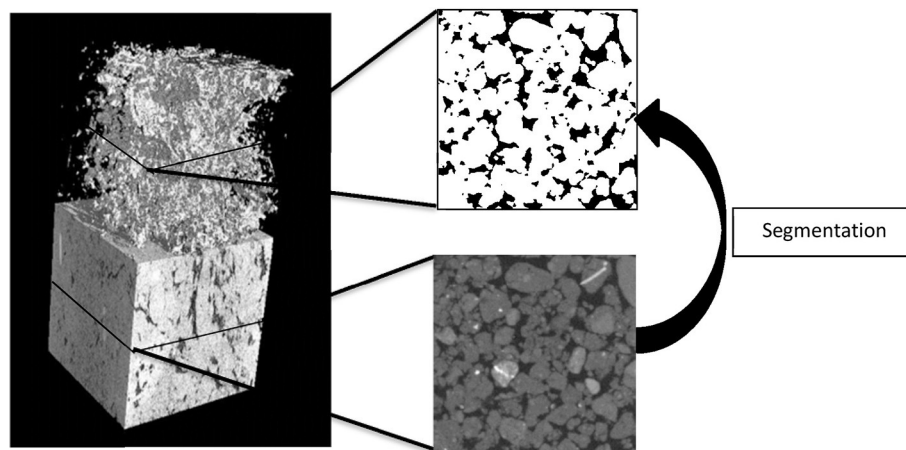
FIGURE 1 | An example of a section of an X-ray CT scan of a repacked sieved soil sample (left) showing the solid and pore volumes and the 3D pore volume). An example of a transect is shown with the solid phase (gray) and pores (black). The pore volume is identified through segmentation which produces a binary image with pores (black) and the solid phase (white).
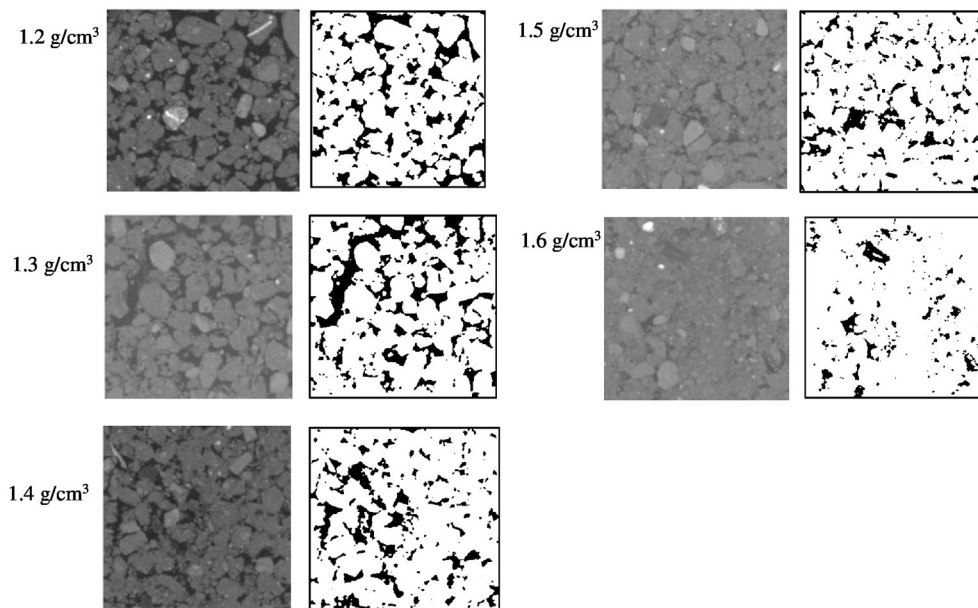

FIGURE 2 | Examples of segmented two-dimensional images of samples packed with 1–2 mm sieved soil at BD ranging from 1.2 to 1.6 g cm^{-3}. The solid phase is represented by different gray-scales and through thresholding transformed into binary images with black representing the pores and white representing the solid phases.

BD = 1.2 g cm^{-3} to 8.7% for BD = 1.6 g cm^{-3}. The connectivity of pores reduced from 98% (s.e. 0.5) for loosely packed soil (1.2 g cm^{-3}) to 58% (s.e 6.1) for densely packed soil (1.6 g cm^{-3}). The mean surface area of soil pores ranged from 43 (s.e 1.7) cm^2 cm^{-3} for soil with a bulk-density of 1.2 g cm^{-3} to 35 (s.e. 5.1) cm^2 cm^{-3} for soil with a bulk-density of 1.6 g cm^{-3}, but this effect was not significant (**Table 2**).

Representative 2D slices selected from the 3D volumes for soil packed with different aggregate sizes are presented in

Figure 3. For the larger aggregate sizes (2–4 mm) the original aggregation of the soil is clearly visible in the resulting soil architecture. Smaller but still recognizable aggregates can also be seen in the other treatments. Overall, aggregate size distribution has a clear effect on pore geometry with wider pores in samples prepared with larger aggregate sizes. No significant difference is found for porosity and connectivity, and the only noticeable change is a minor decline in pore-solid interface with increasing aggregate size (**Table 3**). This is consistent with

expectations, given that the soils were packed at the same bulk-density.

Visualization of Bacterial Cells in Soil Samples

The expression of GFP signals were detected on filter sections under double excitation filter (465–505 and 564–892 nm). GFP-tagged cells appear green in color against reddish color soil background, however the intensity of GFP signals appears very weak (**Figure 4a**). The counterstain DAPI shows that few GFP-tagged cells are not detected. The filter sections treated with CARD-FISH show brighter green signals compared to GFP signals (**Figure 4b**) against the soil background. Therefore, CARD-FISH is a logic choice to apply for enumeration of bacterial cells in all treatments.

The Effect of Different Bulk Soil Densities on Growth of Bacteria

Average number of cell counts of *Pseudomonas* sp. and *Bacillus* sp. bacteria determined in different bulk densities of soil are presented in **Figure 5**. The growth of *Pseudomonas* and *Bacillus* cells in soil is significantly affected by the bulk-density of soil, with the increase in the cumulative number of cell dependent on bulk-density (**Figure 5**). For example, from days 1 to 13 at a bulk-density of 1.3 g cm^{-3} cell counts increase 3.56 times for *Pseudomonas* and 5 times for *Bacillus* with cell densities of 9.37E+08 (s.e 2.80E+07) cells

g^{-1} soil, and 5.12E+08 (s.e 2.61E+07) cells g^{-1} soil for *Pseudomonas* sp. and *Bacillus* sp. at day 13 and 2.66E+08 (s.e 1.42E+07) cells g^{-1} (*Pseudomonas*), and 1.01E+08 (s.e 5.65E+06) cells g^{-1} soil (*Bacillus*) at day 1. This trend is expected due to the growth of bacteria in soil. For all bulk-densities and at all sampling times, the number of cell counts for *Pseudomonas* cells is significantly higher than *Bacillus* cells ($P < 0.05$).

There is a significant effect of bulk-density on the growth of bacteria in soil. As the bulk-density increases, the number of cell counts decreases for both bacterial species ($P < 0.05$) at all sampling times, except for soil packed at bulk-density of 1.2 g cm^{-3} where the average cell counts is lower than for soil packed at 1.3 g cm^{-3} as observed in **Figure 5**. This is a striking result found for both bacteria suggesting there is an optimum density for bacterial growth. At a bulk-density of 1.6 g cm^{-3}, the average number of *Pseudomonas* cells is 63% lower compared to that at a bulk-density of 1.3 g cm^{-3} (**Figure 5A**). A similar trend is observed for *Bacillus* cells where the cumulative number of cell counts is 66% lower at a bulk-density of 1.6 g cm^{-3} ($P < 0.05$, **Figure 5B**). As all cell densities are expressed per gram, these reductions are beyond those one might expect (81%) from an increase in bulk-density alone.

Effect of Aggregate Sizes on Growth of Bacteria

Over time, the growth of *Pseudomonas* and *Bacillus* is significantly increased ($P < 0.05$) for both aggregate size classes (**Figure 6**). For example, from days 1 to 13 in aggregates of size 2–4 mm, cumulative cell counts increase 3.3 times for *Pseudomonas*

TABLE 2 | Mean values of soil pore characteristics packed at bulk-densities (BD) of 1.2, 1.3, 1.4, 1.5, 1.6 g cm^{-3}.

BD (g cm^{-3})	Porosity (%)	Connectivity (%)	Surface area (cm^2 cm^{-3})
1.2	20.0 ± 1.6	98.2 ± 0.5	43.2 ± 1.7
1.3	17.3 ± 0.9	96.5 ± 0.5	43.8 ± 1.5
1.4	12.5 ± 0.6	83.6 ± 3.0	41.1 ± 1.6
1.5	9.4 ± 1.0	66.8 ± 4.0	34.3 ± 3.9
1.6	8.7 ± 0.9	57.5 ± 6.1	35.0 ± 5.1

Mean values ±SE are presented (n = 3).

TABLE 3 | Mean values of pore characteristics in soil of aggregate sizes (AS) 1–2 and 2–4 mm packed at a bulk-density of 1.3 g cm^{-3}.

AS (mm)	Porosity (%)	Connectivity (%)	Surface area (cm^2 cm^{-3})
1–2	22.5 ± 1.1	97.5 ± 0.5	11.6 ± 0.2
2–4	24.2 ± 1.3	96.9 ± 0.4	11.1 ± 0.7

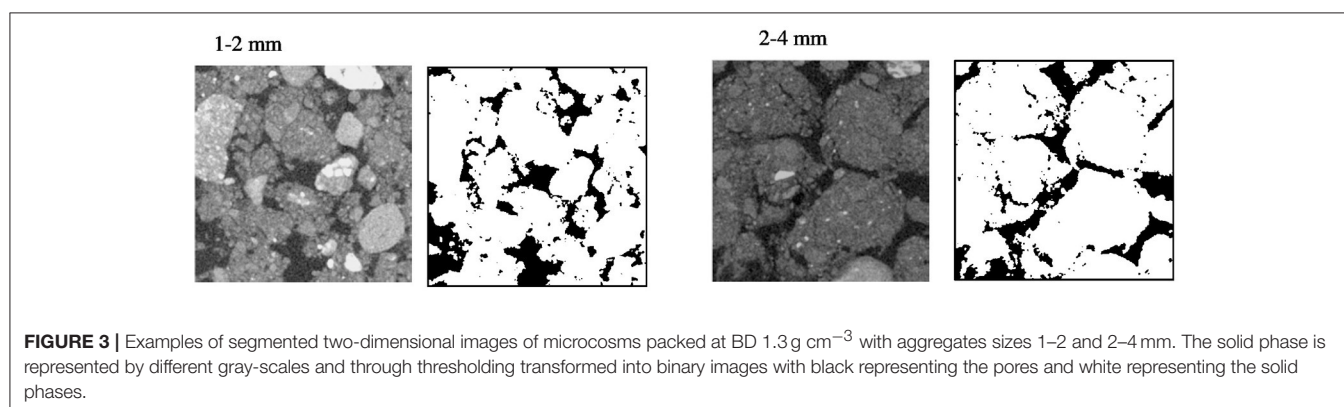*Mean values ±SE are presented (n = 3).*

FIGURE 3 | Examples of segmented two-dimensional images of microcosms packed at BD 1.3 g cm^{-3} with aggregates sizes 1–2 and 2–4 mm. The solid phase is represented by different gray-scales and through thresholding transformed into binary images with black representing the pores and white representing the solid phases.
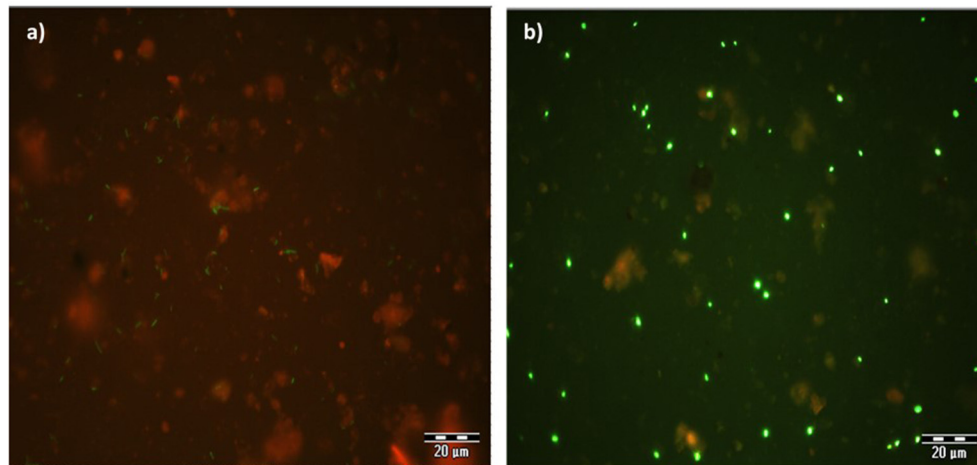
FIGURE 4 | An example of microscopic images GFP-tagged **(a)** and CARD-FISH stained **(b)** *Bacillus subtilis* cells in soil filter sections under double excitation filter (465–505 and 564–892 nm). Scale bar 20 μm.
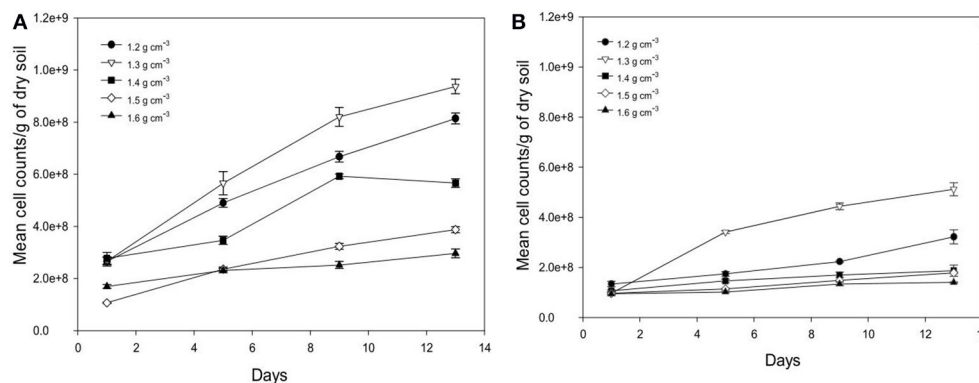

FIGURE 5 | Change in number of cell counts per gram soil with time after inoculation with *P. fluorescens* **(A)** and *B. subtilis* **(B)** in soil at bulk densities of 1.2 g cm^{-3} (•),1.3 g cm^{-3}(∇),1.4 g cm^{-3}(■), 1.5 g cm^{-3}(◊), and 1.6 g cm^{-3}(▲). Data are means ±SE ($n = 3$).

and 3.0 times for *Bacillus* with cell densities of 9.17E+08 (s.e 4.77E+07) cells g^{-1} soil and 3.71E+08 (s.e 9.55E+06) cells g^{-1} soil respectively for *Pseudomonas* and *Bacillus* at day 13 and 2.73E+08 (s.e 2.32E+07) cells g^{-1} soil (*Pseudomonas*), and 1.23E+08 (s.e 1.98E+07) cells g^{-1} soil (*Bacillus*) at day 1. The number of cell counts of *Pseudomonas* is significantly higher than that of *Bacillus* on all sampling days (**Figure 6**).

Between the different aggregate size treatments, the number of cell counts of *Pseudomonas* is unaffected by aggregate size but the cell counts for *Bacillus* is higher in the 1–2 mm size aggregates class compared to 2–4 mm size aggregates (**Figure 6**). For example, on day 13 cell counts in smaller aggregates (1–2 mm) are 1.4 times higher for *Bacillus* than in larger aggregates (2–4 mm), with cell densities of 5.12E+08 (s.e 2.61E+07) cells g^{-1} soil in smaller aggregates (1–2 mm), and 3.71E+08 (s.e 9.55E+06) cells g^{-1} soil in larger aggregates (2–4 mm).

Effect of Bulk-Density on Spread Through Soil

Spread is quantified by a likelihood of spreading, expressed as the number of successful colonizations over time through a layer of soil with a thickness of 15 mm. In all replicates, all baits eventually become colonized irrespective of the bulk-density. However, the time it takes for replicates to become colonized is affected by the bulk-density for both bacterial strains. Increasing bulk-density decreases the movement of *Pseudomonas* and *Bacillus* in soil (**Figure 7**). In Bacillus-inoculated samples, the colonization day (X_o) is 1.62 for soil packed at a lower bulk-density, and 8.70 for soil packed at a higher bulk-density (**Table 4**). The colonization day (X_o) of *Pseudomonas*-inoculated samples is 3.00 in soil packed at lower bulk-density compared to soil packed at higher bulk-density where it is 9.22. In both bulk-density treatments, the spread of *Bacillus* was faster than that of *Pseudomonas*.
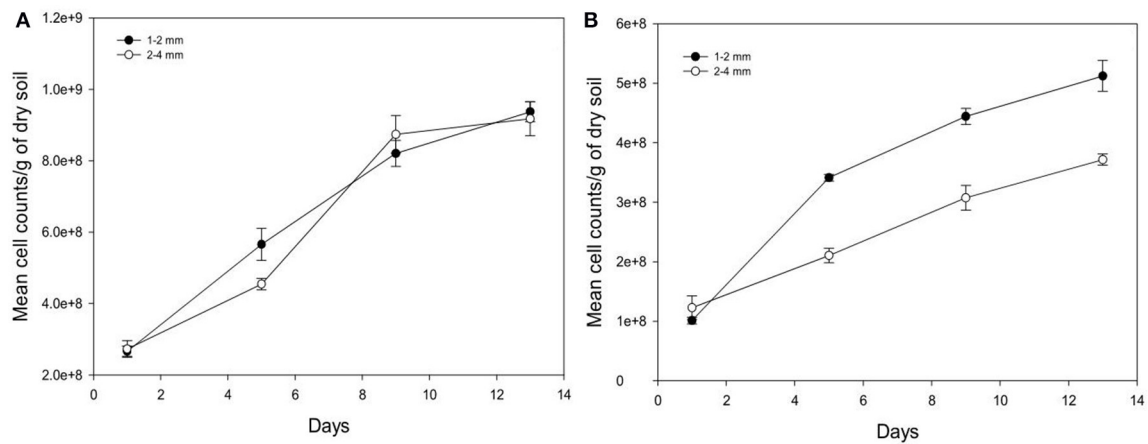
FIGURE 6 | Change in the number of cells per gram soil with time after inoculation with *P. fluorescens* **(A)** and *B. subtilis* **(B)** detected at different sampling time in soil of aggregate size classes 1–2 mm (•) and 2–4 mm (○). Data are means ±SE (*n* = 3).
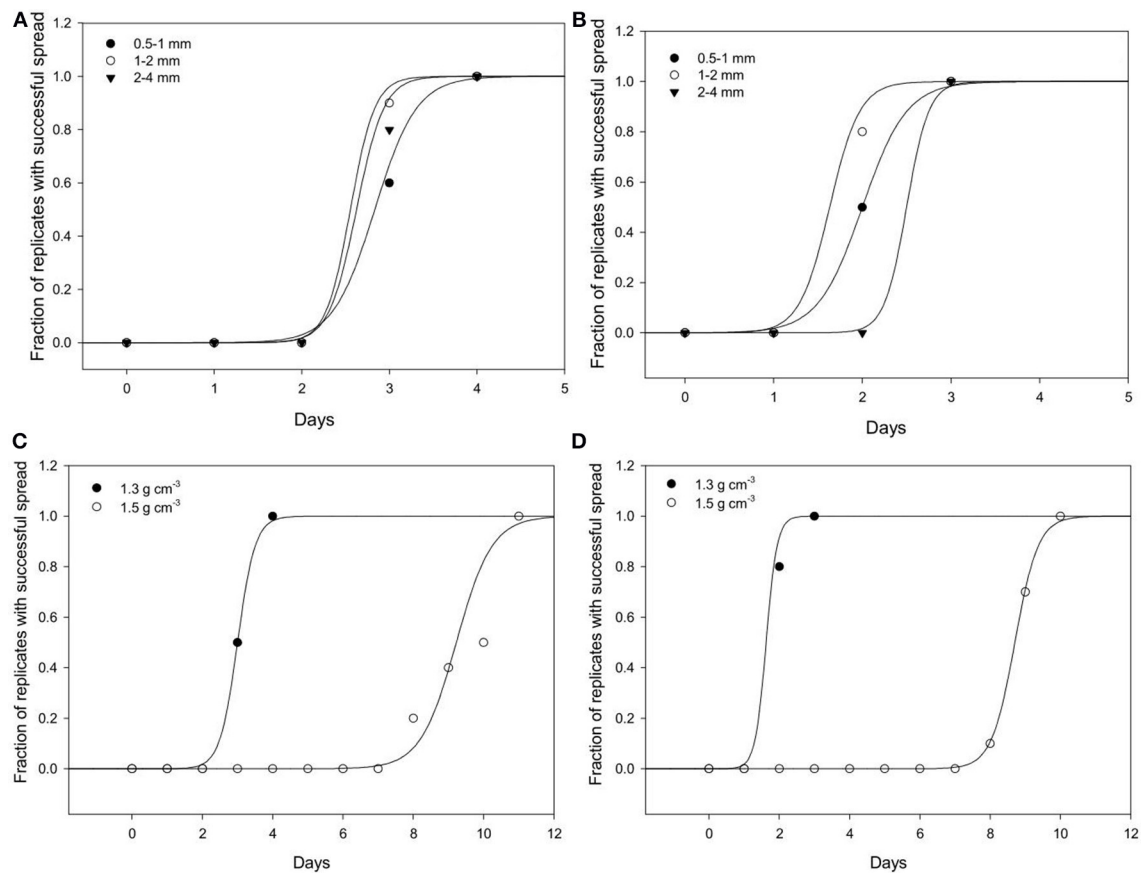
FIGURE 7 | Dynamics of spread of *Pseudomonas* sp. and *Bacillus* sp. through soil. The number of replicates in which *Pseudomonas* **(A)** and *Bacillus* **(B)** successfully spread through soil of aggregates 0.5–1 (•); 1–2 (○); 2–4 (▲) mm packed at a bulk-density of 1.3 g cm^{-3}. The effect of soils packed at a BD of 1.3 or 1.5 g cm^{-3} (AS 1–2 mm and wetness 60%) on the spread of *Pseudomonas* **(C)** and *Bacillus* **(D)**. For all treatments successful colonization was quantified as the number of successful colonizations of target bait placed at specified distances from a source of inoculum.

TABLE 4 | Parameters of sigmoidal curve fitting between fraction of replicates with successful spread and different sampling days for *Pseudomonas* and *Bacillus* inoculated in soil with 60% moisture content packed to bulk densities 1.3 and 1.5 g cm^{-3}.

Strains	Bulk-density (g cm^{-3})	r^2	Parameter a	Parameter b	Parameter X_0
Bacillus	1.3	0.991	1.0	0.15	1.62
	1.5	0.999	1.0	0.33	8.70
Pseudomonas	1.3	0.999	1.0	0.25	3.0
	1.5	0.9436	1.0	0.50	9.22

TABLE 5 | Parameters of sigmoidal curve fitting between fraction of replicates with successful spread and sampling days for *Pseudomonas* and *Bacillus* inoculated in soil with aggregate sizes 0.5–1 mm; 1–2 mm and 2–4 mm with packed to bulk-density 1.3 g cm^{-3}.

Strains	Aggregate size (mm)	r^2	Parameter a	Parameter b	Parameter X_0
Bacillus	0.5–1	0.999	1.0	0.25	2.00
	1–2	0.991	1.0	0.15	1.62
	2–4	0.999	1.0	0.12	2.50
Pseudomonas	0.5–1	0.996	1.0	0.23	2.83
	1–2	0.998	1.0	0.13	2.55
	2–4	0.992	1.0	0.15	2.62

Effect of Aggregate Size on Spread of Bacteria Trough Soil

Regardless of aggregate size, all replicates become colonized within 5 days, demonstrating rapid spread for all treatments. There is however an effect of aggregate size, with a different response for the two bacterial strains (**Figure 7**). In samples inoculated with *Bacillus*, colonization occurs within 2.0 days for packings of 0.5–1 mm aggregates, 1.62 days with 1–2 mm aggregates, and 2.50 days for soil with 2–4 mm aggregate sizes (**Table 5**). The colonization time of *Pseudomonas*-inoculated samples is 2.83 days for soil with 0.5–1 mm aggregates, 2.55 days with 1–2 mm aggregates, and 2.62 days for soil with 2–4 mm aggregate sizes. The spread of *Pseudomonas* and *Bacillus* is faster in soil with 1–2 mm compared to 0.5–1 mm aggregate-sizes. The spread of *Bacillus* was faster than that of *Pseudomonas*.

DISCUSSION

Most laboratory studies of soil processes involving microorganisms tend to be carried out in microcosms with often little consideration of the way soil is packed or what physical conditions are maintained. In the majority of cases, the water content of the soil is mentioned, often as gravimetric water content, but the density at which soil is packed is generally not provided. At best, when these characteristics are provided, they describe bulk-properties summarizing soil over scales that are much larger than those at which microorganisms operate in soil

(Ettema and Wardle, 2002). In this paper we use bulk-density and aggregate size as experimental variables often encountered in soil studies and, via X-ray CT, we demonstrate that significant differences are generated at scales relevant to microorganisms. Our results show that it is possible to alter characteristics of pore geometry with the use of various initial conditions. Increasing aggregate size at the same density leads to formation of pore networks with a majority of macropores and also decreases the surface area of solid-pore interfaces. On the other hand, increasing the bulk-density of soil consisting of aggregates with the same size reduces the volume of pore space, its connectivity, and the pore-solid interface area.

The volume of available pore space and its characteristics have a major impact on a wide range of biological, chemical, and physical processes. Well-connected macro-pores are the preferential paths of fungal colony spread, followed by exploration of smaller connected pores and thin valleys (Otten et al., 2004; Pajor et al., 2010). On the other hand, meso- and micro-pores, where water menisci hold under larger negative pressures, are more suited for organisms that require instant access to water like bacteria (Young and Ritz, 2005). Pore size is a key determinant of the shape of the water retention curve, termed the "curve of life" by Young et al. (2008) since, at the scale relevant to microbial activity, it regulates the abundance of water and air. Macro-pores are the main pathways for the flow of soil water, which has a direct impact on transport of water soluble nutrients (Luo et al., 2010). By applying X-ray CT to a range of microcosms prepared in standard ways often applied in laboratory research, our results show for the first time how we can manipulate soil architecture to assess their impact on microbial dynamics in soil. It is noteworthy that we observed maximum growth at a bulk-density of 1.3, which may indicate that an optimal bulk-density exists for both species. Such an optimum might result from the interplay of contrasting effects. For example, with increasing bulk-density, the OM content per volume soil will increase. From this one might expect an increase in growth. On the other hand, there may also be a reduction in the pore-space and the water content in the sample. This will reduce the volume within which bacteria can grow to a smaller fraction of the soil volume, leading to reduced access to C, and therefore eventually to reduced growth. It is possible that a trade-off between such contrasting processes results in the optimal density for growth, in our case at a density of 1.3 g cm^{-3}.

It is well documented that the pore volume that can be seen by X-ray CT is only a part of the pore volume as any pores smaller than the resolutions remain undetectable (e.g., Baveye et al., 2017). For meaningful samples for microcosm studies this can mean that pores less than 30 μm are not seen. For most soils this is a significant portion of the pore volume. In some soils, it may even represent all of the porosity. Perhaps equally importantly, pores from a few microns to 30 μm in size are in principle accessible to bacteria and archaea. We stress however, that for conditions under which most microcosm studies are conducted, the water content is such that sub-resolution are filled with water. This is certainly the case for our experimental set-up. As anaerobic conditions can occur at very small distances within saturated aggregates and we are here reporting on aerobic

growth, these smaller pores may not play such a major part in the results as one might have assumed. The larger pores will however affect the distribution of water and the air-water interface, the diffusion pathways of dissolved organic carbon and the diffusion pathways of oxygen and hence can be expected to affect bacterial growth and spread. From the discussion above it follows that it is not just the pore geometry that should be considered, but that the water-air ratio within these pores is perhaps of greater relevance. It is clear from the results that the dominant characteristic affected by bulk-density is still the porosity, with connectivity only affected for the more densely packed soils. As expected there is a decrease of porosity values with increasing density of soil, consistent with other studies using thin sections (e.g., Harris et al., 2003) and general theory of porous media. Given that the samples were prepared from repacked sieved aggregates, it is no surprise that high values are reported for connected pore space, with only noticeable declines at higher densities when aggregates are broken during the packing and the pore space collapses. It should be noted that the values reported are for the specific resolutions obtained with X-ray CT, and different values might be expected at higher or lower resolutions as at the current resolution a significant amount of smaller pores is not considered.

We demonstrate clearly that the way microcosms are packed affects the growth and spread of bacteria, demonstrating the importance of reporting physical characteristics in microbial studies involving soil in the laboratory. Experimental results suggest that the rate of growth decreases with increasing bulk-density. These results are consistent with several other studies that report a reduction in the microbial community and its activity at higher bulk-density compared to the soil packed at lower bulk-density (Dick et al., 1988; Li et al., 2002; Tan et al., 2008; Frey et al., 2009; Pupin et al., 2009). For example, Pupin et al. (2009) report a reduction of 22–30% in the number of bacteria at a bulk-density of $1.7 \, g \, cm^{-3}$ compared to the control ($1.3 \, g \, cm^{-3}$). Li et al. (2002) also report a negative relationship of microbial numbers with the bulk-density of soil. A reduction in the microbial biomass carbon and nitrogen was reported due to 13–36% decrease in air-filled porosity caused by compaction of soil. An increase in the bulk-density of soil reduces the number of large pores and the connectivity between the pores. These changes could result in reduced accessibility of organic substances, water movement, and gas exchange. A reduction in O_2 diffusion through soil changes the soil environment into an anaerobic state, thus one of the factor in inhibiting the growth of aerobic microorganisms and its activity (Beylich et al., 2010).

In this study, both *Pseudomonas* sp. and *Bacillus* sp. are aerobic microorganisms and they were both shown to be negatively affected by the increase in bulk-density of soil. We tried to mitigate this effect by choosing a wetness equivalent to 40–60% of the pore space filled with water (and hence 60–40% with air) and maintain this ratio between our treatments. Inevitably, other factors were also altered. For example, as more soil is packed in a microcosm at a higher bulk-density, and the number of cells at inoculation is constant per volume, the cell count expressed per gram of soil is lower in soil with a higher density. This is inherent to quantifying microorganisms

in soil and is the main difference between comparing numbers or densities expressed gravimetrically or volumetrically. However, the differences we found are larger than could be explained by such a simple dilution effect. On the other hand, all other parameters being equal, soil with a higher bulk-density has larger organic matter content per volume of soil. So each microcosm contains more organic matter at a higher bulk-density. The fact that this may also have affected the growth highlights the complex web of interactions that take place between physical space and other conditions. Disentangling this through targeted experimentation is not easy and the way forward would be to develop mathematical models that consider the impact of microscopic heterogeneities on microbial dynamics. Examples of such an approach are given for bacteria in Monga et al. (2014) and for fungi in Falconer et al. (2015) where it was shown how biological, physical, and chemical characteristics interact at the microscale to influence emerging processes at larger scales.

A significant effect of aggregate size on the growth is observed only for samples inoculated with *Bacillus*. The numbers of *Bacillus* cell counts are higher in smaller aggregates of 1–2 mm in size. The possibility of active growth in smaller size aggregates could be due to the availability of more nutrients in smaller sized aggregates. A non-significant effect of aggregate size on *Pseudomonas* cells counts is observed. This result agrees with the finding of Drazkiewicz (1994) who found that soil type had more influence on the number of *Pseudomonas* than the aggregate size.

Spread of microorganism is a critical trait that affects their ability to find food sources, and to interact with other species. Yet data on mobility of bacteria through soil are limited to studies under conditions of convective flow. We developed a simple experimental system that enables the spread of bacteria through soil, following the concept of dispersal kernels commonly used in ecology. Our results show that both species spread significant distances in relatively short timescales even in absence of convective flow. Our results demonstrate spread beyond 1.5 cm in the absence of convective flow and that the spread of bacteria is species-dependent and determined by soil physical conditions. Interestingly, whereas the growth of *Bacillus* is slower than that of *Pseudomonas*, the spread is faster. Potentially this could indicate that energy devoted to spread is diverged from energy devoted to growth. In any case our results show a differential effect of soil physical conditions on the ability of bacteria to grow and spread, which are likely to be significant in relation to the way species explore soil and interact with each other. The results showed a different response to soil architecture on spread than the results we found on growth. Whereas one might expect some similarities to occur, it is also not surprising that factors like connectivity of the water-filled pore space will have a greater effect on spread than it will have on the growth. This is expected as in the growth experiment, bacteria were mixed through the soil, and growth can therefore be initiated in disconnected parts of the pore volume. This in contrast to the spread, where a single source was used, and a connected pathway will be required for spread. The spread would therefore be expected to show a greater dependency on water content that the growth data within the range of water content tested in this study.

Our results have implications for the way soil microbiological studies are reported. We demonstrate in this study that the physical composition of soil has a significant effect on the growth of bacteria in soil. Cell counts of both bacterial strains selected for this study show a significant influence of bulk-density on their growth in soil whereas aggregate size only affected *Bacillus*. We also show that bacterial strains respond differentially to soil physical conditions. This highlights the need to include detailed reporting on soil physical conditions in soil microbiological studies. This is true whether the characteristics are measured in terms of bulk properties, such as bulk-density and aggregate size, or in terms of the microscopic heterogeneity of the pore geometry. We also demonstrate how specific characteristics of the pore volume, such as connectivity of the pore space or the pore-solid interface can be manipulated through bulk properties of soil microcosms.

REFERENCES

Baveye, P., Berthelin, J., and Munch, J. (2016). Too much or not enough: reflection on two contrasting perspectives on soil biodiversity. *Soil Biol. Biochem*. 103, 320–326. doi: 10.1016/j.soilbio.2016.09.008

Baveye, P. C., Pot, V., and Garnier, P. (2017). Accounting for sub-resolution pores in models of water and solute transport in soils based on computed tomography images: are we there yet? *J. Hydrol.* 555, 253–256. doi: 10.1016/j.jhydrol.2017.10.021

Beylich, A., Oberholzer, H.-R., Schrader, S., Hoper, H., and Wilke, B.-M. (2010). Evaluation of soil compaction effects on soil biota and soil biological processes in soils. *Soil Tillage Res.* 109, 133–143. doi: 10.1016/j.still.2010.05.010

Carpenter, S. R. (1996). Microcosm experiments have limited relevance for community and ecosystem ecology. *Ecology* 77, 677–680 doi: 10.2307/2265490

Dick, R. P., Rasmussen, P. E., and Kerle, E. A. (1988). Influence of long-term residue management on soil enzyme activities in relation to soil chemical properties of a wheat-fallow system. *Biol. Fertil. Soils* 6, 159–164. doi: 10.1007/BF00257667

Drake, J. A., Huxel, G. R., and Hewitt, C. L. (1996). Microcosms as models for generating and testing community theory. *Ecology 77,* 670–677. doi: 10.2307/2265489

Drazkiewicz, M. (1994). Distribution of microorganisms in soil aggregates: effect of aggregate size. *Folia Microbiol.* 39, 276–282. doi: 10.1007/BF02814312

Eickhorst, T., and Tippkötter, R. (2008). Improved detection of soil microorganisms using fluorescence in situ hybridization (FISH) and catalyzed reporter deposition (CARD-FISH). *Soil Biol. Biochem.* 40, 1883–1891. doi: 10.1016/j.soilbio.2008.03.024

Ettema, C. H., and Wardle, D. A. (2002). Spatial soil ecology. *Trends Ecol. Evol.* 17 177–183. doi: 10.1016/S0169-5347(02)02496-5

Falconer, R. E., Battaia, G., Schmidt, S., Baveye, P., Chenu, C., andOtten, W. (2015). Microscale heterogeneity explains experimental variability and non-linearity in mineralisation of soil organic matter. *PLoS ONE* 10:e0123774 doi: 10.1371/journal.pone.0123774

Frey, B., Kremer, J., Rudt, A., Sciacca, S., Matthies, D., and Luscher, P. (2009). Compaction of forest soils with heavy logging machinery affects soil bacterial community structure. *Eur. J. Soil Biol.* 45, 312–320. doi: 10.1016/j.ejsobi.2009.05.006

Harris, K., Young, I. M., Gilligan, C. A., Otten, W., and Ritz, K. (2003). Effect of bulk density on the spatial organisation of the fungus *Rhizoctonia solani* in soil. *FEMS Microb. Ecol.* 44, 45–56. doi: 10.1111/j.1574-6941.2003.tb01089.x

Hobley, L., Ostrowski, A., Rao, F. V., Bromley, K. M., Porter, M., Prescott, A. R., et al. (2013). BslA is a self-assembling bacterial hydrophobin that coats the *Bacillus subtilis* biofilm. *Proc. Natl. Acad. Sci. U.S.A.* 110, 13600–13605. doi: 10.1073/pnas.1306390110

Houston, A. N., Otten, W., Baveye, P. C., and Hapca, S. (2013). Adaptive-window indicator kriging: a thresholding method for computed tomography images of porous media. *Comput. Geosci.* 54, 239–248. doi: 10.1016/j.cageo.2012.11.016

Jessup, C. M., Kassen, R., Forde, S. E., Kerr, B., Buckling, A., Rainey, P. B., et al. J. (2004). Big questions, small worlds: microbial model systems in ecology. *Trends Ecol. Evol.* 19, 189–197.doi: 10.1016/j.tree.2004.01.008

King, E. O., Ward, M. K., and Raney, D. E. (1954). Two simple media for the demonstration of pyocyanin and fluorescin. *J. Lab. Clin. Med.*44, 301–307.

Kravchenko, S., Falconer, R., Grinev, D., and Otten, W. (2011). Fungal colonization in soils of contrasting management: modeling growth in 3D pore volumes of undisturbed soil samples. *Ecol. Appl.* 21, 1202–1210. doi: 10.1890/10-0525.1

Li, C. H., Ma, B. L., and Zhang, T. Q. (2002). Soil bulk density effects on soil microbial populations and enzyme activities during the growth of maize (*Zea mays* L.) planted in large pots under field exposure. *Can. J. Soil Sci.* 82, 147–154. doi: 10.4141/S01-026

Luo, L., Lin, H., and Li, S. (2010). Quantification of 3-D soil macropore networks in different soil types and land uses using computed tomography. *J.Hydrol.* 393, 53–64.doi: 10.1016/j.jhydrol.2010.03.031

Monga, O., Garnier, P., Pot, V., Coucheney, E., Nunan, N., Otten, W., et al. (2014). Simulating microbial degradation of organic matter in a simple porous system using the 3-D diffusion-based model MOSAIC. *Biogeosciences* 11, 2201–2209. doi: 10.5194/bg-11-2201-2014

Nunan, N., Ritz, K., Crabb, D., Harris, K., Wu, K., Crawford, J. W., et al. (2001). Quantification of the in situ distribution of soil bacteria by large-scale imaging of thin sections of undisturbed soil. *FEMS Microbiol. Ecol.* 37, 67–77. doi: 10.1111/j.1574-6941.2001.tb00854.x

Or, D., Smets, B. F., Wraith, J. M., Dechesne, A., and Friedman, S. P. (2007). Physical constraints affecting bacterial habitats and activity in unsaturated porous media–a review. *Adv. Water Resour.*30, 1505–1527. doi: 10.1016/j.advwatres.2006.05.025

Otten, W., Gilligan, C. A., Hall, D., Harris, K., Ritz, K., and Young, I. M. (2001). Soil physics, fungal epidemiology and the spread of *Rhizoctonia solani. N. Phytol.* 151, 459–468. doi: 10.1046/j.0028-646x.2001.00190.x

Otten, W., Gilligan, C. A., Watts, C., Dexter, A. R., and Hall, D. (1999). Continuity of air-filled pores and invasion thresholds for a soil-borne fungal plant pathogen, *Rhizoctonia solani. Soil Biol. Biochem.* 31, 1803–1810.

Otten, W., Harris, K., Young, I. M., Ritz, K., and Gilligan, C. A. (2004). Preferential spread of the pathogenic fungus *Rhizoctonia solani* through structured soil. *Soil Biol. Biochem.* 36, 203–210. doi: 10.1016/j.soilbio.2003.09.006

Pajor, R., Falconer, R., Hapca, S., and Otten, W. (2010). Modelling and quantifying the effect of heterogeneity in soil physical conditions on fungal growth. *Biogeosciences* 7, 3731–3740. doi: 10.5194/bg-7-3731-2010

Pupin, B., Freddi, S., and Nahas, E. (2009). Microbial alterations of the soil influenced compaction. *Rev. Bras. Ciênc.* 33, 1207–1213. doi: 10.1590/S0100-06832009000500014

Sun, B., Hallett, P. D., Caul, S., Daniell, T. J., and Hopkins, D. W. (2011). Distribution of soil carbon and microbial biomass in arable soils under different tillage regimes. *Plant Soil* 338, 17–25. doi: 10.1007/s11104-010-0459-2

Tan, X., Chang, S. X., and Kabzems, R. (2008). Soil compaction and forest floor removal reduced microbial biomass and enzyme activities in a boreal aspen forest soil. *Biol. Fertil. Soils.* 44, 471–479. doi: 10.1007/s00374-007-0229-3

Tecon, R., and Or, D. (2017). Biophysical processes supporting the diversity of microbial life in soil *FEMS Microbiol. Rev.* 41, 599–623. doi: 10.1093/femsre/fux039

Verhoef, H. A. (1996). The role of microcosms in the study of ecosystem processes. *Ecology* 77, 685–690 doi: 10.2307/2265492

Young, I. M., Crawford, J. W., Nunan, N., Otten, W., and Spiers, A. (2008). Microbial distribution in soils: physics and scaling. *Adv. Agron.* 100, 81–121.doi: 10.1016/S0065-2113(08)00604-4

Young, I., and Ritz, K. (2005). "The habitat of soil microbes," in *Biological Diversity and Function in Soils*, eds R. Bardgett, M. Usher, and D. Hopkins (Cambridge: Cambridge University Press), 31–43.

Soil Microbial Populations Shift as Processes Protecting Organic Matter Change During Podzolization

Marie-Liesse Vermeire [1,2]*, Jean-Thomas Cornélis [3], Eric Van Ranst [4], Steeve Bonneville [5], Sebastian Doetterl [6,7] and Bruno Delvaux [1]

[1] Soil Science, Earth and Life Institute, Université Catholique de Louvain, Louvain-La-Neuve, Belgium, [2] Department of Biological Sciences, Faculty of Sciences, University of Cape Town, Cape Town, South Africa, [3] TERRA Teaching and Research Centre, Gembloux Agro-Bio Tech, University of Liege, Gembloux, Belgium, [4] Department of Geology (WE13), Faculty of Sciences, Ghent University, Ghent, Belgium, [5] Biogeochemistry and Earth System Modelling, Department of Geosciences, Environment and Society, Université Libre de Bruxelles, Bruxelles, Belgium, [6] Soil and Water Resources Research, Institute of Geography, Universität Augsburg, Augsburg, Germany, [7] Isotope Bioscience Laboratory ISOFYS, Ghent University, Ghent, Belgium

In the upper part of the solum of mineral soils, soil organic and mineral constituents co-evolve through pedogenesis, that in turn impacts the transformation and stabilization of soil organic matter (SOM). Here, we assess the reciprocal interactions between soil minerals, SOM and the broad composition of microbial populations in a 530-year chronosequence of podzolic soils. Five pedons, derived from beach sand, are studied. From young to old soils, net acidification parallels mineral dissolution and the formation of eluvial and illuvial horizons. Organo-mineral associations (OMA) accumulate in the illuvial B horizon of the older soils (330–530 years). Apart from contributing to SOM stabilization and protection, organo-mineral compounds progressively fill up interparticle voids. The subsequent loss of porosity leads to horizon induration, decrease of hydraulic conductivity, which promote redoximorphic processes. While recalcitrant SOM is preserved in the topsoil of the old soils, the largest quantity of protected SOM occurs in the indurated, temporally waterlogged B horizons, through both the OMA accumulation and inhibition of microbial decomposition. SOM protection is thus both time- and horizon-specific. The microbiota also evolve along the chronosequence. Fungi dominate in all horizons of the younger soils and in the topsoil of the older soils, while bacteria prevail in the cemented B horizons of older soils. This shift in microbial community composition is due to the interdependent co-evolution of SOM and minerals during pedogenesis. Our results call for considering the microenvironment and parameters inherent to decomposer microorganisms to understand SOM protection processes in soils.

Keywords: organic matter, microorganisms, amino sugars, carbon fractionation, micromorphology, SOM protection mechanisms, podzol, chronosequence

INTRODUCTION

The fate of SOM involves the decomposition of macromolecules into small oxidized and reactive molecules that can interact with the pedogenic products of mineral weathering, and influence their formation (Cotrufo et al., 2013; Basile-Doelsch et al., 2015; Lehmann and Kleber, 2015). Soil microorganisms accomplish 85–90% of SOM processing (Lavelle et al., 1993) and microbial biomass contributes to about 80% of SOM (Simpson et al., 2007; Grandy and Neff, 2008; Liang and Balser, 2011; Schmidt et al., 2011; Miltner et al., 2012). During the initial stages of SOM decomposition, some organic compounds are selectively preserved because of intrinsic molecular-level properties that limit their biodegradation ("recalcitrant" compounds). This represents a short-to-medium term C stabilization process— i.e., years or decades—(Kögel-Knabner et al., 2008a; Marschner et al., 2008; Schmidt et al., 2011). In later stages of SOM decomposition, the microbial biomass and byproducts bind to reactive, mineral clay-sized surfaces (Kögel-Knabner et al., 2008b; Kleber et al., 2015). The resulting OMA and soil micro-aggregates are responsible for the long-term persistence of SOM—i.e., decades to millennia—(Sollins et al., 1996; Baldock and Skjemstad, 2000; von Lützow et al., 2006; Kögel-Knabner et al., 2008b; Kleber et al., 2015).

In soils, microorganisms live in pore spaces. Therein, water content, pore-size distribution and pore inter-connectivity determine to a large extent the chemical conditions. They thus constrain the abundance and activity of microbial habitats (Tisdall and Oades, 1982; Hassink et al., 1993; Chenu and Stotzky, 2002; Six et al., 2004; Totsche et al., 2010; Kuzyakov and Blagodatskaya, 2015). SOM present in pore spaces that are either physically inaccessible or chemically not favorable for microorganisms is *per se* protected from microbial biodegradation (Hassink et al., 1993; Chenu and Stotzky, 2002; Totsche et al., 2010; Kuzyakov and Blagodatskaya, 2015). In addition, once accessible to microorganisms, SOM can be degraded only if (i) energy costs of enzyme production are paid back by the energy liberated by decomposition reactions, and (ii) microorganisms do not lack other essential nutrients (Neff et al., 2002; Ekschmitt et al., 2005, 2008; Manzoni and Porporato, 2009; Schmidt et al., 2011; Baldock and Broos, 2012).

Understanding complex interactions between OMA and microbial activity thus requires a process-based approach. This study is aimed at (i) assessing the mineralogical changes induced by pedogenesis and the resulting effects on SOM protection, and (ii) relating them with the evolution in microbial community structure.

Soil processes involved in podzolization generate soil horizons characterized by distinct properties in terms of SOM protection: (i) SOM degradation and intense weathering in the surface horizon; (ii) eluviation with percolating water of dissolved organic matter (DOM) complexed with Al and Fe, which will precipitate in soil horizons beneath; (iii) resulting in the formation of secondary mineral phases and OMA accumulation in illuvial horizons. We thus selected a Cambisol-Podzol chronosequence, as it provides an ideal framework to study the mineralogical, physico-chemical and microbial shifts during

soil formation. All horizons of this soil chronosequence were analyzed for their microstructure, pore space organization and their *in situ* organo-mineral associations (OMA). Using chemical extractions, we further characterized those soils for their content in secondary mineral phases and SOM fractions. With respect to SOM, we distinguished three operationally-defined fractions: (1) "oxidizable" C—C oxidized by NaOCl; (2) "mineral-protected" C—C released after dissolution of the minerals by hydrofluoric acid (HF); and (3) "recalcitrant" C—C resistant to both oxidation and HF treatment (Kleber et al., 2005; Mikutta et al., 2005b, 2006; Siregar et al., 2005; von Lützow et al., 2007; Zimmermann et al., 2007; Torn et al., 2009). The microbial populations were characterized by amino-sugar (AS) extractions. AS content provides an estimate of the amount of living and dead microorganisms in soil samples, and is thus a useful biomarker for investigating microbial contribution to SOM (Zhang and Amelung, 1996; Amelung et al., 2001; Glaser et al., 2004; Bodé et al., 2009, 2013). AS occur in living cells, but persist after cell lysis. About 90% of AS is present in microbial residues (Liang et al., 2008; Pronk et al., 2015). In soils, AS are mostly made of glucosamine (Glu), galactosamine (Gal) and muramic acid (Mur) (Bodé et al., 2013). Cell wall of bacteria is made of equal amounts of Mur and Glu while fungal cell walls contain only chitin, a polymer of Glu (Bodé et al., 2009, 2013). Consequently, the Glu:Mur ratio is used as an indicator of the relative contribution of fungi and bacteria to SOM in soil samples (Amelung et al., 2001; Liang et al., 2007). The Glu:Mur ratio of bacteria ranges between <2 and 8 (Amelung et al., 2001), and was estimated around 271 for fungi (Glaser et al., 2004). We complemented this characterization work by performing incubations to measure the potential of SOM to be degraded by microbial heterotrophic activity.

MATERIALS AND METHODS

Study Site

The podzolic chronosequence is located near Cox Bay on the west coast of Vancouver Island, British Columbia (latitude 49° 6′N, longitude 125° 52′W). The sequence was developed under a temperate rain forest and previously described (Cornelis et al., 2014; Vermeire et al., 2016). Mean annual rainfall and temperature amount to 3,200 mm and 8.9°C, respectively. The age of the deposits ranges from 0 to 530 years (Vermeire et al., 2016). The parent material is the Cox Bay beach sand, exhibiting a uniform sequence of deposits emerging at an annual rate of 0.26 m (Singleton and Lavkulich, 1987). The primary minerals are quartz, sodic plagioclase, amphibole (hornblende), pyroxene (augite), kaolinite, mica (illite) and chlorite (Cornelis et al., 2014). Quartz is by far the dominant mineral. A progressive deepening and differentiation of genetic horizons is observed along the chronosequence (Cornelis et al., 2014).

Vegetation progressively develops with increasing soil age along the sequence from shrubs and trees of Sitka spruce (the dominant tree species) to increasing presence of Douglas fir, Hemlock, Red cedar, Salal and Western sword fern. Five pedons (P1–120 years, P2–175 years, P3–270 years, P4–330 years, and P5–530 years) were selected along a transect (0-147 m length)

perpendicular to the present shoreline (**Figure 1**). The thickness of the Oh horizon increased with age, from 6 and 7 cm thick in P1–120 years and P2–170 years locations, to 12 cm in P3–270 years, and 26 cm in P4–330 years. According to the WRB system (IUSS Working Group, 2015), the pedons key out as Dystric Cambisol at the youngest sites (P1–120 years and P2–175 years), Albic Podzol at the intermediate site (P3–260 years) and Albic Podzols (Placic) at the oldest sites (P4–330 years and P5–530 years). The Albic Podzols (Placic) P4 and P5 are characterized by the following sequence of soil horizons from surface to depth (Cornelis et al., 2014): an eluvial albic E horizon, strongly weathered; an illuvial spodic Bh horizon (enriched in OM); a Bhs horizon, enriched in Fe oxides and OM; a Bs horizon, enriched in short-range-order (SRO) aluminosilicates and Fe oxyhydroxides; a weathered Bw horizon; and a poorly structured BC horizon (**Figure 1**).

Soil Sampling

Bulk samples were collected in each horizon of each pedon. In addition, selected undisturbed samples were collected using Kubiëna tins (i.e., square metal boxes, usually 8 × 6 × 4 cm in size with two loose covers), in order to conduct micromorphological analysis. In each soil pit, the Kubiëna boxes were inserted into the various horizons and the sample was cut out from the soil profile. This procedure allowed to collect soils without disturbing the local 3D structure. Boxes were retrieved between (1) 0–10 cm depth in the P1 BC1 horizon, (2) 10–20 cm in the P3 Bh horizon, (3) 13–22 cm in the P4 Bh, Bhs and Bs horizons, (4) at 4–13 cm in the P5 E, Bh, Bhs, and Bs horizons. These undisturbed samples were oven-dried at 50–60°C, and subsequently impregnated under vacuum with a cold-setting polyester resin (Benyarku and Stoops, 2005). Covered small thin sections (2.4 × 4.8 cm) were prepared. The thin sections were studied with a polarizing microscope and described using the terminology of Stoops (2003).

Soil Physico-Chemical Characterization

Bulk samples were air-dried and passed through a 2 mm-sieve according to NF ISO 11464 (AFNOR, 2006) before analysis. Soil pH was measured in 5 g:25 ml soil:water suspension (Page et al., 1982). Cation exchange capacity (CEC) and the content of exchangeable cations were determined according to Page et al. (1982), in ammonium acetate 1 M at pH 7 and measured by inductively coupled plasma/atomic emission spectrometry (ICP-AES). Soil particle-size analysis was achieved by quantitative recovery of clay ($<2 \mu m$), silt ($2–50 \mu m$) and sand ($>50 \mu m$) fractions after sonication and dispersion with Na^+-saturated resins without any previous H_2O_2 oxidation of OM, as described
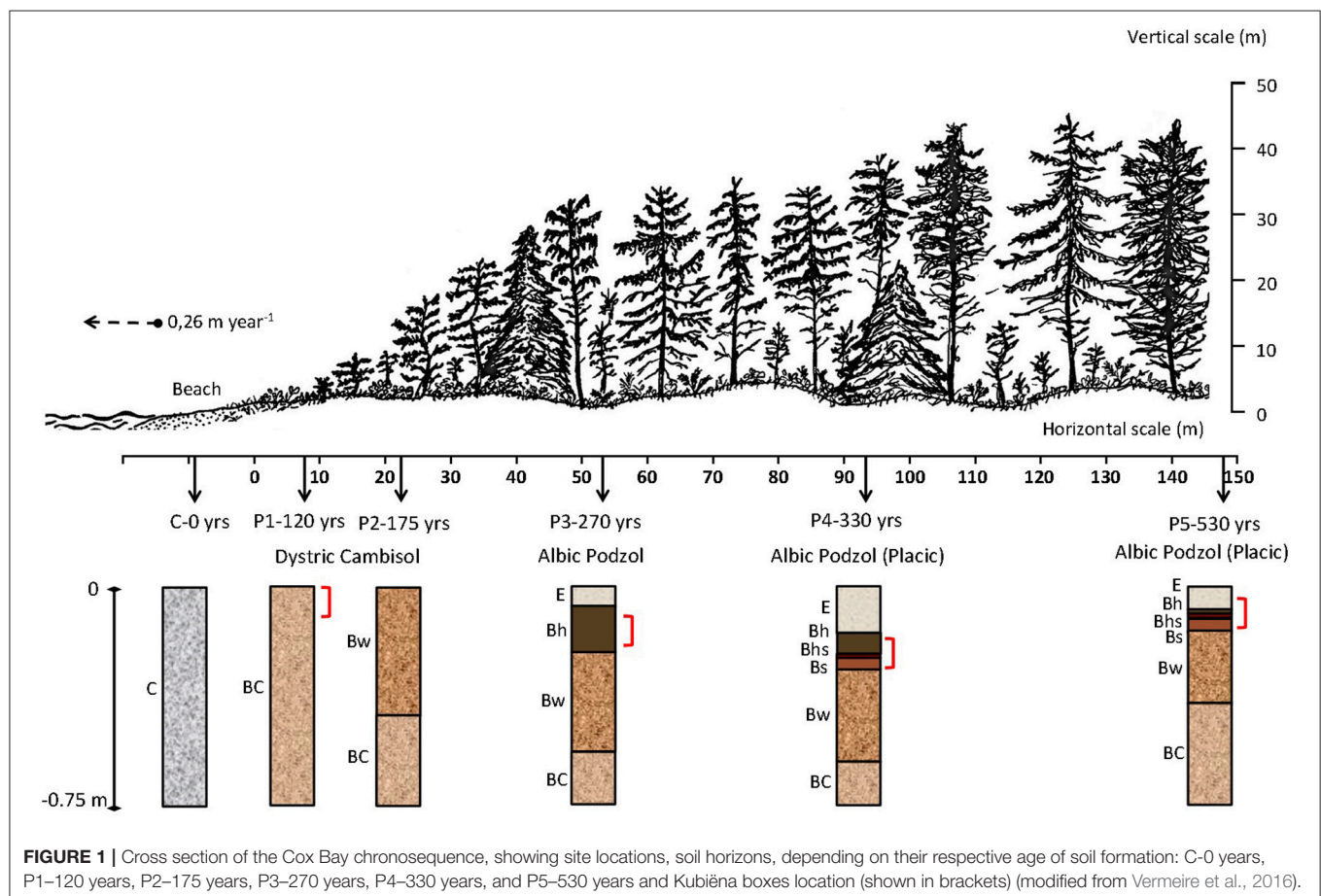

FIGURE 1 | Cross section of the Cox Bay chronosequence, showing site locations, soil horizons, depending on their respective age of soil formation: C-0 years, P1–120 years, P2–175 years, P3–270 years, P4–330 years, and P5–530 years and Kubiëna boxes location (shown in brackets) (modified from Vermeire et al., 2016).

in Henriet et al. (2008). Total element contents (Si, Al, Fe, Ca, K, Mg, Na, Ba, Mn, P, Sr, Zr, Ti) were measured by ICP–AES after fusion in Li-metaborate + Li-tetraborate at 1,000°C of crushed (< 250 μm) subsample (Chao and Sanzolone, 1992). Soil weathering stage was assessed by computing the Total Reserve in Bases (TRB) as the sum of the total contents of major alkaline (K, Na) and alkaline-earth (Ca, Mg) cations (Herbillon, 1986).

Secondary Si-, Fe-, and Al-bearing phases were studied using selective chemical extractions: sodium pyrophosphate (p) (Bascomb, 1968), dark oxalate (o) (Blakemore et al., 1987), and dithionite-citrate-bicarbonate (DCB, d) (Mehra and Jackson, 1960). Si, Fe, and Al concentrations were measured in "p," "o," and "d" extracts by ICP–AES. Al_p and Fe_p are attributed to Al and Fe in organo-metallic complexes. However, this alkaline solution could also extract Al from SRO Al-hydroxide, and Al and Si from SRO aluminosilicates (Schuppli et al., 1983; Kaiser and Zech, 1996). Si_o, Al_o, and Fe_o can be attributed to Si, Al, and Fe SRO minerals such as allophanic substances, SRO Al and Fe oxides. Dark oxalate may, however, dissolve lepidocrocite (Poulton and Canfield, 2005) as well as organo-metallic compounds. DCB-extractable Fe_d is attributed to "free iron," i.e., Fe occurring in (i) in organo-metallic complexes, (ii) SRO oxides, (iii) crystalline Fe oxides such as hematite and goethite. Thus, "crystalline" Fe is estimated by the difference Fe_d-Fe_o. The Fe_d/Fe_t ratio (Fe_t = total iron content) evaluates the relative proportion of free iron in soil and thus reflects soil weathering stage and the evolution of the mineral phases during soil development. However, these assessments must be treated with caution due to partial dissolving side effects of soil minerals.

SOM Fractionation

Total organic carbon and nitrogen concentration (C_T, N_T) were determined on powdered air-dried soil subsamples by dry combustion with a FLASH 2000 Organic Elemental Analyzer (ThermoFisher Scientific). The distribution of C and N was estimated following the chemical separation procedure of Mikutta et al. (2006). In brief, 3 g of air-dried sample were treated three times with 30 mL of 6 wt% NaOCl adjusted to pH 8.0 for a duration of 6 h at 25°C. Samples were further washed twice with 30 mL 1 M NaCl and with deionized water until the solution was chloride free ($AgNO_3$ testing). The samples were then dried at 60°C and homogenized before C and N measurement on powdered soil subsamples by dry combustion with a FLASH 2000 Organic Elemental Analyzer (ThermoFisher Scientific). The amounts of C and N left after NaOCl treatment are quantified as stable C and N (C_S and N_S). The "oxidizable" C and N (C_O and N_O) contents were calculated by subtracting the C_S and N_S contents from the total C and N content (C_T and N_T), respectively.

$$C_O = C_T - C_S \qquad (1)$$

Within the stable, NaOCl-treated fraction, we distinguished mineral-protected (C_{MP} and N_{MP}) from the recalcitrant (C_R and N_R) C and N. HF dissolves mineral moieties of OMA, leaving the NaOCl/HF-treated fraction defined as chemically resistant or recalcitrant (Eusterhues et al., 2003; Mikutta et al., 2006).

"Recalcitrant" organic substances are supposed to exhibit specific molecular properties that can diminish their degradation (e.g., black C and aliphatic compounds such as n-alkanes and n-fatty acids). Although the dominant controls of SOM stability are environmental and biological (von Lützow et al., 2006; Schmidt et al., 2011), molecular structure of SOM influences its decomposition rate by determining the complexity of the decomposition operation (Kleber, 2010; Barré et al., 2016). Briefly, 2.25 g of NaOCl-treated dry samples were transferred into pre-weighed centrifuge tubes, shaken four times with 15 ml 10% HF for a duration of 2 h and then washed five times with 15 ml deionized water. Between each shaking step, the samples were centrifuged and the supernatant discarded. The solid residues were dried at 60°C, crushed and analyzed for C_R and N_R on 10 mg subsamples by dry combustion with a FLASH 2000 Organic Elemental Analyzer (ThermoFisher Scientific). The C_{MP} and N_{MP} contents were derived from the difference between C_S and N_S and C_R and N_R contents, respectively.

$$C_{MP} = C_S - C_R \qquad (2)$$

At each step of the sequential extraction, the initial and residual sample weights were recorded, but the respective C and N contents were expressed on a bulk soil basis (g kg^{-1} soil). The C and N contents in the fractions were measured. The values of the SOM C/N ratio were calculated within each fraction (C_O/N_O, C_R/N_R, C_{MP}/N_{MP}).

Specific Analysis of Amino-Sugars

AS extraction and analysis were carried out according to Bodé et al. (2009, 2013). Yet, the procedure was slightly adapted: instead of using the cation-exchange resin, we used KOH to precipitate Fe and Al impurities. In short, air-dried soil samples (quantity corresponding to 0.3 mg of N) were hydrolyzed and further dried under vacuum in a Rotavap device. The residues were then re-dissolved in MilliQ water and the pH adjusted to 6.6–6.8 with a KOH solution in order to precipitate impurities (mainly Fe and Al). The solutions were then centrifuged and the AS-containing supernatant was freeze dried. The samples were re-dissolved in methanol and centrifuged, and the supernatant (containing the AS fraction) was then transferred into a 10 ml glass tube. The sample was again dried by volatilizing methanol under a stream of nitrogen gas and then freeze dried. After that, the AS were transformed into aldononitrile derivatives and re-dissolved in ethylacetate/hexane. The concentration of basic AS (glucosamine, galactosamine and muramic acid) in the analytical aliquot was determined by liquid chromatography using the method described by Bodé et al. (2009). The liquid chromatographic separation was performed using an LC pump (Surveyor MS-Pump Plus, Thermo Scientific, Bremen, Germany) mounted with a PA20 CarboPac analytical anion-exchange column (3–150 mm, 6.5 μm) and a PA20 guard column (Thermo Scientific, Bremen, Germany).

Soil Respiration Measurements

After being saturated with deionized water, bulk soil samples from each horizon were equilibrated for 15 days in a pressure

plate extractor, to reach a pF of 2.4 (0.25 bar). A quantity equivalent to 40 g of dry soil was transferred into hermetic incubation flasks, containing a 30-mL vial filled with 25 ml of 0.5 M NaOH solution. The CO_2 trapped in NaOH was determined by measuring the changes in electrical conductivity of the solution (Rodella and Saboya, 1999). The incubations were conducted in triplicates per soil horizon and lasted 144 days in a temperature-controlled dark room at 20°C. Incubation flasks without soil samples served as controls. The conductivity within the NaOH vials was determined every 3–7 days. Soil-derived CO_2 was calculated by subtracting the measured values in the soil-containing flasks with values in the blanks measured at the same time (due to atmospheric CO_2). Oxygen was regularly supplied to the incubation by opening the flasks at each measurement time step. The soil samples were kept moist at field capacity by controlling the weight of the incubation flasks and adding deionized water to compensate for the weight loss.

RESULTS

Soil Physico-Chemical Properties

The pH_{H2O} value of the freshly deposited Cox beach sand is 7.7. In P1–120 years and P2–175 years soil pedons, the pH_{H2O} value ranges from 5.8 to 5.9. In P3–270, P4–330, and P5–530 years, from the deepest BC to the surface E horizon, the pH_{H2O} value decreases from 5.4 to 4.6 in P3, from 5.3 to 4.9 in P4, and from 5.1 to 4.4. in P5 (**Table 1**).

The TRB value of the freshly deposited Cox beach sand is 534 $cmol_c$ kg^{-1}. Considering the five pedons (**Table 1**), the TRB of the deepest BC horizon amounts to ($cmol_c$ kg^{-1}) 490 (P1), 368 (P2), 361 (P3), 352 (P4), and 357 in P5. In the surface horizons (P1-BC1, P2-Bw and E in P3, P4, P5), TRB also decreases along the sequence from ($cmol_c$ kg^{-1}) 439 (P1) to 430 (P2), 311 (P3), 236 (P4), and 169 (P5).

In P1, P2, and P3, the oxalate extractable contents (in g kg^{-1}) are low: Fe_o < 2.2, Al_o < 1.4 and Si_o < 0.17 (**Table 1**). In contrast, Fe_o contents are much larger in the Bhs horizon of P4, with 11.6 g kg^{-1}, and P5, with 26.3 g kg^{-1}. Al_o contents are also higher in P4 and P5, compared to the three younger profiles, with a maximum of 9.2 g kg^{-1} in P4-Bhs and 12.6 g kg^{-1} in P5-Bs. Si_o is maximal in P4 and P5-Bs horizons, where it yields 3.5 g kg^{-1} and 4.5 g kg^{-1} respectively. Fe_d contents (g kg^{-1}) are particularly high in P4-Bhs (21.6 g kg^{-1}) and in P5-Bhs (26.1 g kg^{-1}). Pyrophosphate extractable Al and Fe follow the same trends with the largest contents in the Bhs horizons of P4 and P5 (6.7 and 4.1 g kg^{-1} Al_p in P4 and P5 Bhs respectively, and 10.0 and 12.4 g kg^{-1} Fe_p in P4 and P5 Bhs respectively).

In P1 and P2, C_T content does not vary significantly with depth and is ∼ 5.0 g kg^{-1} (**Table 2**). In P3, Bh horizon exhibits a C_T content reaching 17.8 g kg^{-1}. In P4 and P5, C_T further increases in Bh, Bhs and Bs, to reach 25.1 and 43.4 g kg^{-1} in P4- and P5-Bhs, respectively (**Table 2**). In P1 and P2, C_T content is small and mainly consisting of oxidizable C (∼70% of C_T, **Figure 2**). In P3, this oxidizable C fraction is also the largest in all horizons, for example 78% of C_T in the Bh. In P4 and P5 horizons, the oxidizable C still represents an important proportion of C_T, excepted in P4-Bh (5%) and P5-Bs (7%). C_{MP} content amounts

to 11.3, 13.2, and 3.7 g kg^{-1} soil in P4 Bh, Bhs and Bs respectively and thus accounts for 78, 53, and 28% of the C_T. In P5, C_{MP} is 4.3, 15.9 and 7.7 g kg^{-1} in Bh, Bhs and Bs respectively and thus accounts for 14, 37 and 74% of C_T (**Table 2** and **Figure 2**). Recalcitrant C compounds accumulate in the E horizons. C_R represents 30 and 29% of C_T in P3 and P4 E horizons (4.4 and 2.4 g C_R kg^{-1} soil, respectively) and accounts for 69% of C_T in P5 E (10.2 g C_R kg^{-1} soil, **Table 2**, **Figure 2**). In the Bw and BC horizons of all soil profiles, recalcitrant C accounts for ∼1 g kg^{-1} soil; probably due to fire-induced pyrogenic organic matter and "black carbon" present in the sedimentary parent material, as observed in the P1 BC1 thin section.

Soil Respiration

The cumulative CO_2 emission increased linearly over time during the whole experiment (**Figure S1** in Supplementary Material). The respiration rates were thus computed from the slope of the linear regression between cumulated emitted CO_2 and time (all R^2 values were above 0.95). We then normalized the respiration rates to the C content in order to derive the mg CO_2-C emitted per g C per day, which indicates the susceptibility of SOM to be degraded (hereafter called "biodegradability," **Table 2**). The lowest respiration rates were observed in Bw and BC horizons (∼0.13 mg CO_2-C 100 g_{soil} $^{-1}$ day^{-1}), in which C is below 10 g kg^{-1} soil, while the highest respiration rates were observed in E and B horizons (∼0.23 mg CO_2-C 100 g_{soil} $^{-1}$ day^{-1}). The inverse trend was observed for the SOM biodegradability. The lowest biodegradability was measured in the Bh, Bhs and Bs horizons (∼0.11 mg CO_2-C g C $^{-1}$ day^{-1}), the highest in the Bw-BC horizons (∼0.30 mg CO_2-C g C $^{-1}$ day^{-1}) and intermediate biodegradability was measured in E horizons (∼0.21 mg CO_2-C g C $^{-1}$ day^{-1}).

Soil Micromorphological Properties

The P1–120 years BC1 horizon presents a coarse monic (only fabric units larger than a given size limit and associated interstitial pores are present) coarse/fine (c/f) -related distribution pattern (**Figure 3**). Root residues, excrements and charcoal fragments are also observed. The P3–270 years Bh horizon has a similar microstructure. The organic fine material in this horizon results mainly from *in situ* transformation of plant remains and corresponds to polymorphic material as described by De Coninck et al. (1974). Polymorphic material consists of porous aggregates composed of fine organic material, mineral grains and coarse organic elements with a recognizable cell or tissue structure. Roots are mechanically and biochemically fragmented and transformed by soil mesofauna and microbial activity. These transformations result in multiple forms of degraded plant material, including excrements (De Coninck and Righi, 1969; De Coninck et al., 1974; Buurman and Jongmans, 2005). In the spodic horizons of P4–330 years and P5–530 years, the micromorphological features differ from those in the three younger profiles, mainly because of the accumulation of illuvial organic fine material resulting in a mixture of gefuric (bridges of finer material exist between coarser grains), chitonic (finer material coats the coarser grains) and enaulic (the finer material occurs as small aggregates in

TABLE 1 | Soil physico-chemical properties: pH$_{water}$, Total Reserve in Bases (TRB), pyrophosphate (p), oxalate (o), DCB (d)-extractable Al, Fe, and Si (values are given ± one standard deviation).

Profile	Age	Horizon	Depth	pH$_{H2O}$	TRB	Al$_p$	Al$_o$	Fe$_p$	Fe$_o$	Fe$_d$	Si$_o$
			cm		cmol$_c$ kg^{-1}				g kg^{-1}		
P1	120	BC	0–35	5.9	439	0.50 ± 0.03	0.70 ± 0.04	0.54 ± 0.08	1.64 ± 0.15	1.82 ± 0.08	0.12 ± 0.01
P1	120	BC	35–60	5.9	490	0.53 ± 0.03	0.76 ± 0.05	0.49 ± 0.07	1.79 ± 0.16	1.9 ± 0.08	0.13 ± 0.01
P2	175	Bw	3–44	5.8	430	0.68 ± 0.04	0.90 ± 0.06	0.66 ± 0.09	1.73 ± 0.16	2.04 ± 0.09	0.09 ± 0.01
P2	175	BC	44–75	5.9	368	0.42 ± 0.02	0.65 ± 0.04	0.3 ± 0.04	1.04 ± 0.09	1.39 ± 0.06	0.13 ± 0.01
P3	270	E	0–7	4.6	311	0.43 ± 0.03	0.59 ± 0.04	0.87 ± 0.12	1.22 ± 0.11	2.54 ± 0.11	0.12 ± 0.01
P3	270	Bh	7–23	5.1	311	0.93 ± 0.05	1.25 ± 0.08	1.42 ± 0.20	2.17 ± 0.20	2.65 ± 0.11	0.16 ± 0.01
P3	270	Bw	23–57	5.3	299	0.81 ± 0.05	1.10 ± 0.07	1.17 ± 0.17	2.06 ± 0.19	2.38 ± 0.10	0.17 ± 0.01
P3	270	BC	>57	5.4	361	1.05 ± 0.06	1.39 ± 0.09	0.85 ± 0.12	1.7 ± 0.15	2.19 ± 0.09	0.16 ± 0.01
P4	330	E	0–10	4.9	236	1.35 ± 0.08	1.43 ± 0.09	0.75 ± 0.10	1.12 ± 0.10	1.05 ± 0.04	0.22 ± 0.02
P4	330	Bh	10–17	5.5	322	6.02 ± 0.35	8.80 ± 0.55	1.33 ± 0.19	1.71 ± 0.16	3.27 ± 0.14	1.58 ± 0.11
P4	330	Bhs	17–17.5	5.4	329	6.70 ± 0.39	9.16 ± 0.57	9.96 ± 1.42	11.64 ± 1.06	21.63 ± 0.91	1.82 ± 0.13
P4	330	Bs	17.5–23	5.3	378	1.74 ± 0.11	9.11 ± 0.56	0.29 ± 0.04	3.5 ± 0.32	3.69 ± 0.15	3.48 ± 0.25
P4	330	Bw	23–63	5.4	349	1.11 ± 0.06	6.97 ± 0.43	0.09 ± 0.01	1.98 ± 0.18	2.41 ± 0.10	2.79 ± 0.20
P4	330	BC	63–113	5.3	352	0.79 ± 0.05	4.49 ± 0.28	0.05 ± 0.01	0.89 ± 0.08	1.28 ± 0.05	1.88 ± 0.14
P5	530	E	0–8	4.5	169	0.65 ± 0.04	0.68 ± 0.042	0.47 ± 0.07	0.64 ± 0.06	1.59 ± 0.07	0.06 ± 0.004
P5	530	Bh	8–9.5	4.5	241	2.98 ± 0.17	3.19 ± 0.20	3.29 ± 0.47	4.52 ± 0.41	6.74 ± 0.28	0.4 ± 0.03
P5	530	Bhs	9.5–10	4.5	264	4.11 ± 0.24	6.22 ± 0.39	12.44 ± 1.78	26.34 ± 2.40	26.11 ± 1.10	0.84 ± 0.06
P5	530	Bs	10–15	4.8	297	2.43 ± 0.14	12.62 ± 0.78	0.85 ± 0.12	6.93 ± 0.63	9.61 ± 0.40	4.56 ± 0.33
P5	530	Bw	15–40	5.0	352	0.91 ± 0.05	7.96 ± 0.49	0.03 ± 0.004	1.4 ± 0.13	1.77 ± 0.07	3.54 ± 0.25
P5	530	BC	40–60	5.1	357	0.54 ± 0.03	3.9 ± 0.24	0.02 ± 0.003	0.65 ± 0.06	1.18 ± 0.05	1.69 ± 0.12

the spaces between the coarser grains) c/f-related distribution patterns (Stoops, 2003). This homogeneous, colloidal-sized material with a typical cracking pattern and without coarse organic elements corresponds to monomorphic organic matter (De Coninck et al., 1974; De Coninck, 1980). The cracks were interpreted as desiccation features of strongly hydrated OM gels (Buurman and Jongmans, 2005). The cemented (in the field) spodic (Bhs) horizons show all pores filled with monomorphic material, resulting in a porphyric c/f related distribution pattern. This cementation or massive consistence lead to periodic water stagnation in the field, alternating phases of desiccation and waterlogging, and is common in poorly drained Podzols (Buurman and Jongmans, 2005; Legros, 2007).

Evolution of the Microbial Populations

Except in P4, AS content in all pedons is generally the largest in the surface horizon and decreases at depth (**Table 3**). The lowest AS concentrations were measured in P2–175 years and P4–330 years (maximum value of the pedon: 54.1 and 125.8 μg g$_{soil}$$^{-1}$ in P2 and P4 respectively), the largest in P3–270 years and P5–530 years (maximum value: 332.4 and 490.6 μg g$_{soil}$$^{-1}$ in P3 and P5, respectively), while values in P1–120 years were intermediate (maximum value of the pedon: 172.4 μg g$_{soil}$$^{-1}$). In P1, P2, and P3, the Glu:Mur ratio is above 40 in the whole profile, and reaches 98 in P3 Bh, indicating a fungal-dominated microbiota (**Table 3**). A Glu:Mur ratio of 89.0 was measured in beech litter (Amelung et al., 2001) and ascribed to

fungal-derived Glu. In P4 and P5, the composition of microbiota differs between the topmost E and the underlying horizons. In E horizons the population is fungal-dominated (Glu:Mur = 54.9 in P4-E and 62.2 in P5-E) while deeper horizons have low Glu:Mur ratios (between 13.5 and 25.6 in P4; between 13.9 and 29.2 in P5) reflecting a bacteria-dominated microbiota. The Glu:Mur ratio in Bh, Bhs, Bs, Bw, and BC horizons of P4 and P5 is in the range of the values observed in mineral soils by Amelung et al. (2002) (~18–26) and by Glaser et al. (2004) (~15–24).

DISCUSSION

Acidification and Accumulation of Secondary Mineral Phases

With increasing soil age, forest development along the chronosequence induces an increasing SOM input from the litter, favored by humid (excess of precipitation over evapotranspiration) climatic conditions, which promote leaching of solutes produced by mineral weathering. The concomitant decrease of pH and TRB values leads to a net acidification, i.e., a decrease of acid-neutralizing capacity (ANC) (van Breemen et al., 1983; Cornu et al., 2009). The litter of Sitka spruce, which is the dominant tree species, is known to produce strong organic acids promoting soil acidification (Lindeburg et al., 2013). The processes of mineral weathering, Al/Fe complexation and mobilization as well as leaching of alkaline and alkaline-earth cations rapidly

TABLE 2 | C fractions: total (C_T), Stable (C_S), recalcitrant (C_R), mineral-protected (C_{MP}), oxidizable (C_O), bulk soil SOM C_T/N_T ratio (values are given ± one standard deviation); soil respiration rates (slope of the cumulative CO_2 emission with time, calculated by linear regression, and associated R^2-values), and soil respiration rates normalized by the total SOC content (=SOM biodegradability).

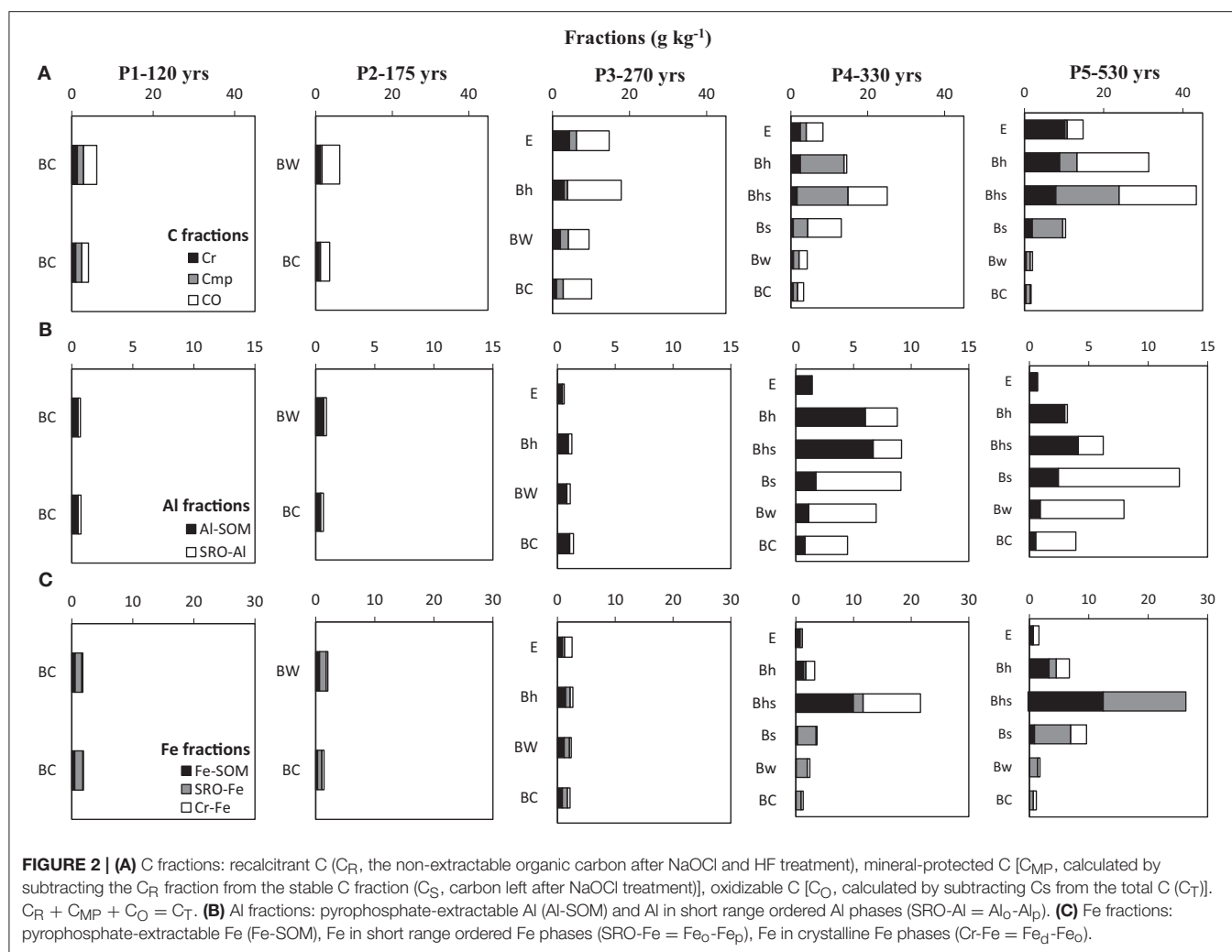| Profile	Horizon	Depth	C_T	C_S	C_R	C_{MP}	C_O	C_T/N_T	Respiration rates		
		cm			g kg^{-1}				mgCO$_2$-C 100 g$_{soil}^{-1}$ day^{-1}	R^2	mgCO$_2$-C g$_C^{-1}$ day^{-1}
P1	BC	0–35	6.14 ± 0.29	2.87 ± 0.21	1.39 ± 0.06	1.48 ± 0.24	3.27 ± 0.37	29.7 ± 1.5	0.16	0.9810	0.26
P1	BC	35–60	4.11 ± 0.20	2.45 ± 0.17	0.97 ± 0.04	1.48 ± 0.24	1.66 ± 0.19	16.8 ± 0.8	0.16	0.9966	0.40
P2	Bw	3–44	6.26 ± 0.3	1.66 ± 0.12	1.15 ± 0.05	0.50 ± 0.08	4.60 ± 0.52	18.2 ± 0.9	0.17	0.9937	0.28
P2	BC	44–75	3.63 ± 0.17	1.23 ± 0.09	0.85 ± 0.04	0.38 ± 0.06	2.40 ± 0.27	10.8 ± 0.5	0.09	0.9710	0.26
P3	E	0–7	14.68 ± 0.70	6.16 ± 0.43	4.41 ± 0.19	1.74 ± 0.28	8.53 ± 0.96	21.2 ± 1.1	0.25	0.9972	0.17
P3	Bh	7–23	17.84 ± 0.86	3.86 ± 0.27	3.05 ± 0.13	0.81 ± 0.13	13.99 ± 1.57	21.6 ± 1.1	0.20	0.9996	0.11
P3	Bw	23–57	9.48 ± 0.46	4.08 ± 0.29	2.04 ± 0.09	2.04 ± 0.32	5.40 ± 0.61	15.8 ± 0.8	0.21	0.9950	0.23
P3	BC	> 57	10.13 ± 0.49	2.8 ± 0.20	1.04 ± 0.04	1.76 ± 0.28	7.33 ± 0.82	16.5 ± 0.8	0.17	0.9974	0.17
P4	E	0–10	8.32 ± 0.40	4.01 ± 0.28	2.44 ± 0.10	1.57 ± 0.25	4.31 ± 0.48	19.9 ± 1.0	0.17	0.9899	0.20
P4	Bh	10–17	14.51 ± 0.70	13.77 ± 1.00	2.49 ± 0.11	11.28 ± 1.79	0.74 ± 0.08	24.8 ± 1.2	0.15	0.9849	0.10
P4	Bhs	17–17.5	25.05 ± 1.20	14.82 ± 1.04	1.64 ± 0.07	13.19 ± 2.10	10.22 ± 1.14	26.7 ± 1.3	0.25	0.9977	0.10
P4	Bs	17.5–23	13.08 ± 0.63	4.35 ± 0.30	0.63 ± 0.03	3.72 ± 0.59	8.73 ± 0.98	20.1 ± 1.0	0.14	0.9866	0.11
P4	Bw	23–63	4.26 ± 0.20	2.1 ± 0.15	0.67 ± 0.03	1.43 ± 0.23	2.16 ± 0.24	14.7 ± 0.7	0.08	0.9582	0.19
P4	BC	63–113	3.33 ± 0.16	1.73 ± 0.12	0.64 ± 0.03	1.09 ± 0.17	1.60 ± 0.18	10.6 ± 0.5	0.12	0.9774	0.35
P5	E	0–8	14.83 ± 0.71	10.76 ± 0.75	10.22 ± 0.44	0.54 ± 0.09	4.06 ± 0.45	18.6 ± 0.9	0.38	0.9996	0.26
P5	Bh	8–9.5	31.43 ± 1.51	13.22 ± 0.93	8.9 ± 0.38	4.31 ± 0.69	18.21 ± 2.04	24.5 ± 1.2	0.27	0.9906	0.09
P5	Bhs	9.5–10	43.42 ± 2.08	23.84 ± 1.67	7.95 ± 0.34	15.89 ± 2.53	19.58 ± 2.19	30.9 ± 1.5	0.52	0.9979	0.12
P5	Bs	10–15	10.39 ± 0.50	9.65 ± 0.70	1.96 ± 0.08	7.69 ± 1.22	0.75 ± 0.08	25.6 ± 1.3	0.18	0.9946	0.17
P5	Bw	15–40	2.01 ± 0.10	1.39 ± 0.10	0.44 ± 0.02	0.96 ± 0.15	0.62 ± 0.07	8.92 ± 0.4	0.10	0.9741	0.51
P5	BC	40–60	1.69 ± 0.08	1.47 ± 0.10	0.4 ± 0.02	1.07 ± 0.17	0.22 ± 0.02	5.61 ± 0.3	0.11	0.9714	0.64

occur, in less than 60 years, i.e., between P3–270 years and P4–330 years (Vermeire et al., 2016; Fekiacova et al., 2017). Such a timing for incipient podzolization is in agreement with several studies reviewed in Sauer et al. (2008), revealing the formation of a bleached E horizon after about 200–500 years.

The formation and transport of aqueous Al/Fe-OM complexes (i.e., "fulvate theory" from McKeague et al., 1978) has been generally accepted as the dominant process of Al/Fe-OM eluviation (Lundström et al., 2000) that initiate podzolization. Due to their large affinity for Fe and Al, the Fe/Al-OM complexes not only enhance mineral weathering (by decreasing the free Fe^{3+} and Al^{3+}, hence, favoring dissolution reactions), but also transport Al and Fe at depth (Lundström et al., 2000; van Hees et al., 2000; Kaiser and Kalbitz, 2012; Gangloff et al., 2014). In the chronosequence, the evidence for podzolization is clear: SOM accumulation is relatively large in the illuvial Bh of P3 and keeps increasing in P4 and P5 while Al- and Fe-rich phases occur in P4 and P5 (**Tables 1**, **2**, **Figure 2**). The main Fe secondary phases in P4 and P5 illuvial horizons are linked to (i) Fe_p (presumably the Fe-SOM complexes), which is largest in P4-Bhs and P5-Bhs (10.0 and 12.4 g kg^{-1}, 46 and 48% of Fe_d, respectively); (ii) SRO Fe oxide (i.e., Fe_o-Fe_p), which is the dominant Fe phase in P4-Bs (3.2 g kg^{-1}, 87% of Fe_d) and P5 Bhs and Bs (13.9 and 6.1 g kg^{-1}, 53 and 63% of Fe_d, respectively) and (iii) crystalline Fe oxide (Fe_d-Fe_o), which is largest in P4-Bhs (10.0 g kg^{-1}, 47% of

Fe_d). The SRO Fe-rich secondary phase is probably ferrihydrite (Fe hydroxides) while crystalline Fe minerals are likely to be goethite. Both are known to be the most abundant Fe mineral phases in Podzols (Cornell and Schwertmann, 2003; Eusterhues et al., 2003, 2005). In parallel, the main Al secondary phase in P4 and P5 Bh and Bhs is bound to SOM (i.e., extracted in Al_p), which represents 68, 73, 93, and 68% of Al_o, in P4-Bh, -Bhs and P5-Bh, -Bhs respectively (6.0, 6.7, 3.0, and 4.1 g kg^{-1}, respectively). In Bs horizons, the main Al secondary phase is a SRO aluminosilicate, likely an "imogolite type material" (ITM) (Farmer et al., 1980). The presence of ITM in P4 and P5 is supported by the several observations: (i) the ratio $(Al_o$-$Al_p)/Si_o$ is ∼ 2 (2.1 in P4 Bs and 2.2 in P5 Bs); (ii) the moderately acidic pH in P4 and P5 (pH > 4.5—**Table 1**) as ITM would readily dissolved for pH<4 (Gustafsson et al., 1995; Lundström et al., 1995; Mossin et al., 2002); (iii) the paucity of Al-SOM (Al_p represents 19% of Al_o, in P4 and P5 Bs) as high levels of those complexes would have hindered the formation of imogolite and proto-imogolite.

Changes in OM Distribution During Soil Development

With increasing soil age, an illuvial Bh-accumulating SOM develops along the chronosequence (**Table 2**, **Figure 2**). As pedogenesis proceeds, the SOM composition also changes, as suggested by the evolution of the C_T:N_T ratio (**Table 2**, **Figure 4**)

FIGURE 2 | (A) C fractions: recalcitrant C (C_R, the non-extractable organic carbon after NaOCl and HF treatment), mineral-protected C [C_{MP}, calculated by subtracting the C_R fraction from the stable C fraction (C_S, carbon left after NaOCl treatment)], oxidizable C [C_O, calculated by subtracting Cs from the total C (C_T)]. $C_R + C_{MP} + C_O = C_T$. **(B)** Al fractions: pyrophosphate-extractable Al (Al-SOM) and Al in short range ordered Al phases (SRO-Al = Al_o-Al_p). **(C)** Fe fractions: pyrophosphate-extractable Fe (Fe-SOM), Fe in short range ordered Fe phases (SRO-Fe = Fe_o -Fe_p), Fe in crystalline Fe phases (Cr-Fe = Fe_d -Fe_o).

from P1 to P5. In P1, values of C_T:N_T ratio for both the mineral BC surface and Oh horizons are roughly similar at 30 and 31, respectively. However, in older pedons, the value of the C_T:N_T ratio in the surface-mineral horizons (Bw in P2 and E in P3, P4 and P5) is lower ($\sim$20) than in the Oh horizons (34, 38, 43, respectively in P2-, P3-, and P4-Oh). This decrease of C_T:N_T ratio might be attributed to an increase of microbially-derived compounds (Schmidt et al., 2000; Kögel-Knabner et al., 2008b; Sollins et al., 2009; Rumpel and Kögel-Knabner, 2011; Miltner et al., 2012). Indeed, the C_T:N_T ratio of bacteria is around 5–8 and that of fungi around 5–30 (Wallander et al., 2003; Kleber et al., 2007). In the deeper illuvial horizons of P3–P5, a progressive increase of the C_T:N_T ratio is observed, from 22 in P3-Bh, to 27 in P4-Bhs and 31 in P5-Bhs. In Podzols, an increase of the C:N ratio in the Bh, Bhs and Bs horizons is frequently observed, and a C:N value > 25 in illuvial horizon is considered as a criterion for podzolization (Baize, 1993).

The composition of SOM fractions evolves along our chronosequence. Recalcitrant C compounds tend to build up in the E horizons from P3 to P5. C_R (i.e., the recalcitrant C fraction) represents 30, 29, and 69% of the total C in the E horizon of P3, P4 and P5 respectively (**Figure 2**) while in parallel, the other main contributing pool of C (i.e., oxidizable C) declines from 58% in P3 to 52% in P4, before reaching 27% of the total C in P5. In P3 and P5 (no data for P4), the low value of the C_O:N_O ratio (i.e., of the oxidizable C fraction) which is $\sim$6-7, suggests a large microbial contribution (**Figure 4**). In contrast, the high C_R:N_R ratio which reaches 47 in P3 and 81 in P5 (**Figure 4**) suggests an input of organic matter derived from vegetation, possibly from Sitka spruce roots which have a very high C:N, from 50 to 420 (Olajuyigbe et al., 2012). The larger fraction of amino-sugars-derived C (AS in mg.g^{-1} C— **Table 3**) in the E horizons compared to the illuvial B horizons also supports an important contribution of microbially-derived compounds to SOM. Buurman et al. (2005) observed similar patterns in a Podzol hydrosequence. In the E horizons of their Podzol, these authors observed that SOM was systematically dominated by (i) recalcitrant plant-derived aliphatic compounds (reflecting residual accumulation) and (ii) easily degradable bacterial products (in particular polysaccharide). In P4 and P5 illuvial Bh, Bhs and Bs horizons, the C_{MP} fraction becomes
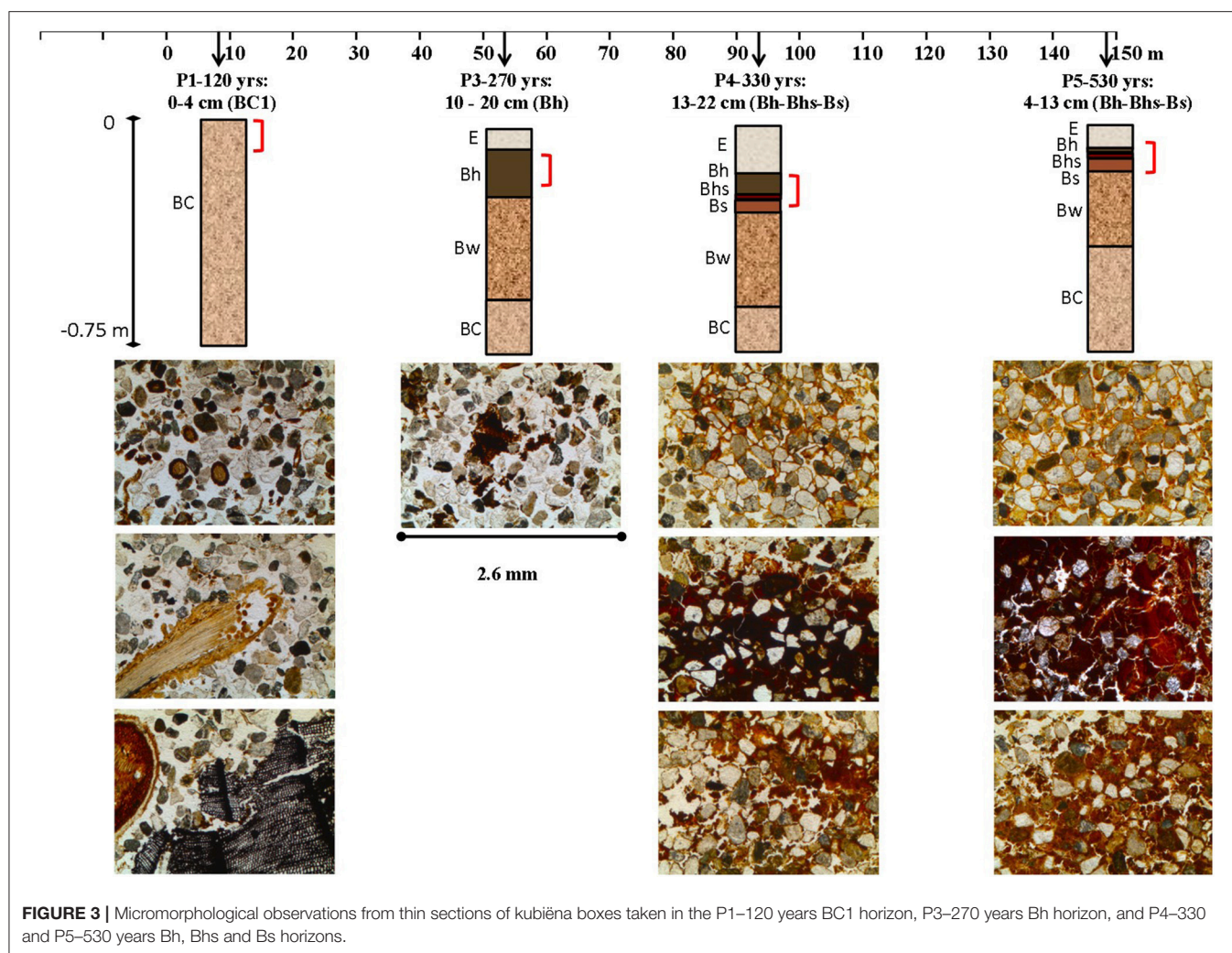
FIGURE 3 | Micromorphological observations from thin sections of kubiëna boxes taken in the P1–120 years BC1 horizon, P3–270 years Bh horizon, and P4–330 and P5–530 years Bh, Bhs and Bs horizons.

important (14–78% of C_T – **Figure 2**). The values of the C:N ratio of the different fractions in those horizons are similar to each other and to the one of the bulk C:N ($\sim$20–30, **Figure 4**).

In contrast to the E horizons in P4 and P5 which are very sandy and exhibit high porosity, the deeper B horizons appear to accumulate large amounts of SOM and secondary Fe/Al phases that induce a clogging of pore space, as revealed by micromorphological features, i.e., the porphyric c/f-related distribution pattern (**Figure 3**). The monomorphic fine organic material filling all pores in the cemented spodic horizons provides evidence of periodic water saturation, and thus anoxic periods. As such, P4 and P5 can be qualified as "hydromorphic" Podzols, in which drainage properties impact OM dynamics and further degradation. According to Buurman and Jongmans (2005), water saturation in hydromorphic Podzols leads to (i) the inaccessibility of the cemented illuvial B horizons for fungi and plant roots, making illuvial DOM the major contributor to SOM accumulation, (ii) the inhibition or slowing of microbial degradation reactions, leading to

a low contribution of microbially derived-compounds to SOM.

Microbial Community Shifts With SOM Protection Processes

Early Stage of Soil Development: Limited SOM Stabilization—Fungi-Dominated Population

In P1–120 years and P2–175 years, primary minerals were not weathered extensively, as is evident from the relatively high TRB values (**Table 1**). Therefore, the content of secondary SRO minerals is low, the potential to form OMA limited and the amount of C_{MP} minimal (**Figure 2**). The main C fraction in these profiles is oxidizable C (between 40 and 73% of C_T), and the degradability of C compounds is relatively large (0.26–0.4 mg CO_2-C g_C^{-1} day^{-1}, **Table 2**). The micromorphological fabric of quartz grains with root residues and excrements in the associated interstitial pores (coarse monic c/f-related distribution pattern in the P1 and P2; **Figure 3**) indicates a microenvironment that does not constrain biological activity; so SOM can continue to decompose.

TABLE 3 | Amino-sugars: Glucosamine (Glu), Galactosamine (Gal), Muramic acids (Mur) content, in $\mu g AS\ g_{soil}^{-1}$, total Amino-sugar content ($\mu g\ AS\ g_{soil}^{-1}$ and mg AS g_C^{-1}) and Glu:Mur ratio (values are given ± one standard deviation).

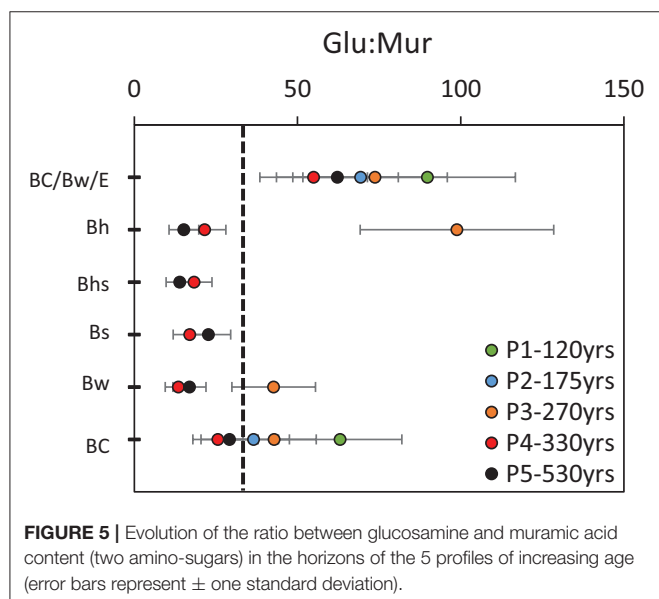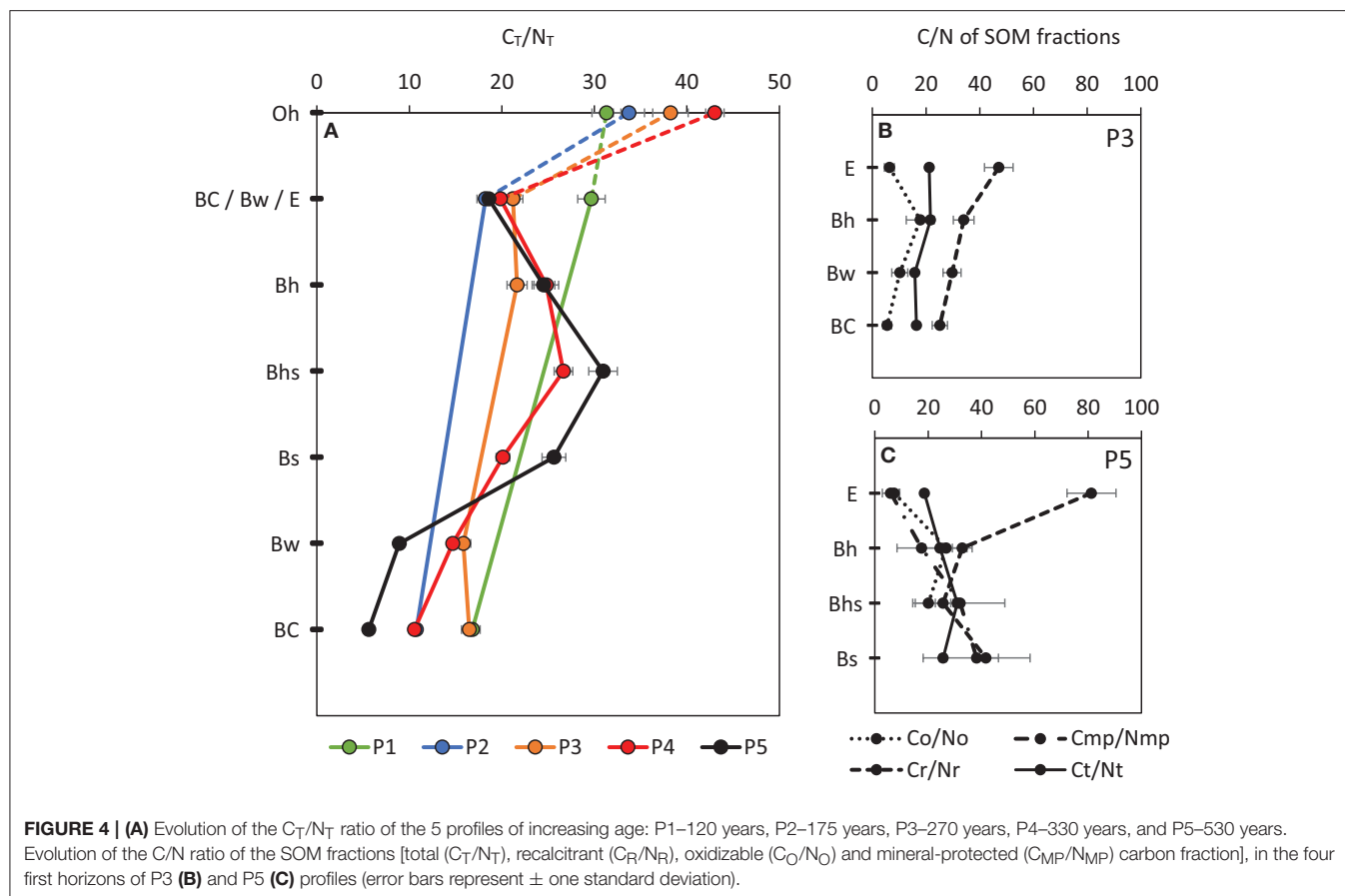| Profile	Horizon	Depth	Glu	Gal	Mur	AS tot	AS tot	Glu:Mur
		cm			$\mu g\ g_{soil}^{-1}$			mg g_C^{-1}	
P1	BC	0–35	142.4 ± 18.4	28.4 ± 4.3	1.6 ± 0.3	172.4 ± 22.4	18.9 ± 5.0	89.8 ± 31.0
P1	BC	35–60	36.3 ± 4.7	5.7 ± 0.9	0.6 ± 0.1	42.6 ± 5.5	5.5 ± 1.8	63.1 ± 21.7
P2	Bw	3–44	45.9 ± 5.9	7.7 ± 1.2	0.7 ± 0.1	54.3 ± 7.1	16.3 ± 1.5	69.4 ± 24.1
P2	BC	44–75	29.6 ± 3.8	10.8 ± 1.6	0.8 ± 0.2	41.1 ± 5.3	16.2 ± 2.0	36.5 ± 12.6
P3	E	0–7	255.7 ± 33.0	73.2 ± 11.1	3.5 ± 0.8	332.4 ± 43.2	26.3 ± 4.0	73.8 ± 25.5
P3	Bh	7–23	251.1 ± 32.4	68.4 ± 10.3	2.5 ± 0.6	322.0 ± 41.9	19.9 ± 3.2	98.8 ± 34.2
P3	Bw	23–57	134.1 ± 17.3	53.0 ± 8.0	3.1 ± 0.7	190.3 ± 24.7	23.3 ± 3.6	42.7 ± 14.8
P3	BC	>57	23.2 ± 3.0	5.3 ± 0.8	0.5 ± 0.1	29.0 ± 3.8	4.2 ± 0.5	42.9 ± 14.9
P4	E	0–10	69.2 ± 8.9	17.9 ± 2.7	1.3 ± 0.3	88.3 ± 11.5	10.4 ± 1.9	54.9 ± 19.0
P4	Bh	10–17	68.5 ± 8.8	19.8 ± 3.0	3.2 ± 0.7	91.5 ± 11.9	5.7 ± 1.1	21.6 ± 7.5
P4	Bhs	17–17.5	91.8 ± 11.8	28.9 ± 4.4	5.0 ± 1.1	125.8 ± 16.3	5.5 ± 0.9	18.3 ± 6.3
P4	Bs	17.5–23	17.5 ± 2.3	6.2 ± 0.9	1.0 ± 0.2	24.8 ± 3.2	5.5 ± 0.3	17 ± 5.9
P4	Bw	23–63	16.2 ± 2.1	6.0 ± 0.9	1.2 ± 0.3	23.5 ± 3.0	8.8 ± 1.0	13.5 ± 4.7
P4	BC	63–113	9.4 ± 1.2	4.6 ± 0.7	0.4 ± 0.1	14.3 ± 1.9	11.4 ± 0.8	25.6 ± 8.8
P5	E	0–8	369.0 ± 47.6	60.3 ± 9.1	5.9 ± 1.3	435.1 ± 56.6	29.4 ± 5.2	62.2 ± 21.5
P5	Bh	8–9.5	363.5 ± 46.9	103.2 ± 15.6	24.0 ± 5.2	490.6 ± 63.8	15.7 ± 2.8	15.2 ± 5.3
P5	Bhs	9.5–10	206.7 ± 26.7	55.3 ± 8.3	14.9 ± 3.2	276.8 ± 36.0	6.8 ± 1.1	13.9 ± 4.8
P5	Bs	10–15	60.8 ± 7.8	7.6 ± 1.1	2.7 ± 0.6	71.1 ± 9.2	6.1 ± 1.2	22.7 ± 7.9
P5	Bw	15–40	9.5 ± 1.2	2.0 ± 0.3	0.6 ± 0.1	12.0 ± 1.6	10.3 ± 1.1	16.9 ± 5.8
P5	BC	40–60	4.5 ± 0.6	0.9 ± 0.1	0.2 ± 0.03	5.5 ± 0.7	8.7 ± 0.6	29.2 ± 10.3

The microbial biomass is lower in these young pedons in comparison with the older profiles, as shown by AS-derived C contents (**Table 3**). In those poorly differentiated profiles, the Glu:Mur ratio is high (>37) and no significant difference was observed at depth, which indicates that the microbiota is dominated by fungi in the whole profile (**Table 3**, **Figure 5**).

Highly Weathered and Leached Soil Horizons: Selective Preservation of Recalcitrant Compounds—Fungi-Dominated Population

In the E horizons of P3–270, P4–330, and P5–530 years, the effect of mineral weathering is evident, as TRB values steeply decline in comparison with P1–120 and P2–175 years values. Selective extractions reveal a low content of secondary Al-, Fe-bearing phases ($Al_o < 1.4\,g\ kg^{-1}$ and $Fe_d < 2.5\,g\ kg^{-1}$, **Table 1**, **Figure 2**). Thus, C_{MP} concentration in E horizons is low ($< 1.7\,g\ kg^{-1}$) and the main mechanism of SOM preservation is probably the intrinsic recalcitrance of organic compounds, which accumulate in those horizons (**Figure 2**).

As in younger pedons, the microbial biomass is mainly fungi-dominated, i.e., a Glu:Mur ratio of 55–74 (**Table 3**, **Figure 5**). Fungi are obligatory aerobes and heterotrophs, more tolerant to acidic conditions and dry events than bacteria (Ekschmitt et al., 2008). Fungi are more abundant in coarse fractions (Kögel-Knabner et al., 2008b) and are generally specialized toward an

assimilation of C directly from the litter (for example lignin) (Poll et al., 2006; Ekschmitt et al., 2008). Furthermore, they are the primary agents of litter and SOM decomposition (Beare et al., 1995; Bardgett and van der Putten, 2014; Keiluweit et al., 2015). It is therefore not surprising to observe fungi prevailing in highly weathered and leached E horizons of Podzols (van Breemen et al., 2000a; Nikonov et al., 2001; Gadd, 2007), which are typically aerated and receive large C input from litter decomposition. Under coniferous forests, mineral weathering has been attributed to acidic excreta from saprotrophic and mycorrhizal fungi (Gadd, 2007). In laboratory studies, ectomycorrhizal fungi were shown to accelerate chemical weathering (Bonneville et al., 2011) (i) by an acidification of their near-environment, (ii) oxidization of redox-sensitive elements such as Fe (Bonneville et al., 2016) which induces exfoliation of biotite and (iii) by combining those chemical weathering strategies with mechanical constraints on their mineral substrates (Bonneville et al., 2009). Ectomycorrhizal fungi have also been shown to "drill" innumerable narrow cylindrical micropores (3–10 μm) in minerals and to excrete micro- to milli-molar concentrations of organic acids in fungal tips (Jongmans et al., 1997; van Breemen et al., 2000a; Hoffland et al., 2002; van Hees et al., 2003; Smits et al., 2005; Bonneville et al., 2011, 2016). Tunnel formation in mineral grains was more intense in nutrient-poor sites, indicating a larger contribution of fungi to plant P, Ca, K supply (van Breemen et al., 2000b; Gadd, 2007). Plant-ectomycorrhizal symbiosis has been proposed as a major driving force in the formation of Podzol E

FIGURE 4 | (A) Evolution of the C_T/N_T ratio of the 5 profiles of increasing age: P1–120 years, P2–175 years, P3–270 years, P4–330 years, and P5–530 years. Evolution of the C/N ratio of the SOM fractions [total (C_T/N_T), recalcitrant (C_R/N_R), oxidizable (C_O/N_O) and mineral-protected (C_{MP}/N_{MP}) carbon fraction], in the four first horizons of P3 **(B)** and P5 **(C)** profiles (error bars represent ± one standard deviation).

FIGURE 5 | Evolution of the ratio between glucosamine and muramic acid content (two amino-sugars) in the horizons of the 5 profiles of increasing age (error bars represent ± one standard deviation).

horizons (van Breemen et al., 2000a,b). As such, the E horizon has been considered as the "fungal-eaten" part of the soil (Baldock and Broos, 2012).

Subsoil Horizons Accumulating Mineral and Organic Phases: Large Physico-Chemical Ability to Stabilize SOM—Bacteria-Dominated Population

In P4 and P5 illuvial horizons, C_{MP} content is strongly and positively correlated with Fe_p ($r = 0.85$), Al_p ($r = 0.91$) and Fe_d-Fe_p ($r = 0.88$) contents, which are proxies for organo-Fe and organo-Al complexes, as well as Fe oxides respectively. Interestingly, the degradability of SOM, measured from respiration rates (**Table 2**), was the lowest in Bh, Bhs and Bs horizons. Those results support the notion that SOM interactions with Fe and Al phases (which accumulate in these horizons) stabilize SOM and protect it from microbial degradation. This observation is in line with a number of studies on Podzols (Eusterhues et al., 2003; Kalbitz et al., 2005; Mikutta et al., 2005a; von Lützow et al., 2006, 2008; Jones et al., 2015), as well as on other soil types (Kleber et al., 2005; Mikutta et al., 2006; Kaiser and Guggenberger, 2007). Fe oxides have a high specific-surface area, usually positively charged (Eusterhues et al., 2005), which readily adsorb negatively-charged OM. Formation of Fe-C coprecipitates can also occur (Kögel-Knabner et al., 2008b; Mikutta et al., 2008). An inhibition of biological activity due to Fe and Al, bound to the organic matter, was reported in several studies (Boudot et al., 1989; Boudot, 1992; Sollins et al., 1996; Jones and Edwards, 1998; Baldock and Skjemstad, 2000). Amelung et al. (2001) showed, for instance, that Al and Fe

oxides decreased the synthesis of bacterial AS by a factor 2. In addition to the physical protection of SOM, P4–330, and P5–530 years illuvial horizons of the chronosequence present a clogged porosity, which—considering the heavy rainfall—favors water saturation and disoxic/anoxic episodes. The resulting decrease in O₂ availability would then drastically inhibit the SOM mineralization process. Overall, our results suggest that lower SOM degradation rates in the Bh, Bhs and Bs of P4 and P5 are explained by the mechanisms of adsorption and co-precipitation of SOM with pedogenic secondary minerals. However, we cannot omit the key role of specific soil physico-chemical properties in the environment of the indurated Bhs horizon. Illuvial horizons

can be considered as "non-preferred soil spaces" (*sensu* Ekschmitt et al., 2008), where microbial activity is limited by suboptimal environmental conditions and low nutrient bioavailability caused by SOM association with reactive surfaces of secondary minerals (Schmidt et al., 2011).

Consistent with this idea, a distinct microbial population was identified in the B horizons of P4 and P5. The Glu:Mur ratio of the latter horizons is significantly lower than in the overlaying E horizons, indicating a bacteria-dominated microbiota (**Table 3**, **Figure 5**). In the chronosequence, there is no correlation between pH and the Glu:Mur ratio ($r^2 = 0.041$), indicating that other factors drive microbial populations composition. It appears

FIGURE 6 | Evolutions in the organic, physico-chemical and mineral compartments, resulting main SOM protection mechanisms and microorganism population, for the five Vancouver profiles of increasing age (P1-120 years, P2-170 years, P3-270 years, P4-330 years, and P5-530 years).
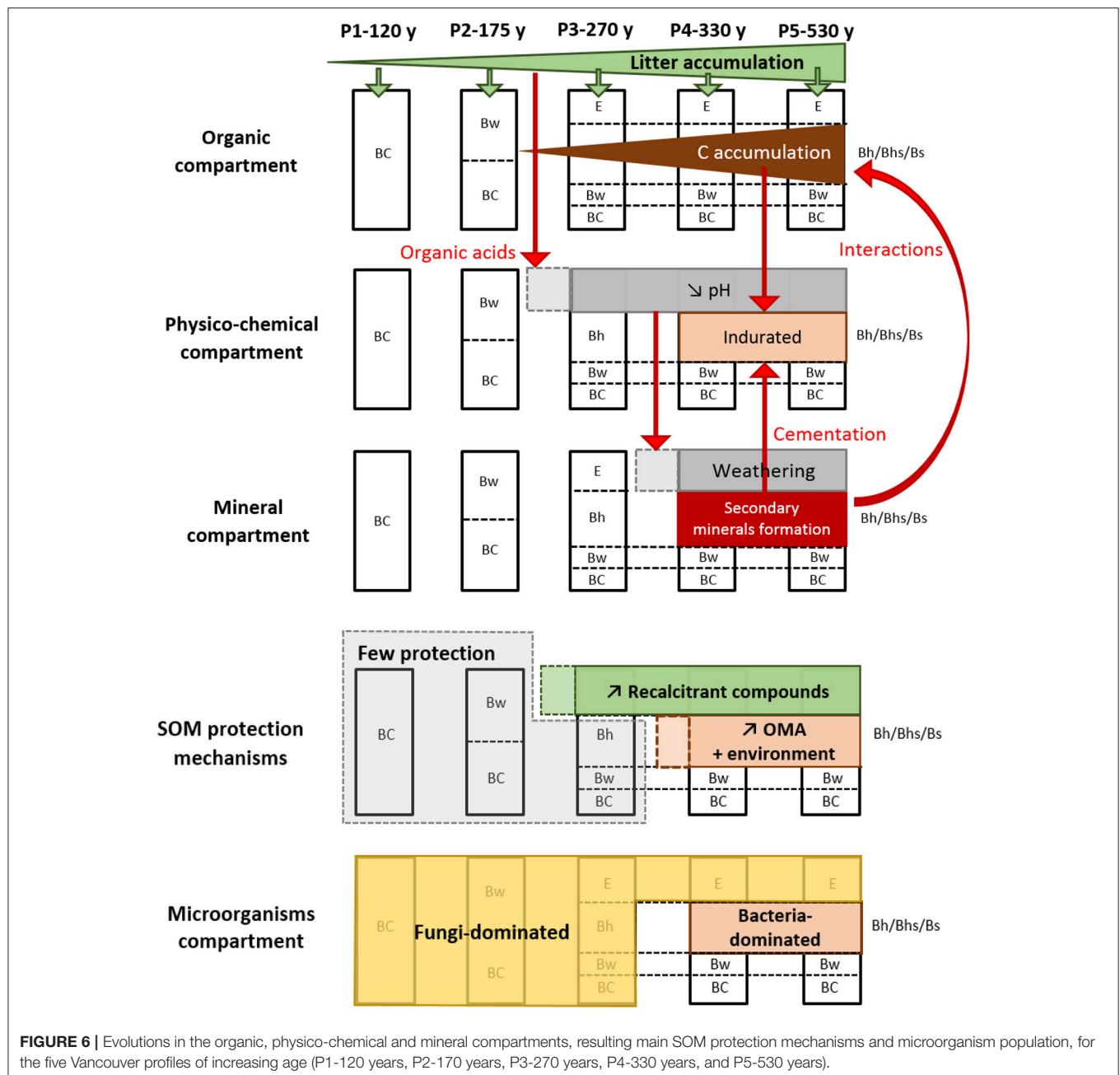
that soil oxygenation status impacts the composition of the microbiota. B horizons which are prone to water saturation are thus less attractive to fungi which are usually highly hydrophobic and water-intolerant due to their aerobic respiration (Slankis, 1974). For instance, mycorrhizal association between fungi and plant roots do not form in waterlogged soils (Theodorou, 1978). This is in line with van Breemen et al. (2000a) who reported a steep decrease of fungal biomass at the transition between E and the B horizons in Podzol. Bacteria require a certain degree of water-saturation and have the capability to quickly adapt to changing chemical conditions by switching electron acceptors [for example from O_2 to Fe(III)] when anoxia sets in (Baldock and Skjemstad, 2000; Chenu and Stotzky, 2002; von Lützow et al., 2006; Kögel-Knabner et al., 2008b). In addition, bacteria generally specialize in utilizing labile C compounds for assimilation reactions in deeper horizons (Poll et al., 2006; Ekschmitt et al., 2008). It is thus coherent that bacteria prevail in the cemented spodic horizons of hydromorphic Podzols, receiving DOC illuviated from the topsoil, and in which roots and/or fungi develop poorly. Bacteria are the main drivers of SOM degradation, but they might also have an important impact on the stability of secondary minerals. Among the bacteria that are able to switch to other electron acceptors in anoxic conditions, iron-reducing bacteria can dissolve secondary Fe(III) phases, producing dissolved Fe(II) which can potentially re-precipitate as new secondary phases. This process might have an important impact on illuvial B horizon evolution in Podzols.

CONCLUSION

Our study objective was to evaluate the co-evolution of SOM protection processes and microbial populations at different stages of soil genesis, in different horizons from five pedons of a podzolic chronosequence.

In the Cox Bay chronosequence, SOM protection processes are constrained in the two younger pedons (P1–120 years and P2–175 years). A weathered eluvial E horizon develops, first observed in P3–270 years, accumulating recalcitrant organic C. In the two well-developed Podzols (P4–330 years and P5–530 years), the accumulation of secondary minerals and associated SOM induces the development of an illuvial B or spodic horizon, cemented and probably undergoing episodic waterlogging. SOM mineralization is hindered in these horizons, due to the formation of OMA and to clogging of soil porosity, leading to a specific low O_2 microenvironment. Our study illustrates that SOM stabilization in soils is time- and horizon-specific and, more specifically, pedogenetically dependent (**Figure 6**).

Soil development and evolution of SOM protection processes along our soil chronosequence induce modifications of the composition of soil microbiota. In the initial stage of pedogenesis (120, 175, and 270 years), fungi are the prevalent group both in topsoil and subsoil. In the older pedons (330 and 530 years), while the topsoil horizons remain fungi-dominated, bacteria dominate in the cemented B horizons where large quantities of SOM are stabilized (**Figure 6**). We assume that this change in microbial community composition potentially has a feedback effect on SOM dynamics. Below-ground community development and functions are poorly known. The important role played by fungi in the E horizon during podzolization is increasingly recognized. However, the bacterial community and function in the B horizon of hydromorphic Podzols still need to be investigated. Given their potential impact on all aspects of soil development (mineral and SOM evolutions), our understanding of the illuvial horizon dynamics would be enhanced by a characterization of its microbial population and their functions.

AUTHOR CONTRIBUTIONS

This research is part of the PhD thesis of M-LV, supervised by J-TC and BD. EVR carried out the micromorphological analysis and was involved in the data interpretation. SD supervised the laboratory work for microbial characterization and was involved in the data interpretation. SB helped with data interpretation. All authors participated to the manuscript revision and discussion. All authors agree to be accountable for the content of the work.

SUPPLEMENTARY MATERIAL

The Supplementary Material for this article can be found online at: https://www.frontiersin.org/articles/10.3389/fenvs.2018.00070/full#supplementary-material

Figure S1 | Cumulative soil respiration (in mg CO_2 100 g^{-1}) over the 144 day incubation from soils for the five Vancouver profiles of increasing age (P1–120 years, P2–170 years, P3–270 years, P4–330 years, and P5–530 years). Values are means of triplicate measurements ± standard error.

REFERENCES

AFNOR (2006). *Qualité du sol - Prétraitement des Echantillons pour Analyses Physico*-Chimiques. La Plaine Saint-Denis. NF ISO 11464, December 2006.

Amelung, W., Lobe, I., and Du Preez, C. C. (2002). Fate of microbial residues in sandy soils of the South African Highveld as influenced by prolonged arable cropping. *Eur. J. Soil Sci.* 53, 29–35. doi: 10.1046/j.1365-2389.2002.00428.x

Amelung, W., Miltner, A., Zhang, X., and Zech, W. (2001). Fate of microbial residues during litter decomposition as affected by minerals. *Soil Sci.* 166, 598–606. doi: 10.1097/00010694-200109000-00003

Baize, D. (1993). *Soil Science Analyses. A Guide to Current Use*. Chichester: John Wiley & Sons Ltd.

Baldock, J. A., and Broos, K. (2012). "Soil organic matter," in *Handbook of Soil Sciences, 2nd, Edn., Vol. 1: Properties and Processes*, eds P. M. Huang, Y. Li, and M. E. Sumner (Boca Raton, FL: CRC Press; Taylor & Francis Group), 11.11–11.52.

Baldock, J. A., and Skjemstad, J. (2000). Role of the soil matrix and minerals in protecting natural organic materials against biological attack. *Org. Geochem.* 31, 697–710. doi: 10.1016/S0146-6380(00)00049-8

Bardgett, R. D., and van der Putten, W. H. (2014). Belowground biodiversity and ecosystem functioning. *Nature* 515, 505–511. doi: 10.1038/nature13855

Barré, P., Plante, A. F., Cécillon, L., Lutfalla, S., Baudin, F., Bernard, S., et al. (2016). The energetic and chemical signatures of persistent soil organic matter. *Biogeochemistry* 130, 1–12. doi: 10.1007/s10533-016-0246-0

Bascomb, C. L. (1968). Distribution of pyrophosphate-extractable iron and organic carbon in soils of various groups. *J. Soil Sci.* 19, 251–268. doi: 10.1111/j.1365-2389.1968.tb01538.x

Basile-Doelsch, I., Balesdent, J., and Rose, J. (2015). Are interactions between organic compounds and nanoscale weathering minerals the key drivers of carbon storage in soils? *Environ. Sci. Technol.* 49, 3997–3998. doi: 10.1021/acs.est.5b00650

Beare, M., Coleman, D., Crossley, D. Jr., Hendrix, P., and Odum, E. (1995). "A hierarchical approach to evaluating the significance of soil biodiversity to biogeochemical cycling" in *The Significance and Regulation of Soil Biodiversity*, eds H. P. Collins, G. P. Robertson, and M. J. Klug (Dordrecht: Springer), 5–22.

Benyarku, C. A., and Stoops, G. (2005). *Guidelines for Preparation of Rock And Soil Thin Sections and Polished Sections*. Departament de Medi Ambient i Ciències del Sòl, Lleida: Universitat de Lleida.

Blakemore, L. C., Searle, P. L., and Daly, B. K. (1987). *Methods for Chemical Analysis of Soils*. New Zealand Soil Bureau Scientific Report No. 80, Lower Hutt.

Bodé, S., Denef, K., and Boeckx, P. (2009). Development and evaluation of a high-performance liquid chromatography/isotope ratio mass spectrometry methodology for delta13C analyses of amino sugars in soil. *Rapid Commun. Mass Spectr.* 23, 2519–2526. doi: 10.1002/rcm.4093

Bodé, S., Fancy, R., and Boeckx, P. (2013). Stable isotope probing of amino sugars–a promising tool to assess microbial interactions in soils. *Rapid Commun. Mass Spectr.* 27, 1367–1379. doi: 10.1002/rcm.6586

Bonneville, S., Bray, A. W., and Benning, L. G. (2016). Structural Fe(ii) oxidation in biotite by an ectomycorrhizal fungi drives mechanical forcing. *Environ. Sci. Technol.* 50, 5589–5596. doi: 10.1021/acs.est.5b06178

Bonneville, S., Morgan, D. J., Schmalenberger, A., Bray, A., Brown, A., Banwart, S. A., et al. (2011). Tree-mycorrhiza symbiosis accelerate mineral weathering: evidences from nanometer-scale elemental fluxes at the hypha–mineral interface. *Geochim. Cosmochim. Acta* 75, 6988–7005. doi: 10.1016/j.gca.2011.08.041

Bonneville, S., Smits, M. M., Brown, A., Harrington, J., Leake, J. R., Brydson, R., et al. (2009). Plant-driven fungal weathering: early stages of mineral alteration at the nanometer scale. *Geology* 37, 615–618. doi: 10.1130/G25699A.1

Boudot, J., Bel Hadj Brahim, A., Steiman, R., and Seigle-Murandi, F. (1989). Biodegradation of synthetic organo-metallic complexes of iron and aluminium with selected metal to carbon ratios. *Soil Biol. Biochem.* 21, 961–966. doi: 10.1016/0038-0717(89)90088-6

Boudot, J.-P. (1992). Relative efficiency of complexed aluminum noncrystalline Al hydroxide, allophane and imogolite in retarding the biodegradation of citric acid. *Geoderma* 52, 29–39. doi: 10.1016/0016-7061(92)90073-G

Buurman, P., and Jongmans, A. G. (2005). Podzolisation and soil organic matter dynamics. *Geoderma* 125, 71–83. doi: 10.1016/j.geoderma.2004.07.006

Buurman, P., van Bergen, P., Jongmans, A., Meijer, E., Duran, B., and van Lagen, B. (2005). Spatial and temporal variation in podzol organic matter studied by pyrolysis-gas chromatography/mass spectrometry and micromorphology. *Eur. J. Soil Sci.* 56, 253–270. doi: 10.1111/j.1365-2389.2004.00662.x

Chao, T. T., and Sanzolone, R. F. (1992). Decomposition techniques. *J. Geochem. Explor.* 44, 65–106. doi: 10.1016/0375-6742(92)90048-D

Chenu, C., and Stotzky, G. (2002). "Interactions between microorganisms and soil particles: an overview," in *Interactions Between Soil Particles and Microorganisms*, eds P. Huang, J. Bollag, and N. Senesi (Manchester: John Wiley & Sons, Ltd.), 1–40.

Cornelis, J.-T., Weis, D., Lavkulich, L., Vermeire, M.-L., Delvaux, B., and Barling, J. (2014). Silicon isotopes record dissolution and re-precipitation of pedogenic clay minerals in a podzolic soil chronosequence. *Geoderma* 235–236, 19–29. doi: 10.1016/j.geoderma.2014.06.023

Cornell, R. M., and Schwertmann, U. (2003). *The Iron Oxides: Structure, Properties, Reactions, Occurrences and Uses*. Weinheim: John Wiley & Sons.

Cornu, S., Montagne, D., and Vasconcelos, P. M. (2009). Dating constituent formation in soils to determine rates of soil processes: a review. *Geoderma* 153, 293–303. doi: 10.1016/j.geoderma.2009.08.006

Cotrufo, M. F., Wallenstein, M. D., Boot, C. M., Denef, K., and Paul, E. (2013). The Microbial Efficiency-Matrix Stabilization (MEMS) framework integrates plant litter decomposition with soil organic matter stabilization: do labile plant inputs form stable soil organic matter? *Glob. Chang. Biol.* 19, 988–995. doi: 10.1111/gcb.12113

De Coninck, F. (1980). Major mechanisms in formation of spodic horizons. *Geoderma* 24, 101–128. doi: 10.1016/0016-7061(80)90038-5

De Coninck, F., and Righi, D. (1969). Aspects micromorphologiques de la podzolisation en Forêt de Rambouillet. *Sci. Sol.* 2, 57–77.

De Coninck, F., Righi, D., Maucorps, J., and Robin, A. (1974). "Origin and micromorphological nomenclature of organic matter in sandy spodosols," in *Soil Microscopy*, ed G. K. Rutherford (Kingston, ON: The Limestone Press), 263–280.

Ekschmitt, K., Kandeler, E., Poll, C., Brune, A., Buscot, F., Friedrich, M., et al. (2008). Soil-carbon preservation through habitat constraints and biological limitations on decomposer activity. *J. Plant Nutr. Soil Sci.* 171, 27–35. doi: 10.1002/jpln.200700051

Ekschmitt, K., Liu, M., Vetter, S., Fox, O., and Wolters, V. (2005). Strategies used by soil biota to overcome soil organic matter stability—why is dead organic matter left over in the soil? *Geoderma* 128, 167–176. doi: 10.1016/j.geoderma.2004.12.024

Eusterhues, K., Rumpel, C., Kleber, M., and Kögel-Knabner, I. (2003). Stabilisation of soil organic matter by interactions with minerals as revealed by mineral dissolution and oxidative degradation. *Org. Geochem.* 34, 1591–1600. doi: 10.1016/j.orggeochem.2003.08.007

Eusterhues, K., Rumpel, C., and Kogel-Knabner, I. (2005). Organo-mineral associations in sandy acid forest soils: importance of specific surface area, iron oxides and micropores. *Eur. J. Soil Sci.* 56, 753–763 doi: 10.1111/j.1365-2389.2005.00710.x

Farmer, V., Russell, J., and Berrow, M. (1980). Imogolite and proto-imogolite allophane in spodic horizons: evidence for a mobile aluminium silicate complex in podzol formation. *J. Soil Sci.* 31, 673–684. doi: 10.1111/j.1365-2389.1980.tb02113.x

Fekiacova, Z., Vermeire, M., Bechon, L., Cornelis, J., and Cornu, S. (2017). Can Fe isotope fractionations trace the pedogenetic mechanisms involved in podzolization? *Geoderma* 296, 38–46. doi: 10.1016/j.geoderma.2017.02.020

Gadd, G. M. (2007). Geomycology: biogeochemical transformations of rocks, minerals, metals and radionuclides by fungi, bioweathering and bioremediation. *Mycol. Res.* 111, 3–49. doi: 10.1016/j.mycres.2006.12.001

Gangloff, S., Stille, P., Pierret, M.-C., Weber, T., and Chabaux, F. (2014). Characterization and evolution of dissolved organic matter in acidic forest soil and its impact on the mobility of major and trace elements (case of the Strengbach watershed). *Geochim. Cosmochim. Acta* 130, 21–41. doi: 10.1016/j.gca.2013.12.033

Glaser, B., Turrión, M. B., and Alef, K. (2004). Amino sugars and muramic acid—biomarkers for soil microbial community structure analysis. *Soil Biol. Biochem.* 36, 399–407. doi: 10.1016/j.soilbio.2003.10.013

Grandy, A., and Neff, J. (2008). Molecular C dynamics downstream: the biochemical decomposition sequence and its impact on soil organic

matter structure and function. *Sci. Total Environ.* 404, 297–307. doi: 10.1016/j.scitotenv.2007.11.013

Gustafsson, J., Bhattacharya, P., Bain, D., Fraser, A., and McHardy, W. (1995). Podzolisation mechanisms and the synthesis of imogolite in northern Scandinavia. *Geoderma* 66, 167–184. doi: 10.1016/0016-7061(95)00005-9

Hassink, J., Bouwman, L., Zwart, K., and Brussaard, L. (1993). Relationships between habitable pore space, soil biota and mineralization rates in grassland soils. *Soil Biol. Biochem.* 25, 47–55. doi: 10.1016/0038-0717(93)90240-C

Henriet, C., De Jaeger, N., Dorel, M., Opfergelt, S., and Delvaux, B. (2008). The reserve of weatherable primary silicates impacts the accumulation of biogenic silicon in volcanic ash soils. *Biogeochemistry* 90, 209–223. doi: 10.1007/s10533-008-9245-0

Herbillon, A. J. (1986). "Chemical estimation of weatherable minerals present in the diagnostic horizons of low activity clay soils," in *Proceedings of the 8th International Classification Workshop: Classification, Characterization, and Utilization of Ultisols. Part, I*, eds M. N. Beinroth, M. N. Camargo, and H. Eswaran (Rio de Janeiro: EMBRAPA), 39–48.

Hoffland, E., Giesler, R., Jongmans, T., and van Breemen, N. (2002). Increasing feldspar tunneling by fungi across a north Sweden podzol chronosequence. *Ecosystems* 5, 11–22. doi: 10.1007/s10021-001-0052-x

IUSS Working Group (2015). *World Reference Base for Soil Resources (WRB) 2014, Update 2015, International Soil Classification System for Naming Soils and Creating Legends for Soil Maps.* World Soil Resources Reports No. 106. Rome: FAO.

Jones, A. R., Sanderman, J., Allen, D., Dalal, R., and Schmidt, S. (2015). Subtropical giant podzol chronosequence reveals that soil carbon stabilisation is not governed by litter quality. *Biogeochemistry* 124, 205–217. doi: 10.1007/s10533-015-0093-4

Jones, D., and Edwards, A. (1998). Influence of sorption on the biological utilization of two simple carbon substrates. *Soil Biol. Biochem.* 30, 1895–1902. doi: 10.1016/S0038-0717(98)00060-1

Jongmans, A., van Breemen, N., Lundström, U., van Hees, P., Finlay, R., Srinivasan, M., et al. (1997). Rock-eating fungi. *Nature* 389, 682–683. doi: 10.1038/39493

Kaiser, K., and Guggenberger, G. (2007). Sorptive stabilization of organic matter by microporous goethite: sorption into small pores vs. surface complexation. *Eur. J. Soil Sci.* 58, 45–59. doi: 10.1111/j.1365-2389.2006.00799.x

Kaiser, K., and Kalbitz, K. (2012). Cycling downwards – dissolved organic matter in soils. *Soil Biol. Biochem.* 52, 29–32. doi: 10.1016/j.soilbio.2012.04.002

Kaiser, K., and Zech, W. (1996). Defects in estimation of aluminum in humus complexes of podzolic soils by pyrophosphate extraction. *Soil Sci.* 161, 452–458. doi: 10.1097/00010694-199607000-00005

Kalbitz, K., Schwesig, D., Rethemeyer, J., and Matzner, E. (2005). Stabilization of dissolved organic matter by sorption to the mineral soil. *Soil Biol. Biochem.* 37, 1319–1331. doi: 10.1016/j.soilbio.2004.11.028

Keiluweit, M., Nico, P., Harmon, M. E., Mao, J., Pett-Ridge, J., and Kleber, M. (2015). Long-term litter decomposition controlled by manganese redox cycling. *Proc. Natl. Acad. Sci. U.S.A.* 112, E5253–E5260. doi: 10.1073/pnas.1508945112

Kleber, M. (2010). What is recalcitrant soil organic matter? *Environ. Chem.* 7:320. doi: 10.1071/EN10006

Kleber, M., Eusterhues, K., Keiluweit, M., Mikutta, C., Mikutta, R., and Nico, P. S. (2015). Chapter one-mineral–organic associations: formation, properties, and relevance in soil environments. *Adv. Agron.* 130, 1–140. doi: 10.1016/bs.agron.2014.10.005

Kleber, M., Mikutta, R., Torn, M. S., and Jahn, R. (2005). Poorly crystalline mineral phases protect organic matter in acid subsoil horizons. *Eur. J. Soil Sci.* 56, 717–725. doi: 10.1111/j.1365-2389.2005.00706.x

Kleber, M., Sollins, P., and Sutton, R. (2007). A conceptual model of organo-mineral interactions in soils: self-assembly of organic molecular fragments into zonal structures on mineral surfaces. *Biogeochemistry* 85, 9–24. doi: 10.1007/s10533-007-9103-5

Kögel-Knabner, I., Ekschmitt, K., Flessa, H., Guggenberger, G., Matzner, E., Marschner, B., et al. (2008a). An integrative approach of organic matter stabilization in temperate soils: linking chemistry, physics, and biology. *J. Plant Nutr. Soil Sci.* 171, 5–13. doi: 10.1002/jpln.200700215

Kögel-Knabner, I., Guggenberger, G., Kleber, M., Kandeler, E., Kalbitz, K., Scheu, S., et al. (2008b). Organo-mineral associations in temperate soils: integrating biology, mineralogy, and organic matter chemistry. *J. Plant Nutr. Soil Sci.* 171, 61–82. doi: 10.1002/jpln.200700048

Kuzyakov, Y., and Blagodatskaya, E. (2015). Microbial hotspots and hot moments in soil: concept and review. *Soil Biol. Biochem.* 83, 184–199. doi: 10.1016/j.soilbio.2015.01.025

Lavelle, P., Blanchart, E., Martin, A., Martin, S., and Spain, A. (1993). A hierarchical model for decomposition in terrestrial ecosystems: application to soils of the humid tropics. *Biotropica* 25, 130–150. doi: 10.2307/2389178

Legros, J. P. (2007). *Les Grands sols du Monde.* Lausanne: Presses Polytechniques et Universitaires romandes.

Lehmann, J., and Kleber, M. (2015). The contentious nature of soil organic matter. *Nature* 528, 60–68. doi: 10.1038/nature16069

Liang, C., and Balser, T. C. (2011). Microbial production of recalcitrant organic matter in global soils: implications for productivity and climate policy. *Nat. Rev. Microbiol.* 9, 75–75. doi: 10.1038/nrmicro2386-c1

Liang, C., Fujinuma, R., and Balser, T. C. (2008). Comparing PLFA and amino sugars for microbial analysis in an Upper Michigan old growth forest. *Soil Biol. Biochem.* 40, 2063–2065. doi: 10.1016/j.soilbio.2008.01.022

Liang, C., Zhang, X., and Balser, T. C. (2007). Net microbial amino sugar accumulation process in soil as influenced by different plant material inputs. *Biol. Fertil. Soils* 44, 1–7. doi: 10.1007/s00374-007-0170-5

Lindeburg, K. S., Almond, P., Roering, J. J., and Chadwick, O. A. (2013). Pathways of soil genesis in the Coast Range of Oregon, USA. *Plant Soil* 367, 57–75. doi: 10.1007/s11104-012-1566-z

Lundström, U. S., van Breemen, N., and Bain, D. (2000). The podzolization process. A review. *Geoderma* 94, 91–107. doi: 10.1016/S0016-7061(99)00036-1

Lundström, U., van Breemen, N., and Jongmans, A. (1995). Evidence for microbial decomposition of organic acids during podzolization. *Eur. J. Soil Sci.* 46, 489–496. doi: 10.1111/j.1365-2389.1995.tb01345.x

Manzoni, S., and Porporato, A. (2009). Soil carbon and nitrogen mineralization: theory and models across scales. *Soil Biol. Biochem.* 41, 1355–1379. doi: 10.1016/j.soilbio.2009.02.031

Marschner, B., Brodowski, S., Dreves, A., Gleixner, G., Gude, A., Grootes, P. M., et al. (2008). How relevant is recalcitrance for the stabilization of organic matter in soils? *J. Plant Nutr. Soil Sci.* 171, 91–110. doi: 10.1002/jpln.200700049

McKeague, J., Ross, G., Gamble, D., and Mahaney, W. (1978). "Properties, criteria of classification and genesis of podzolic soils in Canada," in *Quaternary Soils. Geo Abstracts*, ed W. C. Mahaney (Norwich), 27–60.

Mehra, O. P., and Jackson, M. L. (1960). Iron oxide removal from soils and clays by a dithionite-citrate system buffered with sodium bicarbonate. *Clays Clay Miner.* 7, 317–327. doi: 10.1346/CCMN.1958.0070122

Mikutta, C., Mikutta, R., Bonneville, S., Wagner, F., Voegelin, A., Christl, I., et al. (2008). Synthetic coprecipitates of exopolysaccharides and ferrihydrite. Part I: characterization. *Geochim. Cosmochim. Acta* 72, 1111–1127. doi: 10.1016/j.gca.2007.11.035

Mikutta, R., Kleber, M., and Jahn, R. (2005a). Poorly crystalline minerals protect organic carbon in clay subfractions from acid subsoil horizons. *Geoderma* 128, 106–115. doi: 10.1016/j.geoderma.2004.12.018

Mikutta, R., Kleber, M., Kaiser, K., and Jahn, R. (2005b). Review: organic matter removal from soils using hydrogen peroxide, sodium hypochlorite, and disodium peroxodisulfate. *Soil Sci. Soc. Am.* 69, 120–135. doi: 10.2136/sssaj2005.0120

Mikutta, R., Kleber, M., Torn, M. S., and Jahn, R. (2006). stabilization of soil organic matter: association with minerals or chemical recalcitrance? *Biogeochemistry* 77, 25–56. doi: 10.1007/s10533-005-0712-6

Miltner, A., Bombach, P., Schmidt-Brücken, B., and Kästner, M. (2012). SOM genesis: microbial biomass as a significant source. *Biogeochemistry* 111, 41–55. doi: 10.1007/s10533-011-9658-z

Mossin, L., Mortensen, M., and Nørnberg, P. (2002). Imogolite related to podzolization processes in Danish podzols. *Geoderma* 109, 103–116. doi: 10.1016/S0016-7061(02)00145-3

Neff, J., Townsend, A., Gleixner, G., Lehman, S., Turnbull, J., and Bowman, W. (2002). Variable effects of nitrogen additions on the stability and turnover of soil carbon. *Nature* 419, 915–917. doi: 10.1038/nature01136

Nikonov, V., Lukina, N., Polyanskaya, L., and Panikova, A. (2001). Distribution of microorganisms in the Al–Fe–humus podzols of natural and anthropogenically impacted boreal spruce forests. *Microbiology* 70, 319–328. doi: 10.1023/A:1010459512590

Olajuyigbe, S., Tobin, B., Hawkins, M., and Nieuwenhuis, M. (2012). The measurement of woody root decomposition using two methodologies in a

Sitka spruce forest ecosystem. *Plant Soil* 360, 77–91. doi: 10.1007/s11104-012-1222-7

Page, J. R., Miller, R. H., Keeney, D. H., Baker, D. E., Roscoe, J. R., and Rhoades, J. D. (eds.). (1982). *Methods of Soil Analysis: Part 2, Chemical and Microbiological Properties, 2nd Edn.* Madison, WI: Soil Science Society of America.

Poll, C., Ingwersen, J., Stemmer, M., Gerzabek, M. H., and Kandeler, E. (2006). Mechanisms of solute transport affect small-scale abundance and function of soil microorganisms in the detritusphere. *Eur. J. Soil Sci.* 57, 583–595. doi: 10.1111/j.1365-2389.2006.00835.x

Poulton, S. W., and Canfield, D. E. (2005). Development of a sequential extraction procedure for iron: implications for iron partitioning in continentally derived particulates. *Chem. Geol.* 214, 209–221. doi: 10.1016/j.chemgeo.2004.09.003

Pronk, G. J., Heister, K., and Kögel-Knabner, I. (2015). Amino sugars reflect microbial residues as affected by clay mineral composition of artificial soils. *Org. Geochem.* 83, 109–113. doi: 10.1016/j.orggeochem.2015.03.007

Rodella, A., and Saboya, L. (1999). Calibration for conductimetric determination of carbon dioxide. *Soil Biol. Biochem.* 31, 2059–2060. doi: 10.1016/S0038-0717(99)00046-2

Rumpel, C., and Kögel-Knabner, I. (2011). Deep soil organic matter—a key but poorly understood component of terrestrial C cycle. *Plant Soil* 338, 143–158. doi: 10.1007/s11104-010-0391-5

Sauer, D., Schülli-Maurer, I., Sperstad, R., Sørensen, R., and Stahr, K. (2008). Podzol development with time in sandy beach deposits in southern Norway. *J. Plant Nutr. Soil Sci.* 171, 483–497. doi: 10.1002/jpln.200700023

Schmidt, M. W., Knicker, H., and Kogel-Knabner, I. (2000). Organic matter accumulating in Aeh and Bh horizons of a Podzol—chemical characterization in primary organo-mineral associations. *Org. Geochem.* 31, 727–734. doi: 10.1016/S0146-6380(00)00045-0

Schmidt, M. W., Torn, M. S., Abiven, S., Dittmar, T., Guggenberger, G., Janssens, I. A., et al. (2011). Persistence of soil organic matter as an ecosystem property. *Nature* 478, 49–56. doi: 10.1038/nature10386

Schuppli, P., Ross, G., and McKeague, J. (1983). The effective removal of suspended materials from pyrophosphate extracts of soils from tropical and temperate regions. *Soil Sci. Soc. Am. J.* 47, 1026–1032. doi: 10.2136/sssaj1983.03615995004700050037x

Simpson, A. J., Simpson, M. J., Smith, E., and Kelleher, B. P. (2007). Microbially derived inputs to soil organic matter: are current estimates too low? *Environ. Sci. Technol.* 41, 8070–8076. doi: 10.1021/es071217x

Singleton, G. A., and Lavkulich, M. (1987). A soil chronosequence on beach sands, Vancouver Island, British Columbia. *Can. J. Soil Sci.* 67, 795–810. doi: 10.4141/cjss87-077

Siregar, A., Kleber, M., Mikutta, R., and Jahn, R. (2005). Sodium hypochlorite oxidation reduces soil organic matter concentrations without affecting inorganic soil constituents. *Eur. J. Soil Sci.* 56, 481–490. doi: 10.1111/j.1365-2389.2004.00680.x

Six, J., Bossuyt, H., Degryze, S., and Denef, K. (2004). A history of research on the link between (micro)aggregates, soil biota, and soil organic matter dynamics. *Soil Tillage Res.* 79, 7–31. doi: 10.1016/j.still.2004.03.008

Slankis, V. (1974). Soil factors influencing formation of mycorrhizae. *Annu. Rev. Phytopathol.* 12, 437–457. doi: 10.1146/annurev.py.12.090174.002253

Smits, M. M., Hoffland, E., Jongmans, A. G., and van Breemen, N. (2005). Contribution of mineral tunneling to total feldspar weathering. *Geoderma* 125, 59–69. doi: 10.1016/j.geoderma.2004.06.005

Sollins, P., Homann, P., and Caldwell, B. (1996). Stabilization and destabilization of soil organic matter: mechanisms and controls. *Geoderma* 74, 65–105. doi: 10.1016/S0016-7061(96)00036-5

Sollins, P., Kramer, M. G., Swanston, C., Lajtha, K., Filley, T., Aufdenkampe, A. K., et al. (2009). Sequential density fractionation across soils of contrasting mineralogy: evidence for both microbial- and mineral-controlled soil organic matter stabilization. *Biogeochemistry* 96, 209–231. doi: 10.1007/s10533-009-9359-z

Stoops, G. (2003). *Guidelines for Analysis and Description of Soil And Regolith Thin Sections.* Madison, WI: Soil Science Society of America Inc.

Theodorou, C. (1978). Soil moisture and the mycorrhizal association of Pinus radiata D. *Don. Soil Biol. Biochem.* 10, 33–37. doi: 10.1016/0038-0717(78)90007-X

Tisdall, J., and Oades, J. M. (1982). Organic matter and water-stable aggregates in soils. *J. Soil Sci.* 33, 141–163. doi: 10.1111/j.1365-2389.1982.tb01755.x

Torn, M., Swanston, C., Castanha, C., and Trumbore, S. (2009). "Storage and turnover of organic matter in soil," in *Biophysico-Chemical Processes Involving Natural Nonliving Organic Matter in Environmental Systems,* eds N. Senesi, B. Xing, and P. M. Huang (Hoboken, NJ: Wiley), 219–272.

Totsche, K. U., Rennert, T., Gerzabek, M. H., Kögel-Knabner, I., Smalla, K., Spiteller, M., et al. (2010). Biogeochemical interfaces in soil: the interdisciplinary challenge for soil science. *J. Plant Nutr. Soil Sci.* 173, 88–99. doi: 10.1002/jpln.200900105

van Breemen, N., Finlay, R., Lundström, U., Jongmans, A. G., Giesler, R., and Olsson, M. (2000b). Mycorrhizal weathering: a true case of mineral plant nutrition? *Biogeochemistry* 49, 53–67. doi: 10.1023/A:1006256231670

van Breemen, N., Lundström, U. S., and Jongmans, A. G. (2000a). Do plants drive podzolization via rock-eating mycorrhizal fungi? *Geoderma* 94, 163–171. doi: 10.1016/S0016-7061(99)00050-6

van Breemen, N., Mulder, J., and Driscoll, C. (1983). Acidification and alkalinization of soils. *Plant Soil* 75, 283–308. doi: 10.1007/BF02369968

van Hees, P. A. W., Lundström, U. S., and Giesler, R. (2000). Low molecular weight organic acids and their Al-complexes in soil solution—composition, distribution and seasonal variation in three podzolized soils. *Geoderma* 94(2–4), 173-200. doi: 10.1016/S0016-7061(98)00140-2

van Hees, P., Godbold, D., Jentschke, G., and Jones, D. (2003). Impact of ectomycorrhizas on the concentration and biodegradation of simple organic acids in a forest soil. *Eur. J. Soil Sci.* 54, 697–706. doi: 10.1046/j.1351-0754.2003.0561.x

Vermeire, M.-L., Cornu, S., Fekiacova, Z., Detienne, M., Delvaux, B., and Cornélis, J.-T. (2016). Rare earth elements dynamics along pedogenesis in a chronosequence of podzolic soils. *Chem. Geol.* 446, 163–174. doi: 10.1016/j.chemgeo.2016.06.008

von Lützow, M., Kögel-Knabner, I., Ekschmitt, K., Flessa, H., Guggenberger, G., Matzner, E., et al. (2007). SOM fractionation methods: relevance to functional pools and to stabilization mechanisms. *Soil Biol. Biochem.* 39, 2183–2207. doi: 10.1016/j.soilbio.2007.03.007

von Lützow, M., Kögel-Knabner, I., Ekschmitt, K., Matzner, E., Guggenberger, G., Marschner, B., et al. (2006). Stabilization of organic matter in temperate soils: mechanisms and their relevance under different soil conditions - a review. *Eur. J. Soil Sci.* 57, 426–455. doi: 10.1111/j.1365-2389.2006.00809.x

von Lützow, M., Kögel-Knabner, I., Ludwig, B., Matzner, E., Flessa, H., Ekschmitt, K., et al. (2008). Stabilization mechanisms of organic matter in four temperate soils: development and application of a conceptual model. *J. Plant Nutr. Soil Sci.* 171, 111–124. doi: 10.1002/jpln.200700047

Wallander, H., Nilsson, L. O., Hagerberg, D., and Rosengren, U. (2003). Direct estimates of C: N ratios of ectomycorrhizal mycelia collected from Norway spruce forest soils. *Soil Biol. Biochemi.* 35, 997–999. doi: 10.1016/S0038-0717(03)00121-4

Zhang, X., and Amelung, W. (1996). Gas chromatograph1c determination of muramic acid, glucosamine, mannosamine, and galactosamine in soils. *Soil Biol. Biochem.* 28, 1201–1206. doi: 10.1016/0038-0717(96)00117-4

Zimmermann, M., Leifeld, J., Abiven, S., Schmidt, M. W., and Fuhrer, J. (2007). Sodium hypochlorite separates an older soil organic matter fraction than acid hydrolysis. *Geoderma* 139, 171–179. doi: 10.1016/j.geoderma.2007.01.014

Check for updates

Recognizing Patterns: Spatial Analysis of Observed Microbial Colonization on Root Surfaces

Hannes Schmidt [1]*, Naoise Nunan [2], Alexander Höck [1], Thilo Eickhorst [3], Christina Kaiser [4], Dagmar Woebken [1] and Xavier Raynaud [2]*

[1] Division of Microbial Ecology, Department of Microbiology and Ecosystem Science, Research Network 'Chemistry Meets Microbiology', University of Vienna, Vienna, Austria, [2] Sorbonne Université, CNRS, IRD, INRA, P7, UPEC, Institute of Ecology and Environmental Sciences - Paris, Paris, France, [3] Faculty 2 Biology/Chemistry, University of Bremen, Bremen, Germany, [4] Terrestrial Ecosystem Research, Department of Microbiology and Ecosystem Science, Research Network 'Chemistry Meets Microbiology', University of Vienna, Vienna, Austria

Root surfaces are major sites of interactions between plants and associated microorganisms. Here, plants and microbes communicate via signaling molecules, compete for nutrients, and release substrates that may have beneficial or harmful effects on each other. Whilst the body of knowledge on the abundance and diversity of microbial communities at root-soil interfaces is now substantial, information on their spatial distribution at the microscale is still scarce. In this study, a standardized method for recognizing and analyzing microbial cell distributions on root surfaces is presented. Fluorescence microscopy was combined with automated image analysis and spatial statistics to explore the distribution of bacterial colonization patterns on rhizoplanes of rice roots. To test and evaluate the presented approach, a gnotobiotic experiment was performed using a potential nitrogen-fixing bacterial strain in combination with roots of wetland rice. The automated analysis procedure resulted in reliable spatial data of bacterial cells colonizing the rhizoplane. Among all replicate roots, the analysis revealed an increasing density of bacterial cells from the root tip to the region of root cell maturation. Moreover, bacterial cells showed significant spatial clustering and tended to be located around plant root cell borders. The quantitative data suggest that the structure of the root surface plays a major role in bacterial colonization patterns. Possible adaptations of the presented approach for future studies are discussed along with potential pitfalls such as inaccurate imaging. Our results demonstrate that standardized recognition and statistical evaluation of microbial colonization on root surfaces holds the potential to increase our understanding of microbial associations with roots and of the underlying ecological interactions.

Keywords: microbial ecology, root surface, bacterial colonization, point process, spatial statistics, image analysis, pattern recognition, wetland rice

INTRODUCTION

The rhizosphere is of fundamental importance for nutrient cycling in terrestrial ecosystems. Within this small volume of soil, plants and microorganisms interact closely with each other. These interactions are likely to be strongest at the root surface (i.e., the rhizoplane) where root–derived substrates are accessible to microbial colonizers and microbial metabolites are immediately available for plant uptake. The rhizoplane can therefore be considered as one of the main regions driving nutrient flow and transformation in the rhizosphere. It differs in many aspects from bulk soil, including containing a specific microbial community with high cell density and reduced levels of diversity (Philippot et al., 2013; Reinhold-Hurek et al., 2015). While the diversity of rhizosphere and rhizoplane microorganisms is getting greater attention, information on the spatial organization of this diversity is still scarce. However, detailed knowledge of the spatial localisation and the microniches that root-associated microbes inhabit may shed light on the interactions between plant hosts and their microbiome and allow us to determine the magnitude of these interactions.

Due to their close association with plants, microorganisms colonizing the rhizoplane experience a range of stressors and/or rewards through mechanical or chemical interactions (e.g., root elongation or exudation; Lebeis et al., 2015; Dupuy and Silk, 2016). In turn, plants can be strongly influenced by the rhizoplane fraction of the root microbiome, for instance via the release of signaling molecules or via enzymatic cell wall degradation that may help microbes to enter the endospheric space of roots (Oldroyd, 2013; Reinhold-Hurek et al., 2015; Hacquard et al., 2017). Microbial cells that are able to thrive along this dynamic interface and to act upon plants are likely to colonize nutritional or spatial niches, which may help them to proliferate as clusters of cells or biofilms (Danhorn and Fuqua, 2007; Cardinale, 2014). Qualitative microscopic observations often report non-uniform rhizoplane colonization patterns, which suggests that the bulk of the interactions between roots and associated microorganisms occurs primarily in specific microniches (Foster and Bowen, 1982; Ofek et al., 2012; Cardinale, 2014; Hartmann et al., 2015). For example, nitrogen-fixing bacteria associated with sugar cane or rice were observed to particularly colonize root tips and lateral root junctions, with the latter providing potential entry points into the root endosphere (James et al., 1994; Faoro et al., 2017). While these observations provide us with valuable insights into host-microbe interactions, only quantitative approaches that recognize and evaluate spatial aspects of rhizoplane colonization allow for a reliable identification of potential hotspots of plant-microbe interactions. To date, few studies have measured spatial descriptors of rhizoplane colonization at the micrometer scale, such as bacterial clustering or communication distances between individual cells (Dandurand et al., 1997; Gantner et al., 2006; Watt et al., 2006). However, these microscale data, along with standardized approaches in microscopy and data interpretation (e.g., cell numbers per root unit; Cardinale, 2014; Schmidt and Eickhorst, 2014), are necessary for obtaining comparable data on root colonization and for estimating the dimensions of belowground substrate flux between microbiota and plants.

Spatial statistics provide useful tools to study patterns in sets of 2D points (Ilian et al., 2008), such as those that arise from the growth of microbial cells on a given surface. These methods provide us not only with a means to analyse spatial patterns but also allow us to make hypotheses about the constraints and drivers which underlie observed spatial patterns. In the field of microbial ecology, such approaches have been proven useful to study and model microbial cell distributions within the soil matrix (Raynaud and Nunan, 2014), the affiliation of bacterial phyla with different lichen species (Cardinale et al., 2012), as well as to analyze intra- and inter-specific interactions between bacterial cells on leaf surfaces and their relation to morphological features such as stomata and veins (Remus-Emsermann et al., 2014; Esser et al., 2015).

We therefore aimed at establishing a standardized workflow including fluorescence microscopy, automated signal recognition, and spatial statistics to investigate the arrangement of microbial rhizoplane colonization. The whole procedure has been compiled into imageJ and R scripts that are available online. We will present examples of analyzing the distribution of a putative nitrogen fixing bacterial strain on roots of wetland rice, one of the most important crop plants worldwide. Firstly, we describe the workflow including image acquisition, automated signal recognition, and statistical analyses of spatial patterns. Secondly, we present an application of the analysis pipeline on systematically obtained fluorescence micrographs to show the potential of such analyses in an ecological context. Thirdly, we will discuss the potentials and pitfalls of pattern recognition analyses to study the microbial colonization of root surfaces. The presented protocol and pipeline can be widely used to target mechanistic questions regarding root colonization but also to obtain insights into the ecology of plant-microbe interactions.

MATERIALS AND METHODS

Setup of Gnotobiotic Experiment

The gnotobiotic experiment was performed with young wetland rice plants (*Oryza sativa*) and the in-house bacterial strain *Kosakonia sacchari* which, in previous experiments, has been shown to associate well with rice plants under nitrogen-fixing conditions (unpublished results). The glume of rice seeds (cultivar IR64) was removed by hand and seeds were surface sterilized by washing in 5% NaOCl for 10 min, followed by washing in 2% Na_2SO_3 for 3 min, and 6 successive washes in autoclaved MQ water (1 min each). Rice seedlings were pre-germinated on sterile plates with autoclaved LB medium (Bertani, 1951) in the dark at approximately 25°C for 10 days. Glass tubes (length: 25 cm, diameter: 2.5 cm) were autoclaved, sealed with aluminum foil, and baked at 300°C for 4 h. Nitrogen-free Yoshida solution was prepared according to Yoshida et al. (1976) without the addition of NH_4NO_3. A 1.5% gellan gum medium (Gelrite, Carl Roth, Germany) was autoclaved and kept at 70°C until planting of seedlings in tubes. *K. sacchari* was cultivated in Erlenmeyer flasks filled with 20 mL semisolid nitrogen-free NFCC medium (Mirza and Rodrigues, 2012) in an atmosphere containing 1% oxygen at 19°C without shaking. After reaching exponential phase, the cells were harvested by centrifugation

for 10 min at 5,000 g, the supernatant was discarded, and the cells were resuspended in nitrogen-free Yoshida solution to a concentration of approximately 10^4 cells μL^{-1}.

Only germinated seedlings free of microbial and fungal contamination were used for the gnotobiotic experiments. The radicle of the seedling (root length approximately 1 cm) was submerged in 500 μL of *K. sacchari* for 30 min under sterile conditions. Following inoculation, each seedling was transferred into an individual glass tube filled with 1.5% gellan gum medium with the radicle facing downwards into the medium. A layer of approx. 1 cm nitrogen-free Yoshida solution was added on top of the gel surface to mimic the submerged conditions of rice cultivation without completely drowning the aboveground parts of the plants. Individual tubes were tightly sealed with autoclaved wool and kept in a greenhouse for 2 weeks exposing the plants to a day-and-night cycle of 14 +10 h with average temperatures of 30° and 22°C, respectively. The tubes were opened under sterile conditions every 3 days to allow for an exchange of the atmosphere, to replace the Yoshida solution, and to inspect for potential contamination. Sterile controls without the bacterial inoculum were prepared in the same way.
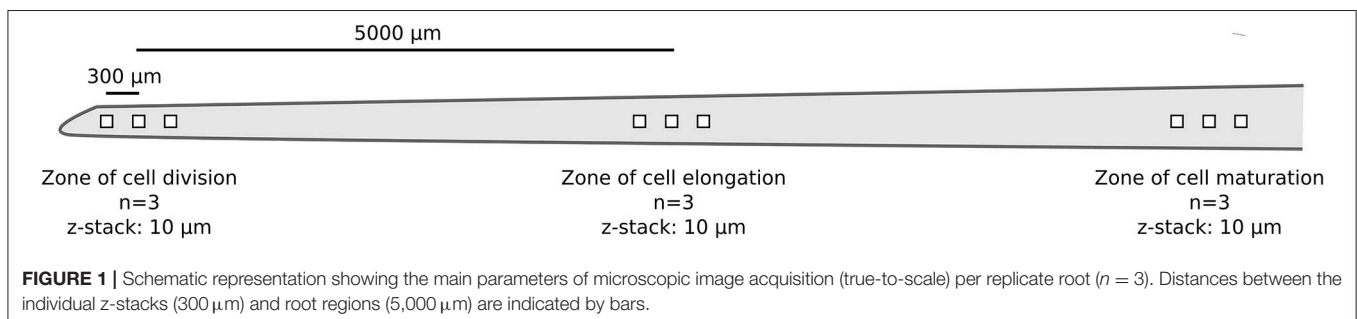
Sample Preparation for Microscopy

After 16 days of growth in the greenhouse, the rice plants were gently removed from the glass tubes under sterile conditions. The roots were immediately subjected to chemical fixation in 4% formaldehyde solution for 3 h at 4°C. Followed by 2 washes in 1 × phosphate-buffered saline (PBS), the roots were stored in a mixture of 2:3 PBS:EtOH (vol:vol) at −20°C until further processing. For downstream microscopic analyses, only primary nodal roots were used to increase comparability among the replicates. Staining of rhizoplane-associated bacteria with SYBR-Green I (Lumiprobe, Germany) and preparation of the roots on objective slides for fluorescence microscopy was performed as described in Richter-Heitmann et al. (2016). In addition, bacteria were visualized on replicate root samples via CARD-FISH as described in Schmidt and Eickhorst (2014) with slight modifications (see Supplementary Materials). To reduce the detachment of bacterial cells from the rhizoplane prior to microscopy the number of washing steps was limited to the minimum (5 washing steps for CARD-FISH) while only soft spring-steel tweezers were used to handle roots at the part that was not used for imaging.

Image Acquisition

One nodal root per replicate rice plant ($n = 3$) was chosen for image acquisition. For each individual root, image stacks were taken in a systematic manner from three root regions: starting from right behind the apical meristem (i.e., zone of cell division; $n = 3$), via the zone of cell elongation ($n = 3$), to the zone of cell maturation ($n = 3$; **Figure 1**). For each root region, a fixed distance of 300 μm between the individual image stacks was chosen to avoid overlap but to ensure that the images were still obtained from the same region. The distance of 5,000 μm between the root regions was selected based on previous observations of nodal root development taken from 4 week old rice plants. A confocal laser scanning microscope (Leica TCS SP8X, Leica, Germany) equipped with a 63x glycerol objective and a white-light laser was used for image acquisition. SYBR Green I was excited at a wavelength of 489 nm and recorded from 500 to 540 nm. In the following, these settings will be referred to as the "dye channel." Background autofluorescence of the root surface, giving information on root cell walls, was recorded via excitation at 565 nm and emission from 580 to 750 nm (in the following referred to as the "autofluorescence channel"). The following settings were used for each z-stack: image size: 184.5 × 184.5 μm, image resolution: 1024 × 1024 pixels, bit depth: 8 per channel, scan speed 100 Hz, line averaging: 4, frame averaging: 1, z-stack thickness: 10 μm, slice distance: 0.5 μm, zoom factor 1, pinhole: 1 AU. Image stacks were stored as Leica *.lif files without post-processing. Two other z-stacks with similar acquisition settings were also acquired to test the generality of the data extraction procedure. These z-stacks corresponded to an additional root region (zone of lateral root emergence; Supplementary Figure S1) and CARD-FISH-stained rhizoplanes (see Supplementary Figure S2).

Image Analysis

All microscopic images (raw *.lif files) were processed with Fiji (Schindelin et al., 2012) to extract information on the spatial distribution of bacterial cells as well as properties of their environment (root cell walls). Extracted data was then loaded into R 3.4 (R Development Core Team, 2017) and converted to *spatstat* objects (Baddeley et al., 2015) for analyses. All codes used in this manuscript (Fiji macro and R codes) are available for download at https://github.com/xraynaud/microbial-cell-detection. The overall detection procedure is shown in **Figure 2** and specific details are given below.

FIGURE 1 | Schematic representation showing the main parameters of microscopic image acquisition (true-to-scale) per replicate root ($n = 3$). Distances between the individual z-stacks (300 μm) and root regions (5,000 μm) are indicated by bars.
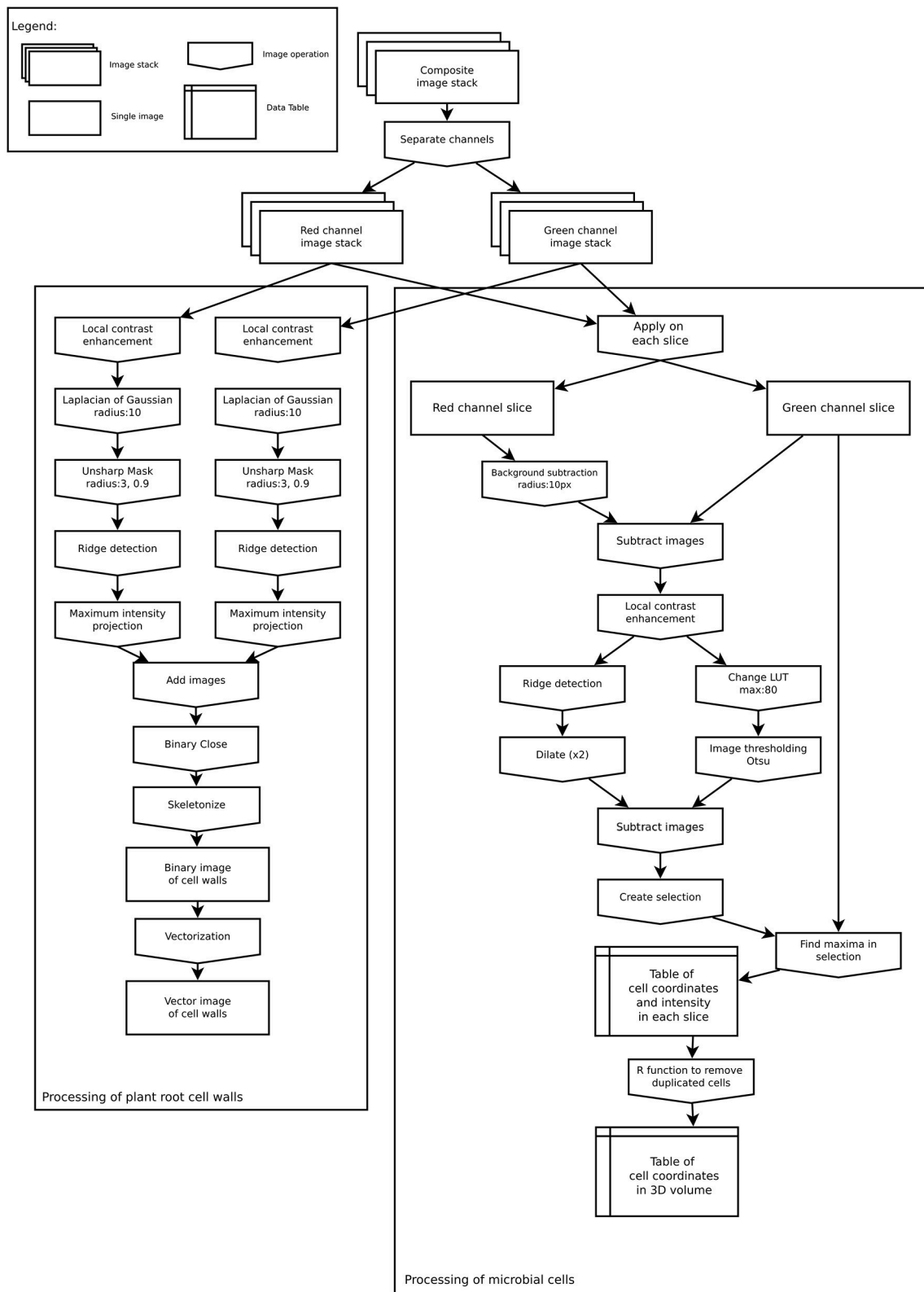
FIGURE 2 | Image analysis workflow to extract root cell walls **(Left)** and microbial coordinates **(Right)**.

Detection of Root Cell Walls

The spatial organization of root cell walls was extracted from both autofluorescence and dye channels. Both channels were processed similarly. First, a local contrast enhancement filter was applied to all slices. Then a 3D Laplacian of Gaussian filter (radius $10 \mu m$) was applied to all slices followed by an Unsharp mask filter. These procedures allowed for the removal of all small features from images (such as bacterial cells), retaining only the larger ones. From these processed images, linear structures were identified in each slice using the Fiji plugin *ij-ridgedetection* (Steger, 1996; Wagner et al., 2017) to produce a binary 3D image set of root cell walls. 3D slices were then merged into a single 2D image, saved as TIFF black and white image, and converted to vector format (SVG) using the software autotrace (http://autotrace.sourceforge.net/). SVG files were then loaded into R and converted to a *spatstat* line segment pattern (psp object) for further analysis.

Detection of Bacterial Cells

The following procedure was applied to extract the coordinates of bacterial cells from each slice in the dye channel. First, the autofluorescence channel was subtracted from the dye channel as root cell walls were visible in both channels. This subtraction allowed for the removal of unwanted features from the dye channel prior to processing. Then, for each slice of the z-stack, a local enhancement filter was applied to the resulting image, which was thereafter thresholded following Otsu's method (Otsu, 1979). In parallel, a ridge detection filter was applied to each slice to identify unwanted linear features in the image. The linear features that were detected were then subtracted from each thresholded image. Because bacterial cells sometimes occur in groups of several individual cells, it was not possible to extract cells from the thresholded image. The thresholded images were thus used as a selection mask to look for signal maxima in the dye channel slice. These signal maxima were assumed to correspond to individual cells and their coordinates were saved into a table. This approach allowed us to obtain coordinates from cell clusters that sometimes appeared as bright spots with low signal variations due to scattered light. In the resulting table, each identified cell was characterized by its *x*, *y*, and *z* coordinates, as well as the measured signal intensity at this position.

As a single bacterial cell (approximately $1 \mu m$ in diameter) could produce a signal in two or three consecutive slices of the z-stack (slice distance: $0.5 \mu m$), the coordinates were processed in R to remove duplicate cells. Coordinates in consecutive slices were assumed to correspond to the same cell if they were less than $0.9 \mu m$ apart. Where this occurred, the *z* coordinate of the cell was linearly interpolated from the signal intensity measured in each slice in which the cell was visible, assuming that the greater the intensity in a slice the closer the cell was to this slice. Finally, the obtained 3D distribution of cells was projected onto the 2D *x,y* plane for analysis. Although this might slightly distort the true distribution of cells due to the cylindrical shape of roots, preliminary tests indicated that this small distortion was very limited and did not alter the geometrical properties of distributions for roots having diameters similar to nodal rice roots at this development stage (data not shown). In rare cases, the extracted data was manually cleaned by removing coordinates that were falsely detected as bacterial cells (see Results section).

Data Analysis

All data analyses were carried out using R 3.4 (R Development Core Team, 2017). The spatial distribution of bacterial cells and root cell walls were analyzed using packages *spatstat* (Baddeley et al., 2015) and *movMF* (Hornik and Grün, 2014). The effect of root region on a number of spatial features was determined using mixed effect ANOVA (*lme4* package, Bates et al., 2015) with root replicates set as the random effect.

Root Cell Walls

Root cells are approximately rectangular in shape when viewed in microscopic images, where the longer sides correspond to the growing direction of the root. For each plant cell, cell walls perpendicular to the microscope focal plane (anticlinal cell walls) were generally identified as several small line segments. To obtain the orientation of plant cells from the image, the angles of each segment with the horizontal were calculated and a mixture of three von Mises distributions was fitted to this data (*movMF* R package, Hornik and Grün, 2014). The total length of segments from the three identified sets was calculated and the orientation of plant cells, which correspond to the growing direction of the root, was assumed to correspond to the set having the greatest total length.

At the surface of roots, these cell walls form grooves which can be colonized by microbial cells. In the following, we will refer to root cell walls when dealing with root features and root cell borders when dealing with these grooves between plant cells.

Bacterial Cell Distributions

Observed distributions of bacterial cells were analyzed assuming they could be described as planar point patterns, i.e., cell distributions were considered to be set of single points (no volume) observed in a window (the image field of view). In order to characterize these distributions, different indices and summary functions were calculated. First, to obtain a broad overview of the spatial organization of cells, we calculated the intensity of the point process (i.e., the number of cells per unit surface) and the Hopkins-Skellam index of aggregation. Second, to get a better view of cell distributions characteristics at different spatial scales, the pair correlation function ($g(r)$), the empty space function ($H(r)$), and the nearest neighbor distance distribution function ($D(r)$) were also calculated. The pair correlation function is related to the number of neighbors a point of the distribution has at a distance r. The empty space function is the distribution of distances between points of the point pattern and an arbitrary location. As $H(r)$ is a probability function, it gives the probability that there will be a point lying within distance r of any arbitrary location in the observed window. The nearest neighbor distance distribution function of a point pattern is the probability distribution of the distance r between a point to its nearest neighbor. Because preliminary inspection suggested that the density of cells was not homogeneous (i.e., the density of points changed depending on the location in the field of view), the inhomogeneous counterparts of these functions
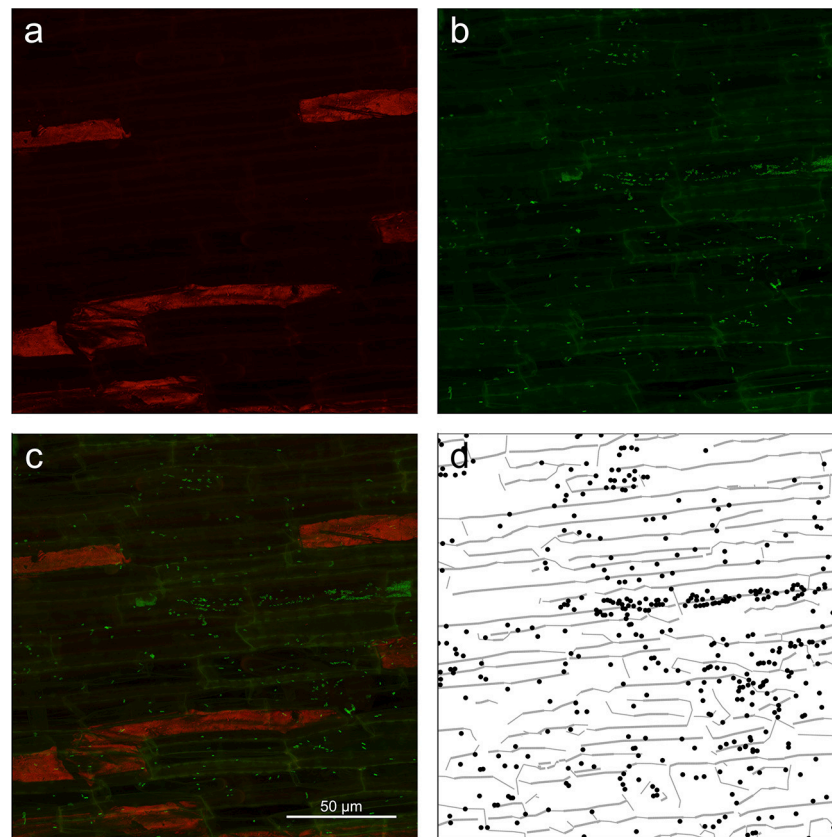
FIGURE 3 | Z-projection from the root mature region of **(a)** autofluorescence channel (shown in red) of the image showing only root cell walls, **(b)** dye channel (in green) showing both plant roots cell walls and microbial cells, **(c)** composite image of the surface of root showing root cell walls (yellowish lines) as well as microbial cells (green dots). **(d)** Extracted data from the image with root cell walls shown as gray lines and microbial cells as black dots.

(Baddeley et al., 2015) were used, which require an estimate of the intensity function of the point distributions across the observed window. This estimate was calculated using a gaussian smoothing kernel with a bandwidth of 60.5 μm for all images. The bandwidth size was chosen because it allowed the capture of the large scale variations in cell density within the image but ignored smaller scale variations. The bandwidth size was also sufficiently large to ensure that interactions between bacterial cells were very limited, as interaction distances between cells have been estimated to lie within 20 μm of cells in most cases (Gantner et al., 2006; Franklin and Mills, 2008). The summary functions of the observed distributions were tested for significant aggregation or regularity using Monte-Carlo simulations envelopes. For this purpose, summary functions of 99 inhomogeneous Poisson processes (i.e., a point process for which the locations of points are independent of the presence of neighbors and in which spatial variations in intensity are accounted for) where calculated and compared to the measured cell distributions using the Diggle-Cressie-Loosmore-Ford goodness-of-fit test (Baddeley et al., 2014).

Finally, the relations between bacterial cells and root cell borders were characterized using two different metrics. First of all, the distances between each bacterial cell and the nearest root

cell wall segment was measured. This was done to determine whether the distributions of bacterial cells were related to root cell borders. For each bacterial cell, the distance was considered to be positive or negative depending on the side of the root cell wall the bacterial cell was found. In this way, the shape of the distribution of distances provided information on the spatial relations between bacterial cells and root cell borders: a uniform distribution indicated no relationship meaning that the cell distributions were independent of cell borders, a humped shaped distribution of distances centered around 0 (the position of the cell walls, $\pm$ 2 μm due to the precision of the data extraction) indicated that cells were distributed preferentially near root cell borders. Secondly, the pair orientation distribution function was calculated for pairs of cells less than 25 μm apart. This function describes the distribution of angles between segments joining two cells and the horizontal (Baddeley et al., 2015). If the distribution of points is isotropic, the orientation of neighboring cells does not have a preferred direction. However, if it is not isotropic, the function determines the angle of the preferred direction with the horizontal. The effect of the root cell border on bacterial distributions was determined by comparing the directions of bacterial cell pair orientations with those of root cell walls in each z-stack.

RESULTS

In the main experiment, we acquired 27 individual z-stacks from three replicate rice roots that were colonized by *K. sacchari* for 16 days after inoculation. A representative example of the z-stacks obtained from the zone of cell maturation and data extracted thereof is shown in **Figure 3**. Z-projections of the dye and autofluorescence channels are shown in **Figures 3a,b** along with the superimposition of both channels (**Figure 3c**) and the extracted data (**Figure 3d**). Images and data extraction for the other root regions are given in Supplementary Figure S3 (zone of cell division) and Supplementary Figure S4 (zone of cell elongation).
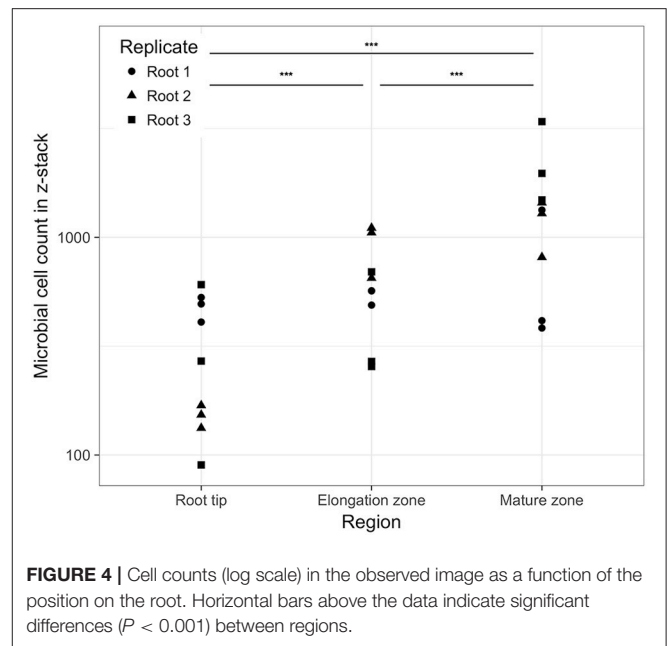
Quality of Data Extracted From Microscopic Images

Careful visual inspection of the microscopic images and the extracted data indicated that the signal extraction procedure allowed for the capture of most of the microbial cells, as well as some important information on their environment, such as root cell walls (**Figure 3**, Supplementary Figures S3, S4). Large unwanted visible structures were automatically and correctly discarded during the data extraction procedure (see large red patches in **Figure 3**). However, we also found that, in some cases, the procedure produced a high number of false positives or did not extract microbial cell coordinates correctly. False detection of cells arose under two conditions: firstly, overall low signal intensity in images (Supplementary Figure S5) or strong differences in signal intensity between the autofluorescence and dye channel (Supplementary Figure S6) resulted in an inefficient first step of the procedure (autofluorescence to dye subtraction; 6 z-stacks affected). In the latter case, junctions between root cell walls were slightly brighter than their surroundings and were detected as false positives. In addition, the overall high intensity level of the images left some bacterial cells undetected (see Supplementary Figure S6). Secondly, SYBR Green I was observed to also bind to root cell nucleic acids. In some z-stacks, plant cell nuclei were visible as green patches and detected as a small cluster of cells (3 z-stacks). Images with a low overall intensity were discarded. In other cases, false positives were manually removed from the images.

Colonization Density and Spatial Distribution of Bacteria on the Rhizoplane

The number of observed cells ranged from 90 to 3,398 per z-stack ($n = 27$), which corresponded to densities of 2.6×10^3-9.9×10^4 cells per mm^2 of root surface. There were significant changes in cell density between the root regions studied (**Figure 4**). On average, there was a significant increase in cell numbers from the zone of cell division via the elongation zone to the mature region (GLM ANOVA, $\chi^2 = 6{,}972.6$, $P < 0.001$). Nevertheless, high variability in cell numbers was visible for each morphological region as well as between individual root replicates.

Across all images, the nearest-neighbor distances ranged from 0.18 to 44.54 μm and bacterial distributions showed significant clustering (Hopkins-Skellam test, $P < 0.001$ for all z-stacks). These distances were highly skewed toward shorter distances. The median distance within images was 2.14 μm on average.

FIGURE 4 | Cell counts (log scale) in the observed image as a function of the position on the root. Horizontal bars above the data indicate significant differences ($P < 0.001$) between regions.

The median of the nearest neighbor distance decreased slightly with the position along the root. Average values of 2.62, 1.93, and 1.88 μm were measured from the zone of cell division to the zone of cell maturation, respectively. Comparisons between summary statistics $g_{inhom}(r)$, $D_{inhom}(r)$, and $H_{inhom}(r)$ were calculated for all observed distributions and simulation envelopes of inhomogeneous Poisson distributions. These comparisons indicated that most observed distributions in the three root regions (21, 18, 27 distributions, respectively) were more aggregated than expected for complete spatial randomness for short distances $<10\,\mu$m (see **Figure 5** for g and D functions of the distribution shown in **Figure 3**).

Relation Between Bacterial Distributions and Rhizoplane Features

In all images, bacterial cells were found to be closer to a root cell border than expected for complete spatial randomness. The distances between individual bacterial cells and the closest root cell border showed a symmetrical hump-shaped distribution (see **Figure 6A** for an example). Careful inspection of observed distributions and the estimation of the pair orientation function further indicated that the orientations of the lines between neighboring bacterial cells were not random and coincided with the orientation of root cells (**Figure 6B**). This was true for most observed distributions, for which the angle at which the pair orientation function reached its maximum was similar to the orientation of root cell walls (**Figure 7**).

DISCUSSION

Imaging Procedure and Data Acquisition

The aim of the paper was to provide a standardized method for analysing microbial cell distributions on the rhizoplane. The image analysis procedure was carried out using the Fiji
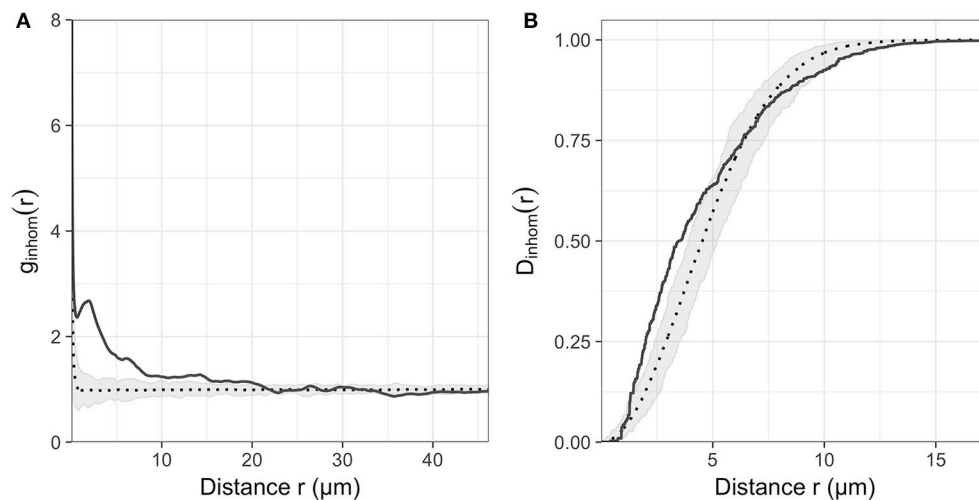
FIGURE 5 | (A) Inhomogeneous pair correlation function $g_{inhom}(r)$ and **(B)** Nearest neighbor distance function $D_{inhom}(r)$ of the microbial distribution shown in **Figure 2**. Gray envelope corresponds to the envelope of 99 realization of an inhomogeneous Poisson process of the same intensity as the observed distribution.
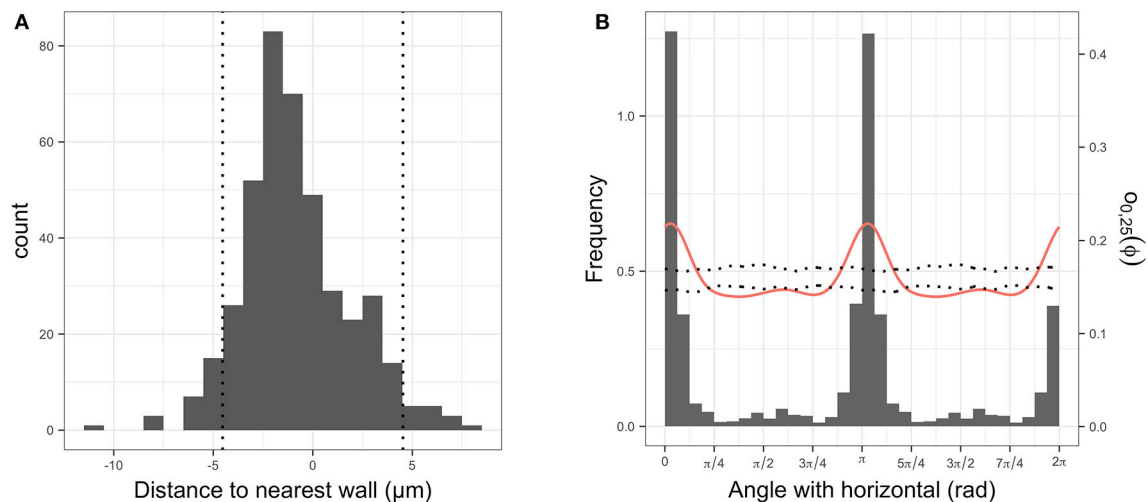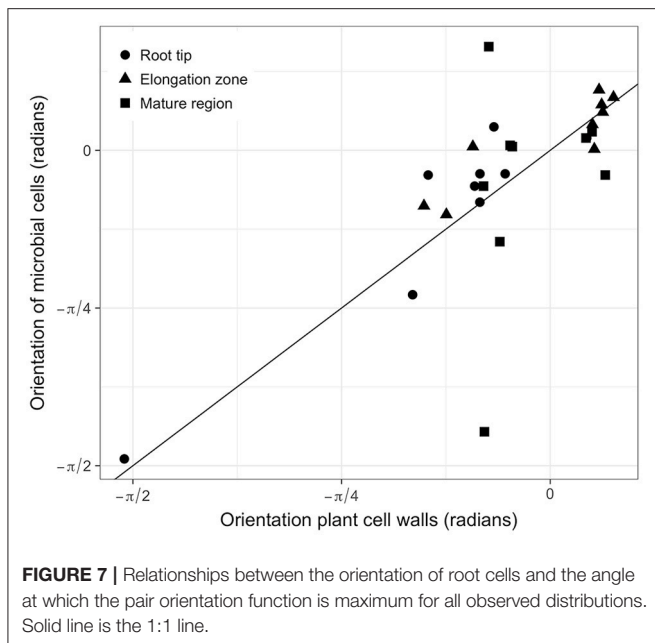

FIGURE 6 | (A) Histogram of signed distances between plant root cells and their nearest cell wall. The two vertical dotted lines indicate the average distance between two parallel cell walls. **(B)** Histogram of angles between walls and horizontal (in gray), observed pair orientation function $O_{0,25}(\Phi)$ for cells less than 25 μm apart (i.e., distribution of angles between two cells and the horizontal; red line) and envelope of the pair orientation function for 99 simulation of complete spatial randomness point processes.

software. Fiji, and ImageJ, upon which it is built, are multi-platform (Windows, Apple, Linux), general purpose, open-source software. Its main features include the availability of numerous plugins (e.g., *ij-ridgedetection,* which is used here), the possibility to develop new plugins for specific applications, as well as the automatized analysis of sets of images through the use of macros. Fiji is also able to directly import image stacks in the native Leica format that was used in this study. Other software such as *daime* (Daims et al., 2006) and IMARIS (Bitplane AG, Zürich, Switzerland) could have been used as well. However, we found that Fiji offered the most complete set of tools to extract the type of data needed for this study (identification of bacterial cells and linear features in images). Nevertheless, there are limitations

to the procedure that the reader should be aware of. These are discussed below.

Choice of Dyes for Microbial Cell Visualization

SYBR Green I has been shown to give strong fluorescent signals that can be used to detect rhizoplane-colonizing microorganisms (Reinhold-Hurek et al., 2015; Richter-Heitmann et al., 2016). The signal-to-noise ratios obtained with SYBR Green I were found to be superior to other general nucleic acid stains such as DAPI. Nevertheless, it is virtually impossible to obtain images with a very high signal-to-noise ratio from rhizoplanes while avoiding capturing root autofluorescence in the dye channel. A lambda scan of an unstained, sterile root revealed that the peaks of root

FIGURE 7 | Relationships between the orientation of root cells and the angle at which the pair orientation function is maximum for all observed distributions. Solid line is the 1:1 line.

autofluorescence are in the regions that overlap with almost all commonly used fluorescent dyes (e.g., DAPI, fluorescein/SYBR Green I, Cyanine 3 - data not shown). Strategies to circumvent problems associated with low signal-to-noise ratios are the use of far-red dyes such as Cyanine 5.5 (Watt et al., 2006) or less commonly used dyes with high fluorescent quantum yields in combination with very narrow emission windows (Lukumbuzya and Daims, personal communication). However, these alternatives come with limitations, such as the inability to observe stained microbial cells by eye due to near-infrared emission wavelengths (e.g., Cy5.5: 694 nm).

Another option to enhance microbial cell detection while using fluorophores in the green and red light spectra is the use of CARD-FISH (Pernthaler et al., 2002). High signal intensities allow for a solid discrimination of microbial target cells on highly autofluorescent rhizoplanes (Schmidt and Eickhorst, 2014; Pett-Ridge and Firestone, 2017). Our pipeline was also tested with a z-stack showing CARD-FISH-stained bacteria on the surface of a soil-grown rice root (Supplementary Figure S2). The coordinates for most cells in the CARD-FISH image were correctly identified with the data extraction procedure. Despite varying signal intensities among target cells, a common feature of FISH applications to environmental samples (Amann and Fuchs, 2008), CARD-FISH is a valuable alternative to the presented approach when the aim is to detect specific target groups of microorganisms on roots.

Avoiding the natural autofluorescence of biological specimens via signal amplification or other strategies is also a reasonable approach to increase signal-to-noise ratios (Peredo and Simmons, 2018). In this study, however, we made use of the natural autofluorescence emitted by roots, a strategy that can be useful for the interpretation of confocal images in the context of plant-microbe interactions (Cardinale, 2014). In principle,

every channel (e.g., blue, green, red) that emits background autofluorescence and that does not interfere with the specific fluorophore can be captured. We decided to acquire information from the red light spectrum to obtain background information on the surroundings of microbial rhizoplane colonizers. In this way it was possible to recognize morphological features such as root cell walls and to correlate them with microbial distribution patterns observed on rhizoplanes.

Image Quality and Data Extraction

Some z-stacks caused minor complications during data extraction (see Results section Quality of data extracted from microscopic images) stressing the importance of meticulous image acquisition prior to data extraction. It is necessary to avoid under- and over-exposure of the channels to enable the removal of the autofluorescence signals from the dye channel and to obtain an image with sufficiently high signal values for the image analysis procedure. It was challenging to record cell coordinates when signal intensities in the dye channel were too low (values <100 for 8 bit images). This can, to a certain extent, be overcome by increasing the dynamic range of both autofluorescence and dye channels to bring values in the 0–255 range prior to image analysis. However, increasing the brightness of images creates additional noise, which in turn leads to an increase in false positives. In such cases, false positives were removed by hand at the end of the cell detection procedure prior to the removal of duplicated cells (**Figure 2**).

Signal recognition was sometimes challenging even with correctly exposed channels. Firstly, bacteria can form clusters at the surface of roots (see dense cluster at the right hand side of **Figure 3** and bottom of Supplementary Figure S1). Such clusters often appear as a bright blur in which the identification of single cells is difficult due to light scattering that causes fluorescence signals to smear around objects (Sanderson et al., 2014). This is one of the reasons the presented analysis procedure does not detect cells based on their sizes but rather on variations in signal intensity within high intensity signal patches. Consequently, this approach might miss some bacteria in dense clusters where variation in signal intensity is not sufficient to allow detection of single cells. Spatial analyses carried out on extracted data (e.g., calculation of the pair correlation function) will underestimate aggregation so that the analyses presented here can be regarded as conservative. We believe, however, that this underestimation had a limited impact on our dataset because not all clusters were missed (see for example bottom of Supplementary Figure S4) and these clusters did not occur frequently. If clusters were more abundant, one way to obtain spatial information of single cells within clusters as well as more isolated cells could be to record images at two different signal intensities: a low intensity to detect features within clusters and a higher intensity to detect isolated cells (Eickhorst and Tippkötter, 2008) and to superimpose the resulting data. Secondly, single microbial cells can appear in two or three successive slices of images. As the extraction of cell coordinates is done independently for each slice of a z-stack, coordinates sets are post-processed in order to remove duplicate cells between two consecutive slices. This post-processing has the potential to make cell distributions more regular than they

naturally occur as two neighboring cells in close proximity (i.e., separated by less than 0.9 μm) in two consecutive slices would be considered as a single cell. This would occur, however, only in very dense clusters of cells and most likely did not affect the results presented here.

Bacterial Cell Distributions on Roots

Overall, the analysis procedure resulted in reliable spatial data of bacterial cells colonizing the rhizoplane in different regions of the roots that matched well with earlier reports on microbial root colonization. The bacterial densities found here were of the same order of magnitude as those quantified manually on soil-grown rice roots (Schmidt and Eickhorst, 2014). Previous observations of increased bacterial densities at the base of lateral roots (e.g., James et al., 1994; Faoro et al., 2017) were in agreement with additional z-stacks analyzed in this study (Supplementary Figure S1), which supports the notion that lateral root junctions provide entry points for nitrogen-fixing bacteria with a facultative endophytic lifestyle. Although our dataset is limited to a small number of roots, in all observed images, bacterial cell distributions were not homogeneous, i.e., cells appeared as patches on the root surface. Taking this inhomogeneity into account the analyses still indicated that cells were clustered within distances of less than 10 μm, which corresponds to measured or modeled interaction distances for bacteria (Gantner et al., 2006; Franklin and Mills, 2008). High interaction rates between bacterial cells are thus to be expected on the rhizoplane even for single species populations.

Bacterial cell distributions also appeared to be strongly associated with root cell borders. Cells were closer to root cell borders than expected for completely random distributions and neighboring cells were oriented in the same direction as the growing direction of the roots. This suggests that root growth and activity is an important determinant of bacterial colonization of root surfaces (Dupuy and Silk, 2016). Indeed, epidermal cells of roots bulge at the surface and create grooves in between neighboring root cells. When observed from the top (as performed in this study), these grooves correspond to the cell walls that are visible in the microscopic images. Microscopic observations have indicated that mucilage and other exudates accumulate in these grooves (Foster and Bowen, 1982), which may create a suitable habitat for microbial growth. Furthermore, these grooves could also offer bacterial cells some physical protection, making them less susceptible to predation. Although replicating these observations is clearly needed, our data provide some elements to sketch how bacteria could colonize the rhizoplane. When roots grow into soil, some cells may attach to the root surface around the apex and near root cell borders, possibly because some exudates are released there, or because they form grooves that offer protection. This would be the origin of colonization of the region of root cell division and could lead to the observed inhomogeneity of microbial colonization patterns. Subsequently, microbial cell populations would grow through cell division with individual daughter cells preferentially growing along the junctions of cell borders. The resulting orientation of neighboring bacterial cells would then resemble the patterns found in this study. Similar observations were also reported for

aboveground plant organs: bacterial cells have been observed to preferentially colonize leaves along cell borders (Verginer et al., 2010; Erlacher et al., 2015; Esser et al., 2015). Although the process of first contact of a microbial cell with a leaf surface may differ from a plant root, the mechanisms of finding a suitable micro-niche and growing along plant cell borders may represent the preferential way to colonize below- and above-ground plant organs by microorganisms.

In our experiment, only the emerging radicle of a seedling was inoculated with *K. sacchari* and immediately transferred into tubes filled with a sterile medium. At root sampling, the roots had an average length of 10 cm and the first centimeter of a root was analyzed for bacterial colonization in the zones of cell division, cell elongation, and cell maturation. The observation of high colonization densities in the zone of cell division after 16 days of root growth suggests that bacterial cells were able to keep up with an average root growth of approximately 0.6 mm per day. In our experimental system, recruitment of bacterial cells from the surrounding medium/soil can be excluded as the medium was sterile and bacterial cells were only introduced into the system through the inoculation process. Furthermore, the actual root cap was devoid of *K. sacchari* in almost all cases (data not shown). Consequently, the colonization of *K. sacchari* had to at least equal the root elongation in order to constantly colonize the zone of cell division behind the root tip.

Sterile controls without inoculum showed no bacterial signals (Supplementary Figure S7) and indicated that only *K. sacchari* cells colonized the roots in this experimental system. The increasing cell densities observed between the different root regions indicate that *K. sacchari* proliferated along the growing root. The strain used in this study is very closely related to type strain *K. sacchari* SP1[T] (99.89% 16S rRNA sequence identity, Chen et al., 2014), a heterotrophic bacterium that has been reported to colonize sugarcane plants and to exhibit plant-growth promotion through nitrogen fixation. In this study, the dense colonization of all observed regions indicates that carbon substrates provided by the plant (i.e., the necessary food source for *K. sacchari* in our experimental system) may not only have been available at the root tip but also at the elongation zone, as well was in the zone of maturity. In addition, our strain was observed to fix atmospheric nitrogen in association with rice roots in parallel experiments (data not shown) and could indeed act upon wetland rice (cultivar IR64) as plant-growth promoting rhizobacterium. However, an *in situ* confirmation of bacterial activity (i.e., nitrogen-fixation) on the single-cell level has yet to be reported for bacteria that colonize the rhizoplane. Such an endeavor (potentially via NanoSIMS) would benefit from the presented approach through the analysis of bacterial colonization patterns and a quantitative identification of hotspots of nutrient flux between roots and microbes. Furthermore, the analysis pipeline could be easily adapted to experiments with natural or synthetic multi-species communities and would allow for the assessment of competitive interactions among species in spatially structured communities. In order to determine how the spatial organization of communities affects these interactions, it would be interesting to trace the fate of stable isotope-labeled carbon, in the form

of ^{13}C-labeled photosynthates, into different components of the microbial communities and to determine how the spatial relations among single microbial cells affect allocation and competition for resources.

As an interesting aside, the significant differences in bacterial density along the rhizoplane, in particular when compared with the densities found in soil (10^1–10^4 mm^{-2}; Raynaud and Nunan, 2014), show quite categorically how the micro-environment can affect microbial communities. To put the range of densities into perspective, a parallel with human societies may be drawn. Assuming that one bacterial cell mm^{-2} is equivalent to 1 person km^{-2}, then the lowest rhizoplane density is roughly equivalent to the population density of a city such as Hamburg, whilst the highest density is greater than the population density of Dhaka, the world's most densely populated city (http://urbandata.unhabitat.org). There is a known super-linear power law relationship between population sizes of cities and many of their qualitative features such as wealth and innovation, which is believed to be driven by an increasing pace of social interactions with population density (Bettencourt et al., 2007). Similarly, microbial density may accelerate and/or alter interactions among microbes, such as competition, signaling (e.g., quorum sensing) or horizontal gene transfer, which may feed-back on the organization of the community in a qualitative way (West et al., 2007). It is therefore reasonable to assume, that not only do micro-environmental properties affect microbial metabolic activities but that they also have a significant effect on the ecology of microorganisms. Just as the practice of ignoring microscale phenomena is believed to have hindered progress in understanding and modeling C dynamics in soil (Wachinger et al., 2000; Falconer et al., 2015), the dramatic range in microbial densities found here and in other studies suggest that a complete understanding of many mechanisms in soil microbial ecology, and their relevance for ecosystem functioning can only be gained from a thorough examination of microscale processes.

AUTHOR CONTRIBUTIONS

HS, NN, TE, CK, DW, and XR designed the study. HS and AH performed the gnotobiotic experiment and acquired the image stacks. XR compiled the imageJ and R scripts. XR, NN, and HS established and tested the analysis pipeline. XR analyzed the data. HS, NN, and XR wrote the manuscript.

FUNDING

ACKNOWLEDGMENTS

SUPPLEMENTARY MATERIAL

The Supplementary Material for this article can be found online at: https://www.frontiersin.org/articles/10.3389/fenvs.2018.00061/full#supplementary-material

REFERENCES

Amann, R., and Fuchs, B. M. (2008). Single-cell identification in microbial communities by improved fluorescence in situ hybridization techniques. *Nat. Rev. Microbiol.* 6, 339–348. doi: 10.1038/nrmicro1888

Baddeley, A., Diggle, P. P. J., Hardegen, A., Lawrence, T., Milne, R. K., and Nair, G. (2014). On tests of spatial pattern based on simulation envelopes. *Ecol. Monogr.* 84, 477–489. doi: 10.1890/13-2042.1

Baddeley, A., Rubak, E., and Turner, R. (2015). *Spatial Point Patterns: Methodology and Applications with R.* London: Chapman and Hall/CRC Press.

Bates, D., Mächler, M., Bolker, B., and Walker, S. (2015). Fitting linear mixed-effects models using lme4. *J. Stat. Softw.* 67, 1–48. doi: 10.18637/jss.v067.i01

Bertani, G. (1951). Studies on lysogenesis. I. The mode of phage liberation by lysogenic *Escherichia coli*. *J. Bacteriol.* 62, 293–300.

Bettencourt, L. M., Lobo, J., Helbing, D., Kühnert, C., and West, G. B. (2007). Growth, innovation, scaling, and the pace of life in cities. *Proc. Nat. Acad. Sci. U.S.A.* 104, 7301–7306. doi: 10.1073/pnas.0610172104

Cardinale, M. (2014). Scanning a microhabitat: plant-microbe interactions revealed by confocal laser scanning microscopy. *Front. Microbiol.* 5:94. doi: 10.3389/fmicb.2014.00094

Cardinale, M., Steinová, J., Rabensteiner, J., Berg, G., and Grube, M. (2012). Age, sun and substrate, triggers of bacterial communities in lichens. *Environ. Microbiol. Rep.* 4, 23–28. doi: 10.1111/j.1758-2229.2011.00272.x

Chen, M., Zhu, B., Lin, L., Yang, L., Li, Y., and An, Q. (2014). Complete genome sequence of Kosakonia sacchari type strain SP1T. *Stand. Genomic Sci.* 9, 1311–1318. doi: 10.4056/sigs.5779977

Daims, H., Lücker, S., and Wagner, M. (2006). Daime, a novel image analysis program for microbial ecology and biofilm research. *Environ. Microbiol.* 8, 200–213. doi: 10.1111/j.1462-2920.2005.00880.x

Dandurand, L. M., Schotzko, D. J., and Knudsen, G. R. (1997). Spatial patterns of rhizoplane populations of *Pseudomonas fluorescens*. *App. Environ. Microbiol.* 63, 3211–3217.

Danhorn,. T., and Fuqua, C. (2007). Biofilm formation by plant-associated bacteria. *Annu. Rev. Microbiol.* 61, 401–422. doi: 10.1146/annurev.micro.61.080706.093316

Dupuy, L., and Silk, W. (2016). Mechanisms of early microbial establishment on growing root surface. *Vadose Zone J.* 15, 1–13. doi: 10.2136/vzj2015.06.0094

Eickhorst, T., and Tippkötter, R. (2008). Detection of microorganisms in undisturbed soil by combining fluorescence *in situ* hybridization (FISH) and micropedological methods. *Soil Biol. Biochem.* 40, 1284–1293. doi: 10.1016/j.soilbio.2007.06.019

Erlacher, A., Cardinale, M., Grube, M., and Berg, G. (2015). Biotic stress shifted structure and abundance of enterobacteriaceae in the lettuce microbiome. *PLoS ONE* 10:e0118068. doi: 10.1371/journal.pone.0118068

Esser, D. S., Leveau, J. H., Meyer, K. M., and Wiegand, K. (2015). Spatial scales of interactions among bacteria and between bacteria and

the leaf surface. *FEMS Microbiol. Ecol.* 91:fiu034. doi: 10.1093/femsec/fiu034

Falconer, R. E., Battaia, G., Schmidt, S., Baveye, P., Chenu, C., and Otten, W. (2015). Microscale heterogeneity explains experimental variability and non-linearity in soil organic matter mineralisation. *PLoS ONE*, 10:e0123774. doi: 10.1371/journal.pone.0123774

Faoro, H., Rene Menegazzo, R., Battistoni, F., Gyaneshwar, P., do Amaral, F. P., Taulé, C., et al. (2017). The oil-contaminated soil diazotroph Azoarcus olearius DQS-4T is genetically and phenotypically similar to the model grass endophyte Azoarcus sp. BH72. *Envir. Microbiol. Rep.* 9, 223–238. doi: 10.1111/1758-2229.12502

Foster, R. C., and Bowen, G. (1982). "Plant surfaces and bacterial growth: the rhizosphere and rhizoplane prokaryotic pathogens and symbionts," in *Phytopathogenic Prokaryotes*, Vol. 1, eds. M. S. Mount and G. H. Lacy (New York, NY: Academic Press), 159–189.

Franklin, R. B., and Mills, A. L. (2008). "The importance of microbial distribution in space and spatial scale to microbial ecology," in *The Spatial Distribution of Microbes in the Environment*, eds R. B. Franklin and A. L. Mills (New York, NY: Kluwer Academic Publishers), 1–30.

Gantner, S., Schmid, M., Dürr, C., Schuhegger, R., Steidle, A., Hutzler, P., et al. (2006). In situ quantitation of the spatial scale of calling distances and population density-independent N-acylhomoserine lactone-mediated communication by rhizobacteria colonized on plant roots. *FEMS Microbiol. Ecol.* 56, 188–194. doi: 10.1111/j.1574-6941.2005.00037.x

Hacquard, S., Spaepen, S., Garrido-Oter, R., and Schulze-Lefert, P. (2017). Interplay Between Innate Immunity and the Plant Microbiota. *Annu. Rev. Phytopathol.* 55, 565–589. doi: 10.1146/annurev-phyto-080516-035623

Hartmann, A., James, E. K., deBruijn, F. J., Schwab, S., Rothballer, M., and Schmid, M. (2015). "*In situ* localization and strain-specific quantification of azospirillum and other diazotrophic plant growth-promoting rhizobacteria using antibodies and molecular probes," in *Handbook for Azospirillum: Technical Issues and Protocols*, eds F. Cassan, Y. Okon, and C. Creus (Heidelberg: Springer), 45–64.

Hornik, K., and Grün, B. (2014). movMF: an R package for fitting mixtures of von Mises-Fisher distributions. *J. Stat. Soft.* 58, 1–31. doi: 10.18637/jss.v058.i10

Ilian, J., Penttinen, A., Stoyan, H., and Stoyan, D. (2008). *Statistical Analysis and Modelling of Spatial Point Patterns*. Chichester: Wiley.

James, E. K., Reis, V. M., Olivares, F. L., Baldani, J. I., and Döbereiner, J. (1994). Infection of sugar cane by the nitrogen-fixing bacterium Acetobacter diazotrophicus. *J. Exper. Bot.* 45, 757–766. doi: 10.1093/jxb/45.6.757

Lebeis, S. L., Paredes, S. H., Lundberg, D. S., Breakfield, N., Gehring, J., McDonald, M., et al. (2015). Salicylic acid modulates colonization of the root microbiome by specific bacterial taxa. *Science* 349, 860–864. doi: 10.1126/science.aaa8764

Mirza, B. S., and Rodrigues, J. L. (2012). Development of a direct isolation procedure for free-living diazotrophs under controlled hypoxic conditions. *Appl. Env. Microbiol.* 78, 5542–5549. doi: 10.1128/AEM.00714-12

Ofek, M., Hadar, Y., and Minz, D. (2012). Ecology of root colonizing Massilia (Oxalobacteraceae). *PLoS ONE* 7:e40117. doi: 10.1371/journal.pone.0040117

Oldroyd, G. E. (2013). Speak, friend, and enter: signalling systems that promote beneficial symbiotic associations in plants. *Nat. Rev. Microbiol.* 11, 252–256. doi: 10.1038/nrmicro2990

Otsu, N. (1979). A Threshold selection method from gray-level histograms. *IEEE Trans. Syst. Man. Cybern.* 9, 62–66. doi: 10.1109/TSMC.1979.4310076

Peredo, E. L., and Simmons, S. L. (2018). Leaf-FISH: Microscale Imaging of Bacterial Taxa on Phyllosphere. *Front. Microbiol.* 9:2669. doi: 10.3389/fmicb.2017.02669

Pernthaler, A., Pernthaler, J., and Amann, R. (2002). Fluorescence in situ hybridization and catalyzed reporter deposition for the identification of marine bacteria. *Appl. Environ. Microbiol.* 68, 3094–3101. doi: 10.1128/AEM.68.6.3094-3101.2002

Pett-Ridge, J., and Firestone, M. K. (2017). Using stable isotopes to explore root-microbe-mineral interactions in soil. *Rhizosphere* 3, 244–253. doi: 10.1016/j.rhisph.2017.04.016

Philippot, L., Raaijmakers, J. M., Lemanceau, P., and van der Putten, W. H. (2013). Going back to the roots: the microbial ecology of the rhizosphere. *Nat. Rev. Microbiol.* 11, 789–799. doi: 10.1038/nrmicro3109

Raynaud, X., and Nunan, N. (2014). Spatial ecology of bacteria at the microscale in soil. *PLoS ONE* 28:e87217. doi: 10.1371/journal.pone.0087217

R Development Core Team (2017). *R: A Language and Environment for Statistical Computing*. Vienna: R Development Core Team.

Reinhold-Hurek, B., Bünger, W., Burbano, C. S., Sabale, M., and Hurek, T. (2015). Roots shaping their microbiome: global hotspots for microbial activity. *Annu. Rev. Phytopathol.* 53, 403–424. doi: 10.1146/annurev-phyto-082712-102342

Remus-Emsermann, M. N. P., Lücker, S., Müller, D. B., Potthoff, E., Daims, H., and Vorholt, J. A. (2014). Spatial distribution analyses of natural phyllosphere-colonizing bacteria on *Arabidopsis thaliana* revealed by fluorescence in situ hybridization. *Environ. Microbiol.* 16, 2329–2340. doi: 10.1111/1462-2920.12482

Richter-Heitmann, T., Eickhorst, T., Knauth, S., Friedrich, M. W., and Schmidt, H. (2016). Evaluation of strategies to separate root-associated microbial communities: a crucial choice in rhizobiome research. *Front Microbiol.* 7:773. doi: 10.3389/fmicb.2016.00773

Sanderson, M. J., Smith, I., Parker, I., and Bootman, M. D. (2014). Fluorescence microscopy. *Cold Spring Harb. Protoc.* 2014, 1042–1065. doi: 10.1101/pdb.top071795

Schindelin, J., Arganda-Carreras, I., Frise, E., Kaynig, V., Longair, M., Pietzsch, T., et al. (2012). Fiji: an open-source platform for biological-image analysis. *Nat. Methods* 9, 676–682. doi: 10.1038/nmeth.2019

Schmidt, H., and Eickhorst, T. (2014). Detection and quantification of native microbial populations on soil-grown rice roots by catalyzed reporter deposition-fluorescence in situ hybridization. *FEMS Microbiol. Ecol.* 87, 390–402. doi: 10.1111/1574-6941.12232

Steger, C. (1996). An unbiased detector of curvilinear structures. *IEEE Trans Pattern Anal. Mach. Intell.* 20, 113–125. doi: 10.1109/34.659930

Verginer, M., Siegmund, B., Cardinale, M., Müller, H., Choi, Y., Míguez, C. B., et al (2010). Monitoring the plant epiphyte Methylobacterium extorquens DSM 21961 by real-time PCR and its influence on the strawberry flavor. *FEMS Microbiol. Ecol.* 74, 136–145. doi: 10.1111/j.1574-6941.2010.00942.x

Wachinger, G., Fiedler, S., Zepp, K., Gattinger, A., Sommer, M., and Roth, K. (2000). Variability of soil methane production on the micro-scale: spatial association with hot spots of organic material and Archaeal populations. *Soil Biol. Biochem.* 32, 1121–1130. doi: 10.1016/S0038-0717(00)00024-9

Wagner, T., Hiner, M., and Raynaud, X. (2017). *Thorstenwagner/ij-ridgedetection: Ridge Detection (Version v1.4.0)*. Zenodo. doi: 10.5281/zenodo.845874

Watt, M., Hugenholtz, P., White, R., and Vinall, K. (2006). Numbers and locations of native bacteria on field-grown wheat roots quantified by fluorescence in situ hybridization (FISH). *Environ. Microbiol.* 8, 871–884. doi: 10.1111/j.1462-2920.2005.00973.x

West, S. A., Diggle, S. P., Buckling, A., Gardner, A., and Griffin, A. S. (2007). The Social Lives of Microbes. *Ann. Rev. Ecol. Evol. Syst.* 38, 53–77. doi: 10.1146/annurev.ecolsys.38.091206.095740

Yoshida, S., Forno, D. A., Cook, J. H., and Gomez, K. A. (1976). *Laboratory Manual for Physiological Studies of Rice*. Manila: International Rice Research Institute.

frontiers
in Microbiology

High Resolution Assessment of Spatio-Temporal Changes in O$_2$ Concentration in Root-Pathogen Interaction

Mirco Rodeghiero [1]*, Simonetta Rubol [2]*, Alberto Bellin [3,4], Elena Turco [1], Giulia Molinatto [5], Damiano Gianelle [1] and Ilaria Pertot [1,4]

[1] Sustainable Agro-Ecosystems and Bioresources Department, Research and Innovation Centre, Fondazione Edmund Mach, San Michele all'Adige, Italy, [2] Energy Resources Engineering, Stanford University, Stanford, CA, United States, [3] Department of Civil, Environmental and Mechanical Engineering, University of Trento, Trento, Italy, [4] Agriculture, Food and Environment Centre (C3A), University of Trento, San Michele all'Adige, Italy, [5] Department of Agricultural, Forest and Food Sciences, University of Turin, Turin, Italy

Fusarium wilt, caused by the fungus *Fusarium oxysporum* f. sp. *lycopersici (Fol)*, is one of the most destructive soil-borne diseases of tomatoes. Infection takes place on the roots and the process starts with contact between the fungus and the roots hairs. To date, no detailed studies are available on metabolic activity in the early stages of the *Fol* and tomato root interaction. Spatial and temporal patterns of oxygen consumption could provide new insights into the dynamics of early colonization. Here, we combined planar optodes and spatial analysis to assess how tomato roots influence the metabolic activity and growth patterns of *Fol*. The results shows that the fungal metabolism, measured as oxygen consumption, increases within a few hours after the inoculation. Statistical analysis revealed that the fungus tends to growth toward the root, whereas, when the root is not present, the single elements of the fungus move with a Brownian motion (random). The combination of planar optodes and spatial analysis is a powerful new tool for assessing temporal and spatial dynamics in the early stages of root-pathogen interaction.

Keywords: fusarium, tomato, soil-borne pathogen, root respiration, planar optodes, spatial moments

INTRODUCTION

Fusarium wilt, caused by the soil-borne fungus *Fusarium oxysporum* f.sp. *lycopersici* (Sacc.) W.C. Snyder & H.N. Hans (*Fol*), is one of the most devastating diseases of the tomato. It is indeed responsible for severe losses in the greenhouse, open field crops and hydroponic cultures. *Fusarium oxysporum* f.sp. *lycopersici* infects tomato roots, starting from a contact with the root hairs and ending with the colonization and necrosis of the root tissue and wilting of the plant (Lagopodi et al., 2002; Mandal et al., 2009). Root colonization by *Fol* is, therefore, a crucial aspect in a successful pathogenesis (Lagopodi et al., 2002). Because of its economic importance, *Fol* has received considerable attention from researchers, especially in terms of root colonization patterns by pathogenic and non-pathogenic strains (Bao and Lazarovits, 2001; Lagopodi et al., 2002; Olivain et al., 2006), with and without the presence of microbial biocontrol agents (Bolwerk et al., 2003, 2005).

Fungal growth has traditionally been studied under the microscope, e.g., by measuring spore germ tube elongation during spore germination, by monitoring radial growth on jellified growth media in Petri dishes or by determining variations in fungal biomass (Cole, 1994; Dhingra and Sinclair, 1995). Moreover, colorimetric and spectrometric methods and microtitre plate assays have also been utilized (Hadacek and Greger, 2000). Oxygen consumption in three fungal species was recently studied with an indirect fluorimetric method, that was found to be highly sensitive and reliable in quantifying fungal activity (Nell et al., 2006). However, these studies did not visualize and quantify the early-stage interaction between the *Fol* mycelium and the tomato roots, especially in terms of spatial and temporal oxygen consumption patterns (i.e., oxidative metabolic activity, Novodvorska et al., 2016; Veillet et al., 2017).

Many biogeochemical processes occur in the roots. As an example, the roots influence the surrounding soil environment by releasing a blend of exudate compounds, which act as signals in plant-pathogen interaction (both for defense and/or pathogen stimulation) and can stimulate, for example, the germination of *Fol* microconidia (Bais et al., 2006; Steinkellner et al., 2009; Baetz and Martinoia, 2014). Besides consuming O_2 for respiratory activities, root O_2 emissions have been observed in plants inhabiting freshwater biomes, such as wetlands or flood-prone environments (McNamara and Mitchell, 1990; Colmer, 2003; Xu et al., 2013; Rudolph-Mohr et al., 2017).

Traditionally, root metabolic activity has been quantified by changes in oxygen concentration using microsensors, which provide local pointwise information, but are invasive. Thus this approach does not make it possible to study biological samples over a large area, or during prolonged periods of time (Tschiersch et al., 2011). Recent advances in imaging methodologies including cameras, scanners, fluorescence, and radiation-based techniques have enabled non-destructive exploration of root growth, including root interaction with soil-borne pathogens (Downie et al., 2015). Fluorescence-based optical sensors, such as non-invasive planar optodes, allow real time measurements of physiological processes offering manifold advantages over other methods including: spatial coverage (from mm^2 to cm^2), micrometric level of resolution and an extended period of measurement (from a few seconds to several days) (Tschiersch et al., 2012). Optodes have been successfully employed to quantify biological O_2 exchange in seagrasses and other aquatic plants (Jovanovic et al., 2015; Larsen et al., 2015; Han et al., 2016), in the roots of terrestrial living plants (Blossfeld et al., 2011; Tschiersch et al., 2011; Rudolph et al., 2012; Rudolph-Mohr et al., 2015), in photosynthetically active leaves (Tschiersch et al., 2011; Ulqodry et al., 2016) and in the sapwood of woody trees (Gansert et al., 2001), as well as to assess oxidative metabolism in soils (Rubol et al., 2016) and biofilm (Rubol et al., 2018). Despite these research efforts, no planar optode studies have assessed soil-borne microorganism activity, either considering the pathogen alone or the pathogen interacting with plant roots. To fill this gap in research and explore the early stages of root-fungus interaction, we combined the use of non-invasive planar optode technology and geostatistical spatial analysis. We investigated how the temporal and spatial dynamics of *Fol* growth (assumed to

be proportional to O_2 consumption) are altered by the presence of tomato roots, and, *vice-versa*, how root physiology is affected by fungus colonization. The interaction was further examined using spatial analysis, to describe the dynamics of the fungus colony during root colonization and to quantify the nature of this interaction.

MATERIALS AND METHODS

Experimental Setup

Seeds of *Lycopersicum esculentum* Mill. var. Marmande were surface disinfected in a 70% ethanol (30 s) and 1% sodium hydrochloride solution (1 min) (both from Sigma Aldrich, USA), carefully rinsed twice in sterile distilled water, and placed in a Petri dish (Ø = 90 mm) on 1/2-strength Murashige and Skoog medium (Murashige and Skoog, 1962). The seeds were then kept in a climate chamber at 23°C, with a day:night cycle of 14:10 h until the plant was at least 90 mm long (25 mm shoot and 65 mm root; reached in approximately 3–5 days).

The fungal material (*Fol* strain FGSC 9935) was acquired from Fungal Genetics Stock Center (US) and stored long-term at −80°C in glycerol (Sigma Aldrich). A conidial suspension obtained from the stock solution was transferred onto 1/4-strength potato dextrose agar (PDA; Oxoid, Italy), incubated for seven days at 25°C and the resulting colonies were used in the experiments. A square Petri dish (10 × 10 × 2 cm; L × W × H) was prepared the day before each measurement session, according to the following procedure. A 2 × 2 cm O_2 sensor foil (SF-RPSu4 Oxygen sensor foil for imaging; Presens, 2013b) was glued to the inside of the Petri dish in the position where the root was supposed to grow and elongate during the experiment. The sensor foil was calibrated according to the Presens instruction manual (Presens, 2013a,b): a droplet of oxygen-free water obtained from a water solution of sodium sulfite (Na_2SO_3; Sigma Aldrich) and cobalt nitrate [$Co(NO_3)_2$; Sigma Aldrich] in nitric acid (HNO_3; Sigma Aldrich) was used as the 0 point, whereas air saturated O_2 (ambient air) was the reference for 100% O_2. Then, a 0.3% agar (Sigma-Aldrich) solution, cooled to 55°C in order to avoid damages to the optode, was poured on the dish until it reached a thickness of 5 mm. Before pouring the medium into the Petri dish, the surface of the sensor foil was gently disinfected with 70% ethanol. Once the agar solution had cooled down to room temperature, a single tomato plant was carefully positioned inside the Petri dish, under the agar layer, so that the root adhered to the sensor foil whilst the stem and leaves were left to protrude outside, through a small hole made in the plastic (**Figure 1**). Similarly, at the same time, a 6 mm plug of fungal mycelium was placed under the agar layer in the upper right corner of the sensor foil (opposite to the aerial part of the plant). This root-fungus interaction experiment was repeated twice (on March 14 and May 21, 2014). Two controls were also performed: on the plant root without the fungus (on April 4, 2014) and on the fungus alone (on April 7, 2014), utilizing a 6 mm mycelium plug positioned in the center of the optode.

The Petri dish was sealed with Parafilm (Sigma Aldrich) along the perimeter and enclosed in a black cardboard to avoid light interference during measurement and at the same time, to protect
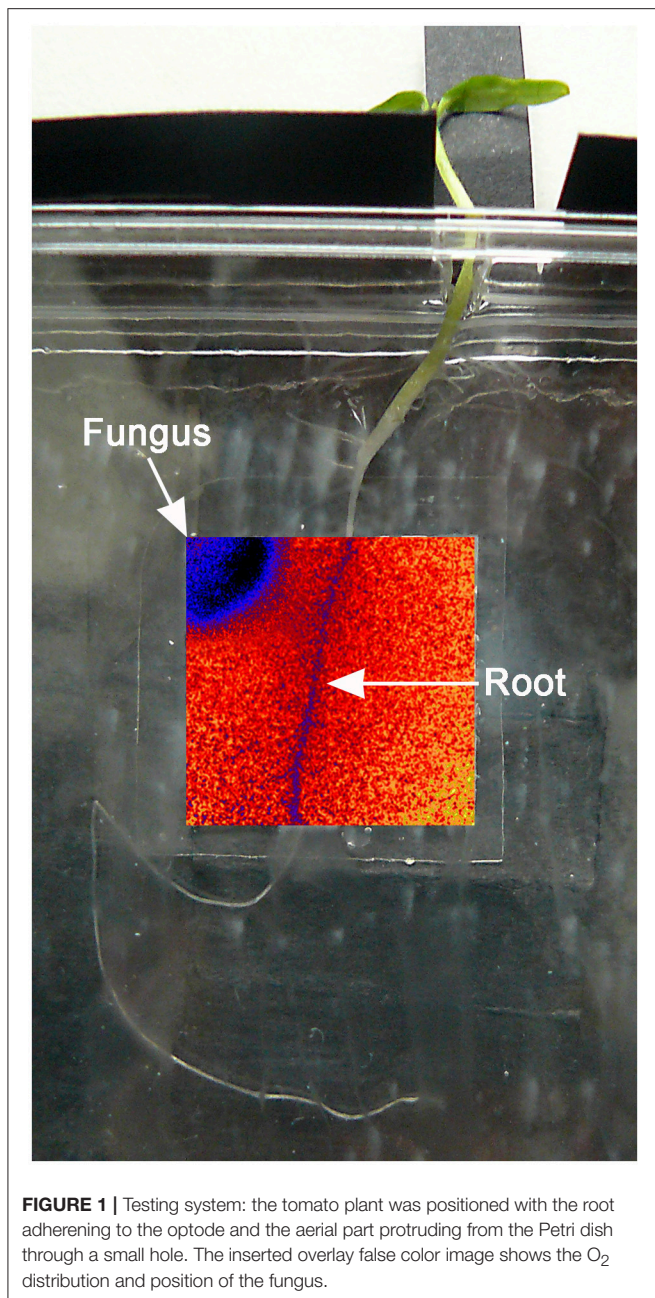
FIGURE 1 | Testing system: the tomato plant was positioned with the root adherening to the optode and the aerial part protruding from the Petri dish through a small hole. The inserted overlay false color image shows the O_2 distribution and position of the fungus.

the sensor foil from light. The shoot of the plant remained outside the black box to allow normal photosynthesis. A removable window the same size of the sensor foil was cut into the bottom side of the black box and covered with a removable cardboard flap, in order to allow the Vivisens detector unit to face the sensor foil. All the above mentioned operations were carried out in the dark and under sterile laminar flow to prevent any alteration of the sensor foil and/or biological contamination of the substrate.

Image Acquisition

The Vivisens detector unit (DU01 detector unit for spectral 2D read-out of fluorescent oxygen sensor foils; Presens, 2013b) was

mounted on a microscope stand modified for the purpose: with this device the distance between the sample and the detector unit lenses was easily adjustable by turning a knob. A foam gasket was positioned between the detector unit and the Petri dish, in order to shield the system from interfering light sources (sunlight and or lab lamps). The distance between the microscope and the sample was set at about 5 cm, which was shown to be optimal in preliminary tests, to acquire images of the entire sensor foil. The detector unit was connected to a laptop, where VA1.12 VisiSens Analytical 1 software (Presens, 2013c) was programmed to measure and record images at 5 min intervals (See also **Supplementary Video 1**). During the experiment the air temperature in the laboratory was continuously recorded at 5 min intervals in close proximity to the Petri dish, with a temperature probe (thermocouple) connected to a CR23X data-logger (Campbell Scientific, USA).

Images Post-processing

Oxygen measurements were expressed as the percentage of O_2 saturation in freshwater at atmospheric equilibrium (% air saturation). Oxygen images were first analyzed with image processing software (VisiSens Analytical 1 VA1.12-RC05; Presens, 2013c), which calculates the ratio of red to green in the emitted fluorescence response (the so-called R-value) provided by the color channels of the CMOS (complementary metal-oxide-semiconductor) chip (Presens, 2013c). The RGB images were calibrated by using the reference images obtained as described above and transformed into a 8-bit gray scale (256 levels of luminance). In the resulting figures white and black correspond to 0 and 100% O_2 saturation, respectively. Subsequently, the images were cropped to remove the crown external to the sensor foil and transformed into a matrix of $O_2\%$ air saturation using the Matlab function *imread* (MathWorks, 2012).

Determination of O_2 Consumption Rates

The O_2 consumption rates were calculated based on the decline of $O_2\%$ air saturation over time (i.e., the slope of the interpolating regression line) as reported by Tschiersch et al. (2011). We selected only specific time intervals where the regression line between $O_2\%$ air saturation and time was highly significant ($p < 0.01$; $R^2 > 0.90$). The slope (σ) was then used to calculate the O_2 content in air-saturated water at temperature (θ) and pressure (p_{atm}) according to the following equation (Presens, 2009):

$$c_S\left(p_{atm}, \theta\right) = \frac{p_{atm} - p_w(\theta)}{p_N} \sigma\, 0.2095\alpha(\theta)\frac{M_{O2}}{V_M} \qquad (1)$$

where: c_S is the water O_2 content in mg l^{-1}; p_w is the water vapor pressure at the temperature θ; p_N is the standard pressure (1013.26 mbar); σ is the slope of the regression line; 0.2095 is the volume of O_2 content in air; α (θ) is the Bunsen absorption coefficient (Benson and Krause, 1980) i.e., the volume of gas dissolved in a unit volume of solvent at standard partial pressure of the gas (1013.26 mbar) at the temperature θ; M_{O2} is the molecular mass of O_2 and V_M is the molar volume of O_2. The atmospheric pressure values (p_{atm}) was recorded at

the nearby weather station (San Michele all'Adige; 46.183498–11.120220) with a PTB220 digital barometer (Vaisala, Finland) whereas temperature (θ) was monitored close to the Petri dish (as explained above). Knowing the time step of image acquisition (5 min) and the surface area (selected for the root and fungus), we could then transform c_S from mg O_2 l^{-1} into g O_2 m^{-2} d^{-1}. Since our agar medium was 0.3%, we performed the above calculations treating the medium as pure water: indeed, according to Van der Meeren et al. (2001), the diffusion coefficient of O_2 in a 0.7–2.0% agar solution only decreases by 1.7 and 2.8%, respectively.

Statistical Analysis

The collected images were transformed into a matrix of oxygen concentration, with each value attributed to the center of the corresponding pixel. The position of each pixel is therefore identified by two indexes (i,j), referring respectively to the row and the column of the matrix (**Figure 2**) whereas N_1 and N_2 are the number of pixels along the horizontal and vertical directions, Δ_{x1} and Δ_{x2} are the respective dimensions of the pixels. The origin of the reference system was fixed in the upper left corner of the cropped image, with the x_1 axis going from left to right and the x_2 axis from top to bottom (**Figure 3**).

Temporal Dynamics of Oxygen Concentration

To quantify the dynamics of fungus and root O_2 concentration, we selected targeted portions of the sensor foil: i.e., the area including the root and its adjacent surroundings (defined as the inner core) and the area including the fungus and its surroundings (upper corner or central part of the optode; **Figure 3**). We than assumed that the density of the fungus, was linearly proportional to the deficit in the O_2 concentration:

$$\rho_{i,j} = \Delta C_{i,j} = (100 - C_{i,j}) \tag{2}$$

where $\rho_{i,j}$ is the O_2 deficit compared to saturation and $C_{i,j}$ is the concentration of O_2 expressed as a percentage of air saturation [the two indexes identify the position within the sensor foil, with $j\Delta x_1$ and $i\Delta x_2$ being the coordinates of the pixel center (i,j), having an O_2 concentration $C_{j,i}$. We also assumed that the mass of the fungus was proportional to its O_2 consumption. Given the above assumptions, we characterized the fungus dynamics by computing the spatial moments of the oxygen deficit ρ.
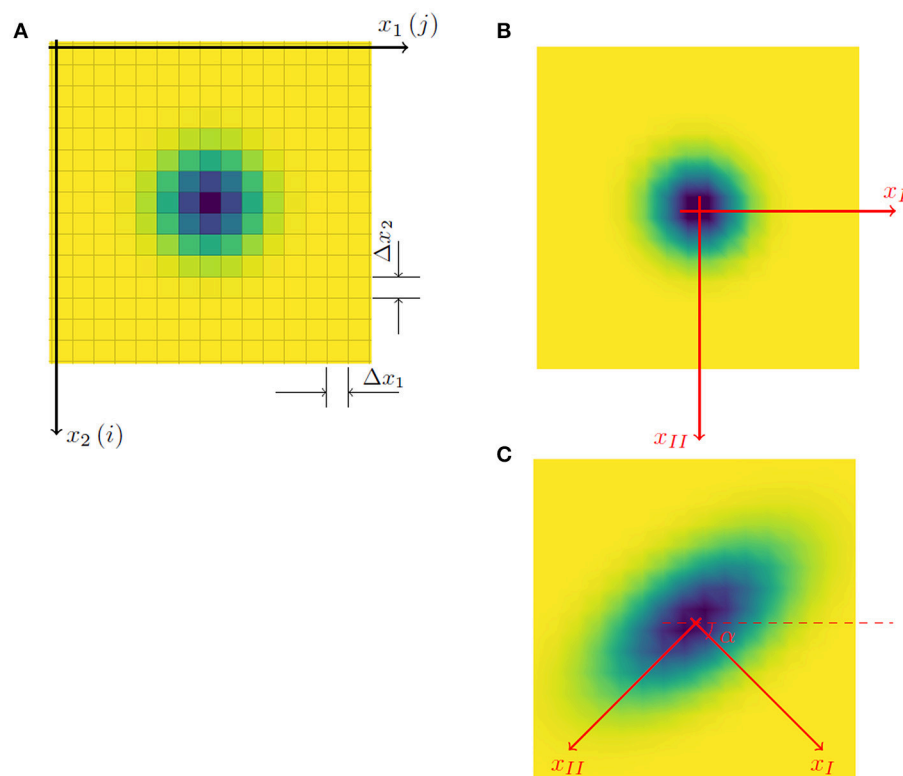
FIGURE 2 | The reference system used to calculate the temporal dynamics of O_2 concentration **(A)** was constituted by a computational grid with Δ_{x1}, Δ_{x2} mesh coinciding with the pixel dimensions in the horizontal and vertical directions respectively (the color of the pixel represents the saturation deficit). **(B)** If the spatial growth of the fungus colony is uniform, the principal directions x_I and x_{II} coincide with x_1 and x_2 respectively, and angle α is 0 compared to the reference axis x_1. **(C)** If the growth of the colony has a preferential direction (e.g., along axis x_{II}) the principal directions are rotated clockwise by an angle α ≠ 0 (e.g., α = π/4). In all cases, the tensor of second moments is diagonal when evaluated in relation to axes x_I and x_{II} instead of x_1 and x_2, (i.e., $X_{I,II} = 0$ and $X_{II,II} > X_{I,I}$).

Spatial Moments

Spatial moments were chosen because they are useful indicators for describing (i) in which direction the fungus is propagating, (ii) how the fungus grows (as expressed by second moments), and (iii) how the fungus is propagating (e.g., whether it is following a diffusive process or not). The first spatial moment illustrates the evolution in time of the center of mass of the fungus of coordinates $\bar{x}_1$ and $\bar{x}_2$, which is also described by the spatial distribution of the O$_2$ deficit:

$$\bar{x}_1 = \frac{1}{M} \sum_{i=1}^{N_2} \sum_{j=1}^{N_1} j \, \rho_{i,j} \Delta x_1 \, \Delta x_1 \, \Delta x_2 \quad (3)$$

$$\bar{x}_2 = \frac{1}{M} \sum_{i=1}^{N_2} \sum_{j=1}^{N_1} i \, \rho_{i,j} \Delta x_2 \, \Delta x_1 \, \Delta x_2 \quad (4)$$

where $M = \sum_{i=1}^{N_2} \sum_{j=1}^{N_1} \rho_{i,j} \, \Delta x_1 \, \Delta x_2$ is proportional to the total mass of the fungus. Similarly, the 2 s order moments X_{11}, X_{12}, and X_{22}, which are descriptors of colony spatial distribution (i.e., spreading around the central mass) compared to the two reference axes x_1 and x_2, are given by:

$$X_{11} = \frac{1}{M} \sum_{i=1}^{N_2} \sum_{j=1}^{N_1} \left(j \, \Delta x_1 - \bar{x}_1 \right)^2 \rho_{i,j} \quad (5)$$

$$X_{22} = \frac{1}{M} \sum_{i=1}^{N_2} \sum_{j=1}^{N_1} \left(i \, \Delta x_2 - \bar{x}_2 \right)^2 \rho_{i,j} \quad (6)$$

$$X_{12} = \frac{1}{M} \sum_{i=1}^{N_2} \sum_{j=1}^{N_1} \left(j \, \Delta x_1 - \bar{x}_1 \right) \left(i \, \Delta x_2 - \bar{x}_2 \right) \rho_{i,j} \quad (7)$$

X_{11}, X_{22}, X_{12}, represent respectively longitudinal, transversal, and cross-directional spreading around the central mass of the fungus.

RESULTS

O$_2$ Dynamics During Root-Fungus Interaction

In the first experimental run, the O$_2$% air saturation in the upper right corner of the sensor foil decreased for about 12 h, from 37.1 to 19.7% ($\Delta = 17.4$%; **Figure 4A**). This was the consequence of an initially high fungal respiration rate (e.g., O$_2$ consumption), which was quantified in 18.2 g O$_2$ m^{-2} d^{-1}, reaching a minimum and then recovering to the initial value (**Figure 4A**). The O$_2$ level in the inner root core peaked at 38.2% at 5.5 h (i.e., $t = 5.5$ h) then decreased due to a high consumption rate, quantified as 19.9 g O$_2$ m^{-2} d^{-1} (**Figure 4A**). Through visual inspection of the image sequence, we observed that the fungus colonized the root between 15 and 20 h from the beginning of the test; subsequently, changes in O$_2$% air saturation were the result of the combined oxidative metabolic activity of two overlapping organisms, quantified as 0.5–1.2 g O$_2$ m^{-2} d^{-1}. When the root-fungus interaction experiment was repeated, similar behavior was observed (**Figure 4B**): fungal respiration increased, with O$_2$ falling from 36.7% at the beginning of the experiment to 24.1% at $t = 12$ h ($\Delta = 12.6$%) and recovered afterwards. The O$_2$ concentration in the inner core (root) peaked at $t = 8.5$ h (37.9%) and then decreased (**Figure 4B**). The fungal
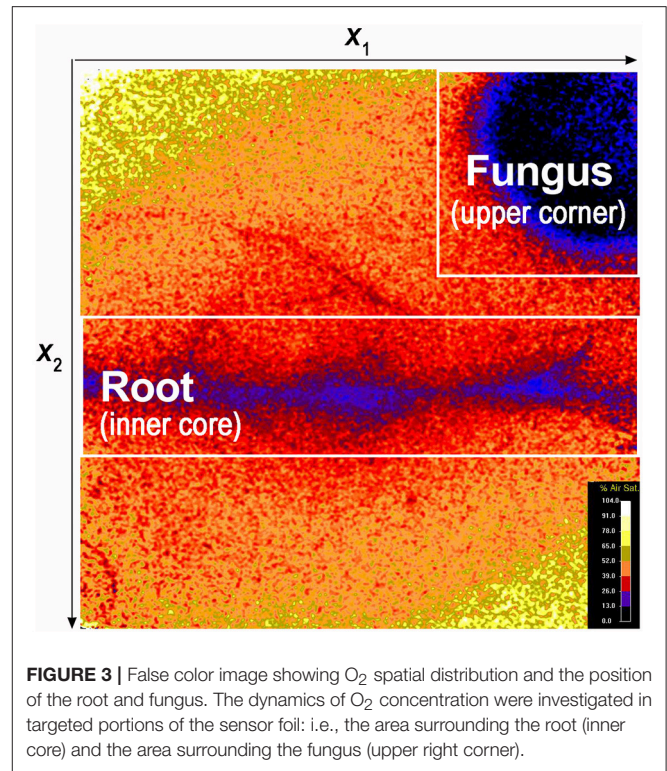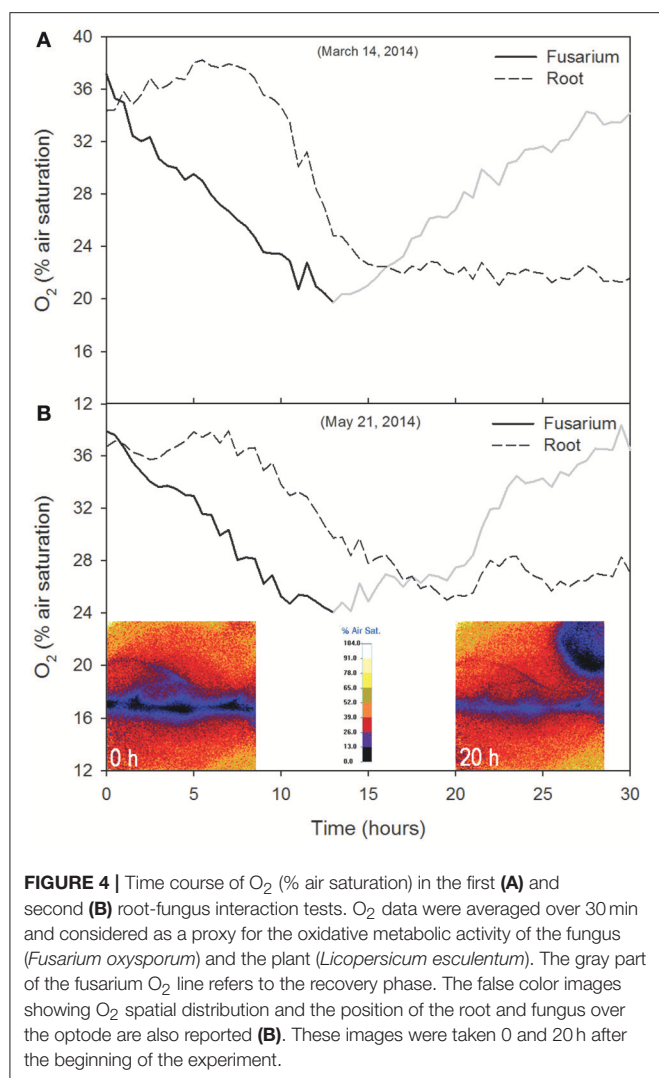

FIGURE 3 | False color image showing O$_2$ spatial distribution and the position of the root and fungus. The dynamics of O$_2$ concentration were investigated in targeted portions of the sensor foil: i.e., the area surrounding the root (inner core) and the area surrounding the fungus (upper right corner).

and root respiration rates were 18.1 and 4.5 g O$_2$ m^{-2} d^{-1}, respectively.

In the control with the plant alone, the root O$_2$% air saturation varied between 27.9 and 32.2% ($\Delta = 4.3$%; **Figure 5A**). The O$_2$ peaks were in phase with temperature peaks (temperature ranged from 20 to 25.4°C; $\Delta = 5.4$; correlation analysis: Pearson $r^2 = 0.44$, $p < 0.01$, $N = 141$; from $t = 0$ to $t = 70$ h), whereas the concentration fluctuated breafly around 13.5% O$_2$ for about 15 h (**Figure 5B**). A release phase followed, coinciding with a decrease in temperature. From $t = 16$ h to $t = 70$, the oxygen trend largely reflected the temperature trend (i.e., O$_2$ concentration decreased with increasing temperature; correlation analysis: Pearson $r^2 = -0.05$, $p < 0.01$, $N = 141$) with O$_2$% air saturation ranging from 13.0 to 21.6% ($\Delta = 8.6$%) and temperature ranging between 19.2 and 24.9°C ($\Delta = 5.7$°C). Respiration rates varied between 37.4 and 101.0 g O$_2$ m^{-2} d^{-1}.

Temporal and Spatial Activity of the Fungus

In the presence of the root, the trajectory of the fungus' center of mass rotated counter-clockwise with the maximum distance from the original position recorded 18 h after inoculation (**Figure 6A**). During this period the barycenter of the colony moved slightly away from the root (from left to right and upwards), the mass grew almost uniformly in the upper corner of the sensor foil. Initially the movement of the center of mass was very fast (after 12 h the distance traveled by the barycenter was about 0.8 mm), while it took about 60 h to return to its original position. At each time step the second moments were computed in the reference system (x_I, x_{II}) rotated by the angle α the reference

FIGURE 4 | Time course of O₂ (% air saturation) in the first **(A)** and second **(B)** root-fungus interaction tests. O₂ data were averaged over 30 min and considered as a proxy for the oxidative metabolic activity of the fungus (*Fusarium oxysporum*) and the plant (*Licopersicum esculentum*). The gray part of the fusarium O₂ line refers to the recovery phase. The false color images showing O₂ spatial distribution and the position of the root and fungus over the optode are also reported **(B)**. These images were taken 0 and 20 h after the beginning of the experiment.

system (x_1, x_2) (**Figures 2B,C**). Angle α was such as to make the tensor diagonal, with maximum second moment $X_{II,II}$, oriented in direction x_{II} and minimum second moment $X_{I,I}$ in direction x_I. These two moments were obtained by making the matrix of second order moments diagonal. The second moment $X_{II,II}$ first increased, reaching a peak 12 h after inoculation, then decreasing to a minimum at $t = 22$ h, and finally increasing again, reaching a stable value slightly lower than the initial one at $t = 40$ h. The second moment $X_{I,I}$ was specular to $X_{II,II}$ (increasing when $X_{II,II}$ reduced and reducing when it increased) and reached a stable value after 25 h, well before the other moment (see **Figure 7A**). Angle α was first reduced by counterclockwise rotation, reaching a minimum after 12 h, when $X_{II,II}$ was at its maximum, then increased with clockwise rotation to a maximum of about 15° at $t = 30$ h to finally stabilize at a value of 10° after 40 h by counterclockwise rotation.

In the control with the fungus alone, the dynamics were completely different. The center of mass was stationary (**Figure 6B**) and the second order moments grew linearly with time experiencing two sudden drops at 18 and 40 h (**Figure 7B**).

These drops, in particular the second, indicated a contraction of the fungus metabolism caused by the decrease in temperature (see the **Figure 5B**). The linear increase in second order moments suggests that the fungus moved randomly with Brownian type movement leading to Fickian diffusion.

DISCUSSION

The comparable results obtained in the two root-fungus interaction experiments demonstrate the consistency and related reliability of the planar optode technique in monitoring O₂ continuously, over a prolonged period of time and without perturbing the system. In both tests, an initially high level of fungal respiration (e.g., O₂ consumption), peaking after 12 h was seen. The respiration rates were almost identical in the two control tests (18.2 and 18.1 g O₂ m⁻² d⁻¹ respectively). A similar trend in *Fol* O₂ consumption was reported by Nell et al. (2006). However, direct comparison with the values recorded by Nell et al. (2006) is not possible, since their data are expressed in terms of relative fluorescence units and the rates measured in our work are the result of different factors, such as root stimulation and presumably root exudates (Bais et al., 2006). Root exudates can indeed stimulate the germination of *Fol* microconidia (Steinkellner et al., 2005, 2009). The peak in fungal respiration was followed by a phase of lower respiration caused by a decrease in fungal metabolic activity present in the reference area (upper corner) due to the fact that the fungus moved out of the investigated area and colonized the root.

Root O₂ consumption at the beginning of the first experiment (19.9 g O₂ m⁻² d⁻¹) was similar to that of the fungus alone, whereas, in the second root-fungus experiment it was lower (4.5 g O₂ m⁻² d⁻¹), probably due to lower physiological activity of the plant (Lai et al., 2016). The measured root respiration rates were of the same order of magnitude as those observed by Dong et al. (2011), in a wetland mesocosm for the aquatic plant *Acorus calamus* L. (14.4–30.3 g O₂ m⁻² d⁻¹). The small number of available studies and the lack of experimental details (e.g., area, temperature, pressure) (Hadas and Okon, 1987; Tschiersch et al., 2012; Han et al., 2016; Rudolph-Mohr et al., 2017; Lenzewski et al., 2018) does not allow additional comparison with *in vitro* respiration rates. The change in O₂% air saturation for the fungus alone ($\Delta = 8.6$) was lower than that measured in the fungus during root-fungus interaction ($12.6 < \Delta < 17.4$). This difference can be explained by the sudden peaks in air temperature recorded during the experiment with the fungus alone. The increase in temperature indeed promoted an increase in respiration rates (up to 101.0 g O₂ m⁻² d⁻¹). The variation in O₂% air saturation of the root alone was even lower ($\Delta = 4.3$) than that measured during interaction. The low rates of O₂ consumption can be related to potential root O₂ emissions. Several studies have shown aerenchyma tissue development and O₂ emissions from tomato roots and for other cultures as well, as a consequence of waterlogging (Kawase and Whitmoyer, 1980; McNamara and Mitchell, 1990; Xu et al., 2013; Vidoz et al., 2016).

Statistical analysis of the data allowed quantification of the aforementioned observations, making it possible to distinguish
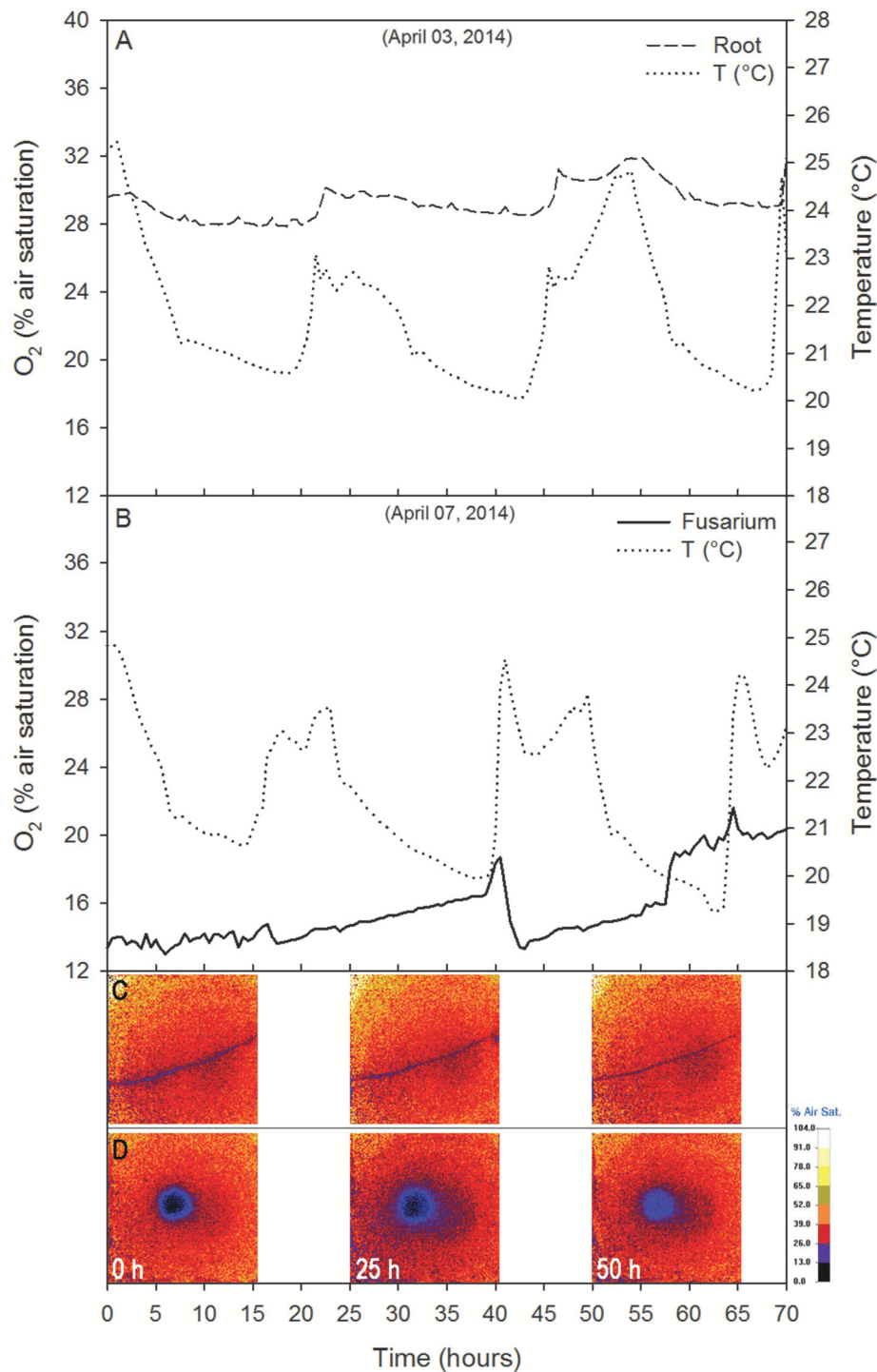
FIGURE 5 | Control tests showing the time course of O$_2$ (% air saturation) for the root alone **(A)** and the fungus alone **(B)**. The temperature recorded near the Petri dish is reported. Data are 30 min averages.

three distinct phases in particular: (i) a peak in oxygen consumption reached at 12 h occupying about 50% of the upper corner area; (ii) occupation of the whole area between 22 h (minimum of $X_{II,II}$) and 25 h (maximum of $X_{I,I}$); (iii) root

colonization (**Figure 7A**). We cannot define the precise moment of contact between the fungus and root, because this would have required microscope investigation at a higher magnification, however we can say that this happened between 12 and 22 h

FIGURE 6 | Time evolution of the barycenter (center of mass) of the fungus' O₂ deficit relative to its initial position, in the presence of the root [**(A)**; March 14, 2014] and without the root **(B)**. The deficit is considered to be proportional to the mass of the fungus and provides information on fungal growth.

FIGURE 7 | Principal second moments of the fungus body in the experiment with the root [**(A)**; March 14, 2014] and with the fungus alone **(B)**. The maximum principal second moment ($X_{II,II}$) was computed with reference to axis x_{II}, forming the α angle with the direction x_1 of the reference system. The minimum principal moment ($X_{I,I}$) was computed with reference to axis x_I orthogonal to x_{II}, forming with it a local rotating orthogonal reference system. The tensor of moments of inertia is diagonal in relation to this reference system. These moments provide an indication of the dispersion around the centroid. The color figures in A are snapshots of the O₂ deficit in the upper corner where the fungus was inoculated. Spatial density was assumed to be proportional to the oxygen deficit in comparison with saturation. The color of the pixels goes from yellow to blue representing low and high oxygen deficit (and fungus density) respectively. The secondary y axis indicates rotation angle α, expressed in degrees, of the principal axes compared to the x_1 direction.

(i.e., the fungus started to move after reaching peak activity). This behavior of *Fol* in colonizing tomato roots is in line with that observed by Lagopodi et al. (2002), although they used a destructive method, using a new biological sample for each subsequent observation and not showing the dynamics of metabolic activity for the two organisms. These complex dynamics ended at about 40 h, when both moments stabilized. From this time on the colony reduced its density uniformly in space. This behavior demonstrates that growth is stimulated by perception of the root and presumably by the diffusion of root exudates through the medium (Bécard and Piché, 1989).

In the experiment with the fungus alone, the barycenter of the object did not move, while second order moments along the principal directions grew linearly with time (**Figures 6B**, **7B** respectively), apart from two sudden drops at 18 and 40 h due to abrupt changes in temperature (data not shown). Angle α oscillated between $-40°$ and $+40°$. The linear, in time, growth of the second moments is indicative of a Brownian motion which is characterized by random movement of a population of particles (Einstein, 1956). This behavior was expected, since fungus has been shown to grow radially on jellified nutritional medium (Trinci, 1969).
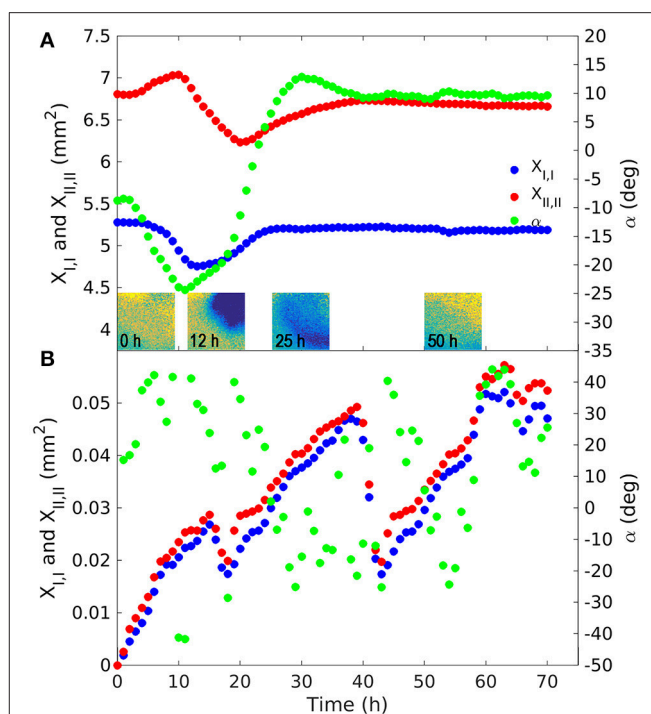
CONCLUSIONS

Overall, the planar optode technique proved to be a useful tool for investigating the O₂ dynamics of root-fungus interaction, due to the flexibility of the system, which technically allows testing of the effect of virtually infinite perturbing factors in interaction and the possibility of studying other plant and fungal species. However, one limitation of the approach presented is the need to work in dark conditions to protect the sensor foil from light interference. This aspect, together with the need for a layer of water between the sample and the optode, make the approach unsuitable for open field studies at the moment. For the first time our work visualizes and quantifies the dynamics of O₂ consumption and related metabolic activity characterizing root-fungus interaction, with the considerable advantage, as compared to standard methods, of not being destructive. Geostatistical analysis made it possible to describe and quantify the spatial motion of the fungus, which was stimulated by the presence of the root and oriented its growth.

This situation was completely different in the experiment with the fungus alone, which was characterized by random Brownian motion.

We conclude that combining optodes and geostatistical analysis is a powerful tool for understanding the temporal and fine scale root-fungus interaction, especially to complement functional studies carried out with other approaches. Translation to real soils needs caution, given the significant effect of heterogeneity in soil and nutrient distribution, which affects the magnitude and direction of fungal growth.

AUTHOR CONTRIBUTIONS

MR, SR, DG, and ET planned and designed the research. MR and ET performed experiments and conducted fieldwork. MR, SR, AB, and IP analyzed and interpreted the data. MR, SR, AB, ET, IP wrote the paper. MR, SR, AB, ET, GM, and IP revised the paper.

ACKNOWLEDGMENTS

SUPPLEMENTARY MATERIAL

The Supplementary Material for this article can be found online at: https://www.frontiersin.org/articles/10.3389/fmicb.2018.01491/full#supplementary-material

Supplementary Video 1 | False color image video showing the O2 spatial distribution during the interaction between 652 the root and the fungus from time $t = 0$ to $t = 40$ h. The O2 % air saturation decreases going 653 from light color (90–100% O2) to dark (0–13% O2).

REFERENCES

Baetz, U., and Martinoia, E. (2014). Root exudates: the hidden part of plant defense. *Trends Plant Sci.* 19, 90–98. doi: 10.1016/j.tplants.2013.11.006

Bais, H. P., Weir, T. L., Perry, L. G., Gilroy, S., and Vivanco, J. M. (2006). The role of root exudates in rhizosphere interactions wiith plants and other organisms. *Annu. Rev. Plant Biol.* 57, 233–266. doi: 10.1146/annurev.arplant.57.032905.105159

Bao, J. R., and Lazarovits, G. (2001). Differential colonization of tomato roots by nonpathogenic and pathogenic *Fusarium oxysporum* strains may influence fusarium wilt control. *Phytopathology* 91, 449–456. doi: 10.1094/PHYTO.2001.91.5.449

Bécard, G., and Piché, Y. (1989). Fungal growth stimulation by Co$_2$ and root exudates in vesicular-arbuscular mycorrhizal symbiosis. *Appl. Environ. Microbiol.* 55, 2320–2325.

Benson, B. B., and Krause, D. (1980). The concentration and isotopic fractionation of gases dissolved in freshwater in equilibrium with the atmosphere. 1. Oxygen. *Limnol. Oceanogr.* 25, 662–671. doi: 10.4319/lo.1980.25.4.0662

Blossfeld, S., Gansert, D., Thiele, B., Kuhn, A. J., and Lösch, R. (2011). The dynamics of oxygen concentration, pH value, and organic acids in the rhizosphere of *Juncus* spp. *Soil Biol. Biochem.* 43, 1186–1197. doi: 10.1016/j.soilbio.2011.02.007

Bolwerk, A., Lagopodi, A. L., Lugtenberg, B. J. J., and Bloemberg, G. V. (2005). Visualization of interactions between a pathogenic and a beneficial fusarium strain during biocontrol of tomato foot and root rot. *Mol. Plant Microbe Interact.* 18, 710–721. doi: 10.1094/MPMI-18-0710

Bolwerk, A., Lagopodi, A. L., Wijfjes, A. H., Lamers, G. E. M., Chin-A-Woeng, T. F. C., Lugtenberg, B. J., et al. (2003). Interactions in the tomato rhizosphere of two pseudomonas biocontrol strains with the phytopathogenic fungus *Fusarium oxysporum* f. sp. radicis-lycopersici. *Mol. Plant Microbe Interact.* 16, 983–993. doi: 10.1094/MPMI.2003.16.11.983.

Cole, M. D. (1994). Key antifungal, antibacterial and anti-insect assays—a critical review. *Biochem. Syst. Ecol.* 22, 837–856. doi: 10.1016/0305-1978(94)90089-2

Colmer, T. D. (2003). Long-distance transport of gases in plants: a perspective on internal aeration and radial oxygen loss from roots. *Plant Cell Environ.* 26, 17–36. doi: 10.1046/j.1365-3040.2003.00846.x

Dhingra, O. D., and Sinclair, J. B. (1995). *Basic Plant Pathology Methods, 2nd Edn.* Boca Raton, FL: CRC Press.

Dong, C., Zhu, W., Zhao, Y. Q., and Gao, M. (2011). Diurnal fluctuations in root oxygen release rate and dissolved oxygen budget in wetland mesocosm. *Desalination* 272, 254–258. doi: 10.1016/j.desal.2011.01.030

Downie, H. F., Adu, M. O., Schmidt, S., Otten, W., Dupuy, L. X., White, P. J., et al. (2015). Challenges and opportunities for quantifying roots and rhizosphere interactions through imaging and image analysis. *Plant. Cell Environ.* 38, 1213–1232. doi: 10.1111/pce.12448

Einstein, A. (1956). *Investigations on the Theory of the Brownian Movement.* New York, NY: Dover.

Gansert, D., Burgdorf, M., and Lösch, R. (2001). A novel approach to the in situ measurement of oxygen concentrations in the sapwood of woody plants. *Plant. Cell Environ.* 24, 1055–1064. doi: 10.1046/j.1365-3040.2001.00751.x

Hadacek, F., and Greger, H. (2000). Testing of antifungal natural products: methodologies, comparability of results and assay choice. *Phytochem. Anal.* 11, 137–147. doi: 10.1002/(SICI)1099-1565(200005/06)11:3<137::AID-PCA514>3.0.CO;2-I

Hadas, R., and Okon, Y. (1987). Effect of Azospirillum brasilense inoculation on root morphology and respiration in tomato seedlings. *Biol. Fertil. Soils* 5, 241–247. doi: 10.1007/BF00256908

Han, C., Ren, J., Tang, H., Xu, D., and Xie, X. (2016). Quantitative imaging of radial oxygen loss from Valisneria spiralis roots with a fluorescent planar optode. *Sci. Total Environ.* 569–570, 1232–1240. doi: 10.1016/j.scitotenv.2016.06.198

Jovanovic, Z., Pedersen, M., Larsen, M., Kristensen, E., and Glud, R. (2015). Rhizosphere O$_2$ dynamics in young *Zostera marina* and *Ruppia maritima*. *Mar. Ecol. Prog. Ser.* 518, 95–105. doi: 10.3354/meps11041

Kawase, M., and Whitmoyer, R. E. (1980). Aerenchyma development in waterlogged plants. *Am. J. Bot.* 67, 18–22.

Lagopodi, A. L., Ram, A. F., Lamers, G. E., Punt, P. J., Van den Hondel, C. A., Lugtenberg, B. J., et al. (2002). Novel aspects of tomato root colonization and infection by *Fusarium oxysporum* f. sp. radicis-lycopersici revealed by confocal laser scanning microscopic analysis using the green fluorescent protein as a marker. *Mol. Plant Microbe Interact.* 15, 172–179. doi: 10.1094/MPMI.2002.15.2.172

Lai, Z., Lu, S., Zhang, Y., Wu, B., Qin, S., Feng, W., et al. (2016). Diel patterns of fine root respiration in a dryland shrub, measured in situ over different phenological stages. *J. For. Res.* 21, 31–42. doi: 10.1007/s10310-015-0511-4

Larsen, M., Santner, J., Oburger, E., Wenzel, W. W., and Glud, R. N. (2015). O2 dynamics in the rhizosphere of young rice plants (*Oryza sativa* L.) as studied by planar optodes. *Plant Soil* 390, 279–292. doi: 10.1007/s11104-015-2382-z

Lenzewski, N., Mueller, P., Meier, R. J., Liebsch, G., Jensen, K., and Koop-Jakobsen, K. (2018). Dynamics of oxygen and carbon dioxide in rhizospheres of *Lobelia dortmanna* - a planar optode study of belowground gas exchange between plants and sediment. *New Phytol.* 281, 131–141. doi: 10.1111/nph.14973

Mandal, S., Mallick, N., and Mitra, A. (2009). Salicylic acid-induced resistance to *Fusarium oxysporum* f. sp. lycopersici in tomato. *Plant Physiol. Biochem.* 47, 642–649. doi: 10.1016/j.plaphy.2009.03.001

The MathWorks, Inc. (2012). *MATLAB and Statistics Toolbox Release.* Natick, MA.

McNamara, S. T., and Mitchell, C. A. (1990). Adaptive stem and adventitious root responses of two tomato genotypes to flooding. *HortScience* 25, 100–103.

Murashige, T., and Skoog, F. (1962). A revised medium for rapid growth and bio assays with tobacco tissue cultures. *Physiol. Plant.* 15, 473–497. doi: 10.1111/j.1399-3054.1962.tb08052.x

Nell, M., Mammerler, R., and Steinkellner, S. (2006). Oxygen consumption-based evaluation of fungal activity. *Mycol. Res.* 110, 760–764. doi: 10.1016/j.mycres.2006.03.012

Novodvorska, M., Stratford, M., Blythe, M. J., Wilson, R., Beniston, R. G., and Archer, D. B. (2016). Metabolic activity in dormant conidia of *Aspergillus niger* and developmental changes during conidial outgrowth. *Fungal Genet. Biol.* 94, 23–31. doi: 10.1016/j.fgb.2016.07.002

Olivain, C., Humbert, C., Nahalkova, J., Fatehi, J., L'Haridon, F., and Alabouvette, C. (2006). Colonization of tomato root by pathogenic and nonpathogenic *Fusarium oxysporum* strains inoculated together and separately into the soil. *Appl. Environ. Microbiol.* 72, 1523–1531. doi: 10.1128/AEM.72.2.1523-1531.2006

Presens (2009). *FB3 LCD Trace UM10*. Regensburg: Presens Precision Sensing GmbH.

Presens (2013a). *Detector Unit DU01/02/03 for Vivisens A1/A2/A3 (Instruction Manual)* (Regensburg), 1–18.

Presens (2013b). *Oxygen Sensor Foils for Imaging SF-RPSu4 (Instruction Manual)* (Regensburg), 1–16.

Presens (2013c). *VisiSens AnalytiCal 1: Software for the VisiSens Imaging System, Version VA1.12 (Instruction Manual)* (Regensburg), 1–49.

Rubol, S., Dutta, T., and Rocchini, D. (2016). 2D visualization captures the local heterogeneity of oxidative metabolism across soils from diverse land-use. *Sci. Total Environ.* 572, 713–723. doi: 10.1016/j.scitotenv.2016.06.252

Rubol, S., Freixa, A., Sanchez-Vila, X., and Roman,í, A. M. (2018). Linking biofilm spatial structure to real-time microscopic oxygen decay imaging. *Biofouling* 34, 200–211. doi: 10.1080/08927014.2017.1423474

Rudolph, N., Esser, H. G., Carminati, A., Moradi, A. B., Hilger, A., Kardjilov, N., et al. (2012). Dynamic oxygen mapping in the root zone by fluorescence dye imaging combined with neutron radiography. *J. Soils Sediments* 12, 63–74. doi: 10.1007/s11368-011-0407-7

Rudolph-Mohr, N., Gottfried, S., Lamshöft, M., Zühlke, S., Oswald, S. E., and Spiteller, M. (2015). Non-invasive imaging techniques to study O$_2$ micro-patterns around pesticide treated lupine roots. *Geoderma* 239–240, 257–264. doi: 10.1016/j.geoderma.2014.10.022

Rudolph-Mohr, N., Tötzke, C., Kardjilov, N., and Oswald, S. E. (2017). Mapping water, oxygen, and pH dynamics in the rhizosphere of young maize roots. *J. Plant Nutr. Soil Sci.* 180, 336–346. doi: 10.1002/jpln.201600120

Steinkellner, S., Mammerler, R., and Vierheilig, H. (2005). Microconidia germination of the tomato pathogen *Fusarium oxysporum* in the presence of root exudates. *J. Plant Interact.* 1, 23–30. doi: 10.1080/17429140500134334

Steinkellner, S., Mammerler, R., and Vierheilig, H. (2009). *Root Exudates as Important Factor in the Fusarium – Host Plant Interaction*. Mutitrophic Interaction Soil IOBC/WPRS Bulletins. 42, 165–168.

Trinci, A. P. J. (1969). A kinetic study of the growth of *Aspergillus nidulans* and other fungi. *J. Gen. Microbiol.* 57, 11–24. doi: 10.1099/00221287-57-1-11

Tschiersch, H., Liebsch, G., Borisjuk, L., Stangelmayer, A., and Rolletschek, H. (2012). An imaging method for oxygen distribution, respiration and photosynthesis at a microscopic level of resolution. *New Phytol.* 196, 926–936. doi: 10.1111/j.1469-8137.2012.04295.x

Tschiersch, H., Liebsch, G., Stangelmayer, A., Borisjuk, L., and Rolletschek, H. (2011). "Planar oxygen sensors for non invasive imaging in experimental biology," in *Microsensors* (Rijeka: InTech), 281–294.

Ulqodry, T. Z., Nose, A., and Zheng, S.-H. (2016). An improved method for the simultaneous determination of photosynthetic O$_2$ evolution and CO$_2$ consumption in *Rhizophora mucronata* leaves. *Photosynthetica* 54, 152–157. doi: 10.1007/s11099-015-0166-6

Van der Meeren, P., De Vleeschauwer, D., and Debergh, P. (2001). Determination of oxygen profiles in agar-based gelled *in vitro* plant tissue culture media. *Plant Cell Tissue Organ Cult.* 65, 239–245. doi: 10.1023/A:10106982265362

Veillet, F., Gaillard, C., Lemonnier, P., Coutos-Thévenot, P., and La Camera, S. (2017). The molecular dialogue between *Arabidopsis thaliana* and the necrotrophic fungus *Botrytis cinerea* leads to major changes in host carbon metabolism. *Sci. Rep.* 7:17121. doi: 10.1038/s41598-017-17413-y

Vidoz, M. L., Mignolli, F., Aispuru, H. T., and Mroginski, L. A. (2016). Rapid formation of adventitious roots and partial ethylene sensitivity result in faster adaptation to flooding in the aerial roots (aer) mutant of tomato. *Sci. Hortic.* 201, 130–139. doi: 10.1016/j.scienta.2016.01.032

Xu, Q. T., Yang, L., Zhou, Z. Q., Mei, F. Z., Qu, L. H., and Zhou, G. S. (2013). Process of aerenchyma formation and reactive oxygen species induced by waterlogging in wheat seminal roots. *Planta* 238, 969–982. doi: 10.1007/s00425-013-1947-4

Conflict of Interest Statement: The authors declare that the research was conducted in the absence of any commercial or financial relationships that could be construed as a potential conflict of interest.

Nitrogen Limitations on Microbial Degradation of Plant Substrates Are Controlled by Soil Structure and Moisture Content

Peter Maenhout[1]*, Jan Van den Bulcke[2], Luc Van Hoorebeke[3], Veerle Cnudde[4], Stefaan De Neve[1] and Steven Sleutel[1]

[1] Research Group of Soil Fertility and Nutrient Management, Department of Environment, Ghent University, Ghent, Belgium, [2] Laboratory of Wood Technology, Centre for X-ray Tomography of Ghent University (UGCT), Department of Environment, Ghent University, Ghent, Belgium, [3] Radiation Physics Research Group, Centre for X-ray Tomography of Ghent University (UGCT), Department of Physics and Astronomy, Ghent University, Ghent, Belgium, [4] PProGRess, Centre for X-ray Tomography of Ghent University (UGCT), Department of Geology, Ghent University, Ghent, Belgium

Mineral nitrogen (N) availability to heterotrophic micro-organisms is known to impact organic matter (OM) decomposition. Different pathways determining the N accessibility depend to a large extent on soil structure. Contact between soil mineral and OM substrate particles can facilitate N transport toward decomposition hot spots. However, the impact of soil structure on N availability to microbes and thus heterotrophic microbial activity and community structure is not yet fully understood. We hypothesized that carbon mineralization (Cmin) from low-N substrate would be stimulated by increased N availability caused by closer contact with soil particles or by a higher moisture level, enhancing potential for N-diffusion. Under opposite conditions retarded heterotrophic activity and a dominance of fungi were expected. A 128-days incubation experiment with CO_2 emission monitoring from artificially reconstructed miniature soil cores with contrasting soil structures, viz. high or low degree of contact between soil particles, was conducted to study impacts on heterotrophic activity. The soil cores were subjected to different water filled pore space percentages (25 or 50% WFPS) and amended with either easily degradable OM high in N (grass) or more resistant OM low in N (sawdust). X-ray μCT image processing allowed to quantify the pore space in 350 μm around OM substrates, i.e., the microbial habitat of involved decomposers. A lower local porosity surrounding sawdust particles in soils with stonger contact was confirmed, at least at 25% WFPS. Mineral N addition to sawdust amended soils with small particle contact at 25% WFPS resulted in a stimulated respiration. Cmin in the latter soils was lower than in case of high particle contact. This was not observed for grass substrate particles or at 50% WFPS. The interactive effect of substrate type and soil structure suggests that the latter controls Cmin through mediation of N diffusion and in turn N availability. Phospholipid fatty acid did not reveal promotion of fungal over bacterial biomarkers in treatments with N-limited substrate decomposition. Combining X-ray μCT with tailoring soil structure allows for more reliable investigation of effects on the soil microbial community, because as also found here, the established soil pore network structure can strongly deviate from the intended one.

Keywords: C mineralization, soil contact, nitrogen availability, microbial community, X-ray μCT

INTRODUCTION

Over the past decades, it has been widely recognized that microbial habitat related constraints, rather than intrinsic chemical recalcitrance of organic matter (OM) control soil C turnover (Schmidt et al., 2011). Ample studies have demonstrated the importance of the so-termed 'physical protection' inside aggregates of otherwise readily biodegradable native OM from microbial heterotrophs in soil (Schmidt et al., 2011; Dungait et al., 2012). But a concept like 'physical protection' is not very manifest and it is obvious that not the arrangement of solid particles *per se* but rather the structure of the soil pore network itself directly impacts microbial activity in soil, by creating micro-environments varying in access to OM and O_2 (Kravchenko and Guber, 2017). Soil pore neck size dictates if a pore will contain moisture at specific bulk soil moisture tension. A decreasing water content also results in a disconnection of water filled pores via water films and as a consequence limits solute diffusion. This interplay between the retention of soil moisture and pore network structure (Crawford et al., 2005) then determines the potential for flux of metabolites and enzymes between microorganisms and their substrates (Sexstone et al., 1985; Prove et al., 1990; Linquist et al., 1997; Or et al., 2007) thus controlling microbial access to OM, and impacting gross soil C mineralization (Chenu and Stotzky, 2002; Juarez et al., 2013; Negassa et al., 2015).

Substrates' location will also determine the contact area with soil particles which finally can impact substrate mineralization (Angers and Recous, 1997; Henriksen and Breland, 2002; Coppens et al., 2006; Giacomini et al., 2007; Garnier et al., 2008). Contact of soil particles and OM will impact potential for diffusion of soluble nitrogen forms (NO_3, dissolved organic N) from and toward micro-organisms (Garnier et al., 2008). Only in circumstances when insufficient N is locally present at decomposition sites, i.e., when organic substrates have a high C:N ratio, impediments on diffusion of dissolved N by limited soil-substrate contact could limit C mineralization by decomposers on the substrate's surface (Angers and Recous, 1997; Garnier et al., 2008). Impediments could logically arise from low soil moisture content, limited contact between substrates and soil or a generally low soil N content. In addition, distribution of microsites, carbon, air filled pores, and soil density can all have an impact on CO_2 produced via respiration by heterotrophic micro-organisms (Ball et al., 2008; Garnier et al., 2008).

With increasingly coarser soil texture or decreasing bulk density, particulate OM resides in an environment that is subject to more frequent drying resulting in moisture stress for the heterotrophic activity. Soils with a higher volume proportion of large pores, like with a coarser texture, require higher volumetric moisture contents to ensure equal diffusion (Moyano et al., 2013) at fixed porosity.

Not only gross microbial activity could be impacted by combinations of these factors, also the abundance of different microbial groups characterized by specific strategies to cope with environmental constraints. Compared to bacteria, fungi should be less sensitive to local variation in moisture content and thus N availability since their hyphal network allows

them to span pores and transfer N from N-rich micro-environments (Frey et al., 2000; Otten et al., 2001; Sleutel et al., 2012; Moyano et al., 2013). Today, information about these small-scale mechanisms is limited.

Investigation of interactive effects of substrate C:N ratio, soil pore network structure and soil moisture content on heterotrophic activity requires a specific experimental setup with due attention to possible artifacts introduced. Intended experimental modifications of the physical habitat surrounding organic substrates needs to be confirmed and this is now possible by advances in X-ray µCT allowing visualization of particulate OM and its spatial distribution in soil. The purpose of this study was to investigate the indirect impact of the soil pore network structure on degradation of N-poor particulate OM via its mediation of contact with soil particles. We hypothesized that the latter factor becomes irrelevant at increasing moisture content and at low C:N ratio of the substrate. A microcosm incubation experiment with miniature soil cores and monitoring of substrate-derived CO_2 emissions was set up to compare the impact of contrasting soil pore network structures using soil cores with two distinct particle size distributions. Additionally, we included different moisture conditions, to see how these modified the effects of soil pore network structure on diffusion of solutes. Lastly, soil cores were prepared with two organic substrates with contrasting C:N ratio. Miniature soil cores were used to allow meaningful analysis of the local environment of the added substrate particles by an innovative approach of X-ray µCT and image processing. We hypothesized that C-mineralization would be stimulated by increased N diffusion toward the organic substrates in soils with a more dense structure and in soils with a higher water content. Secondly, we hypothesized that fungi would dominate C-mineralization in soils characterized by a loose porous structure at low water content, i.e., when N availability impedes activity of bacteria.
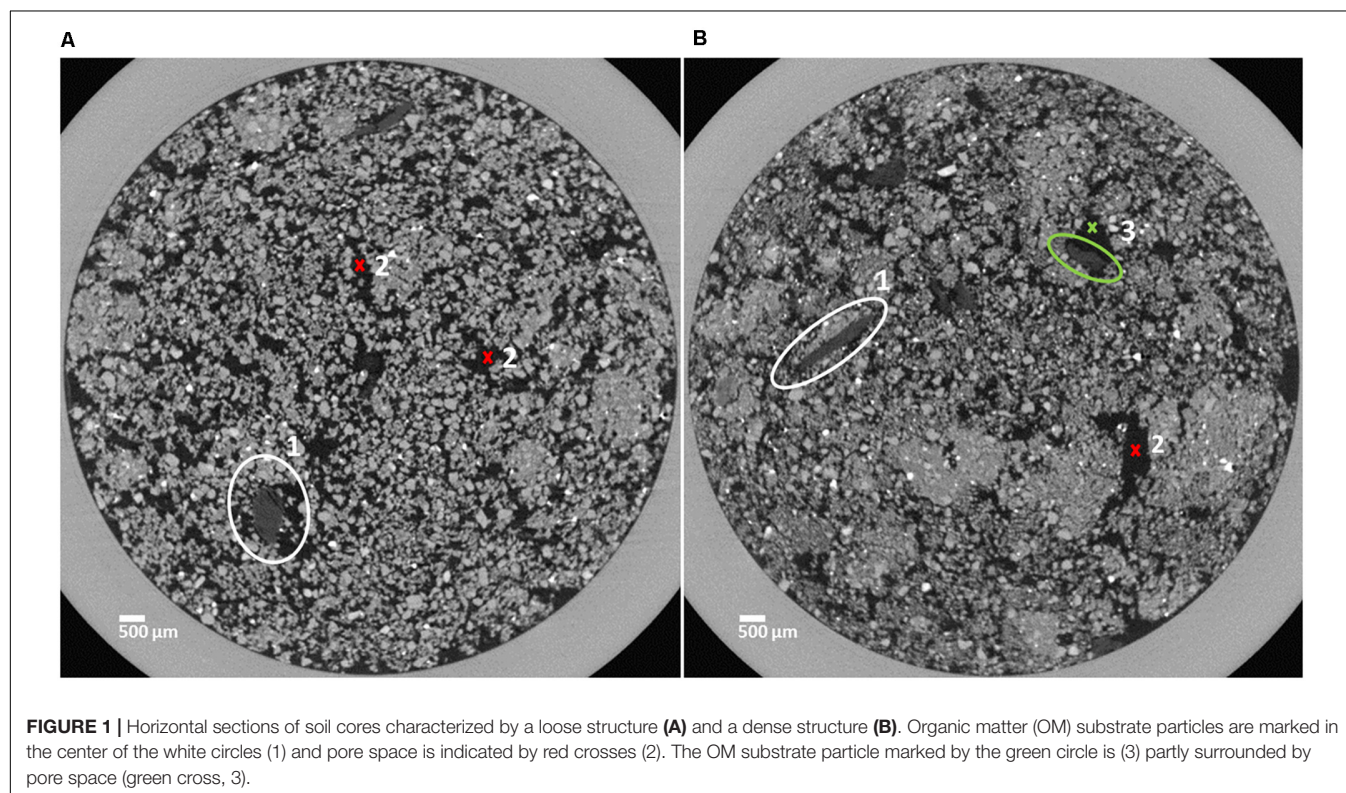
MATERIALS AND METHODS

Soil Characteristics

For the microcosm incubation experiment, a sandy loam soil (7% clay, 42% silt, 51% sand; pH_{H_2O} = 6.3; 0.797% soil organic carbon; 0.061% N) from the 0 to 30 cm depth layer of a cropland field in Lendelede (Belgium) was used. Sand sized and larger soil particulate organic matter (POM) was removed by following procedure. The bulk soil was dry sieved on 2000, 200, and 53 µm (mesh size) sieves. The >2000, >200, and >53 µm fractions were subsequently dispersed by shaking in a 50 g L^{-1} sodium metaphosphate (1:3 w:v^{-1} ratio) solution and these slurries were then sieved once more on the respective sieves, followed by rinsing with deionized water. This resulted in three size fractions: coarse sand (CS: 200–2000 µm), fine sand (FS: 53–200 µm), and silt+clay (S+C: <53 µm). The fine and coarse sand fractions were heated in a muffle furnace at 500°C for 5 h to remove any POM present. These three soil particle size fractions were finally used to create artificial soil mixtures without native POM (which would interfer with identification of added exogenous plant-derived substrate particles in X-ray µCT volumes).

Microcosm Incubation Experiment Set-Up and Carbon Mineralization

The soil incubation experiment had 22 treatments, each in triplicate, and all soils were brought to a fixed bulk density of 1.26 g cm^{-3}. Fixed factors were (i) soil particle size distribution, (ii) soil moisture content, (iii) C:N ratio of added exogenous POM, (iv) addition of extra mineral nitrogen (NO_3^-) and (v) X-ray μCT. Artificial soil mixtures were created at a coarse sand:fine sand:silt+clay (CS:FS:S+C) ratio of 10:40:50 and 20:60:20, and will be called 'densely structured soil' and 'loose structured soil,' respectively (**Figure 1**). Two soil moisture levels were selected, namely dry and near optimal (i.e., non-limiting) conditions for activity of microbial decomposers corresponding to 25 and 50% water filled pore space (WFPS), respectively. Dried plant residues, high and low in N, i.e., grass (42.3% C, 3.10% N) and sawdust (44.8% C, 0.10% N), ground and sieved to a fixed size of 500–1000 μm, were added as substrate to each of the four moisture content/structure combinations. Soil cores without addition of POM were included as controls. Soils were partially brought to the target WFPS% by deionized water and a KNO$_3$-N solution to achieve a mineral N content of 10 μg N g^{-1} soil. A sawdust treatment without mineral N addition was included for each CS:FS:S+C and WFPS combination to assess the interactive effect of these factors with local soil N availability on microbial activity. Soil cores were scanned by X-ray μCT and three additional unscanned replicates for all mineral N amended treatments at 50% WFPS were included to investigate the effect of the X-rays on the microbial community structure and C mineralization.

The soil cores were prepared by mixing the three mineral particle size fractions (and OM) in a watch glass. Subsequently miniature PVC-cylinders (diameter: 1.2 cm and height: 1.2 cm) were gradually filled with this mixture and incubated for 128 days at 18°C (Supplementary Figure 1). All soil cores were kept in open 60 ml containers in the incubation cupboard inside a closed box in which air humidity was maintained to near saturation to limit evaporation from the soils. Throughout the incubation period soil cores were weighed daily until day 41 and afterwards every 2 days to detect any change in moisture content. If needed, water was added by means of a micropippette. To monitor the soil CO_2 emission, each individual soil core was then moved into another 60 ml container fitted with a septum. Incubation of soils in these closed containers proceeded in the incubation cupboard for 6–21 h and the headspace atmosphere was sampled by connecting 12 ml pre-evacuated exetainers® (Labco Limited, United Kingdom) through the septum with a double-sided needle on days 1, 3, 6, 10, 13, 15, 17, 19, 22, 25, 28, 31, 35, 40, 47, 54, 64, 74, 86, 100, 114, 128. An expandable balloon was installed in each closed-chamber to avoid underpressure in the headspace upon gas sampling. After each gas sampling, the 60 ml containers were re-opened to replenish oxygen and put back in the closed box with controlled air humidity in the incubation cupboard until next sampling event. CO_2 concentrations in the exetainers® were measured using a gas chromatograph (Thermo Electron Trace GC Ultra) fitted with a TCD detector and autosampler. Three empty containers were sampled per sampling date to correct for initially present CO_2. CO_2 emission was recalculated to a μg C g^{-1} soil

FIGURE 1 | Horizontal sections of soil cores characterized by a loose structure **(A)** and a dense structure **(B)**. Organic matter (OM) substrate particles are marked in the center of the white circles (1) and pore space is indicated by red crosses (2). The OM substrate particle marked by the green circle is (3) partly surrounded by pore space (green cross, 3).

basis taking into account the soil mass, headspace volume, and pressure.

X-ray Microtomography (X-ray μCT)

The soil cores were scanned with an in-house developed X-ray computed tomography scanner (Nanowood; Dierick et al., 2014) at the Centre for X-ray Tomography of Ghent University (UGCT[1]). The directional target microfocus X-ray tube operated at 60 kV and 255 μA and 1441 projections with an exposure time of 1400 ms were recorded with a Varian Paxscan 2520 detector. The complete system was controlled by in-house developed software (Dierick et al., 2010). Only 35 min were needed per scan, reducing soil moisture loss from the soil cores to a minimum, allowing seemless integration of X-ray μCT into these soil incubation experiments. In addition, we managed to reach an impressive throughput of as much as 12 samples in only 8 h. Unlike in many previous studies, X-ray μCT derived data were produced with a statistically sound number of replicates for all treatments. The in-house developed Octopus Reconstruction software (Vlassenbroeck et al., 2007) (distributed by XRE, Ghent, Belgium[2]) was used to reconstruct the raw data to a 16-bit dataset of 1455 × 1455 × 1274 cubic voxels with 10 μm voxel pitch.

Image Analysis

CT image processing was performed in Octopus Analysis [in-house developed as Morpho+ (Brabant et al., 2011), distributed by XRE, Ghent, Belgium] and started with a contrast enhancement step, followed by conversion from 16 to 8-bit color-depth to reduce computational time and memory use. A region of interest (ROI) in the resulting CT volume was selected to avoid border artifacts (related to the PVC container) during further image processing.

Segmentation of Added OM

Pre-optimization of the scanner and reconstruction parameters resulted in μCT-scans with high contrast between the added substrate particles and the pore space. The volume representing the mineral matrix was firstly selected using a single gray value threshold, which was conservatively chosen to ensure that at this stage only voxels containing mineral material were selected. This segmented mineral matrix volume was subtracted from the entire CT-volume to facilitate further segmentation of OM from the residual CT-volume.

The use of relatively large OM substrate particles (500–1000 μm) in our experiment successfully allowed for gray value thresholding-based segmentation without the need for chemical staining agents. The removal of all native POM before construction of the soil cores (vide supra) completely avoided the risk of misclassification of natural POM with dimensions similar to the added POM. After applying a recursive filter (AVIZO[3]), OM particles were segmented via the application of Octopus Analysis' dual threshold algorithm. Dual

thresholding was performed by selecting a 'strong threshold,' defining voxels at the center of the OM's gray value range, and by setting a 'weak threshold' that led to selection of the remainder of OM. Voxels with a gray value in between the weak and strong threshold are only selected by the dual threshold algorithm if they are directly connected to voxels specified by the strong threshold. This procedure allowed for exclusion of the majority of voxels with a partial volume effect (PVE) between mineral material and pore space.

Segmentation of Pore Space and Pore Neck Size Distributions

CT-visible porosity (pores with diameter > 10 μm) and PND were determined via a sequence of image analysis steps on the previously defined ROI. Next, Octopus Analysis' single threshold algorithm was applied to segment both pore space and applied OM into a single CT volume mask ($VOL_{Pore+OM}$). A very conservative gray value threshold was applied to avoid selection of mineral phase voxels. Subsequently, the previously segmented OM volume (vide supra) was subtracted from the $VOL_{Pore+OM}$, yielding a μCT volume only containing pore space. An Euclidean distance map was calculated, followed by a watershed separation and determination of the PND according to the pore neck diameter, i.e., the diameter of the maximum inscribed sphere in the neck. This parameter describes water distribution and accessibility for micro-organisms more accurately compared to other parameters such as the number of voxels and the equivalent sphere diameter (Sleutel et al., 2008; Brabant et al., 2011).
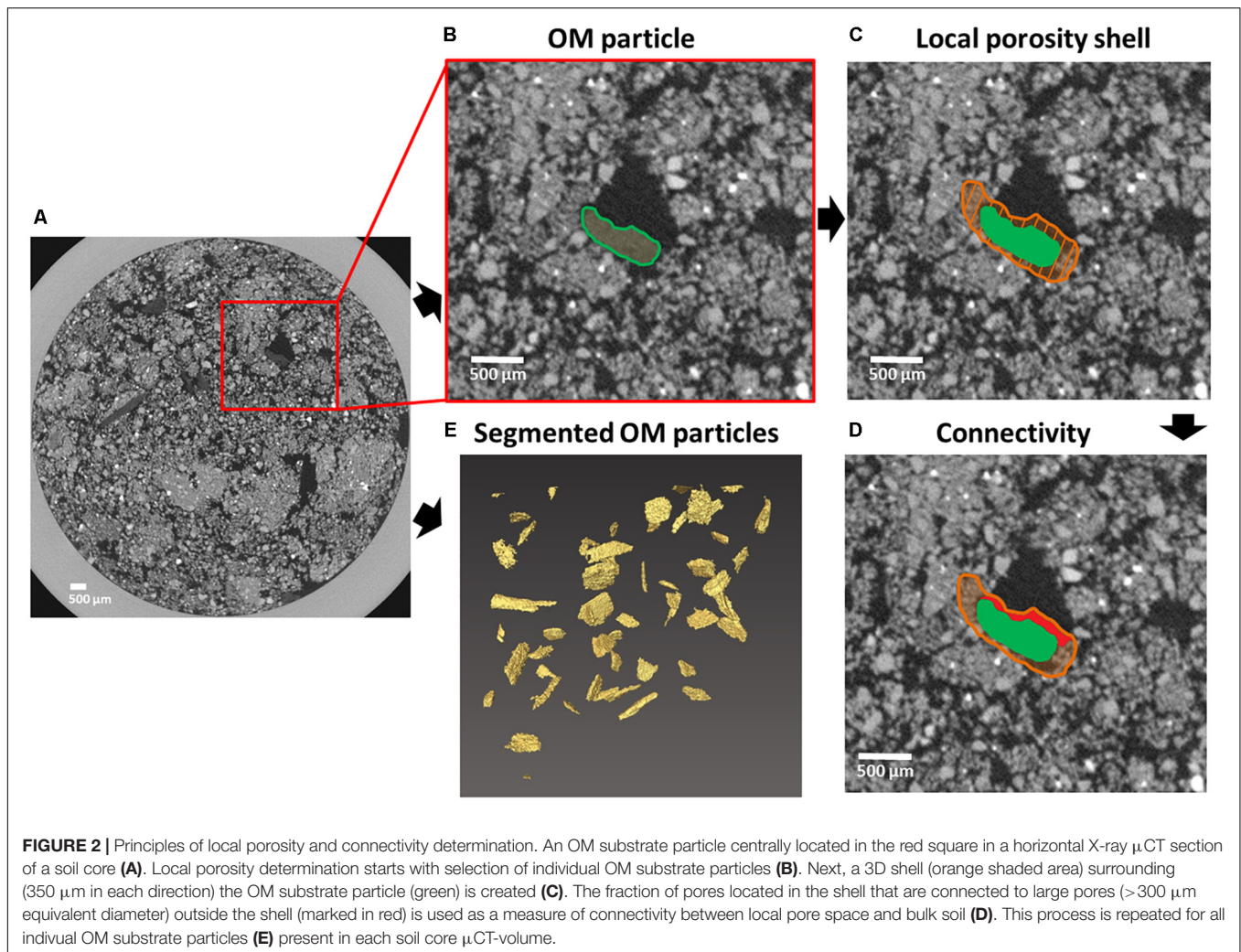
Local Porosity Calculation

The resulting μCT-mask for added particulate OM (**Figure 2E**: 3D representation of mask) was used as input for an in-house developed Matlab-tool (The Mathworks, Natick, MA, United States) to determine porosity of the surrounding soil (**Figure 2**). For each identified (**Figures 2A,B**) OM particle (40–60 per soil core) a buffer/shell volume of 350 μm (**Figure 2C**) was defined and the 'local porosity' inside this shell was calculated. The 350 μm distance was more or less arbitrarily set but was also motivated by the fact that this was the smallest distance at which the variance in local porosity of all substrate particles in a single soil core was minimized. Since large pores connected to the local-porosity shell most often regulate supply of O_2 and evacuation of produced CO_2, we determined the share of 'local pores' that were connected to such large external pores in the bulk soil, termed 'connectivity,' as an indicator for gas diffusion towards the substrate particles (**Figure 2D**). A cutoff of >300 μm equivalent sphere diameter was chosen because these pores should be nearly always dry (only 2.5% should be water-filled) at the selected moisture level. As a result we more closely quantified the habitat of heterotrophs feeding on the added substrate particles, complemented with information on whether or not these pores were part of larger pores not fully contained in the defined 350 μm shells.

FIGURE 2 | Principles of local porosity and connectivity determination. An OM substrate particle centrally located in the red square in a horizontal X-ray μCT section of a soil core **(A)**. Local porosity determination starts with selection of individual OM substrate particles **(B)**. Next, a 3D shell (orange shaded area) surrounding (350 μm in each direction) the OM substrate particle (green) is created **(C)**. The fraction of pores located in the shell that are connected to large pores (>300 μm equivalent diameter) outside the shell (marked in red) is used as a measure of connectivity between local pore space and bulk soil **(D)**. This process is repeated for all indivual OM substrate particles **(E)** present in each soil core μCT-volume.

Phospholipid Fatty Acids Analysis

Phospholipid fatty acids (PLFAs) were extracted based on a methodology described by Moeskops et al. (2010). The protocol was adapted to the small mass of soil in the soil cores. In this study, 3.6 ml phosphate buffer pH 7.0, 4 ml chloroform and 8 ml methanol were added to 1.1 g of freeze-dried soil in glass centrifuge tubes. The PLFA extraction proceeded exactly as described in Moeskops et al. (2010), except for the final step of the extraction. Here the fatty-acid methyl esters were dissolved in 0.2 ml of hexane containing methyl nonadecanoate fatty acid (C19:0), used as an internal standard. Concentrations of PLFAs were determined by GC-MS with a Thermo Focus GC [Varian capillary column CP Sil 88 (100 m × 0.25 mm i.d., 0.2 μm film thickness) Varian, Inc., Palo Alto, CA, United States] coupled to a Thermo DSQ quadrupole MS (Thermo Fisher Scientific, Inc., Waltham, MA, United States) in electron ionization mode.

For statistical data analysis, only those PLFAs that represented more than 1% of the total quantifed PLFA were considered. The fatty acids iC15:0, aC15:0, iC16:0, iC17:0, and aC17:0 were used as indicators of Gram-positive Bacteria (Denef et al., 2009; Moeskops et al., 2010). Gram-negative bacteria were represented by the sum of cyC17:0, cyC19:0, C16:1c9, and C18:1c11 (Denef et al., 2009). The sum of 10MeC16:0 and 10MeC18:0 was used to indicate the actinobacteria (Moeskops et al., 2010; Gebremikael et al., 2015). The sum of marker PLFAs for Gram-positive bacteria and Gram-negative bacteria and C17:0 designated the total bacterial community (Ameloot et al., 2013; Gebremikael et al., 2015). The fatty acid C18:2c9,12 was considered typical for saprotrophic fungi (Moeskops et al., 2010; Sleutel et al., 2012). The bacteria:fungi (B:F) ratio was calculated by dividing the corresponding sums of marker fatty acids. An index for nutrient limitation was calculated as the ratio of saturated PLFAs to mono-unsaturated ones (Bossio and Scow, 1998; Moore-Kucera and Dick, 2008).

Soil Mineral Nitrogen

At the end of the incubations, soil mineral nitrogen content (NO_3^- and NH_4^+) was determined. An equivalent of 0.5 g dry soil was shaken in 4 ml 1 M KCl for 2 h. After extraction, the NO_3^- and NH_4^+ content of the filtrate was colorimetrically measured with a continuous flow analyzer (Chem-lab 4, Skalar 223 Analytical, Breda, Netherlands).
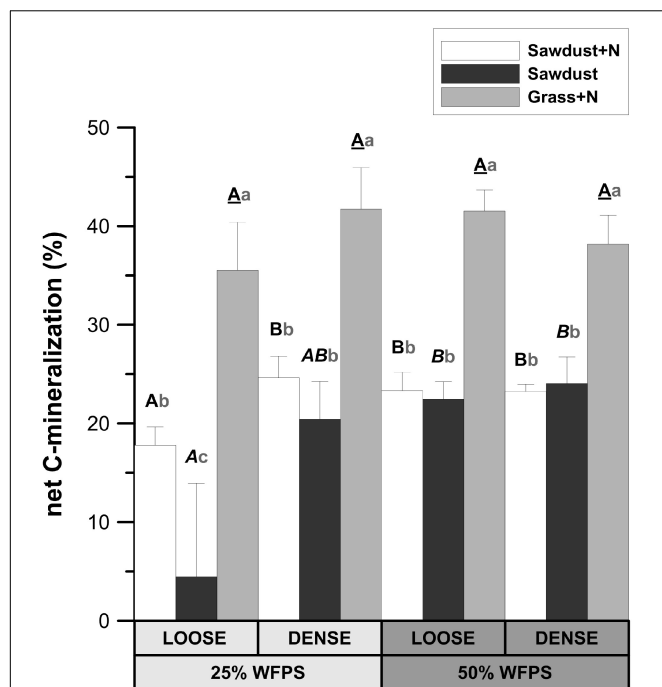
FIGURE 3 | Relative fraction of plant substrate's carbon mineralized after 128 days of incubation in soil cores at either 25 or 50% WFPS moisture level and with a 'loose' or 'dense' soil structure. Error bars represent standard deviations around means (n = 3). Statistically different structure and moisture treatments are indicated by different capital letters, one type per substrate+N treatment: bold letters for the sawdust+N treatment, bold italic letters for the sawdust treatment and underlined bold letters for the grass+N treatment. Statistically different substrate treatments within the same structure and moisture class combination are indicated by gray lowercase letters.
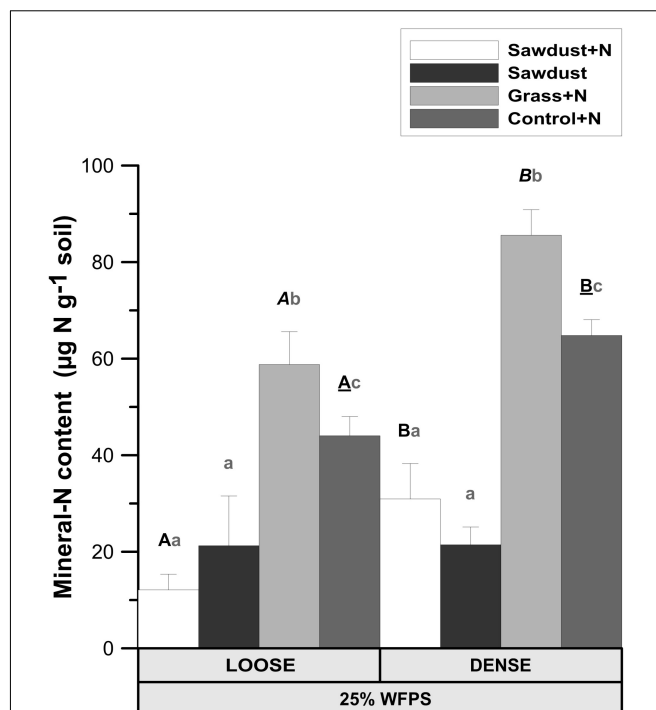

FIGURE 4 | Mineral N content (NO_3^- + NH_4^+) in the soil cores at 25% WFPS after 128 days of incubation for both structure types. Error bars represent standard deviation (n = 3). Statistically different structure treatments are indicated by different capital letters, one type per substrate+N treatment: bold letters for the sawdust+N treatment, bold italic letters for the grass+N treatment and underlined bold letters for the control+N treatment. Statistically different substrate treatments within the same structure class are indicated by gray lowercase letters.

Data Analysis

Statistical analysis of all data was performed using IBM SPSS Statistics 21 (SPSS, Inc., Chicago, IL, United States). Treatment effects were investigated by means of ANOVA and Tukey's *post hoc* test at 5% significance level. In case of heteroscedasticity, data were log-transformed and if unsuccessful the non-parametric Kruskall–Wallis test was used with Mann–Whitney's pairwise comparison.

RESULTS

Net Carbon Mineralization

At 25% WFPS, net Cmin in the grass+N treatment was 17–18% higher ($P < 0.05$) than in the sawdust+N treatment and 21–31% higher ($P < 0.01$) than in the sawdust treatment (**Figure 3**). At 50% WFPS, likewise grass+N amendment led to 14–19% higher ($P < 0.01$) net Cmin compared to sawdust+N and sawdust treatments. Neither soil structure nor moisture treatments had effects on net Cmin from grass amended soils. In contrast, the addition of nitrogen to sawdust amended soil cores with a loose soil structure at 25% WFPS, resulted in increased ($P < 0.05$) net Cmin (**Figure 3**). In the densely structured equivalents, addition

of nitrogen did not result in a significant increase in net Cmin. At 50% WFPS, net Cmin for sawdust+N and sawdust amended soil cores did not differ in both established soil structures. Net Cmin was lower ($P < 0.05$) for the 25% WFPS loose structured sawdust+N treated soil than its densely structured equivalent at 25% WFPS and its loose soil structure equivalent at 50% WFPS.

Mineral Nitrogen

Both OM amendment type ($P < 0.01$) and soil structure treatment ($P < 0.01$) affected soil mineral N. Loose structured sawdust+N, grass+N, and control+N cores all had a lower mineral N content ($P < 0.05$) than the corresponding densely structured treatments (**Figure 4**). Residual mineral N content was 3–5 fold ($P < 0.05$) higher in grass+N than in sawdust(+N) treatments and one third higher ($P < 0.05$) than in the unamended control+N soils for the same soil structure treatment. Regardless of soil structure, the sawdust+N and sawdust treatments contained less residual mineral N than the unamended control+N ($P < 0.05$) soils.

At 50% WFPS, OM amendment ($P < 0.01$) and soil structure treatment ($P < 0.01$) both affected soil mineral N (data not shown). Densely structured sawdust+N, sawdust, grass+N, and control+N soils all had 1.2–5.1 times higher ($P < 0.01$) mineral
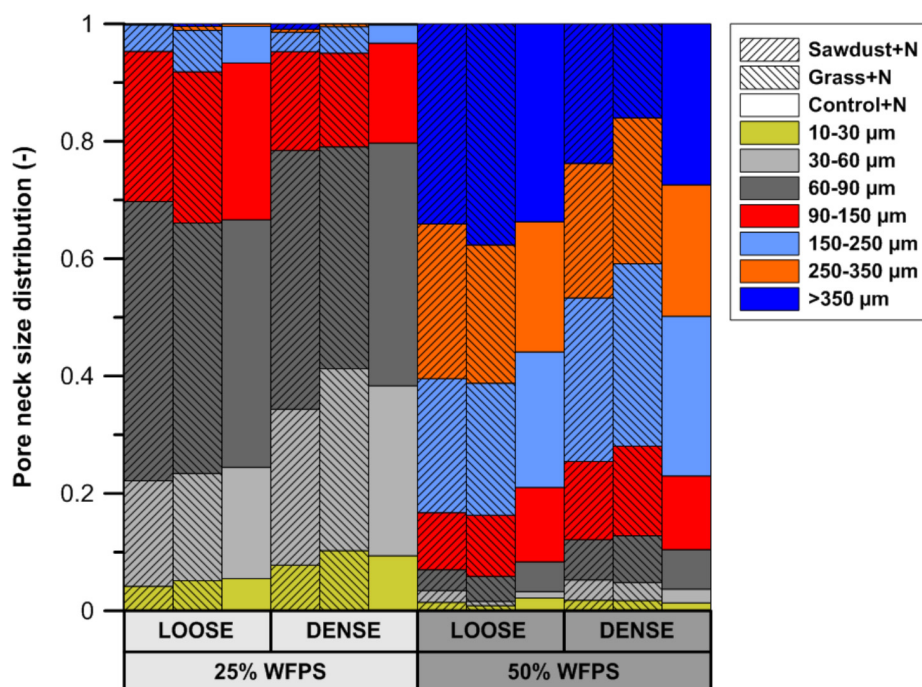
FIGURE 5 | Subdivision of the X-ray μCT visible pore space volume at either 25 or 50% WFPS moisture level and with a 'loose' or 'dense' soil structure, into seven pore neck diameter classes (10–30, 30–60, 60–90, 90–150, 150–250, 250–350, and >350 μm).
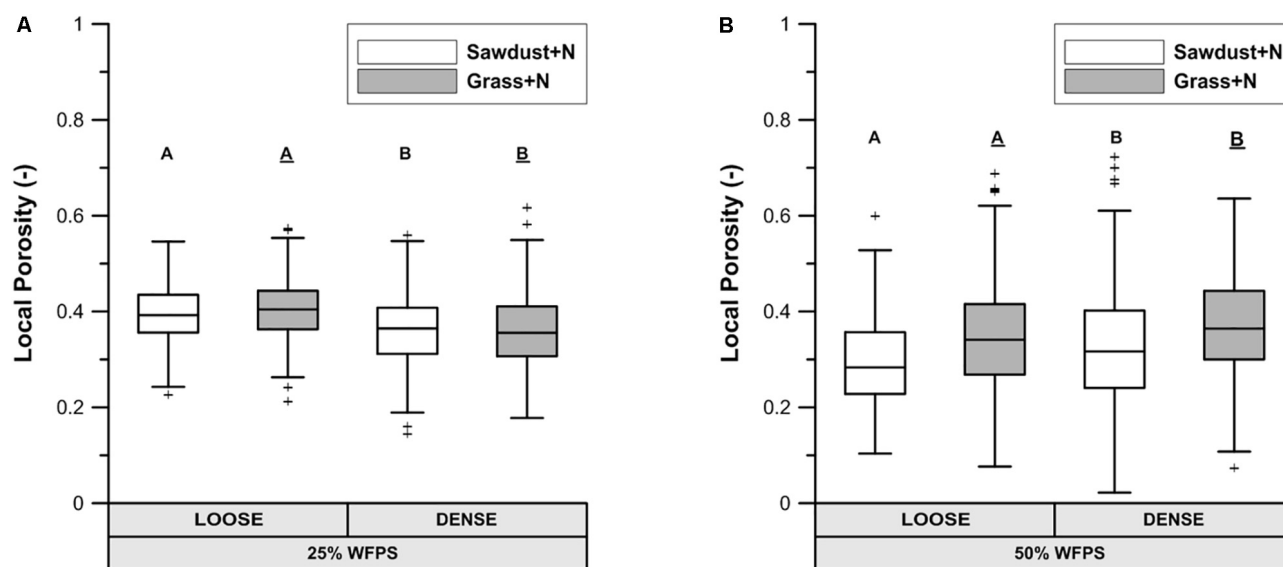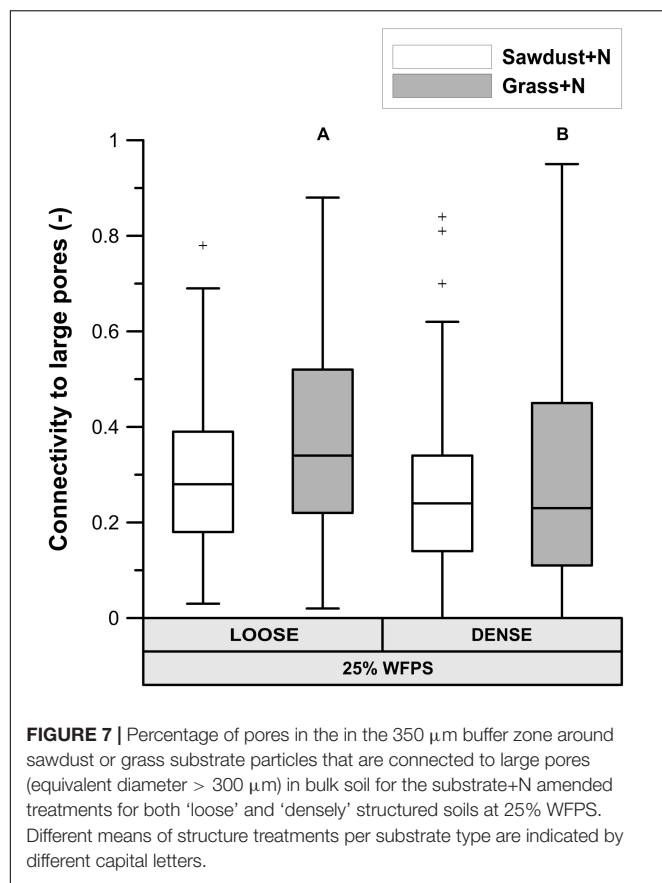

FIGURE 6 | X-ray μCT visible porosity in 350 μm buffer zone around sawdust or grass substrate particles for both loose and densely structured soils at 25% WFPS **(A)** and at 50% WFPS **(B)**, termed 'local porosity'. Statistically different means between both established soil structure treatments per substrate are indicated by different capital letters: plain uppercase letters for the sawdust+N and underlined uppercase letters for the grass+N treatments.

content than the equivalent loose structured treatments. In both soil structures sawdust+N and sawdust soil cores both had lower ($P < 0.01$) mineral N content than the grass+N and control+N treatment. Grass+N treatments on their turn had 1.5–2 times higher ($P < 0.01$) mineral N content than control+N treatments.

Pore Network
Pore Neck Size Distribution

Calculated pore neck size distributions (**Figure 5**) of all soil cores at 25% WFPS revealed pores with medium-sized pore neck diameters, viz. 30–60 and 60–90 μm, to constitute the major part

FIGURE 7 | Percentage of pores in the in the 350 μm buffer zone around sawdust or grass substrate particles that are connected to large pores (equivalent diameter > 300 μm) in bulk soil for the substrate+N amended treatments for both 'loose' and 'densely' structured soils at 25% WFPS. Different means of structure treatments per substrate type are indicated by different capital letters.

of CT-visible pore space. At 25% WFPS, the volume of 10–30 and 30–60 μm neck class pores was 3–5 and 8–13% larger (absolute terms) in densely structured cores than in corresponding loose structured treatments ($P < 0.05$), except for the 10–30 μm class in the sawdust+N amended soils where P was only 0.095. Compared to the dense treatment, loose structured soils at 25% WFPS had a 8–10% higher ($P < 0.05$) volume of the 90–150 μm class.

Unexpectedly, at 50% WFPS PND was very different with mainly large pores (>90 μm). All treatments at 50% WFPS had a higher ($P < 0.05$) pore volume in the 250–350 and >350 μm pore neck classes compared to the treatments at 25% WFPS.

Local Porosity Surrounding OM and Connectivity to Large Pores

At 25% WFPS, calculated 'local porosity' in a 350 μm radius from the OM particles (**Figure 6A**) was higher ($P < 0.05$) in the loose than densely structured sawdust+N or grass+N amended soils. Contrary to our intent, at 50% WFPS (**Figure 6B**) local porosity surrounding the substrate particles was in fact 2.4–3.3% lower ($P < 0.05$) in the loose than in the dense structure treatment. The fraction of local pore space connected to bulk soil large pores (equivalent diameter > 300 μm) was higher in a loose than dense structure for grass+N and sawdust+N treatments at 25% WFPS (**Figure 7**), but this difference was significant ($P < 0.05$) only for grass+N.

Phospholipid Fatty Acids Analysis
Total PLFA

At 25% WFPS (**Figure 8A**) there were no significant differences in total summed PLFAs, though in general values were 37–90% higher in dense OM-amended cores compared to the loose structured counterparts. Regardless of soil structure and moisture level, control+N and grass+N treatments had the lowest and highest mean values, respectively. Since no significant differences were observed, loose and densely packed treatments can be taken together, and then the grass+N treatments had a higher (at $P = 0.078$) total PLFA content than the unamended soils.

At 50% WFPS (**Figure 8B**), all soil cores with a loose structure had statistically equal total PLFA contents, though average contents of densely structured soils were nearly double compared to the corresponding loose structured treatments. Across treatments there were neither consistent nor significant effects of X-ray μCT scanning on total PLFA content.
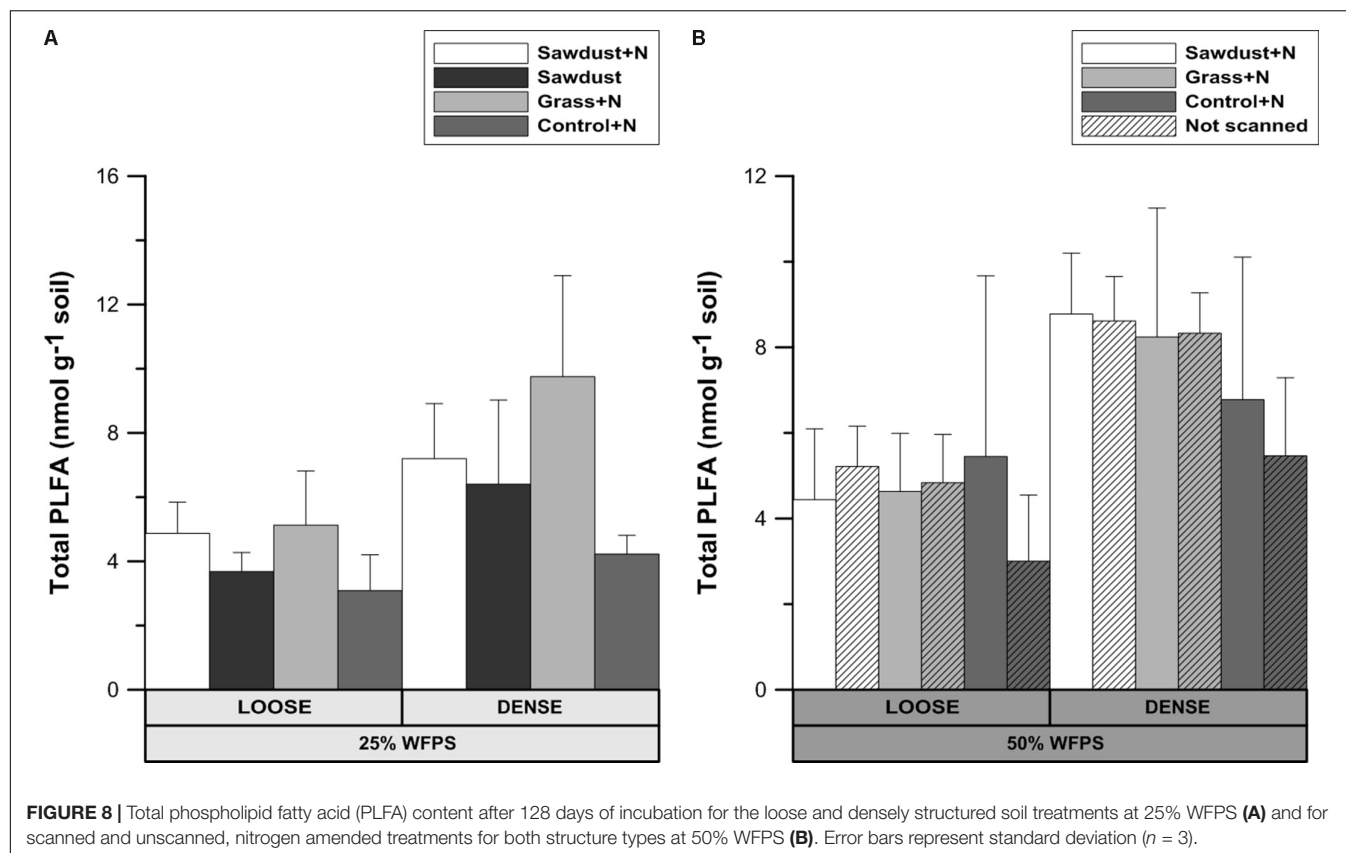
B:F Ratio

No significant differences were detected in the ratio of bacterial and fungal biomarkers within each soil structure/WFPS-% combination or between those combinations. This allows to consider the loose and densely structured soils at 25% WFPS as a one group of OM replicates. In this case, some noteworthy consistent trends existed across treatment combinations. The B:F ratio was higher ($P < 0.05$) for control+N (**Figure 9A**) than for the sawdust+N amended soils. In treatments with a loose structure, the B:F ratio was higher with sawdust than with grass+N addition, while the opposite trend was true for the densely structured treatment. The loose structured treatment amended with sawdust at 25% WFPS had a B:F ratio very similar to the B:F ratio of the unamended soil. The difference in B:F ratio between the sawdust and sawdust+N treatments was larger in loose structured (1.75) than in densely structured (0.45) soils.

At 50% WFPS, the B:F ratio was highest and lowest for the control+N and sawdust+N treatments, respectively, regardless of soil structure treatments. Differences in B:F ratio between corresponding scanned and unscanned treatments were insignificant ($P > 0.05$) and followed no consistent trend across examined treatments.

Principal Component Analysis

At 25% WFPS, principal component analysis (PCA) of the PLFAs resulted in a partial discrimination of the two soil structure treatments (**Figure 10A**) along a combination of PC1 and PC2. Loose structured treatments' scores along PC2 were mainly lower and often negative while densely structured treatments scored mostly positively on PC1. PC1 was positively loaded by cyC19:0, C18:1c11, cyC17:0 and 10MeC18:0, 10MeC16:0, marker PLFAs for Gram-negative bacteria and actinobacteria, respectively. The PLFAs iC15:0, iC16:0, aC17:0, iC17:0 (Gram-positive biomarkers) and C16:1c9 (Gram-negative biomarker) positively loaded on PC2. On the negative side, PC2 was strongly negatively loaded by the fungal marker C18:1c9. Biplots of PC1 and 2 did

FIGURE 8 | Total phospholipid fatty acid (PLFA) content after 128 days of incubation for the loose and densely structured soil treatments at 25% WFPS **(A)** and for scanned and unscanned, nitrogen amended treatments for both structure types at 50% WFPS **(B)**. Error bars represent standard deviation (n = 3).

not yield a clear discrimination according to OM substrate type.

At 50% WFPS scores for soil structural treatments were clustered along combinations of PC1 and PC2 (data not shown), indicating an effect of soil structure on the composition of the microbial community. Densely structured soils had higher summed scores of PC1 and PC2 than loose structured soils, which were mainly situated along the negative sides of PC1 and PC2. PLFAs cyC17:0, cyC19:0, C18:1c11 and aC17:0, iC17:0 and 10MeC18, 10MeC16, biomarkers for Gram-negative bacteria, Gram-positive bacteria and actinobacteria respectively, strongly positively loaded PC1. Fungal biomarker C18:2c9,12 negatively loaded PC1, though at only −0.3. However, since C18:2c9,12 was the sole negative loading variable, it likely had a considerable contribution to the entire variation. Likewise, PC2 was negatively loaded by fungal biomarkers (C18:1c9 and C18:3w3). PC2 was also positively loaded by iC15:0 (indicator for Gram-positive bacteria) and C16:1c9 (indicator for Gram-negative bacteria).

DISCUSSION

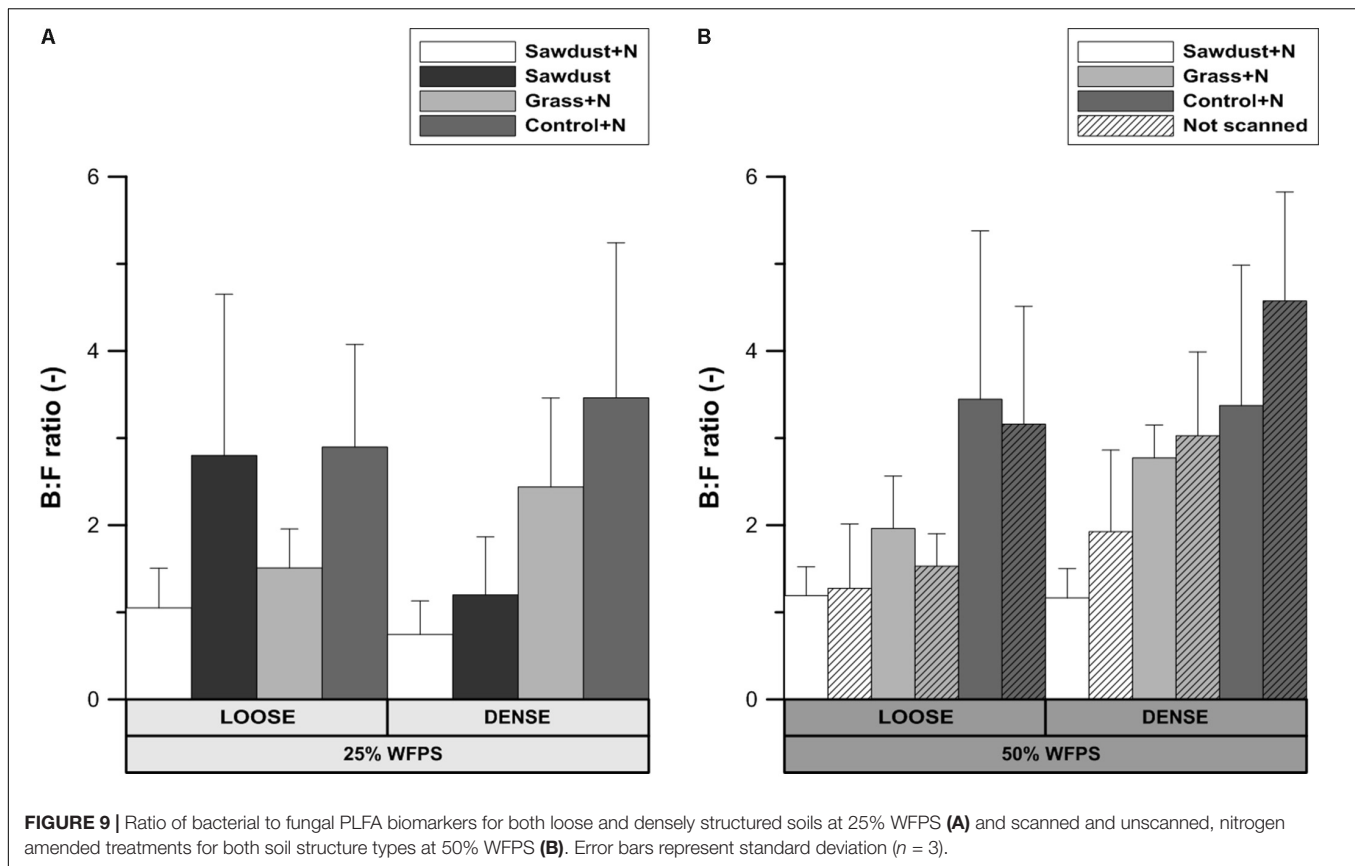### Integration of X-ray μCT in Soil Incubation Experiments

Use of X-ray μCT in soil biological studies is only warranted if the scanning does not impact the microbial community composition and activity. Total PLFA levels and abundances

of groups (**Figures 8B**, **9B**) were not significantly affected by μCT-scanning at 50% WFPS. In addition, there was no effect on cumulative Cmin after 128 days for any of the treatments (data not shown). So, in accordance to Bouckaert et al. (2013) and Schmidt et al. (2015) we conclude an at most minor and acceptable μCT-scanning effect on the microbial community's structure and activity.

We compared C-mineralization for various combinations of soil structure, added substrate, and soil moisture content to test the hypothesis that the impact of soil structure on microbial degradation of organic substrates is not merely by its control on the distribution of moisture and microorganisms in soil, but also through the regulation of N availability. The corresponding experimental design with reconstructed soil cores is not trivial but requires extreme care in creating these artificial soil structures to avoid artifacts. The resulting differences in soil structure need to be extensively validated to ensure correct simulation of the intended effects and proper interpretation of the experimental observations. The application of X-ray μCT uniquely allows to obtain highly accurate information for such validation.

μCT-Based Validation of Soil Structure Manipulations

The PND (**Figure 5**) was used to compare the effectivity of intended soil structural treatments to generate either closer or looser contact between added OM and soil. Soil cores at 25% WFPS all had a PND dominated by pores in medium-sized

FIGURE 9 | Ratio of bacterial to fungal PLFA biomarkers for both loose and densely structured soils at 25% WFPS **(A)** and scanned and unscanned, nitrogen amended treatments for both soil structure types at 50% WFPS **(B)**. Error bars represent standard deviation ($n = 3$).
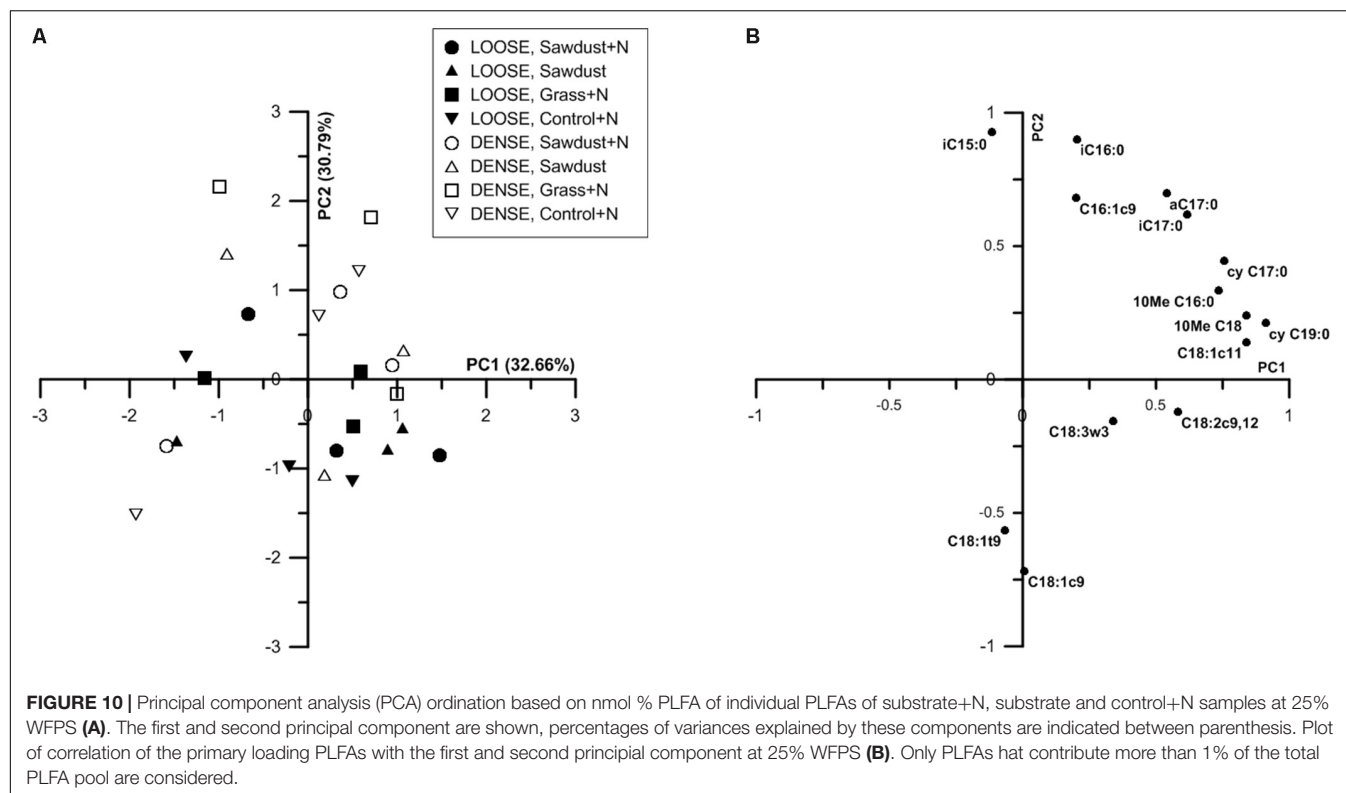
pore neck classes (30–90 μm). The loose structured treatments resulted in both a higher ($P < 0.05$) volume of the 90–150 μm PND class and lower ($P < 0.05$) volume of the 30–60 μm PND class compared to densely structured treatments. In addition, the densely structured treatments also had a 17% larger pore volume of pores with sizes below the 10 μm voxel-resolution. These clear shifts toward smaller pores demonstrate that manipulation of particle size distribution as previously introduced by Sleutel et al. (2012) creates contrasting pore networks at constant soil bulk density. However, at 50% WFPS unexpectedly most pores had neck sizes larger than 150 μm. This very different soil structure must have been generated during the mixing of soil, water and OM. Apparently there was stronger adhesion at higher moisture content with formation of more compact soil aggregates, some of which by chance contained an added substrate particle. This is also indicated by the 19–44% higher pore volume below the 10 μm voxel-resolution at 50% compared to 25% WFPS. The enhanced creation of compact mineral structures was also visually clear from reconstructed μCT volumes and resulted in larger inter-aggregate pores. In addition, at 50% WFPS there was an unexpected and significantly lower ($P < 0.05$) local porosity (**Figure 6B**) in the substrate+N amended loose structured soils compared to the densely structured soils. The resulting pore network structures at 50% WFPS were thus far from the intended ones and this did not allow us to further assess indirect effects of soil structure (at 50% WFPS) on activity and structure of the microbial community through mediation of N-availability. We

therefore just briefly interpret the 50% WFPS net Cmin and local porosity data, and focus on observations made from the 25% WFPS soils.

Impact of Soil Structure, OM Amendment, and Moisture Level on Microbially Mediated OM Decomposition
Low C:N Ratio Substrate

Irrespective of the soil moisture content and soil structure types, net Cmin (**Figure 3**) was higher ($P < 0.05$) in grass+N amended soils compared to sawdust(+N) amended soils, logically owing to the larger content of relatively biodegradable OM (carbohydrates and proteins) at the expense of lignin in grass than in sawdust. We hypothesized that microbially mediated decomposition of a substrate with low C:N ratio (13.7), like grass-derived particles, would not depend on provision of extra N by surrounding soil, which would depend on soil moisture level and structure through their impact on potential for diffusion of N. Neither soil moisture nor structure indeed affected net Cmin in the grass+N amendment, suggesting that the N supply by the grass substrate was sufficient for heterotrophic activity to be non-N limited. Net N mineralization from grass material (**Figure 4**) also evidences that in all cases N availability was not limited. We thus deemed that from the grass amended soil cores we could infer soil moisture level and structure effects on microbial activity *per se*, devoid of any indirect mediation of soil N availability.

FIGURE 10 | Principal component analysis (PCA) ordination based on nmol % PLFA of individual PLFAs of substrate+N, substrate and control+N samples at 25% WFPS (A). The first and second principal component are shown, percentages of variances explained by these components are indicated between parenthesis. Plot of correlation of the primary loading PLFAs with the first and second principal component at 25% WFPS (B). Only PLFAs hat contribute more than 1% of the total PLFA pool are considered.

Grass derived net Cmin turned out to be equal at 25 and 50% WFPS (**Figure 3**) and so even in the relatively dry soil at 25% WFPS there was apparently no inhibition of heterotrophic OM decomposition. Likewise, the factor soil structure did not impact net Cmin. Both observations demonstrate that decomposition of the grass particles proceeded in relative isolation from the surrounding soil conditions. This unresponsiveness of grass-derived Cmin to soil environmental conditions (structure and moisture) has several implications with respect to overall impact of soil gas exchange and solute diffusion on microbial activity in our artificial soil incubations:

1. Enhanced soil air permeability has been positively linked to a faster OM decomposition because pathways created by connected pores support the supply of O_2 toward the micro-organisms (Ruamps et al., 2011; Kravchenko et al., 2015) and simultaneously evacuate the produced CO_2 (Kravchenko et al., 2015). Since the connectivity (**Figure 7**) of the local pore space surrounding the OM substrate toward large air filled pores (>300 μm eq. diameter) was higher for the loose structured soil treatment at 25% WFPS compared to the densely structured, more favorable circumstances for OM decomposition may be expected in the loose structured soils. However, soil physical structure and moisture level directly co-determine air permeability and both differed between the 25 and 50% WFPS treatments. It thus appears that gas transport (O_2 and CO_2) was non-limiting in any of the constructed soils, not surprisingly perhaps given the relatively dry soil

conditions and low bulk density. Gas transport should thus also not have formed a bottleneck to heterotrophic degradation of sawdust with even lower measured net Cmin and thus lower O_2 and CO_2 transport requirement.

2. Secondly, native soil microbial biomass was only derived from the silt+clay fraction, given that sand fractions were free of OM. The fact that net Cmin from grass for loose and dense structures did not differ in spite of their different silt+clay and proportionally microbial biomass content (200 and 500 mg silt+clay g^{-1} soil, respectively), demonstrates that initial soil microbial biomass content had no effect on colonization of the added plant-derived substrates either. Also accessibility of the added grass particles to the native soil microbial community as affected by soil structure treatment and moisture level was apparently no factor of importace for further plant substrate-derived microbial activity.

High C:N Ratio Substrate

Sawdust net Cmin was strongly limited without mineral N application, as expected given its C:N ratio of approximately 450. The probably rapid depletion of locally available N following microbial immobilization logically necessitates diffusion of NO_3^- from the surrounding soil to meet the microbial demand for N. In the loose structured soil at 25% WFPS, the 13.3% higher net Cmin with mineral N addition compared to the corresponding unfertilized treatment confirms that indeed limited N availability impeded heterotrophic activity, in line with our first hypothesis. Moreover, addition of mineral N did not lead to a similar

increase of Cmin in densely structured soils or at 50% WFPS. A 50% higher saturated:monounsaturated PLFA ratio, indicative of nutrient stress (Moeskops et al., 2012) at 25% WFPS in the loose structured sawdust treatment compared to the sawdust+N treatment also confirmed that N was limiting in that particular treatment. On the other hand, the effect of N-addition on Cmin in the densely structured treatments with presumably more water bridging was smaller (4.2%), indicating the more favorable habitat in densely structured soils. This outcome confirms our hypothesis that at periods of combined limited soil N supply and dry soil moisture conditions, soil structure exerts an indirect determining influence on decomposition of N-poor OM.

At 25% WFPS, net Cmin of the sawdust+N treatments was furthermore 6.8% lower ($P < 0.05$) in the 'loose structure' than in the corresponding densely structured treatment, while in both cases N unavailability in bulk soil can be excluded given the initial application of NO_3-N to a constant soil content of 10 µg g^{-1}. Also, without any NO_3^--N added, raising soil moisture to 50% WFPS increased net Cmin to a value comparable to that of sawdust+N treated soil. In sum closer contact with bulk soil or higher moisture level was needed for microbial decomposition of the sawdust particles. Schjonning et al. (2003) demonstrated that CO_2 emission patterns were well-predicted by modeled relative solute diffusivities. In order to more specifically investigate the roles of soil structure and soil moisture content on N availability it seems obvious that their contribution to N diffusion has to be considered, as described below:

1. Logically, the transport of N toward the OM substrate depends on the local contact of the OM particles with water and soil. Information about this contact in the immediate surrounding of sawdust particles was obtained by calculating the local porosity. Local porosity was a bit higher (2.6–5.6 vol%) than total visible porosity (TVP, data not shown). The reduced net Cmin in the loose structured treatments at 25% WFPS (**Figure 3**) was indeed observed in treatments with higher local porosity and thus lesser ($P < 0.05$) contact between substrate particles, soil particles and small pores (**Figure 6A**).

2. In addition to local porosity, obviously pore size distribution needs to be considered. Finer water-filled pores (Kravchenko and Guber, 2017) and more medium-sized pores (30–60 µm) with water films (Strong et al., 2004) contribute to nutrient flux. These pore size classes were indeed more abundantly present in our densely structured soils. Medium-sized pores have also been related to increased Cmin (Strong et al., 2004; Ananyeva et al., 2013; Kravchenko et al., 2015) as well as increased microbial activity (Strong et al., 2004; Ruamps et al., 2011; Kravchenko et al., 2014), probably because they frequently provide suitable habitats for micro-organisms due to a generally optimal water and air distribution (Kravchenko and Guber, 2017). Next to increasing N availability via presence of a higher volume fraction of more small pores in the vicinity of substrate particles, the higher volume fraction of medium-sized pores ($P < 0.05$) in the densely structured soils probably also created circumstances for

stimulated net Cmin (**Figure 3**) and higher total PLFAs (**Figure 8A**) in general.

3. The more than threefold increase in net Cmin in case of N addition led to a much stronger soil mineral N depletion in the sawdust+N treatments compared to the sawdust treatments with strongly inhibited microbial activity. Compared to control and grass amended soils, 2–5 times less mineral N was left in the sawdust(+N) amended soils after incubation, indicating a net microbial N immobilization of 32–34 µg g^{-1} soil by the heterotrophs decomposing the sawdust. Higher final mineral N levels in densely than in loose structured soils logically resulted from higher organic N content in the former (higher silt+clay fraction).

Interactive Effect of Soil Structure, OM Amendment, and Soil Moisture on Microbial Community Structure

Fungal proliferation in soils is related to the connectivity of (large) air filled pores (Otten et al., 1999). The loose structured soils had a higher connection of local pores to macropores in the bulk soil and B:F ratios (**Figure 9A**) of the grass+N and control+N treatments at low moisture content were indeed lower than in the densely structured soils. However, the opposite was true for the sawdust+N and sawdust amended soils. Consequently, a general control of N availability or soil structure on relative abundances of fungi could not be concluded. Our second hypothesis that overall bacterial abundance would be relatively limited by limited N availability was thus not confirmed. Also, due to their limited capacity to decompose lignin-rich substrates compared to fungi (Eskelinen et al., 2009), bacteria were assumed to be more abundant in grass amended than in both sawdust amended and unamended soil. However, treatments with high sawdust or grass-derived net Cmin had a lower B:F ratio than the control treatment, regardless of substrate quality or addition of N. These counter-intuitive observations may be explained taking into account that B:F ratios of the control+N treatments were always higher than when substrates were added. Indeed, it is well-known that fungi are important in fresh OM substrate decomposition because of their ability to decompose cellulose and lignin (Swift et al., 1979; Kogel-Knabner, 2002) and so bacteria dominate native SOM decomposition. The relative contribution of native SOM decomposition versus fresh substrate-derived Cmin appears indeed to have overridingly determined B:F ratio and both were well-correlated ($r = 0.88$) for loose structured soils at 25% WFPS. This then explains why completely contrary to expectation the B:F ratio was highest for the loose structured sawdust treatment: obstruction of microbially mediated decomposition of sawdust (low moisture, no N applied, less contact with soil) resulted in a relatively higher contribution of PLFAs of microorganisms utilizing native SOM as substrate. The difference in B:F ratio between sawdust and the sawdust+N treatments was much larger in the loose structured compared to their densely structured equivalents (**Figure 9A**) and indeed followed ordination of substrate derived C-mineralization. In densely structured soil,

sawdust-derived net Cmin was at a par with 50% WFPS objects and relatively more fungal growth compared to the loose structured equivalent treatment was evidenced by a lower B:F ratio.

Principal component analysis of the relative PLFA concentrations resulted in a partial discrimination based on soil structure treatment (**Figure 10A**). This suggests that more or less specific microbial community profiles existed per soil structure. At 25% WFPS (**Figure 10A**), the densely structured soil treatments were mainly differentiated from the loose structured soils by PC2, aside from three deviating observations. As fungal biomarkers negatively loaded PC2, and fungal PLFA and soil B:F ratio did not differ systematically between dense and loose soils, these results indicate that soil structure effectuated differentiation in either the fungal or bacterial community, or simultaneously in both communities. Closer examination of PC2s loading plots suggests that mainly relatively higher abundances of Gram-positive bacteria (**Figure 10B**) were associated with the denser soil structural treatment.

CONCLUSION

We hypothesized that soil structure controls degradation of OM by regulating potential for diffusion of N. We confirmed such a mediation of heterotrophic microbial activity in conditions of low substrate N content. Soil drying and limited contact between substrates and surrounding soil (in loosely packed soil) limit degradation of OM via a limitation of N supply from surrounding bulk soil, though trends in microbial community structure were unclear. Such conditions frequently occur in well-drained coarse textured soils in drier seasons and perhaps the role of indirect soil structural controls on microbial activity has not been sufficiently acknowledged compared to organo-mineral association and physical occlusion as soil OM stabilizing mechanism. For instance, it is well-known that heathland land-use has resulted in unusually high levels of soil OM with a high C:N ratio in sandy soils throughout North-West Europe.

Soil incubation experiments oriented at studying degradation of exogenous OM, typically rely on well-mixed and repacked soil. Our investigations with X-ray CT in bulk soil and in local surroundings of added substrate particles clearly demonstrate that seemingly comparable treatments can result in completely different soil pore network structure. If such classical incubation experiments are combined with soil N-level as factor, it seems likely that artifacts may emerge, possibly leading to erroneous conclusions. The compatibility of X-ray CT with real-time monitoring of microbial processes was reconfirmed and can

ultimately be used to rule-out flawed parts of experimental designs. Inspection of the local pore space surrounding (350 μm in all directions) OM substrate particles via X-ray CT and image processing now enables for non-invasive inspection of the habitat of decomposers of discrete substrate particles. This expands our ability to further study effects of the degree of OM contact with bulk soil. Such empirically derived information will be useful for developing and testing mechanistic models of soil C cycling which explicitly want to account for soil matrix – OM contact and availability of N.

DATA AVAILABILITY

The raw data supporting the conclusions of this manuscript will be made available by the authors, without undue reservation, to any qualified researcher.

AUTHOR CONTRIBUTIONS

PM, SN, and SS contributed to the concept and design of the study. PM performed all the experiments, statistically evaluated the results, designed the figures and wrote the first draft of the manuscript. JB helped to perform the experiment. JB, LH, and VC helped to design the experiment. All authors contributed to the manuscript revision.

FUNDING

ACKNOWLEDGMENTS

SUPPLEMENTARY MATERIAL

The Supplementary Material for this article can be found online at: https://www.frontiersin.org/articles/10.3389/fmicb.2018.01433/full#supplementary-material

REFERENCES

Ameloot, N., Neve, S., Jegajeevagan, K., Yildiz, G., Buchan, D., Funkuin, Y. N., et al. (2013). Short-term CO_2 and N_2O emissions and microbial properties of biochar amended sandy loam soils. *Soil Biol. Biochem.* 57, 401–410. doi: 10.1016/j.soilbio.2012.10.025

Ananyeva, K., Wang, W., Smucker, A. J. M., Rivers, M. L., and Kravchenko, A. N. (2013). Can intra-aggregate pore structures affect the aggregate's effectiveness in protecting carbon? *Soil Biol. Biochem.* 57, 868–875.

Angers, D. A., and Recous, S. (1997). Decomposition of wheat straw and rye residues as affected by particle size. *Plant Soil* 189, 197–203. doi: 10.1023/A:1004207219678

Ball, B. C., Crichton, I., and Horgan, G. W. (2008). Dynamics of upward and downward N_2O and CO_2 fluxes in ploughed or no-tilled soils in relation to water-filled pore space, compaction and crop presence. *Soil Tillage Res.* 101, 20–30. doi: 10.1016/j.still.2008.05.012

Bossio, D. A., and Scow, K. M. (1998). Impacts of carbon and flooding on soil microbial communities: phospholipid fatty acid profiles and substrate

utilization patterns. *Microb. Ecol.* 35, 265–278. doi: 10.1007/s0024899 00082

Bouckaert, L., Van Loo, D., Ameloot, N., Buchan, D., Van Hoorebeke, L., and Sleutel, S. (2013). Compatibility of X-ray micro-computed tomography with soil biological experiments. *Soil Biol. Biochem.* 56, 10–12. doi: 10.1016/j.soilbio. 2012.02.002

Brabant, L., Vlassenbroeck, J., De Witte, Y., Cnudde, V., Boone, M. N., Dewanckele, J., et al. (2011). Three-dimensional analysis of high-resolution x-ray computed tomography data with Morpho+. *Microsc. Microanal.* 17, 252–263. doi: 10.1017/S1431927610094389

Chenu, C., and Stotzky, G. (2002). *Interactions Between Microorganisms and Soil Particles: An Overview. Interactions Between Soil Particles and Microorganisms: Impact on the Terrestrial Ecosystem.* Manchester: John Wiley & Sons, Ltd., 1–40.

Coppens, F., Garnier, P., De Gryze, S., Merckx, R., and Recous, S. (2006). Soil moisture, carbon and nitrogen dynamics following incorporation and surface application of labelled crop residues in soil columns. *Eur. J. Soil Sci.* 57, 894–905. doi: 10.1111/j.1365-2389.2006.00783.x

Crawford, J. W., Harris, J. A., Ritz, K., and Young, I. M. (2005). Towards an evolutionary ecology of life in soil. *Trends Ecol. Evol.* 20, 81–87. doi: 10.1016/ j.tree.2004.11.014

Denef, K., Roobroeck, D., Wadu, M., Lootens, P., and Boeckx, P. (2009). Microbial community composition and rhizodeposit-carbon assimilation in differently managed temperate grassland soils. *Soil Biol. Biochem.* 41, 144–153. doi: 10. 1016/j.soilbio.2008.10.008

Dierick, M., Van Loo, D., Masschaele, B., Boone, M., and Van Hoorebeke, L. (2010). A LabVIEW (R) based generic CT scanner control software platform. *J. Xray Sci. Technol.* 18, 451–461. doi: 10.3233/XST-2010-0268

Dierick, M., Van Loo, D., Masschaele, B., Van den Bulcke, J., Van Acker, J., Cnudde, V., et al. (2014). Recent micro-CT scanner developments at UGCT. *Nucl. Instr. Methods Phys. Res. B* 324, 35–40. doi: 10.1016/j.nimb.2013. 10.051

Dungait, J. A. J., Hopkins, D. W., Gregory, A. S., and Whitmore, A. P. (2012). Soil organic matter turnover is governed by accessibility not recalcitrance. *Glob. Change Biol.* 18, 1781–1796. doi: 10.1111/j.1365-2486.2012. 02665.x

Eskelinen, A., Stark, S., and Mannisto, M. (2009). Links between plant community composition, soil organic matter quality and microbial communities in contrasting tundra habitats. *Oecologia* 161, 113–123. doi: 10.1007/s00442-009- 1362-5

Frey, S. D., Elliott, E. T., Paustian, K., and Peterson, G. A. (2000). Fungal translocation as a mechanism for soil nitrogen inputs to surface residue decomposition in a no-tillage agroecosystem. *Soil Biol. Biochem.* 32, 689–698. doi: 10.1016/S0038-0717(99)00205-9

Garnier, P., Cambier, C., Bousso, M., Masse, D., Chenu, C., and Recous, S. (2008). Modeling the influence of soil-plant residue contact on carbon mineralization: comparison of a compartmental approach and a 3D spatial approach. *Soil Biol. Biochem.* 40, 2754–2761. doi: 10.1016/j.soilbio.2008.07.032

Gebremikael, M. T., Steel, H., Bert, W., Maenhout, P., Sleutel, S., and De, Neve S (2015). Quantifying the contribution of entire free-living nematode communities to carbon mineralization under contrasting C and N availability. *PLoS One* 10:e0136244. doi: 10.1371/journal.pone.0136244

Giacomini, S. J., Recous, S., Mary, B., and Aita, C. (2007). Simulating the effects of N availability, straw particle size and location in soil on C and N mineralization. *Plant Soil* 301, 289–301. doi: 10.1007/s11104-007-9448-5

Henriksen, T. M., and Breland, T. A. (2002). Carbon mineralization, fungal and bacterial growth, and enzyme activities as affected by contact between crop residues and soil. *Biol. Fertil. Soils* 35, 41–48. doi: 10.1007/s00374-001- 0438-0

Juarez, S., Nunan, N., Duday, A. C., Pouteau, V., Schmidt, S., Hapca, S., et al. (2013). Effects of different soil structures on the decomposition of native and added organic carbon. *Eur. J. Soil Biol.* 58, 81–90. doi: 10.1016/j.ejsobi.2013. 06.005

Kogel-Knabner, I. (2002). The macromolecular organic composition of plant and microbial residues as inputs to soil organic matter. *Soil Biol. Biochem.* 34, 139–162. doi: 10.1016/S0038-0717(01)00158-4

Kravchenko, A. N., and Guber, A. K. (2017). Soil pores and their contributions to soil carbon processes. *Geoderma* 287, 31–39. doi: 10.1016/j.geoderma.2016. 06.027

Kravchenko, A. N., Negassa, W. C., Guber, A. K., Hildebrandt, B., Marsh, T. L., Terence, L., et al. (2014). Intra-aggregate pore structure influences phylogenetic composition of bacterial community in macroaggregates. *Soil Sci. Soc. Am. J.* 78, 1924–1939. doi: 10.2136/sssaj2014.07.0308

Kravchenko, A. N., Negassa, W. C., Guber, A. K., and Rivers, M. L. (2015). Protection of soil carbon within macro-aggregates depends on intra-aggregate pore characteristics. *Sci. Rep.* 5:16261. doi: 10.1038/srep16261

Linquist, B. A., Singleton, P. W., Yost, R. S., and Cassman, K. G. (1997). Aggregate size effects on the sorption and release of phosphorus in an ultisol. *Soil Sci. Soc. Am. J.* 61, 160–166. doi: 10.2136/sssaj1997.036159950061000 10024x

Moeskops, B., Buchan, D., Van Beneden, S., Fievez, V., Sleutel, S., Gasper, M. S., et al. (2012). The impact of exogenous organic matter on SOM contents and microbial soil quality. *Pedobiologia* 55, 175–184. doi: 10.1016/j.pedobi.2012. 03.001

Moeskops, B., Sukristiyonubowo, Buchan, D., Sleutel, S., Herawaty, L., Husen, E., et al. (2010). Soil microbial communities and activities under intensive organic and conventional vegetable farming in West Java, Indonesia. *Appl. Soil Ecol.* 45, 112–120. doi: 10.1016/j.apsoil.2010.03.005

Moore-Kucera, J., and Dick, R. P. (2008). PLFA profiling of microbial community structure and seasonal shifts in soils of a Douglas-fir chronosequence. *Microb. Ecol.* 55, 500–511. doi: 10.1007/s00248-007-9295-1

Moyano, F. E., Manzoni, S., and Chenu, C. (2013). Responses of soil heterotrophic respiration to moisture availability: an exploration of processes and models. *Soil Biol. Biochem.* 59, 72–85. doi: 10.1016/j.soilbio.2013.01.002

Negassa, W. C., Guber, A. K., Kravchenko, A. N., Marsh, T. L., Hildebrandt, B., and Rivers, M. L. (2015). Properties of soil pore space regulate pathways of plant residue decomposition and community structure of associated bacteria. *PLoS One* 10:e0123999. doi: 10.1371/journal.pone.0123999

Or, D., Smets, B. F., Wraith, J. M., Dechesne, A., and Friedman, S. P. (2007). Physical constraints affecting bacterial habitats and activity in unsaturated porous media - a review. *Adv. Water Resour.* 30, 1505–1527. doi: 10.1016/j. advwatres.2006.05.025

Otten, W., Gilligan, C. A., Watts, C. W., Dexter, A. R., and Hall, D. (1999). Continuity of air-filled pores and invasion thresholds for a soilborne fungal plant pathogen, *Rhizoctonia solani*. *Soil Biol. Biochem.* 31, 1803–1810. doi: 10.1016/S0038-0717(99)00099-1

Otten, W., Hall, D., Harris, K., Ritz, K., Young, I. M., Gilligan, C. A., et al. (2001). Soil physics, fungal epidemiology and the spread of *Rhizoctonia solani*. *New Phytol.* 151, 459–468. doi: 10.1046/j.0028-646x.2001. 00190.x

Prove, B. G., Loch, R. J., Foley, J. L., Anderson, V. J., and Younger, D. R. (1990). Improvements in aggregation and infiltration characteristics of a krasnozem under maize with direct drill and stubble retention. *Aust. J. Soil Res.* 28, 577–590. doi: 10.1071/SR9900577

Ruamps, L. S., Nunan, N., and Chenu, C. (2011). Microbial biogeography at the soil pore scale. *Soil Biol. Biochem.* 43, 280–286. doi: 10.1111/j.1574-6941.2008. 00490.x

Schjonning, P., Thomsen, I. K., Moldrup, P., and Christensen, B. T. (2003). Linking soil microbial activity to water- and air-phase contents and diffusivities. *Soil Sci. Soc. Am. J.* 67, 156–165. doi: 10.2136/sssaj2003.1560

Schmidt, H., Vetterlein, D., Kohne, J. M., and Eickhorst, T. (2015). Negligible effect of X-ray mu-CT scanning on archaea and bacteria in an agricultural soil. *Soil Biol. Biochem.* 84, 21–27. doi: 10.1016/j.soilbio.2015.02.010

Schmidt, M. W. I., Torn, M. S., Abiven, S., Dittmar, T., Guggenberger, G., Janssens, I. A., et al. (2011). Persistence of soil organic matter as an ecosystem property. *Nature* 478, 49–56. doi: 10.1038/nature10386

Sexstone, A. J., Revsbech, N. P., Parkin, T. B., and Tiedje, J. M. (1985). Direct measurement of oxygen profiles and denitrification rates in soil aggregates. *Soil Sci. Soc. Am. J.* 49, 645–651. doi: 10.2136/sssaj1985.036159950049000 30024x

Sleutel, S., Bouckaert, L., Buchan, D., Van Loo, D., Cornelis, W. M., and Sanga, H. G. (2012). Manipulation of the soil pore and microbial community structure in soil mesocosm incubation studies. *Soil Biol. Biochem.* 45, 40–48. doi: 10.1016/ j.soilbio.2011.09.016

Sleutel, S., Cnudde, V., Masschaele, B., Vlassenbroek, J., Dierick, M., Van Hoorebeke, L., et al. (2008). Comparison of different nano- and micro-focus X-ray computed tomography set-ups for the visualization of the

soil microstructure and soil organic matter. *Comput. Geosci.* 34, 931–938. doi: 10.1016/j.cageo.2007.10.006

Strong, D. T., De Wever, H., Merckx, R., and Recous, S. (2004). Spatial location of carbon decomposition in the soil pore system. *Eur. J. Soil Sci.* 55, 739–750. doi: 10.1111/j.1365-2389.2004.00639.x

Swift, M. J., Heal, O. W., and Anderson, J. M. (1979). *Decomposition in Terrestrial Ecosystems*. Berkeley, CA: University of California Press.

Vlassenbroeck, J., Dierick, M., Masschaele, B., Cnudde, V., Van Hoorebeke, L., and Jacobs, P. (2007). Software tools for quantification of X-ray microtomography. *Nucl. Instr. Methods Phys. Res. A* 580, 442–445. doi: 10.1016/j.nima.2007.05.073

Conflict of Interest Statement: The authors declare that the research was conducted in the absence of any commercial or financial relationships that could be construed as a potential conflict of interest.

Pore-Scale Monitoring of the Effect of Microarchitecture on Fungal Growth in a Two-Dimensional Soil-Like Micromodel

Raghad Soufan[1], Yolaine Delaunay[2], Laure Vieublé Gonod[1], Leslie M. Shor[3], Patricia Garnier[2], Wilfred Otten[4] and Philippe C. Baveye[1]*

[1] UMR EcoSys, AgroParisTech, Université Paris-Saclay, Thiverval-Grignon, France, [2] UMR EcoSys, Institut National de la Recherche Agronomique, Université Paris-Saclay, Thiverval-Grignon, France, [3] Department of Chemical and Biomolecular Engineering, University of Connecticut, Mansfield, CT, United States, [4] School of Water, Energy and Environment, Cranfield University, Cranfield, United Kingdom

In spite of the very significant role that fungi are called to play in agricultural production and climate change over the next two decades, very little is known at this point about the parameters that control the spread of fungal hyphae in the pore space of soils. Monitoring of this process in 3 dimensions is not technically feasible at the moment. The use of transparent micromodels simulating the internal geometry of real soils affords an opportunity to approach the problem in 2 dimensions, provided it is confirmed that fungi would actually want to propagate in such artificial systems. In this context, the key objectives of the research described in this article are to ascertain, first, that the fungus *Rhizoctonia solani* can indeed grow in a micromodel of a sandy loam soil, and, second, to identify and analyze in detail the pattern by which it spreads in the tortuous pores of the micromodel. Experimental observations show that hyphae penetrate easily inside the micromodel, where they bend frequently to adapt to the confinement to which they are subjected, and branch at irregular intervals, unlike in current computer models of the growth of hyphae, which tend to describe them as series of straight tubular segments. A portion of the time, hyphae in the micromodels also exhibit thigmotropism, i.e., tend to follow solid surfaces closely. Sub-apical branching, which in unconfined situations seems to be controlled by the fungus, appears to be closely connected with the bending of the hyphae, resulting from their interactions with surfaces. These different observations not only indicate different directions to follow to modify current mesoscopic models of fungal growth, so they can apply to soils, but they also suggest a wealth of further experiments using the same set-up, involving for example competing fungal hyphae, or the coexistence of fungi and bacteria in the same pore space.

Keywords: hyphae, spread, microfluidics, fungal highway, microscale

INTRODUCTION

An estimated 1.5 million species of fungi are present in terrestrial ecosystems (Hawksworth, 2001) where they fulfill a wide array of essential ecological functions, in particular in the global carbon cycle (Cromack and Caldwell, 1992). Their role in soil-plant feedback processes in the rhizosphere is widely regarded as key to achieving the estimated 100% increase in overall food production that will be needed in the next 25 years, amidst decreasing availability of suitable land and already overexploited surface- or groundwater resources (e.g., Sposito, 2013; Baveye, 2015; Baveye et al., 2018).

To maximize the benefits that can be derived from the involvement of fungi in these different contexts, we can rely on a wealth of qualitative information about these organisms. For centuries, it has been known that fungal colonies grow as an interconnected network of hyphae, collectively referred to as mycelium (Fricker et al., 2017). In soils, fungal hyphae absorb and mineralize stable biomolecules like cellulose or lignin. Since they can access organic matter and nutrients located in much tinier pores than those typically accessible to plant roots, fungi are able to provide sustenance that otherwise would be difficult for over 90% of vascular plants to take up on their own (Boddy, 1993). Many soil-borne fungi are pathogenic to plants, severely reducing crop production worldwide (Fisher et al., 2012), whereas others have antagonistic properties, or hyperaccumulate metal contaminants, making them particularly suited to remediate polluted soils (Stamets, 2005). Last in this quick overview, but certainly not least, fungi play a crucial role in stabilizing the architecture of soils (e.g., Miller and Jastrow, 2000).

Underpinning these ecologically important processes is the ability of fungi to invade the very convoluted pore space in heterogeneous soil environments, with its tortuous paths, multiple constrictions, and in some cases dead end spaces, all of which may be variably filled with water (Otten et al., 2001; Pajor et al., 2010). Tremendous technological advances over the last two decades, in particular the development of advanced X-ray computed tomography (CT) scanners, now allow the geometrical features of the pore space in which fungal hyphae grow to be determined at resolution of a few microns, which are adequate given typical widths of hyphae of the order of 3–17 μm. Various computer models have been developed in the last decade, which use this information derived from CT images to predict the spread of fungal biomass in soils (e.g., Falconer et al., 2012, 2015; Cazelles et al., 2013). These models predict the amount of fungal biomass that is likely to be present locally in the pore space, and their outputs appear reasonable in light of the few macroscopic observations available. These models have proven very useful to understand the possible effects of various soil parameters, e.g., the connectivity and tortuosity of the pore space, on the proliferation of fungi or the interaction of competing fungal species in soils.

In a number of situations, for example during the bioclogging of soils (e.g., Baveye et al., 1998) or when trying to understand how the presence of fungal hyphae could affect the retention and transport of water in soils, not just the amount of fungal biomass likely to be present locally, but also the precise location and configuration of fungal hyphae in soil pores, may have a significant influence on processes of interest. Unfortunately, the only experimental information available to us at this point, at the microscopic scale, about the growth pattern of fungal hyphae in soil pores has not evolved much in the last 30 years. Some progress has been made in the 3D visualization of the configuration of fungal hyphae in systems constituted of polystyrene beads (Lilje et al., 2013) or in wood. Recent advances in the visualization of root hairs of similar diameter as fungi in small samples using synchrotron X-ray CT does demonstrate that at least in very small samples visualizing fungi might be possible (Koebernick et al., 2017). It is however noted that relative to the scale of fungal colonies and over which nutrient can be translocated such sample sizes would not be representative to capture colony development. Therefore, in actual soils, the only way to visualize fungal hyphae is through snapshots that one can get after preparing soil thin sections (e.g., Harris et al., 2002, 2003), or stabilizing soil samples for electron microscopy (e.g., Foster, 1988). The resulting images provide us with very useful information about hyphae and what surrounds them at discrete locations in soils at specific instants of time. However, it has been so far impossible to derive from these snapshots a reliable picture of the environmental and morphological parameters that control the 3-dimensional path followed by individual fungal hyphae in soil pores. Some fungi, like *Rhizoctonia solani,* exhibit a remarkably constant, undoubtedly genetically-determined behavior when grown in Petri dishes, with virtually constant branching angles and average internodal distances (Boswell and Hopkins, 2008; Boswell and Davidson, 2012; Hopkins and Boswell, 2012; Choudhury et al., 2018). It is tempting to assume that the same characteristics are exhibited when this organism grows in the pore space of a soil, but there is no reason at this point to believe that this assumption is warranted. In fact, it seems safe to take as a working hypothesis that the frequent presence of obstacles in the path of the spreading hyphae in soils is likely to modify significantly the behavior of *R. solani* compared to what it is in Petri dishes. Indeed is has been shown that colony geometry is to a large extent determined by connected tortuous pathways on soil (Otten and Gilligan, 1998; Otten et al., 1999). Following Watts et al. (1998), one might for example assume that fungal hyphae in soils are likely to manifest some type of thigmotropism, by which they would tend to remain in contact with solid surfaces after they encountered them during their foraging in the soil pore space.

Direct dynamic observations of the spread of fungal hyphae in soils are clearly direly needed, to find out to what extent the spreading and branching patterns of fungal hyphae in soils differ from those on Petri dishes. At the moment, the best opportunity we have to get a glimpse of the dynamics of hyphae in soil pores appears to be in two dimensions, by using so-called micromodels or microfuidic devices (e.g., Karadimitriou and Hassanizadeh, 2012; Stanley et al., 2016). Various authors (Hanson et al., 2006; Held et al., 2010, 2011; Hopkins and Boswell, 2012), a few years back, have used micromodels to visualize the spread of fungi. Their micromodels had rectilinear pores intersecting at right angle and of a width just a little bigger than that of hyphae. Since these early investigations, the design and manufacture of micromodels have evolved

noticeably. It is now possible to replicate faithfully the pore geometry of soils, using an inexpensive and biocompatible polymer, polydimethylsiloxane (PDMS), that offers excellent optical clarity. Deng et al. (2015) and Rubinstein et al. (2015) have used such a soil-like micromodel to observe the effect of bacterial activity on water or particle retention and movement in larger pores. Similar work with fungal hyphae has yet to be carried out.

In this general context, the key objective of the research described in the present article was to find out, apparently for the first time, if micromodels can indeed be used to monitor the growth of fungi in confined pore spaces similar to those found in soils, and to elucidate the mechanisms that control this growth. *R. solani* was selected as the target organism in part for the fact that it does not produce spores, which would complicate the dynamics, and for its remarkably predictable behavior in unconfined situations, but also because its growth in Petri dishes is described with particularly striking realism by a computer model developed by Hopkins and Boswell (2012) and extended recently to three dimensions (Vidal-Diez de Ulzurrun et al., 2017). The key ingredients of this model are briefly outlined in the section that follows this introduction, and serve as a guide later on to determine to what extent the growth pattern of hyphae observed in the microcosms differs from the "normal" 2-dimensional behavior out in the open. The article concludes with a quick overview of the many perspectives the preliminary results obtained so far open up for future experimental research and modeling.

THEORETICAL ASPECTS

In the model of Hopkins and Boswell (2012), the mycelium is thought of as a network of inter-connected tubes (representing hyphae) through which various substances (including carbon, nitrogen, trace metals, and tip vesicles) are translocated as part of an internal cytoplasm. Hyphae are modeled as a discrete series of straight line segments. After every time interval of length Δt, the local substrate concentration changes due to translocation, uptake and diffusion. New line segments are included in the fungal network, corresponding to the processes of lengthening of existing tubes (apical extension), and creation of new tubes (subapical branching), according to a set of stochastic rules that depend in part on the local concentrations of internal substrate. A further transformation of the hyphal network may result from the fusion of hyphae that come into contact with each other, a process known as anastomosis. Hopkins and Boswell's (2012) model involves many aspects related to the translocation of chemicals or materials inside the hyphae, as well as a description of the response of hyphal tips to external gradients of an inhibitor produced by the fungus itself, and which diffuses in the surrounding medium. The components of the model that interest us most here, however, are related to parameters that control the elongation and branching of the hyphae.

Apical extension is represented schematically by the creation of a new (virtual) line segment of nominal length Δx that extends from the unconnected end of an existing line segment and represents the movement of the hyphal tip over a discrete time interval Δt. In addition to different tropisms associated with gradients in nutrient- or inhibitor concentrations, hyphal tips

also display small stochastic variations in their growth axis. To simulate the process of tip movement, a "velocity-jump" model is used, which basically assumes that the velocity of hyphal tip undergoes a biased circular random walk with its orientation remaining the same or changing by an angle $\pm\Delta\theta$ (termed a velocity jump) between successive time intervals and where the localized concentration of the inhibitor induces bias so that model tips have a tendency to move in the direction of lower inhibitor concentrations, according to detailed mathematical formulas for the probability of tip re-orientation by an angle $\Delta\theta$, clockwise or anti-clockwise.

Sub-apical branching is modeled by the creation of new line segments emerging from the ends of existing line segments. Since turgor pressure is thought to be implicated in the branching process (Gow and Gadd, 1995; Riquelme and Bartnicki-Garcia, 2004), the model assumes that in the time interval Δt, the probability of an existing line segment k to generate a new line segment from its end position is zero unless the internal substrate concentration exceeds a critical concentration β. The new line segment is oriented at an angle $\pm\phi$ relative to the existing line segment with equal probability (Paulitz and Schroeder, 2005), and the internal substrate is uniformly divided between the existing and the new line segment.

Hopkins and Boswell (2012) parameterize their model with data from the literature, relative to *R. solani*. The hyphal line segment length Δx and the angular step size $\Delta\theta$ are taken to be 50 μm and $\pi/12$ radians (9°), respectively, following Riquelme et al. (1998). The branching angle ϕ is considered to be normally distributed, with mean of 79.2° and a standard deviation of 3.16°. This value of the branching angle may seem a little low, since many authors have pointed out that *R. solani* branches at right angle (90°). Nevertheless, the lower value adopted by Hopkins and Boswell (2012) has been borne out by recent experimental data. The very detailed monitoring of the growth of several fungi in Petri dishes over a 75 h timeframe, carried out by Vidal-Diez et al. (2015) using image analysis techniques, indicates that hyphae of *R. solani* branch at an angle that is in fact slightly lower than 90°, at 81.93 ± 1.15°. Nevertheless, the small standard deviation shows that it is still reasonable to view this value as virtually constant over time. The same feature seems to be also manifested by a parameter, the internodal length, which is not involved in Hopkins and Boswell's (2012) model, but is straightforward to measure in images of fungal hyphae. It corresponds to the average distance between septa (internal cross-walls separating cells in the hyphae). Vidal-Diez et al. (2015) report that the internodal length of *R. solani* first decreases from 175 to 171 μm over the first 17 h of growth, then increases stepwise to reach 180 μm at the end of 75 h. Overall, the average internodal distance they report is 179.29 ± 11.27 μm.

MATERIALS AND METHODS
Micromodel Concept and Fabrication
The microfluidic device, or micromodel, concept adopted in this research, as well as its manufacturing, have been described in detail in the recent article by Deng et al. (2015), which contains full references to earlier work as well as equipment information. To make the present article as self-contained as

possible, we shall reproduce here some information on the design and manufacturing of the micromodels. The original, much more thorough description of Deng et al. (2015) should however be consulted to obtain complete specifications.

In a nutshell, each micromodel is comprised of three parallel channels each one mm wide and 34 μm high connected to a single inlet well and a single outlet well (**Figures 1A,B**). The central, 10-mm long portion of each of the channels consists of a microstructured region, with pillars of varying sizes and shapes representing a two-dimensional slice of the solid phase of a simulated sandy loam soil (**Figure 1C**). The geometry of the microstructured region is based on a realistic computer-generated three-dimensional packing of ellipsoidal particles. The size distribution of the particles is based on an experimentally-determined sandy loam particle size distribution comprised of 56% fine sand and 44% very fine sand (USDA size ranges: 125–250 mm and 50–125 mm, respectively).

To create the soil geometry, ellipsoidal particles were randomly placed in a three-dimensional computational domain, and the packing algorithm DigiPac (Jia and Williams, 2001) was employed to create realistic particle-particle contacts. Then, a two-dimensional slice of the packed three-dimensional domain with a suitable level of pore connectivity was selected. The selected slice was then manually traced using the Raster Design toolset in AutoCAD 2010 and partitioned to completely fill the 1 mm x 10 mm microstructured region in a high-resolution chrome on-glass photomask. The geometrical features of the pseudo-2D soil pattern are as follows: particle diameters averaged

110 μm and ranged from 10 to 300 μm, and the hydraulic pore radius averaged 44 μm and ranged from 16 to 130 μm. In contrast with typical porosities of sandy loam soils, which are in the range of 25–35%, the porosity of Deng's et al. (2015) pseudo-2D emulated soil micromodel is 57%. This increase in porosity is a result of selecting in the simulated porous medium a slice that maintains pore connectivity in 2-D.

The photomask described above was then used to fabricate the reusable casting mold, called the "master," via photolithography. First, a thin layer of SU-8 2025 photoresist was spin-coated onto a 4-inch diameter Si wafer. The thickness of the photoresist coating was 34 ± 3 μm as determined by profilometry. Then, the photoresist was patterned by selectively exposing transparent regions in the photolithography mask to 26.4 mWcm^{-2} ultraviolet light for 6.1 s then finished by cross-linking and developing steps. Finally, the master was "silanized," or coated with (tridecafluoro-1,1,2,2-tetrahydrooctyl)trichlorosilane.

Individual emulated soil micromodels were cast 1 cm thick in PDMS. First, Sylgard 184 base and curing agent were mixed in a 10:1 ratio, degassed at −75 kPa gage for 30 min, then poured over the master and cured at 60°C for 4 h. Cured castings were carefully peeled from the master (silanization facilitates release of the cured PDMS from the master), trimmed, and access ports were manually punched from the patterned side using a 4 mm biopsy punch. Finally, each casting was treated with O_2 plasma for 45 s in an evacuated air atmosphere and irreversibly bonded featured-side down to a clean glass microscope slide. The plasma treatment is desirable in order for the micromodels to better
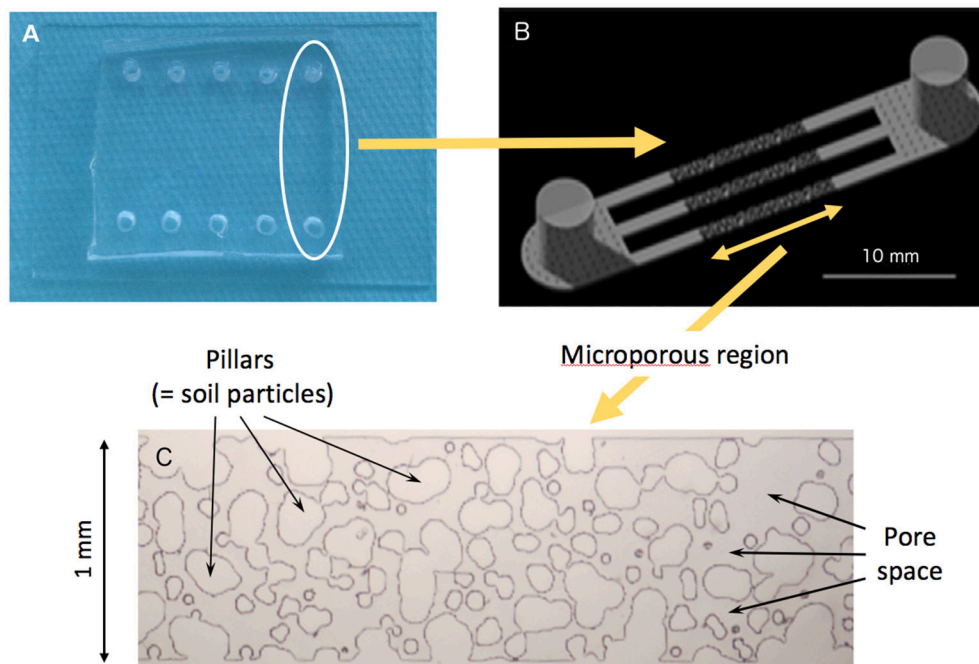

FIGURE 1 | (A) Picture of the experimental system showing the rows of inlet and outlet wells. **(B)** Each channel has a micro-structured region 10 mm long, 1 mm wide, and 34 ± 3 μm-deep, sandwiched between 5 mm-long open channels. Access ports are 1 cm high and 4 mm in diameter. **(C)** Micrograph of the 2-D pore structure, with pores (darker color) located between simulated soil particles (lighter color).

emulate soil since it results in PDMS having a surface charge similar to quartz sand (Roman and Culbertson, 2006), at least as long as the surface of the PDMS remains covered by water. Observations made by Cruz et al. (2017) suggests that the plasma treatment and the emulation of quartz-like surface chemistry are not permanent under unsaturated conditions. In such cases, the macromolecular mobility of the polymer at room temperature allows re-configuration at the surface, and the latter is relatively likely to have properties typical of untreated PDMS.

Cultivation of *R. solani* and Inoculation of Poppy Seeds

Potato dextrose agar (PDA) plates were inoculated with an anastomosis group (5) isolate of *R. solani* and incubated for 3 days at 23°C. Small plugs were cut from the edge of the plates and used as a source of inoculum. Following the inoculation technique adopted by Otten et al. (2012), poppy seeds (*Papaver rhoeas*) were autoclaved twice at 120°C at 1.1 Atm for 1 h over a 48 h period. Sterilized seeds were subsequently sprinkled over the PDA plates previously colonized by *R. solani*, and incubated at 23°C for 3 days.

Operation of Micromodels

The microporous portions of the channels were partially filled with sterile distilled water by injecting a small amount of water inside the access well on one side of the micromodel, and letting the water diffuse in the microporous region over time. Inspection under the microscope was used to determine, for each amount of distilled water applied, the portion of the channel porosity that was saturated.

Once the microporous region had reached equilibrium in terms of the water phase, colonized seeds were removed from the Petri dishes with the PDA, and were placed inside the access wells on the other side of the micromodel, relative to the access wells used to inject water. At this stage, the micromodel was introduced in a sterile Petri dish to maintain a suitable moisture level, but at the same time allow the exchange of oxygen and carbon dioxide with the atmosphere. The Petri dish was incubated for an initial period of 24 h before the microscopic observation of the fungal hyphae began.

Microscopy and Image Processing

Fungal spread in the channels of the micromodels was observed with a Brunel inverted light microscope (Brunel Microscope Limited, Wiltshire, U.K.). Pictures of the hyphae were typically collected as time series at regular intervals, usually one frame every 4 min. at selected locations, before the lens was repositioned on a different spot in the micromodel.

To enhance the quality and contrast of the images obtained with the light microscope, and allow easier visualization of the hyphae, the micrographs showing features of interest were processed with the imaging software Photoshop (Adobe Systems, San José, California), by selecting the green channel in the RGB format and changing its contrast setting. In some cases, false colors were added with an image analysis software (GIMP) to the liquid phase and to the simulated solid particles of the

micromodels, in order to make it clearer where the fungal hyphae spread.

RESULTS AND DISCUSSION

Spread of Hyphae in the Inlet Portion of the Micromodels

Prior to the experiments, it was not clear at all that *R. solani* would manifest any inclination to enter the 34 μm-high inlet section in the micromodels, leading to the microporous region (see **Figure 1**). Our expectation, encouraged by the opinion of several experts we consulted, was that *R. solani* would prefer to stay in the much roomier access well where the poppy seed was deposited, and would have to be enticed to go inside the channel inlet section. This enticement could in principle be carried out in a number of ways, for example via a piece of fresh wood placed in the opposite access well. Based on Fries (1973) observations, the release of volatile compounds by the wood, which would diffuse through the partially saturated microporous section, might be enough of an incentive for the hyphae to penetrate the micromodel. Another option would be to add a source of dissolved carbon to the distilled water injected inside the micromodel, which would have attracted the fungus.

As it turns out, the hyphae do not need any kind of incentive to penetrate the micromodels. Evidence indicates that they do so easily and spread readily away from the poppy seeds, into the inlet portion of the micromodels, and eventually in the microporous sections as well. Near the poppy seeds (**Figure 2a**), branching tends to be abundant, and anastomosis is frequent, making it difficult to determine the range of values exhibited for the branching angle, the hyphal line segment, or the intermodal distance. Close to the entrance of the microporous portion of the micromodel (**Figure 2b**), whenever *Rhizoctonia* does not grow along the wall of the cavity, the branching pattern is very similar to what was observed earlier in the PDA agar plates, which itself was in line with accounts published in the literature. In **Figure 2b**, hyphae, with a constant width of 7 μm, branch at angles of 62, 63, 78, and 63°, respectively, from bottom to top. Branching systematically occurs immediately before the septa on the main hypha, and the segment length is equal to the internodal distance, respectively 227, 236, and 256 μm for the three segments shown in **Figure 2b**. These values for the internodal distances are slightly larger than those of 179.29 ± 11.27 μm measured by Vidal-Diez et al. (2015).

One has to be careful in assigning values to the branching angles in the case of these experiments. Indeed, when growing on agar plates, fungal hyphae have a major incentive to branch out strictly at the surface of the agar, from which they derive energy and carbon. In the experiments described here, however, hyphae derive their sustenance strictly from the poppy seeds, and are therefore not bound metabolically to spread along the bottom surface of the micromodels, as they would be expected to do when growing in agar (even though, even in these cases, it is not infrequent to see them shoot upward as well). Inside the micromodels, branching hyphae can shoot upward at least
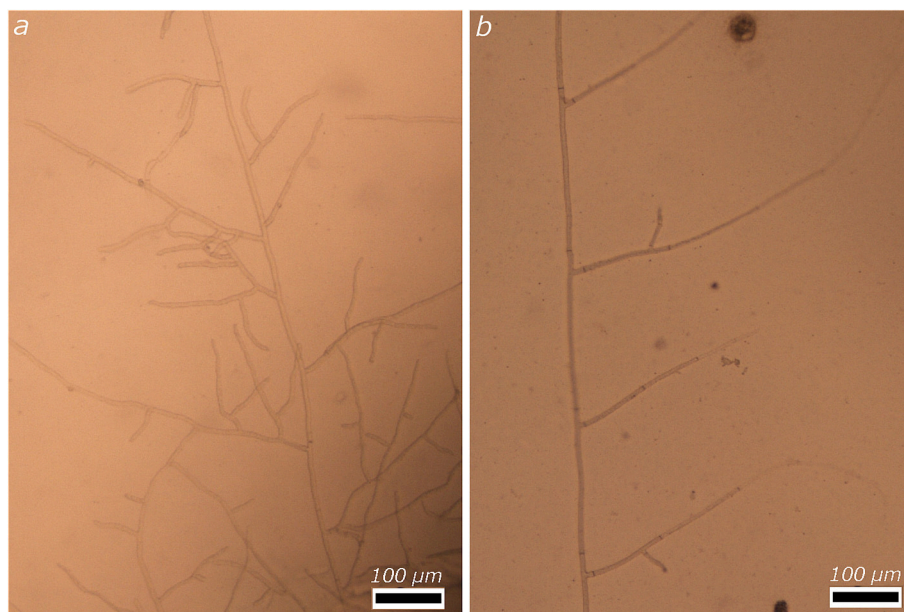
FIGURE 2 | Illustrative example of the growth of *R. solani* in the inlet section of the micromodel, **(a)** near the inoculation point, in the inlet well, and **(b)** hypha with 3 very regular segments, further toward the porous section of the micromodel.

initially, until they reach the 34 μm-high ceiling of the cavities inside the micromodels and are then forced to move horizontally or come back down. Analysis of the resulting images at too coarse a magnification gives the misleading impression of a branching angle that is very different than one would expect, when in fact, close analysis of the images shows sharp bends of the hyphae right after branching. This same process occurs within the microporous regions in the micromodels. In this article, whenever branching angles are mentioned, it is after careful evaluation of the branching at different focal distances of the microscope, to avoid gross misrepresentations.

Influence of Liquid Phase on Fungal Spread

After an initial period during which the hyphae propagate in the inlet regions of the channels, some hyphae tips reach the microporous region, which is variably saturated with distilled water. Based on previous observations by several authors (e.g., Otten et al., 1999), one anticipates at that point that the hyphae would tend to spread preferentially inside larger pores, which are not water filled. Indeed, this behavior is clearly evinced in our experiments (see **Figure 3**). Bundles of hyphae are seen in several images to converge to single air-filled pores and to grow there in preference to other portions of the pore space that are saturated with liquid. One needs to be careful in interpreting these observations because of the fact that the surface of the micromodels in the portions of the pores that are unsaturated are likely not to have properties similar to those of sand particles, because the plasma treatment of the PDMS is not permanent under these conditions. This point will need to be taken into account in future research. Be that as it may, the apparent preference for the unsaturated part of the pore space is not
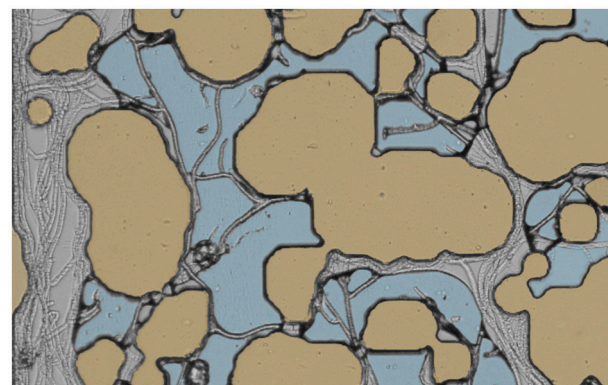

FIGURE 3 | Preferential spread of *R. solani* in air-filled pores. Flas colors have been added to highlight the different phases. The water is represented in blue, and the solid particles in brown. Hyphae are clearly seen to prefer growing in pores without water, even though some hyphae manage to grow inside the liquid phase. The width of the image corresponds to 1 mm.

exclusive. As many authors have pointed out, hyphae are capable of growing through water-filled space if need be, as seen in the water-filled parts of **Figure 3**. Indeed in a series of papers it was shown that *R. solani* used in this study spreads preferentially through water filled pores, larger pores and readily crosses cracks, but when given little choice does spread through smaller and water filled pores (Otten et al., 1999, 2004a,b).

Another feature that is manifested in this same image is the fact that, after a while, as the hyphae undoubtedly consume some of the liquid phase around them, or as the water slowly evaporates from the microcosms, the configuration of the liquid phase that

remains in the pores tends in places to adjust to the presence of the hyphae. Pockets of water exhibit external surfaces that appear to be unphysical from the standpoint of the theory of capillarity, e.g., with a concavity opposite to what one might expect based on the geometry of nearby solid surfaces. However, in many cases, these conflicting observations can be resolved once one realizes upon scrutiny of the micrographs that these interfaces are held in place by one or more fungal hyphae acting as a restraining net.

Linear Apical Extension and Growth Along Pore Walls

In many of the images of the water-saturated microporous regions of the micromodels, hyphae appear to be extending linearly for hundreds of microns without branching (**Figure 4**). Again, one needs to be very careful in that context, and make sure by changing the focal plane of the microscope that one does not miss branching that may occur vertically. But in the absence of such branching, the very long internodal distances that are apparent in these images are in sharp contrast with what has been routinely observed on agar plates.

When a hypha encounters a pore wall, as in **Figure 4** (at point b) and in **Figure 5** (at point a), there is a clear tendency for it to stay in contact with it for a while, as expected according to Watts et al. (1998), a phenomenon termed thigmotropism. This behavior is not entirely surprising and may be due in this case to some extent to electrostatic interactions. *R. solani* might react positively to electrical surface charge, as small as it might be (similar to that on sand particles) on the walls of the pillars in the micromodels. Common wisdom is that if one drags one's finger on a flat surface, producing static electricity in the process, fungal hyphae subsequently colonizing the surface will have a tendency to follow closely the path of the finger. By the same process, hyphae approaching a surface tangentially would have a tendency to keep following it closely afterwards, even if the surfaces curves. Nevertheless, it is clear from **Figures 4**, **5**, that this tendency does not associate the hyphae and surfaces indefinitely. At different stages in the progression of the hypha in **Figure 4**, and at point b in **Figure 5**, the hyphae begin to separate from the surfaces and eventually foray into the open pore space.

Hyphae Encountering Pore Walls "Head on"

Less predictable initially was what happens to fungal hyphae that run straight into a pore wall, as in **Figure 6**. As it touches the wall, the hypha in this image does not branch, as one might have expected. Instead, it seems to keep elongating. The apical region does not move, but the part of the hypha behind it progressively bends to accommodate the extra length that is generated over time. As the bending intensifies, the angle the apex makes with the surface reduces progressively, until the apex is eventually not encumbered by the surface any more, and can grow again, alongside it. This sequence of events, which is observed in many of the pictures we took, clearly deviates from the sequence of steps described by the model of Hopkins and Boswell (2012). In the presence of confining surfaces, fungal hyphae cannot be viewed as series of rigid, straight tubes connected with each other. Provision needs to be made in models for connected tubes to bend in response to constraints.

Branching Pattern

In a previous section, it was mentioned that hyphae can elongate sometimes more than a mm without branching (as in **Figure 4**), unlike what has been routinely observed on Petri dishes. This
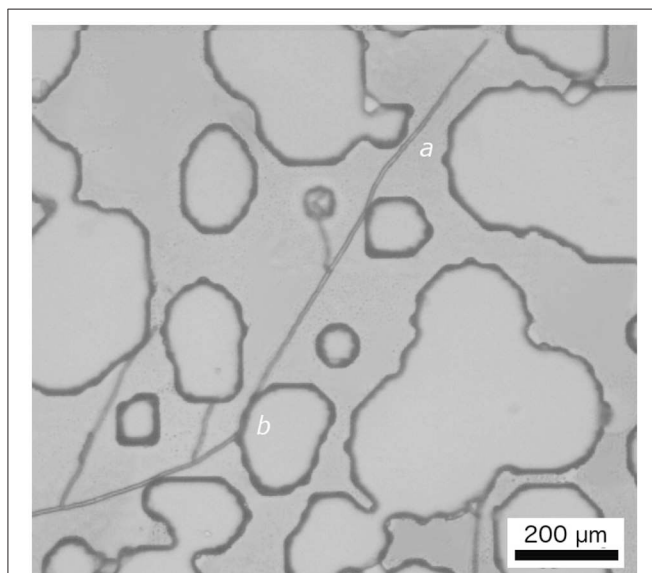

FIGURE 4 | Example of particularly long extension of hyphae in the water-saturated portion of the micromodel. (a) this very long hyphal segment does not show any appearance of branching yet, at the time the picture was taken. (b) At that point, the hypha touches the surface of the pore, and stays in contact with it for a little while, but eventually separates from the surface to return to the pore space.
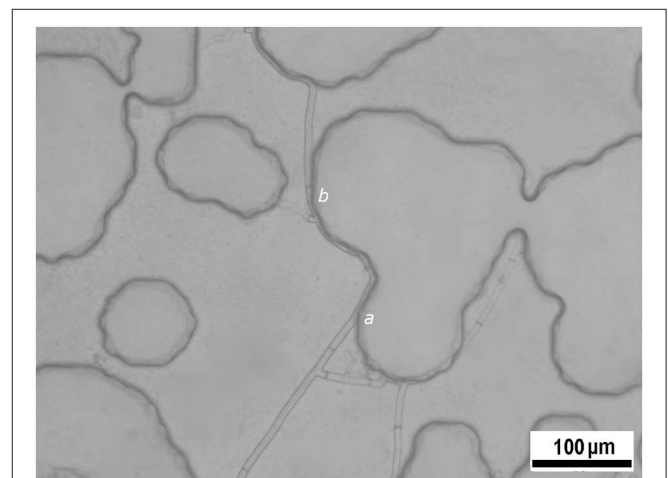

FIGURE 5 | Illustration of the tendency of hyphae to stay in close contact with pore walls once they encounter them (at point a). Nevertheless, this thigmotrophic process does not extend indefinitely, as the hypha eventually dissociates from the surface (at point b).
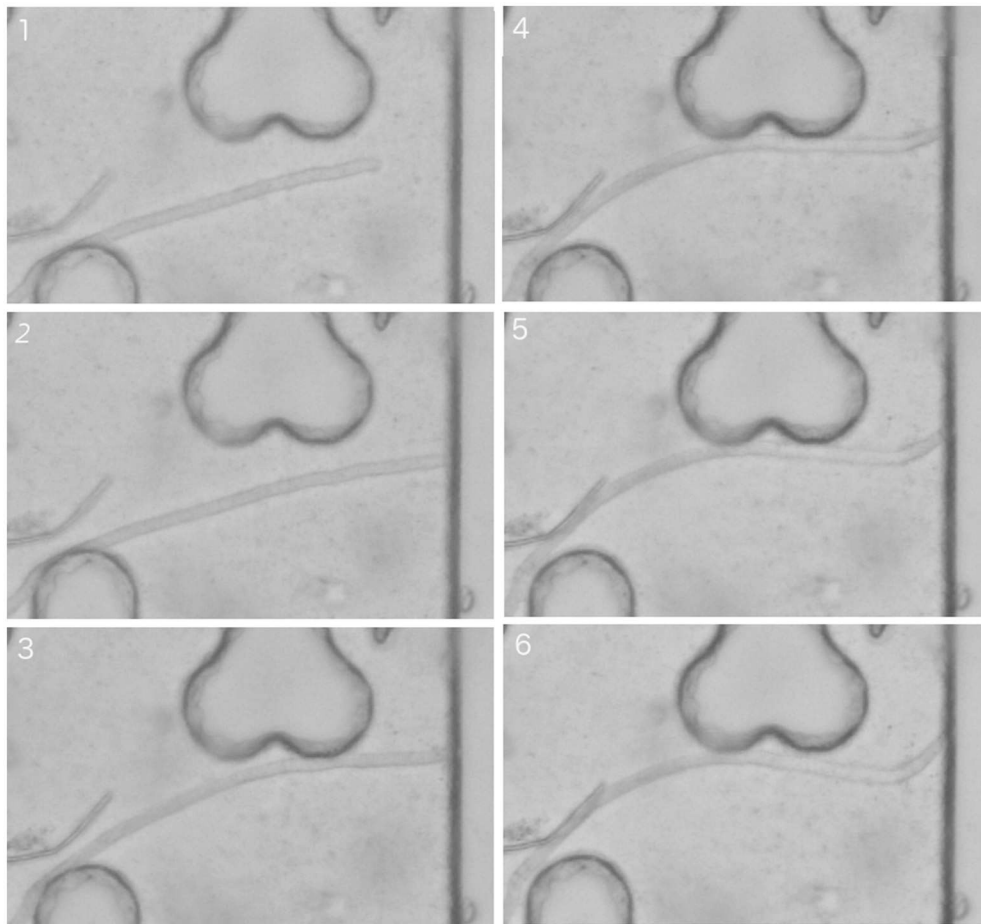
FIGURE 6 | Time sequence of 6 successive snapshots (1 to 6) of the propagation and bending of a hypha and its encounter "head on" with a pore wall.
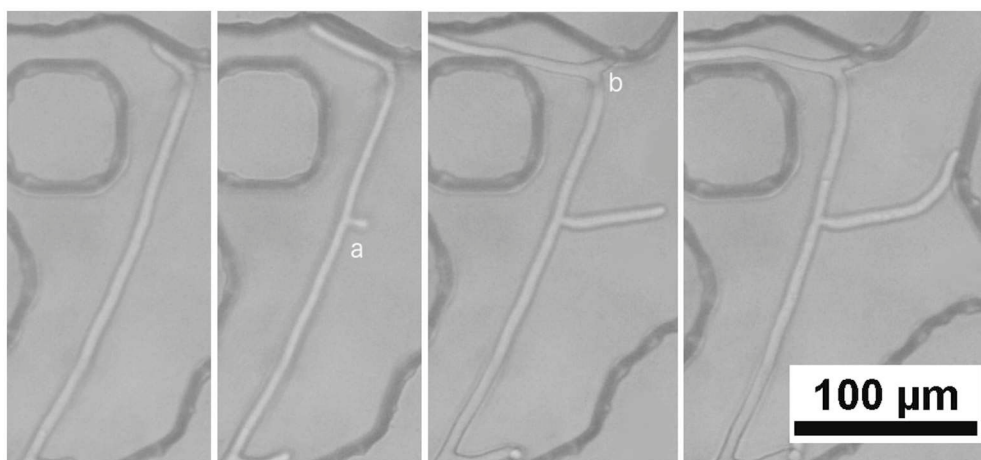

FIGURE 7 | Location and time sequence of the branching of a hypha. (a) at this point, immediately preceding a septum, branching seems to be very much like that observed in Petri dishes or in the inlet portion of the micromodel, whereas at (b) the branching seems to be closely associated with the strong bending of the hypha.

behavior may be due to the fact that hyphae in our experiments are surrounded by distilled water. There is therefore very little reason for the hyphae to branch out to scavenge more nutrients and energy from their environment. Nevertheless, hyphae do branch out at various times. Some of this branching, as in **Figure 7** at point "a," just before a septum, seems to be typical of what happens in Petri dish. But many cases of branching in the hundreds of images that we have taken seem to be as at point "b" in **Figure 7**, associated with bending of the hyphae, following a "head-on collision" with pore walls. The common explanation for the branching process, as mentioned earlier, is that it is related to turgor pressure inside the cell that eventually branch. Turgor pressure is a strictly osmotic process, related to the concentration of electrolyte inside the cytoplasm. However, it could be that the pressure felt inside the branching cell in soil pores is in fact more mechanical than osmotic. As the hypha elongates and is forced to bend, cells walls may be under sizeable stress, just as they would under regular turgor pressure.

CONCLUSION

The research described above corresponds to a first attempt to use a soil-like micromodel to identify the parameters that control the growth of fungal hyphae in the confining pore space of soils. The results suggest that *R. solani*, introduced in the micromodel on a poppy seed from which it subsequently propagates, is indeed able to penetrate into the microporous portion of the micromodel, without having to be enticed to do so. Once the fungus has penetrated inside the micromodel, a working hypothesis in the research was that the geometry of the pores, as well as the presence of hard surfaces in the path of the hyphae would influence the latter's behavior significantly. The experimental results support this hypothesis. Indeed, both the branching pattern as well as the apical elongation of the hyphae appear to be strongly affected by the presence of "obstacles" in soil pores. In particular, far from being series of straight and rigid tubes, hyphae of *R. solani* are able to bend after the forward movement of the apex has stopped. The observations reported in this article therefore suggest that the modeling of hyphal growth in soils cannot simply be viewed as a special case of growth in more open environments. A model tailored to soils will have to encompass very different growth mechanisms and characteristics.

This preliminary experiment shows that it is feasible to use micromodels to study the behavior of fungi under conditions that, although nearly 2-dimensional, are in many respects like those found in real soils. It will be interesting, in future experiments, to try to grasp better, quantitatively, the different parameters that control the growth of *R. solani*, and other fungi as well, in soil pores. This will require systematic replication so that statistics can be computed and the behavior of hyphae characterized in great detail. Further experiments could also address other aspects of the spread of fungal hyphae about which little is yet known, like what happens when different fungal species propagate in the same pore space in a soil, or when bacteria, hopping onto the external surfaces of hyphae, are carried along as the hyphae grows (a process often referred to as "hitchhiking on the fungal highway"). Clearly, there are a lot of avenues that can be pursued in this general context, all of which would result in a far better understanding than is currently available of the ecology of fungi in terrestrial environments.

REFERENCES

Baveye, P. C. (2015). Grand challenges in the research on soil processes. *Front. Environ. Sci.* 3:10. doi: 10.3389/fenvs.2015.00010

Baveye, P. C., Otten, W., Kravchenko, A., Balseiro Romero, M., Beckers, É., Chalhoub, M., et al. (2018). Emergent properties of microbial activity in heterogeneous soil microenvironments: different research approaches are slowly converging, yet major challenges remain. *Front. Microbiol.* 8:1364. doi: 10.3389/fmicb.2017.01364

Baveye, P., Vandevivere, P., Hoyle, B. L., DeLeo, P. C., and de Lozada, D. S. (1998). Environmental impact and mechanisms of the biological clogging of saturated soils and aquifer materials. *Crit. Rev. Environ. Sci. Technol.* 28, 123–191. doi: 10.1080/10643389891254197

Boddy, L. (1993). Saprotrophic cord-forming fungi: warfare strategies and other ecological aspects. *Mycol. Res.* 97, 641–655. doi: 10.1016/S0953-7562(09)80141-X

Boswell, G. P., and Davidson, F. A. (2012). Modelling hyphal networks. *Fungal Biol. Rev.* 26, 30–38. doi: 10.1016/j.fbr.2012.02.002

Boswell, G. P., and Hopkins, S. (2008). Linking hyphal growth to colony dynamics: spatially explicit models of mycelia. *Fungal Ecol.* 1, 143–154. doi: 10.1016/j.funeco.2008.10.003

Cazelles, K., Otten, W., Baveye, P. C., and Falconer, R. E. (2013). Soil fungal dynamics: parameterisation and sensitivity analysis of modelled physiological processes, soil architecture and carbon distribution. *Ecol. Modell.* 248, 165–173. doi: 10.1016/j.ecolmodel.2012.08.008

Choudhury, M. J. A., Trevelyan, P. M. J., and Boswell, G. P. (2018). A mathematical model of nutrient influence on fungal competition. *J. Theor. Biol.* 438, 9–20. doi: 10.1016/j.jtbi.2017.11.006

Cromack, K., and Caldwell, B. A. (1992). "The role of fungi in litter decomposition and nutrient cycling," in *The Fungal Community — Its Organization and Role in the Ecosystem,* eds G. C. Carroll and D. T. Wicklow (New York, NY: Marcel Dekker), 653–668.

Cruz, B. C., Furrer, J. M., Guo, Y. S., Dougherty, D., Hinestroza, H. F., Hernandez, J. S., et al. (2017). Pore-scale water dynamics during drying and the impacts of structure and surface wettability. *Water Resour. Res.* 53, 5585–5600. doi: 10.1002/2016WR019862

Deng, J., Orner, E. P., Chau, F., Anderson, E. M., Kadilak, A. L., Rubinstein, R. L., et al. (2015). Synergistic effects of soil microstructure and bacterial EPS on drying rate in emulated soil micromodels. *Soil Biol. Biochem.* 83, 116–124. doi: 10.1016/j.soilbio.2014.12.006

Falconer, R. E., Battaia, G., Schmidt, S., Baveye, P., Chenu, C., and Otten, W. (2015). Microscale heterogeneity explains experimental variability and non-linearity in soil organic matter mineralisation. *PLoS ONE* 10:e0123774. doi: 10.1371/journal.pone.0123774

Falconer, R. E., Houston, A. N., Otten, W., and Baveye, P. C. (2012). Emergent behavior of soil fungal dynamics: influence of soil architecture and water distribution. *Soil Sci.* 177, 111–119. doi: 10.1097/SS.0b013e31824 1133a

Fisher, M. C., Henk, D. A., Briggs, C. J., Brownstein, J. S., Madoff, L. C., McCraw, S. L., et al. (2012). Emerging fungal threats to animal, plant and ecosystem health. *Nature* 484:186. doi: 10.1038/nature10947.

Foster, R. C. (1988). Microenvironments of soil microorganisms. *Biol. Fertil. Soils* 6, 189–203.

Fricker, M. D., Heaton, L. L. M., Jones, N. S., and Boddy, L. (2017). The mycelium as a network. *Microbiol. Spect.* 5. doi: 10.1128/microbiolspec.FUNK-0033-2017

Fries, N. (1973). Effects of volatile organic compounds on the growth and development of fungi. *Trans. Br. Mycol. Soc.* 60, 1–21. doi: 10.1016/S0007-1536(73)80055-5

Gow, N. A., and Gadd, G. M. (1995). *The Growing Fungus*. London: Chapman and Hall.

Hanson, K. L., Nicolau, D. V. Jr., Filipponi, L., Wang, L., Lee, A. P., and Nicolau, D. V. (2006). Fungi use efficient algorithms for the exploration of microfluidic networks. *Small* 2, 1212–1220. doi: 10.1002/smll.2006 00105

Harris, K., Crabb, D., Young, I. M., Weaver, H., Gilligan, C. A., Otten, W., et al. (2002). *In situ* visualisation of fungi in soil thin sections: Problems with crystallisation of the fluorochrome FB 28 (CalcofluorM2R) and improved staining by SCRI Renaissance 2200. *Mycol. Res.* 106, 293–297. doi: 10.1017/S0953756202005749

Harris, K., Young, I. M., Gilligan, C. A., Otten, W., and Ritz, K. (2003). Effect of bulk density on the spatial organisation of the fungus *R. solani* in soil. *Fems Microbiol. Ecol.* 44, 45–56. doi: 10.1111/j.1574-6941.2003. tb01089.x

Hawksworth, D. L. (2001). The magnitude of fungal diversity: the 1.5 million species estimate revisited* *Paper presented at the Asian Mycological Congress 2000 (AMC 2000), incorporating the 2nd Asia-Pacific Mycological Congress on Biodiversity and Biotechnology, and held at the University of Hong Kong on 9-13 July 2000. *Mycol. Res.* 105, 1422–1432. doi: 10.1017/S09537562010 04725

Held, M., Edwards, C., and Nicolau, D. V. (2011). Probing the growth dynamics of Neurospora crassa with microfluidic structures. *Fungal Biol.* 115, 493–505. doi: 10.1016/j.funbio.2011.02.003

Held, M., Lee, A. P., Edwards, C., and Nicolau, D. V. (2010). Microfluidics structures for probing the dynamic behaviour of filamentous fungi. *Microelectron. Eng.* 87, 786–789. doi: 10.1016/j.mee.2009. 11.096

Hopkins, S., and Boswell, G. P. (2012). Mycelial response to spatiotemporal nutrient heterogeneity: a velocity-jump mathematical model. *Fungal Ecol.* 5, 124–136. doi: 10.1016/j.funeco.2011.06.006

Jia, X., and Williams, R. A. (2001). A packing algorithm for particles of arbitrary shapes. *Powder Technol.* 120, 175–186. doi: 10.1016/S0032-5910(01) 00268-6

Karadimitriou, N. K., and Hassanizadeh, S. M. (2012). A review of micromodels and their use in two-phase flow studies. *Vadose Zone Journal* 11. doi: 10.2136/vzj2011.0072.

Koebernick, N., Daly, K. R., Keyes, S. D., George, T. S., Brown, L. K., Raffan, A., et al. (2017). High-resolution synchrotron imaging shows that root hairs influence rhizosphere soil structure formation. *New Phytol.* 216, 124–135. doi: 10.1111/nph.14705

Lilje, O., Lilje, E., Marano, A. V., and Gleason, F. H. (2013). Three dimensional quantification of biological samples using micro-computer aided tomography (microCT). *J. Microbiol. Methods* 92, 33–41. doi: 10.1016/j.mimet.2012. 10.006

Miller, R. M., and Jastrow, J. D. (2000). "Mycorrhizal fungi influence soil structure," in *Arbuscular Mycorrhizas: Physiology and Function*, eds Y. Kapulnik and D. D. Douds (Dordrecht: Springer), 3–18.

Otten, W., and Gilligan, C. A. (1998). Effect of physical conditions on the spatial and temporal dynamics of the soil-borne fungal pathogen *Rhizoctonia solani*. *New Phytol.* 138, 629–637.

Otten, W., Bailey, D. J., and Gilligan, C. A. (2004a). Empirical evidence of spatial thresholds to control invasion of fungal parasites and saprotrophs. *New Phytol.* 163, 125–132. doi: 10.1111/j.1469-8137.2004. 01086.x

Otten, W., Gilligan, C. A., Watts, C. W., Dexter, A. R., and Hall, D. (1999). Continuity of air-filled pores and invasion thresholds for a soilborne fungal plant pathogen, *R. solani*. *Soil Biol. Biochem.* 31, 1803–1810. doi: 10.1016/s0038-0717(99)00099-1

Otten, W., Hall, D., Harris, K., Ritz, K., Young, I. M., and Gilligan, C. A. (2001). Soil physics, fungal epidemiology and the spread of *R. solani*. *New Phytol.* 151, 459–468. doi: 10.1046/j.0028-646x.2001. 00190.x

Otten, W., Harris, K., Young, I. M., Ritz, K., and Gilligan, C. A. (2004b). Preferential spread of the pathogenic fungus *R. solani* through structured soil. *Soil Biol. Biochem.* 36, 203–210. doi: 10.1016/j.soilbio.2003. 09.006

Otten, W., Pajor, R., Schmidt, S., Baveye, P. C., Hague, R., and Falconer, R. E. (2012). Combining X-ray CT and 3D printing technology to produce microcosms with replicable, complex pore geometries. *Soil Biol. Biochem.* 51, 53–55. doi: 10.1016/j.soilbio.2012. 04.008

Pajor, R., Falconer, R., Hapca, S., and Otten, W. (2010). Modelling and quantifying the effect of heterogeneity in soil physical conditions on fungal growth. *Biogeosciences* 7, 3731–3740. doi: 10.5194/bg-7-3731- 2010

Paulitz, T. C., and Schroeder, K. L. (2005). A new method for the quantification of *R. solani* and *R. oryzae* from soil. *Plant Dis.* 89, 767–772. doi: 10.1094/PD-89-0767

Riquelme, M., and Bartnicki-Garcia, S. (2004). Key differences between lateral and apical branching in hyphae of *Neurosora crassa*. *Fungal Genet. Biol.* 41, 842–851. doi: 10.1016/j.fgb.2004.04.006

Riquelme, M., Reynaga-Peña, C. G., Gierz, G., and Bartnicki-García, S. (1998). What determines growth direction in fungal hyphae? *Fungal Genet. Biol.* 24, 101–109. doi: 10.1006/fgbi.1998.1074

Roman, G. T., and Culbertson, C. T. (2006). Surface engineering of poly(dimethylsiloxane) microfluidic devices using transition metal sol–gel chemistry. *Langmuir* 22, 4445–4451. doi: 10.1021/la 053085w

Rubinstein, R. L., Kadilak, A. L., Cousens, V. C., Gage, D. J., and Shor, L. M. (2015). Protist-facilitated particle transport using emulated soil micromodels. *Environ. Sci. Technol.* 49, 1384–1391. doi: 10.1021/es50 3424z

Sposito, G. (2013). Green water and global food security. *Vadose Zone J.* 12. doi: 10.2136/vzj2013.02.0041

Stamets, P. (2005). *Mycelium Running: How Mushrooms Can Help Save the World*. Berkeley, CA: Ten Speed Press.

Stanley, C. E., Grossmann, G., Casadevall i Solvas, X., and deMello, A. J. (2016). Soil-on-a-Chip: microfluidic platforms for environmental organismal studies. *Lab Chip* 16, 228–241. doi: 10.1039/C5LC0 1285F.

Vidal-Diez de Ulzurrun, G., Baetens, J. M., Van den Bulcke, J., and De Baets, B. (2017). Modelling three-dimensional fungal growth in response to environmental stimuli. *J. Theor. Biol.* 414, 35–49. doi: 10.1016/j.jtbi.2016.11.020

Vidal-Diez de Ulzurrun, G., Baetens, J. M., Van den Bulcke, J., Lopez-Molina, C., De Windt, I., and De Baets, B. (2015). Automated image-based analysis of spatio-temporal fungal dynamics. *Fungal Genet. Biol.* 84, 12–25. doi: 10.1016/j.fgb.2015.09.004

Watts, H. J., Véry, A. A., Perera, T. H., Davies, J. M., and Gow, N. A. (1998). Thigmotropism and stretch-activated channels in the pathogenic fungus *Candida albicans*. *Microbiology* 144 (Pt 3), 689–695. doi: 10.1099/00221287-144-3-689

In Situ X-Ray Tomography Imaging of Soil Water and Cyanobacteria From Biological Soil Crusts Undergoing Desiccation

Estelle Couradeau[1,2†], Vincent J. M. N. L. Felde[3†], Dilworth Parkinson[4], Daniel Uteau[3], Alexis Rochet[4], Charlene Cuellar[4], Geoffrey Winegar[4], Stephan Peth[3], Trent R. Northen[1] and Ferran Garcia-Pichel[2,5*]

[1] Environmental Genomics and Systems Biology, Lawrence Berkeley National Laboratory, Berkeley, CA, United States, [2] School of Life Sciences, Arizona State University, Tempe, AZ, United States, [3] Department of Soil Science, University of Kassel, Witzenhausen, Germany, [4] Advanced Light Source, Lawrence Berkeley National Laboratory, Berkeley, CA, United States, [5] Center for Fundamental and Applied Microbiomics, Biodesign Institute, Arizona State University, Tempe, AZ, United States

Biological soil crusts (biocrusts) are millimeter-sized microbial communities developing on the topsoils of arid lands that cover some 12% of Earth's continental area. Biocrusts consist of an assemblage of mineral soil particles consolidated into a crust by microbial organic polymeric substances that are mainly produced by filamentous bundle-forming cyanobacteria, among which *Microcoleus vaginatus* is perhaps the most widespread. This cyanobacterium is the primary producer for, and main architect of biocrusts in many arid soils, sustaining the development of a diverse microbial community. Biocrusts are only active when wet, and spend most of their time in a state of desiccated quiescence, from which they can quickly recover upon wetting. Despite their ecological importance for arid ecosystems, little is known about the mechanisms that allow biocrust organisms to endure long periods of dryness while remaining viable for rapid resuscitation upon wetting. We had previously observed the persistence of significant rates of light-dependent carbon fixation in apparently dry biocrusts dominated by *M. vaginatus,* indicating that it may be able to remain hydrated against a background soil of very low water potential. One potential explanation for this may be that the abundant exopolysaccharide sheaths of *M. vaginatus* can preferentially retain moisture thus slowing the water equilibration with the surrounding soil allowing for extended activity periods. In order to test this hypothesis we aimed to develop methodologies to visualize and quantify the water dynamics within an undisturbed biocrust undergoing desiccation. We used synchrotron based X-ray microtomography and were able to resolve the distribution of air, liquid water, mineral particles and cyanobacterial bundles at the microscale. We could demonstrate the formation of steep, decreasing gradients of water content from the cyanobacterial bundle surface outward, while the bundle volume remained stable, as the local bulk water content decreased linearly, hence demonstrating a preferential retention of water in the microbes. Our data also suggest a transfer of hydration water from the EPS sheath material into the cyanobacterial filament as

desiccation progresses. This work demonstrates the value of X-ray tomography as a tool to study microbe-scale water redistribution in biocrusts.

INTRODUCTION

Biological soil crusts (biocrusts) are a community of micro and macroscopic organisms that develop in and on the surface layer of many soils worldwide (Belnap et al., 2016). They cover approximately 12% of Earth's terrestrial surface (Rodriguez-Caballero et al., 2018). Although they are widespread and can be found in all macroclimatic regions (Colesie et al., 2016), they are of special importance to dryland ecosystems because the biocrust organisms stabilize the soil against erosive forces through exopolysaccharide production (EPS) and increase soil fertility via the export of C and N to the soils they cover (Johnson et al., 2007; Strauss et al., 2012) and through the lixiviation of many other elements (Beraldi-Campesi et al., 2009). Biocrust organisms have developed various survival mechanisms in order to cope with a multitude of harsh environmental conditions (Pócs, 2009) that include high radiation (Garcia-pichel and Castenholz, 1991) and water scarcity (Rajeev et al., 2013).

Biocrusts are thought to have played an important role in shaping the Earth's terrestrial environments since the precambrian (Beraldi-Campesi and Garcia-Pichel, 2011; Beraldi-Campesi et al., 2014; Zhao et al., 2018). Mergelov et al. (2018) recently showed that the alteration of rocks by endolithic microbial communities is one likely pathway for the beginning of soils on Earth, and that the mechanisms of weathering and organic matter stabilization are strikingly similar to what can be observed in biocrusts nowadays. Present-day biocrusts mostly develop on bare (and often otherwise unconsolidated) substrate or young soils, triggering pedogenetic processes (Dümig et al., 2014). Depending on the various abiotic conditions, the conversion from bare substrate to the first successional stage of biocrust can take around 4 months (Ayuso et al., 2017). This first step is often the result of the activities of pioneer cyanobacteria such as *Microcoleus vaginatus,* a filamentous cyanobacterium that typically encompasses more than 25% of the early biocust microbial community (e.g., Kuske et al., 2012; Couradeau et al., 2016; Ayuso et al., 2017) particularly in areas with moderate temperature (Garcia-Pichel et al., 2013) and supports a community of heterotrophic bacteria and archaea through the release of a large variety of organic metabolites (Baran et al., 2015; Swenson et al., 2018). *M. vaginatus* not only enhances biocrust successional development through metabolic interactions but also directly enables the stabilization of soils particles and crust formation by binding soils particles to its large thallus (Garcia-Pichel and Wojciechowski, 2009), aided by the excretion of abundant exopolymeric substances (Rossi et al., 2012).

Biocrust biological activity is limited by the availability of liquid water. Upon rewetting *M. vaginatus* rapidly resumes

respiration (within seconds), and photosynthetic activity (within minutes) (Rajeev et al., 2013). Genomic analyses have revealed that, upon drying, the cells accumulate intracellular compatible solutes as a means to withstand turgor pressure changes associate with desiccation (Rajeev et al., 2013; Murik et al., 2017). In previous studies of desiccation dynamics in *M. vaginatus*-dominated crusts, extended metabolic activities were detected in apparently dry biocrusts (soil water potential of −85 MPa) (Rajeev et al., 2013) suggesting the presence of a mechanism for sustained metabolic activity past the point of soil hydration. Unlike other bacteria, *M. vaginatus* does not differentiate spores or akinetes while entering dormancy, and yet it is one of the most desiccation resistant cyanobacteria in soil crusts (Fernandes et al., 2018). It is an often mentioned possibility that EPS production may contribute to desiccation resistance, although exact mechanisms or experimental evidence are still lacking. In this regard, it is generally thought that the bacterial EPS matrix may help to slow down cell re-hydration during rapid wetting of the soil, as well as retard the loss of water during desiccation (Volk et al., 2016; Adessi et al., 2018), thereby dampening the severity of osmotic shocks and helping attain gradual reactivation (see, for example, Or et al., 2007). The speed and extent of these processes is likely depending largely on EPS concentration, as well as their amphiphilic property (i.e., their monosaccharidic composition and the amount of proteins and lipids).

Here we hypothesized that the bundle-forming behavior of *M. vaginatus* and its EPS production may play a role in the adaptation of this organism to desiccation stress. To examine this with a new approach, we used synchrotron X-ray microtomography to track in a quantitative manner the dynamics of liquid water distribution in soil and microbes *in situ* in a drying biocrust.

MATERIALS AND METHODS

Sampling Site and Sample Preparation

The biocrust sample was collected in Moab, Utah (38°42′55″ N−109°41′33″ W) in a site dominated by light biocrusts, using a 6 cm diameter Petri dish (**Figures 1A,B**), allowed to air dry before being stored dry, in the dark in a repository. At the time of the experiment, a 4-mm diameter core was taken from the sample using the end of 1 mL pipette tip, and placed on the tomography sample holder. Some 300 μL of MilliQ water (Millipore Corp., USA) was added on top of the core to exceed water retention capacity and form a film of water on the surface. X-ray tomography scans (see below) were recorded sequentially for 3 h every 10 to 40 min as the sample dried.
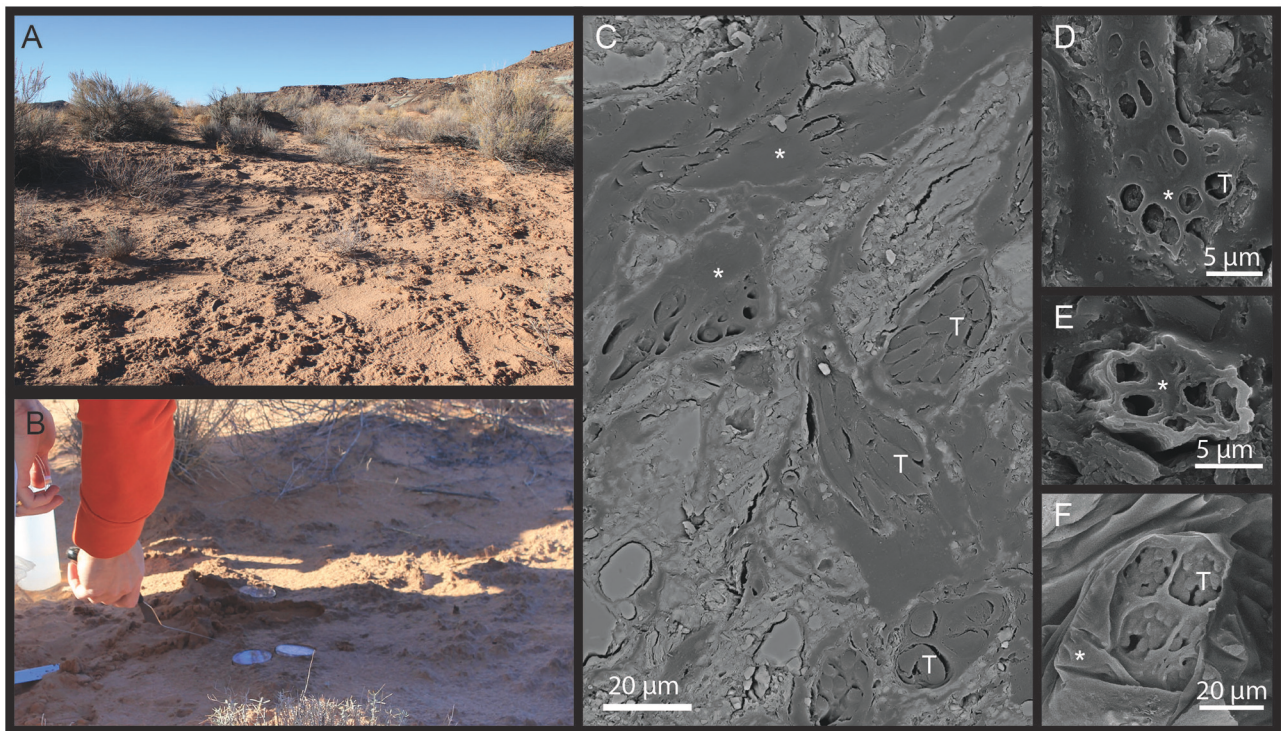
FIGURE 1 | (A) Aspect of the field site and **(B)** sampling illustration. **(C–F)** SEM pictures of a biocrust polished section using backscattered electron **(C)** and secondary electron **(D,E)** showing *Microcoleus* bundle (*) sheath material and cyanobacterial (T) trichomes *in situ*.

X-Ray Tomography Setup and Acquisition

X-ray tomography was performed at Beamline 8.3.2, the Hard X-ray Tomography beamline at the Advanced Light Source at Lawrence Berkeley National Laboratory (MacDowell et al., 2012). An X-ray energy of 25.7 keV was used, detection was accomplished with a 500 micron thick LuAG:Ce scintillator, a 5x Mitutoyo lens, and a PCO.edge sCMOS detector, yielding an effective voxel edge length of 1.3 μm. An exposure time of 250 ms per images was used, and the sample was rotated through 180 degrees while 1,025 images were collected for each scan. The temperature in the acquisition chamber was 24–27°C. The datasets analyzed for this study can be found in the Figshare repository https://doi.org/10.6084/m9.figshare.6447266.v1

Stack Reconstruction and Segmentation

Initial tomographic reconstruction was performed with image normalization and preprocessing implemented in FIJI/ImageJ (Schindelin et al., 2012) and tomographic reconstruction by the Octopus (XRE nv) software package. Subsequent reconstructions were performed using TomoPy (Gürsoy et al., 2014). The reconstructed stacks were processed and analyzed using MAVI (Modular Algorithms for Volume Images, Fraunhofer ITWM, Kaiserslautern) implemented in a Framework called ToolIP (Tool for Image Processing), where numerous analytical solutions can be automatized by means of flow processing charts. Custom python scripts developed for the ALS 8.3.2 beamline and used in this study can be found at https://bitbucket.org/berkeleylab/

als-microct-python/src. A region of interest (ROI), containing a large cyanobacterial bundle, was cropped out for further analysis. The ROIs were filtered with a median filter with a window size of 9^3 voxels to smooth noise effects (**Figure 2**). To avoid ring artifacts and low contrast interfering with the segmentation, we had to segment the images in small steps. To do so, a sobel edge detection was used to exploit the phase contrast of the images. The sobel filter performs a spatial gradient computation that emphasizes regions of high spatial frequency that correspond to edges (Canny, 1986). A watershed segmentation was performed on the edge image, matching the solid phase (sand grains) and segmenting the image in small and more homogeneous pieces. Each watershed was then binarized using the bisection algorithm based on the method of Vogel and Kretzschmar (1996). A low threshold had to be set to identify voxels belonging to the solid phase (lowest gray values correspond to highest density materials) and an upper threshold for the gray values that could be assigned clearly to any phase. A voxel in the intermediate gray value range was assigned to the solid phase, if a neighbor voxel already belonged to it; otherwise it was assigned to the pore space. Both thresholds were calculated as the 10% deviation from the calculated Otsu-threshold (Otsu, 1979). This segmentation procedure allowed a low-noise segmentation without further intervention. During segmentation, most filaments were assigned to the solid phase, as was obvious after visual inspection. As those fragments were 1–2 orders of magnitude smaller in volume than most sand grains, we could label all foreground regions
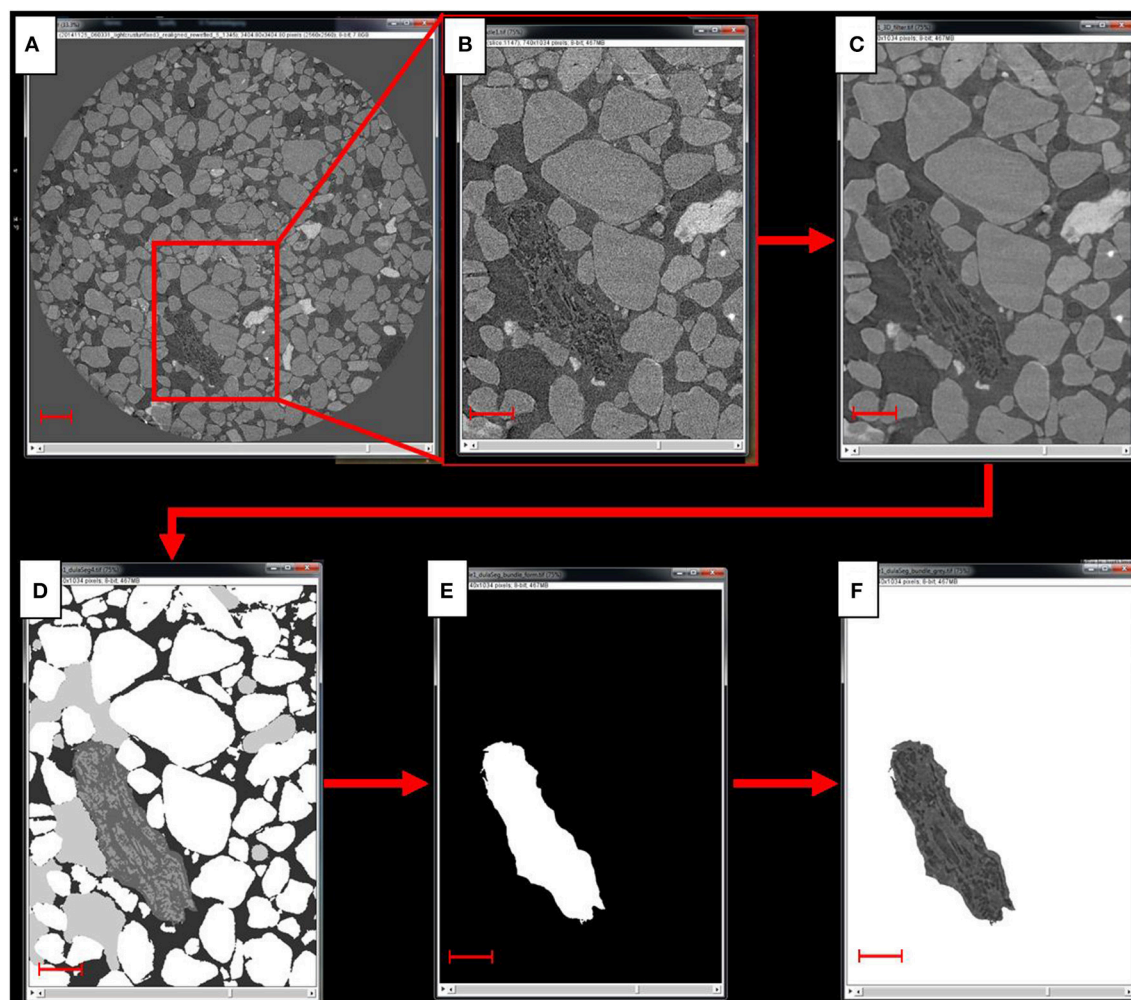
FIGURE 2 | Scheme of the image processing steps. From the reconstructed scan **(A)** a region of interest, or ROI, containing a large cyanobacterial bundle is cropped out **(B)**, to which then a 3D median filter is applied to reduce the noise **(C)**. Next, the image is segmented **(D)** and the segmented bundle **(E)** is used as a mask to cop out the bundle from the grayscale image of the ROI **(F)**. Scale bar in **(A)** equals 300 μm, scale bars in **(B–F)** equal 150 μm.

and eliminate the biggest classes by means of a 3D volume filter implemented in ToolIP-MAVI. Filament fragments but also fine sand grains then remained in the images. A closing operation was performed to merge filament fragments and aggregate them to form a structure that represents the bundle. The remaining fine sand grains were not close to the bundle; they remained more or less isolated from the rest and did not cluster by the effect of the closing operator. A volume filter was applied again, this time filtering all small objects (isolated grains) leaving only the mask of the bundle. A fillhole filter was finally applied to fill remaining holes in the bundle mask. The product of this procedure was used in the next steps. The isolation of the individual components of the cyanobacterial bundle (EPS sheath and cyanobacterial filaments) was performed by tracing them on a slice-by-slice basis using the Avizo (Avizo 3D software, ThermoFisher Scientific) segmentation editor interface, and these boundaries were slightly smoothed in the direction

orthogonal to the slices on which tracing was performed, to eliminate inconsistencies.

Data Analysis
Distribution of Water and Air in the Microenvironment of the Cyanobacterial Bundle

In order to quantify the distribution of water and air close to the cyanobacterial bundle during desiccation, we analyzed the pore space in increasing distances to the bundle. For this, used the segmented bundle to create 8 masks, each of which had a width of 4 μm. This was achieved by applying a dilation algorithm in ImageJ, which inflates the bundle by one voxel. According to the 1.3 μm voxel resolution, we repeated the dilation thrice in order to get distance steps of 3.9 μm. We included the microenvironment around the bundle up to a distance of 32 μm (resulting in 8 masks at different distances from the bundle in steps of of approximately 4 μm). These masks were used

to crop out the the regions from the already segmented ROI. Subsequently, we counted the voxels that were segmented as solid phase, water and air filled pores and calculated the volume by multiplying voxel count by voxel volume.

Bundle Volume and Surface

The volume of the bundle was calculated by counting the total number of voxels and multiplying this number with the voxel volume. The surface area was measured with the "isosurface" feature of the well-established BoneJ algorithm for ImageJ (Doube et al., 2010). This feature uses marching cubes to create a triangular surface mesh and calculates the object surface as the sum of the areas of the triangles (Lorensen and Cline, 1987). Because a larger cube is less sensitve to small differences in surface roughness, we chose a comparatively large size for the marching cube (edge length: 15 voxel) in order to compensate for the different segmentation schemes that were used for different time points.

Scanning Electron Microscopy

A piece of biocrust from the same site was fixed in 2% glutaraldehyde overnight at 4°C before being rinsed 4 times with water. It was then dehydrated in successive bath of increasing concentration of ethanol (20–40–60–80–100%) for 7 min each under slow agitation. Spurr resin was used for impregnation, increasing concentration of resin in ethanol (25–50–75–100%) were used to incubate the sample for 3 h each under slow agitation. A final 100% resin bath was conducted overnight before the polymerisation step that consisted of 24 h incubation at 60°C in 100% resin. Finally the biocrust block was polished down to 0.5 micron using diamond paste and cloth, before being coated with platinum in a Technics Sputter Coater and imaged with a JEOL JSM6300 SEM equipped with a secondary electron detector and a XL30 Environmental FEG (FEI) equipped with a backscattered electron detector.

RESULTS

Suitability of Synchrotron Based X-Ray Microtomography to Track Water Flow *in Situ* in Biocrusts

Synchrotron based X-Ray microtomography was valuable for our purposes in that it is one of the few techniques that enables *in situ* visualization of a hydrated soil with enough contrast to resolve liquid water from air, while providing a spatial resolution sufficient to capture large cells (Aravena et al., 2011, 2014). Here we used it to image bundles of filamentous cyanobacteria *in situ* in a quartz dominated soil and their immediate surroundings. Classic SEM images of dried and embedded pieces of biocrust from the same source showed that individual, dry *Microcoleus vaginatus* filaments are ∼2–3 μm in diameter, assemble into a small bundle that further assembles in larger bundles, each unit being encased by EPS sheath material (**Figure 1**). We used these characteristics to recognize cyanobacterial bundles and their internal structure using synchrotron X-Ray microtomography, choosing one bundle of large size and following its behavior through desiccation. We were able to segment the interfaces

between liquid water, gas phase, soil grains, and bundle as well as the inner components of the bundle, namely trichomes (cellular filaments) and EPS sheath material, (**Figure 2**); we could track them through a complete desiccation time series.

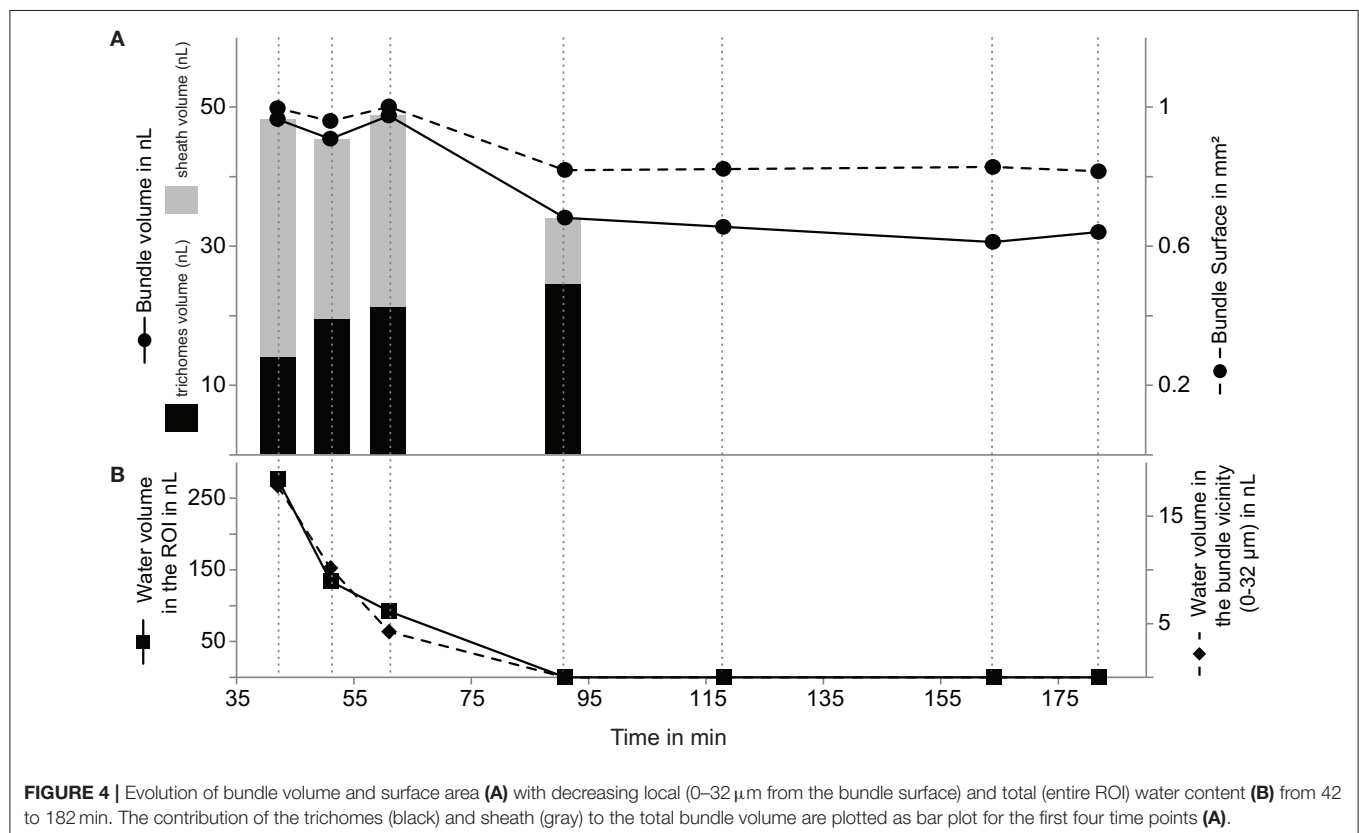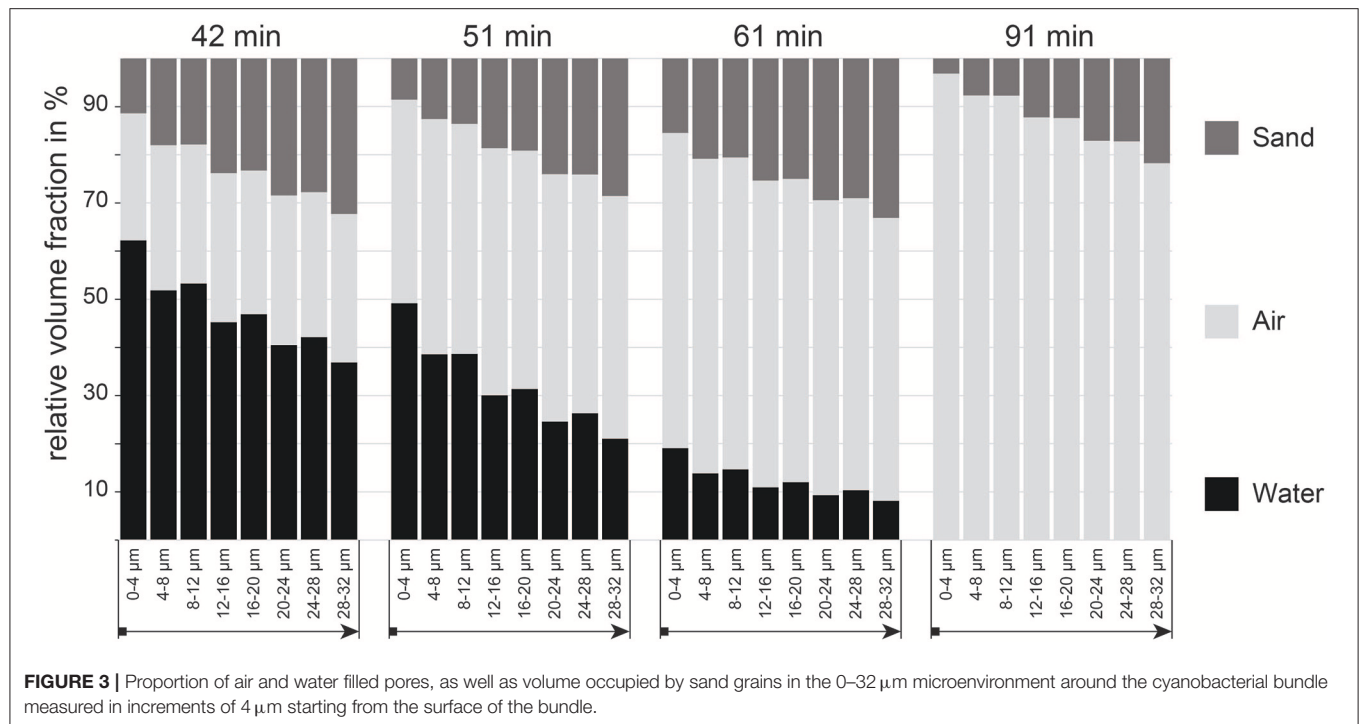## Analysis of the Microenvironment Around the Bundle

The analysis of the pore space around the bundle clearly shows a trend of decreasing water contents and porosity (i.e., more unconsolidated sand particles) with increasing distance away from the bundle (**Figure 3** and Table S1). This is true for the complete time sequence (42–91 min). During the initial phase of desiccation our data indicates the formation of a steep gradient in water availability decreasing away from bundle. The steepness of this gradient (i.e., the difference between the water content in the closest (0–4 μm) and farthest regions (28–32 μm) measured) decreases as the crust dries out. It is also evident from **Figure 3** that the total porosity (that is, the volume around the bundle that is not occupied by sand grains) increases, especially close to the bundle. It is likely that this pattern is caused by the physical shrinking of the bundle, i.e., space that was occupied by the bundle in the (swollen) hydrated state turns to air-filled pore space since sand grains remain at their initial position. This last observation demonstrates that the bundle sheath was not sufficiently strongly attached to the surrounding sand grains, so as to pull them along inwardly as the bundle shrunk (**Figure 4A**).

The Cyanobacterial Bundle Holds on to Water Throughout Desiccation

Expectedly, the volume and surface area of the bundle followed a similar dynamics. Unexpectedly, this dynamics had three differentiated phases. Bundle surface and volume remained relatively constant for the first hour, only to decrease noticeably between 61 and 91 min, then remaining again rather constant until the end of the experiment at 182 min (**Figure 4A**). This is especially noteworthy because the liquid water content in the full region of interests that we measured decreased much faster and more completely than the observed changes in bundle dimensions (**Figure 5**). The same dynamics of complete and linear desiccation could be observed in the water content of the region in the immediate vicinity of the bundle (0–32 μm; **Figure 4B**). This suggests the presence of a mechanism that retards water loss in the trichomes and sheath. Noting that hydrated microbial cells are some 80 percent water (by weight, and roughly volume), the final volume attained is at least 3 times larger than that expected of a completely dry bundle. Judging from the tri-phasic dynamics of shrinkage in the bundle, this mechanism may have at least two distinct components.

Bundle Shrinkage Dynamics and Possible Transfer of Water Between Sheath EPS and Cells

Overall the bundle shrunk by 20% in surface area and 33% in volume during the course of the experiment (see Table S2), however the EPS-sheath and the trichomes (cell filaments), had markedly different responses to drying (**Figure 5**). The volume

FIGURE 3 | Proportion of air and water filled pores, as well as volume occupied by sand grains in the 0–32 µm microenvironment around the cyanobacterial bundle measured in increments of 4 µm starting from the surface of the bundle.

FIGURE 4 | Evolution of bundle volume and surface area **(A)** with decreasing local (0–32 µm from the bundle surface) and total (entire ROI) water content **(B)** from 42 to 182 min. The contribution of the trichomes (black) and sheath (gray) to the total bundle volume are plotted as bar plot for the first four time points **(A)**.

of EPS decreased significantly (by 70%) between 42 and 91 min, from 34.3 to 14.0 nL. During the same period, however, the volume of trichomes increased gradually from 9.5 to 24.6 nL (for a total increase of 75%) (Table S3). This suggests the intriguing possibility that a net water transfer occurred from the sheath material to the trichomes during this period. This ratio change
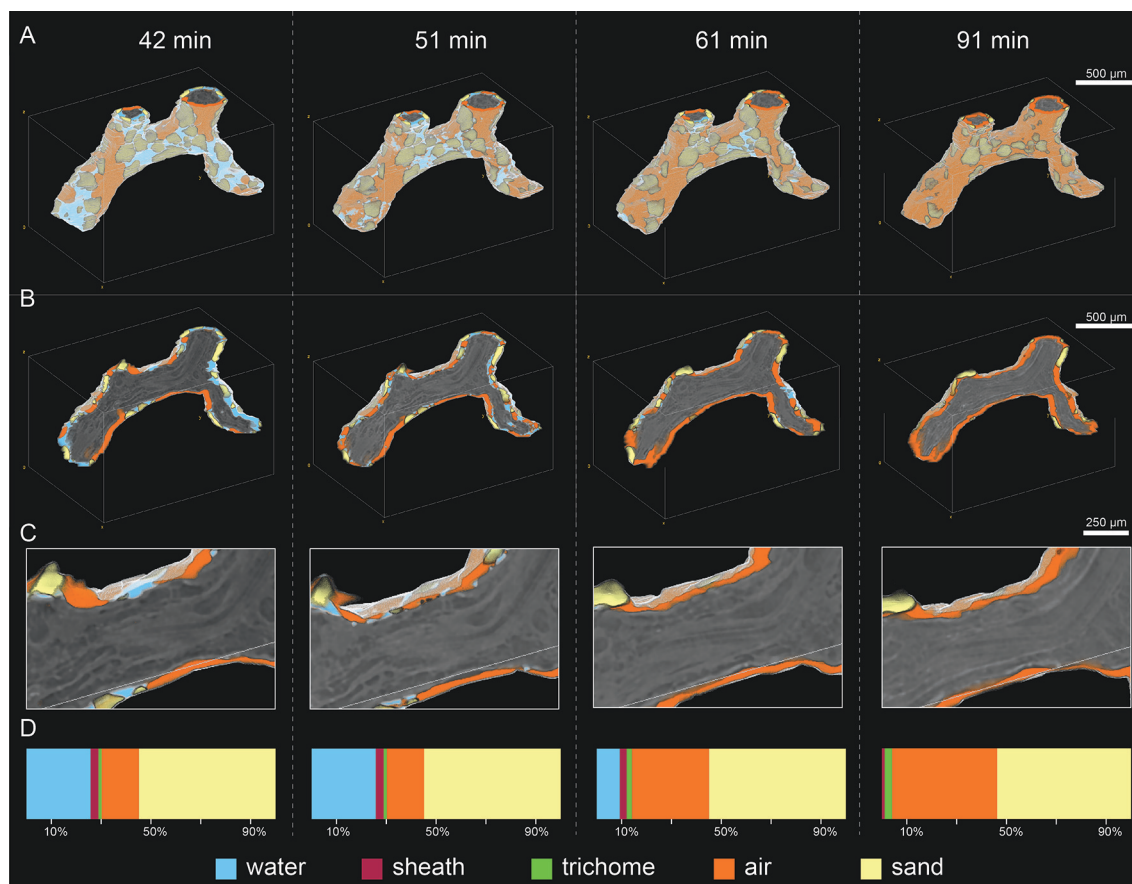
FIGURE 5 | Visualization of the full bundle **(A)**, a cross section of it **(B)** and a close-up cross section view **(C)** showing the distribution of water, air and sand in the 0–32 μm microenvironment around the bundle during desiccation from 42 to 91 min. Percent contribution of water, air, sand, trichome and sheath to the entire ROI are shown in panel **(D)**.

from the sheath-EPS to trichomes is also apparent on the cross section in **Figure 5C**, where one observes a transition from a swollen and hydrated bundle with many hydrated dark regions toward a dehydrated filament (with brighter color and thus, less water).

DISCUSSION

Preferential Water Retention Could Be Behind Sustained Metabolic Activity of *Microcoleus* in Dry Soils

The fact that the volume of the bundle is reduced to 66% of its initial size is likely a result of the loss of water during desiccation from 42 to 182 min. However, the data acquisition might not have captured the total desiccation process as one would expect a water content of 80% in fully hydrated stage. It is therefore possible that the bundle still contained water more than 90 min after the bulk soil was completely devoid of liquid water or that its volume was already less than the initial, fully hydrated at the first time point examined here. Over the course of the desiccation process, the volume ratio of sheath to trichomes changed gradually from 2.45

to 0.38 (**Figure 4A**, Table S3). The most likely explanation is that the trichomes absorbed water from the fully hydrated sheath EPS. A potential mechanism to drive the preferential transfer of sheath hydration water to the trichomes, rather than losing it to the pore space, may be a decreased intracellular water potential caused by the well-known accumulation of trehalose as a compatible solute in *Microcoleus vaginatus* as it undergoes desiccation (Rajeev et al., 2013). This accumulation can occur rather swiftly at the expense of intracellular glycogen reserves (Baran et al., 2013).

Water Holding Capacity of Sheath EPS Results in Effective Halting of Desiccation Fronts

Our results demonstrate for the first time directly that the cyanobacterial bundle and more particularly its sheath EPS material effectively remained hydrated while the surrounding soil pore regions were steadily drying. Although the nature of X-ray tomography limited our analyses to a single region in a single biocrust sample due to the work-intensive manual segmentation process (see methods), the observations that we made with our novel approach are consistent with the long-standing views on

the role of extracellular investments (sheaths capsules, diffuse EPS) in microbial adaptations to desiccation in general (see reviews by Potts, 1994; Rossi and De Philippis, 2015), and in soil crust systems in particular (Campbell, 1979; Or et al., 2007; Fischer et al., 2010). For example, our results also echo the observations made by Rosenzweig et al. (2012) and Adessi et al. (2018) who respectively showed that adding an EPS-analog to any soil increases water retention due to EPS water holding capacity and that preferential EPS extraction from a biocrust results in lessened water retention. These observations were also confirmed by Colica et al. (2014) who described a positive correlation of EPS and water retention in newly formed biocrusts associated with a significantly negative correlation of EPS concentration and hydraulic conductivity. One should be careful, however, in trying to explain the properties of crust EPS, from what one sees in a single species, namely *M. vaginatus*, given that crusts contain a large variety of mucus producing microbes, not only cyanobacteria but many of the bacterial heterotrophs as well (i.e *Sphingomonas mucosissima;* Reddy and Garcia-Pichel, 2007).

Bundle-Mineral Particle Interaction

Our observation that the sheath EPS of *M. vaginatus* may not be strongly adherent to the sand grains can help shed light on previous studies. The fact that the sand grain are pulled away from the bundle during dry-down could be explained by their attachment to matrix EPS rather than sheath EPS, another type of biocrust EPS that would also shrink upon dry-up (Rossi et al., 2017). Rossi et al. (2012) used a non-invasive method for the extraction of EPS and noticed a change in the albedo and in the infiltrability of a variety of crusts after the treatment. This was hypothesized to be the outcome of the collapse of larger pores after the EPS were removed. In order to test this hypothesis, Felde et al. (2016) extracted the EPS from BSCs of four different ecosystems and scanned them before and after the extraction with a high-resolution μCT to quantify structural changes. Unexpectedly, no significant effect of the EPS extraction on the properties of the pore system was found in that study. However, this is consistent with the findings of our present study, where we could show that the EPS from the sheath did not strongly adhere to the sand grains, as their proportion in the microenvironment of the bundle decreased with desiccation, meaning that they stayed in place, while the bundle reduced its volume.

Benefits and Limitations of X-Ray Microtomography for Soil Microbiome Research

X-ray microtomography has been used for more than two decades to elucidate soil properties, such as pore space geometry and connectivity (Spanne et al., 1993; Peth et al., 2008; Ma et al., 2015). The main value of this technique applied to soil studies is that it requires little to no sample preparation, preserves the soil structure, is non-invasive, and enables the imaging of the interior of micrometer to centimeter size samples composed of any mineral phase. However, in the case of synchrotron-CT, it uses specialized facilities that require significant organizational effort

before experimentation. It also requires intense computational efforts combined with expert decision making for segmentation, although these may in the future benefit from improved procedures based on machine learning. Menon et al. (2011) used it for the first time in dry biocrusts, imaging samples from the Kalhari desert to map pore structure and predict pathways of water flow. Neutron tomography (e.g., Tötzke et al., 2017), and X-Ray microtomography are the only techniques that allow resolution of *in situ* water flows (Aravena et al., 2014; Pot et al., 2015), but the spatial resolution of the former (∼10–100 microns) might not be best suited to resolve microbial cells or colonies whose size is typically an order of magnitude smaller. The spatial resolution of X-ray tomography, by contrast, can go down to <1 μm provided that samples are small enough (the voxel resolution is approximately in the order of 1/1,000 of the sample diameter, 1.3 micron in the present study), making it appropriate to advance soil microbiome research at relevant microbial scales. Beyond examination of soil water, Voltolini et al. (2017) for example, characterized the porosity of two soil aggregates to determine the volume accessible to microbial cells of differing size, making it possible to predict how favorable a soil could be to host connected microbial colonies. Further, using osmium to stain organic matter, Peth et al. (2014) were able to localize soil organics within soil aggregates. Here, taking advantage of the biocrust soil system, in which microbial communities are concentrated in the topmost millimeters of soil, and host large bundles of filamentous cyanobacteria, we could segment a large microbial colony (a bundle) and resolve its internal structure. Another point to take into account when considering applying this technique to microbial ecology in general is that even though nominally non destructive, the use of hard X-rays may damage the sample (in particular its biological component). It was shown for instance that it can induce death of large population of selected groups of organisms directly after the scan (Fischer et al., 2013) or have negligible effect depending the dose of X-ray and scan duration (Schmidt et al., 2015). In our case it prevented the cyanobacterium to migrate to the biocrust surface upon rewetting after the experiment (data not shown), which they invariably do when healthy (Pringault and Garcia-Pichel, 2004) suggesting that the imaging process may have impaired their physiology.

Bundle Forming Behavior

The bundle forming behavior clearly limits the ability of light and nutrients to reach cyanobacterial trichomes inside of this crowded conformation, which could be particularly detrimental in an environment where these resources are only available during limited pulses of activity. This seems counter-intuitive, and suggests that bundle-formation must bring about significant adaptive value in some other form. It was already shown that the bundle association behavior serves as an adaptation to soil stabilization (Garcia-Pichel and Wojciechowski, 2009) allowing the establishment of microbial colonies on an otherwise mobile substrate, a feat that is size dependent and unattainable to single filaments. Our work here further suggests that the amount of sheath EPS could be critical to buffer local water dehydration and transfer water to the trichomes. In this sense, bundle formation, i.e., sheath sharing behavior, in an activity

limited environment may also be an adaptive trade-off that favors sustained *Microcoleus* sp. populations in arid lands.

CONCLUSIONS

Our study looked in detail at the process of desiccation of one single bundle inside an early successional stage biocrust. We could show that the bundle remains hydrated while the surroundings are drying, and that the EPS-sheath represents a buffer zone able to redistribute its hydration water to the cyanobacterial cells. We observed that the sand particles were apparently not strongly attached to the bundle since they did not stay close to the bundle through desiccation, increasing pore space around the bundle as desiccation progresses. Our study was somewhat limited by the fact that manual data treatment was required to distinguish liquid water from air and sheath from trichome phases. However, we hope that this study will serve as a pioneer for additional studies, and that machine learning approaches will provide an avenue to improve synchrotron X-ray microtomography approached to the study of water/microbes interactions in soils crusts and other relevant microbial systems.

AUTHOR CONTRIBUTIONS

EC, TN, and FG-P designed the experiment. EC and FG-P collected the sample, acquired the SEM images and wrote the paper. VF analyzed the data and wrote the paper. EC, FG-P, and DP conducted the CT-scans at the Advanced Light Source (LBNL). DU, SP, AR, GW, and CC analyzed the data.

ACKNOWLEDGMENTS

SUPPLEMENTARY MATERIAL

The Supplementary Material for this article can be found online at: https://www.frontiersin.org/articles/10.3389/fenvs.2018.00065/full#supplementary-material

REFERENCES

Adessi, A., Cruz de Carvalho, R., De Philippis, R., Branquinho, C., and Marques da Silva, J. (2018). Microbial extracellular polymeric substances improve water retention in dryland biological soil crusts. *Soil Biol. Biochem.* 116, 67–69. doi: 10.1016/j.soilbio.2017.10.002

Aravena, J. E., Berli, M., Ghezzehei, T. A., and Tyler, S. W. (2011). Effects of root-induced compaction on rhizosphere hydraulic properties–X-ray microtomography imaging and numerical simulations. *Environ. Sci. Technol.* 45, 425–431. doi: 10.1021/es102566j

Aravena, J. E., Berli, M., Ruiz, S., Suárez, F., Ghezzehei, T. A., and Tyler, S. W. (2014). Quantifying coupled deformation and water flow in the rhizosphere using X-ray microtomography and numerical simulations. *Plant Soil* 376, 95–110. doi: 10.1007/s11104-013-1946-z

Ayuso, S. V., Silva, A. G., Nelson, C., Barger, N. N., and Garcia-Pichel, F. (2017). Microbial nursery production of high-quality biological soil crust biomass for restoration of degraded dryland soils. *Appl. Environ. Microbiol.* 83, 1–16. doi: 10.1128/AEM.02179-16

Baran, R., Brodie, E. L., Mayberry-Lewis, J., Hummel, E., Da Rocha, U. N., Chakraborty, R., et al. (2015). Exometabolite niche partitioning among sympatric soil bacteria. *Nat. Commun.* 6, 8289. doi: 10.1038/ncomms9289

Baran, R., Ivanova, N. N., Jose, N., Garcia-Pichel, F., Kyrpides, N. C., Gugger, M., et al. (2013). Functional genomics of novel secondary metabolites from diverse cyanobacteria using untargeted metabolomics. *Mar. Drugs* 11, 3617–3631. doi: 10.3390/md11103617

Belnap, J., Weber, B., and Büdel, B. (2016). "Biological soil crusts as an organizing principle in drylands," in *Biological Soil Crusts: An Organizing Principle in Drylands*, eds B. Weber, B. Büdel, and J. Belnap (Cham: Springer International Publishing), 3–13.

Beraldi-Campesi, H., Farmer, J. D., and Garcia-Pichel, F. (2014). Modern terrestrial sedimentary biostructures and their fossil analogs in mesoproterozoic subaerial deposits. *Palaios* 29, 45–54. doi: 10.2110/palo.2013.084

Beraldi-Campesi, H., and Garcia-Pichel, F. (2011). The biogenicity of modern terrestrial roll-up structures and its significance for ancient life on land. *Geobiology* 9, 10–23. doi: 10.1111/j.1472-4669.2010.00258.x

Beraldi-Campesi, H., Hartnett, H. E., Anbar, A., Gordon, G. W., and Garcia-Pichel, F. (2009). Effect of biological soil crusts on soil elemental concentrations: implications for biogeochemistry and as traceable biosignatures of ancient life on land. *Geobiology* 7, 348–359. doi: 10.1111/j.1472-4669.2009.00204.x

Campbell, S. E. (1979). Soil stabilization by a prokaryotic desert crust: implications for Precambrian land biota. *Orig. Life* 9, 335–348. doi: 10.1007/BF00926826

Canny, J. (1986). A computational approach to edge detection. *IEEE Trans. Pattern Anal. Mach. Intell.* 8, 679–698.

Colesie, C., Felde, V. J. M. N. L., and Büdel, B. (2016). "Composition and macrostructure of biological soil crusts," in *Biological Soil Crusts: An Organizing Principle in Drylands*, eds B. Weber, B. Büdel, and J. Belnap (Cham: Springer International Publishing), 159–172.

Colica, G., Li, H., Rossi, F., Li, D., Liu, Y., and Philippis, R. (2014). Microbial secreted exopolysaccharides affect the hydrological behavior of induced biological soil crusts in desert sandy soils. *Soil Biol. Biochem.* 68, 62–70. doi: 10.1016/j.soilbio.2013.09.017

Couradeau, E., Karaoz, U., Lim, H. C., Nunes da Rocha, U., Northen, T., Brodie, E., et al. (2016). Bacteria increase arid-land soil surface temperature through the production of sunscreens. *Nat. Commun.* 7:10373. doi: 10.1038/ncomms10373

Doube, M., Kłosowski, M. M., Arganda-Carreras, I., Cordelières, F. P., Dougherty, R. P., Jackson, J. S., et al. (2010). BoneJ: free and extensible bone image analysis in ImageJ. *Bone* 47, 1076–1079. doi: 10.1016/j.bone.2010.08.023

Dümig, A., Veste, M., Hagedorn, F., Fischer, T., Lange, P., Spröte, R., et al. (2014). Organic matter from biological soil crusts induces the initial formation of

sandy temperate soils. *CATENA* 122, 196–208. doi: 10.1016/j.catena.2014.0 6.011

Felde, V. J. M. N. L., Rossi, F., Colesie, C., Uteau-Puschmann, D., Horn, R., Felix-Henningsen, P., et al. (2016). Pore characteristics in biological soil crusts are independent of extracellular polymeric substances. *Soil Biol. Biochem.* 103, 294–299. doi: 10.1016/j.soilbio.2016.08.029

Fernandes, V, Machado de Lima, N, Roush, D, Collins, S, Rutgers, J, and Garcia-Pichel, F (2018). Exposure to predicted precipitation patterns decrease population size and alter community structure of cyanobacteria in biological soil crusts from the Chihuahuan Desert. *Environm. Microbiol.* 20, 259–269. doi: 10.1111/1462-2920.13983

Fischer, D., Pagenkemper, S., Nellesen, J., Peth, S., Horn, R., and Schloter, M. (2013). Influence of non-invasive X-ray computed tomography (XRCT) on the microbial community structure and function in soil. *J. Microbiol. Methods* 93, 121–123. doi: 10.1016/j.mimet.2013.0 2.009

Fischer, T., Veste, M., Wiehe, W., and Lange, P. (2010). Water repellency and pore clogging at early successional stages of microbiotic crusts on inland dunes, Brandenburg, NE Germany. *CATENA* 80, 47–52. doi: 10.1016/j.catena.2009.08.009

Garcia-pichel, F., and Castenholz, R. W. (1991). Characterizaton and biological implications of scytonemin, a cyanobacterial sheath pigment. *J. Phycol.* 409, 395–409.

Garcia-Pichel, F., Loza, V., Marusenko, Y., Mateo, P., and Potrafka, R. M. (2013). Temperature drives the continental-scale distribution of key microbes in topsoil communities. *Science* 340, 1574–1577. doi: 10.1126/science.123 6404

Garcia-Pichel, F., and Wojciechowski, M. F. (2009). The evolution of a capacity to build supra-cellular ropes enabled filamentous cyanobacteria to colonize highly erodible substrates. *PLoS ONE* 4:e7801. doi: 10.1371/journal.pone.000 7801

Gürsoy, D., De Carlo, F., Xiao, X., and Jacobsen, C. (2014). TomoPy: a framework for the analysis of synchrotron tomographic data. *J. Synchrotron Radiat.* 21, 1188–1193. doi: 10.1107/S1600577514013939

Johnson, SL, Neuer, S, and Garcia-Pichel, F (2007). Export of nitrogenous compounds due to incomplete cycling within biological soil crusts of arid lands. *Environ Microbiol.* 9, 680–689. doi: 10.1111/j.1462-2920.2006.01187.x

Kuske, C. R., Yeager, C. M., Johnson, S., Ticknor, L. O., and Belnap, J. (2012). Response and resilience of soil biocrust bacterial communities to chronic physical disturbance in arid shrublands. *ISME J.* 6, 886–897. doi: 10.1038/ismej.2011.153

Lorensen, W. E., and Cline, H. E. (1987). Marching cubes: a high resolution 3D surface construction algorithm. *ACM Siggr. Comput. Graph.* 21, 163–169. doi: 10.1145/37401.37422

Ma, R., Cai, C., Li, Z., Wang, J., Xiao, T., Peng, G., et al. (2015). Evaluation of soil aggregate microstructure and stability under wetting and drying cycles in two Ultisols using synchrotron-based X-ray micro-computed tomography. *Soil Tillage Res.* 149, 1–11. doi: 10.1016/j.still.2014.12.016

MacDowell, A. A., Parkinson, D. Y., Haboub, A., Schaible, E., Nasiatka, J. R., Yee, C. A., et al. (2012). "X-ray micro-tomography at the advanced light source," in *Proceedings of SPIE 8506, Developments in X-Ray Tomography* VIII 8506 (San Diego, CA).

Menon, M., Yuan, Q., Jia, X., Dougill, A. J., Hoon, S. R., Thomas, A. D., et al. (2011). Assessment of physical and hydrological properties of biological soil crusts using X-ray microtomography and modeling. *J. Hydrol.* 397, 47–54. doi: 10.1016/j.jhydrol.2010.11.021

Mergelov, N., Mueller, C. W., Prater, I., Shorkunov, I., Dolgikh, A., Zazovskaya, E., et al. (2018). Alteration of rocks by endolithic organisms is one of the pathways for the beginning of soils on Earth. *Sci. Rep.* 8:3367. doi: 10.1038/s41598-018-21682-6

Murik, O., Oren, N., Shotland, Y., Raanan, H., Treves, H., Kedem, I., et al. (2017). What distinguishes cyanobacteria able to revive after desiccation from those that cannot: the genome aspect: desiccation resistance genes in cyanobacteria. *Environ. Microbiol.* 19, 535–550. doi: 10.1111/1462-2920.1 3486

Or, D., Phutane, S., and Dechesne, A. (2007). Extracellular polymeric substances affecting pore-scale hydrologic conditions for bacterial activity in unsaturated soils. *Vadose Zone J.* 6, 298. doi: 10.2136/vzj2006.0080

Otsu, N. (1979). A threshold selection method from gray-level histograms. *IEEE Trans. Syst. Man Cybern.* 9, 62–66. doi: 10.1109/TSMC.1979.4310076

Peth, S., Chenu, C., Leblond, N., Mordhorst, A., Garnier, P., Nunan, N., et al. (2014). Localization of soil organic matter in soil aggregates using synchrotron-based X-ray microtomography. *Soil Biol. Biochem.* 78, 189–194. doi: 10.1016/j.soilbio.2014.07.024

Peth, S., Horn, R., Beckmann, F., Donath, T., Fischer, J., and Smucker, A. J. M. (2008). Three-dimensional quantification of intra-aggregate pore-space features using synchrotron-radiation-based microtomography. *Soil Sci. Soc. Am. J.* 72, 897. doi: 10.2136/sssaj2007.0130

Pócs, T. (2009). Cyanobacterial crust types, as strategies for survival in extreme habitats. *Acta Bot. Hung.* 51, 147–178. doi: 10.1556/ABot.51.2009.1-2.16

Pot, V., Peth, S., Monga, O., Vogel, L. E., Genty, A., Garnier, P., et al. (2015). Three-dimensional distribution of water and air in soil pores: comparison of two-phase two-relaxation-times lattice-Boltzmann and morphological model outputs with synchrotron X-ray computed tomography data. *Adv. Water Resour.* 84, 87–102. doi: 10.1016/j.advwatres.2015.08.006

Potts, M. (1994). Desiccation tolerance of prokaryotes. *Microbiol. Rev.* 58, 755–805. doi: 10.1093/icb/45.5.800

Pringault, O., and Garcia-Pichel, F. (2004). Hydrotaxis of cyanobacteria in desert crusts. *Microb. Ecol.* 47, 366–373. doi: 10.1007/s00248-002-0107-3

Rajeev, L., da Rocha, U. N., Klitgord, N., Luning, E. G., Fortney, J., Axen, S. D., et al. (2013). Dynamic cyanobacterial response to hydration and dehydration in a desert biological soil crust. *ISME J.* 7, 2178–2191. doi: 10.1038/ismej.2013.83

Reddy, G. S. N., and Garcia-Pichel, F. (2007). *Sphingomonas mucosissima* sp. nov. and *Sphingomonas desiccabilis* sp. nov., from biological soil crust in the Colorado Plateau, USA. *Int. J. Syst. Evol. Microbiol.* 57, 1028–1034. doi: 10.1099/ijs.0.64331-0

Rodriguez-Caballero, E., Belnap, J., Büdel, B., Crutzen, P. J., Andreae, M. O., Pöschl, U., et al. (2018). Dryland photoautotrophic soil surface communities endangered by global change. *Nat. Geosci.* 11, 85–189. doi: 10.1038/s41561-018-0072-1

Rosenzweig, R., Shavit, U., and Furman, A. (2012). Water retention curves of biofilm-affected soils using xanthan as an analogue. *Soil Sci. Soc. Am. J.* 76:61. doi: 10.2136/sssaj2011.0155

Rossi, F., and De Philippis, R. (2015). Role of cyanobacterial exopolysaccharides in phototrophic biofilms and in complex microbial mats. *Life* 5, 1218–1238. doi: 10.3390/life5021218

Rossi, F., Mugnai, G., and de Philippis, R. (2017). Complex role of the polymeric matrix in biological soil crusts. *Plant Soil.* doi: 10.1007/s11104-017-3441-4. [Epub ahead of print].

Rossi, F., Potrafka, R. M., Pichel, F. G., and De Philippis, R. (2012). The role of the exopolysaccharides in enhancing hydraulic conductivity of biological soil crusts. *Soil Biol. Biochem.* 46, 33–40. doi: 10.1016/j.soilbio.2011.1 0.016

Schindelin, J., Arganda-Carreras, I., Frise, E., Kaynig, V., Longair, M., Pietzsch, T., et al. (2012). Fiji: an open-source platform for biological-image analysis. *Nat. Methods* 9, 676–682. doi: 10.1038/nmeth.2019

Schmidt, H., Vetterlein, D., Köhne, J.M., and Eickhorst, T. (2015). Negligible effect of X-ray μ-CT scanning on archaea and bacteria in an agricultural soil. *Soil Biol. Biochem.* 84, 21–27. doi: 10.1016/j.soilbio.2015.02.010

Spanne, P., Jones, K. W., Prunty, L. D., and Anderson, S. H. (1993). "Potential applications of synchrotron computed microtomography to soil science," in *1992 Annual Meetings of the American Society of Agronomy, Crop Science Society of America, and Soil Science Society of America* (Minneapolis, MN).

Strauss, S. L., Day, T. A., and Garcia-Pichel, F. (2012). Nitrogen cycling in desert biological soil crusts across biogeographic regions in the southwestern United States. *Biogeochemistry* 108, 171–182. doi: 10.1007/s10533-011-9587-x

Swenson, T. L., Karaoz, U., Swenson, J. M., Bowen, B. P., and Northen, T. R. (2018). Linking soil biology and chemistry in biological soil crust using isolate exometabolomics. *Nat. Commun.* 9:19. doi: 10.1038/s41467-017-02 356-9

Tötzke, C., Kardjilov, N., Manke, I., and Oswald, S. E. (2017). Capturing 3D water flow in rooted soil by ultra-fast neutron tomography. *Sci. Rep.* 7, 1–9. doi: 10.1038/s41598-017-06046-w

Vogel, H. J., and Kretzschmar, A. (1996). Topological characterization of pore space in soil — sample preparation and digital image-processing. *Geoderma* 73, 23–38. doi: 10.1016/0016-7061(96)00043-2

Volk, E., Iden, S. C., Furman, A., Durner, W., and Rosenzweig, R. (2016). Biofilm effect on soil hydraulic properties: experimental investigation using soil-grown real biofilm: HYDRAULIC PROPERTIES OF BIOFILM AMENDED SOIL. *Water Resour. Res.* 52, 5813–5828. doi: 10.1002/2016WR01 8866

Voltolini, M., Taş, N., Wang, S., Brodie, E. L., and Ajo-Franklin, J. B. (2017). Quantitative characterization of soil micro-aggregates: new opportunities from sub-micron resolution synchrotron X-ray microtomography. *Geoderma* 305, 382–393. doi: 10.1016/j.geoderma.2017.06.005

Zhao, M., Reinhard, C. T., and Planavsky, N. J. (2018). Terrestrial methane fluxes and Proterozoic climate. *Geology* 46, 1–4. doi: 10.1130/G39502.1

Comparison of Types and Amounts of Nanoscale Heterogeneity on Bacteria Retention

Scott A. Bradford[1]*, Salini Sasidharan[2], Hyunjung Kim[3] and Gukhwa Hwang[3]

[1] US Salinity Laboratory, USDA, ARS, Riverside, CA, United States, [2] Department of Environmental Sciences, University of California, Riverside, Riverside, CA, United States, [3] Department of Mineral Resources and Energy Engineering, Chonbuk National University, Jeonju, South Korea

Interaction energy calculations that assume smooth and chemically homogeneous surfaces are commonly conducted to explain bacteria retention on solid surfaces, but experiments frequently exhibit signification deviations from these predictions. A potential explanation for these inconsistencies is the ubiquitous presence of nanoscale roughness (NR) and chemical heterogeneity (CH) arising from spatial variability in charge (CH1), Hamaker constant (CH2), and contact angles (CH3) on these surfaces. We present a method to determine the mean interaction energy between a colloid and a solid-water-interface (SWI) when both surfaces contained binary NR and CH. This approach accounts for double layer, van der Waals, Lewis acid-base, and Born interactions. We investigate the influence of NR and CH parameters and solution ionic strength (IS) on interaction energy profiles between hydrophilic and hydrophobic bacteria and the SWI. Increases in CH1 and CH3 reduce the energy barrier and create deeper primary minima on net electrostatically unfavorable surfaces, whereas increasing CH2 diminishes the contribution of the van der Waals interaction in comparison to quartz and makes a more repulsive surface. However, these roles of CH are always greatest on smooth surfaces with larger fractions of CH. In general, increasing CH1 and CH3 have a larger influence on bacteria retention under lower IS conditions, whereas the influence of increasing CH2 is more apparent under higher IS conditions. However, interaction energy profiles are mainly dominated by small fractions of NR, which dramatically lower the energy barrier height and the depths of both the secondary and primary minima. This significantly increases the relative importance of primary to secondary minima interactions on net electrostatically unfavorable surfaces, especially for conditions that produce small energy barriers on smooth surfaces. Energy balance calculations indicate that this primary minimum is sometimes susceptible to diffusive removal depending on the NR and CH parameters.

Keywords: nanoscale, chemical heterogeneity, roughness, hamaker constant, contact angles, XDLVO interaction energy, bacteria, retention

INTRODUCTION

Colloids are particles with diameters of around $10\,nm$ to $10\,\mu m$ and include microorganisms, dissolved and particulate organic matter, clays and mineral precipitates, and nanoparticles (DeNovio et al., 2004). An understanding of factors that control colloid retention and release from surfaces is important for many environmental and industrial applications

(Salata, 2004; Molnar et al., 2015; Stark et al., 2015). Conventional filtration theory considers that retention depends on the mass transfer rate of colloids to the solid-water-interface (SWI) and immobilization on the surface (Yao et al., 1971). The relative magnitude of the forces and torques that act on a colloid adjacent to the SWI will determine whether a colloid will be immobilized or released from a surface (Cushing and Lawler, 1998). Filtration theory considers that the adhesive force dominates colloid retention and release (Tufenkji and Elimelech, 2004).

The adhesive force is typically determined from interaction energy calculations (Bergendahl and Grasso, 1999). The interaction energy between a colloid and the SWI usually considers electrostatic double layer and van der Waals interactions but has also been increasingly extended to include Lewis acid-base, steric, and Born interactions (Grasso et al., 2002). However, many experimental observations of colloid retention and release have not been consistent with such interaction energy calculations (Suresh and Walz, 1996; Huang et al., 2009; Bendersky and Davis, 2011). Traditional interaction energy calculations have been limited to smooth, chemically homogeneous surfaces (Grasso et al., 2002). Conversely, natural surfaces always exhibit some degree of nanoscale roughness (NR) and chemical heterogeneity (CH) (Vaidyanathan and Tien, 1991; Suresh and Walz, 1996). A number of researchers have therefore extended interaction energy calculations to include NR and/or CH as a means to explain colloid retention and release (e.g., Suresh and Walz, 1996; Bhattacharjee et al., 1998; Hoek et al., 2003; Hoek and Agarwal, 2006; Huang et al., 2009; Bendersky and Davis, 2011; Henry et al., 2011).

Consideration of NR and surface charge heterogeneity (CH1) in interaction energy calculations can account for many observed colloid retention and release behavior that were previously unexplained (Shen et al., 2011; Bradford and Torkzaban, 2012, 2013, 2015; Bradford et al., 2017); e.g., a small fraction of the surface contributing to colloid retention on net electrostatically unfavorable and favorable surfaces. Increasing CH1 locally reduces the energy barrier height and increases the depth of the primary minimum under net electrostatically unfavorable conditions, especially for more positively charged and larger sized heterogeneities under higher ionic strength (IS) conditions (Bendersky and Davis, 2011; Bradford and Torkzaban, 2012; Shen et al., 2013; Pazmino et al., 2014). Small NR fractions locally decreases the height of the energy barrier (Suresh and Walz, 1996; Bhattacharjee et al., 1998; Hoek et al., 2003; Hoek and Agarwal, 2006; Huang et al., 2009; Bendersky and Davis, 2011; Shen et al., 2011) and the magnitude of the primary minimum (Shen et al., 2012; Bradford and Torkzaban, 2013), especially for roughness on both the surface of the colloid and the SWI (Bradford et al., 2017). Roughness properties that contribute to colloid retention and release change with the solution IS, the colloid size, and the surface chemical properties (e.g., Bradford et al., 2017). Small NR fractions have been shown to control the shape of the interaction energy profile when surfaces contain both NR and CH1 (Bradford and Torkzaban, 2013, 2015; Bradford et al., 2017).

In addition to CH1 and NR, natural subsurface environments may also exhibit heterogeneity arising from the presence of microorganisms and the degradation of soil organic matter (SOM). A diversity of types and numbers of soil microorganisms may occur in soils and sediments (Stevenson, 1994). SOM is usually divided into fulvic acid, humic acid, and humin fractions (Huang et al., 2003). Fulvic acid has higher contents of carboxylic and phenolic groups than humic acid (Aiken, 1985). Humin is a complex mixture of variably degraded biopolymers such as lignin and polysaccharides (Aiken, 1985), mineral-bound lipids and humic acid-like materials (Rice and MacCarthy, 1990), and kerogen and black carbon (Song et al., 2002).

Although the organic fraction of soils and sediments is usually small in comparison to the inorganic fraction, it can coat large portions of the exposed mineral surface (Doerr et al., 2000). The physical and chemical properties of organic coatings can be vastly different from the underlying mineral surface. For example, NR of microbes and SOM are expected to be very different than pure mineral surfaces (Wilkinson et al., 1999), and to change with the water content (Ma'shum and Farmer, 1985), and the solution pH, IS, and ionic composition (Stevenson, 1994; Sposito, 2008). SOM consists of both hydrophobic and hydrophilic components (Ellerbrock et al., 2005). The wettability of soils and sediments is highly impacted by the types and amounts of SOM (Doerr et al., 2000). Humic acids and humins are reported to contain hydrophobic surfaces (de Blas et al., 2010) such as polyalkyl molecules (e.g., free fatty acids and wax esters) (Ma'Shum et al., 1988; Hudson et al., 1994; Franco et al., 2000). This hydrophobicity can be enhanced in fire-affected soils because of thermal decarboxylation of the humic matter (Almendros et al., 1990), and in dry soils due to conformational changes of the SOM (Ma'shum and Farmer, 1985). In addition, microorganism species are known to exhibit wide variations in hydrophobicity (Van Loosdrecht et al., 1987). The hydrophobicity of a surface is known to have a strong influence on the Lewis acid-base interaction (Bergendahl and Grasso, 1999). In addition, an increase in the presence of organic coatings is expected to reduce the Hamaker constant and the van der Waals interaction (Drummond and Chan, 1997; Tong et al., 2011).

Adsorbed organics on surfaces have frequently been reported to create a brush-like surface that diminishes colloid retention and/or increases colloid stability (Kretzschmar and Sticher, 1997; Yang et al., 2010, 2011, 2013, 2014; Flynn et al., 2012). This diminished colloid retention or increased stability in the presence of adsorbed organics has typically been attributed to steric repulsion which creates a large energy barrier to interaction in a primary minimum (Espinasse et al., 2007; Han et al., 2014). The large energy barrier from steric repulsion predicts no colloid retention on a surface, whereas limited amounts of colloid retention are commonly observed even in the presence of absorbed SOM (Jiang et al., 2012; Han et al., 2014). Furthermore, steric repulsion cannot account for enhanced retention of hydrophobic colloids on SOM surfaces (Amirbahman and Olson, 1993). Alternatively, the brush-like surface of absorbed SOM may be explicitly accounted for in interaction energies calculations through NR heights and fractions parameters. In contrast to the influence of steric repulsion, NR creates colloid stability and low amounts of retention by producing shallow primary minima that are subject to diffusive or hydrodynamic release (Morales et al.,

2011). Spatial differences in roughness parameters on natural surfaces will alter the depth of the primary minimum to produce colloid retention only in some locations (Bradford et al., 2017).

Previous research that has examined the influence of CH on colloid interactions have focused on CH1 (e.g., from metal oxides, mineral defects, and protonation and deprotonation of surface functional groups) (Pazmino et al., 2014; Park and Kim, 2015). No research to date has systematically examined the influence of SOM heterogeneity on the van der Waals and Lewis acid-base components of the interaction energy. Furthermore, the relative importance of various types and amounts of CH (e.g., charge, Hamaker, and contact angle), separately or in combination, has not yet been studied on a single surface let alone on both interacting surfaces. The influence of all of these chemical heterogeneities in the presence of NR on one or both surfaces is also a question that has not yet been addressed.

Bradford et al. (2017) previously presented an approach to simultaneously account for the influence of NR and CH1 on colloid and solid (or another colloid) surfaces on interaction energies. In this case, the interaction energies only considered constant potential double layer electrostatics (Hogg et al., 1966), retarded London-van der Waals attraction (Gregory, 1981), and Born repulsion (Ruckenstein and Prieve, 1976; Oliveira, 1997) for sphere-plate and sphere-sphere geometries. In this work, these equations were further extended to include Lewis acid-base interactions (Van Oss, 1994), and CH arising from Hamaker constants (van der Waals interactions) and contact angles (Lewis acid-base interactions). These changes allow us to consider a wide variety of types, amounts, and combinations of NR and/or CH (charge, Hamaker, and/or contact angle) on one or both surfaces. This tool provides us with valuable information and insight to determine the relative importance of the various heterogeneity types and combinations on colloid retention, release, and stability. A special focus of this research was to better understand the influence of SOM coatings on interactions with mineral surfaces and bacteria.

MATERIALS AND METHODS
Interaction Energies for Homogeneous Surfaces

The total interaction energy between a colloid and the SWI (Φ_{ij}, ML^2T^{-2} where M, L, and T denote units of mass, length, and time, respectively) is associated with a smooth and chemically homogeneous surface. The value of Φ_{ij} was considered to be the sum of electrostatic, van der Waals, Lewis acid-base, and Born repulsion interaction energies as:

$$\Phi_{ij}\left(h\right) = \Phi^{el}\left(h\right) + \Phi^{vdW}\left(h\right) + \Phi^{AB}\left(h\right) + \Phi^{Born}\left(h\right) \quad (1)$$

where Φ^{el} $[ML^2T^{-2}]$, $\Phi^{vdW}[ML^2T^{-2}]$, $\Phi^{AB}[ML^2T^{-2}]$ and $\Phi^{Born}[ML^2T^{-2}]$ are the electric double layer, van der Waals, Lewis acid-base, and Born interaction energies, respectively. The value of Φ_{ij} was made dimensionless by dividing by the product of the Boltzmann constant ($k_B = 1.38 \times 10^{-23}$ J K^{-1}) and the absolute temperature (T_K).

The value of Φ^{el} was determined using the constant surface potential interaction expression of Hogg et al. (1966) for a sphere-plate interaction as:

$$\Phi^{el}\left(h\right) = \pi \varepsilon \varepsilon_o r_c \left\{ 2\zeta_{ci}\zeta_{sj} \ln\left[\frac{1 + \exp\left(-\kappa h\right)}{1 - \exp\left(-\kappa h\right)} \right] \right.$$
$$\left. + \left(\zeta_{ci}^2 + \zeta_{sj}^2\right) \ln\left[1 - \exp\left(-2\kappa h\right)\right] \right\} \quad (2)$$

where ε (dimensionless) is the dielectric constant of the medium, ε_0 $[M^{-1}L^{-3}T^4A^{-2}$, where A denotes ampere] is the permittivity in a vacuum, r_c [L] is the colloid radius, ζ_{ci} is the zeta potential of the colloid, ζ_{sj} is the zeta potential of the solid, and κ [L^{-1}] is the Debye-Huckel parameter.

The value of Φ^{vdW} for a retarded sphere-plate interaction was determined using the expression by Gregory (1981) as:

$$\Phi^{vdW}\left(h\right) = -\frac{A_{cws}r_c}{6h}\left[1 + \frac{14h}{\lambda}\right]^{-1} \quad (3)$$

where A_{cws} $[ML^2T^{-2}]$ is the combined Hamaker constant, and λ is a characteristic wavelength that was taken as 100 nm (Gregory, 1981). The value of A_{cws} can be estimated from Hamaker constants for the various materials (Israelachvili, 1992) as:

$$A_{cws} = \left(\sqrt{A_{ci}} - \sqrt{A_w}\right)\left(\sqrt{A_{sj}} - \sqrt{A_w}\right) \quad (4)$$

where A_{ci} $[ML^2T^{-2}]$, A_{sj} $[ML^2T^{-2}]$, and A_w $[ML^2T^{-2}]$ are the Hamaker constants for the colloid, the solid, and water, respectively. The value of A_w is commonly taken as 3.7×10^{-20} J (Israelachvili, 1992). Values of A_{sj} were estimated from literature values of their surface energies in the air (γ_{sj}) as (Israelachvili, 1992):

$$A_{sj} = 24\pi \gamma_{sj}h_0^2 \quad (5)$$

where h_0 [L] is the value of closest approach taken to be 0.157 nm (Van Oss, 1994). The value of A_{ci} was estimated in an analogous fashion from γ_{ci}.

The value of Φ^{AB} was determined using the approach of Van Oss (1994) as:

$$\Phi^{AB}\left(h\right) = 2\pi r_c \lambda_{AB}\Phi_{AB(h=h_0)}\exp\left[\frac{h_o - h}{\lambda_{AB}}\right] \quad (6)$$

where λ_{AB} [L] is the characteristic decay length of acid-base interactions in water taken as 1 nm (Israelachvili, 1992), and $\Phi_{AB(h=h_0)}[MT^{-2}]$ is the Lewis acid-base free interaction energy per area between the two surfaces when $h = h_0$. The value of $\Phi_{AB(h=h_0)}$ in Equation (6) was determined using the approach of Bergendahl and Grasso (1999) and Yoon et al. (1997) as:

$$\Phi_{AB(h=h_0)} = -\frac{K}{2\pi h_0 \lambda_{AB}} \quad (7)$$

$$\log\left(K\right) = -7.0\left(\frac{\cos\left(\theta_{ci}\right) + \cos\left(\theta_{sj}\right)}{2}\right) - 18.0 \quad (8)$$

where θ_{sj} [degrees] and θ_{ci} [degrees] are the contact angles for the air-water-solid and air-water-colloid systems, respectively, and K [ML^2T^{-2}] is the hydrophobic force constant.

It should be mentioned that values of θ_{sj} and/or θ_{ci} can be theoretically related to A_{sj} and/or A_{ci}, respectively, for dispersive liquids and solids (Drummond and Chan, 1997). However, in the presence of water, this theoretical relationship does not hold because non-dispersive interactions dominate (Hough and White, 1980). In this work, individual material Hamaker constants and contact angles were therefore considered to be independent from each other. This approach is consistent with the assumption that Φ^{vdw} and Φ^{AB} terms account for separate processes.

The value of Φ^{Born} was calculated from Ruckenstein and Prieve (1976) for sphere-plate interactions as:

$$\Phi^{Born}(h) = \frac{A_{cws}\sigma_c^6}{7560}\left[\frac{8r_c + h}{(2r_c + 7)^7} + \frac{6r_c - h}{h^7}\right] \quad (9)$$

where σ_c [L] is the collision diameter that was taken as 0.26 nm in order to achieve a primary minimum depth at 0.157 nm.

Interaction Energies for Heterogeneous Surfaces

An approach of Bradford et al. (2017) to account for the influence of NR and CH on interaction energy calculations between a spherical colloid suspended in a monovalent electrolyte solution and a planar solid surface or another colloid is extended below. Both interacting surfaces may exhibit binary NR and CH within the area of the electrostatic zone of influence (A_z). The zone of electrostatic influence (e.g., proportional to the colloid radius and the Debye length) on the SWI is assumed to contain a NR fraction (f_{sr}) with a height equal to h_{sr}, and the complementary fraction ($1-f_{sr}$) correspond to a smooth surface. Similar NR parameters were defined within the electrostatic zone of influence for the colloid as for the SWI. In this case, parameters f_{sr} and h_{sr} for the SWI correspond to f_{cr} and h_{cr} for the colloid, respectively. The mean dimensionless interaction energy between a colloid and SWI that contains NR on both surfaces (Φ) can be determined as a linear combination of interaction energies for the various NR components as (Bradford et al., 2017):

$$\Phi(h) = a_{r1}\Phi_S(h + h_{sr} + h_{cr}) + a_{r2}\Phi_S(h + h_{sr}) + a_{r3}\Phi_S(h + h_{cr}) + a_{r4}\Phi_S(h) \quad (10)$$

where h [L] is the separation distance from the center of the electrostatic zone of influence at a height h_{sr} from the SWI to the leading face of the colloid center at a height h_{cr}, and a_{r1} [–], a_{r2} [–], a_{r3} [–], and a_{r4} [–] are constants that determine the contributions of the various possible roughness combinations

that are equal to:

$$a_{r1} = (1 - f_{sr})(1 - f_{cr})$$
$$a_{r2} = (1 - f_{sr})f_{cr}$$
$$a_{r3} = f_{sr}(1 - f_{cr})$$
$$a_{r4} = f_{sr}f_{cr}$$

$$(11)$$

Equations (10) and (11) assume that $h > 0$ such that roughness on the colloid and SWI do not overlap, and that lateral components of the interaction energy are insignificant or cancel out.

The value of parameter Φ_S in Equation (10) is the mean dimensionless interaction energy between a smooth colloid and SWI that contains binary CH on both surfaces. Similar to Equation (10), Φ_S can be determined as a linear combination of interaction energies for the various CH components as (Bradford and Torkzaban, 2012).

$$\Phi_S(h) = \sum_{j=1}^{2}\sum_{i=1}^{2} f_{sj}f_{ci}\Phi_{ij}(h) \quad (12)$$

where f_{sj} [–] and f_{ci} [–] are fractions of the electrostatic zone of influence that are associated with binary CH classes on the SWI ($j = 1, 2$) and colloid ($i = 1, 2$), respectively, and Φ_{ij} was defined by Equations (1)–(8) for the various possible CH combinations. It should be mentioned that $f_{s1} = (1-f_{s2})$ and $f_{c1} = (1-f_{c2})$. Note that Equations (10)–(12) are consistent with previous studies that have demonstrated that the mean interaction energy for heterogeneous surfaces can be determined as a linear combination of interaction energies associated with the various heterogeneity combinations (Huang et al., 2009; Bendersky and Davis, 2011; Bradford and Torkzaban, 2013).

Note that our approach for NR in Equations (10) and (11) is independent of the type of CH. Consequently, many types and combinations of CH can be considered using the same approach. For example, the combined CH arising from differences in charge, Hamaker, and contact angle can be simultaneously considered when accounting for separate interaction parameters for each CH class on the SWI and colloid. Alternatively, heterogeneity in charge (CH1), Hamaker constant (CH2), or contact angle (CH3) can be separately determined by only varying these interaction parameters for each CH class. In this case, CH1, CH2, and CH3 reflect the influence of heterogeneity on Φ^{el}, Φ^{vdW} (and Φ^{Born}), and Φ^{AB} components of the total interaction energy (Equation 1), respectively, whereas other interaction energy terms consider homogeneous conditions.

Equations (1)–(12) therefore allow the influence of NR and CH, NR and CH1, NR and CH2, and NR and CH3 to be systematically investigated for various heterogeneity parameters when considering double layer, van der Waals, Lewis acid-base, and Born interactions. All interaction energy profiles were analyzed to determine the energy barrier height (Φ_{max}), and the depths of the secondary (Φ_{2min}) and primary (Φ_{1min}) minima.

Energy Balance

The probability (ε_k) that a colloid interacting in a primary ($k = 1$) or secondary ($k = 2$) minimum would be immobilized in the presence of random kinetic energy fluctuations of a diffusing colloid may be estimated using the Boltzmann factor and Maxwellian kinetic energy models as (Simoni et al., 1998; Shen et al., 2007; Bradford and Torkzaban, 2015; Bradford et al., 2017):

$$\varepsilon_k = \exp(-A) - \exp(-B) \tag{13}$$

$$\varepsilon_k = \left(erf\left(\sqrt{B}\right) - \sqrt{\frac{4B}{\pi}} \exp\left(-B\right) \right)$$
$$- \left(erf\left(\sqrt{A}\right) - \sqrt{\frac{4A}{\pi}} \exp\left(-A\right) \right) \tag{14}$$

where A and B are equal to the dimensionless interaction energies to enter and escape from a minimum, respectively (Bradford and Torkzaban, 2015; Bradford et al., 2017). Note that an infinite depth of the primary minimum has frequently been assumed by setting $B = \infty$ (Bradford and Torkzaban, 2015). Predicted values of ε_1 as a function of A (with $B = \infty$) are shown in Figure S1. Results demonstrate that values of ε_1 are quite similar when using Equations (13) and (14), and we, therefore, choose to employ Equation (14). It should be mentioned that Equations (13) and (14) may also be used to determine the probability that an interacting colloid will be released from a secondary and primary minima (ε_{rk}) by diffusion. In this case, A is equal to the minimum kinetic energy to escape from the minimum and $B = \infty$ (e.g., the maximum kinetic energy) (Bradford and Torkzaban, 2015; Bradford et al., 2017).

The values ε_k and ε_{rk} determine whether a diffusing colloid will interact in a minimum and the reversibility of this interaction, respectively. No colloid interaction in the minimum occurs if ε_k is below a critical threshold (ε_c) that was taken to be 0.01 (Bradford et al., 2017). Reversible interaction occurs when $\varepsilon_k > \varepsilon_c$ and $\varepsilon_c < \varepsilon_{rk}$, and irreversible interaction occurs when $\varepsilon_k > \varepsilon_c$ and $\varepsilon_c > \varepsilon_{rk}$. The condition for irreversible colloid interaction can, therefore, be expressed mathematically using β_k terms as (Bradford and Torkzaban, 2015; Bradford et al., 2017):

$$\beta_k = H_o\left(\varepsilon_k - \varepsilon_c\right) H_o\left(\varepsilon_c - \varepsilon_{rk}\right) \tag{15}$$

where H_o is a Heaviside function that is equal to 1 or 0 depending on whether the quantity in parentheses is greater than or equal to 0 or less than 0, respectively. A value of $\beta_k = 1$ indicates a location of irreversible retention, whereas $\beta_k = 0$ denotes no or reversible retention. In this work, if $\beta_1 = 1$ or $\beta_2 = 1$ we define a parameter β equal to 1 otherwise 0. It should be mentioned that this approach may also be extended to account for the role of hydrodynamics and the spatial distributions of NR and/or CH on colloid immobilization (Bradford and Torkzaban, 2015), but this was not the focus of this study.

Numerical Experiments

Numerical experiments were conducted to examine interaction energy parameters and irreversible retention of hydrophilic and hydrophobic bacteria on quartz surfaces with different types and amounts of CH and/or NR under different IS conditions. Results were presented as interpolated contour graphs which were generated using the marching square graphics algorithm in Plotly (Plotly, Canada).

The individual Hamaker constants for water, pure quartz, and the bacteria were taken as 3.7×10^{-20} J (Israelachvili, 1992), 8.86×10^{-20} J (Bergström, 1997), and 6.46×10^{-20} J, respectively. This yields a commonly employed value for the combined Hamaker constant for bacteria-water-quartz equal to 6.5×10^{-21} J (Rijnaarts et al., 1995a,b). The zeta potential of pure quartz was taken to be -22, -12, and -11.2 mV in 10, 50, and 100 mM NaCl solution, respectively (Torkzaban et al., 2008). The zeta potential of the bacteria in 10, 50, and 100 mM NaCl solution was taken to be -49, -32, and -21 mV, respectively (Torkzaban et al., 2008).

The influence of different amounts and types of organic matter and metal oxide coatings on the quartz surface was considered by systematically changing values of A_{s2}, θ_{s2}, ζ_{s2}, and f_{s2} over hypothetical ranges. The various types of CH (Hamaker, contact angle, or zeta potential) were separately examined to better understand their individual contributions and relative importance. The solid phase Hamaker constant and fraction on site 2 were varied from $A_{s2} = 2.5 \times 10^{-20}$ to 10×10^{-20} J and $f_{s2} = 0$ to 1 when considering heterogeneity in van der Waals interactions. This range in individual Hamaker constants encompassed reported values for humic acid, extracellular polymeric substances, and carbon black that are equal to 4.85×10^{-20}, 7.78×10^{-20}, 1×10^{-19} J, respectively (Tong et al., 2011; Han et al., 2017). The solid phase contact angle and fraction on site 2 were varied from $\theta_{s2} = 0$ to $125°$ and $f_{s2} = 0$ to 1 when considering heterogeneity in Lewis acid-base interactions. This range in contact angles includes reported values for humic acid and fulvic acid of around $20°$ (Lin et al., 2006), and a upper limit similar to black carbon which is equal to $136.6°$ (Hwang et al., 2018). The solid phase zeta potential and fraction on site 2 were varied from $\zeta_{s2} = -20$ to $+30$ mV and $f_{s2} = 0$ to 1 when considering heterogeneity in electrostatic double layer interactions. This range in zeta potentials encompasses a wide range of minerals, metal oxide coatings, and humic materials (Fuerstenau and Pradip, 2005; Tong et al., 2011).

Some calculations considered roughness on the bacteria and solid surfaces. In this case, values of h_{cr} and f_{cr} on the bacteria surface were set to 25 nm and 0.2, respectively, to be consistent with reported values in the literature (King et al., 2014). Tunneling Electron Microscopy of the surface of various bacteria species has also revealed that their macromolecules extend between 5 and 100 nm into solution (Rijnaarts et al., 1995a). Heterogeneity on bacteria cell surface lipopolysaccharides and extracellular polysaccharides have been found to have a role in bacterial adhesion (Camesano and Abu-Lail, 2002; Abu-Lail and Camesano, 2003). The value of h_{sr} and f_{sr} on the solid surface varied from 0 to 80 nm and 0 to 1, respectively, when considering only the influence of NR. When the combined influence of CH and solid phase roughness was considered values of $h_{sr} = 50$ nm and $f_{sr} = 0.1$ (IS = 50 or 100 mM) or 0.05 (IS = 10 mM). These roughness parameters values were selected to be consistent with

published studies that have employed Atomic Force Microscopy to measure the roughness properties on quartz or glass bead surfaces (Han et al., 2016; Rasmuson et al., 2017) or examined the influence of roughness on interaction energies (Bradford et al., 2017).

RESULTS AND DISCUSSION

Chemical Heterogeneity

Figure 1 shows contour plots of Φ_{2min} (**Figure 1A**), Φ_{max} (**Figure 1B**), Φ_{1min} (**Figure 1C**), β_1 (**Figure 1D**), β_2 (**Figure 1E**), and β (**Figure 1F**) for a hydrophilic bacteria when the IS = 100 mM NaCl and heterogeneity in the van der Waals interaction was considered; e.g., the solid phase Hamaker constant and fraction on site 2 were varied from A_{s2} = 2.5 × 10^{-20} to 10 × 10^{-20} J and f_{s2} = 0 to 1. Heterogeneity in double layer and Lewis acid-base interactions was neglected (**Table 1**). The Hamaker constant on solid phase site 1 was A_{s1} = 8.86 × 10^{-20} J to be consistent with quartz (Bergström, 1997). When A_{s2} is less than A_{s1} and f_{s2} > 0 the combined Hamaker is smaller than that of quartz. In this case, the relative importance of the van der Waals interaction is diminished relative to quartz, and conditions for bacteria retention become less favorable. Consequently, a decrease in A_{s2} produces an increase in Φ_{2min}, Φ_{max}, and Φ_{1min}, especially for higher values of f_{s2}. Bacteria release or reversible retention (β = 0 in **Figure 1F**) only occurs for smaller A_{s2} and for larger f_{s2}. Both primary (**Figure 1D**) and secondary (**Figure 1E**) minima contributed to irreversible retention for the complementary conditions. It should be mentioned that the interaction energy profiles were similarly influenced by variability in A_{s2} and f_{s2} under lower IS conditions (Figure S2). However, these changes were not sufficient to eliminate the energy barrier because the influence of the repulsive electrostatic double layer interaction is greater under lower IS conditions. In this case, irreversible retention therefore only occurred in a secondary minimum. Consequently, the influence of variability in the Hamaker constant increased the relative importance of secondary to primary minima retention under lower IS conditions.

Figure 2 shows contour plots of Φ_{2min} (**Figure 2A**), Φ_{max} (**Figure 2B**), Φ_{1min} (**Figure 2C**), and β (**Figure 2D**) for a hydrophilic bacteria when the IS = 50 mM NaCl and heterogeneity in Lewis acid-base interaction on the solid phase was considered. In this case, the solid phase contact angle and fraction on site 2 were varied from θ_{s2} = 0 to 125° and f_{s2} = 0 to 1, and values of θ_{s1} and θ_{c1} were both set to zero. Heterogeneity in double layer and van der Waals interactions was neglected (**Table 1**). An increase in θ_{s2} produces an increase in the attractive Lewis acid-base interaction that reduced Φ_{2min}, Φ_{max}, and Φ_{1min}, especially for larger values of f_{s2}. Higher values of θ_{s2} and f_{s2} created conditions that were favorable for irreversible retention (β = 1 in **Figure 2D**) in either a primary or secondary minima. The influence of variations in Lewis acid-base interactions similarly reduced the energy barrier when the IS = 10 mM, but were insufficient to eliminate that energy barrier and produce irreversible retention in a

primary minimum (Figure S3). Variations in Lewis acid-base interaction only influenced the depth of the primary minimum when the IS = 100 mM because the energy barrier was already eliminated (Figure S4). Similar, calculations were conducted for hydrophobic bacteria (Figure S5). In this case, the influence of Lewis acid-base interactions on interaction energy parameters followed the same trends as for the hydrophilic bacteria, but became even more pronounced (e.g., irreversible retention occurred at lower θ_{s2}, f_{s2}, and IS conditions). It should be mentioned that increasing f_{s2} produced greater amounts of irreversible retention with heterogeneity in θ_{s2}, whereas the opposite trend was observed for heterogeneity in A_{s2} in **Figure 1**.

Figure 3 shows contour plots of Φ_{2min} (**Figure 3A**), Φ_{max} (**Figure 3B**), Φ_{1min} (**Figure 3C**), and β_1 (**Figure 3D**) for a hydrophilic bacteria when the IS = 10 mM NaCl and heterogeneity in electrostatic double layer interaction on the solid phase was considered. In this case, the solid phase zeta potential and fraction on site 2 were varied from ζ_{s2} = −20 to 30 mV and f_{s2} = 0 to 1, and values of ζ_{s1} and ζ_{c1} were equal to −22 and −49, respectively. Heterogeneity in van der Waals and Lewis acid-base interactions was neglected (**Table 1**). Electrostatic repulsion was decreased as ζ_{s2} and f_{s2} were increased, and this produced a decrease in Φ_{2min}, Φ_{max}, and Φ_{1min}. Eventually, the values of ζ_{s2} and f_{s2} were sufficiently large to create an electrostatic attraction which eliminated the energy barrier and produced irreversible retention (β_1 = 1 in **Figure 3D**) in a primary minimum. Other researchers have systematically examined the influence of CH1 on interaction energy profiles under different IS conditions and have observed similar trends (Bendersky and Davis, 2011; Bradford and Torkzaban, 2012; Shen et al., 2013; Pazmino et al., 2014). This information is presented in this work to facilitate the comparison with other CH arising from van der Waals (**Figure 1**) and Lewis acid-base (**Figure 2**) interactions. Comparison of **Figures 1–3** indicates that CH1 can produce irreversible hydrophilic bacteria retention under lower IS conditions than heterogeneity in the solid phase Hamaker constant or contact angle. However, Lewis acid-base interactions become more important for hydrophobic bacteria and this may produce even greater amounts of irreversible retention than CH1 under some solution chemistry conditions (**Figure 3** and Figure S5).

Roughness Heterogeneity

Figure 4 shows contour plots of Φ_{2min} (**Figure 4A**), Φ_{max} (**Figure 4B**), Φ_{1min} (**Figure 4C**), and β_1 (**Figure 4D**) for a hydrophilic bacteria when the IS = 10 mM NaCl and roughness heterogeneity on the bacteria and the solid phase was considered. In this case, the bacteria had f_{cr} = 0.2 and h_{cr} = 25 nm, and the roughness height (h_{sr} = 0–80 nm) and fraction (f_{sr} = 0–1) on the solid phase were varied. The different types of CH were neglected in these calculations (**Table 1**). Roughness on the solid surface had a dramatic influence on interaction energy parameters. In particular, values of Φ_{max} were significantly reduced or eliminated because of differences in van der Waals and electrostatic double layer interactions with separation distance, and Φ_{2min} and Φ_{1min} became shallower for
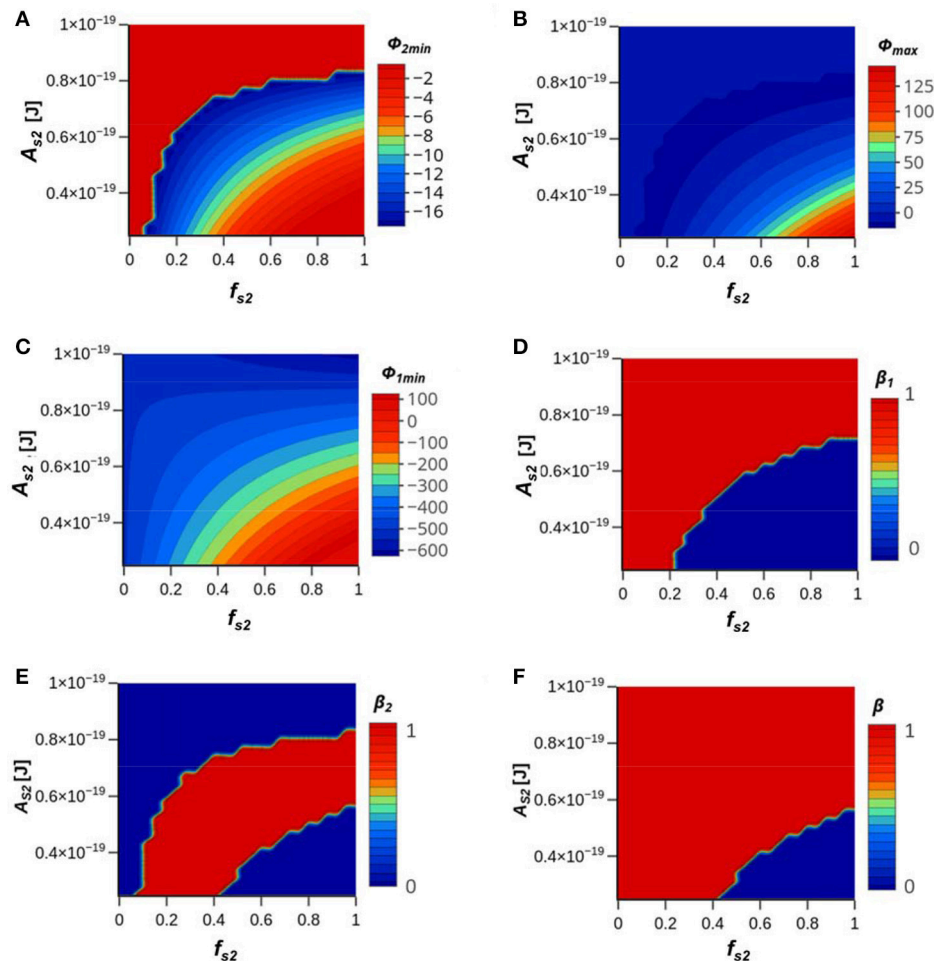
FIGURE 1 | Contour plots of **(A)** Φ_{2min}, **(B)** Φ_{max}, **(C)** Φ_{1min}, **(D)** β_1, **(E)** β_2, and **(F)** β for a hydrophilic bacterium when the IS = 100 mM NaCl and heterogeneity in the van der Waals interaction was considered. The solid phase Hamaker constant and fraction on site 2 were varied from $A_{s2} = 2.5 \times 10^{-20}$ to 10×10^{-20} J and f_{s2} = 0 to 1. **Table 1** gives a summary of all parameters.

small values of f_{sr} because of diminished van der Waals attraction from the underlying surfaces (Torkzaban and Bradford, 2016). Only a small fraction of the solid phase roughness conditions produced irreversible bacteria retention ($\beta_1 = 1$ in **Figure 4D**) in a primary minimum; e.g., when $f_{sr} = 0.05$. Other researchers have previously observed similar trends for solid phase roughness parameters on interaction energies (Suresh and Walz, 1997; Bhattacharjee et al., 1998; Hoek et al., 2003; Hoek and Agarwal, 2006; Huang et al., 2009; Bendersky and Davis, 2011; Shen et al., 2011, 2012; Bradford and Torkzaban, 2013; Bradford et al., 2017). In this research, we compare this behavior to various CH conditions. In particular, small amounts of NR reduces the energy barrier height to a much greater extent than similar amounts of heterogeneity in charge (**Figure 3**), Hamaker constant (**Figure 1**), or contact angle (**Figure 2**) on the solid phase. Furthermore, NR produced shallower Φ_{2min} and Φ_{1min}, whereas heterogeneity in charge (increasing ζ_{s2} and f_{s2}), Hamaker constant (increasing A_{s2} and decreasing f_{s2}), and contact angle (increasing θ_{s2} and f_{s2}) on the solid increased the depth of Φ_{2min} and Φ_{1min}. In the next

section, we investigate the combined influence of NR and the various CH types.

Roughness and Chemical Heterogeneity

Figure 5 shows contour plots of Φ_{2min} (**Figure 5A**), Φ_{max} (**Figure 5B**), Φ_{1min} (**Figure 5C**), and β_1 (**Figure 5D**) for a hydrophilic bacteria when the IS = 100 mM NaCl, the bacteria ($f_{cr} = 0.2$ and $h_{cr} = 25$ nm) and solid phase ($f_{sr} = 0.1$ and $h_{cr} = 50$ nm) have roughness, and the solid phase has the same Hamaker constant heterogeneity conditions as in **Figure 1**. **Table 1** summarizes all parameter values. Note that values of Φ_{max} in **Figure 5** were significantly reduced or eliminated, and Φ_{2min} and Φ_{1min} became shallower in comparison to **Figure 1**. The net effect of these changes was to decrease the amount of irreversible bacteria retention and to increase the relative importance of the primary to the secondary minima. These observations clearly reveal that these roughness conditions dominated the interaction energy profile parameters in the presence of heterogeneity

TABLE 1 | A summary of all model parameters employed in the figures that were varied.

Figure	IS	Hetero	$A_{S2} \times 10\text{-}20$	$\zeta c1 = \zeta c2$	$\zeta s1$	$\zeta s2$	$\theta c1 = \theta c2$	$\theta s2$	f_{S2}	hsr	fsr	hcr	fcr
[No.]	[mM]	[Type]	[J]	[mV]	[mV]	[mV]	[?]	[?]	[−]	[nm]	[−]	[nm]	[−]
1	100	CH2	2.5–10	−21	−11.2	−11.2	0	0	0–1	0	0	0	0
2	50	CH3	8.86	−32	−12	−12	0	0–125	0–1	0	0	0	0
3	10	CH1	8.86	−49	−22	−20–$^{+}$30	0	0	0–1	0	0	0	0
4	10	NR	8.86	−49	−22	−22	0	0	0	0–80	0–1	25	0.2
5	100	CH2+NR	2.5–10	−21	−11.2	−11.2	0	0	0–1	50	0.1	25	0.2
6	10	CH3+NR	8.86	−49	−22	−22	0	0–125	0–1	50	0.05	25	0.2
S2	10	CH2	2.5–10	−49	−22	−22	0	0	0–1	0	0	0	0
S3	10	CH3	8.86	−49	−22	−22	0	0–125	0–1	0	0	0	0
S4	100	CH3	8.86	−21	−11.2	−11.2	0	0–125	0–1	0	0	0	0
S5	10	CH3	8.86	−49	−22	−22	125	0–125	0–1	0	0	0	0
S6	100	CH2+NR	2.5–10	−21	−11.2	−11.2	0	0	0–1	50	0.8	25	0.8
S7	10	CH3+NR	8.86	−49	−22	−22	125	0–125	0–1	50	0.05	25	0.2
S8	10	CH1+NR	8.86	−49	−22	−20–$^{+}$30	0	0	0–1	50	0.05	25	0.2

Constant parameters included: $A_{c1} = A_{c2} = 6.46 \times 10^{-20}$ J, $A_{s1} = 8.86 \times 10^{-20}$ J, and $\theta_{s1} = 0°$.
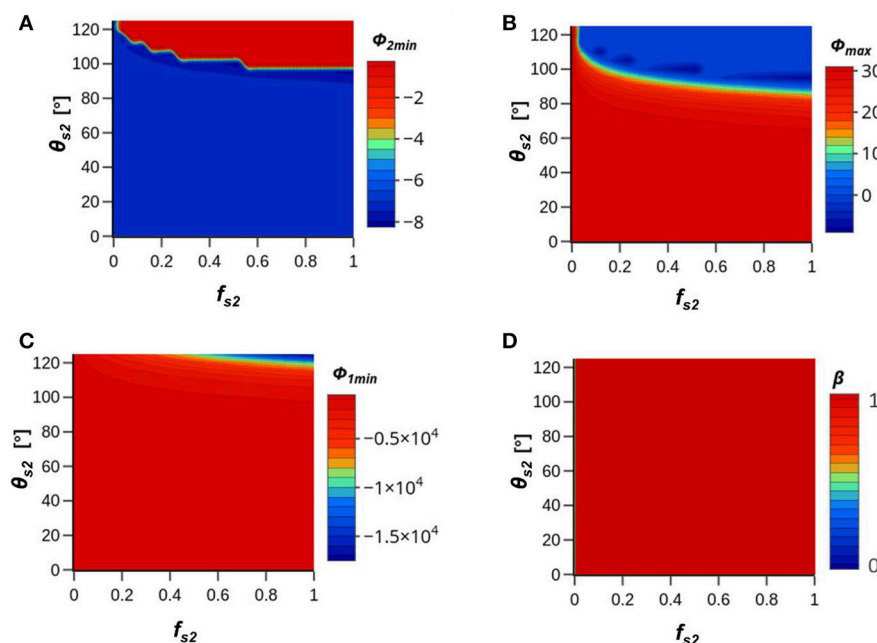

FIGURE 2 | Contour plots of (A) Φ_{2min}, (B) Φ_{max}, (C) Φ_{1min}, and (D) β for a hydrophilic bacterium when the IS = 50 mM NaCl and heterogeneity in Lewis acid-base interaction on the solid phase was considered. The solid phase contact angle and fraction on site 2 were varied from θ_{s2}=0 to 125° and f_{s2}=0 to 1, and values of θ_{s1} and θ_{c1} were both set to zero. Table 1 gives a summary of all parameters.

in solid phase Hamaker constants. However, heterogeneity in solid phase Hamaker constants will control the profile parameters when f_{sr} becomes large and approaches 1 (Figure S6).

Figure 6 shows contour plots of Φ_{2min} (Figure 6A), Φ_{max} (Figure 6B), Φ_{1min} (Figure 6C), and β_1 (Figure 6D) for a hydrophilic bacteria when the IS = 10 mM NaCl, the bacteria ($f_{cr} = 0.2$ and $h_{cr} = 25$ nm) and solid phase ($f_{sr} = 0.05$ and

$h_{cr} = 50$ nm) have roughness, and the solid phase has the same CH3 conditions as in Figure S3. Comparison of Figure S3 and Figure 6 reveals that roughness reduced or eliminated Φ_{max} for the considered CH3 conditions. In addition, the depths of Φ_{2min} and especially Φ_{1min} were reduced in the presence of roughness. CH3 produced no irreversible retention on the smooth surface when the IS = 10 mM (Figure S3). In contrast, the combined influence of roughness and CH3 created irreversible
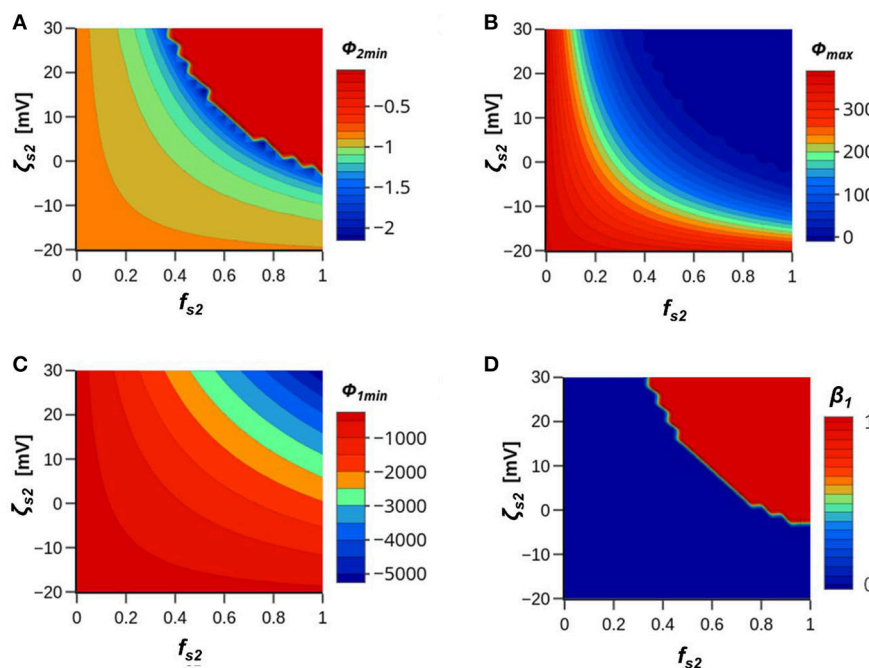
FIGURE 3 | Contour plots of **(A)** Φ_{2min}, **(B)** Φ_{max}, **(C)** Φ_{1min}, and **(D)** β_1 for a hydrophilic bacterium when the IS = 10 mM NaCl and heterogeneity in electrostatic double layer interaction on the solid phase was considered. The solid phase zeta potential and fraction on site 2 were varied from $\zeta_{s2} = -20$ to 30 mV and $f_{s2} = 0$ to 1, and values of ζ_{s1} and ζ_{c1} were equal to -22 and -49, respectively. **Table 1** gives a summary of all parameters.
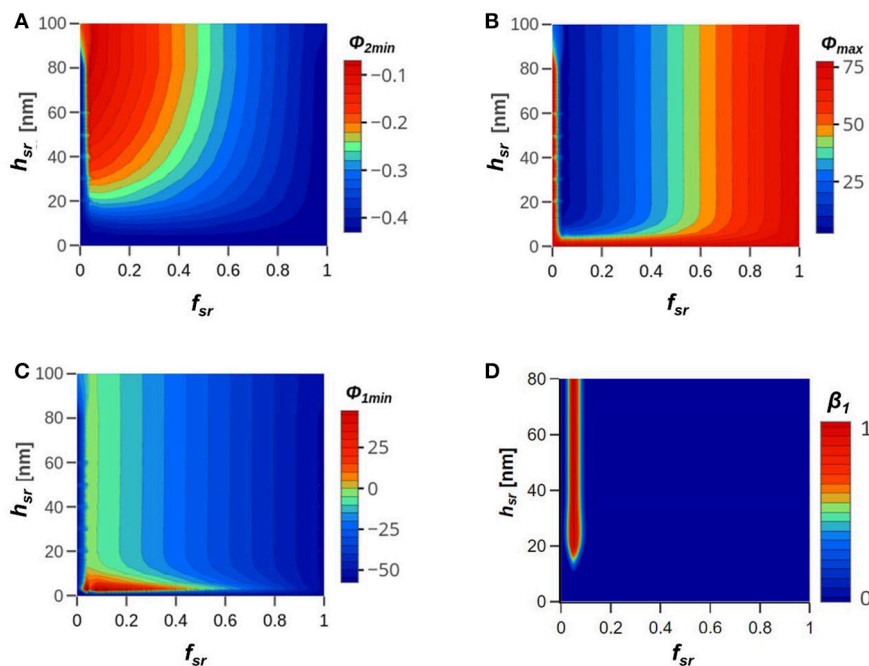
FIGURE 4 | Contour plots of **(A)** Φ_{2min}, **(B)** Φ_{max}, **(C)** Φ_{1min}, and **(D)** β_1 for a hydrophilic bacterium when the IS = 10 mM NaCl and roughness heterogeneity on the bacteria and the solid phase was considered. The bacteria had $f_{cr} = 0.2$ and $h_{cr} = 25$ nm, and the roughness height ($h_{sr} = 0$ to 80 nm) and fraction ($f_{sr} = 0$ to 1) on the solid phase were varied. **Table 1** gives a summary of all parameters.
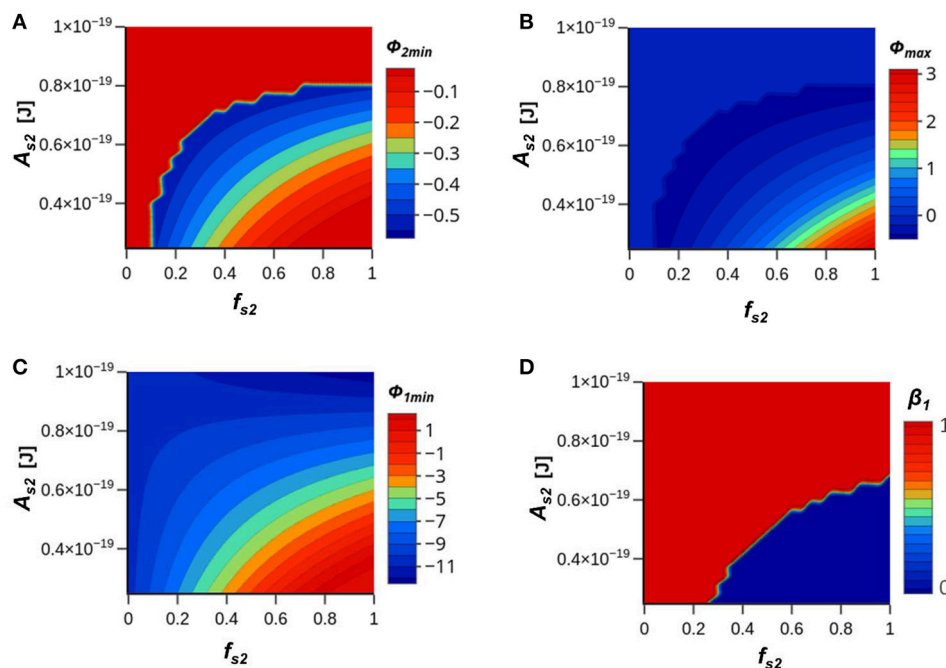
FIGURE 5 | Contour plots of **(A)** Φ_{2min}, **(B)** Φ_{max}, **(C)** Φ_{1min}, and **(D)** β_1 for a hydrophilic bacterium when the IS = 100 mM NaCl, the bacteria (f_{cr} = 0.2 and h_{cr} = 25 nm) and solid phase (f_{sr} = 0.1 and h_{sr} = 50 nm) have roughness. The solid phase Hamaker constant and fraction on site 2 were varied from A_{S2} = 2.5 × 10^{-20} to 10 × 10^{-20} J and f_{s2} = 0 to 1 (**Figure 1**). **Table 1** gives a summary of all parameters.
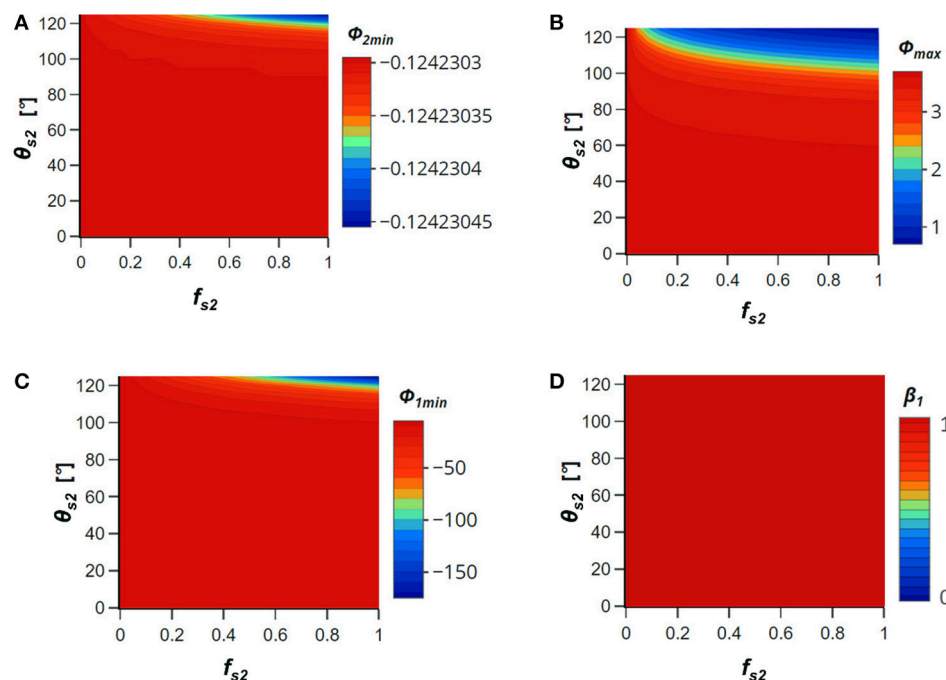
FIGURE 6 | Contour plots of **(A)** Φ_{2min}, **(B)** Φ_{max}, **(C)** Φ_{1min}, and **(D)** β_1 for a hydrophilic bacterium when the IS = 10 mM NaCl, the bacteria (f_{cr} = 0.2 and h_{cr} = 25 nm) and solid phase (f_{sr} = 0.05 and h_{sr} = 50 nm) have roughness. The solid phase contact angle and fraction on site 2 were varied from θ_{s2} = 0 to 125° and f_{s2} = 0 to 1, and values of θ_{s1} and θ_{c1} were both set to zero (**Figure 2**). **Table 1** gives a summary of all parameters.

retention in a primary when the IS = 10 mM for all conditions (**Figure 6D**). These same trends were observed for hydrophobic bacteria when the IS = 10 mM (Figure S7). However, the depth of the primary minimum was much deeper for the hydrophobic than the hydrophilic bacteria. These observations indicate that roughness had a controlling influence on eliminating the energy barrier, but that Lewis acid-base interactions had a significant influence on the depth of the primary minima and may be used to offset some of the influence on roughness. The relative contributions of NR and CH3 are therefore expected to change with the physical and CH parameters, as well as the solution IS.

The combined influence of CH1 and NR on interaction energies has been previously investigated (e.g., Bradford and Torkzaban, 2013; Bradford et al., 2017). However, for completeness Figure S8 shows contour plots of Φ_{2min} (Figure S8A), Φ_{max} (Figure S8B), Φ_{1min} (Figure S8C), and β_1 (Figure S8D) for a hydrophilic bacteria when the IS = 10 mM NaCl, the bacteria (f_{cr} = 0.2 and h_{cr} = 25 nm) and solid phase (f_{sr} = 0.05 and h_{cr} = 50 nm) have roughness, and the solid phase has the same CH1 conditions as in **Figure 3**. Similar to **Figure 6** (NR with CH3), bacteria retention was enhanced in the presence of roughness in comparison to a smooth surface with the same CH1 conditions (**Figure 3** and Figure S8). This occurred because roughness readily reduced the energy barrier, and the combination of roughness and CH1 produced a sufficiently deep primary minimum for retention. It should be mentioned that if f_{cr} and f_{sr} are further decreased that the primary minimum will become shallower and bacteria will be subject to diffusive release even in the presence of CH1 (Bradford et al., 2017).

CONCLUSIONS

An approach was developed to determine interaction energies between a colloid and the solid water interface when both surfaces have binary NR and CH. These interaction energies considered constant potential double layer electrostatics, retarded London-van der Waals attraction, Lewis acid-base interactions, and Born repulsion for a sphere-plate geometry. CH from variability in Hamaker constants (van der Waals interactions), contact angles (Lewis acid-base interactions), and zeta potentials (electrostatic double layer interactions) can be considered separately or in combination with other heterogeneities. Calculated interaction energy parameters were used in conjunction with an energy balance model to determine conditions for irreversible retention in the presence of random fluctuations in kinetic energy of a diffusing colloid.

SOM coatings on mineral surfaces are expected to create heterogeneity by altering their Lewis acid-base (contact angle) and van der Waals (Hamaker constant) interactions. Charge heterogeneity may also occur as a result of SOM as well as metal oxide coatings. Numerical experiments were conducted to investigate the influence of various heterogeneity types, amounts, and combinations on bacteria interaction energy parameters and irreversible retention. Heterogeneity in the solid phase

Hamaker constant over expected ranges for SOM produced a combined Hamaker constant that was smaller than quartz. Increasing Hamaker constant heterogeneity, therefore, tended to increase the relative importance of repulsive double layer interactions over attractive van der Waals interactions and produced a more repulsive surface with less bacteria retention. This effect became more apparent under higher IS conditions when the double layer was compressed, and the energy barrier was smaller.

In contrast to heterogeneity in the Hamaker constant, variability in the solid phase contact angle over expected ranges for SOM produced enhanced attractive Lewis acid-base interactions. This decreased the height of the energy barrier, and increased the depths of the secondary and primary minima and the amount of irreversible bacteria retention under lower IS conditions. These effects were magnified for greater contact angles and fractions on the solid surface, and for more hydrophobic bacteria.

Heterogeneity in the solid phase zeta potential behaved in a similar manner to heterogeneity in the contact angle. In particular, increasing the fraction and zeta potential of site 2 decreased the energy barrier height and increased the depths of the secondary and primary minima and the amount of irreversible retention. In general, increasing CH1 was more effective at reducing the energy barrier height and creating irreversible retention at lower IS conditions than increasing CH3 for hydrophilic bacteria. However, CH3 tended to produce deeper secondary and primary minima than CH1.

Small fractions of NR always significantly reduced and/or eliminated the energy barrier under lower IS conditions. Furthermore, NR tended to control the energy barrier height in the presence of CH in Hamaker constant, contact angle, or zeta potential. Small amounts of NR also significantly decreased the depths of the secondary and primary minima in comparison to a smooth surface. However, the depths of the secondary and primary minima tended to be deeper in the presence of zeta potential and especially CH3, and this made bacteria retention more irreversible.

Collectively, our results demonstrate the critical role of CH and NR in controlling interaction energy parameters and irreversible bacteria retention. In particular, spatial variations in SOM, metal oxide coatings, and especially NR will have important roles in determining bacteria retention on natural surfaces. The relative importance of the various heterogeneity types was found to change with the solution IS and specific ranges in considered heterogeneity parameters. NR tended to be dominant for small roughness fractions. In contrast, SOM and metal oxide coatings are expected to play more important roles on smooth surfaces. In this case, CH1 and CH3 were more important under lower IS conditions, whereas CH2 started to play a role at a higher IS.

AUTHOR CONTRIBUTIONS

SB, SS, HK, and GH contributed to the conceptual processes described in the paper, description of interaction energies,

determination of simulation parameters, and discussion of findings.

SUPPLEMENTARY MATERIAL

The Supplementary Material for this article can be found online at: https://www.frontiersin.org/articles/10.3389/fenvs.2018.00056/full#supplementary-material

REFERENCES

Abu-Lail, N. I., and Camesano, T. A. (2003). The role of lipopolysaccharides in the adhesion, retention, and transport of *Escherichia coli* JM109. *Environ. Sci. Technol.* 37, 2173–2183. doi: 10.1021/es026159o

Aiken, G. R. (1985). *Humic Substances in Soil, Sediment, and Water: Geochemistry, Isolation, and Characterization.* New York, NY: Wiley.

Almendros, G., González-Vila, F., and Martin, F. (1990). Fire-induced transformation of soil organic matter from an oak forest: an experimental approach to the effects of fire on humic substances. *Soil Sci.* 149, 158–168.

Amirbahman, A., and Olson, T. M. (1993). Transport of humic matter-coated hematite in packed beds. *Environ. Sci. Technol.* 27, 2807–2813.

Bendersky, M., and Davis, J. M. (2011). DLVO interaction of colloidal particles with topographically and chemically heterogeneous surfaces. *J. Colloid Interface Sci.* 353, 87–97. doi: 10.1016/j.jcis.2010.09.058

Bergendahl, J., and Grasso, D. (1999). Prediction of colloid detachment in a model porous media: thermodynamics. *AIChE J.* 45, 475–484. doi: 10.1002/aic.690450305

Bergström, L. (1997). Hamaker constants of inorganic materials. *Adv. Colloid Interface Sci.* 70, 125–169.

Bhattacharjee, S., Ko, C. H., and Elimelech, M. (1998). DLVO interaction between rough surfaces. *Langmuir* 14, 3365–3375.

Bradford, S. A., Kim, H., Shen, C., Sasidharan, S., and Shang, J. (2017). Contributions of nanoscale roughness to anomalous colloid retention and stability behavior. *Langmuir* 33, 10094–10105. doi: 10.1021/acs.langmuir.7b02445

Bradford, S. A., and Torkzaban, S. (2012). Colloid adhesive parameters for chemically heterogeneous porous media. *Langmuir* 28, 13643–13651. doi: 10.1021/la3029929

Bradford, S. A., and Torkzaban, S. (2013). Colloid interaction energies for physically and chemically heterogeneous porous media. *Langmuir* 29, 3668–3676. doi: 10.1021/la400229f

Bradford, S. A., and Torkzaban, S. (2015). Determining parameters and mechanisms of colloid retention and release in porous media. *Langmuir* 31, 12096–12105. doi: 10.1021/acs.langmuir.5b03080

Camesano, T. A., and Abu-Lail, N. I. (2002). Heterogeneity in bacterial surface polysaccharides, probed on a single-molecule basis. *Biomacromolecules* 3, 661–667. doi: 10.1021/bm015648y

Cushing, R. S., and Lawler, D. F. (1998). Depth filtration: fundamental investigation through three-dimensional trajectory analysis. *Environ. Sci. Technol.* 32, 3793–3801. doi: 10.1021/es9707567

de Blas, E., Rodríguez-Alleres, M., and Almendros, G. (2010). Speciation of lipid and humic fractions in soils under pine and eucalyptus forest in northwest Spain and its effect on water repellency. *Geoderma* 155, 242–248. doi: 10.1016/j.geoderma.2009.12.007

DeNovio, N. M., Saiers, J. E., and Ryan, J. N. (2004). Colloid movement in unsaturated porous media. *Vadose Zone J.* 3, 338–351. doi: 10.2113/3.2.338

Doerr, S., Shakesby, R., and Walsh, R. (2000). Soil water repellency: its causes, characteristics and hydro-geomorphological significance. *Earth Sci. Rev.* 51, 33–65. doi: 10.1016/S0012-8252(00)00011-8

Drummond, C. J., and Chan, D. Y. (1997). van der Waals interaction, surface free energies, and contact angles: dispersive polymers and liquids. *Langmuir* 13, 3890–3895.

Ellerbrock, R., Gerke, H., Bachmann, J., and Goebel, M.-O. (2005). Composition of organic matter fractions for explaining wettability of three forest soils. *Soil Sci. Soc. Am. J.* 69, 57–66. doi:10.2136/sssaj2005.0057

Espinasse, B., Hotze, E. M., and Wiesner, M. R. (2007). Transport and retention of colloidal aggregates of C60 in porous media: Effects of organic macromolecules, ionic composition, and preparation method. *Environ. Sci. Technol.* 41, 7396–7402. doi: 10.1021/es0708767

Flynn, R. M., Yang, X., Hofmann, T., and von der Kammer, F. (2012). Bovine serum albumin adsorption to iron-oxide coated sands can change microsphere deposition mechanisms. *Environ. Sci. Technol.* 46, 2583–2591. doi: 10.1021/es202048c

Franco, C., Clarke, P., Tate, M., and Oades, J. (2000). Hydrophobic properties and chemical characterisation of natural water repellent materials in Australian sands. *J. Hydrol.* 231, 47–58. doi: 10.1016/S0022-1694(00)00182-7

Fuerstenau, D. W., and Pradip (2005). Zeta potentials in the flotation of oxide and silicate minerals. *Adv. Colloid Interface Sci.* 114–115, 9–26. doi: 10.1016/j.cis.2004.08.006

Grasso, D., Subramaniam, K., Butkus, M., Strevett, K., and Bergendahl, J. (2002). A review of non-DLVO interactions in environmental colloidal systems. *Rev. Environ. Sci. Biotechnol.* 1, 17–38. doi: 10.1023/a:1015146710500

Gregory, J. (1981). Approximate expressions for retarded van der waals interaction. *J. Colloid Interface Sci.* 83, 138–145. doi: 10.1016/0021-9797(81)90018-7

Han, P., Wang, X., Cai, L., Tong, M., and Kim, H. (2014). Transport and retention behaviors of titanium dioxide nanoparticles in iron oxide-coated quartz sand: effects of pH, ionic strength, and humic acid. *Colloids Surfaces A Physicochem. Eng. Aspects* 454, 119–127. doi: 10.1016/j.colsurfa.2014.04.020

Han, Y., Hwang, G., Kim, D., Bradford, S. A., Lee, B., Eom, I., et al. (2016). Transport, retention, and long-term release behavior of ZnO nanoparticle aggregates in saturated quartz sand: role of solution pH and biofilm coating. *Water Res.* 90, 247–257. doi: 10.1016/j.watres.2015.12.009

Han, Y., Hwang, G., Park, T., Gomez-Flores, A., Jo, E., Eom, I-C., et al. (2017). Stability of carboxyl-functionalized carbon black nanoparticles: the role of solution chemistry and humic acid. *Environ. Sci. Nano* 4, 800–810. doi: 10.1039/C6EN00530F

Henry, C., Minier, J.-P., Lefevre, G., and Hurisse, O. (2011). Numerical study on the deposition rate of hematite particle on polypropylene walls: role of surface roughness. *Langmuir* 27, 4603–4612. doi: 10.1021/la104488a

Hoek, E. M. V., and Agarwal, G. K. (2006). Extended DLVO interactions between spherical particles and rough surfaces. *J. Colloid Interface Sci.* 298, 50–58. doi: 10.1016/j.jcis.2005.12.031

Hoek, E. M. V., Bhattacharjee, S., and Elimelech, M. (2003). Effect of membrane surface roughness on colloid-membrane DLVO interactions. *Langmuir* 19, 4836–4847. doi: 10.1021/la027083c

Hogg, R., Healy, T. W., and Fuerstenau, D. W. (1966). Mutual coagulation of colloidal dispersions. *Trans. Faraday Soc.* 62:1638. doi: 10.1039/tf9666201638

Hough, D. B., and White, L. R. (1980). The calculation of Hamaker constants from Lifshitz theory with applications to wetting phenomena. *Adv. Colloid Interface Sci.* 14, 3–41. doi: 10.1016/0001-8686(80)80006-6

Huang, W., Peng, P. A., Yu, Z., and Fu, J. (2003). Effects of organic matter heterogeneity on sorption and desorption of organic contaminants by soils and sediments. *Appl. Geochem.* 18, 955–972. doi: 10.1016/S0883-2927(02)00205-6

Huang, X., Bhattacharjee, S., and Hoek, E. M. V. (2009). Is surface roughness a "scapegoat" or a primary factor when defining particle–substrate interactions? *Langmuir* 26, 2528–2537. doi: 10.1021/la9028113

Hudson, R., Traina, S., and Shane, W. (1994). Organic matter comparison of wettable and nonwettable soils from bentgrass sand greens. *Soil Sci. Soc. Am. J.* 58, 361–367.

Hwang, G., Gomez-Flores, A., Bradford, S. A., Choi, S., Jo, E., Kim, S. B. et al. (2018). Analysis of stability behavior of carbon black nanoparticles in ecotoxicological media: Hydrophobic and steric effects. *Colloids Surf. A Physicochem. Eng. Aspects.*

Israelachvili, J. N. (1992). *Intermolecular and Surface Forces.* London; San Diego, CA: Academic Press.

Jiang, X., Tong, M., and Kim, H. (2012). Influence of natural organic matter on the transport and deposition of zinc oxide nanoparticles in saturated porous media. *J. Colloid Interface Sci.* 386, 34–43. doi: 10.1016/j.jcis.2012.07.002

King, J. D., Berry, S., Clarke, B. R., Morris, R. J., and Whitfield, C. (2014). Lipopolysaccharide O antigen size distribution is determined by a chain extension complex of variable stoichiometry in Escherichia coli O9a. *Proc. Natl. Acad. Sci. U.S.A.* 111, 6407–6412. doi: 10.1073/pnas.1400814111

Kretzschmar, R., and Sticher, H. (1997). Transport of humic-coated iron oxide colloids in a sandy soil: influence of Ca^{2+} and trace metals. *Environ. Sci. Technol.* 31, 3497–3504.

Lin, C.-Y., Chou, W.-C., Tsai, J.-S., and Lin, W.-T. (2006). Water repellency of Casuarina windbreaks (Casuarina equisetifolia Forst.) caused by fungi in central Taiwan. *Ecol. Eng.* 26, 283–292. doi: 10.1016/j.ecoleng.2005.10.010

Ma'shum, M., and Farmer, V. (1985). Origin and assessment of water repellency of a sandy South Australian soil. *Soil Res.* 23, 623–626.

Ma'shum, M., Tate, M., Jones, G., and Oades, J. (1988). Extraction and characterization of water–repellent materials from Australian soils. *Eur. J. Soil Sci.* 39, 99–110.

Molnar, I. L., Johnson, W. P., Gerhard, J. I., Willson, C. S., and O'Carroll, D. M. (2015). Predicting colloid transport through saturated porous media: a critical review. *Water Resour. Res.* 51, 6804–6845. doi: 10.1002/2015WR017318

Morales, V. L., Zhang, W., Gao, B., Lion, L. W., Bisogni, J. J., McDonough, B. A., et al. (2011). Impact of dissolved organic matter on colloid transport in the vadose zone: deterministic approximation of transport deposition coefficients from polymeric coating characteristics. *Water Res.* 45, 1691–1701. doi: 10.1016/j.watres.2010.10.030

Oliveira, R. (1997). Understanding adhesion: a means for preventing fouling. *Exp. Therm. Fluid Sci.* 14, 316–322. doi: 10.1016/S0894-1777(96)00134-3

Park, J.-A., and Kim, S.-B. (2015). DLVO and XDLVO calculations for bacteriophage MS2 adhesion to iron oxide particles. *J. Contam. Hydrol.* 181, 131–140. doi: 10.1016/j.jconhyd.2015.01.005

Pazmino, E., Trauscht, J., Dame, B., and Johnson, W. P. (2014). Power law size-distributed heterogeneity explains colloid retention on soda lime glass in the presence of energy barriers. *Langmuir* 30, 5412–5421. doi: 10.1021/la501006p

Rasmuson, A., Pazmino, E., Assemi, S., and Johnson, W. P. (2017). Contribution of nano- to microscale roughness to heterogeneity: closing the gap between unfavorable and favorable colloid attachment conditions. *Environ. Sci. Technol.* 51, 2151–2160. doi: 10.1021/acs.est.6b05911

Torkzaban, S., and Bradford, S. A. (2016). Critical role of surface roughness on colloid retention and release in porous media. *Water Res.* 88, 274–284. doi: 10.1016/j.watres.2015.10.022

Rice, J. A., and MacCarthy, P. (1990). A model of humin. *Environ. Sci. Technol.* 24, 1875–1877.

Rijnaarts, H. H., Norde, W., Bouwer, E. J., Lyklema, J., and Zehnder, A. J. (1995a). Reversibility and mechanism of bacterial adhesion. *Colloids Surfaces B Biointerfaces* 4, 5–22.

Rijnaarts, H. H., Norde, W., Lyklema, J., and Zehnder, A. J. (1995b). The isoelectric point of bacteria as an indicator for the presence of cell surface polymers that inhibit adhesion. *Colloids Surfaces B Biointerfaces* 4, 191–197.

Ruckenstein, E., and Prieve, D. C. (1976). Adsorption and desorption of particles and their chromatographic separation. *AIChE J.* 22, 276–283. doi: 10.1002/aic.690220209

Salata, O. V. (2004). Applications of nanoparticles in biology and medicine. *J. Nanobiotechnology* 2:3. doi: 10.1186/1477-3155-2-3

Shen, C., Lazouskaya, V., Zhang, H., and Wang, F. (2012). Theoretical and experimental investigation of detachment of colloids from rough collector surfaces. *Colloids Surfaces A Physicochem. Eng. Aspects* 410, 98–110. doi: 10.1016/j.colsurfa.2012.06.025

Shen, C., Lazouskaya, V., Zhang, H., Li, B., Jin, Y., and Huang, Y. (2013). Influence of surface chemical heterogeneity on attachment and detachment of microparticles. *Colloids Surfaces A Physicochem. Eng. Aspects* 433, 14–29. doi: 10.1016/j.colsurfa.2013.04.048

Shen, C., Li, B., Huang, Y., and Jin, Y. (2007). Kinetics of coupled primary- and secondary-minimum deposition of colloids under unfavorable chemical conditions. *Environ. Sci. Technol.* 41, 6976–6982. doi: 10.1021/es070210c

Shen, C., Li, B., Wang, C., Huang, Y., and Jin, Y. (2011). Surface roughness effect on deposition of nano- and micro-sized colloids in saturated columns at different solution ionic strengths. *Vadose Zone J.* 10:1071. doi: 10.2136/vzj2011.0011

Simoni, S. F., Harms, H., Bosma, T. N. P., and Zehnder, A. J. B. (1998). Population heterogeneity affects transport of bacteria through sand columns at low flow rates. *Environ. Sci. Technol.* 32, 2100–2105. doi: 10.1021/es970936g

Song, J., Peng, P., and, a., Huang, W. (2002). Black carbon and kerogen in soils and sediments. 1. Quantification and characterization. *Environ. Sci. Technol.* 36, 3960–3967. doi: 10.1021/es025502m

Sposito, G. (2008). *The Chemistry of Soils.* New York, NY: Oxford university press.

Stark, W. J., Stoessel, P. R., Wohlleben, W., and Hafner, A. (2015). Industrial applications of nanoparticles. *Chem. Soc. Rev.* 44, 5793–5805. doi: 10.1039/C4CS00362D

Stevenson, F. J. (1994). *Humus Chemistry: Genesis, Composition, Reactions.* New York, NY: John Wiley & Sons.

Suresh, L., and Walz, J. Y. (1996). Effect of surface roughness on the interaction energy between a colloidal sphere and a flat plate. *J. Colloid Interface Sci.* 183, 199–213.

Suresh, L., and Walz, J. Y. (1997). Direct measurement of the effect of surface roughness on the colloidal forces between a particle and flat plate. *J. Colloid Interface Sci.* 196, 177–190.

Tong, M., Zhu, P., Jiang, X., and Kim, H. (2011). Influence of natural organic matter on the deposition kinetics of extracellular polymeric substances (EPS) on silica. *Colloids and Surfaces B: Biointerfaces* 87, 151–158. doi: 10.1016/j.colsurfb.2011.05.015

Torkzaban, S., Tazehkand, S. S., Walker, S. L., and Bradford, S. A. (2008). Transport and fate of bacteria in porous media: Coupled effects of chemical conditions and pore space geometry. *Water Resources Res.* 44:W0440. doi: 10.1029/2007wr006541

Tufenkji, N., and Elimelech, M. (2004). Correlation equation for predicting single-collector efficiency in physicochemical filtration in saturated porous media. *Environ. Sci. Technol.* 38, 529–536. doi: 10.1021/es034049r

Vaidyanathan, R., and Tien, C. (1991). Hydrosol deposition in granular media under unfavorable surface conditions. *Chem. Eng. Sci.* 46, 967–983.

Van Loosdrecht, M., Lyklema, J., Norde, W., Schraa, G., and Zehnder, A. (1987). The role of bacterial cell wall hydrophobicity in adhesion. *Appl. Environ. Microbiol.* 53, 1893–1897.

Van Oss, C. (1994). *Interfacial forces in aqueous media, 1. Marcel Dekker.* New York, NY.

Wilkinson, K. J., Balnois, E., Leppard, G. G., and Buffle, J. (1999). Characteristic features of the major components of freshwater colloidal organic matter revealed by transmission electron and atomic force microscopy. *Colloids Surfaces A Physicochem. Eng. Aspects* 155, 287–310.

Yang, X., Deng, S., and Wiesner, M. R. (2013). Comparison of enhanced microsphere transport in an iron-oxide-coated porous medium by pre-adsorbed and co-depositing organic matter. *Chem. Eng. J.* 230, 537–546. doi: 10.1016/j.cej.2013.06.122

Yang, X., Flynn, R., Von der Kammer, F., and Hofmann, T. (2010). Quantifying the influence of humic acid adsorption on colloidal microsphere deposition onto iron-oxide-coated sand.

Environ. Pollut. 158, 3498–3506. doi: 10.1016/j.envpol.2010.0
3.011

Yang, X., Flynn, R., Von Der Kammer, F., and Hofmann, T. (2011).
Influence of ionic strength and pH on the limitation of latex
microsphere deposition sites on iron-oxide coated sand by humic
acid. *Environ. Pollut.* 159, 1896–1904. doi: 10.1016/j.envpol.2011.0
3.026

Yang, X., Lin, S., and Wiesner, M. R. (2014). Influence of natural organic
matter on transport and retention of polymer coated silver nanoparticles in
porous media. *J. Hazard. Mater.* 264, 161–168. doi: 10.1016/j.jhazmat.2013.1
1.025

Yao, K.-M., Habibian, M. T., and O'Melia, C. R. (1971). Water and
wastewater filtration. *Concepts Appl. Environ. Sci. Technol.* 5, 1105–1112.
doi: 10.1021/es60058a005

Yoon, R.-H., Flinn, D. H., and Rabinovich, Y. I. (1997). Hydrophobic interactions
between dissimilar surfaces. *J. Colloid Interface Sci.* 185, 363–370.

Influence of Pore Characteristics on the Fate and Distribution of Newly Added Carbon

Michelle Y. Quigley[1]*, **Wakene C. Negassa**[2], **Andrey K. Guber**[1,3], **Mark L. Rivers**[4] and **Alexandra N. Kravchenko**[1,3]

[1] Department of Plant, Soil and Microbial Sciences, Michigan State University, East Lansing, MI, United States, [2] Faculty of Agriculture and Environmental Science, University of Rostock, Rostock, Germany, [3] Department of Agricultural Soil Science, University of Göttingen, Göttingen, Germany, [4] Argonne National Lab, Center for Advanced Radiation Sources, University of Chicago, Argonne, IL, United States

Pores create a transportation network within a soil matrix, which controls the flow of air, water, and movement of microorganisms. The flow of air, water, and movement of microbes, in turn, control soil carbon dynamics. Computed microtomography (μCT) allows for the visualization of pore structure at micron scale, but quantitative information on contribution of pores to the fate and protection of soil carbon, essential for modeling, is still lacking. This study uses the natural difference between carbon isotopes of C3 and C4 plants to determine how the presence of pores of different sizes affects spatial distribution patterns of newly added carbon immediately after plant termination and then after 1-month incubation. We considered two contrasting soil structure scenarios: soil with the structure kept intact and soil for which the structure was destroyed via sieving. For the experiment, soil was collected from 0–15 cm depth at a 20-year continuous maize (*Zea mays* L., C4 plant) experiment into which cereal rye (*Secale cereale* L., C3 plant) was planted. Intact soil fragments (5–6 mm) were procured after 3 months rye growth in a greenhouse. Pore characteristics of the fragments were determined through μCT imaging. Each fragment was sectioned and total carbon, total nitrogen, δ^{13}C, and δ^{15}N were measured. The results indicate that, prior to incubation, greater presence of 40–90 μm pores was associated with higher levels of C3 carbon, pointing to the positive role of these pores in transport of new C inputs. Nevertheless, after incubation, the association became negative, indicating greater losses of newly added C in such pores. These trends were statistically significant in destroyed-structure soil and numerical in intact-structure soil. In soils of intact-structures, after incubation, higher levels of total carbon were associated with greater abundance of 6.5–15 and 15–40 μm pores, indicating a lower carbon loss associated with these pores. The results indicate that, in the studied soil, pores of 40–90 μm size range are associated with the fast influx of new C followed by its quick decomposition, while pores <40 μm tend to be associated with C protection.

Keywords: computed microtomography, soil carbon dynamics, soil organic matter, soil structure, stable carbon isotopes

INTRODUCTION

Soils contain twice as much carbon as the atmosphere and have the potential to store even more, especially in agricultural soils (Lal, 1999; Swift, 2001; Dungait et al., 2012; Kell, 2012). Soil carbon content is an important component of soil fertility as it drives several defining criteria of soil quality, including cation exchange capacity, soil aggregation, and water holding capacity (Dou et al., 2014). This makes utilization of agricultural management practices that increase and/or conserve soil carbon vitally important to sustainability (Grandy and Robertson, 2007).

One such practice is the utilization of cover crops, a crop that is planted between main crops for the purpose of preventing erosion, decreasing weeds, and increasing soil fertility. The activity of cover crop roots may benefit the physical protection of new carbon inputs. Physical protection of soil carbon occurs when physical disconnections separate decomposers from carbon sources (Dungait et al., 2012). This disconnect is not limited to access of decomposers and their enzymes to soil carbon, but also includes availability of other components necessary for decomposition, such as oxygen and water (Schmidt et al., 2011; Keiluweit et al., 2017).

Long-term cover crop based management increases soil aggregation (Tiemann and Grandy, 2015), and soil carbon is known to be better protected within soil aggregates (Six et al., 2000; Grandy and Robertson, 2007). Yet, mechanistically, it is the soil pore-space that controls not only movement of soil microbes, but also air and water fluxes and transport of nutrients necessary for decomposition (Young and Crawford, 2004; De Gryze et al., 2006; Negassa et al., 2015). Pores within the soil matrix serve as planes of breakage along which the aggregates form; and their sizes and spatial positions not just define soil aggregate-size distributions but determine micro-environmental conditions driving physical carbon protection within the aggregates (Young et al., 2001; Ekschmitt et al., 2005, 2008; Kravchenko and Guber, 2017; Rabot et al., 2018).

Pores of different sizes have different origins, accessibilities, and hydraulic properties. As pore size decreases, higher suction is required to drain the pore. This means that while pores of $>10 \, \mu m$ sizes may only require gravity to fully or partially drain, under normal soil moisture regimes, pores $<10 \, \mu m$ remain water filled (Marshall et al., 1996).

Plant root diameters are typically $>40 \, \mu m$ and, therefore, roots can only access and/or create pores exceeding that size (Wiersum, 1957; Cannell, 1977). Root pores are formed by compressing the soil matrix radially as the root pushes through the soil and then their walls are stabilized through mucilage (Gray and Lissmann, 1938; Greacen and Oh, 1972; Greacen and Sands, 1980; Czarnes et al., 2000; Ruiz et al., 2017). Fungal hyphae are known to create pores of 20–$30 \, \mu m$ size by pushing aside silt particles and exuding binding agents to buttress the pores (Dorioz et al., 1993; Bearden, 2001; Emerson and McGarry, 2003). However, fungi are typically excluded from pores $<10 \, \mu m$ (Six et al., 2006).

Roots provide carbon into the soil system in two ways: as a source of biomass when they die and as a source of easily decomposable carbon via root exudates. Roots tend to

consist of more difficult to decompose molecules (such as lignin and tannin), which, in addition to being harder to decompose, are easier to adsorb to mineral surfaces, sequestering them (Rasse et al., 2005; Jackson et al., 2017). Root exudates, on the other hand, tend to be small, soluble, and easily decomposable materials, such as organic acids, carbohydrates, and amino acids (Dungait et al., 2012) or water insoluble materials, such as mucilage (Brimecombe et al., 2001). The easily decomposable materials stimulate microbial growth, which increases decomposition of native soil organic matter (SOM) (Kuzyakov and Blagodatskaya, 2015). There is some indication that microorganisms can also stimulate root growth and exudation (Neumann et al., 2014).

Agricultural management influences pore size distributions. Wang et al. (2012) showed that soil under long-term conventional tillage had more pores of 37.5–$97.5 \, \mu m$, while primary succession agricultural management had greater proportions of >97.5 and $<15 \, \mu m$ pores. Kravchenko et al. (2014) found that organic management with cover crops had fewer 32–$58 \, \mu m$ pores and a greater amount of $>188 \, \mu m$ pores than conventional tillage management. In that study, the difference in pores from organic cover crop management were attributed to increased root activity, while conventional management promoted 32–$58 \, \mu m$ pores created through wetting/drying cycles. Ananyeva et al. (2013) found that higher carbon concentrations were found in sections of soil aggregates with an increased presence of 15–$37.5 \, \mu m$ pores. The presence of 37.5–$97.5 \, \mu m$ pores was associated with aggregate sections containing less carbon.

Stable carbon isotopic signatures can be used to track carbon within a system. Plants preferentially incorporate ^{12}C into their tissues, but the extent of ^{12}C incorporation depends on which metabolic pathway the plant utilizes. Plants that utilize the C3 photosynthetic pathway incorporate more ^{12}C than plants utilizing the C4 photosynthetic pathway. Therefore, it is possible to differentiate between carbon derived from C3 and C4 plants isotopically due to this natural isotopic difference. Stable carbon isotopes are reported in δ notation as per mil (‰) differences between the $^{13}C/^{12}C$ ratio of the sample compared to a standard:

$$\delta^{13}C = \left[\left(R_{Sample} - R_{Standard} \right) / R_{Standard} \right] * 1000 \qquad (1)$$

SOM and particulate organic matter (POM) $\delta^{13}C$ values reflect the $\delta^{13}C$ values of the original plant material source. Therefore, the measured $\delta^{13}C$ of a soil reflects the C3/C4 history of the soil (Ehleringer et al., 2000; Bowling et al., 2008). Experiments that utilize C3/C4 transitions have been used extensively for determination of soil C turnover rates (Bernoux et al., 1998; Derrien and Amelung, 2011) and for analyses of the fresh carbon input distribution within soil aggregates (Smucker et al., 2007; Urbanek et al., 2011).

The goal of this study was to determine how the abundance of different pore sizes relates to the preservation or loss of newly added carbon. We utilized a C3/C4 natural abundance greenhouse experiment with soil collected from a long term C4 cropping system and planted a C3 plant, cereal rye (*Secale cereale* L.), which is one of the most commonly used cover

crops in the US Midwest. The first objective of this study was to examine the relationships between newly added carbon and soil pores of different sizes. We used $\delta^{13}C$ to "track" newly added C3 carbon and determined pore characteristics via computed microtomography (μCT). The second objective was to examine the relationships between the decomposition of carbon and soil pores sizes after incubating the studied soil.

MATERIALS AND METHODS

Greenhouse Experimental Setup

Soil for the greenhouse study was obtained in the summer of 2013 from the Living Field Lab (LFL) experiment established in 1993 at W. K. Kellogg Biological Station, Hickory Corners, MI (42°24′N, 85°24′W). The soil is a fine-loamy, mixed mesic Typic Hapludalf (Oshtemo and Kalamazoo series) developed on glacial outwash. Soil was collected from the LFL's conventional management continuous maize (*Zea mays* L.) treatment. This treatment has been planted with maize, a C4 plant, and no other crop since 1993. Detailed management and site information is available at http://lter.kbs.msu.edu/Data/LTER and https://lter. kbs.msu.edu/research/long-term-experiments/living-field-lab/.

Six soil blocks of 40 × 26 × 15 cm size were collected at 0 to 15 cm depth. Three of the blocks were placed directly into plastic bins with as little disturbance as possible to retain intact soil structure, and are referred to hereafter as intact-structure treatment. However, we were concerned that, due to the tendency of roots to follow existing pore structure, the root effects generated during out experiment might be masked by the legacy of the existing pores. Therefore, soil from the other three blocks was crushed and sieved through a 1 mm sieve to destroy the existing soil structure, and is referred to hereafter as destroyed-structure treatment. One of the intact soil bins was left unplanted as a control, and the remaining bins had cereal rye (*S. cereale* L.) hand planted at a depth of 3 cm and a plant density of ∼23.5 plants per m². Rye was grown in the greenhouse for 3 months and watered daily to allow for the development of a good stand of rye biomass; the control bin was watered along with the rest. Soil bulk density was taken in each tub using a 7.5 cm brass ring.

After 3 months of rye growth, approximately an eighth of the soil was taken from a random side in each bin was removed using a trowel and allowed to air dry. The soil was allowed to break along natural planes of weakness through manual crushing. Intact soil fragments of 5 mm size were hand selected ($n = 5$, 11, and 11 for control, destroyed-structure and intact-structure treatments, respectively) for analyses and incubation. Soil fragments were selected based on proximity to rye roots to best determine the effect of rye root growth on the aggregates. Two rye roots per bin were hand collected for isotope analysis from intact plants from the soil used for soil fragment selection. Selected intact soil fragments were mounted on top of plastic stands using rubber cement for subsequent scanning and incubation.

The experiment and data collection are briefly summarized here and then described in detail in the sections below. First, all intact soil fragments were air-dried and subjected to μCT scanning (section μCT Image Collection and Analysis). Then

half of the intact soil fragments were physically cut into ∼0.5– 1 mm³ sections, with the physical positions of the procured sections matching their virtual positions in 3D μCT images (section Soil Fragment Cutting and Chemical Analyses). In each cut section, we measured $\delta^{13}C$, $\delta^{15}N$, total C (%C), and total N (%N). These intact soil fragments are hereafter referred to as Pre for preincubation soil. The remaining intact fragments were subjected to a 28 day incubation during which respired CO_2 was measured and collected for $\delta^{13}C$ analysis (section Incubation Experimental Set Up). After incubation, the intact soil fragments were re-scanned and also cut into sections, then $\delta^{13}C$, $\delta^{15}N$, total C (%C), and total N (%N) measurements were taken. These intact soil fragments are hereafter referred to as Post for post incubation soil.

μCT Image Collection and Analysis

The μCT images for both Pre and Post intact soil fragments were obtained on the bending magnet beam line, station 13-BM-D of the GeoSoilEnvironCARS (GSECARS) at the Advanced Photon Source (APS), Argonne National Laboratory (ANL), IL. Images were collected with the Si (111) double crystal monochromator tuned to 28 keV incident energy, the distance from sample to source was ∼55 m, and the X-ray dose is estimated to be 1 kGy. Two-dimensional projections were taken at 0.25° rotation angle steps with a 1 s exposure and combined into a three-dimensional image consisting of 1,040 slices with 1,392 by 1,392 pixels per slice for Pre scans, resulting in a voxel size of 6.5 μm, while Post scans had 1,100 slices with 1,920 by 1,920 pixels, resulting in a voxel size of 6.2 μm. The data were pre-processed by correcting for dark current and flat field and reconstructed using the GridRec fast Fourier transform reconstruction algorithm (Rivers, 2012).

Pore/solid segmentation of the images was conducted using the indicator kriging method in 3DMA-Rock software (Oh and Lindquist, 1999; Wang et al., 2011). Based on the analysis of the segmented data we obtained the total porosity of the intact soil fragments, the total image porosity (pores > 6.5 μm in diameter), and the size distribution of >6.5 μm diameter pores. Total porosity of each intact fragment was calculated using the dry weight of the fragment and its volume as determined from the μCT images. The total image porosity was calculated as the percent of pore voxels within the total intact soil fragment's voxels. Size distribution of image identified pores was determined using the burn number distribution approach in 3DMA-Rock software (Lindquist et al., 2000; Ananyeva et al., 2013). Briefly, the burn number represents the shortest distance from the pore medial axis to the pore wall. For clarity, burn numbers have been converted into pore diameters. We specifically focused the data analyses on the pores of the following four diameter size ranges: 6.5–15, 15–40, 40–95, and >95 μm. These pore sizes were chosen to match pore sizes previously studied in macro-aggregates and which demonstrated strong associations with carbon (Wang et al., 2012, 2013; Ananyeva et al., 2013; Kravchenko et al., 2014, 2015).

Incubation Experimental Set Up

The soil fragments used in incubation (Post soil) consisted of two intact soil fragments from control treatment, 6 intact soil

fragments from destroyed-structure treatment, and 5 intact soil fragments from intact-structure treatment. Water was added to the fragments to achieve 60% of water filled pore space. The fragments were then placed into 10 ml vacutainers (BD Franklin Lakes NJ, USA) with 1 mL of de-ionized water added to the bottom to maintain high humidity. Incubations were carried out for 28 days at $22.4 \pm 0.1°C$. CO_2 emission measurements were taken on days 1, 2.5, 4, 8, 13, 19, and 28. Gas samples for isotope analysis were collected on days 13, 19, and 28 only. The CO_2 emission measurements were conducted using an LI-820 CO_2 infrared gas analyzer (Lincoln, Nebraska, USA). After each sampling, the remaining gas in the headspace was flushed with CO_2-free air. Flushing was found to dry out the soil, so de-ionized water ($\sim$10–20 µL) was added directly to the fragments to maintain the moisture level after day 4. One intact-structure fragment and four destroyed-structure fragments broke during the incubation and, while chemical analyses were possible, the broken fragments could not be re-scanned.

Soil Fragment Cutting and Chemical Analyses

To assess patterns of $\delta^{13}C$, $\delta^{15}N$, total C, and total N and their relationship to pore characteristics, each intact soil fragment was cut into 5–13 sections. This was done to account for variation between the soil fragments. The number of sections into which the fragment was cut depended on its size and shape. To facilitate cutting, de-ionized water was added to fill 30% of the pore volume immediately prior to cutting. Cutting was performed with a #11 scalpel and a 24x magnifying glass. The relative position of each cut was recorded. Then, the relative positions were used to virtually cut the 3D µCT image to match the physical cutting. Virtual cutting yielded regions in the three-dimensional tomographic images that corresponded to the physically cut sections. Image based porosity and pore size distributions were determined in each virtual section of each soil fragment.

Prior to chemical analyses, visibly identifiable particulate organic matter (POM) was separated from physically cut sections and analyzed separately. The identifiable POM consisted primarily of plant root remains, but occasional plant residue fragments of unknown origin were also observed. Soil from cut sections, POM from cut sections, and separately collected rye roots were analyzed for $\delta^{13}C$, $\delta^{15}N$, total C, and total N at the Stable Isotope Facility at the University of California Davis. Fragment sections were analyzed using an Elementar Vario EL Cube or Micro Cube elemental analyzer (Elementar Analysensysteme GmbH, Hanau, Germany) interfaced to a PDZ Europa 20-20 isotope ratio mass spectrometer (Sercon Ltd., Cheshire, UK). POM material and rye roots were analyzed using a PDZ Europa ANCA-GSL elemental analyzer interfaced to a PDZ Europa 20-20 isotope ratio mass spectrometer (Sercon Ltd., Cheshire, UK).

Gas samples were analyzed for $\delta^{13}C$ at the Stable Isotope Facility at the University of California Davis. Gas samples were analyzed using a ThermoScientific GasBench system interfaced to a ThermoScientific Delta V Plus isotope ratio mass spectrometer (ThermoScientific, Bremen, Germany).

The carbon isotopes are reported relative to Vienna PeeDee Belemnite (VPDB) with a 0.1‰ standard deviation for solid samples and 0.02‰ standard deviation for gas samples. The nitrogen isotopes are reported relative to AIR and had a standard deviation of 0.1‰.

Grayscale Gradients

Grayscale gradients were used to identify spatial patterns in the soil matrix adjacent to root pores of 40–90 µm size. The grayscale value of an individual voxel from a µCT image is a function of the atomic number and relative density of the material within the voxel. Higher atomic number elements, such as iron, have higher grayscale values on images, while lower atomic number elements, such as carbon and nitrogen, have lower grayscale values on images. Therefore, the value of each grayscale voxel reflects elements present within it. Quigley et al. (2018) showed that spatial gradients in grayscale values adjacent to the pores formed through plant root activities matched well SOM gradients determined by the osmium staining method (Peth et al., 2014; Rawlins et al., 2016). Thus, in this study we will use the grayscale gradients adjacent to the root pores as indicators of SOM distributions.

Three root pores of 40–90 µm size range were identified on Pre and Post images from 4 soil fragments. The root pores were then 3D dilated by one voxel to exclude any voxels containing both pore and solid material. Voxels were averaged in $\sim$13 µm layers around the pore to a distance of 194 µm and the grayscale gradients were obtained by averaging the grayscale values of each layer (**Figure 1**). Averages excluded 0 values that represented the background and 255 values to prevent skewing the gradients by the occasional presence of inclusions of high atomic number elements, e.g., Fe. For direct comparison of the images, the values were normalized such that the lowest average grayscale value within the gradient was 0 and the highest average grayscale value within the gradient was 1.
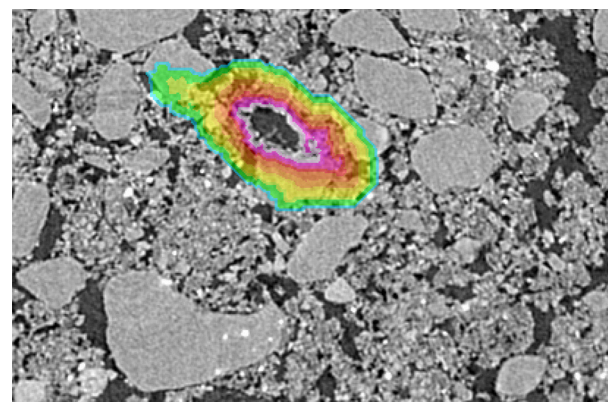

FIGURE 1 | Example of a selected root used for grayscale gradient analyses. The color overlay indicates the extent of the grayscale gradient with the colors indicating each individual 13 µm layer.

Statistical Analysis

Comparisons between intact- and destroyed-structure treatments as well as between Pre and Post in terms of pore characteristics and $\delta^{13}C$, $\delta^{15}N$, total C, and total N were conducted using the mixed model approach implemented in the PROC MIXED procedure of SAS Version 9.4 (SAS, 2009). The statistical model for the analyses consisted of the fixed effects of treatment, Pre and Post, and their interaction; and a random effect of soil fragments nested within treatment and Pre and Post. The normality was visually assessed using normal probability plots and stem-and-leaf plots, while equal variances was assessed using Levene's test. Where the equal variance assumption was violated, analysis with unequal variances was conducted (Milliken and Johnson, 2009).

For analysis of $\delta^{13}CO_2$ and CO_2 data obtained during soil fragment incubations, the statistical model consisted of the fixed effects of treatment, time, and their interaction. Time was treated as a repeatedly measured fixed factor using the REPEATED statement of PROC MIXED. Comparisons between the $\delta^{13}CO_2$ and the $\delta^{13}C$ of the fragments prior to incubation were conducted by defining the $\delta^{13}C$ of the soil in each treatment as a control and analyzed using Dunnett's comparison-with-control test. The significant differences at the 0.05 level were reported, while trends are reported at the 0.1 level.

Regression analyses between pore characteristics and $\delta^{13}C$ and total C were conducted using the PROC REG procedure in SAS Version 9.4 (SAS, 2009). The significant slopes at the 0.05 level were reported.

To investigate the correlation between the pore sizes (6.5–15, 15–40, 40–90, and >90 μm) and chemical measures ($\delta^{13}C$, total C, and total N), canonical correlation analysis was conducted using the cancor function in R (R Core Team, 2013). Canonical correlation compares how one set of variables

is correlated to another set of variables in multidimensional space. The correlations are described through axes, which can be represented as orthogonal planes of maximum correlation, known as correlation axes. Each correlation axis is defined by canonical variates. Canonical variates are latent variables, which are not observed, but derived from a combination of the observed variables. Collinearity within the observed variables was checked through the calculation of the determinant prior to canonical correlation analysis. As canonical correlations requires a larger data set, only the Pre data set was used for canonical correlations due to the small sample size of the Post data set.

RESULTS

Soil and Plant Characteristics

Soil bulk density was lower in the treatments with rye as compared to control treatment (**Table 1**). The average $\delta^{13}C$ values of particulate organic matter (POM), that is, the visible root remains and unidentifiable plant fragments isolated from intact soil fragments during their cutting, showed that the control treatment had significantly more C4 POM than the destroyed-structure treatment and numerically more C4 POM than the intact-structure treatment (**Table 1**). The destroyed-structure and intact-structure treatments were significantly different from each other at $\alpha = 0.1$, but not $\alpha = 0.05$. The $\delta^{13}C$ of rye roots grown in destroyed-structure soil were depleted by ~1.5‰ more than rye roots grown in intact-structure soil, while the $\delta^{15}N$ of rye roots in destroyed-structure was depleted by ~3.3‰ as compared to intact (**Table 1**).

Prior to incubation, intact-structure and destroyed-structure soil had significantly higher total C than the control soil (**Table 2**). However, after incubation, this significance disappeared. The C:N ratio was significantly lower for control soil fragments than for

TABLE 1 | Means of soil bulk density ($n = 2$) and characteristics of rye roots ($n = 4$) from the studied treatments.

Treatment	Bulk density, g/cm^3	$\delta^{13}C$ roots	$\delta^{15}N$ roots	C:N roots	$\delta^{13}C$ POM
Control	1.40 (0.1)**a**	NA	NA	NA	−18.4 (2.3)**a**
Intact	1.13 (0.1)**b**	−28.6 (0.3)b	2.3 (0.4)**b**	18.6 (1.5)b	−22.5 (1.3)**b**
Destroyed	1.16 (0.1)**b**	−30.1 (0.4)a	−1.0 (0.3)**a**	12.1 (1.8)a	−26.0 (1.8)**ab**

Standard errors are shown in parentheses. Letters indicate significant differences among treatments at $\alpha = 0.1$ and bold letters indicate differences at $\alpha = 0.05$.

TABLE 2 | Means of soil carbon and nitrogen characteristics for the three studied treatments Pre and Post.

Time	Treatment	Total C	$\delta^{13}C$	Total N	$\delta^{15}N$	C:N ratio
Pre	Intact	0.87 (0.03)a	−21.4 (0.2)	0.10 (0.01)	3.95 (0.2)	9.14 (0.4)a
	Destroyed	0.87 (0.05)a	−22.0 (0.2)*	0.12 (0.01)	4.21 (0.2)	8.03 (0.4)ab
	Control	0.74 (0.04)b	−21.5 (0.2)	0.10 (0.01)	3.58 (0.3)	7.68 (0.6)b
Post	Intact	0.86 (0.04)	−21.4 (0.2)	0.10 (0.01)	4.26 (0.2)a	8.90 (0.4)a
	Destroyed	0.80 (0.03)	−21.2 (0.2)	0.10 (0.01)	4.80 (0.2)b	8.29 (0.4)ab
	Control	0.77 (0.07)	−21.3 (0.2)	0.11 (0.02)	3.22 (0.3)c	7.13 (0.7)b

Standard errors are shown in parentheses. Means and standard errors in each treatment are calculated based on 2-6 aggregates with 1–13 sections per aggregate. Letters indicate significant differences among treatments within Pre and Post groups at $\alpha = 0.05$. Stars indicate the cases where there was a statistically significant difference between Pre and Post results within each treatment at $\alpha = 0.05$. Total C and total N are expressed as %C and %N.

the fragments from the intact-structure treatment both in Pre and Post. The $\delta^{13}C$ values in destroyed-structure soil significantly increased, indicating losses in C3 carbon during incubation. The numerical trend in $\delta^{15}N$ of Destroyed>Intact>Control observed in the Pre increased and became statistically significant post-incubation. The total N was not affected by either treatment or incubation.

Pore Characteristics

Total porosity of individual soil fragments ranged from 10 to 30% for all three treatments. The average image porosity, that is presence of pores $>6\,\mu m$ in diameter, was around 12% in fragments from control and 20% in fragments from rye treatments (**Figure 2**). After incubation, pore

abundances tended to numerically increase in soils from all three treatments (**Figure 3**), however, the increases were only statistically significant for the pores from the 6.5–$15\,\mu m$ size group (**Figure 2**). Pores with diameters $>90\,\mu m$ tended to be the least abundant in the control treatment, followed by the intact-structure and destroyed-structure soils. This tendency was observed in the soils prior to incubation and remained after incubation. Differences between treatments were only observed for the $>90\,\mu m$ pores.

Associations Between Pores and Chemical Characteristics

In soil from the control treatment there were no significant correlations observed between the two studied carbon
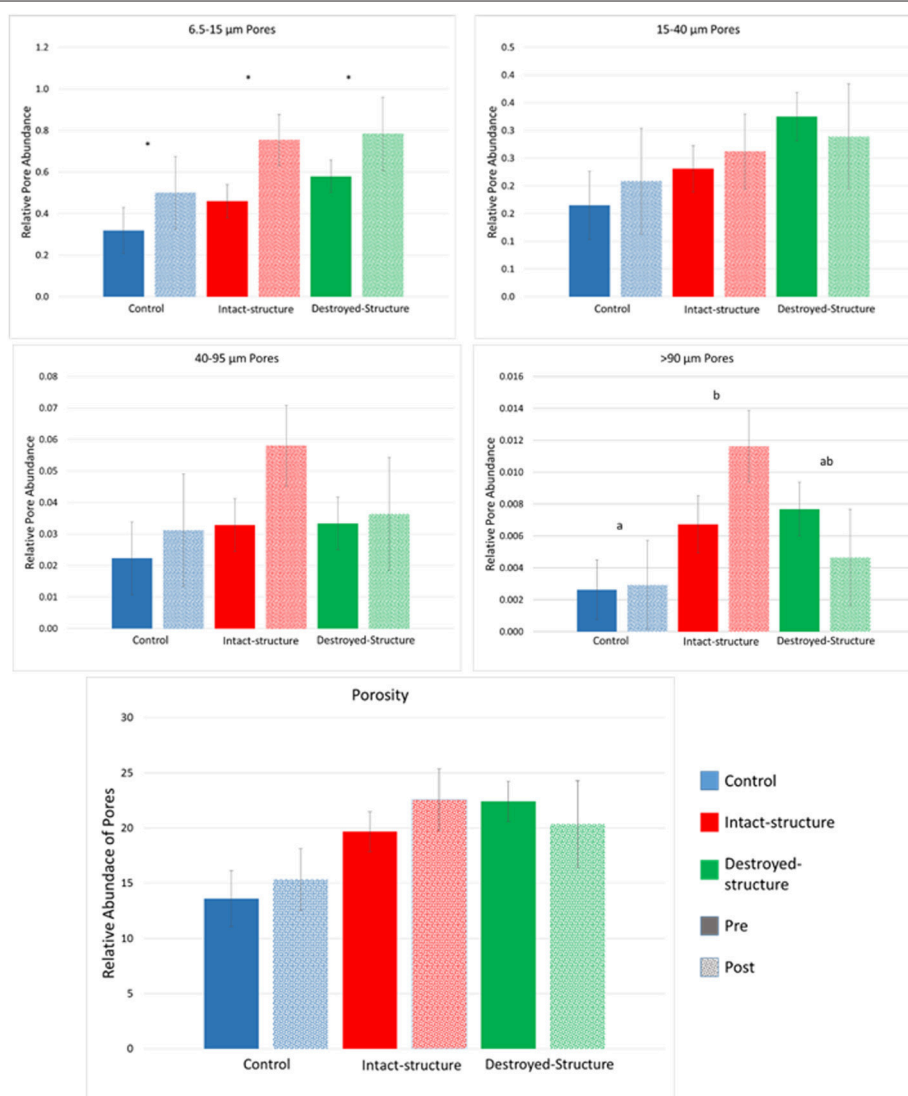
FIGURE 2 | Relative abundances of 6.5–15, 15–40, 40–95, >95 μm pores, and porosity in the soil fragments of the three studied treatments before and after incubation. Relative pore abundance refers to the percent of medial axes per total soil volume as determined from 3DMA-Rock software. Bars represent standard errors. Letters indicate significant differences between treatments, across Pre and Post (α = 0.05). Stars indicated significant differences between Pre and Post within each treatment at α = 0.05.
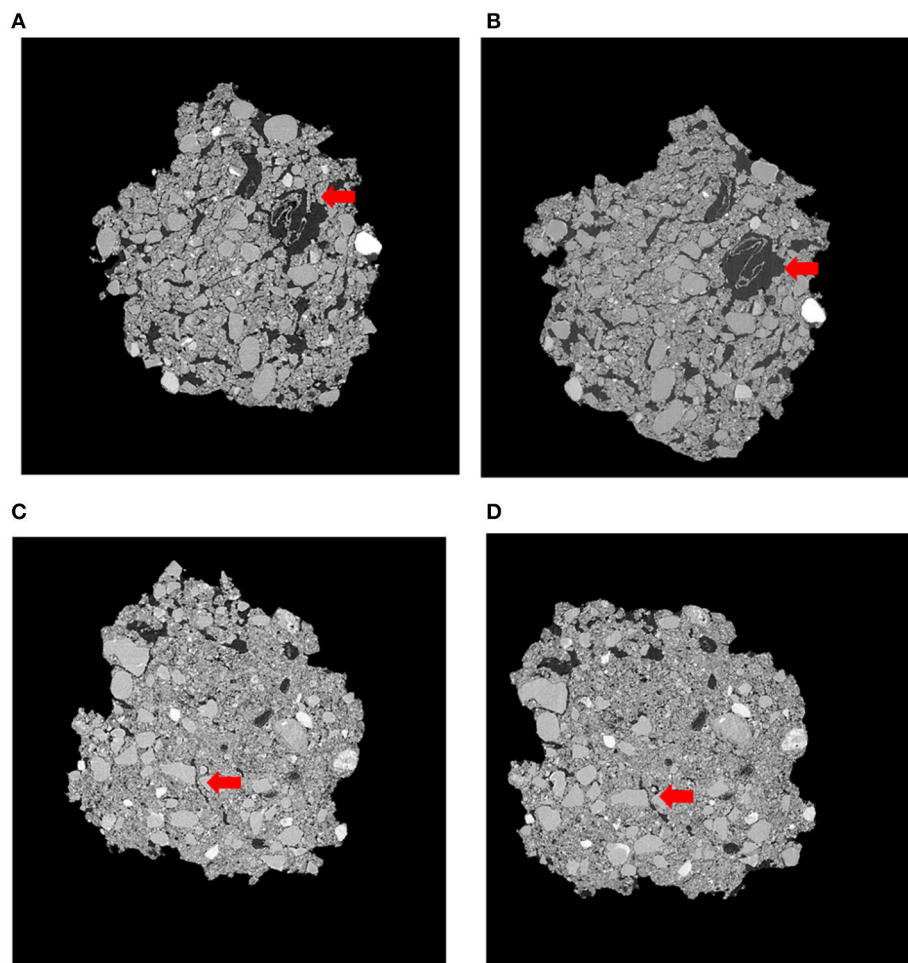
FIGURE 3 | Representative slices of the same soil fragment for Pre-Intact **(A)**, Post-Intact **(B)**, Pre-Destroyed **(C)**, and Post-Destroyed **(D)**. Red arrows highlight an area where porosity visibly increased during incubation. Each soil fragment is approximately 5 mm across.

characteristics (total C and δ^{13}C) and pore abundances of any of the studied sizes, either before or after incubation. There was also no correlation observed between the two nitrogen characteristics (total N and δ^{15}N) and pore abundances (results not shown).

An interesting pattern emerged in the correlation of δ^{13}C and abundance of pores of different sizes in the Pre destroyed-structure treatment. Correlation with 6.5–15 μm pores was positive, no correlation was observed with 15–40 μm pores, and correlation was negative with 40–90 μm pores (**Figure 4**, **Table 3**). This indicates that in the soil from destroyed-structure treatment prior to its incubation, the sections with greater abundance of 6.5–15 μm pores tended to have less C3 carbon while the sections with greater abundance of 40–90 μm tended to have more C3 carbon. Post δ^{13}C was positively correlated with 6.5–15, 15–40, and 40–90 μm pores, indicating that the sections with greater abundance of pores of all three sizes tended to have less C3 carbon after incubation. The trend of negative correlations Pre and positive correlations Post between δ^{13}C and 40–90 μm pores was statistically significant in

destroyed-structure soil and numeric in intact-structure soil. In the soil from the intact-structure treatment, δ^{13}C was positively correlated to 6.5–15 and 15–40 μm pores Post.

There was no significant correlations between total C and any pore sizes in either intact-structure or destroyed-structure soils Pre (**Table 3**). In Post intact-structure soil total C was positively correlated with 6.5–15 μm pores and 15–40 μm pores. However, in destroyed-structure soil total C was negatively correlated with these pores.

Incubation CO_2

The cumulative amount of CO_2 emitted from the soil fragments during the 28-day incubation was the highest in the soil from the intact-structure treatment, followed by the destroyed-structure and control treatments (**Figure 5A**). The δ^{13}C values of the CO_2 emitted during the incubation indicate that microorganisms preferentially used more C3 carbon in the destroyed-structure and intact-structure treatments than in the control, but the difference was only statistically significant on day 28 (**Figure 5B**).

FIGURE 4 | Correlations between total C (%C) and relative abundances of 40–95 μm pores **(A)** and between δ^{13}C and 40–90 μm pores **(B)** for intact-structure treatment and destroyed-structure treatment for both Pre and Post. Relative pore abundances refer to the percent of medial axes per total soil volume as determined from 3DMA-Rock software. Gray area indicates 95% confidence interval. Correlation coefficients are shown in **Table 3**.

TABLE 3 | Correlation coefficients for Pre and Post soil for total C and δ^{13}C with relative abundances of 6.5–15 μm, 15–40 μm, 40–90 μm, and >90 μm pores for intact and destroyed-structure treatments.

Structure	Pore size, μm	Incubation	Total C	δ^{13}C
Destroyed	6.5–15	Pre	−0.25	0.33*
		Post	−0.75*	0.76*
	15–40	Pre	−0.28	0.17
		Post	−0.78*	0.79*
	40–90	Pre	0.05	−0.39*
		Post	−0.47*	0.40*
	>90	Pre	0.25	−0.07
		Post	0.1	−0.19
Intact	6.5–15	Pre	0.19	0.02
		Post	0.50*	0.52*
	15–40	Pre	0.18	0.01
		Post	0.37*	0.45*
	40–90	Pre	0.26	−0.18
		Post	0.11	0.17
	>90	Pre	0.12	−0.14
		Post	0.09	−0.08

Positive correlation with δ^{13}C indicate more new carbon was associated with a higher presence of specified pore. Stars indicate significant correlation at α = 0.05.

The δ^{13}C values of the CO_2 emitted during the incubation indicate that during the last three measurements (days 13, 19, and 28), the CO_2 gas became more depleted for all three treatments.

Grayscale Gradients

Both intact- and destroyed-structure Pre and Post soils had similar general patterns of very high grayscale values directly adjacent to the pores, followed by a sudden decrease (**Figure 6**). Then, the grayscale values slowly increased until reaching a plateau at 120–140 μm distances from the pore. The plateau grayscale value roughly corresponded to the background grayscale value. However, the differences in Pre and Post grayscale gradients had opposite signs in the two treatments. In destroyed-structure soil, Pre soils had lower grayscale values than Post at the same distance, while Pre intact-structure soil had higher grayscale values than the Post soil.

Canonical Correlations

The first two canonical correlation axes were significant at the 0.05 level (**Figure 7**). The first canonical variates can be described by the relationship between total C (negatively correlated) and total N (positively correlated) with 6.5–15 μm (negatively correlated) and 15–40 μm (positively correlated) pores. This indicates that pores of 6.5–15 μm were associated with higher C:N ratios while 15–40 μm pores were associated with lower C:N ratios. There was a treatment difference observed in this axis between destroyed-structure and intact-structure soils: the destroyed-structure soil contained more carbon with lower C:N

ratios and a higher abundance of 15–40 μm pores than intact-structure soil.

The second canonical variates can be described by the relationship between δ^{13}C (positive correlation) and total N (positive correlation) with 40–90 μm pores (positive correlation) and >90 μm pores (negative correlation). This indicates that 40–90 μm pores tend to have newer carbon with higher nitrogen concentrations, while >90 μm pores tend to have older carbon with lower nitrogen concentrations. There was no effect of treatment observed in the second canonical correlation axis.

DISCUSSION

Three months of rye growth increased total C and the C:N ratio within both the intact-structure and destroyed-structured soils. However, in the subsequent incubation, gains of total C tended to disappear. As indicated by the δ^{13}C results, the carbon losses, at least in the destroyed-structure fragments, were dominated by losses in C3 carbon. Gains and losses of C3 and of total carbon were associated with presence of soil pores. However, the relationships between carbon and pores differed for different pore sizes, suggesting different microscale mechanisms by which these pores contribute to carbon accrual processes.

Relationship Between C3 Carbon and 40–90 μm Pores

The correlations between δ^{13}C and pores of the studied size ranges had similar signs in both intact- and destroyed-structure soils, but in the intact-structure soil, the correlations were not

FIGURE 5 | (A) Cumulative CO_2 and (B) average isotopic signature of CO_2 respired during 28 day incubation experiment. Bars represent standard errors. Bold lines indicate the mean $\delta^{13}C$ values of the soil fragment sections prior to incubation for each treatment while boxes indicate the standard errors (-22.0 ± 0.1, -21.4 ± 0.1, and -21.6 ± 0.1‰ for destroyed-structure, intact-structure, and control, respectively). Letters indicate significant differences among treatments at $\alpha = 0.05$. Stars indicate significant differences between the $\delta^{13}C$ of the emitted CO_2 and the soil sections Pre at $\alpha = 0.05$.

FIGURE 6 | Normalized grayscale values from µCT images of soil fragments as a function of distance from 40 to 90 µm pores for intact-structure and destroyed-structure at Pre and Post. Error bars indicate standard error. Note that values of the normalized grayscale reflect a combination of contributors, including atomic numbers of the elements and density of the material located within an image voxel. Specifically, lower normalized values here correspond to lower atomic number elements and lower densities, while higher values correspond to higher atomic number elements and higher densities. As such, lower values roughly represent more carbon in the soil matrix, while higher values represent less carbon in the soil matrix and/or denser soil matrix.

FIGURE 7 | Canonical correlation of pore sizes with total C (%C), total N (%N), and $\delta^{13}C$. The first two canonical correlations were significant at $\alpha = 0.05$ and are shown. The correlation factors that define the latent variables for each axes are shown on the right. The sign indicates the direction of correlation and the number indicates the amount each observed variable contributes to the latent variable. Lines indicate the (0, 1) line (A) and (0, −1) line (B), while letters indicate treatment [destroyed-structure (D) and intact-structure (I)].

statistically significant (**Table 3**). This is likely the outcome of the legacy of soil pore architecture of the intact-structure soil, which contributed to greater variability, thus lowering statistical significance in that treatment, as well as differences in decomposability of plant root material in the two treatments (as discussed below).

Negative correlation between $\delta^{13}C$ and 40–90 µm pores, indicated that greater levels of C3 were associated with the presence of 40–90 µm pores (**Figure 4**, **Table 3**). It is assumed that the increase in C3 carbon is associated with the newly added carbon. We surmise that a possible cause for this association is that many of the 40–90 µm pores, especially those in the destroyed-structure soil, were created by fine plant roots. Since old root pores were destroyed during the sieving process, any 40–90 µm pores in the destroyed-structure soil, which were of root origin, would have been directly produced by the growth of the rye. On the contrary, in the intact-structure
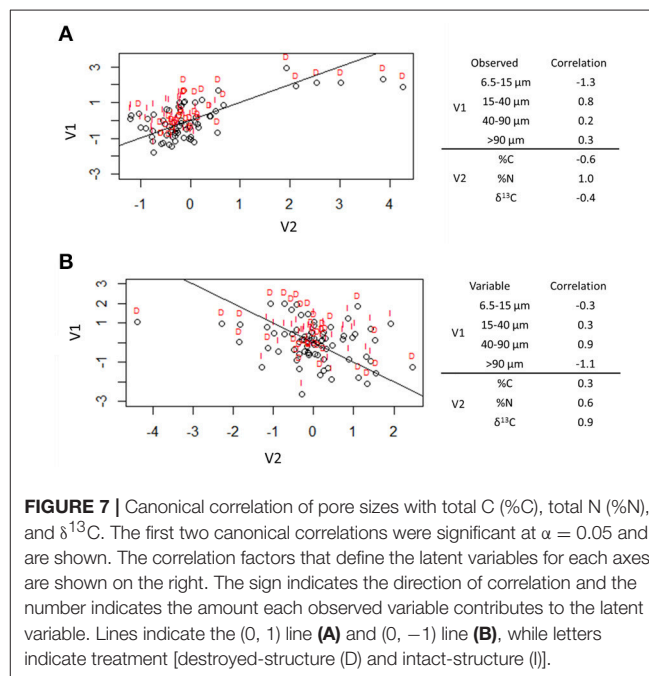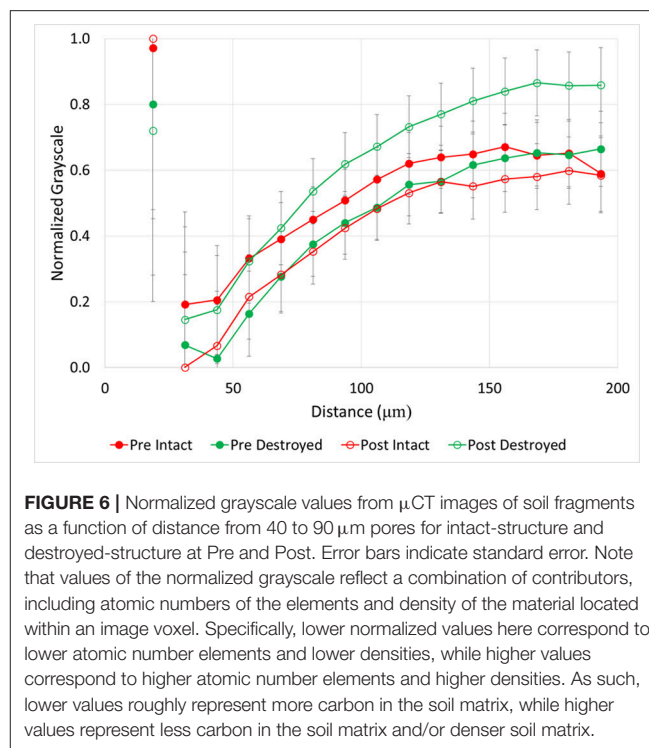
treatment such pores could have been produced by both new and historically grown plants, increasing variability that weakened the correlation.

After incubation, the gains in new carbon in the destroyed-structure soil in relation to the abundance of 40–90 µm pores were quickly lost. The 40–90 µm pores went from being

positively correlated with new carbon in Pre to being negatively correlated with new carbon in Post. The grayscale gradients in the Post destroyed-structure soil had higher grayscale values than in the Pre (**Figure 6**). This further supports the notion that, while prior to incubation the SOM levels in the vicinity of such newly formed pores were relatively high, in samples subjected to incubation the SOM levels adjacent to 40–90 μm pores were low.

Greater decomposition of newly added carbon in 40–90 μm pores could result both from a more labile nature of the new carbon and from greater microbial activites in these pores. The second canonical correlation axis (**Figure 7**) shows that the 40–90 μm pores tend to have newer carbon and a higher concentration of nitrogen, thus possibly, containing more decomposable organic compounds. Indeed, the small plant roots located within such pores could have been more easily decomposable since fine roots tend to have less lignin and a lower lignin:N ratio is an indication of root decomposability (Rasse et al., 2005). Bailey et al. (2017) observed that water extracted from pores between 20 and 200 μm contained more lipids, which are more easily decomposable, than lignin and tannin, which are more difficult to decompose. Moreover, the increased decomposition/carbon loss in such pores was reported as related to greater microbial presence, transport, and activity in 40–90 μm pores (Strong et al., 2004; Wang et al., 2013; Kravchenko et al., 2014).

Some of the differences between the intact- and destroyed-structure treatments in terms of pore associations with new carbon might be related to differences in root decomposability. The intact-structure roots had a higher C:N ratio, as well as δ^{15}N and δ^{13}C (**Table 1**). The δ^{15}N of plant roots is controlled by the nitrogen use efficiency. Large differences between root and shoot δ^{15}N values can result from pooling of nitrate in plant roots (Kalcsits et al., 2015; Kalcsits and Guy, 2016). The shoot δ^{15}N was 2.08‰ for rye samples collected from both intact-structure and destroyed-structure soils, but, while the intact-structure roots were similar to the shoot values, destroyed-structure roots were ∼3‰ more depleted. This suggests that pooling of nitrate could have taken place in the destroyed-structure roots, lowering C:N ratio and increasing decomposability. In addition, more depleted δ^{13}C values of roots from the destroyed-structure soil would make it slightly easier for microorganisms to decompose them than intact-structure roots. The differences in the δ^{13}C of C3 plants are related to water availability with more depleted values occurring where water is more plentiful (Farquhar et al., 1989; Stewart et al., 1995). The differences in overall pore size distributions of the two treatments could be the cause for the differences in nitrate and water availability. However, since the normal range of values for C3 plants is from −24 to −34‰, the difference between intact-structure and destroyed-structure roots observed in this study can be regarded as relatively small.

Relationship Between Carbon and 6.5–15, 15–40, and >90 μm Pores
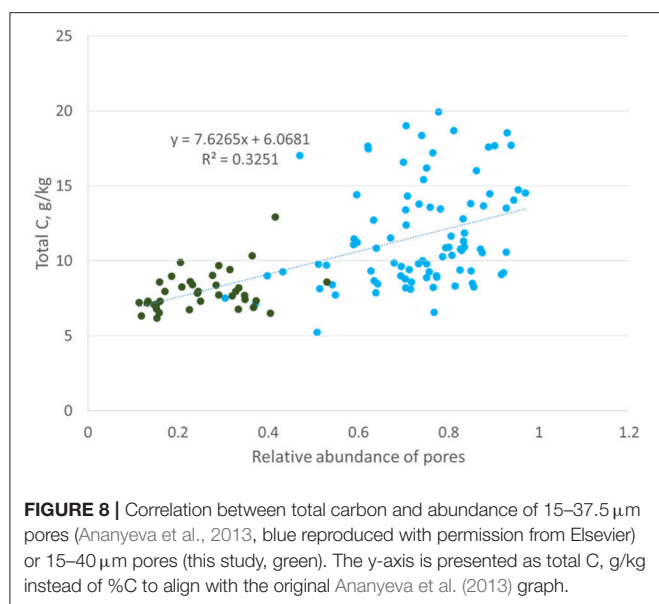
After incubation, there was a notably decreased association with C3 carbon in both intact-structure and destroyed-structure soil. This implies a preferential utilization of newer carbon in these pores. This preference could be the result of anaerobic conditions that existed within the soil. During incubation, the soil moisture level was kept at 60% water filled porosity, which would have resulted in water filling the majority of both the 6.5–15 and 15–40 μm pores during the incubation, resulting in anaerobic conditions prevailing there during incubation. Keiluweit et al. (2017) observed that in anaerobic microsites within upland soils, decomposition rates were reduced by a factor of 10, which may also explain the slower decomposition of materials from these pores as seen in the association with increased amounts of carbon. The anaerobic conditions may also explain why newer carbon was preferentially used in association with these pores. Newer carbon would likely contain more oxidized functional groups than older carbon. These functional groups would be quickly used under anaerobic conditions, resulting in biased decomposition of newer carbon in relation to pores of 6.5–15 and 15–40 μm sizes.

The association between total C and 15–40 μm pores (**Figure 8**) was identical to those observed by Ananyeva et al. (2013). The two data sets, while of the same soil type and collected from the same geographic area, were of two completely different agricultural managements. This study is from a 20 year conventional management continuous corn treatment, while Ananyeva et al. (2013) used aggregates from a 19 year native succession management, which was essentially unmanaged. This seems to suggest a universal mechanism for the relationship between soil carbon and the presence of 15–40 μm pores. One possible driver of this relationship might be the presence of fungi in these pores. The first canonical correlation axis (**Figure 7**), shows a difference in the C:N ratio of the two pore sizes. This potentially could signal a difference in decomposability between 6.5–15 and 15–40 μm pores. Bailey et al. (2017) and Smith et al. (2017) both observed that pores of >6 μm contained more easily decomposable material, while pore <6 μm contained more difficult to decompose material. They attributed this difference to accessibility of fungi, which preferential decompose more complex organic materials, but, as fungal hyphae are typically 10 μm in size, cannot access pores smaller than 10 μm (Six et al., 2006). Fungi are also known to create pores of 20–30 μm size by pushing aside silt particles and extruding binding agents, which would create micro-environments with more decomposable material in these created pores (Dorioz et al., 1993; Bearden, 2001; Emerson and McGarry, 2003). Another potential explanation might be the presence of root hairs. Root hairs are also 10 μm in size and therefore, would also occur in the 15–40 μm pore range. More research is necessary to explore the cause of this correlation between total C and 15–40 μm pores.

Additional Considerations

The CO_2 results seem to indicate a different story than the soil fragment data. In the soil fragment data, destroyed-structure soil lost the most carbon during incubation, while the intact-structure soil losing a negligible amount of carbon during incubation. The CO_2 data, on the other hand, indicates that the intact-structure lost the most carbon as CO_2. This discrepancy is due to the removal of POM from the soil fragments prior to total C, total N, δ^{13}C, and δ^{15}N measurements. The amount of POM removed

FIGURE 8 | Correlation between total carbon and abundance of 15–37.5 μm pores (Ananyeva et al., 2013, blue reproduced with permission from Elsevier) or 15–40 μm pores (this study, green). The y-axis is presented as total C, g/kg instead of %C to align with the original Ananyeva et al. (2013) graph.

from the intact-structure soil was almost twice as large as the amount of POM removed from the destroyed-structure soil. This means that the discrepancy between the CO_2 data and soil fragments was most likely due to the difference in the amount of POM.

We recognize that in terms of exploring associations between carbon and soil pores our work is, in essence, an observational study. Thus, it possesses a limitation common to all observational studies, that is, an inability to unequivocally declare cause and effect relationships. Yet, we posit that, at present it is impossible to recreate soil environments with specific pore characteristics for controlled cause-effect determination. Even though creation of artificial soil materials with contrasting pore architecture by either using soil fractions of different sizes or by soil compaction is possible (De Neve and Hofman, 2000; Stenger et al., 2002; Thomson et al., 2010; Sleutel et al., 2012; Negassa et al., 2015) such constructions fail to recreate biological conditions. By biological conditions, we refer to the structure and abundance of resident microbial communities, formed in pores of different sizes *in situ* and acclimated to specific microenvironments existing there. Since it is microbial activities that largely drive carbon processing, failure to correctly represent them will likely mislead findings. This leaves no alternative, but observational studies, such as this study, to explore the role of pores within soil micro-environments.

CONCLUSION

Our findings confirm previous results on the importance of pores in tens of microns size range for processing of organic carbon in soil, specifically in regards to fate and distribution of newly added carbon. We demonstrated that pores of 40–90 μm size range play a particularly intriguing role in new carbon gains as well as its subsequent losses. Such pores seem to be "easy come easy go" locations which receive the greatest amounts of new carbon from growing plant roots, but then rapidly loose that newly added carbon. On the other hand, both 6.5–15 and 15–40 μm pores are associated with preferential use of newer carbon. Carbon protection associated with the 6.5–15 μm pores could be associated with lack of accessibility by fungal hyphae and pervasiveness of anaerobic conditions when soils are near field capacity. Pores of 15–40 μm pore size are also associated with a prevalence of anaerobic conditions when soils are above field capacity, but fungal hyphae are not excluded and are potential drivers of carbon dynamics in pores of this size.

AUTHOR CONTRIBUTIONS

MQ developed concepts, conducted data analyses and wrote the paper. AK contributed to the development of research concepts, research conduct, and writing. WN contributed to the design of the experiment. AG contributed to the development of research concepts. MR contributed to research conduct.

REFERENCES

Ananyeva, K., Wang, W., Smucker, A. J. M., Rivers, M. L., and Kravchenko, A. N. (2013). Can intra-aggregate pore structures affect the aggregate's effectiveness in protecting carbon? *Soil Biol. Biochem.* 57, 868–875. doi: 10.1016/j.soilbio.2012.10.019

Bailey, V. L., Smith, A. P., Tfaily, M., Fansler, S. J., and Bond-Lamberty, B. (2017). Differences in soluble organic carbon chemistry in pore waters sampled from different pore size domains. *Soil Biol. Biochem.* 107, 133–143. doi: 10.1016/j.soilbio.2016.11.025

Bearden, B. N. (2001). Influence of arbuscular mycorrhizal fungi on soil structure and soil water characteristics of vertisols. *Plant Soil* 229, 245– 258. doi: 10.1023/A:1004835328943

Bernoux, M., Cerri, C. C., Neill, C., and de Moraes, J. F. L. (1998). The use of stable carbon isotopes for estimating soil organic matter turnover rates. *Geoderma* 82, 43–58. doi: 10.1016/S0016-7061(97)00096-7

Bowling, D. R., Pataki, D. E., and Randerson, J. T. (2008). Carbon isotopes in terrestrial ecosystem pools and CO_2 fluxes. *New Phytol.* 178, 24–40. doi: 10.1111/j.1469-8137.2007.02342.x

Brimecombe, M. J., de Leij, F., and Lynch, J. M. (2001). "The effect of root exudates on rhizosphere microbial populations," in *The Rhizosphere: Biochemistry and Organic Substances at the Soil-Plant Interface*, eds R. Pinton, Z. Varanini and P. Nannipieri (New York, NY: Marcel Dekker), 95–140.

Cannell, R. Q. (1977). Soil aeration and compaction in relation to root growth and soil management. *Appl. Biol.* 2, 1–86.

Czarnes, S., Hallett, P. D., Bengough, A. G., and Young, I. M. (2000). Root- and microbial-derived mucilages affect soil structure and water transport. *Eur. J. Soil Sci.* 51, 435–443. doi: 10.1046/j.1365-2389.2000.00327.x

De Gryze, S., Jassogne, L., Six, J., Bossuyt, H., Wevers, M., and Merckx, R. (2006). Pore structure changes during decomposition of fresh residue: X-ray tomography analyses. *Geoderma* 134, 82–96. doi: 10.1016/j.geoderma.2005.09.002

De Neve, S., and Hofman, G. (2000). Influence of soil compaction on carbon and nitrogen mineralization of soil organic matter and crop residues. *Biol. Fertil. Soils* 30, 544–549. doi: 10.1007/s003740050034

Derrien, D., and Amelung, W. (2011). Computing the mean residence time of soil carbon fractions using stable isotopes: impacts of the model framework. *Eur. J. Soil Sci.* 62, 237–252. doi: 10.1111/j.1365-2389.2010.01333.x

Dorioz, J. M., Robert, M., and Chenu, C. (1993). The role of roots, fungi and bacteria on clay particle organization. An experimental approach. *Geoderma* 56, 179– 194. doi: 10.1016/0016-7061(93)90109-X

Dou, F., Hons, F. M., Wright, A. L., Boutton, T. W., and Yu, X. (2014). Soil carbon sequestration in sorghum cropping systems: evidence from stable isotopes and aggregate-size fractionation. *Soil Sci.* 179, 68–74. doi: 10.1097/SS.0000000000000045

Dungait, J. A. J., Hopkins, D. W., Gregory, A. S., and Whitmore, A. P. (2012). Soil organic matter turnover is governed by accessibility not recalcitrance. *Global Change Biol.* 18, 1781–1796. doi: 10.1111/j.1365-2486.2012.02665.x

Ehleringer, J. R., Buchmann, N., and Flanagan, L. B. (2000). Carbon isotope ratios in belowground carbon cycle processes. *Ecol. Appl.* 10, 412–422. doi: 10.1890/1051-0761(2000)010[0412:CIRIBC]2.0.CO;2

Ekschmitt, K., Kandeler, E., Poll, C., Brune, A., Buscot, F., Friedrich, M., et al. (2008). Soil-carbon preservation through habitat constraints and biological limitations on decomposer activity. *J. Plant Nutr. Soil Sci.* 171, 27–35. doi: 10.1002/jpln.200700051

Ekschmitt, K., Liu, M., Vetter, S., Fox, O., and Wolters, V. (2005). Strategies used by soil biota to overcome soil organic matter stability – why is dead organic matter left over in soil? *Geoderma* 128, 167–176. doi: 10.1016/j.geoderma.2004.12.024

Emerson, W. W., and McGarry, D. (2003). Organic carbon and soil porosity. *Aust. J. Soil Res.* 41, 107–118. doi: 10.1071/SR01064

Farquhar, G. D., Ehleringer, J. R., and Hubick, K. T. (1989). Carbon isotope discrimination and photosynthesis. *Annu. Rev. Plant Physiol. Plant Mol. Biol.* 40, 503–537. doi: 10.1146/annurev.pp.40.060189.002443

Grandy, A. S., and Robertson, G. P. (2007). Land-use intensity effects on soil organic carbon accumulation rates and mechanisms. *Ecosystems* 10, 58–73. doi: 10.1007/s10021-006-9010-y

Gray, J., and Lissmann, H. W. (1938). An apparatus for measuring the propulsive forces of the locomotory muscles of the earthworm and other animals. *J. Exp. Biol.* 15, 518–521.

Greacen, E. L., and Oh, J. S. (1972). Physics of root growth. *Nat. New Biol.* 235, 24–25. doi: 10.1038/newbio235024a0

Greacen, E. L., and Sands, R. (1980). Compaction of forest soils. A review. *Aust. J. Soil Res.* 18, 163–189. doi: 10.1071/SR9800163

Jackson, R. B., Lajtha, K., Crow, S. E., Hugelius, G., Kramer, M. G., and Piñeiro, G. (2017). The ecology of soil carbon: pools, vulnerabilities, and biotic and abiotic controls. *Annu. Rev. Ecol. Evol. Syst.* 48, 419–445. doi: 10.1146/annurev-ecolsys-112414-054234

Kalcsits, L. A., and Guy, R. D. (2016). Variation in fluxes estimated from nitrogen isotope discrimination corresponds with independent measures of nitrogen flux in *Populus balsamifera* L. *Plant Cell Environ.* 39, 310–319. doi: 10.1111/pce.12614

Kalcsits, L. A., Min, X., and Guy, R. D. (2015). Interspecific variation in leaf-root differences in $\delta^{15}N$ among three tree species grown with either nitrate or ammonium. *Trees* 29, 1069–1078. doi: 10.1007/s00468-015-1186-3

Keiluweit, M., Wanzek, T., Kleber, M., Nico, P., and Fendorf, S. (2017). Anaerobic microsites have an unaccounted role in soil carbon stabilization. *Nat. Commun.* 8:1771. doi: 10.1038/s41467-017-01406-6

Kell, D. B. (2012). Large-scale sequestration of atmospheric carbon via plant roots in natural and agricultural ecosystems: why and how. *Philos. Trans. R. Soc. B* 367, 1589–1597. doi: 10.1098/rstb.2011.0244

Kravchenko, A. N., and Guber, A. K. (2017). Soil pores and their contributions to soil carbon processes. *Geoderma* 287, 31–39. doi: 10.1016/j.geoderma.2016.06.027

Kravchenko, A. N., Negassa, W. C., Guber, A. K., Hildebrandt, B., Marsh, T. L., and Rivers, M. L. (2014). Intra-aggregate pore structure influences phylogenetic composition of bacterial community in macroaggregates. *Soil Sci. Soc. Am. J.* 78, 1924–1939. doi: 10.2136/sssaj2014.07.0308

Kravchenko, A. N., Negassa, W. C., Guber, A. K., and Rivers, M. L. (2015). Protection of soil carbon within macro-aggregates depends on intra-aggregate pore characteristics. *Sci. Rep.* 5:16261. doi: 10.1038/srep16261

Kuzyakov, Y., and Blagodatskaya, E. (2015). Microbial hotspots and hot moments in soil: concept & review. *Soil Biol. Biochem.* 83, 184–199. doi: 10.1016/j.soilbio.2015.01.025

Lal, R. (1999). Soil management and restoration for carbon sequestration to mitigate the accelerated greenhouse effect. *Prog. Env. Sci.* 1, 307–326.

Lindquist, W. B., Venkatarangan, A., Dunsmuir, J., and Wong, T. (2000). Pore and throat size distributions measured from synchrotron X-ray tomographic images of Fontainebleau sandstornes. *J. Geophys. Res.* 105, 21509–21527. doi: 10.1029/2000JB900208

Marshall, T. J., Holmes, J. W., and Rose, C. W. (1996). *Soil Physics, 3rd Edn.* Cambridge: Cambridge University Press.

Milliken, G. A., and Johnson, D. E. (2009). *Analysis of Messy Data Volume I: Designed Experiments, 2nd Edn.* Boca Raton, FL: CRC Press.

Negassa, W. C., Guber, A. K., Kravchenko, A. N., Marsh, T. L., Hildebrandt, B., and Rivers, M. L. (2015). Properties of soil pore space regulate pathways of plant residue decomposition and community structure of associated bacteria. *PLoS ONE* 10:e0123999 doi: 10.1371/journal.pone.0123999

Neumann, G., Bott, S., Ohler, M. A., Mock, H.-P., Lippmann, R., and R., Grosch, et al. (2014). Root exudation and root development of lettuce (*Lactuca sativa* L. cv. Tizian) as affected by different soils. *Front. Microbol.* 5:2. doi: 10.3389/fmicb.2014.00002

Oh, W., and Lindquist, W. B. (1999). Image thresholding by indicator kriging. *IEEE Trans. Pattern Anal. Mach. Intell.* 21, 590–602. doi: 10.1109/34.777370

Peth, S., Chenu, C., Leblond, N., Mordhorst, A., Garnier, P., Nunan, N., et al. (2014). Localization of soil organic matter in soil aggregates using synchrotron-base X-ray microtomography. *Soil Biol. Biochem.* 78, 189–194. doi: 10.1016/j.soilbio.2014.07.024

Quigley, M. Y., Rivers, M. L., and Kravchenko, A. N. (2018). Patterns and sources of spatial heterogeneity in soil matrix from contrasting long term management practices. *Front. Environ. Sci.* 6:28. doi: 10.3389/fenvs.2018.00028

Rabot, E., Wiesmeier, M., Schlüter, S., and Vogel, H.-J. (2018). Soil structure as an indicator of soil functions: a review. *Geoderma* 314, 122–137. doi: 10.1016/j.geoderma.2017.11.009

Rasse, D. P., Rumpel, C., and Dignac, M.-F. (2005). Is soil carbon mostly root carbon? Mechanisms for a specific stablisation. *Plant Soil* 269, 341–356. doi: 10.1007/s11104-004-0907-y

Rawlins, B. G., Wragg, J., Reinhard, C., Atwood, R. C., Houston, A., Lark, R. M., et al. (2016). Three-dimensional soil organic matter distribution, accessibility and microbial respiration in macroaggregates using osmium staining and synchrotron X-ray computed tomography. *Soil* 2, 659–671. doi: 10.5194/soil-2-659-2016

R Core Team (2013). *R: A Language and Environment for Statistical Computing.* Vienna: R Foundation for Statistical Computing. Available online at: http://www.R-project.org/

Rivers, M. L. (2012). "tomoRecon: High-speed tomography reconstruction on workstations using multi-threading," in *Proceedings of SPIE - The International Society for Optical Engineering* (San Diego, CA), 8506:85060U.

Ruiz, S., Schymanski, S. J., and Or, D. (2017). Mechanics and energetics of soil penetration by earthworms and plant roots: higher rates cost more. *Vadose Zone J.* 16:8. doi: 10.2136/vzj2017.01.0021

SAS Inc (2009). *SAS User's Guide. Verssion 9.2.* Cary, NC: SAS Inst.

Schmidt, M. W., Torn, M. S., Abiven, S., Dittmar, T., Guggenberger, G., Janssens, I. A., et al. (2011). Persistence of soil organic matter as an ecosystem property. *Nature* 478, 49–56. doi: 10.1038/nature10386

Six, J., Elliott, E. T., and Paustian, K. (2000). Soil macroaggregate turnover and microaggregate formation: a mechanism for C sequestration under no-tillage agriculture. *Soil Biol. Biochem.* 32, 2099–2103. doi: 10.1016/S0038-0717(00)00179-6

Six, J., Frey, S. D., Thiet, R. K., and Batten, K. M. (2006). Bacterial and fungal contributions to carbon sequestration in agroecosystems. *Soil Sci. Soc. Am. J.* 70, 555–569. doi: 10.2136/sssaj2004.0347

Sleutel, S., Bouckaert, L., Buchan, D., Van Loo, D., Cornelis, W. M., and Sanga, H. G. (2012). Manipulation of the soil pore and microbial community structure in soil mesocosm incubation studies. *Soil Biol. Biochem.* 45, 40–48. doi: 10.1016/j.soilbio.2011.09.016

Smith, A. P., Bond-Lamberty, B., Benscoter, B. W., Tfaily, M. M., Hinkle, C. R., and Liu, C., et al (2017). Shifts in pore connectivity from precipitation versus groundwater rewetting increases soil carbon loss after drought. *Nat. Commun.* 8:1335. doi: 10.1038/s41467-017-01320-x

Smucker, A. J. M., Park, E.-J., Dorner, J., and Horn, R. (2007). Soil micropore development and contributions to soluble carbon transport within macroaggregates. *Vadose Zone J.* 6, 282–290. doi: 10.2136/vzj2007.0031

Stenger, R., Barkle, G. F., and Burgess, C. P. (2002). Mineralisation of organic matter in intact versus sieved/refilled soil cores. *Aust. J. Soil Res.* 40, 149–160. doi: 10.1071/SR01003

Stewart, G. R., Turnbull, M. H., Schmidt, S., and Erskine, P. D. (1995). ^{13}C natural abundance in plant communities along a rainfall gradient: a biological integrator of water availability. *Aust. J. Plant Physiol.* 22, 51–55. doi: 10.1071/PP9950051

Strong, D. T., De Wever, H., Merckx, R., and Recous, S. (2004). Spatial location of carbon decomposition in the soil pore system. *Eur. J. Soil Sci.* 55, 739–750. doi: 10.1111/j.1365-2389.2004.00639.x

Swift, R. S. (2001). Sequestration of carbon by soil. *Soil Sci.* 166, 858–871. doi: 10.1097/00010694-200111000-00010

Thomson, B. C., Ostle, N. J., McNamara, N. P., Whiteley, A. S., and Griffiths, R. I. (2010). Effects of sieving, drying and rewetting upon soil bacterial community structure and respiration rates. *J. Microbiol. Methods* 83, 69–73. doi: 10.1016/j.mimet.2010.07.021

Tiemann, L. K., and Grandy, A. S. (2015). Mechanisms of soil carbon accrual and storage in bioenergy cropping systems. *Glob. Change Biol. Bioenergy* 7, 161–174. doi: 10.1111/gcbb.12126

Urbanek, E., Smucker, A. J. M., and Horn, R. (2011). Total and fresh organic carbon distribution in aggregate size classes and single aggregate regions using natural ^{13}C/^{12}C tracer. *Geoderma* 164, 164–171. doi: 10.1016/j.geoderma.2011.05.020

Wang, W., Kravchenko, A. N., Johnson, T., Srinivasan, S., Ananyeva, K. A., Smucker, A. J. M., et al. (2013). Intra-aggregate pore structures and *Escherichia coli* distribution by water flow within and movement out of soil macroaggregates. *Vadose Zone J.* 12:4. doi: 10.2136/vzj2013.01.0012

Wang, W., Kravchenko, A. N., Smucker, A. J. M., Liang, W., and Rivers, M. L. (2012). Intra-aggregate pore characteristics: X-ray computed microtomography analysis. *Soil Sci. Soc. Am. J.* 76, 1159–1171. doi: 10.2136/sssaj2011.0281

Wang, W., Kravchenko, A. N., Smucker, A. J. M., and Rivers, M. L. (2011). Comparison of image segmentation methods in simulated 2D and 3D microtomographic images of soil aggregates. *Geoderma* 162, 231–241. doi: 10.1016/j.geoderma.2011.01.006

Wiersum, L. K. (1957). The relationship of the size and structural rigidity of pores to their penetration by roots. *Plant Soil* 9, 75–85. doi: 10.1007/BF01343483

Young, I. M., and Crawford, J. W. (2004). Interactions and self-organization in the soil-microbe complex. *Science* 304, 1634–1637. doi: 10.1126/science.1097394

Young, I. M., Crawford, J. W., and Rappoldt, C. (2001). New methods and models for characterizing structural heterogeneity of soil. *Soil Tillage Res.* 61, 33–45. doi: 10.1016/S0167-1987(01)00188-X

Minkowski Functionals of Connected Soil Porosity as Indicators of Soil Tillage and Depth

Fernando San José Martínez [1]*, Luisa Martín [1] and Carlos García-Gutiérrez [2]

[1] Applied Mathematics, Universidad Politécnica de Madrid, Madrid, Spain, [2] Applied Mathematics and Computer Science in Civil and Marine Engineering, Universidad Politécnica de Madrid, Madrid, Spain

We made use of 3D tomograms from X-ray computed tomography of soil samples from a vineyard in La Rioja (Spain), to explore the ability of Minkowski functionals of connected soil pore space to discriminate between different pore space geometries coming from soils with different management and depth and that, a priori, are expected to have some degree of dissimilarity. We estimate the volume of the connected pore space (V), the surface of the interface soil/void (S), the accumulated mean curvature of that interface (C), and its connectivity (E) out of 3D binary images taken from samples of two different depths of soil where two different managements were undertaken. Logit model showed that V, S, and C are needed to predict soil management and only V is required to infer depths. In our limited experimental circumstances, where we just explain two soil features, it seems natural that not all the four functionals are related to or needed to explain the variety of considered cases of soil structures. Therefore, this could not be an argument to dismiss Minkowski functionals as good candidates as predictors of the geometric structure of soil pore space. Our results suggest just the opposite, and they can be used as discriminants for a wide variety of soil features and behaviors.

Keywords: soil structure, soil pore space, X-ray computed tomography, mathematical morphology, Minkowski functional, soil management

1. INTRODUCTION

Soil structure is intimately related to soil functioning. Soil structure controls many important biophysical processes in soil-plant-microbial systems, related to microbial population dynamics, mass flow, nutrient cycling and uptake by roots (Young and Crawford, 2004). Besides, soil structure also influences soil's response to changes in the surrounding climate or to agriculture (Pot et al., 2015), carbon protection in soil (Kravchenko et al., 2015) or the transport of water and gas through its complex structure (Lehmann et al., 2006). In particular, many of these phenomena are strongly dependent on pore space geometry. A deeper understanding of the geometrical subtleties of soil's pore space topology and its changes due to agricultural management or depth are essential to modeling the previously mentioned processes and to infer the effect of agricultural management and depth on them.

Soil management is intended to affect soil structure to alter its functioning and enhance its productivity, but the geometrical effect of this, sometimes highly invasive, soil perturbations on pore space geometry is not completely elucidated. It is known that a shift from long periods of intensive agriculture to a natural vegetation cover, increases the contents of organic matter present

in the soil and also results in a bigger number of stable micro aggregates (Gryze et al., 2004; Grandy and Robertson, 2007).

The pedologist will manually sample soil *in situ* and classify its structure among several classes that are, somehow, related to its possible functioning and agricultural yield. For many years now, the use of X-ray computerized tomography (CT) has been used as a source of three-dimensional studies of the geometry of the soil pore space (Peyton et al., 1994; Perret et al., 1999; Pierret et al., 2002; Mees et al., 2003; Lehmann et al., 2006; Wildenschild and Sheppard, 2013). In particular, the use of advanced X-ray CT 3D imaging techniques made possible the visualization and study of the pore space inside soil aggregates. Many studies have shown that agricultural practices as tillage and fertilization directly affect the intra-aggregate pore characteristics (Peth et al., 2008; Kravchenko et al., 2011; Wang et al., 2012; Zhou et al., 2013; Zucca et al., 2013).

The vast amount of 3D geometrical data obtained through X-ray CT has been analyzed using tools borrowed from mathematical morphology and integral geometry (Santaló, 1976; Mecke and Stoyan, 2000, 2002; Banhart, 2008). Among these, Minkowski functionals (Arns et al., 2002; Lehmann et al., 2006) are specially interesting. They provide four fundamental geometrical properties of 3D objects, like soil porosity, embedded in three-dimensional space. These properties are the volume, the boundary surface, the integral mean curvature, and the connectivity of the object. Plus they can be computed efficiently. Hadwiger's theorem shows that any functional defined on any three-dimensional object that meets some natural and self-evident geometrical properties is a linear combination of Minkowski functionals (Santaló, 1976). This mathematical theorem could be interpreted as follows: any information that is geometrically relevant for the characterization of the pore space should be encoded in these four parameters. Then, these functionals could be a suitable quantitatively description of the 3D geometry of soil structure. Mecke (1998) and Roth et al. (2005) characterized 2D porous structures using the variation of Minkowski functionals based on the image binarization threshold variation. The same methodology was used by San José Martínez et al. (2013) on soil pore volumes of CT images of undisturbed soil columns. Mecke (2002) and Vogel et al. (2005) studied the variation of Minkowski funcionals based on the morphological effect of the dilation and erosion operations. This technique was also used by Arns et al. (2002, 2004) to characterize 3D images of Fontainebleau sandstone. Furthermore, Renard and Allard (2013) used the Euler numbers variation subject to erosion and dilation to describe connectivity as a means for characterizing heterogeneous aquifers with 2D models. Schlüter et al. (2011) used Minkowski functionals to describe the soil structure development in response to different fertilizations. Falconer et al. (2012, 2015) used Minkowski functionals to study soil fungal and microbial dynamics as functions of pore architecture and carbon distribution. San José Martínez et al. (2015) described exhaustively the morphology of soil aggregates using Minkowski functionals. This work included both the intra-aggregate pore space and the surface features of the aggregates.

Much have been said about the effect that soil tillage and depth have on the geometry of pore space. In this work we focus our attention in another key question: are Minkowski functionals good candidates as indicators of soil structure? We use Minkowski functionals obtained from three-dimensional X-ray CT images of cubic regions of undisturbed soil columns than were extracted from a vineyard in northern Spain as data set to tackle this question. These samples came from different depths of a soil where two different soil management practices were undertaken. In this investigation, first, we elucidate the influence of soil tillage and depth on Minkowski functionals as representative geometrical parameters. Then, we face the study of the power of these functionals to discriminate between different types of soil tillage and different depths.

2. MATERIALS AND METHODS

Soil column samples were taken from an experimental farm, called "La Grajera" which belongs to La Rioja Regional Government (La Rioja, northern Spain). Only the Ap horizon was sampled. Its depth varied between 20 and 39 cm due to the slope. Two different soil managements have been employed, since 2004. These soil managements were established in-between the vines rows, with a row spacing of 5.80 m. The managements tested were (i) tillage and (ii) no tillage with soil natural crop cover. The tillage was done with a cultivator up to depth of 15 cm. The frequency was once every 4–6 weeks, as required to control the weeds that affected the grapevines growth cycle. The dominant species commonly found in vineyards of La Rioja were annual grass and herb. This was the permanent cover crop in between the rows with no tillage. More details on the site can be found in Peregrina et al. (2010). A total of 12 soil columns were extracted in December 2010 using cylinders made out of PVC. The dimensions were 7.5 cm inside diameter and 60 cm height. These cylinders were percussion drilled in the space between the rows. In total, three strips were selected per treatment, six in total. Therefore, two columns per strip and six per treatment were collected.

Soil images were attained with a X-ray CT that used a Feinfocus FXE 225.51 microfocus beam source tube and a PerkinElmer amorphous silicon (a-Si) detector with $2,048 \times 2,048$ pixels. Operation acceleration voltage was $190\,kV$ ($53\,\mu A$) and target power was 20 W. The resulting images were in 16-bit grayscale. The shallow soil layer was analyzed by scanning the top 15 cm of each column. Images were taken of them from the first 7.5 cm and from the 7.5 to 15 cm layer below soil surface. Six images were taken for each layer and treatment, resulting in a total of 24 images. Each column scan resulted in a stack of 1,706 images. Voxel size in 3D reconstructions was $50\,\mu m$ per side. Prior to segmentation, images were enhanced by applying two consecutive 3D nonlinear filters (Müter et al., 2012). The first one, an Unsharp Mask, is used to enhance the edges between the soild and void phases, whilst the second one, a Median Filter, is used to reduce the noise present in the image. Images were segmented using the local adaptive method (Sauvola and Pietikäinen, 2000; Naveed et al., 2012). Cubic volumes 5.1 cm lineal size ($= 1024^3$ voxels) were cut out of the cylinders and used as regions of interest for the study of soil structure. Reconstructions of the

soil pore volumes inside columns can be seen in **Figure 1**. More detailed information can be found in San José Martínez et al. (2017).

When the binary images were available, a computer program (Michielsen and Raedt, 2001) was used to measure geometrical properties and derive the Minkowski functionals. For a 3D object K we can obtain the volume (V), the boundary surface (S), its integral mean curvature (C), and the connectivity (E) of the object of interest as follows

$$V(K) = n_c$$
$$S(K) = -6n_c + 2n_f$$
$$2C(K) = 3n_c - 2n_f + n_e$$
$$E(K) = -n_c + n_f - n_e + n_v$$

where n_c is the number of open cubes, n_f the number open squares or faces, n_e the number of open edges, and n_v the number of vertices that the voxels of the object K has. The property of two voxels being connected must be properly defined to be able to efficiently compute the topological properties of connected voxels by just using the total numbers of vertices, edges, faces and cubes defined above. In this work, two pore space voxels were considered as connected when they had either a face, an edge or a vertex in common (Michielsen and Raedt, 2001). Pores space voxels connected to the boundaries of the sample will be referred to as connected porosity. This is the object of interest in this work.

Soil samples come from two different soil management techniques, i.e., tillage, which will be noted as SMt; and natural cover, or no tillage, noted as SMc. Besides, two different depths are analyzed, first one, the layer between the soil surface and a depth of 7.5 cm, noted as DP1, while the second one ranges from 7.5 to 15 cm, noted as DP2. A total of $n = 22$ samples were considered, divided in the two above described factors with two levels. The inhomogeneity of sampling numbers among factors is due to the loss of a deep sample in the SMt class, and the loss of a superficial sample of the SMc class. We investigate if soil factors, tillage and depth, have any influence on the Minkowski functionals V, S, C, and E. For this purpose ANOVA factor analysis, with two factors and two levels in each factor, was carried out. Additionally, this procedure establishes possible interactions among the factors: sometimes the effect that a factor has on a response variable is dependent on the level at which the other factor is. To check the validity of the model, normality and
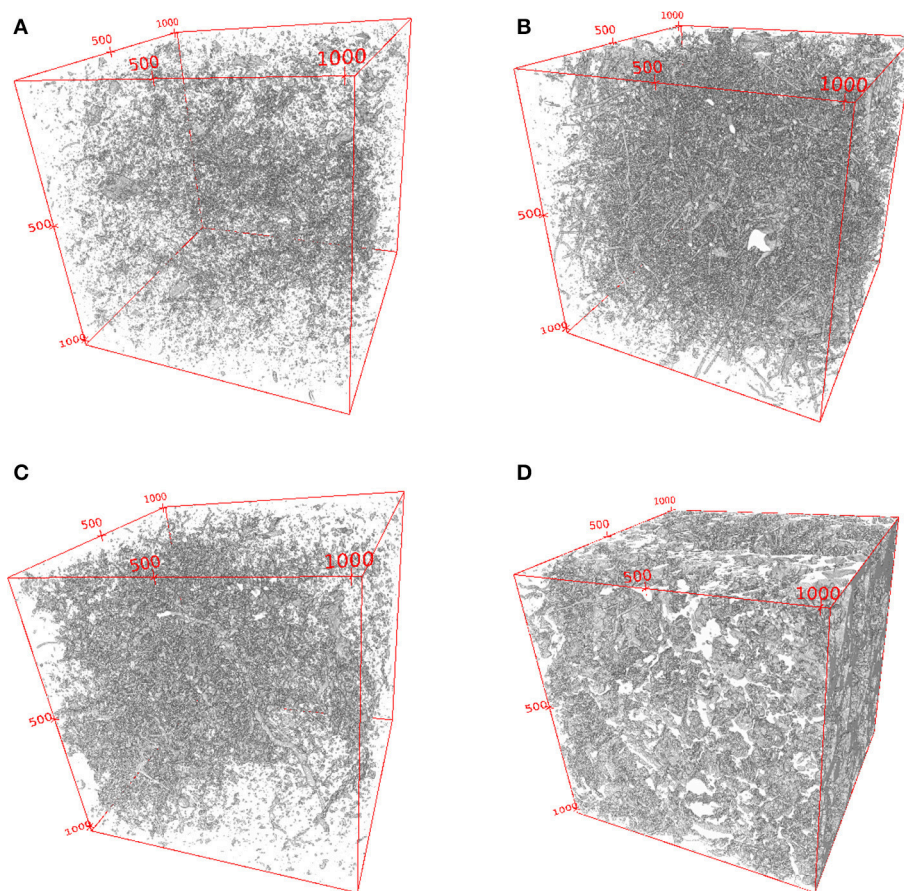

FIGURE 1 | Three-dimensional reconstruction pores space (black). Ticks in the axes correspond to pixel number. **(A)** Top soil sample cube from conventional tillage. **(B)** Bottom soil sample cube from conventional tillage. **(C)** Top soil sample cube from permanent cover crop of natural vegetation. **(D)** Bottom soil sample cube permanent cover crop of natural vegetation.

homoscedasticity of residues were checked. We use Kolmogorov-Smirnov test and Levene test, respectively. We found that at 0.05 significance level the normality and homoscedasticity hypothesis cannot be rejected.

Besides the previous test, we analyze if Minkowski functionals are capable of predicting the particular level of any of the soil available factors that a particular sample is in. Moreover, we want to identify which of the functionals is more relevant in the role of predicting the level of the corresponding soil factor. Classical linear regression is out of the question as the dependent variable is a qualitative binary response variable. A Logit, or logistic regression model, comes at hand: it is a specifically designed non-linear regression model for binary responses. Basically, the nonlinearity forces the estimated values to be in the $[0, 1]$ interval. As this is a regression analysis, it allows us to identify the variables which are most important at explaining the difference among the possible soil levels. We will determine the probability of a given sample to belong to a given soil treatment or a given soil depth based on a given combination of the values of the Minkowski functionals of that sample. The predictive power of the Minkowski functionals is related to the number of samples that are correctly assigned using the model probability function. With a logarithmic transformation we have the following expression for the probability of a given sample belongs to a given soil treatment or a given soil depth

$$\ln\left[\frac{p(\mathbf{X})}{1 - p(\mathbf{X})}\right] = \sum_{j=0}^{4} \beta_j X_j + \varepsilon_i$$

In this expression, $\mathbf{X} = (1, X_1, \ldots, X_4)$, β_j are the coefficient of the regression and ε_i is a random variable with mean 0 and independent values. Variables X_i correspond, in order, to Minkowski functionals, V, S, C, and E. Therefore, there are four explicative variables, or predictors and we need to estimate five values: the independent term β_0 and the coefficients of the four independent variables $\beta_1, \ldots, \beta_4$. The value of the response will be 1 if the probability obtained, for a given combination of the Minkowski functionals, is strictly bigger than 0.5, and zero in the other case. To evaluate the statistical significance of the estimated parameters, a test of hypothesis is performed. The null hypothesis $H_0 : \beta_0 = \beta_1 = \beta_2 = \beta_3 = \beta_4 = 0$ that all parameters are equal to zero, i.e., they have no effect on the soil factors, is tested. Finally, to analyze the goodness-of-fit of the Logit model, we made use of a "leave-one-out-cross-validation" (LOOCV) procedure.

3. RESULTS AND DISCUSSION

3.1. Geometrical Attributes V, S, C, and E as Response Variables

The calculated Minkowski functionals for the different images can be found in **Table 1**. Their mean values and standard deviations are collected in **Table 2**. We performed the ANOVA test for each Minkowski functional, V, S, C, and E, in order to evaluate the statistical significance of the parameters of the model. **Table 3** shows ANOVA results for Minkowski functionals as response variables.

TABLE 1 | Minkowski functionals for the different images.

Sample	SM	DP	V	S	C	E
1	t	1	7.840	904.818	4603.816	−24022
2	t	2	7.104	914.808	5465.367	−22549
3	t	1	2.331	95.081	506.454	424
4	t	2	0.059	8.916	92.836	415
5	t	1	0.184	20.208	166.074	573
6	t	2	2.443	366.351	2625.215	−8148
7	t	1	0.130	13.046	115.861	704
8	t	2	2.853	376.261	2386.790	−6842
9	t	1	0.050	12.631	225.491	1873
10	t	2	1.109	78.736	590.614	888
11	t	1	0.066	9.025	129.447	1370
12	c	2	2.088	311.479	2471.632	−4856
13	c	1	11.021	1239.155	7471.022	−27601
14	c	2	5.542	696.289	5080.058	−8164
15	c	1	6.568	730.389	5469.959	−12082
16	c	2	2.818	401.487	2702.766	−5940
17	c	1	18.538	1002.323	3532.746	−21530
18	c	2	2.613	292.495	2185.564	−2378
19	c	1	35.120	2674.386	4564.505	−111822
20	c	2	1.601	221.020	1976.121	1066
21	c	1	3.077	281.580	1934.588	−105
22	c	2	1.161	130.153	904.289	−424

Units are cm^3 for V, cm^2 for S and cm for C. E has no units.

When using a significance level of 0.05, soil management and the interaction between soil management and soil depth are statistically significant at explaining V. When using a significance level of 0.1, then soil depth also becomes statistically significant. In order to interpret the interaction between the two factors, we can see, in **Figure 2A**, that when in a soil that has undergone tillage (SMt), the mean values of V for the two available soil depths are not visually different. On the other hand, when the soil has kept the natural cover (SMc), there are differences in the mean values of V, meaning that this soil use has no effect on the mean value of the volume of soil pore network, thus it is not altering the soil volume at any depth. On the other hand, tillage removes the soil cover up to a depth of approximately 15 cm. This practice homogenizes soil structure, whilst when soil is kept with its natural cover, this does not happen. Thus, Minkowski functional V captures this expected difference in soil structure due to soil management.

For Minkowski functional S, results of the ANOVA test (**Table 3**), showed that at the 0.05 significance level, only soil

management and the interaction between the two factors are statistically significant. On the other hand, depth has no influence on the mean value of S. The interaction between the two factors can be interpreted using **Figure 2B**, which is very similar to the graph for the interaction of the factors for V. When soil underwent tillage, the mean values of S are similar for both depths, whilst they are different for a naturally covered soil. The homogenization effect of tillage observed for V is also valid for S.
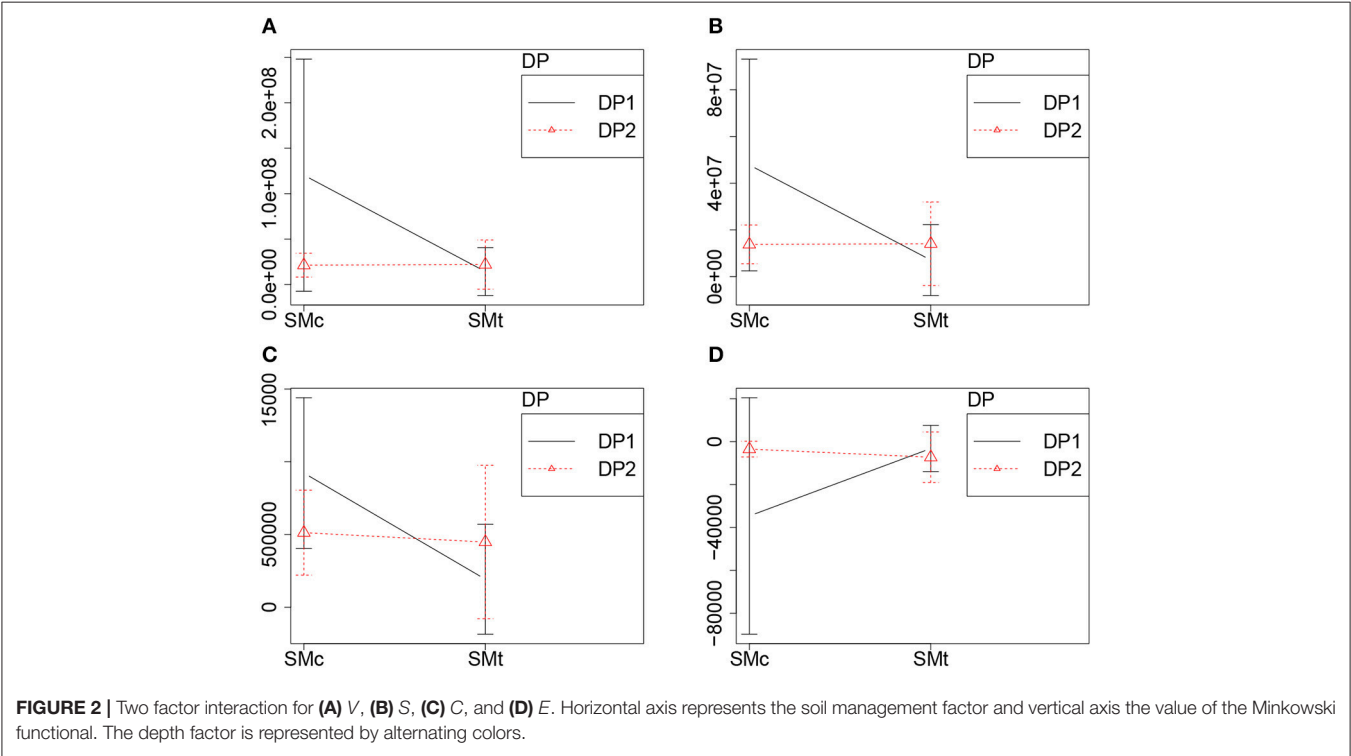
In the case of C response variable, we have (**Table 3**) the same conclusions as for the model with response variable V or S: both the soil management and the interaction between the factors are statistically significant. The interaction between the factors for C can be seen in **Figure 2C**, where we observe the same behavior as we did for the previous functionals V and S.

Lastly, for the model with response variable E (**Table 3**), only the interaction between soil management and soil depth is statistically significant but with a significance level of 0.1. None of the other factors alone has influence on the mean value of E. **Figure 2D** shows the effect of the interaction of the factors in the mean value of E, which is similar to the previous interaction graphs.

We conclude that mean values of V, S, and C become statistically different when altering soil management with a significance level of 0.1. However mean values of V become statistically different when depth changes. It is worth noting that interactions were observed between the two factors for all geometrical attributes V, S, C, and E, with a significance level of 0.1. A soil that has undergone tillage (SMt), did not show different mean values of functionals for the two available soil

TABLE 2 | Means and standard deviation of variables V, S, C, and E.

	Mean	Sd
V	42060060	64747640
S	19755180	24670590
C	503797.2	432376.5
E	-11325	24292.3

FIGURE 2 | Two factor interaction for **(A)** V, **(B)** S, **(C)** C, and **(D)** E. Horizontal axis represents the soil management factor and vertical axis the value of the Minkowski functional. The depth factor is represented by alternating colors.

depths. But, when the soil has kept the natural cover (SMc), there are differences in the mean values of these geometrical attributes. Our results suggest that Minkowski functionals capture the expected difference in soil structure due to soil management when measured at different depths.

3.2. Geometrical Attributes *V*, *S*, *C*, and *E* as Predictors

First we consider that the response variable is the factor type of soil management in the Logit model. We use the level SMt as 1, and SMc as 0 in the model. Thus, the model estimates the probability that a certain sample has undergone tillage, i.e., belongs to the level SMt. **Table 4** shows the estimation of the coefficients of the regression model and the *p*-values associated with the hypothesis tests for those coefficients to be equal to zero. We conclude that all the coefficients are equal to zero except β_0, as all the *p*-values are bigger than the habitual reference values. This could lead to conclude that the response variable is independent of the Minkowski functionals, but this is not reasonable looking at the results of the previous part of this work. A plausible explanation could be the existence of multicolinearity among variables. To study this possible effect the values of the functionals are plotted against one another. **Figure 3** is a matrix of dispersion graphs for all the functionals. All of them present highly aligned graphs. To further analyze this possible colinearity, **Table 5** presents the coefficients of determination among the functionals. It can be observed that *C* is the least correlated functional, to the rest. Taking into account this information and the results of ANOVA, it seems reasonable to use *V*, *S*, and *C* as predictors in the Logit model. **Table 6** shows the results in this case. Now, besides β_0, also the coefficients for *V*, *S*, and *C*, are statistically significant at a level of 0.1.

Now we are considering that soil depth level is the response variable in the Logit model. In this case we take the level DP2

as the value 1, and DP1 as 0 for the model. Thus, the model will estimate the probability that a certain sample belongs to the level DP2. **Table 7** shows the values of the estimated coefficients for this model, along with the *p*-values. In this case only β_1, the coefficient for *V*, is statistically significant at a level of 0.05. This result is also coherent with the results obtained previously in the ANOVA test.

In order to asses the ability of these models to predict the level of factor types SM and DP, we made use of a "leave-one-out-cross-validation" (LOOCV) procedure. With this test, the percentage of failure for predicting the SM was 26.3%, and for predicting DP it was 26.0%.

Interesting to see is that a combination of the three, *V*, *S*, and *C*, discriminates between soil management practices, whilst only *V* is necessary to discriminate between soil depth levels. These results suggest that Minkowski functionals are good predictors of soil management and depth. Nevertheless not all of them are needed to discriminate between the different imprint that soil management or depth has left on pore space geometry. For the soils considered in this investigation, connectivity, as measured by *E*, does not play a major role as a predictor neither for soil management nor for soil depth.

4. CONCLUSIONS

In this investigation we made use of 3D tomograms from X-ray CT of soil samples from a vineyard in La Rioja (Spain), to explore the ability of Minkowski functionals of connected soil pore space to discriminate between different pore space geometries that, a priori, are expected to have some degree of dissimilarity. To do so we measured the volume of the connected pore space (*V*), the surface of the interface soil/void (*S*), the accumulated mean curvature of that interface (*C*) and its connectivity (*E*). These are the Minkowski functionals for the soil pore space.

We first analyzed the Minkowski functionals as response variable of soil management, tillage vs. natural cover; and depth, from topsoil to 7.5 *cm*, and from there to 15 *cm*. We observed, with a significance level of 0.1, that mean values of *V*, *S*, and *C* become statistically different when altering soil management. Also interactions were observed between the two factors for geometrical attributes *V*, *S*, and *C*. A soil that has undergone tillage (SMt), did not show different mean values of these functionals for the two available soil depths. But, when the soil has kept the natural cover (SMc), there are differences in the mean values of these geometrical attributes. Tillage mixes the soil cover up to a depth of approximately 15 *cm*. This practice of soil management homogenizes soil structure, whilst when soil is kept with its natural cover crop, this does not happen. A similar interaction shows connectivity *E*. These results suggest that Minkowski functionals *V*, *S*, and *C* capture this expected difference in soil structure due to soil tillage when measured at different depths. On the other hand, depth has influence only on the volume of the connected pore space. This result should be regarded at the light of the fact that both factors showed interaction for all the Minkowski functionals, as explained above.

TABLE 3 | Results of ANOVA's test of *p*-values for Minkowski functionals as response variables of two factors (SM and DP) with two levels (SMt/SMc and DP1/DP2).

	V	*S*	*C*	*E*
SM	0.02865[**]	0.03288[**]	0.02164[**]	0.16198
DP	0.05407[*]	0.13989	0.63198	0.16988
SM:DP	0.02706[**]	0.03084[**]	0.04945[**]	0.07946[*]

Significance levels at 0.1 (*) and 0.05 (**).

TABLE 4 | Regression results for soil management as soil factor.

	Estimated	Standard error	z-value	Pr(> |z|)
(Intercept)	3.884	1.817	2.137	0.0326[**]
V	−1.069e−07	1.517e−07	−0.705	0.4807
S	9.247e−07	1.080e−06	−0.856	0.3919
C	1.322e−05	1.768e−05	0.748	0.4545
E	−1.003e−03	6.597e−04	−1.520	0.1284

Significance level at 0.05 (**).

FIGURE 3 | Dispersion graphs matrix.
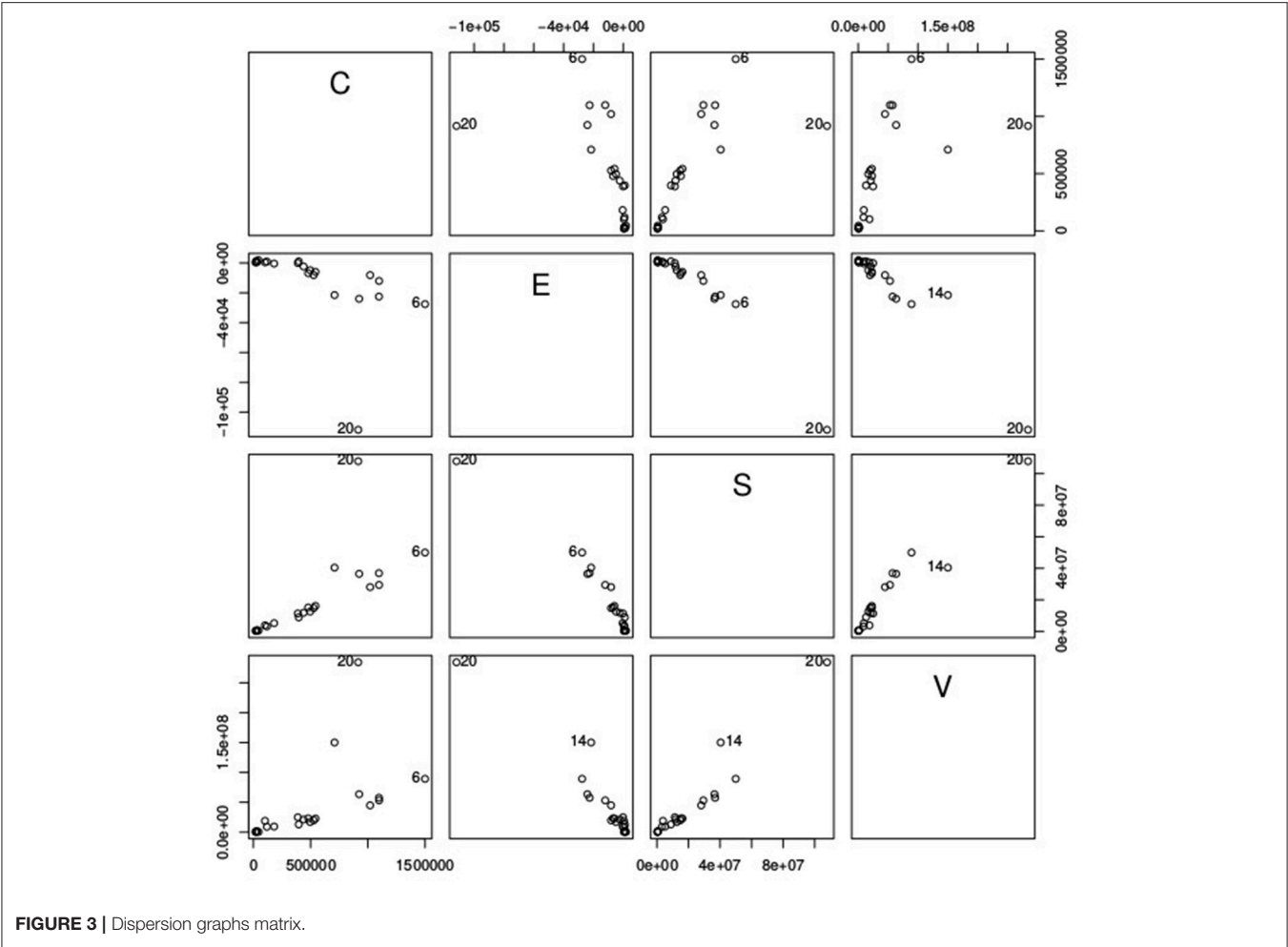
TABLE 5 | Coefficients of determination matrix.

	V	S	C	E
V	1	0.920	0.318	0.903
S	0.920	1	0.533	0.920
C	0.318	0.533	1	0.276
E	0.903	0.920	0.276	1

TABLE 6 | Regression results for soil management as soil factor.

	Estimated	Standard error	z-value	Pr(> |z|)
(Intercept)	2.345	1.190	1.971	0.0487[**]
V	−2.900e−07	1.568e−07	−1.850	0.0644[*]
S	8.609e−07	4.762e−07	1.808	0.0706[*]
C	−1.609e−05	8.540e−06	−1.884	0.0595[*]

Significance levels at 0.1 (*) and 0.05 (**).

Logit model showed that V, S, and C are needed to discriminate between soil tillage practices and only V is required to infer depths. As only a limited type of soil

TABLE 7 | Regression results for soil depth as soil factor.

	Estimated	Standard error	z-value	Pr(> |z|)
(intercept)	−9.984e−01	1.254	−0.796	0.4259
V	−7.471e−07	3.721e−07	−2.008	0.0447[**]
S	1.923e−06	1.319e−06	1.459	0.1447
C	−7.999e−06	1.640e−05	−0.488	0.6258
E	7.024e−04	6.235e−04	1.127	0.2600

Significance level at 0.05 (**).

structures were at hand, it seems fair that not all the four functionals are needed to infer the limited variety of considered cases of soil structures. Therefore, our results suggest that Minkowski functionals could be good predictors of the geometric structure of soil pore space. Nevertheless, this study should be extended to a larger number and variety of samples. This first study suggests that it is reasonable to further develop this theoretical framework. Future work could be to assess the predicting ability of this promising functionals as predictors of soil features related to changes in pore geometric structure.

AUTHOR CONTRIBUTIONS

FS has design the experimental, survey column extraction, X-ray CT imaging and the image analysis for binarization and enhance process. CG-G has carried out the estimation of Minkowski functionals. LM has completed the statistical analysis.

ACKNOWLEDGMENTS

REFERENCES

Arns, C., Knackstedt, M., and Mecke, K. (2002). "Characterizing the morphology of disordered materials," in *Morphology of Condensed Matter. LNP 600*, eds K. R. Mecke and D. Stoyan (Berlin: Springer Verlag), 37–74.

Arns, C., Knackstedt, M., and Mecke, K. (2004). Characterization of irregular spatial structures by parallel sets and integral geometric measures. *Colloids Surf. A Physicochem. Eng. Asp.* 241, 351–372. doi: 10.1016/j.colsurfa.2004.04.034

Banhart, J. (ed.). (2008). *Advanced Tomographic Methods in Materials Research and Engineering.* Oxford: Oxford University Press.

Falconer, R., Battaia, G., Schmidt, S., baveye, P., Chenou, C., and Otten, W. (2015). Microscale heterogeneity explains experimental variability and non-linearity in soil organic matter mineralisatins. *PLoS ONE* 10:e0123774. doi: 10.1371/journal.pone.0123774

Falconer, R., Houston, A., Otten, W., and Baveye, P. (2012). Emergent behaviour of soil fungal dynamics: influence of soil architecture and water distribution. *Soil Sci.* 177, 111–119. doi: 10.1097/SS.0b013e318241133a

Grandy, A., and Robertson, G. (2007). Land-use intensity effects on soil organic carbon accumulation rates and mechanisms. *Ecosystems* 10, 58–73. doi: 10.1007/s10021-006-9010-y

Gryze, S. D., Six, J., Paustian, K., Morris, S., Paul, E., and Merckx, R. (2004). Soil organic carbon pool changes following land-use conversions. *Glob. Change Biol.* 10, 1120–1132. doi: 10.1111/j.1529-8817.2003.00786.x

Kravchenko, A., Negassa, W., Guber, A., and Rivers, M. (2015). Protection of soil carbon within macro-aggregates depends on intra-aggregate pore characteristics. *Sci. Report.* 5:16261. doi: 10.1038/srep16261

Kravchenko, A., Wang, W., Smucker, A., and Rivers, M. (2011). Long-term differences in tillage and land use affect intra-aggregate pore heterogeneity. *Soil Sci. Soc. Am. J.* 75, 1658–1666. doi: 10.2136/sssaj2011.0096

Lehmann, P., Wyss, P., Flisch, A., Lehmann, E., Vontobel, P., Krafczyk, M., et al. (2006). Tomographical imaging and mathematical description of porous media used for the prediction of fluid distribution. *Vadose Zone J.* 5, 80–97. doi: 10.2136/vzj2004.0177

Mecke, K. (1998). Integral geometry and statistical physics. *Int. J. Mod. Phys. B* 12, 861–899. doi: 10.1142/S0217979298000491

Mecke, K. (2002). The shape of parallel surfaces: Porous media, fluctuating interfaces and complex fluids. *Phys. A* 314, 655–662. doi: 10.1016/S0378-4371(02)01047-6

Mecke, K., and Stoyan, D. (eds.). (2000). *Statistical Physics and Spatial Statistics. The Art of Analyzing and Modeling Spatial Structures and Pattern Formation. LNP 554.* Berlin: Springer Verlag.

Mecke, K., and Stoyan, D. (eds.). (2002). *Morphology of Condensed Matter. LNP 600.* Berlin: Springer Verlag.

Mees, F., Swennen, R., van Geet, M., and Jacobs, P., editors (2003). *Applications of X-Ray Computed Tomography in Geosciences. Spec. Publ. 215.* London: Geological Society of London.

Michielsen, K., and Raedt, H. D. (2001). Integral–geometry morphological image analysis. *Phys. Rep.* 347, 461–538. doi: 10.1016/S0370-1573(00)00106-X

Müter, D., Pedersen, S., Sørensen, H., Feidenhans'l, R., and Stipp, S. (2012). Improved segmentation of X-ray tomography data from porous rocks using a dual filtering approach. *Comput. Geosci.* 49, 131–139. doi: 10.1016/j.cageo.2012.06.024

Naveed, M., Moldrup, P., Arthur, E., Wildenschild, D., Eden, M., Lamandé, M., et al. (2012). Revealing soil structure and functional macroporosity along a clay gradient using X-ray computed tomography. *Soil Sci. Soc. Am. J.* 77, 403–411. doi: 10.2136/sssaj2012.0134

Peregrina, F., Larrieta, C., Ibáñez, S., and García-Escudero, E. (2010). Labile organic matter, aggregates, and stratification ratios in a semiarid vineyard with cover crops. *Soil Sci. Soc. Am. J.* 74, 2120–2130. doi: 10.2136/sssaj2010.0081

Perret, J., Prasher, S., Kantzas, A., and Langford, C. (1999). Three-dimensional quantification of macropore networks in undisturbed soil cores. *Soil Sci. Soc. Am. J.* 63, 1530–1543. doi: 10.2136/sssaj1999.6361530x

Peth, S., Horn, R., Beckmann, F., Donath, T., Fischer, J., and Smucker, A. (2008). Three-dimensional quantification of intra-aggregate pore-space features using synchrotron radiation-based microtomography. *Soil Sci. Soc. Am. J.* 72, 897–907. doi: 10.2136/sssaj2007.0130

Peyton, R., Gantzer, C., Anderson, S., Haeffner, B., and Pfeifer, P. (1994). Fractal dimension to describe soil macropore structure using X-ray computed tomography. *Water Resour. Res.* 30, 691–700. doi: 10.1029/93WR02343

Pierret, A., Capowiez, Y., Belzunces, L., and Moran, C. (2002). 3D reconstruction and quantification of macropores using X-ray computed tomography and image analysis. *Geoderma* 106, 247–271. doi: 10.1016/S0016-7061(01)00127-6

Pot, V., Peth, S., Monga, O., Vogel, L., Genty, A., Garnier, P., et al. (2015). Three-dimensional distribution of water and air in soil pores: comparison of two-phase two-relaxation-times lattice-Boltzmann and morphological model outputs with synchrotron X-ray computed tomography data. *Adv. Water Resour.* 84, 87–102. doi: 10.1016/j.advwatres.2015.08.006

Renard, P., and Allard, D. (2013). Connectivity metrics for subsurface flow and transport. *Adv. Water Resour.* 51, 168–196. doi: 10.1016/j.advwatres.2011.12.001

Roth, R., Boike, J., and Vogel, H. (2005). Quantifying permafrost patterns using Minkowski densities. *Permafrost Periglacial Process.* 16, 277–290. doi: 10.1002/ppp.531

San José Martínez, F., Caniego, F., and García-Gutiérrez, C. (2017). Lacunarity of soil macropore space arrangement of ct images: effect of soil management and depth. *Geoderma* 287, 80–89. doi: 10.1016/j.geoderma.2016.09.007

San José Martínez, F., Munoz, F., Caniego, F., and Peregrina, F. (2013). Morphological functions to quantify three-dimensional tomograms of macropore structure in a vineyard soil with two different management regimes. *Vadose Zone J.* 12:vzj2012.0208. doi: 10.2136/vzj2012.0208

San José Martínez, F., Ortega, F. M., Monreal, F. C., Kravchenko, A., and Wang, W. (2015). Soil aggregate geometry: measurements and morphology. *Geoderma* 237–238, 36–48. doi: 10.1016/j.geoderma.2014.08.003

Santaló, L. (1976). *Integral Geometry and Geometric Probability.* Reading, MA: Addison-Wesley.

Sauvola, J., and Pietikäinen, M. (2000). Adaptive document image binarization. *Patt. Recogn.* 33, 225–236. doi: 10.1016/S0031-3203(99)00055-2

Schlüter, S., Weller, U., and Vogel, H.-J. (2011). Soil-structure development including seasonal dynamics in a long-term fertilization experiment. *J. Plant Nutr. Soil Sci.* 174, 395–403. doi: 10.1002/jpln.201000103

Vogel, H., Hoffmann, H., and Roth, K. (2005). Studies of crack dynamics in clay soil. I. Experimental methods, results, and morphological quantification. *Geoderma* 125, 203–211. doi: 10.1016/j.geoderma.2004.07.009

Wang, W., Kravchenko, A., Smucker, A., Liang, W., and Rivers, M. (2012). Intra-aggregate pore characteristics: X-ray computed microtomography analysis. *Soil Sci. Soc. Am. J.* 76, 1159–1171. doi: 10.2136/sssaj2011.0281

Wildenschild, D., and Sheppard, A. (2013). X-ray imaging and analysis techniques for quantifying pore-scale structure and processes in subsurface porous medium systems. *Adv. Water Resour.* 51, 217–246. doi: 10.1016/j.advwatres.2012.07.018

Young, I., and Crawford, J. (2004). Interactions and self-organization in the soil-microbe complex. *Science* 304, 1634–1637. doi: 10.1126/science.1097394

Zhou, H., Peng, X., Perfect, E., Xiao, T., and Peng, G. (2013). Effects of organic and inorganic fertilization on soil aggregation in an Ultisol as characterized by synchrotron based X-ray micro-computed tomography. *Geoderma* 23, 195–196. doi: 10.1016/j.geoderma.2012.11.003

Zucca, C., Vignozzi, N., Madrau, S., Dingil, M., Previtali, F., and Kapur, S. (2013). Shape and intraporosity of topsoil aggregates under maquis and pasture in the mediterranean region. *J. Plant Nutr. Soil Sci.* 176, 529–539. doi: 10.1002/jpln.201200144

Cyanobacteria Inoculation Improves Soil Stability and Fertility on Different Textured Soils: Gaining Insights for Applicability in Soil Restoration

Sonia Chamizo*, Gianmarco Mugnai, Federico Rossi, Giacomo Certini and Roberto De Philippis

Department of Agrifood Production and Environmental Sciences (DISPAA), University of Florence, Florence, Italy

Cyanobacteria are ubiquitous components of biocrust communities and the first colonizers of terrestrial ecosystems. They play multiple roles in the soil by fixing C and N and synthesizing exopolysaccharides, which increase soil fertility and water retention and improve soil structure and stability. Application of cyanobacteria as inoculants to promote biocrust development has been proposed as a novel biotechnological technique for restoring barren degraded areas and combating desertification processes in arid lands. However, previous to their widespread application under field conditions, research is needed to ensure the selection of the most suitable species. In this study, we inoculated two cyanobacterial species, *Phormidium ambiguum* (non N-fixing) and *Scytonema javanicum* (N-fixing), on different textured soils (from silt loam to sandy), and analyzed cyanobacteria biocrust development and evolution of physicochemical soil properties for 3 months under laboratory conditions. Cyanobacteria inoculation led to biocrust formation in all soil types. Scanning electron microscope (SEM) images showed contrasting structure of the biocrust induced by the two cyanobacteria. The one from *P. ambiguum* was characterized by thin filaments that enveloped soil particles and created a dense, entangled network, while the one from *S. javanicum* consisted of thicker filaments that grouped as bunches in between soil particles. Biocrust development, assessed by chlorophyll *a* content and crust spectral properties, was higher in *S. javanicum*-inoculated soils compared to *P. ambiguum*-inoculated soils. Either cyanobacteria inoculation did not increase soil hydrophobicity. *S. javanicum* promoted a higher increase in total organic C and total N content, while *P. ambiguum* was more effective in increasing total exopolysaccharide (EPS) content and soil penetration resistance. The effects of cyanobacteria inoculation also differed among soil types and the highest improvement in soil fertility compared to non-inoculated soils was found in sandy and silty soils, which originally had lowest fertility. On the whole, the improvement in soil fertility and stability supports the viability of using cyanobacteria to restore degraded arid soils.

Keywords: autotrophic organisms, biocrust development, exopolysaccharides, organic carbon, soil nitrogen, soil degradation

INTRODUCTION

Biotechnological techniques based on the use of microorganisms as soil inoculants are regarded as promising potential tools to improve soil quality and counteract soil degradation in disturbed dryland areas (Bowker, 2007; Maestre et al., 2017; Rossi et al., 2017). Indeed, recent studies suggested that manipulation of the soil community by inoculation can be the key for a successful restoration of terrestrial ecosystems (Wubs et al., 2016).

Cyanobacteria are prokaryotic oxygenic phototrophs that inhabit almost every habitat on Earth (Abed and García-Pichel, 2001). They have been widely used as biofertilizers in agriculture, mainly in paddy rice fields in Asia (Prasanna et al., 2009, 2013; Priya et al., 2015; Singh et al., 2016). However, studies on their application for biofertilizing and bioconditioning degraded arid soils are relatively few. Experiments under laboratory (Maqubela et al., 2009, 2012; Mugnai et al., 2018) and outdoor conditions (Wang et al., 2009; Wu et al., 2013; Lan et al., 2017; Park et al., 2017; Zaady et al., 2017) point to positive results in terms of soil stability and fertility.

A successful inoculation procedure employing cyanobacteria can bring to the development of biological soil crusts or "biocrusts," i.e., assemblages of soil particles with bacteria, microalgae, microfungi, cyanobacteria, lichens and bryophytes, in varying proportions. Biocrusts are widespread components in drylands, covering from 40 to 100% of the interplant spaces and providing key ecosystem services in these environments (Maestre et al., 2011; Rodríguez-Caballero et al., in press) by affecting hydrological processes and soil water availability (Colica et al., 2014; Chamizo et al., 2016), soil stability (Rodríguez-Caballero et al., 2012), and nutrient cycling (Delgado-Baquerizo et al., 2013). Due to their recognized functions, biocrusts have been identified as relevant communities to effectively restore disturbed arid soils (Doherty et al., 2015; Antoninka et al., 2016; Velasco Ayuso et al., 2017). Within natural biocrust communities, cyanobacteria are pioneer organisms that improve soil conditions and the colonization of later-successional species, such as lichens and mosses (Belnap and Gardner, 1993; Lan et al., 2013). Both cyanobacterial filaments and their extracellular secretions, which are mostly composed of exopolysaccharides (EPSs), act as gluing agents, binding soil particles, and promoting the formation of soil aggregates, thus increasing soil stability (Mazor et al., 1996). EPSs also enhance water retention (Rossi et al., 2012, in press; Colica et al., 2014; Adessi et al., 2018) and protect microorganisms from desiccation and nutrient limitation, helping them to survive (Mazor et al., 1996; Zhang, 2005). Cyanobacteria fix CO_2 and some species are also able to fix N_2, while also releasing a wide array of substances in the soil, including phytormones, vitamins and phosphorus (Priya et al., 2015). They increase soil fertility in dryland regions (Zhao et al., 2010), where N, together with water, is a major limiting factor for ecosystem functioning (Noy-Meir, 1973). Cyanobacteria also provide a favorable microhabitat for soil biota (Liu et al., 2011) and improve vascular and annual plant performance (Xu et al., 2013; Lan et al., 2014). Due to these features and their high pervasiveness in every environment on Earth, cyanobacteria can be rightfully encompassed between

ecosystem engineers, and regarded as potential soil restoration tools in drylands (Rossi et al., 2017).

Nevertheless, numerous knowledge and methodological gaps still need to be reduced before restoration strategies based on cyanobacteria inoculation guarantee a successful performance under field conditions. Selection of the most suitable species in terms of ease for culture growth, amount and type of EPSs synthesized, and resistance to highly stressing environments are crucial factors to be evaluated before any restoration project (Rossi et al., 2017). In addition, the selection of the species should base chiefly on the capability to promote biocrust development and improve soil properties. This selection must also take into account the soil type. In fact, soil properties such as texture, mineralogy composition, organic matter and nutrients contents, pH, and electrical conductivity greatly influence cyanobacterial growth and EPS production. Soil texture is perhaps the most important of these properties, affecting biocrust formation and structure and water dynamics in soils. So far, most cyanobacteria inoculation experiments have been performed on sandy soils (Rozenstein et al., 2014; Lan et al., 2017; Mugnai et al., 2018), although fine-textured soils are common in many desert areas. In addition, physical crusting is common in fine-textured soils and in combination with biocrust formation greatly affects the structure and hydraulic properties of the soil (Malam Issa et al., 2011; Chamizo et al., 2012a).

In this study, the capability of *Phormidium ambiguum,* a non N-fixing cyanobacterium, and *Scytonema javanicum,* a N-fixing cyanobacterium, to promote biocrust development on four soils with different particle size distribution and organic carbon (C) and nitrogen (N) contents was explored under laboratory conditions. Inoculation of *S. javanicum* and *Phormidium* sp. in varying proportions with other cyanobacterial species has been previously reported to have a positive effect on stability and organic C and N contents of sandy soils (Hu et al., 2002; Xie et al., 2007; Wang et al., 2009; Li et al., 2014). However, the potential of these species alone to induce biocrust formation and modify soil properties in soils with different particle size distributions has not been explored so far, although it would allow having a better understanding of the potential of such species as habitat amelioration agents.

The main goals of this study were to: (i) analyze the effect of inoculation of two cyanobacterial species on biocrust growth and soil stability, hydraulic and fertility properties in different textured soils, under laboratory conditions; (ii) examine changes in biocrust development and soil properties by cyanobacteria inoculation with time.

MATERIAL AND METHODS

Experimental Design

Four types of soil with contrasting particle size distributions were collected from two semiarid areas in the province of Almeria (SE Spain). From the finest to the coarsest, these soils were classified as: (1) silt loam, (2) sandy loam; (3) loamy sand, and (4) sandy. Particle size distribution for each soil type is shown in **Table 1**. The silt loam soil was collected from the Tabernas desert (37°00′37″N, 2°26′37″W), a badlands area

Soil texture	Sand (%)	Silt (%)	Clay (%)
Silt loam	27	59	14
Sandy loam	65	20	15
Loamy sand	73	16	11
Sandy	92	1	7

characterized by shallow soils with poor structure and low N and organic matter content. Mean annual rainfall is 235 mm and mean annual temperature is 18°C. The other three soil types were collected from three different sites within the Cabo de Gata Natural Park. The climate is similar to the one of the Tabernas desert, with mean annual rainfall of 200 mm and mean annual temperature of 18°C (Chamizo et al., 2016). The loamy sand and sand soils were collected near "Las Amoladeras" experimental site (36°49′40″N, 2°16′10″W), a grassland area with flat topography. The sandy loam soil was collected from a semi-intensive rainfed olive crop area (36°48′13″N, 2°08′32″W). The sandy loam and loamy sand soils differ in their structure and chemical composition, the "agricultural" soil being less compact due to occasional tillage and having less carbonate and higher organic C and N contents than the loamy sand soil. The sampled soils were air-dried and sieved to 2 mm, and then autoclaved twice for 20 min at 120°C to suppress biological activity. Two cyanobacterial species were selected for the inoculation experiments: the non N-fixing *Phormidium ambiguum* Gomont NIES-2121, belonging to the order Oscillatoriales, and the widespread desert heterocystous *Scytonema javanicum* Bornet & Flahault NIES-1956, belonging to the order Nostocales. *P. ambiguum* was isolated from an African soil, while *S. javanicum* was isolated from the Tsukuba Botanical Garden (Japan). The genus *Phormidium* is a common colonizer of biocrusts that dwells in the deep soil layers, in contrast to *Scytonema* which preferentially colonizes the uppermost layer (Hu et al., 2002). The two cyanobacteria were grown in $BG11_0$ (*S. javanicum*) or BG11 (*P. ambiguum*) medium in a rotatory shaker (Innova 44B, New Brunswick, USA) at a constant temperature of 30°C, light intensity of 15 μmol photons m^{-2} s^{-1}, and stirring speed of 100 rpm. For the inoculation experiment, the biomass was separated from the culture medium by centrifugation at 4000 x *g* for 30 min and then fragmented in a sterile plastic tube using a sterilized spatula. Finally, the biomass was suspended in distilled water and its dry weight determined. A concentration of 5 g (dry weight) m^{-2} was inoculated on Petri dishes containing the different soil types (henceforth, microcosms). Microcosms had dimensions of 12 mm height × 54 mm diameter and were filled with 30 g of sterilized soil. In these microcosms, ~30 mg of biomass was inoculated. Additionally, bigger microcosms (16 mm height × 88 mm diameter) were prepared with 80 g of each soil type and inoculated with the same concentration of the two cyanobacteria species (5 g m^{-2} or 40 mg on each microcosm). These samples were used to conduct the reflectance measurements and the SEM micrographs at the end of the experiment (90 days) (see below).

Biomass was dispersed using a sterile 10 mL pipette and applying the biomass as homogeneously as possible over the surface, following a spiral distribution (Mugnai et al., 2018). Thus, three conditions were considered on each soil type: soil inoculated with *P. ambiguum*, soil inoculated with *S. javanicum*, and soil without any inoculum (control), each treatment replicated three times on each soil type. Three soil samplings were conducted during the experiment (30, 60, and 90 days after cyanobacteria inoculation), totalizing 108 small Petri dishes, whereas a total of 36 big microcosms (3 treatments × 4 soil types × 3 replicates) were prepared for the measurements at the end of the incubation period (90 days). Microcosms were incubated in a plexiglass growth chamber under controlled temperature (30°C), light intensity (45 μmol photons m^{-2} s^{-1}), and relative humidity (0 %) for 90 days. Twice a week, 2 mm (5 mL in the small microcosms and 13 mL in the bigger microcosms) of distilled water were applied on the microcosms using a sprayer. Such water amount corresponds to the average annual rainfall in the study areas where the soils were from (~215 mm), calculated according to the duration of the experiment.

Crust Sampling and Physico-Chemical Soil Analyses

The crust was collected from the small microcosms after 30, 60, and 90 days since inoculation. Previous to crust sampling, hydrophobicity and penetration resistance were measured in all samples. Then, the crust was collected with a spatula from each microcosm and thickness was measured with a caliber. In the sandy soil, a very thin biocrust (1–2 mm) developed on the surface, while in the silt loam, sandy loam and loamy soils, the crust was thicker (7–8 mm). The entire crust was analyzed and, to compare the effect of biocrusts on soil properties, a weighed mean of all variables with soil depth (considering the 0–2 mm crust and the 2–8 mm underlying soil layer) was calculated for the sandy soil. For the aggregate stability test, a part of the crust was fragmented and sieved, while the rest was manually ground to a fine powder with mortar and pestle for the chemical analyses.

Soil Physical Analyses
Soil hydrophobicity
Soil water repellency was measured in control and inoculated soils at the three sampling dates using two different methods: the water drop penetration time (WDPT, as in Adams et al., 1969) and the repellency index (RI, as in Hallett and Young, 1999). While the former method gives information about the persistence of hydrophobicity in the soil, the latter provides information about the severity of hydrophobicity. The WDPT consists of counting the time a drop of water takes to seep into the soil. Six drops were placed on each microcosm using a small pipette with distilled water. Crusts were classified according to the classification by Adams et al. (1969) as hydrophilic or wettable (<10 s), slightly hydrophobic (10–60 s) and severely hydrophobic (>60 s). The RI was determined from sorptivity measurements at −2 cm pressure head for both water and a 95% ethanol solution using a miniaturized mini-infiltrometer and calculated according

to Equation (1):

$$RI = 1.95 \sqrt{\frac{S_E}{S_W}} \qquad (1)$$

where S_E is the sorptivity of ethanol, S_W is the sorptivity of water, and the factor 1.95 accounts for differences in viscosity and surface tension between the two liquids (Tillman et al., 1989). A soil with $RI < 1.95$ ($S_E < S_W$) is considered non-repellent. Three water and ethanol sorptivity measurements were conducted on each microcosm.
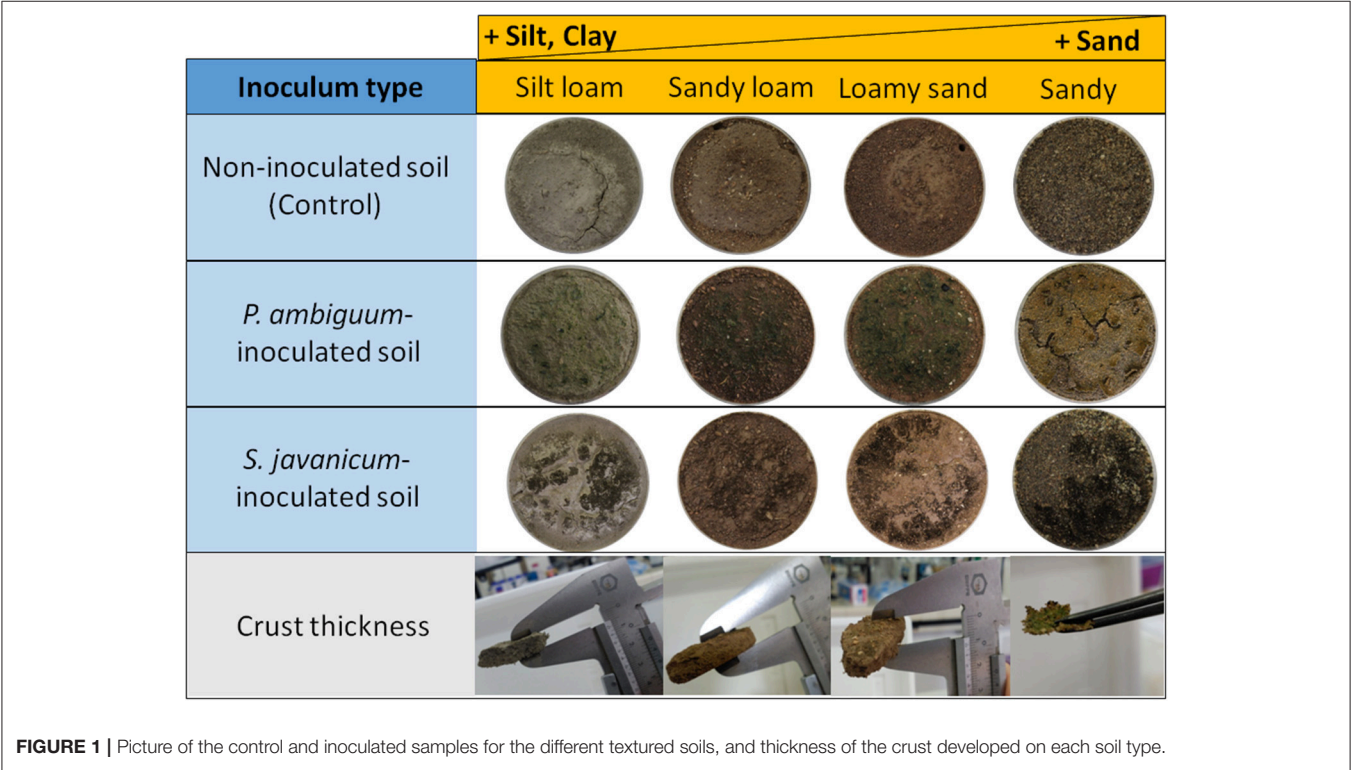
Soil stability
Soil stability was assessed by means of two variables: (1) aggregate stability, and (2) maximum penetration resistance of the surface. Aggregate stability was measured at the three sampling dates (30, 60, and 90 days) using the water drop test (Imeson and Vis, 1984). This test simulates the resistance of crust aggregates to raindrop energy impact. Concretely, the energy of impact of the water drops used was equivalent to the energy of 2.18 mm of rain (Imeson and Vis, 1984). To conduct the test, the crusts were first fragmented and sieved to 4–4.8 mm size. The aggregates were placed on a 2.8-mm metal mesh sieve and water-drops of 0.1 g in weight (obtained by fitting a small silicon tube to the burette nozzle) were dropped from 1 m in height through a burette over the aggregates. We counted the number of drops until the aggregate passed through the sieve. The test was done on 15 aggregates per sample, except on the sandy soil, where the test was not performed due to the absence of crust aggregates with 4–4.8 mm size.

Maximum penetration resistance (PRmax) of the crust was measured at the end of the experiment (90 days) using a digital force gauge (Mark-10 Model M7-5, 25N, Mark-10 Corp, USA) equipped with a cone tip (5 mm length and 6 mm diameter). Samples were placed onto a lifting table that was raised up until the entire tip was inserted into the soil (5 mm soil depth). Four penetration-resistance readings were performed on each sample.

Surface reflectance
At the end of the experiment (90 days), surface reflectance was measured on the samples (previously sprayed with water) with an ASD hand held portable spectroradiometer (ASD Inc., Boulder, Colorado, USA), which measures reflectance over the 325–1075 nm range at a sampling interval of 3.5 nm. Spectral measurements were conducted with a fiber optic oriented 16 cm above the sample to measure the total surface of the Petri dish and using two halogen lamps opposite each other. The spectroradiometer was calibrated using a 99% Spectralon(r) panel prior to measuring each sample. Then, two spectra were taken per sample, each one consisting on the internal average of three individual spectra. All reflectance values were expressed proportional to the 99% Spectralon reflectance panel and normalized to 100% reflectance. Data were acquired with the RS[3] Spectral Acquisition Software on a laptop connected to the spectroradiometer. Spectra processing included removal of noisy bands between 325 and 400 nm and 950 and 1075 nm and data smoothing using the Savitsky–Golay algorithm (Savitzky and Golay, 1964). From the smoothed spectra, two spectral variables that have been used as indicators of biocrust development or

FIGURE 1 | Picture of the control and inoculated samples for the different textured soils, and thickness of the crust developed on each soil type.

recovery after disturbance were calculated: the Brightness Index (BI) and the Normalized Difference Vegetation Index (NDVI). The brightness index was calculated according to equation 2:

$$BI = \sqrt{G^2 + R^2 + NIR^2} \tag{2}$$

where G, R, and NIR are the integrated reflectances for the green (500–600 nm), red (600–700 nm), and near-infrared bands (NIR, 700–950 nm), respectively. The Normalized Difference Vegetation Index (NDVI) was calculated as follow:

$$NDVI = [NIR - R]/[NIR + R] \tag{3}$$

FIGURE 2 | SEM pictures of the soil surface 90 days after inoculation in the different soils. Pictures on the left correspond to *P. ambiguum*-inoculated soils, while pictures on the right correspond to *S. javanicum*-inoculated soils. From the top to the bottom: silt loam **(A,E)**, sandy loam **(B,F)**, loamy sand **(C,G)**, and sandy **(D,H)**.

where R and NIR are the integrated reflectances in the red (600–700) and near-infrared bands (700–950 nm), respectively. Higher positive values of this index indicate greater biocrust development.

Sample's surface structure

After performing the reflectance measurements, small crust pieces were collected from the big microcosms and pre-treated for scanning electron microscopy (SEM) analysis by sputtering them with a thin coating of gold (at 50 mA for 1 min). SEM micrographs were taken using an Environmental Scanning Electron Microscopy (Fei Quanta 200 ESEM, Fei Corporation, Eindhoven, Netherlands) operating in high-vacuum mode (10 kV).

Soil Chemical Analyses

Chlorophyll a

Chlorophyll *a* content was quantified according to Castle et al. (2011). In brief, one g of soil was weighted into a screw-cap vial with 5 mL of ethanol, then shacked in a vortex and heated at 80°C for 5 min. Samples were cooled at 4°C for 24 h and then centrifuged; the supernatant was finally analyzed by a spectrophotometer.

Exopolysaccharide content

Total exopolysaccharides, including both loosely and tightly bound fractions, were recovered from soils using three consecutive extractions with 20 mL of 0.1 M Na_2EDTA each (Rossi et al., in press). The carbohydrate content of the extracts was determined using the phenol-sulfuric acid assay, measuring the absorbance at 488 nm with a UV-VIS spectrophotometer (Dubois et al., 1956). A calibration curve was created using glucose as standard. Three instrumental replicates were used for each sample.

Total organic C and N content

Organic C was measured on finely ground sample once treated with excess HCl to remove inorganic C. Total organic C and N contents were measured on 10–20 mg of the pulverized and oven-dried samples by dynamic dry flash combustion (1030°C under O_2 flow) using a Carlo Erba NA 1500 CNS Analyzer.

Statistical Analyses

The effect of cyanobacteria treatment (control, *P. ambiguum* inoculation, and *S. javanicum* inoculation) and incubation time (30, 60, and 90 days) on RI, chlorophyll content, aggregate stability and total EPS content on each soil type was analyzed using General Linear Models (GLM), after testing for homogeneity of variance and transforming data when necessary. Differences between treatments at each incubation time were further evaluated for significance using the Fisher LSD post hoc test. Statistical differences among cyanobacteria treatments in the variables analyzed at the end of the experiment (organic C and N content, PRmax, BI, and NDVI) were checked by one-way ANOVA and the LSD test. A confidence interval of 95% ($p < 0.05$) was established. All statistical analyses were performed using STATISTICA 8.0 (StatSoft, Inc., Tulsa, Oklahoma, USA).
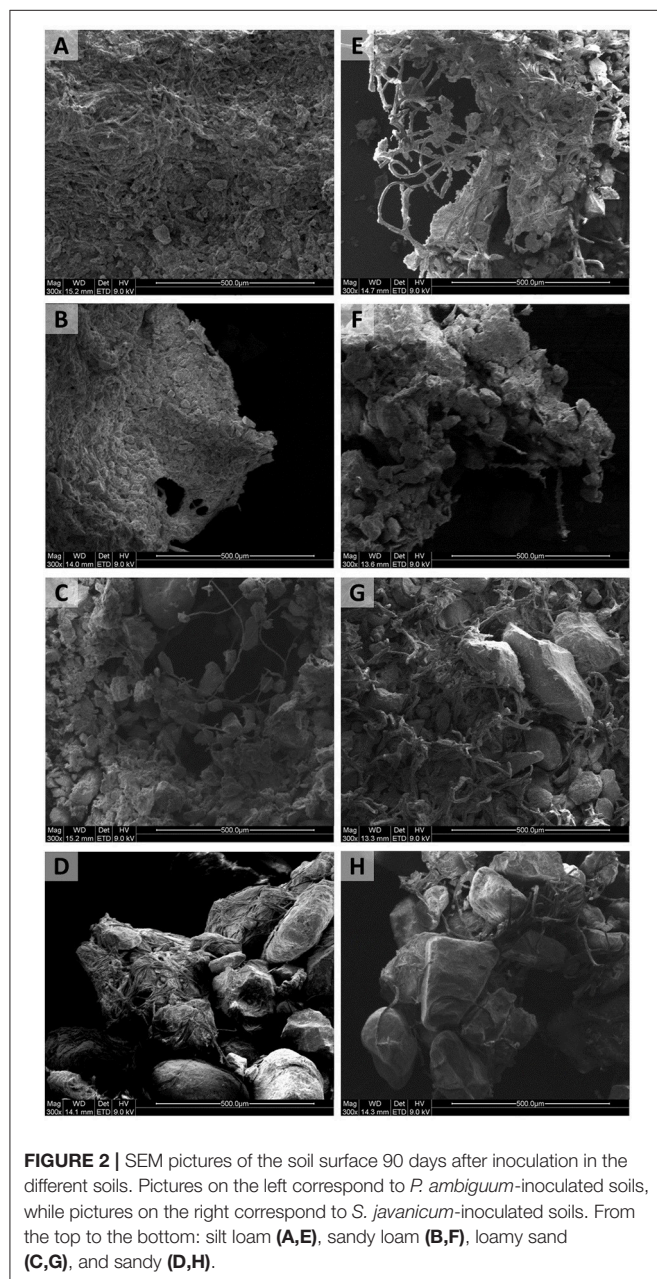
RESULTS

Characteristics of the Developed Biocrusts

Inoculation of the two cyanobacteria led to formation of biocrusts in all soil types. A very thin biocrust developed on the surface of the sandy soil, whereas in the finer soils, which were more prone to soil sealing, a thicker crust was formed by association of cyanobacterial filaments with the compacted soil (**Figure 1**). Average crust thickness was 9.3 ± 1.7 mm in silt loam, 8.3 ± 1.5 mm in sandy loam, 9.2 ± 0.9 mm in loamy sand, and 1.0 ± 0.4 mm in sand soils. Crust thickness was similar for both cyanobacterial species and no significant difference was observed with incubation time.

Cyanobacteria cover distribution over the soil surface differed between the two species. While *P. ambiguum* biomass was more homogeneously spread, *S. javanicum* showed a patchy distribution and tended to form small biomass aggregates near the border of the microcosms (**Figure 1**). In addition, the biocrust induced by *P. ambiguum* inoculation on the sandy soil was characterized by surface cracks, while a more even biocrust layer was observed on the same soil inoculated with *S. javanicum*. The SEM images also revealed differences between the two species in the morphology of cyanobacterial filaments and the spatial organization of soil particles (**Figure 2**). The thin *P. ambiguum* filaments wrapped soil particles and formed an entangled network that appeared as a blanket over the surface, while the relatively thicker *S. javanicum* filaments grouped as bunches in between soil particles, with a structure that resembled a "coral reef." As expected, there were also major differences in the internal structure of the soil types. The microstructure of biocrusts induced by the inoculation of *P. ambiguum* on the silt loam soil (**Figure 2A**) resulted in a dense and tightly packed network without any voids. Conversely, the inoculation of *S. javanicum* on the same substrate produced biocrusts visibly composed by filament bundles and EPSs tightly bound to the filaments (**Figure 2E**). In particular, along the filaments, there were some spots where the sheath covered the filaments and other spots where filaments appeared thinner and

without any sticky material attached. In the sandy loam soil (**Figures 2B–F**), biocrust induced by *P. ambiguum* inoculation resulted in a dense structure formed by web-like patterns of thin filaments. In contrast, *S. javanicum*-induced biocrust presented a non-homogeneous surface with low-density filaments where the sheath materials kept the soil particles together acting as cementing agents. Biocrust formation triggered by the inoculation of *P. ambiguum* on loamy sand soil (**Figure 2C**) was characterized by stable microaggregates where inter-particle cohesion was enhanced by polymer bridges. On the contrary, the *S. javanicum* crust (**Figure 2G**) showed filaments bundles that embedded soil particles and were distributed in an upward discontinuous surface without interspaces or porous structures. The biocrust developed on the sandy soil (**Figures 2D–H**) showed a lighter structure, with frequent air spaces between the sand grains. *P. ambiguum* tended to envelope soil particles in a thin layer of filaments that surrounded and bound sand particles into a tangled network (**Figure 2D**). On the same substrate, *S. javanicum* showed a lower number of filaments, with thicker shape compared to *P. ambiguum*, which entrapped and interconnected the sand grains (**Figure 2H**).
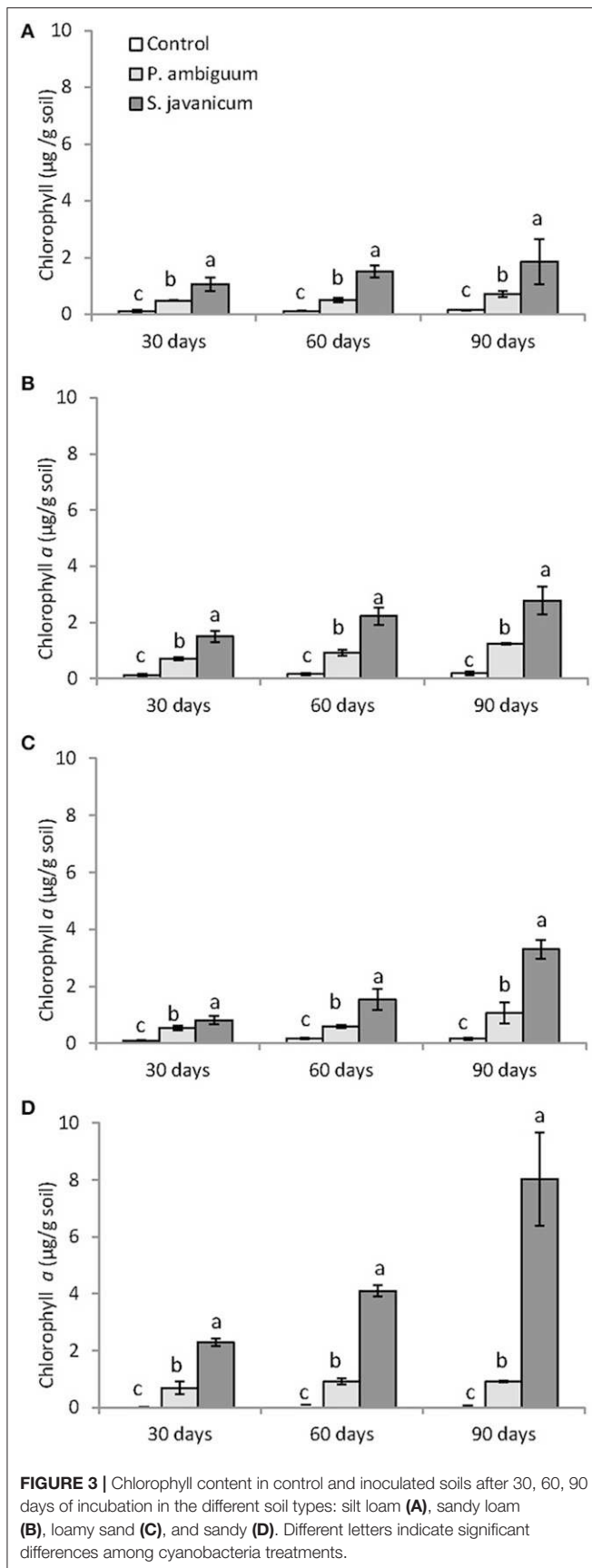
Biocrust Growth

Cyanobacteria inoculation and incubation time had significant effects on chlorophyll content (**Table 2**). The interaction between both factors was also significant, indicating that the effect of cyanobacteria depended on incubation time. Chlorophyll *a* content increased with time in both *P. ambiguum*-inoculated soils and, more significantly, in *S. javanicum*-inoculated soils, which showed the highest values after 90 days (**Figure 3**). From 30 to 90 days of incubation, the *S. javanicum*-inoculated soils showed an average increase in chlorophyll content of 121, 86, 321, and 251% in silt loam, sandy loam, loamy sand, and sand soils, respectively, while *P. ambiguum*-inoculated soils showed an average increase of 48, 75, 97, and 44%, respectively.

The higher chlorophyll content in inoculated soils and, especially in those inoculated with *S. javanicum*, was supported

TABLE 2 | *p*-values resulting from the GLM analysis considering as categorical predictors the cyanobacteria treatment (control, *P. ambiguum*, *S. javanicum*) and time of incubation (30, 60, and 90 days).

Soil texture	Predictor factors	RI	Chlorophyll content	Aggregate stability	Total EPS
Silt loam	Cyanobacteria treatment	0.001	0.000	0.000	0.000
	Time	0.000	0.034	0.004	0.000
	Cyanobacteria treatment * time	0.002	0.359	0.006	0.020
Sandy loam	Cyanobacteria treatment	0.000	0.000	0.000	0.000
	Time	0.000	0.000	0.001	0.000
	Cyanobacteria treatment * time	0.001	0.007	0.000	0.000
Loamy sand	Cyanobacteria treatment	0.000	0.000	0.003	0.000
	Time	0.787	0.000	0.000	0.000
	Cyanobacteria treatment * time	0.099	0.000	0.356	0.001
Sandy	Cyanobacteria treatment	0.000	0.000	–	0.000
	Time	0.000	0.000	–	0.000
	Cyanobacteria treatment * time	0.000	0.000	–	0.000

FIGURE 3 | Chlorophyll content in control and inoculated soils after 30, 60, 90 days of incubation in the different soil types: silt loam **(A)**, sandy loam **(B)**, loamy sand **(C)**, and sandy **(D)**. Different letters indicate significant differences among cyanobacteria treatments.

by the deeper spectral absorption at 670 nm, which was absent in the non-inoculated soils (**Figure 4**). Biocrust development in inoculated soils was also reflected by changes in BI and NDVI compared to the non-inoculated ones. Cyanobacteria inoculation significantly decreased BI in sandy and, more notably, in the light-colored silt loam soil, while had no significant effect in the darker sandy loam and loamy sand soils (**Table 3**). Cyanobacteria inoculation had a significant effect on NDVI in all soils ($p < 0.05$). NDVI was higher in inoculated soils than in the control ones, and the highest values were observed in those inoculated with *S. javanicum*. The increase in NDVI differed between soils and was more remarkable in the silt loam and sandy soils compared to the sandy loam and loamy sand ones (**Table 3**).

Soil Hydrophobicity

All soils showed WDPT values lower than 5 s, thus indicating a hydrophilic behavior. The GLM analysis showed a significant effect of cyanobacteria treatment and time on RI (**Table 2**). However, such differences did not change substantially the soil water repellency in the presence of biocrusts, as all RI values were lower than 1.95 (**Table 4**). Noteworthy is the relatively higher RI values in control and *P. ambiguum*-inoculated soils compared to the *S. javanicum*-inoculated ones 30 days after the soil incubation (**Table 4**), with average values of 1.52 ± 0.45, 1.60 ± 0.26, and 1.00 ± 0.44, respectively. The small differences observed diminished at the end of the incubation period, when average RI values in the control, *P. ambiguum*-inoculated and *S. javanicum*-inoculated soils were 1.20 ± 0.50, 1.15 ± 0.45, and 1.02 ± 0.33, respectively.

Soil Stability

Aggregate stability was low in all the samples and, in general, less than 10 water drop impacts were enough to break crust aggregates. Cyanobacteria treatment and time, and their interaction, showed a significant effect on aggregate stability (**Table 2**). Aggregate stability increased with incubation time. However, this increase varied with inoculant and soil type. *S. javanicum* inoculation promoted the highest increase in aggregate stability with time, especially in the silt loam soil, which showed higher values than the sandy loam and loamy sand soils (**Table 5**). Although to a lesser extent, *P. ambiguum* inoculation as well increased aggregate stability compared to the control soil, mainly at the end of the incubation period (**Table 5**).

Cyanobacteria inoculation increased penetration resistance of soil surface after 90 days of soil incubation, as shown by the significant effect of cyanobacteria treatment on PR_{max} in all soils ($p = 0.029$ in silt loam, $p = 0.008$ in sandy loam, $p = 0.030$ in loamy sand, and $p = 0.002$ in sandy soil). In contrast to the pattern observed in aggregate stability, soils inoculated with *P. ambiguum* showed higher PR_{max} than those inoculated with *S. javanicum*. *P. ambiguum* inoculation significantly increased penetration resistance in all soil types compared to the control soil, while *S. javanicum* inoculation significantly increased penetration resistance in the loamy sand and sandy soils. Important differences in PR_{max} were also observed among the four soils, the sandy soil showing lower values than the finer soils.
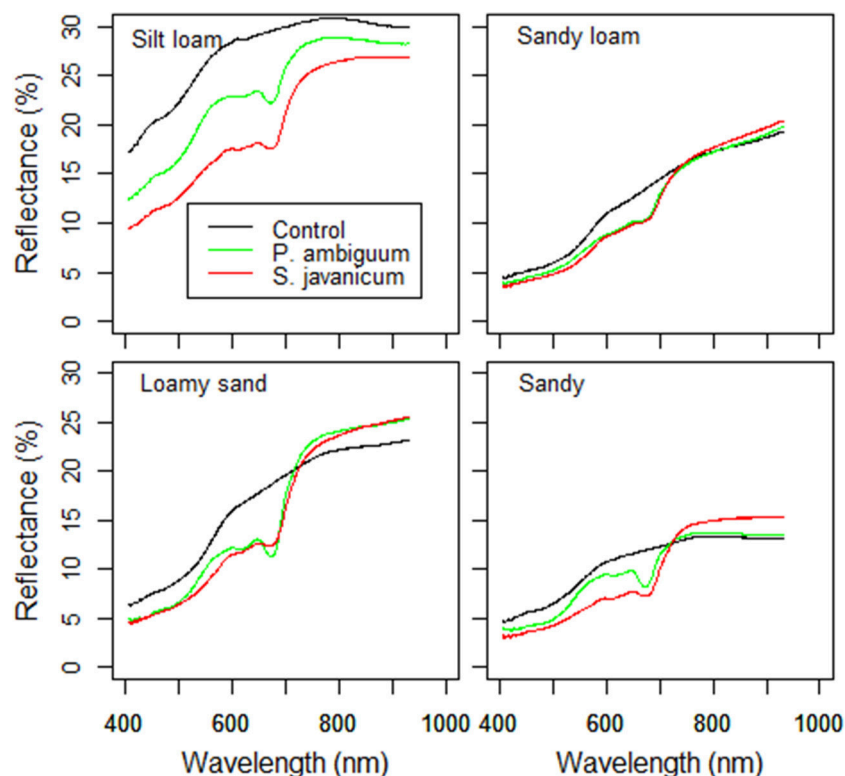
FIGURE 4 | Surface reflectance of control and inoculated soils at the end of the incubation period (90 days).

TABLE 3 | Mean ± sd of the Brightness Index (BI) and Normalized Difference Vegetation Index (NDVI) in control and inoculated soils at the end of the incubation period (90 days).

	Silt loam		Sandy loam		Loamy sand		Sandy	
	BI	NDVI	BI	NDVI	BI	NDVI	BI	NDVI
p-value	0.001	0.000	0.161	0.002	0.258	0.000	0.020	0.000
Control	49.6 ± 1.5[a]	0.02 ± 0.01[c]	22.9 ± 1.0[a]	0.16 ± 0.00[b]	30.8 ± 2.5[a]	0.11 ± 0.00[b]	19.5 ± 1.0[a]	0.06 ± 0.00[c]
P. ambiguum	42.0 ± 2.6[b]	0.10 ± 0.01[b]	21.2 ± 1.5[a]	0.26 ± 0.03[a]	28.5 ± 1.7[a]	0.30 ± 0.01[a]	18.0 ± 0.2[b]	0.18 ± 0.01[b]
S. javanicum	35.3 ± 2.4[c]	0.18 ± 0.01[a]	21.3 ± 0.4[a]	0.28 ± 0.04[a]	27.9 ± 1.8[a]	0.30 ± 0.04[a]	17.3 ± 0.7[b]	0.32 ± 0.01[a]

The p-value indicating the effect of cyanobacteria treatment is also shown. Different letters indicate significant differences within column.

Organic Carbon and Nitrogen Content of the Soil

Cyanobacteria inoculation promoted a significant increase in EPS content with time in all soils (**Table 2**, **Figure 5**). The *P. ambiguum*-inoculated soils showed higher EPS content than the *S. javanicum*-inoculated soils in all soils except in the sandy one, where *S. javanicum*-inoculated soils showed the highest EPS content after 90 days. There were also differences in EPS content among soil types mainly associated to the inherent EPS content of the tested soils. Thus, the sandy loam soil, which was collected from an agricultural arid site, showed per se higher EPS content than the other soils, all from natural arid sites. After 90 days of soil incubation, the *P. ambiguum*-inoculated soils showed an average increase in EPS content compared to the control soil of 44, 39,

22, and 195% in silt loam, sandy loam, loamy sand, and sandy soils, respectively, while *S. javanicum*-inoculated soils showed an average increase of 27, 22, 24, and 355%, respectively. The EPS content represented between 9 and 18% of organic C content (on average, 13.1% ± 2.0) in inoculated silt loam, sandy loam, and loamy sand soils, while in the sandy soil, EPS content was 29–36% of organic C.

Cyanobacteria inoculation significantly increased organic C compared to the control soil only in the sandy soil, where *P. ambiguum* and *S. javanicum* inoculation caused an organic C increase of 42 and 83%, respectively (**Table 6**). Cyanobacteria inoculation had a significant effect on total N in all soils but in the sandy loam one. The effect of cyanobacteria on the N content depended on the species. In fact, *P. ambiguum* inoculation only

TABLE 4 | Repellency index (RI) in control and inoculated soils after 30, 60, 90 days of incubation.

REPELLENCY INDEX (RI)			
Silt loam	**30 days**	**60 days**	**90 days**
Control	1.92 ± 0.24[a]	1.43 ± 0.18[a]	1.58 ± 0.20[a]
P. ambiguum	1.86 ± 0.03[b]	1.60 ± 0.02[a]	1.77 ± 0.09[ab]
S. javanicum	1.48 ± 0.24[c]	1.54 ± 0.14[a]	1.35 ± 0.12[ac]
Sandy loam	**30 days**	**60 days**	**90 days**
Control	1.31 ± 0.05[b]	1.06 ± 0.07[b]	0.94 ± 0.09[a]
P. ambiguum	1.78 ± 0.08[a]	1.37 ± 0.05[a]	1.09 ± 0.15[a]
S. javanicum	1.13 ± 0.08[c]	1.04 ± 0.18[bc]	1.13 ± 0.16[a]
Loamy sand	**30 days**	**60 days**	**90 days**
Control	1.62 ± 0.24[a]	1.54 ± 0.06[a]	1.73 ± 0.23[a]
P. ambiguum	1.35 ± 0.23[a]	1.09 ± 0.10[b]	1.17 ± 0.12[b]
S. javanicum	0.99 ± 0.06[b]	1.20 ± 0.09[b]	1.08 ± 0.07[b]
Sandy	**30 days**	**60 days**	**90 days**
Control	1.01 ± 0.09[a]	0.66 ± 0.10[a]	0.61 ± 0.05[a]
P. ambiguum	1.42 ± 0.11[b]	0.75 ± 0.04[a]	0.59 ± 0.08[a]
S. javanicum	0.53 ± 0.02[c]	0.50 ± 0.04[a]	0.53 ± 0.07[a]

Different letters indicate significant differences among cyanobacteria treatments on each soil type.

significantly increased N content in the sandy soil, where the inoculated samples showed 15% higher N content compared to the non-inoculated ones. *S. javanicum* significantly increased the N content in all soils but the sandy loam one. Average increases in N were 11%, 10%, 14%, and 55% in silt loam, sandy loam, loamy sand, and sandy soils, respectively.

DISCUSSION

The soils utilized in this study for the inoculation experiments diverged not only in terms of particle size distribution. The sand soil showed the lowest organic C and N contents and very low penetration resistance, while the silt loam soil showed low organic C and N content, as expected for soils from badlands (Chamizo et al., 2016). The loamy sand soil showed relatively high organic C and N contents due to better conditions of the site where the soil was from, a flat area where runoff erosion is infrequent (Chamizo et al., 2016). The sandy loam soil had even higher organic C and N contents, but lower aggregate stability due to aggregate disruption by occasional tillage. These differences between the soils used for the inoculation tests were functional for investigating the effects of the inoculation of the two cyanobacteria on a range as broad as possible.

A thick and resistant crust developed upon inoculation in the soils with less than 80% of sand, whereas a very thin and more fragile biocrust developed in the sandy soil. In fine-textured soils, biocrusts commonly co-exist with different types of physical crusts (Malam Issa et al., 2011), which increase soil compaction compared to coarser textures. Actually, the SEM images of the inoculated fine-textured soils clearly showed a firmer attachment of the cyanobacterial filaments to finer particles (**Figure 2**).

The two cyanobacteria showed a completely different way of biocrust formation: *P. ambiguum* grew forming a homogeneously dispersed biocrust, whereas *S. javanicum* induced the formation of a patchy biocrust, with areas covered by the cyanobacterium and areas apparently without any filament (**Figure 1**), as further confirmed by the SEM images (**Figure 2**).

The two tested species increased soil stability in all soils (**Table 5**), but in different ways probably owing to the different volume of the two cyanobacterial species as well as differences observed in the microstructure of the biocrusts. The volume of *S. javanicum* can be more than 100-fold higher than that of *Phormidium* sp. (Hu et al., 2003). Indeed, SEM images pointed out that *S. javanicum* filaments were thicker and organized as branches in between soil particles, binding them and leading to greater aggregate stability than *P. ambiguum* (**Figure 2**). However, *P. ambiguum* spred more uniformly over the surface and its thinner filaments surrounded soil particles, creating an entangled web that significantly enhanced crust resistance to penetration. Greater surface resistance could be also due to the higher EPS content of the biocrusts promoted by *P. ambiguum* inoculation (**Figure 5**). In addition, *S. javanicum* and *P. ambiguum* colonize different soil depths in natural desert crusts, with the former dominating at a depth of 0.02-0.05 mm and the latter growing deeper into the soil and dominating at a depth of 1.0–3.0 mm (Hu et al., 2003; Wu et al., 2011). This capacity of *P. ambiguum* to occupy a deeper niche in the soil and subsequent dispersion of its EPS in the first millimeters of soil is expected to have a more effective role in increasing soil penetration resistance compared to *S. javanicum*, whose growth and effects in soil stability could be mostly restricted to the surface. Previous experiments have also shown that inoculation of *Nostoc* sp., *Scytonema* sp., *Microcoleus vaginatus,* and *Phormidium* sp. increase soil aggregation on sand (McKenna Neuman et al., 1996; Hu et al., 2002; Chen et al., 2006; Xie et al., 2007), sandy loam (Malam Issa et al., 2007), silty and silt loam (Maqubela et al., 2009, 2012) and clay soils (Falchini et al., 1996; de Caire et al., 1997; Nisha et al., 2007).

The above reported microscale differences in the biocrusts are correlated to both the morphological differences of the two cyanobacteria used as inoculants and their different capability of growing in the soil. *S. javanicum*-inoculated soils showed the highest chlorophyll content with time in all soil types and, more remarkably, in the sandy soil (**Figure 3**). Higher size of *S. javanicum* filaments could provide them with a greater ability to trap and grow on coarse soil particles, while the colonization by *P. ambiguum* seems more confined due to lower size of their filaments and easier movement down into the large pores between coarse sand grains, as reported also for *Microcoleus vaginatus* (Rozenstein et al., 2014). The greater synthesis of chlorophyll observed in *S. javanicum* is most probably due to the efficient N metabolism typical of heterocystous cyanobacteria (Hu et al., 2003). *S. javanicum* is also a desiccation-tolerant species capable of synthesizing UV screening pigments (García-Pichel and Castenholz, 1991; Chen et al., 2013; Rastogi et al.,

TABLE 5 | Aggregate stability and maximum penetration resistance (mean ± sd) in inoculated and control soils.

	Aggregate stability (number of raindrop impacts)			Maximum penetration resistance (kPa)
Silt loam	**30 days**	**60 days**	**90 days**	**90 days**
Control	4.37 ± 0.40[b]	5.93 ± 0.00[b]	5.36 ± 0.88[c]	177.9 ± 35.3[b]
P. ambiguum	7.21 ± 0.52[a]	6.49 ± 0.45[b]	7.16 ± 0.27[b]	297.8 ± 34.3[a]
S. javanicum	7.23 ± 0.28[a]	8.42 ± 0.62[a]	9.72 ± 1.26[a]	231.9 ± 48.7[ab]
Sandy loam	**30 days**	**60 days**	**90 days**	**90 days**
Control	2.18 ± 0.22[c]	2.96 ± 0.31[b]	2.97 ± 0.42[b]	166.6 ± 21.0[b]
P. ambiguum	3.43 ± 0.29[b]	3.76 ± 0.21[a]	3.88 ± 0.61[b]	234.3 ± 24.0[a]
S. javanicum	4.41 ± 0.11[a]	3.14 ± 0.17[ab]	5.28 ± 0.78[a]	153.1 ± 19.1[b]
Loamy sand	**30 days**	**60 days**	**90 days**	**90 days**
Control	3.26 ± 0.67[b]	3.06 ± 0.19[b]	4.13 ± 0.61[a]	157.8 ± 12.2[b]
P. ambiguum	3.42 ± 0.20[b]	4.00 ± 0.42[a]	5.02 ± 0.31[a]	276.6 ± 39.1[a]
S. javanicum	4.21 ± 0.30[a]	4.06 ± 0.25[a]	4.75 ± 0.83[a]	280.6 ± 70.1[a]
Sandy	**30 days**	**60 days**	**90 days**	**90 days**
Control	na	na	na	5.6 ± 3.4[b]
P. ambiguum	na	na	na	23.8 ± 2.8[a]
S. javanicum	na	na	na	22.4 ± 5.0[a]

Different letters indicate significant differences among cyanobacteria treatments on each soil type. na, not available (no aggregates).

2014). Despite the low light intensity used in this study, the dry conditions imposed by high temperature and low water availability during the experiment could have favored the synthesis of UV screening and other photosynthetic pigments by *S. javanicum,* explaining the higher chlorophyll content compared to *P. ambiguum*.

Together with chlorophyll content, surface spectral indices were good indicators of biocrust development in the different soil types, as also shown by previous studies (Zaady et al., 2007; Belnap et al., 2008; Chamizo et al., 2012b; Rodríguez-Caballero et al., 2015). The BI index reflected the increase in surface darkness with biocrust development and was closely related to chlorophyll content, showing the highest values in *S. javanicum*-inoculated soils (**Table 3**). The NDVI was a good indicator not only of biocrust development but also of soil quality, as values of this index were higher in soils which had higher EPS, organic C and N content (**Table 3**). The NDVI values found in inoculated soils in the current study were in the range reported by Fischer et al. (2012) for incipient and well-developed biocrusts and showed maxima of 0.30 units, similarly to those found for lower plants (Karnieli et al., 1996); this indicates a considerable photosynthetic biomass growth promoted by cyanobacteria inoculation.

Biocrusts have been previously reported to increase soil hydrophobicity through the synthesis of hydrophobic organic compounds or swelling of cyanobacteria filaments and EPS upon wetting (Fischer et al., 2010; Lichner et al., 2012). However, in the current study, in agreement with Mugnai et al. (2018), soil hydrophobicity was not significantly increased by cyanobacteria

inoculation, as supported by WDPT < 5 s and RI < 1.95 (**Table 4**). Moreover, the RI values were slightly higher in the control soils, suggesting that improvement in soil aggregation and EPS content by cyanobacteria addition could even have a decreasing effect on soil water repellence.

Several studies have shown increases in nutrients content in natural and agricultural soils after cyanobacteria inoculation (Nisha et al., 2007; Maqubela et al., 2009; Lan et al., 2013; Singh et al., 2016; Rossi et al., 2017). In the current study, cyanobacteria growth was accompanied by a significant increase in EPS amount in the soil with time. *P. ambiguum*-inoculated soils, despite showing lower chlorophyll content, generally exhibited higher EPS content than *S. javanicum*-inoculated soils (**Figure 5**). Higher synthesis of EPS by *P. ambiguum* could be a strategy to cope with stress conditions imposed by water scarcity and more limited N availability compared to *S. javanicum*. Only in the sand soil, inoculation of *S. javanicum* led to higher EPS content than *P. ambiguum*, which was associated to a much greater photosynthetic biomass.

The increase in EPS was more remarkable in the sandy soil due to the very low EPS content of such soil compared to the silt loam, loamy sand, and sandy loam ones, which initially showed higher values. Despite the increase in EPS content with cyanobacteria inoculation, no significant increase in organic C content was observed in inoculated compared to control soils, with the exception of *S. javanicum* on sandy soils. Nevertheless, cyanobacteria inoculation did increase N content of soils, with different effects depending on species (**Table 6**). The presence of heterocysts in *Scytonema* sp. enables them to fix N and make
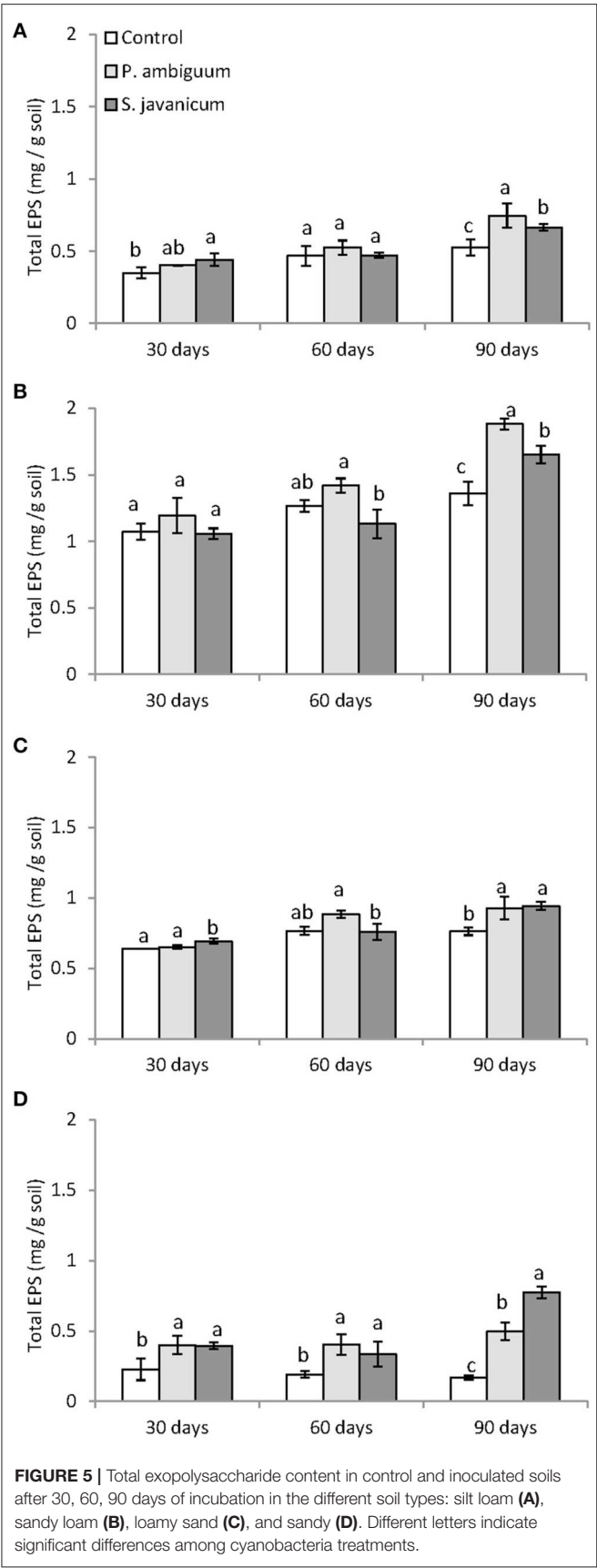
FIGURE 5 | Total exopolysaccharide content in control and inoculated soils after 30, 60, 90 days of incubation in the different soil types: silt loam **(A)**, sandy loam **(B)**, loamy sand **(C)**, and sandy **(D)**. Different letters indicate significant differences among cyanobacteria treatments.

TABLE 6 | Total organic carbon and total nitrogen content (mean ± sd) in inoculated and control soils.

	Silt loam		Sandy loam		Loamy sand		Sandy	
	Organic C (mg g^{-1})	N (mg g^{-1})	Organic C (mg g^{-1})	N (mg g^{-1})	Organic C (mg g^{-1})	N (mg g^{-1})	Organic C (mg g^{-1})	N (mg g^{-1})
p-value	0.787	0.058	0.984	0.904	0.140	0.074	0.002	0.000
Control	4.73 ± 1.00[a]	0.90 ± 0.02[b]	12.63 ± 1.86[a]	1.12 ± 0.15[a]	6.36 ± 0.63[a]	0.79 ± 0.04[b]	1.23 ± 0.28[c]	0.21 ± 0.01[c]
P. ambiguum	5.11 ± 0.49[a]	0.97 ± 0.01[b]	12.68 ± 0.88[a]	1.12 ± 0.05[a]	7.25 ± 0.52[a]	0.82 ± 0.06[ab]	1.68 ± 0.04[b]	0.24 ± 0.00[b]
S. javanicum	5.03 ± 0.47[a]	1.00 ± 0.06[a]	12.85 ± 1.68[a]	1.16 ± 0.14[a]	7.21 ± 0.38[a]	0.90 ± 0.04[a]	2.15 ± 0.11[a]	0.32 ± 0.02[a]

The p-value is also shown. Different letters indicate significant differences among cyanobacteria treatments on each soil type.

an efficient use of light to fix N compared to non-heterocystous species (Johnson et al., 2005; Yeager et al., 2007; Abed et al., 2010). Thus, soils inoculated with *S. javanicum* showed higher N content than *P. ambiguum*-inoculated soils. Nonetheless, contribution of non-heterocystous cyanobacteria to N fixation can be important (Abed et al., 2010). In this regard, we found that the inoculation of *P. ambiguum* also increased the N content in the sandy soil (**Table 6**).

In summary, our results point out a higher ability of *S. javanicum* to increase some soil properties crucial for fertility and a greater effect of *P. ambiguum* in increasing soil stability. In this regard, a recent study has shown that the species *Phormidium tenue* was dominant in crusts of different ages in the Loess Plateau (China) and, together with *Oscillatoria* sp., could increase carbon and nitrogen content in later biocrust successional stages, thus making it a suitable candidate for artificial cultivation in both early and later biocrust successional stages (Zhang et al., 2017). On the whole, our findings highlight the appropriateness of species selection to increase the success of restoration strategies based on cyanobacteria application under field conditions.

CONCLUSIONS

Soil inoculation with two cyanobacteria species, one N-fixing and one non N-fixing, led to rapid biocrust formation and improved soil stability and/or fertility properties on different soils. The positive effects greatly varied depending on species and soil characteristics, mainly soil texture. A thinner and more fragile biocrust developed in the sandy soil, while a stable and resistant cyanobacterial biocrust developed in the finer soil textures. Inoculation of *S. javanicum* had a greater effect on photosynthetic biomass and soil nitrogen content, while inoculation of *P. ambiguum* had a more important effect on EPS amount and soil strength. Moreover, increase in soil fertility properties was greater in soils with initially lower physical and chemical soil quality. In light of these results, it is worth stressing

that the selection of cyanobacterial species to be used as soil inoculants based on their main functional roles and suitability for a given soil is an important issue to consider to maximize the positive effects on soil quality. Further research about the applicability of cyanobacteria inoculation in different ecosystems with different soil types and climate conditions are needed to develop a complete, versatile, and applicable decision system for restoration of arid lands based on the induction of biocrust formation.

AUTHOR CONTRIBUTIONS

SC conceived the idea, designed the experiment, performed the laboratory analyses, and wrote the manuscript. GM and FR designed the experiment, performed the laboratory analyses and improved manuscript editing. GC performed the laboratory analyses and improved manuscript editing. RD conceived the idea, designed the experiment, and wrote the manuscript. All authors contributed with constructive comments to the manuscript.

FUNDING

ACKNOWLEDGMENTS

REFERENCES

Abed, R. M., Al Kharusi, S., Schramm, A., and Robinson, M. D. (2010). Bacterial diversity, pigments and nitrogen fixation of biological desert crusts from the Sultanate of Oman. *FEMS Microbiol. Ecol.* 72, 418–428. doi: 10.1111/j.1574-6941.2010.00854.x

Abed, R. M. M., and Garcia-Pichel, F. (2001). Long-term compositional changes after transplant in a microbial mat cyanobacterial community revealed using a polyphasic approach. *Environ. Microbiol.* 3, 53–62. doi: 10.1046/j.1462-2920.2001.00159.x

Adams, S., Strain, B. R., and Adams, M. S. (1969). "Water-repellent soils and annual plant cover in desert scrub community of south eastern California," in *Proceedings of the Symposium on Water-Repellent Soils, University of California* (Riverside), 289–295.

Adessi, A., Cruz de Carvalho, R., De Philippis, R., Branquinho, C., and Marques da Silva, J. (2018). Microbial extracellular polymeric substances improve water retention in dryland biological soil crusts. *Soil Biol. Biochem.* 116, 67–69. doi: 10.1016/j.soilbio.2017.10.002

Antoninka, A., Bowker, M. A., Reed, S. C., and Doherty, K. (2016). Production of greenhouse-grown biocrust mosses and associated cyanobacteria to

rehabilitate dryland soil function. *Restor. Ecol.* 24, 324–335. doi: 10.1111/rec.12311

Belnap, J., and Gardner, J. S. (1993). Soil microstructure in soils of the Colorado Plateau: the role of the cyanobacterium *Microcoleus vaginatus*. *Great Basin Nat.* 53, 40–47.

Belnap, J., Phillips, S. L., Witwicki, D. L., and Miller, M. E. (2008). Visually assessing the level of development and soil surface stability of cyanobacterially dominated biological soil crusts. *J. Arid Environ.* 72, 1257–1264. doi: 10.1016/j.jaridenv.2008.02.019

Bowker, M. A. (2007). Biological soil crust rehabilitation in theory and practice: an underexploited opportunity. *Restor. Ecol.* 15, 13–23. doi: 10.1111/j.1526-100X.2006.00185.x

Castle, S. C., Morrison, C. D., and Barger, N. N. (2011). Extraction of chlorophyll a from biological soil crusts: a comparison of solvents for spectrophotometric determination. *Soil Biol. Biochem.* 43, 853–856. doi: 10.1016/j.soilbio.2010.11.025

Chamizo, S., Cantón, Y., Lázaro, R., Solé-Benet, A., and Domingo, F. (2012a). Crust composition and disturbance drive infiltration through biological soil crusts in semiarid ecosystems. *Ecosystems* 15, 148–161. doi: 10.1007/s10021-011-9499-6

Chamizo, S., Cantón, Y., Rodríguez-Caballero, E., and Domingo, F. (2016). Biocrusts positively affect the soil water balance in semiarid ecosystems. *Ecohydrology* 9, 1208–1221. doi: 10.1002/eco.1719

Chamizo, S., Stevens, A., Cantón, Y., Miralles, I., Domingo, F., and Van Wesemael, B. (2012b). Discriminating soil crust type, development stage and degree of disturbance in semiarid environments from their spectral characteristics. *Eur. J. Soil Sci.* 63, 42–53. doi: 10.1111/j.1365-2389.2011.01406.x

Chen, L., Deng, S., De Philippis, R., Tian, W., Wu, H., and Wang, J. (2013). UV-B resistance as a criterion for the selection of desert microalgae to be utilized for inoculating desert soils. *J. Appl. Phycol.* 25, 1009–1015. doi: 10.1007/s10811-012-9906-1

Chen, L., Xie, Z., Hu, C., Li, D., Wang, G., and Liu, Y. (2006). Man-made desert algal crusts as affected by environmental factors in Inner Mongolia, China. *J. Arid Environ.* 67, 521–527. doi: 10.1016/j.jaridenv.2006.02.018

Colica, G., Li, H., Rossi, F., Li, D., Liu, Y., and De Philippis, R. (2014). Microbial secreted exopolysaccharides affect the hydrological behavior of induced biological soil crusts in desert sandy soils. *Soil Biol. Biochem.* 68, 62–70. doi: 10.1016/j.soilbio.2013.09.017

de Caire, G. Z., de Cano, M. S., Zaccaro de Mulé, M. C., Palma, R. M., and Colombo, K. (1997). Exopolysaccharide of Nostoc muscorum (Cyanobacteria) in the aggregation of soil particles. *J. Appl. Phycol.* 9, 249–253. doi: 10.1023/A:1007994425799

Delgado-Baquerizo, M., Maestre, F. T., and Gallardo, A. (2013). Biological soil crusts increase the resistance of soil nitrogen dynamics to changes in temperatures in a semi-arid ecosystem. *Plant Soil* 366, 35–47. doi: 10.1007/s11104-012-1404-3

Doherty, K. D., Antoninka, A. J., Bowker, M. A., Ayuso, S. V., and Johnson, N. C. (2015). A novel approach to cultivate biocrusts for restoration and experimentation.. *Ecol. Restor.* 33, 13–16. doi: 10.3368/er.33.1.13

Dubois, M., Gilles, K. A., Hamilton, J. K., Rebers, P. A., and Smith, F. (1956). Colorimetric method for determination of sugars and related substances. *Anal. Chem.* 28, 350–356. doi: 10.1021/ac60111a017

Falchini, L., Sparvoli, E., and Tomaselli, L. (1996). Effect of Nostoc (Cyanobacteria) inoculation on the structure and stability of clay soils. *Biol. Fert. Soils* 23, 346–352. doi: 10.1007/BF00335965

Fischer, T., Veste, M., Eisele, A., Bens, O., Spyra, W., and Hüttl, R. F. (2012). Small scale spatial heterogeneity of Normalized Difference Vegetation Indices (NDVIs) and hot spots of photosynthesis in biological soil crusts. *Flora* 207, 159–167. doi: 10.1016/j.flora.2012.01.001

Fischer, T., Veste, M., Wiehe, W., and Lange, P. (2010). Water repellency and pore clogging at early successional stages of microbiotic crusts on inland dunes, Brandenburg, NE Germany. *Catena* 80, 47–52. doi: 10.1016/j.catena.2009.08.009

García-Pichel, F., and Castenholz, R. W. (1991). Characterization and biological implications of scytonemin, a cyanobacterial sheath pigment. *J. Phycol.* 27, 395–409. doi: 10.1111/j.0022-3646.1991.00395.x

Hallett, P. D., and Young, I. M. (1999). Changes to water repellence of soil aggregates caused by substrate-induced microbial activity. *Eur. J. Soil Sci.* 50, 35–40. doi: 10.1046/j.1365-2389.1999.00214.x

Hu, C., Liu, Y., Song, L., and Zhang, D. (2002). Effect of desert soil algae on the stabilization of fine sands. *J. Appl. Phycol.* 14, 281–292. doi: 10.1023/A:1021128530086

Hu, C., Zhang, D., Huang, Z., and Liu, Y. (2003). The vertical microdistribution of cyanobacteria and green algae within desert crusts and the development of the algal crusts. *Plant Soil* 257, 97–111. doi: 10.1023/A:1026253307432

Imeson, A. C., and Vis, M. (1984). Assessing soil aggregate stability by water-drop impact and ultrasonic dispersion. *Geoderma* 34, 185–200. doi: 10.1016/0016-7061(84)90038-7

Johnson, S. L., Budinoff, C. R., Belnap, J., and Garcia-Pichel, F. (2005). Relevance of ammonium oxidation within biological soil crust communities. *Environ. Microbiol.* 7, 1–12. doi: 10.1111/j.1462-2920.2004.00649.x

Karnieli, A., Shachak, M., Tsoar, H., Zaady, E., Kaufman, Y., Danin, A., et al. (1996). The effect of microphytes on the spectral reflectance of vegetation in semiarid regions. *Remote Sens. Environ.* 57, 88–96. doi: 10.1016/0034-4257(95)00209-X

Lan, S., Wu, L., Yang, H., Zhang, D., and Hu, C. (2017). A new biofilm based microalgal cultivation approach on shifting sand surface for desert cyanobacterium Microcoleus vaginatus. *Bioresource Technol.* 238, 602–608. doi: 10.1016/j.biortech.2017.04.058

Lan, S., Wu, L., Zhang, D., and Hu, C. (2013). Assessing level of development and successional stages in biological soil crusts with biological indicators. *Microb. Ecol.* 66, 394–403. doi: 10.1007/s00248-013-0191-6

Lan, S., Zhang, Q., Wu, L., Liu, Y., Zhang, D., and Hu, C. (2014). Artificially accelerating the reversal of desertification: cyanobacterial inoculation facilitates the succession of vegetation communities. *Environ. Sci. Technol.* 48, 307–315. doi: 10.1021/es403785j

Li, H., Rao, B., Wang, G., Shen, S., Li, D., Hu, C., et al. (2014). Spatial heterogeneity of cyanobacteria-inoculated sand dunes significantly influences artificial biological soil crusts in the Hopq Desert (China). *Environ. Earth Sci.* 71, 245–253. doi: 10.1007/s12665-013-2428-6

Lichner, E., Holko, L., Zhukova, N., Schacht, K., Rajkai, K., Fodor, N., et al. (2012). Plants and biological soil crust influence the hydrophysical parameters and water flow in an aeolian sandy soil. *J. Hydrol. Hydromech.* 60, 309–318. doi: 10.2478/v10098-012-0027-y

Liu, Y., Li, X., Jia, R., Huang, L., Zhou, Y., and Gao, Y. (2011). Effects of biological soil crusts on soil nematode communities following dune stabilization in the Tengger Desert, Northern China. *Appl. Soil Ecol.* 49, 118–124. doi: 10.1016/j.apsoil.2011.06.007

Maestre, F. T., Bowker, M. A., Cantón, Y., Castillo-Monroy, A. P., Cortina, J., Escolar, C., et al. (2011). Ecology and functional roles of biological soil crusts in semi-arid ecosystems of Spain. *J. Arid Environ.* 75, 1282–1291. doi: 10.1016/j.jaridenv.2010.12.008

Maestre, F. T., Solé, R., and Singh, B. K. (2017). Microbial biotechnology as a tool to restore degraded drylands. *Microb. Biotechnol.* 10, 1250–1253. doi: 10.1111/1751-7915.12832

Malam Issa, O., Défarge, C., Le Bissonnais, Y., Marin, B., Duval, O., Bruand, A., et al. (2007). Effects of the inoculation of cyanobacteria on the microstructure and the structural stability of a tropical soil. *Plant Soil* 290, 209–219. doi: 10.1007/s11104-006-9153-9

Malam Issa, O., Valentin, C., Rajot, J. L., Cerdan, O., Desprats, J. F., and Bouchet, T. (2011). Runoff generation fostered by physical and biological crusts in semi-arid sandy soils. *Geoderma* 167–168, 22–29. doi: 10.1016/j.geoderma.2011.09.013

Maqubela, M. P., Mnkeni, P. N. S., Issa, O. M., Pardo, M. T., and D'Acqui, L. P. (2009). Nostoc cyanobacterial inoculation in South African agricultural soils enhances soil structure, fertility, and maize growth. *Plant Soil* 315, 79–92. doi: 10.1007/s11104-008-9734-x

Maqubela, M. P., Muchaonyerwa, P., and Mnkeni, P. N. S. (2012). Inoculation effects of two South African cyanobacteria strains on aggregate stability of a silt loam soil. *Afr. J. Biotechnol.* 11, 10726–10735. doi: 10.5897/AJB11.2111

Mazor, G., Kidron, G. J., Vonshak, A., and Abeliovich, A. (1996). The role of cyanobacterial exopolysaccharides in structuring desert microbial crusts. *FEMS Microbiol. Ecol.* 21, 121–130. doi: 10.1111/j.1574-6941.1996.tb00339.x

McKenna Neuman, C., Maxwell, C. D., and Boulton, J. W. (1996). Wind transport of sand surfaces crusted with photoautotrophic microorganisms. *Catena* 27, 229–247. doi: 10.1016/0341-8162(96)00023-9

Mugnai, G., Rossi, F., Felde, V. J. M. N. L., Colesie, C., Büdel, B., Peth, S., et al. (2018). Development of the polysaccharidic matrix in biocrusts induced by a cyanobacterium inoculated in sand microcosms. *Biol. Fert. Soils* 54, 27–40. doi: 10.1007/s00374-017-1234-9

Nisha, R., Kaushik, A., and Kaushik, C. P. (2007). Effect of indigenous cyanobacterial application on structural stability and productivity of an organically poor semi-arid soil. *Geoderma* 138, 49–56. doi: 10.1016/j.geoderma.2006.10.007

Noy-Meir, I. (1973). Desert ecosystems: environment and producers. *Annu. Rev. Ecol. Syst.* 4, 25–51. doi: 10.1146/annurev.es.04.110173.000325

Park, C. H., Li, X. R., Zhao, Y., Jia, R. L., and Hur, J. S. (2017). Rapid development of cyanobacterial crust in the field for combating desertification. *PLoS ONE* 12:e0179903.. doi: 10.1371/journal.pone.0179903

Prasanna, R., Babu, S., Rana, A., Kabi, S. R., Chaudhary, V., Gupta, V., et al. (2013). Evaluating the establishment and agronomic proficiency of cyanobacterial consortia as organic options in wheat-rice cropping sequence. *Exp. Agr.* 49, 416–434. doi: 10.1017/S001447971200107X

Prasanna, R., Jaiswal, P., Nayak, S., Sood, A., and Kaushik, B. D. (2009). Cyanobacterial diversity in the rhizosphere of rice and its ecological significance. *Indian J. Microbiol.* 49, 89–97. doi: 10.1007/s12088-009-0009-x

Priya, H., Prasanna, R., Ramakrishnan, B., Bidyarani, N., Babu, S., Thapa, S., et al. (2015). Influence of cyanobacterial inoculation on the culturable microbiome and growth of rice. *Microbiol. Res.* 171, 78–89. doi: 10.1016/j.micres.2014.12.011

Rastogi, R. P., Sonani, R. R., and Madamwar, D. (2014). The high-energy radiation protectant extracellular sheath pigment scytonemin and its reduced counterpart in the cyanobacterium Scytonema sp. R77DM. *Bioresour. Technol.* 171, 396–400. doi: 10.1016/j.biortech.2014.08.106

Rodríguez-Caballero, E., Cantón, Y., Chamizo, S., Afana, A., and Solé-Benet, A. (2012). Effects of biological soil crusts on surface roughness and implications for runoff and erosion. *Geomorphology* 145–146, 81–89. doi: 10.1016/j.geomorph.2011.12.042

Rodríguez-Caballero, E., Castro, A. J., Chamizo, S., Quintas-Soriano, C., Garcia-Llorente, M., Cantón, Y., et al. (in press). Ecosystem services provided by biocrusts: from ecosystem functions to social values. *J. Arid Environ.* doi: 10.1016/j.jaridenv.2017.09.005

Rodríguez-Caballero, E., Knerr, T., and Weber, B. (2015). Importance of biocrusts in dryland monitoring using spectral indices. *Remote Sens. Environ.* 170, 32–39. doi: 10.1016/j.rse.2015.08.034

Rossi, F., Li, H., Liu, Y., and De Philippis, R. (2017). Cyanobacterial inoculation (cyanobacterisation): Perspectives for the development of a standardized multifunctional technology for soil fertilization and desertification reversal. *Earth-Sci. Rev.* 171, 28–43. doi: 10.1016/j.earscirev.2017.05.006

Rossi, F., Mugnai, G., and De Philippis, R. (in press). Complex role of the polymeric matrix in biological soil crusts. *Plant Soil.* doi: 10.1007/s11104-017-3441-4

Rossi, F., Potrafka, R. M., Pichel, F. G., and De Philippis, R. (2012). The role of the exopolysaccharides in enhancing hydraulic conductivity of biological soil crusts. *Soil Biol. Biochem.* 46, 33–40. doi: 10.1016/j.soilbio.2011.10.016

Rozenstein, O., Zaady, E., Katra, I., Karnieli, A., Adamowski, J., and Yizhaq, H. (2014). The effect of sand grain size on the development of cyanobacterial biocrusts. *Aeolian Res.* 15, 217–226. doi: 10.1016/j.aeolia.2014.08.003

Savitzky, A., and Golay, M. J. E. (1964). Smoothing and differentiation of data by simplified least squares procedures. *Anal. Chem.* 36, 1627–1639. doi: 10.1021/ac60214a047

Singh, J. S., Kumar, A., Rai, A. N., and Singh, D. P. (2016). Cyanobacteria: a precious bio-resource in agriculture, ecosystem, and environmental sustainability. *Front. Microbiol.* 7:529. doi: 10.3389/fmicb.2016.00529

Tillman, R., Scotter, D., Wallis, M., and Clothier, B. (1989). Water repellency and its measurement by using intrinsic sorptivity. *Soil Res.* 27, 637–644. doi: 10.1071/SR9890637

Velasco Ayuso, S., Giraldo Silva, A., Nelson, C., Barger, N. N., and Garcia-Pichel, F. (2017). Microbial nursery production of high-quality biological soil crust biomass for restoration of degraded dryland soils. *Appl. Environ. Microb.* 83:e02179–16. doi: 10.1128/AEM.02179-16

Wang, W., Liu, Y., Li, D., Hu, C., and Rao, B. (2009). Feasibility of cyanobacterial inoculation for biological soil crusts formation in desert area. *Soil Biol. Biochem.* 41, 926–929. doi: 10.1016/j.soilbio.2008.07.001

Wu, L., Lan, S., Zhang, D., and Hu, C. (2011). Small-scale vertical distribution of algae and structure of lichen soil crusts. *Microb. Ecol.* 62, 715–724. doi: 10.1007/s00248-011-9828-5

Wu, Y., Rao, B., Wu, P., Liu, Y., Li, G., and Li, D. (2013). Development of artificially induced biological soil crusts in fields and their effects on top soil. *Plant Soil* 370, 115–124. doi: 10.1007/s11104-013-1611-6

Wubs, E. R., Van Der Putten, W. H., Bosch, M., and Bezemer, T. M. (2016). Soil inoculation steers restoration of terrestrial Ecosystems. *Nat. Plants* 2:16107. doi: 10.1038/nplants.2016.107

Xie, Z., Liu, Y., Hu, C., Chen, L., and Li, D. (2007). Relationships between the biomass of algal crusts in fields and their compressive strength. *Soil Biol. Biochem.* 39, 567–572. doi: 10.1016/j.soilbio.2006.09.004

Xu, Y., Rossi, F., Colica, G., Deng, S., De Philippis, R., and Chen, L. (2013). Use of cyanobacterial polysaccharides to promote shrub performances in desert soils: a potential approach for the restoration of desertified areas. *Biol. Fert. Soils* 49, 143–152. doi: 10.1007/s00374-012-0707-0

Yeager, C. M., Kornosky, J. L., Morgan, R. E., Cain, E. C., García-Pichel, F., Housman, D. C., et al. (2007). Three distinct clades of cultured heterocystous cyanobacteria constitute the dominant N_2-fixing members of biological soil crusts of the Colorado Plateau, USA. *FEMS Microbiol. Ecol.* 60, 85–97. doi: 10.1111/j.1574-6941.2006.00265.x

Zaady, E., Karnieli, A., and Shachak, M. (2007). Applying a field spectroscopy technique for assessing successional trends of biological soil crusts in a semi-arid environment. *J. Arid Environ.* 70, 463–477. doi: 10.1016/j.jaridenv.2007.01.004

Zaady, E., Katra, I., Barkai, D., Knoll, Y., and Sarig, S. (2017). The coupling effects of using coal fly-ash and bio-inoculant for rehabilitation of disturbed biocrusts in active sand dunes. *Land Degrad. Dev.* 28, 1228–1236. doi: 10.1002/ldr.2510

Zhang, Y. (2005). The microstructure and formation of biological soil crusts in their early developmental stage. *Chinese Sci. Bull.* 50, 117–121. doi: 10.1007/BF02897513

Zhang, Y., Duan, P., Zhang, P., and Li, M. (2017). Variations in cyanobacterial and algal communities and soil characteristics under biocrust development under similar environmental conditions. *Plant Soil.* doi: 10.1007/s11104-017-3443-2

Zhao, Y., Xu, M., and Belnap, J. (2010). Potential nitrogen fixation activity of different aged biological soil crusts from rehabilitated grasslands of the hilly Loess Plateau, China. *J. Arid Environ.* 74, 1186–1191. doi: 10.1016/j.jaridenv.2010.04.006

Patterns and Sources of Spatial Heterogeneity in Soil Matrix From Contrasting Long Term Management Practices

Michelle Y. Quigley [1]*, Mark L. Rivers [2] and Alexandra N. Kravchenko [1,3]

[1] Department of Plant, Soil and Microbial Sciences, Michigan State University, East Lansing, MI, United States, [2] Argonne National Lab, Center for Advanced Radiation Sources, The University of Chicago, Chicago, IL, United States, [3] Department of Agricultural Soil Science, University of Göttingen, Göttingen, Germany

With the advent of computed microtomography (μCT), *in situ* 3D visualization of soil at micron scale became easily achievable. However, most μCT-based research has focused on visualization and quantification of soil pores, roots, and particulate organic matter (POM), while little effort has been put in exploring the soil matrix itself. This study aims to characterize spatial heterogeneity of soil matrix in macroaggregates from three differing long term managements: conventionally managed and biologically based row-crop agricultural systems and primary successional unmanaged system, and explore the utility of using grayscale gradients as a proxy of soil organic matter (SOM). To determine spatial characteristics of the soil matrix, we completed a geostatistical analysis of the aggregate matrix. It demonstrated that, while the treatments had the same range of spatial correlation, there was much greater overall variability in soil from the biologically based system. Since soil from both managements have the same mineralogy and texture, we hypothesized that greater variability is due to differences in SOM distributions, driven by spatial distribution patterns of soil pores. To test this hypothesis, we applied osmium (Os) staining to intact micro-cores from the biologically based management, and examined Os staining gradients every 4 μm from 26 to 213 μm from pores of biological or non-biological origin. Biological pores had the highest SOM levels adjacent to the pore, which receded to background levels at distances of 100–130 μm. Non-biological pores had lower SOM levels adjacent to the pores and returned to background levels at distances of 30–50 μm. This indicates that some of the spatial heterogeneity within the soil matrix can be ascribed to SOM distribution patterns as controlled by pore origins and distributions. Lastly, to determine if the grayscale values could be used as a proxy for SOM levels, gradients of grayscale values from biological and non-biological pores were compared with the Os gradients. Grayscale gradients matched Os gradients for biological pores, but not non-biological pores due to an image processing artifact. Grayscale gradients would, therefore, be a good proxy for SOM gradients near biological origin pores, while their use for non-biological pores should be conducted with caution.

Keywords: microtomography, soil organic matter, geostatistics, spatial variability, particulate organic matter

INTRODUCTION

The use of computed microtomography (μCT) has allowed for the *in situ* characterization of the physical structure of soil, specifically, positions, size distributions, and shapes of soil pores (Gibson et al., 2006; Chun et al., 2008; Peth et al., 2008; Papadopoulos et al., 2009; Kravchenko et al., 2011; Wang et al., 2012). It also enabled identification of large organic fragments, including particulate organic matter (POM) (Kravchenko et al., 2014a) and intact plant roots (Mooney et al., 2012). These advances led to quantitative insights into the contribution of pore characteristics to residue decomposition, carbon protection, and spatial patterns of bacterial distributions (De Gryze et al., 2006; Ananyeva et al., 2013; Wang et al., 2013; Kravchenko et al., 2014b; Negassa et al., 2015). However, little focus has been given to μCT information regarding mineral soil matrix, that is, solid material containing no pores or organic fragments visible at the μCT image resolution. Of particular interest is how characteristics of the solid material may relate to soil organic matter (SOM) dynamics, specifically SOM protection.

Solid material is represented in μCT images by a range of grayscale values that are correlated to the attenuation of x-rays, which is controlled by the density and atomic number (Z) of the elements occurring within an image voxel (Ketcham, 2005; Peth, 2010). Voxels that contain primarily low Z elements, such as nitrogen, carbon, and oxygen, have lower grayscale values (appear darker) on μCT images, while voxels containing higher Z elements, such as iron, silicon, and aluminum, have higher grayscale values (appear brighter). A voxel's overall grayscale value is the average attenuation of the elements occurring within that voxel. Spatial variability in grayscale values of the solid material originates from multiple sources, including variations in mineralogy, presence of pores with sizes below image resolution, and SOM distribution patterns. The first two of these factors are important drivers of SOM protection, while the third one is an indicator of where such protection has occurred. Mineralogy influences SOM protection by affecting organic matter binding via electrostatic forces. Small pores can contribute to SOM protection by a combination of restricting decomposers' access and retardation of decomposition due to anaerobic conditions prevalent in these pores (Bailey et al., 2017; Keiluweit et al., 2017). Thus, overall SOM distribution patterns are likely controlled by a combination of mineralogy and pore architecture, i.e., pore size and connectivity (Dungait et al., 2012; Kravchenko et al., 2015).

Soil pores function as the soil transport network; regulating the flow of nutrients, microorganisms, oxygen, and organic material (Young and Crawford, 2004; De Gryze et al., 2006; Kuzyakov and Blagodatskaya, 2015; Negassa et al., 2015). Soil pores are created through either biological or non-biological means. Biological pores are formed by macrofauna, such as earthworms, or through action of roots and root hairs as they spread and grow. Non-biological pores are primarily produced in a course of wetting/drying and freeze/thaw cycles and are controlled by soil texture, specifically clay content. Biological and non-biological pores also play different roles in the cycling of organic matter within the soil. Biological pores are generally thought of as a source of new carbon inputs, either through direct

organic addition, such as decaying roots, or through ancillary organic matter additions, such as root exudates. Organic matter that then diffuses out from biological pores typically occurs as dissolved organic matter (DOM). DOM can be bound to minerals by electrostatic forces (Kiem and Kögel-Knabner, 2002; Six et al., 2002; Dungait et al., 2012), where, due to the electrostatic force being greater than the enzyme binding energy, it can be protected from microbial attack and results in SOM protection (Dungait et al., 2012). While biological origin pores are sources of organic matter and SOM protection, they also compress adjacent solid material as roots push through the soil resulting in denser material closer to root pores (Bengough et al., 2011; Aravena et al., 2014). Thus, the net effect of biological pores on proximate densities is uncertain. Formation of non-biological pores, on the other hand, created through the shrinking and swelling of clay minerals, can expose previously inaccessible carbon to microbial attack, resulting in a net carbon loss (Sørensen, 1974; Denef et al., 2001; Smucker et al., 2007). However, quantitative data on how presence, abundance, and characteristics of pores of different origins influence SOM accrual and protection is currently lacking. Falconer et al. (2015) noted that despite identical bulk characteristics, including average porosity, POM turnover rate varied widely due to micro-scale properties. Their results indicated that an understanding of micro-scale pore properties may be vital to achieve more accurate modeling of soil carbon dynamics.

The grayscale values of the solid material in μCT images could potentially provide insights into spatial patterns of SOM and the associations between such patterns and pores of different origins. As noted previously, a voxel's overall grayscale value is the average attenuation of the elements occurring within that voxel. While mineralogy plays the largest role in the spatial characteristics of the solid material and would normally override any spatial characteristics from distribution of SOM and presence of pores with below image resolution sizes, samples with similar mineralogy would allow for the spatial patterns caused by these other factors to be observed. There is some experimental evidence that, in samples with similar mineralogy, grayscale values of μCT images and SOM are correlated (Ananeyva, personal communications).

Studies have shown that geostatistics is helpful for describing the spatial characteristics of pores and, therefore, can be expected to also model well the spatial characteristics of the solid material (De Gryze et al., 2006; Feeney et al., 2006; Nunan et al., 2006). Therefore, to assess spatial patterns within the solid material, geostatistics will be used to quantify the range of spatial correlation, overall spatial variability, and the contribution of spatial variability that is below image resolution to the overall spatial variability.

Here we would like to explore the utility of using the spatial patterns of grayscale values in μCT images as a proxy for the spatial patterns of SOM distribution. As such, we will focus on SOM distribution patterns in the vicinity of soil pores of both non-biological and biological origin. This focus is driven by an expectation that, due to the role of biological pores in supplying new organic inputs and the role of non-biological pores in contributing to carbon losses, their comparison should

yield contrasting gradients in SOM distributions. Identification of such gradients will indicate that grayscale values can provide useful information on SOM distribution patterns within intact soil samples.

To further verify the utility of grayscale values as indicators of SOM spatial patterns, we will compare the gradients of grayscale values from conventional μCT images with gradients of Osmium (Os) stained organic matter from Os dual-energy images. Os staining has been proposed as an effective tool to visualize organic matter in μCT images (Peth et al., 2014) and was applied to estimate SOM spatial patterns (Rawlins et al., 2016). Os strongly binds with carbon-carbon double bounds and its high atomic number increases the visibility of organic matter on μCT images. By taking images above and below the K-edge of Os, 3D maps of SOM within an intact soil sample can be constructed. From such maps we can then obtain direct measurements of SOM gradients in the vicinity of non-biological and biological soil pores.

Agricultural management is known to have an effect on overall SOM levels (Oades, 1984; Six et al., 2000; Syswerda et al., 2011; Paul et al., 2015), as well as on micro-scale SOM patterns (Ananyeva et al., 2013; Kravchenko et al., 2015). Since pores are known drivers of SOM protection, any change in the spatial pattern of pores would result in a change in SOM spatial patterns and potentially SOM levels. The distribution of non-biological and biological pores is known to be affected by agricultural management. Wang et al. (2012) and Kravchenko et al. (2014b) both that observed non-biological pores tended to dominate in systems with tillage, while pores of biological origin tended to dominate in conservation managements with little soil disturbance.

We hypothesize that areas dominated by non-biological pores will have relatively uniform microenvironmental conditions, thus relatively uniform SOM spatial distribution patterns. Together with lack of point sources of organic matter in such pores, this will lead to smaller SOM gradients in their vicinity. On the other hand, areas dominated by biological pores provide spatially variable SOM inputs as well as a more diverse range of microenvironmental conditions for microorganisms. Thus, we expect greater spatial variability in SOM, as well as greater SOM gradients, in the vicinity of biological pores. In addition, we hypothesize that agricultural management practices that lead to a greater presence of biological pores will increase SOM spatial variability and result in larger SOM gradients than the management practices with greater presence of non-biological pores.

The first objective of the study is to explore utility of grayscale values of solid material from μCT images to characterize SOM patterns by comparing grayscale value spatial patterns with Os spatial patterns. The second objective is to explore spatial characteristics of the solid material in μCT images of intact soil samples from three contrasting land use and management practices and to analyze relationships between the spatial characteristics and the SOM levels of these practices. Our third objective is to explore SOM and grayscale value gradients at distances from pores of different origins and in soils from different managements.

MATERIALS AND METHODS

Soil Collection and Imaging

The studied soil was collected from three different managements at Kellogg Biological Station Long Term Ecological Research station, Hickory Corners, MI (42°24′N, 85°24′W). The three managements were a conventional corn-soybean wheat management maintained with current best management practices, a biologically based corn-soybean-wheat with rye cover after corn and red clover interseeded into wheat with no additional inputs and rotary tillage between rows for weed management, and a primary successional management, which is burned annually, but otherwise unmanaged. These management practices represent a management gradient with a highly managed system (conventional), a conservation management system (biologically based), and an unmanaged system (primary successional). Further details can be found in Kravchenko et al. (2015).

The soil (from 0 to 15 cm depth) was dry sieved and aggregates of 4–6.3 mm were collected for imaging. μCT images were obtained from beamline 13-BM-D of the GeoSoilEnvironCARS (GSECARS) at the Advanced Photon Source (APS), Argonne National Laboratory (ANL) in Argonne, Illinois. Two-dimensional projections were taken at 0.25° rotation angle steps with a 1 s exposure and combined into a three-dimensional image consisting of 520 slices with 696 by 696 pixels per slice for grayscale analysis and 1,200 slices with 1,920 by 1,920 pixels per slice for analysis of pores below image resolution. The voxel size of the images was 13 μm for grayscale analysis and 2 μm for analysis of pores below image resolution. Pores were identified using the indicator kriging method in 3DMA-Rock (Oh and Lindquist, 1999; Wang et al., 2011) for grayscale analysis and through simple thresholding with Otsu's method for analysis of pores below image resolution.

Geostatistical Analysis

A total of 32 soil aggregate images were used in the geostatistical analysis, namely, 11 images from conventional and biologically based management and 10 images from primary successional management. On each image we identified 5 soil cubes, 130 × 130 × 130 μm in size (**Figure 1**). Positions of the cubes were initially randomly selected, with further adjustments made to avoid major overlaps with other cubes, coarse sand grains that would not reflect the overall spatial characteristics of the aggregate, and aggregate boundaries. Soil pores identified by 3DMA-Rock were removed from the cubes prior to geostatistical analysis allowing for analysis of spatial patterns in the solid material only. 3D variograms were obtained using the gstat package in R (Pebesma, 2004) run on the High Performance Computing Center at Michigan State University. Variograms (Supplementary Presentation 1) were fit with an exponential model using PROC NLIN in SAS 9.3 (SAS Inc, 2009). Spatial characteristics of the solid material can be determined from the components of the 3D variograms. The sill, where the variogram flattens out, indicates the total spatial variability within a sample. The range of a variogram, lag distance at which the sill occurs, is the distance for which spatial correlation exists in a sample. The nugget, the
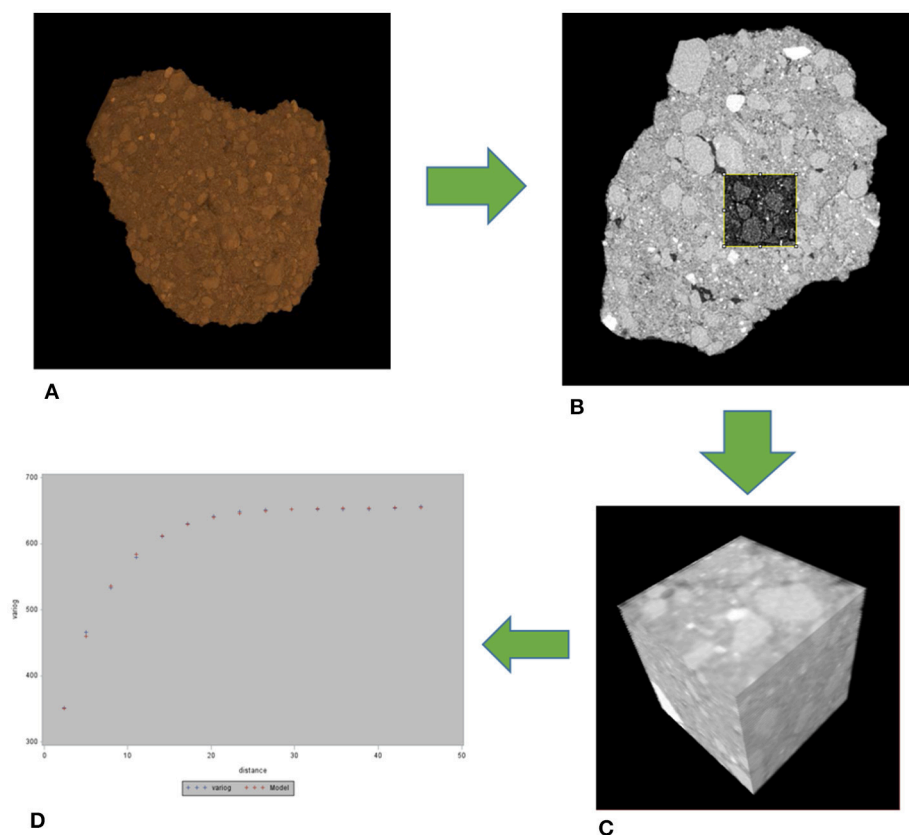
FIGURE 1 | Workflow for the geostatistical analysis. From each whole aggregate **(A)**, 5 cubes were selected **(B,C)** and then a 3D variogram obtained **(D)**. The whole aggregate is 5 mm in size, while the cubes in the slice **(B)** and 3D **(C)** are 130 μm on a side.

difference between the zero and the y-intercept, represents both measurement error and the variability at scales below the image resolution. The nugget to sill ratio describes the relative amount of spatial dependence at the voxel size.

Os Gradients

Soil samples for Os analysis were taken as mini-cores. Only three mini-cores, all from the biological based management practice, were analyzed. The reason for the small number of samples used for this analysis is the very long image collection time for dual-energy Os scanning limiting the number of samples that could be processed. We choose biologically based management for these analyses, since we expected that pores of both non-biological and biological origin would be well represented in soil under this management. Samples were taken as mini-cores, as opposed to dry sieved aggregates, because of concerns that aggregates would be too fragile for the multiple handling steps required by this method.

The mini-cores were taken at 3.5–5 cm depth using a beveled 3 mL Luer-Lok polypropylene syringe with a 8 mm inner diameter (BD, Franklin Lakes NJ, USA). There was minimal interference with Os staining from polypropylene syringes as they contained almost no carbon-carbon double bounds. Cores were air dried and exposed to OsO_4 gas in a fume hood for 1 week. This allowed ample time for the OsO_4 gas to diffuse throughout the soil and to ensure maximum binding of Os to the soil organic material. The cores were then scanned at beamline 13-BM-D, GSECARS, APS ANL. Two-dimensional projections were taken at 0.25° rotation angle steps with a 2 s exposure and combined into a three-dimensional image consisting of 1,200 slices with 1,920 by 1,920 pixels per slice. Final images had a 4 μm resolution. Three energies were used for the scans, 74, 73.8, and 28 keV. These energies provided, respectively, an image above Os K-edge, an image below Os K-edge, and an image at an energy optimal for soil pore and POM identification. By taking the difference between the above and below K-edge images, a map of the stained soil organic materials was created (**Figure 2**). Using the 28 keV images, non-biological pores were identified using simple thresholding, while POM pieces of both root and non-root origin were visually identified by hand. POM of non-root origin was defined as stand-alone organic fragments of round or irregular shape that were not connected to any obvious root remains.

Two pores containing non-root derived POM (POM-NS), two pores containing root-derived POM (POM-Root) and four pores of non-biological origin were identified by hand for the analyses in each mini-core image (**Figure 3**). Identified pores
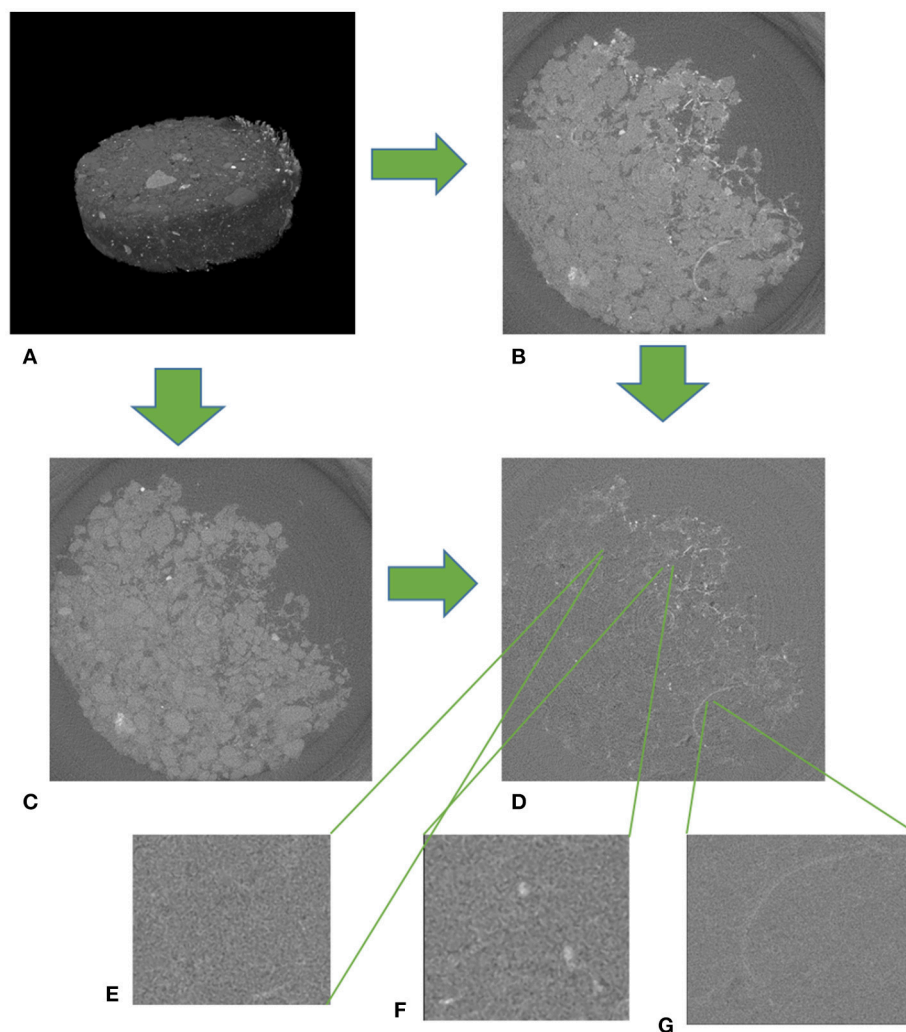
FIGURE 2 | An example of a μCT image from an Os stained soil sample from biologically based management at 4 μm resolution. **(A)** A 3D scan of an entire Os stained sample. The thickness of the sample was 1 mm. **(B)** Image of a slice of an Os stained sample above the K-edge (74 keV). **(C)** Image of a slice of an Os stained sample below the K-edge (73.8 keV). **(D)** Difference between above and below K-edge images with non-biological pore **(E)**, POM-NS **(G)**, and POM-Root **(F)** expanded. Total image size is 8 × 8 mm for **(B–D)**.

varied in size from 20 to 300 μm. The identified pores were dilated by ~13 μm in all three dimensions to match the grayscale gradient results (described below). Then, a set of 4 μm layers were identified around each pore to a maximum distance of 213 μm. Grayscale values of the Os stained map were averaged for each 4 μm layer to obtain an Os gradient. The averages excluded the 0 value as that was the color of the image background. To ensure comparability among the mini-cores, the Os gradients were standardized by subtracting the Os map's average grayscale value from each mini-core.

Grayscale Gradients

From each of the 32 images used in the geostatistical analysis, we identified three POM-NS, three POM-Root, and five non-biological origin pores (**Figure 3**). Identified pores ranged in sizes from 40 to 300 μm. In order to remove partial volume

effects, the identified pores were dilated by one voxel in all three dimensions, thus they did not include the layer of border voxels that contained both pore and solid material. The grayscale value gradients were obtained by averaging voxels from 13 μm layers around each pore to a maximum distance of 208 μm (**Figure 4**). Averages did not include the 0 and 255 grayscale values as the 0 value was the value of the image background and excluding the 255 value corrected for any overly dense material, such as iron minerals like magnetite or limonite, in the samples that might have skewed the grayscale averages. To enable direct comparisons between images, the grayscale value gradients were normalized so that the minimum grayscale value was 0 and the maximum grayscale value was 1 for each gradient. Calculation of the distance over which the gradient had influence was done by fitting the individual gradients using PROC NLIN in SAS 9.4 (SAS Inc, 2009) with the following
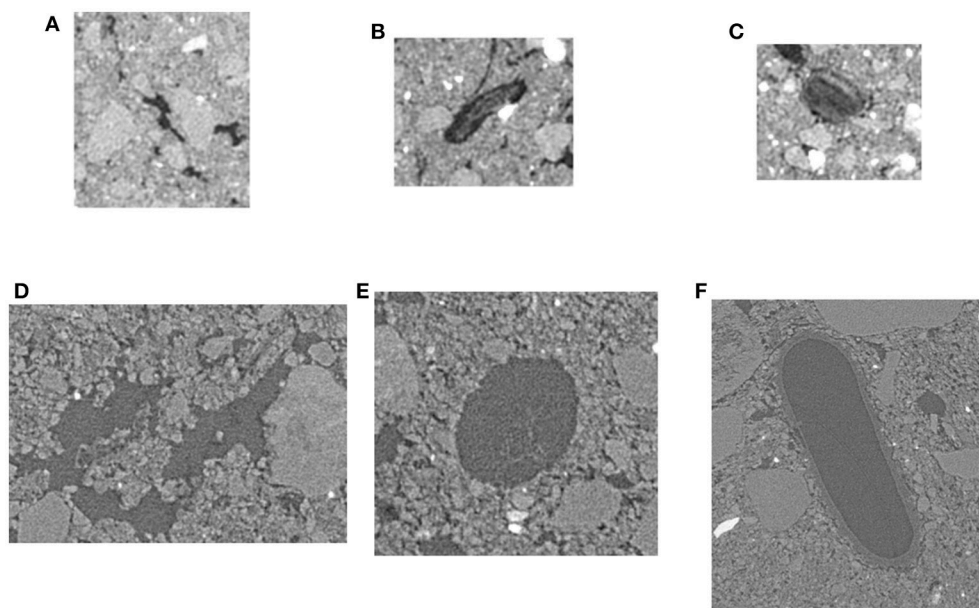
FIGURE 3 | Examples of selected non-biological **(A,D)**, POM-Root **(B,E)**, and POM-NS pores **(C,F)** for 13 and 2 μm resolution. Non-biological pores were chosen so that no organic matter was visible in the pores and the pores were not round or oval in shape. POM-Root pores were chosen such that organic material was visible in the pores and were root shape, i.e., round or oval with an elongated shape. POM-NS was chosen such that organic material was visible within the pores and the pore did not have a root like shape.

non-linear model:

$$f(x) = n + (s - n) \times \left(1 - e^{\left(-\frac{3x}{d}\right)}\right) \quad (1)$$

where x is distance from the pore, n is the y-intercept, s is the average grayscale value of the image, and d is the distance at which the pore stops affecting the grayscale values or effective distance of pore influence (EDPI).

Analysis of Pores Below Image Resolution (2–13 μm)

Presence of pores with sizes below the image resolution (<13 μm) can potentially affect gradients of grayscale values. If that were the case, then it would not be possible to attribute the observed gradients in grayscale values to SOM. In order to explore the potential effect of such pores on the studied grayscale gradients, we scanned six of the 32 studied aggregates at 2 μm resolution. Two aggregates from each management were scanned.

We explored the differences among the studied managements in terms of presence of 2–13 μm pores. The purpose of this analysis was to ensure that the observed differences among the management practices were driven by SOM and not by below-resolution pores. For that, four cubes, 140 × 140 × 140 μm in size, were selected, using a selection process identical to that described above for the geostatistical analysis. Using Otsu's method, the overall porosity of each cube was determined. Binning was then used to compress the cube image to ∼13 μm voxel size (**Figure 5**). Overall porosity of the binned image was

then determined using the same threshold as the 2 μm samples. Subtracting the porosity of the binned images from the un-binned images resulted in the 2–13 μm porosity, referred to hereafter as the below image resolution porosity.

Statistical Analysis

Data analyses for all studied variables were conducted using the mixed model approach implemented in the PROC MIXED procedure of SAS Version 9.4 (SAS Inc, 2009). For comparisons of the geostatistical characteristics and total below image resolution porosity, the statistical model consisted of the fixed effect of management and the random effect of aggregates nested within management. For investigation of pore type and management effects on the grayscale gradients, the statistical model consisted of the fixed effects of management, pore types, distances from the pores, and their interactions, as well as the random effect of aggregates nested within management and the random effect of individual pores nested within respective pore types and aggregates. In this analysis, distance was treated as a repeated measure factor. Comparisons among pore types for the Os gradients were conducted using the statistical model with the fixed effects of pore type, distance, and their interaction and the random effects of soil core and soil core by pore type interaction. As with the grayscale gradients, the Os gradients distance factor was treated as a repeated measure. Comparisons among managements and pore types for the gradient influence distance were evaluated using the statistical model with the fixed effects of management, pore type, and the interactions between them and the random effect of aggregates nested within
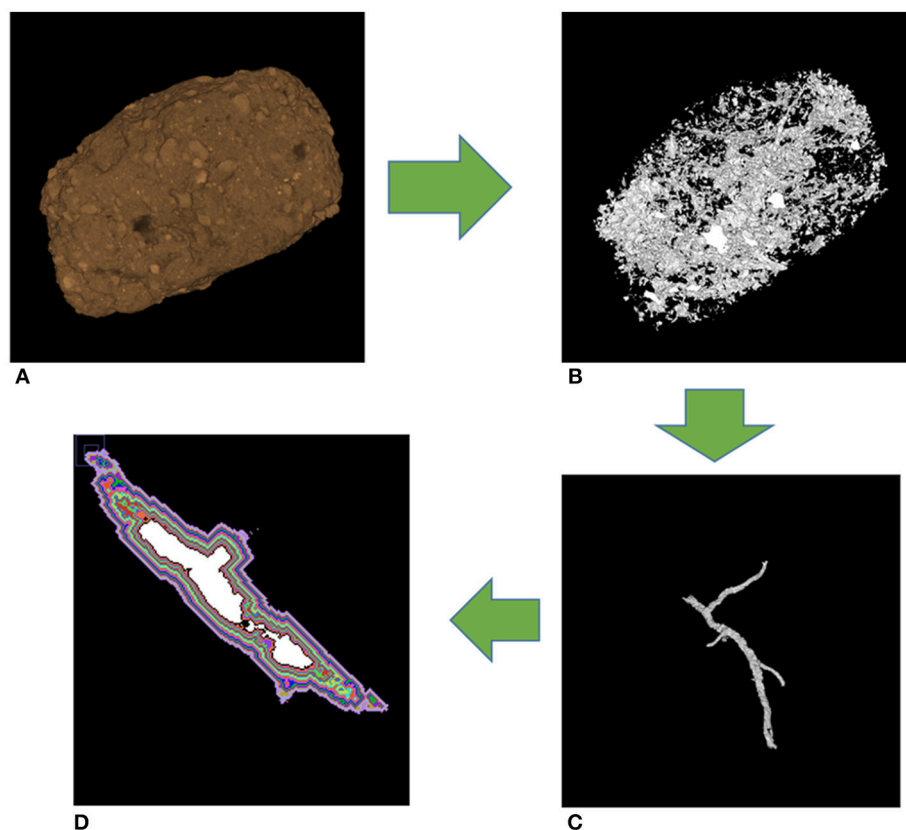
FIGURE 4 | Workflow for grayscale gradients. The whole aggregate **(A)** has all pores identified **(B)**. Individual pores are then identified **(C)**. Layers are collected for analyses of grayscale gradients **(D)**. Each color represents a different layer, while the white in the middle is the actual pore, and the black layer adjacent to white accounts for partial volume effects.

management. The normality of residuals in all analyses was visually assessed using normal probability plots and stem-and-leaf plots, while equal variances assumption was assessed using Levene's test. Results are reported as statistically significant at $\alpha = 0.05$ level.

For all analyses, if the interactions were not significant, pairwise comparisons of the main effects using the LSMEANS statement were used. In the case where interactions were significant, slicing using the LSMEANS statement was employed. All distance graphs were created from slicing results. T-tests were conducted to determine if the mean values differed from zero.

RESULTS

Geostatistical Analysis of Grayscale Spatial Patterns

Biologically based and primary successional managements had greater overall variability in grayscale values of the solid material than the conventional management system, as indicated by their higher sill values (**Table 1**). Spatial variations at distances greater than the image resolution ($13 \, \mu m$) accounted for more than 50% of the overall variability, as indicated by nugget-to-sill ratios ranging from 39% in biologically based management to 46 and

TABLE 1 | Characteristics of the variograms of soil material containing no $>13 \, \mu m$ pores in three studied land use and management practices.

Variogram characteristic	Conventional	Biologically based	Primary successional
Range (μm)	334.1(1.4)a	309.4(1.4)a	297.7(1.4)a
Nugget	313(26)a	321(26)a	357(28)a
Sill	641(45)a	822(45)b	778(47)b
Nugget to Sill	0.48(0.02)a	0.39(0.02)b	0.46(0.02)a

Shown are means and standard errors (in parentheses) calculated based on a total of 157 subsection cubes from 32 aggregates. Different letters within each row denote statistically significant differences among the managements at $\alpha = 0.05$.

48% in primary successional and conventional managements. The three managements did not differ in terms of their nugget and range values, indicating similarities in terms of variabilities at distances $<13 \, \mu m$ and of distances at which spatial correlation were present.

Os Levels as a Function of Distance From Soil Pores

The Os gradients were markedly different in pores of non-biological and biological origin (**Figure 6**). However, Os gradients did not differ between biological pores associated with
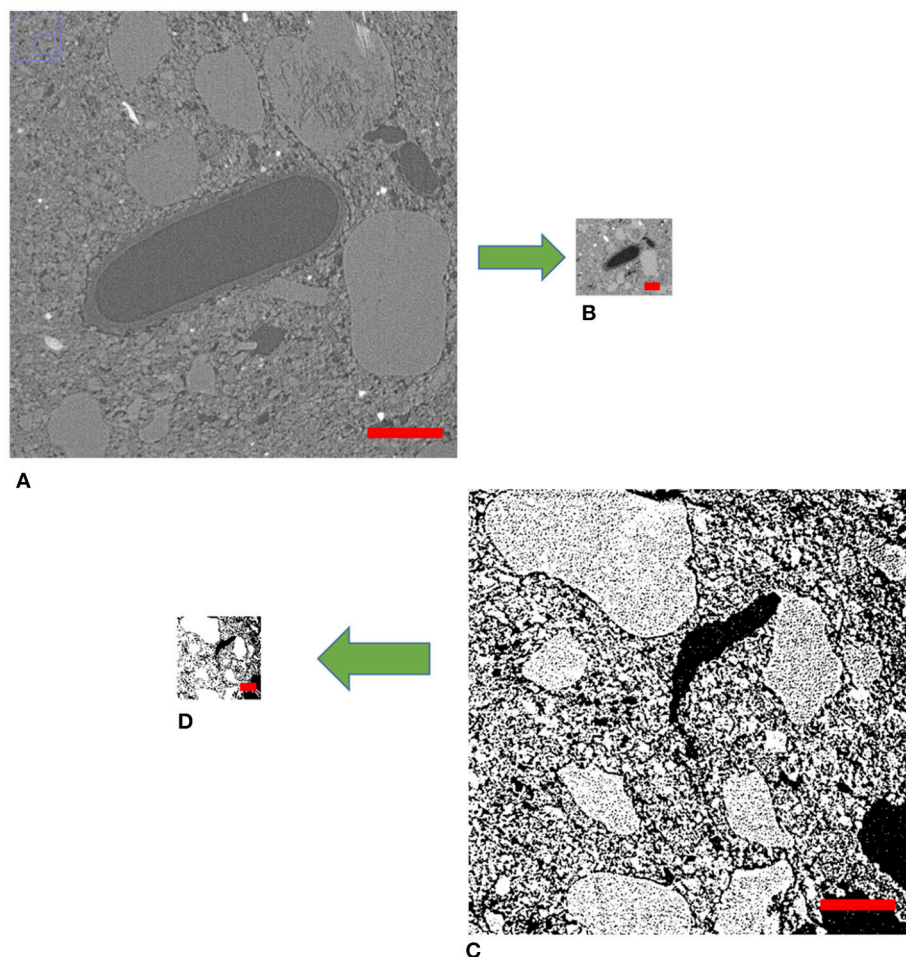
FIGURE 5 | Example of a 2 μm image **(A)** and the same image reduced to 13 μm resolution **(B)**. Example of thresholding with Otsu's method of the same image at 2 μm **(C)** and 13 μm **(D)**.

POM-NS and POM-Root. Pores of biological origin had a large increase in Os labeled SOM immediately adjacent to the pores, which then slowly declined until returning to background levels at distances of 100–130 μm. Non-biological pores, on the other hand, had levels of Os labeled SOM that were statistically lower than background levels ($P = 0.0454$) at distances up to 30 μm from the pores.

Grayscale Levels as a Function of Distance From Soil Pores

The grayscale gradients for all managements and pore types had decreased grayscale values closer to the pores that increased as distances from the pore increased (**Figure 6**). This was similar to the biological pore results from the Os gradients. For biological pores, the grayscale gradients matched the Os gradients almost identically. When both grayscale and Os gradients for POM-NS and POM-Root in biologically based management were normalized (**Figure 7**), the overlap between the relationships was almost perfect, indicating that Os and grayscale value gradients were equivalent.

The grayscale levels in the solid material adjacent to non-biological pores were lower than the background grayscale values (average grayscale value of the whole aggregate). However, they increased much faster with increasing distance (**Figure 6**) and reached the background levels at much shorter distances than those of biological pores (**Table 2**). For POM-NS and POM-Root, grayscale values returned to background levels at 123 μm, while non-biological pores at 74 μm.

While no differences were observed between POM-NS and POM-Root grayscale gradients for biologically based and primary successional managements ($P = 0.4217, 0.2311$), POM-NS retained decreased grayscale values over longer distances than POM-Root in conventional management ($P < 0.001$; **Figure 8**). No significant differences were observed between managements for non-biological and POM-Root pores ($P = 0.8516, 0.3629$), but conventional management again showed a shallower POM-NS grayscale gradient than the other managements ($P = 0.0096$). EDPI only varied by pore type, indicating that management had no effect on this characteristic of grayscale value distributions (**Table 2**).
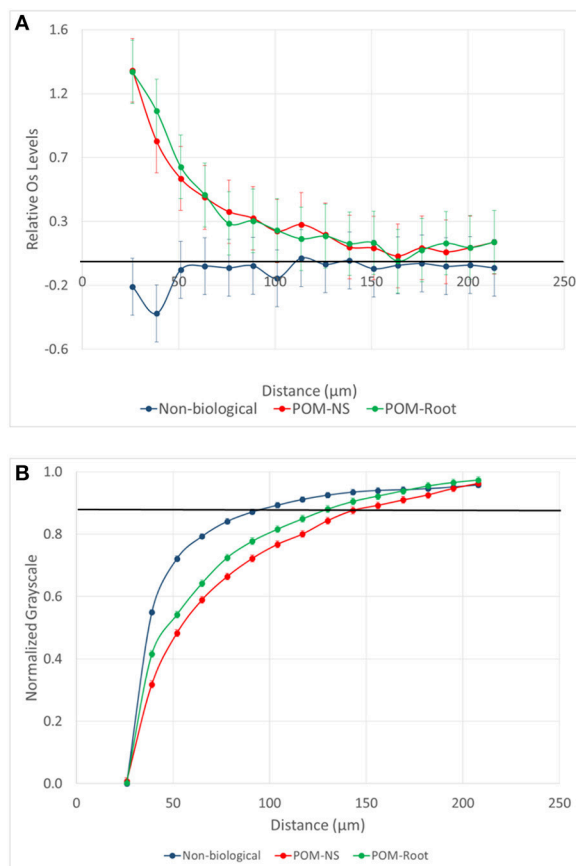
FIGURE 6 | (A) Mean difference from the background level for Os stained samples as a function of distance from pores of biological origin with plant roots (POM-Root) and with non-root derived POM (POM-NS) and from non-biological pores ($n = 6$). The samples are from the biologically based system. Positive values indicate increased presence of Os labeled SOM, while negative values indicate a decrease in Os labeled SOM. **(B)** Normalized grayscale values for all three studied pore types from all three management practices. Dots are averages and the standard errors are equal to the size of the dots at each distance. The solid black lines represent the background Os labeled level (on **A**) and the background grayscale value (on **B**).

FIGURE 7 | Normalized Os values from Os stained samples ($n = 6$) and grayscale values ($n = 96$) from non-stained samples as a function of distance from POM-NS and POM-Root pores in the soil of the biologically based management.

TABLE 2 | Effective distance of pore influence (EDPI) for the three studied pore types averaged across all studied aggregates.

Pore type	EDPI(μm)
Non-biological	74.2(5.0)a
POM-Root	123.3(6.2)b
POM-NS	122.7(6.2)b

Means were calculated based on 32 aggregates with 3 POM-NS, 3 POM-Root, and 5 non-biological pores from each aggregate. Standard errors are shown in parentheses. Different letters denote significant differences among pore types at $\alpha = 0.05$.

Pores Below Image Resolution

While the $>2\,\mu$m and the $>13\,\mu$m porosity differed among the managements ($P = 0.0435$), the below image resolution porosity (2–13 μm) was the same for all three managements ($P = 0.4513$; **Figure 9**). The $>13\,\mu$m porosity and the $>2\,\mu$m porosity were greater in the biologically based management than the conventional management, while the primary successional management was not significantly different from either management.

DISCUSSION

Image Grayscale Values as a Proxy for SOM Patterns

Our findings indicate that grayscale values can be a useful proxy for SOM, however, caution needs to be exercised in such
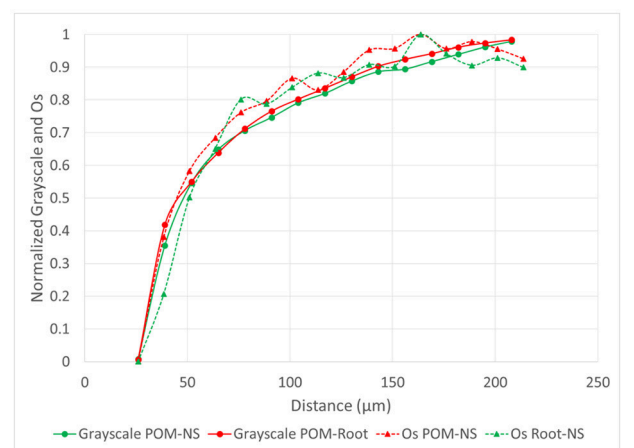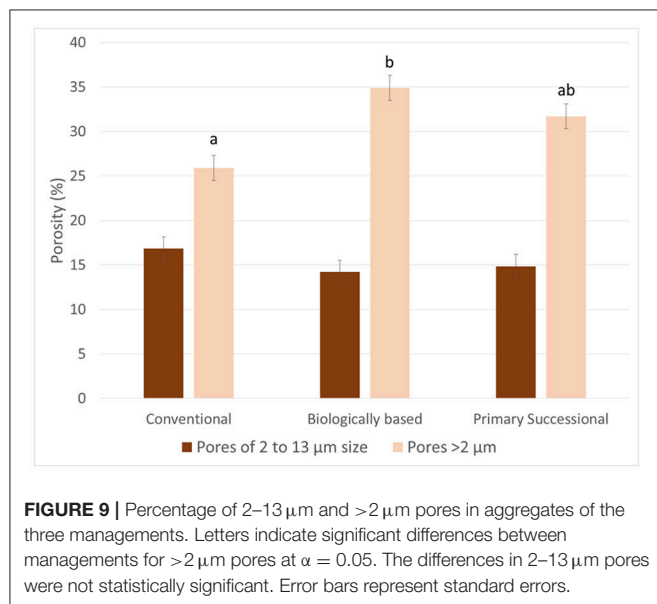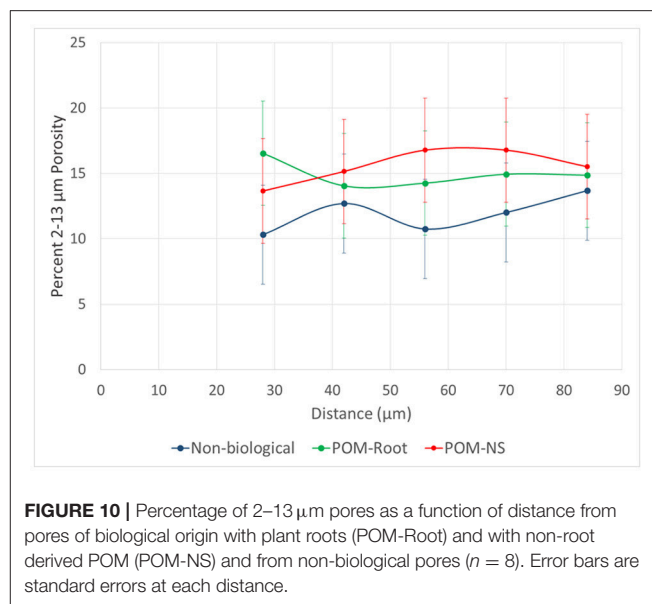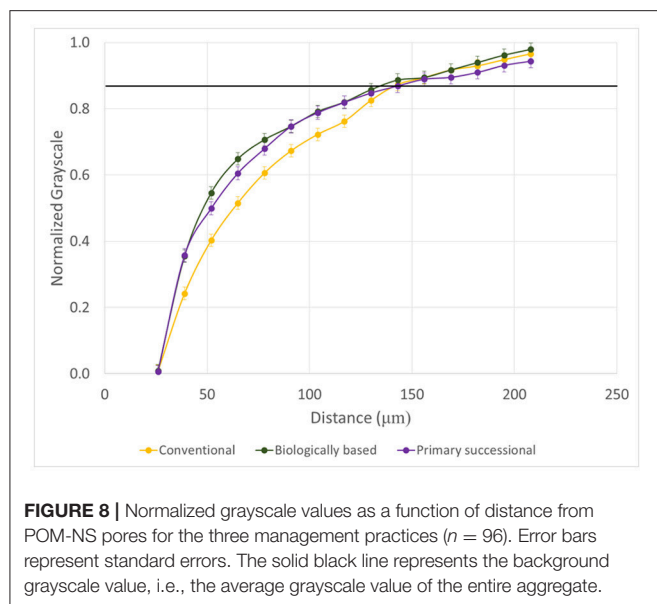
use. Specifically, in the studied soil, a reliable correspondence between SOM gradients as determined via Os staining and grayscale value gradients was achieved only for pores of biological origin. As can be seen from **Figure 7**, the Os and grayscale gradients corresponded to each other remarkably well, indicating that grayscale gradients can be used as a suitable proxy when exploring SOM patterns near pores of biological origin. It should be noted that the EDPI observed (123 μm) is consistent with previously reported ranges for SOM distributions in soil of 38–175 μm determined through the use of Os staining and geostatistical analyses, although these analyses were not correlated to pores specifically (Rawlins et al., 2016). Previous studies utilizing isotopically labeled materials have reported movement of decomposition products as far as 5–10 mm from carbon sources during soil incubations (Gaillard et al., 1999, 2003; Toosi et al., 2017). However, these studies do not specifically measure transport of DOM from individual pores, but overall transport of isotopic labeled materials from its source, which would account for the larger transport ranges seen in previous studies. Direct imaging of the spatial distribution of SOM near individual pores has previously been achieved using NanoSIMS, however, at spatial scales much lower (nm) than those used in this study. Mueller et al. (2012) showed that, in

FIGURE 8 | Normalized grayscale values as a function of distance from POM-NS pores for the three management practices ($n = 96$). Error bars represent standard errors. The solid black line represents the background grayscale value, i.e., the average grayscale value of the entire aggregate.

FIGURE 10 | Percentage of 2–13 μm pores as a function of distance from pores of biological origin with plant roots (POM-Root) and with non-root derived POM (POM-NS) and from non-biological pores ($n = 8$). Error bars are standard errors at each distance.

FIGURE 9 | Percentage of 2–13 μm and >2 μm pores in aggregates of the three managements. Letters indicate significant differences between managements for >2 μm pores at $\alpha = 0.05$. The differences in 2–13 μm pores were not statistically significant. Error bars represent standard errors.

the 5 mm and <63 μm samples used in their study, DOM moved ~2 μm from a carbon source, but also found indications of possibly larger spatial ranges at larger spatial scales. The 123 μm distance may indicate the typical diffusion distance of DOM from biological pores into the soil matrix in similarly textured soils.

For non-biological pores, Os staining and grayscale value gradient trends did not match. The grayscale levels increased with the distance from the pore, which could be interpreted as increased SOM concentrations near the pore. Yet, the Os gradients clearly indicate lower SOM levels in immediate vicinity (<30 micron) of non-biological pores (**Figure 6**). This result was hypothesized to be due to increased <13 μm porosity closer to non-biological origin pores. However, no difference in <13 μm

porosity was observed among pore types (**Figure 10**). A possible explanation for this discrepancy is an artifact of image processing via 3DMA. 3DMA uses indicator kriging as a thresholding method, while the distance measures were conducted using Otsu's method due to computational and time limits resulting from the smaller image resolution. Indicator kriging performs well for identifying pores well above the image resolution, but may misidentify pores of sizes at or only slightly larger than the image resolution (**Figure 11**). Thus, the decreases in the grayscale values might be due to such missed porosity in non-biological pores. For non-biological pores, indicator kriging fails to identify small visible connections between larger pores, that extend for several voxels between adjacent pores due to using the surrounding voxels to help determine if a voxel is pore or not, while Otsu's method correctly identifies these pores because it only uses the raw grayscale value to identify pores. This artifact is less pronounced in biological pores as biological pores have no such small connections and, therefore, the true extent of the pore was accounted for.

The reason for this artifact to be present in pores of non-biological but not biological origin can be explained by the processes that create the pores of these two different types. Biological pores are created through the radial compression of the surrounding matrix as a root or macrofauna pushes through the soil and is then supported by organic binding agents, such as mucilage, mucus, and large amounts of DOM from decomposing organic matter, resulting in a clear boundary between pore and solid material (Gray and Lissmann, 1938; Greacen and Oh, 1972; Greacen and Sands, 1980; Czarnes et al., 2000; Ruiz et al., 2017). Additionally, Helliwell et al. (2017) found that while porosity near roots increased initially in sandy soils, which is similar to the texture of these soils, after 8 days of growth, porosity was found to decreased adjacent to roots at this image resolution. Non-biological pores are created through the shrinking and expanding of clays, resulting in neither clear nor stable boundaries (Peng
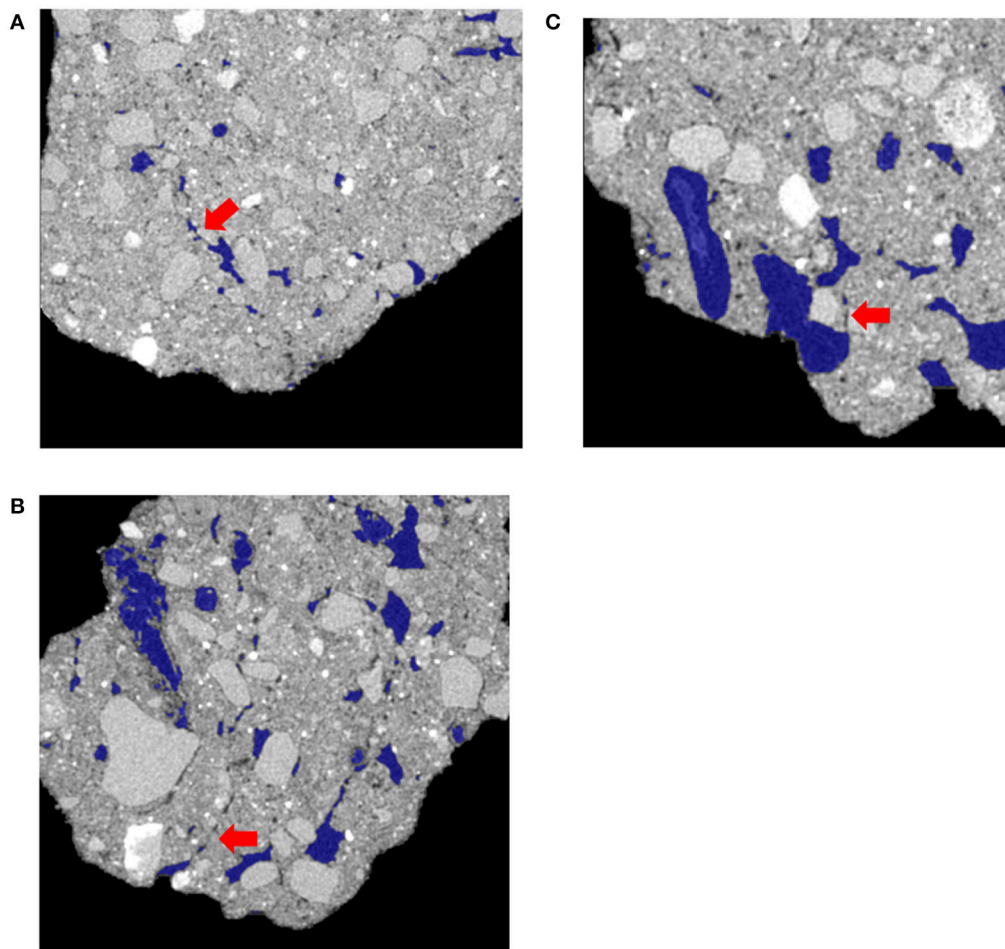
FIGURE 11 | Examples from the three different managements of how 3DMA missed pore material adjacent to non-biological pores, but identifies POM-Root and POM-NS pores correctly. **(A)** is from the conventional management, **(B)** is from the biologically based, and **(C)** is from the primary successional. The blue outlines are the pores identified by 3DMA. Red arrows on each figure indicate an example of missed porosity on each figure.

et al., 2007). However, using a different thresholding method may overcome the artifact effect.

Spatial Patterns of Grayscale Values

The nugget to sill ratio values of the studied samples indicate that approximately 50–60% of the spatial variability in grayscale values of the solid material is accounted for at $>13\,\mu m$ distances. This matches the porosity data, where approximately 50% of the porosity occurs at $>13\,\mu m$ (**Figure 9**). Biologically based management had the most porosity above $13\,\mu m$ and the lowest nugget to sill ratio, while conventional management had the lowest porosity above $13\,\mu m$ and the highest nugget to sill ratio. Since nugget to sill ratio indicates the relative amount of spatial dependence at voxel size, this may indicate a connection between spatial dependence and porosity at image scale. This would support our hypothesis that spatial variability in the solid material of similar mineralogy is driven by pores. However, more research would be necessary to confirm this connection.

The lack of difference in spatial correlation ranges among the aggregates from the three managements was surprising. Tillage, utilized both in conventional and biologically based management, homogenizes the soil, which, according to our expectations and previous findings (Garrett, 2009), should be manifested in greater spatial correlation range values. Lack of such an effect in our samples may indicate that the spatial correlation range in this soil is controlled more by the inherent mineralogy and/or texture, which are similar for the soil of all three managements, than by the management-driven SOM differences. The EDPI was much smaller than the spatial correlation range (123 vs. $312\,\mu m$) lending further support to the notion that the SOM distribution was not a driver of the spatial correlation range values. Rawlins et al. (2016) investigated the spatial ranges of SOM, pores, minerals, and bulk from μCT images. While the spatial ranges for SOM (38–175 μm) were greater than mineral and pores alone, the spatial ranges for bulk variograms were $<250\,\mu m$, which is congruent with our results.

Observed similarity in the nugget values from the three studied managements was in agreement with the results of Nunan et al. (2006), who found similar nuggets between three different amendment managements. The lack of differences between nuggets corroborates the below image resolution porosity measurements where the below image resolution porosity was similar between all three managements (**Figure 9**). The differences observed in the overall porosity matched results previously reported for these aggregates with biologically based ≥ primary successional ≥ conventional (Kravchenko et al., 2015).

Greater overall spatial variability in conservational practices, i.e., biologically based and primary successional managements, manifested via greater sill values (**Table 1**), is likely a result of management-induced changes in SOM. As mentioned above, soil mineralogy and texture of the studied managements were very similar, as well as their below image resolution porosity values (**Figures 9**, **10**). Yet, after almost 20 years of implementation, the biologically based and primary successional management practices resulted in higher SOM than the conventionally managed practice (Paul et al., 1999; Senthilkumar et al., 2009). Observed greater variability in grayscale values of biologically based and primary successional managements suggests that these SOM inputs were not uniformly distributed. This assertion is supported by previous findings of Ananyeva et al. (2013) who reported greater variability in soil carbon within the macro-aggregates from primary successional management as compared to conventional management practice; while Feeney et al. (2006) observed that active biota, in particular roots, increased spatial correlation of soil pores. Spatial gradients in SOM associated with pores of biological origin is one possible mechanism contributing to the increased variability.

The increased spatial variability observed in the grayscale values of the biologically based and primary successional managements, if driven by SOM distributions, would indicate increased occurrence of different microenvironments of either increased or decreased amounts of SOM, while conventional management would have less of these differing microenvironments. Greater presence of biological pores may result in an increased diversity of microenvironmental conditions, including different levels of microbial accessibility, nutrient availability, and potentially water and gas fluxes. Such microenvironmental differences affect microbial activities (Ekschmitt et al., 2005, 2008; Kravchenko and Guber, 2017); and greater SOM decomposition can be expected in microenvironments conducive to high microbial activity, while SOM protection in microenvironments where microbial activity is reduced. This increase in microenvironment heterogeneity, and therefore, greater presence of microsites where SOM might not be available to microbial decomposers and/or reduction of microbial decomposition due to anaerobic microsites (Keiluweit et al., 2016, 2017), may be reflective of the increased carbon protection/sequestration observed in the biologically based and primary successional managements as compared to conventional management (Paul et al., 1999; Senthilkumar et al., 2009).

SOM Pattern in Relation to Soil Pores

Our Os results demonstrated that pores were the drivers of SOM's spatial variability in the studied soil (**Figure 6**). Biological pores, had a clear spatial gradient of SOM with highest levels in the vicinity of pores and decreasing when moving into the surrounding solid material. Biological pores are observed more frequently in biologically based and primary successional managements as biological pores tend to be $< 90 \mu m$, which have a higher abundance in these managements. Non-biological pores, had a small decrease in SOM adjacent to the pores, but otherwise their presence was not related to SOM distribution patterns. Non-biological pores are observed more frequently in conventional management as non-biological pores tend to be $40-90 \mu m$ in size, which have a higher abundance in this management. Oxygen availability may control the decrease in SOM observed adjacent to non-biological pores. In the studied soil, $<13 \mu m$ pores (below image resolution sizes) are water filled during most of the year. This would hamper the diffusion of oxygen and lead to dominance of anaerobic conditions, which can result in as much as a 10-fold decrease in decomposition rates (Keiluweit et al., 2017). The likely outcome is, thus, organic's decomposition near large $(20-300 \mu m)$ pore boundaries, where oxygen is available, and organic's preservation in anaerobic $(<13 \mu m$ pore) zones.

Effect of Management Practices on SOM Pattern in Relation to Soil Pores

The effect of management on the SOM gradients as inferred from the grayscale gradient was unanticipated. There were no differences between managements observed for non-biological and POM-Root pores. However, there was observed differences between the managements in POM-NS pores. Biologically based and primary successional managements had no differences between POM-Root and POM-NS pores. Conversely, in conventional management, POM-NS gradients tended to retain decreased grayscale values over longer distances. It is inferred that this decrease would be related to an increase in SOM content. A possible explanation is that, per visual observations. POM-NS within conventional soil aggregates tended to be located closer to the interior of soil aggregates and/or away from pores of $>13 \mu m$ size, while POM-NS in biologically based and primary successional managements were located closer to the aggregate exterior and/or nearer to pores of $>13 \mu m$ size. Such isolation in conventional soil would result in restriction of microorganism, water, and oxygen access to POM-NS, resulting in incomplete decomposition. The incomplete decomposition produces decomposition products of a more hydrophobic nature. This hydrophobicity would decrease the ability of these products to be transported by water, resulting in a build-up of organic matter closer to the pore. Toosi et al. (2017) observed that as maximum pore size decreases the presence of SOM compounds with fewer oxygen functional groups and greater aromaticity increases; this observation supports our increased hydrophobicity explanation.

CONCLUSION

Analysis of grayscale gradients near pores of biological origin were found to be a useful proxy for assessing SOM spatial distribution patterns at micro-scale. Grayscale gradients of non-biological pores, in contrast, were found to be different from SOM gradients due to a pore identification artifact. Utilizing a different thresholding method may overcome this limitation.

Os and grayscale value gradients indicate increased SOM concentrations adjoining biological pores, decreasing to background levels as distance from the pore increases. The average distance of positive influence of biological pores on SOM levels was 123 μm. Os gradients indicate that SOM concentrations decreased in the direct vicinity of non-biological pores then returning to the background levels. The average distance of negative influence of non-biological pores on SOM levels was 30 μm.

Soil material without >13 μm pores was more variable in its grayscale values in biologically based and primary successional management than in conventional management practice. The greater variability is believed to be driven by SOM spatial distribution patterns, which reflect presence of soil pores, especially, pores of biological origin. This spatial variability likely results in greater variability of microenvironmental conditions for microbial functioning with possible implications for soil carbon protection.

AUTHOR CONTRIBUTIONS

MQ developed concepts, conducted data analyses and wrote the paper; MR contributed to research conduct; AK contributed to the development of research concepts, research conduct and writing.

SUPPLEMENTARY MATERIAL

The Supplementary Material for this article can be found online at: https://www.frontiersin.org/articles/10.3389/fenvs.2018.00028/full#supplementary-material

REFERENCES

Ananyeva, K., Wang, W., Smucker, A. J. M., Rivers, M. L., and Kravchenko, A. N. (2013). Can intra-aggregate pore structures affect the aggregate's effectiveness in protecting carbon? *Soil Biol. Biochem.* 57, 868–875. doi: 10.1016/j.soilbio.2012.10.019

Aravena, J. E., Berli, M., Ruiz, S., Suárez, F., Ghezzehei, T. A., and Tyler, S. W. (2014). Quantifying coupled deformation and water flow in the rhizosphere using X-ray microtomography and numerical simulations. *Plant Soil.* 376, 95–110. doi: 10.1007/s11104-013-1946-z

Bailey, V. L., Smith, A. P., Tfaily, M., Fansler, S. J., and Bond-Lamberty, B. (2017). Differences in soluble organic carbon chemistry in pore waters sampled from different pore size domains. *Soil Biol. Biochem.* 107, 133–143. doi: 10.1016/j.soilbio.2016.11.025

Bengough, A. G., McKenzie, B. M., Hallett, P. D., and Valentine, T. A. (2011). Root elongation, water stress, and mechanical impedance: a review of limiting stresses and beneficial root tip traits. *J. Exp. Bot.* 62, 59–68. doi: 10.1093/jxb/erq350

Chun, H. C., Giménez, D., and Yoon, S. W. (2008). Morphology, lacunarity and entropy of intra-aggregate pores: aggregate size and soil management effects. *Geoderma* 146, 83–93. doi: 10.1016/j.geoderma.2008.05.018

Czarnes, S., Hallett, P. D., Bengough, A. G., and Young, I. M. (2000). Root- and microbial-derived mucilages affect soil structure and water transport. *Eur. J. Soil Sci.* 51, 435–443. doi: 10.1046/j.1365-2389.2000.00327.x

De Gryze, S., Jassogne, L., Six, J., Bossuyt, H., Wevers, M., and Merckx, R. (2006). Pore structure changes during decomposition of fresh residue: x-ray tomography analyses. *Geoderma* 134, 82–96. doi: 10.1016/j.geoderma.2005.09.002

Denef, K., Six, J., Bossuyt, H., Frey, S. D., Elliot, T. E., Merckx, R., et al. (2001). Influence of dry-wet cycles on the interrelationship between aggregate, particulate organic matter, and microbial community dynamics. *Soil Biol. Biochem.* 33, 1599–1611. doi: 10.1016/S0038-0717(01)00076-1

Dungait, J. A. J., Hopkins, D. W., Gregory, A. S., and Whitmore, A. P. (2012). Soil organic matter turnover is governed by accessibility not recalcitrance. *Global Change Biol.* 18, 1781–1796. doi: 10.1111/j.1365-2486.2012.02665.x

Ekschmitt, K., Kandeler, E., Poll, C., Brune, A., Buscot, F., Friedrich, M., et al. (2008). Soil-carbon preservation through habitat constraints and biological limitations on decomposer activity. *J. Plant Nutr. Soil Sci.* 171, 27–35. doi: 10.1002/jpln.200700051

Ekschmitt, K., Liu, M., Vetter, S., Fox, O., and Wolters, V. (2005). Strategies used by soil biota to overcome soil organic matter stability–why is dead organic matter left over in soil? *Geoderma* 128, 167–176. doi: 10.1016/j.geoderma.2004.12.024

Falconer, R. E., Battaia, G., Schmidt, S., Baveye, P., Chenu, C., and Otten, W. (2015). Microscale heterogeneity explains experimental variability and non-linearity in soil organic matter mineralization. *PloS ONE* 10:e0123774. doi: 10.1371/journal.pone.0123774

Feeney, D. S., Crawford, J. W., Daniell, T., Hallett, P. D., Nunan, N., Ritz, K., et al. (2006). Three-dimensional microorganization of the soil-root-microbe system. *Microb. Ecol.* 52, 151–158. doi: 10.1007/s00248-006-9062-8

Gaillard, V., Chenu, C., and Recous, S. (2003). Carbon mineralization in soil adjacent to plant residues of contrasting biochemical quality. *Soil Biol. Biochem.* 35, 93–99. doi: 10.1016/S0038-0717(02)00241-9

Gaillard, V., Chenu, C., Recous, S., and Richard, G. (1999). Carbon, nitrogen and microbial gradients induced by plant residues decomposing in soil. *Eur. J. Soil Sci.* 50, 567–578. doi: 10.1046/j.1365-2389.1999.00266.x

Garrett, R. G. (2009). Relative spatial soil geochemical variability along two transects across the United States and Canada. *Appl. Geochem.* 24, 1405–1415. doi: 10.1016/j.apgeochem.2009.04.011

Gibson, J. R., Lin, H., and Bruns, M. A. (2006). A comparison of fractal analytical methods on 2- and 3-dimensional computed tomographic scans of soil aggregates. *Geoderma* 134, 335–348. doi: 10.1016/j.geoderma.2006.03.052

Gray, J., and Lissmann, H. W. (1938). An apparatus for measuring the propulsive forces of the locomotory muscles of the earthworm and other animals. *J. Exp. Biol.* 15, 518–521.

Greacen, E. L., and Oh, J. S. (1972). Physics of root growth. *Nat. New Biol.* 235, 24–25. doi: 10.1038/newbio235024a0

Greacen, E. L., and Sands, R. (1980). Compaction of forest soils. A review. *Aust. J. Soil. Res.* 18, 163–189. doi: 10.1071/SR9800163

Helliwell, J. R., Sturrock, C. J., Mairhofer, S., Craigon, J., Ashton, R. W., Miller, A. J., et al. (2017). The emergent rhizosphere: imaging the development of the porous architecture at the root-soil interface. *Sci. Rep.* 7:14875. doi: 10.1038/s41598-017-14904-w

Keiluweit, M., Nico, P. S., Kleber, M., and Fendorf, S. (2016). Are oxygen limitations under recognized regulators of organic carbon turnover in upland soils? *Biogeochemistry* 127, 157–171. doi: 10.1007/s10533-015-0180-6

Keiluweit, M., Wanzek, T., Kleber, M., Nico, P., and Fendorf, S. (2017). Anaerobic microsites have an unaccounted role in soil carbon stabilization. *Nat. Commun.* 8:1771. doi: 10.1038/s41467-017-01406-6

Ketcham, R. A. (2005). Three-dimensional grain fabric measurements using high-resolution X-ray computed tomography. *J. Struc. Geol.* 27, 1217–1228. doi: 10.1016/j.jsg.2005.02.006

Kiem, R., and Kögel-Knabner, I. (2002). Refractory organic carbon in particle-size fractions of arable soils II: organic carbon in relation to mineral surface area and iron oxides in fractions <6 μm. *Org. Geochem.* 33, 1699–1713. doi: 10.1016/S0146-6380(02)00112-2

Kravchenko, A. N., and Guber, A. K. (2017). Soil pores and their contributions to soil carbon processes. *Geoderma* 287, 31–39. doi: 10.1016/j.geoderma.2016.06.027

Kravchenko, A. N., Negassa, W., Guber, A. K., and Schmidt, S. (2014a). New approach to measure soil particulate organic matter in intact samples using X-ray computed microtomography. *Soil Sci. Soc. Am. J.* 78, 1177–1185. doi: 10.2136/sssaj2014.01.0039

Kravchenko, A. N., Negassa, W. C., Guber, A. K., Hildebrandt, B., Marsh, T. L., and Rivers, M. L. (2014b). Intra-aggregate pore structure influences phylogenetic composition of bacterial community in macroaggregates. *Soil Sci. Soc. Am. J.* 78, 1924–1939. doi: 10.2136/sssaj2014.07.0308

Kravchenko, A. N., Negassa, W. C., Guber, A. K., and Rivers, M. L. (2015). Protection of soil carbon within macro-aggregates depends on intra-aggregate pore characteristics. *Sci. Rep.* 5:16261. doi: 10.1038/srep16261

Kravchenko, A. N., Wang, W., Smucker, A. J. M., and Rivers, M. L. (2011). Long-term differences in tillage and land use affect intra-aggregate pore heterogeneity. *Soil Sci. Soc. Am. J.* 75, 1658–1666. doi: 10.2136/sssaj2011.0096

Kuzyakov, Y., and Blagodatskaya, E. (2015). Microbial hotspots and hot moments in soil: concept & review. *Soil Biol. Biochem.* 83, 184–199. doi: 10.1016/j.soilbio.2015.01.025

Mooney, S. J., Pridmore, T. P., Heliwell, J., and Bennett, M. J. (2012). Developing X-ray computed tomography to non-invasively image 3-D root systems architecture in soil. *Plant Soil* 352, 1–22. doi: 10.1007/s11104-011-1039-9

Mueller, C. W., Kölbl, A., Hoeschen, C., Hillion, F., Heister, K., Herrmann, A. M., et al. (2012). Submicron scale imaging of soil organic matter dynamics using NanoSIMS–from single particles to intact aggregates. *Org. Geochem.* 42, 1476–1488. doi: 10.1016/j.orggeochem.2011.06.003

Negassa, W. C., Guber, A. K., Kravchenko, A. N., Marsh, T. L., Hildebrandt, B., and Rivers, M. L. (2015). Properties of soil pore space regulate pathways of plant residue decomposition and community structure of associated bacteria. *PLoS ONE* 10:e0123999 doi: 10.1371/journal.pone.0123999

Nunan, N., Ritz, K., Rivers, M., Feeney, D. S., and Young, I. M. (2006). Investigating microbial micro-habitat structure using X-ray computed tomography. *Geoderma* 133, 398–407. doi: 10.1016/j.geoderma.2005.08.004

Oades, J. M. (1984). Soil organic matter and structural stability: mechanisms and implications for management. *Plant Soil* 76, 319–337. doi: 10.1007/BF02205590

Oh, W., and Lindquist, W. B. (1999). Image thresholding by indicator kriging. *IEEE Trans. Pattern Anal. Mach. Intell.* 21, 590–602. doi: 10.1109/34.777370

Papadopoulos, A., Bird, N. R. A., Whitmore, A. P., and Mooney, S. J. (2009). Investigating the effects of organic and conventional management on soil aggregate stability using X-ray computed tomography. *Eur. J. Soil Sci.* 60, 360–368. doi: 10.1111/j.1365-2389.2009.01126.x

Paul, E. A., Harris, D., Collins, H. P., Schulthess, U., and Robertson, G. P. (1999). Evolution of CO_2 and soil carbon dynamics in biologically managed, row-crop agroecosystems. *Appl. Soil Ecol.* 11, 53–65. doi: 10.1016/S0929-1393(98)00130-9

Paul, E. A., Kravchenko, A., Grandy, S., and Morris, S. (2015). "Soil organic matter dynamics: controls and management for sustainable ecosystem functioning," in *The Ecology of Agricultural Landscapes: Long-Term research on the Path to Sustainability*, eds S. K. Hamilton, J. E. Doll, and G. P. Robertson (New York, NY: Oxford University Press), 104–134.

Pebesma, E. J. (2004). Multivariable geostatistics in S: the gstat package. *Comput. Geosci.* 30, 683–691. doi: 10.1016/j.cageo.2004.03.012

Peng, X., Horn, R., and Smucker, A. (2007). Pore shrinkage dependency of inorganic and organic soils on wetting and drying cycles. *Soil Sci. Soc. Am. J.* 71, 1095–1104. doi: 10.2136/sssaj2006.0156

Peth, S. (2010). "Applications of microtomography in soils and sediments," in *Developments in Soil Science,* Vol. 34, eds B. Singh and M. Gräfe, (The Netherlands: Elsevier B. V), 73–101.

Peth, S., Chenu, C., Leblond, N., Mordhorst, A., Garnier, P., Nunan, N., et al. (2014). Localization of soil organic matter in soil aggregates using synchrotron-base X-ray microtomography. *Soil Biol. Biochem.* 78, 189–194. doi: 10.1016/j.soilbio.2014.07.024

Peth, S., Horn, R., Beckmann, F., Donath, T., Fischer, J., and Smucker, A. J. M. (2008). Three-dimensional quantification of intra-aggregate pore-space features using synchrotron-radiation-based microtomography. *Soil Sci. Am. J.* 72, 897–907. doi: 10.2136/sssaj2007.0130

Rawlins, B. G., Wragg, J., Reinhard, C., Atwood, R. C., Houston, A., Lark, R. M., et al. (2016). Three-dimensional soil organic matter distribution, accessibility and microbial respiration in macroaggregates using osmium staining and synchrotron X-ray computed tomography. *Soil* 2, 659–671. doi: 10.5194/soil-2-659-2016

Ruiz, S., Schymanski, S. J., and Or, D. (2017). Mechanics and energetics of soil penetration by earthworms and plant roots: higher rates cost more. *Vadose Zone J.* 16:8. doi: 10.2136/vzj2017.01.0021

SAS Inc (2009). *SAS User's Guide.* Version 9.2. Cary, NC: SAS Inst.

Senthilkumar, S., Basso, B., Kravchenko, A. N., and Robertson, G. P. (2009). Contemporary evidence of soil carbon loss in the U.S. corn belt. *Soil Sci. Soc. Am. J.* 73, 2078–2086. doi: 10.2136/sssaj2009.0044

Six, J., Conant, R. T., Paul, E. A., and Paustian, K. (2002). Stabilization mechanisms of soil organic matter: implications for C-saturation of soils. *Plant Soil* 241, 155–176. doi: 10.1023/A:1016125726789

Six, J., Elliott, E. T., and Paustian, K. (2000). Soil macroaggregate turnover and microaggregate formation: a mechanism for C sequestration under no-tillage agriculture. *Soil Biol. Biochem.* 32, 2099–2103. doi: 10.1016/S0038-0717(00)00179-6

Smucker, A. J. M., Park, E.-J., Dorner, J., and Horn, R. (2007). Soil micropore development and contributions to soluble carbon transport within macroaggregates. *Vadose Zone J.* 6, 282–290. doi: 10.2136/vzj2007.0031

Sørensen, L. H. (1974). Rate of decomposition of organic matter in soil as influenced by repeated air drying-rewetting and repeated additions of organic material. *Soil Biol. Biochem.* 6, 287–292. doi: 10.1016/0038-0717(74)90032-7

Syswerda, S. P., Corbin, A. T., Mokma, D. L., Kravchenko, A. N., and Robertson, G. P. (2011). Agricultural management and soil carbon storage in surface vs. deep layers. *Soil Sci. Soc. Am. J.* 75, 92–101. doi: 10.2136/sssaj2009.0414

Toosi, E. R., Kravchenko, A. N., Mao, J., Quigley, M. Y., and Rivers, M. L. (2017). Effects of management and pore characteristics on organic matter composition

of macroaggregates: evidence from characterization of organic matter and imaging. *Eur. J. Soil Sci.* 68, 200–211. doi: 10.1111/ejss.12411

Wang, W., Kravchenko, A. N., Johnson, T., Srinivasan, S., Ananyeva, K. A., Smucker, A. J. M., et al. (2013). Intra-aggregate pore structures and *Escherichia coli* distribution by water flow within and movement out of soil macroaggregates. *Vadose Zone J.* 12:4. doi: 10.2136/vzj2013.01.0012

Wang, W., Kravchenko, A. N., Smucker, A. J. M., Liang, W., and Rivers, M. L. (2012). Intra-aggregate pore characteristics: x-ray computed microtomography analysis. *Soil Sci. Soc. Am. J.* 76, 1159–1171. doi: 10.2136/sssaj2011. 0281

Wang, W., Kravchenko, A. N., Smucker, A. J. M., and Rivers, M. L. (2011). Comparison of image segmentation methods in simulated 2D and 3D microtomographic images of soil aggregates. *Geoderma* 162, 231–241. doi: 10.1016/j.geoderma.2011.01.006

Young, I. M., and Crawford, J. W. (2004). Interactions and self-organization in the soil-microbe complex. *Science* 304, 1634–1637. doi: 10.1126/science.1097394

Correlative Visualization of Root Mucilage Degradation Using X-ray CT and MRI

Arjen van Veelen[1], Monique C. Tourell[2], Nicolai Koebernick[1], Giuseppe Pileio[2] and Tiina Roose[1]*

[1] Bioengineering Sciences Research Group, Faculty of Engineering and the Environment, University of Southampton, Southampton, United Kingdom, [2] Department of Chemistry, Faculty of Natural and Environmental Sciences, University of Southampton, Southampton, United Kingdom

Root exudates are a crucial component of the rhizosphere. Often, they take a form of a gel exuded by the plant roots and are thought to influence the soil aggregation, root penetration into soil, soil nutrient availability, immobilization of toxic cations, and microbial activity amongst other things. In addition, the capacity of exudates to store water makes the plants potentially less susceptive to drought. Major components of root exudates are high molecular weight organic compounds consisting of predominantly polysaccharides and proteins, which makes it challenging to visualize using current rhizosphere visualization techniques, such as X-ray computed tomography (CT). In this contribution, we use correlative X-ray CT (resolution ∼20 μm) in combination with Magnetic Resonance Imaging (MRI, resolution ∼120 μm) to set up groundwork to enable *in situ* visualization of mucilage in soil. This multimodal approach is necessary because mucilage density closely matches that of water. We use chia seeds as mucilage analog, because it has been found to have a similar consistency to root mucilage. Moreover, to understand mucilage development in time, a series of samples made by chia seeds placed in different porous media were prepared. Structurally and chemically, mucilage breaks down toward a water-like substance over a course of 2 weeks. Depending on its relative concentration, these changes were found to be less dominant when seeds were mixed in porous media. Having set up the groundwork for correlative imaging of chia seeds in water and an artificial soil (Nafion and sand/beads) this enables us to expand this imaging to deal with plant root exudates under natural conditions.

Keywords: chia, mucilage, [1]H-MRI, X-ray CT, root-exudate, polysaccharides, rhizosphere

INTRODUCTION

We rely on soil to support the crops on which we depend. Less obviously we also rely on soil for a host of "ecosystem services": for example, soil contains large quantities of carbon which would otherwise be released into the atmosphere where it would contribute to climate change, and soil buffers the hydrological system, greatly reducing the risk of flooding after heavy rain. Given its importance it is not surprising that soil, especially its interaction with plant roots, has been a focus for many researchers. However, the complex and optically opaque nature of soil has always made it a difficult medium to study. Soil is a complex medium. It is composed of different materials

(minerals, organic matter, water, microorganisms) of diverse morphologies and length-scales (from centimeters to nanometers), which aggregate together to form an intricate porous material. While many key properties of soil are determined by processes taking place at the micrometer-scale (often called pore scale), within this complex material we have traditionally only been able to measure and observe soil function at the larger, meter-scale (usually referred to as the macroscale or field scale). We can manipulate soil systems at the macroscale and empirically observe what occurs, and this empirical description is useful, but it offers no scope to truly predict how the system would respond to modification. Critical to soil function are processes (nutrient cycling, carbon storage, water movement etc.) that occur at the pore scale and root scale. This is important because we have the potential, and most likely the future need, to manipulate the underlying soil processes at the microscale.

The role of root mucilage in the rhizosphere is manifold: it can aid in the contact between plant roots and rock mineral phases in the changing soil hydration situation; it can be important for nutrient solubilization reactions on the soil mineral surfaces; it can immobilize heavy metals; and it has been hypothesized to be an important habitat for other soil microorganisms (Bais et al., 2006; Watanabe et al., 2008; Carminati et al., 2010; Fox et al., 2012; Ahmed et al., 2016). Thus, it is important to learn how mucilage influences the root-soil interface physically. Root cap derived mucilage is usually in the form of a viscoelastic substance that is exuded by the roots, primarily by the root cap cells into the rhizosphere. Chemically, mucilage is a high molecular weight (HMW) carbohydrate, consisting predominantly of polysaccharides, organic acids, amino acids, fatty acids, and alcohols (Knee et al., 2001; Watanabe et al., 2008; Naveed et al., 2017). The sugar, amino acid, and glycosidic linkage composition of mucilage is complex and quite similar between different plant species. These glycosidic compositions, which are comparable to kinds found in arabinogalactan proteins (AGP), are known for high-water-binding and gel-forming properties (Fincher et al., 1983). Therefore, mucilage, when fully hydrated, can achieve a water retention of 27–589 times its weight (McCully and Boyer, 1997; Huang and Gutterman, 1999; Capitani et al., 2013). Hydration of mucilage is thought to happen quickly with rapid root surface hydration and diffusion of the exudate gel into the soil (McCully and Boyer, 1997; Salgado-Cruz et al., 2013). In addition, the carbohydrate nature makes it possible to form a dense three-dimensional micro to nano-sized fibril network. These characteristics make it especially useful for the adsorption of cations due to its high concentration of active binding sites (Watanabe et al., 2008; Goh et al., 2016). Therefore, the rhizosphere is potentially at least a four-phase domain, i.e., mineral, water with colloidal microparticles, air, and mucilage.

Plant roots exude ∼20–25% of the total reduced carbon in the rhizosphere with roughly half of it in the form of mucilage, which therefore acts as a major carbon source for soil biota (Chaboud, 1983; Knee et al., 2001; Walker et al., 2003). The extent and rate of root mucilage degradation or mineralization by soil microbes is unclear, although the ability of biota to utilize root mucilage as a carbon source may be an important

factor in successful root colonization in soils (Knee et al., 2001; Carminati and Vetterlein, 2013). Polysaccharides in mucilage are harder to hydrolyse by microbes in order to gain access to monomers that induce growth than soluble root exudates. Therefore, the make-up of the microbial community and the level of microbes in the direct vicinity of roots is thought to be directly influenced by root exudates, such as mucilage, and root border cells (Benizri et al., 2007). As a result, microbes that are capable to mineralize polysaccharides will therefore alter the structure and water holding properties of the rhizosphere, which can have detrimental effects on plant function (Mary et al., 1993; Knee et al., 2001; Naveed et al., 2017).

^{1}H Magnetic Resonance Imaging (^{1}H-MRI) relaxometry has a potential to be used to study the state of water in soil-root-mucilage interactions *in-situ* (Jaeger et al., 2006). The relaxation rate (both T_1 and T_2) of the ^{1}H-NMR signal acquired in any sample (soil, root, or mucilage) varies as a result of the different molecular environments experienced by water molecules (Jaeger et al., 2006; Brax et al., in press). These differences can be measured and manifest as a shift of relaxation rates. Likewise, the changes in the mucilage structure, i.e., during degradation, can potentially cause shifts in these relaxation rates and can be useful in studying the progress of mucilage aging and decomposition in the rhizosphere *in situ*. In this paper, we set out to establish the groundwork for further experimental imaging techniques to enable imaging of mucilage in the soil. We will do this by utilizing correlative X-ray computed tomography and NMR imaging which, in combination, are suited for imaging soft biological materials in 4D, i.e., in 3D space and in time.

MATERIALS AND METHODS

Sample Preparation

Three different samples were prepared, (i) pure chia seeds, (ii) chia seeds with Nafion artificial soil, and (iii) chia seeds with quartz sand (**Figure 1**). As to mimic mucilage release under "soil" conditions, Nafion and quartz were chosen as model soils for this exploratory study. Analytical grade sand (quartz, Sigma Aldrich, 212–300 μm) was used as received. Nafion was prepared by first washing Nafion beads (NR50 and R1100) in 2% HNO_3 and MilliQ and then subsequently mixing NR50 and R1100 precursor beads in a 1:1 ratio. Finally, the mixture was cryo-milled using liquid nitrogen and subsequently sieved between 105 and 850 μm ending up with a mean particle size of 152 μm (determined from CT).

Chia mucilage (*Salvia hispanica* L.) was chosen as model mucilage in this study since it has been investigated as a model compound in various rhizosphere studies (Kroener et al., 2014; Benard et al., 2017). In addition, chia seeds are known for their relatively high yield of mucilage. Chia seed samples were prepared in three separate 2.5 mL syringes which contained a rectangular capillary. The long axis of the capillary was placed parallel to the long axis of the syringe (**Figure 1**) to be used as internal bulk water reference (MilliQ). For sample (i), the syringe contained only chia seeds and was prepared as a control. As to test the behavior of different mucilage concentrations in different environments, two distinct chia regions were created in the sand
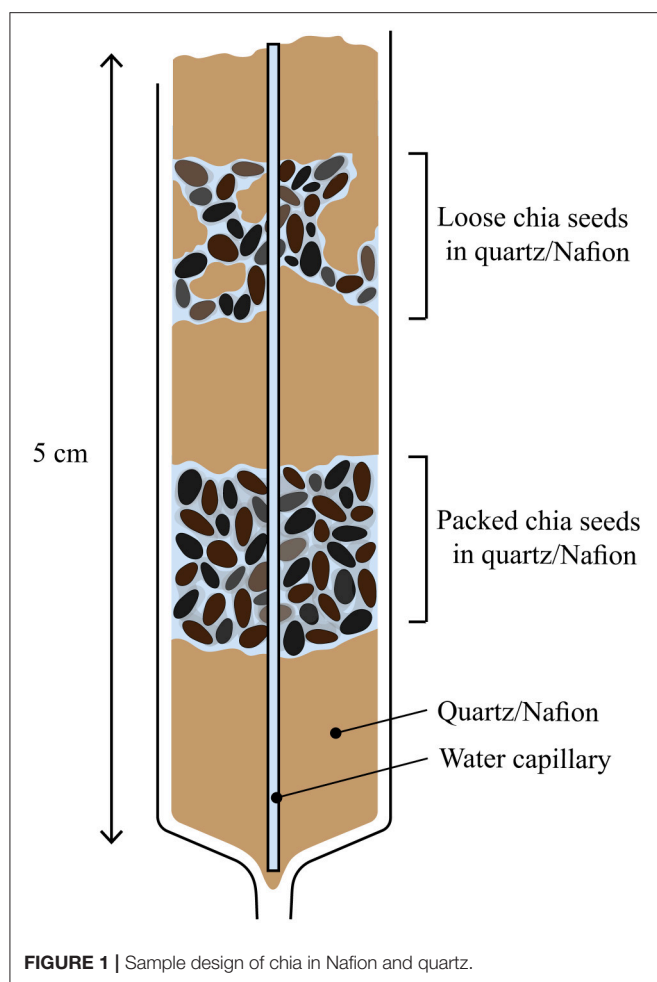
FIGURE 1 | Sample design of chia in Nafion and quartz.

and Nafion treatment (**Figure 1**) which were prepared as follows, (i) loose chia which consisted of chia mixed in a 1:1 ratio with either Nafion or quartz, and (ii) packed chia which consisted of just chia seeds. The interlayers consisted of either Nafion or quartz as to separate out these layers. This resulted in a total of five chia regions across all samples (one pure chia, two chia and Nafion, and two chia and quartz). All samples were then wetted and saturated (matric potential 0 MPa) and left to equilibrate in a beaker with ultra-pure water (MilliQ, 18 Ω) for 6 h (±0.5 h) prior to the first NMR imaging session. The start of these imaging time series was chosen to be the first NMR imaging session, set at $t = 0$ h. Prior to the start of the NMR imaging series, both ends of the syringes were sealed with parafilm and agarose at the bottom and top, respectively as to prevent sample dehydration.

MRI

All MRI experiments were carried out on a 7 T Bruker Avance III spectrometer equipped with a micro-imaging probe carrying a ^{1}H/^{13}C 10 mm resonator with a triple-axis gradient set able to deliver a maximum gradient amplitude of 1.5 T/m. The syringes were placed in the instrument such that the long axis of the syringe was parallel to the static magnetic field, and the smallest

axis of the water-containing rectangular capillary was aligned parallel to the coronal slice direction. A series of T_2-weighted images for each of the five chia regions (pure chia, Nafion packed, Nafion loose, quartz packed, and quartz loose) at six different time points (0, 42, 97, 168, 284, and 325 h) were acquired using a CPMG pulse sequence. These consisted of 40 echoes for 8 adjacent coronal slices within each chia region, slice thickness 0.5 mm, with the parameters: TE = 12–480 ms; TR = 4,000 ms; matrix size (NP × NR) = 128 × 256; in-plane resolution of 120 × 120 μm; and $N = 2$ image averages. The total acquisition time for each scan was under 15 min. As a reference for pore water, we also measured T_2 of packed Nafion and quartz saturated with ultra-pure water, respectively. Post-processing of the images was completed in *Mathematica* (Wolfram Inc., Illinois) using an analysis code written in-house. Briefly, three regions of interest (ROIs) were selected manually: 1. Regions of water-only within the capillaries were used as a reference; 2. Regions on either side of the capillary, containing chia seeds, surrounding gel and any soil substitutes; and 3. Regions of just chia seed. A three-parameter least-squares fit was performed on the intensity S from each voxel in an ROI to the function

$$S = S_0 \, exp\,(-R_2 \, t) + c \qquad (1)$$

where R_2 is the transversal relaxation rate given by $\frac{1}{T_2}$, S_0 is the initial signal, t is time, and c is the final noise level. From this data R_2 maps and histograms were constructed.

Finally, to measure the degradation rate of chia mucilage, the R_2 of each time step was measured and averaged by carefully segmenting regions of mucilage. Although the voxel sizes are big (120 μm) and there might be an error associated with this, the regions were chosen in such a way that the bulk of the ^{1}H signal is from water trapped in the mucilage. Hydrated mucilage contains 99.9% H_2O compared to 5–10% H_2O in the seed cellular structure (Muñoz et al., 2012). The R_2 values are used to measure the changes of both physical and chemical properties of mucilage in time. As such, the resulting data was averaged over each sample per time point and fitted against a simple degradation rate model, described as

$$y = a + C_0 \, exp\,(-K \, t) \qquad (2)$$

where K is the degradation constant of mucilage, C_0 is the initial signal, and t is time expressed in hours.

X-ray CT

All X-ray computed tomography (XCT) measurements were carried out in the μ-VIS X-ray Imaging Centre at the University of Southampton using a X-Tek 160 kV Benchtop Micro-CT scanner (X-Tek Systems Ltd, Tring, Hertfordshire, UK) equipped with a 1 248 × 1 248 pixels flat panel detector. Each of the samples was scanned within 24 h after the first MRI measurement, and after the total series of MRI scans was finished spaced 325 h apart ($t = 349$ h). Each syringe was scanned separately at two different heights, which corresponded to the conditions "packed" and "loose" in the samples. Samples were scanned using a tube voltage of 120 kV and a current of 131 μA. A series of 2001 projections were recorded at an exposure time of 534 ms. Volume

reconstructions were carried out using the CT Pro software package. The resulting volumes had an isotropic voxel side length of 20.8 μm. Images were processed and analyzed using the open source image analysis platform ImageJ (Schindelin et al., 2012) except for the correlation of CT and MRI scans, which was performed in VGStudio Max (Volume Graphics GmbH, Heidelberg, Germany). Images were cropped to a cylindrical region with a radius of 8 mm to remove the syringe wall. The glass capillary was segmented using a manual threshold followed by a dilation and a "Fill holes" operation in ImageJ. A seeded region growing was applied to remove any quartz/Nafion particles that were erroneously segmented during this step. Contrast of the remaining materials was enhanced manually based on the gray value histograms. In the pure chia seed sample a single threshold was computed with the default histogram based thresholding algorithm (also known as iterative intermeans) in ImageJ to segment air-filled voids. The remaining volume consisted of the chia seeds and hydrated mucilage. In the images containing porous media no robust automated thresholding method was found to classify the image into three different phases. Therefore, two thresholds were defined manually: A lower threshold separating air-filled voids from the seeds and hydrated mucilage and an upper threshold separating seeds and hydrated mucilage from solid quartz/Nafion particles, respectively. Volume fractions of the different materials were computed within ROI which were manually defined to match ROI on either side of the capillary used in the processing of the NMR scans. To this end, CT images and the corresponding NMR images taken at the nearest time point were co-registered using the "simple registration" tool in VG Studio Max. The volume fraction of any material was defined as the volume of said material divided by the total volume of the ROI. The pore size distribution of the liquid phase was estimated using the local thickness plugin in ImageJ. Local pore diameter was evaluated for the Chia loose regions in both Nafion and quartz at $t = 325$ h. A rough classification into soil pores and pores containing chia seeds was done by manually thresholding the local thickness map with threshold that segmented all the chia seeds (see **Figure S2** in Supplementary Information).

RESULTS

MRI

By using the ^{1}H transverse relaxation rates ($R_2 = 1/T_2$) from MRI images, it was possible to distinguish between (i) the water phase by using an internal standard in the capillary, (ii) the mucilage gel phase, and (iii) the chia seeds. Due to the relatively small pore sizes between the seeds and relative large voxel sizes required by MRI experiments, the probability diagrams are presented as (i) seeds separate, and (ii) total signal from seeds and gel together (**Figures 2–5**, and also **Figure S1** in Supporting Information).

Across all five regions investigated (chia pure, Nafion/sand loose, and Nafion/sand packed) the relaxation rates measured differ from (a) the rate of bulk water in the glass capillary ($R_2 = 0.016 \pm 0.009$ ms^{-1}), (b) the rate of water in the pore space of the Nafion-only sample (0.016 ± 0.002 ms^{-1}), and (c) the rate of the water measured in the quartz-only sample (0.0595 ± 0.004 ms^{-1}). Since mucilage excretion will change the

relaxation rate, the results presented here in combination with the CT images, confirm the successful mucilage release from chia seeds in all five samples regions.

In the chia-only sample, the region containing both seeds and mucilage shows, in general, a slower relaxation rate compared to that measured in the seeds alone. This suggests that the water molecules present in the mucilage itself have a slower relaxation rate than those in the seeds. When compared to X-ray CT, these phases can generally be distinguished easier by NMR (**Figures 2a,b**). Moreover, the total NMR signal has a range of relaxation times, which is composed of more concentrated mucilage at the seed surface, dilute mucilage in the pores, and pore water. Although not significant, the overall R_2 value seems to shift toward that of bulk water (vertical dashed line in **Figure 2c**) and back. The seeds, on the other hand, seem to hydrate from 284 h and follow an opposite trend. The fact that this is not represented in the total signal suggests that this is a small fraction of the total ^{1}H signal.

The overall NMR relaxation rates of mucilage in the loose and packed Nafion regions differ substantially (**Figure 3**). The loose chia layer (**Figures 3a,c**) has an overall R_2 similar to that of bulk capillary water. **Figures 3b,d** show that the packed layer has a higher R_2, similar to the pure chia sample, which is consistent with the formation of a densely formed mucilage network and more tightly bound water molecules. In both layers the overall signal, is again predominantly affected by mucilage and pore water. In the loose layer, where the gel:water ratio is lower, the overall signal is similar to that of water and no significant changes occur over time. In contrast, the packed layer shows unequivocally a continuous shift toward lower R_2 values with increasing time. Moreover, the degradation constant (**Table 1**, **Figure 4**) is bigger, which means that the R_2 from mucilage changes significantly. In this region, the R_2 values of mucilage decreases rapidly within the first 97 h.

Similar to the Nafion regions, the packed and loose chia layers in quartz differ significantly (**Figures 4**, **5**) and degradation is slightly faster than in the Nafion treatment. Mucilage in the loose quartz region (**Figures 5a,c**) shows a broader range of R_2 values compared to the other samples (**Table 1**). This is indicative of a wider range of gel concentrations throughout this region. At 97 h, the R_2 in this region shifts toward higher values, away from bulk water reference (0.016 ± 0.009 ms^{-1}; black dashed line **Figure 5c**), but toward the value for pore water measured in pores of quartz particles (0.0595 ± 0.004 ms^{-1}; gray dashed line **Figure 5c**). In addition, the degradation curve of mucilage shows a slight R_2 increase over time (**Figures 4**, **5c**). In the packed region, the same evidence of mucilage degradation occurs. The packed region shows a continuous shift in the opposite direction toward that of bulk water. Similar to Nafion, also in this region a rapid decrease in the mucilage R_2 occurs in the first 97 h. However, compared to the loose packed region, the gel:water ratio remains higher.

Seed hydration changes are minimal in chia and chia-quartz treatments and changes are only observed in the chia-Nafion treatment (**Figures 3**, **5**). The hydration in these samples sets in immediately and seems to increase over time. In contrast,
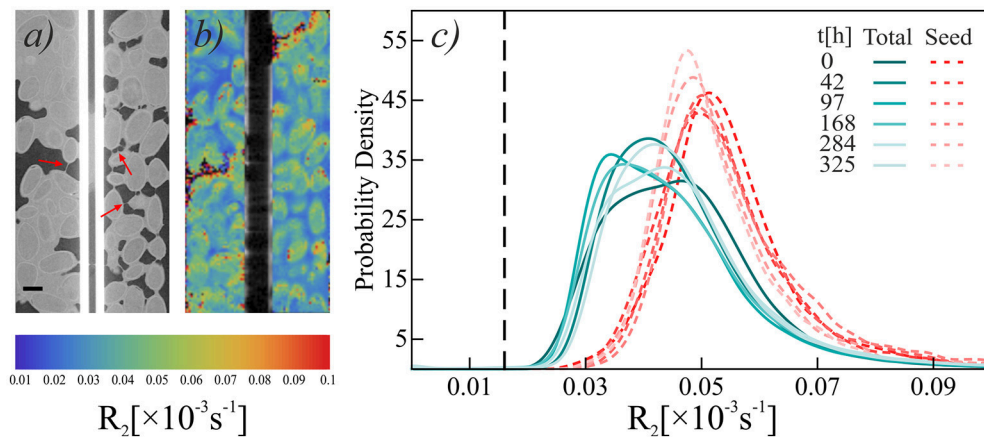
FIGURE 2 | Aligned CT **(a)** and NMR **(b)** scans of pure chia seeds at $t = 325$ h. Scale bar at bottom left of the CT image is 1 mm. X-ray CT images show filaments spanning across air-filled voids (red arrows). Colors in the NMR image indicate relaxation rate R_2. **(c)** Histograms of relaxation rate R_2 of pure chia. Blue-green solid lines show R_2 in "Total" region, red dashed lines show R_2 in "Seed" region. Black dashed reference line shows mean R_2 of water in the capillary. Note that the thickness of a single MRI slice is 500 µm compared to 20 µm of X-ray CT, which results in a perceived misalignment of geometrical features.

FIGURE 3 | Temporal development relaxation rate R_2 of chia seeds in Nafion. **(a,b)** Temporal sequence of NMR scans of **(a)** loose chia in Nafion and **(b)** packed chia in Nafion. Colors indicate relaxation rate R_2. Scale bars are 2 mm. **(c,d)** Histograms of relaxation rate R_2 of **(c)** loose chia in Nafion and **(d)** packed chia in Nafion. Blue-green solid lines show R_2 in "Total" region, red dashed lines show R_2 in "Seed" region. Black dashed reference line shows mean R_2 of water in the capillary, which is equal to the mean R_2 of water in Nafion pores ($R_2 = 0.016$).

TABLE 1 | Estimated volume fractions of the different materials within the XCT imaged regions of interest at time points $t = 0$ h and $t = 325$ h.

Condition	ϕ_{liquid}[a] t [h]		ϕ_{air}[b] t [h]		ϕ_{solid}[c] t [h]		R_2 total[d] t [h]		R_2 seed t [h]		K[e]
	0	325	0	325	0	325	0	325	0	325	
Chia pure	0.957	0.828	0.043	0.172	–	–	0.046 (13)*	0.048 (15)	0.055 (12)	0.052 (11)	∼0
Nafion chia loose	0.647	0.583	0.071	0.099	0.281	0.318	0.031 (18)	0.028 (14)	0.060 (20)	0.035 (13)	0.010
Nafion chia packed	0.878	0.847	0.018	<0.001	0.104	0.153	0.057 (17)	0.040 (13)	0.053 (06)	0.037 (13)	0.013
Quartz chia loose	0.592	0.563	0.010	0.032	0.399	0.405	0.050 (21)	0.053 (20)	0.053 (14)	0.049 (11)	−0.024
Quartz chia packed	0.808	0.831	0.03	0.002	0.161	0.166	0.058 (16)	0.047 (15)	0.055 (09)	0.054 (13)	0.020

[a] ϕ_{liquid} is the volume fraction of Chia seeds. [b] ϕ_{air} is the volume fraction of air-filled voids. [c] ϕ_{solid} is the volume fraction of solid "soil" constituents, i.e., quartz or Nafion particles. [d] Transverse relaxation rates $R_2 = 1/T_2$ (ms^{-1}) in different regions of interest (ROIs) given as a mean. The R_2 of the capillary water was 0.0016 ± 0.009 ms^{-1}. [e] Degradation rate constant of chia mucilage. *Standard deviation on the last two digits of R_2.

in the other samples changes are only observed from 284 h onwards.

X-ray CT Imaging

In the CT images, it was possible to distinguish between three different phases: (i) a *solid* phase made up by the porous material, i.e., either Nafion or sand, (ii) a *liquid* phase consisting of hydrated chia seeds, mucilage, and pore water, and (iii) an *air* phase containing air-filled voids. Change in the volume fraction (ϕ_i, where i denotes the material) of the materials between the start and the finish of the experiment is shown in **Table 1**. Most prominently, in the chia pure sample, ϕ_{air} increased by ∼12%. Moreover, in both the Nafion and quartz samples, ϕ_{air} increased in the chia loose regions, while it decreased in the chia packed regions. Change of ϕ_{air} is in most cases accompanied by a change of ϕ_{liquid} with opposite sign, except for Nafion chia packed, where both ϕ_{liquid} and ϕ_{air} decreased over the course of the experiment. This was explained by an increase of ϕ_{solid}. Change of ϕ_{solid}, which was deemed constant, was < 5% in the Nafion sample and < 1% in the quartz sample and was likely caused by the shrinkage of mucilage.

A portion of the air-filled void volume at $t = 325$ h was occupied with a dense network of slightly sub-resolution filaments. Segmentation of these filaments was not possible at the given resolution and signal/noise ratio. However, projection of the maximum gray value over 200 μm (10 voxels) along the z-axis (longitudal) enabled the visualization of this network in a portion of the air-filled voids (**Figure 6a**). The network consisted of long filaments with diameters of ∼20 μm, and irregularly shaped agglutinations of hydrated material at the junctions of multiple filaments (red arrows in **Figure 6a**). The diameter of these agglutinations varied between ∼40 and 200 μm. After the experiment, images recorded with a light microscope, confirmed the formation of filaments and a branched network of filaments from the degraded gel (**Figures 6b–d**).

The local thickness measure of the liquid fraction in Nafion loose and chia loose in sand at $t = 325$ h showed marked differences in pore size distribution (**Figure S3** in Supplementary Information). Both histograms showed a clear separation of local thickness into a soil pore fraction and a fraction containing chia seeds. Total fraction of pores classified as soil pores was similar
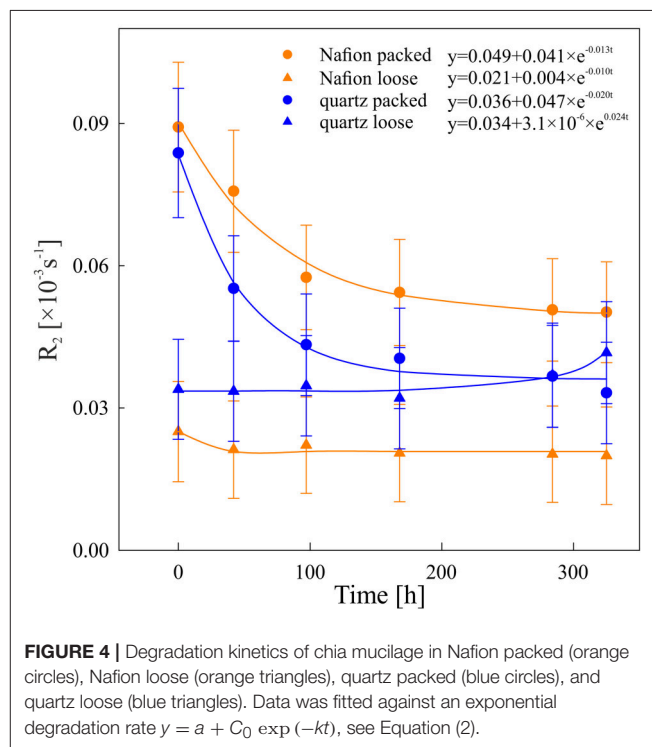
FIGURE 4 | Degradation kinetics of chia mucilage in Nafion packed (orange circles), Nafion loose (orange triangles), quartz packed (blue circles), and quartz loose (blue triangles). Data was fitted against an exponential degradation rate $y = a + C_0 \exp{(-kt)}$, see Equation (2).

in Nafion (0.39) and in sand (0.38), while the sand contained a greater fraction (0.12) of meso- and micro-pores (Brewer, 1964) than the Nafion (0.07).

DISCUSSION

The purpose of this paper was to image chia seed mucilage in soil *in situ* and demonstrate how it is changing with time; this provides a way forward for further studies using plant derived mucilage.

We were able to successfully image the gel-phase around the Chia seeds. The broad range of observed relaxation times of mucilage at the start of the experiment are consistent with mucilage data published by Muñoz et al. (2012). Their research
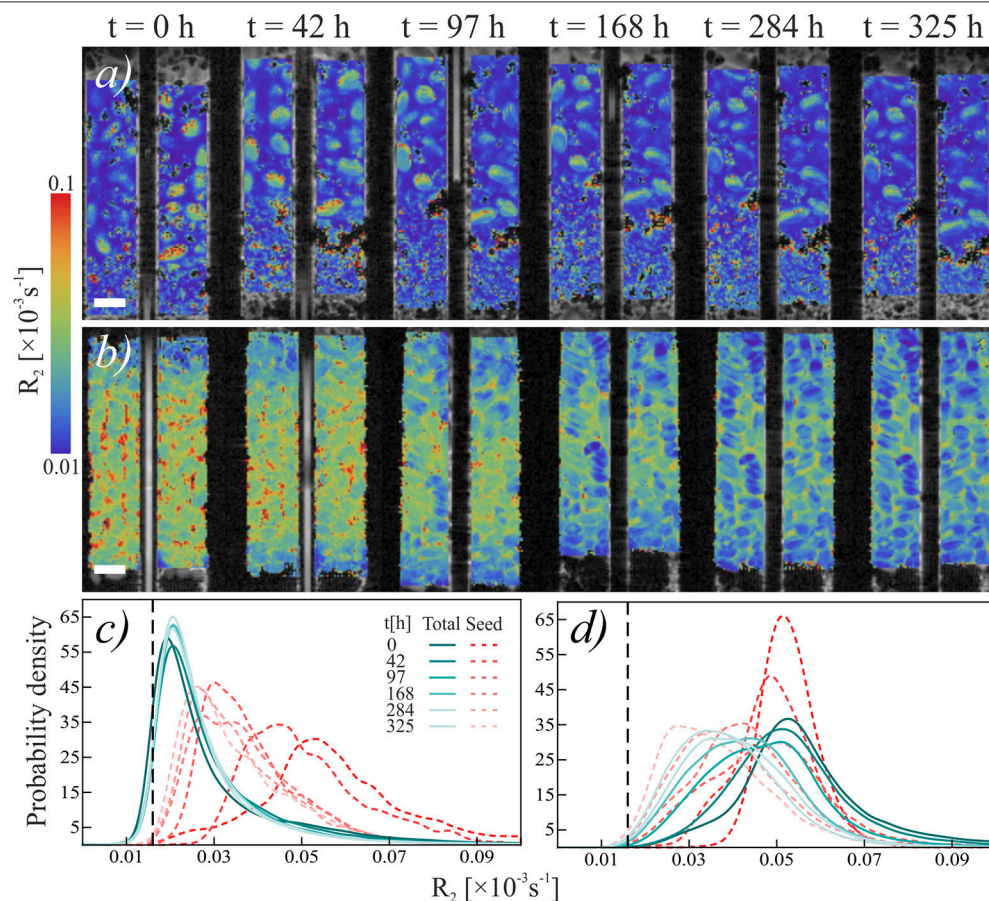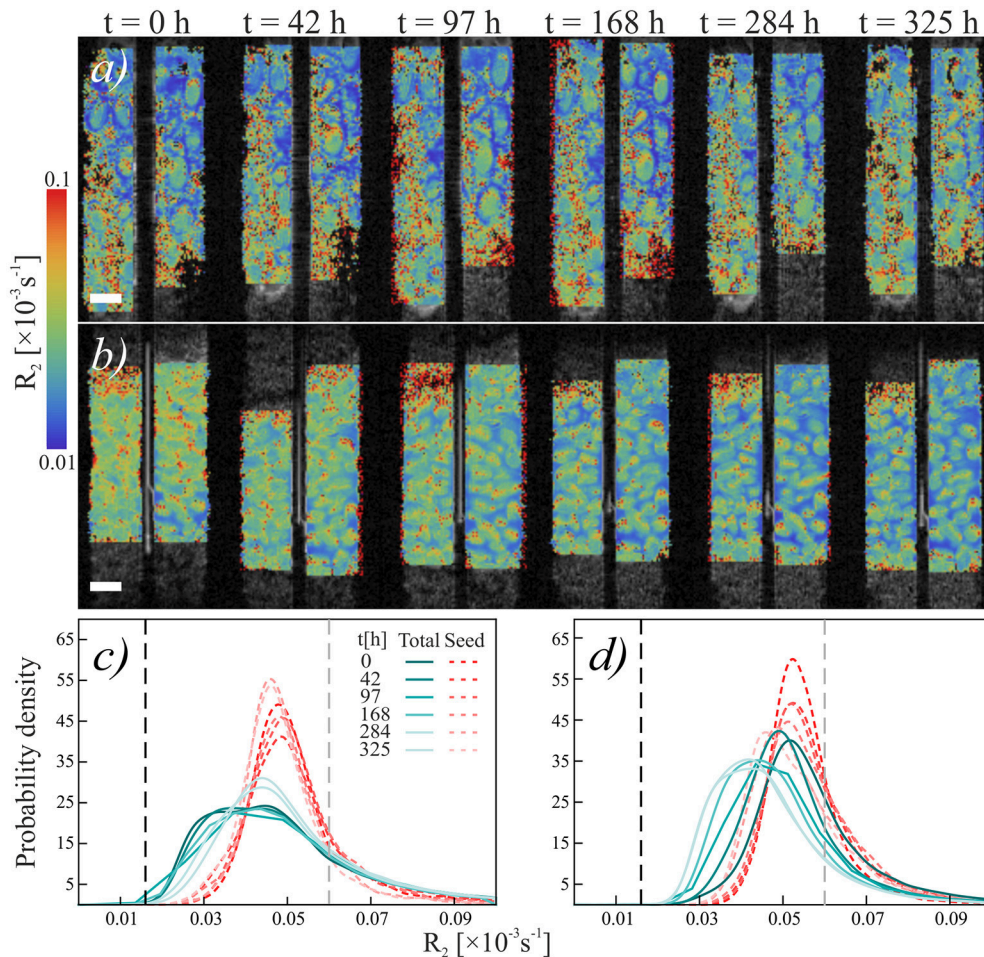
FIGURE 5 | Temporal development relaxation rate R_2 of chia seeds in quartz sand. **(a,b)** Temporal sequence of NMR scans of **(a)** loose chia in sand and **(b)** packed chia in sand. Colors indicate relaxation rate R_2. Scale bars are 2 mm. **(c,d)** Histograms of relaxation rate R_2 of **(c)** loose chia in sand and **(d)** packed chia in sand. Blue-green solid lines show R_2 in "Gel" region, red dashed lines show R_2 in "Seed" region. Black dashed reference line shows mean R_2 of water in the capillary, gray dashed reference line shows mean R_2 of water in quartz sand ($R_2 = 0.0595$).

showed that there is a concentration gradient of mucilage right at the interface of the chia seed. After 42 h, the degradation of mucilage gel manifests as a shift in ^{1}H transverse relaxation rate from faster to slower values, with the exception of the loosely packed quartz sample. In the loosely packed quartz sample, partly due to the smaller pore sizes (see **Figure S3**), this R_2 value is increasing to that of quartz pore water. Therefore, this implies a change in the mucilage molecular structure from a higher to a lower viscosity, which is consistent with degradation of mucilage to a more aqueous gel. Moreover, in both loosely packed regions there was less gel produced compared to the pure regions. Therefore, the starting R_2 and changes in the relaxation time were much smaller in these regions. The results here are consistent to those of Brax et al. (in press), where it is shown that a decrease in mucilage concentration decreases the R_2. X-ray CT results corroborate this finding, also showing that degradation of mucilage is accompanied by an increase in the air-filled void fraction, likely due to the breakdown by-product CO_2. Changes

in hydraulic and mechanical properties of chia mucilage from gel-like to water-like properties have previously been reported by Naveed et al. (2017). The key difference of chia mucilage, when compared to root mucilage, is the relatively high content of polysaccharides. This component of chia seed mucilage is responsible for the gel formation and higher viscosity (Read and Gregory, 1997; Goh et al., 2016). The decomposition of these sugar chains will cause a release of both trapped water in the dense fibril network and structurally absorbed water. In the present experimental setup this led to an increase of the matric potential and decrease of the viscosity of decomposed mucilage, and caused it to drain toward the lower compartment in the sample due to gravity. This is corroborated by the decrease in air-filled and increase in water-filled void fraction in the lower packed regions.

Structurally, at $t = 325$ h the remainder of the mucilage will consist of the more insoluble and slow-degrading long chain sugar fraction. These dehydrated long chain fibril structures form

FIGURE 6 | (a) Cutout of a horizontal slice of CT scan (chia pure) showing the filamentous network within air-filled voids including agglutinations (red arrows) of hydrated material. Larger hydraulic bridge indicated by blue arrow. Filamentous network was visualized by projecting the maximum gray value over 208 μm along the z-axis. Hydraulic bridge between chia seeds indicated by blue arrow. Pixel size in x- and y-direction is 20.8 μm. **(b–d)** Light microscope images of dehydrated chia mucilage in Nafion **(b)** and in sand **(c,d)**.

large bridging features between soil particles and seeds which are very similar to those described in Benard et al. (2017). These fibrils are found to be very stable and persist for over a month after the experiment. In the loosely packed regions in both Nafion and quartz, this degraded network of fibrils would have a lower capacity to retain water in the direct vicinity of the seeds, which is due to the relatively higher porosity in the gel-phase. These filaments do not represent the shape of the porous polymer network in a hydrated state, but may still play an important role in aggregate stability.

Although this is a first attempt in visualizing and quantifying the properties of mucilage *in situ* in 3D, more data under more realistic conditions is needed and this study should be viewed as a first step toward root exudate imaging. Many challenges, such as problems with salts and paramagnetic effects in soil, still remain. Although our study has shown the potential of NMR in visualizing organic material in a porous medium, more data under natural conditions is necessary. In this study, Nafion, which has been previously used in rhizosphere imaging studies (Downie et al., 2012), and quartz (to enhance contrast in CT scanning) were chosen to prevent the effects of high salts and paramagnetic effects, but data on real soil would be necessary to corroborate our observed results. Nevertheless, a correlative NMR imaging and CT study of bean roots within a mixed agricultural topsoil have been successfully applied and enabled the visualization of a dense root network (Zappala et al., 2013; Metzner et al., 2015). Depending on sample size, MRI in Metzner's study generally yielded a higher density of roots, compared to CT, where challenges remain with limited contrast between soil water and roots. Due to the big differences

in the molecular environment of water between soil-water and root-moisture, the root architecture was made visible in NMR relaxometry. Furthermore, Schaumann et al. (2005) investigated the differences in wetting and swelling kinetics of an organic-rich soil sample. ^{1}H-NMR relaxometry was successfully used in this contribution to distinguish between both swelling and wetting phenomena, which fundamentally investigated changes in pore size distribution in easily wettable pores and slowly wettable pores within soil organic matter (SOM). Additionally, Jaeger et al. (2006) investigated the effects of microbial activity on the relaxation time shifts within humous soil material. Even though in these studies no imaging was performed, it was found that hydration of organic matter and the formation of biofilms caused lower relaxation times and could be used to separate out different phases. However, it was stated that more investigation is needed on the exact effects of biofilms as well as paramagnetic substances, e.g., Fe and Mn, have on the relaxation times. Since mucilage is effectively a "humous" and porous medium, ^{1}H-NMR imaging might be potentially an effective tool to image rhizosphere processes *in situ* and *in vivo*. The combination with X-ray CT additionally allows to disentangle the effect of changing chemical properties of mucilage and pore geometry on the resulting relaxation rates. Nevertheless, challenges such as natural abundant artifacts and the differences between different mucilage types and concentrations need to be overcome. However, the information of mucilage provided by this technique might be paramount in understanding key processes in the rhizosphere and direct vicinity, which is currently not clearly understood.

AUTHOR CONTRIBUTIONS

AvV, MT, NK, GP, and TR all co-designed the study, analyzed the data, and co-wrote the manuscript.

FUNDING

ACKNOWLEDGMENTS

SUPPLEMENTARY MATERIAL

The Supplementary Material for this article can be found online at: https://www.frontiersin.org/articles/10.3389/fenvs.2018.00032/full#supplementary-material

Figure S1 | Three-dimensional segmentation of chia mucilage degradation in quartz loose region at $t = 0$ h and $t = 168$ h.

Figure S2 | Three major image processing steps on CT images. **(a)** Vertical raw CT slice after removal of capillary (black vertical stripe), **(b)** classification result of solid particles (red) and liquid phase (blue) and airfilled voids

(black), and **(c)** pore-size distribution of the liquid phase, warmer colors indicate bigger pore-sizes and cluster bigger than 0.3 are colored white.

Figure S3 | Histograms of local radius of the liquid phase in Nafion loose and sand loose at $t = 325$ h. Histogram bins are 20 μm, smallest detectable pore size is 40 μm. The red shaded area indicates the range of soil pores, the blue shaded area indicates the range covered by chia seeds.

REFERENCES

Ahmed, M. A., Kroener, E., Benard, P., Zarebanadkouki, M., Kaestner, A., and Carminati, A. (2016). Drying of mucilage causes water repellency in the rhizosphere of maize: measurements and modelling. *Plant Soil* 407, 161–171. doi: 10.1007/s11104-015-2749-1

Bais, H. P., Weir, T. L., Perry, L. G., Gilroy, S., and Vivanco, J. M. (2006). The role of root exudates in rhizosphere interactions with plants and other organisms. *Annu. Rev. Plant Biol.* 57, 233–266. doi: 10.1146/annurev.arplant.57.032905.105159

Benard, P., Zarebanadkouki, M., Hedwig, C., Holz, M., Ahmed, M. A., and Carminati, A. (2017). Pore-scale distribution of mucilage affecting water repellency in the rhizosphere. *Vadose Zone J.* 17:170013. doi: 10.2136/vzj2017.01.0013

Benizri, E., Nguyen, C., Piutti, S., Slezack-Deschaumes, S., and Philippot, L. (2007). Additions of maize root mucilage to soil changed the structure of the bacterial community. *Soil Biol. Biochem.* 39, 1230–1233. doi: 10.1016/j.soilbio.2006.12.026

Brax, M., Buchmann, C., and Schaumann, G. E. (in press). Effect of mucilage on water properties in the rhizosphere monitored by 1H-NMR relaxometry. *Microporous Mesoporous Mater.* doi: 10.1016/j.micromeso.2017.07.044

Brewer, R. (1964). *Fabric and Mineral Analysis of Soils*. New York, NY: Wiley.

Capitani, M. I., Ixtaina, V. Y., Nolasco, S. M., and Tomás, M. C. (2013). Microstructure, chemical composition and mucilage exudation of chia (*Salvia hispanica* L.) nutlets from Argentina. *J. Sci. Food Agric.* 93, 3856–3862. doi: 10.1002/jsfa.6327

Carminati, A., Moradi, A. B., Vetterlein, D., Vontobel, P., Lehmann, E., Weller, U., et al. (2010). Dynamics of soil water content in the rhizosphere. *Plant Soil* 332, 163–176. doi: 10.1007/s11104-010-0283-8

Carminati, A., and Vetterlein, D. (2013). Plasticity of rhizosphere hydraulic properties as a key for efficient utilization of scarce resources. *Ann. Bot.* 112, 277–290. doi: 10.1093/aob/mcs262

Chaboud, A. (1983). Isolation, purification and chemical composition of maize root cap slime. *Plant Soil* 73, 395–402. doi: 10.1007/BF02184316

Downie, H., Holden, N., Otten, W., Spiers, A. J., Valentine, T. A., and Dupuy, L. X. (2012). Transparent soil for imaging the rhizosphere. *PLoS ONE* 7:e44276. doi: 10.1371/journal.pone.0044276

Fincher, G. B., Stone, B. A., and Clarke, A. E. (1983). Arabinogalactan-proteins: structure, biosynthesis, and function. *Annu. Rev. Plant Physiol.* 34, 47–70. doi: 10.1146/annurev.pp.34.060183.000403

Fox, D. I., Pichler, T., Yeh, D. H., and Alcantar, N. A. (2012). Removing heavy metals in water: the interaction of cactus mucilage and arsenate (As (V)). *Environ. Sci. Technol.* 46, 4553–4559. doi: 10.1021/es2021999

Goh, K. K., Matia-Merino, L., Chiang, J. H., Quek, R., Soh, S. J., and Lentle, R. G. (2016). The physico-chemical properties of chia seed polysaccharide and its microgel dispersion rheology. *Carbohydr. Polym.* 149, 297–307. doi: 10.1016/j.carbpol.2016.04.126

Huang, Z., and Gutterman, Y. (1999). Germination of Artemisia sphaerocephala (Asteraceae), occurring in the sandy desert areas of Northwest China. *South Afr. J. Bot.* 65, 187–196. doi: 10.1016/S0254-6299(15)30972-8

Jaeger, F., Grohmann, E., and Schaumann, G. E. (2006). 1H NMR relaxometry in natural humous soil samples: insights in microbial effects on relaxation time distributions. *Plant Soil* 280, 209–222. doi: 10.1007/s11104-005-3035-4

Knee, E. M., Gong, F. C., Gao, M., Teplitski, M., Jones, A. R., Foxworthy, A., et al. (2001). Root mucilage from pea and its utilization by rhizosphere bacteria as a sole carbon source. *Mol. Plant-Microbe Interact.* 14, 775–784. doi: 10.1094/MPMI.2001.14.6.775

Kroener, E., Zarebanadkouki, M., Kaestner, A., and Carminati, A. (2014). Nonequilibrium water dynamics in the rhizosphere: how mucilage affects water flow in soils. *Water Resour. Res.* 50, 6479–6495. doi: 10.1002/2013WR014756

Mary, B., Fresneau, C., Morel, J. L., and Mariotti, A. (1993). C and N cycling during decomposition of root mucilage, roots and glucose in soil. *Soil Biol. Biochem.* 25, 1005–1014. doi: 10.1016/0038-0717(93)90147-4

McCully, M. E., and Boyer, J. S. (1997). The expansion of maize root-cap mucilage during hydration. 3. changes in water potential and water content. *Physiol. Plant.* 99, 169–177. doi: 10.1111/j.1399-3054.1997.tb03445.x

Metzner, R., Eggert, A., van Dusschoten, D., Pflugfelder, D., Gerth, S., Schurr, U., et al. (2015). Direct comparison of MRI and X-ray CT technologies for 3D imaging of root systems in soil: potential and challenges for root trait quantification. *Plant Methods* 11:17. doi: 10.1186/s13007-015-0060-z

Muñoz, L. A., Cobos, A., Diaz, O., and Aguilera, J. M. (2012). Chia seeds: microstructure, mucilage extraction and hydration. *J. Food Eng.* 108, 216–224. doi: 10.1016/j.jfoodeng.2011.06.037

Naveed, M., Brown, L. K., Raffan, A. C., George, T. S., Bengough, A. G., Roose, T., et al. (2017). Plant exudates may stabilize or weaken soil depending on species, origin and time. *Eur. J. Soil Sci.* 68, 806–816. doi: 10.1111/ejss.12487

Read, D. B., and Gregory, P. J. (1997). Surface tension and viscosity of axenic maize and lupin root mucilages. *New Phytol.* 137, 623–628. doi: 10.1046/j.1469-8137.1997.00859.x

Salgado-Cruz, M. d. l. P., Calderón-Domínguez, G., Chanona-Pérez, J., Farrera-Rebollo, R. R., Méndez-Méndez, J. V., and Díaz-Ramírez, M. (2013). Chia (*Salvia hispanica* L.) seed mucilage release characterisation. a microstructural and image analysis study. *Indust. Crops Prod.* 51, 453–462. doi: 10.1016/j.indcrop.2013.09.036

Schaumann, G. E., Hobley, E., Hurrab, J., and Rotard, W. (2005). H-NMR relaxometry to monitor wetting and swelling kinetics in high-organic matter soils. *Plant Soil* 275, 1–20. doi: 10.1007/s11104-005-1708-7

Schindelin, J., Arganda-Carreras, I., Frise, E., Kaynig, V., Longair, M., Pietzsch, T., et al. (2012). Fiji: an open-source platform for biological-image analysis. *Nat. Methods* 9, 676–682. doi: 10.1038/nmeth.2019

Walker, T. S., Bais, H. P., Grotewold, E., and Vivanco, J. M. (2003). Root exudation and rhizosphere biology. *Plant Physiol.* 132, 44–51. doi: 10.1104/pp.102.019661

Watanabe, T., Misawa, S., Hiradate, S., and Osaki, M. (2008). Characterization of root mucilage from Melastoma malabathricum, with emphasis on its roles in aluminum accumulation. *New Phytol.* 178, 581–589. doi: 10.1111/j.1469-8137.2008.02397.x

Zappala, S., Mairhofer, S., Tracy, S., Sturrock, C. J., Bennett, M., Pridmore, T., et al. (2013). Quantifying the effect of soil moisture content on segmenting root system architecture in X-ray computed tomography images. *Plant Soil* 370, 35–45. doi: 10.1007/s11104-013-1596-1

in Environmental Science

frontiers

Can The Pore Scale Geometry Explain Soil Sample Scale Hydrodynamic Properties?

Sarah Smet [1]*, Eléonore Beckers [1], Erwan Plougonven [2], Angélique Léonard [2] and Aurore Degré [1]

[1] Soil Water Plant Exchanges, BIOSE, Gembloux Agro-Bio Tech, University of Liège, Gembloux, Belgium, [2] Chemical Engineering, University of Liège, Liège, Belgium

For decades, the development of new visualization techniques has brought incredible insights into our understanding of how soil structure affects soil function. X-ray microtomography is a technique often used by soil scientists but challenges remain with the implementation of the procedure, including how well the samples represent the uniqueness of the pore network and structure and the systemic compromise between sample size and resolution. We, therefore, chose to study soil samples from two perspectives: a macroscopic scale with hydrodynamic characterization and a microscopic scale with structural characterization through the use of X-ray microtomography (X-ray μCT) at a voxel size of 21.5^3 μm^3 (resampled at 43^3 μm^3). The objective of this paper is to unravel the relationships between macroscopic soil properties and microscopic soil structure. The 24 samples came from an agricultural field (*Cutanic Luvisol*) and the macroscopic hydrodynamic properties were determined using laboratory measurements of the saturated hydraulic conductivity (Ks), air permeability (ka), and retention curves (SWRC). The X-ray μCT images were segmented using a global method and multiple microscopic measurements were calculated. We used Bayesian statistics to report the credible correlation coefficients and linear regressions models between macro- and microscopic measurements. Due to the small voxel size, we observed unprecedented relationships, such as positive correlations between log(Ks) and a μCT global connectivity indicator, the fractal dimension of the μCT images or the μCT degree of anisotropy. The air permeability measured at a water matric potential of -70 kPa was correlated to the average coordination number and the X-ray μCT porosity, but was best explained by the average pore volume of the smallest pores. Continuous SWRC were better predicted near saturation when the pore-size distributions calculated on the X-ray μCT images were used as model input. We also showed a link between pores of different sizes. Identifying the key geometrical indicators that induce soil hydrodynamic behavior is of major interest for the generation of phenomenological pore network models. These models are useful to test physical equations of fluid transport that ultimately depend on a multitude of processes, and induce numerous biological processes.

Keywords: soil, X-ray micro-computed tomography, saturated hydraulic conductivity, soil water retention curve, air permeability, Bayesian statistics

INTRODUCTION

The development of visualization techniques has played a major role in fully describing soil functions. Serial sectioning, a well-established method (Cousin et al., 1996), has been replaced by replaced by 3D non-destructive visualization techniques are becoming more easily available, with added benefit of less time-consuming procedures that provide higher resolution images (Grevers et al., 1989). However, Roose et al. (2016) have wisely said, "Technological advances alone are not sufficient. Real advances in our understanding will only be achieved if these data can be integrated, correlated, and used to parameterize and validate image based and mechanistic models." X-ray micro-computed tomography (X-ray μCT) has been widely used in soil science making comparisons between studies possible. (Taina et al., 2008) and Wildenschild and Sheppard (2013) discuss the use of X-ray μCT to study the vadose zone. We also will mention the visual analysis of the air and water distributions within pore spaces, which are both important physical variables for activity of soil biota (e.g., Young et al., 1998; Or et al., 2007; Falconer et al., 2012; Monga et al., 2014; Vogel et al., 2015). One approach is to visualize the soil at high resolution to identify hot-spots of microbial activity (e.g., Gutiérrez Castorena et al., 2016), simulate air-water interfaces within the pore network (e.g., Pot et al., 2015) or quantify the impact of the pore network architecture on the microorganism's activity (e.g., Kravchenko and Guber, 2017). Another approach is to provide a more specific description of the fluid transport capacities (Vogel et al., 2015) which could ultimately improve field-scale models of microbial activity and biochemical processes (Blagodatsky and Smith, 2012). De facto, when dealing with agricultural and environmental properties of the soil, an accurate description and prediction of its transport capacities in the unsaturated state is the overarching goal.

It is well-known that, due to natural or anthropogenic actions, there is quite a range in the variability in fluid transport parameters [e.g., saturated hydraulic conductivity (Ks) or air permeability (ka)] between samples with homogenous textures (Baveye and Laba, 2015; Naveed et al., 2016), due to the uniqueness of the porosity distribution and the connectivity within a sample. Studies have, therefore, focused on the link between the inner pore space structure of a sample and its specific fluid transport properties. On one hand, experimentally visualized infiltration studies shed light on the effective conducting pore network which represents only a small portion of the total network (Luo et al., 2008; Koestel and Larsbo, 2014; Sammartino et al., 2015). The procedures developed in these studies are promising, but restricted to the analysis of large macropores because of the trade-off between resolution and acquisition time. On the other hand, numerical simulations based on pore space are used to predict conductivity. Many studies focused on idealized porous structures (e.g., Vogel et al., 2005; Schaap et al., 2007) and a few deal with actual soil (Elliot et al.,

Abbreviations: h, water matric potential; θ, water content; SWRC, soil water retention curve; Ks, saturated hydraulic conductivity; ka, air permeability; LabPO, laboratory measured air-filled porosity at a water matrix potential of 1 kPa; BF, Bayes factor. The rest of the uncommon abbreviations are defined in **Table 1**.

2010; Dal Ferro et al., 2015; Tracy et al., 2015). The latter show encouraging results, but are restricted to a defined resolution and/or sample size (Baveye et al., 2017). Indeed, the direct approach of linking one structure to one function is limited by the difficulty in analyzing the structure in a representative way, so that the soil is adequately characterized (Vogel et al., 2010). The description of soil microscopic structure via global characteristics could encompass that challenge and comparisons of one soil microscopic structure to its own macroscopic properties have indeed gained attention.

Luo et al. (2010) were among the first to measure Ks and the break through curve characteristics on soil samples that were also scanned with X-ray μCT and analyzed in 3D (16 soil cores of 5×6 cm and 10.2×35 cm and voxel sizes ranging from $250^2 \times 1,000$ μm^3 to $1^2 \times 10$ mm^3). They found that μCT macroporosity, the number of independent macropore, macropore hydraulic radius and angle were identified as the most important microscopic characteristics to explain fluid transport. From 18 soils cores (10×9 cm) scanned at a voxel size of 186^3 μm^3 and 17 soil cores (19×20 cm) scanned at $430^2 \times 600$ μm^3, respectively, Naveed et al. (2012) and Katuwal et al. (2015b) found that the lowest μCT macroporosity value for any quarter length of sample height adequately explained air permeability (ka) measured at a water matric potential (h) of −3 or −2 kPa, respectively. Paradelo et al. (2016) showed that the minimum value of macroporosity along a sample depth was most correlated to Ks and ka (45 soil cores of 20×20 cm and voxel size of $430^2 \times 600$ μm^3). Mossadeghi-Björklund et al. (2016) also demonstrated that Ks was significantly correlated to μCT macroporosity within a compaction experiment (32 soils cores of 20×20 cm and voxels size of $430^2 \times 600$ μm). Eventually, Naveed et al. (2016) suggested that biopore-dominated and matrix-dominated flow soil cores should be distinguished before analyzing relationships between microscopic and macroscopic soil properties. They indeed found distinct significant power regressions between Ks or ka (measured at $h = -3$ and −0 kPa) and μCT macroporosity for the two categories of the 65 soil cores (6×3.5 cm and voxel size of 129^3 μm^3). These observed relationships between flow parameters and μCT porosity are actually intuitive, but they depend on image resolution, water matric potential and soil type. For example, Lamandé et al. (2013) did not find the expected relationship between μCT porosity and ka measured at $h = -10$ kPa, but rather a linear positive relationship between the number of pores and ka (32 soil cores of 19×20 cm and voxel size of 600^3 μm^3). Finally, Anderson (2014) found that Ks could reasonably be estimated from the μCT number of pores and the μCT macroporosity fractal dimension (336 soil cores of 7.62×7.62 cm and voxel size of $0.19^2 \times 0.5$ μm^3).

The μCT porosity, number of pores, average pore radius, surface area, and pore network connectivity and tortuosity all depend on the minimal visible pore size, in other words, on the resolution of the binary X-ray μCT images used to obtain the pore network (Houston et al., 2013; Peng et al., 2014; Shah et al., 2016), additionnaly, useful information about conducting pores is lost with increased voxel size. One strategy to minimize this limitation is to use grayscale information. Crestana et al. (1985) demonstrated a linear dependence between the gray value of the

soil matrix in Hounsfield unit (HU) and the soil water content. More recently, Katuwal et al. (2015a) found the CT number of the soil matrix (average grayscale value in HU) as a useful descriptor for determining the magnitude of preferential flow, and Paradelo et al. (2016) showed that global macroporosity values combined with the CT-matrix number best explained the variation in air and water transport parameters. Another strategy would be to scan soil samples at higher resolutions. For example, Sandin et al. (2017) worked at a voxel size of 120^3 μm^3 and observed significant correlations between Ks and a global measure of the pore network connectivity (from the percolation theory) which had, to our knowledge, never been observed (20 soil samples of 6.8×10 cm). Pore network connectivity and tortuosity are important indicators of flow capacities (Perret et al., 1999; Vogel, 2000). There is still a lack of information on the links between global pore network complexity indicators and flow parameters. It is indeed challenging to identify and describe the part of the conducting pore network that dominates flow. We, however, hypothesize that it might come from the resolution at which previous studies were performed.

Within that context, the objectives of this study are to: (i) characterize the microscopic structure of twenty-four soil samples at a resolution of 21.5 μm resampled to 43 μm; and (ii) explore the relationships between soil microscopic characteristics and its saturated hydraulic conductivity, air permeability and retention capacities using Bayesian statistics.

MATERIALS AND METHODS

Soil Sampling
Twenty-four vertical undisturbed soil samples (3 cm in diameter and 5 cm in height) were taken at the surface of an agricultural soil in Gembloux, Belgium (50°33′N, 4°42′E). According to the WRB soil system (2006), this soil is classified as a *Cutanic Luvisol* with an average of 14.3% of clay, 78.3% of silt and 7.4% of sand. This type of soil is representative of the intensive central agricultural area in Belgium. Sampling was performed 24 to 48 h after a rain. In order to minimize sampling disturbance, the plastic cylinders were manually driven into the soil until the top of the cylinder was at the surface level and then manually excavated.

Macroscopic Measurements
Soil samples were first upward saturated with distilled water. Their characteristic soil water retention curve (SRWC) was then measured using pressure plates (Richards, 1948; DIN ISO 11274, 2012). After being weighed at a water matric potential of −7, −10, −30 and −70 kPa, the air permeability of the samples was measured by applying an air flow across the sample and measuring the resulting inner-pressure with an Eijkelkamp air permeameter 08.65 (Eijkelkamp Agrisearch Equipment, Giesbeek, The Netherlands). As recommended by the constructor, each measure was repeated five times and kept as short as possible. Corey's law was then applied to calculate the air permeability [L²] (Corey, 1986 in Olson et al., 2001). At −70 kPa, the soil samples were scanned using an X-ray microtomograph (see next section) before the end of their SWRC

was measured (water matric potential of −100, −500, and −1500 kPa). After reaching −1,500 kPa, the soil samples were saturated once again and the saturated hydraulic conductivity (Ks [LT^{-1}]) was measured using a constant head device (Rowell, 1994) and applying Darcy's law. Finally, the soil samples were oven-dried at 105° for 7 days to obtain their dry weight. Porosity [L^3L^{-3}] was calculated as the ratio between the volume of water within the saturated soil sample and its total volume (McKenzie et al., 2002). From McKenzie et al. (2002), the bulk density (BD) [ML^{-3}] was deduced from the porosity value (PO) assuming a particle density of 2.65 g/cm³.

Microscopic Measurements
Image Acquisition
After reaching a water matric potential of −70 kPa, the soil samples were scanned using a Skyscan-1172 desktop micro-CT system (Bruker microCT, Kontich, Belgium). The choice of scanning parameters (filters, number of projections, 180 or 360°, projection averaging) was made by evaluating reconstruction quality over acquisition time. The X-ray source was set at 100 kV and 100 μA and an aluminum-copper filter was used to reduce the beam hardening artifacts in the reconstruction. The rotation step was set at 0.3° over 180° and, to improve the signal-to-noise ratio, the average of 2 projections was recorded at each rotation step. The exposure time was 600 ms. The field of view was 21 × 14 mm and, to cover the entire sample, a 2 × 4 grid of sub-regions were scanned (in the Skyscan software this corresponds to using both the "wide image" mode and "oversize scan" mode). Given these parameters, the total acquisition time was ∼4 h. We adjusted the detector configuration (16-bit X-ray camera with 4 × 4 binning, creating 1000 × 666 pixel radiograms) and the distance between the camera and the soil sample in order to obtain radiographs with a pixel size of 21.5 μm.

Image Processing
Tomographic reconstruction was performed with the NRecon® software, freely provided by Brüker. Automatic misalignment compensation was used along with a level 7 (out of 20) ring artifact correction. No beam hardening post-corrections were applied. The lower limit for the histogram grayscale range was set at zero, as recommended by Tarplee and Corps (2008). The upper limit, the same for all samples, was the maximum value between the automatically generated upper limit for each sample. After reconstructions, the 3D images were cropped to only select the volume within the sampling cylinders (radius of 700 pixels) and the image's contrast was improved in Matlab (MathWorks, UK).

Prior to segmentation, a 3D median filter with a radius of 2 pixels was applied to the images to decrease noise (Smet et al., 2017). Because of computational cost, sub-sampling was performed and the final voxel size was 43 μm in all directions. This process follows recommendation from Houston et al. (2013) and Shah et al. (2016), which is to scan a sample at the highest possible resolution even if a post-scan coarsening is necessary. We then applied the global porosity-based segmentation method developed by Beckers et al. (2014b). To that purpose, we firstly calculated the potential maximal visible pore size from capillary

law and voxel size information ($43^3\,\mu m^3$). Then, from the laboratory SWRC data, the potential visible porosity for each soil samples was obtained; it was the air-filled porosity at $h = -1$ kPa (equivalent radius of $150\,\mu m$). The porosity-based segmentation method selects an initial global threshold with Otsu's method (Otsu, 1979), and then compares the porosity of the resulting binary image (ratio of pore voxels over the total amount of voxels) to the estimated soil sample visible porosity. Through an iterative loop, the threshold is then adjusted to minimize the difference between this calculated porosity and the estimated soil sample visible-porosity. This method has been proven satisfactory (Beckers et al., 2014b; Smet et al., 2017) and the Matlab R2015a (MathWorks, UK) code was provided by the authors. Finally, a visual inspection was performed to evaluate the segmentation quality and, in case the porosity-based segmentation method failed, Otsu's segmentation was used. A post-segmentation cleanup was applied to remove any pores smaller than five voxels.

Quantification of Soil Microscopic Features

After segmentation, the images were imported into Avizo where codes developed by Plougonven (2009) were used. Those codes provide a 3D morphological quantification of the pores based on the skeleton where a pore is defined as "part of the pore space, homotopic to a ball, bounded by the solid, and connected to other pores by throats of minimal surface area" (Plougonven, 2009), the pore boundaries are demarcated by the local geometry. The resulting 3D quantification information regarding pores chambers connected by pores throats included pore localization, volumes, specific surface, connected surfaces, number of connections, deformation and inertia tensor. From those data, we calculated several microscopic parameters (**Table 1**) as well as the pore-size distribution with radius calculated from the assumption that pores were elliptic cylinders (Beckers et al., 2014a). After morphological processing in Avizo, we imported the binary images in ImageJ (Schneider et al., 2012) where the BoneJ plugin (Doube et al., 2010) functionalities were used; all the measurements into ImageJ were performed in 3D. The skeletonisation tool was used to find the pore's centerline and extract a skeleton made of branches that are connected by junctions. It was achieved by external erosion with a 3D medial axis thinning algorithm. All the calculated microscopic parameters presented in **Table 1** are commonly used in studies regarding the use of X-ray in soil science. We calculated the large porosity (Large_PO) in order to be comparable to the results discussed in the introduction of this paper where the voxel size was ~10 times larger.

3D Visualization

In order to obtain clear 3D representations, all 24 soil X-ray μCT images were subjected to the following process: any pore that was not part of the largest connected component was removed using the MorphoLib plugin (Legland et al., 2016) in ImageJ (Schneider et al., 2012), a cylindrical region of interest of 295 pixels in radius was then used to remove the edge effects caused by sampling with the initial height going unchanged. Visualization was performed

using the 3DViewer plugin (Schmid et al., 2010) in ImageJ (Schneider et al., 2012).

Results Analysis

Basic descriptive statistics were performed on the macroscopic and microscopic data. The correlation coefficients (ρ) between the different microscopic parameters were then calculated using Bayesian statistics (see next section) to account for data uncertainty. Then, Bayesian correlation coefficients were calculated between relevant microscopic and macroscopic measurements as well as Bayesian linear regression models. Before implementation, the data were randomly split into calibration (18 soil samples) and validation (6 soil samples) sets. To that purpose, a number was assigned to each of the 24 soil samples and six numbers were randomly picked. Therefore, the soil samples have a sequential numbering. The calibration set includes samples from #1 to #18 and the validation set from #19 to #24.

Bayesian Statistics for Correlation and Linear Regression

When a linear relationship was visually assumed between two variables, the correlation coefficient between those two variables was calculated using Bayesian statistics. In Bayesian statistics a probability is assigned to a model [P(observations|model)] rather than to an observation, as in frequentist statistics. From the observations, the models (the *prior*) are updated to *posterior* distributions [P(model|observations)] and the uncertainty of the statistic description is expressed in a probabilistic way through the posterior distributions parameters. We refer to Marin and Robert (2007) for more information about Bayesian statistics. In this study, we used the package "BayesMed" (Nuijten et al., 2015) in R (R Core Team, 2015), which computes a Bayesian correlation test, the null hypothesis (H_0) being that the correlation coefficient is null. The correlation test is based on a linear regression between two variables with a Jeffreys-Zellner-Siow (JZS) prior as a mixture of g-priors (Liang et al., 2008; Wetzels and Wagenmakers, 2012). The correlation coefficient is extracted from the posterior variance matrix. We computed the test without expectation about the direction of the correlation effect (Wagenmakers et al., 2016). The credibility of the test is assumed by comparing the marginal likelihoods of the regression model to the same regression model without the explaining variable (Bayes Factor, BF), which quantify the evidence for one or the other hypothesis. Another advantage of using the Bayesian approach is the possibility of quantifying the evidence for the null hypothesis (Wetzels and Wagenmakers, 2012). Non-significant tests in frequentist statistics are interpreted in favor of the null hypothesis although the result could be induced by a noisy data set. Therefore, because the posterior distributions are updated from the observations, the conclusion of the test will not depend on the number of observations and it is possible to recalculate BF as the observations are logged-in and stop the collect when the evidence is compelling. Adapted from Jeffreys (1961) in Wetzels and Wagenmakers (2012), BF's larger than 100 were interpreted as decisive evidence for H_1; BF's between 30 and 100 as a very strong evidence for H_1, BF's between 10 and 30 as a strong

TABLE 1 | Calculated microscopic parameters on the X-ray μCT images and their definition.

	Microscopic parameter (abbreviation, metric)	Definition
Avizo	Porosity (μCT_PO, %)	Ratio of pore voxels over the total amount of voxels
	Large porosity (Macro_PO,%)	Part of the porosity composed by pores of at least 1,000 voxels
	Number of pores (NP, –)	Total number of pores
	Averaged pore volume (Avg_vol, mm^3)	Ratio of the total volume of pores over the number of pores
	Averaged pore volume of the biggest pores (Avg_Bvol, mm^3)	The biggest pores are the ones that account for 90% of the pores volumes by only representing 10% of the number of pores
	Averaged pore volume of the smallest pores (Avg_Svol, mm^3)	The smallest pores are the ones that account for 10% of the pores volumes by representing 90% of the number of pores
	Proportion of isolated pores (IP, %)	Ratio of the number of pores that have no connection over the total number of pores
	Proportion of isolated porosity (IPO, %)	Ratio of the isolated porosity over the total porosity
	Averaged coordination number(Avg_Z, –)	The average of Z, which is the number of connections at one point (Perret et al., 1999), of the connected pores
	Averaged surface connectivity (SC, L^{-1})	The average of sc which is sc = Nc * Ac / Vp, where Nc is the number of connections, Ac the mean surface area of the connections (L^2) and Vp the pore volume (L^3)
	Total surface connected (Con_surf, mm^2)	The sum of each pore's connected surface
	Specific surface (SS, m^{-1})	Sum of the specific surface of each pore which is the ratio of the pore surface area over its volume
Av. + IJ	Global connectivity (Γ, –)	The sum of each pore's volume squared divided by the total volume of pores. It measures the probability that two pores voxel are part of the same pore (Renard and Allard, 2013).
Image J	Total length of the pore network (L, m)	After skeletonization, it is the sum of all the branches length
	Total nomber of branches (B, –)	After skeletonization
	Total number of junctions (J, –)	After skeletonization
	Degree of connectivity (B/J, –)	Ratio of the number of branches over the number of junctions. As negative is the ratio, as connected should be the medium
	Global tortuosity (τ, m^{-1})	The geometric tortuosity between two points is the ratio between the effective pore path and the shortest distance between the two extreme points (Perret et al., 1999). We calculated the global tortuosity (τ) of the pore network as the average of the tortuosity of each branch
	Fractal dimension (FD, –)	FD was calculated with a box-counting algorithm (Perret et al., 2003)
	Degree of anisotropy (DA, –)	The value of DA is between 0 and 1, 0 for an isotropic medium. DA was calculated with the mean intercept length method (Harrigan and Mann, 1984)
	Euler number (ε, –)	The Euler number is a quantification of the connectivity. Originaly calculated as ε =N-L+O, where N is the number of isolated objects; L is the number of redundant connections and O the number of cavities or holes (Vogel et al., 2010). As negative is the Euler number, as connected is the medium
	Lowest Euler number (Min_ε, –)	The Euler number of the largest connected component of the pore network

evidence for H$_1$, BF's between 3 and 10 as a substantial evidence for H$_1$ and BF's below 3 as an anecdotal evidence for H$_1$. The values of BF's that were inferior to one (1/100; 1/30; 1/10; 1/3) were interpreted in the same way as the BF values superior to one, the evidence going for H$_0$.

We also established a Bayesian linear regression design to extract relationships between micro- and macroscopic measurements. All combinations between Y and $X_1 + X_2$ were tested and regression models were compared against the same models without the explaining variable (BF). The variables priors were JZS prior as a mixture of g-priors (Liang et al., 2008). We used the "BayesFactor" package (Morey and Rouder, 2015) in R (R Core Team, 2015), the autocorrelation and the convergence were verified. In Bayesian statistics, the starting point is not to identify the best regression equation but rather evaluate the unknown values of the equation explaining variables and intercept. We did it through the quantification of the 2.5 and 97.5% quantiles. The regression equations are reported in the Supplementary Materials section. Afterwards, we aimed at

predicting the validation data points through the use of the slopes and intercepts posterior mean. The relative root mean square errors (RRMSE) were calculated as follows:

$$RRMSE = \sqrt{\frac{1}{n} \sum_{i=1}^{n} \left(\frac{d_i - D_i}{D_i} \right)^2} \qquad (1)$$

Where n is the number of data points, d_i is the predicted data point and D_i the observed data point.

RESULTS AND DISCUSSIONS
Macroscopic Measurements
The agricultural soil we studied showed large variations between samples with porosity values ranging from 43.09 to 57.70% and density from 1.12 to 1.51 g/cm^3. **Table 2** presents the maximum, minimum, and average values as well as the associated standard deviations of the logarithmic saturated hydraulic conductivities

Logarithmic saturated hydraulic conductivities (Ks, cm/day) and air permeability (ka, μm^2) measured after applying a draining pressure of -4, -7, -10, -30, and -70 kPa for the calibration and validation data sets [minimum values (Min), maximum values (Max), mean values (Mean), and standard deviation (St dev)].

	[cm/d]	log [μm^2]				
	log(Ks)	ka(-4 kPa)	ka(-7 kPa)	ka(-10 kPa)	ka(-30 kPa)	ka(-70 kPa)
CALIBRATION DATA SET						
Max	1.591	2.920	3.076	2.992	3.235	3.231
Min	0.443	0.059	0.017	0.095	0.418	0.936
Mean	1.015	1.681	1.735	1.916	2.164	2.318
St error	0.149	0.505	0.478	0.478	0.603	0.400
VALIDATION DATA SET						
Max	1.709	1.773	2.532	2.718	2.837	3.217
Min	0.352	0.395	-0.051	0.581	1.077	0.402
Mean	1.149	1.132	1.018	1.601	1.852	1.885
St error	0.400	0.801	1.028	1.013	0.893	0.891
ALL DATA						
Max	1.709	2.920	3.076	2.992	3.235	3.231
Min	0.352	0.059	-0.051	0.095	0.418	0.402
Mean	1.049	1.584	1.572	1.853	2.086	2.220
St error	0.147	0.443	0.445	0.424	0.496	0.376

[Ks (cm/day)] and air permeabilitys [ka (μm^2)]. As expected, the range of Ks and ka values is large due to the singular nature of pore network organization and the resulting transfer properties. For all studied soil samples, we observed a power-law type relationship between ka and the associated air-filled porosity measured from the SWRC (e.g., Ball and Schjønning, 2002). There was, however, no linear relationship between log(Ks) and log(ka) as opposed to what has been shown in other studies (e.g., Loll et al., 1999; Mossadeghi-Björklund et al., 2016). Those transport properties, as well as the water content at various matric potentials, were compared to the microscopic measurements made on the X-ray images.

X-ray μCT Images Analysis

The segmentation step, within the image processing scheme, has a great impact on the visible porosity calculated on the X-ray μCT image and on the extracted microscopic measurements (Lamandé et al., 2013; Smet et al., 2017). We, therefore, visually verified the accuracy of the global segmentation on each of the 24 X-ray μCT images by superimposing the grayscale images on the binary images. It appears that the porosity-based global segmentation method did not provide satisfactory results for two soil X-ray μCT images (#6 from the calibration set and #20 from the validation set). Those samples had a large air-filled porosity at $h = -1$ kPa (Lab_PO); the porosity-based segmentation method increased the threshold (increased μCT_PO) in order to obtain a μCT_PO as close as possible to Lab_PO [resulting threshold of 94 (0–255)]. In addition, the algorithm did not converge for one soil sample (#2), which had a large Lab_PO. Otsu's method was, therefore, applied to those three samples and the global threshold values for samples #2, #6, and #20 were 67, 69, and 69 (0–255), respectively. The threshold values

comparisons obtained with the porosity-based method for the other samples supported this processing choice; the averaged threshold value was 63 ($\pm$ 0.75). Finally, the samples #10, #13, #16 and #17 were segmented using the Otsu's method because their soil water retention curves (SWRC) were not measured. **Figure 1** presents a 3D visualization of each soil sample (calibration and validation sets) followed by a 2D vertical slice from the middle of the soil sample. We will refer to this figure within the Results section.

Microscopic Measurements

Table 3 presents the data ranges, averages and associated standard deviations for all the previously introduced microscopic measurements made on the X-ray μCT soil images (**Table 1**). The calculated μCT porosities, taking into account pores of at least five voxels, were only slightly higher than those calculated taking into account pores of at least 1,000 voxels. The differences represented $\pm$ 90% of the number of pores (the pores having a volume between five and 1,000 voxels happened to be the "small pores" as defined in **Table 1**). There was no surprise that we observed longer pore networks (L), higher numbers of pore branches (B) and junctions (J) than Katuwal et al. (2015b) or Garbout et al. (2013) who both worked with larger voxel sizes. Consequently to the high number of pores (NP), the observed Euler numbers (ε) were frequently highly positive and the differences between the percentage of isolated pore (IP) and isolated porosity (IPO) was large. Comparisons to others studies are however tricky because the pore network skeleton is highly sensitive to the scanning equipment and procedure, the image processing, the skeletonisation process and the pore identification.

Table 4 provides the credible (BF > 3) Bayesian correlation coefficients between each of the microscopic measurements. The coefficients were initially calculated for the calibration data and then the validation data were included. In Bayesian statistics, the number of observations does not count for the credibility of a hypothesis, so when a BF was improved with the addition of the validation data, it meant that the correlation was more credible thanks to the observation *values*. The BF were highlighted with colors according to the classes described in the Materials and Methods section. We did not compute the Bayesian regression equations between microscopic measurements since it was not in the scope of this paper. We did not observe any substantial evidence for the null hypothesis between any of the microscopic measurements.

As Perret et al. (1999) observed, μCT_PO and NP were not correlated; NP cannot be a measure of porosity, but rather expresses a notion of pore density and distribution through the soil sample. The positive correlation between μCT_PO and the fractal dimension (FD) has often been observed in the literature (Rachman et al., 2005; Larsbo et al., 2014) and its dependence on μCT_PO is actually the main drawback of being used as an indicator of pore network heterogeneity and complexity. FD was also correlated to the specific surface area (SS), L, B, J, and NP, which is consistent with studies from Kravchenko et al. (2011)
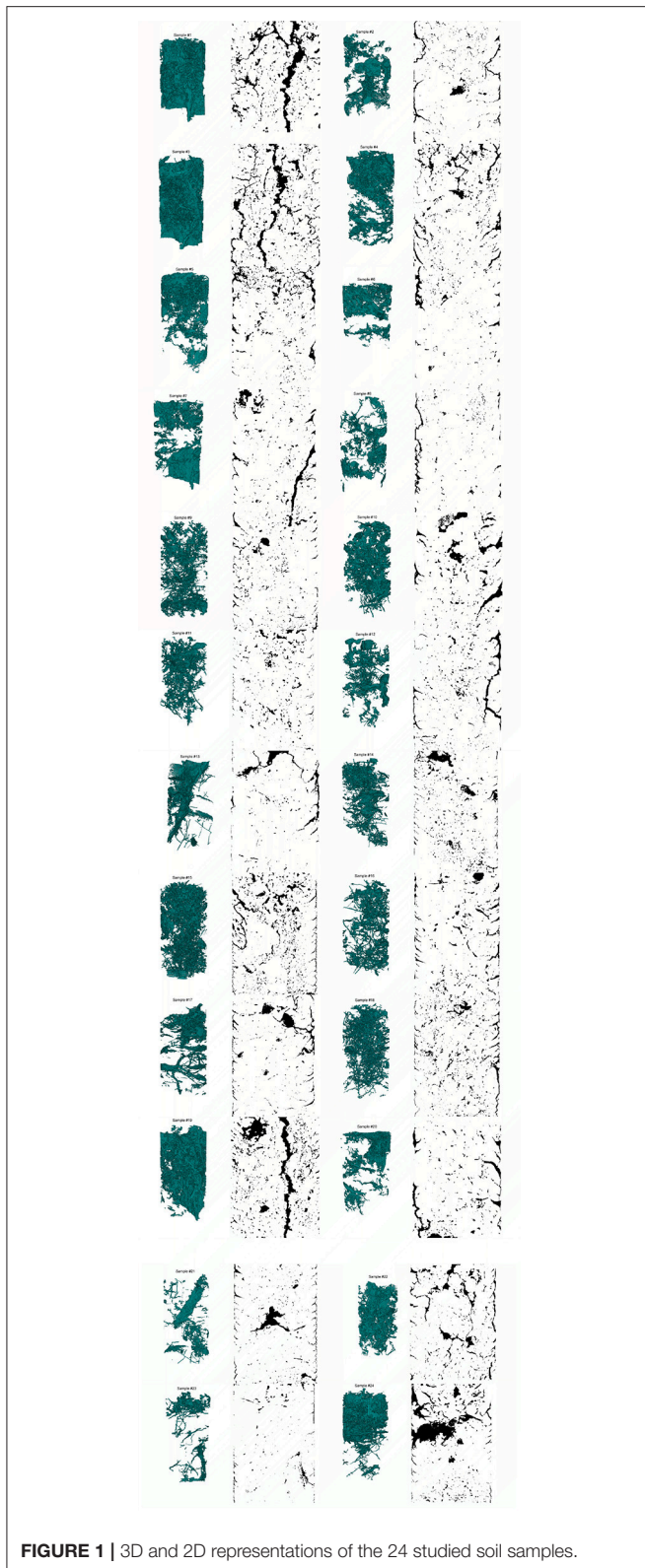
FIGURE 1 | 3D and 2D representations of the 24 studied soil samples.

and Anderson (2014). Those five parameters were all highly correlated to each other but selecting one to represent the other could distort the analysis.

The correlation between μCT_PO and average pore volumes (Avg_vol, Avg_Bvol, and Avg_Svol) also made sense since the average pore volumes were not negatively correlated to NP. The average pore volumes were all slightly correlated to Avg_Z; we observed that larger pores tended to be more connected; Avg_Z and Large_PO were also correlated. This is consistent with the results from Luo et al. (2010); Larsbo et al. (2014); Katuwal et al. (2015a,b). Regarding the other connectivity indicators [degree of connectivity (B/J), the Euler number [ε], and the average surface connectivity (SC)], we observed that AvgZ was correlated to B/J but not to ε or to SC while B/J was correlated to ε and not to SC, and SC was correlated to ε. Those connectivity indicators did not carry the exact same information and should, therefore, be used for their potential explanatory power, as pointed out by Renard and Allard (2013) and Katuwal et al. (2015a), Jarvis et al. (2017), and Sandin et al. (2017) have focused on connectivity indicators based on the percolation theory, and they found that four indicators of connectivity were interchangeable and dependent on soil porosity. We calculated the global connectivity (Γ) indicator from the pore size distribution extracted from Avizo and, from the cluster distribution extracted from BoneJ to be comparable to Jarvis et al. (2017) and Sandin et al. (2017). We observed drastically different Γ values from the two methods of computation. As Houston et al. (2017) assessed it, the software, and the decomposition method that goes with it, influence the final pore size distribution. The very low values of Γ from Avizo came from the decomposition of the pore space into a large amount of connected (or not) pores and the resulting smaller (by two orders of magnitude) largest component than the one identified in BoneJ, where cluster of connected pores are quantified. In the following, to be comparable to Sandin et al. (2017), we used the Γ value computed from the BoneJ's cluster size distribution.

Relationships Between the Microscopic and Macroscopic Measurements
Measured, Calculated, and Predicted Soil Water Retention Curves
In the following section, samples #10, #13, #16, and #17 were not included because SWRC were not measured; the calibration data set included 14 samples instead of 18.

Air-filled porosity at h = −1 kPa
In the calibration data set, the relationship between μCT_PO and Lab_PO was neither linear nor credible because of three outliers (#1, #2, #7, **Figure 2**). As discussed above, samples #2 and #7 were segmented with Otsu's method. In the case of sample #7, Lab_PO was too large for the porosity-based method, introducing unrealistic porosity that would explain the deviations. Lab_PO was calculated by weighing the soil samples after draining. If the pore surfaces were rough or loose, water films could have covered up the pores surface by adsorption and pores could appear smaller than they are. Difference between adsorption and desorption curves, also known as the hysteresis effect, can indeed be substantial close to saturation (McKenzie et al., 2002). A physical explanation for sample #1 could be that it had large pores which drained just before being weighed at

TABLE 3 | Microscopic measurements on μCT X-ray images for the calibration and validation data set [minimum values (Min), maximum values (Max), mean values (Mean), and standard deviation (St dev)].

Microscopic measurements	Calibration data set				Validation data set			
	Min	Max	Mean	St dev	Min	Max	Mean	St dev
μCT_PO [%]	3.71	14.23	7.66	2.69	2.76	12.77	8.55	4.06
Macro_PO [%]	2.87	13.22	6.69	2.68	1.97	11.86	7.54	3.93
NP [−]	31,770	79,749	46,649	12,957	32,197	66,192	44,478	12,346
Avg_vol [mm^3]	0.0260	0.1110	0.0567	0.0223	0.0260	0.1010	0.0620	0.0294
Avg_Bvol [mm^3]	0.1350	1.3450	0.5958	0.3656	0.1210	2.0190	0.7795	0.7191
Avg_Svol [mm^3]	3.000E-03	1.200E-02	6.278E-03	2.372E-03	3.000E-03	1.100E-02	7.000E-03	3.162E-03
IP [%]	66.29	87.32	76.58	5.97	64.28	83.76	75.51	7.31
IPO [%]	3.10	12.76	8.44	2.62	4.16	12.88	7.93	3.02
Avg_Z [−]	3.07	5.40	4.29	0.83	3.58	5.24	4.36	0.59
SC [voxel^{-1}]	0.206	0.304	0.250	0.029	0.209	0.315	0.258	0.036
Con_surf [mm²]	2553	7921	4722	1321	2696	5984	4703	1282
SS [m^{-1}]	2.040E-03	5.078E-03	2.991E-03	8.484E-04	2.027E-03	4.008E-03	2.843E-03	7.034E-04
Γ [−] / Avizo	9.200E-04	4.817E-02	5.152E-03	1.080E-02	1.400E-03	4.100E-02	1.307E-02	1.601E-02
Γ [−] / BoneJ	0.8613	0.5356	0.7386	0.0820	0.8286	0.6724	0.7365	0.0649
L [m]	28.22	71.58	43.83	10.95	30.97	57.57	43.63	12.17
B[−]	77,776	22,3143	126,510	36,757	81,850	158,219	124,115	30,407
J [−]	28,480	94,542	51,812	16,524	32,605	65,150	51,595	13,053
B/J [−]	2.230	2.930	2.529	0.183	2.280	2.740	2.443	0.166
Tortuosity [mm^{-1}]	1.240	1.280	1.257	0.014	1.240	1.276	1.258	0.013
FD [−]	2.405	2.642	2.527	0.072	2.313	2.653	2.507	0.118
DA [−]	0.112	0.384	0.206	0.080	0.104	0.352	0.252	0.092
ε [−]	−14,125	27,434	8,761	10,969	−9,897	30,112	6,534	13,836
Min_ε [−]	−39,624	−7,196	−20,034	9,141	−2,7461	−9,747	−19,667	6410

The abbreviations of the microscopic measurements are listed in **Table 1**.

saturation. Therefore, the volume of water used to calculate the total laboratory porosity could have been under-evaluated. This is most likely since one gram of water can change the Lab_PO from 8.02 to 14.21%. The 3D visualization of sample #1 shows that a large part of its porosity was connected from top to bottom (**Figure 1**). The validation data were in agreement with the calibration data except for sample #20, which was segmented with Otsu for the same reasons as sample #7, and sample #22, which showed a behavior similar to sample #1.

Eventually, the samples that were segmented with the porosity-based method displayed similar Lab_PO and μCT_PO values. Lab_PO was used as a target during the segmentation process. Elliot et al. (2010) also found congruent air-filled porosity values measured by X-ray μCT (voxel size of $45^3 \mu m^3$) and by weight determination. The slope of the relationship between Lab_PO and μCT_PO was higher than one and Lab_PO was indeed positively correlated to the difference between Lab_PO and μCT_PO. The applied capillary theory to calculate Lab_PO and μCT_PO simplifies the pore network to capillaries. We, therefore, suggest that the difference between Lab_PO and μCT_PO reflected the systematic error produced by considering pores as capillaries, and increasing the volume of data to which the theory was applied (PO) had increased the *error* (the difference). The difference between Lab_PO and μCT_PO, whether in absolute value or not, could, however, not be

correlated to any microscopic measurements. We presumed that the pore network real connectivity would explain the imperfect applicability of the capillary law. For example, Parvin et al. (2017) reported that the percentage of isolated pores explained the difference in volumetric water content (between laboratory evaporation measurements and X-ray μCT calculation) at a water matric potential ranging from −0.35 to −0.4 kPa by only considering pores larger than 350 μm (pores that should drain at a matric potential of −0.42 kPa from capillary law). The isolated pores were actually connected to others by throats smaller than the voxel size and may not have drained at the required potential calculated from capillary law.

From discrete to continuous data

Beckers et al. (2014a) and Parvin et al. (2017) applied nearly the same methodology to compare predicted SWRC with the bimodal version (Durner, 1994) of the van Genuchten (1980) model. On one hand, they only used macroscopic input data [from pressure plates weighting procedure for Beckers et al. (2014a) and from the evaporation method for Parvin et al. (2017)], and on the other hand, they used those macroscopic data in combination with microscopic data (pore-size distribution extracted from X-ray μCT images) as input. They both found that using the X-ray μCT data allows a better prediction of SWRC close to saturation in terms of RRMSE. We noted, however,

TABLE 4 | Significant Bayesian correlation coefficients between the microscopic measurements for the calibration data set (Cal. data) or the complete data set (All data).
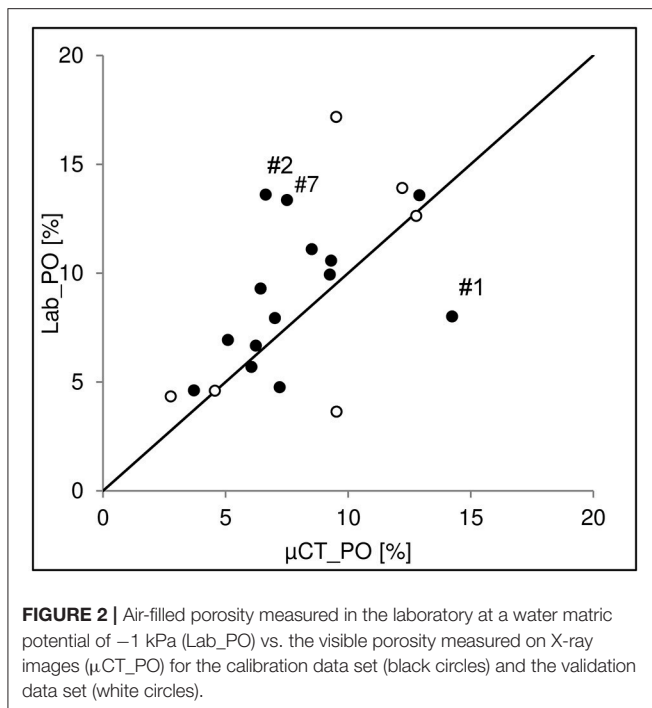
		Large_PO	NP	Avg_vol	Avg_Bvol	Avg_Svol	IP	IPO	Avg_Z	SC	Con_surf	SS	Γ/Avizo	Γ/Bonej	L	B	J	B/J	τ	FD	DA	ε	Min_ε
µCT_PO	Cal. data	0.98		0.78	0.58	0.80					0.87									0.59			
	All data	0.98		0.77	0.56	0.80				−0.49	0.87									0.69			
Large_PO	Cal. data			0.86	0.68	0.87		0.70	0.53		0.79												
	All data			0.83	0.63	0.85				−0.48	0.82									0.61			
NP	Cal. data											0.98			0.87	0.90	0.84			0.70			
	All data											0.98			0.87	0.89	0.82			0.71			
Avg_vol	Cal. data				0.87	0.98		0.49	0.62			0.52		0.50									
	All data				0.88	0.99		−0.47	0.57		0.52												
Avg_Bvol	Cal. data			0.87		0.83			0.55			0.54				−0.54	−0.54						
	All data			0.88		0.86	0.50	−0.47	0.51														
Avg_Svol	Cal. data								0.62		0.52												
	All data									−0.49	0.55												
IP	Cal. data									−0.68								0.80	−0.60			0.86	0.68
	All data									−0.73								0.78	−0.67			0.87	
IPO	Cal. data												0.46	−0.78								0.49	
	All data												0.56	−0.76									
Avg_Z	Cal. data																	0.52					
	All data																	0.51	−0.56				
SC	Cal. data																		0.79			−0.78	
	All data																		0.80	−0.55		−0.80	−0.66
Con_surf	Cal. data														0.59					0.73			
	All data														0.67					0.77			
SS	Cal. data														0.83	0.90	0.83			0.61			
	All data														0.83	0.90	0.83			0.63			
Γ/Avizo	Cal. data																						
	All data																						

TABLE 4 | Continued

		Large_PO	NP	Avg_vol	Avg_Bvol	Avg_Svol	IP	IPO	Avg_Z	SC	Con_surf	SS	L/Avizo	L/BoneJ	L	B	J	B/J	τ	FD	DA	ε	Min_ε
L/BoneJ	Cal. data																						
	All data																						
L	Cal. data															0.95	0.95			0.72			−0.70
	All data															0.94	0.93			0.75			−0.74
B	Cal. data																0.95	−0.51		0.57			−0.83
	All data																0.99			0.58			−0.85
J	Cal. data																	−0.60		0.53			−0.84
	All data																	−0.49		0.53			−0.86
B/J	Cal. data																					0.64	0.63
	All data																		−0.52			0.71	
τ	Cal. data																						0.60
	All data																					−.84	−.49
FD	Cal. data																						
	All data																						
DA	Cal. data																						
	All data																						
ε	Cal. data																						.62
	All data																						

*The abbreviations of the microscopic measurements are listed in **Table 1**. Red BF > 100, orange 30 < BF < 100, yellow 10 < BF < 30 and green 3 < BF < 10.*

FIGURE 2 | Air-filled porosity measured in the laboratory at a water matric potential of −1 kPa (Lab_PO) vs. the visible porosity measured on X-ray images (µCT_PO) for the calibration data set (black circles) and the validation data set (white circles).

FIGURE 3 | Measured and predicted soil-water retention curves for three samples. Unlike the samples, the SWRC for #1 predicted with the pressure plates data alone (plain line, Pred_PP_DP) performed better than with X-ray µCT data (dotted line, Pred_PP+µCT_DP). Black circles represent the X-ray µCT data and white circles the pressure plate measurements.

that those studies used macroscopic data from one set of soil samples and microscopic data from another set of soil samples. We aimed at validating the results by using the same samples for both types of measurements. To that purpose, capillary theory was applied to the pore-size distribution extracted from the X-ray µCT images and the calculated SWRC were adjusted to the total laboratory porosity. **Figure 3** illustrates the SWRC for three samples and shows that for all samples, except #1, the volumetric water content (θ) close to saturation was higher when predicted with the combination of X-ray µCT data and pressure plates data (µCT+PP) than with only the pressure plates data (PP), confirming previous results from Beckers et al. (2014a) to Parvin et al. (2017). We also observed that according to the RRMSE values, prediction with µCT+PP data were better than with only the PP data (**Table 5**), except for sample #1. Lamandé et al. (2013) also found that X-ray µCT measurements (voxel size of 600^3 µm^3) allowed a more complete description of the pore space than classical laboratory measurements, and Rab et al. (2014) have concluded that X-ray µCT was likely a better method than laboratory SWRC measurements for determining air-filled macroporosity (pores larger than 300 µm in diameter). The poor performance from sample #1 came from the fact that Lab_PO was lower than µCT_PO, as discussed in **Figure 2**. Apart from sample #1, the use of microscopic information undeniably improved the prediction of continuous SWRC with the bimodal version (Durner, 1994) of the van Genuchten model (1980).

Altogether
The determination of SWRC through pressure plate measurements are likely more representative of the *in-situ* soil hydrodynamic, but those are not free of artifacts; for
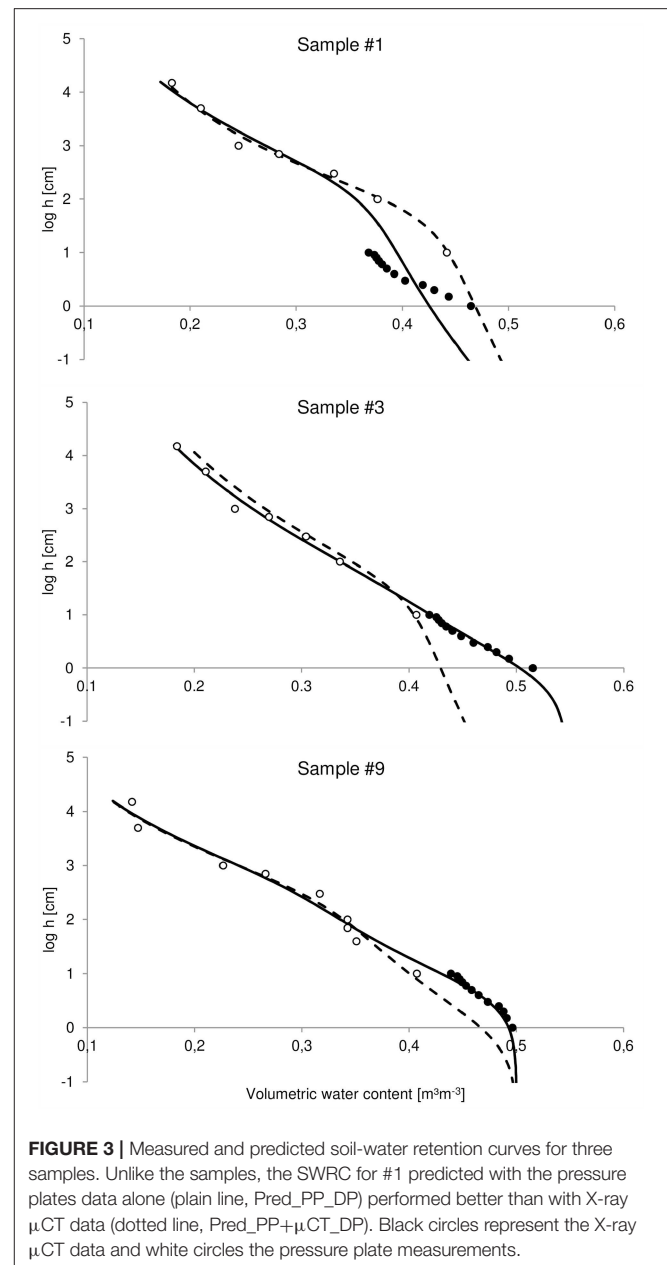
example, air entrapment might result in incomplete saturation leading to inaccurate estimation of the air-filled macroporosity. And, although the connectivity of the pore network was not taken into account with the X-ray µCT SWRC calculation, we still observed that the combination of laboratory measurements and X-ray µCT data improved the SRWC prediction close to saturation. The accurate characterization of the air-filled macroporosity is important for the study of microorganism development (e.g., soil fungal growth in Falconer et al., 2012).

Saturated Hydraulic Conductivity and Soil Porous Structure
The saturated hydraulic conductivity was positively correlated to the global connectivity indicator (Γ) computed from the

TABLE 5 | Relative root mean squared error (RRMSE, %) for the predicted soil water retention curves with the pressure plates data (PP) or the μCT data plus the pressure plates data (μCT + PP) for the calibration data set samples.

Sample	RRMSE	
	PP	**μCT+PP**
#1	3.445	0.0538
#2	1.816	0.0157
#3	2.867	0.0201
#4	3.617	0.0254
#5	3.711	0.0300
#6	2.311	0.0165
#7	1.727	0.0134
#8	2.906	0.0216
#9	6.526	0.0474
#11	2.427	0.0232
#12	6.135	0.0556
#14	2.734	0.0223
#15	3.840	0.0275
#18	4.781	0.0385

BoneJ cluster size distribution (**Figure 4A**, $\rho = 0.593$, BF = 9.5) as observed in Sandin et al. (2017), unlike that study, we did not observe a credible correlation, but a positive trend between μCT_PO and Γ/BoneJ. It is worth noticing again that Sandin et al. (2017) worked with a resolution close to our but with a different textural soil. Pöhlitz et al. (2018) also reported similar trend of Ks and connectivity values (and μCT_PO) between cultural practices. They worked with a voxel size of $60^3 \mu m^3$ on different samples for the Ks and microscopic measurements, with although a large number of repetitions. **Figure 4A** shows the observations of the calibration data (black circles), the observations of the validation data (white circles), the predicted validation points with the 50% quantiles of the regression model (crosses) and the 25 and 75% quantiles of the regression models (dotted lines). The 50% quantiles of the regression models provided a RRMSE of 0.492 for the validation data and the predicted data points were, in most cases, underestimated. The reported regression models that included two explaining variables reported light credible evidence in the cases where Γ was one of the explaining variables. We did not observe relationships between μCT_PO and log(Ks), despite what the literature reported (Kim et al., 2010; Luo et al., 2010; Mossadeghi-Björklund et al., 2016; Naveed et al., 2016). The measured Ks from those studies were, however, higher by several orders of magnitude. We did observe a positive correlation between log(Ks) and FD when the calibration samples were visually separated in two groups according to their Ks value (**Figure 4B**, black circles). Samples #1, #2, #3, #4, #7, #11, #12, #14, #15, #16, #18 were part of group 1 and samples #5, #6, #8, #9, #10, #13, #17 were part of group 2. No microscopic measurements explained that separation and it was difficult to visually distinguish a pore distribution trend within the pore space (**Figure 1**). We noticed that some of the less conductive samples presented one or two large macropores (not necessarily vertically oriented
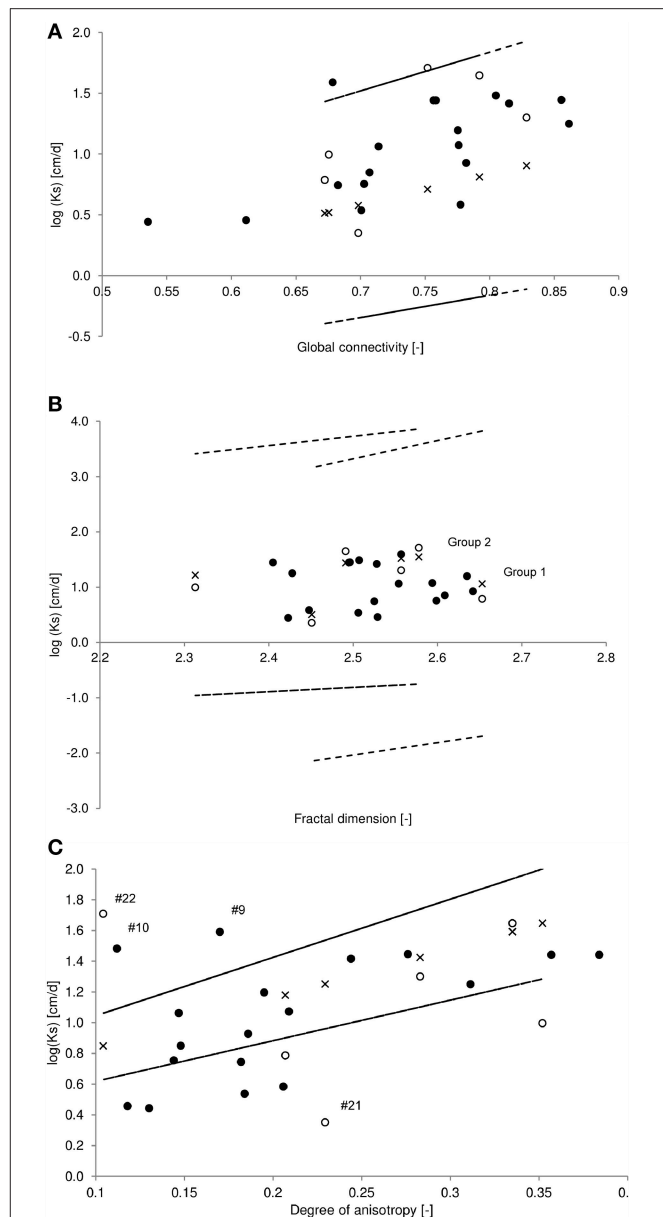

FIGURE 4 | Logarithmic saturated hydraulic conductivity (Ks) vs. **(A)** global connectivity calculated from the pore size distribution extracted from BoneJ, **(B)** the fractal dimension measured on X-ray μCT images, and **(C)** the soil degree of anisotropy measured on X-ray μCT images. Black and white circles represent the observations from the calibration and validation data sets, respectively. Crosses represent predicted validation data points and dotted lines represent the 25 and 75% regression model quantiles.

nor connected from top to bottom) while some of the more conductive samples had more dispersed pore networks, and we observed a negative trend (not credible) between FD and the degree of anisotropy (DA) for group 2, but not for group 1. This suggested that the porosity arrangement led to the composition of two groups for the relationship between FD and log(Ks). By using the Ks value as a boundary, the validation data were assigned to a group (**Figure 4B**, white circles). FD measures the

ability of the studied object to fill the Euclidian space within which it is integrated and, the larger the FD, the closer to a real fractal the object gets, meaning that its shape is similar at different scales. Although Pachepsky et al. (2000) reported that soils are far from being real fractal, Perret et al. (2003) and Kravchenko et al. (2011) pointed out that FD can be used as a global measure of the pore network complexity. For example, FD was found to vary with depth or soil treatment (Rachman et al., 2005; Udawatta and Anderson, 2008; Kim et al., 2010). Anderson (2014) also observed a positive correlation between log(Ks) and FD. By applying the regression equations, log(Ks) of group 1 equal to log(Ks) of group 2, when FD = 3.03, which was close to the upper limit of the possible FD values of a 3D object. At FD = 3, the object (the porosity) occupies each point of 3D Euclidian space, but that also meant that log(Ks) was limited to 128 cm/day. It is reasonable to ask if more groups would be created with increasing conductivity and if the slopes of the relationships would decrease, or if the solutions of the regression equations would be identical when the fractal dimension equals three, which is the fractal dimension upper limit for an Euclidian 3D object. The global RRMSE was 0.260, which is a rather good performance (**Figure 4B**, crosses). The 25 and 75% regression model quantiles were highly dispersed (**Figure 4B**, dotted lines) inducing uncertainty about the regression model.

Anisotropy has been shown to impact soil conductivity (Ursino et al., 2000; Raats et al., 2004; Zhang, 2014). **Figure 4C** plots log(Ks) as a function of DA (black circles for the observations of the calibration data) and by removing two outliers from the calibration data set (#9 and #10), we obtained a correlation coefficient of 0.74 (BF = 125.3), which presents a convincing link that has, to our knowledge, not been seen before. Such a positive correlation could be interpreted as a consequence of preferential flow through large macropores. For example, Dal Ferro et al. (2013) have found that anisotropy was scale-dependent by showing higher average DA in soil cores (DA of 0.32 and voxel size of 40 µm) than in soil aggregates (DA of 0.14 and voxel size of 6.25 µm), they hypothesized that as a possible consequence of biological and mechanical macropores. This was later confirmed by a second study where they showed that only the macropores in the range of 250–500 µm were correlated to the global DA (Dal Ferro et al., 2014). From the DA calculation decomposition (in the Supplementary Materials section), it was possible, but not straightforwardly, to evaluate the main direction of the anisotropy which could be represented by a small amount of pores in that direction, or as the direction of the preferential orientation of one large pore. Ks was measured along the z-axis (vertically) but the main direction of anisotropy was not systematically in that direction. Therefore, the positive correlation between DA and log(Ks) was not necessarily a result of preferential pore networks paths. Moreover, the directions of the pore connections showed that a majority of the pores junction were horizontal (x- and y-axis). The repartition was practically the same between samples, 60% horizontal and 40% vertical connections. Applying the regression model to the validation data gave consistent results for four samples with a RRMSE for those of 0.414 (**Figure 4C**, crosses). Sample #21 gave poor results with a predicted log(Ks) of 1.03

cm/day instead of an observed log(Ks) of 0.35 cm/day and a resulting RSE of 3.742. As well, sample #22 gave a RSE of 0.433, its low DA and large log(Ks) made it similar to the two outliers of the calibration data (#9 and #10). The relationship between DA and log(Ks) may not be suitable for highly conductive soil sample presenting isotropic-like porosity distribution (Samples #9, #10, #22, **Figure 1**). Subjective comparisons between 3D representations and DA need to be made cautiously. We observed that, compared to samples #9, #10, #22, samples #15 and #18 had similar visually homogenous porosity (and equivalent low DA) but with a lower Ks. Samples from group 2 in **Figure 4** (#5, #6, #8, #13, #17 and #20, #23, #24) had higher log(Ks) with a more heterogeneous porosity (and higher DA). The narrower distribution of the 25 and 75% regression model quantiles came from the exclusion of two outliers in the model computation.

The prediction of the hydraulic conductivity curve is frequently extracted from the SWRC shape and absolute values of K(h) can be obtained by matching both curves with a specific point, which is often Ks (Vogel and Roth, 1998). Ks is however cumbersome and time-consuming to measure *in-situ*. We reported here that the porosity arrangement described by the global connectivity, the fractal dimension, and degree of anisotropy had an impact on the soil conductivity, the combination of those indicators provided information that could be used across scales and to eventually better estimate Ks. No other relationships between log(Ks) or Ks and the other microscopic measurements were reported.

Air Permeability Variations Explained by Microscopic Structure

Macroscopic measurements showed, as expected, that the air permeability increased with air-filled porosity. We also observed positive credible Bayesian correlation coefficients between log(ka) measured at various h and microscopic indicators of the porosity (µCT_PO, Large_PO, Avg_vol, Avg_Bvol, and Avg_Svol), although only log(ka, −70 kPa) was positively correlated to µCT_PO (**Table 6**). Given the X-ray µCT image resolution, µCT_PO should be representative of the air-filled PO measured at $h = -1$ kPa although th e soil samples were scanned at $h = -70$ kPa. The choice to scan soil samples at $h = -70$ kPa was a compromise between the fact that all the potential visible porosity should be air-filled and without cracks due to drying, and this particular correlation suggests that all the potential visible porosity was indeed air-filled. In their study, Katuwal et al. (2015b.) and Naveed et al. (2016) both observed a power-law function between, respectively, ka(−2 kPa) or ka(−3 kPa) and µCT_PO. The µCT_PO calculated on their images is equivalent to the Large_PO on our images as previously stated, and we also reported a correlation between Large_PO and log(ka) (**Table 6**). Therefore, the difference between µCT_PO and Large_PO might be the part of the PO that should have drained at low negative potential (from the capillary law), but was actually drained at higher negative potential (due to unusable pathways). We refer to Hunt et al. (2013) to name that part of porosity, the *inaccessible porosity*. This assumption was confirmed by the credible correlations between the inaccessible PO and microscopic parameters which expresses a notion of pore

network complexity (B, J, L, NP, SS, IPO, FD). We previously pointed out the drawback that, when calculating SWRC from the X-ray μCT data (namely from the visual pore size distribution), the connectivity was not taken into account. We here confirmed that the pore network connectivity play a role in the desorption process.

Lamandé et al. (2013) found a positive correlation between log(ka, −10 kPa) and NP. We observed negatives correlations (as well as with B, J, and SS). Many pores of our samples were connected to others with connections smaller than the voxel size and were considered isolated (high IP and ε, **Table 3**). It would make sense, that an increasing volume of small (invisible) connections reduces the airflow through the pore network. The air permeability is also largely dependent on the tortuosity and connectivity of the pore network (Ball and Schjønning, 2002; Moldrup et al., 2003), but to our knowledge, no study has reported these links from μCT measurements. From **Table 6**, it appears that the air permeability increased with a growing average number of connections (Avg_Z) as well with a growing global connectivity (Γ/BoneJ), but also with Min_ε and B/J. The last two parameters indicate a decreasing connectivity with an increasing value. First, from **Table 4**, it was observed that B/J increased with decreasing B or decreasing J. That purely algebraic relationship might explain why the air permeability would decrease with decreasing B/J (increasing connectivity). Then, Min_ε was calculated over the largest connected pore component, and, because there are no cavities in real soil pore space (Vogel and Roth, 1998), Min_ε decreased as the number of redundant connections increased. When calculating Avg_Z by class of pore according to their volumes, it appeared that the values of Avg_Z we observed came from a large number of small pores having few connections; the biggest pores had ten times

more connections. Avg_Z was correlated to Avg_Z calculated on the pores having a radius between 250 and 375 μm. Therefore, air permeability was correlated to the fact that "medium" size pores had more connections. Moreover, there was a negative trend between log(ka) and Avg_Z calculated on the largest pores which corroborated the positive correlation between ka and Min_ε.

The best regression models calculated on the calibration data (Bayes factor) and applied on the validation data reported that the best explaining variable for all measures of log(ka) (RRMSE) was the average pore volume of the smallest pores (Avg_Svol). That parameter might be seen as a limiting factor, and this suggested that ka was more related to pore size distribution than porosity. **Figure 5A** displays log(ka, −70 kPa) as a function of Avg_Svol and the distribution of the 25 and 75% regression model quantiles are rather narrow. The RRMSE was 1.256 or 0.0649 when the two worst predicted validation data points were not taken into account. The RRMSE for log(ka, −30 kPa) and log(ka, −10 kPa) were around 0.800 with one bad validation data point, and the RRMSE for log(ka, −7 kPa) was very high (8.154) with three

TABLE 6 | Credible Bayesian correlation coefficients between microscopic measurements and logarithmic air permeability (ka) measured at water matric potentials of −70, −30, −10, and −7 kPa for the calibration data set.

	log			
	ka (−7 kPa)	ka (−10 kPa)	ka (−30 kPa)	ka (−70 kPa)
μCT_PO				0.53
Large_PO	0.54	0.60		0.64
Avg_Vol	0.72	0.76	0.72	0.79
Avg_Svol	0.75	0.85	0.75	0.84
Avg_Bvol	0.69	0.76	0.69	0.77
NP		−0.70	−0.76	
Avg_Z	0.55	0.78	0.85	0.69
SS	−0.64	−0.73	−0.80	−0.54
IPO	−0.70	−0.76	−0.82	−0.62
B	−0.56	−0.68	−0.72	
J	−0.52	−0.68	−0.71	
B/J			0.62	0.63
Γ/BoneJ	0.54			0.54
Min_ε		0.68	0.73	

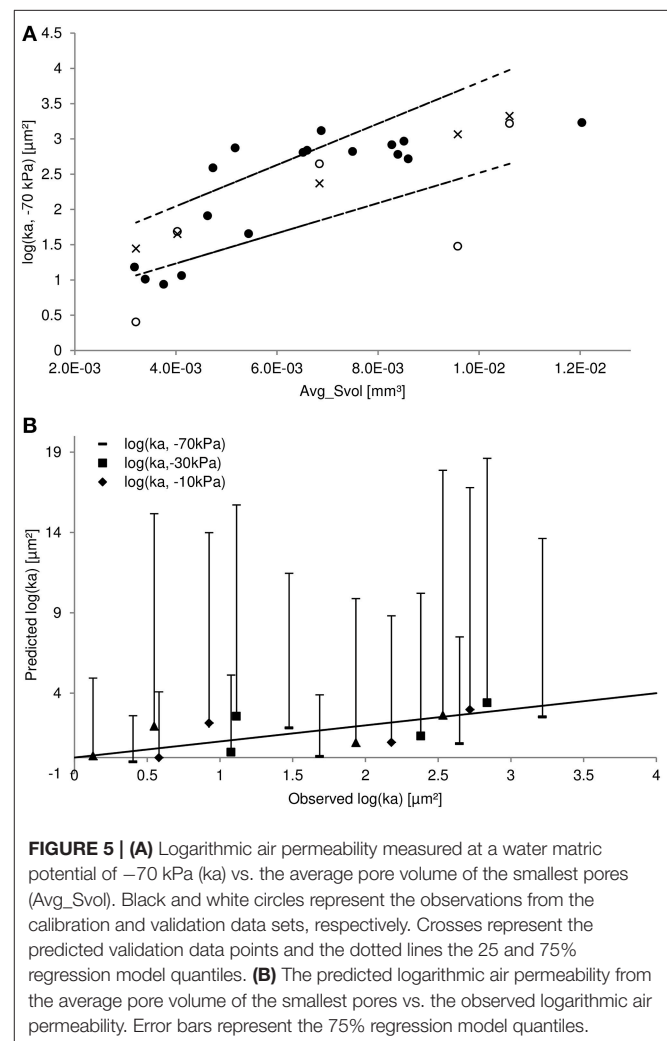*The abbreviations of the microscopic measurements are listed in **Table 1**.*

FIGURE 5 | (A) Logarithmic air permeability measured at a water matric potential of −70 kPa (ka) vs. the average pore volume of the smallest pores (Avg_Svol). Black and white circles represent the observations from the calibration and validation data sets, respectively. Crosses represent the predicted validation data points and the dotted lines the 25 and 75% regression model quantiles. **(B)** The predicted logarithmic air permeability from the average pore volume of the smallest pores vs. the observed logarithmic air permeability. Error bars represent the 75% regression model quantiles.

badly predicted data points out of five. The combination of Avg_Svol and average pore volume of all pores (Avg_Vol) performed slightly better in some cases, and slightly worse in others. **Figure 5B** shows the predicted log(ka) from Avg_Svol vs. the observed log(ka) values. Although the RRMSE were acceptable, the regression model distributions (the error bars represent the 75% regression models quantiles) were high which induce large uncertainty. That combination of two explaining variables was, in all cases, the best regression model of two explaining variables. Other important explaining variables were the average coordination number (Avg_Z), the proportion of isolated porosity (IPO), the average pore volume of the biggest pores (Avg_Bvol) and the combination of µCT_PO and Large_PO.

With soil air diffusivity, soil air permeability is one of the main processes governing the exchange of gases with the atmosphere, including therefore soil aeration. Through our experimentations, we aimed at unraveling the main physical drivers of air fluxes through the soil. We have previously observed that subdividing the pore volume averages into three categories (all of the pores, the biggest, and smallest) was not informative; in this study, we have shown the opposite. Avg_Svol was the average volume of the pores having a volume between 4×10^5 and $\pm 8 \times 10^7$ μm^3, in contrast to other cited studies; those pores were visible because of our high resolution (43 µm). Eventually, we suggested that Avg_Svol worked as a limiting factor.

CONCLUSION

X-ray microtomography, among other visualization techniques, has brought new insight into the study and the understanding of soil function. The challenge, however, is the representativeness of the studied soil samples (Vogel et al., 2010) and, to that purpose, the analysis of the same soil samples at two scales has become more prevalent. The resulting next challenge is the resolution at which the soil samples should be studied. To our knowledge, very few studies dealt with equivalent voxel size (43^3 μm^3) and, we did not find any micro-macro correlations such as the ones we observed.

Starting with the comparison of the calculated visible porosity for all pores and for those of at least 1,000 voxels in volume, it appeared that the difference was rather small but positively correlated to indicators of the pore network complexity. The uncommon relationships we observed might be due to the higher resolution we worked with and the resulting finer details of the pore network structure. For example, the calculated fractal dimension and degree of anisotropy are both global indicators of the pore network complexity and both were positively correlated to the saturated hydraulic conductivity, although with some limitations. The global connectivity showed interesting results although highly dependent on the decomposition software used to extract the pore size distribution. Identifying the key parameters that convey the complexity of the pore network is a motivating goal to reach. Pore network modeling has already

proven useful (e.g., Vogel and Roth, 1998, or more recently, Köhne et al., 2011), and those three indicators are values that could be used for the generation of a phenomenological model.

Furthermore, we have reported various positive correlations between the air permeability measured at several water matric potentials and microscopic measurements. The average volume of the smallest pores (as small as $\pm 4 \times 10^5$ μm^3) showed the best link with air permeability. Due to our high resolution, we observed a higher number of pores than in other studies and consequently more isolated pores. The Euler number based on the connected space was expected to correlate well with air permeability, but this was not the case. Other measures that provide similar types of information (total pore length, total number of branches, and junctions) proved equally unsatisfactory. In fact, a pertinent link was the positive relationship between the average pore volume of the biggest pores and that of the smallest ones, suggesting dependence between pores of different volumes.

We also reported that the soil water retention curve was better predicted near saturation with the pore size distribution extracted from the X-ray µCT data. Indicators can be derived from the SWRC to characterize soil quality or extrapolate microorganism development (Rabot et al., 2018); its accurate description is therefore a prerequisite. The degree of saturation is also important in the modeling of microbial growth, the dissolution of O_2, the soil respiration, the NO and N_2O production. These processes are affected by the so-called water filled pore space, by soil oxygen content and by soil temperature, which all vary with the volumetric water content (Smith et al., 2003). Blagodatsky and Smith (2012) concluded that the microbial growth models (and we add to this statement: "among others") including "an explicit description of microbial growth, i.e., growth rate and efficiency, humidification ratios and their relationship with N availability, need to be coupled with well-developed soil transport models." The fluid transport predictions for a continuous range of water contents and from discrete measurements are possible through models that are, today, mostly not physically-based. From the pore space structures analyzed, we aimed at contributing to a better understanding of the potential influences of the pore network topology on the physical hydrodynamic properties of soil. Strong unequivocal conclusions could not be drawn because of the limited number of repetitions; image processing and analysis are time-consuming and will be increase with increasing resolution. The comparisons to others studies, as discussed multiple times, depends on many factors and we, therefore, strongly urge the open access to gray scale X-ray µCT images.

DATA AVAILABILITY

Grayscale images and soil physical properties data are available upon request (contact the corresponding author).

AUTHOR CONTRIBUTIONS

FUNDING

ACKNOWLEDGMENTS

SUPPLEMENTARY MATERIAL

The Supplementary Material for this article can be found online at: https://www.frontiersin.org/articles/10.3389/fenvs.2018.00020/full#supplementary-material

REFERENCES

Anderson, S. H. (2014). Tomography-measured macropore parameters to estimate hydraulic properties of porous media. *Procedia Comput. Sci.* 36, 649–654. doi: 10.1016/j.procs.2014.09.069

Ball, B. C., and Schjønning, P. (2002). "Air permeability,"in *Methods of Soil Analysis, Part 1*, ed. J. H. Dane and G. C Topp (Madison, WI: Soil Science Society of America), 1141–1158.

Baveye, P. C., and Laba, M. (2015). Moving away from the geostatistical lamppost: why, where, and how does the spatial heterogeneity of soils matter? *Ecol. Model.* 298, 24–38. doi: 10.1016/j.ecolmodel.2014.03.018

Baveye, P. C., Pot, V., and Garnier, P. (2017). Accounting for sub-resolution pores in models of water and solute transport in soils based on computed tomography images: are we there yet? *J. Hydrol.* 555, 253–256. doi: 10.1016/j.jhydrol.2017.10.021

Beckers, E., Plougonven, E., Gigot, N., Léonard, A., Roisin, C., Brostaux, Y., et al. (2014a). Coupling X-ray microtomography and macroscopic soil measurements: a method to enhance near saturation functions? *Hydrol. Earth Syst. Sci.* 18, 1805–1817. doi: 10.5194/hess-18-1805-2014

Beckers, E., Plougonven, E., Roisin, C., Hapca, S., Léonard, A., and Degr,é, A. (2014b). X-ray microtomography: a porosity-based thresholding method to improve soil pore network characteristization? *Geoderma* 219–220, 145–154. doi: 10.1016/j.geoderma.2014.01.004

Blagodatsky, S., and Smith, P. (2012). Soil physics meets soil biology: towards better mechanistic prediction of greenhouse gas emissions from soil. *Soil Biol. Biochem.* 47, 78–92. doi: 10.1016/j.soilbio.2011.12.015

Corey, A. T. (1986). "Air permeability," in *Methods of Soil Analysis. Part I. 2nd Edn,* ed A. Klute (Madison, WI: Agronomy Monograph 9, American Society of Agronomy, Inc.; Soil Science Society of America, Inc.,), 1121–1136.

Cousin, I., Levitz, P., and Bruand, A. (1996). Three-dimensional analysis of a loamy-clay soil using pore and solid chord distributions. *Eur. J. Soil Sci.* 47, 439–452. doi: 10.1111/j.1365-2389.1996.tb01844.x

Crestana, S., Mascarenhas, S., and Pozzi-Mucelli, R. S. (1985). Static and dynamic three-dimensional studies of water in soil using computed tomographic scanning. *Soil Sci.* 140, 326–332. doi: 10.1097/00010694-198511000-00002

Dal Ferro, N., Charrier, P., and Morari, F. (2013). Dual-scale micro-CT assessment of soil structure in a long-term fertilization experiment. *Geoderma* 204–205, 84–93. doi: 10.1016/j.geoderma.2013.04.012

Dal Ferro, N., Sartori, L., Simonetti, G., Berti, A., and Morari, F. (2014). Soil macro- and microstructure as affected by different tillage systems and their effects on maize root growth. *Soil Til. Res.* 140, 55–65. doi: 10.1016/j.still.2014.02.003

Dal Ferro, N., Strozzi, A. G., Duwig, C., Delmas, P., Charrier, P., and Morari, F. (2015). Application of smoothed particle hydrodynamics (SPH) and pore morphologic model to predict saturated water conductivity from X-ray CT imaging in a silty loam Cambisol. *Geoderma* 255–256, 27–34. doi: 10.1016/j.geoderma.2015.04.019

DIN ISO 11274 (2012). *Soil Quality–Determination of the Water Retention Characteristics–Laboratory Methods (ISO 11274:1998 + Cor. 1:2009) English Translation of DIN ISO 11274, 2012-04*. Deutsches Institut für Normung, Berlin.

Doube, M., Klosowski, M. M., and Arganda-Carreras, I., et al. (2010). Bone-J: free and extensible bone image analysis in ImageJ. *Bone* 47, 1076–1079. doi: 10.1016/j.bone.2010.08.023

Durner, W. (1994). Hydraulic conductivity estimation for soils with heterogeneous pore structure. *Water Resour. Res.* 30, 211–223. doi: 10.1029/93WR02676

Elliot, T. R., Reynolds, W. D., and Heck, R. J. (2010). Use of existing pore models and X-ray computed tomography to predict saturated soil hydraulic conductivity. *Geoderma* 156, 133–142. doi: 10.1016/j.geoderma.2010.02.010

Falconer, E. R., Houston, A. N., Otten, W., and Baveye, P. C. (2012). Emergent behavior of soil fungal dynamics: influence of soil architecture and water distribution. *Soil Sci.* 177, 111–119. doi: 10.1097/SS.0b013e318241133a

Garbout, A., Munkholm, L. J., and Hansen, S. B. (2013). Tillage effects on topsoil structural quality assessed using X-ray CT, soil cores and visual soil evaluation. *Soil Til. Res.* 128, 104–109. doi: 10.1016/j.still.2012.11.003

Grevers, M. C. J., De Jong, E., and St Arnaud, R. J. (1989). The characterization of soil macroporosity with CT scanning. *Can. J. Soil Sci.* 69, 629–637. doi: 10.4141/cjss89-062

Gutiérrez Castorena, E. V., Gutiérrez Castorena, M. D. C., Vargas, T. G., Bontemps, L. C., Martinez, J. D., Mendez, E. S., et al. (2016). Micromapping of microbial hotspots and biofilms from different crops using image mosaics of soil thin sections. *Geoderma* 279, 11–21. doi: 10.1016/j.geoderma.2016.05.017

Harrigan, T. P., and Mann, R. W. (1984). Characterization of microstructural anisotropy in orthotropic materials using a 2nd rank tensor. *J. Mater. Sci.* 19, 761–767. doi: 10.1007/BF00540446

Houston, A. N., Otten, W., Falconer, R., Monga, O., Baveye, P. C., and Hapca, S. M. (2017). Quantification of the pore size distribution of soils: assessment of existing software using tomographic and synthetic 3D images. *Geoderma* 299, 73–82. doi: 10.1016/j.geoderma.2017.03.025

Houston, A. N., Schmidt, S., Tarquis, A. M., Otten, W., Baveye, P. C., and Hapca, S. (2013). Effect of scanning and image reconstruction settings in X-ray computed microtomography on quality and segmentation of 3D soil images. *Geoderma* 207–208, 154–165. doi: 10.1016/j.geoderma.2013.05.017

Hunt, A. G., Ewing, R. P., and Horton, R. (2013). What's wrong with soil physics? *Soil Sci. Soc. Am. J.* 77, 1877–1887. doi: 10.2136/sssaj2013.01.0020

Jarvis, N., Larsbo, M., and Koestel, J. (2017). Connectivity and percolation of structural pore networks in a cultivated silt loam soil quantified by X-ray tomography. *Geoderma* 287, 71–79. doi: 10.1016/j.geoderma.2016.06.026

Jeffreys, H. (1961). *Theory of Probability.* Oxford, UK: Oxford University Press.

Katuwal, S., Moldrup, P., Lamandé, M.,Tuller, M., and de Jonge, L. W. (2015a). Effect of CT number derived matrix density on preferential flow and transport in a macroporous agricultural soil. *Vadose Zone J.* 14, 1–13. doi: 10.2136/v15.01.0002

Katuwal, S., Norgaard, T., Moldrup, P., Lamandé, M., Wildenschild, D., and de Jonge, L. W. (2015b). Linking air and water transport in intact soils to macropore characteristics inferred from X-ray computed tomography. *Geoderma* 237–238, 9–20. doi: 10.1016/j.geoderma.2014.08.006

Kim, H., Anderson, S. H., Motavalli, P. P., and Gantzer, C. J. (2010). Compaction effects on soil macropore geometry and related parameters for an arable field. *Geoderma* 160, 244–251. doi: 10.1016/j.geoderma.2010.09.030

Koestel, J., and Larsbo, M. (2014). Imaging and quantification of preferential solute transport in soil macropores. *Water Resour. Res.* 50, 4357–4378. doi: 10.1002/2014WR015351

Köhne, J. M., Schlüter, S., and Vogel, H.-J. (2011). Predicting solute transport in structured soil using pore network models. *Vadose Zone J.* 10, 1082–1096. doi: 10.2136/vzj2010.0158

Kravchenko, A. N., and Guber, A. K. (2017). Soil pores and their contributions to soil carbon processes. *Geoderma* 287, 31–39. doi: 10.1016/j.geoderma.2016.06.027

Kravchenko, A. N., Wang, A. N. W., Smucker, A. J. M., and Rivers, M. L. (2011). Long-term differences in tillage and land use affect intra-aggregate pore heterogeneity. *Soil Sci. Soc. Am. J.* 75, 1658–1666. doi: 10.2136/sssaj2011.0096

Lamandé, M., Wildenschild, D., Berisso, F. E., Garbout, A., Marsh, M., Moldrup, P., et al. (2013). X-ray CT and laboratory measurements on glacial till subsoil cores: assessment of inherent and compaction-affected soil structure characteristics. *Soil Sci.* 178, 359–368. doi: 10.1097/SS.0b013e3182a79e1a

Larsbo, M., Koestel, J., and Jarvis, N. (2014). Relations between macropore network characteristics and the degree of preferential solute transport. *Hydrol. Earth Syst. Sci.* 18, 5255–5269. doi: 10.5194/hess-18-5255-2014

Legland, D., Arganda-Carreras, I., and Andrey, P. (2016). MorphoLibJ: integrated library and plugins for mathematical morpholofy with ImageJ. *Bioinformatics* 32, 3532–3534. doi: 10.1093/bioinformatics/btw413

Liang, F., Paulo, R., Molina, G., Clyde, M. A., and Berger, J. O. (2008). Mixtures of g-priors for Bayesian variable selection. *J. Am. Stat. Assoc.* 103, 410–423. doi: 10.1198/016214507000001337

Loll, P., Moldrup, P., Schjønning, P., and Riley, H. (1999). Predicting saturated hydraulic conductivity from air permeability: application in stochastic water infiltration modeling. *Water Resour. Res.* 35, 2387–2400. doi: 10.1029/1999WR900137

Luo, L., Lin, H., and Halleck, P. (2008). Quantifying soil structure and preferential flow in intact soil using X-ray computed tomography. *Soil Sci. Soc. Am. J.* 72, 1058–1069. doi: 10.2136/sssaj2007.0179

Luo, L., Lin, H., and Schmidt, J. (2010). Quantitative relationships between soil macropore characteristics and preferential flow and transport. *Soil Sci. Soc. Am. J.* 74, 1929–1937. doi: 10.2136/sssaj2010.0062

Marin, J.-M., and Robert, C. P. (2007). *Bayesian Core. A Pratical Approach to Computational Bayesian Statistics*. New York, NY: Springer.

McKenzie, N., Coughlan, K., and Cresswell, H. (2002). *Soil Physical Measurement and Interpretation for Land Evaluation*. Collingwood: CSIRO Publishing.

Moldrup, P., Yoshikawa, S., Olesen, T., Komatsu, T., and Rolston, D. E. (2003). Air permeability in undisturbed volcanic ash soils: predictive model test and soil structure finderprint. *Soil Sci. Soc. Am. J.* 67, 32–40. doi: 10.2136/sssaj2003.3200

Monga, O., Garnier, P., Pot, V., Coucheney, E., Nunan, N., Otten, W., et al. (2014). Simulating microbial degradation of organic matter in a simple porous system using the 3-D diffusion-based model MOSAIC. *Biogeosciences* 11, 2201–2209. doi: 10.5194/bg-11-2201-2014

Morey, R. D., and Rouder, J. N. (2015). *BayesFactor: Computation of Bayes Factors for Common Designs.* R package version 0.9.12-2. Available online at: https://CRAN.R-project.org/package=BayesFactor

Mossadeghi-Björklund, M., Arvidsson, J., Keller, T., Koestel, J., Lamandé, M., Larsbo, M., et al. (2016). Effects of subsoil compaction on hydraulic properties and preferential flow in a Swedish clay soil. *Soil Til. Res.* 156, 91–98. doi: 10.1016/j.still.2015.09.013

Naveed, M., Moldrup, P., Arthur, E., Wildenschild, D., Eden, M., Lamandé, M., et al. (2012). Revealing soil structure and functional macroporosity along a clay gradient using X-ray computed tomography. *Soil Sci. Soc. Am. J.* 77, 403–411. doi: 10.2136/sssaj2012.0134

Naveed, M., Moldrup, P., Schaap, M. G., Tuller, M., Kulkarni, R., Vogel, H.-J., et al. (2016). Prediction of biopore- and matrix-dominated flow from X-ray CT-derived macropore networkds characteristics. *Hydrol. Earth. Syst. Sci.* 20, 4017–4030. doi: 10.5194/hess-20-4017-2016

Nuijten, M. B., Wetzels, R., Matzke, D., Dolan, C. V., and Wagenmakers, E.-J. (2015). *BayesMed: Default Bayesian Hypothesis Tests for Correlation, Partial Correlation, and Mediation.* R package version 1.0.1. Available online at: http://CRAN.R-project.org/package=BayesMed

Olson, M. S., Tillman, F. D. Jr., Choi, J.-W., and Smith, J. A. (2001). Comparison of three techniques to measure unsaturated-zone air permeability at Picatinny Arsenal, N. J. *J. Contam. Hydrol.* 53, 1–19. doi: 10.1016/S0169-7722(01)00135-8

Or, D., Smets, B. F., Wraith, J. M., Deschene, A., and Friedman, S. P. (2007). Physical constraint affecting bacterial habitats and activity in unsaturated porous media – a review. *Adv. Wat. Res.* 30, 1505–1527. doi: 10.1016/j.advwatres.2006.05.025

Otsu, N. (1979). A threshold selection method from gray-level histograms. *IEEE Trans. Syst. Man Cybern.* 9, 62–66. doi: 10.1109/TSMC.1979.4310076

Pachepsky, Y. A., Giménez, D., Crawford, J. W., and Rawls, W. J. (2000). "Conventional and fractal geometry in soil science," in *Developments in Soil Science*, eds Y. A. Pachepsky, J. W. Crawford and W. J. Rawls (Elsevier), 7–18.

Paradelo, M., Katuwal, S., Moldrup, P., Norgaard, T., Herath, L., and de Jonge, L. W. (2016). X-ray CT-derived characteristics explain varying air, water, and solute transport properties across a loamy field. *Vadose Zone J.* 192, 194–202. doi: 10.2136/vzj2015.07.0104

Parvin, N., Beckers, E., Plougonven, E., Léonard, A., and Degré, A. (2017). Dynamic of soil drying close to saturation: what can we learn from a comparison between X-ray computed microtomography and the evaporation method? *Geoderma* 302, 66–75. doi: 10.1016/j.geoderma.2017.04.027

Peng, S., Marone, F., and Dultz, S. (2014). Resolution effect in X-ray microcomputed tomography imaging and small pore's contribution to permeability for a Berea sandstone. *J. Hydrol.* 510, 403–411. doi: 10.1016/j.jhydrol.2013.12.028

Perret, J. S., Prasher, S. O., and Kacimov, A. R. (2003). Mass fractal dimension of soil macropores using computed tomography: from the box-counting to the cube-counting algorithm. *Eur. J. Soil Sci.* 54, 569–579. doi: 10.1046/j.1365-2389.2003.00546.x

Perret, J. S., Prasher, S. O., Kantzas, A., and Langford, C. (1999). Three-dimensional quantification of macropore networks in undisturbed soil cores. *Soil Sci. Soc. Am. J.* 63, 1530–1543. doi: 10.2136/sssaj1999.6361530x

Plougonven, E. (2009). *Link between the Microstructure of Porous Materials and their Permeability*. Ph.D. thesis, Université Sciences et Technologies, Bordeaux.

Pöhlitz, J., Rücknagel, J., Koblenz, B., Schlüter, S., Vogel, H.-J., and Christen, O. (2018). Computed tomography and soil physical measurements of compaction behavior under strip tillage, mulch tillage and no tillage. *Soil Til. Res.* 175, 205–2016. doi: 10.1016/j.still.2017.09.007

Pot, V., Peth, S., Monga, O., Vogel, L. E., Genty, A., Garnier, P., et al. (2015). Three-dimensional distribution of water and air in soil pores: comparison of two-phase two-relaxation-times lattice-Boltzmann and morphological model outputs with synchrotron X-ray computed tomography data. *Adv. Water Res.* 87, 87–102. doi: 10.1016/j.advwatres.2015.08.006

Raats, P. A. C., Zhang, Z. F., Ward, A. L., and Gee, G. W. (2004). The relative connectivity-tortuosity tensor for conduction of water in anisotropic unsaturated soils. *Vadose Zone J.* 3, 1471–1478. doi: 10.2136/vzj2004.1471

Rab, M. A., Haling, R. E., Aarons, S. R., Hannah, M., Young, I. M., and Gibson, D. (2014). Evaluation of X-ray computed tomography for quantifying macroporosity of loamy pasture soils. *Geoderma* 213, 460–470. doi: 10.1016/j.geoderma.2013.08.037

Rabot, E., Wiesmeier, M., Schlüter, S., and Vogel, H.-J. (2018). Soil structure as an indicator of soil functions: a review. *Geoderma* 314, 122–137. doi: 10.1016/j.geoderma.2017.11.009

Rachman, A., Anderson, S. H., and Gantzer, C. J. (2005). Computed-Tomographic measurement of soil macroporosity parameters as affected by stiff-stemmed grass hedges. *Soil Sci. Soc. Am. J.* 69, 1609–1616. doi: 10.2136/sssaj2004.0312

R Core Team (2015). *R: A Language and Environment for Statistical Computing*. Vienna: R Foundation for Statistical Computing.

Renard, P., and Allard, D. (2013). Connectivity metrics for subsurface flow and transport. *Adv. Wat. Res.* 51, 168–196. doi: 10.1016/j.advwatres.2011.12.001

Richards, L. A. (1948). Porous plate apparatus for measuring moisture retention and transmission by soils. *Soil Sci.* 66, 105–110. doi: 10.1097/00010694-194808000-00003

Roose, T., Keyes, S. D., Daly, K. R., Carminati, A., Otten, W., Vetterlein, D., et al. (2016). Challenges in imaging and predictive modeling of rhizosphere processes. *Plant Soil.* 407, 9–38. doi: 10.1007/s11104-016-2872-7

Rowell, D. L. (1994). *Soil Science: Methods and Application*. Harlow, UK: Longman Group Limited, Longman Scientific & Technical.

Sammartino, S., Lissy, A.-S., Bogner, C., Van Den Bogeart, R., Capowiez, Y., et al. (2015). Identifying the functional macropore network related to preferential flow in structured soils. *Vadose Zone J.* 14, 1–16. doi: 10.2136/vzj2015. 05.0070

Sandin, M., Koestel, J., Jarvis, N., and Larsbo, M. (2017). Post-tillage evolution of structural pore space and saturated and near-saturated hydraulic conductivity in a clay loam soil. *Soil Til. Res.* 165, 161–168. doi: 10.1016/j.still.2016.08.004

Schaap, M. G., Porter, M. L., Christensen, B. S. B., and Wildenschild, D. (2007). Comparison of pressure-saturation characteristics derived from computed tomography and lattice Boltzmann simulations. *Water Resour. Res.* 43:W12S06. doi: 10.1029/2006WR005730

Schmid, B., Schindelin, J., Cardona, A., Longhair, M., and Heisenberg, M. (2010). A high-level 3D visualization API for Java and ImageJ. *BMC Bioinformatics* 11:274. doi: 10.1186/1471-2105-11-274

Schneider, C. A., Rasband, W. S., and Eliceiri, K. W. (2012). NIH Image to ImageJ: 25 years of image analysis. *Nat. Methods* 9, 671–675. doi: 10.1038/nmeth.2089

Shah, S. M., Gray, F., Crawshaw, J. P., and Boek, E. S. (2016). Micro-computed tomography pore-scale study of flow in porous media: effect of voxel resolution. *Adv. Wat. Res.* 95, 276–287. doi: 10.1016/j.advwatres.2015.07.012

Smet, S., Plougonven, E., Léonard, A., Degré, A., and Beckers, E. (2017). X-ray Micro-CT: how soil pore space description can be altered by image processing. *Vadose Zone J.* 17:160049. doi: 10.2136/vzj2016.06.0049

Smith, K. A., Ball, T., Conen, F., Dobbie, K. E., Massheder, J., and Rey, A. (2003). Exchange of greenhouse gases between soil and atmosphere: interactions of soil physical factors and biological processes. *Eur. J. Soil Sci.* 54, 779–791. doi: 10.1046/j.1351-0754.2003.0567.x

Taina, I. A., Heck, R. J., and Elliot, T. R. (2008). Application of X-ray computed tomography to soil science: a literature review. *Can. J. Soil Sci.* 88, 1–20. doi: 10.4141/CJSS06027

Tarplee, M., and Corps, N. (2008). *Skyscan 1072 desktop X-ray microtomograph. sample scanning reconstruction, analysis and visualisation (2D and 3D) Protocols*. Guidelines, notes, selected references and F.A.Qs.

Tracy, S. R., Daly, K. R., Sturrock, C. J., Crout, N. M. J., Mooney, S. J., and Roose, T. (2015). Three-dimensional quantification of soil hydraulic properties using X-ray computed tomography and image-based modeling. *Water Resour. Res.* 51, 1006–1022. doi: 10.1002/2014WR016020

Udawatta, R. P., and Anderson, S. H. (2008). CT-measured pore characteristics of surface and subsurface soils influenced by agroforestry and grass buffers. *Geoderma* 145, 381–389. doi: 10.1016/j.geoderma.2008.04.004

Ursino, N., Roth, K., Gimmi, T., and Flühler, H. (2000). Upscaling of anisotropy in unsaturated Miller-similar porous media. *Water Resour. Res.* 36, 421–430. doi: 10.1029/1999WR900320

van Genuchten, M. T. (1980). A closed-form equation for prediction the hydraulic conductivity of unsaturated soils. *Soil Sci. Soc. Am. J.* 44, 892–898. doi: 10.2136/sssaj1980.03615995004400050002x

Vogel, H.-J. (2000). A numerical experiment on pore size, pore connectivity, water retention, permeability, and solute transport using network models. *Eur. J. Soil Sci.* 51, 99–105. doi: 10.1046/j.1365-2389.2000.00275.x

Vogel, H.-J., and Roth, K. (1998). A new approach for determining effective soil hydraulic functions. *Eur. J. Soil Sci.* 49, 547–556. doi: 10.1046/j.1365-2389.1998.4940547.x

Vogel, H.-J., Tölke, J., Schulz, V. P., Krafczyk, M., and Roth, K. (2005). Comparison of a lattice-boltzmann model, a full-morphology model, and a pore network model for determining capillary pressure–saturation relationships. *Vadose Zone J.* 4, 380–388. doi: 10.2136/vzj2004.0114

Vogel, L. E., Makowski, D., Garnier, P., Vieublé-Gonod, L., Coquet, Y., Raynaud, X., et al. (2015). Modeling the effect of soil meso- and macropores topology on the biodegradation of a soluble carbon substrate. *Adv. Water Res.* 83, 123–136. doi: 10.1016/j.advwatres.2015.05.020

Vogel, H.-J., Weller, U., and Schlüter, S. (2010). Quantification of soil structure based on Minkowski functions. *Comput. Geosci.* 36, 1236–1245. doi: 10.1016/j.cageo.2010.03.007

Wagenmakers, E.-J., Verhagen, J., and Ly, A. (2016). How to quantify the evidence for the absence of correlation. *Behav. Res.* 48, 412–426. doi: 10.3758/s13428-015-0593-0

Wetzels, R., and Wagenmakers, E.-J. (2012). A default Bayesian hypothesis test for correlations and partial correlations. *Psychon. Bull. Rev.* 19, 1057–1064. doi: 10.3758/s13423-012-0295-x

Wildenschild, D., and Sheppard, A. P. (2013). X-ray imaging and analysis techniques for quantifying pore-scale structure and processes in subsurface porous medium systems. *Adv. Water Res.* 51, 217–246. doi: 10.1016/j.advwatres.2012.07.018

Young, I. M., Blanchart, E.,Chenu, C., Dangerfield, M., Fragoso, C., Grimaldi, M., et al. (1998). The interaction of soil biota and soil structure under global change. *Global Change Biol.* 4, 703–712. doi: 10.1046/j.1365-2486.1998.00194.x

Zhang, Z. F. (2014). Relationship between anisotropy in soil hydraulic conductivity and saturation. *Vadose Zone J.* 13:vzj2013.09.0172. doi: 10.2136/vzj2013.0 9.0172

Conflict of Interest Statement: The authors declare that the research was conducted in the absence of any commercial or financial relationships that could be construed as a potential conflict of interest.

Denitrification in Soil Aggregate Analogues-Effect of Aggregate Size and Oxygen Diffusion

Steffen Schlüter [1]*, Sina Henjes [2], Jan Zawallich [3], Linda Bergaust [4], Marcus Horn [2], Olaf Ippisch [3], Hans-Jörg Vogel [1,5] and Peter Dörsch [6]

[1] Department of Soil System Sciences, Helmholtz-Centre for Environmental Research-UFZ, Halle, Germany, [2] Institute of Microbiology, Leibniz University, Hannover, Germany, [3] Institue of Mathematics, TU Clausthal, Claustal-Zellerfeld, Germany, [4] Faculty of Chemistry, Biotechnology and Food Science, Norwegian University of Life Sciences, NMBU, Ås, Akershus, Norway, [5] Institute of Soil Science and Plant Nutrition, Martin Luther University of Halle-Wittenberg, Halle, Germany, [6] Faculty of Environmental Sciences and Natural Resource Management, Norwegian University of Life Sciences, NMBU, Ås, Akershus, Norway

Soil-borne nitrous oxide (N_2O) emissions have a high spatial and temporal variability which is commonly attributed to the occurrence of hotspots and hot moments for microbial activity in aggregated soil. Yet there is only limited information about the biophysical processes that regulate the production and consumption of N_2O on microscopic scales in undisturbed soil. In this study, we introduce an experimental framework relying on simplified porous media that circumvents some of the complexities occuring in natural soils while fully accounting for physical constraints believed to control microbial activity in general and denitrification in particular. We used this framework to explore the impact of aggregate size and external oxygen concentration on the kinetics of O_2 consumption, as well as CO_2 and N_2O production. Model aggregates of different sizes (3.5 vs. 7 mm diameter) composed of porous, sintered glass were saturated with a defined growth medium containing roughly 10^9 cells ml^{-1} of the facultative anaerobic, *nosZ*-deficient denitrifier *Agrobacterium tumefaciens* with N_2O as final denitrification product and incubated at five different oxygen levels (0–13 vol-%). We demonstrate that the onset of denitrification depends on the amount of external oxygen and the size of aggregates. Smaller aggregates were better supplied with oxygen due to a larger surface-to-volume ratio, which resulted in faster growth and an earlier onset of denitrification. In larger aggregates, the onset of denitrification was more gradual, but with comparably higher N_2O production rates once the anoxic aggregate centers were fully developed. The normalized electron flow from the reduced carbon substrate to N-oxyanions (e_{denit}^-/e_{total}^- ratio) could be solely described as a function of initial oxygen concentration in the headspace with a simple, hyperbolic model, for which the two empirical parameters changed with aggregate size in a consistent way. These findings confirm the important role of soil structure on N_2O emissions from denitrification by shaping the spatial patterns of microbial activity and anoxia in aggregated soil. Our dataset may serve as a benchmark for constraining or validating spatially explicit, biophysical models of denitrification in aggregated soil.

Keywords: greenhouse gas emissions, denitrification kinetics, microbial hotspots, microsites, anoxic aggregate centers, *Agrobacterium tumefaciens*, physically-based modeling

1. INTRODUCTION

Emission and uptake of greenhouse gases (CO_2, CH_4, N_2O) by soil are subject to pronounced spatial and temporal fluctuations. Emission patterns in space and time appear to be controlled by the spatial and temporal distribution of labile organic matter (e.g., roots, crop residues, animal manure, particulate organic matter) and the occurrence of physicochemical conditions (e.g., temperature, soil moisture, anoxic volumes) favorable for specific microbial processes (e.g., nitrification, denitrification). This has led to the notion that the bulk of microbially driven greenhouse gas (GHG) turnover occurs in "hot spots" and during "hot moments" (Groffman et al., 2009; Vos et al., 2013; Kuzyakov and Blagodatskaya, 2015; Tecon and Or, 2017). While the emission of carbon dioxide (CO_2) through soil respiration exhibits a fairly low spatio-temporal variability, nitrous oxide emissions (N_2O) are a notorious example for extreme variability. Sampling campaigns with undisturbed soil often exhibit a log-normal distribution of denitrification activity in aerated soil with numerous "coldspots" without emissions and some samples with very high emissions (Röver et al., 1999; Mathieu et al., 2006). In a seminal study Parkin (1987) demonstrated that 25–85% of denitrification activity was associated with particulate organic matter that comprised <1% of the soil volume. Thus, a better understanding of denitrification activity on microscopic scales is required to improve predictions of N_2O emissions at relevant spatial scales.

Denitrifiers are facultative aerobes that start to denitrify when oxygen becomes limiting. The reduction of nitrate (NO_3^-) to dinitrogen (N_2) occurs via a series of enzymatic steps and intermediates (NO_2^-, NO, N_2O) (Philippot et al., 2007). The basic requirements for heterotrophic denitrification in soil are (1) the presence of decomposable carbon supplying electrons for anaerobic respiration, (2) a shortage of O_2 as electron acceptor, (3) the availability of NO_3^- as an alternative electron acceptor and (4) a microbial community that has the capacity to express the enzymes for some or all reduction steps in denitrification. Key soil environmental factors that govern denitrification are well understood and can be roughly grouped into biochemical constraints and physical constraints, but it is the interaction of all factors that causes the seemingly erratic nature of denitrification activity in soils. Firstly, denitrification is constrained biochemically by the availability and quality of carbon substrates in soil such as root exudates, plant litter and soil organic matter. Besides sustaining denitrification, organic substrates fuel aerobic respiration, thus enhancing local anoxia in micro-sites. Secondly, the denitrifier community is composed of species exhibiting different regulatory phenotypes (Bergaust et al., 2011) that differ in completeness and timing of denitrification gene transcription. This causes the onset of denitrification as well as the accumulation of intermediates to be different for different denitrifying communities (Dörsch et al., 2012). Notably, a significant fraction of the denitrifiers does not have the genetic capacity to reduce N_2O (Jones and Hallin, 2010) and it is debated whether functional redundancy enabling complete denitrification is always warranted in soil microbial consortia at a micro-scale (Philippot et al., 2011, 2013). Simplistic

estimates of spatially explicit bacterial diversity in soil suggest that moderately active soil (10^9 cells g^{-1} soil) harbors around 100 bacterial species within interaction distance ($< 20\ \mu m$) and this number remains below 400 in hotspots (10^{10} cells g^{-1} soil) (Raynaud and Nunan, 2014). Thirdly, microbial activity as well as post-transcriptional regulation are controlled by environmental factors such as the presence of N-oxides (NO_2^-, NO, N_2O), temperature and pH. It is well-known, for instance, that a low pH suppresses the N_2O reductase enzyme post-transcriptionally so that the molar ratio between N_2O and N_2 is shifted toward N_2O (Šimek and Cooper, 2002; Liu et al., 2010; Bakken et al., 2012). On the other hand, diffusion of reactants and products to and from the sites of microbial denitrification are constrained physically in the soil matrix. The diffusion pathways for gaseous fluxes are mainly governed by the water content, because the diffusion coefficients are many orders of magnitudes smaller in water than in air. This leads to the well-known phenomenon that N_2O emissions exhibit a threshold behavior around a water saturation of 70% and peaks around 90% (Linn and Doran, 1984; Ruser et al., 2006) at which the air becomes discontinuous. With lost air continuity the average distance for dissolved oxygen to reach a microbial hotspot starts to diverge from the size of the hotspot itself to typical aggregate sizes. If aggregation is poorly developed, then the mean diffusion length amounts to the average half distances between air-filled macropores. At higher saturation, the N_2O/N_2 ratio shifts toward N_2, because large fractions of the soil become anoxic so that dissolved N_2O is consumed where it is produced or during its extended diffusion path toward the atmosphere. Even the role of wet soils as a sink for atmospheric N_2O is debated but poorly investigated (Chapuis-Lardy et al., 2007; Kolb and Horn, 2012). Finally, denitrification activity in hotspots can also be constrained by nitrate diffusion to sites of active denitrification (Smith, 1990). The well-known observation that nitrate amendment leads to increased denitrification activity is often interpreted from a biochemical standpoint as the effect of a high half-saturation constant of dissimilatory NO_3^- reductase (Firestone, 1982). Yet, by employing Fick's law it can be shown that the diffusion flux into a hotspot also scales linearly with the concentration gradient between the NO_3^- depleted hotspot and the external NO_3^- concentration regulated by the nitrate amendment (Myrold and Tiedje, 1985). Hence, the high half-saturation constant can simply be a consequence of a NO_3^- diffusion constraint.

Microscale denitrification models that combine the aforementioned biochemical and physical controls based on a set of reaction-diffusion equations typically employ individual soil aggregates as a model domain (Leffelaar and Wessel, 1988; Arah and Smith, 1989). Assuming a steady-state situation and uniform initial substrate concentration, the denitrification activity typically scales with the volume fraction of the anoxic aggregate center which, in turn, is mainly controlled by the aggregate size. The resulting oxygen profiles as a function of distance to the aggregate boundary typically exhibit an exponential decline at a rate that scales with microbial activity. This has been confirmed experimentally with micro-sensors (Sexstone et al., 1985; Zausig et al., 1993; Højberg et al., 1994). Currently, new models are underway that allow for numerical experiments on the role of

substrate location for denitrification activity through spatial self-organization of aerobic and anaerobic species along oxygen gradients (Ebrahimi and Or, 2015). A major outcome is that an internal carbon source such as sequestered particulate organic matter is more efficient in invoking denitrification activity in an anoxic micro-site than an external carbon source like dissolved organic matter.

Such new insights into spatially explicit, micro-scale denitrification models call for new, systematic laboratory experiments on denitrification in soil aggregates. The objective of this study was to explore the impact of aggregate size and external oxygen concentration on aerobic and anaerobic respiration in model soil aggregates. For this, we inoculated the aggregates with a single bacterial strain (*Agrobacterium tumefaciens*), which is able to switch from aerobic respiration to denitrification. In this way, the physical constraints on denitrification kinetics could be studied without the added complexity of spatial or temporal patterns in denitrification activity through interactions within bacterial consortia. Furthermore, the delicate balance between N_2O and the difficult to quantify N_2 production could be neglected as *A. tumefaciens* lacks the *nosZ* gene encoding N_2O reductase and hence has N_2O as its final denitrification product. This still leaves a wealth of diffusion and reaction processes co-occurring within an aggregate as depicted in **Figure 1**. Denitrification activity was assessed by incubating differently sized aggregates loosely placed in closed bottles and monitoring O_2 depletion and N_2O accumulation in the headspace of the bottles at high resolution until the added carbon source (succinate) or the electron acceptor (NO_3^-) were depleted. We did not measure dissolved oxygen directly, but inferred the spatial extent of the anoxic volume from denitrification kinetics. The data can be used to predict the critical aggregate size for denitrification in *A. tumefaciens* to occur at different external O_2 concentrations.

2. MATERIALS AND METHODS

2.1. Bacterial Strain and Growth Medium

We used a pure culture of the bacterial strain *Agrobacterium tumefaciens* C58 (ATCC 33970), a facultative anaerobic α-proteobacterium, which lacks the genes encoding nitrous oxide reductase (Baek and Shapleigh, 2005; Bergaust et al., 2008). Therefore, N_2O was the final denitrification product. Sistrom's medium (Sistrom, 1960) with an initial pH of 7 was used as growth medium. The medium contained (l^{-1}): K_2HPO_4 3.48 g, NH_4Cl 0.195 g, succinic acid 4 g, L-glutamic acid 0.1 g, L-aspartic acid 0.04 g, NaCl 0.5 g, nitrolotriacetic acid 0.2 g, $MgSO_4 * 7H_2O$ 0.3 g, $CaCl_2 * 7H_2O$ 15 mg, and $FeSO_2 * 7H_2O$ 7 mg. In addition, trace elements and vitamins were added (l^{-1}): EDTA (triplex 3) 1.765 mg, $ZnSO_4 * 7H_2O$ 10.95 mg, $FeSO_4 * 7H_2O$ 5 mg, $MnSO_4 * 7H_2O$ 1.54 mg, $CuSO_4 * 5H_2O$ 0.392 mg, $Co(NO3)_7 * 6H_2O$ 0.248 mg, H_3BO_3 0.114 mg, nicotinic acid 1 mg, thiamine HCl 0.5 mg, biotin 0.01 mg. pH was brought to 7.0 with 10 M KOH and the medium was sterilized by autoclaving. KNO_3 was added to the medium to a concentration of 5 mM as a substrate for denitrification. A stirred culture was grown aerobically at 25°C. Cells were harvested during

exponential growth by centrifugation (10,000 rpm for 7 min). The resulting cell pellets were immediately resuspended in fresh growth medium to a density of $\approx 3 \times 10^9$ cells ml^{-1} which is typical for hotspots in real soil (Raynaud and Nunan, 2014). The cultures were kept on ice to inhibit growth until the start of the experiment.
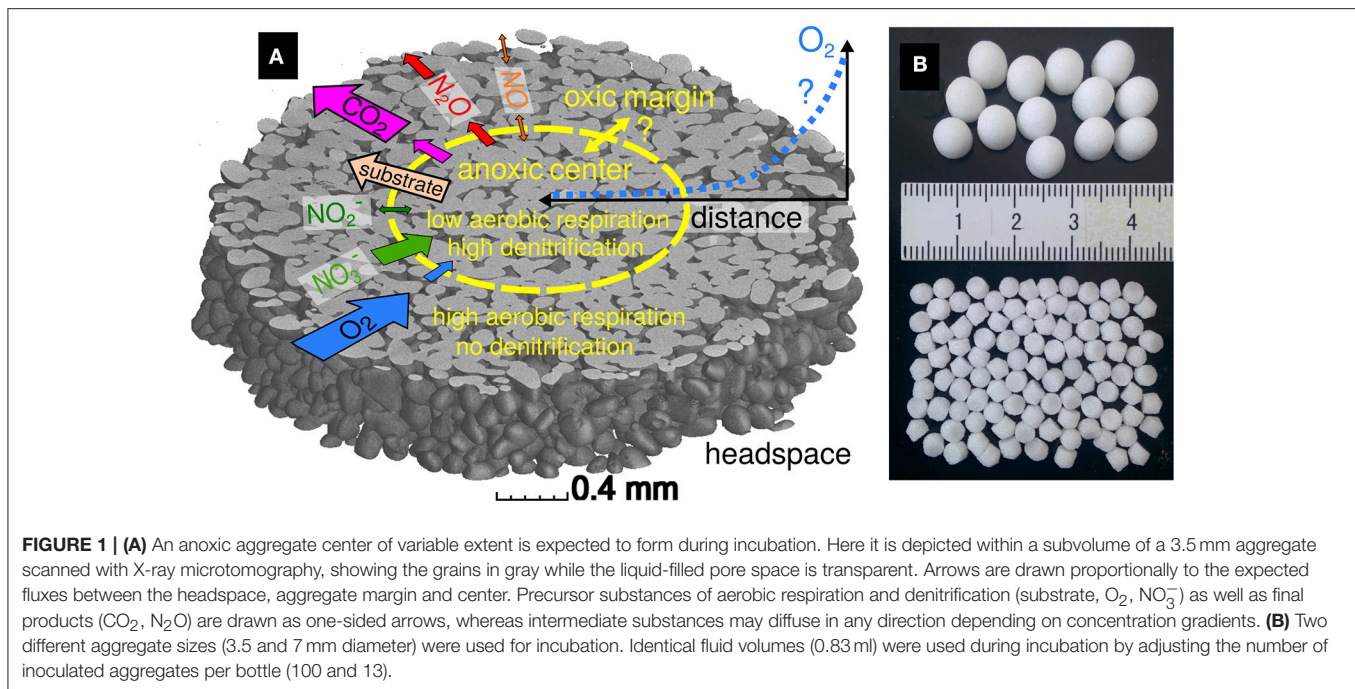
2.2. Aggregate Inoculation

Porous borosilicate glass beads (VitraPOR P100, ROBU Glasfilter Geräte GmbH, Hattert Germany) served as a simplified analogue for soil aggregates. The sintered glass beads had a porosity of 32% and an internal pore size in the range of 45–100 μm. Two different bead sizes were used with a diameter of 3.5 and 7 mm and an internal pore volume of 8.3 $\pm$ 0.2 μl and 64.0 $\pm$ 0.6 μl, respectively. In the following these will be referred to as small and large aggregates. The shape and internal pore structure as obtained via X-ray microtomography are depicted in **Figure 1**. After submersion of the aggregates in the growth cultures, roughly 3% of the pore space was filled with entrapped air (data not shown). These bubbles were removed completely from the submersed aggregates through vacuum application in a gas-tight bottle for 1–2 min.

Either 100 small or 13 large aggregates were placed into empty 120 ml glass bottles so that in both cases the pore volume inside of the aggregates filled with cell culture was about 830 μl per bottle, with some 10–20% additional liquid adhering to aggregate surfaces by weak capillary forces. After closing the bottles with an air-tight butyl rubber septum, the bottles were purged with helium by applying five cycles of vacuum and He filling. The bottles were immediately spiked with oxygen, to adjust final concentrations (v/v) of 13, 7, 3.5, 2, and 0% O_2 in the head space. Hence, the pre-incubation of the cell cultures was aerobic during the entire sample preparation, except for the short intervals of degassing and He purging. Two replicates were prepared for each aggregate size and initial oxygen concentration, resulting in a total of ten treatments and twenty bottles. Finally, the bottles were moved from the ice bath to a water bath kept at 20°C to initiate microbial activity and the overpressure that built up due to spiking with O_2 and warming of the bottles was released, before the gas chromatography (GC) measurements started.

2.3. Incubation

The incubations were carried out with a robotized incubation system consisting of an autosampler (GC-PAL, CTC Analytics, Zwingen, Switzerland) connected to a GC (Agilent Model 7890A, Santa Clara, CA, USA) and an NO analyzer (Teledyne T200, San Diego, CA, USA), allowing for repeated headspace analysis of oxygen (O_2) and carbon dioxide (CO_2) as well as the denitrification products nitric oxide (NO), nitrous oxide (N_2O) and dinitrogen (N_2) via a peristaltic pump (Molstad et al., 2007). The gas volume ($\approx$ 1 ml) lost with each sampling was automatically replaced by He, so that the pressure in the bottles was kept at $\approx$1 atm. The bottles were sampled every 3 h for 45 h. The nitrate (NO_3^-) and nitrite (NO_2^-) concentrations that remained in the aggregates at the end of the experiment were measured with a colorimetric assay. To do so, all bottles were kept on ice after the experiment and

FIGURE 1 | (A) An anoxic aggregate center of variable extent is expected to form during incubation. Here it is depicted within a subvolume of a 3.5 mm aggregate scanned with X-ray microtomography, showing the grains in gray while the liquid-filled pore space is transparent. Arrows are drawn proportionally to the expected fluxes between the headspace, aggregate margin and center. Precursor substances of aerobic respiration and denitrification (substrate, O_2, NO_3^-) as well as final products (CO_2, N_2O) are drawn as one-sided arrows, whereas intermediate substances may diffuse in any direction depending on concentration gradients. **(B)** Two different aggregate sizes (3.5 and 7 mm diameter) were used for incubation. Identical fluid volumes (0.83 ml) were used during incubation by adjusting the number of inoculated aggregates per bottle (100 and 13).

aggregates from each treatment were thoroughly crushed in a mortar and taken up with 0.9% NaCl solution. The turbid fluid containing medium, cells and bead fragments was collected in Eppendorf tubes and centrifuged (10,000 rpm, 5 min) to obtain a clear solution. The protocols for nitrite and nitrite + nitrate quantification were adapted from Keeney and Nelson (1982) and Doane and Horwáth (2003). Nitrate concentrations were obtained through subtraction using two technical replicates per assay. The spectrophotometric measurement was carried out at 540 nm (Tecan infinite F50, Tecan, Männedorf, Switzerland) and converted into concentrations through calibration curves.

3. RESULTS

3.1. Aggregate Size Effects

Aerobic microbial respiration as determined by decrease in O_2 and increase in CO_2 over time in **Figures 2A,B** was clearly limited by the carbon substrate in the aerobic cultures. Depletion of succinate was indicated by a slow-down of O_2 consumption, which occurred in the small aggregates, depending on initial O_2 level, between 15 and 30 h into the incubation. O_2 consumption after this period was reduced substantially. The slow-down in O_2 consumption and CO_2 accumulation occurred synchronously. The added succinate in the fresh growth medium amounted to 68 μmol C/bottle, of which 27–35 μmol/bottle were converted to CO_2, which suggests a yield factor between assimilation and total carbon consumption of 0.4–0.5 depending on treatment. However, the absolute accumulation of CO_2 in the headspace might have been reduced by an increase in CO_2 solubility due to a pH increase caused by the reduction of NO_3^- to NO_2^-. Respiration kinetics in **Figures 2A,B** show that microbial activity was clearly delayed in the large aggregates as compared to the

small aggregates. Irrespective of aggregate size, the onset of substrate depletion as well as the total amount of produced CO_2 at the end of the experiment scaled positively with the O_2 concentration in the headspace. The higher the amount of external O_2, the steeper the gradient between dissolved O_2 at the aggregate boundary and in the aggregate center, which in turn results in a larger diffusive flux, a better supply with O_2 and eventually a smaller extent of anoxic centers.

Note that microbial respiration in the completely anoxic treatments (0% O_2) was exceptionally small, irrespective of aggregate size. This effect can be explained by unbalanced kinetics of denitrification associated enzyme induction in *A. tumefaciens*. Sudden anoxia in growing cultures resulted in pronounced NO release, accumulating NO to more than 1 μmol/bottle, which corresponds to more than 0.5 μM in the liquid medium (**Figure 2C**). Dissolved NO concentrations > 0.3 μM have been shown to repress metabolic activity in *A. tumefaciens* (Bergaust et al., 2008). In all oxic treatments the NO concentrations were 1–2 orders of magnitude smaller. In the small aggregates the NO peak coincided with the depletion of the primary carbon substrate, after which NO was quickly consumed by the microbes inside the aggregates. The oxic treatment with the lowest oxygen concentration (2% O_2) showed an interesting double peak in NO, one at a very early stage in the logarithmic growth phase and another shortly before succinate was depleted. Except for the 2% O_2 treatment, large aggregates did not show a clear NO peak but higher steady-state NO concentrations than small aggregates toward the end of the incubation, suggesting different denitrification kinetics in small and large aggregates.

N_2O accumulation in the headspace followed a characteristic pattern with respect to initial O_2 concentration (**Figure 2D**). The lower the initial O_2 concentration in the headspace, and
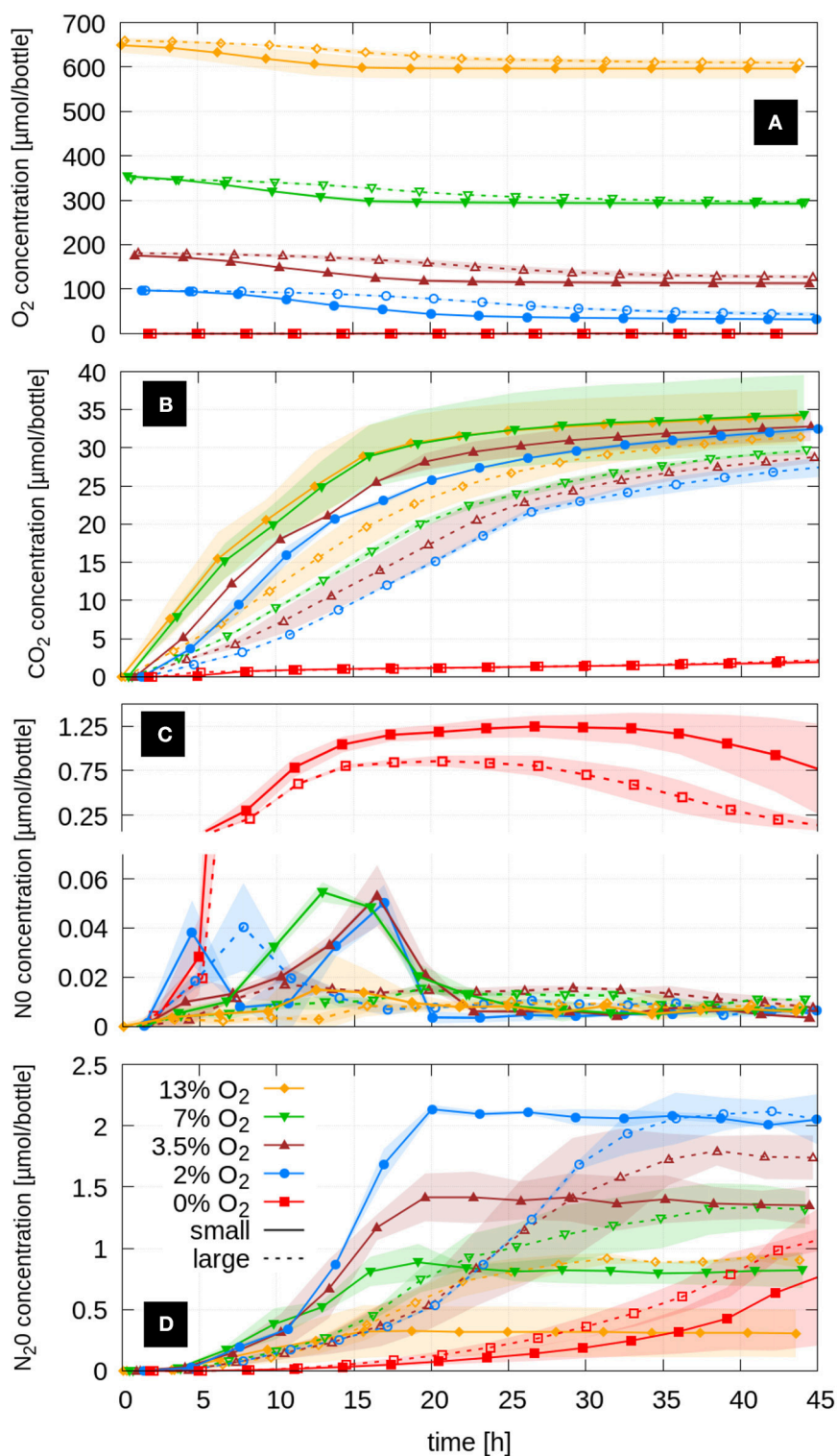
FIGURE 2 | Respiration kinetics of *A. tumefaciens* in small and large aggregates at five initial oxygen concentrations shown as average headspace concentrations (*n* = 2) of **(A)** O_2, **(B)** CO_2, **(C)** NO and **(D)** the final denitrification product N_2O. Shaded areas represent standard deviations.

the less oxygen was available for aerobic growth, the more N_2O accumulated as the final denitrification product. In the small aggregates denitrification abruptly stopped after ca. 18 h. At this point all succinate was consumed (as judged from the O_2 and CO_2 kinetics, **Figures 2A,B**).
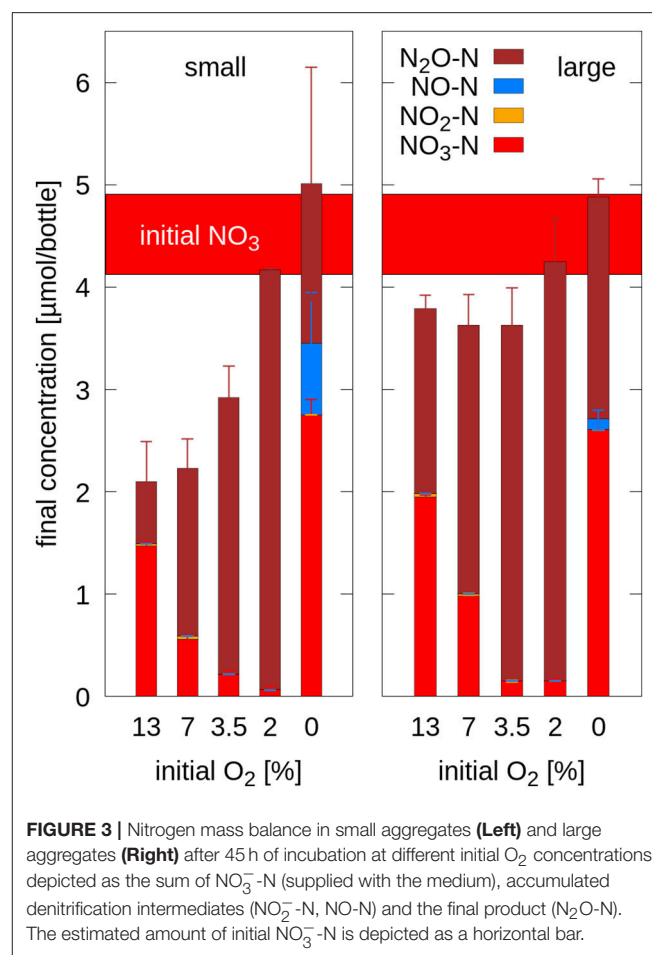
Microbial respiration beyond the point of succinate depletion was small and likely fell below the rate of O_2 diffusion into the aggregate so that the anoxic centers vanished. Larger aggregates released N_2O more gradually because slower aerobic growth led to less anoxia initially. The point in time when the N_2O accumulation in the large aggregates exceeded the value from small aggregates decreased with increasing oxygen concentration in the headspace from 36 h (2% O_2) to 28 h (3.5% O_2), 21 h (7% O_2) to 16 h (13% O_2). The total N_2O production by large aggregates was either as large (2% O_2) or 25% (3.5% O_2), 50% (7% O_2), and 100% (13% O_2) larger than in the small aggregates with comparable oxygen concentrations. Here as well, N_2O accumulation leveled off when O_2 consumption decreased due to C-limitation. Aggregates incubated without O_2 (0 vol-%) exhibited a delayed accumulation of N_2O. Only after $\approx$24 h did NO start to be net consumed and N_2O production rates increased.

The recovery of the initially added NO_3^--N (4.15 μmol per bottle) ranged between 88 and 102% in the oxic treatments with large aggregates (**Figure 3**). Less N was recovered in the treatments with small aggregates (51–100%) and the mismatch increased with increasing oxygen levels. Presumably, with higher oxygen availability, cell growth exceeded the supply of ammonia contained in the medium so that some nitrate was assimilated. In both anoxic treatments more N was recovered than supplied with the added nitrate when estimated from the internal porosity of the aggregates, but was still within a range that could be explained with surplus of medium by liquid adhering to aggregate surfaces (118–122%). In general, the N-mass balances indicate that negligible amounts of denitrification intermediates (NO_2^-, NO) accumulated, while the partitioning into N still present as nitrate after 45 h incubation and N denitrified to N_2O followed a similar pattern over O_2 availability for both aggregate sizes.

4. DISCUSSION

4.1. Denitrification Kinetics

Denitrifying bacteria fall into different categories denoted as denitrification regulatory phenotypes (Bergaust et al., 2011), depending on how they manage the transition from oxic to anoxic conditions. The optimal switch between respiration strategies is important for two reasons: (1) The ATP yield by aerobic respiration is higher than by denitrification, thus, electrons should be directed toward oxygen when possible. (2) The enzymes for denitrification activity have to be expressed before oxygen is completely depleted, so that cells do not get caught in a situation of metabolic arrest. Batch incubation experiments with stirred cultures with nitrate amendment and the same growth medium have shown that *Agrobacterium tumefaciens* belongs to a common denitrification regulatory phenotype with a sequential production of denitrification intermediates (Bergaust et al., 2008, 2011). Nitrate reduction

FIGURE 3 | Nitrogen mass balance in small aggregates **(Left)** and large aggregates **(Right)** after 45 h of incubation at different initial O_2 concentrations depicted as the sum of NO_3^--N (supplied with the medium), accumulated denitrification intermediates (NO_2^--N, NO-N) and the final product (N_2O-N). The estimated amount of initial NO_3^--N is depicted as a horizontal bar.

is induced while oxygen is still present, whereas nitrite and NO reduction commence after oxygen depletion. In cultures where oxygen depletion was too rapid, NO accumulated to toxic concentrations, resulting in respiratory arrest (Bergaust et al., 2008). This general pattern was confirmed by our study. Indeed, NO production was maximal and growth delayed when the aerobic inoculum was suddenly subjected to 0% oxygen conditions. In the oxic treatments NO and N_2O accumulation in the headspace commenced simultaneously. In larger aggregates, the NO peak was widened into a broad plateau at lower levels. Presumably, the oxic aggregate margins were thicker in larger aggregates with more gradual growth, so that a quick NO release was buffered by longer diffusion distances between the production sites in the anoxic aggregate center and the headspace, causing longer residence times which increased the chance for NO reduction along the way.

4.2. Anoxic Aggregate Centers

The purpose of our experiment was to study denitrification kinetics under dynamic growth conditions, in contrast to steady-state conditions which are typically invoked as a simplifying assumption in physically-based denitrification models (Leffelaar and Wessel, 1988; Arah and Smith, 1989). Hence, we needed

to account for the different growth rates when comparing the denitrification kinetics in both aggregate sizes, since the cells grew faster in small aggregates due to a better oxygen supply caused by a larger surface-to-volume ratio. A correction for growth effects can be achieved by analyzing N_2O/CO_2 ratios as depicted in **Figure 4A**, i.e., the amount of N_2O as the final product of denitrification is normalized against CO_2 as the final production of respiration. There was hardly any difference in normalized denitrification between the two aggregate sizes at the same initial oxygen level during the first 12 h. Only after the anoxic centers were fully established in the aggregates two consistent trends evolved. First, denitrification was always larger in the large aggregates, irrespective of external O_2 concentration, implying that the volume fraction of anoxic centers is smaller in small aggregates. Second, denitrification increased with decreasing external O_2 concentration, as the diffusive flux of O_2 was driven by the gradient between the oxygen depleted aggregate centers and the dissolved O_2 at the aggregate boundary, which is in equilibrium with the concentration of gaseous O_2 in the headspace of the bottle. Interestingly, doubling of the aggregate size had roughly the same effect on the final N_2O/CO_2 ratio as a reduction of external O_2 concentration by 50%. The absolute values of the N_2O/CO_2 ratio, however, should not be taken for granted due to the expected pH increase caused by nitrate reduction that changes CO_2 solubility.

A more direct approach to assess denitrification activity is to compute the fraction of electron flow diverted to electron acceptors for anaerobic respiration (e^-_{denit}, including NO_3^-, NO_2^-, NO) and total respiration (e^-_{total}, including NO_3^-, NO_2^-, NO and O_2) (Bergaust et al., 2011). Time series of these electron flows are shown for selected treatments in **Figure 4B**, inset. The ratio of cumulative electron flows at the end of incubation exhibited a systematic trend (**Figure 4B**) that is described by a hyperbolic relationship between the e^-_{denit}/e^-_{total} ratio [%] and the initial oxygen concentration C_{O_2} [%]:

$$\frac{e^-_{denit}}{e^-_{total}} = 100\left(1 - \left(\frac{C_{O_2}}{100}\right)^a\right)^b \qquad (1)$$

where a and b are dimensionless fitting parameters. The values of the fitting parameters are shown in **Table 1**. The fit across all investigated oxygen levels was excellent for both aggregate sizes. Note that a similar model of the form $\left[a/\left(a - C_{O_2}\right)\right]^b$ was also capable to reproduce the sharp decline in the electron flow ratio with only slightly larger errors, whereas an exponential model resulted in a too smooth decline (data not shown). The good model fit across a wide oxygen range may allow for extrapolation toward higher O_2 concentrations. At ambient conditions (21% O_2), small aggregates are likely to be devoid of anoxia, whereas large aggregates may still have roughly 2% of electron flow diverted to denitrification. The outer exponent b was roughly increased by a factor of two, as the aggregate diameter was doubled. This consistent scaling of the exponent suggests that predictions for larger aggregates are feasible, but this

can not be validated on a set of two different aggregate diameters. Further experiments would be necessary.

4.3. Consequences for Greenhouse Gas Emissions From "Hotspots" in Soil

The delicate balance between growth rates and the transient formation of anoxic centers led to a rich variety of denitrification dynamics which resulted from the interplay of a number of diffusive fluxes summarized in **Figure 1A**. The diffusive flux of oxygen into the aggregates and the diffusive flux of the final respiration products (CO_2 and N_2O) out of the aggregates can be considered as uni-directional processes that solely depend on concentration gradients, since the diffusion coefficient does not change at constant (complete) saturation. Likewise, the diffusive flux of the dissolved carbon substrate (succinate) from the less active, anoxic aggregate center into the more substrate-depleted, oxic aggregate margin as well as the diffusive flux of nitrate from the well O_2-supplied aggregate margin into the actively denitrifying aggregate center are uni-directional, yet without any exchange with the headspace. Finally, the diffusion of intermediates (NO_2^-, NO) is bi-directional and changing during incubation. Therefore, it might look surprising that a rather simple model with two empirical parameters is able to capture the denitrification behavior for a large range of oxygen concentrations and different aggregate sizes. However, this can be ascribed to the fact that (1) all oxic treatments were equally constrained by electron-donor and not electron-acceptor limitation and (2) that the model describes cumulative electron fluxes and not denitrification kinetics.

There are several reasons why our findings cannot be directly transferred to natural conditions. Natural consortia and a more complex composition of reduced carbon in soil would lead to coexistence and spatially separated niches causing spatial and temporal variability of aerobic respiration and denitrification activity (Vos et al., 2013; Kuzyakov and Blagodatskaya, 2015) as well as other N_2O forming processes (e.g., nitrification) to occur simultaneously (Philippot et al., 2007; Stange et al., 2013). While the sudden removal of oxygen that was induced in the anoxic treatments could certainly occur under natural conditions, e.g., after a heavy rainfall, the toxic NO accumulation would not happen in natural consortia with a certain amount of functional redundancy (Schimel and Schaeffer, 2012). Moreover, a mobile carbon substrate like dissolved organic matter is likely to evoke a different spatio-temporal pattern in aerobic respiration and denitrification than a stationary carbon substrate like particulate organic matter (Ebrahimi and Or, 2015). An exponentially growing culture foraging on a low-molecular carbon substrate like in our experiments may also occur under natural conditions, when easily decomposable organic matter is added to the soil (e.g., animal manure, plant residues after harvest or plowing). But this scenario is rather an exception, whereas a steady-state or gradual change in microbial activity typically prevails in soil. Nevertheless, dynamic growth also poses an interesting case for modeling. Even though hotspots of microbial activity are believed to be the dominating sites of denitrification in soil, they cannot readily be investigated in isolation from the surrounding
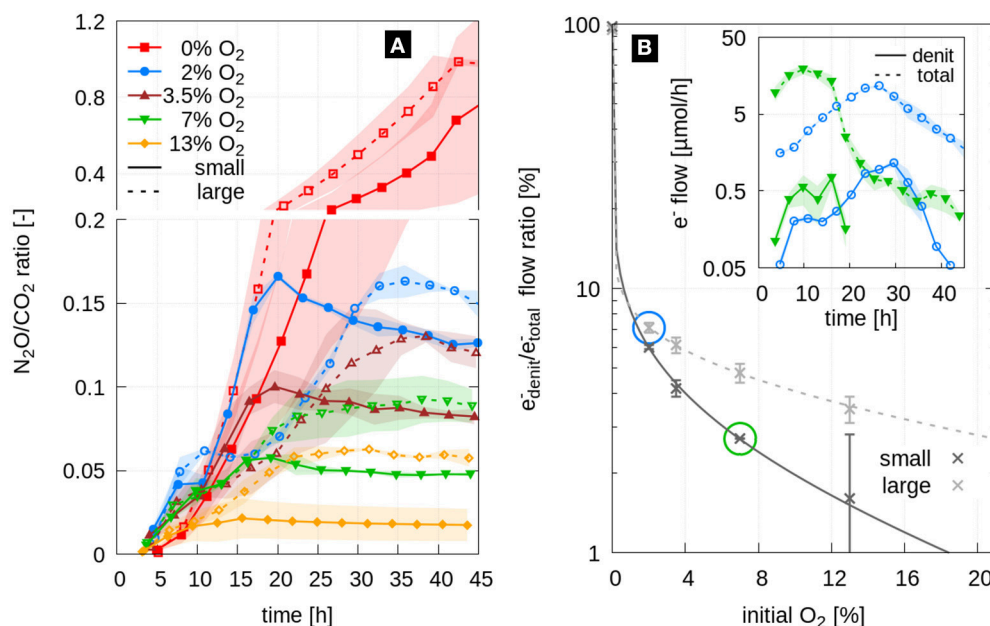
FIGURE 4 | (A) Time series of the N_2O/CO_2 ratio shown as average (lines) and standard deviation (shaded area) for two replicates of small aggregates (solid) and large aggregates (dashed) at five different initial O_2 concentrations. **(B)** Ratio of electron flow diverted in denitrification and total electron flow both measured and modeled with Equation 1. The inset shows the time series of electron flows for two selected treatments (large aggregates at 2%O_2, blue, and small aggregates at 7%O_2, green).

TABLE 1 | Fitting parameters (*a*,*b*) for the hyperbolic relationship between initial oxygen concentration and the ratio of electron flows (Equation 1) for large and small aggregates.

size	a	b	weighted error	RMSE
large	0.0955	2.4189	0.0016	0.0414
small	0.0240	1.0935	0.0016	0.0712

Fitting is done by minimizing the weighted errors between the measurements and model using the standard deviation between two technical replicates as weighting factor. The root mean square error (RMSE) is also reported.

soil matrix, as the varying water content in the soil matrix acts as a major control on the micro-environmental conditions in the hotspots. Changing the external O_2 concentration as a substitute for changing water contents is only an indirect analogue as it does not account for dilution of nitrate and carbon substrate as well as the osmotic effects induced by a rewetting event (Fierer and Schimel, 2003; Groffman et al., 2009). Moreover, undisturbed soil structure does typically not manifest itself as isolated, well-sorted aggregates but a coherent soil matrix pervaded with a complex pore network (Rabot et al., 2018). Hence, the aggregate size should rather be interpreted as the typical distance to the closest air-filled pore (Schlüter and Vogel, 2016) and the varying oxygen levels for instance as a depth gradient in the partial pressure of O_2 within a soil profile. Finally, experiments in closed systems affect the residence time of gaseous intermediates which increases the chances of soil to act as a sink for NO and N_2O (Chapius-Lardy et al., 2007).

Despite those limitations our simplified incubation experiment may serve as an interesting case for studying the dynamics of soil denitrification as an important source of N_2O. Thus, the experiments with artificial aggregates may provide a useful benchmark data set for physically-based diffusion-reaction models of microbial activity in model soil aggregates. The pioneering studies of Leffelaar and Wessel (1988) and Arah and Smith (1989), which assumed simplified one-dimensional, radial domains, are gradually superseded by spatially explicit, three-dimensional models of the pore space (Ebrahimi and Or, 2014, 2015; Falconer et al., 2015) that can be directly derived from X-ray CT scans like shown in **Figure 1A**. These models can inherently take into account the fragmentation of microbial niches under normal hydraulic conditions due to a discontinuous water phase as well as increased microbial dispersal after a rewetting event (Tecon and Or, 2017). They have the potential to explore microscopic biochemical processes, which are impossible to measure directly, in order to inform or improve macroscopic models of greenhouse gas emission, which operate with emergent properties on much larger scales like transient, anoxic soil volumes (Li et al., 2000; Ebrahimi and Or, 2016). The development of a new spatially-explicit, physically-based model of denitrification kinetics based on the modeling framework of Hron et al. (2015) is currently underway, but beyond the scope of the study.

5. CONCLUSIONS

This incubation experiment clearly demonstrates how denitrification in fully saturated aggregates is governed by

physical constraints that give rise to a transient formation of anoxic aggregate centers. The spatial gradients in dissolved oxygen which drive the diffusive flux are controlled by the aggregate size and the external oxygen concentration in very predictable ways. The better supply with oxygen in small aggregates leads to faster growth and an earlier onset of N_2O emission, whereas larger aggregates have a larger N_2O accumulation and larger N_2O/CO_2 production ratio on the long run. The main conclusions for physically-based modeling is that under dynamic growth conditions denitrification activity can only be predicted if both the aggregate size and the oxygen concentration at the aggregate surface are known.

The reduction of external oxygen concentration consistently leads to a reduction in aerobic respiration as well as to an increase in the denitrification activity and the N_2O/CO_2 production ratio. The cumulative diversion of electrons from reduced carbon to N-oxyanions is perfectly described by a simple, empirical model across a large oxygen concentration range, which confirms the dominant role of physical constraints on N_2O emissions from these simplified model aggregates inoculated with a single bacterial strain and a simple growth medium.

Incubation studies with these simplified soil aggregates can be extended toward more realistic soil conditions in several ways. We are currently working with experimental setups, in which aggregates are inoculated with different bacterial strains and embedded in explicit geometries in a sandy soil matrix adjusted to different water contents to account for interactions between hotspots and to explore the role of spatial distribution of hotspots on greenhouse gas emissions.

AUTHOR CONTRIBUTIONS

SS, H-JV, MH, OI, and PD conceived the experiment. LB provided the bacterial strain. SS, SH, LB, and PD conducted the experiments. SS, SH, JZ, and PD analyzed the data. All authors contributed to writing the manuscript.

FUNDING

ACKNOWLEDGMENTS

REFERENCES

Arah, J. R. M., and Smith, K. A. (1989). Steady-state denitrification in aggregated soils: a mathematical model. *J. Soil Sci.* 40, 139–149. doi: 10.1111/j.1365-2389.1989.tb01262.x

Baek, S.-H., and Shapleigh, J. P. (2005). Expression of nitrite and nitric oxide reductases in free-living and plant-associated *Agrobacterium tumefaciens* C58 cells. *Appl. Environ. Microbiol.* 71, 4427–4436. doi: 10.1128/AEM.71.8.4427-4436.2005

Bakken, L. R., Bergaust, L., Liu, B., and Frostegård, Å. (2012). Regulation of denitrification at the cellular level: a clue to the understanding of N_2O emissions from soils. *Philos. Trans. R. Soc. Lond. B Biol. Sci.* 367, 1226–1234. doi: 10.1098/rstb.2011.0321

Bergaust, L., Bakken, L. R., and Frostegård, Å. (2011). Denitrification regulatory phenotype, a new term for the characterization of denitrifying bacteria. *Biochem. Soc. Trans.* 39, 207–212. doi: 10.1042/BST0390207

Bergaust, L., Shapleigh, J., Frostegård, Å., and Bakken, L. (2008). Transcription and activities of NO_x reductases in *Agrobacterium tumefaciens*: the influence of nitrate, nitrite and oxygen availability. *Environ. Microbiol.* 10, 3070–3081. doi: 10.1111/j.1462-2920.2007.01557.x

Chapuis-Lardy, L., Wrage, N., Metay, A., Chotte, J.-L., and Bernoux, M. (2007). Soils, a sink for N_2O? A review. *Glob. Change Biol.* 13, 1–17. doi: 10.1111/j.1365-2486.2006.01280.x

Doane, T. A., and Horwáth, W. R. (2003). Spectrophotometric determination of nitrate with a single reagent. *Anal. Lett.* 36, 2713–2722. doi: 10.1081/AL-120024647

Dörsch, P., Braker, G., and Bakken, L. R. (2012). Community-specific pH response of denitrification: experiments with cells extracted from organic soils. *FEMS Microbiol. Ecol.* 79, 530–541. doi: 10.1111/j.1574-6941.2011.01233.x

Ebrahimi, A., and Or, D. (2015). Hydration and diffusion processes shape microbial community organization and function in model soil aggregates. *Water Resour. Res.* 51, 9804–9827. doi: 10.1002/2015WR017565

Ebrahimi, A., and Or, D. (2016). Microbial community dynamics in soil aggregates shape biogeochemical gas fluxes from soil profiles–upscaling an aggregate biophysical model. *Glob. Change Biol.* 22, 3141–3156. doi: 10.1111/gcb.13345

Ebrahimi, A. N., and Or, D. (2014). Microbial dispersal in unsaturated porous media: characteristics of motile bacterial cell motions in unsaturated angular pore networks. *Water Resour. Res.* 50, 7406–7429. doi: 10.1002/2014WR015897

Falconer, R. E., Guillaume, B., Sonja, S., Philippe, B., Claire, C., and Wilfred, O. (2015). Microscale heterogeneity explains experimental variability and non-linearity in soil organic matter mineralisation. *PLoS ONE* 10:e0123774. doi: 10.1371/journal.pone.0123774

Fierer, N., and Schimel, J. P. (2003). A proposed mechanism for the pulse in carbon dioxide production commonly observed following the rapid rewetting of a dry soil. *Soil Sci. Soc. Am. J.* 67, 798–805. doi: 10.2136/sssaj2003.7980

Firestone, M. (1982). "Biological denitrification," in *Nitrogen in Agricultural Soils*, ed F. J. Stevenson (Madison, WI: American Society of Agronomy), 289–326.

Groffman, P., Butterbach-Bahl, K., Fulweiler, R., Gold, A., Morse, J., Stander, E., et al. (2009). Challenges to incorporating spatially and temporally explicit phenomena (hotspots and hot moments) in denitrification models. *Biogeochemistry* 93, 49–77. doi: 10.1007/s10533-008-9277-5

Højberg, O., Revsbech, N. P., and Tiedje, J. M. (1994). Denitrification in soil aggregates analyzed with microsensors for nitrous oxide and oxygen. *Soil Sci. Soc. Am. J.* 58, 1691–1698. doi: 10.2136/sssaj1994.03615995005800060016x

Hron, P., Jost, D., Bastian, P., Gallert, C., Winter, J., and Ippisch, O. (2015). Application of reactive transport modeling to growth and transport of microorganisms in the capillary fringe. *Vadose Zone J.* 14:vzj2014.07.0092. doi: 10.2136/vzj2014.07.0092

Jones, C. M., and Hallin, S. (2010). Ecological and evolutionary factors underlying global and local assembly of denitrifier communities. *ISME J.* 4, 633. doi: 10.1038/ismej.2009.152

Keeney, D., and Nelson, D. W. (1982). "Nitrogen—inorganic forms," in *Methods of Soil Analysis. Part 2. Chemical and Microbiological Properties,* 2nd Edn., eds A. L. Page, R. H. Miller, and D.R. Keeney (Madison, WI: American society of Agronomy), 643–698.

Kolb, S., and Horn, M. A. (2012). Microbial CH_4 and N_2O consumption in acidic wetlands. *Front. Microbiol.* 3:78. doi: 10.3389/fmicb.2012.00078

Kuzyakov, Y., and Blagodatskaya, E. (2015). Microbial hotspots and hot moments in soil: concept & review. *Soil Biol. Biochem.* 83, 184–199. doi: 10.1016/j.soilbio.2015.01.025

Leffelaar, P., and Wessel, W. (1988). Denitrification in a homogeneous, closed system: experiment and simulation. *Soil Sci.* 146, 335–349.

Li, C., Aber, J., Stange, F., Butterbach-Bahl, K., and Papen, H. (2000). A process-oriented model of N_2O and NO emissions from forest soils: 1. Model development. *J. Geophys. Res. Atmos.* 105, 4369–4384. doi: 10.1029/1999JD900949

Linn, D., and Doran, J. (1984). Effect of water-filled pore space on carbon dioxide and nitrous oxide production in tilled and nontilled soils. *Soil Sci. Soc. Am. J.* 48, 1267–1272. doi: 10.2136/sssaj1984.03615995004800060013x

Liu, B., Mørkved, P. T., Frostegård, Å., and Bakken, L. R. (2010). Denitrification gene pools, transcription and kinetics of NO, N_2O and N_2 production as affected by soil pH. *FEMS Microbiol. Ecol.* 72, 407–417. doi: 10.1111/j.1574-6941.2010.00856.x

Mathieu, O., Lévêque, J., Hénault, C., Milloux, M.-J., Bizouard, F., and Andreux, F. (2006). Emissions and spatial variability of N_2O, N_2 and nitrous oxide mole fraction at the field scale, revealed with ^{15}N isotopic techniques. *Soil Biol. Biochem.* 38, 941–951. doi: 10.1016/j.soilbio.2005.08.010

Molstad, L., Dörsch, P., and Bakken, L. R. (2007). Robotized incubation system for monitoring gases (O_2, NO, N_2O, N_2) in denitrifying cultures. *J. Microbiol. Methods* 71, 202–211. doi: 10.1016/j.mimet.2007.08.011

Myrold, D. D., and Tiedje, J. M. (1985). Diffusional constraints on denitrification in soil. *Soil Sci. Soc. Am. J.* 49, 651–657. doi: 10.2136/sssaj1985.03615995004900030025x

Parkin, T. B. (1987). Soil microsites as a source of denitrification variability. *Soil Sci. Soc. Am. J.* 51, 1194–1199. doi: 10.2136/sssaj1987.03615995005100050019x

Philippot, L., Andert, J., Jones, C., Bru, D., and Hallin, S. (2011). Importance of denitrifiers lacking the genes encoding the nitrous oxide reductase for N_2O emissions from soil. *Glob. Change Biol.* 17, 1497–1504. doi: 10.1111/j.1365-2486.2010.02334.x

Philippot, L., Hallin, S., and Schloter, M. (2007). "Ecology of denitrifying prokaryotes in agricultural soil," in *Advances in Agronomy*, Vol. 96, *Advances in Agronomy*. (Academic Press), 249–305.

Philippot, L., Spor, A., Henault, C., Bru, D., Bizouard, F., Jones, C. M., et al. (2013). Loss in microbial diversity affects nitrogen cycling in soil. *ISME J* 7, 1609–1619. doi: 10.1038/ismej.2013.34

Rabot, E., Wiesmeier, M., Schlüter, S., and Vogel, H.-J. (2018). Soil structure as an indicator of soil functions: a review. *Geoderma* 314, 122–137. doi: 10.1016/j.geoderma.2017.11.009

Raynaud, X., and Nunan, N. (2014). Spatial ecology of bacteria at the microscale in soil. *PLoS ONE* 9:e87217. doi: 10.1371/journal.pone.0087217

Röver, M., Heinemeyer, O., Munch, J. C., and Kaiser, E.-A. (1999). Spatial heterogeneity within the plough layer: high variability of N_2O emission rates. *Soil Biol. Biochem.* 31, 167–173. doi: 10.1016/S0038-0717(97)00271-X

Ruser, R., Flessa, H., Russow, R., Schmidt, G., Buegger, F., and Munch, J. (2006). Emission of N_2O, N_2 and CO_2 from soil fertilized with nitrate: effect of compaction, soil moisture and rewetting. *Soil Biol. Biochem.* 38, 263–274. doi: 10.1016/j.soilbio.2005.05.005

Schimel, J. P., and Schaeffer, S. M. (2012). Microbial control over carbon cycling in soil. *Front. Microbiol.* 3:348. doi: 10.3389/fmicb.2012.00348

Schlüter, S., and Vogel, H.-J. (2016). Analysis of soil structure turnover with garnet particles and x-ray microtomography. *PLOS ONE* 11:e0159948. doi: 10.1371/journal.pone.0159948

Sexstone, A. J., Revsbech, N. P., Parkin, T. B., and Tiedje, J. M. (1985). Direct measurement of oxygen profiles and denitrification rates in soil aggregates. *Soil Sci. Soc. Am. J.* 49, 645–651. doi: 10.2136/sssaj1985.03615995004900030024x

Šimek, M., and Cooper, J. E. (2002). The influence of soil pH on denitrification: progress towards the understanding of this interaction over the last 50 years. *Eur. J. Soil Sci.* 53, 345–354. doi: 10.1046/j.1365-2389.2002.00461.x

Sistrom, W. R. (1960). A Requirement for sodium in the growth of rhodopseudomonas spheroides. *Microbiology* 22, 778–785.

Smith, K. A. (1990). *Anaerobic Zones and Denitrification in Soil: Modelling and Measurement.* Boston, MA: Springer, 229–244.

Stange, C., Spott, O., Arriaga, H., Menéndez, S., Estavillo, J., and Merino, P. (2013). Use of the inverse abundance approach to identify the sources of NO and N_2O release from Spanish forest soils under oxic and hypoxic conditions. *Soil Biol. Biochem.* 57, 451–458. doi: 10.1016/j.soilbio.2012.10.006

Tecon, R., and Or, D. (2017). Biophysical processes supporting the diversity of microbial life in soil. *FEMS Microbiol. Rev.* 41, 599–623. doi: 10.1093/femsre/fux039

Vos, M., Wolf, A. B., Jennings, S. J., and Kowalchuk, G. A. (2013). Micro-scale determinants of bacterial diversity in soil. *FEMS Microbiol. Rev.* 37, 936–954. doi: 10.1111/1574-6976.12023

Zausig, J., Stepniewski, W., and Horn, R. (1993). Oxygen concentration and redox potential gradients in unsaturated model soil aggregates. *Soil Sci. Soc. Am. J.* 57, 908–916. doi: 10.2136/sssaj1993.03615995005700040005x

Impact of Pore-Scale Wettability on Rhizosphere Rewetting

Pascal Benard [1,2*], Mohsen Zarebanadkouki [2] and Andrea Carminati [2]

[1] Division of Soil Hydrology, University of Göttingen, Göttingen, Germany, [2] Chair of Soil Physics, University of Bayreuth, Bayreuth, Germany

Vast amounts of water flow through a thin layer of soil around the roots, the rhizosphere, where high microbial activity takes place—an important hydrological and biological hotspot. The rhizosphere was shown to turn water repellent upon drying, which has been interpreted as the effect of mucilage secreted by roots. The effects of such rhizosphere water dynamics on plant and microbial activity are unclear. Furthermore, our understanding of the biophysical mechanisms controlling the rhizosphere water repellency remains largely speculative. Our hypothesis is that the key to describe the emergence of water repellency lies within the microscopic distribution of wettability on the pore-scale. At a critical mucilage content, a sufficient fraction of pores is blocked and the rhizosphere turns water repellent. Here we tested whether a percolation approach is capable to predict the flow behavior near the critical mucilage content. The wettability of glass beads and sand mixed with chia seed mucilage was quantified by measuring the infiltration rate of water drops. Drop infiltration was simulated using a simple pore-network model in which mucilage was distributed heterogeneously throughout the pore space with a preference for small pores. The model approach proved capable to capture the percolation nature of the process, the sudden transition from wettable to water repellent and the high variability in infiltration rates near the percolation threshold. Our study highlights the importance of pore-scale distribution of mucilage in the emergent flow behavior across the rhizosphere.

Keywords: rhizosphere, water percolation, mucilage, water repellency, rewetting, pore scale, connectivity

INTRODUCTION

The rhizosphere is defined as the layer of soil particles actively modified by plant root growth and exudation (Gregory, 2006; Hinsinger et al., 2009). Regardless of its narrow extent ranging from millimeters to a few centimeters, this region is crossed by an immense amount of water. About 40% of all terrestrial precipitation flows across the root-soil interface when taken up by plants (Bengough, 2012; Sposito, 2013). In this context, the importance of the hydraulic properties of the rhizosphere, hosting a tremendous biodiversity (Philippot et al., 2013) ought to be acknowledged.

Alterations in rhizosphere physical and hydraulic properties induced by plant roots have been reported by an increasing number of studies (Young, 1995; Hallett et al., 2003; Carminati et al., 2010; Zarebanadkouki et al., 2016; Naveed et al., 2017). Several of these rhizosphere alterations were attributed to the presence of root exuded mucilage, such as hysteretic fluctuations in water content during drying-wetting cycles in the rhizosphere of lupins (*Lupinus albus*) (Carminati et al., 2010). In this case, the authors related the observed increased water retention during drying and

decreased wettability during rewetting to root exuded mucilage. Low rhizosphere wettability was also observed in maize (*Zea Mays*) (Ahmed et al., 2016).

Mucilage is a polymeric substance released from the root tip. It is mainly composed of polysaccharides and about 1% of lipids (Oades, 1978; Read et al., 2003). It can be classified as a hydrogel (Brinker and Scherer, 1990) and its polymer network is capable to increase the water retention when embedded in a soil matrix (Kroener et al., 2018). Recently, Kroener et al. (2018) hypothesized that mucilage polymers need to be anchored to soil particles to withstand shrinkage and subsequent collapse during soil drying. It has been shown that mucilage and other highly polymeric substances, like bacterial EPS (extracellular polymeric substances) and their analogs, form distinct structures within the soil pore space during drying (Roberson et al., 1993; Albalasmeh and Ghezzehei, 2014; Benard et al., 2018). At low content, mucilage forms thin threads between particles. When a critical mucilage content is reached, these threads extend throughout the pore space forming large 2D lamellar structures (Benard et al., 2018). The authors proposed that this critical mucilage content determines the onset of water repellency in the rhizosphere. A physical explanation for the formation of these structures in drying soil was provided by Carminati et al. (2017) and was related to the high viscosity of mucilage.

Dry root mucilage deposits reduce soil wettability depending on plant species and concentration (Zickenrott et al., 2016; Naveed et al., 2017) and they can potentially turn hydrophobic (Ahmed et al., 2016). Kroener et al. (2015) and Benard et al. (2016, 2018) made a first attempt to estimate the amount of mucilage needed to induce water repellency in the rhizosphere for varying soil textures. Using a percolation model the authors were able to predict the mucilage content at which water could no longer penetrate into the soil. In the present paper, we aimed to further develop this model by including the temporal dynamics of water infiltration.

The water drop penetration time (WDPT) is typically used to characterize soil wettability. The method consists in placing water drops of known volume onto soil and capturing the time of their complete penetration into the pore space (van't Woudt, 1959; Dekker and Ritsema, 1996). We used this method to assess the water repellency of sand particles and glass beads mixed with chia seed mucilage, which is used as a preliminary model of the rhizosphere. Our hypothesis is that the water penetration time across the rhizosphere has a percolation nature which originates from the non-uniform distribution of mucilage (preferably deposited in small pores). This results in a heterogeneous distribution of wettability on the pore-scale, which in turns determines the on-set of water repellency. At a critical mucilage content (the percolation threshold), when a sufficient fraction of pores are non-wettable, the water penetration time increases and becomes highly variable. Above this threshold, the non-wettable pores block the water penetration, which becomes very slow, and macroscopic water repellency occurs. Surface roughness is expected to induce a more homogeneous distribution of mucilage and the percolation threshold is expected to occur at higher mucilage content. The effect of particle size on macroscopic wettability has been analyzed in a previous study (Benard et al., 2018), where it was shown that the finer are the soil particles, the higher is their specific surface and the critical mucilage content at which water repellency occurs.

Here, we focused on the temporal dynamics of water infiltration measured in sand and glass beads embedded with mucilage and simulated using a new percolation method. The model was designed as basic as possible to allow for an unbiased evaluation of its capabilities to capture the percolation nature of the process and assess the impact of pore-scale wettability on rhizosphere rewetting dynamics.

MATERIALS AND METHODS

Mucilage Extraction and Sample Preparation

A detailed description of mucilage extraction and sample preparation can be found in Benard et al. (2018). In summary, we mixed different amounts of mucilage with glass beads of 0.1–0.2 mm, and fine sand of 0.125–0.2 mm in diameter to achieve different dry mucilage contents (weight of dry mucilage per weight of particles). As an analog for root exuded mucilage, we used mucilage extracted from chia seeds (*Salvia hispanica* L.). Its physical properties are similar to mucilage exuded by maize roots in the sense that for increasing mucilage content the contact angle increases (Ahmed et al., 2016). The mixtures of mucilage and glass beads (and of mucilage and sand) were spread on glass slides and let dry at 20°C for 48 h. Upon drying the samples were not repacked to avoid artificial alterations of the microscopic mucilage distribution in the pore space. Dry mucilage content of the samples ranged from 0.9 to 6 mg g^{-1} in glass beads, and 2.8 to 9.3 mg g^{-1} in sand. These ranges of mucilage content were selected according to preliminary tests. At higher contents the samples were repellent (contact angle above 90°), while at lower contents the samples were wettable. We focused on the interesting ranges of mucilage content when the samples switched between the two states. Sample thickness was ∼1.5 ± 0.1 mm.

Wettability Quantification

In a classical WDPT (water drop penetration time) test, drops of known volume are placed on a soil and the time for complete penetration is captured. The water drop penetration times are divided in discrete classes to characterize the wettability of different soils (van't Woudt, 1959; Dekker and Ritsema, 1996). In this study we focused on the infiltration dynamics in soil affected by dry mucilage deposits of reduced wettability. To capture the effect of mucilage on infiltration dynamics we placed 1 µL drops of deionized water on the dry samples and the infiltration process was recorded at intervals of about 200 ms (CCD camera; Drop Shape Analyzer DSA30, Krüss GmbH). The drop volume was estimated from the optically detected drop geometry and a manually set baseline. For each mucilage content two slides were prepared and the infiltration of at least 10 drops per slide was captured. Note that the decrease in volume could not always be easily captured from recorded image sequences. Due to that

reason, the number of captured drop infiltrations per mucilage content ranged from 13 to 20 in glass beads and 19 to 31 in sand.

For high mucilage content, water did not completely infiltrate within the observation time of 5 min. Therefore, we calculated the WDPT from the slope of the infiltration rate over the square root of time. For consistency we followed this procedure for all measurements.

Measurements were conducted in a temperature controlled room at about 25°C. Humidity was not measured in the process of wettability quantification. Evaporation loss was approximated for a relative humidity of 65%.
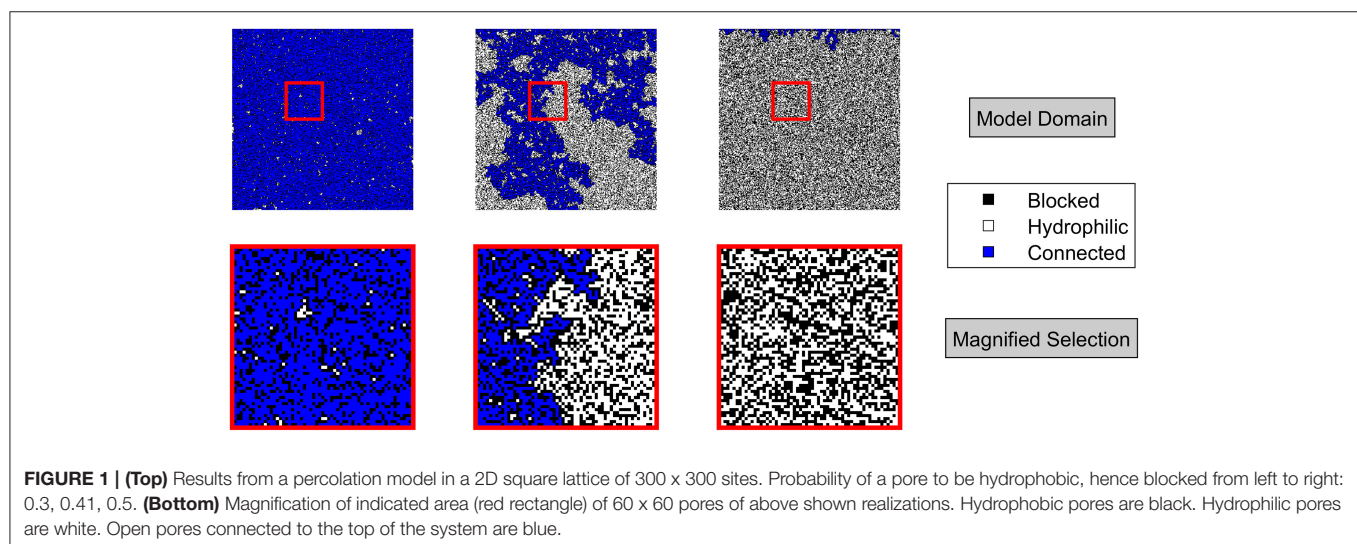
Model Description

We developed a simple pore-network model based on the concept of percolation theory. In a percolation system, pores are randomly assigned open or closed. When a critical fraction of pores is blocked, the connectivity of the open pores is strongly reduced and the system switches from conductive to non-conductive. Our idea is that such a concept can be used to predict and describe the transition of soils mixed with hydrophobic substances such as mucilage from wettable to water repellent. We assume that the distribution of pore sizes of our model system is random and during drying mucilage is preferentially deposited in the small pores. The contact angle in each pore depends on its specific surface and the amount of mucilage. If the contact angle is above 90° the pore is blocked.

The effect of the pore-scale distribution of wettability is illustrated in **Figure 1**, in which pores are distributed on a 2D square lattice. When the fraction of hydrophobic pores reaches a critical value (at the percolation threshold), small variations in their number and distribution can cause a substantial change in macroscopic wettability, as in the central image of **Figure 1**. For a low mucilage content in soil, most pores are wettable and so is the soil (left image). At the threshold mucilage content, there is a 50% chance for a connected cluster of wettable pores to span from the upper to the lower side of the system

(central image). Macroscopic wettability is most critically affected by the pore-scale distribution of wettability at this point and preferential flow is likely to be observed. Above this threshold, the rhizosphere turns water repellent (right image).

The percolation model described hereafter was used to simulate the water drop infiltration experiments. The numerical model was written in MATLAB 2017b (The MathWorks, Inc.). Capillarity was considered to be the main driving force for infiltration of 1 μL of water. Pores can be filled only through saturated adjacent pores. In consecutive steps, the shortest time to fill a pore is calculated. The time is derived by approximation of water flow through a cylindrical pore, with the flow rate depending on the contact angle, pathway distance and pore radius. Saturation of each pore currently being filled is updated according to this interval. Simultaneously, the decrease in drop volume is corrected for loss by evaporation according to the approximation by Hu and Larson (2002). Final water drop penetration time is derived by summation of all consecutive infiltration and/or evaporation time steps needed to deplete a drop volume of 1 μL.

The soil pores are placed on a cubic lattice with a coordination number of 6, hence each pore is connected to its six adjacent neighbors. Pore volume is estimated from a random normal distribution of grain diameters between 0.1 and 0.2 (glass beads), respectively 0.125–0.2 mm (sand), assuming a porosity of 0.36, which is the porosity of a random close packing (RCP) of equally sized spheres (Torquato et al., 2000). The surface area of a pore derived for a cubic packing is corrected to fit the increase in surface area by 1.22 for a unit volume of an RCP of spheres. The surface area was doubled for simulations in sand, to account for roughness which induced an increase in the number of sites for preferential mucilage deposition (Benard et al., 2018). The mucilage content of each pore is derived from a random normal distribution of mucilage contents. Mucilage contents from high to low are assigned to pore volumes from small to large. In this way we mimicked the preferential deposition of mucilage in small pores.

FIGURE 1 | (Top) Results from a percolation model in a 2D square lattice of 300 x 300 sites. Probability of a pore to be hydrophobic, hence blocked from left to right: 0.3, 0.41, 0.5. **(Bottom)** Magnification of indicated area (red rectangle) of 60 x 60 pores of above shown realizations. Hydrophobic pores are black. Hydrophilic pores are white. Open pores connected to the top of the system are blue.

Flow of water from a filled to an empty accessible (wettable) pore is calculated through a cylindrical capillary of length L, which is equal to the sum of the two grain radii of particles defining adjacent pores. The radius of the cylinder r is derived from the biggest circle that can be fit into the bottleneck of the smaller particle pack. The term bottleneck refers to the minimum radius of the six pathways toward the central pore in a cubic packing of spheres.

Flow from a filled into an empty pore through a cylindrical capillary is calculated employing the Hagen-Poiseuille Equation (1):

$$Q = \frac{\pi r^4 \Delta p}{\eta 8 L} \tag{1}$$

where the volumetric flow rate Q [mm^3 ms^{-1}] depends on the radius of the connecting capillary r [mm], viscosity of water η [mN ms mm^{-2}], flow length L [mm], and the pressure gradient Δp [mN mm^{-2}]. The capillary pressure in a cylindrical tube is approximated employing the Young-Laplace Equation (1):

$$P_c = \frac{2 \gamma \cos(\alpha)}{r} \tag{2}$$

with surface tension γ [mN mm^{-1}], contact angle α [deg.], and pore radius r [mm].

Integrating (2) into (1) and given $Q = V/t$ one obtains the time t [ms] it takes to fill a pore of defined volume V [mm^3] through a cylindrical pipe (3):

$$t = \frac{\eta\, 8}{\pi r^4} \frac{r}{2\, \gamma\, \cos(\alpha)} \frac{L_{tot}\, V}{1} \tag{3}$$
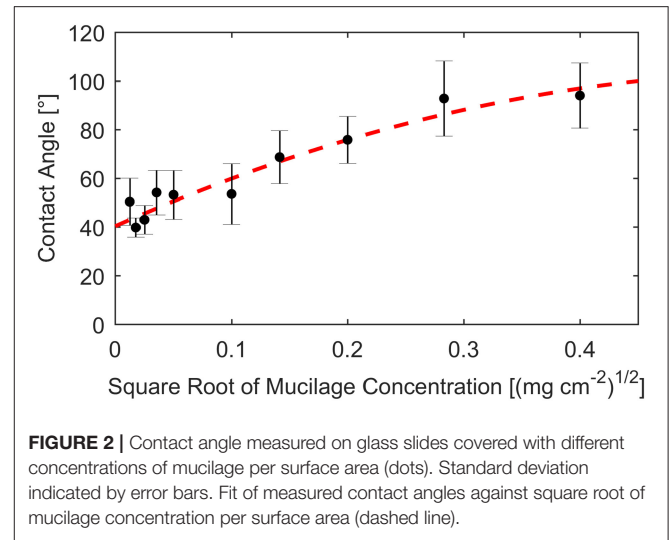
Note that L_{tot} is the length of the flow path from the placed drop of water through water filled pores to an empty accessible pore. The derived time to fill a pore and the current flux Q into a pore is updated for additional flow paths emerging in the process of water percolation through the system. In other words, when water finds an additional route to a partially unsaturated pore, this pore is filled quicker.

The contact angle α was calibrated using the measurements by Benard et al. (2016). In this study, the contact angle was measured for different concentrations of mucilage per surface area. Contact angles were derived after fitting the contact angle against the square root of dry mucilage concentration per surface area (**Figure 2**).

Since our measurements were based on optical measures of the decrease in drop volume, the decrease was corrected for loss by evaporation. In water repellent conditions when the contribution of infiltration diminishes, evaporation substantially contributes to the decrease in drop volume over time. The current evaporation rate $e(t)$ [μL s^{-1}] is approximated according to Hu and Larson (2002):

$$e(t) = -\pi R D\, (1 - H)\, c_v \left(0.27 \alpha(t)^2 + 1.30\right) \tag{4}$$

with contact-line radius R [mm], water vapor diffusivity D [mm^2 s^{-1}], relative humidity H [-], saturated water vapor

FIGURE 2 | Contact angle measured on glass slides covered with different concentrations of mucilage per surface area (dots). Standard deviation indicated by error bars. Fit of measured contact angles against square root of mucilage concentration per surface area (dashed line).

concentration c_v [g mm^{-3}], and drop contact angle α [rad.] which changes over time. R [mm] was derived from the mean size of the 9 randomly generated grains in x- and y-direction below the imposed drop center. In this way a mean base radius of 0.68 mm for 0.1 to 0.2 mm particles (glass beads) and 0.73 mm for 0.125–0.2 mm particles (sand) was achieved.

For known initial drop volume (i.e., 1 μL), the contact angle α is derived integrating the height of the drop h [mm] in its center (5) into (6). The initial contact angle of a water drop on a sample is approximated in this first step based on the initial volume [$V(t = 0)$, i.e., 1 μL] and base radius R. The drop volume is decreased by the sum of evaporated and infiltrated volume in each time step. As long as additional pores are being filled, α is adapted for a decrease in drop volume according to the shortest time step t needed to saturate an additional pore. Maximum time step for infiltration was fixed to 1000 ms to assure a constant update of evaporation and avoid overestimation of infiltration times, especially in the water repellent regime. When the infiltration of water was incomplete, due to a lack of accessible empty pores, the time step of constant evaporation was fixed to 1000 ms. In this way the contact angle was adapted over time and evaporation was approximated stepwise with decrease in drop volume.

$$h(t) = R \tan\left[\frac{\alpha(t)}{2}\right] \tag{5}$$

$$V(t) = \frac{\pi (h(t)) * (3R^2 + h(t)^2)}{6} \tag{6}$$

$$V(t) = \frac{\pi \left(R \tan\left(\frac{\alpha(t)}{2}\right)\right) * \left(3R^2 + \left(R \tan\left(\frac{\alpha(t)}{2}\right)\right)^2\right)}{6} \tag{7}$$

RESULTS

Wettability Quantification

Measurements of decrease in drop volume over time were performed for a range of dry mucilage contents across the

transition to water repellency. Individual infiltration slopes were obtained by fitting the decrease in drop volume as a function of square root of time. Results are presented as a summary of fitted slopes of infiltration curves at each mucilage content (**Figure 3**).

The infiltration dynamics in glass beads showed a threshold-like decrease in wettability with increase in dry mucilage content. For 0.9 mg g^{-1} all drops penetrated within 300 ms corresponding to a slope of $\geq$0.058 μL ms$^{-1/2}$. At 2.2 mg g^{-1} a high variation was observed, with the infiltration slopes ranging from 0.015 to 0.004 μL ms$^{-1/2}$. Standard deviation decreased with increase in mucilage content. Mean infiltration slopes decreased to 0.0023, 0.0018, and 0.0018 μL ms$^{-1/2}$ for 3.5, 4.7, and 6 mg g^{-1} respectively (**Figure 3A**).

For the lowest content of 2.8 mg g^{-1} in sand, all drops infiltrated within the detection limit of 300 ms (slope of $\geq$0.058 μL ms$^{-1/2}$). At 4.7 mg g^{-1} a high variability in infiltration slopes was observed. Slopes ranged from 0.003 to 0.038 μL ms$^{-1/2}$ with a mean of 0.003 μL ms$^{-1/2}$. With an increase to 6.5 mg g^{-1} variation in infiltration slope decreased to values between 0.011 and 0.002 μL ms$^{-1/2}$. The highest mucilage content of 9.3 mg g^{-1} resulted in a mean infiltration slope of 0.002 μL ms$^{-1/2}$ (**Figure 3B**).

Water Drop Penetration Time (WDPT)

The derived water drop penetration time (WDPT) from measurements and simulations are shown alongside exemplary top views of average final water saturation from simulations (**Figures 4**, **5**).

The square root of the Pearson product moment correlation coefficient (r^2) of the mean WDPT of measurements and simulations including the lowest mucilage content measured with an approximated WDPT of 150 ms was 0.16. For glass beads it was 0.18 and for sand it was 0.55.

Fitted measurements and simulations of infiltration in glass beads showed increasing WDPT with increasing mucilage

content (**Figure 4**). The threshold mucilage content was identified between 2.5 and 2.8 mg g^{-1} from the simulations, marked by a maximum in variability in penetration time and followed by a drastic change in wettability. Likewise, a maximum in diversity of connected, water filled pore clusters (wetted front) was observed across the threshold. Mean WDPT from simulations above the repellent transition ($>$3 mg g^{-1}) was about 19.7 min.

Fitted WDPT and simulations in sand showed a similar trend as in glass beads with a high variability and rapid change in wettability at 4.9 mg g^{-1} (**Figure 5**). Derived mean WDPT from simulations above the repellent transition ($>$5.5 mg g^{-1}) was about 19.1 min.

DISCUSSION

The main hypothesis was that the occurrence of macroscopic water repellency and the critical nature of water infiltration in soils mixed with mucilage was related to the heterogeneous distribution of wettability on the pore-scale. We tested this hypothesis by monitoring the infiltration of water drops placed on particles of comparable size and different surface roughness mixed with varying mucilage content. Subsequently, a simple pore-network model was used to simulate the drop infiltration experiments.

The water drop penetration time in glass beads and sand mixed with mucilage showed the expected threshold-like behavior, with a sudden increase in penetration time. Infiltration times increased from milliseconds to minutes for mucilage contents ranging from 1 to 6 mg g^{-1} in glass beads, respectively 3 to 9 mg g^{-1} in sand. The derived threshold for sand is in agreement with the results of Kroener et al. (2015), who observed it between 5 and 10 mg g^{-1}.

The highest variability in infiltration time was observed at the percolation threshold, confirming the percolation nature of the process. The threshold in penetration time was well predicted by
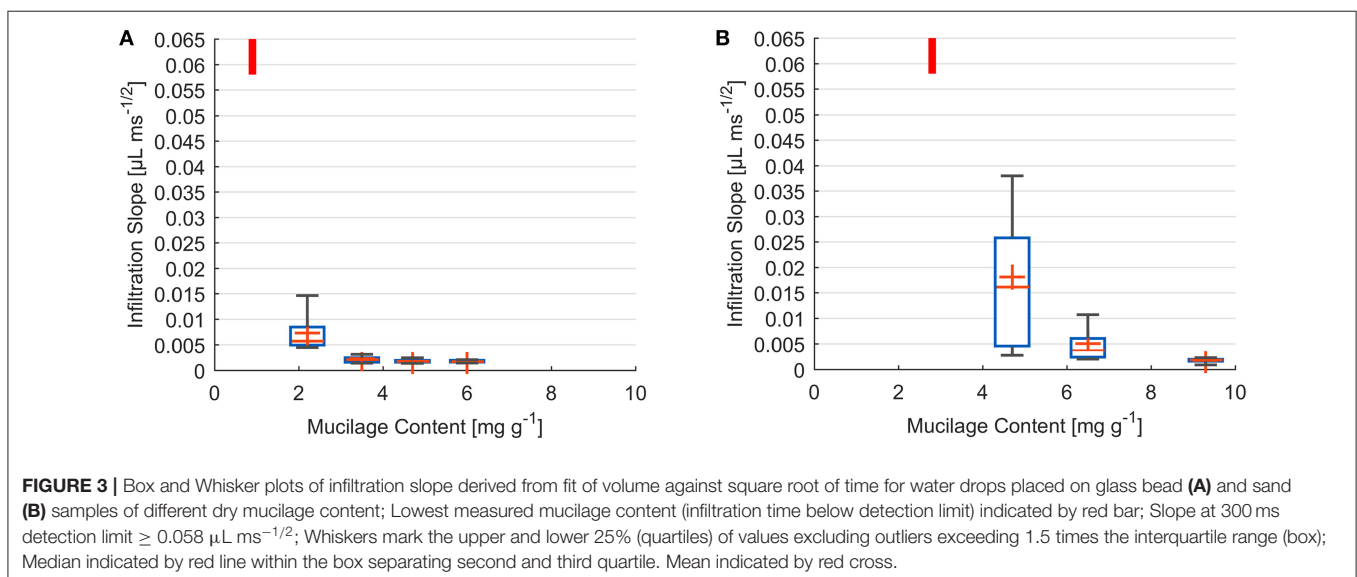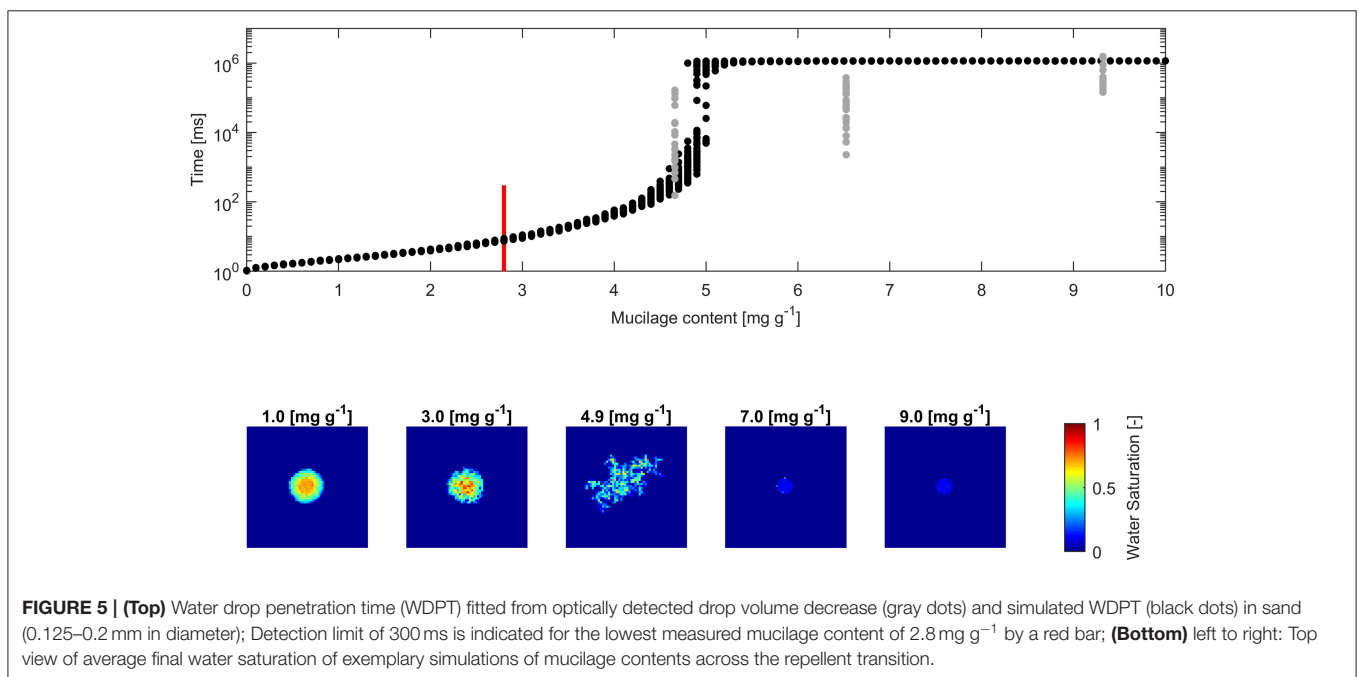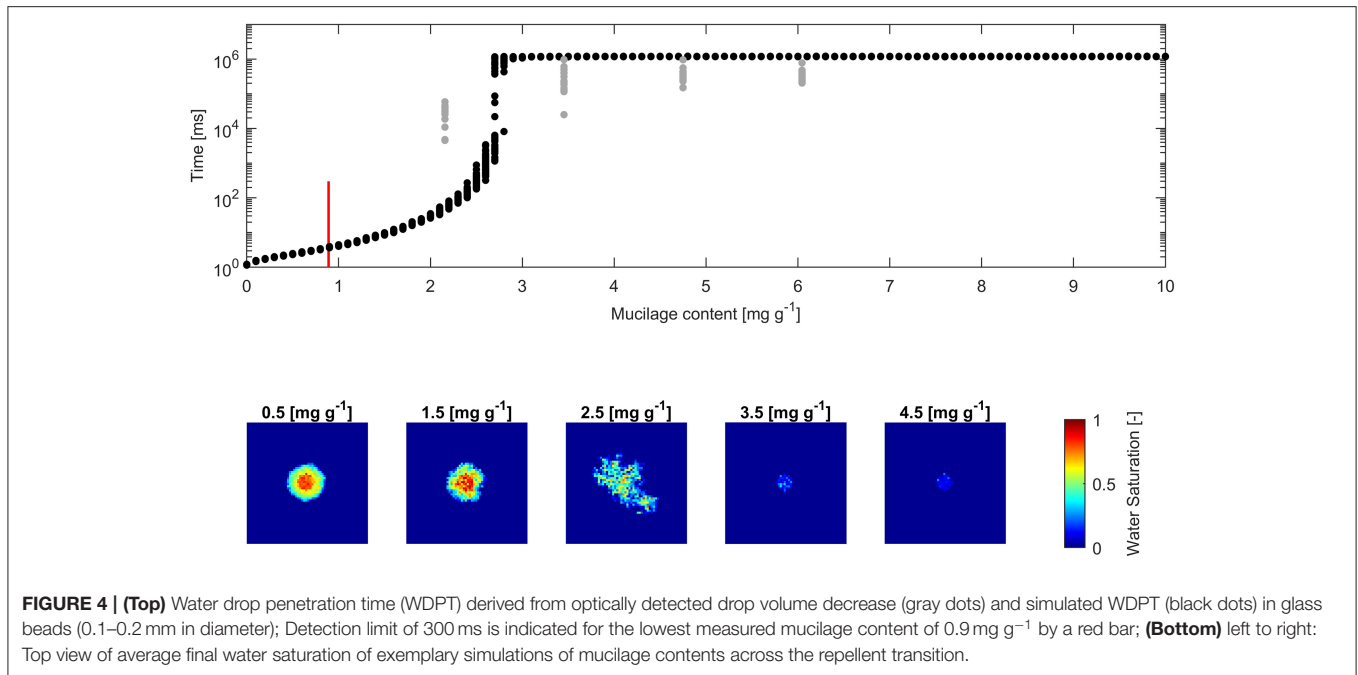

FIGURE 3 | Box and Whisker plots of infiltration slope derived from fit of volume against square root of time for water drops placed on glass bead **(A)** and sand **(B)** samples of different dry mucilage content; Lowest measured mucilage content (infiltration time below detection limit) indicated by red bar; Slope at 300 ms detection limit $\geq$ 0.058 μL ms$^{-1/2}$; Whiskers mark the upper and lower 25% (quartiles) of values excluding outliers exceeding 1.5 times the interquartile range (box); Median indicated by red line within the box separating second and third quartile. Mean indicated by red cross.

FIGURE 4 | (Top) Water drop penetration time (WDPT) derived from optically detected drop volume decrease (gray dots) and simulated WDPT (black dots) in glass beads (0.1–0.2 mm in diameter); Detection limit of 300 ms is indicated for the lowest measured mucilage content of 0.9 mg g^{-1} by a red bar; **(Bottom)** left to right: Top view of average final water saturation of exemplary simulations of mucilage contents across the repellent transition.

FIGURE 5 | (Top) Water drop penetration time (WDPT) fitted from optically detected drop volume decrease (gray dots) and simulated WDPT (black dots) in sand (0.125–0.2 mm in diameter); Detection limit of 300 ms is indicated for the lowest measured mucilage content of 2.8 mg g^{-1} by a red bar; **(Bottom)** left to right: Top view of average final water saturation of exemplary simulations of mucilage contents across the repellent transition.

the model in which mucilage was preferentially deposited in small pores inducing a heterogeneous spatial distribution of wettability. Measurements and simulations confirm the substantial impact of the heterogeneous pore-scale wettability on water flow through the rhizosphere. When the continuity of wettable pores was blocked, the onset of macroscopic soil water repellency was observed. Increased surface roughness in sand caused the expected shift to higher mucilage content needed to induce macroscopic water repellency.

The simulations showed a sharper transition in wettability than the measurements. This might be related to the assumption that mucilage is mainly deposited in small pores. This caused large pores to remain almost unaffected and highly conductive. An underestimation of infiltration time is therefore likely to occur below the repellent transition. Additionally, the difference might arise from the time dependent properties of mucilage not considered in the model. Wettability of substrates mixed with mucilage is expected to increase over time as a consequence of

mucilage rehydration and decrease in contact angle, as reported in Moradi et al. (2012) and Zickenrott et al. (2016). Below the percolation threshold, water penetration is matter of milliseconds to seconds. Due to this reason, a decrease in contact angle upon rewetting does not impact water penetration. Nevertheless, pore clogging due to mucilage rehydration and swelling might slow down the infiltration process at and above the wettability threshold. Above the repellent transition, mean infiltration time deviated by several minutes from measurements in glass beads and sand. Water adsorption by previously dry, hydrophobic mucilage deposits could be an explanation for the overestimated water penetration time.

The variability in infiltration times across the wettability threshold was bigger and the transition smoother in sand than in glass beads. This difference between sand and glass beads is possibly related to the increased surface roughness of sand particles. Rough surface leads to an increase in number of sites for preferential mucilage deposition (Benard et al., 2018), inducing a more uniform distribution of wettability and resulting in a smoother transition across the threshold. It also explains the higher mucilage content needed to achieve a similar magnitude of water repellency as observed in glass beads in terms of infiltration time.

This study shows that macroscopic water repellency in substrates mixed with mucilage emerges from the distribution of mucilage on the pore-scale and it has a percolation nature. Toward and above the percolation threshold, the fraction of non-wettable pores increases and eventually blocks the pathway for water infiltration and the porous medium turns water repellent. The fact that water repellency was observed repeatedly in the rhizosphere (Carminati et al., 2010; Moradi et al., 2012; Ahmed et al., 2016) indicates that mucilage content around the roots is close to or above the percolation threshold. If we assume that the size of connected pore clusters affected by high mucilage content (high enough to induce water repellency) increases across the percolation threshold[1], then the combination of water retention and preferential distribution has the potential to keep

---

[1]This assumption implies that the coordination number of pores critically affected by mucilage is bigger than the one of hydraulically connected (hydrophilic) pores.

pores hydraulically connected at low matric potential, when otherwise this crucial link would be lost. Additionally, close to the percolation threshold, roots could effectively control the wettability, and therefore also the diffusion of oxygen, by slightly changing the exudation rate or the chemical composition of exudates.

In summary this study reveals that the wettability of soils embedded with mucilage emerges from pore-scale mechanisms and has a percolation nature—the connectivity of hydrophobic pores determines the switch from wettable to non-wettable soil. The mixture of sand (or glass beads) with chia mucilage has been used as analog of the rhizosphere. Doing so, we implicitly assumed that (1) mucilage is the primary factor controlling the rhizosphere wettability, (2) mucilage from chia seeds is a good analog of root mucilage, and (3) the processes can be easily scaled for finer soil textures. All these assumptions are (over)simplifications of rhizosphere dynamics. First of all, mucilage from different plant species showed different degrees of water repellency (Zickenrott et al., 2016; Naveed et al., 2018). Secondly, in the rhizosphere root exudates are degraded by microorganisms, which can secret other highly polymeric blends altering the properties of the soil solution. Such complexities need to be studied and applied to varying soil textures, including structured soils. The importance of the current study is that it points to the pore-scale distribution of hydrophilic/hydrophobic region as the key factor determining the rhizosphere properties and it proposes the percolation theory as the key concept to link pore-scale to transport properties across the rhizosphere.

AUTHOR CONTRIBUTIONS

PB, MZ, and AC conceived the experimental set-up. PB conducted the experiments and processed the data. PB and AC developed the conceptual model. PB developed the numerical code and wrote the manuscript in consultation with MZ and AC.

FUNDING

REFERENCES

Ahmed, M. A., Kroener, E., Benard, P., Zarebanadkouki, M., Kaestner, A., and, Carminati, A. (2016). Drying of mucilage causes water repellency in the rhizosphere of maize: measurements and modelling. *Plant Soil* 407, 161–171. doi: 10.1007/s11104-015-2749-1

Albalasmeh, A. A., and Ghezzehei, T. A. (2014). Interplay between soil drying and root exudation in rhizosheath development. *Plant Soil* 374, 739–751. doi: 10.1007/s11104-013-1910-y

Benard, P., Kroener, E., Vontobel, P., Kaestner, A., and Carminati, A. (2016). Water percolation through the root-soil interface. *Adv. Water Resour.* 95, 190–198. doi: 10.1016/j.advwatres.2015.09.014

Benard, P., Zarebanadkouki, M., Hedwig, C., Holz, M., Ahmed, M. A., and Carminati, A. (2018). Pore-scale distribution of mucilage affecting water repellency in the rhizosphere. *Vadose Zone J.* 17:17001. doi: 10.2136/vzj2017.01.0013

Bengough, A. G. (2012). Water dynamics of the root zone: rhizosphere biophysics and its control on soil hydrology. *Vadose Zone J.* 11. doi: 10.2136/vzj2011.0111

Brinker, C. J. and Scherer, G. W. (1990). *Sol-gel Science: The Physics and Chemistry of Sol-gel Processing*. Boston, MA: Academic Press.

Carminati, A., Moradi, A. B., Vetterlein, D., Vontobel, P., Lehmann, E., Oswald, U., et al. (2010). Dynamics of soil water content in the rhizosphere. *Plant Soil* 332, 163–176. doi: 10.1007/s11104-010-0283-8

Carminati, A., Benard, P., Ahmed, M. A., and Zarebanadkouki, M. (2017). Liquid bridges at the root-soil interface. *Plant Soil* 417, 1–15. doi: 10.1007/s11104-017-3227-8

Dekker, L. W., and Ritsema, C. J. (1996). Variation in water content and wetting patterns in Dutch water repellent peaty clay and clayey peat soils. *Catena* 28, 89–105. doi: 10.1016/S0341-8162(96)00047-1

Gregory, P. J. (2006). Roots, rhizosphere and soil: the route to a better understanding of soil science? *Eur. J. Soil Sci.* 57, 2–12. doi: 10.1111/j.1365-2389.2005.00778.x

Hallett, P. D., Gordon, D. C., and Bengough, A. G. (2003). Plant influence on rhizosphere hydraulic properties: direct measurements using a miniaturized infiltrometer. *New Phytol.* 157, 597–603. doi: 10.1046/j.1469-8137.2003.00690.x

Hinsinger, P., Bengough, A. G., Vetterlein, D., and Young, I. M. (2009). Rhizosphere: biophysics, biogeochemistry and ecological relevance. *Plant Soil* 321, 117–152. doi: 10.1007/s11104-008-9885-9

Hu, H., and Larson, R. G. (2002). Evaporation of a sessile droplet on a substrate. *J. Phys. Chem. B* 106, 1334–1344. doi: 10.1021/jp0118322

Kroener, E., Ahmed, M. A., and Carminati, A. (2015). Roots at the percolation threshold. *Phys. Rev. E* 91:042706. doi: 10.1103/PhysRevE.91.042706

Kroener, E., Holz, M., Zarebanadkouki, M., Ahmed, M., and Carminati, A. (2018). Effects of mucilage on rhizosphere hydraulic functions depend on soil particle size. *Vadose Zone J.* 17:170056. doi: 10.2136/vzj2017.03.0056

Moradi, A. B., Carminati, A., Lamparter, A., Woche, S. K., Bachmann, J., Oswald, D., et al. (2012). Is the rhizosphere temporarily water repellent? *Vadose Zone J.* 11. doi: 10.2136/vzj2011.0120

Naveed, M., Brown, L. K., Raffan, A. C., George, T. S., Bengough, A. G., Hallett, T., et al. (2017). Plant exudates may stabilize or weaken soil depending on species, origin and time: effect of plant exudates on rhizosphere formation. *Eur. J. Soil Sci.* 68, 806–816. doi: 10.1111/ejss.12487

Naveed, M., Brown, L. K., Raffan, A. C., George, T. S., Bengough, A. G., Hallett, T., et al. (2018). Rhizosphere-scale quantification of hydraulic and mechanical properties of soil impacted by root and seed exudates. *Vadose Zone J.* 17:170083. doi: 10.2136/vzj2017.04.0083

Oades, J. M. (1978). Mucilages at the root surface. *Eur. J. Soil Sci.* 29, 1–16. doi: 10.1111/j.1365-2389.1978.tb02025.x

Philippot, L., Raaijmakers, J. M., Lemanceau, P., and van der Putten, W. H. (2013). Going back to the roots: the microbial ecology of the rhizosphere. *Nat. Rev. Microbiol.* 11, 789–799. doi: 10.1038/nrmicro3109

Read, D. B., Bengough, A. G., Gregory, P. J., Crawford, J. W., Robinson, D., Zhang, C. M., et al. (2003). Plant roots release phospholipid surfactants that modify the physical and chemical properties of soil. *New Phytol.* 157, 315–326. doi: 10.1046/j.1469-8137.2003.00665.x

Roberson, E. B., Chenu, C., and Firestone, M. K. (1993). Microstructural changes in bacterial exopolysaccharides during desiccation. *Soil Biol. Biochem.* 25, 1299–1301. doi: 10.1016/0038-0717(93)90230-9

Sposito, G. (2013). Green water and global food security. *Vadose Zone J.* 12. doi: 10.2136/vzj2013.02.0041

Torquato, S., Truskett, T. M., and Debenedetti, P. G. (2000). Is random close packing of spheres well defined? *Phys. Rev. Lett.* 84:2064. doi: 10.1103/PhysRevLett.84.2064

van't Woudt, B. D. (1959). Particle coatings affecting the wettability of soils. *J. Geophys. Res.* 64, 263–267. doi: 10.1029/JZ064i002p00263

Young, I. M. (1995). Variation in moisture contents between bulk soil and the rhizosheath of wheat (*Triticum aestivum* L. cv. Wembley). *New Phytol.* 130, 135–139. doi: 10.1111/j.1469-8137.1995.tb01823.x

Zarebanadkouki, M., Ahmed, M. A., and Carminati, A. (2016). Hydraulic conductivity of the root-soil interface of lupin in sandy soil after drying and rewetting. *Plant Soil* 398, 267–280. doi: 10.1007/s11104-015-2668-1

Zickenrott, I.-M., Woche, S. K., Bachmann, J., Ahmed, M. A., and Vetterlein, D. (2016). An efficient method for the collection of root mucilage from different plant species-A case study on the effect of mucilage on soil water repellency. *J. Plant Nutr. Soil Sci.* 179, 294–302. doi: 10.1002/jpln.201500511

Advantages of publishing in Frontiers

OPEN ACCESS
Articles are free to read
for greatest visibility
and readership

FAST PUBLICATION
Around 90 days
from submission
to decision

HIGH QUALITY PEER-REVIEW
Rigorous, collaborative,
and constructive
peer-review

TRANSPARENT PEER-REVIEW
Editors and reviewers
acknowledged by name
on published articles

REPRODUCIBILITY OF RESEARCH
Support open data
and methods to enhance
research reproducibility

DIGITAL PUBLISHING
Articles designed
for optimal readership
across devices

FOLLOW US
@frontiersin

IMPACT METRICS
Advanced article metrics
track visibility across
digital media

EXTENSIVE PROMOTION
Marketing
and promotion
of impactful research

LOOP RESEARCH NETWORK
Our network
increases your
article's readership